Ling Qin
Harry K. Genant
James Griffith
Kwok-Sui Leung

Editors
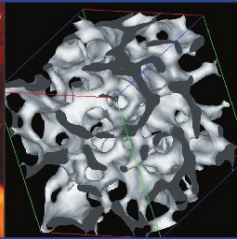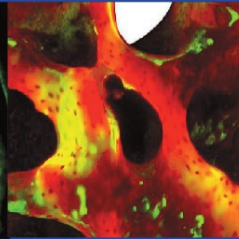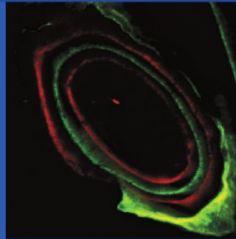
Advanced Bioimaging Technologies in Assessment of the Quality of Bone and Scaffold Materials

Techniques and Applications

Springer

Advanced Bioimaging Technologies in Assessment of the Quality of Bone and Scaffold Materials

Techniques and Applications

L. Qin · H.K. Genant
J.F. Griffith · K.S. Leung
(Editors)

Advanced Bioimaging Technologies in Assessment of the Quality of Bone and Scaffold Materials

Techniques and Applications

With 333 Figures and 44 Tables

Springer

Ling Qin
Professor of Department of Orthopaedics and Traumatology,
The Chinese University of Hong Kong, Hong Kong SAR, China
e-mail: lingqin@cuhk.edu.hk

Harry K. Genant
Professor Emeritus, University of California, San Francisco,
Chairman Emeritus; Board of Directors, Synarc, Inc
e-mail: harry.genant@radiology.ucsf.ucsf

James F. Griffith
Department of Radiology and Organ Imaging,
The Chinese University of Hong Kong, Hong Kong SAR, China
e-mail: Griffith@ruby.med.cuhk.edu.hk

Kwok Sui Leung
Professor of Department of Orthopaedics & Traumatology,
The Chinese University of Hong Kong, Hong Kong SAR, China
e-mail: ksleung@cuhk.edu.hk

Foreword (I)

As the Emeritus Professor and Executive Director of the Osteoporosis and Arthritis Research Group of the University of California San Francisco, and as Chairman of the WHO Task Force on Osteoporosis, I am pleased to write this preface to *Advanced Bio-imaging Technologies in Assessment of Quality of Bone and Scaffold Biomaterials* edited by Ling Qin, Harry K. Genant, James F. Griffith, and Kwok-Sui Leung. This book results largely from the contributions provided by the scientists and physicians who participated in the 2005 International Symposium on Advanced Biotechnologies for Assessing Quality of Bone and Scaffold Biomaterials, which was organized by Ling Qin, Ph.D, in Hong Kong, 17–19 October, 2005. This unique congress convened the world's leading researchers and clinicians in the fields of osteoporosis, imaging sciences, and biomechanics.

With the collective knowledge of the participating faculty, it seemed timely and appropriate to assemble this volume, which addresses the advances in imaging and bio-engineering technologies and their applications, and enables researchers and clinicians to examine and understand the pathophysiology of osteoporosis, its natural evolution, and its response to both conventional and novel treatments. These noninvasive and/or nondestructive imaging techniques, and the various destructive biomechanical methods, can provide important structural information about bone beyond standard bone mineral densitometry (BMD). Although BMD provides important information about osteoporosis diagnosis and fracture risk assessment, considerable evidence indicates that BMD only partially explains bone strength and fracture resistance. The information obtained from quantitative assessment of macro- and microstructural characteristics undoubtedly improves our understanding of bone diseases, and enhances our ability to estimate bone strength and predict fractures. The rationale for imaging and biomechanically testing bone macro- and micro-structure, therefore, is to obtain information beyond BMD, improve fracture risk prediction, clarify the pathophysiology of skeletal disease, define the skeletal response to therapy, and assess important biomechanical relationships.

Specifically, this book introduces cutting-edge bio-imaging technologies for studying the musculoskeletal system at the molecular level to the organ level, and for examining related biomaterials, including nano- and micro-computed tomography (CT), peripheral and axial quantitative CT (pQCT and aQCT), magnetic resonance imaging (MRI), quantitative ultrasound (QUS), transmission and scanning electron microscopy (TEM and SEM), confocal microscopy, polarized and florescence microscopy, near-field scanning optical microscopy, scanning acoustic microscopy, cell traction force microscopy, nano-micro-indentation, high-fidelity 3D microscopy, microradiography, fiber-optic nano-biosensors, and other advanced and unique contact and non-contact bio-imaging modalities.

Finally, this book examines the use of the above advanced bio-engineering and imaging techniques in studying: the quality of intact, osteoporotic, osteonecrotic,

osteo-arthritic, and healing bone and cartilage, and examines the role of these technologies in assessing the vascularity of relevant hard and soft tissues along with various scaffolding materials developed for musculoskeletal applications.

Harry K. Genant, M.D, FACR, FRCR (Honorary)
Emeritus Professor and Director, Osteoporosis and Arthritis Research Group, UCSF
Chairman, WHO Task Force on Osteoporosis
Emeritus Chairman and Member, Board of Directors, Synarc, Inc.

Foreword (II)

Bone is a hard tissue and yet bone is constantly undergoing the most active dynamic processes of metabolism, which are the basic forces behind the rapidly changing internal structure. Bone has a complex internal structure. On the gross anatomical level, it is comprised of a closely writhing, intermingled collection of hard columns, trabeculations, tubes, fat and vascular components. On the histomorphometry level, it contains fine blood vessels, canals, minute pathways, different cells with widely divergent responsibilities. On the molecular level, it is even more complex: the different stages of growth and metabolism produce chemicals, metabolites, biochemical markers and binders, all of which take part in the colourful changes of bone.

The knowledge of bone as a complex structure was gathered over at least half a century: from gross anatomical histomorphometric studies to biochemical investigations. In this long march to the understanding of the mysterious bone there occurred many breakthroughs, on which today's knowledge is based. Radiological imaging was probably the first technique that allowed the external appearance and a summation of the internal structure to be revealed. With radiological images surgeons could handle fractures logically and scientifically. Many decades of radio-imaging refinement and the application of computer interpretation advanced the simple technology to a detailed gross revelation. What followed were the special screening techniques with various radioisotopes and finally magnetic resonance technology, which illustrated on the images both soft tissues and bone activities. It is no surprise that the scientists who were responsible for the different stages of imaging earned the utmost honour of the Nobel Prize.

Bone imaging is still advancing. With the need to manage bone degradation as one ages, many generations of equipment to detect bone density have matured and are still undergoing refinement, since it is important to understand the gross values as well as the fine structures. The fine structures are gaining more and more significance since bone metabolism is continuously being affected by mechanical forces. The biomechanical influences directly and indirectly guide the degeneration and regeneration processes. Today the fine structures are revealed with imaging technology.

With this brief background, readers can appreciate this new volume, which covers current bioimaging techniques, focusing on the quality and fine structures of bone. We all look forward to more contributions from this group of image experts, engineers, bioengineers and surgeons.

Prof. Ping-Chung Leung
President
International Society of Orthopedic
Research and Traumatology

Foreword (III)

It was an honor for the International Chinese Hard Tissue Society to be a co-sponsor at the 2005 International Symposium on Advanced Bio-imaging Technologies in Assessment of Quality of Bone and Scaffold Biomaterials, held at the Chinese University of Hong Kong, Hong Kong, 17–19 October 2005. The conference brought together scientists worldwide to discuss cutting-edge technologies and the organizers were resourceful enough to convince speakers to contribute chapters to make this unique material available to the scientific community. The realization that one technology cannot unravel the complexities that contribute to bone, cartilage, and fracture healing has led numerous investigators to employ various technologies; thus, the chapters in this book contain uses of micro-CT, nano-CT, digital radiography, radioactive contrast medium, pQCT, backscattering electron microscopy, histochemistry, immunochemistry, mineralization, collagen fiber orientation, polarized light microscopy, histology, finite element analysis, etc., mostly in combination, to evaluate anti-osteoporotic drugs, bone and cartilage quality, fracture healing, and scaffolding biomaterials. Many of these technologies are non-invasive, with high precision or reproducibility, repeatability, and rapidity. They also reduce labor and do not require necropsy. Micro-CT was coupled with X-ray contrast agent to allow for the analyses of vasculature and articular cartilage. Nano-CT made it possible to quantify osteocytes, microcracks, and resorption lacunae. The development of the cutting-edge technologies and paragons was not for the sake of development or basic science alone, but were employed in translational research in the treatment of fracture healing, osteoporosis, osteoporotic fracture repair, regional bone adaptation, ovariectomy rat models, osteonecrosis, osteoarthritis, scoliosis, and evaluation of efficacy of various scaffold biomaterials. A few exciting examples include the in vivo micro-CT studies used to monitor change in trabecular structure in rats sequentially treated with bisphosphonate and parathyroid hormone, imaging the subtle erosive lesion in subchondral bone caused by inflammation processes in TNF-alpha transgenic mice and monitoring the progressive osteolytic response following administration and treatment of tumor cells in the tibial metaphyses of nude mice. In addition, series with in vivo micro-CT studies of human early osteo-arthritis (OA) and guinea pig OA showed subchondral cancellous bone to be thicker and markedly plate-like, but weaker in mechanical properties, supporting the concept that the bone changes come before cartilage deterioration.

Each chapter contains new developments and findings; therefore, I strongly suggest this revolutionary book to all personnel and investigators working in the fields of musculoskeletal research and development.

Webster S.S. Jee, Ph.D
Professor of Neurobiology and Anatomy
Chairman of the Board
International Chinese Hard Tissue Society

Foreword (IV)

It is without exception that osteoporosis and other disorders and injury of bone and cartilage, as well as its repairing and regeneration, are omnipresent to relate with the relevant changes in its metabolism, microstructure, vasculature, quantity, and mechanical properties.

The evaluation of the quality and quantity of bone, cartilage, vasculature, and scaffold materials provide the basic elements for the diagnosis, prevention, and treatment of such diseases, which serves as the main evidence to evaluate the curative effect and prognosis. By understanding the biological and biomechanical status of the musculoskeletal tissues, the diagnosis and scientific evaluations can be made after analysis of imaging characteristics and the status of turnover. This is the foundation for the prevention, management, and control of musculoskeletal diseases.

In recent years, both methods and equipment for evaluating structure, function, and mechanical properties of bone, cartilage, vasculature, and scaffold materials developed for musculoskeletal applications have evolved rapidly. There is no doubt that, to a great extent, how to use such equipment in a logical and scientific way, by exerting the strength of different facilities, avoiding its shortcomings and the possible errors, as well as integrating analyses from the exam results, will determine the correctness and validity of the evaluation results. In this context, the knowledge and experience of the researchers involved are essential as well. It is likely that the same facilities in different users' hands might result in different applications, results, and interpretations.

It is true that in animal experiments, some invasive examinations still have great value for research and applications, where we could get the direct results of bone and cartilage microstructure, bone histomorphometry, cell and molecular biological analysis, and tissue and biomaterial interactions or integrations. But in clinical practice, the patients obviously are more willing to receive the non-invasive exams. The non-invasive nature of recent developments in musculoskeletal imaging presented in this book contributes definitively to our clinical applications.

This book provides detailed introductions from different aspects on the working principles and operating techniques of micro-CT, pQCT/QCT, MRI, and other imaging-related modalities. It also presents the related knowledge and experiences concerning in vitro and in vivo assessments for bone and cartilage on its microarchitecture, vasculature, fracture healing, and scaffolds for tissue engineering.

The contributors of this book are renowned experts and avant-garde researchers in their respective professions. It will serve as a unique reference book with both high academic and applied values for medical doctors, scientists, technologists, postgraduate students, and related persons. It may be expected that this book will bring inspiration and technological insights for our readers to enhance quality of research and develop new applications.

Kerong Dai
Academician, Chinese Academy of Engineering
Life Tenured Professor and Dean Ninth Hospital Medical School
Shanghai Jiaotong University

Preface

The purpose of this book is to provide a perspective on the current status of bio-imaging technologies developed for assessment of quality of musculoskeletal tissues, with emphasis on bone and cartilage, and evaluations of scaffold biomaterials developed for enhancement of repair of musculoskeletal tissues; these include QCT, pQCT, micro-CT for animals and humans, nano-CT, MRI, ultrasound and other advanced imaging modalities. The contents of this book are from the contributions provided by the leading scientists and physicians in the related professions, who participated in the *2005 International Symposium on Advanced Biotechnologies for Assessing Quality of Bone and Scaffold Biomaterials* at the Chinese University of Hong Kong, Hong Kong SAR, China. Some other leading groups who were not able to attend this symposium have also contributed to this book. Their participation makes this book more comprehensive, with an even wider spectrum in musculoskeletal imaging technologies and their applications, from molecular imaging to visualization and simulation of human body with applications extended from musculoskeletal to cardiovascular research.

This book provides a unique platform for multidisciplinary research and may help to facilitate collaborations in development of science and technology, basic and applied biomedical education, as well as research and service among various professions, including biomedical engineering, biomaterials, and basic and clinical medicine. How to make full use of the advanced technologies is essential for further improvement of these biotechnologies. As such, this book is categorized into Part I, with emphasis on technologies, and Part II, the specific applications of those technologies. The subject index is also summarized in this way; therefore, the readership covers medical doctors, clinical and material scientists, bioengineers, technologists, postgraduate students and related personnel.

As we are now in the middle of the Bone-Joint Decade (BJD), the editors hope that this book will contribute to BJD in a specific way, especially in diagnosis, prevention and treatment of aging-related disorders of musculoskeletal, cardiovascular and other relevant living tissues, organs, and systems.

Ling Qin, Ph.D
Professor and Director, Musculoskeletal Research Laboratory
Department of Orthopaedics and Traumatology
The Chinese University of Hong Kong, Hong Kong SAR, China

List of Contents

Part I Perspectives of Advances in Musculoskeletal and Scaffold Biomaterial Imaging Technologies and Applications

I-1 Advances in Assessment of Quality of Bone and Orthopaedic Applications

**Part II Specific Applications of Advances in Musculoskeletal and Scaffold
Biomaterial Imaging Technologies**

II-1 In Assessment of Osteoporosis and Treatment

II-2 In Assessment of Fracture Repair

II-3 In Assessment of Osteonecrosis

II-4 In Assessment of Osteoarthritis

Perspectives of Advances in Musculoskeletal and Scaffold Biomaterial Imaging Technologies and Applications

Advances in Assessment of Quality of Bone and Orthopaedic Applications

Perspectives on Advances in Bone Imaging for Osteoporosis

Harry K. Genant (✉) [1,2] and Ye-Bin Jiang [3]

[1] Professor Emeritus, University of California, San Francisco, California, USA
  e-mail: harry.genant@ucsf
[2] Chairman Emeritus, Board of Directors, Synarc, Inc., San Francisco, California, USA
[3] Director, Osteoporosis and Arthritis Lab, Division of Musculoskeletal Radiology, Department of Radiology, University of Michigan, Michigan, USA

Abstract

Noninvasive and/or nondestructive techniques can provide structural information about bone, beyond simple bone densitometry. While the latter provides important information about osteoporotic fracture risk, many studies indicate that BMD only partly explains bone strength. Quantitative assessment of macro-structural characteristics, such as geometry, and microstructural features, such as relative trabecular volume, trabecular spacing, and connectivity, may improve our ability to estimate bone strength. Methods for quantitatively assessing macrostructure include (besides conventional radiographs) dual X-ray absorptiometry (DXA) and computed tomography (CT), particularly volumetric quantitative computed tomography (vQCT). Methods for assessing microstructure of trabecular bone noninvasively and/or nondestructively include high-resolution computed tomography (hrCT), micro-computed tomography (μCT), high-resolution magnetic resonance (hrMR), and micro-magnetic resonance μmR. Volumetric QCT, hrCT, and hrMR are generally applicable in vivo; μCT and μmR are principally applicable in vitro. Despite progress, problems remain. The important balances between spatial resolution and sampling size, or between signal-to-noise ratio and radiation dose or acquisition time, need further consideration, as do the complexity and expense of the methods vs their availability and accessibility. Clinically, the challenges for bone imaging include balancing the advantages of simple bone densitometry vs the more complex architectural features of bone, or the deeper research requirements vs the broader clinical needs. The biological differences between the peripheral appendicular skeleton and the central axial skeleton must be addressed further. Finally, the relative merits of these sophisticated imaging techniques must be weighed with respect to their applications as diagnostic procedures, requiring high accuracy or reliability, vs their monitoring applications, requiring high precision or reproducibility.

Introduction

More than standard bone densitometry (Genant et al. 1996), noninvasive and/or nondestructive techniques are capable of providing macro- or micro-structural infor-

mation about bone (Faulkner et al. 1990). While the bone densitometry provides important information about osteoporotic fracture risk, numerous studies indicate that bone strength is only partially explained by BMD. Quantitative assessment of macrostructural characteristics, such as geometry, and microstructural features, such as relative trabecular volume, trabecular spacing, and connectivity, may improve our ability to estimate bone strength.

The methods available for quantitatively assessing macrostructure include computed tomography and particularly volumetric quantitative computed tomography (vQCT). Noninvasive and/or nondestructive methods for assessing microstructure of trabecular bone include high-resolution computed tomography (hrCT), micro-computed tomography (μCT), high-resolution magnetic resonance (hrMR), and micro-magnetic resonance μmR. Volumetric QCT, hrCT, and hrMR are generally applicable in vivo, whereas μCT and μmR are principally applicable in vitro.

Volumetric Computed Tomography

The use of standard QCT has centered on two-dimensional characterization of vertebral trabecular bone, but there is also interest in developing three-dimensional, or vQCT, techniques to improve spinal measurements and extend QCT assessments to the proximal femur. These three-dimensional techniques encompass the entire object of interest with stacked slices or spiral CT scans, and can use anatomic landmarks to automatically define coordinate systems for reformatting CT data into anatomically relevant projections.

Volumetric CT can determine BMC or BMD of the entire bone or subregion, such as a vertebral body or femoral neck, as well as provide separate analysis of the trabecular or cortical components (Figs. 1, 2). Since a true and highly accurate volumetric rendering is provided, important geometrical and biomechanically relevant assessments, such as cross-sectional moment of inertia and finite element analyses, can be derived (Faulkner et al. 1990; Keyak et al. 1998; Lang et al. 1997, 1999, 2002;

Figure 1. Volumetric QCT of the spine may be used to analyze bone mineral density in bone compartments and accurately measure vertebral geometry. (Courtesy of T. Lang)
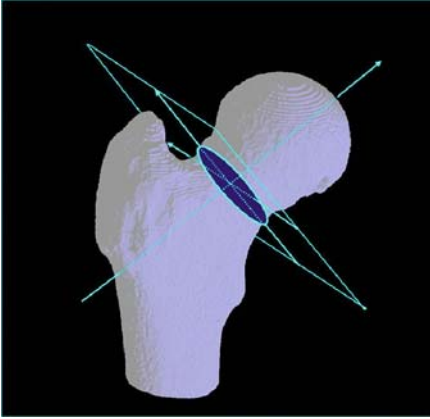
Figure 2. Volumetric QCT of the hip may be used to analyze bone mineral density in bone compartments and accurately measure proximal femoral geometry. (Courtesy of K. Engelke)

Lotz et al. 1990; McBroom et al. 1985). Highly accurate assessment of bone size and density, independent of the artifacts of projectional radiographic and densitometric techniques (such as absorptiometry), can also be derived for epidemiological studies and for studies of nutritional, racial, and genetic influences on bone size and density (Jergas et al. 1995).

Because of the complex anatomy of the proximal femur and its dramatic three-dimensional variations in bone density, vQCT has particularly important ramifications for both research and clinical applications at this biologically relevant site. vQCT and finite element analysis modeling have been used by Lotz et al. (1990) and by Keyak and colleagues (1998), Lang et al. (1990), and Sode et al. (2004) to improve estimations of proximal femoral strength over global projectional densitometry (Fig. 3). In-vitro studies by Lang et al. (1997, 1999) have shown enhanced prediction of in vitro fracture load using subregional vQCT of the hip. The QCT 3D finite element model of the proximal femur shows moderate reproducibility in postmenopausal women (Sode et al. 2004). The QCT-based finite element models of the hip in 51 women aged 74 ($\pm$5) years showed different risk factors for hip fracture during single-limb stance and falls, which agree with epidemiological findings of different risk factors for cervical and trochanteric fractures (Lang et al. 2003).

The geometry of the proximal femur is much more complicated than that of the vertebral body. Trabecular structural parameters obtained from multidetector-row CT in four femoral head specimens were highly correlated with their ultimate load, whereas the volumetric BMD and trabecular structural parameters obtained from multidetector-row CT in the vertebral body of postmenopausal women revealed a strong association with prevalent vertebral fracture (Jiang et al. 2005). The CT examination shows that an increase in volumetric trabecular BMD at total hip and femoral neck in PTH-treated postmenopausal osteoporotic women ($n = 62$) for 1.5 years was due primarily to an increase in volumetric trabecular BMC. Cortical bone volume increased significantly at both hip regions. The increase in volumetric cortical BMC was smaller than the increase in bone volume, and therefore there was a decrease in volumetric cortical BMD that was significant at the total hip, but not at
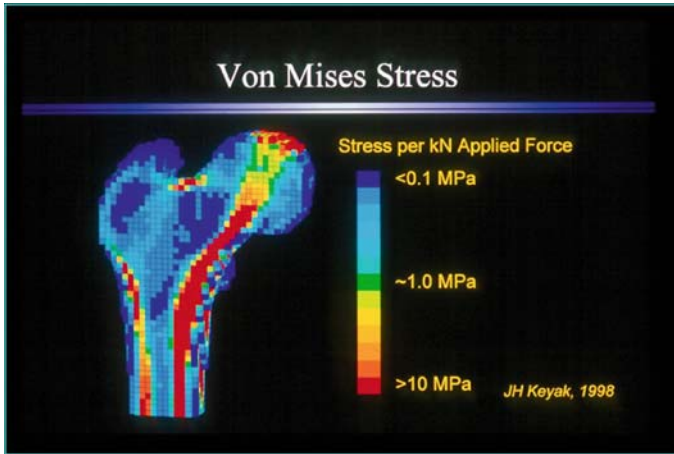
Figure 3. Volumetric QCT of the hip provides a basis for finite element analyses (FEM). (Courtesy of J. Keyak and T. Lang)

the femoral neck (Bogado et al. 2005). Helical volumetric quantitative CT examination of 14 crew members of the International Space Station demonstrated that total femur integral BMC, but not integral volumetric BMD or trabecular BMD, recovered to its pre-flight value, 12 months after flights lasting 4 – 7 months. Recovery of bone mass involved increasing both bone density and bone size. Incomplete recovery of BMD in the hip in the year after long-duration spaceflight was observed. As shown by an increase in the minimum femoral neck cross-sectional area and integral tissue volume, the proximal femur appears to adapt to resumed load bearing by periosteal apposition (Lang et al. 2005). In 3158 men aged 65+ years in the US who are enrolled in the Osteoporotic Fractures in Men Study (MrOS), the femoral neck, and lumbar spine volumetric BMD was greatest in African Americans, whereas the femoral neck and lumbar spine cross-sectional area was lowest in African Americans and greatest in Caucasians, which might contribute to some of the ethnic difference in hip and vertebral fracture epidemiology (Zmuda et al. 2005).

Finite element models derived from QCT scans may improve the prediction of vertebral strength because they mechanically integrate all the geometrical and material property data within the scans. The QCT BMD values of each bone voxel can be converted into elastic modulus values using pre-determined correlation between the elastic modulus and QCT-derived BMD. Finite element models integrate mechanically all of the anisotropic, inhomogeneous, and complex geometry of the bone structure examined. It has been demonstrated that voxel-based finite element model-derived estimates of strength are better predictors of in vitro vertebral compressive strength than clinical measures of bone density derived from QCT with or without geometry (Crawford et al. 2003a). A pilot study in 20 randomly selected postmenopausal women treated with PTH (1 – 84) for 1 year indicate that about half the overall increase in vertebral strength can be attributed to an average increase in bone

density, and the remaining half of the effect is due to alterations in the distribution of bone density within the vertebra (Black et al. 2005). Although imaging resolution is not critical in cross-sectional studies using clinical CT scanners, longitudinal studies that seek to track more subtle changes in stiffness over time should account for the small but highly significant effects of voxel size (Crawford et al. 2003b).

High-Resolution Computed Tomography

There is much research underway in the areas of high-resolution computed tomography (hrCT). The spatial resolution of clinical CT scanners (typically > 0.3 mm) is inadequate for highly accurate cortical measurements and for analysis of discrete trabecular morphological parameters, and new CT developments address this issue. There are two main approaches: the development of new image acquisition and analysis protocols using state-of-the-art clinical CT scanners; and the development of new hrCT scanners for in vivo investigations of the peripheral skeleton, or of new µCT scanners for in vitro 2D or 3D structural analysis of very small bone samples (typically < 4 cm^3).

State-of-the-art spiral CT scanners utilize a relatively high-resolution (~ 0.3 × 0.3 mm) thin slice (~ 1.0 mm) to provide images of the spine and hip that clearly display structural information; however, it requires a higher radiation exposure than is employed for standard QCT. Also, the extraction of the quantitative structural information is difficult and the results vary substantially according to the threshold and image-processing techniques used. This is due to substantial partial-volume effects at this resolution relative to the typical dimensions of trabeculae (100–400 µm) and trabecular spaces (200–2000 µm; Fig. 4)

High-resolution CT has been employed to measure a feature called the trabecular fragmentation index (length of the trabecular network divided by the number of
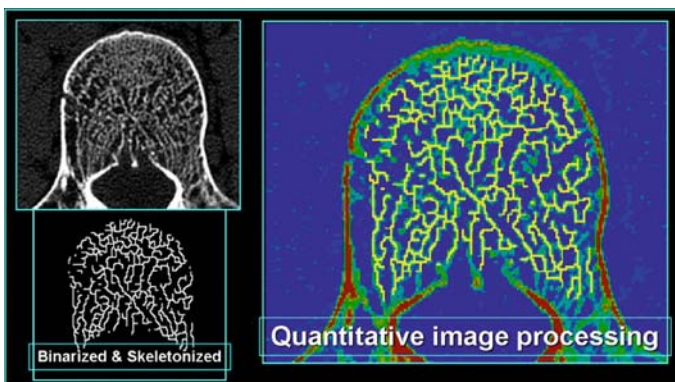
Figure 4. High-resolution thin-slice CT provides a basis for image processing and extraction of parameters approximating trabecular and cortical structure, but with considerable partial-volume affects. (Courtesy K. Engelke)

discontinuities) in an effort to separate osteoporotic subjects from normal subjects (Chevalier et al. 1992), and a similar trabecular textural analysis approach has been reported by Ito et al. (1995). Gordon et al. (1998) reported on a hrCT technique that extracted a texture parameter reflecting trabecular hole area, analogous to star volume, that appears to enhance vertebral-fracture discrimination relative to BMD. One in vitro study showed that a combination of BMD and trabecular structural parameters of bone cubes examined by pQCT improved prediction of bone biomechanical properties (Jiang et al. 1998). Link (2003a) has provided a comprehensive analysis of multislice hrCT with hrMR applied to the peripheral skeleton.

In a recent in vivo study, the voxel size of $156-187\,\mu m$ in-plane, and $300-500\,\mu m$ through-plane, from vertebrae of osteoporotic women demonstrated that differences in spatial resolution of the different CT scanners used had a significant influence on measured structural variables but did not affect longitudinal analyses (Timm et al. 2005). Long-term precision errors were 13% for bone volume fraction and 11% for trabecular thickness, corresponding to monitoring time intervals of 1 and 1.2 years. In another study, all measured structural variables in 67 patients treated with teriparatide at $20\,\mu g$/day for 1 year showed significant improvements. Increases were consistently larger during the first 6 months of treatment (Graeff et al. 2005).

More recent studies of high-resolution and volumetric CT have further documented the unique capabilities of these techniques, including 3D rendering (Fig. 5; Ito et al. 2005). Some have shown that trabecular structural analysis from multidetector-row CT images can better discriminate postmenopausal women with vertebral fracture than DXA (Takada et al. 2004). High-resolution spiral CT assessment of the trabecular structure of the vertebral body in combination of BMD improves prediction of biomechanical properties (Bauer et al. 2004). In elderly men, there is an independent association of sex steroid levels with cortical and trabecular area and their QCT volumetric BMD, but lack such association in young men (Khosla et al. 2004).
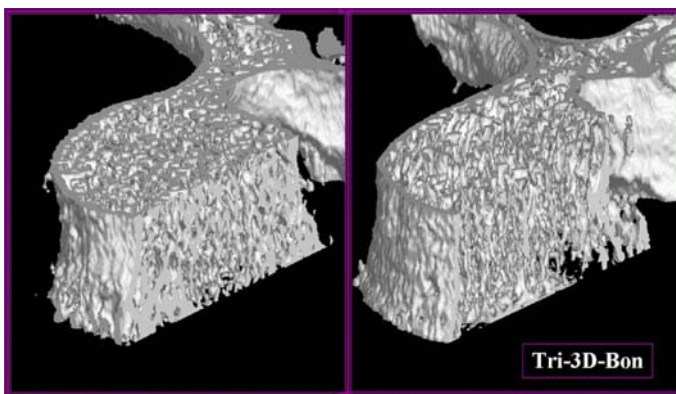
Figure 5. Multi-slice high-resolution in vivo images of the spine rendered in three dimensions have been reported by Ito, Link, and others. (Courtesy of M. Ito)

Higher-resolution pCT scanners for peripheral skeletal measurements in vivo have been developed and evaluated by Durand and Rüegsegger (1992) and Müller et al. (1996a,b). The images show trabecular structure in the radius, with a spatial resolution of 170 µm isotropic. The images can be used for quantitative trabecular structure analysis and also for a separate assessment of cortical and trabecular BMD. (Note, however, that these state-of-the-art scanners may approach the limits of spatial resolution achievable in vivo with acceptable radiation exposure; Engelke et al. 1993.)

Micro-Computed Tomography

To achieve very high spatial resolution images, Feldkamp et al. (1989) and Kuhn et al. (1990) constructed a unique µCT system for 3D in vitro analyses of small bone samples. The system employed cone-beam geometry and a 3D reconstruction algorithm. The spatial resolution of ≈ 60 µm clearly visualized individual trabeculae, allowing a 3D analysis of trabecular network. Goulet (1994) utilized images of bone cubes generated by this system to examine standard histomorphometric parameters as well as additional parameters such as Euler number, an index of connectivity, and mean intercept length, a means of determining anisotrophy. He also related these image-based parameters to Young's modulus, a measure of elasticity of bone. Based on data sets from Feldkamp's µCT, Engelke (1994, 1996) developed a 3D digital model of trabecular bone for comparing 2D and 3D structural analysis methods, and to investigate the effects of spatial resolution and image-processing techniques on the extraction of structural parameters (Fig. 6). Three-dimensional data sets from these µCT systems can be used for calculating classical histomorphometric parameters, such as trabecular thickness and separation (Parfitt et al. 1983a,b; Odgaard 1993), as well as for determining topological measurements such as the Euler number and connectivity.

Another in vitro µCT scanner with a spatial resolution of $15-20$ µm^3 was developed by Rüegsegger et al. (1996; Müller 2001) and has been used extensively in lab-
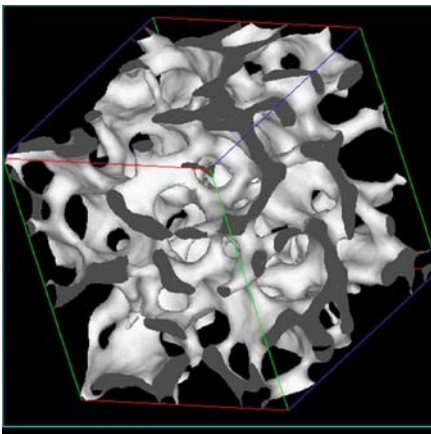
Figure 6. A 3D digital model of trabecular bone based on µCT image at approximately 60 µm^3 resolution. (Courtesy of K. Engelke)

oratory investigations. Its high accuracy in relation to standard 2D histomorphometry as well as to serial grindings and their derived 3D parameters has been reported (Gordon 1998). The relationship of these parameters to in vitro measures of strength and their application to micro-finite element modeling has been shown (Muller et al. 1996a,b; van Rietbergen 1995). More recently, additional special-purpose, ultra-high-resolution μCT systems have been developed for imaging bone microstructure at resolutions approaching 10 μm or better (Engelke et al. 1998). These various μCT systems have found wide application in both preclinical animal studies and clinical research settings (Jiang et al. 2005a). Similarly, in animal studies, micro-CT has recently found applications in the assessment of skeletal phenotype in gene knock-out mice (Sohaskey et al. 2004; Sorocéanu et al. 2004; Takeshita et al. 2002; Bergo et al. 2002), and in osteoporotic (Lane et al. 2004) or arthritic rodents (Jiang et al. 2004).

In a human study by Jiang et al. (2005a), the rapid deterioration in trabecular micro-architecture in women experiencing menopause was documented by paired iliac crest biopsies before and approximately 5 years after the menopause. Prominent thinning of trabeculae and conversion of plate-like to rod-like trabecular structure was observed (Fig. 7).

Jiang et al. (2005a) also used micro-CT with 3D analyses compared with standard 2D histomorphometry to study the longitudinal impact of teriparatide (PTH 1–34) treatment vs placebo on the skeleton of postmenopausal women. In this analysis the changes of the more simple 2D indices pertaining to cancellous bone structure, such as trabecular number, thickness, and spacing, did not reach significance after PTH treatment; however, more stereologically correct indices, such as marrow star volume and μCT-based 3D indices, revealed significant changes, further corroborating
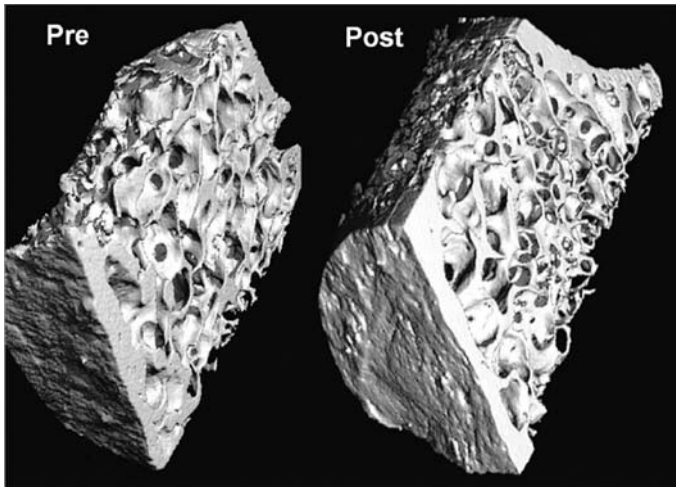
Figure 7. Micro-CT image at ∼ 20 μm^3 resolution of trabecular structure of serial iliac crest biopsies from a postmenopausal woman before and 2 years after estrogen replacement therapy. (Courtesy of Y. Jiang)

the superiority of these techniques for structural analysis of small samples such as bone biopsies (Fig 8). The root mean square CV as reproducibility of µCT examination after rescanned and re-analyzed 20 human biopsy specimens was 2–6% for trabecular structural parameters (Jiang et al. 2003a,b).

While the µCT scanners described above use an X-ray tube as radiation source, other investigators have explored the potential of high-intensity, tight collimation synchrotron radiation, which allows either faster scanning or higher spatial resolution in imaging bone specimens. These systems have been referred to as X-ray tomographic microscopy (XTM) and can achieve spatial resolution of 10 µm or better. Bonse et al. (1994), Engelke et al. (1991), and Graeff and Engelke (1991) were among the first to apply this approach to imaging of bone specimens. Kinney et al. (1995) and Lane et al. (1995) have applied the XTM approach to imaging the rat tibia at ultra-high resolution, both in vitro and in vivo, and have documented the impact of oophorectomy and PTH treatment on two- and three-dimensionally derived trabecular bone indices. Peyrin et al. (1998) have utilized synchrotron based XTM to image trabecular bone ultrastructure at resolutions approaching 1–2 µm, thereby providing the capability to assess additional features such as resorption cavities. In recently reported studies using synchrotron radiation, micro-CT examination of sequential iliac biopsies showed that treatment with a bisphosphonate treatment did not cause significant hypermineralization but did increase the mineralization at the tissue level (Fig. 9; Borah et al. 2004). Also, standard micro-CT and histomorphometric assessments of serial iliac crest bone biopsies from postmenopausal women treated with another bisphosphonate for 10 years showed normal micro-architecture (Recker et al. 2004).

At recent international congresses there have been many additional studies using micro-CT, including technical developments and various applications. An in vivo human micro CT scanner developed in Europe has been used to examine distal radius or distal tibia with isotropic resolution of about 90 µm (Fig. 10; Neff et al. 2004; Dambacher et al. 2005).
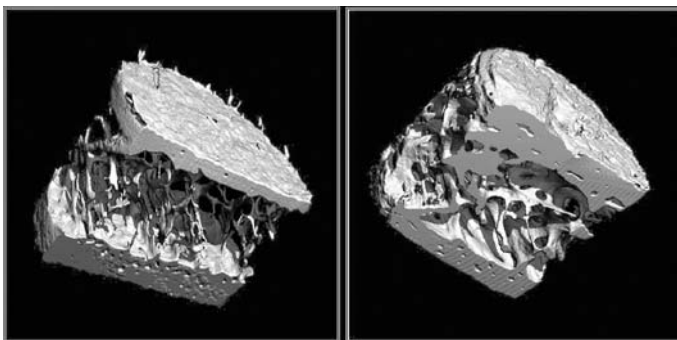
Figure 8. Paired biopsy sample was obtained from a 65-year-old woman treated with PTH. Compared with the baseline biopsy (*L*), PTH treatment (*R*) increased trabecular bone volume, trabecular connectivity, and cortical thickness, and shift trabecular morphology from a rod-like structure to a more plate-like pattern. (Courtesy of Y. Jiang)
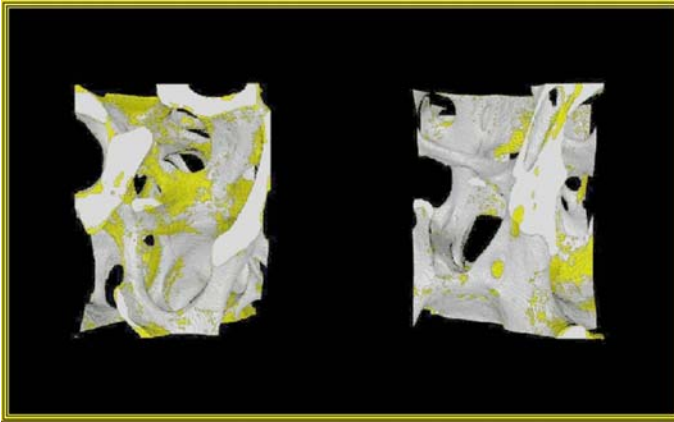
Figure 9. Syncrotron-based micro-CT images of iliac crest biopsies used to assess the degree of mineralization pre- and post-bisphosphonate treatment. (Courtesy of B. Borah)

Applying this technique, no significant differences in bone architecture were found between radius and tibia in young healthy women (Backstroem et al. 2005). Three-dimensional pQCT of the radius, but not hip and spine DXA, could differentiate osteopenic women with and without a fracture history (Boutroy et al. 2005). A population-based study showed that relative to women, men begin adult life with a more plate-like, and thus stronger, trabecular microstructure, and that no change over life in trabecular number or separation occurs in men, as compared with significant decreases in trabecular number and increases in trabecular separation in women (Khosla et al. 2005). The 3D analysis of weight-bearing (distal tibia) and non-weight-bearing (distal radius) sites suggests that Colle's fracture is related mainly to local cortical low mineral density instead of trabecular bone structure, whereas hip fractures are associated with a combination of both trabecular and cortical quantitative
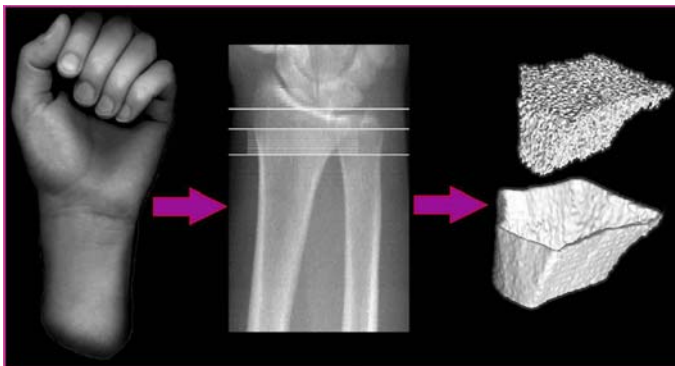
Figure 10. In-vivo micro-CT of the distal radius (*arrows*) using the XtremCT system. (Courtesy B. Koehler)
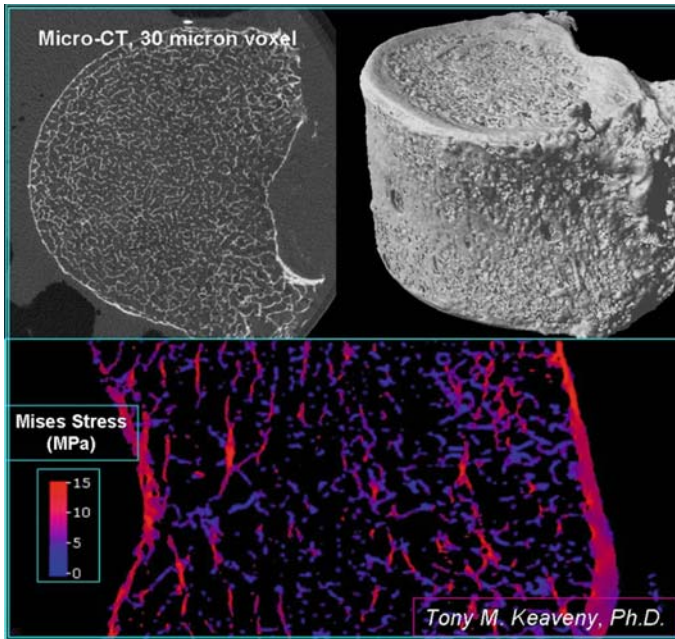
Figure 11. Micro-CT of vertebral body at 30-μm resolution, and generation of micro-finite element model at the trabecular level. (Courtesy of T. Keaveny)

and qualitative damages occurring in both weight-bearing and non-weight-bearing bones (Zouch et al. 2005).

Advanced micro-finite analyses with models based on 3D peripheral micro-CT systems (at isotropic voxel resolution of 165 μm) have predicted the failure load of the human radius Colles' fractures better than by DXA or bone morphology and geometry measurements (Pistoia et al. 2002). Micro-CT (and micro-MRI, see below) replicate the complex trabecular architecture on a macroscopic scale for visual or biomechanical analysis. A complete set of 3D micro-CT image data provides a basis for micro-finite element modeling for virtual biomechanics to predict mechanical properties (Fig. 11; Sode et al. 2004; Crawford et al. 2003a,b; van Rietbergen et al. 1995; Borah et al. 2001).

MR Microscopy

High-resolution MR and micro-MR, referred to collectively as MR microscopy, have received considerable attention as research tools and as potential clinical tools for assessment of trabecular bone architecture. Magnetic resonance is a complex technology based on the application of high magnetic fields, transmission of radio-frequency (RF) waves, and detection of RF signals from excited hydrogen protons. A noninvasive, nonionizing radiation technique, MR can provide 3D images in arbitrary ori-

entations and can depict trabecular bone as a negative image by virtue of the strong signal generated by the abundant fat and water protons in the surrounding marrow tissue. The appearance of the MR image is affected by many factors beyond spatial resolution, including the field strength and specific pulse sequence used, the echo time, and the signal-to-noise ratio achieved (Majumdar et al. 1993, 1994, 1995). Analysis and interpretation of MR images are more complicated than for the X-ray-based images of CT. Nevertheless, MR microscopy holds much promise for improved quantitative assessment of trabecular structure both in vivo and in vitro.

Because of the relation of signal-to-the-field strength in MR, special-purpose, small-bore, high-field magnets have been employed to obtain very high resolution or μmR images of bone specimens in vitro (Chung et al. 1993; 1995a,b; Hwang et al. 1997). Wehrli and colleagues (1998, 2001, 2002) obtained 78-μm isotopic resolution of human and bovine bone cubes using 3D imaging at 9.4 T, and derived anisotropy ellipsoids from the analysis of mean intercept length. They also found good correlations between MR-derived parameters and standard histomorphometric measures. Antich et al. (1994) conducted similar experiments and found changes in accordance with histomorphometry measures. Kapadia et al. (1993) extended the in vitro techniques to obtain images in an ovariectomized rat model and were able to measure changes in trabecular structure following ovariectomy. Simmons and Hipp (1997) examined bovine cubes in a small bore microimaging spectrometer at 60-$μm^3$ resolution and found 3D results heavily dependent upon the threshold and image processing algorithm. Majumdar et al. (1996) examined human cadaver specimens using a standard clinical MR scanner at 1.5 T and a spatial resolution of $117 \times 117 \times 300\,μm$, and compared these images with XTM images and with serial grindings to determine the impact of in-plane resolution and slice thickness on both 2D and 3D structural and textural parameters (Fig. 12). Considerable resolution dependence was observed
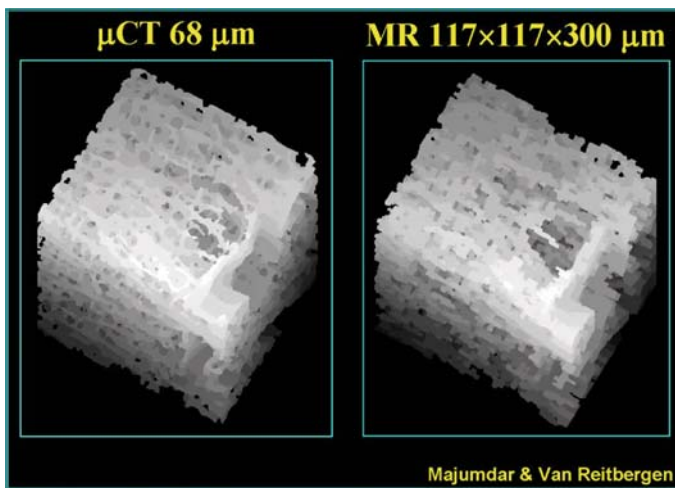
Figure 12. Comparison micro-MR and micro-CT images of trabecular bone specimens. (Courtesy of S. Majumdar and B. Van Reitbergen)

for traditional stereological parameters, some of which could be modulated by appropriate thresholds and image-processing techniques.

Limitations of the signal-to-noise ratio, spatial resolution, and total imaging time prevent resolution of smaller individual trabeculae in vivo at clinical field strengths, but the images show the larger trabeculae and the texture of the trabecular network. The trabecular structure can still be quantified using standard techniques of stereology as well as textural parameters such as fractal analysis. In an early study by Majumdar et al. (1994) establishing the feasibility of using such images to quantify trabecular structure, MR images of the distal radius were obtained using a modified gradient-echo sequence, a 1.5-T imager, a spatial resolution of $156\,\mu m^2$, and a slice thickness of 0.7 mm. Representative axial sections from normal and osteoporotic subjects clearly depicted the loss of the integrity of the trabecular network with the development of osteoporosis (Fig. 13). Similar images of the calcaneus of normal subjects showed that the orientation of the trabeculae is significantly different in various anatomic regions. Ellipses, representing the mean intercept length, showed a preferred orientation and hence mapped the anisotropy of trabecular structure. In preliminary in vivo studies of the calcaneus, gray-scale reference values from fat, muscle, and tendon were used to calculate reproducible threshold values (Ouyang et al. 1997). This approach gave a midterm in vivo precision of $\approx 3.5\%$ CV for trabecular width and spacing.
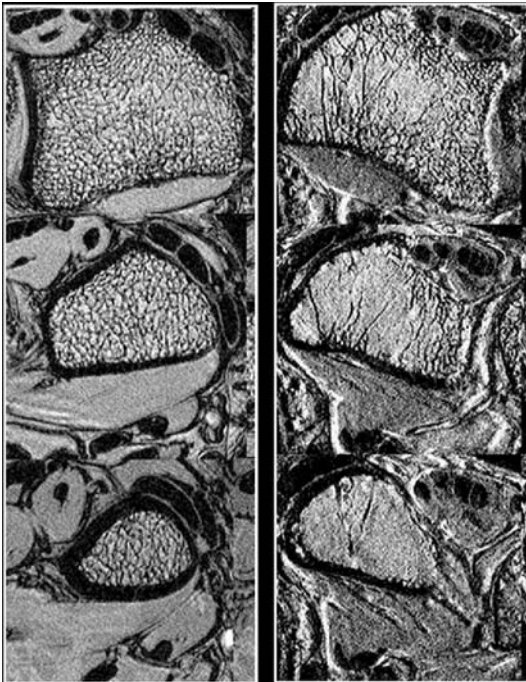
Figure 13. High-resolution ($\sim 150 \times 150 \times 500\,\mu m$) axial gradient-echo MR images of the distal radius of a young woman (*left*) and an elderly osteoporotic woman (*right*). (Courtesy of S. Majumdar)

Jara and colleagues (1993), Kühn et al. (1997), and Stamper et al. (1998, 2002) have utilized clinical imagers at 1.5 T with special RF coil designs and have measured trabecular and cortical bone in the phalanges, a convenient anatomic site particularly suitable for obtaining high signal-to-noise ratio and high spatial resolution images in vivo. Resolution of 78 – 150 μm and slice thickness of 300 μm have been achieved in the phalanges. Stampa et al. (2002) used these phalangeal images to derive quantitative 3D parameters based on an algorithm and model for defining trabecular rods and plates. Other authors, including Link et al. (1998), Majumdar (1997), and Wehrli et al. (1998, 2001, 2002), have shown the ability to discriminate spine and/or hip fractures using trabecular structure or textural parameters from in vivo MR images of the radius or calcaneus (Fig. 14). Recently, an in vivo study in early postmenopausal women, MR images of the distal radius and tibia acquired at $137 \times 137 \times 410 \, \mu m^3$ voxel size at baseline and 11 – 13 months showed significant structural changes (8 – 10%) in control subjects but little or no significant change in the HRT group (Ladinsky et al. 2005).

Engelke has provided a comprehensive analysis of threshold effects in hrMR of the calcaneus when compared with ultra-high-resolution anatomic sectioning in vitro (Engelke et al. 2001). Newitt (2001) has reported promising results on the application of micro-finite-element analyses based on hrMR images of the distal radius in vivo. Structure parameters determined in high-resolution MR images of the proximal femur specimen correlated significantly with bone strength, with the highest correlations obtained combining DXA BMD and structure measures (Link et al. 2003b).

The resolution achievable in vivo by MRI is not sufficient to depict precisely individual trabeculae and, thus, does not permit the quantification of the "true" trabecular bone morphology and topology. Trabecular samples of the distal radius imaged using MRI at $156 \times 156 \times 300 \, \mu m$ correlate well with micro-CT at $34 \times 34 \times 34 \, \mu m$, with r^2 ranging from 0.57 to 0.64 for morphological measurements (Fig. 13; Pothuaud et al. 2002). Trabecular bone structure parameters assessed in the distal radius on high-resolution MR and multislice CT images are significantly correlated with those
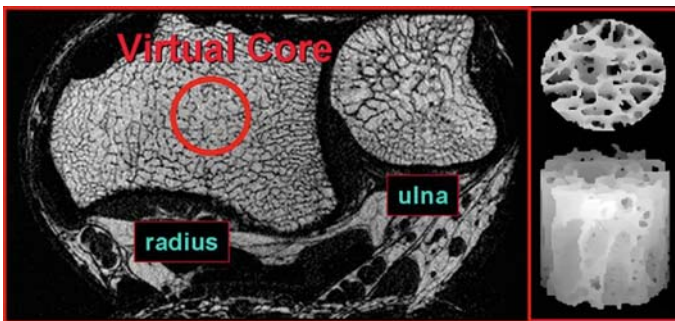
Figure 14. Virtual core biopsy is illustrated for in vivo MR imaging of the distal radius. (Courtesy of F. Wehrli)
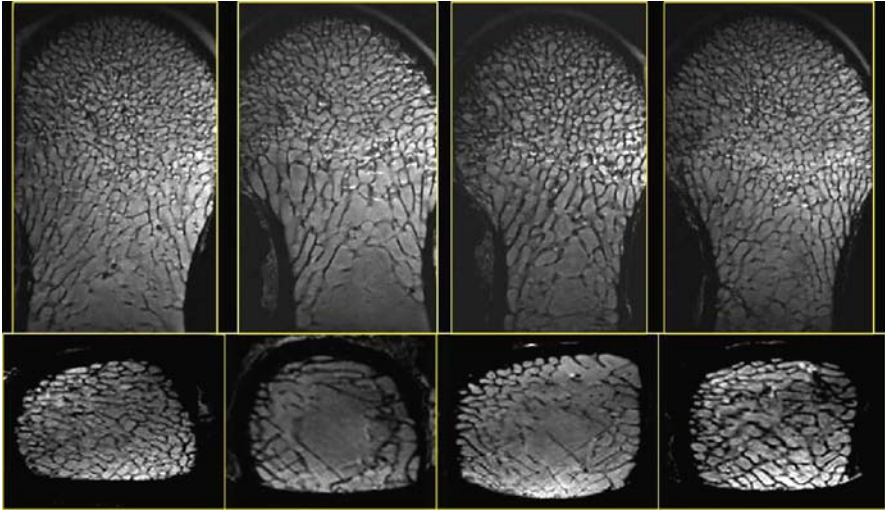
Figure 15. Magnetic resonance microscopic images of the proximal femur show that the ovariectomy (OVX)-induced loss in trabecular microstructure in the femoral neck is prevented by the treatment of salmon calcitonin (sCT) at 50 or 100 IU

determined on contact radiographs of the corresponding specimen sections. For the MR imaging, the threshold algorithm used for binarizing the images substantially affected these correlations (Link et al. 2003c).

In an animal study by Jiang et al. (2005), MRI microscopy showed that ovariectomy induces deterioration of trabecular microstructure and the biomechanical properties in the femoral neck of ewes. Calcitonin treatment prevented OVX-induced changes in a dose-dependent manner (Fig. 15). The femoral neck trabecular microstructure significantly correlates with biomechanical properties, and its combination with BMD further improved the prediction of bone quality.

Challenges for Bone Imaging

Despite the considerable progress that has been made over the past decade in advanced bone imaging for osteoporosis assessment, a number of challenges remain. Technically, the challenges reflect the balances and trade-offs between spatial resolution, sample size, signal-to-noise ratio, radiation exposure, and acquisition time, or between the complexity and expense of the imaging technologies vs their availability and accessibility. Clinically, the challenges for bone imaging include balancing the advantages of standard BMD information vs the more complex architectural features of bone, or the deeper research requirements of the laboratory vs the broader needs of clinical practice. The biological differences between the peripheral appendicular skeleton and the central axial skeleton and their impact on the relevant bone imaging methods must be clarified further.

Finally, the relative merits of these sophisticated imaging techniques must be weighed with respect to their applications as diagnostic procedures, which require high accuracy and reliability, vs their applications as monitoring procedures, which requires high precision and reproducibility.

References

Adapted in part from Genant HK, Gordon C, Jiang Y, Lang TF, Link TM Majumdar S (1999) Advanced imaging of bone macro and micro structure Bone 25:149–152

Antich P, Mason R, McColl R, Zerwech J, Pak C (1994) Trabecular architecture studies by 3D MRI microscopy in bone biopsies. J Bone Miner Res 9S1:327

Backstroem M, Armbrecht G, Beller G, Reeve J, Alexandre C, Rizzoli R, Berthier A, Braak L, Binot R, Koller B, Felsenberg D (2005) First data of forearm and tibia bone micro architecture in young, healthy women, using high resolution 3DpQCT in vivo. J Bone Miner Res 20 (Suppl 1):S336

Bauer JS, Mueler D, Fischbeck M, Eckstein F, Rummeny EJ, Link TM (2004) High resolution spiral-CT for the assessment of osteoporosis: Which site of the spine and region of the vertebra is best suited to obtain trabecular bone structural parameters? J Bone Miner Res 19:S169

Bergo MO, Gavino B, Ross J, Schmidt WK, Hong C, Kendall LV, Mohr A, Meta M, Genant H, Jiang Y, Wisner ER, Van Bruggen N, Carano RA, Michaelis S, Griffey SM, Young SG (2002) Zmpste24 deficiency in mice causes spontaneous bone fractures, muscle weakness, and a prelamin A processing defect. Proc Natl Acad Sci USA 99:13049–13054

Black DM, Crawford RP, Palermo L, Bilezikian JP, Greenspan S, Keaveny TM (2005) Finite element biomechanical analysis of the PTH and alendronate (PaTH) study: PTH increases vertebral strength by altering both average density and density distribution. J Bone Miner Res 20 (Suppl 1):S15

Bogado CE, Zanchetta JR, Mango A, Mathisen AL, Fox J, Newman MK (2005) Effects of parathyroid hormone 1 – 84 on cortical and trabecular bone at the hip as assessed by QCT: results at 18 months from the TOP study. J Bone Miner Res 20 (Suppl 1):S22

Bonse U, Busch F, Gunnewig O, Beckmann F, Pahl R, Delling G, Hahn M, Graeff W (1994) 3D computed X-ray tomography of human cancellous bone at 8 μm spatial and 10 – 4 energy resolution. Bone Mineral 25:25–38

Borah B, Gross GJ, Dufresne TE, Smith TS, Cockman MD, Chmielewski PA, Lundy MW, Hartke JR, Sod EW (2001) Three-dimensional microimaging (MRmicro and microCT), finite element modeling, and rapid prototyping provide unique insights into bone architecture in osteoporosis. Anat Rec 15:101–110

Borah B, Ritman EL, Dufresne TE, Liu S, Chmielewski PA, Jorgensen SM, Reyes DA, Turner RT, Phipps RJ, Manhart MD, Sibonga JD (2004) Five year risedronate therapynormalizes mineralization: synchrotron radiation micro computed tomography study of sequential triple biopsies. J Bone Miner Res 19:S308

Boutroy S, Bouxsein ML, Munoz F, Delmas PD (2005) Non-invasive measurement of trabecular architecture by 3D-pQCT discriminates osteopenic women with and without fractures. J Bone Miner Res 20 (Suppl 1):S91

Chevalier F, Laval-Jeantet AM, Laval-Jeantet M, Bergot C (1992) CT image analysis of the vertebral trabecular network in vivo. Calcif Tissue Int 51:8-13

Chung H, Wehrli FW, Williams JL, Kugelmass SD (1993) Relationship between NMR transverse relaxation, trabecular bone architecture, and strength. Proc Natl Acad Sci 90:10250–10254

Chung HW, Wehrli FW, Williams JL, Kugelmass SD, Wehrli SL (1995a) Quantitative analysis of trabecular microstructure by 400 MHz nuclear magnetic resonance imaging. J Bone Miner Res 10:803–811

Chung HW, Wehrli FW, Williams JL, Wehrli SL (1995b) Three-dimensional nuclear magnetic resonance microimaging of trabecular bone. J Bone Miner Res 10:1452–1461

Crawford RP, Cann CE, Keaveny TM (2003a) Finite element models predict in vitro vertebral body compressive strength better than quantitative computed tomography. Bone 33:744–750

Crawford RP, Rosenberg WS, Keaveny TM (2003b) Quantitative computed tomography-based finite element models of the human lumbar vertebral body: effect of element size on stiffness, damage, and fracture strength predictions. J Biomech Eng 125:434–438

Dambacher MA, Neff M, Radspieler H, Rizzoli R, Delmas P, Qin L (2005) Bone microarchitecture evaluation in vivo in humans. J Bone Miner Res 20 (Suppl 1):S334

Durand EP, Rüegsegger P (1992) High-contrast resolution of CT images for bone structure analysis. Med Phys 19:569–573

Engelke K, Dix W, Graeff W et al. (1991) Quantitative microtomography and microradiography of bones using synchrotron radiation. Presented at the 8th Int Workshop on Bone Densitometry, Bad Reichenhall, Germany

Engelke K, Graeff W, Meiss L, Hahn M, Delling G (1993) High spatial resolution imaging of bone mineral using computed microtomography. Comparison with microradiography and undecalcified histologic sections. Invest Radiol 28:341–349

Engelke K, Klifa C, Munch B, Glüer C, Genant H (1994) Morphological analysis of the trabecular network: the influence of image processing technique on structural parameters. Tenth Int Bone Densitometry Workshop, Venice, Italy. J Bone Miner Res 25 (Suppl 2) S8

Engelke K, Song SM, Glüer CC, Genant HK (1996) A digital model of trabecular bone. J Bone Miner Res 11:480–489

Engelke K, Karolczak M, Schaller S, Felsenberg D, Kalender WA (1998) A cone beam micro computed tomography (μCT) system for imaging of 3D trabecular bone structure. Presented at the 13th Int bone Densitometry Workshop, 4–8 October 1998, Wisconsin

Engelke K, Hahn M, Takada M et al. (2001) Structural analysis of high resolution in vitro MR images compared to stained grindings. Calcif Tissue Int 68:163–171

Faulkner KG, Cann CE, Hasegawa BH (1990) CT-derived finite element model to determine vertebral cortex strength In: Loew MH (ed) Medical imaging IC: image processing, vol 1233. SPIE, Newport Beach, California, pp 194–202

Feldkamp LA, Goldstein SA, Parfitt AM, Jesion G, Kleerekoper M (1989) The direct examination of three-dimensional bone architecture in vitro by computed tomography. J Bone Miner Res 4:3–11

Genant HK, Engelke K, Fuerst T, Glüer CC, Grampp S, Harris ST, Jergas M, Lang T, Lu Y, Majumdar S, Mathur A, Takada M (1996) Noninvasive assessment of bone mineral and structure: state of the art. J Bone Miner Res 11:707–730

Gordon CL, Lang TF, Augat P, Genant HK (1998) Image-based assessment of spinal trabecular bone structure from high-resolution CT images. Osteoporos Int 8:317–325

Goulet RW, Goldstein SA, Ciarelli MJ, Kuhn JL, Brown MB, Feldkamp LA (1994) The relationship between the structural and orthogonal compressive properties of trabecular bone. J Biomech 27:375–389

Graeff W, Engelke K (1991) Microradiography and microtomography. In: Ebashi S, Koch M, Rubenstein E (eds) Handbook on synchrotron radiation. North-Holland, Amsterdam, pp 361–405

Graeff C, Timm W, Farrerons J, Nickelsen TN, Blind E, Kekow J, Möricke R, Boonen S, Audran M, Glüer CC (2005) Structural analysis of vertebral trabecular bone structure allows to assess the effect of teriparatide treatment independently of BMD. J Bone Miner Res 20 (Suppl 1):S411

Hwang SN, Wehrli FW, Williams JL (1997) Probability-based structural parameters from three-dimensional nuclear magnetic resonance images as predictors of trabecular bone strength. Med Phys 24:1255–1261

Ito M, Ohki M, Hayashi K, Yamada M, Uetani M, Nakamura T (1995) Trabecular texture analysis of CT images in the relationship with spinal fracture. Radiology 194:55–59

Ito M, Ikeda K, Uetani M, Orimo H (2005) In vivo analysis of vertebral microstructure for evaluation of fracture risk. J Bone Miner Res 20 (Suppl 1):S91

Jara H, Wehrli FW, Chung H, Ford JC (1993) High-resolution variable flip angle 3D MR imaging of trabecular microstructure in vivo. Magn Reson Med 29:528–539

Jergas M, Breitenseher M, Glüer CC, Yu W, Genant HK (1995) Estimates of volumetric bone density from projectional measurements improve the discriminatory capability of dual X-ray absorptiometry. J Bone Miner Res 10:1101–1110

Jiang Y, Zhao J, Augat P, Ouyang X, Lu Y, Majumdar S, Genant HK (1998) Trabecular bone mineral and calculated structure of human bone specimens scanned by peripheral quantitative computed tomography: relation to biomechanical properties. J Bone Miner Res 13:1783–1790

Jiang Y, Zhao J, Mitlak BH, Wang O, Genant HK, Eriksen EF (2003a) Recombinant human parathyroid hormone (1–34) (teriparatide) improves both cortical and cancellous bone structure. J Bone Miner Res 18:1932–1941

Jiang Y, Zhao J, Eriksen EF, Genant HK (2003b) Reproducibility of micro CT quantification of 3D microarchitecture of the trabecular and cortical bone in the iliac crest of postmenopausal osteoporotic women and their treatment with teriparatide [rhPTH(1–34)]. RSNA'03:571

Jiang Y, Zhao JJ, Mangadu R, Medicherla S, Protter AA, Genant HK (2004) Assessment of 3D cortical and trabecular bone microstructure and erosion on micro CT images of a murine model of arthritis. J Bone Miner Res 19:S474

Jiang Y, Zhao, P, Liao EY, Dai RU, Wu XP, Genant HK (2005a) Application of micro CT assessment of 3D bone microstructure in preclinical and clinical studies. J Bone Miner Metab 23(Suppl):122–131

Jiang Y, Zhao J, Geusens P, Liao EY, Adriaensens P, Gelan J, Azria M, Boonen S, Caulin F, Lynch JA, Ouyang X, Genant HK (2005b) Femoral neck trabecular microstructure in ovariectomized ewes treated with calcitonin: MRI microscopic evaluation. J Bone Miner Res 20:125–130

Kapadia RD, High W, Bertolini D, Sarkar SK (1993) MR microscopy: a novel diagnostic tool in osteoporosis research. In: Christiansen C (ed) Fourth Int Symposium on Osteoporosis and Consensus Development Conference, Hong Kong, p 28

Keyak JH, Rossi SA, Jones KA, Skinner HB (1998) Prediction of femoral fracture load using automated finite element modeling. J Biomech 31:125–133

Khosla S, Melton LJ, Atkinson EJ, Oberg AE, Robb R, Camp J, Riggs BL (2004) Relationship of volumetric density, geometry and bone structure at different skeletal sites to sex steroid levels in men. J Bone Miner Res 19:S88

Khosla S, Riggs BL, Oberg AL, Atkinson EJ, McDaniel L, Peterson JM, Melton LJ (2005) Effects of gender and age on bone microstructure at the wrist: a population-based in vivo bone biopsy study. J Bone Miner Res 20 (Suppl 1):S20

Kinney JH, Lane NE, Haupt DL (1995) In vivo, three-dimensional microscopy of trabecular bone. J Bone Miner Res10:264–270

Kuhn JL, Goldstein SA, Feldkamp LA, Goulet RW, Jesion G (1990) Evaluation of a microcomputed tomography system to study trabecular bone structure. J Orthop Res 8:833–842

Kühn B, Stampa B, Glüer C-C (1997) Hochauflösende Darstellung und Quantifierung der trabekulären Knochenstruktur der Fingerphalangen mit der Magnetresonanztomographie. Z Med Phys 7:162–168

Ladinsky GA, Vasilic B, Popescu AM, Zemel B, Wright AC, Song HK, Saha PK, Peachy H, Snyder PJ, Wehrli FW (2005) MRI based virtual bone biopsy detects large one-year changes in trabecular bone architecture of early postmenopausal women. J Bone Miner Res 20 (Suppl 1):S15

Lane NE, Thompson JM, Strewler GJ, Kinney JH (1995) Intermittent treatment with human parathyroid hormone (hPTH[1-34]) increased trabecular bone volume but not connectivity in osteopenic rats. J Bone Miner Res 10:1470–1477

Lane NE, Balooch M, Zhao J, Jiang Y, Yao W (2004) Glucocorticoids induce changes around the osteocyte lacunae that reduces bone strength and bone mineral content independent of apoptosis: preliminary data from a glucocorticoid-induced bone loss model in male mice. J Bone Miner Res 19:S434–435

Lang TF, Keyak JH, Heitz MW, Augat P, Lu Y, Mathur A, Genant HK (1997) Volumetric quantitative computed tomography of the proximal femur: precision and relation to bone strength. Bone 21:101–108

Lang TF, Li J, Harris ST, Genant HK (1999) Assessment of vertebral bone mineral density using volumetric quantitative computed tomography. J Comput Assist Tomogr 23:130–137

Lang TF, Guglielmi G, van Kuijk C, de Serio A, Cammisa M, Genant HK (2002) Measurement of bone mineral density at the spine and proximal femur by volumetric quantitative computed tomography and dual-energy X-ray absorptiometry in elderly women with and without vertebral fractures. Bone 30:247–250

Lang TF, Keyak JH, Yu A, Lu Y, Do L, Li J (2003) Determinants of proximal femoral strength in elderly women. J Bone Miner Res 18:S266

Lang TF, LeBlanc A, Evans H, Lu Y (2005) Recovery of proximal femoral density and geometry after long-duration spaceflight. J Bone Miner Res 20 (Suppl 1):S44

Link T, Majumdar S, Augat P, Lin J, Newitt D, Lang T, Lu Y, Lane N, Genant HK (1998) In vivo high resolution MRI of the calcaneus: differences in trabecular structure in osteoporotic patients. J Bone Miner Res 13:1175–1182

Link TM, Vieth V, Stehling C et al. (2003a) High-resolution MRI vs multislice spiral CT: Which technique depicts the trabecular bone structure best? Eur Radiol 13:663–671

Link TM, Vieth V, Langenberg R, Meier N, Lotter A, Newitt D, Majumdar S (2003b) Structure analysis of high resolution magnetic resonance imaging of the proximal femur: in vitro correlation with biomechanical strength and BMD. Calcif Tissue Int 72:156–165

Link TM, Vieth V, Stehling C, Lotter A, Beer A, Newitt D, Majumdar S (2003c) High-resolution MRI vs multislice spiral CT: Which technique depicts the trabecular bone structure best? Eur Radiol 13:663–671

Lotz JC, Gerhart TN, Hayes WC (1990) Mechanical properties of trabecular bone from the proximal femur: a quantitative CT study. J Comput Assist Tomogr 14:107–114

Majumdar S, Genant H, Gies A, Guglielmi G (1993) Regional variations in trabecular structure in the calcaneus assessed using high resolution magnetic resonance images and quantitative image analysis. J Bone Miner Res 8S:351

Majumdar S, Genant H, Grampp S, Jergas M, Newitt D, Gies A (1994) Analysis of trabecular bone structure in the distal radius using high resolution MRI. Eur Radiol 4:517–524

Majumdar S, Newitt DC, Jergas M, Gies AA, Chiu EC, Osman D, Keltner J, Keyak J, Genant HK (1995) Evaluation of technical factors affecting the quantification of trabecular bone structure using magnetic resonance imaging. Bone 17:417–430

Majumdar S, Newitt D, Mathur A, Osman D, Gies A, Chiu E, Lotz J, Kinney J, Genant H (1996) Magnetic resonance imaging of trabecular bone structure in the distal radius: relationship with X-ray tomographic microscopy and biomechanics. Osteoporos Int 6:376–385

Majumdar S, Genant HK, Grampp S, Newitt DC, Truong VH, Lin JC, Mathur A (1997) Correlation of trabecular bone structure with age, bone mineral density and osteoporotic status: in vivo studies in the distal radius using high resolution magnetic resonance imaging. J Bone Miner Res 12:111–118

McBroom RJ, Hayes WC, Edwards WT, Goldberg RP, White AA III (1985) Prediction of vertebral body compressive fracture using quantitative computed tomography. J Bone Joint Surg (Am Vol) 67:1206–1214

Muller R, Rüegsegger P (1996) Analysis of mechanical properties of cancellous bone under conditions of simulated bone atrophy. J Biomech 29:1053–1060

Muller R, Hahn M, Vogel M, Delling G, Rüegsegger P (1996a) Morphometric analysis of non-invasively assessed bone biopsies: comparison of high-resolution computed tomography and histologic sections. Bone 18:215–220

Muller R, Hildebrand T, Hauselmann HJ, Rüegsegger P (1996b) In vivo reproducibility of three-dimensional structural properties of noninvasive bone biopsies using 3D-pQCT. J Bone Miner Res 11:1745–1750

Müller R, Bauss F, Smith SY, Hannan MK (2001) Mechano-structure relationships in normal, ovariectomized and Ibandronate treated aged macaques as assessed by micro-tomographic imaging and biomechanical testing. Trans Orthop Res Soc 26:66

Neff M, Dambacher M, Haemmerle S, Rizzoli R, Delmas P, Kissling R (2004) 3D evaluation of bone microarchitecture in humans using high resolution pQCT; a new in vivo, non-invasive and time saving procedure. J Bone Miner Res 19:S236

Newitt DC, Majumdar S, van RB, van Rietbergen B, Ingersleben G, Harris ST, Genant HK, Chesnut C, Garnero P, MacDonald B (2002) In vivo assessment of architecture and micro-finite element analysis derived indices of mechanical properties of trabecular bone in the radius. Osteoporos Int 13:6–17

Odgaard A, Gundersen HJG (1993) Quantification of connectivity in cancellous bone, with special emphasis on 3-D reconstructions. Bone 14:173–182

Ouyang X, Selby K, Lang P, Engelke K, Klifa C, Fan B, Zucconi F, Hottya G, Chen M, Majumdar S et al. (1997) High resolution magnetic resonance imaging of the calcaneus: age-related changes in trabecular structure and comparison with dual X-ray absorptiometry measurements. Calcif Tissue Int 60:139–147

Parfitt AM, Matthews C, Villanueva A (1983a) Relationships between surface, volume and thickness of iliac trabecular bone in aging and in osteoporosis. J Clin Invest 72:1396–1409

Parfitt AM (1983b) The stereologic basis of bone histomorphometry: theory of quantitative microscopy and reconstruction of the third dimension. In: Recker R (ed) Bone histomorphometry: techniques and interpretations. CRC Press, Boca Raton, pp 53–87

Peyrin F, Salome M, Cloetens P, Ludwig W, Ritman EL, Rüegsegger P, Laval-Jeantet AM, Baruchel J (1998) What do micro CT examinations reveal at various resolutions: a study of the same trabecular bone samples at the 14, 7, and 2 micron level. Presented at the Symposium on Bone Architecture and the Competence of Bone, Ittingen, Switzerland, 3–5 July 1998

Pistoia W, van Rietbergen B, Lochmuller EM, Lill CA, Eckstein F, Rüegsegger P (2002) Estimation of distal radius failure load with micro-finite element analysis models based on three-dimensional peripheral quantitative computed tomography images. Bone 30:842–848

Pothuaud L, Laib A, Levitz P, Benhamou CL, Majumdar S (2002) Three-dimensional-line skeleton graph analysis of high-resolution magnetic resonance images: a validation study from 34-microm-resolution microcomputed tomography. J Bone Miner Res 17:1883–1895

Recker R, Ensrud K, Diem S, Cheng E, Bare S, Masarachia P, Roschger P, Fratzl P, Klaushofer K, Lombardi A, Kimmel D (2004) Normal bone histomorphometry and 3D microarchitecture after 10 years alendronate treatment of postmenopausal women. J Bone Miner Res 19:S45

Rüegsegger P, Koller B, Muller R (1996) A microtomographic system for the nondestructive evaluation of bone architecture. Calcif Tissue Int 58:24–29

Simmons CA, Hipp JA (1997) Method-based differences in the automated analysis of the three-dimensional morphology of trabecular bone. J Bone Miner Res 12:942–947

Sode M, Keyak J, Bouxsein M, Lang T (2004) Assessment of femoral neck torsional strength indices. Bone Miner Res 19:S238

Sohaskey ML, Jiang Y, Zhao J, Mohr A, Roemer F, Genant HK, William C, Skarnes WC (2004) Insertional mutagenesis of osteopotentia, a novel transmembrane protein essential for skeletal integrity. J Bone Miner Res 19:S21

Sorocéanu MA, Miao D, Jiang Y, Zhao JJ, Bai XY, Su H, Genant HK, Amizuka N, Goltzman D, Karaplis AC (2004) *Pthrp* haploinsufficiency impairs bone formation but potentiates the bone anabolic effects of PTH (1 – 34). J Bone Miner Res 19:S97

Stampa B, Kühn B, Heller M, Glüer C-C (1998) Rods or plates: a new algorithm to characterize bone structure using 3D magnetic resonance imaging. Presented at the 13th Int Bone Densitometry Workshop, 4 – 8 October 1998, Wisconsin

Stampa B, Kühn B, Liess C, Heller M, Glüer CC (2002) Characterization of the integrity of three-dimensional trabecular bone microstructure by connectivity and shape analysis using high-resolution magnetic resonance imaging in vivo. Top Magn Reson Imaging 13:357–363

Takada M, Kikuchi K, Unau S, Murata K (2004) Three-dimensional analysis of trabecular bone structure of human vertebra in vivo using image data from multi-detector row computed tomography: correlation with bone mineral density and ability to discriminate women with vertebral fracture. J Bone Miner Res 19:S371

Takeshita S, Namba N, Zhao J, Jiang Y, Genant HK, Silva MJ, Brodt MD, Helgason CD, Kalesnikoff J, Rauh MJ, Humphries RK, Krystal G, Teitelbaum SL, Ross FP (2002) SHIP-deficient mice are severely osteoporotic due to increased numbers of hyper-resorptive osteoclasts. Nature Med 8:943–949. (Published online on 5 August 2002)

Timm W, Graeff C, Vilar J, Nickelsen TN, Nicholson T, Lehmkuhl L, Barkmann R, Glüer CC (2005) In vivo assessment of trabecular bone structure in human vertebrae using high resolution computed tomography. J Bone Miner Res 20 (Suppl 1):S336

van Rietbergen B, Weinans H, Huiskes R, Odgaard A (1995) A new method to determine trabecular bone elastic properties and loading using micromechanical finite-element models. J Biomech 28:69–81

Wehrli FW, Hwang SN, Ma J, Song HK, Ford JC, Haddad JG (1998) Cancellous bone volume and structure in the forearm: noninvasive assessment with MR microimaging and image processing. Radiology 206:347–357

Wehrli FW, Gomberg BR, Saha PK et al. (2001) Digital topological analysis of in vivo magnetic resonance microimages of trabecular bone reveals structural implications of osteoporosis. J Bone Miner Res 16:1520–1531

Wehrli FW, Saha PK, Gomberg BR, Song HK, Snyder PJ, Benito M, Wright A, Weening R (2002) Role of magnetic resonance for assessing structure and function of trabecular bone. Top Magn Reson Imaging 13:335–355

Zmuda JM, Chan BKS, Marshall LM, Cauley JA, Lang TF, Ensrud KE, Lewis CE, Stefanick ML, Barrett-Conner E, Orwoll ES (2005) Ethnic diversity in volumetric bone density and geometry in older men: the osteoporotic fractures in men study (MrOS). J Bone Miner Res 20 (Suppl 1):S35

Zouch M, Gerbay B, Thomas T, Vico L, Alexandre C (2005) Patients with hip fracture exhibit bone microarchitectural deterioration compared to patients with Colle's fracture as assessed with in vivo high resolution 3D micro-pQCT. European Advanced Detection of Bone Quality(ADOQ) Study. J Bone Miner Res 20 (Suppl 1):S45

Bone Structure and Biomechanical Analyses Using Imaging and Simulation Technology

Edmund Y.S. Chao

Professor Emeritus (the Holleren-Brook Professor of Bioengineering),
the Mayo Medical School, Baltimore, Maryland, USA
Professor Emeritus (the Lee Riley, Jr. Professor of Orthopaedics),
the Johns Hopkins University, Baltimore, Maryland, USA
Department of Orthopaedics, University of California, Irvine, California
e-mail:yebin.jiang@radiology.ucsf.edu

Abstract

Bio-imaging technology has been used to study bone structure and biomechanics ever since the discovery of roentgenograms (X-ray) by Wilhelm Konrad Roentgen in the late nineteenth century. Recent advancements of CT- and MRI-based imaging techniques plus various digital image processing and 3D and 4D reconstruction algorithms have made these studies easier with expanded scope and greater depth and enabling biomechanical analysis with unprecedented clarity using computer graphics in static and dynamic animations. These capabilities formed the foundation of computer-aided simulation and analysis of the musculoskeletal system in an interactive environment. To perform biomechanical analysis of bone and other connective tissues at both the material and structure levels, one needs accurate and effective models and reliable material properties. In addition, bone and joint loading depend on muscle contraction and the interaction among all connective tissues engaged in body and limb functions. This chapter presents a variety of bio-imaging techniques and a number of selected application examples of using these techniques to conduct structure and biomechanical investigations involving the normal and abnormal compositions and functions of the musculoskeletal system. A unique simulation software and database, the Virtual Interactive Musculoskeletal System (VIMS), which incorporates model-making techniques, biomechanical analysis algorithms, and a graphic image-based virtual laboratory environment to present the model, data and analysis results, is introduced. It is hoped that this exciting technology will provide the tools and motivation to bring musculoskeletal biomechanics back to the centre of attention in the fields of bioengineering, orthopaedic surgery and rehabilitation.

Introduction

The main goals of bone structural analysis at the tissue level are to determine its strength, fracture healing progression, callus distraction maturation and skeletal density change after bone or joint reconstruction. To accomplish these goals, the bone

geometry, architecture, mineral density, repairing tissue material property and their time-related changes must be quantified. If possible, this information should be determined using non-destructive methods and that is where various bio-imaging techniques would be utilized; however, for validation purposes or in animal model experiments, destructive methods would be necessary in order to obtain the specimens, relying on the similar image capturing, processing and analysis techniques to extract useful data and information. The traditional method of determining bone structure, composition and strength is to conduct specimen analysis and biomechanical testing combined with standard histomorphological methods. Although some of this information can be deduced using non-destructive methods, their reliability and consistency are still questionable and require further refinement.

The key information to be established in biomechanical analysis involving skeletal structures are their motions, the internal loading condition and the stress and strain born by bone and other connective tissues interacting with bone. To conduct such analysis, a physical model of the musculoskeletal system is mandatory before the application of mechanical laws and mathematical theories. In the past, such models were constructed using cadaver-dissecting data, skeleton measurements and information gathered from anatomy textbooks to construct crude line diagrams. The accuracy and visual fidelity of these diagrams were generally poor, which significantly affected the confidence and the acceptability of the data generated in the medical community. Furthermore, such an approach would be extremely difficult when applied to a living person. With the aid of X-ray and CT-based non-invasive imaging techniques, the skeletal geometry data from a normal subject or a patient can be used for model extraction using more advanced image-processing algorithms. For the non-osseous connective tissues interacting with the bone, MRI technique is strongly indicated; however, during activities, the musculoskeletal system is constantly changing its configuration and sometimes these tissues may involve subtle deformation under large loads. To reconstruct these models incorporating body and limb movement and tissue deformation including the micro-motion of the internal devices or prostheses in the body relative to the bone where they are anchored presents new challenges to current state-of-the-art bio-imaging.

Following the major breakthrough in engineering design, analysis and manufacturing in the 1980s, biomechanical analysis of the musculoskeletal system has recently adapted the computer-aided design (CAD), computer-aided analysis (CAA) and computer-aided manufacturing (CAM) concepts, as well as technology using graphically attractive, anatomically accurate and mechanically realistic models while permitting system and physical parameter changes interactively. Involved tissue material properties from existing databases or specifically defined are being adapted. In addition, biomechanical analysis programs for bone structure and musculoskeletal system function are being incorporated with the models for the specific investigation. Finally, the analysis results can be presented together with the model in a real-time fashion under a graphic simulation environment to enhance the visual impact of the analysis and the credibility of the theoretical approach in understanding and predicting the effect of normal and pathological conditions on tissue response and limb function.

One such simulation software is the VIMS for biomechanical analysis (Chao 2003). This system contains three major parts: (a) the model-making programs; (b) the analysis tools; and (c) a virtual laboratory to execute experiments or theoretical studies while being able to inspect and document analysis results incorporated on a computer-based working platform (Fig. 1). Although individualized working platforms are located in each laboratory or the investigator's office, all users can be connected and interactive through the Internet. Different commercial or custom-made programs can easily be adapted to the general platform to suit each user's own specific needs. In addition, the VIMS system also includes a robust database containing skeletal and implant/device models and analysis results. This software and database will be available in the public domain and can be acquired by joining a network on a co-op basis. This image-based biomechanical modelling and analysis technology is expected to help the specialty of biomechanics to regain its essential utility once rigorously shared by orthopaedic surgeons and bioengineers alike. It will also elevate the quality and relevance of this discipline, with strong emphasis on clinical application, so that it can compete for research funding from all sources.

This chapter provides an arguable justification for utilizing bio-imaging and simulation technology to refine the quality and expand the scope of bone structural and biomechanical studies with clear end point of generating clinically relevant data and knowledge to promote health maintenance in normal population of all ages and to improve treatment outcome in patients with skeletal trauma, joint diseases, degeneration, deformity and various neoplastic conditions. The scope and objectives of bone structure and biomechanics analysis are reviewed with specific emphasis on the application of bio-imaging and simulation technology. The currently used imaging techniques are briefly introduced and their procedural details are presented together with selected application examples to demonstrate their utilization. The contents of this chapter end with a discussion of future developmental needs of imaging science and technology with the aim of advancing our understanding of normal and abnormal musculoskeletal system function and the current and future treatment modalities and prevention strategies. Computer-generated graphic models and their biomechanical analysis results are included to fully demonstrate the visualization capa-
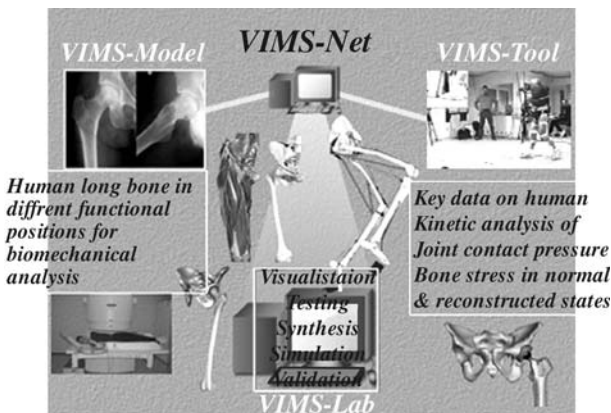
Figure 1. The Virtual Interactive Musculoskeletal System (VIMS) simulation software platform consists of three major components: the VIMS-Model; the VIMS-Tools; and the VIMS-Lab, for biomechanical analysis and results visualization

bility of this technology to appreciate the complex musculoskeletal system function, injury mechanism and treatment options in a dynamic 4D space.

Scope and Objectives of Bone Structural and Biomechanical Analyses

From a structural point of view, bone has two basic types, the compact or cortical bone and the cancellous or trabecular bone in their matured stages. Although the basic compositions in these two types of bone are similar, their structural characteristics, biomechanical function and biological responses are quite different. In addition, the cortical and cancellous bones follow separate pathways in response to development, formation/resorption, injury, reparation and the stress-induced remodelling. Furthermore, soft tissue attachment to bone varies according to bone type, anatomical location and loading condition; hence, bone structural analysis has a broad scope ranging from cell and molecular compositions to tissue or structural response from metabolic, pathological and functional changes. From a narrower viewpoint, however, by treating bone as a structural material, the following objectives are commonly sought in most basic and clinical studies:

1. Quantification of bone mineral density (BMD) and estimate of its material properties in different degrees of normality and stages of pathological involvements
2. Description of various osseous tissues' architectural characteristics in order to correlate their structure with mechanical strength
3. Assessment of bone disease process, degeneration, resorption, fracture healing, defect repair and callus distraction osteogenesis, and the remodelling capability according to pathological, anatomical and biomechanical pre-dispositions.

The scope of bone biomechanical analysis overlaps with that for bone structural studies since they are closely related and mutually dependent. It is also prudent to involve the entire musculoskeletal system in the investigation since bone cannot function alone. Hence, imaging techniques allow us to do the following:

1. Determine the geometry and connectivity of bone, related soft tissue and possible implants or devices in order to develop a realistic working model from the anatomical, functional and biomechanical points of view
2. Conduct static and kinetic analyses to quantify muscle, ligament, as well as bone and joint loading under activities
3. Based on the loading conditions and the estimated material property of the model, determine the internal state of stress and strain in the bone, implant and their interface to speculate the risk of fracture or loosening failure due to trauma, repetitive stress or disuse atrophy
4. Study bone responses in the presence of orthopaedic implant/device or their wear particles concerning bone resorption, overgrowth or remodelling
5. Conduct preoperative planning in different bone fixation or reconstructive procedures based on optimal loading and functional requirements
6. Validate proposed bone remodelling theories using simulation models combined with animal experiments

It is quite clear that these study objectives are extremely broad, but the information to be generated should remain closely related to what clinical patient care would need to improve treatment outcome. The majority of this knowledge is either unknown or inadequately established. The urgency of filling this information void is critical and it will impact on the quality of our life, work and medical service. The currently available bio-imaging techniques are more that adequate to help in achieving these goals. It is also important to realize that the cost involved in generating this pertinent and relevant information is only a small fraction of what we have spent in biotechnology.

General Imaging Techniques Used for Bone Structural and Biomechanical Analyses

There are numerous imaging techniques currently being used for bone and connective tissue structural and biomechanical analyses. Each of these techniques also has different image processing and reduction methods to make the raw data reliable, useful and consistent. As the contents of this book will no doubt provide an exhaustive coverage on each of these methods, only the most common and pertinent techniques germane to the applications contained in this chapter are briefly summarized herein.

Digital Black-and-White and Colour Photography

Digital black-and-white and colour photography is probably the oldest method to record bone and other connective tissue images for composition and geometric analysis. The best example of such application is the huge database established in the Visible Human project in the 1990s (Spitzer et al. 1996). Digital photography is undeniably the simplest and most reliable method, but the process involved to obtain the specimen surface for photo image preparation is very tedious and time-consuming. Serial cross-sectional images of intact anatomy provide the best resolution and fidelity of the tissues involved and their relative orientation (Fig. 2), based on which

Figure 2. The ultra-high-resolution digital image (3.4 GB) of human cross-sectional anatomy through the pelvis at the level of femoral head from the Visible Human Dataset (from Spitzer et al. 1996) available on the Internet

many 3D musculoskeletal models were constructed and utilized, some of which are presented in this chapter. The shortcomings of this method are obvious, and because it is totally destructive, costly and extremely time-consuming, its wide utilization has been prevented.

Roentgenographic Method

The commonly used radiographic method providing non-destructive bone image in 2D projection with different grey levels according to the mineral density of the tissue involved is still the gold standard to study bone integrity and normality. Using refined X-ray energy source, film quality, cassette design, processing technique plus the use of staged scaling phantoms and digital image processing algorithms, this method still has its lasting values in bone material and structural analyses. When trabecular bone is assumed to be a homogeneous and anisotropic material its elastic modulus and strength can be estimated using a 2D Fourier analysis of the radiographic image to estimate the principal directions of the trabecular orientation and intensities (Inoue 1987). This technique also allows analysis of image data with a grey-level gradient without binalization of the grey level (Fig. 3). It is noted, however, that this method does not allow analysis of geometrical characteristics of individual trabeculae such as connectivity and thickness of the trabeculae.

Reflecting and Transmission Light Microscopy and Scanning Electron Microscopy

These are the standard methods used to provide high-magnification and high-resolution surface histomorphological data of connective tissue specimens. With different specimen-preparation techniques, both calcified and uncalcified bone tissue can
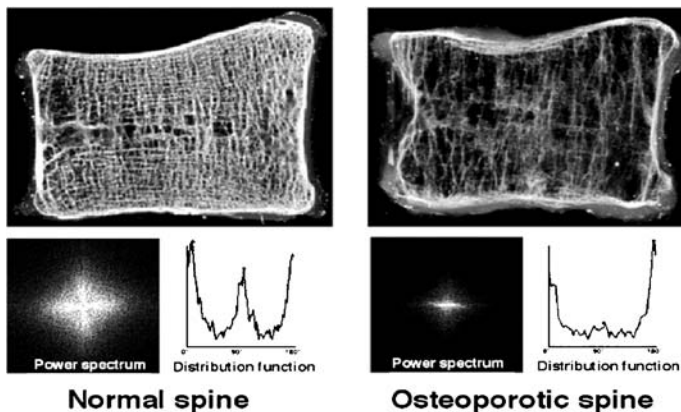
Figure 3. The 2D Fourier Spectrum analysis of the grey level of thin slices of normal and osteoporotic vertebral body X-ray images. The power spectrum, density and distribution give the trabecular orientation and intensity for the architectural of the cancellous bone structure

be studied qualitatively as well as quantitatively. Using different light sources, electron emission, confocal technique, the use of immuno-fluorescence staining agents, etc., the surface and internal structure and topography of tissue and their collagen type, cellular structure, and chemical composition can be visualized and studied in detail. In un-decalcified osseous tissue, micro-indentation test may be performed to estimate the mechanical property of the tissue and correlate that with morphology. These are obviously destructive techniques and there is no non-destructive method available at the present time to provide such detailed information at the tissue level.

Single- or Dual-Photon Densitometry

The single- or dual-photon densitometry methods are particularly useful to determine mineral density of bone in a totally non-invasive manner; however, the image obtained is a 2D projection of a 3D object which lacks resolution as well as specificity. In addition, such data does not correlate well in predicting bone structural strength since it provides no architectural information especially for the trabecular bone (Aro et al. 1990; Markel et al. 1990). Using an optical image spectrum analysis method similar to that described before, significant structural information could be produced to estimate bone strength loss along with mineral density.

Computed Tomography and Micro-CT

Both regular CT and micro-CT are able to produce a wide spectrum of image data on a voxel-based material density non-invasively for bone structural and biomechanical analyses. This technology is further strengthened by the powerful image processing algorithms in terms of surface and volume rendering, image segmentation, etc.; hence, 3D objects with complex geometrical shape and material composition can be reconstructed, providing unprecedented information concerning skeleton shape, surface topography and cross-sectional imaging in any orientation and depth, even with material property estimation (Fig. 4). With recent improvement in scanning speed, image resolution, object volumetric reconstruction efficiency and cost reduction, this technology will be the workhorse for bone structural and biomechanical analyses at different levels of resolution. Dynamic scanning techniques able to record skeleton in motion are being developed with the ultimate goal of detecting small deformation of bone tissue under large functional loads.
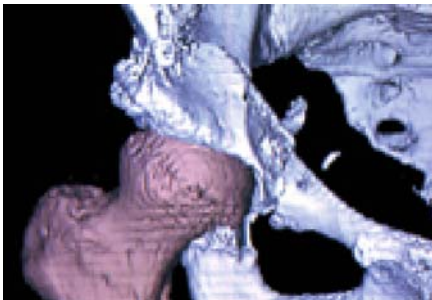
Figure 4. A 3D solid structure reconstruction of the pelvis and proximal femur in a patient after peri-acetabular osteotomy using CT scan data

Magnetic Resonance Imaging and Emission Tomography

For the non-osseous connective tissue, including cartilage, menisci, intervertebral disc, ligament, tendon and muscles, magnetic resonance imaging (MRI) and emission tomography are the only non-invasive techniques that can provide geometrical and material structural information for biomechanical analysis. The MRI technology is advancing rapidly with specialized coils, open primary coil design, new sequences, radio-frequency tagging, etc. Minute changes in tissue composition and physical property in the soft connective tissue due to water-content variation and deformation under loading can be visualized with surprising clarity. This method is especially useful for musculoskeletal tumour biopsy and diagnosis for local lesion resection and reconstruction surgery planning and execution (Fig. 5). In patients with osteonecrosis, MRI can detect early disease involvement in the subchondral bone structure enabling consideration of prophylactic treatment to prevent bone collapse. Dynamic MRI is being developed to provide time-related activity of soft tissues, offering the most unique information to study musculoskeletal system function and degeneration. With further improvement in accuracy and resolution, tendon-to-bone insertion sites can be studied in a dynamic and totally non-invasive manner. The use of special radio energy emission labelling agents, such as the radio-isotope applied to specific tissue type, can produce 3D integrated multi-modality visualization, which will revolutionize musculoskeletal system biomechanical analysis in normal persons and patients with a wide variety of musculoskeletal conditions.
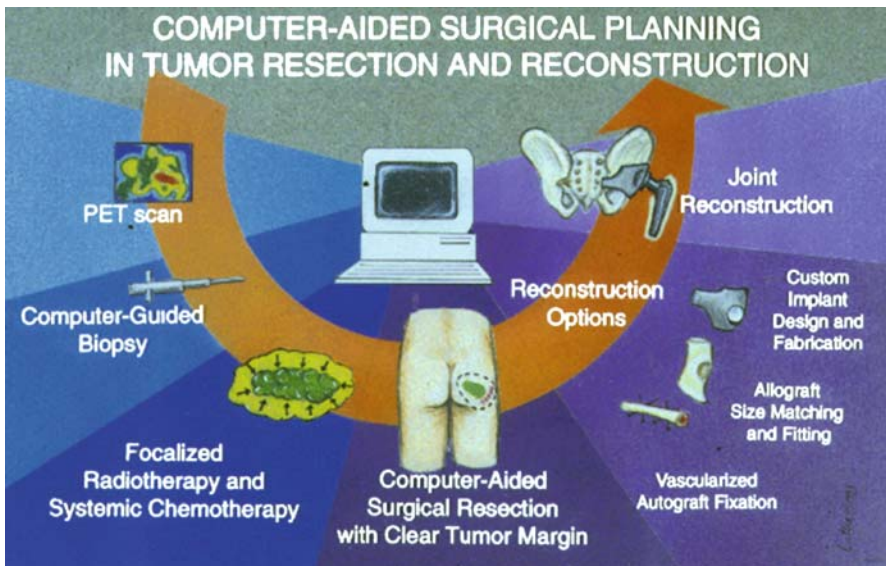
Figure 5. The concept of computer-aided diagnostics, biopsy, neo-adjuvant treatment, surgical resection and reconstruction planning in limb salvage operation using image-based technology involving musculoskeletal tumour management

Ultrasound Tomography Imaging

Ultrasound imaging has a well-established advantage in imaging soft tissue shape changes with time using a non-radiation energy source. This technique can also provide osseous tissue material properties, since the sonic wave propagation velocity in bone is directly related to its material's elastic modulus and Poisson's ratio. Using special wave spectrum and intensity analysis on sonic wave propagating through the bone allows estimation of its mechanical strength and anisotropy. Ultrasound imaging in the form of tomography can provide visual depiction of bone structure as well as its structural properties for biomechanical analysis.

Any one type, or a combination of several types, of the above-mentioned imaging techniques will be required to fulfil the bone structural and biomechanical analysis objectives. It is important to realize that bio-imaging only provides the basic data, and additional image processing and analysis procedures are required to generate the additional information on bone and soft tissue composition, material properties and musculoskeletal system models for the final biomechanical investigations. The model and analysis results visualized using 3D and 4D graphic technology will further accentuate the need and efficacy of these esoteric investigations. These technical advancements will offer a win-win situation in several clinical disciplines involving human musculoskeletal system health maintenance, injury prevention, treatment and rehabilitation. This technology will also enrich the medical devices and implant industry in improving their product design, lowering manufacturing cost and optimizing the application skills among surgeons, thus enhancing clinical care outcome measures.

Rationales for Biomechanical Analysis in a Simulation Environment

The "Virtual Human" provides an ideal environment for biomechanical analyses and simulation, which is demonstrated later in this chapter (Spitzer 1996). With further development, this technology will form a broad technical resource with full-featured analysis capability, robust model library and database, and a well-facilitated environment to conduct biomechanical analysis in a virtual laboratory for basic science and clinical investigations. This simulation technology unites the expertise in biomechanical analysis and graphic modelling to investigate joint and connective tissue mechanics and to visualize the results in both static and animated forms. Adaptable anatomical models, including implants and fracture fixation devices and a computational infrastructure, are readily available for static, kinematic, inverse and forward dynamic, joint contact pressure, as well as stress and strain analyses under varying boundary and loading conditions (Fig. 6). These models and computational algorithms, incorporated on a common software platform, are a timely and significant advance in the field of musculoskeletal biomechanics to revive its vital interest and impetus among surgeons and basic science investigators.

This simulation technology will in no way completely replace the need to conduct experimental testing using human and animal bone and soft tissue specimens
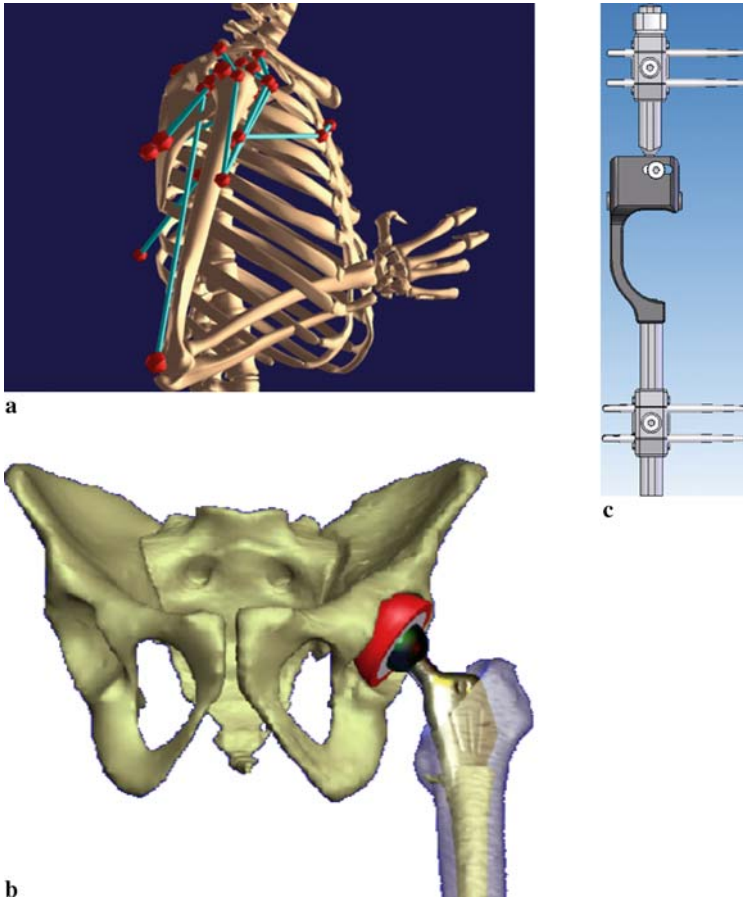
Figure 6a–c. Archived musculoskeletal joint and orthopaedic device models in VIMS database. **a** The skeletal joint model of human upper torso and arm system with key shoulder muscle attachments and orientation for biomechanical analysis. **b** The composite pelvis-proximal femur and hip-joint replacement prosthesis model used to study the effect of implant design and placement on joint range of motion in activities of daily living. **c** The EBI's Dimension (EBI, L.P., Parsippany, N.J.) external fixator model for distal forearm fracture immobilization and limited wrist movement. The model contains all key mechanical properties of the device including joint motion and pin placement to simulate fracture reduction and wrist continuous passive of motion

mounted on universal testing machines or custom-made joint simulators. Any time-related simulation on material fatigue failure or tissue growth and remodelling will require bench testing and animal experiments. The results generated from all of these experimental studies, experimental or theoretical, will rely on controlled clinical studies to validate their relevance and efficacy. What the simulation software, VIMS, can offer is to provide a generic database for comparative study purpose among the normal and patient population. In individual patients, specific models can be gen-

erated using innovative scaling techniques to provide unprecedented information to assist physicians and surgeons to optimize treatment and minimize risk.

Several computational algorithms, robust model library, and databases are integrated into the VIMS software platform on a SGi super computer main frame under the Unix operating system. All of the independent analysis components of the software are accessible through a single graphical user interface (GUI). This software package could be modified to fit the X-Windows/OpenGL environment. The users get the access to the VIMS database and search through the model library to select the desirable musculoskeletal region and the orthopaedic implant or device for the intended simulation and analysis. The kinematic data of the anatomic system involved in activities of daily living or sports activities can be adapted from the literature or measured to serve as the input data for biomechanical analysis on the generic models. The analysis results will be graphically presented and animated using the VisLab software (EAI, Ames, Iowa) or other commercial software and utility programs in the public domain. Although this utility software plus the VisModel package are no longer being served by the commercial firm, other equivalent commercial or free software can provide the same effect on a PC-based operating system for the VIMS to gain acceptance in the community.

This integrated simulation system will make the learning of functional anatomy easier and create a virtual laboratory environment for biomechanical analysis of musculoskeletal system among investigators with similar interest. Such networking will expand the scope and utility of this bioengineering specialty without relying on the use of animals or cadaver specimens with no restrictions on loading conditions. This broad-based technology will make the development and testing process of orthopaedic implants and devices more efficient and cost-effective while improving their clinical performance and reliability. Such technology is expected to make biomechanics competitive in landing government and foundation research funding as well as attracting industrial developmental contracts. Finally, the development of biomechanically justified preoperative planning strategy and the associated execution procedures guided by an intraoperative navigation system form the foundation of computer-aided orthopaedic surgery (CAOS). Another potential area of benefit is the computer-aided rehabilitation (CAR).

Examples of Bone Biomechanical Analysis Using Imaging and Simulation Technology

The applications of bio-imaging and VIMS simulation technology on bone structural and biomechanical analysis to date have been limited by the availability of models and the ability to incorporate soft tissue structures in the system; however, several examples are presented here to demonstrate the unlimited potential of this technology in a virtual laboratory environment to conduct biomechanical analyses not possible in the past. These analyses also help to demonstrate that the technology introduced here is not and should not be regarded as merely a graphic-based tool for visualization purpose alone.

Hip Joint Contact Pressure in Activities of Daily Living

Intrinsic pathomechanical changes in articular cartilage and subchondral bone depend upon local stress levels rather than global joint loading. To estimate the acetabulam and femoral head contact area and pressure distribution under daily activities is essential in predicting joint disease progression, patient management and pre-treatment planning in patients at different stages of osteonecrosis. This loading data provides the biomechanical rationale for femoral head subchondral bone collapse prevention and the selection of an effective method of reconstruction for varying degrees of osteonecrotic involvement. In-vitro studies to quantify contact pressure of the hip joint have been performed in limited loading conditions. Numerical simulation technique and a radiograph-based joint model, combined with measured joint loading data in living subjects with instrumented prosthesis, would be ideal for population-based studies as well as for analyzing individual patients. The purpose of this study was to use the Discrete Element Analysis (DEA; Schuind et al. 1995; Yoshida et al. 2005) technique on a realistic joint model to predict hip joint contact area and pressure distribution based on the in vivo joint motion and force data during activities of daily living (ADL; Yoshida et al. 2005). Simulation software was used to visualize the analysis results together with the model during ADL.

By assuming a spherical shape of the femoral head, a geometrical model was created from an anteroposterior (AP) radiograph of a subject's hip joint (Genda et al. 2001). To obtain the acetabular potential contact area, the radiographic contour line of the femoral head was digitized and the radius and centre of the best-fit circle were calculated using the acetabular sourcil line and a least-squares-fit method. Anterior and posterior edges of the acetabulum were then digitized on the radiograph. The approximate joint surface of contact on the acetabulum was divided into approximately 4000 rectangular mesh elements. The joint surface was assumed to be congruent. The shape of the corresponding femoral head and neck were adapted from an existing proximal femur model with matching head diameter.

At the centre of each mesh element, one compressive spring was placed normal to the opposing mesh of the femoral head surface. The stiffness property of the linear springs was determined from the cartilage Young's modules of 11.85 MPa (Kempson et al. 1980), Poisson ratio of 0.45 (Blankevoort 1991) and thickness of 2.66 mm (Athanasiou et al. 1994). Since the majority of the joint deformation under load occurs in the acetabulum and femoral head cartilage, the underlying subchondral bone structures were assumed to be rigid. In the DEA technique, small deformation was assumed and the system of equilibrium equations was derived using the minimum strain energy principle (Schuind et al. 1996; Genda et al. 2001). The rigid body displacement field provided the deformation of the springs, which approximated the joint contact area and pressure. Hip joint motion and joint contact forces during ADL were taken from Bergmann et al. (1993), which were based on the in vivo measurements in patients with instrumented hip replacement prosthesis. The graphic animation feature of the simulation software, Virtual Interactive Musculoskeletal System (VIMS), was used to display the analysis results for visualization purposes. The contact area and pressure on the femoral head were identical to that on the acetabulum

based on the action-and-reaction principle; however, the location of the contact area on the head would change due to the relative position of the femur with regard to the pelvis during activity.
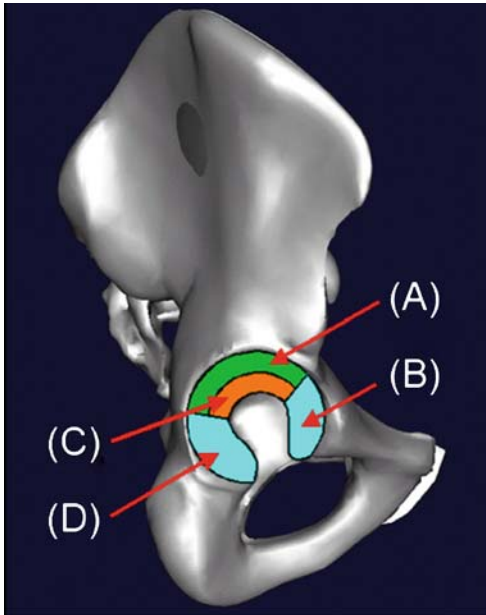
Figure 7. Hip-joint contact area location defined on the surface of the acetabulum. *A* Lateral roof. *B* Anterior horn. *C* Medial roof. *D* Posterior horn
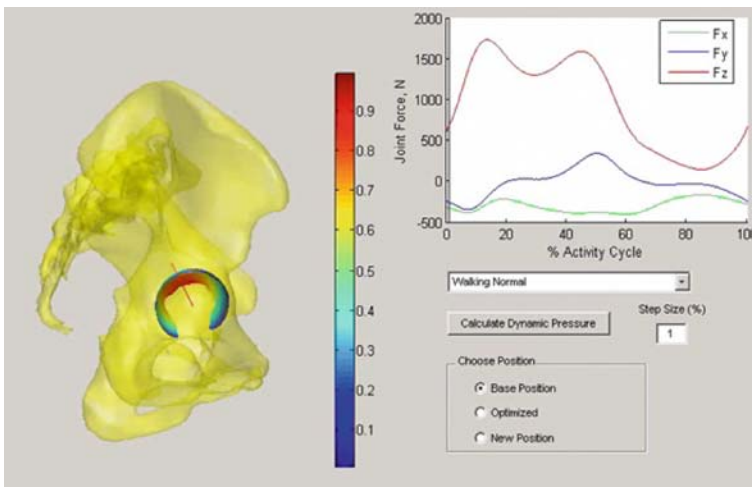
Figure 8. Hip-joint contact force, area and pressure distribution during normal gait. The model and analysis illustrated here allow variation of load and acetabulum orientation to minimize contact pressure and maximize contact area in peri-acetabular osteotomy planning
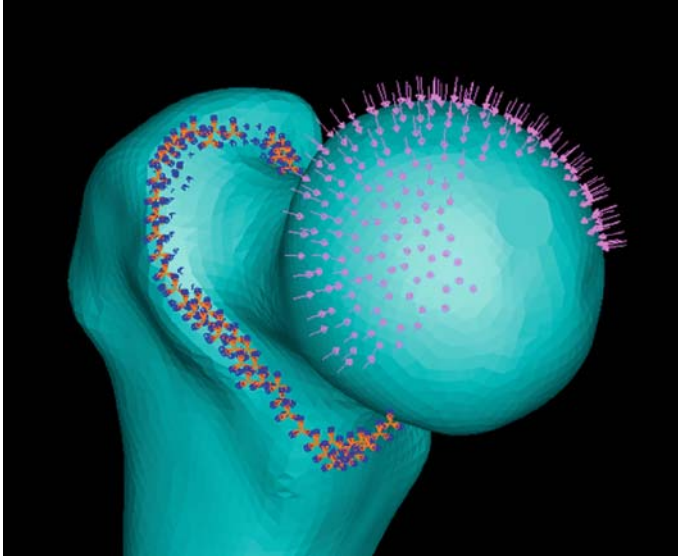
Figure 9. Femoral-head FEM model with inverted contact pressure from the acetabulum at the loading condition to predict bone collapse due to osteonecrosis condition and the reconstruction effect using the Eigenvalue buckling analysis algorithm in ABAQUS software

The acetabulum available contact area was divided into four regions to describe the peak pressure location (Fig. 7). In normal walking, the maximum contact pressure was relatively low due to the large area of joint contact throughout the gait cycle (Fig. 8). The magnitude and occurrence of the peak contact pressure coincided with that of the ground reaction force during gait cycle for different walking speeds. In stair walking, the peak pressure going upstairs (5.71 MPa) was higher than that going downstairs (3.77 MPa), although the measured joint contact force magnitudes were in opposite order. During the closed kinetic chain activity, the hip peak con-

Table 1. Hip joint peak contact pressure (location on the acetabulum surface) and contact area during activities of daily living, and the activity cycle locations

Activities of daily living	Peak pressure (Mpa)	Contact area (% of total area)	Activity cycle (%)
Fast walking	3.28 (Lateral roof)	78.7	12.5
Normal walking	3.26 (Lateral roof)	76.3	16.5
Slow walking	2.87 (Lateral roof)	81.2	16.0
Standing up	8.97 (Posterior horn)	19.7	35.0
Sitting down	9.36 (Posterior horn)	17.6	50.5
Knee bending	3.65 (Posterior horn)	51.6	53.0
Going upstairs	5.71 (Lateral roof)	52.1	11.0
Going downstairs	3.77 (Lateral roof)	80.6	55.0

tact pressure was moderate (3.65 MPa). The highest joint contact pressure occurred during sitting down on a chair (9.36 MPa) or standing up from it (8.97 MPa), due mainly to the small contact area at the edge of the posterior horn of the acetabulum. The peak pressure, the contact area, the activity cycle percentage and the joint contact force data of all ADL are given in Table 1. The pressure distribution on the femoral head was the reverse of that on the acetabulum (Fig. 9). The area of contact on the femoral head varies significantly in different activities.

Cortical Defect: A Model To Study Bone Repair and Remodelling

Several mechanistic theories have been developed to describe bone modelling and re-modelling to describe bone adaptation mechanisms; however, there is a lack of well-formed experimental models with minimal co-morbidity effects to validate these theories. The cortical defect healing in intact long bone is not yet well understood. In addition, the repair process seemed to follow a unique pathway (Chao et al. 1998), and such process often remains incomplete with no effect on long bone structural strength (Claes 2002). It was propose that cortical-defect repair follow a two-phase process. The initial phase is marked by an angiogenic response, characterized by microvascular invasion into the defect area followed by an intramembranous ossification process. The second phase is related to remodelling by transforming the woven bone into cortical bone. We hypothesized that the deformation gradient around the defect has a direct effect on vascular network and woven bone formation during the repair phase. In the remodelling phase, we assumed that bone material property and morphology are regulated by minimizing the strain energy gradient in bone

a   b
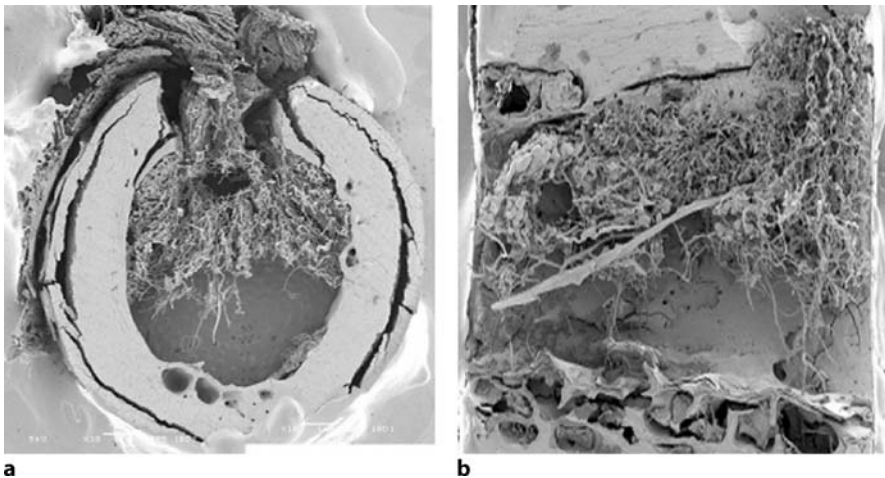
Figure 10. The SEM images of cortical defect healing 1 week after surgery in a canine tibia. Dense vascular network formation adjacent to the defect corner region corresponds with greatest strain energy gradient. **a** Cross-section at the cortical defect corner. **b** Longitudinal section across the defect
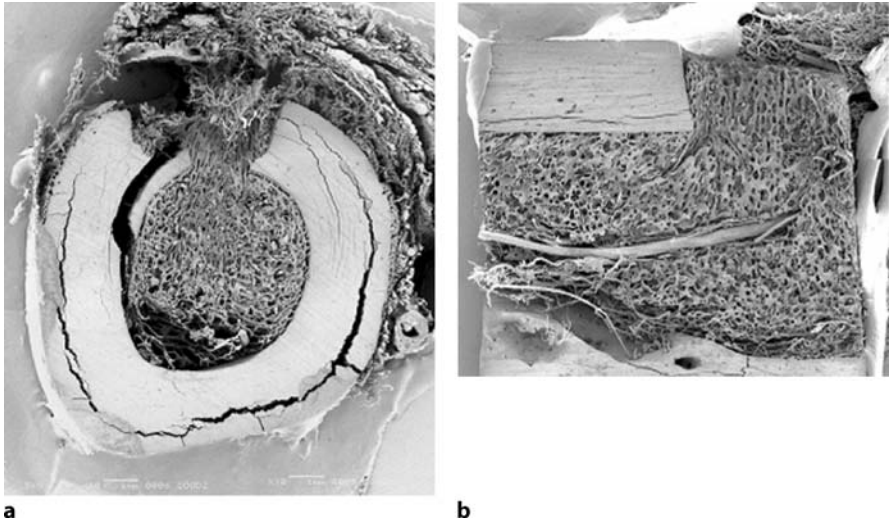
Figure 11. The SEM images of cortical defect healing 2 weeks after surgery. Dense woven bone formation following the vascular network orientation. The defect corner region corresponds to greatest strain energy gradient. **a** Cross-section at the cortical defect corner. **b** Longitudinal section across the defect
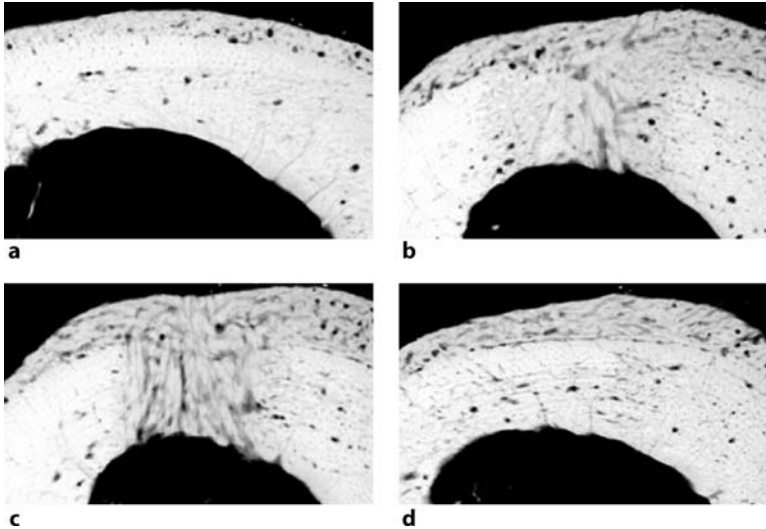
Figure 12. The microradiographs of normal cortical bone defect healing 16 weeks after surgery. **a** Intact cortex 5 mm away from defect (note the periosteal new bone formation). **b** Bone healing at the edge of the defect (note that the new bone in the defect area is less dense compared with that in the cortex). **c** Healing at the defect mid-section (note that the new bone in the defect is less dense than that at the defect edge and the periosteal new bone is most prominent). **d** Intact bone at the defect edge (note that its periosteal new bone is more than that at 5 mm away from the defect). The formation of periosteal new bone provides an alternative means to recover the cortex's structural strength and stiffness

around the defect while attempting to recover bone structural strength measured by the sectional modulus of the tubular structure. This study was to investigate the proposed defect repair and remodel regulating mechanisms using an animal model (canine with mid-tibia cortical defect) and a corresponding numerical simulation model (FEM; Elias et al. 2000; Chao 2005).

Fourteen skeletally matured adult male canines were used for this study. Unilateral longitudinal rectangular cortical bone defects were created in the antero-medial surface of the mid-diaphysis of the tibia. Defect length was equal to the tibial outer diameter (1 OD) and the defect width was 0.25 OD. One dog each was killed 1 and 2 weeks after surgery for microvascular analysis. The remaining 12 dogs were killed 6 each at 4 and 16 weeks, respectively. A vascular corrosion casting method was used for the microvascular analysis. The specimens were coated gold for SEM study. Routine microradiographic biomechanical and histological analyses were performed for the 16-week group specimens.

A mid-diaphysis length of 5 OD was used for the analysis. Identical defect was created in the anterior-medial bone surface. Twenty-node reduced-integration brick elements were used in each FEM model. The transversely isotropic properties of the human cortical bone were used for the engineering constants. The defect had the same transversely isotropic material properties and only the elastic modules were changed
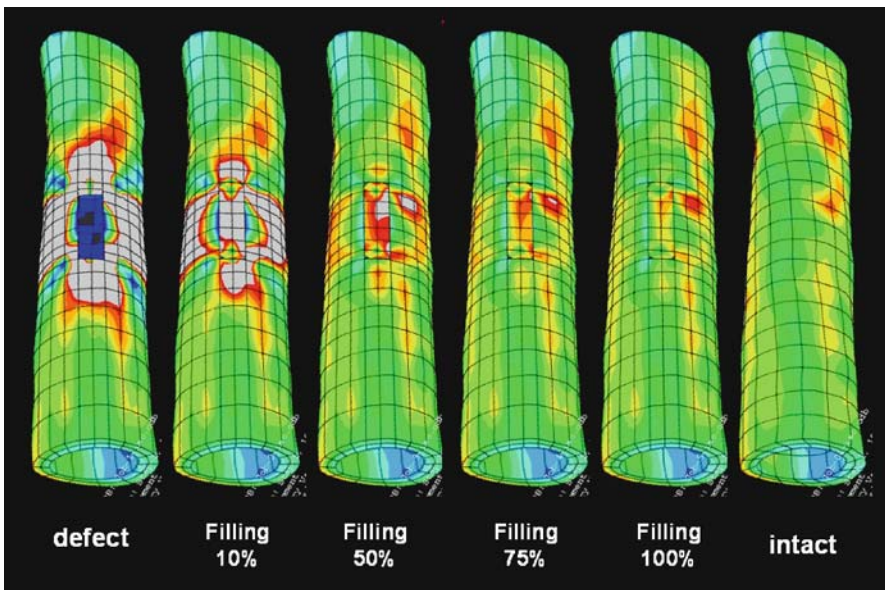
Figure 13. The strain energy density (SED) plot of the cortical bone around the rectangular defect of simulated healing stages of 0, 10, 50, 75 and 100% when compared with the intact cortex. This simulated healing was not observed in the animal experiment, which may suggest a different bone repair and remodelling regulatory mechanism based on both the tissue healing and biomechanical criteria

to simulate the healing stages. The distal end was rigidly fixed and the proximal edge had coupled constraint under torsional load. ABAQUS CAE (Hibbitt, Karlsson and Sorensen, Pawtucket, Rhode Island) was used to create the FEM models for analysis and post-process the results.

There was dense microvascular formation at 1 week (Fig. 10) which was transformed into woven bone in 2 weeks (Fig. 11). Capillaries formed from the medullary canal to the bone defect where the deformation gradient was maximal. At 16 weeks, the torsional strength was completely recovered as compared with the intact bone but with entirely different morphological architecture (Fig. 12). The stain energy density was distributed equally in the intact model; however, that of the defect model was increased dramatically in the surrounding of the defect part in comparison with that of the intact model (Fig. 13). The strain energy density surrounding the defect and at its corners were decreased significantly by the repair process. According to the increasing material properties of the repair tissues, the strain energy density decreased gradually around the defects. The torsional load of 1000 Nmm was applied and the torsional stiffness was calculated by dividing the torsional load by the rotational displacement, which also incorporated the "open section" effect. The torsional stiffness of the intact model at the defect centre section was 0.248, whereas the defect model with no repair was 0.198. Under varying degrees of repair and remodelling at 10, 50 and 75% of defect recover (only on material modulus), the corresponding torsional stiffness values were increased to 0.238, 0.239 and 0.239, respectively (Chao et al. 2005).

Femoral Head Collapse and Reconstruction in Avascular Necrosis

Estimation of the hip joint contact pressure during activities of daily living (ADL) is useful for both preoperative planning and postoperative rehabilitation in different conditions that lead to osteoarthritis. Avascular necrosis (AVN) or osteonecrosis (ON) of the femoral head is one of those conditions, and it is a relentless process that leads to articular surface collapse (Volokh et al. 2006). The ideal treatment should aim at the arrest of the progression of the disease in the pre-collapse stage; therefore, in the management of the pre-collapse stage, appropriate structural reinforcement of the femoral head is essential and the development of a method for the prediction of the head failure is desirable. Careful biomechanical analysis using computer simulation can help rationalize the development of this method and optimize the head reinforcement reconstructive method based on individualized AVN conditions. The purpose of the present study was to reveal the biomechanical rationale for predicting failure of the femoral head at the early stages of AVN. It was hypothesized, particularly, that the loss of the mass density and stiffness of the bone during necrosis development led to an inability of the cortical shell structure due to failure of the cancellous bone responsible for supporting the system exposed to high femoral head loading. The well-known mechanical concept of shell structure buckling can cause femoral head collapse. Such a scenario immediately rationalizes the need to reconstruct the femoral head using biostructural augmentation techniques.

Computer analysis of the hip joint included two stages. At the first stage, the shapes of the femoral head and the acetabulum were created from the Visible Human data set (Spitzer et al. 1996) and the potential contact area for an individual was established from his/her anteroposterior radiograph data (Genda et al. 2001). The cartilage between the acetabulum and the femoral head was mimicked by 4000 "equivalent" unilateral springs. In order to find the joint pressure distribution, the acetabulum and the femoral head were assumed to be rigid bodies. The loads at the joint were chosen as the hip contact forces during ADL. The pressure distribution was obtained by using the discrete element analysis (DEA; Genda et al. 2001; Yoshida et al. 2005). At the second stage, the hip pressure obtained from the DEA was inverted to a distributed load on the femoral head for the subsequent finite element (FE) analysis (Fig. 14).

The spatial finite element model used continuum brick elements for the cancellous bone and thin shell elements for the cortical bone. The nodal points of the contacting brick and shell elements were properly adjusted. The femoral head was rigidly fixed at the plane separating it from the femoral neck. The necrotic area was considered as a cone with the base angle of $2\pi/3$ radian (Brown, et al. 1981). The ABAQUS software was utilized for the Eigenvalue Buckling (instability) Analysis (EBA) of the cortical shell under the normal and necrotic cancellous bone foundation (Fig. 15).

The normal walking contact pressure calculated from DEA, and varying from 0 to 3 MPa over the contact area, was used as the "initial" load for the buckling analysis of the normal and necrotic femoral heads. Isotropy was assumed for both cancellous
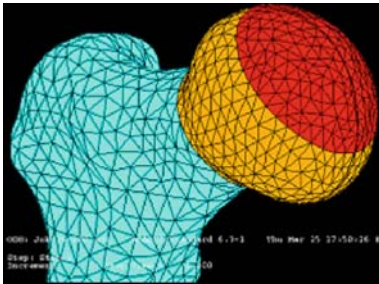
Figure 14. The 3D finite element analysis model of the femoral head using a shell structure with cortical bone covering the surface and the cancellous bone filling the inner cavity space similar to a positive pressure for external loading requirements of the femoral head
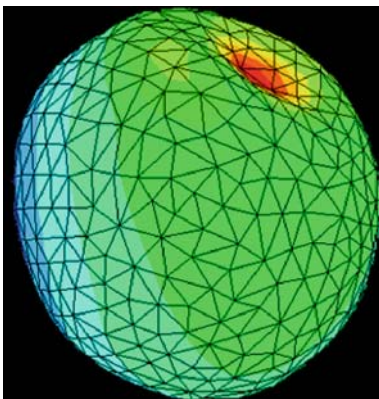
Figure 15. Using the linear Eigenvalue buckling analysis algorithm to predict the femoral head collapse under defective cortical and cancellous bone property due to osteonecrosis effect. This figure provides the estimated lowest mode of structure buckling failure under the critical pressure profile applied based on the activities of daily living data
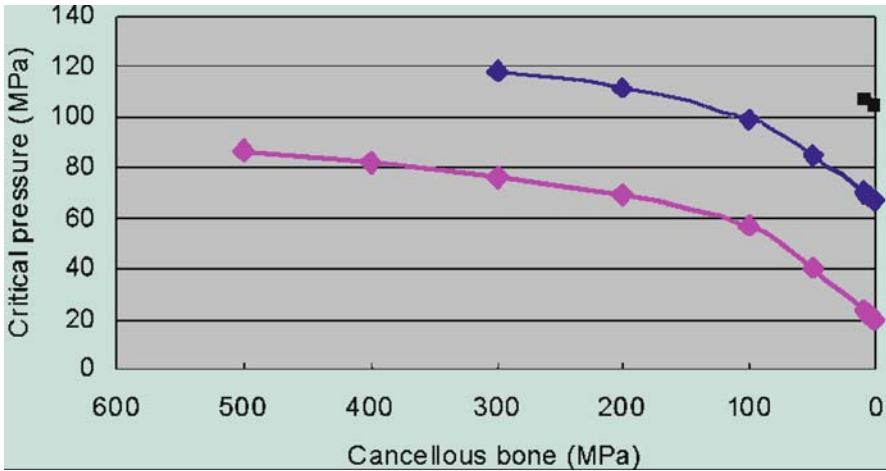
Figure 16. The femoral head model collapse critical pressure (using the peak pressure of the profile) resulted from the Eigenvalue buckling analysis based on varying cancellous bone yielding stress estimate due to osteonecrosis involvement and the assumed cortical bone yield stresses: $\sigma_y = 10\,\text{GPa}$; $\sigma_y = 5\,\text{GPa}$; $\sigma_y = 1\,\text{GPa}$

and cortical bones and the Poisson ratio was chosen to be 0.25 for the cortical and 0.3 for the cancellous bone in all simulations. The critical pressure obtained from the EBA is a multiplication factor for the "initial" load to become critical. Bone material property affected by AVN was estimated by adapting different Young's moduli for either the cancellous or the cortical bones.
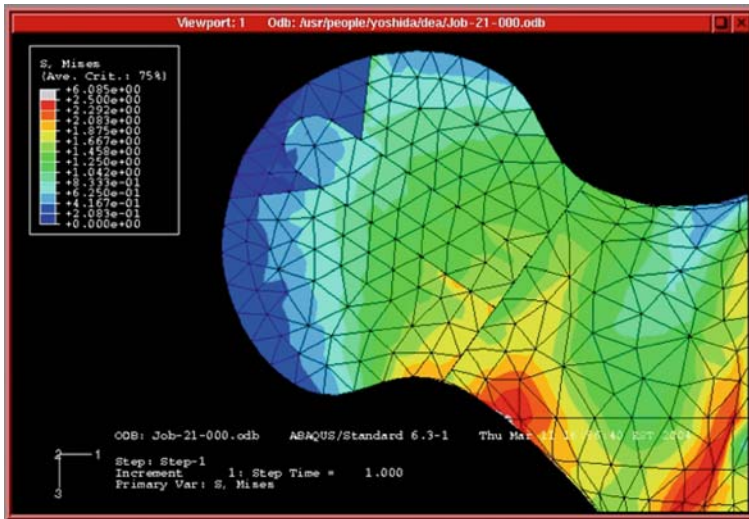
Figure 17. The effect of bio-structural augmentation using allograft bone screw and osteoinductive material to reconstruct the osteonecrotic area. Bone collapse could be effectively avoided if the bone screw and the interfacing cancellous bone are integrated, regenerated and remodelled

A. Osteoinductive Material

B. 'Support Bone Screws'

C. Core Decompression Paths
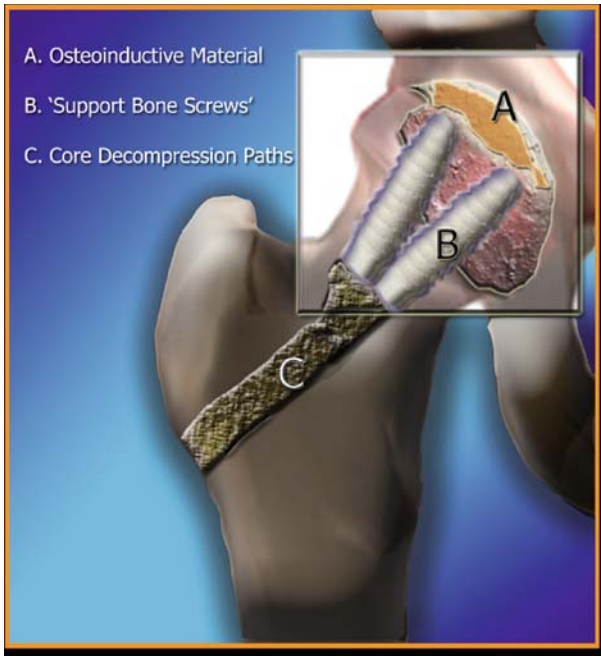
Figure 18. The concept of the bio-structural augmentation method to reconstruct the femoral head affected by osteonecrosis (adapted from Volokh, et al. 2006). The size, number and location of the bone screws is determined using the Eigenvalue buckling analysis assuming that the head is a composite shell structure

Two EBAs were performed under the AVN conditions of degrading elastic properties of the femoral head. Firstly, the Young modulus of the cortical shell was chosen to be equal 1.0 GPa and the critical pressure was computed for the varying Young modulus of the cancellous bone. Secondly, the Young modulus of the cancellous bone was chosen to be 1.0 MPa and the critical pressure was computed for the varying Young modulus of the cortical shell. When the normal femoral head was considered where the Young modulus was chosen to be equal 10.0 and 1.0 GPa for the cortical and cancellous bone accordingly, negative critical pressure was obtained (Fig. 16). A biostructural reconstruction method using allograft bone screws and demineralized bone matrix (DBM) reinforcement was introduced (Fig. 17). This reconstruction not only reduces the collapse risk; the DBM will allow bone regeneration to reconstitute the subchondral bone structure as illustrated in Fig. 18.

Discussion and Future Perspectives

Bio-imaging technology has helped musculoskeletal biomechanical studies by providing reliable methods to estimate connective tissues composition, physical properties and healing or remodelling progression. Furthermore, it offers the unique opportunity to reconstruct anatomically realistic and biomechanically effective models, including both soft and hard tissues for research investigations, studying functional anatomy, surgical planning, intraoperative monitoring and many other applications. These models allow computer-aided analysis of bone and joint system

in a virtual-reality environment. On the other hand, image-based bone structural and biomechanical analyses also expand the bio-imaging field beyond its traditional diagnostic and interventional roles in medicine. With the aid of functional assessment before and after surgical or non-operative management of patients with injured or diseased bone and joint systems, bio-imaging technology can be viewed as a tool to provide effective pre-treatment planning to improve clinical treatment outcome.

To accomplish these goals, one needs an effective and accurate means to produce patient-specific musculoskeletal joint models. Using the raw CT or MRI data of the patient would be extremely time-consuming as well as costly; therefore, innovative methods of using limited imaging data from the patient as a guide combined with archived model data pool through a scaling approach would seem more attractive. Parametric and non-parametric scaling techniques have been tried with disappointing results due to the complexity of the bone deformity and the disease related joint changes involved. A feature-based method taking into account anatomic location, skeletal shape characteristics, deformity type, reconstructive method being considered, patient demographic information, etc., would be the ideal way of constructing patient-specific models. Although a robust model database and an accurate scaling method would be highly desirable, biomechanical results to be produced from such analysis will still be approximate in nature since many assumptions are necessary in the solution process while the problem itself is often indeterminate; hence, no one really knows what the real in vivo results should be. However, the objective for the model-based analysis is to produce comparative results for the purpose of rationalizing the surgical procedure, as well as optimizing the implant selection and placement, which do not require the exact biomechanical solution if it ever exists.

Under dynamic function, limb movements are being monitored using various motion analysis systems with surface markers placed on the patient's body; however, no information can be extracted from these data on the underlying skeletal and soft tissue structure for biomechanical analysis. There is no bio-imaging technique available at the present time to provide such information on a reliable and cost-effective way. Although cineradiography is being utilized, the image resolution is inadequate to provide subtle information on the normal, diseased or reconstructed joint function. Better imaging techniques and data processing software, including data segmentation and object reconstruction, are needed. Low radiation exposure and acceptable time and cost involved for data capturing and reduction are other developmental considerations. These new technologies must be able to handle metals, synthetic materials, bone as well as soft tissue with acceptable data accuracy and consistency.

Model reconstruction and biomechanical analysis results should be validated using mechanical simulators, parametric analysis and clinical trial follow-up studies. Although exact results are nearly impossible to predict, limited data extracted from patients with instrumented implants should be used to assess the model and the analysis method in predicting the joint loading results theoretically. Using data generated from the model according to a systematic trend of parameter variation could produce qualitative information to evaluate the efficacy and reliability of the VIMS soft-

ware for biomechanical analysis. Limited cadaver experiments conducted on special testing machines or custom-made mechanical simulators with precisely controlled loading condition and joint movement of the musculoskeletal system would produce valuable information to assess the acceptability of the model-based analytical data. Patient functional data before and after treatment based on the preoperative planning criteria should be evaluated in the light of the historical data reported in the literature. Through these validation studies, the image-based model and the computer-aided simulation and analysis technology can be substantiated and further improved, if necessary, to establish the credibility of image-based biomechanical analysis in a simulation environment.

Although the technologies discussed herewith are far less expensive and easier to use when compared with those in other biotechnology fields, the need to share the models and the analysis tools through close collaboration must be emphasized. Although biomechanical analysis will remain in the limelight of the medical arena, those who are engaged in such esoteric effort will always be regarded as the minority. The VIMS technology shall provide the tool and work platform to foster such collaborative effort and thus benefit medicine, surgery, and biomedical engineering alike. If the simulation technology introduced in this chapter is further improved by new imaging techniques, biomechanicians working in the musculoskeletal field will take on a new role to advance musculoskeletal sciences and clinical care. In addition, these technologies should also benefit orthopaedic devices and rehabilitation equipment industries to optimize design, product quality control, application implementation and cost reduction.

Conclusion

Both bio-imaging and biomechanical analysis have a long and rewarding history in medical science and patient care. These two fields are mutually dependent and can cross-fertilize in a productive manner. When the specialists in these two fields are able to collaborate seamlessly, innovative diagnostic methods, interventional planning and post-treatment function monitoring can be developed and applied in an effective, reliable and affordable manner. The new and highly innovative technology of computer-aided and image-based biomechanical analysis (the VIMS technology) will no doubt provide the tools needed to generate new knowledge of musculoskeletal joint system function unknown or not available previously. It will also enhance its competitive edge in gaining funding support from both the medical and engineering fields. This technology and its analysis capability can also benefit other medical specialty areas in research, education and clinical patient care. It is hoped that the image-based biomechanical analysis can set the standard on how to utilize engineering principles and technical know-how to improve medical care quality and reduce the overall social service cost – the underpinning pre-requisite of the bioengineering profession.

References

Athanasiou KA, Agarwal A, Dzida FJ (1994) Comparative study of the intrinsic mechanical properties of the human acetabular and femoral head cartilage. J Orthop Res 12:340–349

Bergmann G, Graichen F, Rohlmann A (1993) Hip joint loading during walking and running, measured in two patients. J Biomech 26:969-990

Blankevoort L, Kuiper JH, Huiskes R, Grootenboer HJ (1991) Articular contact in a three-dimensional model of the knee. J Biomech 24:1019–1031

Brown TD, Way ME and Ferguson AB (1981) Mechanical characteristics of bone in femoral capital aseptic necrosis. Clin. Orthop. Relat. Res., 156, pp 240–247

Chao EY (2003) Graphic-based musculoskeletal model for biomechanical analysis and animation. J Med Eng Phys 4:3:1:687-699

Chao EYS, Inoue N, Elias JJ, Aro H (1998) Enhancement of fracture healing by mechanical and surgical intervention. Clin Orth Rel Res 355:S163–S178

Chao EYS, Yoshida H, Inoue N, Toda I, Ito K, Schneider E (2005) Cortical defect: a model to study bone repair and remodeling. Transactions of 51st Annual Meeting of Orthopaedic Research Society, Washington, DC

Claes L, Eckert-Hubner K, Augat P (2002) The effect of mechanical stability on local vascularization and tissue differentiation in callus healing. J Orthop Res 20:1099–1105

Elias JJ, Frassica FJ, Chao EYS (2000) The open section effect in a long bone with a longitudinal defect: a theoretical modeling study. J Biomech 33:1517-1522

Genda E, Iwasaki N, Li GA, MacWilliams BA, Barrance PJ, Chao EYS (2001) Normal hip joint contact pressure distribution in single-leg standing: effect of gender and anatomic parameters. J Biomech 34:895–905

Inoue N (1987) Mechanical properties of cancellous bone: dependence of strength and elastic modulus on trabecular orientation. J Kyoto Pref Univ Med 96:847–865

Kempson GE (1980) The joints and synovial fluid. Academic Press, New York, pp 177–238

Markel MD, Wikenheiser MA, Chao EYS (1990) A study of fracture callus material properties: relationship to the torsional strength of bone. J Orthop Res 8:843–850

Schuind F, Cooney WP, Linscheild RL, An KN, Chao EYS (1995) Force and pressure transmission through the normal wrist. A theoretical two-dimensional study in the posterioanterior plane. J Biomech 28: 587–601

Spitzer V, Ackerman MJ, Scherzinger AL, Whitlock D (1996) The visible human male: a technical report. J Am Med Inform Assoc 3:118-130

Volokh KY, Yoshida H, Leali A, Fetto JF, Chao EYS (2006) Prediction of femoral head collapse in osteonecrosis. J Biomech Eng 128:467–470

Yoshida H, Kitagawa M, Faust A, Wilckens J, Fetto JF, Chao EYS (2005) 3-D hip contact area and pressure distribution in activities of daily living. Transactions of 51st Annual Meeting of Orthopaedic Research Society, Washington, DC

Imaging Technologies for Orthopaedic Visualization and Simulation

Pheng Ann Heng

Department of Computer Science and Engineering and Shun Hing Institute of Advanced Engineering, The Chinese University of Hong Kong, Shatin, N.T., Hong Kong, China
e-mail: pheng@cse.cuhk.edu.hk

Abstract

Computerized techniques have long been applied in the field of biomedical imaging. In the past, the heavy burden induced by medical-related imaging or visualization process was always coupled with bulky and expensive workstation or server-grade computer. The recent advancement in graphics processing unit has unleashed the personal computer (PC) as the major platform for medical image processing, analysis, visualization as well as surgical simulation. In light of this, our group has worked out different high-performance computing techniques exploiting affordable PC graphics boards. These techniques include advancement in segmentation, rendering, deformation as well as surgical simulation. In this chapter, we discuss some of our advancements in this area with applications to biomedical imaging.

We discuss our experience in performing efficient tissue identification in the area of interest in different types of medical image. In particular, the latest advances in the processing of Chinese Visible Human (CVH) data are described. Different tissue can be identified within the images through semi-automatic methods. Based on the tissue-tagged images, we can further reconstruct structural models which represent different organs or tissues. The structural modelling process involves mesh generation and the development of appropriate mathematical models for simulating various operations being applied on the structures. In this part, we have proposed hybrid finite element models (FEM) which are computational efficient for processing of soft tissue deformation and other surgical procedure simulation. To demonstrate the practical application of our techniques, we also discuss our recent research and development process in various virtual reality (VR) surgical simulators, including virtual orthopaedic training and virtual knee arthroscopy.

Imaging Modalities

Computed tomography (CT), magnetic resonance imaging (MRI) and ultrasound (US) are common medical imaging modalities. Different modalities provide different form of anatomical or functional information. Although these imaging techniques can acquire in vivo patient data, true colour dissection anatomical details cannot be
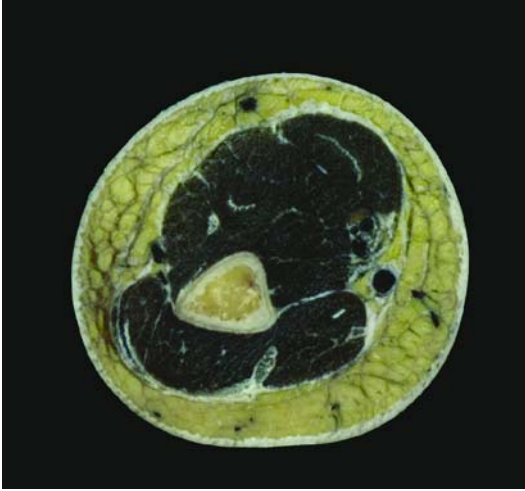
Figure 1. An original slice from the Chinese Visible Human (CVH) data is shown

obtained. Visible Human Project founded in 1983 (Ackerman 1998) by National Library of Medicine in United States has provided a revolutionary way of presenting human data, the true dissection anatomical data. The emergence of the latest Chinese Visible Human (Zhang et al. 2003, 2004) data sets feature another milestone in the true colour anatomical imaging.

The first CVH data set was collected in 2002, by the Third Military Medical University, Chongqing, China. The latest CVH data set consists of 18200 serial cross-sectional colour digital images. The resolution of each sectional image is 4064×2704 with 48 bits per pixel (Fig. 1). The whole data set is acquired at 0.1 mm intervals. Compared with different modalities, such as MRI or CT, such a high-resolution data can provide fruitful anatomical detail which can benefit medial imaging analysis, human anatomy education as well as surgical simulation. On the other hand, the new data sets also impose new challenges to the imaging research community. Tissue identification is one of these challenges. The data size of CVH is large compared with other common medical imaging modalities. Efficient storage, processing and rendering of the data set is another important problem to be tackled. We discuss these issues in the following sections.

Tissue Identification

Based on the raw image obtained from any one of the image modalities, one would have to distinguish different tissues or organs. In computer science terminology, the act of dividing or partitioning out of an image is called segmentation. For a set of subsequent image slices, after one of the slices is segmented, the contour front can be used in propagating on subsequent slices. We call this technique tracking.

To identify different anatomical structures from the CVH volumetric data set, we make use of both manual and semi-automatic methods. Manual segmentation is a very labour-intensive task. Skin, fat, septum, bone, bone marrow, muscle, ligament,
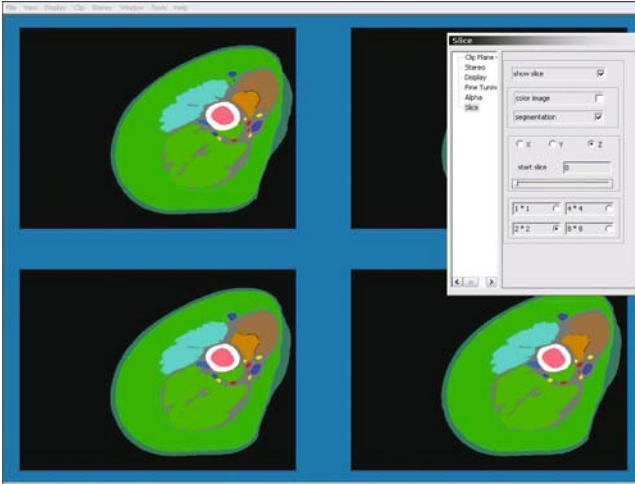
Figure 2. Manually segmented results are shown from a segmented CVH volume

nerve and blood vessels are scribbled by hand slice by slice (Fig. 2). Although medical professionals would find the result very acceptable, the progress can be slow. For the semi-automatic method, we have proposed a modified level set method (Qu et al. 2004) to deal with both segmentation and tracking.

The level set method, developed by Osher and Sethian (1988), is a zero equivalent surface method. The basic idea is to convert the track of a planar curve movement into the track of a three-dimensional surface movement. Although this conversion may complicate the solution, it exhibits many other advantages: parameter free representation, higher topological flexibility and ability to handle local deformations are its main strengths. These properties make the level set framework a suitable choice for segmenting tissue structures out of different imaging modalities.

Although the CVH data set brings more difficulties to segmentation methods when dealing with high-resolution information, on one hand, it brings convenience to the tracking-based serial images segmentation, on the other hand.

Our main idea is to incorporate the colour feature, the texture feature as well as the gradient feature within the image in augmenting the overall level-set-based tissue identification process. In this sense, a two-step scheme based on level-set segmentation and tracking is proposed herein.

Segmentation

In this step, we segment the first slice of a volumetric data (in form of a sequence of serial images). A speed function, which incorporates the gradient, texture and colour information, is introduced for the segmentation purpose. The user needs to lay the initial seed by simply clicking on the AOI.

$$F = K_I(x,\, y)(\varepsilon K + F_A) + \beta \frac{(\nabla c \cdot \nabla \phi)}{|\nabla \phi|} + \gamma(BPV)\,, \tag{1}$$

where εK is to prevent the sharp corner developing; K_I is defined as $e^{-|\nabla G_\sigma \cdot I(x,y)|}$; $\nabla c \cdot \nabla \phi$ proposed by Yezzi et al. (1997) is a pull-back stress dependent on the gradient; and BPV is to measure the texture feature.

The basic idea in constructing the speed term for segmentation is to make speed F tends to be zero when it is close to the boundary. According to our previously proposed model (Qu et al. 2004), BPV texture feature (Loone 1997) and gradient feature are incorporated into our speed function.

Tracking

The 0.1 mm inter-layer distance of CVH data makes the tracking possible and reliable for segmentation task. We also extended the speed model in (Qu et al. 2004) for the tracking problem. Due to the visual consistency constraint between two continuous layers, we can assume the transformation of edge between images I_n and I_{n+1} is between a narrow band with width δ. The following calculation is done entirely within the narrow band.

For the subsequent image slices, after the first segmentation step, the level-set segmentation can be initialized by evolving the result from the previous image, and propagates the front with a newly proposed speed function, which is designed for tracking.

$$F = KI_{n+1}(\varepsilon K + F_D) + \beta F_C . \tag{2}$$

$$F_D = Sig \cdot (I_n - I_{n+1})^2 , \quad F_C = Sig \cdot dist(C_n, C_{n+1}) . \tag{3}$$

$$Sig = Sign(dist(CID, C_+^n) - dist(CID, C_-^n)) . \tag{4}$$

We propose a new speed function to evolve the contour, from slice I_n to the next slice I_{n+1}. The segmentation result (i.e. the resultant contour) obtained in slice I_n can be exploited as the initial contour for slice I_{n+1}, and the front propagates under the speed function given in Eq. (2) which can attract the front moving towards the new AOI boundary. Here, the curvature term K is adopted to avoid the "swallowtail" during propagation. F_D is the cost function between the two slices I_n and I_{n+1}, which can be measured by the sum of square differences between the image intensities in a window, as shown in Fig. 3. Equation (3) tells how to decide the magnitude and the signal of F_D, where $+n$ and $-n$ indicate whether the pixels are outside or respectively,
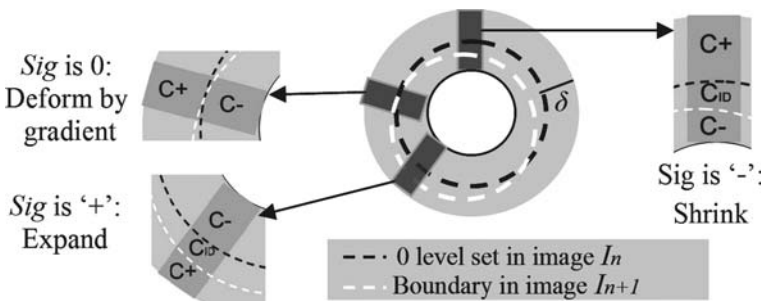
Figure 3. The design of the speed function for tracking is shown: value and signal
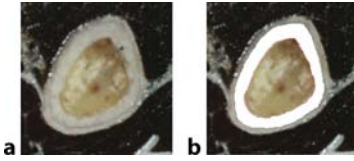
Figure 4. Level-set-based segmented bony tissue is shown

in slice I_n; C_+^n and C_-^n are the content model of these pixels in slice I_n. *ID* represents the pixels in the overlapped inhomogeneous areas (see Fig. 3). We note that F_D, convolved by KI_{n+1}, forces the front to move in the homogeneous area and to stop at the boundaries in I_{n+1}. The sign of F_D influences the curve to expand or shrink.

With this semi-automatic way of identifying tissues, different structures can be separated at a much faster pace. Figure 4 shows the segmentation of bony tissue in the upper limb region. Although we have not yet successfully identified all major tissues semi-automatically, there has been great progress. Manual and semi-automatic segmentation need not be performed separately. An integration of both methods can achieve better results in some cases. One of the possible approaches is to segment one particular organ in the first slice manually and then make use of the level-setbased tracking to extract the same organ in subsequent slices. This method is particularly useful when the organ boundary is not very clear but the slicing intervals are not very long. Having segmented the tissues, the next step is structural modelling.

Geometric Modelling

Having identified various tissues within the colour images, we can further generate the geometric models for representing individual organs and tissues. Modelling refers to the process of representing structural topology through a number of methods such as parametric representation, mathematical form or meshes. In surgical simulation applications, meshes are one of the most common modelling methods. Mesh, in computer graphics, is a network of connected nodes or vertices for representing structural models.

In general, we can roughly divide mesh models into surface representation and volume representation. Surface mesh refers to connected nodes bounding certain volume with no inner nodes. A list of connecting triangles or quadrilaterals is usually used in modelling surface meshes. Volume meshes bound certain volume region, but inner connecting nodes are included in the representation. Connected tetrahedrons or cubes are common form of representing volume meshes.

For one particular tissue structure, the choice of surface or volume representation depends on the tissue itself. In general, the operations being applied to the structure is the major concern. For instance, bony tissue is seldom cut in almost every normal situation. In such a case, we usually choose surface meshes to represent bone. On the other hand, soft tissues, such as muscle, fat and ligament, would be better represented

by volume meshes, because cutting or more vigorous topological changes are likely to happen in these tissues (Fig. 5).

The reconstruction of surface mesh is relatively simpler making use of a series of 2D contours within the medical image. We can use the Ganapathy and Dennehy (1982) method to model the surfaces. A typical correspondence problem in this method can be solved if each contour of every single slice can be identified by its two neighbouring tissues. Comparatively speaking, the reconstruction of volume mesh, likely in the form of tetrahedral mesh, is not as trivial as is the case in surface mesh reconstruction. Here, we only consider the case of tetrahedral mesh construction. Since the size and shape of the tetrahedral generated affect the performance later on tissue deformation or cutting being used in surgical simulators, the reconstruction process has to be designed carefully.

Traditionally, interval volume tetrahedralization (Nielson and Sung 1997) and 3D Delaunay tetrahedralization (Sullivan et al. 2005) are two major methods in creating tetrahedral mesh out of a volume. The number of tetrahedrons generated by the first method is usually too large. This would complicate the overall simulation process. Moreover, the shape of the tetrahedrons generated is not good (too sharp) in general. The second method can create well-shaped tetrahedrons; however, gaps may be introduced between the two generated meshes if multiple organs are extracted simultaneously.

In order to deal with these issues, we have developed a constrained tetrahedral mesh generation method (Yang et al. 2002). This algorithm can be applied in extracting human organs from the tissue-identified volume. Our method creates tetrahedral directly from the volume with no need to generate isosurfaces in advance. This can be regarded as an incremental insertion algorithm in the 3D Delaunay triangulation category. The algorithm involves two main steps: vertex placement and boundary-preserved Delaunay tetrahedralization.
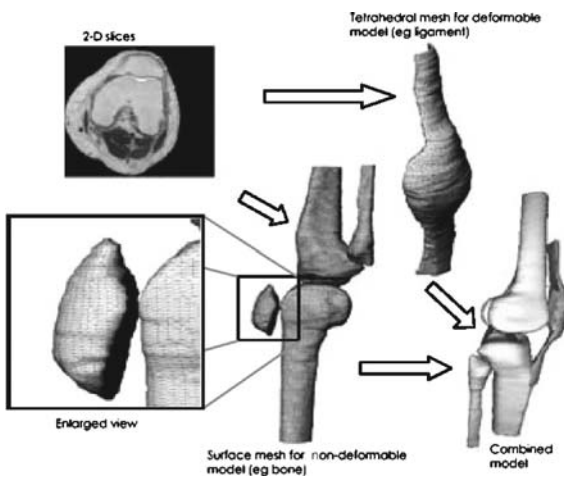
Figure 5. The generation of surface meshes (for non-deformable structures) and tetrahedral meshes (for deformable structures) from the slices of medical images is shown

Vertex Placement

Vertex placement is a process for placing vertices on a polyhedron common to three or more sides in order to facilitate the subsequent tetrahedralization. Two types of vertices, feature points (points that lie on the boundary) and Steiner points (inferior points), are inserted. The step can affect the density of the mesh and its conformation to the tissue boundaries.

Boundary-Preserved Delaunay Tetrahedralization

Boundary-preserved Delaunay tetrahedralization is a process for generating the tetrahedral mesh based on the feature points and Steiner points obtained in the previous step. All these points are used as the input for the 3D Delaunay algorithm. At every single time one new point is added and the tetrahedral mesh grows up gradually. After a new tetrahedron is added, in order to preserve the boundary positions between different structures, a flipping-based algorithm is integrated in order to restore tissue boundaries by a step called re-meshing.

The main advantage of our method is that many geometric details can be preserved while the size and shape of the tetrahedral can be kept well. This is particularly important for the finite element analysis (FEA) in surgical simulation (see below).

Surgical Simulation

To simulate surgical procedures in the virtual reality, many difficult issues have to be tackled. Realism of the physical simulation and real-time interactivity is somehow a trade-off (Delingette 1998). The most crucial computation processes in surgery simulation include soft tissue deformation, soft tissue cutting and collision detection. A well-balanced surgical simulation, which exhibits realism as well as interactivity, demands highly efficient algorithmic design and software implementation.

Soft Tissue Deformation

Carefully designed mathematical model is crucial for carrying out realistic soft tissue modelling (Bielser et al. 1999; Bielser and Gross 2000; Cotin et al. 2000; Mor and Kanade 2000). Finite element models (FEMs) are one of the most common used mathematical models used in dealing with soft tissue interaction; however, real-time deformation using FEM is quite a challenge problem since computation involved in FEM is quite intensive. In light of this, we have introduced two methods to lessen the computational burden in the FEM deformation process. The first one is to simplify the formulation of FEM and the second one is to shift several key computation modules from standard central processing unit (CPU) to the graphics processing unit (GPU; Wu and Heng 2004).

The simplification we have made to the FEM formulation is called hybrid FEM. The basic idea of this method is to divide the model into two regions, namely the operational region and the non-operational region (Fig. 6). Operational refers to the
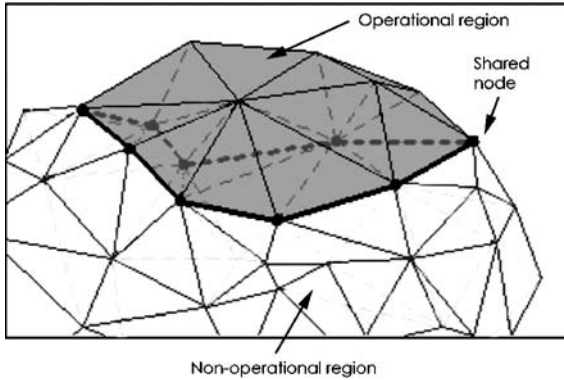
Figure 6. The hybrid model is shown

application of surgical operations. In other words, the operational region is for modelling pathological area on which operations will be done. The non-operational region simulates the area that is not likely to be modified by surgical tools. In this case, we have made an assumption here that topological changes within the surgical simulation should occur only in the operational region. Different mathematical models are designed to handle regions with different physical properties (Duck 1990). This strategic approach can balance the computational burden with the level of visual realism.

In particular, a complex FEM, which incorporates non-linear deformation and topological change, is used to simulate the operational region. On the contrary, a linear and topology fixed FEM is used for the non-operational region in order to accelerate the overall simulation efficiency. Based on such a configuration, additional boundary conditions can be introduced to both models through their shared vertices. Inferior vertices of the non-operational region can be regarded as duplicated vertices, and thus can be removed by a condensation process (Nielsen and Cotin 1996) during the actual simulation. As a result, the dimension of matrices in the FEA computation can be reduced, thus improving the ultimate simulation performance.

The GPU-based acceleration relates to the application of the programmable graphics hardware to compute certain numerical procedures. Vector-based computations are the most favourable processes for being accelerated under the GPU architecture. In the FEM computation, one of the main steps involves the use of the conjugate gradient solver, which is an algorithm for the numerical solution of particular systems of linear equations. Since the core component of this solver is the multiplication of sparse matrix and vector, the computation can be greatly accelerated in the programmable graphics architecture. By deploying the GPU in performing the core computation, the real-time FEM-based deformation has become feasible.

Soft Tissue Cutting

Within the operational region, soft tissue cutting is one of the most common surgical procedures to be simulated. An efficient cutting algorithm on the tetrahedrons

mesh is crucial for the interactivity of the surgery simulator. Our strategy in cutting tetrahedrons is based on a concept called minimal new-element creation, which is a method for generating as few new tetrahedrons as possible during every new cut (Sun et al. 2002).

Tetrahedrons are subdivided by tracking the intersection between the cutting tool and every tetrahedron. Such a subdivision process undergoes a number of steps. Firstly, we determine the initial intersection between the surface boundaries and the cutting tool. Once an intersection is detected, all intersected tetrahedrons are recorded. The intersection test is then propagated to all neighbouring tetrahedrons that share the intersected faces and edges. In this sense, any involved tetrahedrons can be detected promptly. Once the subdivision is completed, cut surfaces between these intersection points can be generated.

The visual update during the whole cutting process can affect the realism of simulation. In some cases, immediate visual feedback "on the fly" is mostly preferred. A simple way to handle the process is that we update the tetrahedron subdivision at certain time steps. We based this on the cutting result of the previous time instance to update the subdivision; however, this may lead to a dramatic increase in the total number of tetrahedrons during the simulation.

To ensure interactive visual feedback, progressive cutting (Hoppe 1996; Mor 2001) with temporary subdivision is one of the concepts being used in our subdivision process. In view of this, we subdivide a tetrahedron temporarily until it is cut completely, whereas those temporary tetrahedrons can be discarded after display. If the topology of the subdivided tetrahedron does not change along with the movement of the cutting tool, we can just update the position of the intersection points. On the other hand, if the topology does change, the temporarily subdivided tetrahedrons are deleted and the tetrahedron will undergo another subdivision again. Such an implementation can lower the latency between the user input and visual feedback. Moreover, the total number of tetrahedrons will increase moderately.

Virtual Orthopaedics Training System

Traditionally, high-quality rendering of huge medical data have to be performed at workstation or server-grade super computer. With the advance of novel graphics architecture, PC-based system is another evolving platform for the medical society to preview, interact and process the data. Exploiting the CVH data and innovative volume-rendering algorithms, we have developed a virtual anatomy system for orthopaedics training of the upper limb region. This is a pilot application of CVH data in interactive volume visualization as well.

In the system, we first perform tissue identification on the CVH volume data. Then, a volume-rendered visualization algorithm is used. Using voxel as the basic modelling unit, we can render the body directly. To improve the rendering performance, we have optimized the data set so that our application can be performed interactively on a single PC.

The user can make use of the mouse cursor to perform translational and rotational transformation on the volume data set (Fig. 7). Arbitrary cross-sectional
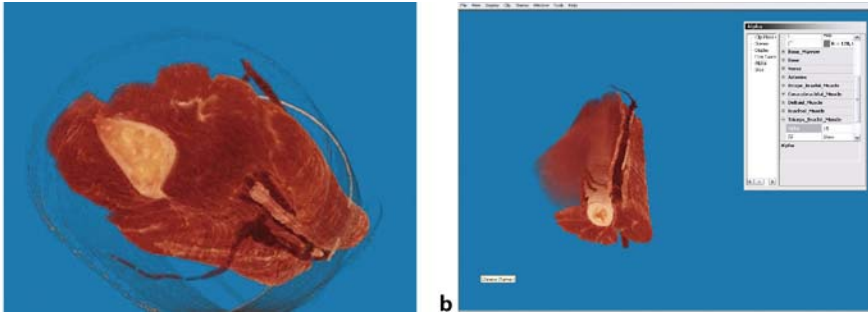
Figure 7. Muscular tissue is shown with different orientation and transparency
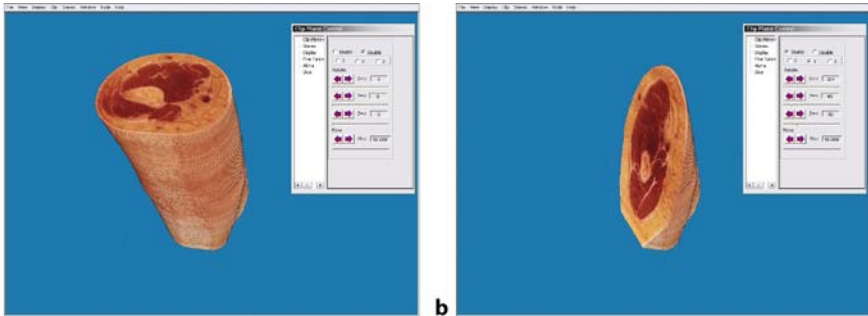
Figure 8. Arbitrary clip-plane can be added to the original volume. **a** An original volume rendered view of the upper limb model is shown. **b** A clipped view is shown

clip-plane can be added to the data visualization (Fig. 8). Users can add one single axis-aligned (i.e. aligned to x-, y- or z-axis) clip-plane to the volume, whereas the movement of the plane can be adjusted interactively. Skeletal tissue, muscular tissue, blood vessels and nerve, for example, can be visualized separately with adjustable transparency (Fig. 9). Moreover, the user can freely assign different pseudo-colour
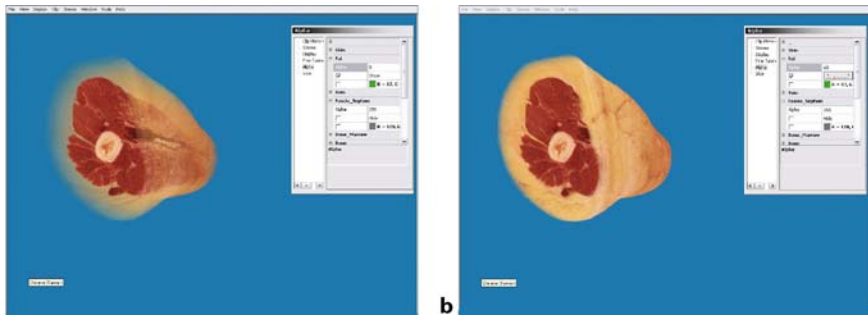
Figure 9. Transparency adjustment can be applied to the rendered volume. **a** Original volume-rendered shot. **b** A semi-opaque fatty tissue is visualized

to different tissue. The user-friendly interface can help medical professionals to comprehend the anatomical structure in depth.

Virtual Knee Arthroscopy

Minimally invasive surgery (MIS) relies on small incisions in the patient and makes use of endoscopic devices to carry out different types of operations which could only be done by open surgery in the past. Endoscopic surgery introduces less trauma, reduced pain and quicker patient convalescence, and its advantages are apparent; however, the hand-to-eye coordination in MIS requires extensive training so that the surgeons can be able to handle complex cases. Training on animals or plastic models cannot optimally deliver the realism of operations compared with that of real surgery. In light of this, virtual-reality (VR)-based training systems (Downes et al. 1998; Mabrey et al. 2002) provide another effective alternative to this issue, and VR surgical simulators are beneficial to both experienced surgeons and medical novices.

The virtual knee arthroscopy training system is one of the MIS simulator systems we have developed in recent years. We collaborate with the Department of Orthopaedics and Traumatology in the Prince of Wales Hospital, Hong Kong. Our system consists of a virtual environment that supports standard inspection and various surgical operations through a homemade virtual knee user interface. Real-time soft tissue deformation is supported for more realistic simulation of ligament and meniscus inside the compartments of knee. The interactive navigation is augmented with force feedback (Fig. 10). Users can manipulate a virtual endoscope and a probe to perform a series of surgical procedures in the simulator. To improve the realism, a 30° adjustable offset viewing at the tip of the virtual endoscope is available.

During the simulation process, different views can be rendered in the virtual environment (Fig. 11). Internal view and external view can be displayed side by side in order to give users better understanding in the correlation between the endoscopic
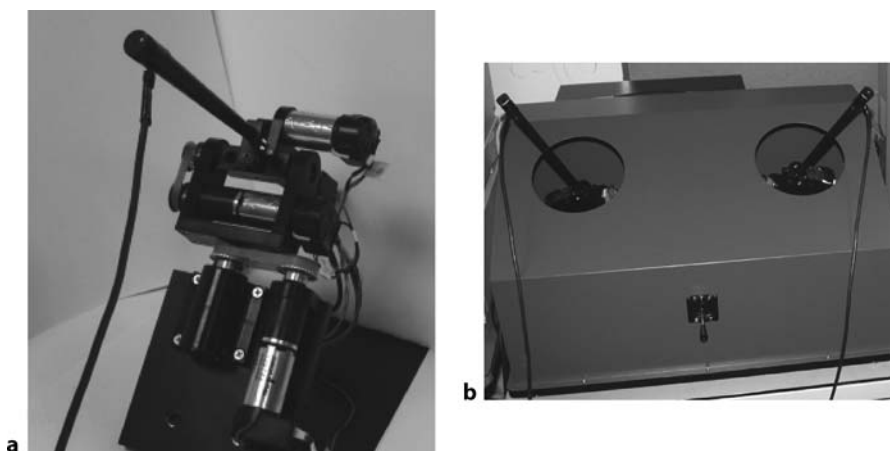
Figure 10. The tailor-made haptics device is shown. **a** The outlook of the bare device is shown. **b** The two-handed interface is shown
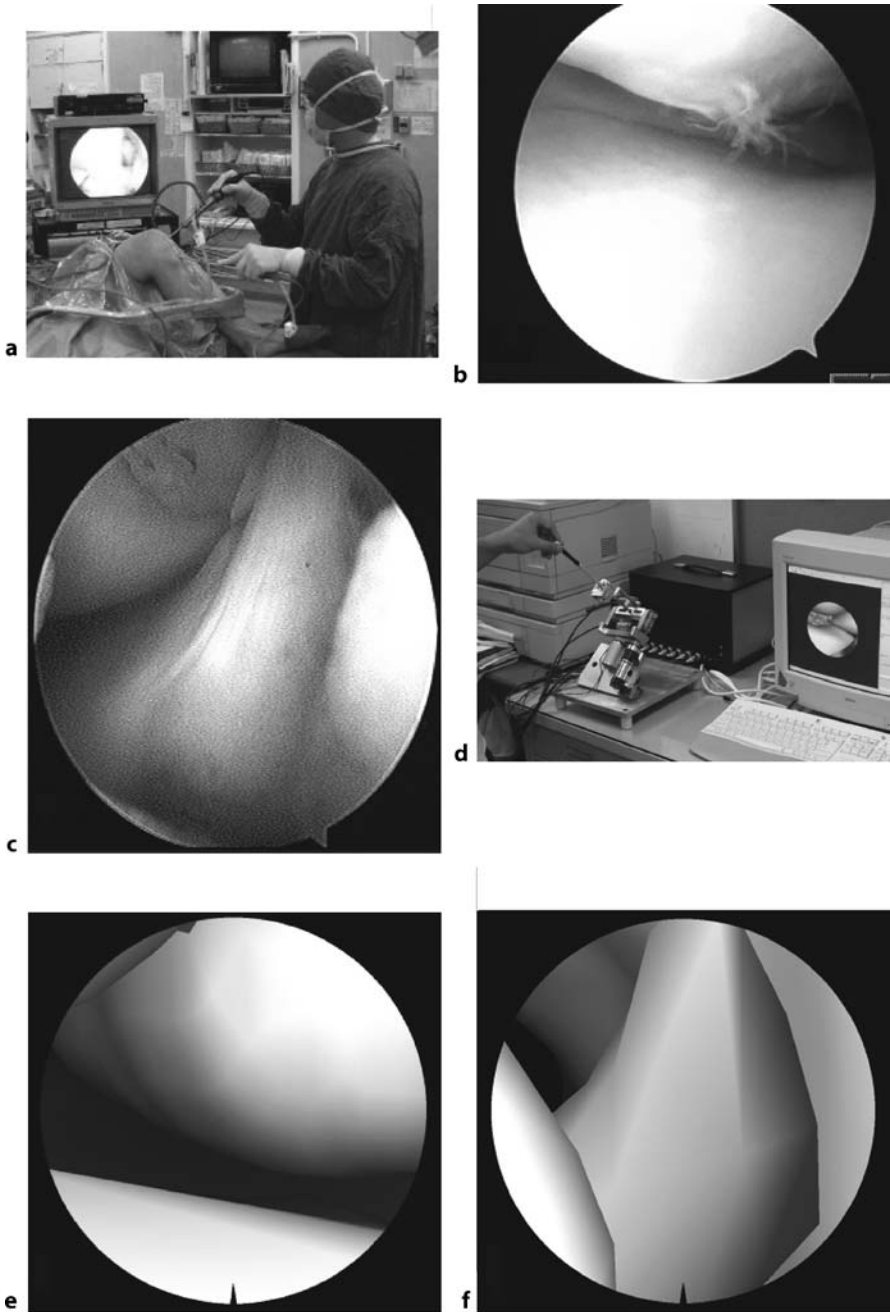
Figure 11. A comparison of real arthroscopic surgery with our virtual-reality-based surgery system is shown. **a** A real interface for the knee arthroscopic surgery is shown. **b,c** Real screen shots from the knee arthroscope are shown. **d** A virtual two-hand haptic input interface is shown. **e,f** Simulated views are shown

view and the actual location of the tools when viewed outside. Users can also record an operation procedure within the simulator so that any deficiencies in the skill set can be identified by other medical professionals. This is particularly important for training medical students in acquiring certain difficult skill sets. In this sense, practices of dangerous procedures on real patients can be largely avoided.

Conclusion

In this chapter we discuss the techniques in medical imaging and image analysis as real-time mathematical models being used in surgical simulations. Particularly, the latest advancement in semi-automatic segmentation with application to CVH data and the novel hybrid FEMs for simulating soft tissue are introduced.

References

Ackerman M (1998) The visible human project. Proceedings of IEEE 86:504–511

Bielser D, Gross M (2000) Interactive simulation of surgical cuts. In: Proc Pacific Graphics 2000. IEEE Computer Society Press, UK, pp 116–125

Bielser D, Maiwald V, Gross M (1999) Interactive cuts through 3-dimensional soft tissue. Proc Eurographics 18:31–38

Cotin S, Delingette H, Ayache N (2000) A hybrid elastic model allowing real-time cutting, deformations and force-feedback for surgery training and simulation. Vis Comput 16:437–452

Delingette H (1998) Towards realistic soft tissue modeling in medical simulation. In: Proc IEEE special issue on surgery simulation, pp 521–523

Downes M, Cavusoglu M, Gantert W, Way L, Tendick F (1998) Virtual environment for training critical skills in laparoscopic surgery. In: Proc Medicine Meets Virtual Reality, pp 316–322

Duck F (1990) Physical properties of tissue. A comprehensive reference book. Academic Press, London

Ganapathy S, Dennehy T (1982) A new general triangulation method for planar contours. Comput Graphics Proc SIGGRAPH 16:69–75

Hoppe H (1996) Progressive meshes. Comput Graphics Proc SIGGRAPH'96, pp 99–108

Loone CG (1997) Pattern recognition using neural network. Oxford University Press, London

Mabrey J, Gilogly S, Kasser J (2002) Virtual reality simulation of arthroscopy of the knee. J Arthroscop Relat Surg 18:28–32

Mor A (2001) Progressive cutting with minimal new element creation of soft tissue models for interactive surgical simulation. PhD thesis, The Robotics Institute, Carnegie Mellon University

Mor A, Kanade T (2000) Modify soft tissue models: progressive cutting with minimal new element creation. In: Proc Med Image Computing and Computer-Assisted Intervention, pp 598–607

Nielsen M, Cotin S (1996) Real-time volumetric deformable models for surgery simulation using finite elements and condensation. In: Proc Eurographics'96 Computer Graphics Forum 15:57–66

Nielson G, Sung J (1997) Interval volume tetrahedralization. In: Proc Visualization'97, pp 221–228

Osher S, Sethian J (1988) Fronts propagating with curvature-dependent speed: algorithms based on Hamilton–Jacobi formulations. J Comput Phys 79:12–49

Qu YG, Chen Q, Heng PA, Wong TT (2004) Segmentation of left ventricle via level set method based on enriched speed term. Int Conf Med Image Comput Comput Assist Interv Lect Note Comput Sci 1:435–442

Sullivan J, Wu Z, Kulkarni A (2005) Three-dimensional finite-element mesh generation of anatomically accurate organs using surface geometries created from the visible human data set. Proc Third Visible Human Project Conference, 5–6 October 2000, ISSN 1524-9008.: http://www.nlm.nih.gov/research/visible/vhpconf2000/MAIN.HTM

Sun J, Guo W, Chai J, Tang Z (2002) Simulation of surgery cutting. In: Proc Fourth China–Japan–Korea Joint Symposium on Medical Informatics, July 2002, Beijing, China

Wu W, Heng PA (2004) A hybrid condensed finite element model with GPU acceleration for interactive 3D soft tissue cutting. Comput Anim Virtual Worlds J 15:219–227

Yang X, Heng PA, Tang Z (2002) Constrained tetrahedral mesh generation of human organs on segmented volume. In: Proc Int Conf on Diagnostic Imaging and Analysis, August 2002, Shanghai, China, pp 294–299

Yezzi A, Kichenassamy S, Kumar A, Olver P, Tannenbaum A (1997) A geometric snake model for segmentation of medical imagery. IEEE Trans Med Imaging 16:199–209

Zhang SX, Heng PA, Liu ZJ et al. (2003) Creation of the Chinese visible human data set. Anat Rec 275B:190–195

Zhang SX, Heng PA, Liu ZJ et al. (2004) The Chinese visible human (CVH) data sets incorporate technical and imaging advances on earlier digital humans. J Anat 204:165–173

In-Vivo Bone Mineral Density and Structures in Humans: From Isotom Over Densiscan to Xtreme-CT

Maximilian A. Dambacher (✉) , Maurus Neff, Helmut R. Radspieler,
Peter Rüegsegger, and Ling Qin

Zurich Osteoporosis Research Group (Zurich-Munich-Hong Kong)
e-mail: m.dambacher@bluewin.ch

Brief History of Device Development and Related Studies

In the early 1960s, Prof. Rüegsegger, Institute for Medical Technology and Medical Informatics, Eidg. Technische Hochschule (ETH) and University in Zurich, was asked by the NASA to develop a device cable of quantifying bone loss in astronauts and people working or training under conditions of weightlessness (micro-gravity).

The result was the Isotom, a small tomograph for peripheral quantitative computed tomography (pQCT), which allowed us in these early days to perform measurements of the trabecular compartment of the bone only, as the cortical part of the bone was not yet accessible (Fig. 1; Rüegsegger et al. 1976, 1981). Our first step was to perform "bed-rest studies" in male volunteers in 1969. After 15 weeks of immobilization, trabecular bone loss exceeded 15% in the radius, a tremendously high bone loss as compared with the approximately 1% of yearly trabecular bone loss in perimenopausal women.

Having completed these studies, the device was transferred back to Zurich and we decided to adapt it in order to match the specific needs of our patients with osteoporosis. This laid the basis for Generation 2, i. e. the Densiscan 1000, manufactured by

Figure 1. Generation 1, Isotom (pQCT)

Figure 2. Generation 2, Densiscan 1000 (pQCT)

Scanco Medical AG in Bassersdorf/Zurich, Switzerland (Fig. 2). The key characteristics include separate measurement of trabecular and cortical bone in vivo at a lateral resolution of 0.2 mm. The default measurement program includes 16 tomograms in total at both distal radius and tibia (Fig. 3).
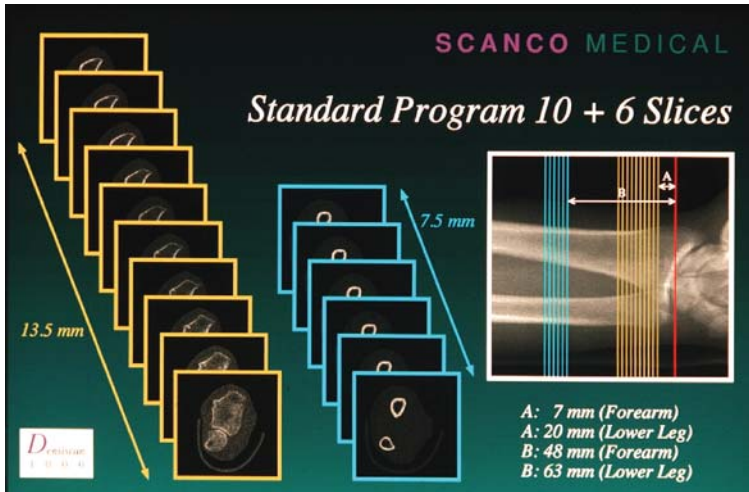
Figure 3. Real imaging of multilayer pQCT (Densiscan 1000) with standard measurement program with ten tomograms for the ultradistal radius and six tomograms for the distal radial midshaft

Strength of the Device Generation 2 in Research and Clinical Evaluations

By the end of 2005, we delivered 150 in vitro and in vivo devices from our Densiscan Series to worldwide leading research organizations. With the Densiscan System, now we are working on the five typical research areas or questions given herein, among others.

Separate Evaluation of Cortical and Metabolically More Active Trabecular Bone

Do the trabecular and the cortical compartments of bone belong to one and the same system, responding to identical rules and factors, or do they differ, eventually even showing differences in bone dynamics? The answer is "Yes".

In perimenopausal women, cortical bone was found to remain relatively stable, but trabecular bone underwent a marked loss, reaching up to 5% over these 20 months of observation (Fig. 4; Rüegsegger et al. 1981). A similar phenomenon was observed over 12 months in tetra- and paraplegics, in the radius as well as the tibia, whereby trabecular bone loss was shown to be far more pronounced than cortical bone loss (Frey-Rindova et al. 2000; de Bruin et al. 1999, 2000, 2005). Fast rate of bone loss in trabecular bone as compared with that of cortical bone found in Caucasian women (Dambacher 1999a,b, 2001a) was also shown in studies from Asian population (Ito et al. 1998; Qin et al. 2000, 2002a, 2003a,b).

Because of the differences in rate of bone loss between cortical and trabecular bone, pQCT was used to explore the exercises in prevention of bone loss in postmenopausal women, such as the studies related to the Chinese martial art Tai Chi Chuan, where significant preventive effects were demonstrable more in trabecular bone (Qin et al. 2002b, 2003a,b, 2005; Chan et al. 2004). The pQCT also showed its
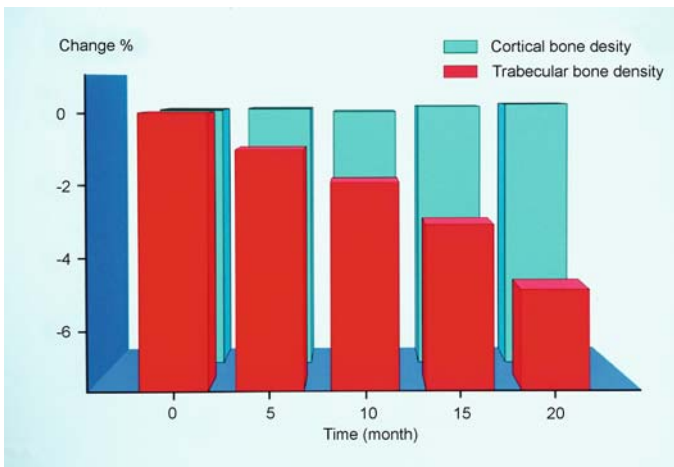
Figure 4. Perimenopausal trabecular and cortical bone loss over 20 months of observation

advantages in detecting inactivity-induced bone loss, such as changes of bone mineral status in weight-bearing tibia bone properties after spinal cord injury (de Bruin et al. 1999, 2000, 2005).

Regional Variations in Bone Mineral Density and Structure

As our pQCT is a 3D technique, its advantage to 2D techniques is seen in its recent applications in studying regional variations in volumetric BMD in perpendicular skeletons in conjunction with biomechanical evaluations of weight-bearing or loading effects (Lai et al. 2005a,b).

pQCT Measurement at Perpendicular Skeletons and its Relationship with Central or Axial Devices

It was repeatedly alleged, thereby reflecting the knowledge gaps, that peripheral measurements would not be representative for the lumbar spine. Ito et al. (1998, 1999) performed longitudinal and cross-sectional examinations with our device and showed a highly significant correlation between axial and peripheral measurements, *when comparing what should be compared*, i. e. trabcular bone with trabecular bone. Similar conclusions applied to the dynamics of trabecular bone loss were drawn in Ito et al.'s study with a follow-up of up to 5 years after menopause (Fig. 5; Ito et al. 1998).
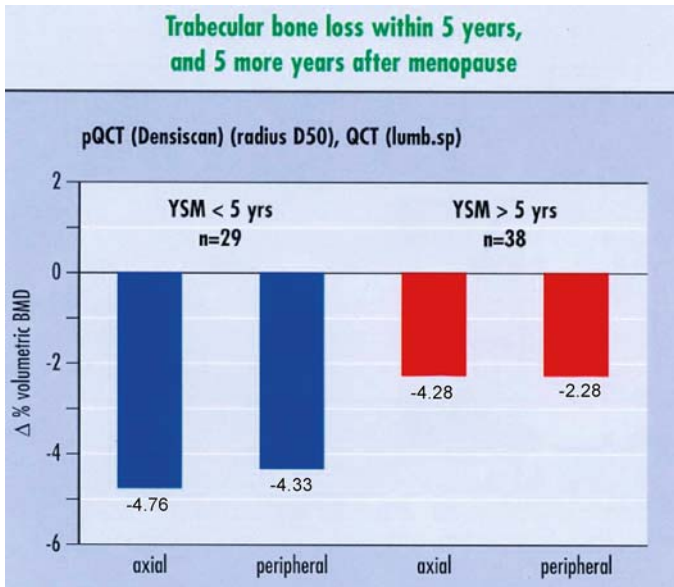
Figure 5. Similar rate of bone loss in trabecular bone compared between axial QCT and pQCT in both pre- and postmenopausal women
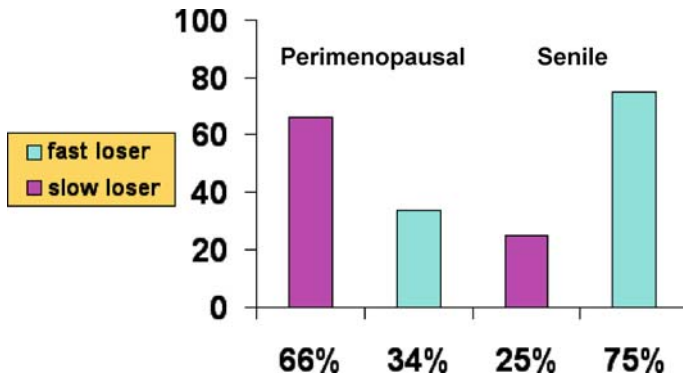
Figure 6. Distribution of fast and slow loser in perimenopausal and severely osteoporotic (senile) patients. Rate of bone loss is based on the rate of trabecular bone loss at non-dominant distal radius

Types of Osteoporosis and Rate of Bone Loss

The individualization of osteoporosis into two distinct types, type I and type II, is still actual, whereby rapid bone loss is referred to as type-I osteoporosis, and type-II osteoporosis would apply to stable bone dynamics or to a slow rate of bone loss. To differentiate between rapid and slow rates of loss of bone substance, we categorized our patients into "fast" and "slow" losers, reflecting the bimodal distribution of the rates of trabecular bone loss in women aged between 45 and 55 years, whereby patients defined as "fast losers" lost more than 3.5% of trabecular BMC per year (Dambacher et al. 1998; Rüegsegger et al. 1996; Qin et al. 2003a,b).

During perimenopause, 34% of our patients only showed a "fast bone loss", and the remaining 66% had a normal rate of loss in volumetric bone density (Fig. 6). This is consistent with the observation that only one of three women will effectively develop osteoporosis and therefore become eligible for treatment. During those days, we were accused of "acting like rebels", as we disagreed with the dogma which required that every post-menopausal woman underwent estrogen replacement therapy. In contrast, the proportion of "fast losers" reached 75% in patients with severe (senile) osteoporosis (type II). This contradicts common current scientific knowledge, a contradiction which can be explained by the fact that trabecular bone is not examined independently but only in combination with cortical bone, although these two bone compartments act as totally different systems with distinct dynamics. Another problem arises from the presentation of rates of bone loss in relative and not absolute values.

Reproducibility and Pitfalls of Devices

Long-Term Reproducibility

The long-term reproducibility is a relative measure of the precision of repeated measurements over a more or less prolonged period of time. Reproducibility depends

Table 1. Reproducibility and the required time frame between two measurements for evaluation of "fast bone losers" (at 95% confidence level)

	Multi-layer pQCT				DXA (%)				QUS (%)		
Precision error	±0.3	±0.5	±1.0	±1.5	±2.0	±2.5	±3.0	±3.5	±4.0	±4.5	±5.0
Minimal time	*3*	*5*	*9*	*14*	*19*	*24*	28	33	38	42	47
interval	*3*	*5*	*10*	*15*	*21*	26	31	36	41	46	51
between two	*3*	*6*	*11*	*17*	*23*	28	34	40	45	51	57
repeated	*4*	*6*	*13*	*19*	25	31	38	44	50	57	63
measurements	*4*	*7*	*14*	*21*	28	35	42	50	57	64	71
(months)	*5*	*8*	*16*	*24*	32	40	49	57	65	73	81
	6	*9*	*19*	28	38	47	57	66	75	85	94
	7	*11*	*23*	34	45	57	68	79	91	102	113
	8	*14*	28	42	57	71	85	99	113	127	142

Data highlighted in italics and boldface: measurement interval < 2 years and the rest refers to measurement interval > 2 years

on the method used and the value of bone density at baseline. Table 1 shows the level of reproducibility required to be able to identify a fast loser patient within a given time frame. With the high-resolution pQCT measurement method and assuming a baseline bone density value of 50% and a reproducibility of 0.3%, 7 months would be required to identify a fast-loser patient (Dambacher et al. 1998; Qin et al. 2002a, 2003a,b). When using a routine DXA method for bone density measurement, with a reproducibility of 1–2%, this time frame increases to more than 24 months (Rüegsegger 1996). In this regard, the following statement from Delmas (1999) is of interest: "In patients with osteoporosis and with high bone turnover (fast loser condition) antiresorptive agents like Bisphosphonates, SERMS and calcitonin should be used. In patients with low bone turnover (slow loser condition) fluorides should be applied, regardless of the discussion about fluorid medication".

Pitfalls

The pitfalls or limitations of the above-mentioned device are found in either "false-positive" or "false-negative" conditions, including measurement sites with microfractures (misinterpreted as an increase in BMD) or with healing of microfractures (misinterpreted as a "fast-loser" status (Figs. 7a-c).

The Latest Development: Generation 3, Xtreme-CT for In-Vivo Human Studies

Rationale of Device Development

On 22 September 2003, in Minneapolis, Harry Genant organized a symposium entitled "Beyond". In his mind, the measurement of bone density in humans alone was
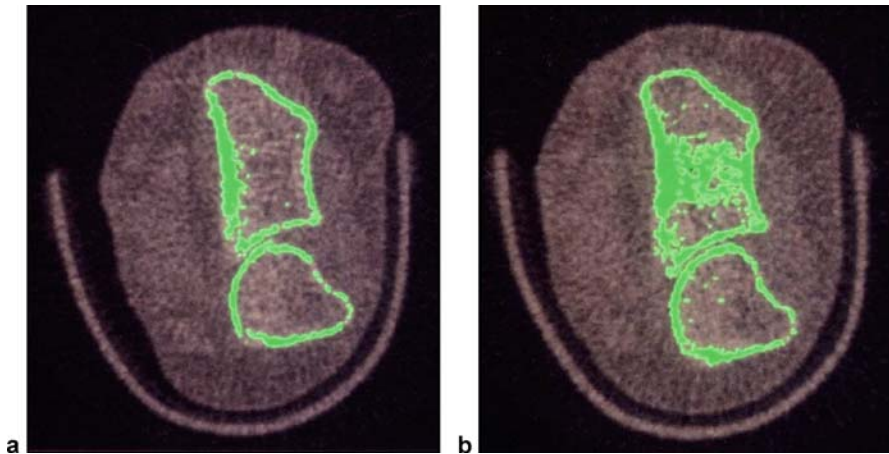
Figure 7. Microfracture results in "false-positive" results in BMD values. **a** At the time of fracture at distal radius. **b** A few months after fracture, with increased trabecular BMD in the central part of the distal radius on the pQCT image, i. e. formation of micro-fracture

to be considered as insufficient. In fact, all proposed definitions or consensus statements of osteoporosis (Copenhagen 1990, Hong Kong 1993, Amsterdam 1996 and the Consensus Development Conference 2001) do highlight the importance of bone structure. During the past years, it has become increasingly clear that an increase in BMD is not accompanied by a parallel decrease of fracture risk. Table 2 shows very

Table 2. The increase in BMD does not correlate with the decrease in fracture risk

Fracture end-point studies	Difference in BMD as compared with placebo (%)	Reduction of vertebral fractures (%)
Calcitonine (PROOF) (Chestnut et al. 1993)	0.5	36
Raloxifene (MORE) (Ettinger et al. 1999)	2.6	40
Alendronate (FIT 1) (Black et al. 1999)	6.2	47
Risedronate (Reginster et al. 2000)	6.3	49
Fluoride (Meunier et al. 1998)	8.4	No difference
Teriparatide (Neer et al. 2001)	14.2	65
Strontium ranelate (Meunier et al. 2004)	12.7	41
Ibandronate (Recker et al. 2004)	5.7	50

Figure 8. Generation 3, Xtreme-CT

clearly that BMD is accountable for only 20% of the observed fracture risk reduction (Dambacher et al. 2004a,b).

Additionally, a poster was presented by Watts (2005), with the following title: "Risedronate demonstrates efficacy to reduce fragility fractures independent of treatment related BMD changes". Moreover, at 2005 ASBMR Pierre Delmas stated: "Half of incident fractures occur in osteopenic women who have BMD values above the WHO defined diagnostic threshold for osteoporosis". Similar thoughts triggered us, much earlier, to go ahead with the development of the Generation 3 of our device, i. e. Xtreme-CT, for the representation and the quantitative measurement of 3D structures in vivo in humans (Figs. 8, 9; Dambacher et al. 2001b, 2004a,b; Neff et al. 2002). This device features a reproducibility of total, trabecular and cortical BMD of 0.7–1.5% and of 2.5–4.4% for trabecular architecture (P. Delmas, pers. commun.), with a resolution of 100 µm.

The Specific Features of In-Vivo Human Xtreme-CT

The recent application of this latest development suggests that Xtreme-CT may have the following characteristics:

1. Its ability to discriminate between osteopenic women with and without a prior history of fracture. In contrast, spine and hip BMD measured by DXA were not different between the two groups (P. Delmas, pers. commun.).
2. Its quantitative assessment of trabecular microarchitecture (Figs. 10–12) allows an improved assessment of fracture risk.
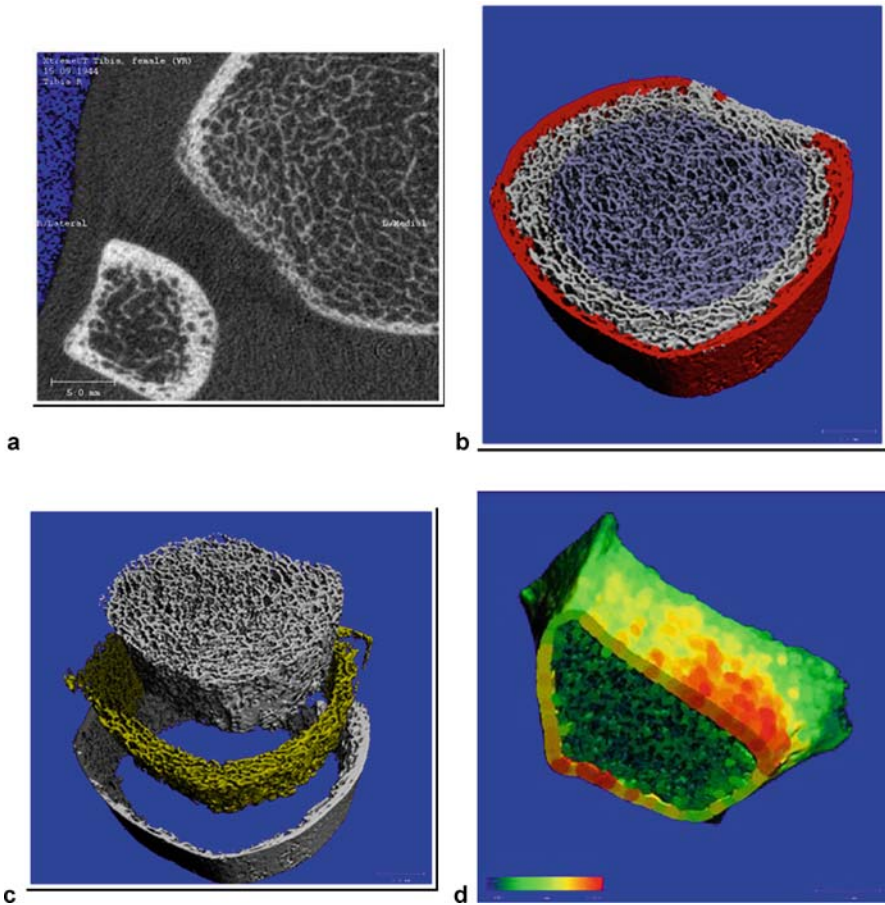
Figure 9. In-vivo Xtreme-CT for human application with 3D reconstructions. **a** A 2D image of ultradistal radius. **b** A 3D reconstruction with defined region of interests. **c** A "cut out" of region of interests defined in **b**. **d** A 3D reconstruction of radial cortical shell at distal radial diaphysis

3. Better monitoring of treatment effects (Fig. 13).
4. It allows prospective studies to assess osteopenic patients at increased risk for fracture.

The technical details of the above-mentioned devices are summarized on the home-page of the devices: http://www.scanco.ch.

Conclusion

The motivation for development of 3D bone densitometry was attributed to NASA space flight in early 1960s. Over the years, we have been able to advance our engi-
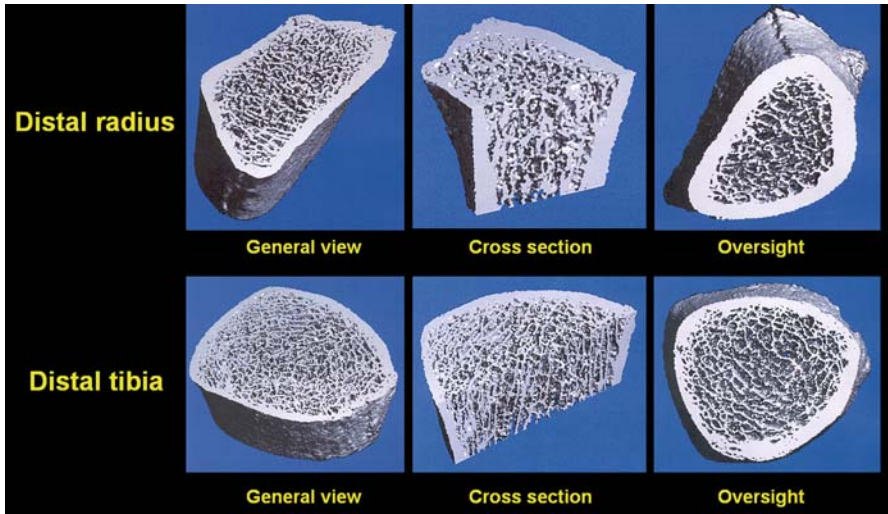
Figure 10. The Xtreme-CT: 3D structure presentations at various views of normal distal extremities
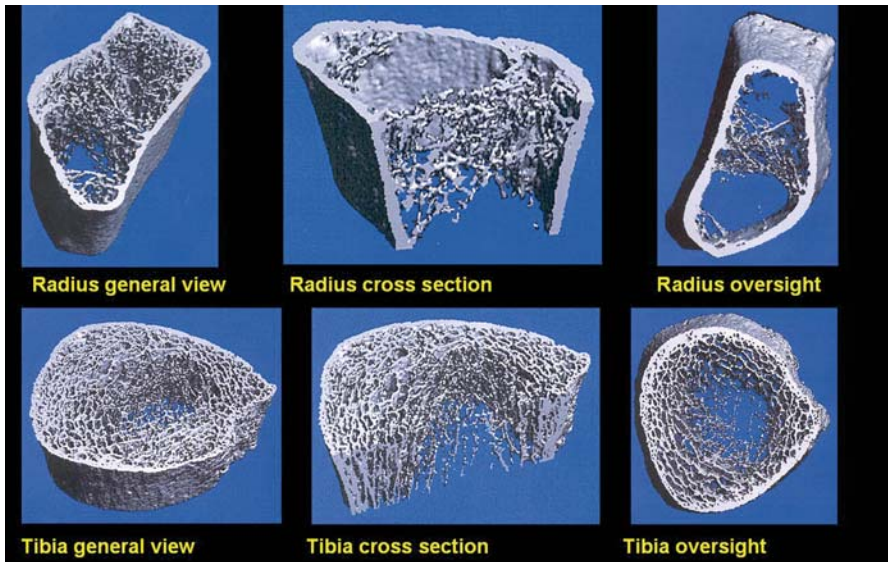
Figure 11. The Xtreme-CT: 3D structure presentations at various views of osteoporotic distal extremities

neering significantly, and our latest development in this area is the in vivo human Xtreme-CT, which enables us to measure and monitor the changes of 3D bone structures in vivo in humans. This opens a new horizon to evaluate the efficacy of the drugs developed for prevention and treatment of osteporosis, and potentially also for monitoring osteoporotic fracture repair.
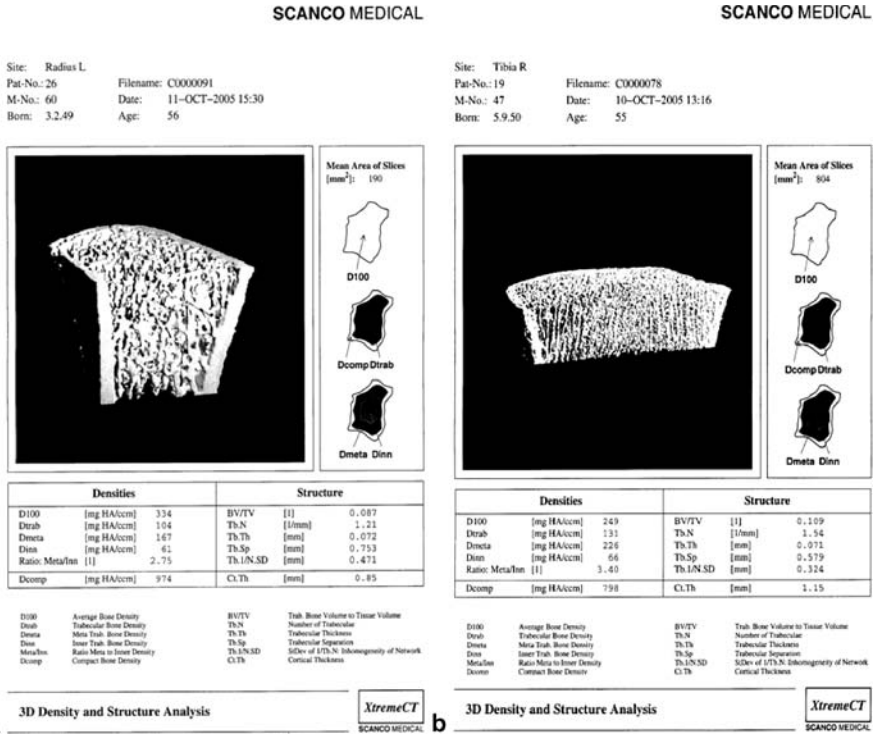
Figure 12. Datasheets of in vivo Xtreme-CT 3D reconstructions (corresponding to Figs. 10 and 11). **a** Datasheet of distal radius. **b** Datasheet of distal tibia
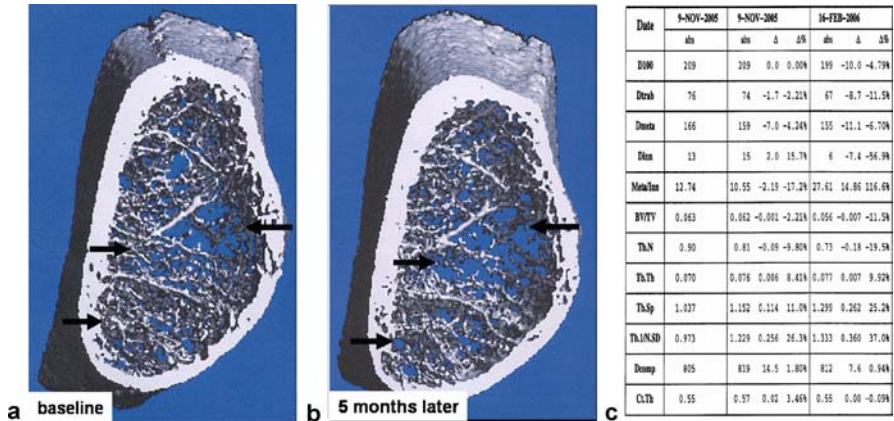
Figure 13. The Xtreme-CT: monitoring of trabecular bone loss of at distal radius of a post-menopausal women. **a** A 3D distal radius at baseline (*arrows*). **b** A 3D distal radius of the same region made 5 months after baseline measurement (*arrows*: demonstrating trabecular bone structural deterioration and loss). **c** Datasheet for comparison of density and structural values

References

Black DM, Thompson DE (1999) The effect of alendronate therapy on osteoporotic fracture in the vertebral fracture arm of the Fracture Intervention Trial. Int Clin Practice 101:46–50

Chan KM, Qin L, Lau MC, Woo J, Au SK, Choy WY, Lee KM, Lee SH (2004) A randomized, prospective study of the Tai Chi Chun exercise on bone mineral density in postmenopausal women. Arch Phy Med Reha 85(5):717–722

Chestnut CH III (1993) Calcitonin in the prevention and treatment of osteoporosis. Osteoporosis Int 3 (Suppl 1):206–207

Dambacher MA, Neff M, Kissling R, Qin L (1998) Highly precise peripheral quantitative computed tomography for the evaluation of bone density, loss of bone density and structures. Drugs Aging 12:15–24

Dambacher MA, Neff M, Radspieler H, Qin L (1999a) Ist die herrschende Meinung "Perimenopausal schneller – Senile Osteoporose langsamer Knochenverlust" korrekt? J Menopause 6:10–11

Dambacher MA, Radspieler H, Neff M, Schacht E, Qin L., Kissling R (1999b) "Fast" und "slow-loser" Patienten: Eine sinnvolle Unterscheidung? Konsequenzen für die Praxis. ("Fast-" and "slow-loser" patients: A useful differentiation? Consequences for our daily practice). Osteologie 8:152–160

Dambacher MA, Neff M, Kissling R, Qin L (2001a) Das fast/slow bone loser Konzept. Osteopor Rheum Aktuelle 3:38–45

Dambacher MA, Neff M, Qin L, Rüegsegger P (2001b) 2- und 3-Dimensionale Knochenstrukturen in vivo und in vitro. J Miner Stoffwechsel 3:26–33

Dambacher MA, Schmitt S, Schacht E, Ito M, Neff M, Müller R, Qin L, Zhao YL (2004a) Bone structures in vitro and in vivo in animals and in men: a view into the future. J Miner Stoffwechs 11:13–19

Dambacher MA, Schmitt S, Schacht E, Ito M, Neff M, Müller R, Qin L, Zhao YL (2004b) Bone structures in vitro and in vivo in animals and in men: a view into the future. J Miner Stoffwechs 2:22–28

de Bruin ED, Frey-Rindova P, Herzog RE, Dietz V, Dambacher MA, Stussi E (1999) Changes of tibia bone properties after spinal cord injury: effects of early intervention. Arch Phys Med Rehab 80:214–220

de Bruin ED, Dietz V, Dambacher MA, Stussi E (2000) Longitudinal changes in bone in men with spinal cord injury. Clin Rehab 14:145–152

de Bruin ED, Vanwanseele B, Dambacher MA, Dietz V, Stussi E (2005) Long-term changes in the tibia and radius bone mineral density following spinal cord injury. Spinal Cord 3:96–101

Delmas P (1999) Presentation at the 1999 European Congress on calcified Tissue, Maastricht

Ettinger B, Black DM, Mitlak BH, Knickerbocker RK, Nickelsen T, Genant HK, Christiansen C, Delmas PD, Zanchetta JR, Stakkestad J, Gluer CC, Krueger K, Cohen FJ, Eckert S, Ensrud KE, Avioli LV, Lips P, Cummings SR (1999) Reduction of vertebral fracture risk in postmenopausal women with osteoporosis treated with raloxifene: results from a 3-year randomized clinical trial. Multiple Outcomes of Raloxifene Evaluation (MORE) Investigators. J Am Med Assoc 282:637–645

Frey-Rindova P, de Bruin ED, Stussi E, Dambacher MA, Dietz V (2000) Bone mineral density in upper and lower extremities during 12 months after spinal cord injury measured by peripheral quantitative computed tomography. Spinal Cord 38:26–32

Ito M (1998) Trabecular bone loss within 5 years and 5 years and more after menopause. Bone 23:S619

Ito M, Nakamura T, Tsurusaki K, Uetani M, Hayashi K (1999) Effects of menopause on age-dependent bone loss in the axial and appendicular skeletons in healthy Japanese women. Osteoporos Int 10:377–383

Lai YM, Qin L, Hung VWY, Chan KM (2005a) Regional differences in cortical bone mineral density in weight-bearing long bone shaft: a pQCT study. Bone 36:467–471

Lai YM, Qin L, Yeung HY, Lee KM, Chan KM (2005b) Regional differences in trabecular BMD and microarchitecture of weight bearing bone under habitual gait loading: a pQCT and microCT study in human subject. Bone 37:274–282

Meunier PJ, Sebert JL, Reginster JY, Briancon D, Appelboom T, Netter P, Loeb G, Rouillon A, Barry S, Evreux JC, Avouac B, Marchandise X (1998) Fluoride salts are no better at preventing new vertebral fractures than calcium-vitamin D in postmenopausal osteoporosis: the FAVO Study. Osteoporosis Int 8:4–12

Meunier PJ, Roux C, Seeman E, Ortolani S, Badurski JE, Spector TD, Cannata J, Balogh A, Lemmel EM, Pors-Nielsen S, Rizzoli R, Genant HK, Reginster JY (2004) The effects of strontium ranelate on the risk of vertebral fracture in women with postmenopausal osteoporosis. N Engl J Med 350:459–468

Neer RM, Arnaud CD, Zanchetta JR, Prince R, Gaich GA, Reginster JY, Hodsman AB, Eriksen EF, Ish-Shalom S, Genant HK, Wang O, Mitlak BH (2001) Effect of parathyroid hormone (1-34) on fractures and bone mineral density in postmenopausal women with osteoporosis. N Engl J Med 344:1434–1441

Neff M, Dambacher MA, Kissling R, Qin L, Rüegsegger P (2002) Quantified 2- and 3-dimensional evaluation of bone structures in vitro and in vivo. Osteologie 11:67–77

Qin L, Au SK, Chan KM, Lau MC, Woo J, Dambacher MA, Leung PC (2000) Peripheral volumetric bone mineral density in pre- and postmenopausal Chinese women in Hong Kong. Calcif Tissue Int 67:29–36

Qin L, Au SK, Leung PC, Lau MC, Woo J, Choy WY, Hung WY, Dambacher MA, Leung KS (2002a) Baseline BMD and bone loss at distal radius measured by pQCT in peri- and postmenopausal Hong Kong Chinese women. Osteoporosis Int 13:962–970

Qin L, Au SZ, Choy YW, Leung PC, Neff M, Lee KM, Lau MC, Woo J, Chan KM (2002b) Regular Tai Chi exercise may retard bone loss in postmenopausal women: a case control study. Arch Phys Med Rehab 83:1355–1359

Qin L, Au SZ, Choy YW, Leung PC, Neff M, Lee KM, Lau MC, Woo J, Chan KM (2003a) Tai Chi Chuan and bone loss in postmenopausal women. Arch Phys Med Rehab 84:621–623

Qin L, Dambacher MA, Leung PC, Neff M (2003b) Fast and slow bone loss: diagnostic and therapeutic implications in osteoporosis. In: Schneider HPG (ed) Menopause the state of art: in research and management. Parthenon, New York, pp 124–130

Qin L, Choy WY, Leung KS, Leung PC, Au SK, Hung WY, Dambacher MA, Chan KM (2005) Beneficial effects of regular Tai Chi exercise on musculoskeletal system. J Bone Miner Metabol 23:186–190

Recker RR, Weinstein RS, Chesnut CH III, Schimmer RC, Mahoney P, Hughes C, Bonvoisin B, Meunier PJ (2004) Histomorphometric evaluation of daily and intermittent oral ibandronate in women with postmenopausal osteoporosis: results from the BONE study. Osteoporosis Int 15:231–237

Reginster J, Minne HW, Sorensen OH, Hooper M, Roux C, Brandi ML, Lund B, Ethgen D, Pack S, Roumagnac I, Eastell R (2000) Randomized trial of the effects of risedronate on vertebral fractures in women with established postmenopausal osteoporosis. Vertebral Efficacy with Risedronate Therapy (VERT) Study Group. Osteoporosis Int 11:83–91

Rüegsegger P (1996) Bone density measurement. In: Bröll H, Dambacher MA (eds) Osteoporosis: a guide to diagnosis and treatment. Rheumatology 18:103–116

Rüegsegger P, Elsasser U, Anliker M, Gnehm H, Kind H, Prader A (1976) Quantification of bone mineralization using computed tomography. Radiology 121:93–97

Rüegsegger P, Anliker M, Dambacher MA (1981) Quantification of trabecular bone with low dose computed tomography. J Comput Assist Tomogr 5:384–390

Watts NB (2005) Risedronate demonstrates efficacy to reduce fragility fractures independent of treatment related BMD changes (poster). ASBMR, September, Nashville

Calibration of Micro-CT Data for Quantifying Bone Mineral and Biomaterial Density and Microarchitecture

Bruno Koller (✉) and Andres Laib

Scanco Medical AG, Bassersdorf, Switzerland
e-mail: bkoller@scanco.ch

Abstract

With the awareness of the importance of the bone architecture to the overall stability of bone, micro-CT has become the gold standard for 3D static histomorphometry in bone research over the past 10 years. Nevertheless, bone densitometry is still the method of choice in the clinical environment. It is, however, anticipated that only a combination of the two methods, densitometry and morphometry, will improve the diagnosis and treatment of patients. This chapter introduces the calibration of micro-CT for quantification of bone mineral and material density at both organ and tissue levels and its impact in bone and mineral research based on bone biopsy. This approach may also be widely applied to measure the density of other appreciated materials.

A Need for Quantification of Bone Material Density

Our early micro-CT mainly provided measurements of structural or microarchitectural futures of bone and related materials to supplement our pQCT (Densiscan), which measured volumetric bone mineral density (BMD) at organ level (Lai et al. 2005a,b). As the demands on quantification of bone material density at tissue level became increasingly high (Gong et al. 2005; Lai et al. 2005b), consequently we added densitometric features to our micro-CT device, and developed the XtremeCT, a new pQCT densitometry system that assesses bone microarchitecture (Fig. 1).

Micro-CT and XtremeCT Features

For both high-resolution micro-CT and Xtreme CT systems, the techniques and procedures are more or less identical and consist of the following features: Firstly, both systems must have a very good stability over many years. This is achieved with self-calibration and control of the signal before each measurement. Quality-control (QC) phantoms are provided to control the stability of the systems.
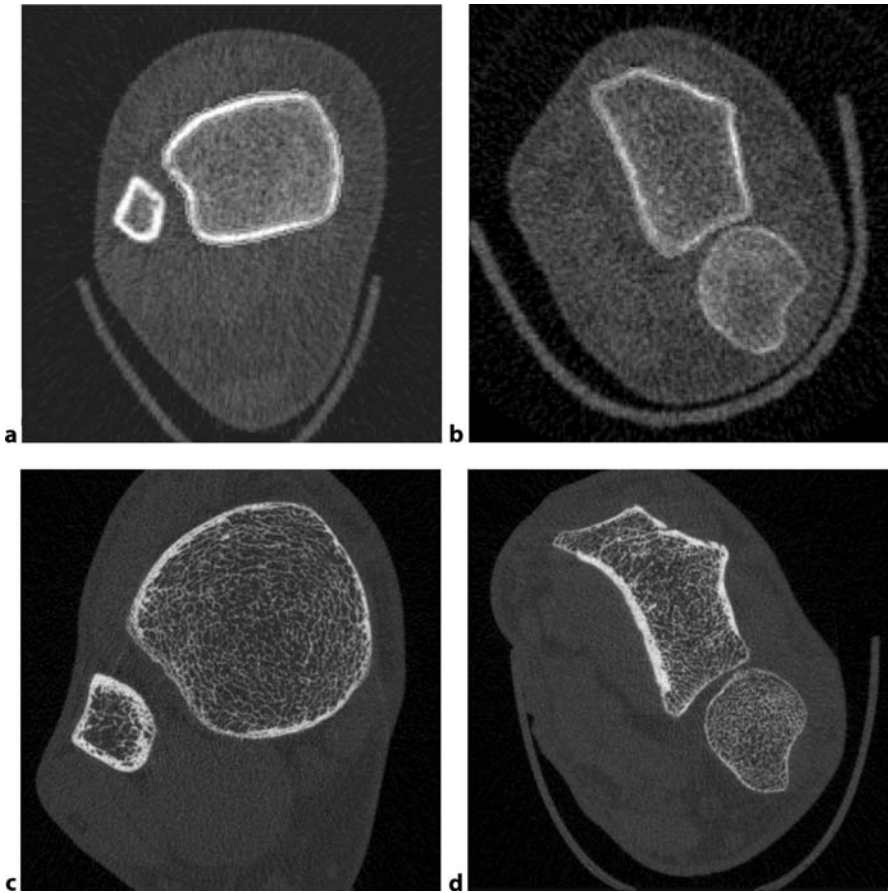
Figure 1. Human tibia (**a**) and radius (**b**) scanned at 300 μm voxel size by pQCT (Densiscan) compared with human tibia (**c**) and radius (**d**) scanned at 82 with XtremeCT

Secondly, due to the polychromatic beam of X-ray sources, the beam-hardening artifact has to be addressed very carefully. The beam hardening effect leads to a dependence of the density readout from the object size. Densities, therefore, may vary between smaller and larger people or smaller and larger biopsies just because of their size. This artifact is eliminated by filtering the primary beam and by applying a correction function to the measured signal. By applying special beam-hardening correction curves that are adapted to scanning bone, the cupping artifact can be avoided, and the gray-scale image values are homogeneous throughout the region of interest (Fig. 2).

Thirdly, CT systems can measure the absorption of the X-rays, but not directly the density of the material; however, assuming a proper beam-hardening correction, the density is linearly correlated to the absorption (within our energy range); therefore, we can measure reference materials of known density and then apply a conversion function to the bone measurements.
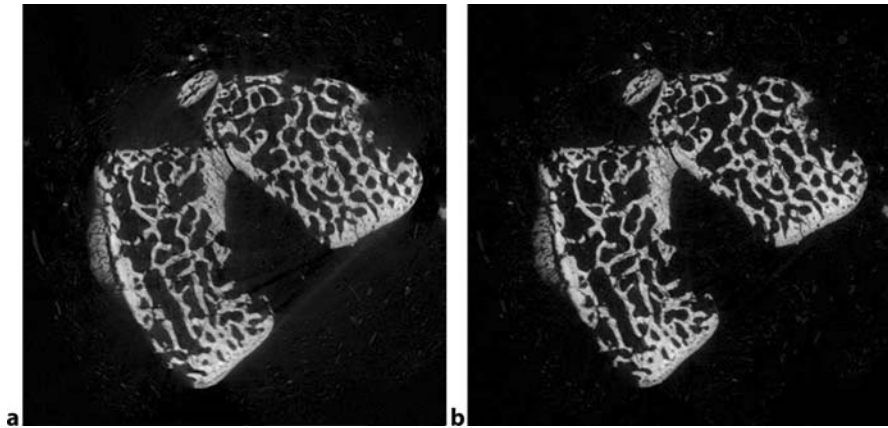
Figure 2. Dry excised distal rat femur. **a** Without specialized beam-hardening correction. **b** With beam-hardening correction for bone

Evaluation of Bone Mineral Density at Organ and Tissue Level

For the purpose of BMD measurement, we designed reference phantoms made of five different hydroxyapatite (HA) densities for the whole line of our micro-CT scanners (Fig. 3), which only vary in size for the different instruments; therefore, we are able to cross-calibrate all our systems. The whole procedure of density calibration can also be applied to different materials and reference phantoms, so users can build their own calibration sets, e. g., for Al, Mg, or scaffold scanning. Since all our systems are calibrated, they provide true volumetric BMD for both patients and bone specimens.

The DXA densitometry is limited to areal BMD measurement. This means one cannot distinguish between different parts or regions within the bone. Calibrated mi-
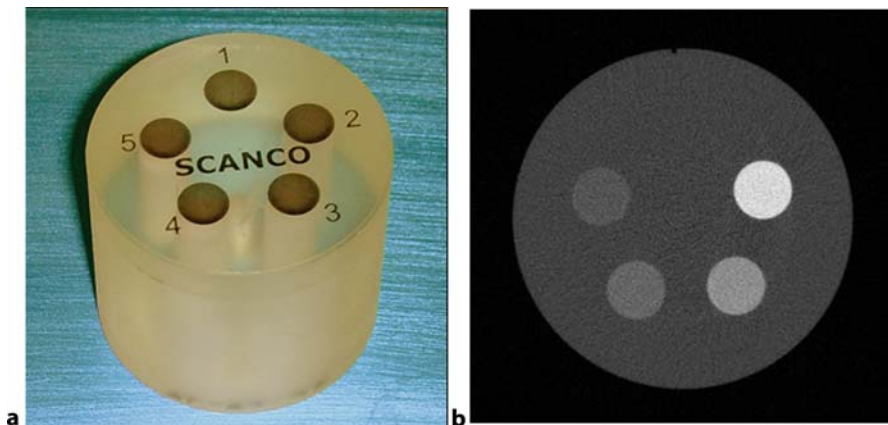
Figure 3. Quality control and density calibration phantom (**a**) and its CT scan (**b**)
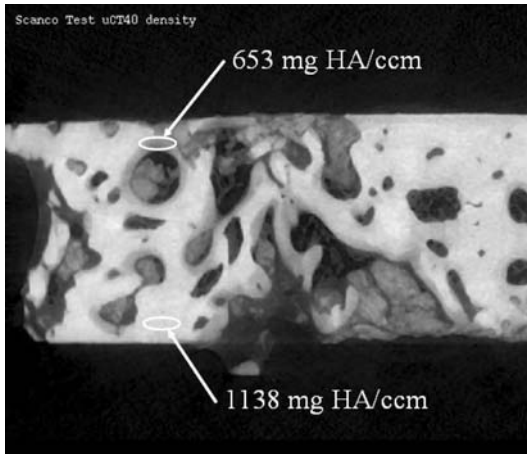
Figure 4. Local changes in BMD within a bone sample

crotomography now offers true volumetric densitometry for apparent density (bone and marrow space) within different regions of the specimen. In addition to the apparent density, we can also measure the material density within the cortex and trabecular bone at organ level and even local changes of bone matrix density at tissue level, i. e., within a single trabecula.

For material density measurements, it is very important to have a very high resolution, as otherwise partial-volume effects may affect the results. For this reason, the outermost layer is excluded from analysis for achieving precise results. This is shown by measuring different bone specimens using micro-CT and then ash. An example of local changes within a bone sample is illustrated in Fig. 4.

Evaluation of Structural Parameters

Once the object is scanned and segmented, the whole 3D structure can be visualized. In contrast to traditional 2D histomorphometry, the trabecular bone structure can now also be quantified in 3D, and therefore one does not have to rely on any model assumptions about the shape of bone anymore (no plate model assumption).

By filling the trabeculae with overlapping maximal spheres (Hildebrand and Rüegsegger 1997a,b) the local thickness of the bone at each place can be calculated as the diameter of the biggest sphere that fits inside the bone at this place. The mean value of all local thickness values then gives trabecular thickness (Tb.Th). Since this calculation is done for every point of bone, histograms of local thickness values can also be plotted. Applying the same technique to the marrow space, trabecular separation Tb.Sp is calculated, and the histogram of local separations can be given. From the histogram, the homogeneity of the trabecular network can now be quantified as the standard distribution of Tb.Sp: Tb.Sp.SD is large for networks that are less regular and contain large "holes" (Laib et al. 2002).
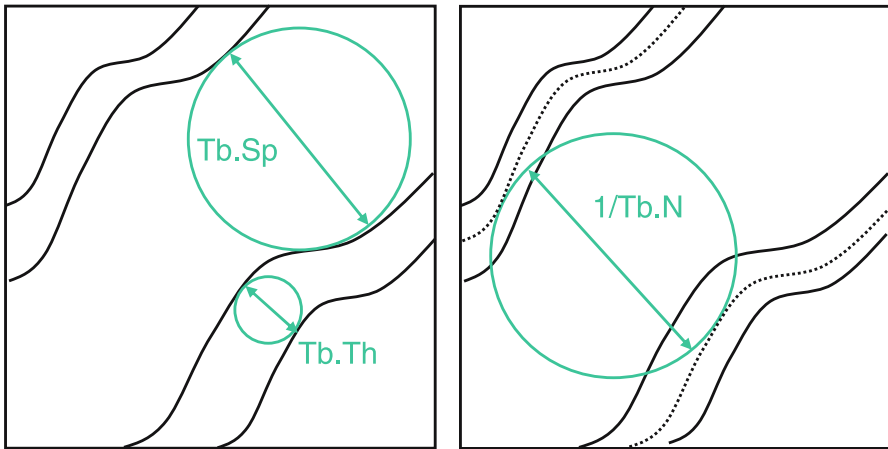
Figure 5. The determination of Tb.Th, Tb.Sp and Tb.N

Trabecular number is usually defined as the number of trabeculae an observer meets per millimeter of flight-path through the bone, averaged over all directions of the flight. By determining the mean distance of the skeletonized structure and inverting this number, Tb.N can now be quantified without model assumptions, e. g., Tb.N = 3 trabeculae per millimeter of flight length, i. e., the distance between the midpoints of the trabeculae is 0.333 mm, thus 1 divided by 0.333 mm is the desired Tb.N of 3 [1/mm]; (Fig. 5).

With the method of Odgaard and Gundersen (1993), the topology of the trabeculae can be assessed, and the number of connections and the connectivity density (number of connections divided by total volume) can be calculated based on Euler numbers. When trabecular bone is visualized, it is interesting to note that some bone sites look more plated-like (e. g., human femoral head), whereas other bone sites have distinctly rod-like bone (e. g., human spine). This feature of bone architecture can now be quantified with the structure model index (SMI; Hildebrand and Rüegsegger 1997a,b) with perfectly plate-like bone having an SMI of 0, and perfectly rod-like bone having an SMI of 3. Values of SMI in-between denote a mixture of plate- and rod-like bone, or bone with "rods" with elliptical cross-section.

Triangulating the surface model of bone then allows to also quantify bone surface and assess the potentially active remodeling surface of trabecular bone (Hildebrand and Laib 1999; Lorensen and Cline 1987).

Conclusion

The interests on quantification of bone material density at tissue level in vivo for human became increasingly high in bone and mineral research. The new generation of pQCT, i. e., the XtremeCT is developed, which is able to assess both bone microarchitecture and BMD at both organ and tissue levels.

References

Gong H, Zhang M, Yeung HY, Qin L (2005) Regional variations in microstructural properties of vertebral trabeculae with ageing. J Bone Miner Metabol 23:174–180

Hildebrand T, Laib A (1999) Direct three-dimensional morphometric analysis of human cancellous bone: microstructural data from spine, femur, iliac crest, and calcaneus. J Bone Miner Res 14:1167-1174

Hildebrand T, Rüegsegger P (1997a) A new method for the model independent assessment of thickness in three-dimensional images. J Microsc 185:67–75

Hildebrand T, Rüegsegger P (1997b) Quantification of bone microarchitecture with the structure model index. Comput Methods Biomech Biomel Eng 1:15–23

Lai YM, Qin L, Hung VWY, Chan KM (2005a) Regional differences in cortical bone mineral density in weight-bearing long bone shaft: a pQCT study. Bone 36:467–471

Lai YM, Qin L, Yeung HY, Lee KM, Chan KM (2005b) Regional differences in trabecular BMD and microarchitecture of weight bearing bone under habitual gait loading: a pQCT and micro-CT study in human subject. Bone 37:274–282

Laib A, Newitt DC, Lu Y, Majumdar S (2002) New model-independent measures of trabecular bone structure applied to in vivo high-resolution MR images. Osteoporosis Int 13:130–136

Lorensen WE, Cline HE (1987) Marching cubes: a high resolution 3D surface construction algorithm. Comput Graphics 21:163–169

Odgaard A, Gundersen HJG (1993) Quantification of connectivity in cancellous bone, with special emphasis on 3-D reconstruction. Bone 14:173–182

Repositioning of the Region of Interest in the Radius of the Growing Child in Follow-up Measurements by pQCT

Thomas N. Hangartner (✉) , Dhruman Goradia, and David F. Short

BioMedical Imaging Laboratory, Wright State University, Dayton, Ohio, USA
e-mail:thomas.hangartner@wright.edu

Abstract

The assessment of changes in bone mineral density (BMD) requires follow-up measurements. In order to compute accurate changes, it is important that the region of interest (ROI) of the initial and follow-up measurements match in terms of location. Our present focus is the evaluation of bone at the distal end of the radius by peripheral quantitative computed tomography (pQCT). In adults, in whom the bones have ceased to grow, repositioning of the ROI has been attempted either by matching the measurement location defined as a fixed percentage of the bone length away from an anatomical landmark or by matching the cross-sectional areas of the bone in the conic distal region of the radius; however, in the case of children, whose bones are growing, these methods cannot be applied blindly. The aim of this study was to propose a model that aids in the relocation of the ROI during follow-up measurements in children.

From a long-term research study of multiple generations of volunteers, we were able to obtain sets of radiographs of forearms taken regularly from birth until the age of 18 years. From the radiographs of each subject, the bone lengths and widths were measured. The shapes of the bones were analyzed, and a model that predicts change in width based on change in length was developed. This model was modified to predict change in cross-sectional area based on change in length, assuming a cross-sectional geometry derived from a set of pQCT images over the same age range. It was observed that the shape of the radiographically projected radius between distal and proximal growth plates for a given subject did not vary with age. The model was tested by matching pairs of pQCT scans based on the cross-sectional areas predicted by the model. The pairs of images were compared qualitatively for a match in shape of the cross-section of the bone. If the cross-sectional shape matched closely, the two sections were considered to belong to the same region. From 26 evaluated pairs of cross-sections, 21 pairs had matching shapes. From this study we concluded that the proposed model produced satisfactory results in 81% of the tested cases. The failures were observed mostly at an age when the increase in length ceased but the increase in cross-section continued. The results of the qualitative evaluation is deemed encouraging and warrants further tests to see if ROIs defined with this model provide clinically meaningful results.

Introduction

Bone mineral density (BMD) measurements are commonly used to diagnose bone diseases and to evaluate the effectiveness of treatment (Glüer et al. 2005; Harris et al. 1999). In the first case, measured bone values are compared with those of normal controls, and the amount of deviation from the normal average provides an indicator of the severity of the disease. In the second case, bone measurements taken of a subject at different ages or time points are compared with each other. Increases or decreases in the measured parameters are usually assessed against given thresholds that represent the error of the method, to decide if an observed change is significant.

Our current interest is in the use of peripheral quantitative computed tomography (pQCT) for the assessment of trabecular BMD (TBD) of the forearm. In the case of long bones, the regions closest to the growth plates have a high proportion of trabecular bone; thus, scans are usually taken near the distal growth plate. Once a scan is obtained, the TBD is computed by segmenting the trabecular region from the cortical and subcortical bone.

After an initial measurement, follow-up measurements to compare TBD need to be taken in the same bone region every time. It is important to measure the same region because if the measured slice is off, even by 1 mm, the error in the TBD value can be as large as 6% (Rauch et al. 2001). A 6% change in the TBD value is large compared with the expected change of about 3% per year (WHO study group 1994).

Relocating the same region of bone is currently achieved using one of two methods. One method is the fixed-percentage method, and the other method involves the fitting of cross-sectional areas. In the fixed-percentage method (Grampp et al. 1995), the length of the forearm is measured from the elbow to the ulnar styloid process. A slice that is at a given distance from a reference line is then scanned. For the radius, the reference line may be the articular cartilage of the radius or the place where the radius and ulna overlap, and the distance for selecting the slice to be measured is usually a fixed percentage of the length of the forearm; however, in this method, only one slice is measured, and, hence, the reproducibility of relocating the same slice may be influenced by potential patient movement between scout scan and axial scan and by error in locating the same reference line as the one selected during the initial measurement. To overcome this problem of reproducibility, a second method has been developed.

The second method involves fitting of cross-sectional areas (Hangartner and Overton 1982); scans of multiple adjacent slices in the distal conic region of the radius are taken during initial and follow-up measurements. The cross-sectional areas of the bone obtained for follow-up measurements are compared with the cross-sectional areas of the initial measurement. If the cross-sectional areas in the follow-up measurements match the cross-sectional areas of the initial measurement closely, it is assumed that they represent the same region of bone.

When applied to adult patients, both methods to relocate the same region of bone during follow-up measurements are based on the assumption that the bones are mature, the growth process has ceased, and there is no change in length or cross-sectional area of the bone; however, in the case of children, in whom the bones are

still growing and who show a continued change in cross-sectional area and length, the above two methods may fail (Bilezikian et al. 2002). This failure may lead to erroneous results while examining the change in TBD values.

The thrust of this study is the investigation of problems in relocating the same bone region in children for obtaining longitudinal measurements using pQCT. It aims to propose a model that can be used in relocating the same region in the radius of children.

Change of Radius in Projection Radiographs

Radiographic Data Sets

For the purpose of this study, a longitudinal data set was obtained to investigate changes in bone structure, size, and shape of individuals as they age. We used the radiographs of the forearms of 17 subjects who were measured every 6 months from birth until the age of 10 years and once a year from 10 to 18 years.

The radiographs were digitized using a Howtec film digitizer (iCAD, Nashua, N.H.) at its maximum resolution of 292 dpi. For each digitized radiograph, the regions of interest consisted of the complete radius and ulna, saved as 12-bit TIFF images and tagged with the subject's initials and age. In accordance with the privacy protection policy of the Lifespan Health Research Center, the identities of subjects were masked if they were visible in the digitized images.

Growth in Length

Growth in the length of the radius is known to be different for the distal section as compared with the proximal section. To assess this difference in growth, we have to rely on a landmark that does not change over time. There is a natural marker in the mid-shaft of long bones, the nutrient foramen, which can be identified on a radiograph of the bone. This nutrient foramen can be used as a consistent visual marker, irrespective of how the bone grows (Pritchett 1991), as the point of penetration of the blood vessel into the bone does not vary with age; however, the nutrient foramen is not a prominent feature in all images. Nevertheless, we were able to identify two sets of successive images in which the nutrient foramen was clearly visible.

The first set consisted of seven images, the second set of five images between 2 and 15 years of age. We identified and marked three key locations on each bone image: the proximal end, the distal end, and the nutrient foramen. The distance between the two end points represented the length of the bone. Since the location of the nutrient foramen is fixed, it was used as a reference point from which the percentage contribution of each growth plate towards the increase in length was computed.

The average percentage contribution of the distal growth plate for subject 1 was 65.9% with a standard deviation of 6.8%, and for subject 2 it was 64.6% with a standard deviation of 3.5%. An unpaired Student's t-test for the analysis of difference in the means of the two subjects gave a p-value of 0.74, indicating that the difference between the two means is not statistically significant; thus, we felt comfortable pooling

Table 1. Change in bone length and distal length by age and by subject

Subject	Age range (years)	Difference in bone length (pixels)	Difference in distal length (pixels)	Contribution of distal growth plate (%)
1	2–3	190	112	58.9
1	3–4	144	97	67.4
1	4–7	380	252	66.3
1	7–8	124	72	58.1
1	8–11	316	216	68.4
1	11–15	509	389	76.4
2	2–4	481	306	63.6
2	4–7	385	232	60.3
2	7–9	262	179	68.3
2	9–15	564	374	66.3
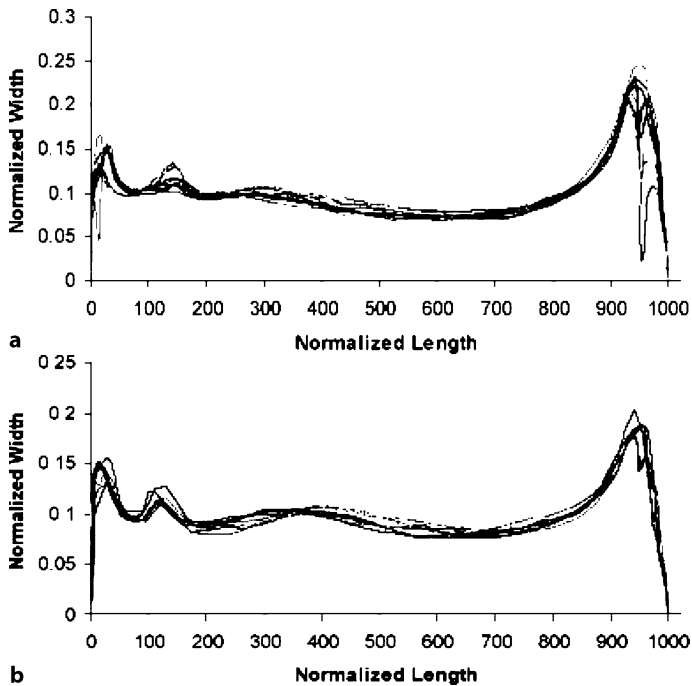
Figure 1. Line profiles of normalized bone shape **a** for subject 1 and **b** for subject 2. The plots consist of bone profiles at ten different ages. The bone profiles match closely for each subject, indicating that the general shape of the bone is age-invariant; however, there are discernable differences between the profiles of the two subjects

the data of the two subjects into one data set (Table 1). For the combined set the average percentage contribution of the distal growth plate was 65.4% with a standard deviation of 5.5%. This deviates from the published value of 75% contribution of the distal growth plate (Lovell et al. 2001), but not enough to be statistically significant. Further experimental measurements to increase the statistical power are needed to confirm if the value of 65% obtained from our limited data set is a better approximation than the published 75%.

Change in Shape

The goal of this analysis was to understand the changes in the shape of the radius of an individual during growth. To normalize the bone with respect to size, the images of the radius of a given subject, taken at different ages, were scaled so that they showed the same length and area of the bone. We investigated whether the shape of the bone is age-invariant and unique for each subject. The following steps were performed:

1. A mask was created covering the region of the bone.
2. The length of the radius was measured in terms of pixels.
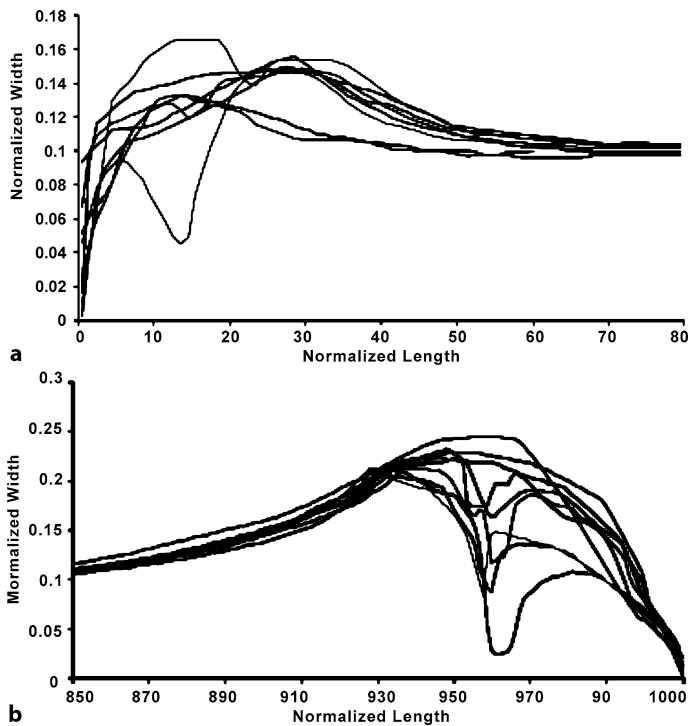
Figure 2. Changes in the profile of the bone with age in the growth-plate regions **a** for the proximal growth-plate region and **b** for the distal growth plate region for subject 1. There is a major change in the shape of the profile as the bone grows because the epiphyses gradually fuse with the metaphyses
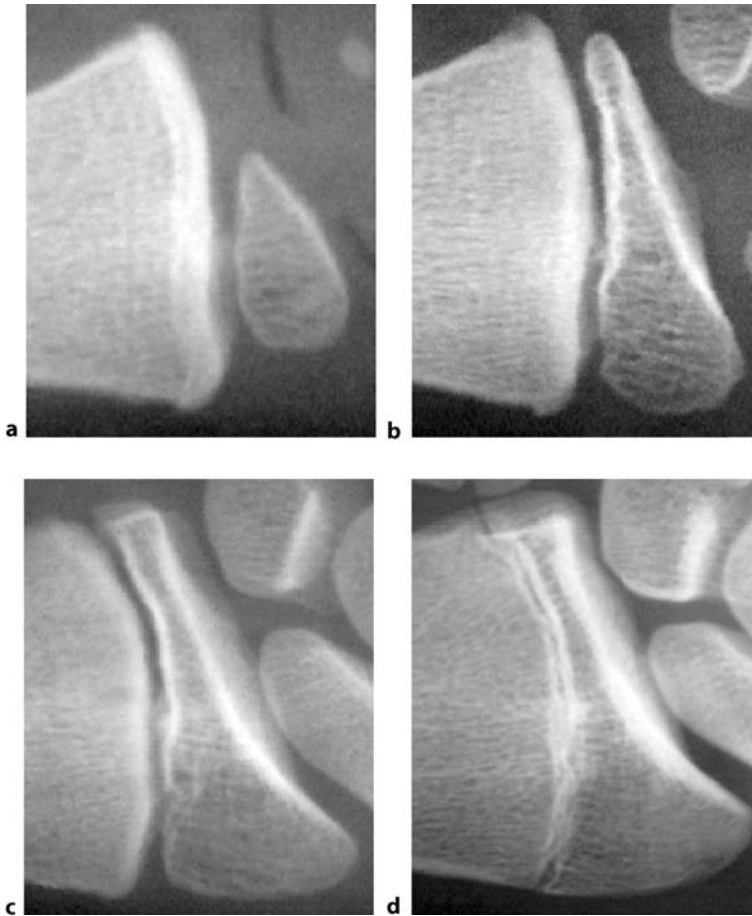
Figure 3. Changes in the shape and structure of the distal epiphysis as the bone grows. Images **a–d** correspond to ages 4, 8, 13, and 17 years

3. The bone width was measured at every point along the length of the bone in terms of pixels. The 1D vector obtained in this step represents the width profile of the radius.
4. The length of the bone was normalized to 1000 pixels. The actual lengths of the bones were always greater than 1000 elements, so normalization of the length to 1000 was achieved by resampling and linear interpolation.
5. The width profile of each bone was normalized to result in a 2D bone area of 100.

A plot of the combined bone profiles of two subjects (Fig. 1) shows that the general shape of the bone does not change much with age; however, the profiles at both ends of the bone show considerable differences (Fig. 2). This is because the epiphyses at both ends undergo major changes and eventually fuse with the metaphyses (Fig. 3). If the profiles are restricted to the diaphyseal and distal metaphyseal region,
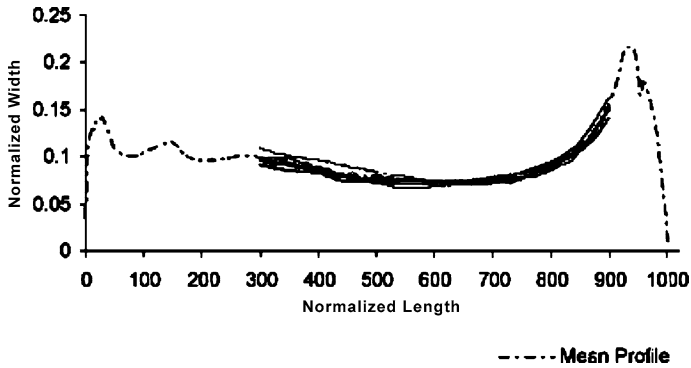
Figure 4. Profiles of the radius of a subject from the diaphysis to the distal growth plate. It is observed that, in the mid-shaft and distal metaphyseal region, the shape of the profile does not change drastically

representing the sites of interest for pQCT measurements, the normalized shape of the bone matches closely for all ages (Fig. 4).

Since the shape of the radius in the diaphyseal and distal metaphyseal region is age-invariant for an individual, it was of interest to check whether the shape of the radius is similar between individuals. To test the shape invariance among different individuals, a uniqueness test was performed, in which the mean profile and the combined sum-of-mean-square (SMS) errors of all profile points were computed from bone profiles of a given subject at three different ages. To compute the mean profile, the normalized width values were averaged at each point of the profile. To test the uniqueness of radius shape, the mean profile of another subject was computed, and the two profiles were compared (Fig. 5). We observed that the mean profile of the two subjects did not match, thereby indicating that radius shapes were different between individuals.
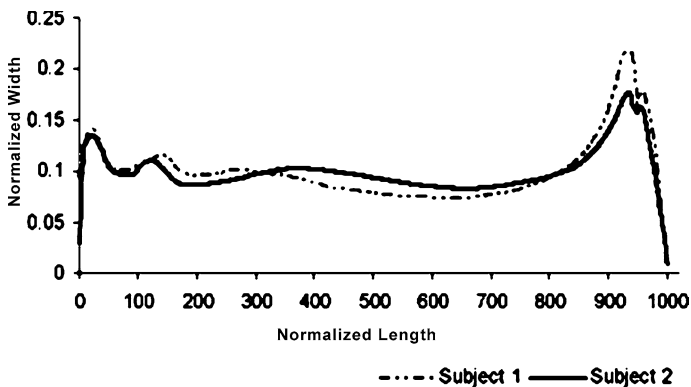
Figure 5. Overlayed plots of mean profiles for two subjects. The mean profiles of the two subjects are different, indicating that the profile for each individual is unique

To evaluate the significance of the differences between the bone profiles and the mean profiles, two types of combined SMS errors were computed: first the differences for all points of each bone profile relative to all points of the mean profile of subject 1; secondly, the differences for all points of each bone profile of subject 1 relative to all points of the mean profile of subject 2 (Fig. 6; Table 2). The combined SMS error of a subject appeared to be greater if it is computed relative to the mean profile of another subject. We performed the same evaluation for all 17 subjects and obtained similar results. Figure 7 shows an example of the combined SMS errors of the bone profiles of subject 7 relative to his own mean profile and relative to the mean profiles of the remaining 16 subjects. We observed that the least error is obtained when the SMS error is computed using the subject's own mean profile; however, this is not always true, as we observed a better match with another subject's mean profile in 113 of 2363 comparisons.

Figure 8a shows the plot of combined SMS errors of the subjects relative to their own mean profiles; Fig. 8b shows the plot of combined SMS errors of each subject relative to the mean profile of the other subjects. It can be seen that the error obtained using the mean profiles of the subjects themselves is smaller than the error obtained
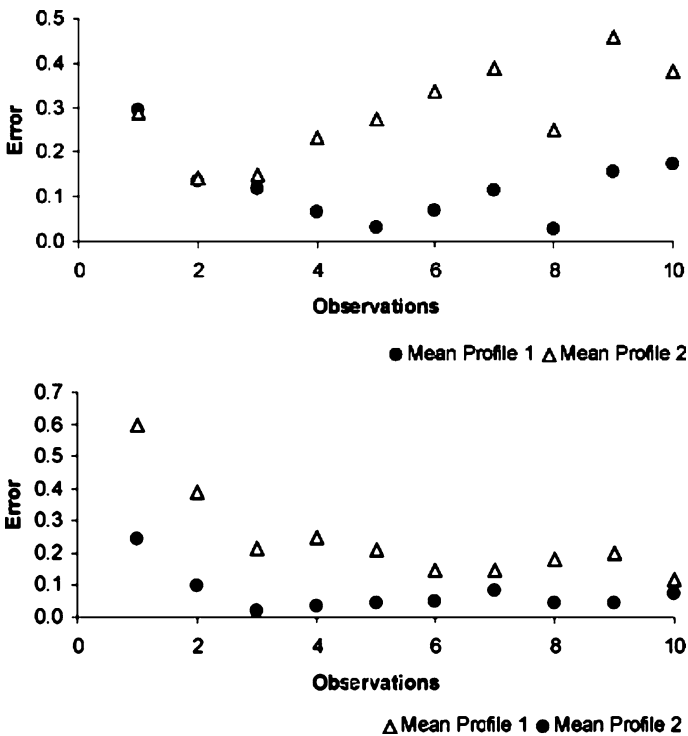
Figure 6. Combined sum-of-mean-square (SMS) error for **a** subject 1 relative to the mean profile of subject 1 and the mean profile of subject 2 and for **b** subject 2 relative to the mean profile of subject 1 and the mean profile of subject 2. The plots show that the SMS error is smallest when it is computed relative to the mean profile of the subject itself

Table 2. Combined sum-of-mean-square errors for both subjects

Observation	Subject	Age (years)	Error relative to mean profile of subject 1	Error relative to mean profile of subject 2
1	1	2	0.296	0.289
2	1	3	0.134	0.144
3	1	4	0.117	0.149
4	1	7	0.068	0.232
5	1	8	0.031	0.275
6	1	9	0.068	0.337
7	1	10	0.115	0.389
8	1	11	0.028	0.250
9	1	13	0.155	0.459
10	1	15	0.173	0.380
11	2	2	0.599	0.244
12	2	4	0.391	0.095
13	2	6	0.212	0.017
14	2	7	0.246	0.033
15	2	8	0.208	0.045
16	2	9	0.145	0.047
17	2	10	0.146	0.081
18	2	12	0.180	0.046
19	2	13	0.199	0.045
20	2	15	0.116	0.071
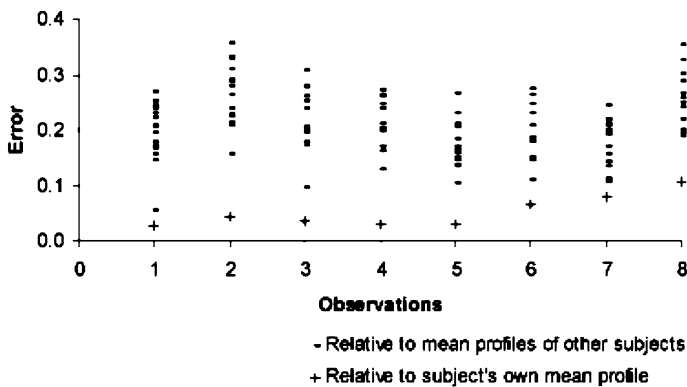
Figure 7. The SMS errors of a subject's individual bone profile relative to the mean of other subjects' profiles and relative to the subject's own mean profile. The least amount of error is obtained relative to the subject's own mean profile

using the mean profile of other subjects. The higher error observed at both ends of the graphs is due to the epiphysis of the bone, which changes its shape drastically with age; however, if the combined SMS errors are computed for the diaphyseal and metaphyseal regions, the errors are reduced (Fig. 9).
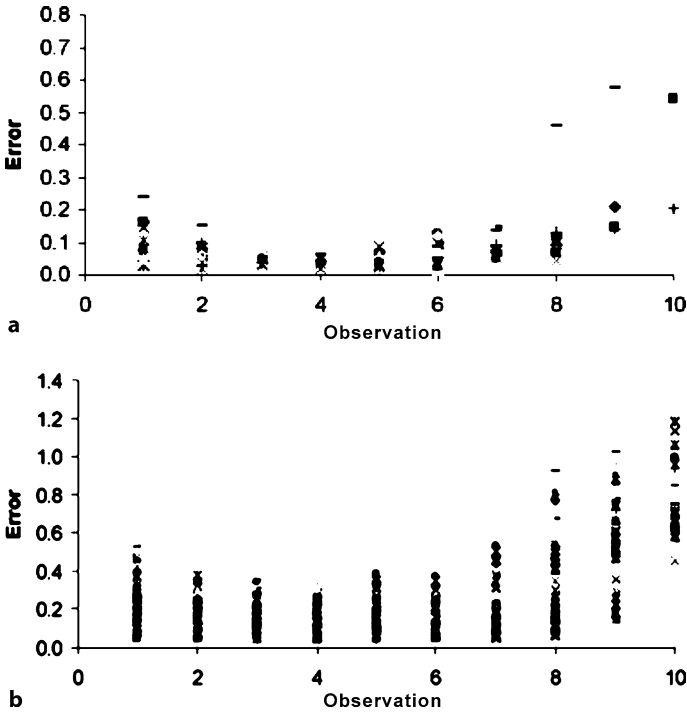
Figure 8. Combined SMS errors of the subjects relative to their own mean profiles (**a**) and relative to the mean profiles of other subjects (**b**). Note that the error axis is scaled differently for the two graphs

△ Relative to subject's own mean profile for the midshaft region

○ Relative to subject's own mean profile for entire bone
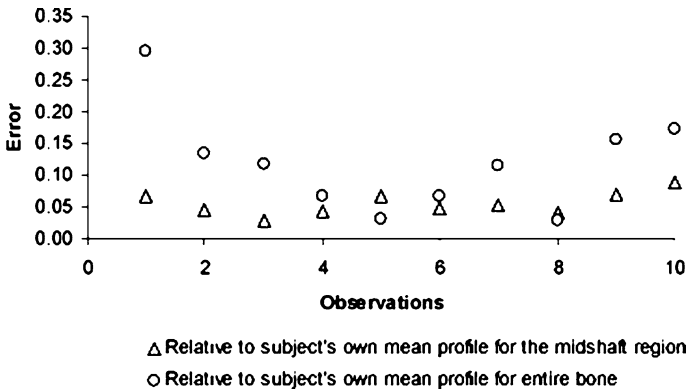
Figure 9. Comparison of error relative to a subject's own mean profile for the mid-shaft region and for the entire bone. The plot shows a reduction in error at lower and higher ages if the epiphyseal regions are excluded

The error tests show qualitatively that the bone profiles between subjects are different; however, statistical analysis using the chi-squared test suggested no significance in the differences of the error values between subjects; however, it can be con-

cluded that, even though the contribution of both growth plates towards the longi-
tudinal growth is not equal, the cross-sectional growth is related to the longitudinal
growth, allowing the bone to maintain its shape throughout the growth process. If
this relationship between cross-sectional growth and longitudinal growth is mathe-
matically modeled, an expression can be obtained that predicts change in width based
on change in length. Such a model will aid in relocating the same region during lon-
gitudinal measurements in children.

Change in Width

A mathematical expression that relates appositional growth to longitudinal growth
would provide the desired model. Since the shape of the bone in the diaphyseal and
metaphyseal regions is invariant with age, the projected bone area will be a function
of its length. The bone area changes with change in width and length. Due to the
shape of the bone being invariant, the change in width is proportionately the same
in all regions of the bone; thus, the average width will vary by the same function of
length. The average width is computed as the ratio of the radiographically projected
area to the length.

To develop a predictive model, the images of the 17 subjects were used. The bone
masks were generated, resulting in a set of binary images with the radius being white
and the background black. Then, the average width $\bar{w}_i$ of each bone was computed
as the 2D area of the bone divided by the length L_i of the bone (Fig. 10). A linear
regression model was fitted through all points:

$$\bar{w} = 0.0475 \cdot L + 37.995 \ . \tag{1}$$

The regression Eq. (1) defines a slope and an intercept. The intercept provides the
average width when the length of the bone is zero. Of course, the length of the bone
is never zero, even at birth, so the intercept information is not useful; however, the
slope, which is the ratio of change between the average width and the length, can be
used to compute changes in width. This change in width can then be added to the
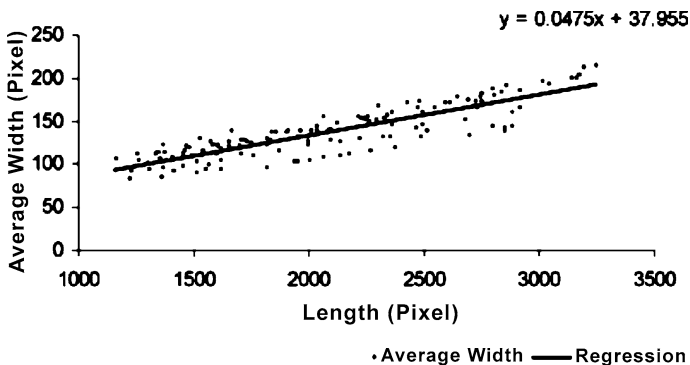
Figure 10. Average width vs length of 139 radius images from 17 subjects
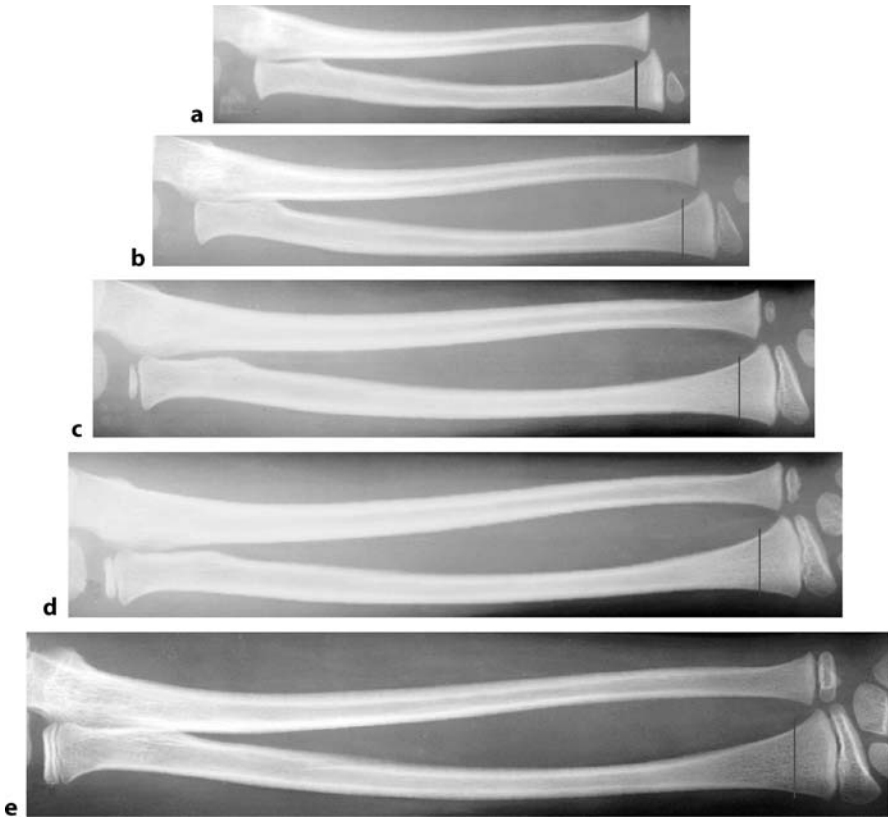
Figure 11. Forearm bone images of a subject corresponding to ages 2, 4, 7, 8, and 11 years. **a** The image at age 2 years where the initial slice is selected. **b–e** The relocated slices at age 4, 7, 8 and 11 years, respectively. The images show qualitatively that, by using the predictive model, the relocated slices are consistently positioned in the distal conic region

width of the slice obtained during an initial measurement to estimate the width of the relocated slice during a follow-up measurement:

$$NewWidth = 0.0475 \cdot \Delta L + InitialWidth \,, \tag{2}$$

where ΔL is the change in radius length from a younger to an older age. After computing the new width, the task of relocation is reduced to finding a slice in the conic region in the more recent radius image that corresponds in width to the new width computed.

The model was developed based on 139 radius images of the 17 subjects. Since the subjects were not classified by gender, the model developed is not gender specific. This model has been based on radius only and, thus, is not necessarily a generalized solution for any other type of long bone.

The model was tested on five different images of a given subject, taken at ages 2, 4, 5, 8, and 11 years. The following steps were performed to test the model:

1. On the earliest forearm image, the length of the radius was measured and recorded.
2. A slice was selected in the distal conic region, and its width was measured and recorded (Fig. 11a).
3. For the subsequent bone images, the length of the radius was measured and recorded.
4. Using the predictive model, the new slice widths were computed based on the change in bone length of images taken after the first bone image.
5. The slices were relocated by matching the computed width on their respective bone images. The closest match of the computed width on the bone is marked as the relocated slice (Fig. 11b–e).

It can be seen that the relocated slices are always in the conic region of the radius. It also appears qualitatively that the relocated slices are in the same region as the slice initially selected in the first forearm bone image, taken when the subject was 2 years of age. This indicates that the predictive model developed is successful in *predicting* the position of the relocated slice. If a multi-slice approach is used in collecting pQCT data, there is no need for a reference landmark, hence reducing the error in relocation due to potential patient movement between scanning the scout view and the transaxial slices.

Conversion of Width to Cross-Sectional Area

The method of CT provides cross-sectional images, from which the cross-sectional area (CSA) of objects, such as a bone, can be extracted. In the distal conic region of the radius, this cross-sectional area is greatly dependent on the position of the measurement slice. Conversely, the cross-sectional area is a sensitive parameter for establishing the location of a measurement slice. As has been shown in adult subjects, relocation based on matching CSA results in greatly improved repeatability of bone-density assessment compared with repositioning based on scout views (Hangartner and Overton 1982). The goal of the next step is to calculate the new CSA based on the growth in bone length and, thus, avoid the need to rely on repositioning based on a scout view and a reference landmark.

Mathematical Expression

The extension of the predictive model to compute change in cross-sectional area was derived as follows:

$$Area \propto Width^2 \ . \tag{3}$$

Therefore,

$$Area_1 = c \cdot Width_1^2 \quad \text{and} \quad Area_2 = c \cdot Width_2^2 \ , \tag{4}$$

where c is a proportionality constant that considers the actual geometry of the cross-section instead of assuming the shape to be circular; thus,

$$Area_2 - Area_1 = c \cdot \left(Width_2^2 - Width_1^2 \right) . \tag{5}$$

A further proportionality constant g takes care of the ratio between the average width and the width at the slice of interest:

$$Area_2 - Area_1 = c \cdot g \cdot \left(\bar{w}_2^2 - \bar{w}_1^2 \right) . \tag{6}$$

Substituting $\bar{w}$ with Eq. (1) we obtain:

$$Area_2 - Area_1 = c \cdot g \cdot \left[\left(0.0475 \cdot L_2 + 37.955 \right)^2 - \left(0.0475 \cdot L_1 + 37.955 \right)^2 \right] . \tag{7}$$

Simplifying Eq. (7) results in

$$Area_2 - Area_1 = c \cdot g \cdot \left[0.0475^2 \cdot \left(L_2^2 - L_1^2 \right) + 2 \cdot 0.0475 \cdot 37.955 \cdot \left(L_2 - L_1 \right) \right] ; \tag{8}$$

thus, the new area is:

$$Area_2 = c \cdot g \cdot \left[0.0475^2 \cdot \left(L_2^2 - L_1^2 \right) + 3.606 \cdot \left(L_2 - L_1 \right) \right] + Area_1 . \tag{9}$$

Calculation of Constants

Converting the multiplicative constant g into an additive constant, which disappears in the difference expression of Eq. (8), we can calculate the value of c for each individual longitudinal data set from the cross-sectional images using the following steps:

1. A line is drawn tangential to the posterior boundaries of both the radius and ulna (Fig. 12). This creates a reference line replicating the orientation of the film used for the posterior-anterior view of the radiographs, from which the width measurements were obtained.
2. Two lines are drawn perpendicularly to the aforementioned reference line: one tangential to the lateral boundary and the other tangential to the medial boundary of the radius.
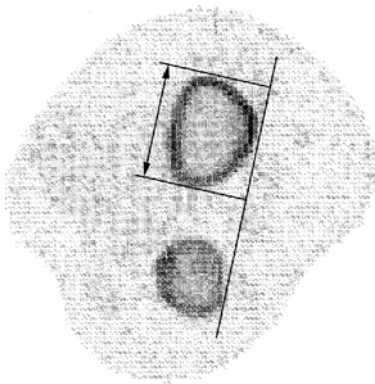
Figure 12. Measurement of the width of the radius to compute the value of c. The width (*arrowed line*) is parallel to the reference line that is tangential to both radius and ulna

3. The distance between the lateral and medial lines is measured using a ruler and noted as the width of the radius.
4. The variable c is computed by dividing the area of the bone with the square of its measured width. The area of the bone is obtained as part of the regular segmentation process from the pQCT image.

To use the model for pQCT of longitudinal measurements of children, the following procedure needs to be carried out:

1. During the initial measurement, the length of the forearm is noted, and a site is located in the distal conic region. For this site, the CSA is recorded.
2. During a follow-up measurement, the length of the forearm is measured and the change in length is computed.
3. The value of c is computed from the baseline measurement.
4. Using the model with known initial cross-sectional area and change in length, the new CSA is computed.
5. The position of the relocated slice in the new measurement set is identified where the area of the slice is equal to the computed CSA.

To use this model, it is necessary to measure multiple slices in the conic region during follow-up measurements. The predicted area can, then, be matched with the cross-sectional area of the slices measured during follow-up measurements. The slice that matches closely with the predicted area gives the position of the relocated slice; however, if the predicted area does not match with any of the measured slices but instead lies between two measured slices, then the bone parameter of interest for the relocated slice may be computed by interpolating between the two measured slices. The same procedure is valid for relocating and then averaging multiple adjacent slices.

Evaluation of Repositioning Algorithm

Data sets from our laboratory consisting of radial pQCT measurements of three subjects were used to assess the relocation approach. Each data set included the length of the forearm, the location of the ulnar and radial styloid processes from a scout view as well as the cross-sectional areas and densities at known distances from the styloid processes. Six to eight sections were available for each data set at 2-mm intervals in the distal conic region of the radius.

Using the area of the initial slice and the corresponding $c \cdot g$ value, the new areas were computed using Eq. (9). Each new area was compared with the areas measured during the follow-up measurements. If the difference in two areas was <60 pixels (out of an area of about 3000 pixels), the slice was considered to be a match with the corresponding slice in the initial measurement. Once a match was obtained, the cross-sectional shapes of the two images were visually compared. If the shapes matched reasonably well, the match was considered successful (Fig. 13). Conversely, if the shape did not match even though the areas matched, the match was considered a failure.
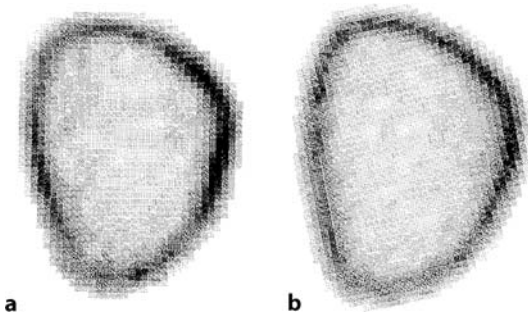
Figure 13. Sample images for successfully matching cross-sections from **a** initial measurement to **b** follow-up measurement. The area of the second slice differs by <60 pixels from the area predicted by the growth in length, and the shape of the two cross-sections are considered to match closely

The foregoing evaluation was conducted to find matching pairs in the data sets of the three subjects. A total of 26 area matches were obtained of which 21 were considered successful shape matches and the remaining 5 failures.

Discussion

The analysis of a limited set of radiographs allowed us to establish an estimate for the relative contribution of the distal and proximal growth plates to the increase in length of the radius. Using the nutrient foramen as a fixed landmark, the average contribution of the distal growth plate was measured to be 65%, the contribution of the proximal growth plate 35%. Considering the standard deviation observed in the given data set, this estimate was similar to the published value of 75% contribution of the distal growth plate (Lovell et al. 2001). There is potentially a variation in contribution of the two growth plates at various ages, and this was not considered in this initial study.

The longitudinal data set represented by the projection radiographs of the forearm provided a rare opportunity to study the shape changes during growth. Although our final interest is in relocating the measurement position for pQCT analysis, the establishment of an appropriate pQCT database would require a 20-year-long study. The necessary pQCT measurements would have to include a large number of adjacent slices to characterize the dependence of the various bone parameters on position. The limited measurement speed of pQCT would likely not allow a sufficiently dense coverage of the region of interest, making such an approach impractical. Modern volumetric CT does have the capability of measuring large numbers of slices in a short period of time, but this technique was not available to us at the time when we started this research project; however, some of the findings could be verified with a follow-up study using volumetric CT, although not easily over the same time period of 20 years covered by our radiographic data set.

The two major findings from the radiographs are (a) that the projected posterior/anterior shape, as defined in our approach, is invariant for a given subject as long as we exclude the growth plates, which is not a problem, as pQCT measurements usually attempt to exclude the growth plates anyway, and (b) that the shape is different between subjects. The first finding implies that an anatomically similar measurement position is reasonably defined based on a certain percentage of the bone length from a given landmark. The second finding implies that some normalization needs to be subject specific and cannot be assumed to be the same for all subjects.

If it was possible to reliably reposition the measurement slices in follow-up scans based on the identification of given landmarks from the scout view, no further investigations would be necessary; however, the combination of limited axial resolution of the scout view (±1 mm at best), potentially large gradients of bone density with axial position (5 – 10%/mm), and a certain amount of possible arm movement between scout view and axial scan makes the sole reliance on the scout view for repositioning unsatisfactory.

The most sensitive parameter for repositioning is the CSA of the bone. Due to growth, it is necessary to estimate the new CSA from the increase in bone length. The CSA, however, can only be established after the slice has been scanned, which means that several slice positions need to be available to evaluate the bone parameters of interest at the right location; thus, a single-slice approach is not acceptable for accurate repositioning of the slices in longitudinal studies.

Our approach of normalizing length and width separately accounts for growth in length and width. Although we fitted a linear curve to obtain a simple expression describing the change in width relative to the change in length, it is not necessarily true that the calculated dependence is the same in all phases of growth. A refined model might take the chronological age, the bone age, or the pubertal status into account.

The final formula for calculating the new cross-sectional area relies on an average dependence of width based on length and on a patient-specific relationship between width and cross-sectional area. This assumes that the width-to-area relationship is constant for the two time points in a given patient. We do not have independent proof for the constancy of this relationship, but we inferred it from the constancy of the posterior-anterior shape.

The evaluation of the success of our algorithm relied on a small set of measurements. We declared success if a qualitative match in cross-sectional shape was observed. Again, we assumed consistency in cross-sectional shape. Better quantitative assessment of the similarity of the shape is possible by using some of the tools developed for active shape models (Cootes et al. 1994).

The qualitative match experiment resulted in 21 of 26 matches, indicating an 81% success rate. This result is encouraging but needs to be verified by a more rigorous quantitative matching method. With some of the refinements suggested above, we expect that our success rate can be improved, allowing this approach to be used in clinical practice.

Conclusion

Our proposed model produced satisfactory results in 81% of the tested cases. The failures were observed mostly at an age when the increase in length ceased but the increase in cross-section continued. The results of the qualitative evaluation is deemed encouraging and warrants further tests to see if ROIs defined with this model provide clinically meaningful results.

References

Bilezikian JP, Raisz LG, Rodan GA (2002) Principles of bone biology. Academic Press, San Diego

Cootes T, Hill A, Taylor C, Haslam J (1994) The use of active shape models for locating structures in medical images. Image Vision Comput 12:355–366

Glüer M, Minne H, Glüer C, Lazarescu A, Pfeifer M, Perschel F, Fitzner R, Pollähne W, Scholtthauer T, Pospeschill M (2005) Prospective identification of postmenopausal osteoporotic women at high vertebral fracture risk by radiography, bone densitometry, quantitative ultrasound, and laboratory findings: results from the PIOS study. J Clin Densitom 8:386–395

Grampp S, Lang P, Jergas M, Glüer CC, Mathur A, Engelke K, Genant HK (1995) Assessment of the skeletal status by peripheral quantitative computed tomography of the forearm: short-term precision in vivo and comparison to dual X-ray absorptiometry. J Bone Miner Res 10:1566–1576

Hangartner TN, Overton TR (1982) Quantitative measurement of bone density using gamma-ray computed tomography. J Comput Assist Tomogr 6:1156–1162

Harris S, Watts N, Genant H, McKeever C, Hangartner T, Keller M, Chestnut III C, Brown J, Eriksen E, Hoseyni M, Axelrod D, Miller P (1999) Effects of risedronate treatment on vertebral and nonvertebral fractures in women with postmenopausal osteoporosis: a randomized controlled trial. J Am Med Assoc 282:1344–1352

Lovell W, Morrissy B, Winter R, Morrissy R, Weinstein S (2001) Lovell and Winter's pediatric orthopaedics. Lippincott Williams and Wilkins, Philadelphia

Pritchett J (1991) Growth plate activity in the upper extremity. Clin Orthop Rel Res 268:235–242

Rauch F, Tutlewski B, Fricke O, Rieger-Wettengl G, Schauseil-Zipf U, Herkenrath P, Neu CM, Schönau E (2001) Analysis of cancellous bone turnover by multiple slice analysis at distal radius: a study using peripheral quantitative computed tomography. J Clin Densitom 4:257–262

WHO study group (1994) Assessment of fracture risk and its application to screening for postmenopausal osteoporosis. World Health Organization, Geneva

Non-invasive Bone Quality Assessment Using Quantitative Ultrasound Imaging and Acoustic Parameters

Yi-Xian Qin (✉) [1], Wei Lin[1], Yi Xia[1], Erik Mittra[1], Clint Rubin[1], and Ralph Müller[2]

[1] Department of Biomedical Engineering, Stony Brook University, NY 11794-2580, USA
e-mail:Yi-Xian.Qin@sunysb.edu
Tel: 631-632-1481, Fax: 631-632-8577
[2] Institute for Biomechanics, ETH and University, Zürich, Switzerland

Abstract

Musculoskeletal complications, i. e., osteoporosis, affect not only bone's mineral density, but also quality. Early diagnosis of such poor bone quality leads to prompt treatment and thus will dramatically reduce the risk of complications. Using a newly developed scanning confocal acoustic diagnostic (SCAD) system, trabecular bone quality was evaluated by quantitative ultrasound on 63 sheep bone samples. The structural and strength properties of bone were confirmed using μCT and mechanical testing in three orthogonal directions. While there are good correlations between broadband ultrasonic attenuation and μCT determined parameters, such as bone volume fraction (BV/TV; $R = -0.68$), strong correlations exist between ultrasound velocity and bone strength and structural parameters such as bulk modulus ($R = 0.82$), and BV/TV ($R = 0.93$). The correlations between SCAD prediction and bone quantity and quality parameters were improved by using a parameter to combine BUA and UV in a linear regression analysis, yielding $R = 0.96$ (BV/TV) and $R = 0.82$ (bulk modulus). A stratified model was proposed to study the effect of transmission and reflection of ultrasound wave within the trabecular architecture on the relationship between ultrasound and BMD. The results demonstrated that ultrasound velocity in trabecular bone was highly correlated with the bone apparent density ($r = 0.97$). Moreover, a consistent pattern of the frequency dependence of ultrasound attenuation has been observed between simulation using this model and experimental measurement of trabecular bone, in which the peak magnitude of nBUA was observed at approximately 60% of the bone porosity. These results suggest that image-based quantitative ultrasound has demonstrated the potentials to predict not only the bone mass, but also bone's mechanical strength in the region of interests of bone.

Introduction

Clinical Relevance of Osteoporosis

Musculoskeletal complications induced by age-related diseases, such as osteoporosis, and in functional disuse induced disorders, e. g., osteopenia generated by microgravity during extended space missions and bed rest, represent key health problems. Such a skeletal disorder changes both the structural and strength properties of bone, and the latter plays a critical role in ultimately leading to fracture. Early diagnosis of progressive bone loss or poor bone quality would allow prompt treatment and thus would dramatically reduce the risk of bone fracture. Most osteoporotic fractures occur initially in cancellous bone; hence, non-invasive assessment of trabecular strength and stiffness is extremely important in evaluating bone quality.

Osteoporosis is a reduction in bone mass or density that leads to deteriorated and fragile bones and is the leading cause of bone fractures in postmenopausal women and in the elderly population for both men and women. About 13–18% of women aged 50 years and older, and 3–6% of men aged 50 years and older, have osteoporosis in the U.S. alone. These rates correspond to 4 ~ 6 million women, and 1 ~ 2 million men who suffer from osteoporosis (Looker and Johnson 1998). One-third of women over 65 years will have vertebral fractures and 90% of women aged 75 years and older have radiographic evidence of osteoporosis (Melton 1995, 1996; Wahner and Fogelman 1994). Another 37–50% of women aged 50 years and older, and 28–47% of men of the same age group, have some degree of osteopenia; thus, approximately a total of 24 million people suffer from osteoporosis in the U.S. alone, with an estimated annual direct cost of over $18 billion to national health programs. Hence, early diagnosis that can predict fracture risk and result in prompt treatment is extremely important. Early identification of fracture risk, most commonly caused by osteoporosis-induced bone fragility, is also important in implementing appropriate treatment and preventive strategies. Indeed, the ability to accurately assess bone fracture risk non-invasively is essential for improving the diagnostis as well as therapeutic goals (i. e., assessing temporal changes in bone during therapy) for bone loss from such varied etiologies as osteoporosis, microgravity, bed rest, or stress-shielding around an implant.

Current Non-invasive Evaluation Methods for Osteoporosis

Assessment of bone mineral density (BMD) has become as essential element in the diagnosis of osteopenia and osteoporosis (Genant 1998; Kanis 1997a,b; Kanis et al. 2005a,b; Melton et al. 1998, 2001, 2003, 2005; Melton 1995). Bone density was initially estimated from the conventional X-ray by comparing the image density of the skeleton to the surrounding soft tissues. While de-mineralized bone has image density closer to soft tissues, dense mineralized skeletal tissues appear relatively white on an X-ray image; hence, the mineral density of bone can be estimated by the degree of gray color of the X-ray image in the bone region. However, because of its resolution and variations generated in the X-ray image, it has been suggested that bone

mineral losses of at least 30% are required before they may be visually measured using a conventional X-ray (Sartoris and Resnick 1990a,b). Growing awareness of the impact of osteoporosis on the elderly population and the consequent costs of health care, together with development of new treatments to prevent fractures, have led to a rapid increase in the demand for bone densitometry measurements. Many image modalities and techniques have been developed to improve the quality and accuracy of the measurement for bone mineral and density assessment.

The BMD measurement using dual-energy X-ray absorptiometry (DXA) is currently a gold standard technique used because of its relative precision ($\sim$ 2%), and whole body and/or multi-site imaging ability (spine, hip, wrist, and total skeleton); however, because the source and the detector cross the whole bone (including layers of cortex and trabeculae), current techniques *apparently* are too insensitive for quantifying trabecular bone mass separately. In other words, a certain percent of bone mass must be lost before significant radiation attenuation occurs (Chesnut 1993). In addition, DXA, as well as CT, has limitations on X-ray ionizing radiation (70 – 140 kVp, 10 mrem), imprecision due to surrounding soft tissue variations, and issues of non-repeatability due to patients' position (Chesnut 1993; Wahner and Fogelman 1994). Importantly, the measurements obtained do not provide information about the integrity of the trabecular architecture, or information about the mechanical properties of the composing trabeculae. Due to these issues, the quality of bone, whether in normal or osteopenic people, remains largely unknown (i. e., it is extremely difficult to monitor the strength and the conductivity in vivo). As a result, an improved diagnostic tool is needed to evaluate both the quantity and the quality of bone, which will help in the early detection and therefore the possible prevention and treatment of this disease.

Bone Quality As a Factor of Assessment of Fracture

Unfortunately, a skeleton at risk of fracture cannot simply be determined by the amount of bone (e. g., BMD) that exists. To a large degree, the *quality* of the bone is just as important. While a formal definition of bone quality is somewhat elusive, at the very least it incorporates architectural, physical, and biological factors that are critical to bone strength, such as bone morphology (i. e., trabecular connectivity, cross-sectional geometry, longitudinal curvature), the tissue's material properties (e. g., stiffness, strength), and its chemical composition and architecture (e. g., calcium concentration, collagen orientation, porosity, permeability). The ability to directly assess both bone density and quality (i. e., strength) would have great impact in predicting the risk of fracture.

If not only bone mineral density but also bone quality, e. g., stiffness and/or modulus, can be monitored or determined instantly in the early stage of such diseases, then one can better understand the skeleton adaptation on a daily basis. In the case of osteopenia and/or osteoporosis, fractures can occur without a singular traumatic event. Such a database would provide detailed progressive information of the skeleton modeling/remodeling response, which would potentially direct treatment regimens to prevent or recover bone loss.

Quantitative Ultrasonometry

Quantitative ultrasound (QUS) for measuring the peripheral skeleton has raised considerable interest in recent years. New methods have emerged with the potential to estimate trabecular bone modulus more directly. The QUS provides an intriguing method for characterizing the material properties of bone in a manner which is non-invasive, non-ionizing, non-destructive, and relatively accurate. The primary advantage of QUS is that it is capable of measuring not only bone quantity (e. g., BMD), but also bone quality (i. e., estimation of the mechanical property) of bone. Over the past 15 years, a number of research approaches have been developed to quantitate bone mass and structural stiffness using QUS (Ashman et al. 1984, 1987; Ashman and Rho 1988; Nicholson et al. 2001; Nicholson and Bouxsein 2002). Preliminary results for predicting osteoporosis using QUS are quite promising, and it has great potential for widespread application (including screening for prevention). As such, many QUS machines have been developed, and there are currently many different devices on the market. Most of the available systems measure the calcaneus using plane waves that utilize either water or gel coupling (Table 1), e. g., Sahara (Hologic, Bedford, Mass.), QUS-2 (Metra Biosystems, Santa Clara, Calif.), Paris (Norland, Fort Atkinson, Wisconsin), and UBA 575 (Walker Sonix, Worcester, Mass.). Recently, an image-based bone densitometry device for calcaneous ultrasound measurement was also made available using an array of plane ultrasound wave (GE-Lunar, Madison, Wis.). Using several available clinical devices, studies in vivo have shown the ability of QUS to discriminate between patients with osteoporotic fractures and age-matched controls (Cheng et al. 1997; Gregg et al. 1997; Njeh et al. 1997, 1999a, 2001). It has been demonstrated that QUS predicts risk of future fracture generally as well as DXA (Bauer et al. 1997; Hans et al. 1993, 1995, 1998; Njeh et al. 1997, 1999a); however, there are several noted limitations, including the tissue boundary interaction, non-linear function of density associated with bone ultrasonic attenuation, single index covering broad

Table 1. Summary of current QUS devices for calcaneus

Device	Performance	Resolution	Predict parameter	Cost ($K)
Sahara (Hologic)	Index	Non-image	Z score	20~25
QUS-2 (Metra Biosystem)	Index	Non-image	Z score	20~25
UBA 575 (Walker Sonix)	Index	Non-image	Z score	20~25
Achilles (GE-Lunar)	Index+image	Image, 5 mm	Z score	40~50
UBIS 5000 (DMS)	Index+image	Image, 2 mm	Z score	30~35
DTU-one (Osteometer)	Index+image	Image, 2 mm	Z score	25~30
New SCAD/SCAN	Image+index	Image, 1 mm	Stiffness, BMD, Z	20

range of tissues (including cortical and trabecular regions), and the interpolation of the results. Recently, a focused ultrasound sonometer device was developed to obtain likelihood BUA image in the human calcaneus region (center frequency 0.5 MHz, focus 50 mm; Laugier et al. 1996, 1997, 2000; UBIS 5000, Diagnostic Medical Systems; and DTU-one, Osteometer MediTech). These devices provide ultrasound images in the calcaneus region, in which the parameter compares to DXA data. Perhaps the major drawbacks of these ultrasound osteometers are low resolution and lack of physical interrelation with meaningful bone strength. While only showing the correlation between BUA data and BMD, these devices mostly provide qualitative information for assessment of osteoporosis, not the true prediction for bone structural and strength properties; therefore, QUS remains at a stage as a screening tool (Fig. 1), because of the non-uniformity of the porous structure in the bone tissue and its associated affects in resolution (Njeh et al. 1999b). Research attention is focused on developing systems to provide true images reflecting bone's structural and strength properties at multiple skeletal sites, i. e., in the hip, which can provide a true diagnostic tool (instead of just for screening) that surpasses the radiation-based DXA machines.

If QUS bone densitometry can be developed to provide a "true" bone quality parameter-based diagnostic tool, i. e., directly related to bone's structural and strength properties, and to target multiple and critical skeletal sites, e. g., hip and distal femur, QUS would have greater impact on the diagnosis of bone diseases (e. g., osteoporosis) than current available bone densitometry. Research efforts are being made in this regard (Laugier et al. 1996, 1997, 2000; Qin et al. 2001, 2003). As an example, a new QUS modality, known as scanning confocal acoustic diagnostic system, has been developed (Qin et al. 2001, 2002, 2003; Xia et al. 2005). This system is intended to provide true images reflecting to bone's structural and strength properties at particular skeletal sites at peripheral limb and potentially at deep tissue such as greater trochanter (Nicholson et al. 2001; Nicholson and Bouxsein 2002). The technology may further provide both density and strength assessment in the region of interests for the risk of fracture (Qin et al. 2001, 2002, 2003; Xia et al. 2005).

Figure 1. A QUS bone densitometry test in a heel region. (Reproduced courtesy of GE-Lunar, Inc.)

Fundamental QUS Parameters in Bone Measurement

In an effort to utilize QUS for predicting bone quality, a variety of approaches have been explored with a large number of studies published in the past decade which have examined the utility of QUS and its potential application as a diagnostic tool for osteoporosis. The physical mechanisms of ultrasound applied to bone may include a number of fundamental approaches, i. e., speed of sound (SOS) or ultrasonic wave propagating velocity (UV), sound-energy attenuation (ATT), broadband ultrasound attenuation (BUA), and critical angle ultrasound parameters which closely relate to acoustic transmission in a porous structure. Most commonly parameters for QUS measurement are BUA and SOS, which can be used to identify those individuals at risk of osteoporotic fracture as reliably as BMD (Bauer et al. 1997; Frost et al. 1999, 2001; Hans et al. 1993, 1995, 1998). It has been shown that both BUA and SOS are decreased in individuals with risk factors for osteoporosis, i. e., primary hyperparathyroidism (Gomez et al. 1998; Guo et al. 1996; Minisola et al. 1989, 1995, 1998), kidney disease (Wittich et al. 1998), and glucocorticoid use (Blanckaert et al. 1997; Cortet et al. 1997). The proportion of women classified into each diagnostic category was similar for BMD and QUS. Using the World Health Organization (WHO) criteria to classify osteoporosis for BMD measurement use DXA and QUS testing, approximately one-third of postmenopausal women aged 50+ years with clinical risk factors were diagnosed as osteoporotic, compared with only 12% of women without clinical risk factors. This suggests that the measurement of QUS with calcaneal BUA and SOS is to some extent the same as BMD Z-score measurement.

Background of BUA in Trabecular Bone Measurement

The BUA and SOS are currently two commonly used methods for QUS measurements, which make it potentially possible to predict bone density and strength. As an ultrasound wave propagates through a medium, BUA measures the acoustic energy that is lost in bone (unit: dB/MHz). The slope, at which attenuation increases with frequency, is generally between 0.2 and 0.6 MHz, and characterizes BUA. The slopes of the frequency spectrum may reflect the density and structure of bone. Although relatively little is known about the fundamental interactions that determine ultrasound attenuation in bone, the potential sources contributing to the attenuation include absorption, scattering, diffraction and refraction (Madsen et al. 1999; Wear and Garra 1998; Wear 1999; Wear et al. 2000). While absorption predominates in cortical bone attenuation, the mechanism of BUA in cancellous bone is believed to be scattering (Njeh et al. 1999b; Strelitzki and Evans 1996, 1998; Strelitzki et al. 1999). The importance of scattering has been alluded to in the literature. Scattering is also suggested to contribute to the non-linear variation in BUA with density seen in cancellous bone and porous medium (Aindow and Chivers 1988; Chivers 1977, 1981; Chivers and Parry 1978).

Background of SOS or UV for Bone Measurement

The strength of trabecular bone is an important parameter for bone quality. In-vitro studies have correlated the ultrasound velocity with stiffness in trabecular bone sam-

ples (Ashman et al. 1989; McKelvie and Palmer 1991; Turner and Eich 1991). This indicates that ultrasound has the potential to be advantageous over the X-ray based absorptiometry in assessing the quality of bone in addition to the quantity of bone. The mechanism of SOS in predicting bone strength is believed to be due to the fact that the velocity of an ultrasound wave depends on the material properties of the medium through which it is propagating, but also depends on the mode of propagation. By determining the wave velocity through a bone, the elastic modulus of bone specimens can be evaluated, or at least be approximated (Ashman et al. 1989; McKelvie and Palmer 1991; Rho et al. 1993; Turner and Eich 1991). When ultrasound travels through a porous material, e. g., trabecular bone, it carries information concerning material properties, such as density, elasticity, and architecture. A relationship exists between the ultrasound velocity (unit: meters per second) and the material elasticity E and density ρ (Ashman et al. 1989; Njeh et al. 1999b).

$$V = \sqrt{E/\rho} \tag{1}$$

The velocity, with which ultrasound passes through normal bone, is quite fast and varies depending on whether the bone is cortical or trabecular. Speeds of 2800 – 3000 m/s are typical in cortical bone, whereas speeds of 1550 – 2300 m/s are typical in trabecular bone.

It is demonstrated that trabecular bone strength is highly correlated with elastic stiffness (Hou et al. 1998). With the introduction of QUS, a number of new diagnostic parameters and experimental results, both in vitro and in vivo, have shown potential for evaluating not only bone quantity (i. e., BMD), but also bone quality (i. e., structure and strength). Two principal variables, BUA and UV, have been confirmed to identify those individuals at risk of osteoporotic fracture as reliably as BMD from DXA; however, SOS and BUA are related to bone density and strength as well as to trabecular orientation, the proportion of trabecular bone and cortical shell, the composition of organic and inorganic components, and conductivity of cancellous structure; thus, QUS of trabecular bone depends on a variety of factors that contribute to the measured ultrasound parameters.

QUS Assessment for Bone Quality

Beyond bone quantity, the quality (the integrity of its structure and strength) has become an equally or even more important measure to understand the bone structure and mechanical integrity. Most osteoporotic fractures occur in cancellous bone; therefore, non-invasive assessment of trabecular bone strength and stiffness is extremely important in predicting the quality of the bone. The strength of trabecular bone depends mostly on the mechanical properties of the bone at the local and bulk tissue level, and on its spatial distribution (i. e., the microarchitecture). A better understanding of the factors that influence bone strength is a key to developing improved diagnostic techniques and more effective treatments. To overcome the current hurdles, to improve the "quality" of the non-invasive diagnostic instrumentations, and to apply the technology for future clinical application, new clinical modalities

should concentrate on several main areas: (a) increasing the resolution, sensitivity, and accuracy in diagnosing osteoporosis through unique methods for improvement of signal/noise ratio; (b) directly measurement of bone's strength as one of the primary parameters for the risk of fracture; (c) generating real-time compatible imaging to identify local region of interest; (d) validation of structural and strength properties with new modalities; and (e) predicting local trabecular and bulk stiffness and microstructure of bone, and generating physical relationship between measurement and bone quality. In an attempt to achieve these goals, recent advances of emerging technologies have been developed primarily for animal studies at this stage. These developments include high-resolution pQCT, micro-MR-derived measures of structure, micro-CT-based BMD, and combined assessment of strength using geometry, density, and computational simulation. These methods will further lead to better understanding of the progressive deterioration of bone in aging populations, and ultimately may provide early prediction of fracture risk and associated musculoskeletal complications such as osteoporosis.

Trabecular Bone Quality Assessment using Scanning Confocal Acoustic Diagnostic Technology

Background and QUS and Ultrasound Imaging for Bone

Recently, new methods have emerged with the potential to estimate cancellous bone modulus more directly. Quantitative ultrasonic techniques provide an intriguing method for characterizing the material properties of bone in a manner, which is non-invasive, non-ionizing, non-destructive, and relatively accurate. The primary advantage of QUS is that it is capable of measuring not only bone quantity, but also bone quality, i. e., estimation of the mechanical property of bone. Over the past 15 years, a number of research approaches have been developed to quantitate bone mass and structural stiffness using QUS (Ashman et al. 1984, 1987; Ashman and Rho 1988). The QUS is an emerging physical modality in the evaluation of bone material properties because it is simple, inexpensive, non-invasive and free of ionizing radiation. Preliminary results for predicting osteoporosis using QUS are quite promising, and it has much greater potential for widespread application (including screening for prevention) than traditional X-ray bone densitometry methods. As such, many QUS technologies have been developed, and there are currently used (Njeh et al. 1999b). Using several available clinical devices, studies in vivo have shown the ability of QUS to discriminate patients with osteoporotic fractures from age-matched controls (Cheng et al. 1997; Gregg et al. 1997; Njeh et al. 1997). It has been demonstrated that QUS predicts risk of future fracture generally as well as DXA (Bauer et al. 1997; Hans et al. 1993, 1995); however, there are several noted limitations, including the tissue boundary interaction, non-linear function of density associated with bone ultrasonic attenuation, single index covering broad range of tissues (including cortical and trabecular regions) and the interpolation of the results. Recently, using imaging based technology, ultrasound is used for evaluating region of interests of bone, e. g., using array

plane ultrasound wave (Calle et al. 2003; Gomez et al. 2002; Njeh et al. 1999b). These methods provide ultrasound images in the calcaneus region, in which the parameter compares to DXA data. Perhaps the major drawbacks of current ultrasound osteometers are low resolution and lack of physical interrelation with meaningful bone strength. While only showing the correlation between BUA data and BMD, these devices mostly provide qualitative information for assessment of osteoporosis, not the true prediction for bone structural and strength properties; therefore, QUS remains at an initial stage, as a screening tool, because of the non-uniformity of the porous structure in the bone tissue and its associated affects in resolution (Njeh et al. 1999b).

To overcome these hurdles and improve the specificity of non-invasive ultrasonic assessment, we have initiated a new modality of QUS by developing a scanning confocal acoustic diagnostic (SCAD), or scanning confocal acoustic navigation (SCAN) technology particularly for identifying the strength of trabecular bone. Our new design of SCAD system is intended to provide true images reflecting bone's structural and strength properties at particular skeletal sites, which can provide a true diagnostic tool (instead of just for screening) that surpasses the radiation-based DXA machines.

The principal goal of this study was to evaluate both bone mineral density and strength properties using ultrasound scanning, μCT-determined BMC and structural properties, and the mechanical testing.
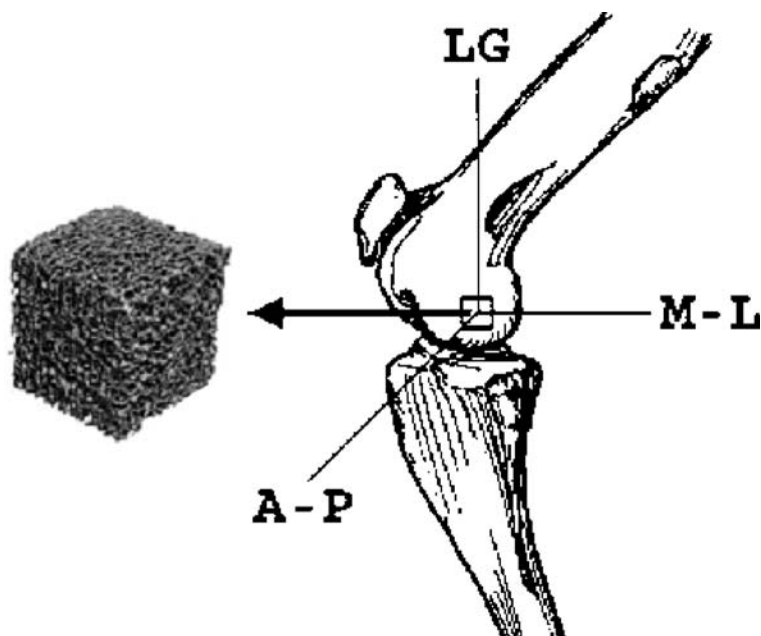
Figure 2. Trabecular bone samples were carefully extracted from sheep distal femoral condyle. *LG* longitudinal direction in weight-bearing (45° with the long axis of bone), *M–L*: medial–lateral direction, *A–P* anterior–posterior direction

Methods

A total of 63 sheep trabecular bone cubes ($1 \times 1 \times 1$ cm) were harvested from the distal femoral condyle. Prior to cutting, the femoral shaft was placed at a 45° to the blade (Fig. 2) such that the axes of the resultant samples corresponded to the physiologic and anatomic directions, i. e., longitudinal (LG; animal's weight-bearing direction), anteroposterior (AP), and mediolateral (ML). These bones were stored in the solution of half 70% ethanol and half normal saline at 4°C.

SCAD Measurement

Using a newly developed SCAD technology, the bone cubes were measured ultrasonically in three orthogonal directions. The measurement procedure consisted of confocal scanning of ultrasonic beam through the central region (2D plane) of the sample with a resolution of 0.5 mm pixel size. A recording of ultrasound wave was made over an 80×80 array (40×40 mm field of view). These waveforms were processed to calculate the attenuation coefficient (ATT; dB), the log-ratio of the energy of reference wave to testing wave, the broadband ultrasound attenuation (BUA; dB/MHz), which is the slope of the frequency-dependent attenuation at bandwidth 300–700 kHz, and the ultrasound velocity (UV; m/s) at each scanning point. These ultrasonic values were further processed to generate images of ATT, BUA, and UV. A 14×14 grid (0.5 mm pixel size, 7×7 mm field of view) region of interest (ROI) was then determined from the images of ATT, BUA, and UV to derive ultrasound parameters.

μCT Determining Microarchitecture and Density of Bone

A series of structural parameters of the trabecular samples, such as the total volume (TV), bone volume (BV), bone mineral density (BMD), trabecular width (TbTh) and space, connectivity, and structural model index (SMI), were determined from the 3D images of the trabecular sample from the μCT 3D reconstruction with a 20 μm resolution (μCT40, Scanco).

Tissue Mechanical Modulus

Contact force-displacement testing was used to determine the elastic modulus of trabecular bones. Using a mechanical testing machine (MTS Systems), the cubes were uniaxially loaded in compression using displacement control (Fig. 3). To overcome slight deviations from surface parallelism, a smoothly curved nail head was placed above the bone cube such that the force would be distributed evenly to the bone in the loading direction. An upper limit of 300 N, determined by prior loading of non-experimental but otherwise identical bone cubes, was established to prevent the plastic yielding of any specimens while the loading was achieved in bone's elastic region. The loading rate was approximately 1000 $\mu\varepsilon$/s for the samples. Both displacement and force were digitized and analyzed using MTS BasicTestware software.

The material properties studied included elastic moduli in three orthogonal directions, and bulk modulus, which was the averaged value of the elastic moduli from the three orthogonal directions. Finally, the samples were compressively loaded up
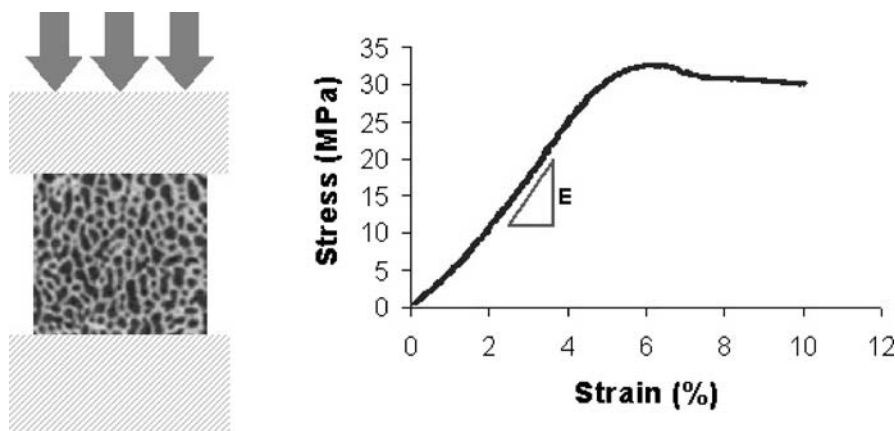
Figure 3. Mechanical testing of bone cubic samples. The modulus of bone was calculated by the linear slope of the strain–stress curve

to their failure in the longitudinal direction, and the yield strength and the ultimate strength were recorded.

Interrelationships between QUS parameters and μCT determined structural values, and between QUS parameters and mechanical properties, were evaluated through multiple correlations. Finally, a combined linear regression of BUA and UV was used to interpret the complex structure of trabecular bone and its interactive influence on derived ultrasound signals. The data were analyzed using Pearson product moment correlation coefficients and the significance level was set at $p < 0.05$.

Results

Among the quantity and quality parameters, these trabecular bone samples showed a variety of values of structural (Fig. 4) and stiffness parameters. The value of BV/TV averaged 49 ± 7% (mean ± SD), whereas the mechanical strength averaged 415 ± 100 MPa for bulk modulus, 16.5 ± 6.7 MPa for yield strength, and 18.6 ± 6.9 MPa for ultimate stress. Ultrasound scanning was capable of predicting the bone's quality parameters via multiple correlations.

Statistical correlation was preformed between the ultrasound parameter and the trabecular structural parameters and mechanical parameters. When ultrasound parameters were correlated to the Young's modulus of the trabecular bone in three orthogonal directions, the ultrasound velocity and BUA in the corresponding directions were used; otherwise, the averaged ultrasound velocity and BUA from the three orthogonal directions were used. Figure 5 shows a good correlation between BUA and BV/TV with r^2 of 0.53. Since BV/TV is independent of the direction of measurement, the averaged BUA was used. Figure 6 demonstrates a better correlation between the bulk stiffness of the trabecular bone and the average ultrasound velocity with r^2 of 0.67.
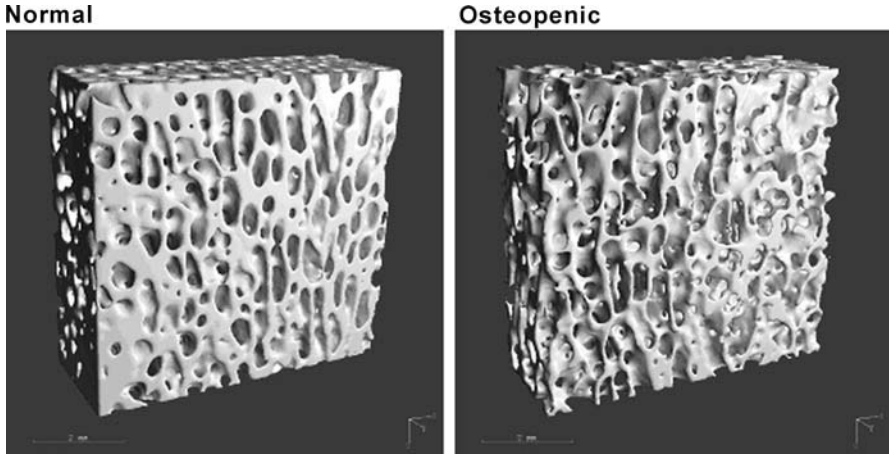
Figure 4. Micro-CT measured trabecular bone structure, 34 μm resolution. *Left*: normal bone. *Right*: the sample with osteopenia
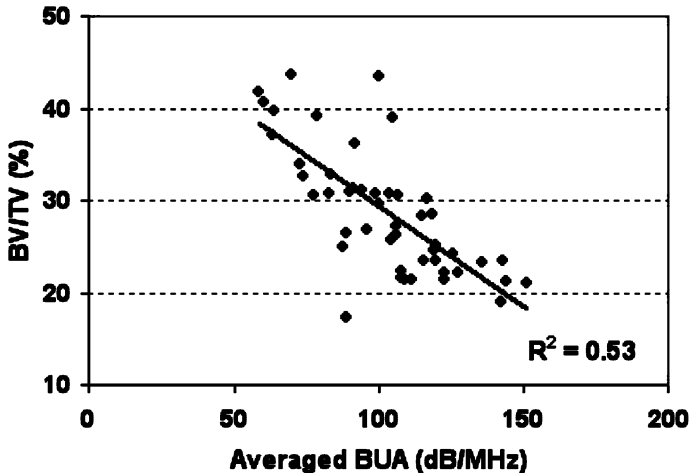
Figure 5. The correlation of average BUA with the BV/TV from μCT analysis

Table 2 shows the overall correlation coefficients. While there were weak correlations between BUA and μCT, determined structural parameters, such as bone volume fraction (BV/TV; $R = -0.68$), trabecular width (TbTh; $R = -0.34$) and connectivity ($R = 0.07$), as well as tissue bulk modulus ($R = -0.31$), demonstrated strong correlations between UV and bone strength and structural parameters such as bulk modulus ($R = 0.82$), BV/TV ($R = 0.93$), and TbTh ($R = 0.69$). It was also interesting to find that the variation of the correlation coefficients between BUA and the mechanical modulus was also greater than those between the ultrasound velocity and the mechanical modulus. The ultrasound attenuation coefficient (ATT) was shown
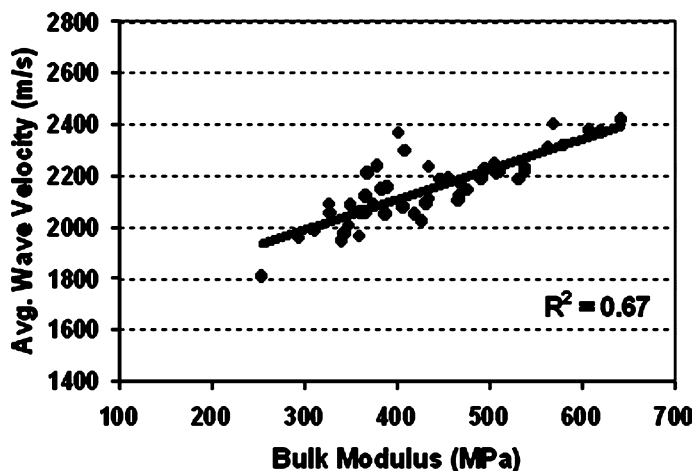
Figure 6. The correlation of averaged UV with the bulk modulus

Table 2. Relative correlation coefficients (r values) for QUS, μCT and mechanical testing consistently above 0.75 with regard to the elastic modulus, bulk modulus, yield or ultimate strength. All r values above 0.3 are significant

	ATT	UV	BUA	Combo BUA & UV
AP Modulus	−0.71	0.79	−0.66	–
LG Modulus	−0.75	0.79	−0.70	–
ML Modulus	−0.36	0.89	−0.34	–
Bulk Modulus	−0.75	0.82	−0.31	0.84
Yield Strength	−0.72	0.90	−0.85	0.93
Ultimate Strength	−0.75	0.90	−0.85	0.94
BV/TV	−0.37	0.93	−0.68	0.96
BMD	0.74	0.85	0.75	0.87
SMI	0.3	0.9	0.66	0.93
Connectivity	−0.12	−0.33	0.07	0.28
Trab.Thickness	−0.17	0.69	−0.34	0.67

to be equivalent to BUA when it was correlated to the mechanical modulus and BMD of the trabecular bone.

The correlations were improved by using a new parameter that combined BUA and UV in a linear regression analysis, yielding values of $r = 0.96$ for BV/TV, $r = 0.67$ for trabecular thickness, and $r = 0.84$ for bulk modulus. Figure 7 demonstrates that the linear combination of ultrasound velocity and BUA could predict 70% of the bulk modulus ($r^2 = 0.70$), and Fig. 8 shows that the linear combination of ultrasound velocity and BUA could predict 87% of the BV/TV.
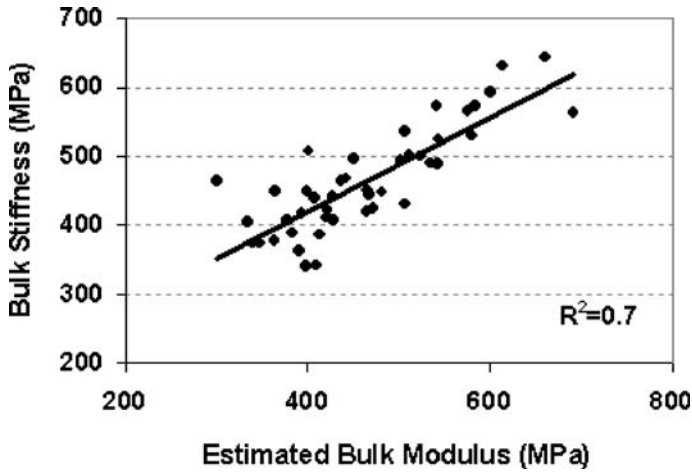
Figure 7. Prediction of bulk modulus by the linear combination of ultrasound velocity and BUA also showed high correlation ($R^2 = 0.7$, $p < 0.01$)
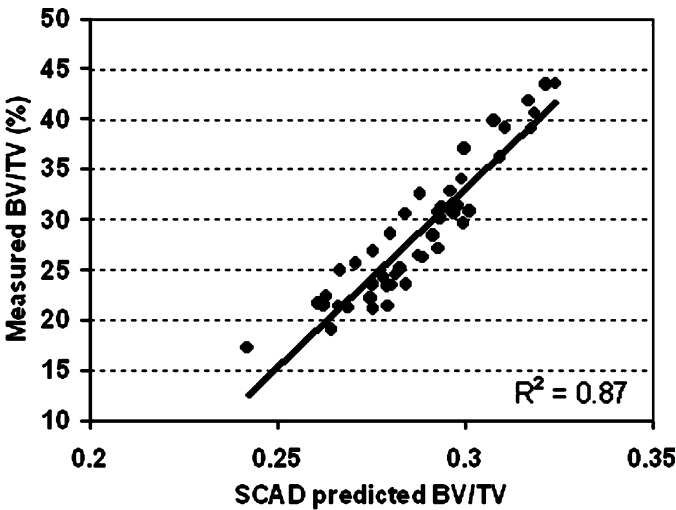
Figure 8. Prediction of BV/TV by the linear combination of ultrasound velocity and BUA showed high correlation ($R^2 = 0.87$, $p < 0.01$)

Discussion

Ultrasound is a promising tool for the efficient and non-invasive assessment of bone status. Contrary to the conventional ultrasound technique, The SCAD system can provide images instead of individual parameters from the ultrasonic measurement of bone samples. These images can also help to determine the region of interest on the bone samples so that the ultrasound data can best represent the bone properties. In our study, the edge effect of ultrasound on bone can be excluded when only the

data in the region of interest are used. Although the inhomogeneity in the trabecular cubes was not obvious because of the small size of the samples, different patterns of ultrasound images were discovered. This indicated that when this new technology was applied on large bone samples, such as the calcaneous, the inhomogeneity revealed by SCAD could be of clinical interest.

The ultrasound parameters used in the correlation with the bone properties are the averaged values from the region of interest. They included the ultrasound velocity (UV) and the broadband ultrasound attenuation (BUA). When single ultrasound parameter was used, the ultrasound velocity was generally a better predictor of the trabecular properties than BUA. The r^2 from the correlation results can be considered as an indicator of the percentage of trabecular properties information embedded in the individual ultrasound properties. The UV is best in characterizing the mechanical stiffness and yield strength as well as BMD and BV/TV. Although BUA is not as good as UV as an individual parameter for the assessment of bone properties, its correlations with yield strength, ultimate strength, BV/TV, and BMD are fairly good. This implies that BUA might also contain the bone properties, some of which might not be revealed in UV.

Considering the complex architecture of trabecular bone, it can be a better prediction of bone's quality for determining osteogenic conditions if the combination of UV and BUA are used. The advantage of combining the ultrasound velocity and BUA to predict the trabecular properties was that it could combine the information in both velocity and attenuation BUA and increased the accuracy of prediction. The combination of the ultrasound velocity and attenuation has improved the prediction of bone quality indexes such as the yield strength and ultimate strength and bone quantity index of BMD. This was attributed to the additional stiffness information provided in BUA.

As such, various ultrasound methods are available to optimize the correlations with the true mechanical properties of bone and ultimately fracture risk; thus, a well-established database using this newly developed system may provide an insight into non-invasive diagnosis of osteoporosis and bone quality using ultrasound. More generally, it is both interesting and promising that, when looking at either mechanical properties or μCT parameters, it is the more global and clinically relevant properties that are best described by ultrasound. Yield and ultimate strength, the best indicators of true fracture risk, are better correlated than elastic modulus, a simple measure of stiffness. Furthermore, with respect to μCT, the ultrasound values are best correlated with overall parameters such as bone volume fraction and structural model index, which are again the best indicators of global quality of the bone, rather than specific parameters such as connectivity density and trabecular thickness.

Quantitative Ultrasound Propagation in Bone using a Simplified Stratified Model

Background

Ultrasonic assessment of bone has shown the potential of its capability in detecting not only the density but also the strength of bone tissue; however, the lack of

understanding of ultrasound interaction with bone, particularly in the trabeculae, has become one of the obstacles preventing ultrasound from being a fully developed diagnosis technique. At present, a few theoretical models exist that can robustly explain the ultrasound propagation in bone, especially physical interactions with bone. One such study applied Biot's theory (Biot 1956, 1962) to characterize the ultrasound propagation in porous trabecular bone. Analytically, Biot's theory was effective in explaining ultrasound velocity in trabecular bone, yet its predicted attenuation of the ultrasound in trabecular bone had great discrepancy with the experimental data (Acotto et al. 2004; Cvijetic et al. 2003; Hosokawa and Otani 1997; McKelvie and Palmer 1991). This may be because the attenuation mechanism in trabecular bone is not limited to the friction loss between the relative motion of bone marrow and the trabecular struts (Williams 1992, 2001). Also, the limitation inherent in assessing bone to be a homogenous porous material by Biot's theory ignored the sensitivity of ultrasound attenuation to trabecular architecture, which is complex, inhomogeneous, and anisotropic (Cowin 1989). Upon closer inspection, Biot's theory involved more than ten material parameters, most of which, e. g., permeability in the trabecular structure, were theoretical and hard to determine by experimental methods (Haire and Langton 1999; Prins et al. 1998), and thus might cause difficulty in predicting results.

Recently, models other than the Biot's theory have come into light. Hughes et al. (1999) used a stratified model to simulate the ultrasound propagation in trabecular bone and demonstrated the existence of both slow and fast waves as predicted by Biot's theory. They also showed that the fast wave was strongly anisotropic and suggested that the simplification of the trabecular structure by the stratified model had potential for the study of ultrasound interaction with trabecular bone. Regarding the ultrasound propagation in stratified medium, the frequency response of stratified media to an ultrasonic wave can provide clues to a more complete understanding of wave propagation in porous media (Schoenberg 1984). The objective of this work was to extend the stratified model and to simulate the interaction of ultrasound velocity and broadband ultrasound attenuation with the trabecular architecture. The stratified model was applied to investigate the relationship of ultrasound velocity and normalized broadband ultrasound attenuation (nBUA) with the bone density and porosity at a series of frequencies, in which the stratified model focuses on the reflection and transmission of ultrasound at the marrow-trabeculae interfaces. This simplicity makes the study of the interrelationship of the apparent density and porosity of bone with ultrasound attenuation and wave velocity more straightforward. We hypothesize that transmission and reflection are the two defining factors affecting ultrasound propagation in trabecular bone, and thus the stratified model can more cohesively explain the relationship between ultrasound and trabecular properties such as porosity and apparent density.

Method

Stratified Model

Trabecular architecture is a complex solid matrix of trabecular struts, with marrow filling the spaces. When ultrasound enters this complex architecture, a portion of
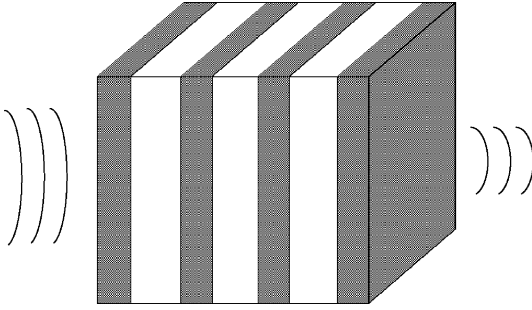
Figure 9. Stratified model for trabecular bone. The *shaded area* represents trabecular material. The marrow is sitting between trabecular layers

the acoustic energy is reflected at the marrow-trabeculi boundary, whereas a portion of the energy is transmitted through the boundary. Since numerous such boundaries exist within the trabecular architecture, it is clear that accounting for the reflections and transmissions of the signal is a key aspect of the ultrasound interaction with the bone. The stratified model (Fig. 9) simplifies this trabecular architecture but keeps the wave reflection and transmission features similar to that which is encountered within the bone. In this model, the solid phase is composed of bone material and the liquid phase is composed of marrow. The model begins with the solid phase at left and ends with the same material at right. The solid layers have equal thickness, as do the liquid layers. The porosity of the model determines the thickness of both solid and liquid layers. Plane ultrasonic wave enters the model at left and exits the model at the right. Only the normal incident wave is considered in the model, and therefore it is assumed that no shear wave is generated in the solid layers.

Density of the Stratified Model
The apparent density ρ of trabecular bone is directly related to the trabecular bone porosity β. It is defined as the mass of trabecular material by the whole bone volume. It can be calculated using the following equation:

$$\rho = (1 - \beta)\rho_s \tag{2}$$

where ρ_s is the density of the trabecular material. This density agrees with the later calculation of BMD from micro-CT data, which is the bone mineral content divided by the total volume. Apparent density and BMD are closely related. Han et al. (1996a,b) reported that BMD was 80% of the apparent density of the same bone specimen.

Ultrasonic Wave Velocity in the Stratified Model
When ultrasound travels through the model, it takes t_s seconds in the solid phase and t_l seconds in liquid phase. If the porosity is β and thickness of the model is l, then the total thickness in solid phase is $(1 - \beta)l$ and the thickness in liquid phase is βl; therefore, t_s and t_l are:

$$t_s = \frac{(1-\beta)l}{v_s} \tag{3}$$

$$t_l = \frac{\beta l}{v_l} \tag{4}$$

where v_s and v_l are the ultrasonic wave velocities in the solid and liquid phase respectively; therefore, the ultrasound velocity in the stratified model is:

$$v = \frac{l}{t_s + t_l} \tag{5}$$

or

$$v = \frac{v_s v_l}{(1-\beta)v_l + \beta v_s} . \tag{6}$$

Ultrasound Attenuation in the Stratified Model

Ultrasound attenuation in trabecular bone is usually measured by the insertion method (Langton et al. 1984; Langton and Hodgskinson 1997; Langton and Njeh 1999). While the ultrasound signal is initially recorded between the transmitter and receiver without the interference of the bone sample to serve as a reference signal, the trabecular bone sample is inserted into the ultrasound pathway and the attenuated ultrasound signal is recorded. The difference of the logarithm of the amplitude frequency spectrum between the reference and attenuated signals is defined as the ultrasound attenuation coefficient in trabecular bone. The slope of the linear section of the ultrasound attenuation coefficient vs frequency is defined as broadband ultrasound attenuation (BUA). The normalized BUA (nBUA) is the BUA normalized to the specimen thickness to eliminate the effect of specimen thickness.

Pressure and velocity are two parameters that describe an ultrasound field and are functions of position. The velocity described here is distinct from the ultrasonic wave velocity, and represents the motion of a medium particle at a specified position. The pressure becomes the normal stress in the solid media if only a longitudinal plane wave is involved. In each layer of the model, the pressure and velocity at the right side, P_r, V_r, are related to pressure and velocity at the left side, P_l, V_l, through the transfer matrix:

$$\begin{bmatrix} P_r \\ V_r \end{bmatrix} = \begin{bmatrix} \cos(kx) & -Z_c \sin(kx) \\ \frac{\sin(kx)}{Z_c} & \cos(kx) \end{bmatrix} \tag{7}$$

$$k = \frac{2\pi}{\lambda} Z_c = \rho c \tag{8}$$

In the above equations, k is wave number derived from wavelength λ and is the function of the ultrasound frequency. Z_c is the characteristic impedance of the medium, which is the multiplication of medium density ρ and ultrasonic wave velocity c in the medium. The thickness of the layer is defined by x. This equation stipulates that the pressure and velocity at one point of the sound field is associated with the pressure and velocity at another point through the transfer matrix $[T]$; therefore, only the pair of pressure and velocity at the left side of each layer is needed to describe the ultrasound field in that layer.

It is assumed that the stratified model has n layers and that the media on both sides of the stratified model are semi-infinite, which are the same as the media in the liquid phase in the model. P_0 and V_0 are the pressure and velocity of the incident ultrasonic wave at the left side of the model, and P_{n+1}, V_{n+1} are the pressure and velocity of the transmitted ultrasonic wave at the right side of the model. The pressure and velocity at the right side of each layer are then calculated from those at left side using the transfer matrix. The boundary conditions between layers are such that the pressure and velocity are considered continuous. This means that the pressure and velocity at the left side of the layer are equal to the pressure and velocity at the right side of previous layer.

Measurement of Ultrasound Velocity and Attenuation in Trabecular Bone

To verify the model, the measurement of ultrasound velocity and attenuation were conducted to provide experimental data. Ultrasound velocity was measured using ultrasound pulse and calculated using the time-of-flight method (Prins et al. 1998, 2000). A total of 17 cubic trabecular bone samples ($1 \times 1 \times 1$ cm) were harvested from the femoral condyle of sheep. Micro-CT (µCT20, Scanco, Bassersdorf, Switzerland) tests were conducted on each sample to obtain bone mineral content and bone porosity. The BMD was calculated by the ratio of the bone mineral content and the total volume of the specimen. Two identical broadband unfocused ultrasound transducers (25.4 mm in diameter) with a center frequency at 500 kHz (Panametrics) were mounted on opposite sides of a $10 \times 10 \times 15$ cm water tank (Fig. 10). Bone specimens were positioned in the ultrasound path using a specimen holder. The transmitting
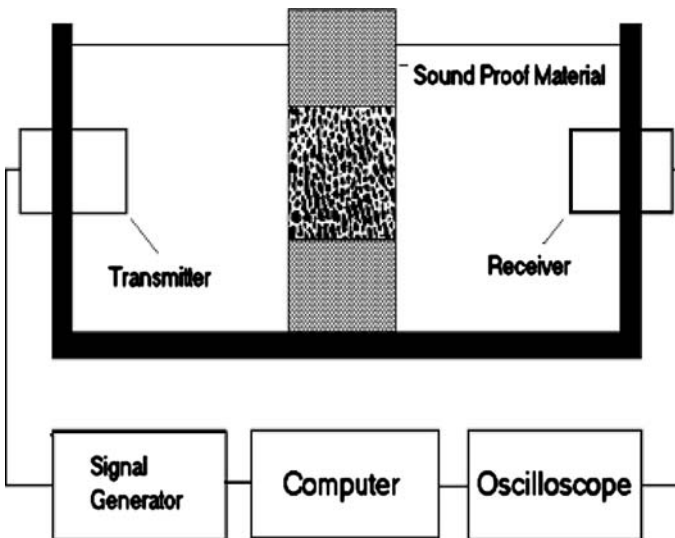
Figure 10. Experimental setup for ultrasound measurement of trabecular bone. In ultrasound velocity measurement, the signal generator is a pulse generator. In ultrasound attenuation measurement, the signal generator is a waveform generator

transducer was driven by a 100 V pulse with 0.5 μs duration generated by a pulse generator (Hewlett Packard model HP214B). The ultrasound response from the receiver was collected by a digital oscilloscope with sampling frequency of 25 MHz (Tektronix model TDS430A). The time difference between the transit delays of the reference wave (without bone in sound path) and the testing wave (with bone in sound path) were measured by choosing the second zero crossing point as the characteristic point for the purpose of comparison. Ultrasound velocity was calculated by:

$$V_b = \frac{V_w D_s}{D_s - V_w \Delta t} \tag{9}$$

where V_b is the velocity in bone, D_s is the thickness of bone sample, V_w is the velocity in water, and Δt is the time difference.

Ultrasound attenuation was measured with the same setup, except that the signal was generated by the waveform generator (model DS345, Stanford Research Systems). Both waveform generator and oscilloscope were controlled by a laptop computer (Dell Latitude) using LabView software (National Instruments). The ultrasound attenuation was measured using a frequency-scanning method. For each measured frequency, a tone burst of three cycles of sinusoidal wave at the tone frequency was used to drive the transmitting transducer. This ensured that the energy of the signal was concentrated at the tone frequency. The reference signal was first established and then the bone signal was recorded with the specimen placed between transmitter and receiver. Both the reference and bone signals are integrated to calculate the energy of the signals. The energy difference in decibels between reference and bone signals was calculated as the attenuation coefficient at the tone burst frequency. The range of frequency scanning was between 200 and 800 kHz with an interval of 50 kHz.

Ultrasound Velocity and Attenuation Calculated by the Stratified Model

Both ultrasound velocity and attenuation were calculated with changing bone porosity using the stratified model. Since marrow properties are close to water, a density of 1000 kg m^{-3} and wave velocity of 1500 m s^{-1} were used. The infinite medium on both sides of the model was water. Trabecular material also has similar properties as cortical bone (Turner et al. 1999); thus, values used in the model were based on the measurements of cortical bone from the sheep femur. A density of 2000 kg m^{-3} and a wave velocity of 3680 m s^{-1} for trabecular material were used. Since the apparent density of bone was highly correlated to BMD ($r = 0.98$; Han et al. 1996a,b, 1997), the apparent density was used in the numerical model in place of the BMD. The thickness of the stratified model was chosen as 1 cm. The values of thickness for solid and liquid layer were calculated from porosity of the model based on the assumption that solid layers and fluid layers had the same thickness shown in Eqs. (10) and (11).

$$T_{tr} = \frac{(1 - \beta) w}{n + 1} \tag{10}$$

$$T_{ma} = \frac{\beta w}{n} \tag{11}$$

where T_{tr} and T_{ma} are the thickness of the trabecular layer and marrow layer, n is the number of marrow layer, β is the porosity, and w is the model thickness. To determine the number of trabecular layers in the model, a series of simulation were done at different number of trabecular layers. The results showed that ten trabecular layers best represented the attenuation coefficient vs frequency curve, where the linear section was between 300 and 700 kHz. The current model includes ten trabecular layers and nine marrow layers, which generated the thickness of 0.5 mm of trabecular layer and the thickness of 0.55 mm of the marrow layer at the porosity of 50%. With these values, the relationship between velocity and porosity of the model was simulated using Eqs. (4) and (5). To simulate the nBUA of the model of a specific porosity, a series of tone bursts, using three cycles of a frequency from 200 to 800 kHz at 50 kHz intervals, were created. For each tone burst, the attenuation coefficient was calculated; thereby, the frequency distribution of ultrasound attenuation coefficient in the stratified model was obtained. The nBUA of the model was calculated from the slope of the linear section of the attenuation coefficient curve where the r-value of the correlation of attenuation coefficient to frequency is above 0.98. This section was normally between 300 and 700 kHz. The porosity ranged from 10 to 90% and simulations were done at 10% intervals between the porosity of 10 and 40% and between 70 and 90%, and at 5% intervals between 40 and 70%.

Results

Although the theoretical relationship between ultrasound velocity and bone porosity was not strictly linear, the stratified model established a high correlation ($r = -0.97$) when bone porosity changed from 0 to 100% (Fig. 11). Because the apparent density was inversely proportional to bone porosity, a positive correlation was observed be-
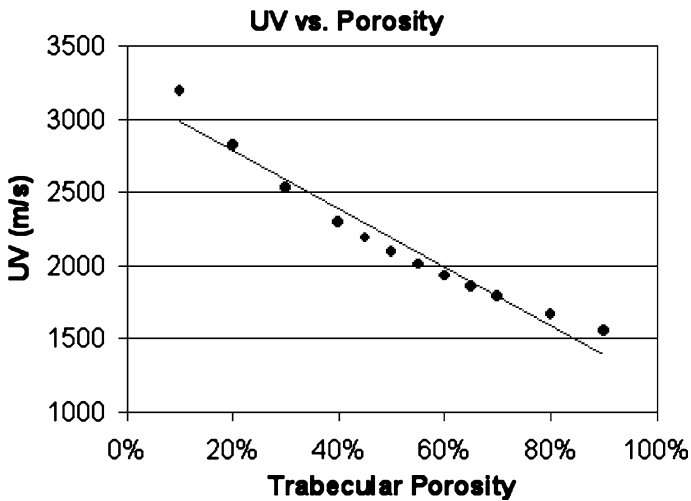
Figure 11. Simulated ultrasound wave velocity vs porosity in the stratified model. As porosity increases, the wave velocity decreases ($r = -0.97$). (From Lin et al. 2001)

tween ultrasound velocity and the apparent density (r = 0.97). These results were in an agreement with published results by other researchers (Han et al. 1996b, 1997; Langton et al. 1984; Langton and Njeh 1999). For the experimental measurement, the results showed that the correlation between ultrasound velocity and bone porosity of the trabecular sample from the sheep femoral condyle demonstrated a significant r-value of −0.93, and correlation of ultrasound velocity and BMD had an r-value of 0.93 (Fig. 12).
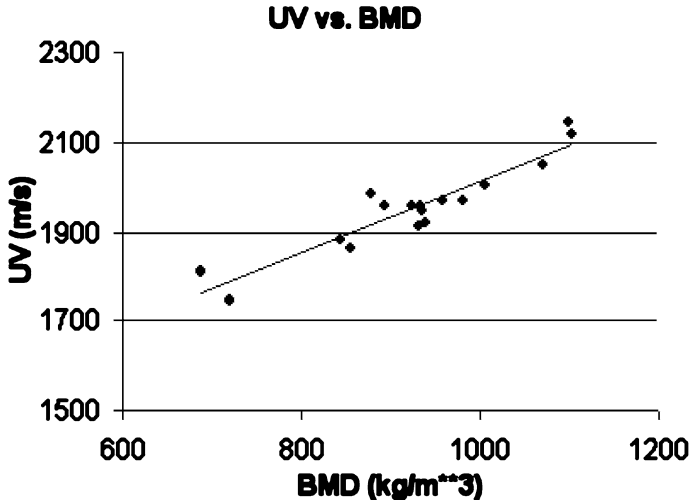
Figure 12. Ultrasound wave velocity was positively correlated with the bone mineral density (BMD) in the trabecular bone from sheep femoral condyle (r = 0.93). (From Lin et al. 2001)
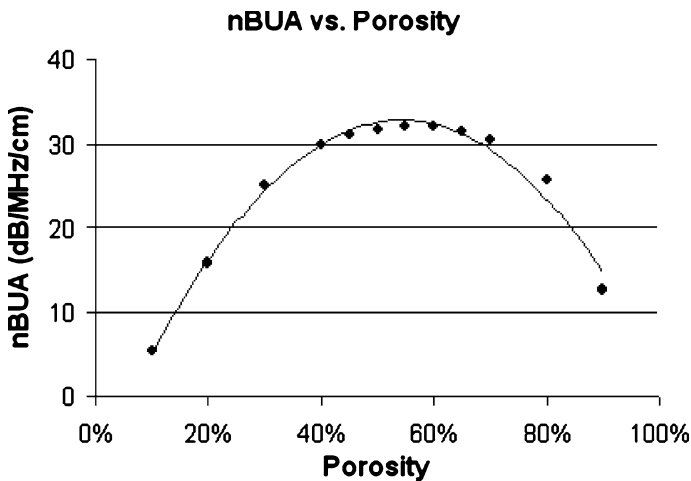
Figure 13. The broadband ultrasound attenuation (nBUA) of the stratified model is non-linear with respect to porosity. The peak of nBUA is reached when porosity is 60%. (From Lin et al. 2001)

Ultrasound attenuation is dependent on ultrasound frequency, increasing as frequency increases. In the stratified model for trabecular bone, attenuation coefficient at different porosities was calculated. A linear relationship ($r \geq 0.98$) existed between attenuation and frequency from 300 to 700 kHz. The slope of the data in this linear region normalized to the model thickness is referred to as the nBUA. The simulated pattern at the porosity of 50% was the same as that of the experimental data from a trabecular sample with an established porosity of 50%, as measured by micro-CT. The difference between experimental attenuation data and model data was from 5 to 10 dB.

The simulation demonstrated that the nBUA as defined in the stratified model shows a non-linear relationship with the porosity (Fig. 13). In the low-porosity region, nBUA increased as porosity increased; however, in the high-porosity region, the relationship was inverted and began to decline. The maximum nBUA occurs at the porosity of 60% or with an apparent density of $800\,\mathrm{kg\,m^{-3}}$.

Discussion

The stratified model is capable of explaining the complex interaction of ultrasound with trabecular bone structure. Whereas nBUA is a widely used index of ultrasound in the assessment of bone density, e. g., BMD, the experimental studies have indicated that nBUA is non-linear with respect to BMD as porosity decreases from osteoporotic trabecular bone to normal cortical bone, thereby confounding interpretation of the results (Fig. 13). The stratified model has successfully represented this non-linear relationship, and thus appeared to be a valuable tool to evaluate the interaction of ultrasound with trabecular bone. According to the simulation result, the nBUA reached maximum at the porosity of 60%. The porosity of trabecular bone varies between 30 and 90% depending on bone quality (Njeh et al. 1999b, 2001). For normal trabecular bone, the porosity is well below 60%, and thus the nBUA increases with the trabecular porosity because it selects the rising part of the non-linear curve; however, if the trabecular bone is osteoporotic, the porosity can easily exceed 60%, and the relationship of nBUA and porosity is represented by the falling part of the non-linear curve, indicating that the trabecular porosity is inversely proportional to BMD. This non-linear dependence of nBUA on porosity, therefore, may explain some of the wide variability in ultrasound results and provide insight to explain the experimental measurement by ultrasound. These results also agree with published data. Using phantom material, Strelitzki et al. (1997) demonstrated the similar parabolic shaped relationship between nBUA and phantom material porosity, with nBUA peaked at 50%. Serpe (1996) demonstrated in their in vitro study that nBUA is non-linear over a wide range of BMD and the peak nBUA occurred at the BMD value around $600\,\mathrm{kg\,m^{-3}}$. Based on the relationship of apparent density and BMD given by Han et al. (1996a), the BMD is about 80% of the apparent density; therefore, the BMD of $600\,\mathrm{kg\,m^{-3}}$ was equivalent to the apparent density of $750\,\mathrm{kg\,m^{-3}}$, which was also close to $800\,\mathrm{kg\,m^{-3}}$ predicted by the stratified model.

Ultrasound attenuation is considered as the combine result of absorption and scattering. The difference of attenuation between the experimental data and simu-

lation model implies that other energy absorption factors exist. This indicates that absorption was also an important contribution to the total ultrasound attenuation. The backscattered model proposed by Wear (2000a,b, 2004) demonstrated that the scattering in all directions is approximately proportional to the frequency cubed; therefore, absorption could be a considerable component of attenuation since the ultrasound attenuation is approximately linear to the frequency. The simulated ultrasound attenuation was about 5–10 dB below the experimental data, demonstrating the significance of the role of absorption in ultrasound attenuation.

The stratified model has demonstrated that ultrasound velocity is proportional to bone density in this study. Trabecular bone has two phases, the solid phase of trabeculae and the liquid phase of bone marrow. Since the trabecular structure is porous, high BMD represents low porosity, or more trabecular material within a given volume. As the ultrasonic wave velocity is faster in trabecular material than in marrow, ultrasonic wave travels faster in trabecular bone of high BMD than that of low BMD. This agreed well with the in vitro results reported by Tavakoli et al. (1991). In their study, they used nitric acid to demineralize the bone specimen so that the effect of BMD was isolated. They reported that the ultrasound velocity was highly correlated with BMD ($r = 0.99$). This agreement is the strong support of the stratified model, since only the BMD of the model was changed. The lower-than-predicted correlation coefficient ($r = 0.93$) between ultrasound velocity and BMD from our experiment indicated that factors other than BMD had influence on ultrasound velocity. The characteristic point, such as the second zero crossing point, in the ultrasound signal can introduce error in the determination of the transit delay in the trabecular bone due to pulse distortion as a result of attenuation (Wear 2000b, 2001, 2004). The pathway of ultrasound is more complicated in real trabecular architecture than in the stratified model. Due to the heterogeneity of trabecular bone, the trabecular thickness varies from point to point. These results in the uneven distribution of local ultrasound velocity within the trabecular specimen, indicating that the trabecular architecture will affect the measured velocity.

The limitations of the stratified model include the simplification of the model. Firstly, the wavelength of ultrasound in the trabecular bone is around 4 mm, much larger than the size of any given trabeculae and Rayleigh scattering occurs inside the trabecular specimen. The use of reflection to simulate scattering will leave out factors unique to scattering. If the trabeculae are considered cylindrical scatterers (Wear 1999), the intensity of the scattering wave is proportional to the third power of the frequency of the incident wave. This phenomenon is not reflected in the stratified model. Secondly, the solid bone material in the stratified model was not connected between layers and therefore could not simulate the connectivity of the trabecular structure. Thirdly, no indication of trabecular stiffness and strength could be found from the model. As the marrow layer cannot withstand stress load, the bulk stiffness of the model cannot be established. Fourthly, the stratified model can represent well the BMD and porosity at the bulk level; however, work is still needed to link the number and thickness of the layers in the model to the microstructure of the trabecular bone. Finally, the absorption mechanism of ultrasound in the trabecular bone was not included in the model and could account for the difference between the simulated

ultrasound attenuation and the experimental results. Despite the above limitations, the close match of the simulated data and the experimental data demonstrated that the stratified model, though simple, is an effective means of revealing the mechanism of ultrasound interaction with bone.

Conclusion

Quantitative ultrasound image has demonstrated its ability in assessing quantity and quality of bone non-invasively. While osteoporoses occur initially in the trabecular region, scanning confocal acoustic diagnostic technology provides high signal-to-noise ratio in the trabecular bone. The stratified model of trabecular architecture is simple but powerful. It indicates that wave reflection and transmission play important roles in the ultrasound interaction with trabecular bone. High correlation between bone modulus and ultrasound parameters suggest that QUS image is a unique modality for bone quality evaluation. This study also indicates that, when ultrasound is used in the diagnosis of osteoporosis, a better understanding of the signal diagnostics will potentially improve the precision and accuracy of the measurement of bone's physical properties.

References

Acotto CG, Niepomniszcze H, Vega E, Mautalen CA (2004) Ultrasound parameters and markers of bone turnover in hyperthyroidism: a longitudinal study. J Clin Densitom 7:201–208
Aindow JD, Chivers RC (1988) Ultrasonic wave fluctuations through tissue: an experimental pilot study. Ultrasonics 26:90–101
Ashman RB, Rho JY (1988) Elastic modulus of trabecular bone material. J Biomech 21:177–181
Ashman RB, Cowin SC, Van Buskirk WC, Rice JC (1984) A continuous wave technique for the measurement of the elastic properties of cortical bone. J Biomech 17:349–361
Ashman RB, Corin JD, Turner CH (1987) Elastic properties of cancellous bone: measurement by an ultrasonic technique. J Biomech 20:979–986
Ashman RB, Rho JY, Turner CH (1989) Anatomical variation of orthotropic elastic moduli of the proximal human tibia. J Biomech 22: 895–900
Bauer DC, Gluer CC, Cauley JA, Vogt TM, Ensrud KE, Genant HK, Black DM (1997) Broadband ultrasound attenuation predicts fractures strongly and independently of densitometry in older women. A prospective study. Study of Osteoporotic Fractures Research Group. Arch Intern Med 157:629–634
Biot MA (1956) Theory of propagation of elastic waves in a fluid-saturated porous solid. J Acoust Soc Am 28:168–191
Biot MA (1962) Generalized theory of acoustic propagation in porous dissipative media. J Acoust Soc Am 34:1254–1264

Blanckaert F, Cortet B, Coquerelle P, Flipo RM, Duquesnoy B, Marchandise X, Delcambre B (1997) Contribution of calcaneal ultrasonic assessment to the evaluation of postmenopausal and glucocorticoid-induced osteoporosis. Rev Rhum Engl Ed 64:305–313

Calle S, Remenieras JP, Bou MO, Defontaine M, Patat F (2003) Application of nonlinear phenomena induced by focused ultrasound to bone imaging. Ultrasound Med Biol 29:465–472

Cheng S, Tylavsky F, Carbone L (1997) Utility of ultrasound to assess risk of fracture. J Am Geriatr Soc 45:1382–1394

Chesnut CH III (1993) Noninvasive techniques for measuring bone mass. A comparative review. Clin Obstet Gynecol 30:812–819

Chivers RC (1977) The scattering of ultrasound by human tissues: some theoretical models. Ultrasound Med Biol 3:1–13

Chivers RC (1981) Tissue characterization. Ultrasound Med Biol 7:1–20

Chivers RC, Parry RJ (1978) Ultrasonic velocity and attenuation in mammalian tissues. J Acoust Soc Am 63:940–953

Cortet B, Flipo RM, Blanckaert F, Duquesnoy B, Marchandise X, Delcambre B (1997) Evaluation of bone mineral density in patients with rheumatoid arthritis. Influence of disease activity and glucocorticoid therapy. Rev Rhum Engl Ed 64:451–458

Cowin SC (1989) Bone mechanics. CRC Press, Boca Raton

Cvijetic S, Baric IC, Bolanca S, Juresa V, Ozegovic DD (2003) Ultrasound bone measurement in children and adolescents. Correlation with nutrition, puberty, anthropometry, and physical activity. J Clin Epidemiol 56:591–597

Frost ML, Blake GM, Fogelman I (1999) Contact quantitative ultrasound: an evaluation of precision, fracture discrimination, age-related bone loss and applicability of the WHO criteria. Osteoporos Int 10:441–449

Frost ML, Blake GM, Fogelman I (2001) Quantitative ultrasound and bone mineral density are equally strongly associated with risk factors for osteoporosis. J Bone Miner Res 16:406–416

Genant HK (1998) Current state of bone densitometry for osteoporosis. Radiographics 18:913–918

Gomez AC, Schott AM, Hans D, Niepomniszcze H, Mautalen CA, Meunier PJ (1998) Hyperthyroidism influences ultrasound bone measurement on the Os calcis. Osteoporos Int 8:455–459

Gomez MA, Defontaine M, Giraudeau B, Camus E, Colin L, Laugier P, Patat F (2002) In vivo performance of a matrix-based quantitative ultrasound imaging device dedicated to calcaneus investigation. Ultrasound Med Biol 28:1285–1293

Gregg EW, Kriska AM, Salamone LM, Roberts MM, Anderson SJ, Ferrell RE, Kuller LH, Cauley JA (1997) The epidemiology of quantitative ultrasound: a review of the relationships with bone mass, osteoporosis and fracture risk. Osteoporos Int 7:89–99

Guo CY, Thomas WE, al Dehaimi AW, Assiri AM, Eastell R (1996) Longitudinal changes in bone mineral density and bone turnover in postmenopausal women with primary hyperparathyroidism. J Clin Endocrinol Metab 81:3487–3491

Haire TJ, Langton CM (1999) Biot theory: a review of its application to ultrasound propagation through cancellous bone. Bone 24:291–295

Han S, Medige J, Ziv I (1996a) Combined models of ultrasound velocity and attenuation for predicting trabecular bone strength and mineral density. Clin Biomech 11:348–353

Han S, Rho J, Medige J, Ziv I (1996b) Ultrasound velocity and broadband attenuation over a wide range of bone mineral density. Osteoporos Int 6:291–296

Han S, Medige J, Davis J, Fishkin Z, Mihalko W, Ziv I (1997) Ultrasound velocity and broadband attenuation as predictors of load-bearing capacities of human calcanei. Calcif Tissue Int 60:21–25

Hans D, Schott AM, Meunier PJ (1993) Ultrasonic assessment of bone: a review. Eur J Med 2:157–163

Hans D, Schott AM, Arlot ME, Sornay E, Delmas PD, Meunier PJ (1995) Influence of anthropometric parameters on ultrasound measurements of Os calcis. Osteoporos Int 5:371–376

Hans D, Njeh CF, Genant HK, Meunier PJ (1998) Quantitative ultrasound in bone status assessment. Rev Rhum Engl Ed 65:489–498

Hosokawa A, Otani T (1997) Ultrasonic wave propagation in bovine cancellous bone. J Acoust Soc Am 101:558–562

Hou FJ, Lang SM, Hoshaw SJ, Reimann DA, Fyhrie DP (1998) Human vertebral body apparent and hard tissue stiffness. J Biomech 31:1009–1015

Hughes ER, Leighton TG, Petley GW, White PR (1999) Ultrasonic propagation in cancellous bone: a new stratified model. Ultrasound Med Biol 25:811–821

Kanis JA (1997a) Diagnosis of osteoporosis. Osteoporos Int 7 (Suppl 3):S108–S116

Kanis JA (1997b) Osteoporosis: a view into the next century. Neth J Med 50:198–203

Kanis JA, Borgstrom F, De Laet C, Johansson H, Johnell O, Jonsson B, Oden A, Zethraeus N, Pfleger B, Khaltaev N (2005a) Assessment of fracture risk. Osteoporos Int 16:581–589

Kanis JA, Borgstrom F, Zethraeus N, Johnell O, Oden A, Jonsson B (2005b) Intervention thresholds for osteoporosis in the UK. Bone 36:22–32

Langton CM, Hodgskinson R (1997) The in vitro measurement of ultrasound in cancellous bone. Stud Health Technol Inform 40:175–199

Langton CM, Njeh CF (1999) Acoustic and ultrasonic tissue characterization: assessment of osteoporosis. Proc Inst Mech Eng [H] 213:261–269

Langton CM, Palmer SB, Porter RW (1984) The measurement of broadband ultrasonic attenuation in cancellous bone. Eng Med 13:89–91

Laugier P, Fournier B, Berger G (1996) Ultrasound parametric imaging of the calcaneus: in vivo results with a new device. Calcif Tissue Int 58:326–331

Laugier P, Droin P, Laval–Jeantet AM, Berger G (1997) In vitro assessment of the relationship between acoustic properties and bone mass density of the calcaneus by comparison of ultrasound parametric imaging and quantitative computed tomography. Bone 20:157–165

Laugier P, Novikov V, Elmann–Larsen B, Berger G (2000) Quantitative ultrasound imaging of the calcaneus: precision and variations during a 120-day bed rest. Calcif Tissue Int 66:16–21

Lin W, Qin Y-X, Rubin CT (2001) Ultrasonic wave propagation in trabecular bone predicted by the stratified model. Ann Biomed Eng 29:781-790

Looker AC, Johnson CL (1998) Prevalence of elevated serum transferrin saturation in adults in the United States. Ann Intern Med 129:940–945

Madsen EL, Dong F, Frank GR, Garra BS, Wear KA, Wilson T, Zagzebski JA, Miller HL, Shung KK, Wang SH, Feleppa EJ, Liu T, O'Brien WD Jr, Topp KA, Sanghvi NT, Zaitsev AV, Hall TJ, Fowlkes JB, Kripfgans OD, Miller JG (1999) Interlaboratory comparison of ultrasonic backscatter, attenuation, and speed measurements. J Ultrasound Med 18:615–631

McKelvie ML, Palmer SB (1991) The interaction of ultrasound with cancellous bone. Phys Med Biol 36:1331–1340

Melton LJI (1995) How many women have osteoporosis now? J Bone Miner Res 10:175–177

Melton LJI (1996) Epidemiology of hip fracture: implications of the exponential increase with age. Bone 18:121S–125S

Melton LJ III, Atkinson EJ, O'Connor MK, O'Fallon WM, Riggs BL (1998) Bone density and fracture risk in men. J Bone Miner Res 13:1915–1923

Melton LJ III, Orwoll ES, Wasnich RD (2001) Does bone density predict fractures comparably in men and women? Osteoporos Int 12:707–709

Melton LJ III, Gabriel SE, Crowson CS, Tosteson AN, Johnell O, Kanis JA (2003) Cost-equivalence of different osteoporotic fractures. Osteoporos Int 14:383–388

Melton LJ III, Kanis JA, Johnell O (2005) Potential impact of osteoporosis treatment on hip fracture trends. J Bone Miner Res 20:895–897

Minisola S, Scarnecchia L, Carnevale V, Bigi F, Romagnoli E, Pacitti MT, Rosso R, Mazzuoli GF (1989) Clinical value of the measurement of bone remodelling markers in primary hyper-parathyroidism. J Endocrinol Invest 12:537–542

Minisola S, Rosso R, Scarda A, Pacitti MT, Romagnoli E, Mazzuoli G (1995) Quantitative ul-trasound assessment of bone in patients with primary hyperparathyroidism. Calcif Tissue Int 56:526–528

Minisola S, Pacitti MT, Ombricolo E, Costa G, Scarda A, Palombo E, Rosso R (1998) Bone turnover and its relationship with bone mineral density in pre- and postmenopausal women with or without fractures. Maturitas 29:265–270

Nicholson PH and Bouxsein ML (2002) Bone marrow influences quantitative ultrasound measurements in human cancellous bone. Ultrasound Med Biol 28:369–375

Nicholson PH, Muller R, Cheng XG, Ruegsegger P, Van der PG, Dequeker J, Boonen S (2001) Quantitative ultrasound and trabecular architecture in the human calcaneus. J Bone Miner Res 16:1886–1892

Njeh CF, Boivin CM, Langton CM (1997) The role of ultrasound in the assessment of osteo-porosis: a review. Osteoporos Int 7:7–22

Njeh CF, Fuerst T, Hans D, Blake GM, Genant HK (1999a) Radiation exposure in bone mineral density assessment. Appl Radiat Isot 50:215–236

Njeh CF, Hans D, Fuerst T, Gluer C-C, Genant HK (1999b) Quantitative Ultrasound assess-ment of osteoporosis and bone status. Dunitz, Munich

Njeh CF, Saeed I, Grigorian M, Kendler DL, Fan B, Shepherd J, McClung M, Drake WM, Genant HK (2001) Assessment of bone status using speed of sound at multiple anatomical sites. Ultrasound Med Biol 27:1337–1345

Prins SH, Jorgensen HL, Jorgensen LV, Hassager C (1998) The role of quantitative ultrasound in the assessment of bone: a review. Clin Physiol 18:3–17

Prins SH, Jorgensen HL, Jorgensen LV, Hassager C (2000) Quantitative ultrasound bone mea-surements. Ugeskr Laeger 162:2731–2735

Qin Y-X, Lin W, Rubin C (2001) Interdependent relationship between trabecular bone quality and ultrasound attenuation and velocity using a scanning confocol acoustic diagnostic system. J Bone Miner Res 16:S470–S470

Qin Y-X, Xia Y, Lin W, Chadha A, Gruber B, Rubin C (2002) Assessment of bone quantity and quality in human cadaver calcaneus using scanning confocal ultrasound and DEXA measurements. J Bone Miner Res 17:S422

Qin Y-X, Mittra E, Lin W, Xia Y, Gruber B, Rubin C (2003) Non-invasive evaluation of trabec-ular bone density and strength using scanning ultrasound. Bone 32:S182

Rho JY, Ashman RB, Turner CH (1993) Young's modulus of trabecular and cortical bone ma-terial: ultrasonic and microtensile measurements. J Biomech 26:111–119

Sartoris DJ, Resnick D (1990a) Current and innovative methods for noninvasive bone densit-ometry. Radiol Clin North Am 28:257–278

Sartoris DJ, Resnick D (1990b) X-ray absorptiometry in bone mineral analysis. Diagn Imaging 12:108–113, 159, 183

Schoenberg M (1984) Wave propagation in alternating solid and fluid layers. Wave Motion 6:303–321

Serpe L, Rho JY (1996) The nonlinear transition period of broadband ultrasound attenuation as bone density varies. J Biomech 29:963–966

Strelitzki R, Evans JA (1996) An investigation of the measurement of broadband ultrasonic attenuation in trabecular bone. Ultrasonics 34:785–791

Strelitzki R, Evans JA (1998) Diffraction and interface losses in broadband ultrasound attenuation measurements of the calcaneum. Physiol Meas 19:197–204

Strelitzki R, Evans JA, Clarke AJ (1997) The influence of porosity and pore size on the ultrasonic properties of bone investigated using a phantom material. Osteoporos Int 7:370–375

Strelitzki R, Metcalfe SC, Nicholson PH, Evans JA, Paech V (1999) On the ultrasonic attenuation and its frequency dependence in the os calcis assessed with a multielement receiver. Ultrasound Med Biol 25:133–141

Tavakoli MB, Evans JA (1991) Dependence of the velocity and attenuation of ultrasound in bone on the mineral content. Phys Med Biol 36:1529–1537

Turner CH, Eich M (1991) Ultrasonic velocity as a predictor of strength in bovine cancellous bone. Calcif Tissue Int 49:116–119

Turner CH, Rho J, Takano Y, Tsui TY, Pharr GM (1999) The elastic properties of trabecular and cortical bone tissues are similar: results from two microscopic measurement techniques. J Biomech 32:437–441

Wahner HW, Fogelman I (1994) The evaluation of osteoporosis: dual energy X-ray absorptiometry in clinical practice. Martin Dunitz, London

Wear KA (1999) Frequency dependence of ultrasonic backscatter from human trabecular bone: theory and experiment. J Acoust Soc Am 106:3659–3664

Wear KA (2000a) Anisotropy of ultrasonic backscatter and attenuation from human calcaneus: implications for relative roles of absorption and scattering in determining attenuation. J Acoust Soc Am 107:3474–3479

Wear KA (2000b) The effects of frequency-dependent attenuation and dispersion on sound speed measurement: applications in human trabecular bone. IEEE Trans Ultrason Ferroelectr Freq Control 47:265–273

Wear KA (2001) A stratified model to predict dispersion in trabecular bone. IEEE Trans Ultrason Ferroelectr Freq Control 48:1079–1083

Wear KA (2004) Measurement of dependence of backscatter coefficient from cylinders on frequency and diameter using focused transducers: with applications in trabecular bone. J Acoust Soc Am 115:66–72

Wear KA, Garra BS (1998) Assessment of bone density using ultrasonic backscatter. Ultrasound Med Biol 24:689–695

Wear KA, Stuber AP, Reynolds JC (2000) Relationships of ultrasonic backscatter with ultrasonic attenuation, sound speed and bone mineral density in human calcaneus. Ultrasound Med Biol 26:1311–1316

Williams JL (1992) Ultrasonic wave propagation in cancellous and cortical bone: prediction of some experimental results by Biot's theory. J Acoust Soc Am 91:1106–1112

Williams JL (2001) Is there a causal relationship between quantitative ultrasound and the elastic constants of cancellous bone? J Bone Miner Res 16:966–969

Wittich A, Vega E, Casco C, Marini A, Forlano C, Segovia F, Nadal M, Mautalen C (1998) Ultrasound velocity of the tibia in patients on haemodialysis. J Clin Densitom 1:157–163

Xia Y, Lin W, Qin Y (2005) The influence of cortical end-plate on broadband ultrasound attenuation measurements at the human calcaneus using scanning confocal ultrasound. J Acoust Soc Am 118:1801–1807

Advances Microscopic Technologies and Applications

Cortical Bone Mineral Status Evaluated by pQCT, Quantitative Backscattered Electron Imaging and Polarized Light Microscopy

Yau-Ming Lai (✉) [1] and Wing-Chi Chan[2]

[1] Department of Health Technology and Informatics, The Hong Kong Polytechnic University, Hong Kong SAR, China
    e-mail: htymlai@polyu.edu.hk
[2] The Hong Kong Polytechnic University,Hong Kong SAR, China
    e-mail: htlchan@polyu.edu.hk

Abstract

Synergy can be achieved using multiple imaging modalities to reveal cortical bone adaptation at organ, tissue and ultrastructural levels. Peripheral quantitative computed tomography (pQCT) measurement showed significant regional variations of cortical bone mineral density (cBMD) in the distal tibia and distal radius, independent of menopausal status. The higher cBMD was related to its prevalent compressive stress. Circularly polarized light (CPL) microscopy supported this by showing a preferred transverse to oblique collagen fibre orientation. Quantitative backscattered electron (QBSE) imaging study of osteon morphometry and degree of mineralisation in the cadaveric tibia and radius showed that the variation of cBMD was due to differences in percentage of intracortical porosity (IP), rather than to the variation of mineralisation. The distal tibia had significantly lower cBMD than the distal radius. This lower cBMD was compensated by having greater cortical thickness, polar moment of inertia, and collagen fibre orientation index. The tibia, being subject to habitual dynamic compressive loading as compared with the non-weight-bearing nature of the radius, may activate a higher remodelling rate, which does not allow full secondary mineralisation. This was evidenced in the study showed lower cBMD and greater percentage of IP; thus, the compensatory increase in bone geometry is meant to withstand the sustained bend and torsion loading in this region. This chapter demonstrates that compressive loading is more osteogenic bringing about greater regional BMD. The design of exercise intervention programs to enhance bone quality should consider the strain mode effect. Compensation between the material density and structure is evidenced which allows bone strengthening. Regional bone adaptation, as revealed by multiple imaging modalities, allows better understanding of changes at different levels of bone organization.

Introduction

A review of human exercise intervention studies in pre- and postmenopausal women shows that exercise generally has a positive effect on bone mineral density (BMD), with the size of the effect varying between different anatomical sites (Chilibeck et al. 1995; Schoutens et al. 1989; Wolff et al. 1999). The exercise regimes reported in these studies are characterized by type, frequency, intensity, and duration. These parameters define the mechanical milieu to which the bone is subject. Nevertheless, they may not be directly related to exercise induced-changes in bone, and specific strain parameters have been shown to relate to bone response (Judex et al. 1997; Lanyon et al. 1982; O'Connor et al. 1982; Rubin and Lanyon 1984, 1985); however, these studies have been biased towards the invariant stimuli of mechanical strain. A growing number of animal experimental studies has demonstrated that, in response to disparities in the habitual strain mode, variant stimuli of mechanical strain, such as compression vs tension cortices, have exhibited significant differences in material organization in terms of osteon micromorphology, bone mineral content (BMC), and preferred collagen fibre orientation in deer calcaneus, turkey ulna, and equine third metacarpal (Skedros et al. 1994a,b, 1996, 2003b); however, designs of the animal studies are unable to address the issue of bone adaptation in human subjects under the influence of habitual loading. The straight embryonic long bone becomes curved via modelling drifts in response to an increase in muscle strength and a combined bend and compressive loading during growth (Jee and Frost 1992). The bone curvature appears to optimize the strength of the bone as well as to improve the predictability of the loading direction (Bertram and Biewener 1988). The combined loading shifts the neutral axis and results in an asymmetric stress distribution in which compressive stresses are greater than tensile stresses. Compressive strain is sustained on the concave side, whereas tensile strain is concentrated on the convex side of the long bone shaft (Panjabi and White 2001). This difference in strain mode/magnitude may bring about adaptation in material and structural organization via intracortical bone remodelling (Skedros et al. 2003b).

Peripheral quantitative computed tomography (pQCT) offers a new dimension in bone densitometry, which measures volumetric BMD at the organ level. The cross-sectional tomographic images allow the cortices at different regions to be evaluated separately (Muller et al. 1989). A recent study by Lai et al. (2005) using pQCT in postmenopausal subjects also illustrated that the volumetric BMD at the posterior cortex was significantly higher at 6.5% than the anterior cortex, whereas no significant difference in vBMD was shown between the medial and lateral cortices; however, the anterior cortical wall showed the greatest thickness compared with the other three regions, and was significantly 21.3% greater in thickness than the posterior cortex. It is suggested that geometric adaptation in terms of cortical thickness may be the mechanism to adapt such vBMD differences in response to different strain mode in these regions. Further investigation of collagen fibre orientation, degree of mineralisation and osteon morphology, which are determinants of bone strength (Felsenberg and Boonen 2005), at a microscopic level, may lead to a better understanding of regional bone adaptation. The material density of cortical bone is a function of both

the degree of mineralisation and the intracortical porosity (Schaffler and Burr 1988). Nevertheless, in terms of resolution, it is beyond the capacity of current pQCT scanners to depict the porosity and osteon morphology of cortical bone.

In consideration of the above review, studying material organization in terms of osteon morphology, degree of bone mineralisation, and collagen fibre orientation is necessary to obtain an understanding of regional bone adaptation to differential strain magnitudes/modes; however, such a study would involve the use of invasive techniques applicable in animals that may not be suitable for use in human subjects. To circumvent this problem, a model comprising both human subjects and human cadavers was employed to investigate the long bone regional adaptation under habitual loading using pQCT, quantitative backscattered electron (QBSE) imaging and polarized light microscopic imaging. This in vivo and in vitro study model may provide us with complementary information in terms of material and structural organization at both the organ and tissue levels, to understand skeletal adaptations under weight-bearing and non-weight-bearing loading differences. Regional differences in adaptation between the anterior, posterior, medial, and lateral cortices in the same individual long bone subject to different strain magnitudes/modes (compression verse tension) are examined. The strengths of this self-controlled model are that it allows the non-mechanical factors to be adjusted because the same individual long bone is examined, and allows an understanding of end-point bone adaptations under such influences.

Role and Principles of Quantitative Backscattered Electron Imaging

The study by Currey (1984) illustrates that there is a considerable range of mineralisation measured by ash density ranging from 45 to 58% in non-pathological cortical bone. This range of mineralisation results in an even variability of mechanical properties, with the Young modulus of elasticity ranging from 4 to 32 GPa, bending strength from 50 to 300 MPa and the toughness from 200 to 7000 J/m^2. These mechanical properties are compromised in a bone so as to adapt to the requirement of stiffness, strength and toughness. The same amount of bone mass but with high or lower degree of mineralisation corresponds to a high or a low BMD measured either by X-ray absorptiometric and quantitative computed tomographic (QCT) techniques; however, the characteristics of bone mineralisation in terms of its degree can be determined by contact microradiography (CMR), QBSE imaging (Bloebaum et al. 1990, 1997; Roschger et al. 1998), ash weight (An et al. 2000), infrared imaging (Camacho et al. 2003; Faibish et al. 2005; Paschalis et al. 2005), Raman microspectroscopy (Akkus et al. 2003), histomorphometry with Toluidine blue (TB) staining (Qin et al. 2001), scanning acoustic microscopy (SAM; Qin et al. 2004), bench-top micro-computed tomography (micro-CT) with hydroxyapatite phantom calibration (Dufresne et al. 2003) and synchrotron radiation computed tomography (SRCT; Borah et al. 2006; Ito et al. 2003).

Microradiography is the conventional method for evaluating the degree of mineralisation of bone; however, its utility is limited by its volumetric resolution. The errors

caused by the projection effect further reduce its accuracy in BMD and histometric analyses. Added to this, calibration between laboratories has yet to be established (Bloebaum et al. 1997). Use of ash weight as a measure of degree of mineralisation is the gold standard, but the method is destructive and does not allow further evaluation of the specimen. Histomorphometry with TB staining is cost-effective. The TB staining intensities in the osteons moderately correlated with the degree of mineralisation as measured by CMR using aluminium step wedge as the calibration (r = 0.567), but reliable imaging quantification can be achieved provided that bone matrix is not physiologically fully mineralised (Qin et al. 2001). Reflection coefficient as measured by SAM highly correlated with CMR (r = 0.786; Qin et al. 2004, 2001). The QBSE imaging has been developed as a tool with high consistency and image resolution (Roschger et al. 1998; Vajda et al. 1995). Experimental studies showed that BSE images from canine cortical and trabecular bone had excellent morphological resolution, accurate bone histomorphometry and the ability to quantify accurately the bone mineralisation compared with micro-radiographic images (Bachus and Bloebaum 1992). It is also advantageous in that it does not have partial-volume effect and beam-hardening effect as encountered in micro-CT and QCT. These effects do not render the depiction of subtle regional changes in the degree of mineralisation. The use of SRCT with the high intensity, monochromatic X-ray beam provides excellent contrast resolution, which has been applied clinically in the prospective study of the efficacy of antiresorptive drugs on the accretion of bone mineralisation and preservation of bone micro-architecture (Borah et al. 2006, 2005; Roschger et al. 2001); however, the limited access of SRCT in worldwide precludes its common use.

The efficacy of the degree of mineralisation, measured by BSE imaging, in the prediction of bone strength has been validated in experimental studies using standardized machined bovine bone samples (Martin and Boardman 1993; Martin and Ishida 1989), in baboon (Meunier and Boivin 1997) and human studies prescribed with antiresorptive Alendronate (Boivin et al. 2000) and anabolic teriparatide (Paschalis et al. 2005) and in comparing the efficacy weight-bearing and non-weight-bearing exercise interventions (Huang et al. 2003). The study by Follet et al. (2004) using human cadaveric calcanei supported the findings that the increase in bone strength was augmented by degree of mineralisation within the physiological range without necessary changes of bone matrix volume and micro-architecture. Similar findings were also observed in ovariectomized baboons treated with alendronate (Meunier and Boivin 1997), in postmenopausal osteoporotic patients treated with alendronate (Boivin et al. 2000) and postmenopausal osteoporotic patients treated with risedronate (Borah et al. 2006, 2005).

Figure 1 summarizes the work flow of the surface preparation the bone specimen necessary for QBSE imaging, CPL microscopy and osteon morphometry. The methyl methacrylate embedded bone slice is mounted on a plastic slide, which is then attached to a resin mould made by the automatic mounting press (Figs. 1a,b; Simplimet 3000 Mounting Press, Buehler, Illinois). The distal surface of the bone slice is then grinded and polished to a 1 µm finish using the Beta Grinder/Polisher fitted with Vector Power heads (Fig. 1c; Vector, Buehler, Illinois). The surface topology of the bone specimen is monitored by a reflected light microscope (Fig. 2).
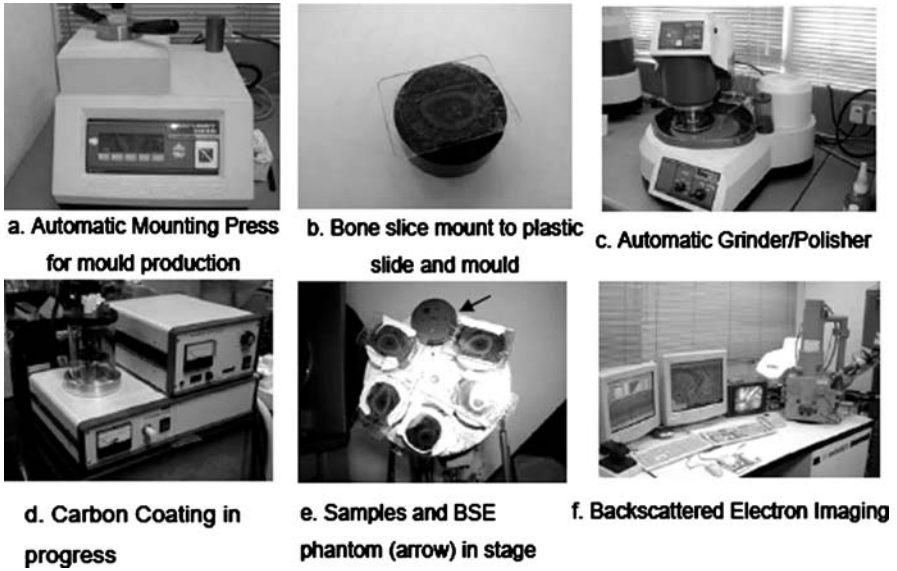
Figure 1. Workflow shows the preparation of a bone specimen for backscattered electron (BSE) imaging and osteon morphometry

Figure 2. Nikon Epiphot 200 inverted light microscope on line with a computer to monitor the bone surface topology
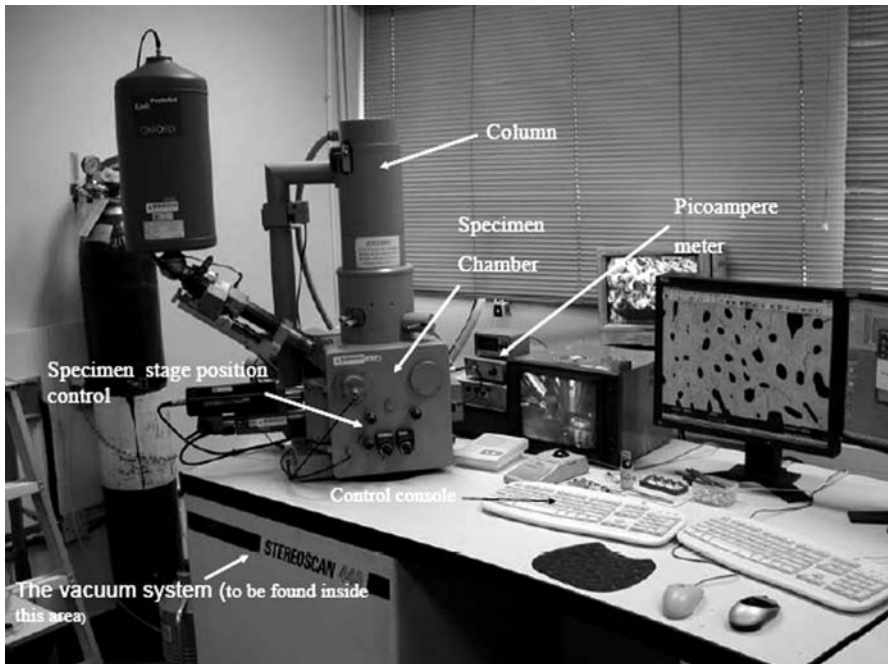
Figure 3. The major components of a scanning electron microscope

The major components of a scanning electron microscope are shown in Fig. 3. The column is used to generate and focus a narrow beam of electrons upon the specimen mounted in the specimen chamber. The electron gun has a tungsten hairpin filament in which the source of electrons is produced via thermionic emission. A series of electromagnetic lens beneath the gun serves to focus and shape the electron beam before it strikes the specimen surface (in case of biological material, such as bone, it should be coated with carbon to make it conductive) in a raster scan pattern. The electron beam energy and the electron beam currently can be varied from 300 V to 30 kV and from 1 pico-amp to 1 micro-amp, respectively, to tailor for the type of examination in progress. The examined specimen is put in a stage inside the chamber. The position of stage can be controlled manually via control knob at the front of the stage door to allow for the different views of the specimen.

The operation of the electron optical column and specimen scanning requires a highly vacuum status in the range of $10^{-4} - 10^{-6}$ torr. The vacuum system is operated by a turbomolecular pump, backed up a rotary pump, is mounted underneath the lower face of the specimen chamber. When the electron beam strikes on the specimen surface, beam specimen interaction gives rise to the emission of Auger electrons, secondary electrons, backscattered electrons, continue and characteristic X-rays from the specimen surface. To study the degree of bone mineralisation, a four quadrant backscattered detector. as shown in Fig. 4, is employed to collect the backscattered electrons from the bone specimen. There are several confounding
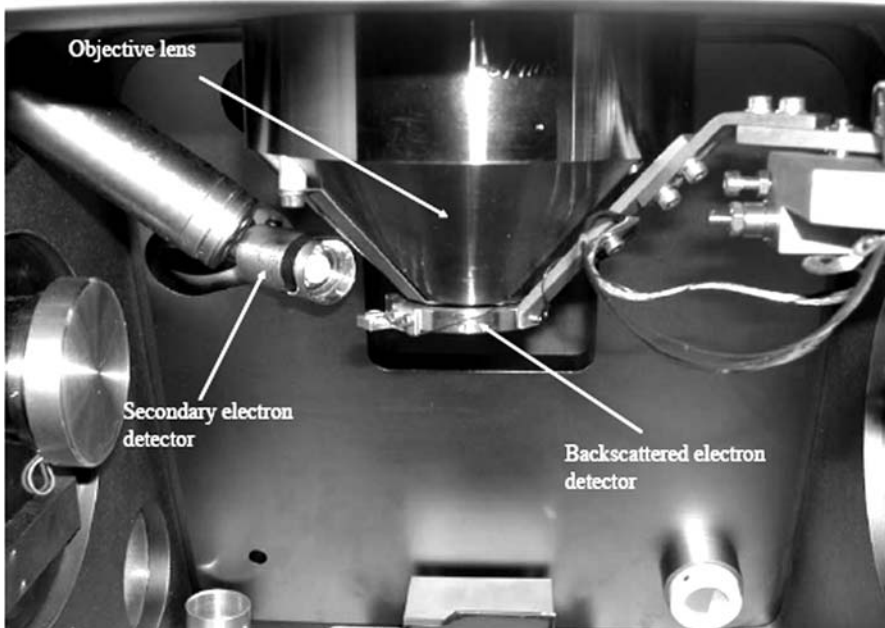
Figure 4. A four-quadrant backscattered detector in situ to collect the backscattered electron signals for BSE imaging

factors in quantitative BSE analysis of bone, which need to be controlled. It is requisite that the incident electron beam maintains the same incident angle and working distance with the specimen (Bloebaum et al. 1990). Also, the specimen surface should be highly polished to eliminate the variation of surface topography (Vajda et al. 1999). Beam current consistency should be monitored using a Faraday cup and a picoampere meter (Roschger et al. 1998). During each scanning session, the specimen current should be monitored using a Faraday cup (Fig. 5a, labeled as *F*) in the BSE calibration phantom. Next, a four-quadrant BSE detector set at the atomic contrast mode is used to image the carbon (C) (Grey value: 27.0 ± 5.2) and Aluminium (Al; Grey value: 223.4 ± 3.3) reference standards in the phantom (Fig. 5a). This procedure aims to standardize the working conditions and calibrate the grey scale of the BSE images. The amount of backscattered electrons varies directly with the average atomic number of a matter. Accordingly, it allows differentiation of the bone specimen with different degrees of mineralisation of the bone matrix as well as the depiction of osteon morphology and porosity (Fig. 6).

Different degrees of mineralisation appear as various shades of grey in the BSE image, which depict the mineralisation intensity distribution. The bone area of the BSE image is segmented from the porosities, MMA areas and fracture lines (due to tissue processing) using Ostu's method and user-specific algorithms written by Matlab (The MathWorks, Natick, Mass.). This image processing left behind an image with a mineral phase. The mineralisation intensity of the mineral phase image is quantified

a. BSE Phantom

b. BSE image of Al

c. BSE image of C

d. Histograms of Al BSE images

f. Histograms of C BSE images
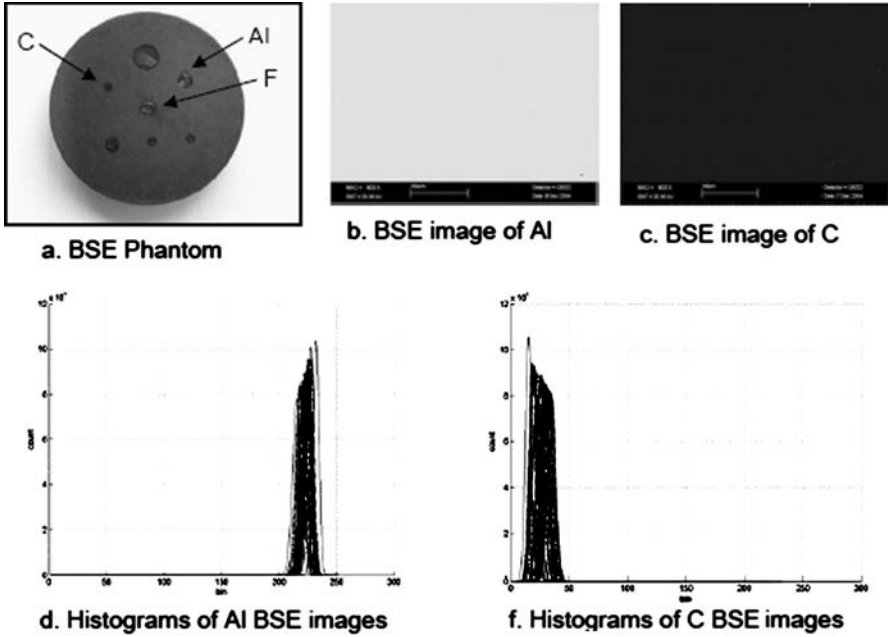
Figure 5. a BSE phantom calibration using aluminium (Al) and carbon (C) standards and Faraday cup (*F*). **b** Typical BSE image of Al standard. **c** Typical BSE image of C standard. **d,e** Cluster of histograms of Al and C images acquired over the imaging sessions
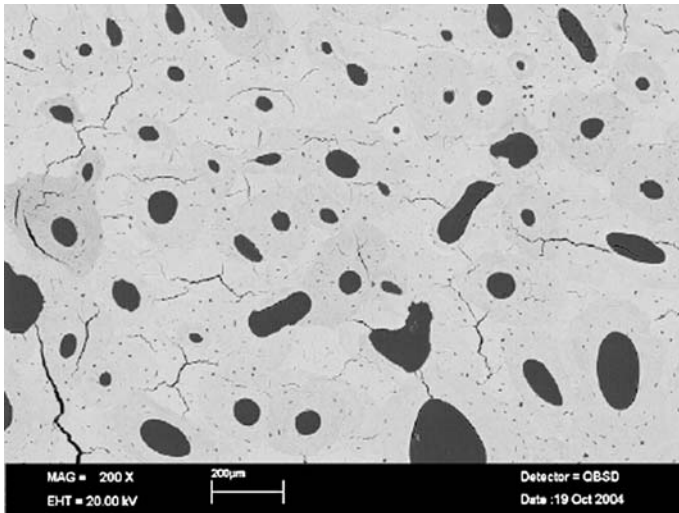
Figure 6. Typical BSE image of a cadaveric tibia cortical bone (lateral region), 200×
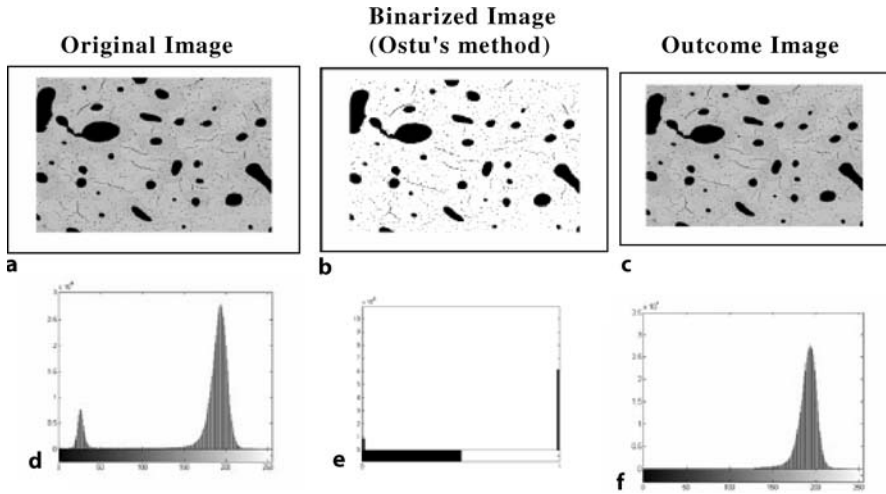
Figure 7. a–c Segmentation of bone phase from porosities using Ostu's method and the corresponding histogram (**d–f**). **d** Histogram of the original BSE image. **e** Histogram of the binarized image. **f** Histogram of the outcome image when the original image is multiplied by its binarized image resulting in a grey-scale distribution of the bone mineral phase

by a weighted mean grey-scale level (WMGL*; Eq. (1)), which measures the position of the grey value histogram in the axis (Fig. 7; Bloebaum et al. 1990; Bloebaum et al. 1997; Skedros et al. 1993).

$$WMGL^* = \sum \frac{NiGi}{C} \qquad (1)$$

Equation (1) shows determination of WMGL as a measure of the degree of mineralisation (Bloebaum et al. 1990, 1997; Skedros et al. 1993).

With the use of same BSE image for studying mineralisation, the osteon morphometry is performed at the anterior, posterior, medial and lateral mid-cortices of the radius and tibia using the image processing software, MetaMorph (Universal Imaging Corporation). Morphometric measurements included:

1. Osteon Area (OA) $\times 10^{-3}$ mm^2
2. Osteon Cortical area (OCA) $\times 10^{-3}$ mm^2
3. Osteon Density (ODen); 1/mm^2
4. Osteon Diameter (ODia; μm); a circular model was assumed
5. Percentage of Fractional Area of secondary bone (FASB)
6. Percentage of Fractional Area of interstitial bone (FAIB)
7. Haversian Canal Area (HCA), $\times 10^{-3}$ mm^2
8. Percentage of Intracortical Porosity (IP).

Details of the definition of the osteon morphometry are listed in Table 1.

In accordance with Barth et al. (1992), the following criteria are used to define measurable osteon in the present study:

Table 1. Definition of osteon morphometric parameters. (From Barth et al. 1992; Skedros et al. 1994b)

Osteon area = total osteon area (includes the laminar bone and Haversian canal)/ no. of measurable osteons

Osteon cortical area = (total osteon area minus total Haversian canal area)/ no. of measurable osteons

Osteon density = total no. of measurable and countable osteons/ image area

Osteon diameter: assuming that the osteon is circular in shape and this parameter can be determined by the following formula: 2 × square root of (osteon area /pi)

Percentage of fractional area of secondary bone = total osteon bone area/ image area ×100%

Percentage of fractional area of interstitial bone = (image area minus total osteon area)/ image area ×100%

Haversian canal area = total Haversian canal area/ no. of measurable osteons

Percentage of intracortical porosity = (image area minus total bone area)/ image area ×100%

Image area: area occupied by the cortical bone in the BSE micrograph

1. The Haversian canal is patent and distinct. Haversian canals that merge with other canals or with Volkmann's canals are not measured.
2. The osteon is identified, with more than 80% of its area distinguishable from contiguous osteons.
3. The borders of the osteon are distinguishable.
4. Osteons at the periphery of the field are measured if the above criteria are satisfied.

Also, the following criteria are used to determine whether an osteon was to be counted:

1. The Haversian canal is patent and distinct. Haversian canals that merge with other canals are not measured.
2. The osteon is identified, with more than 80% of its area distinguishable from contiguous osteons.
3. Osteons at the periphery of the field are measured if the above criteria are satisfied.

Role and Principles of Polarized Light Microscopy

The orientation of collagen fibres can be demonstrated using polarized light microscopy (Boyde and Riggs 1990; Carando et al. 1989; Martin and Ishida 1989; Martin et al. 1996; Skedros 2001; Skedros et al. 2003a). The use of circularly polarized light (CPL), as opposed to linearly polarized light, to study collagen fibre orientation has been validated in terms of its better correlation with mechanical properties. Also, the quantification of fibre orientation using circularly polarized light microscopy is superior in that it is independent of the orientation of a specimen in the field of view and is without maltase cross artefacts (Fig. 8; Martin et al. 1996).
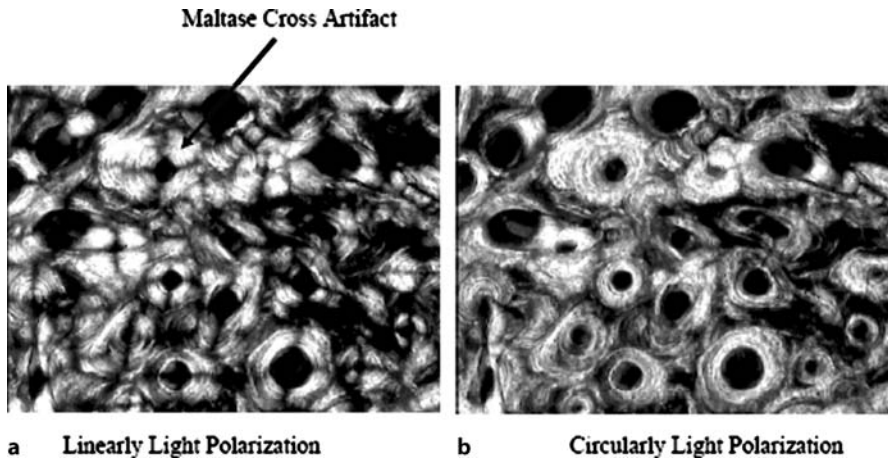
Figure 8. a Linearly polarized microscopy of cadaveric tibia cortex with maltase cross artefact (*arrow*). **b** Circularly polarized microscopy of the same specimen, free of the artefact

Preferred longitudinal collagen fibre orientation (CFO) has been shown in the tension cortex, whereas a more transverse-to-oblique direction is seen in the compression cortex of the equine radius (Boyde and Riggs 1990; Riggs et al. 1993) and in human upper and lower limb shafts (Carando et al. 1989, 1991); thus, the use of CPL in the demonstration of CFO may add evidence to the regional differences in cortical cBMD of long bone shaft (Lai et al. 2005). The CFO quantified as the predominant longitudinal direction explained the greatest percentage of variance in the total amount of energy absorbed in the ultimate tensile stress using equine third metacarpals at mid-diaphysis (Skedros et al. 2001). It was also the best predictor of tensile strength (Martin and Ishida 1989) and bending elastic modulus and ultimate stress using bovine cortical bone (Martin and Boardman 1993).

The principle of circularly polarized light microscopy has been described in detail (Bromage et al. 2003). The plane polarized light incident on the quarter wave plate resolves into two orthogonal wave components (birefringent effect) with equal magnitude but propagating with a phase difference of a quarter wavelength ($\lambda/4$). This results in a CPL wave with its electric vector rotating 360°. The CPL refracts in the bone specimen such that its birefringent effect allows transmission of peak light intensities on condition that the collagen fibres are lying parallel (transverse orientation) with plane of bone section. The emerging CPL from the bone specimen incident on the quarter wave plate is then converted into linearly polarized light and aligns with the transmission axis of the analyser.

Quantification of collagen fibre orientation (CFO) can be determined from the researcher-defined CFO index obtained from these images. To determine the CFO index, the original CPL image is first binarized by thresholding using Image J image processing software (National Institutes of Health, Bethesda, Maryland). This is to separate the collagen fibres lying relatively more transverse to oblique orientation (bright pixels) from the background of the image (dark pixel). The CFO index is

$$CFO\ index = \frac{Pixel\ counts\ of\ gray\ value = 1}{Total\ pixel\ counts\ of\ the\ image\ area}$$
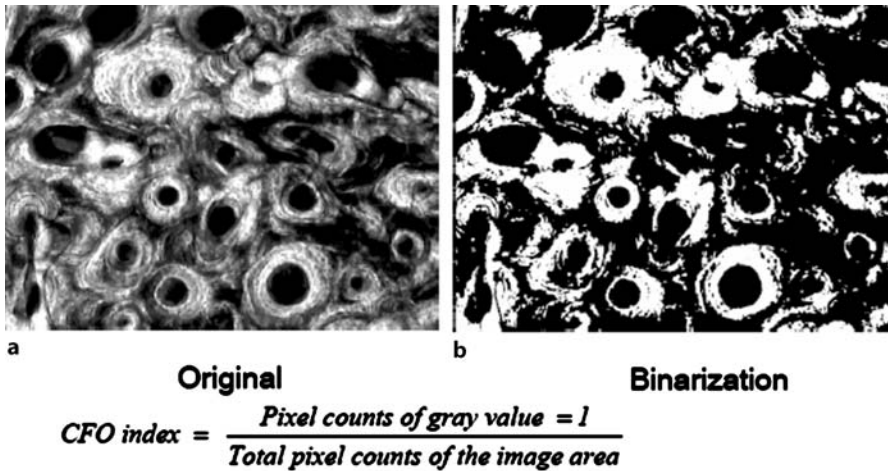
Figure 9. a Original CFO image. **b** Binarization of the original CFO image using thresholding to separate the bright collagen from the image background. The CFO index is determined according to the pixel counts in this binarized image

defined as a ratio of the number of pixels above a threshold value (single threshold for bright pixels under CPL) to the total number of pixels in this binary image (Fig. 9). The question of brightness (degree of transverse orientation) or darkness (degree of longitudinal orientation) is not considered; thus, the effect of cortical thickness on the brightness of the image is then eliminated. The proportion of CPL bright area in the image indicates the relative amount of collagen fibre in the transverse-to-oblique orientation.

Application of pQCT, QBSE Imaging and CPL Microscopy in the Study of Long Bone Adaptation Under Habitual Loading

A model comprising of both human subjects and human cadavers was used to study the regional bone adaptation in distal tibia and radius under habitual loading using pQCT (Densiscan 2000, Scanco Medical, Bassersdorf, Switzerland) with standard protocol to measure the cBMD, cortical thickness and polar moment of inertia (Qin et al. 2000, 2002b), QBSE imaging (Stereoscan 440, Cambridge 440) and CPL microscopy (Nikon Optiphot-Pol, Japan), as discussed previously. Ninety-nine healthy Hong Kong Chinese women were recruited; of these, 72 were postmenopausal, aged 47–60 years (mean ± SD: 53.7 ± 3.1 years); and 27 were perimenopausal, aged 42–53 years (mean±SD: 49.1 ± 2.6 years). Subjects who were undergoing hormone replacement therapy, corticosteroid therapy, suffering from hypo- or hyperthyroidism, hypo- or hyperparathyroidism, and renal or liver disease were excluded. Other conditions known to affect bone metabolism, such as patients with a history of fracture in the non-dominant forearm and lower leg in the region of the pQCT measurements,

were also excluded. All of the subjects reported that they did not engage in regular exercise (not > 0.5 h/week), and gave their informed consent before participating in the study.

Twenty cadavers of Chinese ethnicity, embalmed using an intra-arterial injection of fixatives, were recruited in the present study. They consisted of 2 females and 18 males aged 70.8 ± 8.5 years without history of metabolic diseases and macroscopic bone deformities as confirmed by computed radiography. A forearm and a lower leg were harvested from each of the cadavers, for a total of 20 left forearms, 16 left lower legs and 4 right lower legs.

Overall Findings of the Study

This was the first study to report on the regional differences in material and structural organization in both weight-bearing (tibia) and non-weight-bearing (radius) long bone under the influence of habitual loading in human subjects and cadavers at both the macroscopic and microscopic levels. Our main findings indicated that the intra-skeletal comparison in postmenopausal and perimenopausal women showed a significant regional difference in cBMD in the distal tibia and radius (Figs. 8,10a,b). The radius medial and tibia posterior cortices had the greatest cBMD compared with the other regions. Perimenopausal women had a greater cBMD in both tibia and radius than postmenopausal women; however, no interaction effect of strain mode and menopausal status on regional cBMD was demonstrated. In an intra-skeletal site comparison of human cadavers (Table 2), the tibia by itself also showed significant regional differences in the following osteon morphometric parameters: ODen, percentage of FASB, percentage of FAIB, and percentage of IP, whereas a significant regional difference only in the CFO index was shown in the radius. An inter-skeletal site comparison of human cadavers (Table 3), the tibia and radius demonstrated significant differences in cBMD, cortical thickness, PMI, WMGL, CFO index, OA, ODia, HCA, and percentage of IP. In an intra-skeletal correlation study of human cadavers (Table 4), a significant positive correlation was demonstrated between cBMD and OA, OCA and ODia in distal radial cortices, whereas a significant negative correlation was found between these parameters in the distal tibial cortices. A significant correlation was shown between cBMD and HCA and ODen, in the distal tibial cortices, but these parameters were not significantly correlated in the distal radial cortices. Also, a significant negative relationship between cBMD and CFO was demonstrated in both the distal radial and tibial cortices.

Intra-skeletal Regional Adaptation of Cortical Bone: Evaluation of Distal Tibia and Radius in Postmenopausal and Perimenopausal Women Under Habitual Loading

Measurement of tibial cBMD using pQCT showed that the posterior cortex had volumetric cBMD a significant 6.4% higher than the anterior cortex; however, there was no significant difference in cBMD between the medial and the lateral cortices. Also, there was no interaction effect between menopausal status and strain mode on cBMD. This indicates that the differential mechanical loading magnitude/mode

Table 2. Intra-skeletal comparison of regional cBMD (n = 99 human subjects). WMGL, the CFO index, and osteon morphometric parameter, summarized in mean (SD), in distal tibia and radius (n = 20 human cadavers)

Parameter	Tibia				Radius			
	Anterior	Posterior	Medial	Lateral	Anterior	Posterior	Medial	Lateral
PQCT (cBMD, mg/cm^3)[a]	1828.3 (109.5)	1946.1 (124.6)	1885.5 (101.2)	1849.4 (113.9)	1983.9 (74.2)	1968.5 (108.5)	2054.1 (71.9)	1943.7 (127.7)
BSE (WMGL)	182.3 (5.1)	184.3(5.9)	184.3 (5.1)	184.9 (6.4)	189.7 (7.5)	188.5 (7.7)	189.1 (7.6)	189.1 (8.7)
CPL (CFO index)[a]	0.309 (0.041)	0.336 (0.075)	0.338 (0.066)	0.320 (0.045)	0.287 (0.040)	0.255 (0.053)	0.303 (0.067)	0.270 (0.034)
Osteon morphometry								
No. of osteon	473	385	518	552	424	479	322	430
OA (10^{-3} mm^2)[a] measured	35.2(7.9)	35.8 (11)	31.6 (8.7)	32.6 (7)	32.3 (7.8)	29.3 (6.8)	32.6 (9.2)	27.4 (5.5)
OCA (10^{-3} mm^2)	28.9(6.5)	29.5(7.9)	26.1(6.8)	28.5 (6.5)	28.3 (6.7)	26.2 (6.1)	28.3 (7.5)	24.3 (4.8)
ODen (1/mm^2)[a]	10.3(4.1)	8.1(4.2)	11.3(4.2)	11.7 (3.4)	10.1 (2.9)	10.1 (3.5)	8.4 (2.5)	11.1 (3.9)
ODia (μm)	210.4(24.2)	211.3(31.7)	198.7(28.5)	202.8 (22.4)	201.2 (24.9)	192.1 (21.8)	201.6 (29.5)	185.9 (19.3)
%FASB[a]	27.7(8.4)	22.9(9.2)	28.8(11.5)	32.9 (11.2)	27.7 (8.4)	26.8 (7.2)	23.0 (7.6)	26.1 (7.9)
%FAIB[a]	66.0(9.8)	72.7(10.6)	65.5(12.6)	62.3 (12.3)	68.5 (9.6)	69.4 (7.8)	73.6 (8.9)	70.4 (9.2)
HCA (10^{-3} mm^2)[a]	6.2(2.6)	6.3(4.4)	5.6(3.8)	4.2 (1.6)	3.9 (1.9)	3.1 (1.3)	4.3 (2.5)	3.2 (1.1)
% IP[a]	14.2(4.2)	11.2(3.7)	11.1 (3.5)	10.3 (2.7)	9.5 (2.8)	8.8 (3.1)	9.2 (3.2)	10.3 (4.0)

cBMD cortical bone mineral density, *WMGL* weighted mean grey-scale level, *CFO index* collagen fibre orientation index, *OA* osteon area, *OCA* osteon cortical area, *ODen* osteon density, *ODia* osteon diameter, *%FASB* fractional area of secondary bone, *%FAIB* fractional area of interstitial bone, *HCA* Haversian canal area, *%IP* intracortical porosity. *pQCT* peripheral quantitative computed tomography, *BSE* backscattered electronimaging, *CPL* circular polarized light

[a] A one-way ANOVA test showed significant regional differences in these parameters in both the tibia and radius.
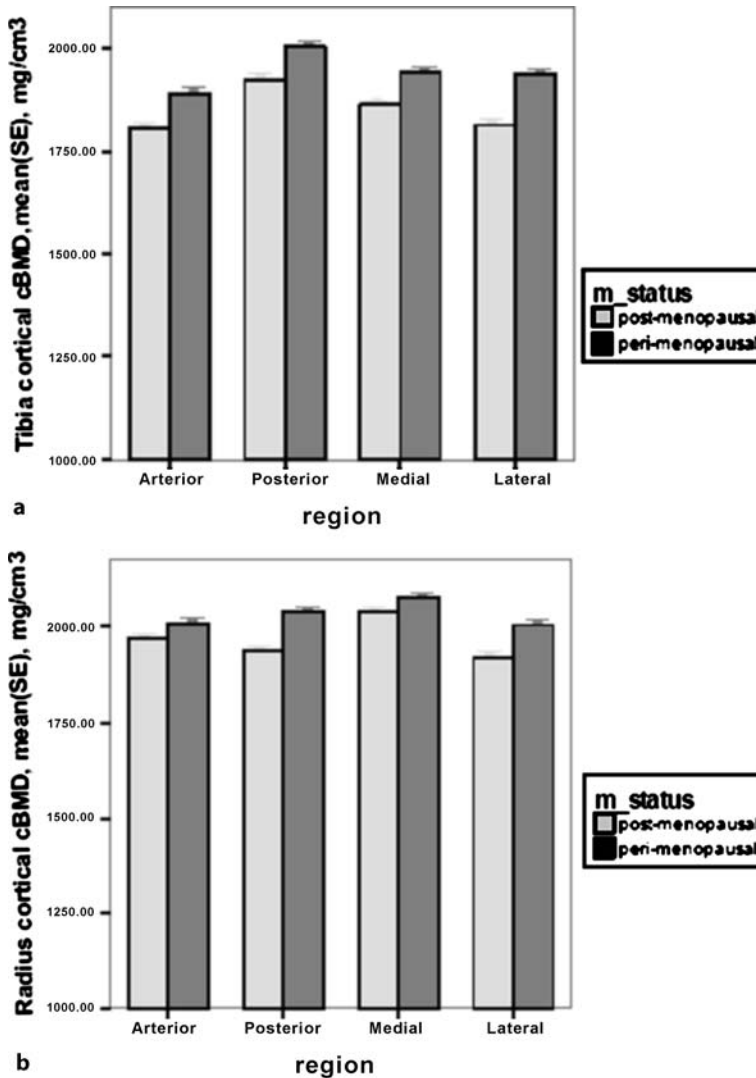
Figure 10. a The main effects of menopausal status (m_{status}) and the cortical region on tibia cBMD were significant (two-way ANOVA; $P < 0.001$), whereas no interaction effect was demonstrated ($P = 0.467$). **b** The main effects of menopausal status (m_{status}) and the cortical region on radius cBMD were significant (two-way ANOVA; $P < 0.001$), whereas no interaction effect was demonstrated ($P = 0.059$)

prevalent in a cortex brings about bone density adaptation, which is independent of the effect of menopausal status. Alternatively, such regional difference may be a result of ontogeny of bone adaptation (Pearson and Lieberman 2004; Skedros et al. 2003b). Strain gauge studies on the loading environment may shed light on these findings.

Table 3. Inter-skeletal comparison of pQCT-acquired cBMD, cortical thickness, PMI, BSE-acquired WMGL, CPL acquired CFO index, and the osteon morphometric parameters between the distal tibia and distal radius (n = 20 human cadavers): combining the results from all the regions, summarized in mean (SD)

	Tibia	Radius	(%) Differences[a]	p-value (paired samples t-test)
pQCT				
cBMD (mg/cm^3)	1604.3 (214.1)	1831.2 (148.0)	−12.4	< 0.001[b]
Cortical thickness (mm)	3.09 (0.58)	2.45 (0.39)	26.1	< 0.001[b]
PMI($\times 10^2$ mm^4)	239.4 (58.7)	26.6 (7.4)	800.0	< 0.001[b]
BSE				
WMGL	183.9 (4.5)	189.1 (7.7)	−2.7	0.005[b]
CPL				
CFO index	0.326 (0.038)	0.278 (0.028)	17.3	< 0.001[b]
Osteon morphometry				
OA (10^{-3} mm^2)	33.8 (6.4)	30.4 (5.9)	11.2	0.043[b]
OCA (10^{-3} mm^2)	28.3 (5.0)	26.8 (5.2)	5.6	0.229
ODen (1/mm^2)	10.3 (3.3)	9.9 (2.3)	4.0	0.639
ODia (μm)	205.8 (19.7)	195.2 (19.4)	5.4	0.051[c]
%FASB	28.1 (8.3)	25.9 (6.0)	8.5	0.320
%FAIB	66.6 (9.5)	70.5 (6.6)	−5.5	0.111
HCA (10^{-3} mm^2)	5.6 (1.9)	3.6 (1.2)	55.6	0.001[b]
%IP	11.7 (2.5)	9.5 (2.5)	23.2	0.006[b]

cBMD cortical bone mineral density, *PMI* polar moment of inertia, *WMGL* weighted mean grey-scale level, *CFO index* collagen fibre orientation index, *OA* osteon area, *OCA* osteon cortical area, *ODen* osteon density, *ODia* osteon diameter, *%FASB* fractional area of secondary bone, *%FAIB* fractional area of interstitial bone, *HCA* Haversian canal area, *%IP* intracortical porosity
[a] Difference in parameter between the tibia and radius calculated with respect to the radius
[b] Significant difference (significance level set at p = 0.05)
[c] Marginal significant difference (significance level set at p = 0.05)

In a recent study by Peterman et al. (2001), a robust cadaver model was used to simulate walking and measured the strain during the gait cycle with seven rosettes. The rosettes were evenly distributed around the tibial cortex, with one rosette attached to the anterior crest and two each bonded to the antero-medial, antero-lateral and posterior facets. The results showed that the primary mode of tibial loading was bending with peak compressive and tensile strains, which occurred within the posterior aspect and anterior crest of the tibia, respectively. The magnitude of the compressive strain was also higher than that of the tensile strain during the whole cycle of the stance of the gait. Furthermore, the neutral axis of bending aligned with the medial and

Table 4. Correlation coefficient between cBMD and BSE-measured WMGL, osteon morphometric parameters, and collagen fibre orientation by pooling the data from the four regions in both the radius and tibia of human cadavers ($n = 20$)

Parameter	Radius (pQCT-cBMD)	Tibia (pQCT-cBMD)
BSE		
WMGL	−0.105	−0.163
Osteon morphometry		
OA	0.233[a]	−0.258[a]
OCA	0.247[a]	−0.212[b]
Oden	−0.153	0.316[a]
Odia	0.241[a]	−0.267[a]
%FASB	0.009	0.198
%FAIB	0.034	−0.176
HCA	0.096	−0.244[a]
%IP	−0.232[a]	−0.157
CPL		
CFO	−0.246[a]	−0.277[a]

[a] Correlation is significant at the 0.05 level (two-tailed) [b] Marginally significant ($P = 0.059$)

lateral region with a slight variation of 10° during the stance phase of the gait. The findings of these experimental studies may indicate that the posterior cortex, subjected to higher compressive loading, adapts with a significantly higher BMD than the tensile anterior cortex. By contrast, no significant difference in cBMD was shown between the medial and lateral tibial cortices where both regions coincide near the neutral plane, and the difference in normal strain was small compared with that of the anterior and posterior cortices. The normal strain at these regions is zero, but the shear strains are prevalent, which is in accordance with engineering principles (Bertram and Biewener 1988; Hayes and Bouxsein 1997).

In the case of the distal radius, the medial and anterior cortices had greater cBMD compared with the lateral and posterior cortices, respectively. On average, the medial cortex had a significant 3.5, 4.3 and 5.7% greater cBMD than the anterior, posterior and lateral cortices, respectively. Similar to the tibia, the main effects of the strain mode and menopausal status on cBMD are independent. Biomechanical studies and a macroscopic examination of radial shaft morphology may provide evidence of the relationship between bone structure and mechanical loading. Firstly, functional/daily activities involving gripping and lifting applied to the hand can generate a significant wrist and elbow joint reaction force. A biomechanical study using a grip transducer illustrated that humero-ulnar forces of up to 1600 N, humero-radial forces of up to 800 N and wrist joint forces of up to 2800 N can be generated during a moderate level of gripping activity (Chadwick and Nicol 2000). A study by Karnezis using a free body analysis of the sagittal-plane forces acting on the supinated distal radius during lifting demonstrated that the radiocarpal joint reaction force amounted to 4.24 times the

lifted weight and occurred at a forearm position of 13.4° above the horizontal plane (Karnezis 2005). The study only considered the wrist flexor in action. If a heavier weight is lifted, stronger forearm flexors (Biceps, Brachialis, Brachioradialis) with large physiological cross-sectional areas would be recruited (An et al. 1981; Neumann 2002). The result could be an even higher joint reaction force to encounter the muscle tension and external loading. Force transmission studies using a cadaveric forearm demonstrated that about 70–80% of compressive loading was shared by the distal radius and the balance by the distal ulna when axial loading was applied to the wrist (Birkbeck et al. 1997; Pfaeffle et al. 2000). Furthermore, a cadaveric forearm study by Pfaeffle et al. (2000) illustrated that the interosseous ligament, with an average force vector at an angle of 21 – 25° with the long axis of the ulna, exerts longitudinal forces on the radius when compressive loading is applied to the hand.

Secondly, by examining the surface form of the radial shaft, both the upper three-fourths of the anterior surface and medial border extending down from the radial tuberosity were shown to be concave, whereas both the lateral surface, through its entire extent, and the posterior surface, for its middle third and lower third, are convex (Gray 1974). Added to that, the characteristic macroscopic radial bow allows room for attaching muscle and interosseous membranes; thus, it engenders a bending load in the radius as a result of compressive loading at the radiocarpal joint and radial head. It follows that the concave (anterior and medial cortices) and convex (lateral and posterior cortices) sides of the radius cortical shaft are sustained to compressive and tensile loading, respectively, as evidenced by a recent strain gauge study using cadaveric upper extremities (Kaufmann et al. 2002). Our results from the CPL analyses further substantiated such a loading distribution in that both the anterior and medial cortices had a higher CFO index than the posterior and lateral cortices, respectively. The abovementioned findings of the descriptive anatomy and those of experimental studies of elbow and forearm kinetics may provide support to the loading milieu of the distal radius; thus, the anterior and medial concave cortices are subject to compressive loading, which may be more osteogenic and results in higher cBMD compared with posterior and lateral convex cortices. Since the interosseous ligament attaches to the radius at the medial border, longitudinal forces generated by the interosseous ligament increases the compressive force magnitude at this region. This may account for the greatest cBMD at the radial medial cortices compared with other regions.

Intra-skeletal Regional Adaptation of Cortical Bone: Evaluation of Human Cadaveric Tibia and Radius Under Habitual Loading

An increasing amount of experimental data suggest that mechanical signals determine regional variations in the material organization of cortical bone at the tissue level (Mason et al. 1995; Skedros et al. 1994a,b, 1996, 2003a). Our findings also provide evidence of bone adaptation in response to differential loading modes as such. The volumetric cortical bone mineral density measured by pQCT is a function of both the degree of mineralisation of the organic matrix and intracortical porosity. The present study showed that there was no significant difference in the degree of mineralisation as measured by WMGL between the anterior tibial and posterior tibial cortices; how-

ever, the anterior tibial cortex showed a 14.2% greater intracortical porosity than the posterior tibial cortex. This illustrates that the posterior tibial cortex may adapt to the compressive loading, resulting in lower intracortical porosity but with a similar degree of mineralisation compared with the anterior tibial tensile cortex. This finding supports the hypothesis put forward by Martin et al. (1998) that change in volumetric BMD is a reflection of change in intracortical porosity rather than the mineralisation of the tissue, achieved via intracortical bone remodelling; thus, the lower volumetric cBMD in the anterior tensile cortex may reflect increased porosity rather than decreased mineralisation of the organic bone matrix. Osteon morphometry may further substantiate this argument. The results showed that the compression cortex had the smallest osteon density and the lowest percentage of FASB/highest percentage of FAIB compared with the anterior tension cortex, and medial and lateral cortices situated near the neutral plane (see Table 3), although significant differences in percentage of FASB and percentage of FAIB were not demonstrated between the anterior and posterior cortices. The lower osteon density concurs with the lowest percentage of FASB/highest percentage of FAIB in the posterior cortex under compression. Osteon morphometric pattern as such explains that the higher cBMD may be attributed to slower remodelling activity in the region (Skedros et al. 1997). The interstitial lamellar bone, which is the remnant of an older generation of the Haversian system, had a higher degree of mineralisation following continuing intracortical reorganization than the secondary bone; thus, either an increase in percentage of FAIB or a decrease in percentage of FASB or percentage of IP contributes to an increase in cBMD; however, the present correlation study (see Table 4) demonstrated that there was significant linear relationship between the cBMD and percentage of IP, but it was not significant with percentage of FASB, and percentage of FAIB in tibia. Our findings illustrated that in the distal tibia, the posterior cortex had a significantly lower porosity than the anterior cortex, but insignificant regional differences in both percentage of FAIB and percentage of FASM. The latter finding concurred that there was no significant difference in the degree of mineralisation as measured by WMGL between the anterior and posterior regions. The present correlation study showed that there was significant relationship between the porosities due to the Haversian canal/other pores and cBMD, but no significant relationship between the cBMD and degree of mineralisation as measured by WMGL. Altogether these findings supported that regional adaptation of cBMD via intracortical remodelling may be attributed to differences in intracortical porosity, rather than in the degree of mineralisation in response to differential strain magnitudes/modes. Such variations in regional cBMD and porosities shown in the distal tibia may be explained in accordance with Frost's strain-magnitude related bone adaptation theories (Frost 1983, 1987, 1990). There are three minimum effective strains (MES) that govern bone remodelling activities. The loading magnitude sustained in the posterior compression cortex may be such that remodelling is regressed by conditions of normal mechanical usage; however, the loading magnitude sustained in the anterior tensile cortex may be such that remodelling is activated below an MES and ultimately yields increased porosity.

The present osteon morphometric study of radial cortical regions showed that there were no significant differences in the osteon morphometric parameters; how-

ever, the medial cortex showed a relatively higher percentage of FAIB, lower percentage of FASB and lower percentage of IP compared with the other three radial cortical regions. This may explain the increase in cBMD in this region; however, the loading sustained in the distal forearm, apart from a combination of bending and compression, also involves rotation in most daily activities (ranging from 50° of pronation to 50° of supination; Morrey et al. 1981). This may add substantial torsional/shear force in the distal forearm and result in a more complex loading environment. Previous studies (Skedros 2001; Skedros et al. 2001; Skedros et al. 1994b; Skedros et al. 1996) used animal skeletal tissue characteristics of a cantilever beam, in which there was a clear strain history in the concave compression and convex tension cortices. The results showed that there was strain magnitude/mode-specific material and structural adaptation of bone; thus, as was explained, the influences of complex kinetics and kinematics in the forearm could reduce the sensitivity and specificity of bone adaptation to loading. This may defy the use of strain-magnitude-based rules of Frost's Mechanostat Theory of mechanically induced bone adaptation under the milieu of mechanical loading.

Evidence has also been shown for a functional association of the collagen fibre orientation with the loading demand. At the ultrastructural level, regional strain-mode specific CFO has been reported in human upper and lower extremities (Carando et al. 1989, 1991) and in animals using horse radius, and sheep, deer and horse calcanei that had been subjected to relatively simple bend loading (Mason et al. 1995; Riggs et al. 1993; Skedros 2001). In these studies, cortex that receives predominant compression exhibits relatively more transverse-to-oblique fibre orientation, while cortex with predominant tension has more longitudinal collagen. In the present study the radius, with its concave anterior and medial cortices subjected to prevalent compressive loading, exhibited more transverse-to-oblique fibre orientation as measured by the CFO index, an average of 12% higher than that of the posterior and the lateral cortices with prevalent tensile loading; however, there was no significant regional difference in fibre orientation as measured by the CFO index in the tibial cortices. Previous in vivo strain gauge measurements of the human tibia shaft during walking have illustrated that torsional loading associated with the external rotation of the tibia during stance and push brings about a maximum shear stress of 2.5 MPa (Lanyon et al. 1975). This prevalent shear stress may produce shear-related adaptations in such a way that the CFO appears relatively uniform as evidenced by turkey ulna (Skedros et al. 2003b). Also, a cadaveric study of the geometric properties of tibia has shown that the principal major axis of the moment of inertia of the slender distal tibia shaft has a 40° deviation with respect to the anterior-posterior axis of the tibia (Piziali et al. 1980). It follows that this entails a change in the direction of the maximum bending rigidity. Also, the small cross-sectional area in the lower tibial shaft weakens the tibia's capacity to withstand torsion activity. This change in mechanical properties paralleled the change in position of the concentration of the transverse-to-oblique fibres normally found in the posterior compression cortex (Carando et al. 1989). This was shown in our data, in which both medial (0.338 ± 0.066) and lateral (0.320 ± 0.045) cortices had a CFO index similar to that of the posterior cortex (0.336 ± 0.075). That explained why no significant regional differences in the CFO

index were seen in response to changes in the bend loading direction and prevalent torsional loading.

Inter-skeletal Regional Adaptation of Cortical Bone: Evaluation of Human Cadaveric Tibia and Radius Under Habitual Loading

An inter-skeletal comparison of the regional differences between the tibia and radius showed that, at the macroscopic level, the cBMD of the tibia is a significant 12.4% lower than that of the radius. The difference in cBMD between the tibia and radius has been reported in a study on Chinese peri- and postmenopausal women using pQCT, but has yet to be explained (Qin et al. 2000, 2002a,b). The present study using cadavers demonstrated that, microscopically, the radial cortex has a significantly 2.8% higher WMGL, 35.7% smaller HCA and 18.8% lower percentage of IP than that of tibia cortex (see Table 3). It concurs with the intra-skeletal comparison that porosity from Haversian canals and other pores contributed more to the decrease in cBMD compared with the degree of mineralisation. It follows that the aforementioned differences in osteon morphometric parameters together explain the greater cBMD shown in the radius than the tibia. The relative large porosities and reduced degree of mineralisation seen in the tibia may be due to the differential bone remodelling rates between the tibia and radius (Pearson and Lieberman 2004). The tibia, being subject to habitual dynamic compressive loading as compared with the non-weight-bearing nature of the radius, may activate a higher remodelling rate, which does not allow full secondary mineralisation. This was evidenced in the present study by showing lower cBMD and greater percentage of IP in tibial cortices. Being subject to habitual dynamic loading, these physiological strains may produce more micro-damage in the tibia cortices. This damage will weaken bone; thus, the bone activates a higher remodelling rate in order to remove the damage. The higher remodelling rate concurs with the findings in the present study that the tibia has a 4% higher osteon density compared with radius. It was not yet investigated in the present study whether there are differential differences in micro-damage morphology between the tibia and radius. Regional differences in micro-damage morphology in terms of numerical density and crack length between interstitial lamellae and osteon cortical bone has been demonstrated recently (Qiu et al. 2005). Studies on micro-damage had used dog limbs (Burr et al. 1998; Mori and Burr 1993), human ribs (Burr et al. 1997; Qiu et al. 2005) as the models, but intra-skeletal and inter-skeletal site differences in micro-damage are still to be determined. With the exception of the femur, the tibia is the longest and largest bone in the skeleton. It has been suggested that fatigue failure is more likely in larger structures containing a significant flaw. The high remodelling rate is an advantage in that it allows the tibia to be of light weight for efficient movement, to reduce the accumulation of micro-damage and to maintain an extended fatigue life (Martin 2003). To compensate for the lower cBMD in the tibia, the present study demonstrated a geometric adaptation in terms of an average increase of 26% and eight times greater in cortical thickness and PMI, respectively. Such observation in geometric adaptation, but at ultrastructural level, was also supported in the present correlation study, in that there was a significant negative re-

lationship between the CFO index and cBMD. It follows that the lower cBMD may be compensated for by the more transverse-to-oblique fibre orientation so as to offer strength to compression. The concept that a bone's geometry and material characteristics can function in a compensatory manner has been suggested in previous studies (Burr et al. 1990; Lai et al. 2005; Martin et al. 1980; Skedros et al. 2003b). In the present study, the synergy brought about by an increase in cortical thickness, PMI, and the CFO index in tibia, apart from acting to compensate for the lower mineralisation, would increase the tolerance of the dynamic loading of the lower leg during walking.

Rigour of the Study Design

The strength of the present study may lie in the following aspects: Firstly, the use of the in vivo and in vitro model provides an enhanced understanding of bone adaptation at both the macroscopic and microscopic levels using multiple imaging modalities. This model also allows regional differences in bone mineral density, bone geometry, collagen fibre orientation and osteon morphology to be evaluated in a long bone under the same mechanical influences. Secondly, other confounding variables that may affect bone metabolism were excluded in the design of the present study, and this made possible valid comparative studies of intra-skeletal and inter-skeletal variations of the material and structural organizations. Thirdly, the use of multiple imaging modalities with high-precision, calibrated measurements and well-defined measurement parameters have led to synergies in substantiating the variation of bone morphology at different levels and enabled valid comparisons to be made. Finally, use of male cadavers, because of the limited sources, in the in vitro study did not match with the gender in the in vivo study. Gender difference on the regional cortical bone adaptation cannot be excluded in the present study. Nevertheless, the long bones are subject to the same mechanical loading influence, and similar intra/inter-skeletal site differences are contemplated.

Conclusion

This chapter demonstrates that there were significant regional variations in cBMD in both the distal tibia and radius. The higher cBMD in the cortex was related to its prevalent compressive stress as evidenced at the ultrastructural level by showing a preferred transverse-to-oblique collagen fibre orientation; thus, compressive loading may be more osteogenic and beneficial to bone strength. The intra-skeletal and inter-skeletal measurement of osteon morphometry and the degree of mineralisation in the tibia and radius showed that the variation of cBMD was due to differences in percentage of IP rather than to the variation of mineralisation, whereas both percentage of FAIB and percentage of FASB make no significant contribution to the cBMD differences between compressive and tensile cortices. An inter-skeletal comparison between the tibia and radius showed that the long bone may work in a compensatory manner, whereby the lower cBMD is compensated for by bone geometry with

increased cortical thickness, PMI, and the CFO index. The tibia, being subject to habitual dynamic compressive loading as compared with the non-weight-bearing nature of the radius, may bring about more bone micro-damage and activate a higher remodelling rate, resulting in lower cBMD and greater percentage of IP. Recent study in human cortical bone shows that micro-damage in terms of numerical density and crack length are significantly greater in interstitial bone parallel with a significantly lower osteocyte lacunae density when compared with the osteonal bone. Investigation of the micro-damage morphology between the tibia and radius cortices subject to differential strain/mode may provide further understanding of the regional vBMD differences.

The compensatory increase in bone geometry shown in the distal tibia compared with distal radius is meant to enhance the strength to the bend and torsion loading. A high remodelling rate in tibia may be an advantage in that it allows a larger volume of bone, but of a lighter weight, to be carried over and maintain an extended fatigue lifetime.

In conclusion, this work demonstrates that compressive loading is more osteogenic bringing about greater regional BMD. Design of exercise intervention programs to enhance bone quality should consider the strain mode effect. A compensation between material density and structure is shown which allows bone strengthening. Regional bone adaptation as revealed by multiple imaging modalities allows better understanding of changes at different levels of bone organization.

References

Akkus O, Polyakova-Akkus A, Adar F, Schaffler M B (2003) Aging of microstructural compartments in human compact bone. J Bone Miner Res 18(6):1012–1019

An KN, Hui FC, Morrey B F, Linscheid R L, Chao E Y (1981) Muscles across the elbow joint: a biomechanical analysis. J Biomech 14(10):659–669

An Y H, Barfield W R, Knets I (2000) Methods of evaluation for bone dimensions, densitites, contents, morphology, and structures. Mechanical testing of bone and the bone-implant interface. Y. H. An and R. A. Draughn, eds. CRC Press, Boca Raton, pp 103–118

Bachus KN, Bloebaum RD (1992) Projection effect errors in biomaterials and bone research. Cells Mater 2(4):347–355

Barth RW, Williams JL, Kaplan FS (1992) Osteon morphometry in females with femoral neck fractures. Clin Orthop 283:178–186

Bertram J E, Biewener A A (1988) Bone curvature: sacrificing strength for load predictability? J Theor Biol 131(1):75–92

Birkbeck D P, Failla J M, Hoshaw S J, Fyhrie D P, Schaffler M (1997) The interosseous membrane affects load distribution in the forearm. J Hand Surg [Am] 22(6):975–980

Bloebaum R D, Bachus K N, Boyce T M (1990) Backscattered electron imaging: the role in calcified tissue and implant analysis. J Biomater Appl 5(1):56–85

Bloebaum R D, Skedros J G, Vajda E G, Bachus K N, Constantz B R (1997) Determining mineral content variations in bone using backscattered electron imaging. Bone 20(5):485–490.

Boivin G Y, Chavassieux P M, Santora A C, Yates J, Meunier P J (2000) Alendronate increases bone strength by increasing the mean degree of mineralization of bone tissue in osteoporotic women. Bone 27(5):687–694.

Borah B, Ritman E L, Dufresne T E, Jorgensen S M, Liu S, Sacha J, Phipps R J and Turner R T (2005) The effect of risedronate on bone mineralization as measured by micro-computed tomography with synchrotron radiation: correlation to histomorphometric indices of turnover. Bone 37(1):1–9

Borah B, Dufresne T E, Ritman E L, Jorgensen S M, Liu S, Chmielewski P A, Phipps R J, Zhou X, Sibonga J D, Turner R T (2006) Long-term risedronate treatment normalizes mineralization and continues to preserve trabecular architecture: sequential triple biopsy studies with micro-computed tomography. Bone 39(2):342–345

Boyde A, Riggs C M (1990) The quantitative study of the orientation of collagen in compact bone slices. Bone 11(1):35–39

Bromage T G, Goldman H M, McFarlin S C, Warshaw J, Boyde A, Riggs C M (2003) Circularly polarized light standards for investigations of collagen fiber orientation in bone. Anat Rec B New Anat 274(1):157–168

Burr D B, Ruff C B, Thompson D D (1990) Patterns of skeletal histologic change through time: comparison of an archaic native American population with modern populations. Anat Rec 226(3):307–313

Burr D B, Forwood M R, Fyhrie D P, Martin R B, Schaffler M B, Turner C H (1997) Bone microdamage and skeletal fragility in osteoporotic and stress fractures. J Bone Miner Res 12(1):6–15

Burr D B, Turner C H, Naick P, Forwood M R, Ambrosius W, Hasan M S, Pidaparti R (1998) Does microdamage accumulation affect the mechanical properties of bone? J Biomech 31(4):337–345

Camacho N P, Carroll P, Raggio C L (2003) Fourier transform infrared imaging spectroscopy (FT-IRIS) of mineralization in bisphosphonate-treated oim/oim mice. Calcif Tissue Int 72(5):604–609

Carando S, Portigliatti Barbos M, Ascenzi A, Boyde A (1989) Orientation of collagen in human tibial and fibular shaft and possible correlation with mechanical properties. Bone 10(2):139–142

Carando S, Portigliatti-Barbos M, Ascenzi A, Riggs C M, Boyde A (1991) Macroscopic shape of, and lamellar distribution within, the upper limb shafts, allowing inferences about mechanical properties. Bone 12(4):265–269

Chadwick E K, Nicol A C (2000) Elbow and wrist joint contact forces during occupational pick and place activities. J Biomech 33(5):591–600

Chilibeck P D, Sale D G, Webber C E (1995) Exercise and bone mineral density. Sports Med 19(2):103–122

Currey J D (1984) Effects of differences in mineralization on the mechanical properties of bone. Philos Trans R Soc Lond B Biol Sci 304(1121):509–518

Dufresne T E, Chmielewski P A, Borah B (2003) A novel method for the measurement of degree of mineralization using bench-top microCT. J Bone Miner Res 18(Suppl 2): s319

Faibish D, Gomes A, Boivin G, Binderman I, Boskey A (2005) Infrared imaging of calcified tissue in bone biopsies from adults with osteomalacia. Bone 36(1):6–12

Felsenberg D, Boonen S (2005) The bone quality framework: determinants of bone strength and their interrelationships, and implications for osteoporosis management. Clin Ther 27(1):1–11

Follet H, Boivin G, Rumelhart C, Meunier P J (2004) The degree of mineralization is a determinant of bone strength: a study on human calcanei. Bone 34(5):783–789

Frost H M (1983) A determinant of bone architecture. The minimum effective strain. Clin Orthop(175):286–292

Frost H M (1987) Bone "Mass" and the "Mechanostat": a proposal. Anat Rec 219(1):1–9

Frost H M (1990) Skeletal structural adaptations to mechanical usage (SATMU): 1. Redefining Wolff's law: the bone modeling problem. Anat Rec 226(4):403–413

Gray H (1974) Gray's anatomy. Running Press, Philadelphia, pp 134–215

Hayes W C, Bouxsein M L (1997) Biomechanics of cortical and trabecular bone: implications for assessment of fracture risk. Basic orthopaedic biomechanics. V. C. Mow and W. C. Hayes, eds. Lippincott-Raven, New York, pp 69–111

Huang T H, Lin S C, Chang F L, Hsieh S S, Liu S H, Yang R S (2003) Effects of different exercise modes on mineralization, structure, and biomechanical properties of growing bone. J Appl Physiol 95(1):300–307

Ito M, Ejiri S, Jinnai H, Kono J, Ikeda S, Nishida A, Uesugi K, Yagi N, Tanaka M, Hayashi K (2003) Bone structure and mineralization demonstrated using synchrotron radiation computed tomography (SR-CT) in animal models: preliminary findings. J Bone Miner Metab 21(5):287–293

Jee W S, Frost H M (1992) Skeletal adaptations during growth. Triangle 31(2/3):77–88

Judex S, Gross T S, Zernicke R F (1997) Strain gradients correlate with sites of exercise-induced bone-forming surfaces in the adult skeleton. J Bone Miner Res 12(10):1737–1745

Karnezis I A (2005) Correlation between wrist loads and the distal radius volar tilt angle. Clin Biomech (Bristol, Avon) 20(3):270–276

Kaufmann R A, Kozin S H, Barnes A, Kalluri P (2002) Changes in strain distribution along the radius and ulna with loading and interosseous membrane section. J Hand Surg [Am] 27(1):93–97

Lai Y M, Qin L, Hung V W Y, Chan K M (2005) Regional differences in cortical bone mineral density differences in the weight-bearing long bone shaft: a pQCT study. Bone 36:465–471

Lanyon L E, Rubin C T (1984) Static vs dynamic loads as an influence on bone remodelling. J Biomech 17(12):897–905

Lanyon L E, Hampson W G, Goodship A E, Shah J S (1975) Bone deformation recorded in vivo from strain gauges attached to the human tibial shaft. Acta Orthop Scand 46(2):256–268

Lanyon L E, Goodship A E, Pye C J, MacFie J H (1982) Mechanically adaptive bone remodelling. J Biomech 15(3):141–154

Martin R B (2003) Fatigue microdamage as an essential element of bone mechanics and biology. Calcif Tissue Int 73(2):101–107

Martin R B, Boardman D L (1993) The effects of collagen fiber orientation, porosity, density, and mineralization on bovine cortical bone bending properties. J Biomech 26(9):1047–1054

Martin R B, Ishida J (1989) The relative effects of collagen fiber orientation, porosity, density, and mineralization on bone strength. J Biomech 22(5):419–426

Martin R B, Pickett J C, Zinaich S (1980) Studies of skeletal remodeling in aging men. Clin Orthop Relat Res(149):268–282

Martin R B, Lau S T, Mathews P V, Gibson V A, Stover S M (1996) Collagen fiber organization is related to mechanical properties and remodeling in equine bone. A comparison of two methods. J Biomech 29(12):1515–1521

Martin R B, Burr D B, Sharkey N A (1998) Skeletal tissue mechanics. Springer, Berlin Heidelberg New York, pp 127–180

Mason M W, Skedros J G, Bloebaum R D (1995) Evidence of strain-mode-related cortical adaptation in the diaphysis of the horse radius. Bone 17(3):229–237

Meunier P J, Boivin G (1997) Bone mineral density reflects bone mass but also the degree of mineralization of bone: therapeutic implications. Bone 21(5):373–377

Mori S, Burr D B (1993) Increased intracortical remodeling following fatigue damage. Bone 14(2):103–109

Morrey B F, Askew L J, Chao E Y (1981) A biomechanical study of normal functional elbow motion. J Bone Joint Surg Am 63(6):872–877

Muller A, Ruegsegger E, Ruegsegger P (1989) Peripheral QCT: a low-risk procedure to identify women predisposed to osteoporosis. Phys Med Biol 34(6):741–749

Neumann D A (2002) Elbow and forearm complex. Kinesiology of the musculoskeletal system: foundations for physical rehabilitation. D. A. Neumann, ed. Mosby, St. Louis, pp 133–171

O'Connor J A, Lanyon L E, MacFie H (1982) The influence of strain rate on adaptive bone remodelling. J Biomech 15(10):767–781

Panjabi M M, White A A (2001) Biomechanics in the musculoskeletal system. Churchill Livingston, New York, p 196

Paschalis E P, Glass E V, Donley D W, Eriksen E F (2005) Bone mineral and collagen quality in iliac crest biopsies of patients given teriparatide: new results from the fracture prevention trial. J Clin Endocrinol Metab 90(8):4644–4649

Pearson O M, Lieberman D E (2004) The aging of Wolff's "law": ontogeny and responses to mechanical loading in cortical bone. Am J Phys Anthropol Suppl 39:63–99

Peterman M M, Hamel A J, Cavanagh P R, Piazza S J, Sharkey N A (2001) In vitro modeling of human tibial strains during exercise in micro-gravity. J Biomech 34(5):693–698

Pfaeffle H J, Fischer K J, Manson T T, Tomaino M M, Woo S L, Herndon J H (2000) Role of the forearm interosseous ligament: Is it more than just longitudinal load transfer? J Hand Surg (Am) 25(4):683–688

Piziali R L, Hight T K, Nagel D A (1980) Geometric properties of human leg bones. J Biomech 13(10):881–885

Qin L, Au S K, Chan K M, Lau M C, Woo J, Dambacher M A, Leung P C (2000) Peripheral volumetric bone mineral density in pre- and postmenopausal Chinese women in Hong Kong. Calcif Tissue Int 67(1):29–36

Qin L, Hung L, Leung K, Guo X, Bumrerraj S, Katz L (2001) Staining intensity of individual osteons correlated with elastic properties and degrees of mineralization. J Bone Miner Metab 19(6):359–364

Qin L, Au S, Choy W, Leung P, Neff M, Lee K, Lau M, Woo J, Chan K (2002a) Regular Tai Chi Chuan exercise may retard bone loss in postmenopausal women: a case-control study. Arch Phys Med Rehabil 83(10):1355–1359

Qin L, Au S K, Leung P C, Lau M C, Woo J, Choy W Y, Hung W Y, Dambacher M A, Leung K S (2002b) Baseline BMD and bone loss at distal radius measured by pQCT in peri- and postmenopausal Hong Kong Chinese Women. Osteoporosis Int 13(12):962–970

Qin L, Bumrerraj S, Leung K, Katz L (2004) Correlation study of scanning acoustic microscope reflection coefficients and image brightness intensities of micrographed osteons. J Bone Miner Metab 22(2):86–89

Qiu S, Rao D S, Fyhrie D P, Palnitkar S, Parfitt A M (2005) The morphological association between microcracks and osteocyte lacunae in human cortical bone. Bone 37(1):10–15

Riggs C M, Lanyon L E, Boyde A (1993) Functional associations between collagen fibre orientation and locomotor strain direction in cortical bone of the equine radius. Anat Embryol (Berl) 187(3):231–238

Roschger P, Fratzl P, Eschberger J, Klaushofer K (1998) Validation of quantitative backscattered electron imaging for the measurement of mineral density distribution in human bone biopsies. Bone 23(4):319–326

Roschger P, Rinnerthaler S, Yates J, Rodan G A, Fratzl P, Klaushofer K (2001) Alendronate increases degree and uniformity of mineralization in cancellous bone and decreases the porosity in cortical bone of osteoporotic women. Bone 29(2):185–191

Rubin C T, Lanyon L E (1984) Regulation of bone formation by applied dynamic loads. J Bone Joint Surg Am 66(3):397–402

Rubin C T, Lanyon L E (1985) Regulation of bone mass by mechanical strain magnitude. Calcif Tissue Int 37(4):411–417

Schaffler M B, Burr D B (1988) Stiffness of compact bone: effects of porosity and density. J Biomech 21(1):13–16

Schoutens A, Laurent E, Poortmans J R (1989) Effects of inactivity and exercise on bone. Sports Med 7(2):71–81

Skedros J G (2001) Collagen fiber orientation: a characterisitcs of strain-mode-related regional adaptation in cortical bone. Bone 28: S110-S111

Skedros J G, Bloebaum R D, Bachus K N, Boyce T M (1993) The meaning of graylevels in backscattered electron images of bone. J Biomed Mater Res 27(1):47–56

Skedros J G, Bloebaum R D, Mason M W, Bramble D M (1994a) Analysis of a tension/compression skeletal system: possible strain-specific differences in the hierarchical organization of bone. Anat Rec 239(4):396–404

Skedros J G, Mason M W, Bloebaum R D (1994b) Differences in osteonal micromorphology between tensile and compressive cortices of a bending skeletal system: indications of potential strain-specific differences in bone microstructure. Anat Rec 239(4):405–413

Skedros J G, Mason M W, Nelson M C, Bloebaum R D (1996) Evidence of structural and material adaptation to specific strain features in cortical bone. Anat Rec 246(1):47–63

Skedros J G, Su S C, Bloebaum R D (1997) Biomechanical implications of mineral content and microstructural variations in cortical bone of horse, elk, and sheep calcanei. Anat Rec 249(3):297–316

Skedros J G, Dayton M R, Bachus K N (2001) Strain-mode specific loading of cortical bone reveals important role for collagen fiber orientation in energy absorption. Trans Orthop Res Soc 26: 519

Skedros J G, Hunt K J, Dayton M R, Bloebaum R D, Bachus K N (2003a) The influence of collagen fiber orientation on mechanical properties of cortical bone of an artiodactyl calcaneus: implications for broad applications in bone adaptation. Trans Orthop Res Soc 28: 411

Skedros J G, Hunt K J, Hughes P E, Winet H (2003b) Ontogenetic and regional morphologic variations in the turkey ulna diaphysis: implications for functional adaptation of cortical bone. Anat Rec A Discov Mol Cell Evol Biol 273(1):609–629

Vajda E G, Skedros J G, Bloebaum R D (1995) Consistency in calibrated backscattered electron images of calcified tissues and minerals analyzed in multiple imaging sessions. Scanning Microsc 9(3):741–753

Vajda E G, Humphrey S, Skedros J G, Bloebaum R D (1999) Influence of topography and specimen preparation on backscattered electron images of bone. Scanning 21(6):379–387

Wolff I, van Croonenborg J J, Kemper H C, Kostense P J, Twisk J W (1999) The effect of exercise training programs on bone mass: a meta-analysis of published controlled trials in pre- and postmenopausal women. Osteoporos Int 9(1):1–12

High-Fidelity Histologic Three-Dimensional Analysis of Bone and Cartilage

Russell Kerschmann

Microscience Group, Inc., 100 Tamal Plaza, Corte Madera, California, USA
e-mail: rkerschmann@microsciencegroup.com

Abstract

Optical-resolution three-dimensional (3D) imaging of adequate volumes of tissues and other materials has been an elusive goal since microscopy was popularised over a century ago. For much of that time, microanatomists and other life science researchers contented themselves with artists' recreations, based on manual examination of often hundreds of glass slide-mounted serial sections. The relatively recent appearance of "real" 3D imaging technologies has brought the quest for true volumetric microscopy a new level of discipline. Confocal microscopy, micro-CT/MRI, optical coherence tomography, and other approaches have been shown to generate real data from actual tissue samples; however, none of these methods are capable simultaneously producing histochemically accurate volumetric data at the micron level of resolution while addressing samples of tissue in the size range of hundreds of cubic millimeters. This is a sample size range that encompasses a class of commercially important materials including standard tissue biopsies, biopolymer scaffolds for tissue engineering, and many other important materials. Digital volumetric imaging (DVI) is a new approach to this old problem that addresses adequate volumes of material, preserves full histochemical data, and produces image data with sufficient detail to address important questions about the 3D arrangement of cells and other microanatomical structures.

Introduction

Micron-resolution three-dimensional (3D) visualization and analysis of relatively large volumes of tissue (hundreds of cubic millimeters per sample) at optical-level resolution is a problem that has challenged and frustrated researchers since histologic microscopy first appeared in the mid-nineteenth century. Despite some Herculean efforts involving the construction of massive physical models or drawings requiring hundreds of man-hours per sample, attempts to create accurate 3D replicas of tissue by serial reconstruction from glass slide-mounted sections have not produced practical results. Attesting to this situation, most 3D images of microscopic biostructure seen in the twentieth century biomedical literature are artist's renderings, indeed valuable for teaching but not sufficiently authentic for routine scientific investigation.

The reasons for this failure are multiple: the high labor content for each glass-slide section, coupled with the large number of sections required for high-fidelity reconstruction, drives costs out of reach for most researchers. Bringing all these sections back into alignment to produce a usable image is a difficult task to perform by hand. Furthermore, the distortion inevitably introduced during manual sectioning makes micron-level realignment of tissue structures nearly impossible. Even with the advent of computers the immense models or data sets produced by serial histologic reconstruction had been beyond what could be practically manipulated and analyzed.

More recently, computers have become more powerful and systems able to overcome some of these deficiencies have been developed. Confocal microscopy, microradiological methods, optical coherence tomography, and some other technologies can now produce real data in 3D space, and have come into routine use in research laboratories. The key to high-resolution 3D digital replication of microscopic structures is the elimination of the need for producing glass slide-mounted tissue sections. All the currently available 3D microscope technologies take this approach by performing optical sectioning, as in the case of confocal microscopy; or by avoiding optical imaging altogether, as in the case of micro-CT/MRI; however, despite their obvious success, these technologies have not yet attained the "holy grail" of 3D microscopy: full projection into 3D space of a full volume of tissue recapitulating all the histochemical and cytologic detail present in traditional histologic microscopy sections, e.g., a fully mineralized, fluorochrome-labeled metabolic bone sample.

Digital volumetric imaging (DVI; also called surface imaging microscopy, or SIM) is a new approach specifically developed to solve this problem. DVI produces 3D histologic images routinely and economically by eliminating the need to work from a large set of serial glass slide-mounted sections. Instead, tissues are first en bloc stained with low molecular weight fluorochrome compounds or labeled lectins or antibodies, and are embedded in an optically conditioned polymer that suppresses the transmission of light. The resulting block, which is black, is physically sectioned by automated microtomy. Serial sectioning on a diamond blade exposes faces on the block cut through the sample, and it is these faces, rather than the thin sections, that are then imaged on a modified digital epi-illumination fluorescence microscope (Fig. 1).

The high opacity of the embedding polymer combined with the strong signal output of the fluorochrome staining provides very high contrast images of the most superficial $0.25-4.0\,\mu m$ of the tissue embedded in the block. These are the component "virtual section" of the 3D reconstruction comprising the DVI image. The "thickness" of a virtual section is user-selectable by varying the concentration of the opacification agent added to the polymer, thereby controlling the depth into the block that excitation light can travel, and also limiting the depth into which tissue can be viewed. This approach means that unlike confocal microscopy, the high quality of the image generated (Fig. 2) does not decline as deeper images are added to the stack, because the intervening tissue is continuously removed in the microtomy process.

The system automatically collects and aligns thousands of these images per reconstruction, resulting in a high-resolution volume with near-perfect registration and no distortion (Fig. 3); thus, there is no theoretical limit to the thickness of a tissue
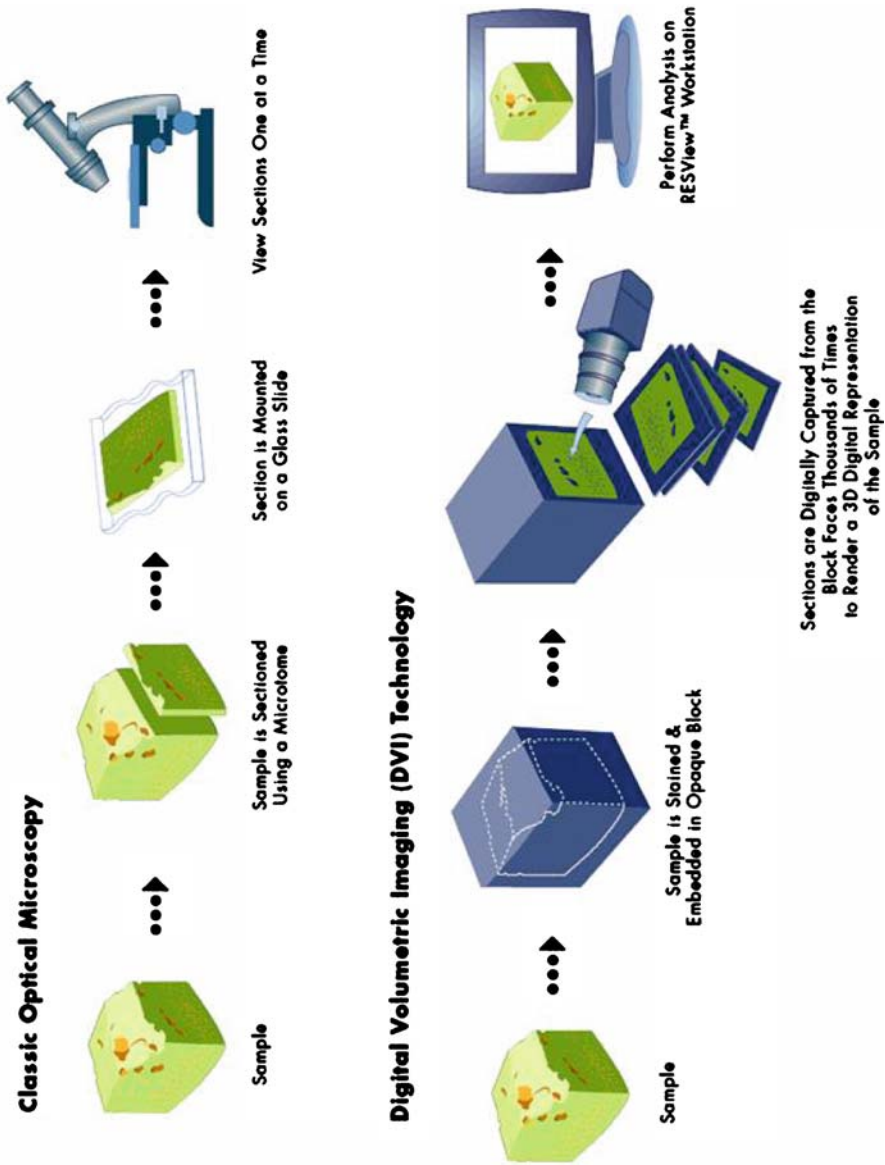
Figure 1. Principal of digital volumetric imaging (DVI). Classical optical microscopy (*top*) requires cutting a section from a block and mounting and staining it on a glass slide for viewing through a microscope. With DVI (*bottom*), the sample is first stained en bloc with fluorochrome dyes. Prior to cutting a section, the face of the block is imaged electronically, and the resulting data are transformed computationally into a high-quality image, or digital section, which is displayed on a visualization workstation in 2D or 3D
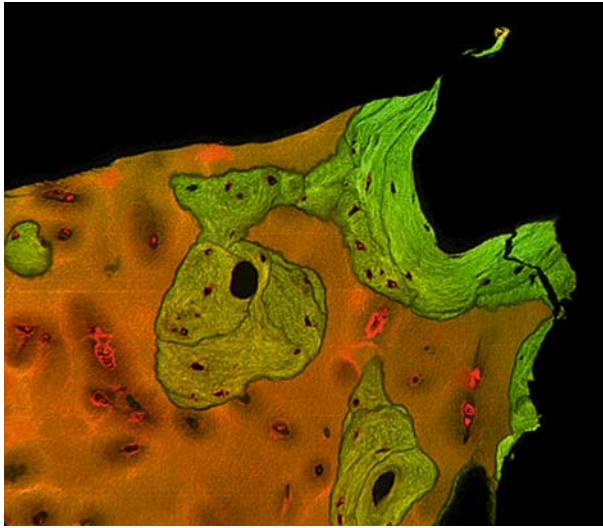
Figure 2. Basic DVI 2D image. Digital view of freshly cut DVI block face shows high-fidelity 2D image of interface between articular cartilage and bone (decalcified, bovine). (Stain: acridine orange/eosin; *green* bone, *orange* nuclei and perilacunar cartilage, *mixed* cartilage matrix)
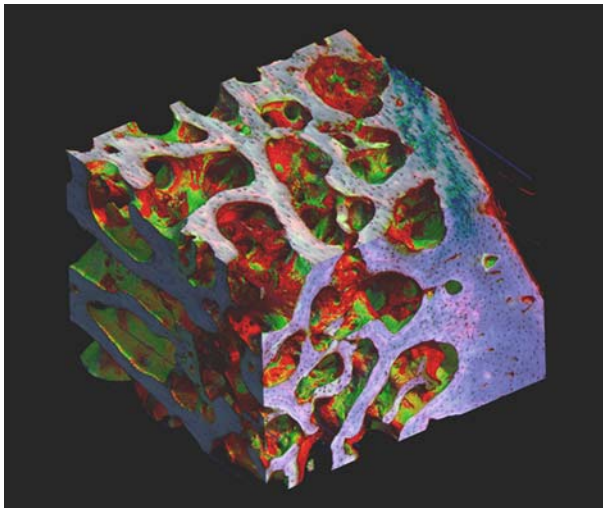
Figure 3. A DVI 3D reconstructed trabecular bone with fluorochrome label. Near-perfect registration of thousands of 2D images produces a high-fidelity 3D reconstruction of this fluorochrome-labeled undermineralized sample from rat tail vertebra. (Stain: modified Villanova; *blue* bone, *red* osteoid, *green* label)

sample that can be imaged, the practical limitations imposed only by the total *z*-axis excursion of the microtome or other mechanical factors.

The resulting multi-gigabyte data sets constitute the raw material for precision visualization and microanalysis. While the *x*- and *y*-axis resolutions of the DVI data are determined by the optics of the microscope, the *z*-axis resolution is independently determined by manipulating the chemistry of the stain and embedding material. In this way, x, y, and z resolutions can be brought into close concordance and isotropic data is generated, making possible precision 3D morphometrics. Isotropic data also means that high-resolution 2D images may be re-extracted from the data stack at any angle. To complete the compatibility with conventional histologic microscopy, the

DVI system includes a computational capacity to transform the raw dark-field image data into familiar bright-field histologic images, even including a digital analog of hematoxylin and eosin stain.

The system extends the capabilities of conventional volumetric techniques such as confocal microscopy and microtomography, to allow for the first time the integrated 2D and 3D analysis of important tissue structural relationships in the context of full histochemical expression. Cellular microanatomy can be seen in a larger anatomical context, and precision tissue metrics, accurate cell enumeration, and the 3D analysis of extended structures, such as bone trabeculae or blood vessels are made possible.

DVI is a new technology, with a developing base of supporting studies. The technology has been compared favorably to confocal microscopy in a study of embryos conducted at the California Institute of Technology Biological Imaging Center (Ewald et al. 2002), and is in use at the University of California San Diego for cartilage morphometrics (Jadin et al. 2005). The technology is also in use at the University of Washington, North Carolina State University, the University of Texas and other academic and industrial laboratories.

This article reviews three DVI applications for orthopedics research: 3D quantification of articular cartilage cell distribution, 3D analysis of fluorochrome labeling for metabolic bone studies, and computational simulation for bone analysis.

Quantification of Articular Cartilage Cell Distribution

For research into arthritis, developmental orthopedics, prosthetic joint replacement, and other applications, precise quantification of chondrocyte distribution in articular cartilage is a useful option. The distribution of resident cells in this tissue is complex and investigations to date have been carried out using methods that give only a limited view of the full 3D properties of cartilage and the adjacent bone.

It is known that both chondrocyte density and pattern of distribution vary with depth into articular cartilage, particularly in mature cartilage. Hunziker (1992) defined the superficial zone as the first 10% of depth from the surface, the middle zone as 10–40%, and the deep zone as 40–100%, and has further described how each of these layers displays their own anatomical and physiologic characteristics. Chondrocytes near the surface tend to be present in higher densities, and arranged in chondron clusters aligned with the surface, whereas cells deeper in the tissue are less dense and formed into vertical columns (Schumacher et al. 2002). Probably these architectures have something to do with maintenance of the matrix domain surrounding each chondron, but detailed investigations of this phenomenon have been inhibited by the lack of a high-fidelity 3D microscope that fully reveals the histochemical features of the tissue.

The Department of Bioengineering at the University of California, San Diego, is one of the first laboratories to apply DVI routinely to the problems of quantitative tissue analysis in cartilage by producing high-resolution data on the entire thickness of bovine articular cartilage samples (Jadin et al. 2005). Once this data is obtained, arbitrary subvolumes from anywhere in the cartilage can be delimited via 3D analysis

software, the matrix removed computationally, and precision cell counts performed (Jadin et al. 2005). This is more precise and informative than older bulk analysis techniques, such as the quantification of DNA content by layer (Kim et al. 1988).

Additionally, the 3D arrangement of the chondrocytes is readily apparent in the data, and can also be quantitated through nearest-neighbor analysis. Unique proximity maps can be generated using this data, showing the distance to the nearest nucleus from any point in the cartilage (Fig. 4). This can be an important tool for under-
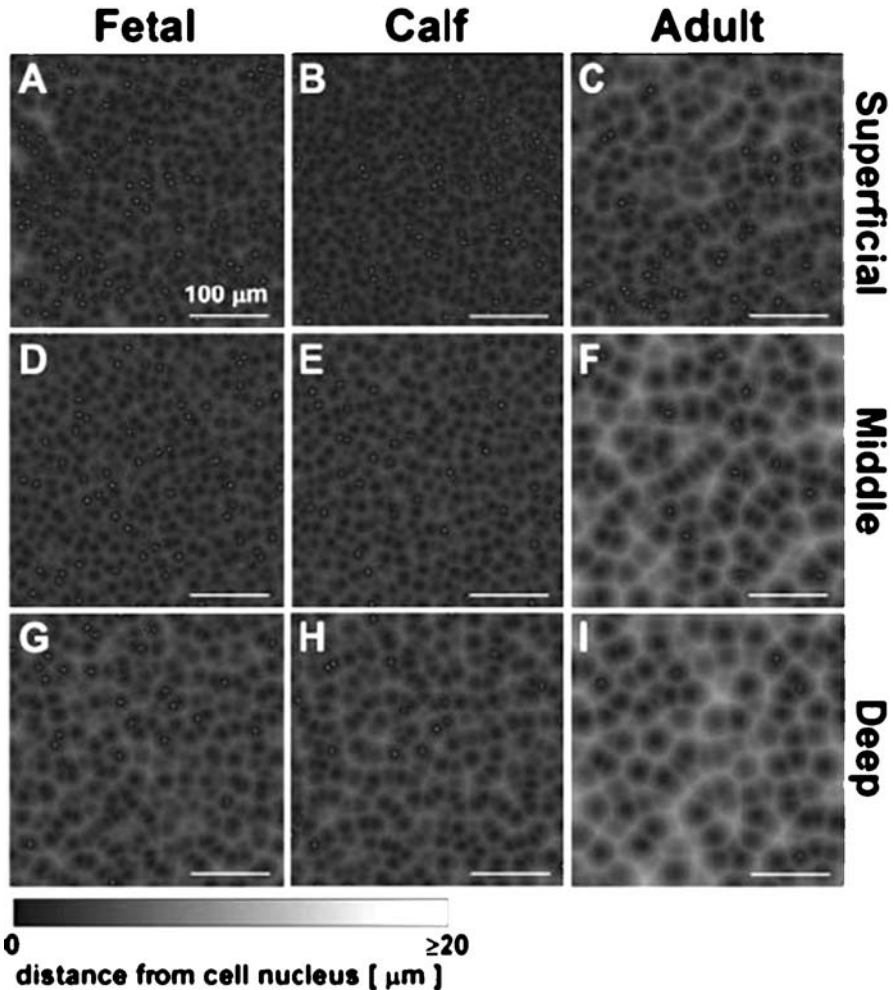
Figure 4. Proximity maps illustrate distance from each location to the nearest cell nucleus. The DVI image data were analyzed by distance transforms of superficial (**a–c**), middle (**d–f**), and deep (**g–i**) regions of articular cartilage corresponding to fetal, calf, and adult stages of development. Gray-scale intensity indicates 3D distance as shown (0–20 μm). Cell nuclei centroids within 0.5 μm of the cross-section plane are indicated as *white dots*. (From Jadin et al. 2005)

standing the geometry of the pericellular matrix domain serviced by each chondrocyte (Hunziker 1992), and can facilitate 3D watershed analysis and other theoretical physiology approaches to cartilage metabolism, substrate turnover, and ultimately to the development of cartilage disease.

Three-Dimensional Analysis of Metabolic Bone Disease

Another area of study wherein DVI can carry conventional 2D techniques into 3D space is metabolic bone analysis. The technical basis of this work resides in in vivo labeling of human or animal bone, with subsequent harvesting of trabecular bone samples and investigation under fluorescent microscopy. By carefully timing the dosing of the fluorochrome labels, an accurate measure of bone growth can be related to microscopic features. Non-toxic fluorochromes used for bone labeling include calcein, oxytetracycline, and xylenol orange (Lee et al. 2003).

Measuring bone turnover via in vivo fluorochrome labeling is an excellent example of a technique requiring histochemical analysis, but historically there has been no 3D counterpart to conventional 2D fluorescent microscopy; thus, the higher-level distribution of new bone formation in animal and man has not been well investigated. The DVI provides such highly detailed maps of the distribution of any fluorescent label used in conventional 2D metabolic bone preparations.

Because of its high surface to volume ratio relative to cortical bone, trabecular bone shows changes in turnover earlier and is more amenable to micromorphometric analysis for measurement of metabolic bone disturbances. But trabecular bone has a highly 3D tissue and requires volumetric imaging for adequate analysis. For example, it is known that in primary hyperparathyroidism the average trabecular thickness is reduced, which can ultimately lead to perforation of trabecular plates by deep resorption lacunae (Christiansen et al. 2001). This process can be estimated on conventional 2D bone sections, but the complex geometry coupled with the limited view imposes serious constraints on the accuracy of the results. Full 3D data provides a more authentic index of this change, and may require a smaller sample to do so.

Activation frequency is an index of the initiation of new remodeling sites on the trabecular bone surface. A 2D analysis does not allow the researcher to directly differentiate an early, small patch of new bone formation from a tangential cut through a larger, older focus. 3D analysis with preservation of histochemical label is the only method that makes possible distinct visualization and fully accurate quantification of this parameter (Fig. 5). By maintaining histochemical data into an actual 3D volume, the location of new remodeling sites can more accurately be related to the precise spatial anatomy of dissolution and reformation of trabecular structure in diseases such as osteoporosis. This may obviate the need for applying approximating mathematical extrapolations from 2D methods, such as node-strut analysis (Garrahan et al. 1986; Abe et al. 1999).
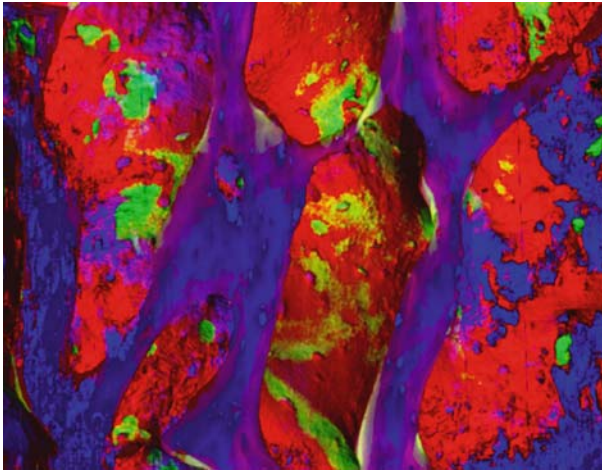
Figure 5. Detail of sample from Fig. 3 shows fluorochrome-labeled initiation sites on surfaces of trabecular bone (*green*). These areas can be computationally extracted and measured to give a quantitative analysis of bone remodeling, fully integrated with the histologic context. (Stain: modified Villanova; *blue/purple* bone, *red* osteoid, *green* label)

More Accurate Computational Simulation of Bone Dynamics

High-Level Computerized Modeling of Bone Growth Adaptation, response to disease states, reaction to prosthetic implants, and other processes, such as fracture healing, have become an important tool for some bone researchers. With this approach, methods such as finite element analysis can be applied to study healing of trabecular fractures (Shefelbine et al. 2005), remodeling due to metabolic states (Muller 2005), and other interesting processes can be studied in silico without resorting to human or animal models; however, the accuracy of these digital models depends to some extent on the raw spatial information upon which they are built. To date, the best 3D data that can be supplied to such software comes from microradiology systems; but this approach does not provide histochemical data such as in vivo fluorochrome labeling of growth centers. Also, the lack of cellular-level resolution in micro-CT systems, combined with the lack of histochemical labeling of individual cells is a significant liability when trying to understand, for example, the role of osteoclasts and other cell types in the genesis of menopause-related bone loss (McNamara et al. 2005).

In another example, a uniform stress hypothesis of bone remodeling states that bone resorption and production will tend to produce structures that equilibrate compressive loads throughout the trabecular structure (Tsubota et al. 2002). This theoretical work is based on micro-CT data employing voxel finite element analysis, but the final proof will require 3D data that incorporates remodeling information in the form of metabolic labels, and only histologic 3D imaging has that capacity.

There is over a century of accumulated knowledge based on standard, chemically stained 2D histomicroscopy waiting to be expanded and reinterpreted based on rou-

tinely available 3D histologic images. The DVI provides the most accurate models that combine 3D spatial data, and is significantly higher in resolution (approximating 0.25 μm) than that available by microradiology. This, combined with color histochemical labeling of cells, growth centers, blood vessels, and other tissue elements familiar to those using standard microscopy, provides a powerful tool for investigation. This allows for a more integrated analysis of total bone anatomy and physiology than was previously possible, leading to breakthroughs in understanding of bone anatomy and physiology.

References

Abe T, Sato K, Miyakoshi N, Kudo T, Tamura Y, Tsuchida T, Kasukawa Y (1999) Trabecular remodeling processes in the ovariectomized rat: modified node-strut analysis. Bone 24:591–596

Christiansen P (2001) The skeleton in primary hyperparathyroidism: a review focusing on bone remodeling, structure, mass and fracture. APMIS (Suppl) 102:1–52

Ewald AJ, McBride H, Reddington M, Fraser SE, Kerschmann R (2002) Surface imaging microscopy, an automated method for visualizing whole embryo samples in three dimensions at high resolution. Dev Dyn 225:369–375

Garrahan NJ, Mellish RW, Compston JE (1986) A new method for the two-dimensional analysis of bone structure in human iliac crest biopsies. J Microsc 142:341–349

Hunziker EB (1992) Articular cartilage structure in humans and experimental animals. In: Kuettner KE, Schleyerbach R, Peyron JG, Hascall VC (eds) Articular cartilage and osteoarthritis. Raven Press, New York, pp 183–199

Jadin KD, Wong BJ, Bae WC, Li KW, Williamson AK, Shumacher BL, Price JH, Sah RL (2005) Depth-varying density and organization of chondrocytes in immature and mature bovine articular cartilage assessed by 3D imaging and analysis. J Histochem Cytochem 53:1–11

Jadin KD, Wong BL, Won CB, Li KW, Williamson AK, Schumacher BL, Price JH, Sah RL (2005) Depth-varying density and organization of chondrocytes in immature and mature bovine articular cartilage assessed by 3D imaging and analysis. J Histochem Cytochem 53:1–11

Kim YJ, Sah RL, Doong JY, Grodzinsky AJ (1988) Fluorometric assay of DNA in cartilage explants using Hoechst 33258. Anal Biochem 174:168–176

Lee TC, Mohsin S, Taylor D, Parkesh R, Gunnlaugsson T, O'Brien FJ, Giehl M, Gowin W (2003) Detecting microdamage in bone. J Anat 203:161–172

McNamara LM, Prendergast PJ (2005) Perforation of cancellous bone trabeculae by damage-stimulated remodeling at resorption pits: a computational analysis. Eur J Morphol 42:99–109

Muller R (2005) Long-term prediction of three-dimensional bone architecture in simulations of pre-, peri- and post-menopausal microstructural bone remodeling. Osteoporos Int 2:S25-S35

Schumacher BL, Su J-L, Lindley KM, Kuettner KE, Cole AA (2002) Horizontally oriented clusters of multiple chondrons in the superficial zone of ankle, but not knee articular cartilage. Anat Rec 266:241–248

Shefelbine SJ, Augat P, Claes L, Simon U (2005) Trabecular bone fracture healing simulation with finite element analysis and fuzzy logic. J Biomech 38:2440–2450

Application of Laser Scanning Confocal Microscopy in Musculoskeletal Research

Kwong-Man Lee (✉) [1] and Hiu-Yan Yeung[2]

[1] Lee Hysan Clinical Research Laboratories, The Chinese University of Hong Kong,
Hong Kong, China
e-mail: simonlee@ort.cuhk.edu.hk
[2] Department of Orthopaedics and Traumatology, The Chinese University of Hong Kong,
Hong Kong, China

Abstract

Laser scanning confocal microscopy (LSCM) produces three-dimensional (3D) images of thick objects. The recent advances in LSCM and the power of computer for image processing and analysis provides a very useful tool for orthopaedic research to further look at the details of cell biology of different skeletal cells such as osteocytes and chondrocytes. The application of LSCM is also extended to the study of osteoclasts and osteoblasts. The present chapter describes LSCM applications in cartilage cell biology and study of fluid flow in cortical bone as well as other structures.

Introduction

The main advantage of laser scanning confocal microscopy (LSCM) is its ability to produce three-dimensional (3D) images of thick objects. This is possible because of its so-called optical sectioning property, which allows sections to be imaged with minimal blur from other parts of the sample. At present its major application areas are in biology and medicine, where it is widely used in a fluorescence mode.

After the development of the principle of confocal microscopy in 1953 by Marvin Minsky (1988), the first commercial instrument was launched in 1982. The technology became widely known to biological researchers after wide publicity in the late 1980s.

In a laser scanning confocal microscope, a laser beam passes a light source aperture and then is focused by an objective lens into a focal volume within a fluorescent specimen. A mixture of emitted fluorescent light as well as reflected laser light from the illuminated spot is then recollected by the objective lens. Then the recollected lights passes a beam splitter separating both kinds of light into the laser light, which is reflected away from the detector, and the fluorescent light which is passed through the splitter to the detection apparatus. After passing a pinhole, the fluorescent light is detected by a photo-detector transferring the signal to a computer imaging system.
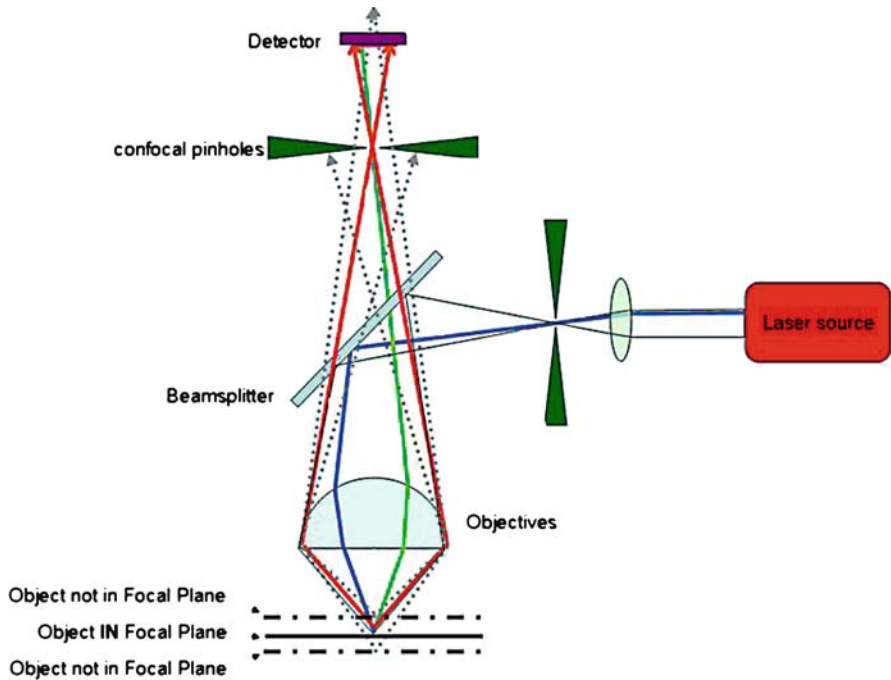
Figure 1. The principle of the laser scanning confocal microscopy

As seen in Fig. 1, the detector aperture obstructs the "out-of-focus" fluorescent light. Light rays from below the focal plane come into focus before reaching the detector pinhole, and then they expand out so that most of the rays are physically blocked from reaching the detector by the pinhole. In the same way, light from above the focal plane is focused behind the detector pinhole, so that most of this light also hits the edges of the pinhole and is not detected; however, all the light from the focal plane (*solid red lines*) is focused at the pinhole and passed to the detector. In turn, a sharper image is obtained when compared with conventional light microscopy because all the information that is not in the focal plane is blocked. The detected light originating from an illuminated volume element within the specimen represents one pixel in the final image. As the laser scans over the plane of interest a whole image is obtained pixel by pixel and line by line, while the brightness of a final image pixel corresponds to the relative intensity of detected fluorescent light. The beam is scanned across the sample in the horizontal plane using one or more oscillating mirrors. This scanning method usually has a low reaction latency and the scan speed can be varied as slower scans provide a better signal-to-noise ratio resulting in better contrast and higher resolution. Information can be collected from different focal planes by raising or lowering the microscope stage. The computer can generate a 3D picture of a specimen by assembling a stack of these 2D images from successive focal planes.

Since Boyde et al. (1990) first applied laser confocal scanning microscopy (LCSM) to explore the microstructure of bone, LCSM has become one of the major tools used to study different cell biology related to the skeletal system and the microstructure of bone and cartilage. The examples given herein are various applications of LSCM in the musculoskeletal system.

Application of LSCM in Cartilage Cell Biology

Calcium Metabolism in Growth Plate Chondrocytes

Endochondral ossification involves a series of progressive stages of cartilage development ultimately leading to mineralization of the extracellular matrix. Although it is generally acknowledged that growth plate chondrocytes are vital to the mineralization process, some investigators suggest that these cells are involved primarily in producing an extracellular matrix capable of inducing mineral deposition. Nevertheless, there is a growing awareness that the cells may be directly involved in the acquisition and processing of the calcium ion and inorganic phosphate before the appearance of the initial crystalline mineral in the extracellular domain.

Previous studies established that matrix vesicles are primary initiators of extracellular mineral deposition in endochondral calcification. Recently, there have been studies showing that cellular metabolism of calcium (Ca^{2+}) and inorganic phosphate (Pi), and cellular interaction with the matrix, are involved in the formation of calcifiable matrix vesicles. Chondrocytes in growth plate cartilage are envisioned to induce the formation of calcifiable matrix vesicles. Chondrocyte cell membrane processes from which matrix vesicles arise have been found to be tightly linked to the cartilage-specific extracellular matrix collagens and proteoglycans. The interaction between the extracellular matrix and chondrocytes appears to facilitate calcium loading of chondrocytes, formation of Ca^{2+} and Pi-primed matrix vesicles, and rapid induction of mineralization in growth plate cartilage (Fernandez et al. 1988; Genge et al. 1992).

One of the fundamental questions pertaining to the induction of mineral deposition in tissues concerns whether cellular metabolism of Ca^{2+} and Pi is directly involved in this process. There is now considerable morphological and biochemical evidence in endochondral calcification that growth plate chondrocytes acquire substantial amounts of Ca^{2+} and Pi before the onset of extracellular mineralization (Brighton and Hunt 1976; Gunter et al. 1990; Iannotti and Brighton 1989; Shapiro and Lee 1975). Growth plate chondrocytes produce matrix vesicles that contain large amounts of Ca^{2+} and Pi (Arsenault et al. 1988; Wuthier 1977) and mediate the induction of extracellular mineralization (Ali 1976; Anderson 1969; Bonucci 1970). Although the mechanism of matrix vesicle mineralization is not fully understood, there is strong evidence that matrix vesicles derive from the plasma membrane of growth plate chondrocytes by blabbing of vesicles from cell processes (Bonucci 1970; Hale and Wuthier 1987).

The combination of collagen-binding and Ca^{2+} ion channel properties make annexin V and annexin VI, a less abundant matrix vesicle protein with even tighter collagen-binding properties (Wu et al. 1991), promising candidates for stretch-activated Ca^{2+} ion channels (Wuthier et al. 1992). Such properties would enable influx of Ca^{2+} into the cells to be coordinated with mechanical stress to the tissue (Watson 1991). The binding of the annexins to collagen and their Ca^{2+}-dependent binding to alkaline phosphatase also help to explain the formation of matrix vesicles (Hale and Wuthier 1987), which are enriched in APL (Wuthier 1975) and, in Ca^{2+} and Pi (Arsenault et al. 1988; Wuthier 1977); thus, the metabolism of Ca^{2+} and Pi, by growth plate chondrocytes, now can be seen to be intimately involved in matrix vesicle formation, and are clearly integral features of endochondral ossification.

The present study was carried out to establish a model for in situ monitoring of intracellular and extracellular Ca^{2+} from each zone of the mammalian growth plate using LSCM.

Protocol of Using LSCM to Detect the Ca^{2+} Ion Changes

Longitudinal Costal Growth Plate Slices

Three pigs between 4 and 5 weeks of age were used. After the animal was euthanized by over-dosage of 2.5% pentobarbital, the rib cage was aseptically dissected and cleaned until free from soft tissue. The growth plate cartilage was taken out at the osteochondral junctions of all ribs. The growth plate block was then placed in a DMEM (Sigma, St. Louis, Mo.). Approximately $300\,\mu m$-thick longitudinal sections of growth plate were then prepared with vibrating microtone (Campdem Instruments, UK).

Intracellular Ca^{2+} Level Determination by LSCM

Determination of intracellular Ca^{2+} level by LSCM was done by labelling the Ca^{2+} with Fluo-3, a Ca^{2+} fluorescent indicator, used to monitor changes in the intracellular Ca^{2+} level. Growth plate sections were placed in a culture disk of 3 cm diameter and loaded with fluo-3/AM ($6-8\,\mu g/ml$) at room temperature for 2 h in Na^+-N-2-hydroxyethylpiperazine-N'-2-ethanesulfonic acid (HEPES) buffer (pH 7.2).

After washing, one section was mounted on the glass bottom plate of a tailor-made stainless-steel holder with 0.5 ml Na+-HEPES buffer for further studies. Resting, proliferative or hypertrophic zones in the growth plate section were selected under the transmitted light microscope for confocal microscopy. Change in fluorescence was measured with confocal imaging system at room temperature. At various time intervals, x-y images were acquired with 0.2 mm pixel size on a Multiprobe 2001 confocal laser scanning system (Molecular Dynamics) which is fitted with an Argon laser (8 mW) and a Nikon diaphot inverted microscope. For the fluorescence determination, an excitation filter with 488 nm wavelength and a long pass emission filter of 510 nm were used. Cells were scanned using a $60\times$ oil objective (1.4 NA, Nikon). The voltage for the photomultiplier tube (PMT) was set at $550-750\,mV$ and the diameter of the pinhole before the PMT was 50 mm. Images were processed and the averaged fluorescent intensity in the subcellular compartment was calculated by an

image analysis software (Imagespace 3.03, Molecular Dynamics). For the pseudo-colour images, black-blue represents a low fluorescence while orange-red illustrates a high degree of fluorescence.

Variations of Calcium Levels in Subcellular Regions

The intracellular Ca^{2+} distribution of growth plate chondrocytes among different subcellular regions varies according to the different maturational stages. In resting chondrocytes, the free calcium is concentrated in the nuclear regions with relatively low level observed in the cytoplasm (Fig. 2a). For the proliferative chondrocytes adjacent to the resting zone, the intracellular Ca^{2+} distribution pattern is similar to the resting chondrocytes, although the shape of these cells has becomes more spindle (Fig. 2b); however, the Ca^{2+} concentration in proliferative chondrocytes from the maturation zone (adjacent to hypertrophic zone) was found to be more evenly distributed within the whole cell (Fig. 2b). For the hypertrophic chondrocytes, the Ca^{2+} seems to distribute in a manner similar to that of the adjacent proliferative zone (Fig. 2c).

Evidence of Cellular Exfoliation of Calcium-Rich Matrix Vesicles

From the investigation of Ca^{2+} in extracellular matrix, we have also found that the Ca^{2+} distribution patterns changed during chondrocyte differentiation. In the resting zone, no Ca^{2+} could be seen in the pericellular matrix and other cartilage matrix from the confocal image (Fig. 2d). In the proliferative zone, islands of Ca^{2+} were found in the horizontal edges of proliferative chondrocytes beside the chondrocyte columns (Fig. 2e). In the hypertrophic zone, arcs of Ca^{2+} surrounding the hypertrophic chondrocyte by a distance were illustrated (Fig. 2f). The Ca^{2+} arcs from one hypertrophic chondrocyte was interrupted by the adjacent Ca^{2+} arcs.

Stability of Intracellular Free Calcium

From serial confocal scanning, the stability of intracellular free calcium of chondrocytes in various maturation zones was monitored. Although there were variations among individual cells, the Ca^{2+} level in most of the resting chondrocytes increased during multiple UV confocal scanning, whereas small amounts of cells show no change (Fig. 3a). In the proliferative zone, column-specific responses were observed. The proliferative chondrocytes in the same cell column exhibited similar intracellular Ca^{2+} stability. The majority of cell columns showed declining response in multiple scanning, whereas increased Ca^{2+} was observed in some other cell columns (Fig. 3b). In hypertrophic chondrocytes, the intracellular free calcium level was unstable and unsystematic. Two adjacent cells always demonstrated different response during the testing period of 400 s (Fig. 3c).

According to the observation of the LSCM data on the growth plate chondrocytes, there is evidence of a general trend for intracellular Ca^{2+} to concentrate in the nuclear region among the resting chondrocytes. In the proliferative and hypertrophic chondrocytes, the intracellular calcium concentration appears to distribute
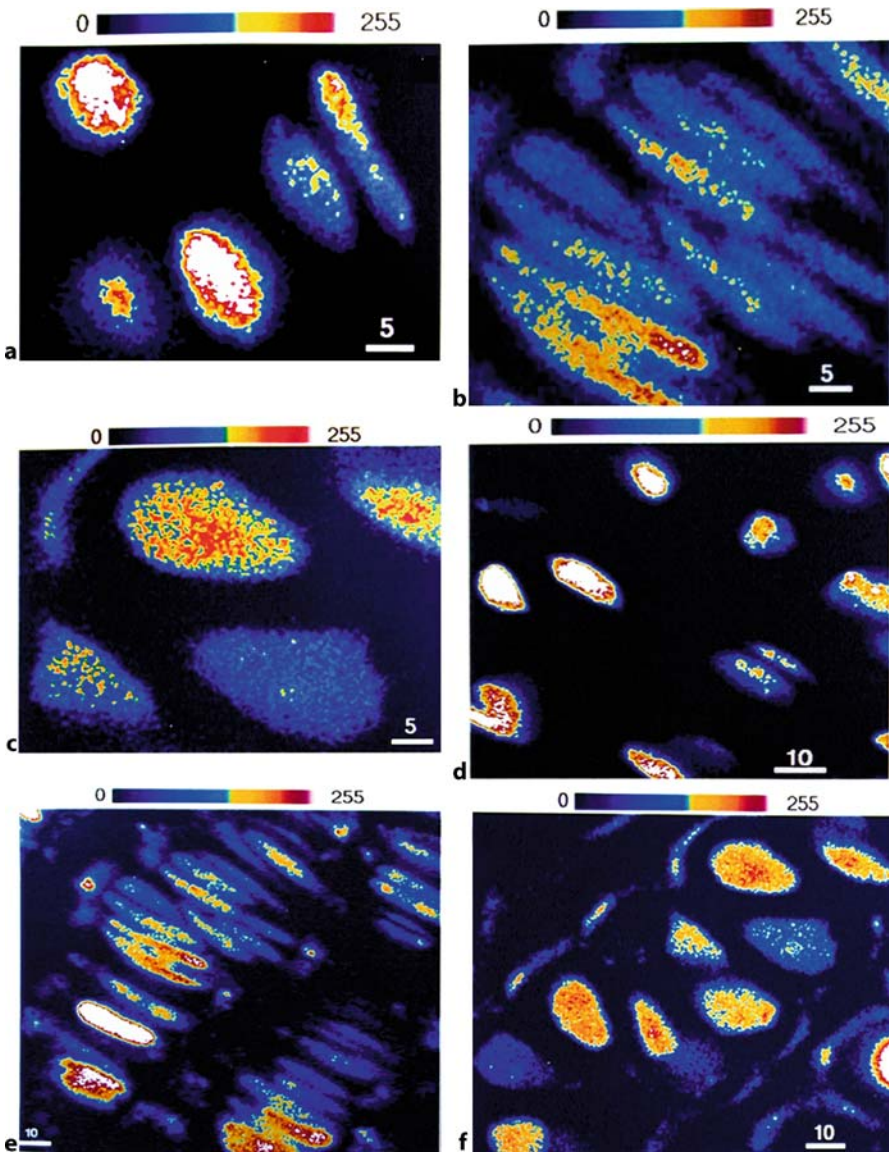
Figure 2. The calcium ion distribution in different region of chondrocytes in growth plate. **a** Intracellular Ca^{2+} distribution of resting chondrocytes. **b** Intracellular Ca^{2+} distribution of proliferative chondrocytes. **c** Intracellular Ca^{2+} distribution of hypertrophic chondrocytes. **d** Extracellular matrix Ca^{2+} distribution of resting zone. **e** Extracellular matrix Ca^{2+} distribution of proliferative zone. **f** Extracellular matrix Ca^{2+} distribution of hypertrophic zone. The Ca^{2+} were stained with Fluo-3 fluorescence dye. The unit of the bar is in microns
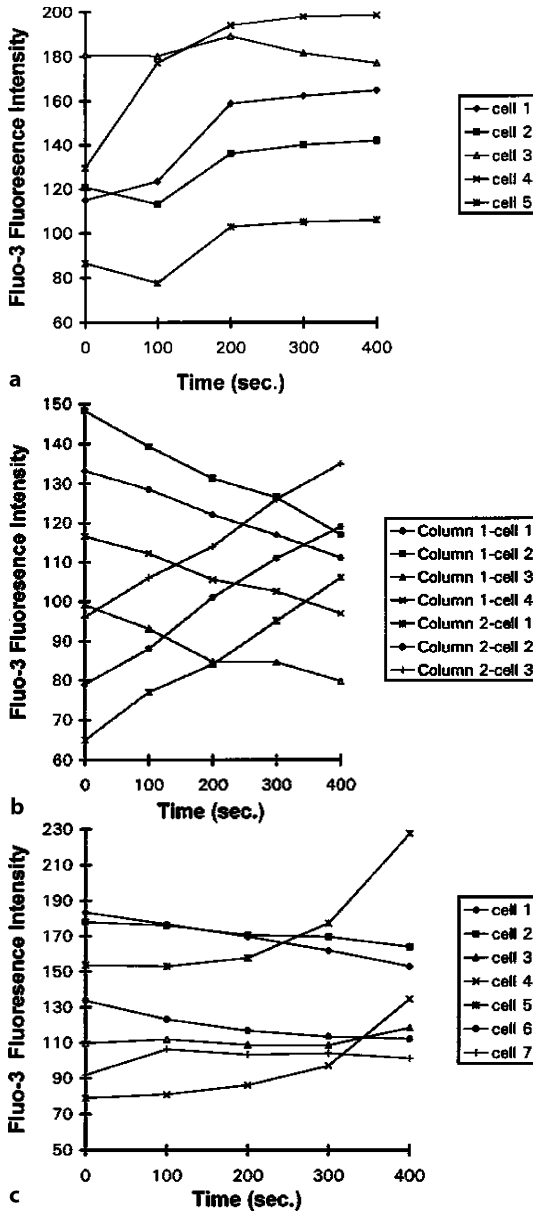
Figure 3. a Stability of intracellular free calcium in resting chondrocytes. **b** Stability of intracellular free calcium in proliferative chondrocytes. **c** Stability of intracellular free calcium in hypertrophic chondrocytes

in a different pattern. The cytoplasmic Ca^{2+} increased to a similar level to that of the nuclear region. This indicates that in the proliferative chondrocytes and hypertrophic chondrocytes of maturation zone, the Ca^{2+} are mainly trapped inside the Golgi apparatus and/or endoplasmic reticulum for secretion through matrix vesi-

cles. This finding was also supported by evidence that Ca^{2+} arcs and islands were detected in the matrix surrounding the chondrocytes of hypertrophic and proliferative zones, respectively. Similar results on the avian growth plate has been reported recently (Wuthier 1993).

The intracellular Ca^{2+} is unstable in various stages of chondrocyte development especially in the hypertrophic zone. The Ca^{2+} level in resting chondrocytes increased in multiple UV confocal scanning. It may indicate that Ca^{2+} releasing mechanism from the cellular calcium pool in resting chondrocytes is heat-sensitive since UV scanning can generate heat. For the proliferative chondrocytes, we are the first group to report cell column-specific stability of intracellular free calcium. This can be explained by the fact that one column of proliferative chondrocytes originates from a single chondrocyte. That is why they show similar Ca^{2+} activity. The large Ca^{2+}-level fluctuation in hypertrophic chondrocytes may be due to the extremely active calcium metabolism during matrix mineralization. This model can be used for further in situ study for the effects of modulators on calcium metabolism in mammalian growth plate.

In addition to the study of chondrocyte biology with LSCM, the authors also developed another model to study the 3D fine structure of Haversian canal in bone and the fluid flow.

Study of Fluid Flow in Cortical Bone by LSCM

Bone is a highly structuralized and dynamic organ that functions in load bearing and adapting to the changing biomechanical demands of the body. Mature cortical bone is the major load-bearing tissue which is organized into osteons. Osteon in cortical bone is similar to a cylindrical shape with concentric lamellae around the vasculature-containing Haversian canal. The tiny lacunae-canaliculi around the bone cells builds a hierarchical network of flow channel with longitudinal Haversian and transverse Volkmann's canals (Atkinson and Hallsworth 1982; Cooper et al. 1966; Kaplan et al. 1994; Qin et al. 1999; Seliger 1970). This hierarchical network is essential for osteogenesis, maintenance of bone vitality, bone growth, and fracture repair (Rhinelander 1968; Eitel et al. 1981; Bronk et al. 1993; Kaplan et al. 1994; Judex et al. 1997). The flows are very much related to bone electromechanics, namely the streaming potential phenomena. In cortical bone, the streaming potential induced by fluid flow is considered as one of the most important mechanisms to moderate the function of osteoblasts and osteocytes in bone growth, remodelling, and fracture repair.

Conventionally, thin decalcified bone sections (7 μm) were used to study cortical fluid pattern labeled with trace markers (Knothe Tate et al. 1998). The investigators established a histological method for research based on thick undecalcified sections (60 μm); however, there were difficulties in focusing the regions of interest for objective evaluation (Mak et al. 2000; Qin et al. 1999). The present study indicates that using LSCM will be advantageous to study fluid flow in cortical bone.

Protocol of Using LSCM to Track the Fluid Flow

Animal and Calcein Injection

In this protocol the author used goat as the model of investigation. The animals were anesthetized with intravenous pentobarbital (4 mg/kg). Both tibiae were surgically exposed and the nutrient arteries to the tibiae were isolated and cannulated. Catheters were connected to a hydraulic pump (LKB Bromma 213, Microperpex) which delivered a controlled volume of fluid to each tibia. At the start of the experiment, plasma was infused at a calculated physiological rate of $2\,ml/100\,g\,min^{-1}$. Calcein green solution (0.7% w/v; Sigma, St. Louis, Mo.) was injected into the catheter and then flushed with a volume of plasma equal to its capacity. After calcein green was fully injected into the nutrient artery, the blood circulation was immediately stopped by clamping the femoral vein of the experimental hindlimb. During this time plasma infusion was maintained. The goat was immediately killed with an intravenous overdose of thiopentone. One tibia without calcein green injection was used to validate the use of calcein green as a tracer for cortical bone fluid flow (Mak et al. 2000; Nesbitt and Horton 1997; Qin et al. 1999).

Sample Preparation for LSCM

After cleaning the tibia, two blocks of bone, each 6 mm in length, were transversely sectioned from the entrance of the tibial nutrient artery at the distal tibia. The bony blocks were washed with distilled water before dehydration through graded alcohol and acetone. After dehydration, the blocks were then embedded in methyl methacrylate (MMA) without decalcification and cured at $30\,^\circ C$ for 3 days until the blocks were hardened. The blocks were cut transversely and longitudinally at $200\,\mu m$ in thickness using a saw microtome (Leitz 600, Leica, Germany) and the surface was polished for LSCM.

The cortical fluid flow was evaluated under LSCM (LSM 510 META, Carl Zeiss, Oberkochen, Germany). An objective magnification of 20 times and florescence mode at excitation of wavelength 488 nm were used for demonstrating green dye. Stock sequential scanning at $0.49\,\mu m$ resolution (layer thickness) for 150 planes was performed and reconstructed for visualizing 3D cortical fluid flow patterns. Bright-field image was also used to compare the spatial fluid pattern with respect to cortical microscopic structure.

Three-Dimensional Images of the Fluid Flow in Cortical Bone

Both 2D and 3D confocal images from transverse or longitudinal sections showed calcein distributed only in some of the Haversian or Volkmann's capillaries or network of canaliculi and lacunae. More intensely labeled osteocyte lacunae were associated with those where osteocyte underwent cell death (empty lacunae; Figs. 4, 5).
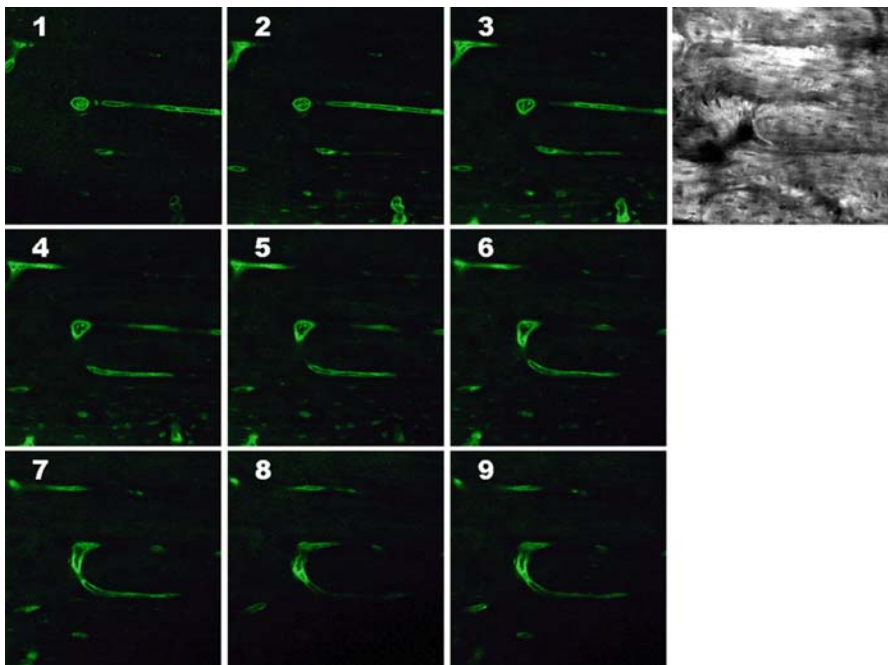
Figure 4. Sequential two-dimensional images of the canaliculi at an increasing depth from top (1) to bottom (9). The *panel on the right* is the bright-field image taken at the same site

Establishment of Evaluation Protocol for the Cortical Fluid Flow with LSCM

Calcein green has been conventionally used for studying bone remodelling (apposition rate) via in vivo injection days before specimen harvesting. This study demonstrated the feasibility of LSCM to use calcein green as a reliable florescent trace marker in studying cortical fluid flow on the undecalcified thick specimens. The non-destructive confocal evaluation and 3D reconstruction of the fluid pattern demonstrated technical advantages as compared with conventional microscopy. Goat cortical bone was used for the present study as it has similarities to human skeletons in bone structure and bone remodelling, fracture repair, and osteoporosis (Lai et al. 2005; Mak et al. 2000; Qin et al. 1999; Siu et al. 2004). Only part of Haversian or Volkmann's capillaries or network of canaliculi and lacunae was labeled with calcein green or filled with fluid flow at one time, and, consistent with our previous findings, this may be explained by flow regulation mechanism controlled by arteriolar sphincter of Haversian capillaries. The possibility of LSCM in in vivo monitoring of cortical fluid movement experimentally may need to be explored further.

This example demonstrates for the first time that LSCM is an advanced technique in the study of cortical fluid flow labeled with florescence dye in vivo and evaluated in vitro in 3D manner. This method may also provide the technical possibility of studying the effect of mechanical and biophysical intervention on cortical fluid flow.
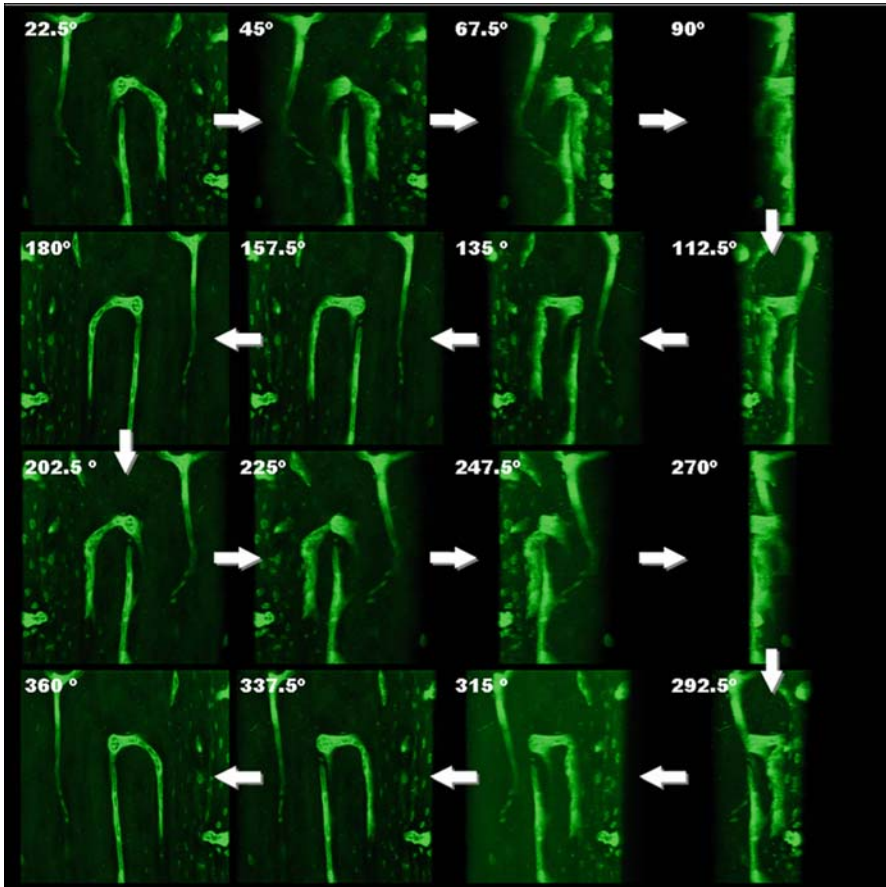
Figure 5. Three-dimensional reconstruction images of network of canaliculi and lacuna. The diagram shows the 360° turn of the reconstructed image

Other Applications of LSCM in Osteocytes and Microcracks

The development of the bone is mainly by membranous ossification and endochondral ossification. Membranous ossification is mainly for the formation of the flat bones in the body, whereas endochondral ossification is the process to form long bones and vertebral body. The cells involved in these processes are mainly osteoblasts, osteoctyes, osteoclasts, and growth plate chondrocytes. Often surrounded heavily by extracellular matrix, these cells require extensive communication network, such as cell processes and the Haversian system, to cooperate with each other to from bones in addition to the cell-cell interaction. To study their cell biology and the communication network, previously the main tools were histology and histocytology from tissue and cell culture; however, these tools can only provide 2D and static information about cells. Bone is a dynamic and structuralized tissue designed to sup-

port the body, protect major organs, and be a storehouse of calcium and phosphorus. It is important to understand the cell biology of the bone in a 3D and dynamic way. The LSCM technique offers the advantage of providing information on living cell biology and morphology as well as 3D organization of the communication network.

In both cortical and trabecular bone, osteocytes are the most abundant cells. Their functions were shown to be a calcium sensor (Kamioka et al. 1994, 1995; Ypey et al. 1992), a regulator for osteoid matrix maturation and mineralization (Mikuni-Takagaki et al. 1995), and mechanosensor (Ajubi et al. 1996; Burger and Klein-Nulend 1999; Klein-Nulend et al. 1995; Tanaka-Kamioka et al. 1998; Terai et al. 1999). Previous studies have attempted to use traditional histology by decalcified section or transmission electron microscope (TEM) to obtain serial images. A 3D reconstruction was then done by computer-aided imaging processing and analysis. This approach had the advantage of unlimited depth of sampling but was very labor intensive and technically challenging in obtaining complete tissue sections and perceive the relationship between structures. Allowing for the complexity of the fine structural detail of osteocyte processes and 3D networking, it is not possible to fully obtain morphological data by traditional histology.

With the rapid development of the LSCM and supplementary fluorescent labels, several studies have used LSCM to study the osteocyte density and the osteocyte-process network with osteoblasts. (Hernandez et al. 2004; Kamioka et al. 2001; McCreadie et al. 2004; Sugawara et al. 2005). In a study using LSCM to evaluate osteocyte density in different types of bone (Hernandez et al. 2004), it was found that the lacunar density of lamellar cortical bone in the rat did not differ significantly from that of perioseal woven bone formed via intramembranous osteogenesis; however, the lacunar density of the woven bone of fracture callus formed via endochondral ossification was 100% greater than that of cortical bone, whereas the lacunar density of the newly formed bone from the growth plate was 40% greater than that in lamellar cancellous bone. In additional to the cellularity of the bone, the size and shape of the lacunae were also observed by LSCM. It was found that the size of the lacunae of the healthy and fractured bone was similar and the shape was estimated as an ellipsoid with the images from LSCM plus the extensive imaging-processing technique (McCreadie et al. 2004).

Another study on osteocyte processes network using confocal microscopy (Sugawara et al. 2005) used Texas red-X-conjugated phalloidin to label the osteocyte processes for LSCM. With a commercially available image-processing software "IMARIS", (Bitplane, Zurich), it was shown that the average of ten osteocytes was about 53 processes and the total length of the processes was approximately 1 mm. From these studies employing the LSCM to observe the cell density, shape, and the process network, the power of LSCM in studying the osteocyte and its biology is appreciated.

It was observed that there is a difference between bone formed by membranous ossification and endochondral ossification in terms of the osteocyte density. This can be explained by another study on osteocytes using LSCM (Kamioka et al. 2001) in which the osteocyte was observed to widely spread its processes to osteoblasts and

that a very limited number of processes reach the vascular facing surface of the osteoblast layer. It was also shown that the number of processes that contacted with one osteoblast was 4.8 on average. Osteoblasts directly beneath an osteoid-osteocyte contained numerous processes, but osteoblasts somewhat further away contained only very few processes. Interestingly, it was rare to see an osteoblast that had a connection with several osteocytes at one time, i.e. usually one osteoblast had connection with only one osteoid-osteocyte. This suggests that an osteocyte might have its territory of osteoblasts contacted by osteocyte processes. Furthermore, it is reported that only a limited number of osteoblasts can become osteocytes, and that this unique selection is done by committed osteocytes (Palumbo et al. 1990). Since the intermediate osseous tissue formed in membranous and endochondral ossification is different, it is possible that the osteocytes control the maturation and differentiation of the osteoblasts into osteocytes in membranous ossification. This leads to the lower osteocyte density in membranous ossification when compared with that in endochondral ossification (Hernandez et al. 2004).

In addition to the osteocytes, which are not easily studied in situ without LSCM as they are buried in the mineralized matrix, microcracks in bone is another feature that is attracting much attention recently because fatigue damage in bone occurs in the form of microcracks which contribute to the formation of stress fractures and fragility fractures and contribute to the loss of bone quality in osteoporosis (Schaffler et al. 1995). The scale of the microcracks is very small (of the order of 10 µm), and they are visible only as diffuse matrix microdamage by traditional light microscopy (Boyce et al. 1998; Fazzalari et al. 1998; Reilly and Currey 1999; Schaffler and Jepsen 2000; Vashishth et al. 2000). Although the microdamage in bone has been described as a small crack with linear-type morphology under light microscopy, it is important to understand the nature of the microcrack in the 3D bone structure. Again the LSCM becomes a useful tool to provide the microcrack morphological data in 3D. In studies using human cadavers to study the size and shape of the microcracks (Fazzalari et al. 1998; O'Brien et al. 2000), the microcracks were shown to have an average length of 404 ± 145 µm and an average width of 97 ± 38 µm. The shape of the microcracks was described as elliptical which is consistent with the theoretical shape (Taylor and Lee 1998). Later, another study also used LSCM to study the propagation of the microcracks in bone (Zarrinkalam et al. 2005). The study not only depicted the 3D microcracks but also used sequential fluorochrome labelling technique to see the propagation of the microcracks under LSCM. Through a series of z-series images, a close association was found between microdamage and osteocytic lacunae and their canaliculi in 3D. It is still unknown, however, whether the close association between the osteocyte lacunae and microdamage would result in osteocytic cell death and damage to the canaliculi. Both are considered important with regard to the ability of the osteocytes to sense matrix strain. Confocal microscopic imaging of fluorochrome-labeled microdamage in vivo was shown to be used in conjunction with a fluorescent viability cell marker to directly determine which osteocytes apoptosis in response to microdamage (Zarrinkalam et al. 2005).

Conclusion

The recent advances in LSCM and the power of computer for image processing and analysis provides a very useful tool for orthopedic research to further look at the details of cell biology of different skeletal cells such as osteocytes and chondrocytes. Actually, the usage of LSCM is also extended to the study of osteoclasts (Nesbitt and Horton 1997, 2003) and osteoblasts (Ramires et al. 2002). The application of LSCM is very wide and will give us increasingly more understanding of the cells related to the skeletal system as well as the complex 3D structure of the bone and cartilage future.

References

Ajubi NE, Klein-Nulend J, Nijweide PJ, Vrijheid-Lammers T, Alblas MJ, Burger EH (1996) Pulsating fluid flow increases prostaglandin production by cultured chicken osteocytes: a cytoskeleton-dependent process. Biochem Biophys Res Commun 225:62–68

Ali SY (1976) Analysis of matrix vesicles and their role in the calcification of epiphyseal cartilage. Fed Proc 35:135–142

Anderson HC (1969) Vesicles associated with calcification in the matrix of epiphyseal cartilage. J Cell Biol 41:59–72

Arsenault AL, Ottensmeyer FP, Heath IB (1988) An electron microscopic and spectroscopic study of murine epiphyseal cartilage: analysis of fine structure and matrix vesicles preserved by slam freezing and freeze substitution. J Ultrastruct Mol Struct Res 98:32–47

Atkinson PJ, Hallsworth AS (1982) The spatial structure of bone. In: Harrison RJ, Havaratman V (eds) Progress in anatomy. Cambridge University Press, Cambridge, pp 179–199

Bonucci E (1970) Fine structure and histochemistry of calcifying globules in epiphyseal cartilage. Z Zellforsch Mikrosk Anat 103:192–217

Boyce TM, Fyhrie DP, Glotkowski MC, Radin EL, Schaffler MB (1998) Damage type and strain mode associations in human compact bone bending fatigue. J Orthop Res 16:322–329

Boyde A, Hendel P, Hendel R, Maconnachie E, Jones SJ (1990) Human cranial bone structure and the healing of cranial bone grafts: a study using backscattered electron imaging and confocal microscopy. Anat Embryol (Berl) 181:235–251

Brighton CT, Hunt RM (1976) Histochemical localization of calcium in growth plate mitochondria and matrix vesicles. Fed Proc 35:143–147

Bronk JT, Meadows TH, Kelly PJ (1993) The relationship of increased capillary filtration and bone formation. Clin Orthop Relat Res:338–345

Burger EH, Klein-Nulend J (1999) Mechanotransduction in bone: role of the lacuno-canalicular network. FASEB J 13:S101-S112

Cooper RR, Milgram JW, Robinson RA (1966) Morphology of the osteon. An electron microscopic study. J Bone Joint Surg Am 48:1239–1271

Eitel F, Klapp F, Jacobson W, Schweiberer L (1981) Bone regeneration in animals and in man. A contribution to understanding the relative value of animal experiments to human pathophysiology. Arch Orthop Trauma Surg 99:59–64

Fazzalari NL, Forwood MR, Manthey BA, Smith K, Kolesik P (1998) Three-dimensional confocal images of microdamage in cancellous bone. Bone 23:373–378

Fernandez MP, Selmin O, Martin GR, Yamada Y, Pfaffle M, Deutzmann R, Mollenhauer J, von der Mark K (1988) The structure of anchorin CII, a collagen binding protein isolated from chondrocyte membrane. J Biol Chem 263:5921–5925

Genge BR, Cao X, Wu LN, Buzzi WR, Showman RW, Arsenault AL, Ishikawa Y, Wuthier RE (1992) Establishment of the primary structure of the major lipid-dependent Ca2+ binding proteins of chicken growth plate cartilage matrix vesicles: identity with anchorin CII (annexin V) and annexin II. J Bone Miner Res 7:807–819

Gunter TE, Zuscik MJ, Puzas JE, Gunter KK, Rosier RN (1990) Cytosolic free calcium concentrations in avian growth plate chondrocytes. Cell Calcium 11:445–457

Hale JE, Wuthier RE (1987) The mechanism of matrix vesicle formation. Studies on the composition of chondrocyte microvilli and on the effects of microfilament-perturbing agents on cellular vesiculation. J Biol Chem 262:1916–1925

Hernandez CJ, Majeska RJ, Schaffler MB (2004) Osteocyte density in woven bone. Bone 35:1095–1099

Iannotti JP, Brighton CT (1989) Cytosolic ionized calcium concentration in isolated chondrocytes from each zone of the growth plate. J Orthop Res 7:511–518

Judex S, Gross TS, Bray RC, Zernicke RF (1997) Adaptation of bone to physiological stimuli. J Biomech 30:421–429

Kamioka H, Sumitani K, Tagami K, Miki Y, Terai K, Hakeda Y, Kumegawa M, Kawata T (1994) Divalent cations elevate cytosolic calcium of chick osteocytes. Biochem Biophys Res Commun 204:519–524

Kamioka H, Miki Y, Sumitani K, Tagami K, Terai K, Hosoi K, Kawata T (1995) Extracellular calcium causes the release of calcium from intracellular stores in chick osteocytes. Biochem Biophys Res Commun 212:692–696

Kamioka H, Honjo T, Takano-Yamamoto T (2001) A three-dimensional distribution of osteocyte processes revealed by the combination of confocal laser scanning microscopy and differential interference contrast microscopy. Bone 28:145–149

Kaplan FS, Hayes WC, Kearney TM, Boskey A, Einhorn TA, Iannotti JP, Simon SR (2000) Form and function of bone. In: Buckwalter JA, Einhorn TA, Simon SR (eds) Orthopaedic basic science: biology and biomechanics of the musculoskeletal system. American Academy of Orthopaedic Surgeons, Rosemont, Illinois, pp 127–184

Klein-Nulend J, Semeins CM, Ajubi NE, Nijweide PJ, Burger EH (1995) Pulsating fluid flow increases nitric oxide (NO) synthesis by osteocytes but not periosteal fibroblasts: correlation with prostaglandin upregulation. Biochem Biophys Res Commun 217:640–648

Knothe Tate ML, Niederer P, Knothe U (1998) In vivo tracer transport through the lacunocanalicular system of rat bone in an environment devoid of mechanical loading. Bone 22:107–117

Lai YM, Qin L, Yeung HY, Lee KM, Chan KM (2005) Regional differences in trabecular BMD and microarchitecture of weight bearing bone under habitual gait loading: a pQCT and microCT study in human subject. Bone 37:274–282

Mak AF, Qin L, Hung LK, Cheng CW, Tin CF (2000) A histomorphometric observation of flows in cortical bone under dynamic loading. Microvasc Res 59:290–300

McCreadie BR, Hollister SJ, Schaffler MB, Goldstein SA (2004) Osteocyte lacuna size and shape in women with and without osteoporotic fracture. J Biomech 37:563–572

Mikuni-Takagaki Y, Kakai Y, Satoyoshi M, Kawano E, Suzuki Y, Kawase T, Saito S (1995) Matrix mineralization and the differentiation of osteocyte-like cells in culture. J Bone Miner Res 10:231–242

Minsky M (1988) Memoir on inventing the confocal scanning microscope. Scanning 10:128–138

Nesbitt SA, Horton MA (1997) Trafficking of matrix collagens through bone-resorbing osteoclasts. Science 276:266–269

Nesbitt SA, Horton MA (2003) Fluorescence imaging of bone-resorbing osteoclasts by confocal microscopy. Methods Mol Med 80:259–281

O'Brien FJ, Taylor D, Dickson GR, Lee TC (2000) Visualisation of three-dimensional microcracks in compact bone. J Anat 197:413–420

Palumbo C, Palazzini S, Zaffe D, Marotti G (1990) Osteocyte differentiation in the tibia of newborn rabbit: an ultrastructural study of the formation of cytoplasmic processes. Acta Anat (Basel) 137:350–358

Qin L, Mak AT, Cheng CW, Hung LK, Chan KM (1999) Histomorphological study on pattern of fluid movement in cortical bone in goats. Anat Rec 255:380–387

Ramires PA, Giuffrida A, Milella E (2002) Three-dimensional reconstruction of confocal laser microscopy images to study the behaviour of osteoblastic cells grown on biomaterials. Biomaterials 23:397–406

Reilly GC, Currey JD (1999) The development of microcracking and failure in bone depends on the loading mode to which it is adapted. J Exp Biol 202:543–552

Rhinelander FW (1968) The normal microcirculation of diaphyseal cortex and its response to fracture. J Bone Joint Surg Am 50:784–800

Schaffler MB, Choi K, Milgrom C (1995) Aging and matrix microdamage accumulation in human compact bone. Bone 17:521–525

Schaffler MB, Jepsen KJ (2000) Fatigue and repair in bone. Int J Fatigue 22:839–846

Seliger WG (1970) Tissue fluid movement in compact bone. Anat Rec 166:247–255

Shapiro IM, Lee NH (1975) Effects of Ca2+ on the respiratory activity of chondrocyte mitochondria. Arch Biochem Biophys 170:627–633

Siu WS, Qin L, Cheung WH, Leung KS (2004) A study of trabecular bones in ovariectomiezed goats with micro-computed tomography and peripheral quantitative computed tomography. Bone 35:21–26

Sugawara Y, Kamioka H, Honjo T, Tezuka K, Takano-Yamamoto T (2005) Three-dimensional reconstruction of chick calvarial osteocytes and their cell processes using confocal microscopy. Bone 36:877–883

Tanaka-Kamioka K, Kamioka H, Ris H, Lim SS (1998) Osteocyte shape is dependent on actin filaments and osteocyte processes are unique actin-rich projections. J Bone Miner Res 13:1555–1568

Taylor D, Lee TC (1998) Measuring the shape and size of microcracks in bone. J Biomech 31:1177–1180

Terai K, Takano-Yamamoto T, Ohba Y, Hiura K, Sugimoto M, Sato M, Kawahata H, Inaguma N, Kitamura Y, Nomura S (1999) Role of osteopontin in bone remodeling caused by mechanical stress. J Bone Miner Res 14:839–849

Vashishth D, Tanner KE, Bonfield W (2000) Contribution, development and morphology of microcracking in cortical bone during crack propagation. J Biomech 33:1169–1174

Watson PA (1991) Function follows form: generation of intracellular signals by cell deformation. FASEB J 5:2013–2019

Wu LN, Genge BR, Lloyd GC, Wuthier RE (1991) Collagen-binding proteins in collagenase-released matrix vesicles from cartilage. Interaction between matrix vesicle proteins and different types of collagen. J Biol Chem 266:1195–1203

Wuthier RE (1975) Lipid composition of isolated epiphyseal cartilage cells, membranes and matrix vesicles. Biochim Biophys Acta 409:128–143

Wuthier RE (1977) Electrolytes of isolated epiphyseal chondrocytes, matrix vesicles, and extracellular fluid. Calcif Tissue Res 23:125–133

Wuthier RE (1993) Involvement of cellular metabolism of calcium and phosphate in calcification of avian growth plate cartilage. J Nutr 123:301–309

Wuthier RE, Wu LN, Sauer GR, Genge BR, Yoshimori T, Ishikawa Y (1992) Mechanism of matrix vesicle calcification: characterization of ion channels and the nucleational core of growth plate vesicles. Bone Miner 17:290–295

Ypey DL, Weidema AF, Hold KM, Van der LA, Ravesloot JH, Van der PA, Nijweide PJ (1992) Voltage, calcium, and stretch activated ionic channels and intracellular calcium in bone cells. J Bone Miner Res 7 (Suppl 2):S377-S387

Zarrinkalam KH, Kuliwaba JS, Martin RB, Wallwork MA, Fazzalari NL (2005) New insights into the propagation of fatigue damage in cortical bone using confocal microscopy and chelating fluorochromes. Eur J Morphol 42:81–90

Fiber-optic Nano-biosensors and Near-Field Scanning Optical Microscopy for Biological Imaging

Kin-Fai Wu[1], Yuan-Ting Zhang (✉) [1], and Mary Miu Yee Waye[2]

[1] Department of Electronic Engineering, the Chinese University of Hong Kong, Hong Kong, China
e-mail: ytzhang@ee.cuhk.edu.hk
[2] Department of Biochemistry (Medicine), Croucher Laboratory for Human Genomics, the Chinese University of Hong Kong, Hong Kong

Abstract

In recent decades, the rapid development of nanotechnology has led to the broadening of application in many areas. Among these technologies, near-field optics is the one which can provide sufficient resolution suitable for measurement in molecular level in the biological area. Although current light and electron microscopies can yield images in many scales, they do not fit the measurement in the submicrometer scale, which is important for the study of functional molecular complexes ranging from chromosomes to membrane domains. For electron microscopy, even though it is able to resolve structures of samples down to nanometer scales, the samples must be dry and dead. Traditional light microscopy can be applied to the investigation of molecular complexes in living cells, but as its resolution is limited by the diffraction of light (~250 nm), molecular complex structures cannot be resolved. On the other hand, the near-field scanning optical microscopy (NSOM) allows fluorescence imaging at a resolution of a few tens of nanometers. Also, as a result of the extremely small excitation volume, the background fluorescence is greatly reduced and so single-molecule detection becomes possible. In addition, both topography and fluorescent images can be collected simultaneously. As a result, NSOM provides great advances in biological research. Fiber-optic nano-biosensor (FONBS), which is derived from NSOM, is commonly used to investigate intracellular measurement. Taking the advantages of NSOM as well as biological methods, FONBS opens new horizons in environmental and biological monitoring of chemicals and biomolecules within single cells. In this chapter, the basic concepts and developments of both techniques are discussed. The mechanisms and their application to biological systems are also provided in brief.

Near-Field Probes

A fiber probe is the most important component of the two near-field optical techniques. Fabrication of such probes is, therefore, the first issue about which we should
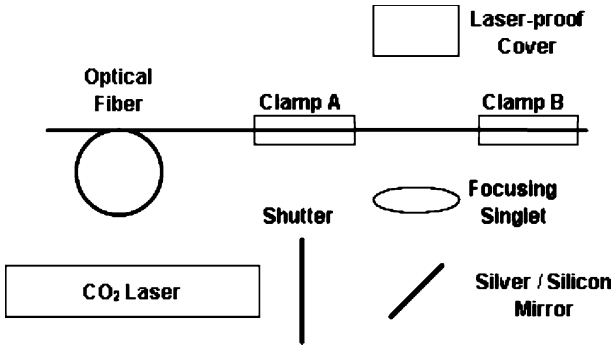
Figure 1. Structure of a micropipette puller. The laser spot focuses on an optical fiber at the middle position between the two clamps. A shutter is used to control the duration of laser heating while clamps *A* and *B* provide the outward pulling force to separate the optical fiber into two parts with tiny tips

be concerned. The main purpose of such probes is to transmit the light from the source end to the fiber tip, and with some mechanisms, the transmitted light can be used to elicit the optical responses which are directly proportional to the concentration of the detecting species.

The fiber probes are commonly fabricated through a multistage heating-pulling process (Fig. 1; Cullum and Vo-Dinh 2000; Hecht et al. 2000; Valaskovic et al. 1995). A tapered optical fiber is prepared by a micropipette puller. The fiber is heated by a carbon dioxide laser and pulled along its major axis by a tension device. By adjusting the heating temperature and the tension applied to the fiber, tip diameters varying from 20 to 500 nm can be produced (Fig. 2). This technique can provide a fast and simple way to fabricate the fiber probes with reproducible tip diameters.

Another method for probe fabrication is chemical etching (Cullum and Vo-Dinh 2000; Hecht et al. 2000). Two different etching methods, Turner etching and tube
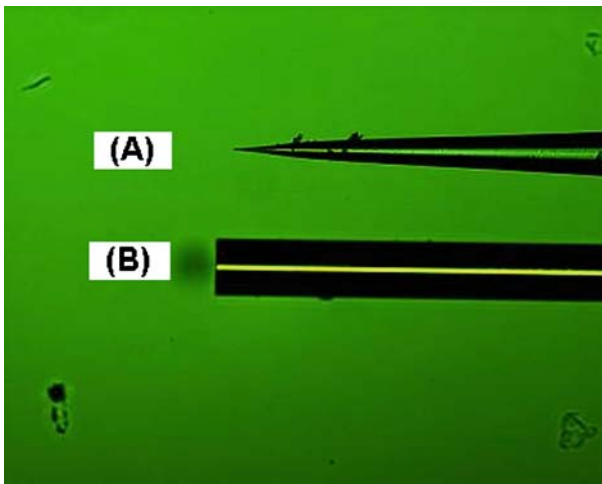
Figure 2. A pulled (*A*) and an unpulled (*B*) optical fiber with core diameter of 400 nm
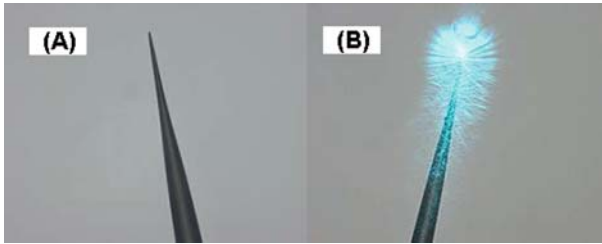
Figure 3 A,B. A pulled optical fiber (**A**) with core diameter of 400 nm. Light transmits along the optical fiber and is emitted from the tip (**B**). There is some leakage of light from the tapered side wall of the optical fiber due to the absence of metallic coating

etching, have been reported. In general, hydrofluoric acid together with another organic substance is used to prepare a fiber probe. Large taper angles and tip diameters comparable to those obtained by the pulling method have been reported; however, the chemical nature, temperature fluctuations, vibrations and other environmental factors can cause variations in tip characteristics.

Another equally important fabrication step is tip coating (Fig. 3; Valaskovic et al. 1995). To prevent leakage of the excitation light on the tapered side of the fiber, the outside of the tapered end is usually coated with a thin layer of metal, such as silver, aluminum, or gold (100–300 nm), leaving the distal end of the fiber free as an aperture. The fiber probe is attached to a rotating device with an angle to the horizon inside a thermal evaporation chamber. The metal is, therefore, allowed to evaporate evenly onto the tapered side of the fiber tip to form a thin layer of metallic coating.

A fiber probe is regarded as a simple waveguide along its length, but with a complex structure at the tapered tip. Two critical characteristics, including lateral resolution and transmission efficiency, are highly governed by the tip geometry (Hecht et al. 2000; Valaskovic et al. 1995). The tip diameter is typically fabricated <100 nm. Owing to this tiny aperture which is below the half-wavelength diffraction limit of visible light (~250 nm) governed by the optics, evanescent waves, rather than propagating waves, are emitted from the aperture. The intensity of the evanescent light decays exponentially to an insignificant level of <100 nm from the aperture. As a result, the excitation light can be only effective within a very small volume from the aperture.

Near-Field Scanning Optical Microscopy

Near-field scanning optical microscopy (NSOM), or scanning near-field optical microscopy (SNOM), is one of the scanning probe microscopy (SPM) techniques that is capable of very high-resolution imaging and spectroscopy at visible wavelengths without lenses. The NSOM breaks the diffraction limit (~ 250 nm) and is capable of investigating an aggregate of cells, and even a single cell, with superior resolution. Besides two-dimensional imaging, surface topography can also be obtained simultaneously. That is why NSOM has a prominent position in biological imaging compared

with ordinary light microscopies (de Lange et al. 2001; Hosaka et al. 1999; Lewis et al. 1999).

The principle of NSOM is to place the light source with effective volume in nanometer level close to the sample surface and then collect the optical responses by a photon-counting device (Fig. 4). Through the pixel-by-pixel scanning, a two-dimensional image of the selected area can be revealed on a computer. To accomplish this idea, NSOM consists of several techniques which are used to control the tip-sample separation in nanometer scale and provide ways to specifically reflect the localized concentration of the testing subject.

Generally, the tip-sample separation is controlled through the application of another SPM called atomic force microscopy (AFM). The AFM basically exploits the knowledge of intermolecular forces to implement this control (Fig. 5). The tapered optical fiber probe acts as a cantilever in an AFM system. When the tip of the probe is brought into close proximity of a sample surface, the intermolecular force between the tip and the sample leads to a deflection of the cantilever. A feedback mechanism is employed to adjust the tip-sample distance to keep the force between the tip and the sample in a suitable range ($< 10\,nm$) by the piezoelectric materials. Typically, the optical method, where an additional laser spot is reflected from the top of the bent-version fiber probe into an array of photodiodes, is applied to measure such a deflection (Jenkins et al. 1995). Another method is a mechanical method, where a quartz tuning fork is attached to an erect fiber probe and oscillates at its resonance frequency. When the tip is very close to the sample, the oscillation slows down due to intermolecular forces (Lu et al. 2001). On the other hand, topographic data can be collected during the whole scanning process.

To make NSOM a powerful tool for biological imaging, the target molecules should be prepared to specifically respond to the excitation light. Samples prepared
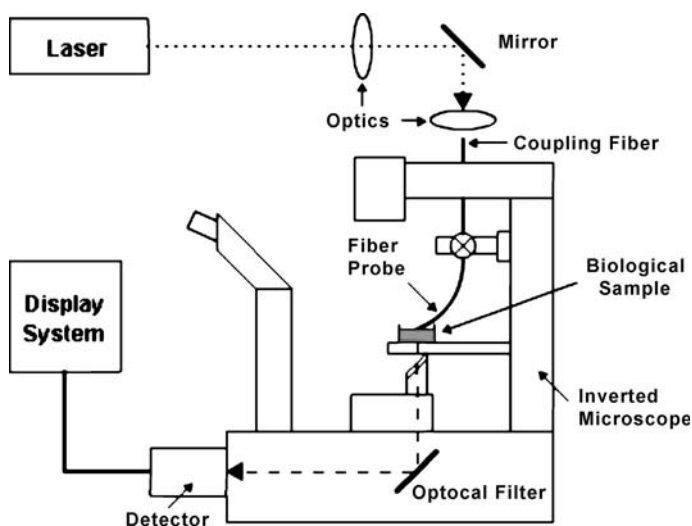
Figure 4. Experimental setup of a near-field scanning optical microscope
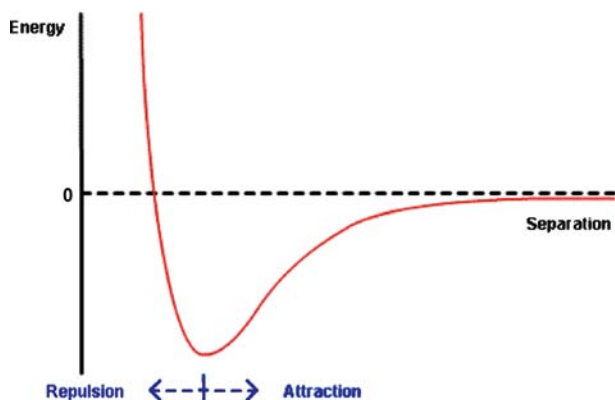
Figure 5. The curve of intermolecular energy of both the fiber probe tip and the sample. At long distances there is very little force between the fiber and the sample, and their intermolecular energy is regarded as zero. As they approach each other there is an increasing attractive force. Motion in the direction of force lowers energy. As a result, the energy becomes increasingly negative. At some point the force becomes zero, and the energy is a minimum. At closer separations the force is repulsive and the energy increases, finally becoming positive

for imaging, in general, are treated to label the target molecules with fluorescent chemicals or biochemicals, called fluorophores, such as Texas Red (TR), fluorescein isothiocyanate (FITC), and green fluorescent protein (GFP; Garcia-Parajo et al. 1999). Immunofluorescence technique is usually applied in the measurements. In general, this technique employs two sets of antibodies: a primary antibody is used against the antigen of interest; subsequently, a secondary, dye-coupled antibody that recognizes the primary antibody is used. During near-field imaging, a monochromatic light emitted from the aperture of the fiber probe is significant within a volume smaller than 100 nm from it. Effectively, only the fluorophores within a layer of < 100 nm from the tip of fiber probe can be excited (Fig. 6). Under Raman scattering, the fluorescence of another wavelength is collected by a photomultiplier tube or an avalanche photodiode. As a result, the response from each position is processed and the whole image can be created on the computer. Due to localized excitation, autofluorescence of the fluorophores is highly reduced. In addition, since only fluorophores
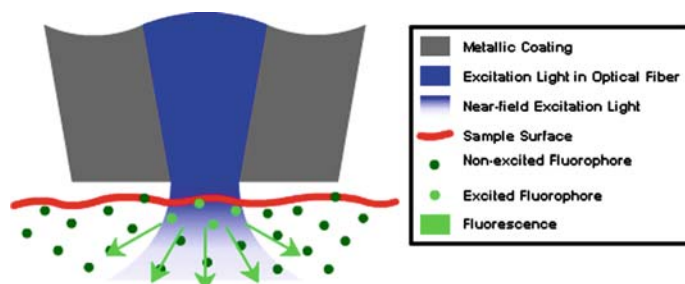
Figure 6. Conceptual diagram of near-field excitation of fluorophores

Table 1. Determination of erbB2 cluster diameter on quiescent and activated cells. (From Nagy et al. 1999)

Cells and treatments	Manual (μm)	Segmentation (μm)	Autocorrelation (μm)
SKBR3			
Quiescent	0.48 ± 0.08	0.59 ± 0.16	0.36 ± 0.08
Quiescent, labeled with Fab	0.45 ± 0.08	0.62 ± 0.07	0.42 ± 0.12
4D5-activated	0.62 ± 0.11[*]	0.75 ± 0.26[*]	0.63 ± 0.21[*]
EGF-activated	0.60 ± 0.11[*]	0.80 ± 0.31[*]	0.60 ± 0.12[*]
EGF-treated, in the presence of PD153035	0.39 ± 0.09	0.49 ± 0.12	0.29 ± 0.06
Heregulin-activated	0.66 ± 0.14[*]	0.86 ± 0.31[*]	0.84 ± 0.20[*]
MDA453			
Quiescent	0.51 ± 0.09	0.61 ± 0.18	0.40 ± 0.08
CB2			
Quiescent	0.83 ± 0.13[*]	0.95 ± 0.31[*]	0.71 ± 0.18[*]

Cell were stained with TAMRA-labeled anti-erbB[2] monoclonal antibodies or with Fab if indicated, and were activated with the indicated agents

Manual (method 1): determination of cluster size by measuring the diameter of particles on the screen

Segmentation (method 2): entropy thresholding of background-filtered images

Autocorrelation (method 3): determination of the angle-averaged autocorrelation function of the images

Indicated values are mean ± SD of at least three different experiments

[*]Significant difference ($p < 0.05$) from untreated SKBR3 cells using Student's t-test

located in the outermost layer of the sample is excited, NSOM is a very specific tool for studies of plasma membranes of living cells.

Currently, NSOM is applied to a variety of aspects in the biological area, such as the study of biomolecules and their interactions, the mechanisms and effects of drugs and toxins in cellular levels, and the structure-function relationships of biomolecules (Badhan and Penny 2006; Enderle et al. 1997; Hwang et al. 1998; Jauss et al. 2002; Lei et al. 2001; Nagy et al. 1999). For example, we have tried to visualize the distribution of P-glycoproteins in hepatocellular carcinoma cells (Fig. 7; HepG2). The cells were fixed on a cover slip and the P-glycoproteins were labeled with FITC. Through near-field scanning, P-glycoproteins were found to be located on the plasma membranes. These types of experiments might be useful to validate the in-silico modeling studies of P-glycoprotein (Badhan and Penny 2006). On the other hand, Enderle et al. (1997) demonstrated the mapping and colocalization of malarial and host skeletal proteins in plasmodium-falciparum-infected erythrocyte by dual-color NSOM (Fig. 8; Enderle et al. 1997). Two types of secondary antibodies were used and labeled with FITC and TR, respectively. Since both fluoresceins shared the same wavelength of excitation light, a perfect pixel-by-pixel registry can be done by using two sets of photodiodes and optical filters. This method provides a possible way to study colocalization
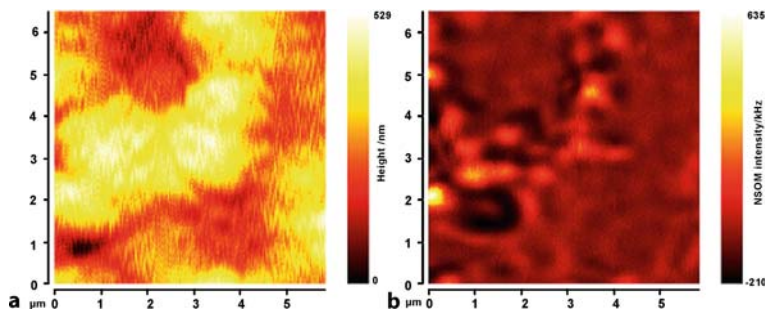
Figure 7 a,b. Result of NSOM imaging in topography (**a**) and fluorescence (**b**; 256 × 256 pixels, 22.5 nm/pixel). The hepatocellular carcinoma cells (*HepG2*) were fixed and reacted with primary antibodies from mouse against the P-glycoproteins. Secondary antibodies labeled with FITC (anti-mouse) were used

of biomolecules at the cellular level and helps in many areas of biological research. In addition, Nagy et al. applied NSOM to the detection of large-scale clustering of the erbB2 receptor tyrosine kinase (Table 1; Nagy et al. 1999). Fluorescent anti-erbB2 antibody-labeled breast tumor cells (SKBR3 and MDA453) were investigated. Interestingly, patches with mean diameter of 0.5 µm formed by erbB2 were found in the plasma membranes of both kinds of cells. Experiments in both quiescent and activated cells were also implemented. An increase in cluster size was found to increase with the activation level of erbB2 in cells. This relationship and the related findings offer a better knowledge of protein-protein interactions and structure-function relationship in the plasma membrane at the submicrometer level. In conclusion, studies towards these directions can be benefited greatly by the application of NSOM.

Fiber-optic Nano-biosensors

A fiber-optic nano-biosensor (FONBS) is a modified version of the probing system used in NSOM. It is used to suit investigations of fast intracellular measurements, especially examination of processes within living cells. This ability provides great advances in understanding of cellular functions. The probes used in FONBS are the same as those used in NSOM; thereby, FONBS also achieves superior resolution, which enables scientists to probe for specific target molecules in highly localized areas of three-dimensional structures. As a result, it broadens our horizon of intracellular concentration gradients and spatial inhomogeneities in submicroscopic environments (Cullum and Vo-Dinh 2000; Vo-dinh and Kasili 2005). In addition, owing to the low production cost of the fiber probes, FONBS provides an economical way for mass investigation on an array of samples. It can thus assist in rapid data collection for biological, biochemical, and medical research studies.

The main structural difference between FONBS and NSOM is that the tip of the fiber probes used in FONBS are commonly immobilized, by covalent binding, with receptors which are capable of producing optical responses specifically to their target
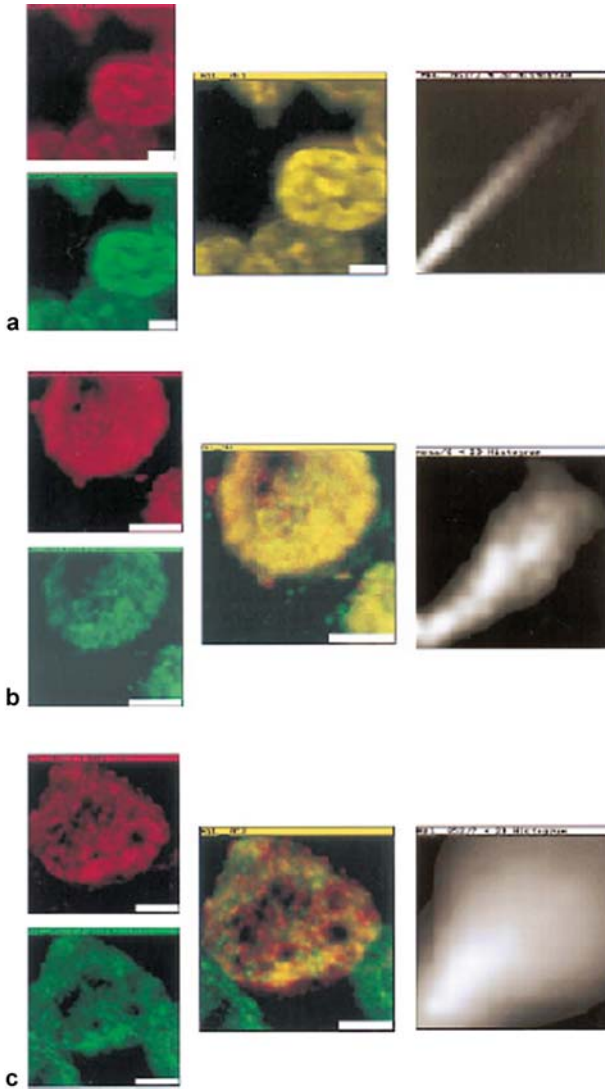
Figure 8 a–c. Colocalization of malarial and host proteins in the erythrocyte membrane. A blood smear of erythrocytes infected with the trophozoite-stage parasites was fixed and then reacted with two different antibodies (from rabbit and mouse) against the proteins under study. Secondary antibodies labeled with FITC (anti-rabbit) and TR (anti-mouse) were used, respectively. The *left column* shows the two simultaneously acquired fluorescence channels by NSOM dual-color imaging. The *center column* presents the corresponding overlay of the fluorescence images and the *right column* is pixel-by-pixel correlation between the *red* and *green* images. **a** Control experiment: primary antibodies against PfHRP1 (128×128 pixels, 86 nm/pixel). **b** Colocalization of MESA and protein 4.1 (128×128 pixels, 48 nm/pixel). **c** Colocalization of PfHRP1 and protein 4.1 (256×256 pixels, 30 nm/pixel). (*Scale bars* = 2μm)

molecules under the exposure of the excitation light. A variety of receptors, including chemicals, antibodies, enzymes, and molecular beacons, is exploited to probe different types of targets inside a cell.

Using chemicals as the receptors, chemical changes of the immobilized chemicals during redox reactions with the targets are applicable to amplify (or enhance) the measurements. Specific optical responses usually accompany such chemical changes when exposed to the excitation light, and so act as the indicators of target concentrations; therefore, this type of FONBS is commonly used to probe the pH and the ion concentration in the intracellular space. For instance, Bui et al. (1999) monitored the cellular responses to drug administration in NG108-15 neuroblastoma cells and vascular smooth muscle cells (VSMC) by detecting the calcium ions (Ca^{2+}) increase in a precise intracellular space. Fura-2/AM or fluo-3/AM calcium dye-loaded cells were stimulated with drugs and the responses were recorded by a CCD camera and an avalanche photon detector simultaneously. As a result, possible real-time visualization of intracellular events can be obtained. This monitoring technique helps in understanding of many physiological processes and functions.

The antibody-based FONBS is usually used to probe the fluorescent targets in cells (Cullum et al. 2000; Vo-dinh et al. 2000a,b). Based on antibody-antigen interactions, this type of FONBS is a very powerful monitoring tool as a result of its excellent specificity and sensitivity. The antibody-based FONBS is specifically used to probe proteins, biomolecules, viruses, microorganism components, and toxins. A great biomedical interest in the detection of benzopyrene tetrol (BPT) was demonstrated by Vo-dinh et al. (2000a). The BPT is a fluorescent analyte, and also a metabolite of the carcinogen benzo[a]pyrene (BaP). In the beginning, anti-BPT FONBS was employed to target BPT in calibration solutions with different known BPT concentrations. Consequently, the cells (rat liver epithelial clone-9 cell line) were treated with BPT and detected by the anti-BPT FONBS. By comparing the data obtained in the calibration solutions, the intracellular BPT concentration of the detected cells can be estimated. This method provides a fast and simple way to monitor DNA damage due to BaP exposure and for possible precancer diagnosis.

For the enzyme-based FONBS (Cullum and Vo-Dinh 2000), the optical responses are commonly generated by the reaction products or the chemical changes of the enzymes during binding to the substrates under the exposure of the excitation light. Due to the enzymatic natures of the receptors, this type of FONBS should be possible to continuously monitor the target chemicals located in the intracellular region. A review paper stated that glutamate, one of the major neurotransmitters in the central nervous system, could be indirectly monitored by the glutamate-dehydrogenase-immobilized FONBS (Cullum and Vo-Dinh 2000). When glutamate was bound to the glutamate dehydrogenase, a cofactor, oxidized nicotinamide adenine dinucleotide (NAD^+), was reduced to NADH, and the fluorescence of NADH could be measured and related to the glutamate levels. Owing to its chemical regeneration ability, it could be used in continuous glutamate measurements of individual cells and achieve a better understanding of the neurotransmission mechanisms of sensations.

Molecular beacons (MBs; Liu and Tan 1999; Liu et al. 2000) are hairpin-shaped oligonucleotides, each of them is composed of two complementary arm sequences
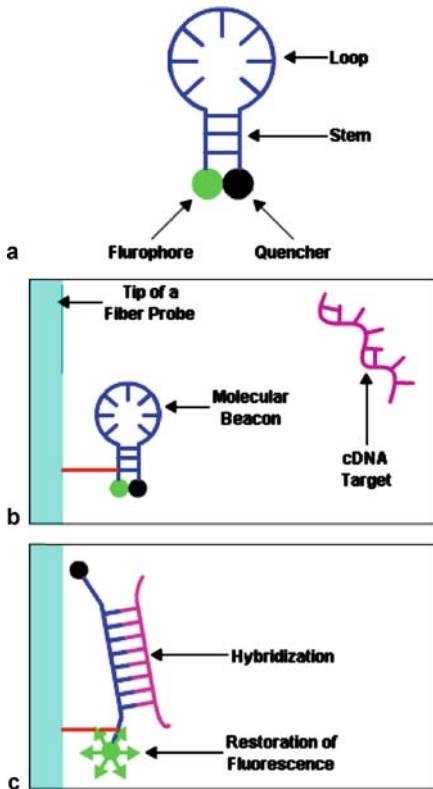
Figure 9 a–c. Structure of a molecular beacon (**a**). A molecular beacon is immobilized onto the tip of a fiber probe by covalent binding (**b**). The stem keeps the fluorophore and the quencher in close proximity to each other; thereby the fluorescence of the fluorophore is quenched by the quencher through energy transfer. Until the probe is put in close proximity to a complementary DNA target, the loop hybridizes to it and separates the two arms, leading to the restoration of fluorescence (**c**)

and a probe sequence composed of a base sequence complementary to the gene of interest (Fig. 9). A fluorophore is attached to the end of one arm, while a quencher is attached to the end of another arm. Originally, since the stem keeps the fluorophore and the quencher in close proximity to each other, the fluorescence of the fluorophore is quenched by the quencher through energy transfer. When the probe sequence hybridizes to its complementary target sequence, the stem opens and the fluorophore separates from the quencher in the stem, leading to the restoration of the fluorescence emitted by the fluorophore (Fig. 9). As a result, by immobilizing MBs onto the tip of FONBS, the concentration of a specific sequence of nucleic acids in a localized area can be measured. Liu et al. (2000) have used MB-immobilized FONBS to quantify a rat γ-actin mRNA sequence amplified by polymerase chain reaction (Fig. 10). The MBs were immobilized onto the tip of optical fiber probes through avidin-biotin binding. Since their probe sequence was complementary to the specific mRNA sequence, high specificity and fast response time was shown in the experiment. Single base-pair mismatch of the mRNA sequence was tested and the MB-immobilized FONBS showed a good identification capability; therefore, this type of FONBS can be applied to DNA mutation studies and disease diagnosis with neither complex preparations nor long reaction time.
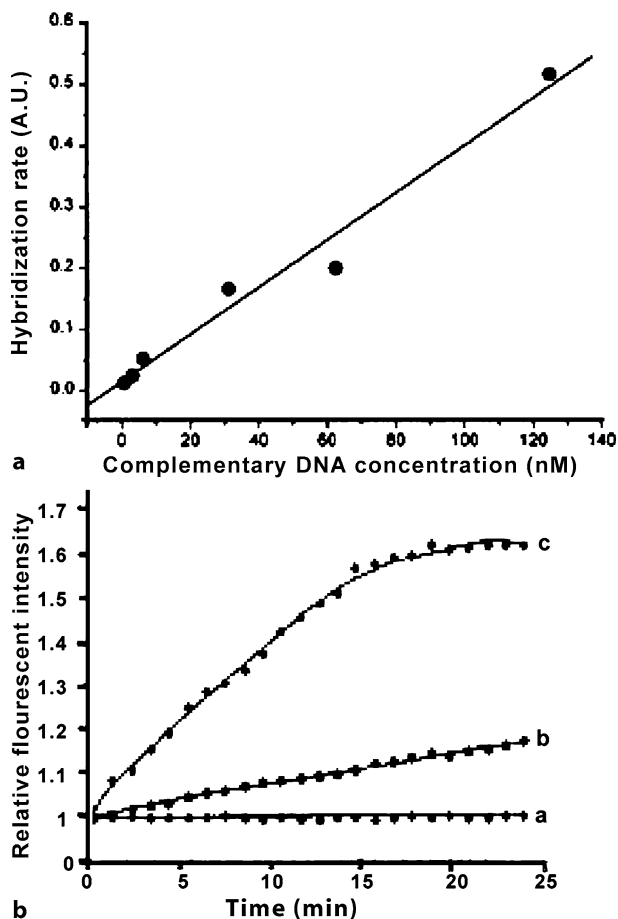
Figure 10. a Molecular beacon DNA biosensor sensitivity test. Change in MB hybridization rate vs concentration of the target oligonucleotide is linear. The initial hybridization rate was calculated using the slope of the linear portion of the time course of hybridization. Both initial and steady-state reaction rates can be used for sensor characterization; however, when cDNA concentration is low, it takes a long time to reach steady state. So it is more appropriate to use the initial rate for sensor characterization in our experiments. **b** Time course of hybridization of (a) 30-nM non-complementary oligonucleotide, (b) 30-nM 1-base mismatch oligonucleotide, and (c) 30-nM complementary oligonucleotide to the immobilized molecular beacon optical fiber biosensor

Conclusion

This chapter introduces near-field optics, which can provide sufficient resolution suitable for measurements in molecular levels in biological research. On the other hand, NSOM allows fluorescence imaging at a resolution of a few tens of nanometers. As a result of the extremely small excitation volume, the background fluorescence

is greatly reduced and so single-molecule detection becomes possible. Fiber-optic nano-biosensor, which is derived from NSOM, provides a unique means in environmental and biological monitoring of chemicals and biomolecules within single cells. The adaptation of these advanced bioimaging technologies into musculoskeletal and related biomaterial research might open a now horizon and enhance their in-depth studies at cellular and molecular levels in the near future.

References

Badhan R, Penny J (2006) In silico modelling of the interaction of flavonoids with human P-glycoprotein nucleotide-binding domain. Eur J Med Chem (Epub ahead of print)

Bui JD, Zelles T, Lou HJ, Gallion VL, Phillips MI, Tan W (1999) Probing intracellular dynamics in living cells with near-field optics. J Neurosci Meth 89:9–15

Cullum BM, Vo-Dinh T (2000) The development of optical nanosensors for biological measurements. Tren Biotechnol 18:388–393

Cullum BM, Griffin GD, Miller GH, Vo-Dinh T (2000) Intracellular measurements in mammary carcinoma cells using fiber-optic nanosensors. Anal Biochem 277:25–32

de Lange F, Cambi A, Huijbens R, de Bakker B, Rensen W, Garcia-Parajo M, van Hulst N, Figdor CG (2001) Cell biology beyond the diffraction limit: near-field scanning optical microscopy. J Cell Sci 114:4153–4160

Enderle TH, Ha T, Ogletree DF, Chemla DS, Magowan C, Weiss S (1997) Membrane specific mapping and colocalization of malarial and host skeletal proteins in the Plasmodium falciparum infected erythrocyte by dual-color near-field scanning optical microscopy. Proc Natl Acad Sci 94:520–525

Garcia-Parajo MF, Veerman JA, Segers-Nolten GM, de Grooth BG, Greve J, van Hulst NF (1999) Visualising individual green fluorescent proteins with a near-field optical microscope. Cytometry 36:239–246

Hecht B, Sick B, Wild UP, Deckert V, Zenobi R, Martin OJF, Pohl DW (2000) Scanning near-field optical microscopy with aperture probes: fundamentals and applications. J Chem Physics 112: 7761–7774

Hosaka S, Shintani T, Kikukawa A, Itoh K (1999) Evaluation of nano-optical probe from scanning near-field optical microscope images. J Microsc 194:369–373

Hwang J, Gheber LA, Margolis L, Edidin M (1998) Domains in cell plasma membranes investigated by near-field scanning optical microscopy. Biophys J 74:2184–2190

Jauss A, Koenen J, Weishaupt K, Hollricher O (2002) Scanning near-field optical microscopy in life science. Single Mol 3:232–235

Jenkins DFL, Cunningham MJ, Clegg WW, Bakush MM (1995) Measurement of the modal shapes of inhomogeneous cantilevers using optical beam deflection. Measur Sci Technol 6:160–166

Lei FH, Shang GY, Troyon M, Spajer M, Morjani H, Angiboust JF, Manfait M (2001) Nanospectrofluorometry inside single living cell by scanning near-field optical microscopy. Appl Phys Lett 79:2489–2491

Lewis A, Radko A, Ami NB, Palanker D, Lieberman K (1999) Near-field scanning optical microscopy in cell biology. Tren Cell Biol 9:70–73

Liu XJ, Tan WH (1999) A fiber-optic evanescent wave DNA biosensor based on novel molecular beacons. Anal Chem 71:5054–5059

Liu XJ, Farmerie W, Schuster S, Tan WH (2000) Molecular beacons for DNA biosensors with micrometer to submicrometer dimensions. Anal Biochem 283:56–63

Lu NH, Lin WC, Tsai DP (2001) Tapping-mode tuning-fork near-field scanning optical microscopy of low power semiconductor lasers. J Microsc 202:172–175

Nagy P, Jenei A, Kirsch AK, Szollosi J, Damjanovich S, Jovin TM (1999) Activation-dependent clustering of the erbB2 receptor tyrosine kinase detected by scanning near-field optical microscopy. J Cell Sci 112:1733–1741

Valaskovic GA, Holton M, Morrison GH (1995) Parameter control, characterization, and optimization in the fabrication of optical fiber near-field probes. Appl Optics 34:1215–1228

Vo-Dinh T, Kasili P (2005) Fiber-optic nanosensors for single-cell monitoring. Anal Bioanal Chem 382:918–925

Vo-Dinh T, Alarie JP, Cullum BM, Griffin GD (2000a) Antibody-based nanoprobe for measurement of a fluorescent analyte in a single cell. Nature Biotechnol 18:764–767

Vo-Dinh T, Griffin GD, Alarie JP, Cullum BM, Sumpter B, Noid D (2000b) Development of nanosensors and bioprobes. J Nanoparticle Res 2:17–27

Changes of Biological Function of Bone Cells and Effect of Anti-osteoporosis Agents on Bone Cells

Hong-Fu Wang (✉), Weif-Ang Jin, Jian-Jun Gao, and Hui Sheng

Department of Bone Metabolism, Institute of Radiation Medicine, Fudan University, Xietu Rd. 2094, Shanghai 200032, China
e-mail: hfwang@shmu.edu.cn

Abstract

Osteoporosis is a disorder of bone remodeling in adults, which results from decreased bone formation and/or increased bone resorption. Osteoblast and osteoclast are two major functional cells involved in bone remodeling. Based on the understanding of normal biological functions of bone cells, many traditional western anti-osteoporotic agents and some alternative Chinese herbs were tested with in vitro cultured osteoblasts and osteoclasts. The results showed that diphosphonate (Ibandronate), calcitonin (Elcatonin) and kidney-tonifying herb preparations could greatly inhibit the resorption activity of osteoclasts including decreased TRAP-positive multinucleated osteoclasts, inhibited resorption pits on dentine and osteoclast fusion index, and increased osteoclasts apoptosis, whereas rhPTH(1-34), calcitonin (Miacalcic) and Chinese herb extract *Jinjier* could significantly enhance bone-forming activity of osteoblasts including increased osteoblast proliferation, enhanced ALP activity and mineralization capability. This indicates that the established in vitro bone cell models, including osteoblasts and osteoclasts, provide a rapid and effective screening strategy for anti-osteoporotic agents.

Introduction

Bone maintains its mass and structure by constant bone remodeling in adults. Bone remodeling, as a process of bone turnover, includes the removal of old bone and subsequent formation of new bone. This process is initiated in response to physiological or pathological changes including injuries, fatigue stresses, aging, inflammations and metabolic needs. Bone-forming osteoblasts and bone-resorbing osteoclasts are coupled functionally to keep the homeostasis of bone metabolism. The biological activity of osteoblasts and osteoclasts are modulated by systematic hormones including parathyroid hormone (PTH), vitamin D, calcitonin and leptin, and by local factors including insulin growth factor (IGF), transforming growth factor-β (TGF-β), bone morphogenetic protein (BMP), fibroblast growth factor (FGF), prostaglandin E2 (PGE2), interleukin (IL), receptor for activation of nuclear factor kappa B ligand (RANKL), osteoprotegerin (OPG), etc. (Deng and Liu 2005).

Physiological and pathological changes of bone influence the bone remodeling process, such as prolonged resorption phase, increased bone resorption, extended reversal phase and suppressed bone formation. This results in bone loss, microarchitecture deterioration and matrix mineralization disturbance, and eventually leads to osteoporosis and osteoporotic fracture. Osteoporosis, by nature, is a kind of metabolic bone disorder due to abnormal bone remodeling (Raisz 2005; Seeman 2003). Although there are many factors involved in bone remodeling disorder, the bone-forming osteoblasts and bone-resorbing osteoclasts are the two main contributors (Recker 1996). Research at cellular level is of obvious importance for exploring the pathogenesis of osteoporosis and developing corresponding agents for prevention and treatment of osteoporosis. Based on the understanding of biological function of normal bone cells, this chapter focuses on the change of biological function of bone cells and the effects of anti-osteoporotic agents on bone cells.

Bone Cell Morphology and Their Biological Functions

Osteoclasts, osteoblasts and osteocytes are major functional cells in bone remodeling. The biological functions of bone cells play a key role in bone health. Bone cells are functional elements in constant bone remodeling, which maintain the flexibility and stiffness of bone as well as maintaining bone mass and microarchitecture.

Osteoclasts

Osteoclasts are bone-resorbing cells that are hematopoietic in origin. Mononuclear cells, also called colony-forming unit granulocyte/macrophage (CFU-GM), are osteoclast progenitors that differentiate into multinuclear osteoclast progenitors in the presence of mononuclear colony-stimulating factor (M-CSF). When osteoclast progenitors make contact with osteoblasts, they differentiate into mature osteoclasts. During this process, receptor activator of NF-KB ligand (RANKL) from osteoblasts interact with the receptor activator of nuclear factor kappa B (RANK) in osteoclasts. The osteoclasts then differentiate into functional mature osteoclasts (Fig. 1). The mature osteoclasts are recruited to bone-resorbing surface and the mononuclear osteoclasts then merge into multinuclear osteoclasts, acting as functional bone-resorbing osteoclasts (Boyle et al. 2003).
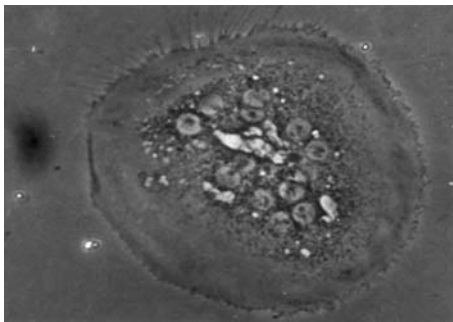
Figure 1. Phase-contrast micrograph of a rat osteoclast with several nuclei (× 200)

Osteoclasts are multinucleated giant cells with a diameter ranging from 20 to 100 μm. Osteoclast contains several to dozens of nuclei (Fig. 1). The nucleus is orbicular-ovate in shape and contains tiny and homogeneous chromatin, and one to two nucleoli. Osteoclasts are rich in mitochondrium, endocytoplasmic reticulum, glycogen granules, and also rich in vesicles and mineralized crystal phagocytotic vesicles (Fig. 2). Laser confocal microscopy may demonstrate dense microtubular structure within osteoclast (Fig. 3).

Osteoclast cytoplasm is acidophilia and stains positive for acid phosphatase (ACP; Fig. 4). Tartrate resistant acid phosphatase (TRAP) and tartrate-resistant acid adenosine triphotase (TrATP) are characteristic enzymes expressed by osteoclasts, which usually serve as osteoclasts markers after being stained cytochemically (Figs. 5, 6).
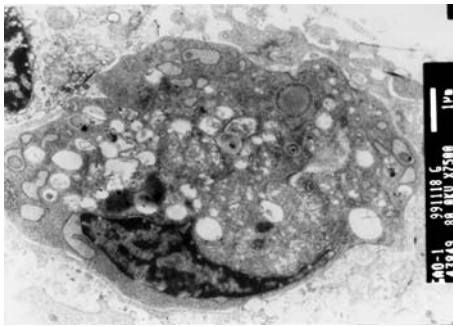
Figure 2. Ultrastructure of a rat osteoblast with nucleus (*N*), mitochondria (*M*), endoplasmic reticulum (*ER*), Golgi apparatus (*Go*), and phagosome containing hydroxyapatite crystal (*p*; SEM × 7500)
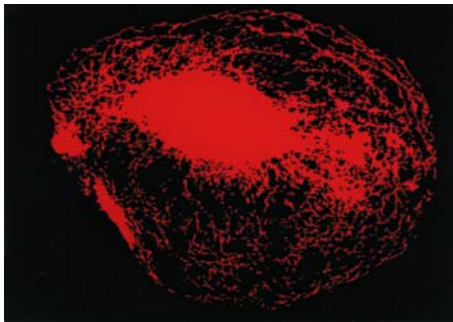
Figure 3. Laser scanning confocal micrograph of rhodamine labelled microtube within a rat osteoclast (× 400)

Figure 4. Rat osteoclast with red deposits stained by acid phosphatase (ACP; × 200)

Calcitonin receptor is also a unique marker of osteoclast, which stains positive immunocytochemically (Fig. 7; Lee et al. 1995; Lindunger et al. 1990).

The osteoclast is not only functionally a unique cell that specializes in degrading bone matrix; it also possesses distinct morphorlogical features that support its unique function. Ruffled border membrane, one of the distinguishing features of osteoclast, is a form of series of deeply interfolded finger-like projections of the plasma and cytoplasmic membranes adjacent to the bone surface. Another characteristic feature is called the clear zone (Fig. 8), which is the cell surface next to bone characterized by close apposition of the plasma membrane to bone and an adjacent, organelle-free area, which is rich in actin filaments. Ruffled border membrane and clear zone constitute characteristic bone-resorbing compartment. This instrument attaches closely to bone matrix by integrin.
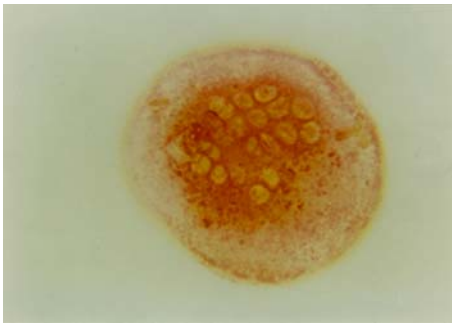
Figure 5. Rat osteoclast with red granules indicating intense reaction with tartrate-resistant acid phophatase (TRAP; × 200)

Figure 6. Rat osteoclast with dark brown granules stained by tartrate-resistant acid adenosine triphosphatase (TrATPase; × 200)

Figure 7. Rat osteoclast with calcitonin receptor stained by immunohistochemical method (× 200)
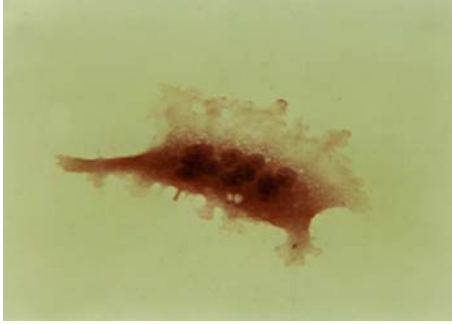
Figure 8. Micrograph of a rat femur-derived osteoclast stained by hematoxylin and eosin showing pseudopids, clear zone, and nuclei (× 200)
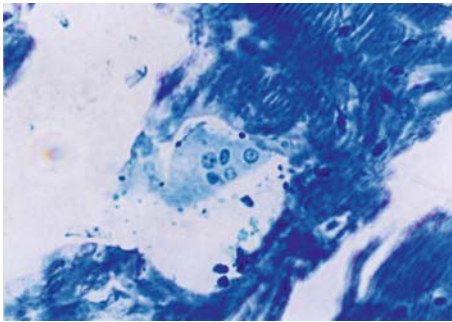
Figure 9. Micrograph of rat femur stained by toluidine blue showing the active osteoclast in lacuna (× 100)

Figure 10. Scanning electron microscopy of one wandering osteoclast after bone resorption (a lacuna formed on the right of the cell; × 1500)

Osteoclasts are rich in H^+ and lysosomal proteinase vesicles, which are released into bone-resorbing compartment via ruffled border membrane in terms of exocytosis. The secreted matrix metalloproteinases (MMPs), acidic proteinases and other proteinases degrade organic components of bone matrix including collagen protein. Osteoclasts keep a low pH (pH = 4.5) in the resorption compartment by H^+-ATPase
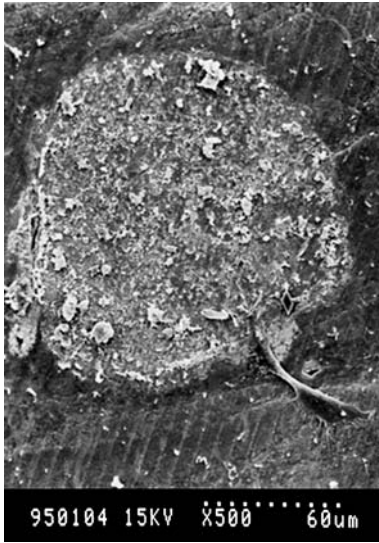
Figure 11. Scanning electron microscopy of an osteoclast with resorption lacuna, which was cultured 30 h on a bovine slice ($\times$ 500)
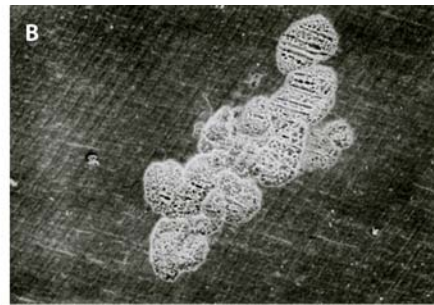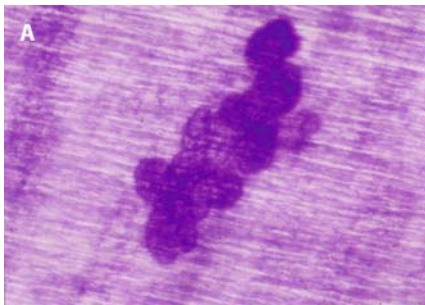
Figure 12. Lacunae on the dentine slice. **A** Observed by light microscopy stained with toluidine blue ($\times 200$). **B** Observed with SEM ($\times 500$)

transports protons and carbonic anhydrase, then degrade crystalline hydroxyapatite and release calcium [$Ca_{10}(PO_4)_6(OH)_2 + 8H^+ \rightarrow 6HPO_4^{2-} + 10Ca^{2+} 2H_2O$]. Osteoclasts cultured in vitro form resorption pits on dentine slices, and the active osteoclasts form a series of resorption pits (Figs. 9–12; Teitelbaum 2000; Vaananen et al. 2000).

Osteoblasts

Osteoblasts are bone-forming cells that are derived from osteoblast precursors or mesenchymal stem cells (MSCs). Bone envelopes covering the endosteum, periosteum, trabeculae, as well as the Haversian canals and Volkmann's canals are rich in osteoblast precursors. The MSCs are rich in bone marrow and other mesenchymal-derived tissues, which are multipotential stem cells and can be induced to differentiate between osteoblasts and adipocytes. The change of MSC activity, including the decreased number of MSCs and/or its priority differentiation into adipocytes,

is believed to be one of the important pathogenesis of osteoporosis associated with steroid and aging (Chen 2004; D'Ippolito et al. 1999; Walsh et al. 2001). For evaluation of MSC activity from different donors, the number of MSCs can be reflected by colony-forming unit fibroblastic (CFU-Fs) counting, which is believed to be derived from one mesenchymal stem cell (Castro-Malaspina et al. 1980). In addition, the change of differentiation potential into osteoblasts and adipocytes can also be evaluated in osteogenic or adipogenic culture medium in vitro (Fig. 13; Sheng et al. 2003; Yang et al. 2003). As a bone-specific transcript factor, the core-binding factor
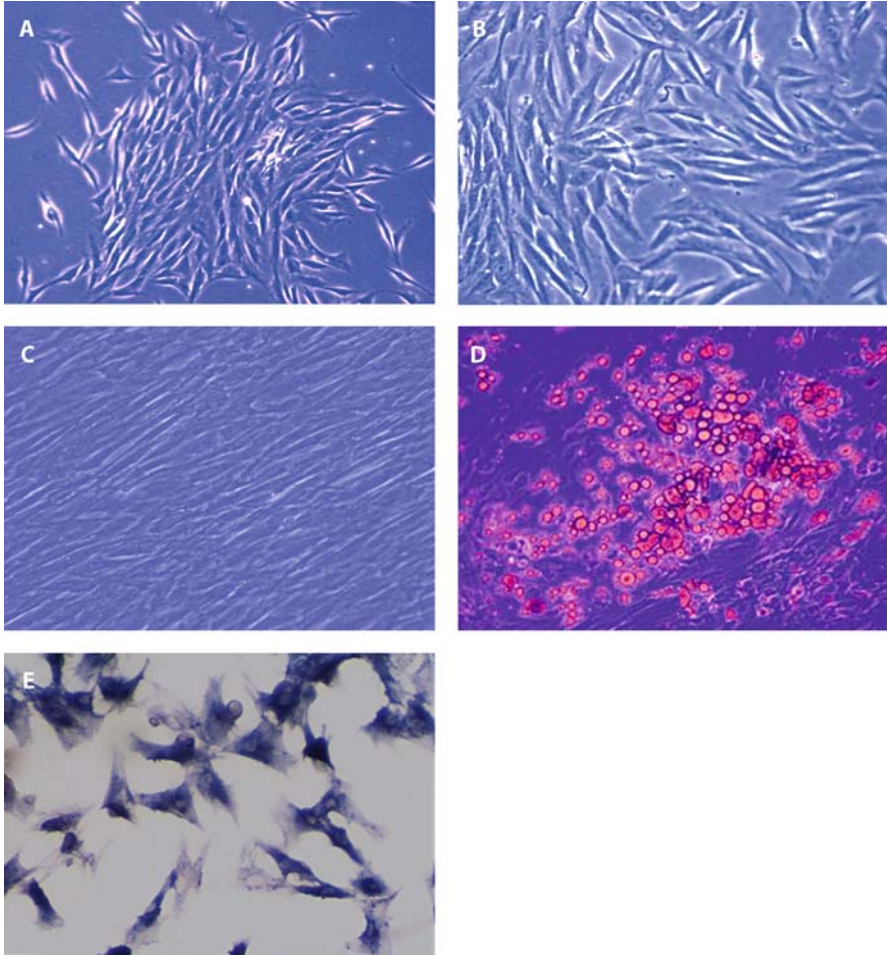
Figure 13 A–E. Micrographs of rabbit mesenchymal stem cells from bone marrow and their differentiation into osteoblast and adipocytes in vitro. **A** Colony of MSCs in 5 days (× 100). **B** Half confluence of MSCs in 9 days (× 100). **C** Confluent MSCs showing spindle shape (× 100). **D** Adipocyte-like cells formed after induction in adipogenic medium. Lipid droplets stained positive with Oil Red O (× 100). **E** Osteoblast-like cells formed after induction in osteogenic medium. Cytochemical staining showed positive staining for ALP (× 200)
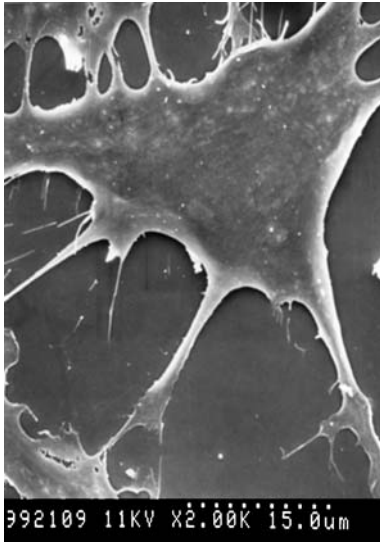
Figure 14. Scanning electron microscopy of a cultured rat osteoblast with protrusions (× 2000)

alpha-1 (Cbfa1) plays a key role in the process of MSC differentiation into osteoblasts, in bone development and maturation as well. Other factors involved in osteoblast differentiation and bone formation include BMP, TGF-β, IGF-1, platelet-derived growth factor (PDGF), FGF, and 1,25(OH)2D3 (Ducy et al. 2000; Karsenty 2001).

Functional active osteoblasts are cuboidal or cylindrical in shape and contain big and elliptic nucleus with one to two clear nucleoli. They are 20–50 μm in diameter with tiny and long projections connected to each other (Fig. 14). Osteoblasts proliferate through mitotic division growth (Figs. 15, 16).

Osteoblast cytoplasm is basophilic and rich in alkaline phosphatase (ALP). The ALP in cytoplasm stains black with Gomori method (Fig. 17) and stains red with nitrogen-couple staining (Fig. 18). The cytoplasm is also rich in mucopolysaccharide, which stains positive with periodic acid Schiff (PAS; Fig. 19). Osteoblast cytoplasm is also rich in rough endoplasmic reticulum, mitochondrium, ribosome, advanced Golgi's apparatus, as well as high-density particles, matrix vesicles, lysosomes, lipid droplet and glycogen granules (Fig. 20). Laser confocal microscopy may show F-actin skeleton framework of osteoblasts with red fluorescence after being marked with phalloidine (Fig. 21).

Osteoblasts are protein-secreting cells. Their secreted proteins play an important role in bone formation. One of them is collagen protein, which is the major component in osteoid (Fig. 22); another one is ALP, which is of great importance in bone mineralization. During the process of mineralization, ALP reacts with phosphonolipid and releases inorganic phosphoric acid locally. The inorganic phosphoric acid then binds with calcium to form hydroxyapatite crystal and deposit between collagens, facilitating osteoid mineralization (Sugawara et al. 2002). Osteoblasts cultured in vitro in the presence of β-sodium glycerophosphate and ascorbate can form mineralized nodules, which show red calcium matrix after being stained with alizarin red (Fig. 23). Mineralized nodules are one of the main parameters indicating the bone-
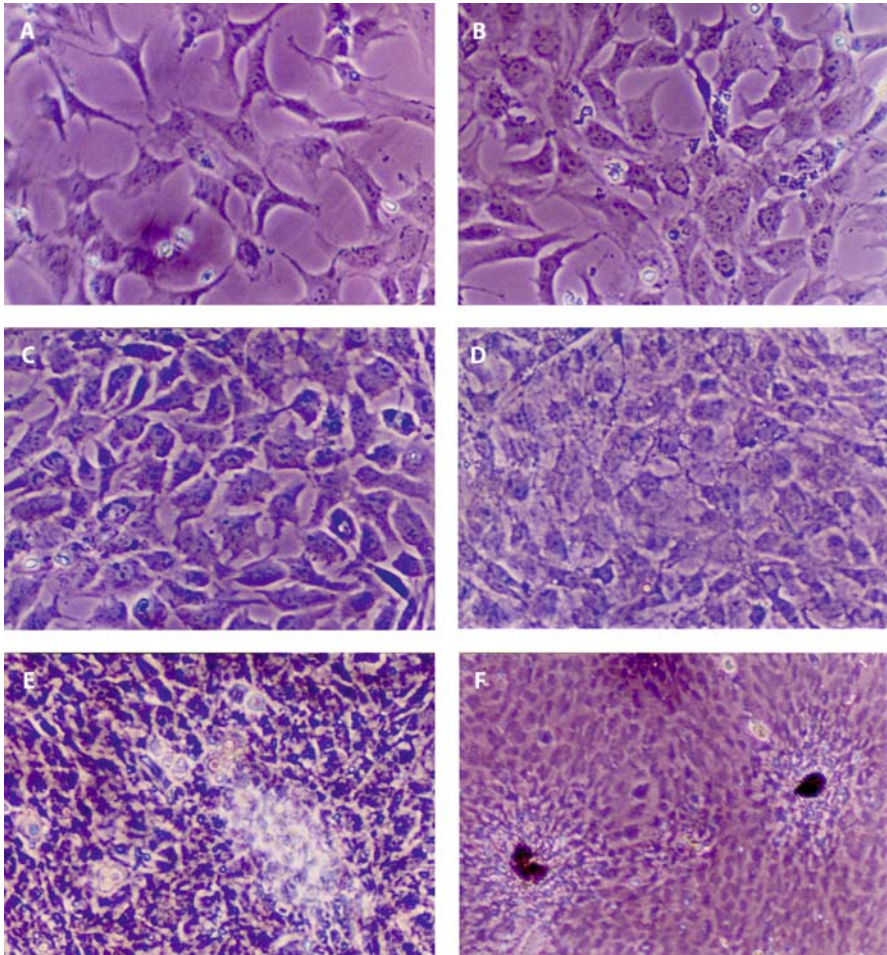
Figure 15 A–F. Phase-contrast micrographs of rat calvaria-derived osteoblasts in vitro. **A** Attachment and spreading in 1 day. **B** Proliferation in 3 days. **C** Half-confluence in 5 days. **D** Confluence in 7 days. **E** Merging in 9 days. **F** Matrix deposit in 12 days

formation function of osteoblasts. Many kinds of non-collagen proteins are also secreted by osteoblasts to regulate bone formation and bone remodeling including bone sialprotein, osteocalcin, bone morphogenic protein and osteonectin, IGF-1(2)TGF-β1(β2)PDGF(IL-6)RANKL and OPG (Nefussi et al. 1997).

There are many hormone receptors on osteoblast membrane, such as receptor of oestrogen, PTH, parathyroid hormone-related protein (PTHrp) and $1.25(OH)_2D_3$, growth factor (GH). These hormones and some agents regulate the function of osteoblast/osteoclast through corresponding receptors. Osteoblasts may enhance biological functions by releasing factors such as cyclic AMP (CAMP), ALP, IGF-1, and calcium in response to stimulating signals (Mundy 1996; Yu et al. 2002).
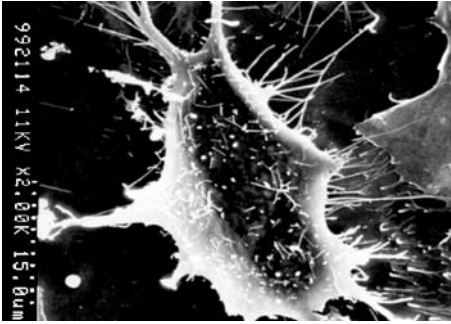
Figure 16. Scanning electron microscopy of a dividing osteoblast (× 2000)
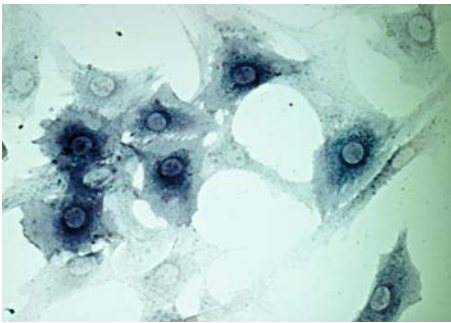
Figure 17. Rat calvaria-derived osteoblasts with black deposits in cytoplasm; cytochemical staining for ALP (Gomori method; × 200)
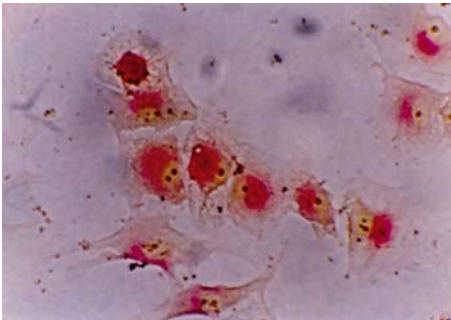
Figure 18. Rat clavaria-derived osteoblasts with red deposits in cytoplasm; cytochemical staining for ALP (nitrogen-couple staining; × 200)
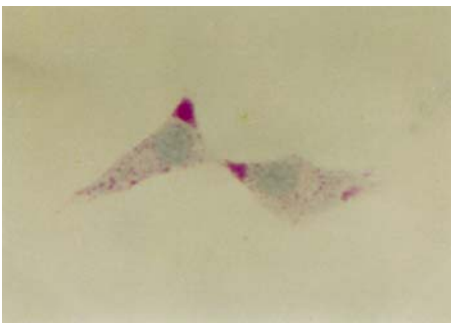
Figure 19. Rat calvaria-derived osteoblasts with red deposits in cytoplasm; cytochemical staining for pro-matrix (PAS staining; × 200)
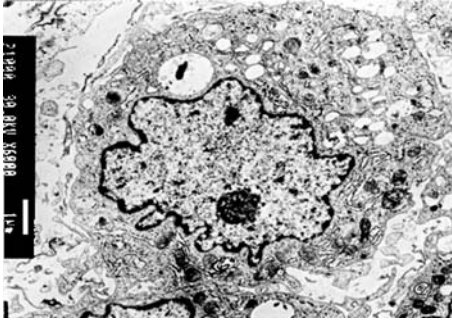
Figure 20. Transmission electron micrograph of one dissociative osteoblast (× 6000)
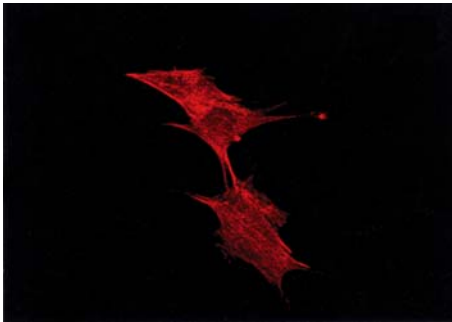
Figure 21. A confocal laser scanning micrograph of rat calvaria-derived osteoblasts with rhodamine-phalloidian stained F-actin (× 200)
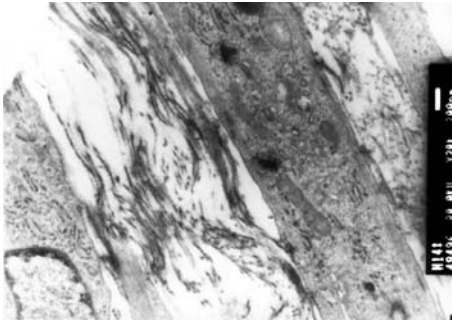
Figure 22. A transmission electron micrograph shows osteoblast and its secreted tropocollagen (× 20.00 K)

Figure 23. Light micrograph of mineralized nodes stained in red by ARS (× 40)

Bone Cell Responses to Anti-osteoporosis Agents

The pathogenesis of osteoporosis is related mainly to enhanced bone resorption of osteoclasts and/or inhibited bone formation of osteblasts in bone remodeling (Seeman 2003). This implies that the strategy for prevention and treatment of osteoporosis should focus on developing agents that could inhibit osteoclast differentiation, maturation and activation, and/or enhance osteoblast differentiation, proliferation and bone-forming function. With the establishment and perfection of bone cell in vitro culture and related biological function evaluation indices, screening of anti-osteoporotic agents has been greatly facilitated (Wang et al. 1999).

The following sections review the results of some anti-osteoporotic agents, including conventional western agents and alternative Chinese herbs using osteoblast and osteoclast in vitro culture model in the authors' laboratory.

Inhibition of Osteoclast Activity

Increased osteoclast activity leads to accelerated bone turnover, which results in deeper and wider resorption cavities, increased trabeculae perforation and deterioration, and porosity in cortical bone. These changes are typical findings in osteoporosis; therefore, inhibition of osteoclast activity will moderate or inhibit bone turnover, increase the reparative efficacy of resorption cavity and decrease bone loss.

Indices for evaluation of drug effects on osteoclasts in vitro include TRAP-stained positive cell counting, osteoclast fusion index, histomorphometry of bone resorption pits and ostoeclast apoptosis test. These parameters may comprehensively reflect the effects of drugs on differentiation, maturation, bone resorption capability and viability of osteoclasts (Gao et al. 2004; Wang et al. 1999, 2001). Results from our studies showed that agents, including diphosphonate, calcitonin and kidney-tonifying herbs, can significantly inhibit the bone resorption activity of osteoclasts (Gao et al. 2000, 2002; Jin et al. 1999, 2001).

Number of TRAP-Positive Multinucleated Osteoclasts

Osteoclasts inoculated on dentin slices were cultured in medium with agent for 24, 48, 72 and 120 h. Then the slices were stained with TRAP staining kit (Sigma). Cells stained positive for TRAP containing more than two nuclei were counted as osteoclasts under light microscopy. The inhibition rate at a certain time point = (TRAP-positive osteoclasts in control group minus TRAP-positive osteoclasts in drug group)/TRAP positive osteoclasts in control group ×100).

Ibandronate (National Key Laboratory, Institute of Nuclear Medicine, Jiangsu, China) inhibited the formation of osteoclasts in a dose-dependent manner. The osteoclast inhibition rates of Ibandronate at doses of 10^{-12}, 10^{-10}, to 10^{-8} M were 13.5, 33.6 and 71.3%, respectively ($p < 0.01$).

Elcatonin (Asahi Kasei, Japan) significantly inhibited the formation of TRAP-positive osteoclasts, and the inhibition rates for 1×10^{-9} M at different time points of 48, 96, and 144 h were 59.2% ($p < 0.01$), 33.3% ($p < 0.05$) and 27.2%, respectively ($p < 0.05$).

Table 1. The effects of Elcatonin on formation of TRAP-positive multinuclear and mononuclear osteoclasts

Culture time (h)	Multinuclear osteoclasts		Multinuclear osteoclasts	
	Control	Elcatonin	Control	Elcatonin
48	229.3 ± 39.2	93.5 ± 23.9^{a}	441.0 ± 67.1	458.3 ± 61.8
96	335.0 ± 30.1	223.3 ± 53.4^{b}	474.0 ± 69.3	502.0 ± 52.9
144	285.0 ± 57.7	207.5 ± 24.4^{b}	483.5 ± 61.2	399.8 ± 45.4

^{a} Mean $\pm$ SD
^{b} $n = 4$

Inhibition Rate of Osteoclast Fusion Index

Both mononuclear and multinuclear osteoclasts are stained positive for TRAP. The ratio of mononuclear and multinuclear osteoclasts is called osteoclast fusion index (OFI). Although mononuclear osteoclasts may also be stained positive for TRAP, they do not have bone-resorbing ability until fused into multinuclear osteoclasts. The osteoclast fusion index may therefore indicate the maturation of osteoclasts. The osteoclast fusion index at a certain time point = (osteoclast fusion index in control group minus osteoclast fusion index in drug group)/osteoclast fusion index in control group ×100).

Elcatonin at concentration of 1×10^{-9} M obviously inhibited the formation of TRAP-positive multinuclear osteoclasts, but did not show effect on the formation of TRAP-positive mononuclear osteoeclasts (Table 1). The osteoclast fusion indices were 0.2, 0.44 and 0.51 in Elcatonin-treated group and 0.52, 0.70 and 0.65 in control group at different culture time points of 48, 96 and 144 h; thus, the inhibition rates of osteoclast fusion index for Elcatonin were 61.5, 37.0 and 21.5% at culture time points of 48, 96 and 144 h, respectively.

Inhibition Rate of Osteoclast Resorption Pits on Dentine

Osteoclasts inoculated on dentine slices were cultured in α-MEM medium with drugs described below for 72 or 120 h. Then the dentine slices were processed and stained with 1% toluidine blue. The resorption pits were stained purple with clear border and rough bottom, showing different shapes, such as round shape, ellipse shape and allanto-like shape. The number and area of resorption pits were evaluated under light microscopy with Image-Pro Plus 5.1 software (Media Cybernetics). The osteoclast resorption pits identified under light microscopy were confirmed by scanning electron microscopy (SEM; Fig. 24; Gao et al. 1998).

Ibandronate inhibited the formation of resorption pits in a concentration-dependent manner. The inhibition rate at doses of 10^{-12}, 10^{-10} and 10^{-8} M were 31.6% ($p > 0.05$), 76.3%, ($p < 0.01$) and 88.0% ($p < 0.01$), respectively. The inhibition rates of Elcatonin at doses of 10^{-12}, 10^{-10} and 10^{-8} M were 28.6% ($p > 0.05$), 75% ($p < 0.05$) and 86.2% ($p < 0.01$), respectively.

The rat drug sera from three different kidney-tonifying herbal formulas, *Jinkuibushenwan, Zhibodihuangwan* and Prematin, were prepared and used to cul-
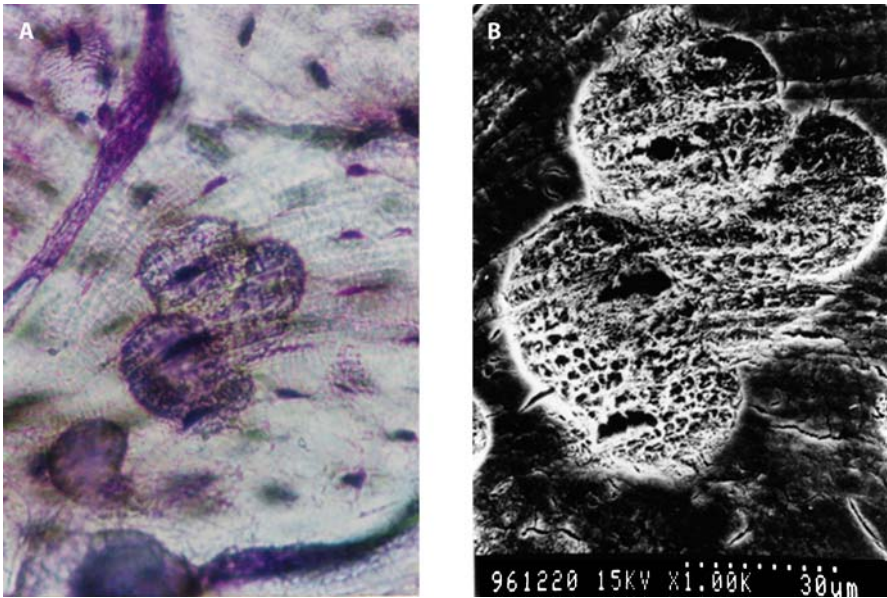
Figure 24 A,B. Lacunae on bovine slice. **A** Observed by light microscopy with toluidine blue staining (× 200). **B** Observed under SEM (× 1000)

ture ostoeclasts inoculated on dentine slices for 7 days. The resorption pits on dentine slices were then quantified. The mean inhibition rates for osteoclast resorption pits were 46.3% ($p < 0.05$), 77.3% ($p < 0.01$) and 50.8% ($p < 0.05$) in *Jinkuibushenwan*, *Zhibodihuangwan* and Prematin group, respectively.

Osteoclast Apoptosis Test

Apoptosis is the main fate of osteoclasts. The drugs described below, which induce osteoclast apoptosis, may decrease the number of osteoclasts and thus inhibit bone resorption. Apoptosis can be identified using fluorescent staining together with morphology feature, which is a fast, simple and reliable method to confirm apoptosis. Osteoclast apoptosis was identified on the basis of orange?red fluorescence, membrane shrinkage, broken or margined nucleus and apoptotic bodies (Fig. 25; Li et al. 1999).

Ibandronate-induced apoptosis of osteoclasts is dose dependent. For example, the apoptosis rates increased from 20.8 ± 4.0% in the control group to 22.5 ± 12.0% ($p > 0.05$), 33.5 ± 16.0% ($p < 0.05$), 52.0 ± 9.0% ($p < 0.01$) and 62.0 ± 23.0% ($p < 0.01$) in 10^{-10}, 10^{-8}, 10^{-6} and 10^{-4} M in the drug-treated groups, respectively.

Bone-Forming Effects of Osteoblasts

The decreased activity of osteoblasts also plays an important role in the pathogenesis of osteoporosis. Modalities are being explored as a hot topic to enhance bone-forming
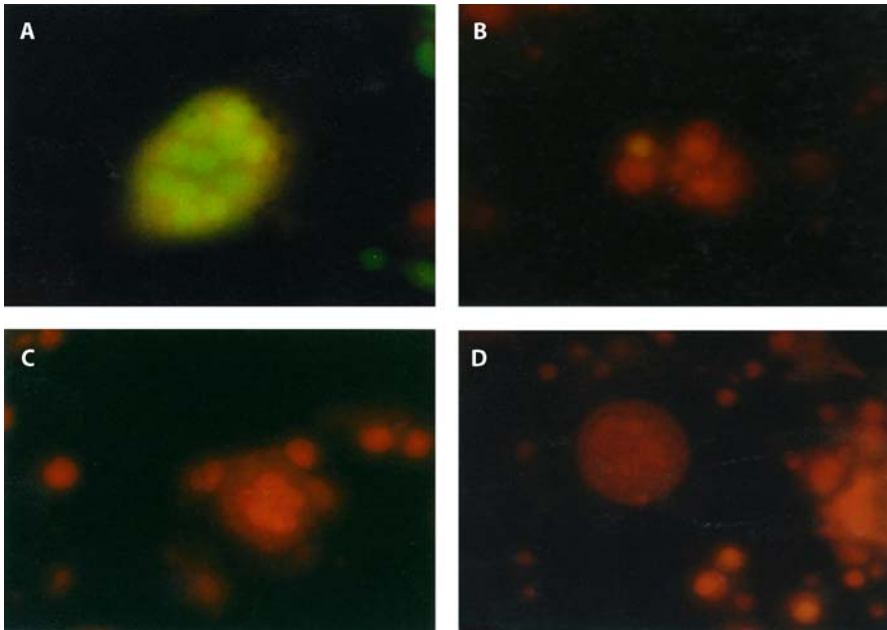
Figure 25 A–D. Fluorescent photomicrographs of osteoclasts stained by acridine orange show **A** normal cell, **B** a apoptotic cell, **C** apoptotic bodies, and **D** a necrotic cell ($\times$ 200)

activity of osteoblasts to increase osteoid secretion and mineralization rate, and to decrease resorption pits. The established in vitro parameters for evaluation of anabolic effects of anti-osteoporotic agents include osteoblast proliferation rate, ALP activity, mineralization quantification and cytokine measurements such as bone Gla protein (BGP), procollagen type-I carboxyterminal propeptide (PICP) and IGF-1 (Wang et al. 1999, 2001). Anti-osteoporotic agents, including rhPTH(1-34), calcitonin and herbs, have been studied in the authors' laboratory. The results showed that they all were able to significantly enhance the bone-forming functions of osteoblasts (Gao et al. 2002; Jin et al. 2001; Sheng 2003a,b).

Enhancement of Osteoblast Proliferation Rate

The MTT (3-(4,5-dimethylthiazol-2-yl)-2,5-diphenyltetrazolium bromide) method can be used to show the proliferation rate of osteoblasts in vitro. Osteoblasts were cultured in 96-cell plates with drug for 1–10 days. Absorbance value (OD) for the osteoblasts was measured dynamically using auto-microplate reader (Bio-Tek ELx800). The proliferation rate = (OD value in drug group minus OD value in control group)/OD value in control group $\times$ 100).

rhPTH(1-34) (Shanghai Zhongkeshenglongda Biotechnical Company, Shanghai, China) increased osteoblast proliferation in a dose-dependent manner. The results showed that the proliferation rate of rhPTH(1-34) increased by 3.4% ($p > 0.05$),

19.3% ($p < 0.001$), 22.7% ($p < 0.05$) and 39.9% ($p < 0.001$) at doses of 10^{-12}, 10^{-11}, 10^{-10} and 10^{-9} M, respectively.

Miacalcic (Calcitonin, Novartis, Switzerland) enhanced osteoblast proliferation rate by 17.9% ($p > 0.05$), 50.7% ($p < 0.05$) and 26.2% ($p > 0.05$), at doses of 10^{-12}, 10^{-10} and 10^{-8} g/l, respectively.

Herb extraction of *Jinjier* (Natural Herbs Lab, Pharmacy Faculty, Shanghai Medical University), containing mainly chrysophenine, showed stimulating effects on osteoblast proliferation. The osteoblast proliferation rates increased by 16.7% ($p < 0.05$), 25.6% ($p < 0.01$) and 32.3% ($p < 0.001$) at doses of 10^{-10}, 10^{-8} and 10^{-6} g/ml, respectively.

Enhancement of Osteoblast ALP Activity

The ALP secreted by osteoblast plays an important role in promoting osteoid mineralization. The ALP was expressed strongly in active osteoblasts. Osteoblasts were cultured in medium with drugs described in the following paragraph, and the ALP activity was measured by p-nitro-phenyl phosphate (PNPP) method, and normalized to total protein. The ALP activity = (ALP activity in drug group minus ALP activity in control group)/ALP activity in control group × 100).

rhPTH(1-34) increased ALP activity of osteoblasts. As compared with the control group, the ALP activity was increased by 13.0% ($p < 0.01$), 17.5% ($p < 0.01$), 27.1% ($p < 0.001$) and 44.6% ($p < 0.001$) treated with 10^{-12}, 10^{-11}, 10^{-10} and 10^{-9} M, respectively. For Miacalcic, the ALP activity of osteoblasts was increased by 28.4% ($p < 0.01$) at the concentration of 10^{-10} g/l.

Enhancement of Mineralization

Osteoblasts form mineralized nodules in vitro in the presence of ascorbate and β-sodium glycerophosphate. Mineral nodules can be stained positively with alizarin red and used as a parameter for mineralization capability of osteoblasts. Osteoblasts were cultured in vitro in the medium containing the drugs described below. Ascorbate and β-sodium glycerophosphate were added 10 days later. The mineralization nodules stained positively with alizarin red were quantified histomorphometrically. Mineralization capacity = (Number or area of mineralization nodules in drug group -Number or area of mineralization nodules in control group)/ Number or area of mineralization nodules in control group × 100).

In rhPTH groups the mineralization nodules were increased by 18.6 ($p < 0.01$), 65.8 ($p < 0.01$), 108.3% ($p < 0.01$) and 146.0% ($p < 0.01$) when treated at doses of 10^{-12}, 10^{-11}, 10^{-10} and 10^{-9} M respectively. This showed that rhPTH(1-34) enhanced osteoblast mineralization capacity in the tested doses. Mineralization nodules were also increased by 283% treated with Miacalcic at the dose of 10^{-10} g/l.

The herbal extraction *Jinjier* also increased the formation of mineralization nodules. The mineralization nodules were increased by 10.4, 7.9 and 13.5% ($p < 0.05$) at doses of 10^{-10}, 10^{-8} and 10^{-6} g/ml, respectively.

Conclusion

The drug effects of anti-osteoporotic agents have been successfully tested using established in vitro bone cell models, including osteoblasts, osteoclasts and mesenchymal stem cells. In-vitro cell models are rapid, effective and economic for drug screening; however, the efficacy of the drugs must be tested preclinically using in vivo experimental animal models, and clinically in patients, including multicenter clinical trails.

References

Boyle WJ, Simonet WS, Lacey DL (2003) Osteoclast differentiation and activation. Nature 15:423(6937):337–342

Castro-Malaspina H, Gay RE, Resnick G, Kapoor N, Meyers P, Chiarieri D, McKenzie S, Broxmeyer HE, Moore MA (1980) Characterization of human bone marrow fibroblast colony-forming cells (CFU-F) and their progeny. Blood 56:289–301

Chen TL (2004) Inhibition of growth and differentiation of osteoprogenitors in mouse bone marrow stromal cell cultures by increased donor age and glucocorticoid treatment. Bone 35(1):83–95

Deng HW, Liu YZ (2005) Current topics in bone biology. World Scientific Publishing, UK

D'Ippolito G, Schiller PC, Ricordi C, Roos BA, Howard GA (1999) Age-related osteogenic potential of mesenchymal stromal stem cells from human vertebral bone marrow. J Bone Miner Res 14(7):1115–1122

Ducy P, Schinke T, Karsenty G (2000) The osteoblast: a sophisticated fibroblast under central surveillance. Science 289:1501–1504

Gao JJ, Jin WF, Wang HF (1998) Osteoclast resorption activity evaluation by quantifying resorption pits on bone dentine under light microscopy. J Shanghai Med Uni 25 (1):71–73

Gao JJ, Li LB, Jin WF, Wang BC, Wang HF (2000) The effects of Ibandronate (BM210955) on osteoclasts activity and its related mechanism. J Shanghai Med Uni 27 (3):171–173

Gao JJ, Zhou Y, Gu SZ, Jin WF, Wang HF (2002) The effects of Elcatonin on in vitro osteoclasts activity. Chin J Osteoporosis 8 (3):248–249

Gao JJ, Gu SZ, Zhou Y, Jin WF, Wang HF (2004) The change of rat osteoclasts in number and biological functions with aging. Chin J Geriat 23(3):184–187

Jin WF, Gao JJ, Wang HF, Wang BC, Hu MY (1999) The effects of Ibandronate (BM210955) on in vitro osteoclasts resorption activity. Chin J Osteoporosis 5 (1):10–12

Jin WF, Zhu WQ, Wang HF, Luo HF, Hu CQ (2001) The effects of kidney-tonifying herb HU-ECS on osteoblasts proliferation, differentiation and mineralization. Chin J Osteoporosis 7(1):9–11

Karsenty G (2001) Minireview: transcriptional control of osteoblast differentiation. Endocrinology 142(7):2731–2733

Lee SK, Goldring SR, Lorenzo JA (1995) Expression of the calcitonin receptor in bone marrow cell cultures and in bone: a specific marker of the differentiated osteoclast that is regulated by calcitonin. Endocrinology 136(10):4572–4581

Li LB, Gao JJ, Jin WF, Wang HF (1999). Gamma(γ) radiation induced apoptosis of osteoclasts. J Radiat Res Radiat Proc 17 (1):45–47

Lindunger A, MacKay CA, Ek-Rylander B, Andersson G, Marks SC Jr (1990) Histochemistry and biochemistry of tartrate-resistant acid phosphatase (TRAP) and tartrate-resistant acid adenosine triphosphatase (TrATPase) in bone, bone marrow and spleen: implications for osteoclast ontogeny. Bone Miner 10(2):109–119

Mundy GR (1996) Regulation of bone formation by bone morphogenetic proteins and other growth factors. Clin Orthop Relat Res 324:24–28

Nefussi JR, Brami G, Modrowski D, Oboeuf M, Forest N (1997) Sequential expression of bone matrix proteins during rat calvaria osteoblast differentiation and bone nodule formation in vitro. J Histochem Cytochem 45(4):493–503

Raisz LG (2005) Pathogenesis of osteoporosis: concepts, conflicts, and prospects. J Clin Invest 115(12):3318–3325

Recker RR (1996) Bone remodeling abnormalities in osteoporosis. Osteoporosis. Academic Press, California, pp 703–712

Seeman E (2003) Invited review: Pathogenesis of osteoporosis. J Appl Physiol 95(5):2142–2151

Sheng H, Wang HF, Gao JJ, Jin WF, Gu SZ (2003a) The effects of different doses of dexamethasome on the differentiation of rat mesenchymal stem cells into osteoblasts. J Fudan Uni 30 (2):164–166

Sheng H, Wang HF, Zhu GY (2003b) Effects of rhPTH(1–34) on rat bone marrow stromal cells differentiation into osteoblasts. Chin J Bone Miner Res 1(2):56–58

Sugawara Y, Suzuki K, Koshikawa M, Ando M, Iida J (2002) Necessity of enzymatic activity of alkaline phosphatase for mineralization of osteoblastic cells. Jpn J Pharmacol 88(3):262–269

Teitelbaum SL (2000) Bone resorption by osteoclasts. Science 289:1504–1507

Vaananen HK, Zhao H, Mulari M, Halleen JM (2000) The cell biology of osteoclast function. J Cell Sci 113:377–381

Walsh S, Jordan GR, Jefferiss C, Stewart K, Beresford JN (2001) High concentrations of dexamethasone suppress the proliferation but not the differentiation or further maturation of human osteoblast precursors in vitro: relevance to glucocorticoid-induced osteoporosis. Rheumatol (Oxford) 40(1):74–83

Wang HF, Jin WF, Gao JJ (1999) The evaluation of anti-osteoporosis agents using in vitro osteoblasts and osteoclasts. Chin J Osteoporosis 5(2):58–62

Wang HF, Jin WF, Gao JJ (2001) An atlas of bone cells and cell culture techniques. Shanghai Scientific and Technical Publishers, Shanghai, pp 60–68

Yang X, Tare RS, Partridge KA, Roach HI, Clarke NM, Howdle SM, Shakesheff KM, Oreffo RO (2003) Induction of human osteoprogenitor chemotaxis, proliferation, differentiation, and bone formation by osteoblast stimulating factor-1/pleiotropin: J Bone Miner Res 18:47–57

Yu MX, Jin WF, Gu SZ, Wang HF (2002) The biological function change of human osteoblasts with aging. Chin J Endocrinol 18(2):116–119

Bone Histomorphometry in Various Metabolic Bone Diseases Studied by Bone Biopsy in China

Mei Zhu (✉) and Ming-cai Qiu

Division of Endocrinology, Tianjin Medical University Hospital, Tianjin 300052, China
e-mail:mingcaiqiu@sina.com.cn

We use this opportunity to review what we have done in the past 20 years in studying various metabolic bone disorders by bone biopsy. Before our investigation, the normal reference for bone histomorphometry had to be established as the basis for further study on bone quantity and bone quality from iliac crest biopsies of 259 normal Chinese subjects. Among them, there were 178 patients with minor orthopedic problems and 81 normal subjects who died suddenly. A total of 259 bone specimens was available for bone histomorphometric study.

In adults, bone consists of cortical and cancellous (trabecular) bone as well as bone marrow. The function of osteoclasts and osteoblasts in cancellous bone is controlled primarily by factors produced by adjacent bone marrow cells. Similar cells in Haversian systems of cortical bone are removed from the myriad of osteotropic cytokines that are produced by marrow mononuclear cells. Metabolic bone disease in adults is fundamentally a disorder of bone remodeling, which can be directly studied by performing histomorphometric analysis of undecalcified sections of trabecular bone from transiliac bone biopsies. Fluorochromes, such as tetracycline, can be given as tissue-time markers before the bone biopsy. The fluorescence of tetracycline uptake can be seen at the location where bone mineralization takes place near the cement line, showing a pattern of labels around the Harvasian canal within the normal cortex and trabeculae. There is newly formed osteoid on the mineralizing surface containing double tetracycline labels. With better staining and embedding technique, under fluorescent microscopy, measurement of the distance between the two labels can be performed as well as osteoid seams width on the same undecalcified section.

Illiac bone specimens were studied from 114 normal Chinese subjects. Bone quality depends not only on bone volume and its 3D structure. In our study, only MTPS among the three calculated parameters showed a significant difference between the two categories of females at difference ages. It suggests that MTPS might be a more sensitive parameter for predicting bone strength. It suggests that bone loss may be related to a sharp lowering of estrogen after menopause; thus, it is easier to understand why there are more compression fractures of vertebrae in females than in males. Bone dynamic parameters of normal subjects provide a basis for studying metabolic bone disorders. In this work, 62 normal Chinese subjects with age range of 22–60 years were divided into several groups on the basis of gender and age, including 28 women and 34 men. The possibility of a metabolic bone disorder had been ruled out before the experiment was started. On a specially designed schedule of 3-11-3-5 days double tetracycline labeling was undertaken and bone biopsies were performed below the

crest. The bone blocks were pre-stained with Villanova bone stain for 72 h and 10 µm undecalcified sections were made. Some of the sections were further stained with 1% toludine blue. By light and fluorescent microscopy, the trabecular dynamic parameters were evaluated. On Villanova bone-stained section, the old mineralized bone was slightly green and the new bone showed dark staining. The osteoid was red and easy to differentiate from mineralized bone. The results indicated that there was a difference between male and female in mean osteoid seam width which was higher in males than females, but no significant difference was found between the two groups. It was probably caused by the imbalance of intrinsic hormone.

Bone mass changes with age. Bone mass reaches a peak in young adult life, but then steadily declines in both men and women. In women there is a rapid phase of bone loss, which is associated with estrogen withdrawal and lasts for about 10 years after menopause. The two critical determinants of bone mass are peak bone mass and rates of bone loss after mid-life. Since women have lower peak bone mass than men and lose bone rapidly because of estrogen withdrawal, bone mass in later life is less than it is in men. Loss of bone with age is a universal phenomenon in humans, the bone marrow cavity becomes larger, the cortex becomes thinner, and the trabeculae become decreased in number and size. Bone is lost mostly from the endosteal surface. The number of remodeling sites on the corticoendosteal or trabecular bone surface does not increase with age, nor does the ratio of resorption to formation site. The appositional rate and the tissue-level bone formation rate decreases, and so does the bone turnover rate. From these observations it has been concluded that age-related bone loss results from the summation of minute negative bone balances occurring within each individual microscopic site of bone turnover on the endosteal surfaces implying a preferential recruitment of osteoclasts over osteoblasts or in impairment of osteoblast function. A progressive loss of bone from the endosteal surface, however, leads to a second mechanism which accelerates or amplifies the first and renders the bone loss irreversible. As the plates and trabeculae become thinner than the depth of the resorption thrust, circular defects in the trabeculae occur and it is too extensive to refill again with new bone. In time, they add to a substantial net loss of trabeculae bone and to erosion or trabeculation of the cortex.

Osteoporosis is a metabolic bone disease in which there is both a decrease in the amount of normally mineralized bone and disturbance in bone microarchitecture, with a consequent increase in bone fragility and susceptibility to fractures. The abnormalities in patients with osteoporosis include thinning and fragmentation of the trabecular bone plates; endosteal bone resorption leading to decreased cortical bone width and increased porosity of the Haversian canals. Bone loss associated with advanced age and estrogen deficiency in women is accompanied by a disturbance of bone microarchitecture. There is focal perforation of cancellous bone plates caused by osteoclastic resorption, leading to loss of connectivity of these plates and the presence of unconnected vertical rods and bars dispersed throughout the marrow cavity. The static and dynamic histomorphometric data collected from iliac bone biopsies do not differ greatly between subject with osteoporosis and the rest of the aging population. Some researchers consider osteoporosis to be an extension of physiological bone loss to the point of fracture, a quantitative but not qualitative difference from aging.

In addition, we found a case of T1VDDR, a young girl at the age of 18 years, who was mistakenly diagnosed as having idiopathic osteoporosis or hypophosphotamic rickets because of the low phosphate in the serum while ALP was significantly elevated. On the other hand, 25OHD3 and 1.25(OH)2D3 were extremely low. The disease was so severe that the girl could not move at all. Kidney and muscular biopsies showed that there was plenty of immunoglobulin and complex deposition. On pathological evidence, vitamin D3 was injected while prednisone was initiated. After treatment for 3 months, the girl could walk and even ride a bike while bone density was doubled. Now the patient is getting increasingly better. This suggest that bone loss in young patients may be related to autoimmune damages to multiple organs, especially to the renal tubules which is a location used to biosynthesize 1,25(OH)2D3, a critical hormone for bone quality.

Cell Traction Force Microscopy

James H.-C. Wang (✉) [1], Jeen-Shang Lin[2], and Zhao-Chun Yang[1]

[1] MechanoBiology Laboratory, Departments of Orthopaedic Surgery, Bioengineering, and Mechanical Engineering, University of Pittsburgh, Pittsburgh, PA 15213, USA
e-mail: wanghc@pitt.edu

[2] Department of Civil and Environmental Engineering, University of Pittsburgh, Pittsburgh, PA 15213, USA

Abstract

Cell traction forces are vital for many biological processes, including angiogenesis, inflammation, wound healing, and metastasis. The study of cell traction forces enables us to better understand the mechanisms of these biological processes at the cellular and molecular levels. Because of the small size of a cell and low magnitude of cell traction forces ($\sim 10\,\mathrm{nN}$), it is a daunting task to determine cell traction forces reliably and accurately. In this chapter we review the current methods for determining cell traction forces, with special focus on a new technology for cell traction force microscopy (CTFM) we have recently developed. We conclude this chapter by discussing possible areas for improvement in CTFM and also suggesting potential applications of this technology.

Introduction

Cells in culture are typically anchorage dependent, which means that they must adhere to a solid substrate to survive and grow (Ruoslahti and Reed 1994). These adherent cells develop tension via actomyosin interactions inside cells. The cellular tension is transmitted to the underlying substrate through focal adhesions (FAs) located on the substrate and linked with actin stress fibers inside the cell (Balaban et al. 2001). This tensile force is referred to as cell traction force (Fig. 1). Cells use traction forces to organize extracellular matrix, maintain cell shape, probe physical environments, and generate mechanical signals (Pelham and Wang 1997); therefore, the ability to measure and characterize cell traction forces is crucial to a better understanding of cellular and molecular mechanisms of many fundamental biological processes, including embryogenesis, angiogenesis, wound healing, and metastasis.

It is known that cell traction force at a single FA is $\sim 10\,\mathrm{nN}$ (Balaban et al. 2001; Burton et al. 1999; Tan et al. 2003). The magnitude of cell traction force, however, varies from one cell type to another. Even within the same cell type or the same cell, various conditions such as substrate properties (e.g., stiffness), cell shape, and growth cycle can affect the cell traction force. As a result, it is a technically challenging task
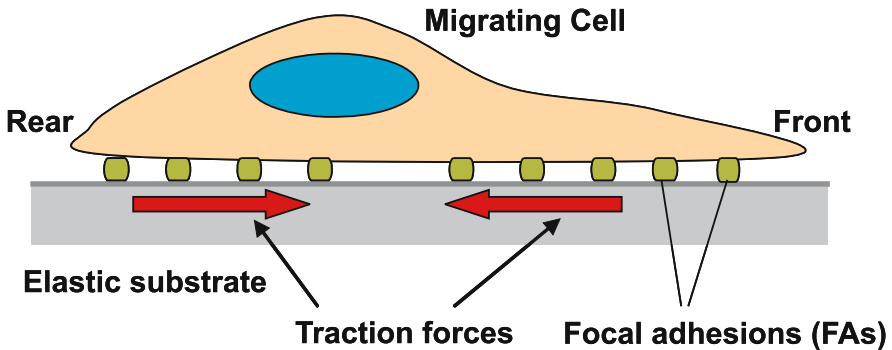
Figure 1. An illustration of cell traction forces. The forces are the cell tension that is generated by actomyosin interactions and transmitted to underlying substrate through focal adhesions

to determine cell traction force reliably and accurately. Herein we review the current methods used for determining cell traction forces, with a focus on the method of cell traction force microscopy (CTFM).

Techniques for Determining Cell Traction Forces

Various methods have been developed to measure cell traction forces; among the earliest was cell-populated collagen gel (CPCG; Bell et al. 1979). In this method, cells are mixed with liquid collagen to form a polymerized gel disk. When the cells inside the gel generate traction forces, the gel contracts, decreasing the gel's diameter (Campbell et al. 2004; Moon and Tranquillo 1993). Cell traction forces from a population of cells are estimated by measuring the change in the diameter of the gel disk. This approach is only semi-quantitative, and hence cell force monitor was later developed to quantify mechanical forces generated by the CPCG through the use of strain gauges (Campbell et al. 2003; Delvoye et al. 1991); however, even such a modification still falls short of actually measuring traction forces of individual cells (Ferrenq et al. 1997); instead, it measures gel contraction caused by the "averaged" traction forces of the embedded population of cells. As the embedded cells actively remodel the collagen gel, the rigidity, composition, and number of cells keep changing in complex ways, which prevents the CPCG approach from determining traction forces of individual cells in a controlled manner.

Another technique developed shortly after the CPCG approach was the use of a poly-dimethylsiloxane (PDMS) membrane floating in growth medium (Harris et al. 1980). In this technique, cell traction forces are made "visible" because cells generate wrinkles on the PDMS surface during locomotion. Although this approach is qualitative in nature, it has led to the development of various substrate methods for quantitative measurement of cell traction forces. For example, using the same silicone membrane approach, traction forces generated during cytokinesis of individual cells can be estimated using a calibration technique that uses a flexible micro-needle to reverse the wrinkles on the PDMS surface (Burton and Taylor 1997); however, because

wrinkling poses a highly nonlinear problem, there is currently no known mathematical method to quantify the wrinkles caused by a complex, non-isotropic cell traction force field.

Years later, a micro-machined substrate in which cantilevers were etched was developed to measure cell traction forces (Galbraith and Sheetz 1997). This approach uses an array of cantilever beams with calibrated stiffness, and these cantilevers allow cell traction forces to be determined quantitatively; however, the approach can only determine the force in one direction and still cannot measure the complex, non-isotropic traction force field within the entire cell-spreading area. This problem was solved using flat substrates with embedded markers (fluorescent beads; Pelham and Wang 1997), and this effort eventually brought about the development of CTFM. We discuss this technology in detail in the following section.

Micro-patterned elastomer has been used in the CTFM method (Balaban et al. 2001). Strictly speaking, the micro-patterned elastomer does not provide a complete flat substrate, as its surface consists of micro-dots ($0.3\,\mu m$ high) that modulate the surface topography. These dots serve as markers, thereby allowing the substrate deformation to be determined by analysis of phase-contrast images, while the site of each FA is located by vinculin labeled with green fluorescent protein (GFP). The traction force at each FA can then be obtained by using elasticity theory to solve an inverse problem. This method is elegant in its combined use of elasticity theory and GFP labeling technology to obtain cell traction forces. Its advantage is that the displacement can be readily quantified without too much effort; however, there are also major disadvantages, which include: (a) the GFP gene has to be introduced into cells by transfection, making this method both technically demanding and time-consuming; and (b) the transfection effect on cellular generation of traction forces is uncertain. Moreover, the elastomer is much stiffer: its Young's modulus varied between 12 and $1000\,kPa$, as the ratio of the silicone elastomer to curing agent varied from 50:1 to 10:1 (Schwarz et al. 2002). While the stiffness of the silicone membrane cannot be adjusted low enough to sense small substrate deformations, poly-acrylamide gel (PG), in contrast, can be made more compliant. By changing the proportions of acrylamide and bis-monomers, its Young's modulus may vary from 1.2 to $100\,kPa$ (Butler et al. 2002; Wang and Pelham 1998). In addition, the PG substrate is highly elastic, transparent, mechanically stable, and easy to prepare; therefore, it is the most commonly used substrate for CTFM.

Cell Traction Force Microscopy

There are currently three cell traction force microscopy (CTFM) methods that use elastic PG substrate in measuring cell traction forces. These procedures have been developed by Dembo and Wang (1999), Butler et al. (2002), and the authors (Yang et al. 2006), respectively. The CTFM methods involve three major steps. The first step is to fabricate elastic PG substrate with a flat surface. The next step is to obtain a pair of "null force" and "force loaded" microscopy images, from which the displacement field can be determined based on the movement of markers on the surface of the PG

substrate. In the final step, the substrate deformation is used to compute cell traction forces. The three CTFM methods have the first step in common but differ in how they carry out the second and third steps.

Fabricating PG Substrate

In the CTFM method, an acrylamide/bis-acrylamide mixture with a pre-determined acrylamide to bis-acrylamide ratio is added to a pretreated cover-glass of a circular dish after being mixed with fluorescent micro-beads. The mixture is then covered with a small, circular cover-glass and turned upside down to assure that the micro-beads move to the surface of the cover-glass by gravity.

After the mixture has solidified to form a small gel disk, HEPES is added to the gel surface to allow a matrix protein to be conjugated. Following exposure to ultraviolet light and the removal of Sulfo-SANPAH solution, the dish is washed. The gel is then coated with collagen type I.

Determining Substrate Displacement Field

Several separate cells on the PG substrate in each dish are chosen for imaging at different time intervals using a CCD camera system on an inverted microscope. This yields "force loaded" images. Then, the cells in the dish are detached by trypsinization, and an image of the same location is taken. This is denoted as the "null force" image. These images are then used to determine substrate displacement field.

The underlying principle for determining the displacement field is to locate the positions of the fluorescent micro-beads near the transparent substrate surface. By locating the micro-beads in the images taken before and after straining PG substrate, micro-bead movements can be determined. These changes in position provide the basis for deriving the substrate displacement field. Micro-beads are brighter than the background in the images and can be identified in theory through the brightness contrast in a given image. Each pixel on an image has a Gray value characterized by an 8-bit integer. The higher the Gray value, the brighter is the pixel. Figure 2 shows a tendon fibroblast on PG substrate (a) and a pair of "null force" (b) and "force loaded" (c) image samples.

The process of determining the substrate displacement field is complicated by the fact that there are several thousand micro-beads present in each image. Dembo and Wang (1999) and Butler et al. (2002) methods rely on the similarities in local contrast between a pair of images to identify substrate deformation. Of particular interest is the "optical flow" algorithm (Marganski et al. 2003). One starts by setting a grid on the "null force" image. For each grid point, a small patch of pixels surrounding the point is selected, and the contrast correlation of this patch with a corresponding patch in the "force loaded" image, within a predefined range, is computed. The two patches that have the highest correlation are considered a match, and the displacement for a grid point is calculated from the coordinates of the centers of the matched patches. The procedure is repeated with a finer grid and smaller search range until the target search range is reached.
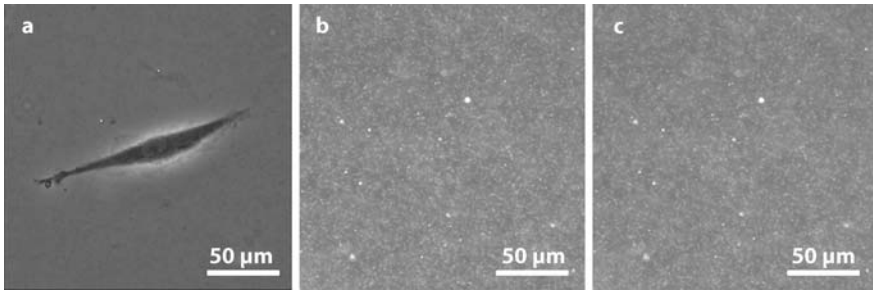
Figure 2. A tendon fibroblast on the elastic polyacrylamide gel (**a**). Fluorescent bead images before cell detachment (**b**). Fluorescent bead image after cell detachment (**c**). (The beads appear as fine white dots in the two images.)

We have developed a different procedure in which the movement of an individual micro-bead is identified (Yang et al. 2006). This procedure first distinguishes a bead from its background by applying a local threshold over an image. A pixel whose Gray value is higher than the local threshold is turned into 1, and 0 otherwise. In the connected "1" pixels of this converted binary image lie the micro-beads. We limit the potential micro-beads to be connected to clusters with sizes between 4 and 8 pixels. After this process is carried out on both "null force" and "force loaded" images, a line search is initiated to match beads from the two images. The range of search is guided by the expected strain levels due to cell traction forces on the PG substrate. For the sample image pair, the derived displacement field obtained with this procedure is presented in Fig. 3.

max. displacement = 1.57 μm
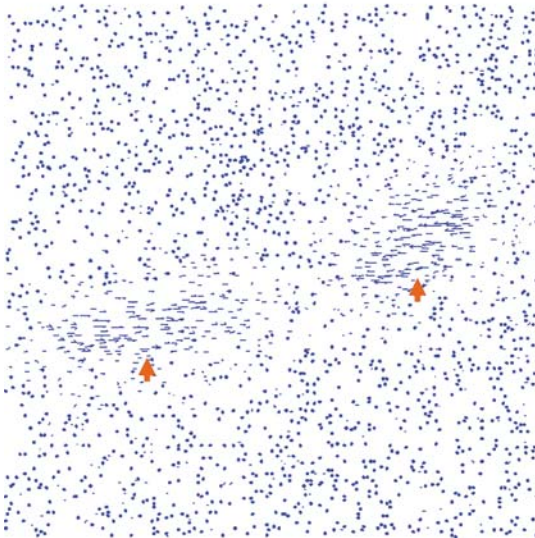
Figure 3. The substrate displacement field determined by our new algorithms. Note the larger displacements that concentrate around the front and rear ends of the cell (*arrows*) compared with the rest of the area

Determining Cell Traction Forces

Determining cell traction forces involves a solution to an inverse problem: Given the measured displacements, solve for the cell traction forces that cause them. Depending on how a problem is formulated, an inverse problem may be ill-posed. According to Hadamard (Lavrentev et al. 1986), a problem which fails to meet all the following conditions is ill-posed: (a) a solution always exists; (b) the solution is unique; and (c) the solution to the problem depends continuously on the data of the problem. The last condition basically requires a system to be stable and that a small perturbation in the displacement measurements should not induce a large variation in the resulting forces. An ill-posed problem may be solved with the aids of regularization.

To solve an inverse problem, one also needs a forward model. Both, the Dembo and Wang (1999) and Butler et al. (2002) methods, use the Boussinesq analytical solution (Landau and Lifshitz 1986) as the forward model. The Boussinesq solution gives the surface displacement of an infinite half-space due to a point surface load. Considering the finite thickness of the PG substrate used, this approximation may introduce modeling errors. Given a point load, the Boussinesq solution gives a larger displacement than its counterpart that considers actual substrate thickness. Conversely, given a displacement, the Boussinesq solution projects a smaller force. To address this concern, our procedure uses three-dimensional (3D) finite elements and takes into account the actual thickness of a substrate (Yang et al. 2006).

In applying the Boussinesq solution, the expected displacement at any point, x_j, of an elastic substrate due to n cell traction forces can be expressed in a general discrete convolution form as follows:

$$\mathrm{d}(x_j) = \sum_{i=1}^{n} G(x_i - x_j) \cdot F(x_j) , \tag{1}$$

where $F(x_i)$ is a point force acting at x_t, and $G(x_i - x_j)$ represents the forward model that computes the displacement at x_j due to a unit force at x_i. The convolution can also be written in a matrix form as follows:

$$[A]\{F\} = \{d\} \quad where \quad A_{i,j} = G(x_i - x_j) . \tag{2}$$

If $[A]$ is a full rank matrix, $\{F\}$ can readily be found by simple inversion. This is basically the approach Butler et al. (2002) take. It poses the forward convolution equation in the frequency domain and obtains the inversion through inverse Fourier transform. To conduct the computation in the frequency domain, Butler et al. (2002) consider both the force points and the displacement points to reside on a regular grid. A back substitution of forces obtained from inversion does not give back the input displacement, and the method carries out iteration until the forces in the interior of a cell converge.

The Dembo and Wang (1999) method, on the other hand, first covers the interior of a cell with a mesh, and the goal of its inverse problem is to find the unknown forces at these mesh nodes. The method enables the incorporation of subjective a priori error information, and obtains the forces through Bayesian a posteriori statistics

(Dembo et al. 1996). The method is flexible and allows the number of measured displacements used to be much greater than that for the forces. Regularization is required to guarantee a stable solution, and that results in an intensive computation with a high computational cost.

In an FEM formulation, forces are often known and displacements are to be found. The adoption of adequate interpolation functions and the subsequent application of weighted residual (Zienkiewicz et al. 2005) relate the stiffness matrix $[K]$ with the force vector $\{F\}$ as follows:

$$[K]\{d\} = \{F\} \tag{3}$$

This makes the computation of forces a forward process. In our procedure of applying 3D FEM in obtaining cell traction forces, an FE model is first built using a regular lattice. The Dirichlet boundary condition of zero displacement, or the fixed boundary condition, is imposed on all the nodes at the base of the substrate. The rest of the nodes that do not directly contact the cell are assigned the free traction boundary condition, whereas the nodes that are in direct contact with the cell are prescribed with the known measured displacements. By expressing the displacements at the traction-free nodes as a function of those at the prescribed displacement nodes, the cell traction force can be obtained through multiplication as follows:

$$\{F'\} = [K']\{\hat{d}\} , \tag{4}$$

where $\{\hat{d}\}$ represents the measured displacements and $\{F'\}$ the corresponding cell traction forces.

We applied this procedure for the displacement field depicted in Fig. 3; the traction forces so obtained are summarized in Fig. 4. This force calculation took less than 1 min using a 1.2-GHz Pentium PC.
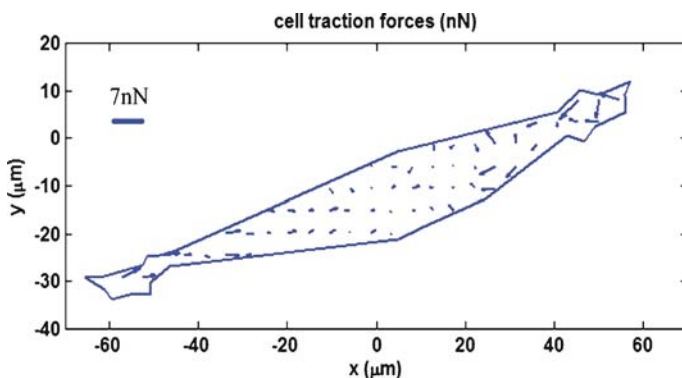
Figure 4. The cell traction forces determined by finite element analysis based on the estimated displacement field

Conclusion

The past decade has seen significant advances in the quantification of cell traction forces. The use of compliant elastic substrate is an attractive approach, and major issues associated with the inverse problem posed by this approach have mostly been resolved; however, further refinements are needed to reduce errors, improve efficiency, and maintain consistency. An exciting task ahead would be to improve the current CTFM technology such that automation and real-time tracking of cell traction forces may be achieved, thereby providing new insights into cell behavior, such as migration. Also, it would be an exciting challenge to explore ways to extend the current CTFM technology to determine traction forces of cells within 3D matrices in addition to 2D substrates.

In addition, it is known that cell traction forces are generated by actomyosin interactions, and both cellular components, actin and myosin, are involved in almost all cellular biological processes; therefore, cell traction forces likely alter in response to biological, biochemical, and biomechanical stimuli, and as a result, they may serve as a useful "biophysical marker" to characterize cell phenotypic changes.

References

Balaban NQ, Schwarz US, Riveline D, Goichberg P, Tzur G, Sabanay I, Mahalu D, Safran S, Bershadsky A, Addadi L, Geiger B (2001) Force and focal adhesion assembly: a close relationship studied using elastic micropatterned substrates. Nat Cell Biol 3(5):466–472

Bell E, Ivarsson B, Merrill C (1979) Production of a tissue-like structure by contraction of collagen lattices by human fibroblasts of different proliferative potential in vitro. Proc Natl Acad Sci USA 76(3):1274–1278

Burton K, Park JH, Taylor DL (1999) Keratocytes generate traction forces in two phases. Mol Biol Cell 10(11):3745–3769

Burton K, Taylor DL (1997) Traction forces of cytokinesis measured with optically modified elastic substrata. Nature 385(6615):450–454

Butler JP, Tolic-Norrelykke IM, Fabry B, Fredberg JJ (2002) Traction fields, moments, and strain energy that cells exert on their surroundings. Am J Physiol Cell Physiol 282(3):595–605

Campbell BH, Clark WW, Wang JH (2003) A multi-station culture force monitor system to study cellular contractility. J Biomech 36(1):137–140

Campbell BH, Agarwal C, Wang JH (2004) TGF-beta1, TGF-beta3, and PGE(2) regulate contraction of human patellar tendon fibroblasts. Biomech Model Mechanobiol 2(4):239–245

Delvoye P, Wiliquet P, Leveque JL, Nusgens BV, Lapiere CM (1991) Measurement of mechanical forces generated by skin fibroblasts embedded in a three-dimensional collagen gel. J Invest Dermatol 97(5):898–902

Dembo M, Wang YL (1999) Stresses at the cell-to-substrate interface during locomotion of fibroblasts. Biophys J 76(4):2307–2316

Dembo M, Oliver T, Ishihara A, Jacobson K (1996) Imaging the traction stresses exerted by locomoting cells with the elastic substratum method. Biophys J 70(4):2008–2022

Ferrenq I, Tranqui L, Vailhe B, Gumery PY, Tracqui P (1997) Modelling biological gel contraction by cells: mechanocellular formulation and cell traction force quantification. Acta Biotheor 45(3–4):267–293

Galbraith CG, Sheetz MP (1997) A micromachined device provides a new bend on fibroblast traction forces. Proc Natl Acad Sci USA 94(17):9114–9118

Harris AK, Wild P, Stopak D (1980) Silicone rubber substrata: a new wrinkle in the study of cell locomotion. Science 208(4440):177–179

Landau LD, Lifshitz EM (1986) Theory of elasticity, 3rd edn. Pergamon, Oxford

Lavrentev MM, Romanov VG, Shishatskii SP (1986) Ill-posed problems of mathematical physics and analysis, 3rd edn. American Mathematical Society, Providence, Rhode Island

Marganski WA, Dembo M, Wang YL (2003) Measurements of cell-generated deformations on flexible substrata using correlation-based optical flow. Methods Enzymol 361:197–211

Moon AG, Tranquillo RT (1993) Fibroblast-populated collagen microsphere assay of cell traction force 1. Continuum model. AIChE J 39(1):163–177

Pelham RJ, Wang Y (1997) Cell locomotion and focal adhesions are regulated by substrate flexibility. Proc Natl Acad Sci USA 94(25):13661–12665

Ruoslahti E, Reed JC (1994) Anchorage dependence, integrins, and apoptosis. Cell 77(4):477–478

Schwarz US, Balaban NQ, Riveline D, Bershadsky A, Geiger B, Safran SA (2002) Calculation of forces at focal adhesions from elastic substrate data: the effect of localized force and the need for regularization. Biophys J 83(3):1380–1394

Tan JL, Tien J, Pirone DM, Gray DS, Bhadriraju K, Chen CS (2003) Cells lying on a bed of microneedles: an approach to isolate mechanical force. Proc Natl Acad Sci USA 100(4):1484–1489

Wang YL, Pelham RJ (1998) Preparation of a flexible, porous polyacrylamide substrate for mechanical studies of cultured cells. Methods Enzymol 298:489–496

Yang ZC, Lin J-S, Chen J, Wang J-C (2006) Determining substrate displacement and cell traction fields: a new approach. J Theoret Biol 242:607–616

Zienkiewicz OC, Taylor RL, Nithiarasu P, Zhu JZ (2005) The finite element method: its basis and fundamentals, 6th edn. Butterworth-Heinemann, London

Advances in Vascular Research and Applications

Contrast-Enhanced Micro-CT Imaging of Soft Tissues

Angela S.P. Lin (✉) , Ashley W. Palmer, Craig L. Duvall, Galen C. Robertson, Megan E. Oest, Bina Rai, Marc E. Levenston, and Robert E. Guldberg

Georgia Institute of Technology, 315 Ferst Drive, Atlanta, Georgia 30332, USA
e-mail: angela.lin@me.gatech.edu

Abstract

Analyzing the three-dimensional (3D) structure of specimens has become increasingly important in biomedical research fields, and microcomputed tomography (micro-CT) has emerged as an effective method for rapidly and non-destructively quantifying the geometry and morphology of tissues. Though micro-CT was originally designed to assess cortical and trabecular bone microarchitecture, applications for micro-CT now extend to the imaging of soft tissues. In particular, vascular anatomy and articular cartilage degradation are of major interest to investigators in the orthopedic research areas. This chapter outlines processes and results involved in utilizing X-ray contrast agents to enhance micro-CT analyses of vasculature and articular cartilage.

Introduction

Micro-CT analysis offers distinct advantages including its non-destructive nature and high-resolution 3D imaging. Typical scanning is performed using voxel sizes from 5 to 100 μm, with no physical sectioning required. In addition, micro-CT scanning provides rapid generation of 3D images and quantitative volumetric analyses. These capabilities provide advantages over other imaging techniques, such as light microscopy and histology, where specimens must be destructively processed, quantitative 3D data on specimen geometry is not readily ascertained, and analysis time is high (H.S. Tuan et al., in preparation). Micro-CT has traditionally been utilized as a method for quantifying the geometry and morphology of hard tissues such as trabecular and cortical bone. Recently, the scope of quantitative micro-CT analysis has grown to include 3D, high-resolution imaging and analysis of non-mineralized structures such as soft tissue and vasculature; however, due to the comparatively low radiodensity of soft tissues and vasculature, application of a radiopaque contrast agent is necessary.

Typical Contrast Agents

Iodine, barium, and other metallic elements are radiopaque substances commonly used to enhance the contrast of low-attenuating materials. Barium sulfate combined with gelatin has been injected to aid in micro-CT imaging of mouse hindlimb vas-

culature (Duvall et al. 2004); however, clumping of the contrast agent within vessels resulted in inhomogeneous distribution of contrast throughout the vasculature. Instead, a silicone rubber contrast agent containing lead chromate (Microfil MV-122, FlowTech, Carver, Mass.) was found to be more suitable for vascular imaging. Iodinated contrast agents such as sodium meglumine ioxaglate (Hexabrix, Mallinckrodt, Hazelwood, Mo.), iodixanol (Visipaque), and sodium diatrizoate are also commercially available. Hexabrix and Visipaque are used for visualizing vessels and other soft tissue areas in the clinical setting, whereas sodium diatrizoate is only indicated for laboratory use.

Vascular Imaging Applications

Motivation and Significance

The current approaches to vascular imaging and analysis have significant limitations that can potentially be overcome with the high-resolution, 3D, and quantitative capabilities of micro-CT. Immunohistochemistry is the most commonly used method for counting capillary and arteriole density. The main advantage it provides over other methodologies is the ability to fully resolve capillary-sized vessels; however, the technique is relatively subjective, semi-quantitative, and not necessarily representative of the 3D vasculature throughout the entire specimen. Histological sections can be stacked to render 3D images (Brey et al. 2002), but this approach is subject to artifacts and requires large processing times. Laser Doppler perfusion imaging allows for semi-quantitative analysis of the functional blood flow (Abe et al. 2003; Amano et al. 2003; Couffinhal et al. 1998; Scholz et al. 2002; Silvestre et al. 2003), but the technique is limited because anatomical information cannot be ascertained and only superficial blood flow can be measured.

X-ray angiography is also a widely used method for visualizing 2D projections of contrast agent perfused vascular networks (Amano et al. 2003; Mallat et al. 2002; Silvestre et al. 2002). This approach provides high-resolution angiograms, but it lacks the ability to employ a robust 3D quantitative analysis. Another technique involves injecting colored or fluorescent microspheres and using spectrophotometric analysis to quantify functional vessel perfusion (Brevetti et al. 2001; Deveci and Egginton 1999; Kowallik et al. 1991; Prinzen and Glenny 1994; Van Oosterhout et al. 1995). One advantage of this approach is that it allows for longitudinal injection of different colored microspheres so multiple time points can be measured within a single animal; however, for small animal models, performing the required arterial catheterization or direct injection of microspheres into the left ventricle or atrium can be extremely challenging. Magnetic resonance angiography and positron emission tomography have also been used to analyze vascular growth but may not provide sufficient image resolution for small animal models.

Contrast Agent Perfusion Technique

For vascular imaging of mouse hindlimbs, a technique has been developed by Duvall et al. (2004) for perfusing a lead chromate-based contrast agent (Microfil MV-

122, FlowTech) through the vasculature to enhance X-ray attenuation of the lumen spaces. The full protocol has previously been described in its entirety (H.S. Tuan et al., in preparation) but is only briefly explained here. Blood is first flushed from the vasculature at physiologic pressure with heparanized 0.9% saline through a needle inserted into the left ventricle. Subsequently, vessels are pressure fixed with 10% neutral buffered formalin (NBF) and flushed again with heparanized saline. Then, Microfil at full concentration is pressure perfused throughout the vasculature. The contrast agent is allowed to polymerize overnight at 4°C, and the hindlimbs are dissected and placed in 10% NBF for 4 days for tissue fixation. This contrast agent perfusion technique can be utilized for any angiogenesis or vascular anatomy related models in mice, such as fracture healing. The procedure can also be adapted for use in other small animal models.

Imaging Vasculature Near Bone Structures

Bone and vascular structures are in proximity to one another in most regions of interest for micro-CT analysis, including the hindlimbs. A scan containing both perfused vessels and mineralized bone can easily be accomplished following Microfil perfusion; however, characterizing the vasculature in a scan that also includes bone can be challenging. Processing images containing both bone and vasculature using higher thresholds may eliminate bone but at the same time diminish the accuracy of the resulting images of vasculature (Duvall et al. 2004). In addition, histograms of X-ray attenuation for an image containing both bone and Microfil-perfused vessels show that the attenuation for those materials have overlapping regions (Fig. 1a).

For ideal segmentation between two materials, the attenuation histogram for one material must not overlap with another. In the case of bone and Microfil-perfused vessels, it is difficult to precisely segment one material from the other using global thresholding techniques (Figure 1b,c). To image and analyze perfused vasculature only, it is therefore crucial to decalcify the mineralized tissue prior to scanning. Figure 1d shows a micro-CT image of vasculature alone after decalcification. One method for decalcifying bone tissues is to place the specimen in Cal Ex II (a formic acid-based solution) for 48 h, rinse in water for 1 h, and then store specimens in 10% NBF at 4°C until scanning with micro-CT. Ethylenediamine tetraacetic acid (EDTA) may also be used for decalcification. While EDTA treatment is less harsh for the specimen, the processing time is significantly longer. Depending on sample size, the decalcification can take up to 2–3 weeks.

Hindlimb Ischemia Model

The mouse hindlimb ischemia model is a well-characterized technique in which a length of the superficial femoral artery and vein are ligated and excised to simulate peripheral artery disease (Couffinhal et al. 1998). This stimulates remodeling of the surrounding vascular network in order to restore function to the limb. Micro-CT has been utilized to quantitatively evaluate the mechanisms involved in the arteriogenic remodeling process immediately following hindlimb ischemia (Duvall et al.

Figure 1a–e. The vasculature of a mouse was pressure perfused with Microfil MV-122 lead chromate-based contrast agent to enhance X-ray attenuation. Hindlimbs were extracted, retaining all soft tissue. A volume of interest, including bone and vasculature near the distal femur, was scanned using a Scanco vivaCT 40 at a voxel size of 21 µm. **a** From the gray-scale image, a histogram of X-ray attenuation was generated; threshold range from 0 – 1000. The bone peak and contrast-enhanced vessel peak have overlapping regions, marked by *dotted curves*. **b** Threshold of 110 was used to capture both bone and vessels. **c** Segmenting for bone using a threshold range of 110 – 165 produced poor bone image quality and did not eliminate vessels. **d** Vessel segmentation at threshold of 220 eliminated low-attenuation vessel voxels but included high-attenuation bone voxels. **e** When bone tissue is decalcified, vasculature alone can be completely visualized at threshold of 110

2004). Wild-type C57BL/6 mice underwent surgeries on right hindlimbs, and the left hindlimbs were used as the unoperated contralateral controls. Upper hindlimb vascular morphology was then analyzed post-operatively at 0, 3, and 14 days via micro-CT scans performed at various voxel resolutions (16, 30, and 36 µm). Several global, model-independent parameters were computed using direct transformation methods (Hildebrand et al. 1999; Hildebrand and Ruegsegger 1997; Odgaard and Gundersen 1993) including vessel volume, thickness/diameter, separation, number/density, and connectivity. Results of these studies showed that at 3 and 14 days post-surgery, the reconstituted vascular volume for surgically manipulated limbs was not significantly different from the control limbs. Other morphologic parameters obtained through micro-CT analysis were used to explain the microarchitectural mechanisms behind this recovery of vascular volume. Average vessel number for the surgical limbs at 3 and 14 days post-surgery was significantly increased over 0 day surgery limbs as well as control limbs. Average vessel thickness was significantly smaller for surgical limbs compared with control limbs at all time points. In addition, average vessel separation at 3 and 14 days post-surgery was significantly smaller for the surgical limbs compared with day 0 and control limbs.

The vessel number, thickness, and separation data show that a network of smaller, more closely packed collateral vessels formed to compensate for the restricted blood flow caused by femoral artery ligation. Also, vascular connectivity of surgery limbs increased significantly by day 14 over day 0 and control limbs. This demonstrated that the network of collateral vessels became more interconnected over time and supported the evidence that these collaterals rapidly formed to reconstitute perfusion throughout the limb. Preferential analyses of vessels of varying sizes were also performed. Histograms were generated to compare the distribution of vessel diameter measurements between surgical and control limbs. The control limbs represented the normal distribution of vessel diameters. At day 0, the surgery limbs had a decreased number of occurrences at all vessel diameters compared with the control limbs. By day 3, the surgery limbs had an increased number of small collateral vessels but decreased number of large conduit-sized vessels. To visually depict the vessel size variations, the vessel diameter measurements were mapped onto 3D color-coded images (Fig 2b,c).
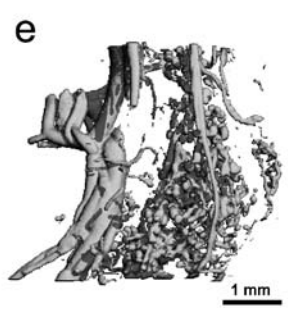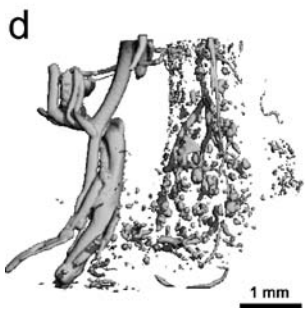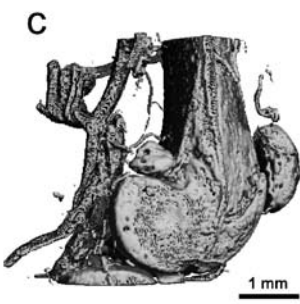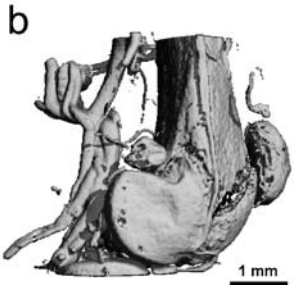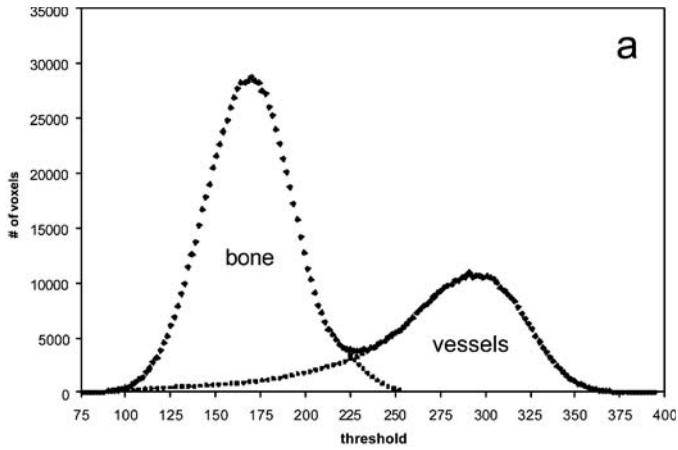
Fracture Healing Angiogenesis

Vascular response during fracture healing plays an important role in the conversion of cartilaginous callus to mineralized tissue and therefore recovery of mechanical integrity. A unilateral femoral fracture model (Bonnarens and Einhorn 1984) has been used to study the process of bone repair including early neovascularization in a fracture site. Following anesthesia, the femora are fixed via retrograde insertion of a nee-
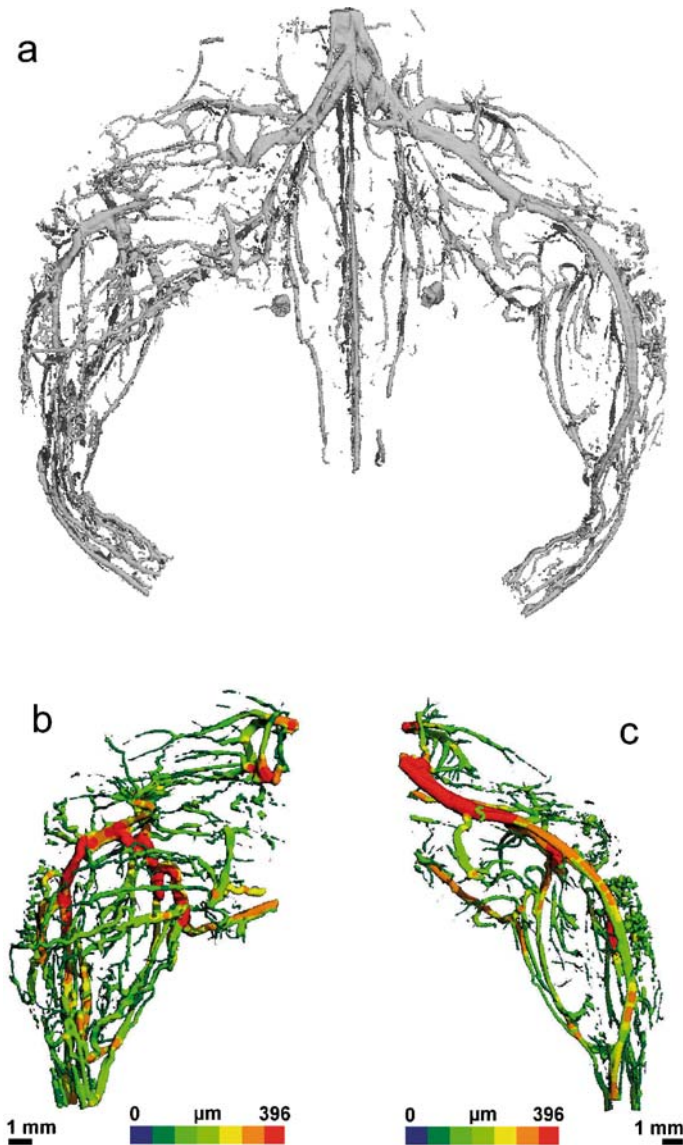
Figure 2 a–c. Representative micro-CT images of mouse hindlimb vasculature following ligation and excision of the femoral artery and vein in the right leg. No surgical procedure was performed on the left leg. Microfil MV-122 lead chromate-based contrast agent was pressure perfused throughout the vasculature to enhance X-ray attenuation, and the images were obtained at the 14-day post-surgery time point using a Scanco μCT 40. **a** Image from an entire perfused hindlimb, scanned at 36-μm voxel size. Images of surgical (**b**) and control (**c**) volumes of interest (36-μm voxel size) have been mapped with color-coded vessel diameter data derived from direct transformation methods. *Red* indicates vessels with diameter 396 μm and larger, and the color scale decreases linearly to zero (*blue*)

dle between the femoral condyles into the intramedullary canal. A transverse fracture was then created at the mid-diaphysis of this surgical leg, and the contralateral leg was left intact as a control. At multiple time points, mice were sacrificed and perfused with lead chromate-based radiopaque contrast agent as described previously for the hindlimb ischemia model. After contrast agent polymerization, fractured femurs were dissected from the surrounding soft tissue under a dissecting microscope to ensure calluses remained intact. The fixation pins were then removed from the intramedullary canals, and femora were stored in 10% NBF at 4°C for 48 h. Specimens were then decalcified in Cal Ex II formic acid-based solution for 48 h. Immediately following decalcification, femora were washed in water and stored in 10% NBF at 4°C until micro-CT imaging. Femurs were scanned along the longitudinal axis at 10.5-μm voxel resolution, and global segmentation values were used to render 3D binarized images of the vascular networks. Figure 3 shows a representative image of vasculature within an entire fractured mouse femur. Quantitative morpho-
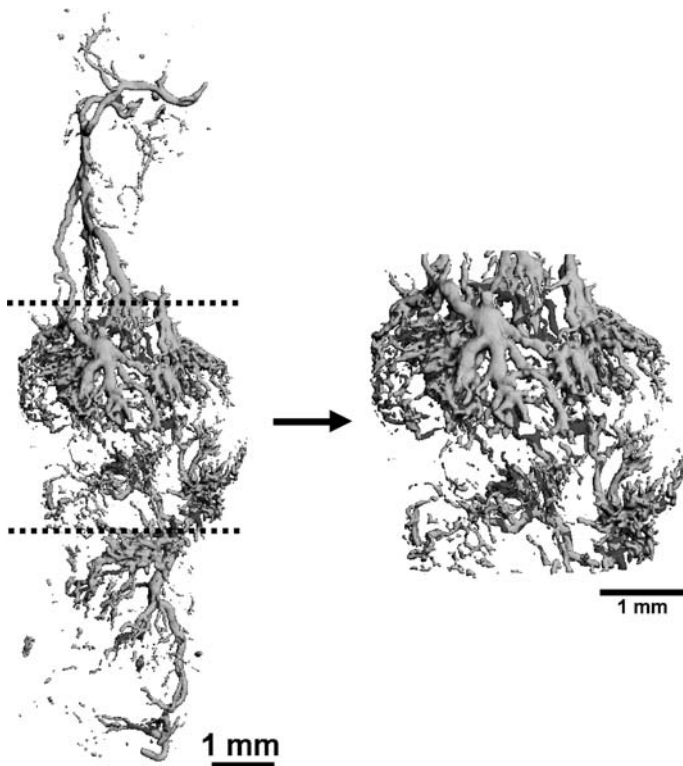
Figure 3. A representative vascular micro-CT image obtained from a mouse femur 14 days post-fracture, scanned with a Scanco vivaCT 40 at 10.5-μm voxel size. The vasculature was pressure-perfused with Microfil MV-122, and bone was decalcified prior to scanning. Morphometric parameters were quantified for a standardized callus length, as marked by *dotted lines* and depicted in an expanded view to the right

metric parameters, such as total callus volume, vessel volume, volume fraction, connectivity, number/density, thickness/diameter, and separation, were then computed within standardized callus lengths marked by dotted lines. The isolated volume of interest containing only the callus vasculature is also shown. This technique provides a methodology for quantifying differences in vascular development between transgenic and wildtype animals or animals undergoing treatments to either stimulate or inhibit angiogenesis.

Revascularization in Segmental Defect Repair

Another application utilizing vascular micro-CT imaging is evaluating the infiltration of vessels into an implanted tissue engineering construct. A rat femoral segmental defect model has been developed to study the efficacy of using porous polymer biodegradable scaffolds as bone graft materials in critical-sized defects (M.E. Oest et al., submitted). Revascularization of the construct is an essential requirement for integration of the graft with native bone and ultimately restoration of function. Implantation of a construct into the segmental defect combined with perfusion of a vascular contrast agent (Microfil MV-122) and micro-CT analysis provide a method for quantitatively assessing the vascular ingrowth within implanted constructs (M.E. Oest et al., submitted). For the implantation procedure, rats were anesthetized using isoflurane continuously administered via induction chamber and face mask. A longitudinal incision was made along the upper hindlimb, and the quadriceps musculature was teased aside to reveal the entire femur. A custom modular fixation plate was af-

PRP-treated PCL-TCP scaffold   PCL-TCP scaffold

a   b
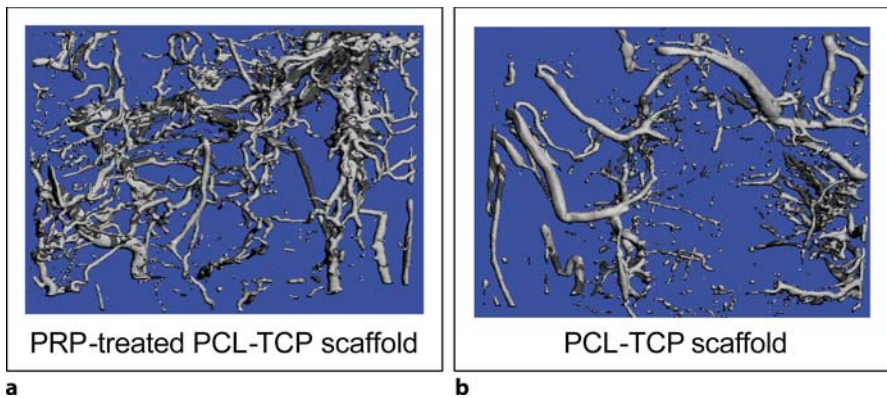
Figure 4 a,b. Micro-CT images of vasculature within scaffolds implanted in 8-mm rat femoral segmental defects. Three weeks after implantation, animals were sacrificed and perfused with Microfil MV-122 vascular contrast agent for micro-CT scanning using a Scanco vivaCT 40 at 21-μm voxel size. A volume of interest 6 mm in length was analyzed for vascular growth. **a** Vasculature within a poly(ε-caprolactone) scaffold containing tricalcium phosphate particles (*PCL-TCP*; 80:20) and loaded with autologous platelet rich plasma (*PRP*). **b** Vasculature within a PCL-TCP scaffold alone. The PRP-loaded PCL-TCP scaffolds had approximately 70% higher vascular volume fraction than their unloaded PCL-TCP counterparts

fixed to stabilize the femur, then a defect 8 mm in length was created using a miniature oscillating saw. Several polymer scaffold types have been implanted, including scaffolds produced using poly(L-DL-lactide) (PLDL), poly(ε-caprolactone) (PCL), and poly(ε-caprolactone) with tricalcium phosphate particles (PCL-TCP). In one study, the effects of delivering autologous platelet rich plasma (PRP) on neovascularization, mineralization, and mechanical properties were evaluated (Rai et al. 2005). Defects of 8-mm length in rat femora were filled with PRP-treated PCL-TCP constructs or PCL-TCP scaffolds alone (contralateral controls). After 3 weeks post-surgery, animals were killed and perfused with Microfil to enhance contrast of the lumen spaces of the vasculature. Mineral was decalcified using a formic acid treatment in order to facilitate imaging of the vasculature. Micro-CT scans were performed at a voxel resolution of 20 μm, and a volume of interest 6 mm in length in the central portion of the defect region was analyzed. Representative images of the vascularization within these volumes of interest for PRP-treated and control scaffolds are shown in Fig. 4. The PRP-treated defects possessed 70% greater vascular volume fraction compared with the non-treated controls.

Advantages and Limitations

As the examples in this chapter show, combining micro-CT scanning with perfusion of an appropriate contrast agent provides a powerful method for quantifying 3D vascular morphology at high resolutions; however, several concerns must be addressed when considering contrast-enhanced micro-CT imaging of vascular anatomy.

Challenges with Micro-CT Analysis

Many choices are required when performing micro-CT analyses on vasculature including determining an appropriate voxel size, segmentation values, and volume of interest. Varying these parameters causes changes in all morphometric measurements; thus, careful consideration must be taken to choose application-specific parameters. Users must also be aware of inherent limitations in both micro-CT imaging and contrast agent perfusion techniques.

Voxel Size Sensitivity

In the mouse hindlimb ischemia model, a voxel size of 36 μm was found to be optimal for focusing on the collateral-sized vessels of the upper limb (Duvall et al. 2004). When analyzing a localized region of angiogenesis, such as in the fracture healing model, it was appropriate to use a small voxel size (10.5 μm) to accurately measure the newly forming capillary-sized vessels; however, the associated tradeoffs when scanning at high voxel resolutions are longer scan times and large data sets requiring increased processing resources and time.

Segmentation

Compromises must be made when defining global segmentation values for vascular image analysis. Choosing a high binarization threshold may obscure smaller-sized

vessels, but choosing a low threshold causes larger vessel diameters to appear arti-factually large. Lowering the Gauss filter values (sigma and support) allows for finer details to be captured but produces a 3D image that is less smooth. The optimal values are typically chosen based on visual inspection of 2D tomograms, often with the guidance of X-ray attenuation histograms.

Vascular Structure and Function

One limitation of micro-CT analysis is that it provides purely anatomical data regarding the vascular structure. To most effectively and comprehensively assess functional vascular perfusion, it may be necessary to combine the quantitative structural analyses of micro-CT with techniques that provide data on vascular functionality, such as Laser Doppler perfusion imaging.

Contrast Agent Perfusion Limitations

A potential limitation of the Microfil vascular perfusion technique is that the analysis must be performed post-mortem. Using this methodology, it is therefore impossible to perform sequential in vivo vascular scans at various time points for a single animal. This increases the number of animals necessary to complete a study, which increases the cost compared with other techniques that allow for sequential scanning. In-vivo vascular contrast agents are currently being developed; however, longitudinal in vivo scans on a single animal increase the amount of total X-ray exposure, and the potential biological effects of this amplified radiation dose must be considered. In-vivo scanning would also eliminate the possibility of decalcifying bone tissue, thus reducing the accuracy of analyzing vascular networks in proximity to bone structures. Finally, it is noteworthy that vascular imaging using micro-CT combined with contrast agent perfusion allows for analysis of lumen spaces only. It is therefore challenging to employ this technique to examine the remodeling of vessel walls.

Despite limitations, this technique is becoming utilized more widely to generate quantitative data regarding the structure of vascular networks in small animal models (Bentley et al. 2002; Garcia-Sanz et al. 1998; Jorgensen et al. 1998; Maehara 2003; Ortiz et al. 2000; Rodriguez-Porcel et al. 2000; Simopoulous et al. 2001; Holdsworth and Thornton 2002; Wilson et al. 2002). Vessels within other organs of interest, such as the brain and heart of mice and rats, have also been imaged (Fig. 5).

Cartilage Imaging Applications

Motivation and Significance

Articular cartilage is a hydrated soft tissue that lines the articulating surfaces of diarthroidial joints and consists of an extracellular matrix (ECM) composed primarily of type-II collagen, proteoglycans (PGs), and interstitial fluid. Ionic interactions between the negatively charged sulfated glycosaminoglycans (sGAGs) attached to the PG backbone and mobile ions in the surrounding interstitial fluid create an osmotic
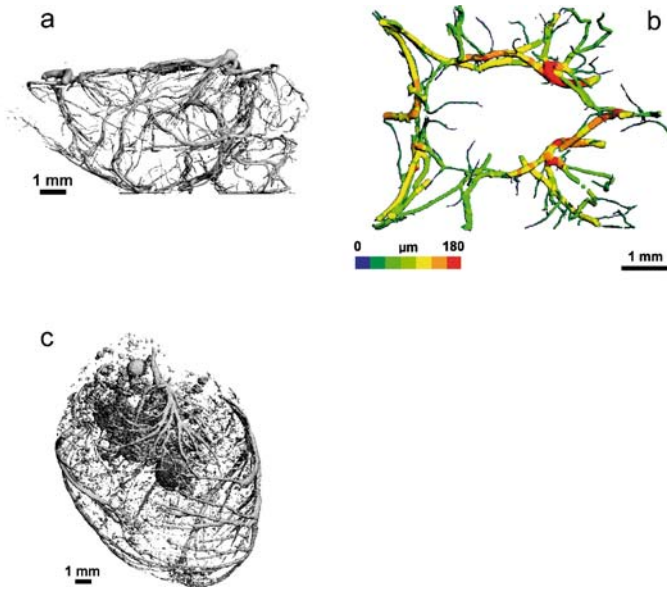
Figure 5 a–c. Vascular anatomy for various organs of interest can be visualized by micro-CT imaging. **a** Micro-CT image of the vasculature within a mouse brain, lateral view. **b** Direct transformation computations were used to produce a color-coded mapping of vessel diameters to the vasculature within and surrounding a mouse circle of Willis. The color scale is linear, with *red* indicating diameters of 180 μm or larger and *blue* indicating 0 μm. **c** Vasculature of a rat heart. All scans were performed using a Scanco vivaCT 40 at a voxel size of 10.5 μm following perfusion with Microfil MV-122 contrast agent

swelling pressure. The collagen fiber network entrapping the PGs offers resistance to this osmotic pressure, regulating the overall mechanical properties of articular cartilage (Mow and Ratcliffe 1997). Monitoring changes in the amount and distribution of PGs and their attached sGAGs may therefore provide an indication of the health and integrity of the articular cartilage matrix. This approach may be beneficial in developing diagnostic tools for degenerative joint conditions such as osteoarthritis, where early PG depletion has been observed, and for in vitro monitoring of matrix accumulation in tissue-engineered constructs prior to implantation.

A wide range of techniques have previously been used to examine the PG composition of cartilage, but these techniques are ill-suited for monitoring changes in PG composition in small animal models. For instance, safranin-O histology is a commonly used method for obtaining the spatial distribution of sGAGs in tissue sections, but the approach requires destruction of the sample and provides only semi-quantitative information regarding PG content. Biochemical assays, including dimethylmethylene blue and alcian blue, offer quantitative data regarding sGAG content but do not provide spatial information and require sample destruction. A contrast-enhanced magnetic resonance imaging (MRI) technique called delayed gadolinium-enhanced MRI of cartilage (dGEMRIC) has successfully been used to
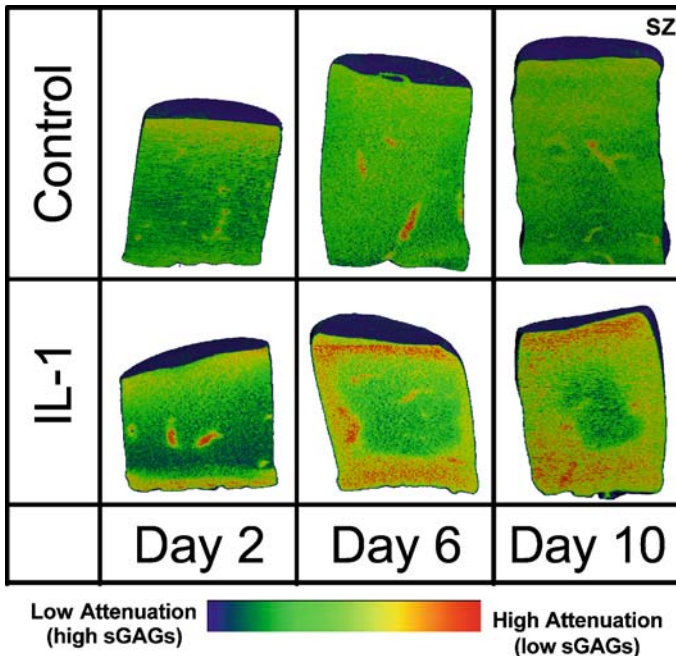
Figure 6. Representative micro-CT images of interleukin-1α-treated (IL-1) and control bovine articular cartilage explants at days 2, 6, and 10. Explants were analyzed by a technique that utilizes the equilibrium partitioning of an ionic contrast agent (Hexabrix) combined with micro-CT (EPIC-μCT). Distribution of X-ray attenuation through the explants, which is inversely related to sulfated glycosaminoglycan (*sGAG*) content, is represented by the color scale with *blue* indicating low attenuation (high sGAG content) and *red* indicating high attenuation (low sGAG content). Day-6 and day-10 IL-1-treated explants contain more regions of low sGAG content than either the control explants or the day-2 IL-1-treated explants. In all images, superficial zone (*SZ*) is at the top. (Reprinted from Palmer et al. 2006)

examine human articular cartilage both in vitro and in vivo (Bashir et al. 1999; Nieminen et al. 2002; Kim et al. 2003; Kurkijarvi et al. 2004; Nieminen et al. 2004; Samosky et al. 2005; Tiderius et al. 2001, 2003; Williams et al. 2004, 2005). This technique relies on the equilibrium partitioning of a negatively charged paramagnetic contrast agent within the PG-rich ECM of articular cartilage (Bashir et al. 1996; 1997). While this approach allows for non-invasive, longitudinal monitoring of PG content, the current in-plane resolution of clinical MRI systems (~ 300 μm) is not sufficient for imaging small animal joints. Recent efforts using microscopic MRI (μMRI) improve the imaging resolution, but these systems are costly and typically have substantially lower out-of-plane resolutions (Faure et al. 2003; Watrin et al. 2001).

Micro-CT combined with a suitable contrast agent is an attractive alternative to these approaches due to its ability to provide rapid, non-destructive, 3D quantitative assessments of articular cartilage PG distribution and 3D morphology at high resolutions.

EPIC-μCT Technique for Imaging Articular Cartilage

A micro-CT technique that relies on the *E*quilibrium *P*artitioning of an *I*onic *C*ontrast agent with the cartilage ECM has been developed to monitor PG content in articular cartilage (Palmer et al. 2006). The technique, EPIC-μCT, exploits the negative charge of sGAGs within the ECM by assuming that an anionic, radiopaque solute introduced into the cartilage environment will distribute in an inverse relationship with the sGAGs. High X-ray attenuation readings (corresponding to high concentrations of the anionic, radiopaque solute) would therefore indicate regions of sGAG depletion. Hexabrix, the contrast agent used in EPIC-μCT, is a sterile, non-pyrogenic, low osmolar, aqueous solution consisting of 39.3% (w/v) ioxaglate meglumine and 19.6% (w/v) ioxaglate sodium. Ioxaglate, the negatively charged dissociate of Hexabrix, is a hexa-iodinated dimer. The higher iodine content of hexa-iodinated dimers was found to improve radiopacity without increasing osmolality when compared with tri-iodinated monomers such as sodium diatrizoate.

In Vitro Cartilage Degradation Model

EPIC-μCT imaging of articular cartilage has been validated in an in vitro model of cartilage degradation (Palmer et al. 2006). Full-thickness bovine articular cartilage explants were obtained from the patellar groove and femoral condyles of a 1–2 week old calf. Cartilage degradation was induced in some explants with 20 ng/ml interleukin-1α (IL-1), a cytokine implicated in osteoarthritis. Following culture of control and IL-1-treated explants for up to 10 days, specimens were placed in full-strength Hexabrix™ supplemented with protease inhibitors for 24 h at 37 °C with gentle agitation. After the immersion period, explants were removed, blotted to eliminate excess Hexabrix™, and scanned at a voxel resolution of 21 μm using a Scanco vivaCT 40. Two full-thickness explants could be scanned in parallel in approximately 15 min. For each explant, average X-ray attenuation was computed. Mean attenuation values for the IL-1-treated explants were found to be significantly higher than controls starting at 6 days, which suggested lower sGAG content within IL-1-treated explants by that time point. Analysis of culture media with the dimethylmethylene blue (DMMB) assay showed higher levels of sGAGs were released by IL-1-treated explants throughout the culture period. Longitudinally sectioned images depicting color-coded X-ray attenuation values in control and IL-1-treated explants are shown in Fig. 6. There was no change in control explants but a progressive increase in X-ray attenuation with time in IL-1-treated explants. The increase in X-ray attenuation in IL-1-treated explants progressed radially inward from the outer surface, which was consistent with patterns of PG loss in safranin-O stained sections from IL-1-treated explants. A separate study was undertaken to determine the ability of EPIC-μCT attenuation to predict sGAG content in cartilage. Explants were treated for 3-48 h with chondroitinase ABC, an enzyme with specificity for sGAGs, to produce samples with a range of sGAG contents. These treated explants were scanned by EPIC-μCT at a voxel resolution of 21 μm, digested, and analyzed for sGAGs by the DMMB assay. A strong, significant correlation was found between X-ray attenuation and sGAG/water, indicating the ability of EPIC-μCT to predict sGAG content (Fig. 7).
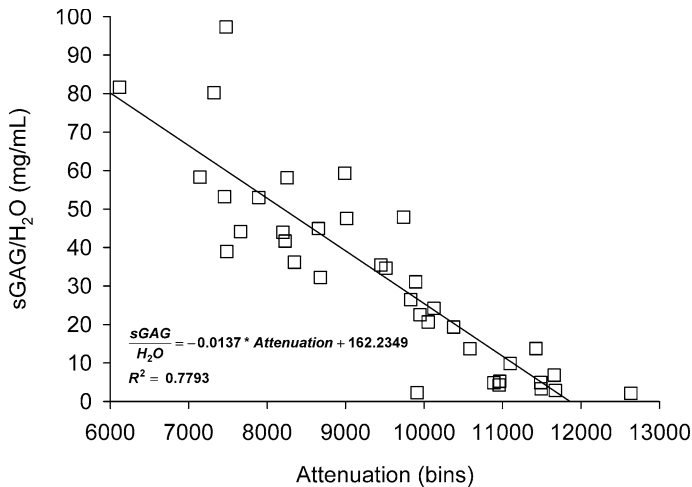
Figure 7. X-ray attenuation values are inversely related to sGAG content as described in this plot. Data to define this relationship were generated from EPIC-µCT scans of bovine articular cartilage explants following exposure for varying lengths of time to chondroitinase ABC. The scans were performed on a Scanco vivaCT 40 at $E = 45\,\text{kVp}$, $I = 133\,\mu\text{A}$, and voxel size $= 21\,\mu\text{m}$

In-Situ Articular Cartilage Imaging

To determine the feasibility of utilizing EPIC-µCT to image articular cartilage surface characteristics and thickness in situ, a rabbit femur was dissected from surrounding soft tissue (Fig. 8a) and the distal end was soaked in Hexabrix at varying concentrations (Palmer et al. 2006). Initial attempts using Hexabrix at full concentration allowed for imaging of the soft tissue surface characteristics; however, due to the similarity in X-ray attenuation between Hexabrix and subchondral bone, segmentation of the two materials was not possible. To lower the attenuation of contrast-enhanced soft tissue, the femur was immersed in 40/60% (v/v) Hexabrix/0.15 M PBS at 37°C for 1 h under gentle agitation. The femur was subsequently scanned at 21-µm voxel resolution (Fig. 8b), revealing surface features on the native femur that were not visible without the use of Hexabrix. A histogram of X-ray attenuation for the scanned volume of interest contained two partially overlapping but distinct peaks corresponding to soft tissues contrast-enhanced by Hexabrix and bone. Based on the histogram, the volume of soft tissue was isolated using dual thresholds. Soft tissue thickness measurements were obtained using direct transformation algorithms (Hildebrand and Ruegsegger 1997). These thickness measurements were applied to the 3D image to render the color-coded thickness mapping in Fig. 8c. Figure 8d shows a sectioned view of the distal femur, containing subchondral cortical and trabecular bone (gold) and the layer of articular cartilage lining the surface (blue). The range of thickness values obtained using this approach was qualitatively consistent with expected values of rabbit articular cartilage thickness. This demonstrates the potential of EPIC-µCT for measuring cartilage thickness; however, experimental validations of EPIC-µCT thickness measurements still need to be performed.
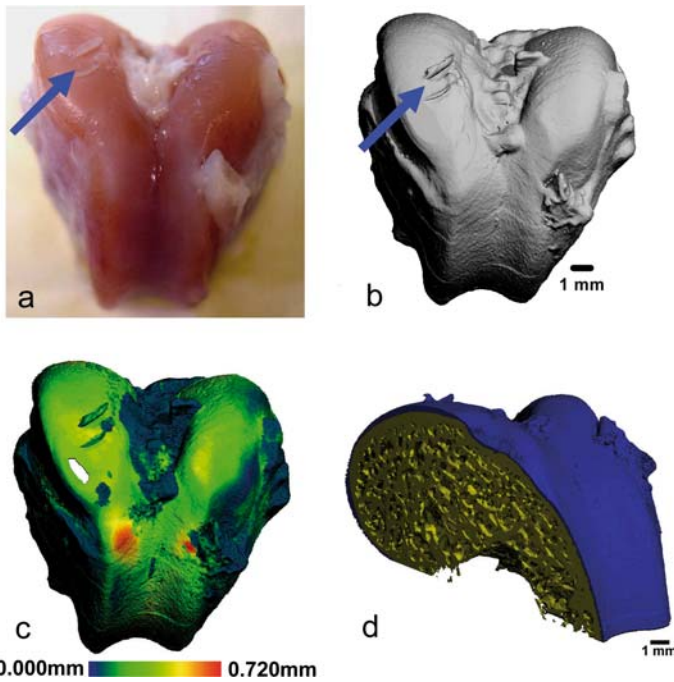
Figure 8 a–d. The distal end of a rabbit femur was imaged using EPIC-µCT to visualize articular cartilage in situ. **a** Macroscopic digital image depicts surface structures of the articular cartilage on the femoral condyles and patellar groove. **b** EPIC-µCT image at 40% Hexabrix concentration of articular cartilage surface characteristics. Note the two corresponding scalpel marks (*arrows*) in **a** and **b**. **c** Direct transformation thickness measurements were mapped to the articular cartilage image according to a linear color scale where *blue* = 0 µm and *red* = 720 µm and thicker. **d** A sectioned view of the distal femur, including subchondral cortical and trabecular bone in *gold* and articular cartilage in *blue*. (Reprinted from Palmer et al 2006)

Advantages and Limitations

The previous in vitro and in situ EPIC-µCT applications exemplify the advantages of utilizing micro-CT imaging for contrast enhanced soft tissue analyses in small animal models. These advantages include high-resolution imaging, non-invasiveness, quantitative morphological analysis, and shorter scan times compared with MRI. This technique has great potential, particularly for assessing the degradation of articular cartilage, which could lead to advances in the study and diagnosis of osteoarthritis; however, EPIC-µCT does require more complete development and characterization. For example, contrast-enhanced vascular analyses using micro-CT showed that quantitative measurements were sensitive to choice of voxel resolution. Voxel size optimization for EPIC-µCT applications presents a potential area of further development. The application of EPIC-µCT to in vivo cartilage tissue visualization is of major interest; however, a number of technical concerns must be addressed, including optimizing Hexabrix delivery and limiting non-specific localization.

References

Abe M, Sata M, Nishimatsu H, Nagata D, Suzuki E, Terauchi Y, Kadawaki T, Minamino N, Kangawa K, Matsuo H, Hirata Y, Nagai R (2003) Adrenomedullin augments collateral development in response to acute ischemia. Biochem Biophys Res Commun 306:10–15

Amano K, Matsubara H, Iba O, Okigaki M, Fujiyama S, Imada T, Kojima H, Nozawa Y, Kawashima S, Yokoyama M, Iwasaka T (2003) Enhancement of ischemia-induced angiogenesis by eNOS overexpression. Hypertension 41(1):156–162

Bashir A, Gray ML, Burstein D (1996) Gd-DTPA2- as a measure of cartilage degradation. Magn Reson Med 36(5):665–673

Bashir A, Gray ML, Boutin RD, Burstein D (1997) Glycosaminoglycan in articular cartilage: in vivo assessment with delayed Gd(DTPA)(2-)-enhanced MR imaging. Radiology 205(2):551–558

Bashir A, Gray ML, Hartke J, Burstein D (1999) Nondestructive imaging of human cartilage glycosaminoglycan concentration by MRI. Magn Reson Med 41(5):857–865

Bentley MD, Ortiz MC, Ritman EL, Romero JC (2002) The use of microcomputed tomography to study microvasculature in small rodents. Am J Physiol Regul Integr Comp Physiol 282(5): R1267-R1279

Bonnarens F, Einhorn TA (1984) Production of a standard closed fracture in laboratory animal bone. J Orthop Res 2(1):97–101

Brevetti LS, Paek R, Brady SE, Hoffman JI, Sarkar R, Messina LM (2001) Exercise-induced hyperemia unmasks regional blood flow deficit in experimental hindlimb ischemia. J Surg Res 98(1):21–26

Brey EM, King TW, Johnston C, McIntire LV, Reece GP, Patrick CW Jr (2002) A technique for quantitative three-dimensional analysis of microvascular structure. Microvasc Res 63(3):279–294

Couffinhal T, Silver M, Zheng LP, Kearney M, Witzenbichler B, Isner JM (1998) Mouse model of angiogenesis. Am J Pathol 152(6):1667–1679

Deveci D, Egginton S (1999) Development of the fluorescent microsphere technique for quantifying regional blood flow in small mammals. Exp Physiol 84:615–630

Duvall CL, Taylor WR, Weiss D, Guldberg RE (2004) Quantitative microcomputed tomography analysis of collateral vessel development after ischemic injury. Am J Physiol Heart Circ Physiol 287(1): H302–H310

Faure P, Doan BT, Beloeil JC (2003) In-vivo high resolution three-dimensional MRI studies of rat joints at 7 T. NMR Biomed 16(8):484–493

Garcia-Sanz A, Rodriguez-Barbero A, Bentley MD, Ritman EL, Romero JC (1998) Three-dimensional microcomputed tomography of renal vasculature in rats. Hypertension 31(1 Pt 2):440–444

Hildebrand T, Ruegsegger P (1997) A new method for the model-independent assessment of thickness in three-dimensional images. J Microsc 185:67–75

Hildebrand T, Laib A, Muller R, Dequeker J, Ruegsegger P (1999) Direct three-dimensional morphometric analysis of human cancellous bone: microstructural data from spine, femur, iliac crest, and calcaneus. J Bone Miner Res 14(7):1167–1174

Holdsworth DW, Thornton MM (2002) Micro-CT in small animal and specimen imaging. Trends Biotechnol 20:S34–S39

Jorgensen SM, Demirkaya O, Ritman EL (1998) Three-dimensional imaging of vasculature and parenchyma in intact rodent organs with X-ray micro-CT. Am J Physiol 275(3 Pt 2):H1103–H114

Kim YJ, Jaramillo D, Millis MB, Gray ML, Burstein D (2003) Assessment of early osteoarthritis in hip dysplasia with delayed gadolinium-enhanced magnetic resonance imaging of cartilage. J Bone Joint Surg Am 85A(10):1987–1992

Kowallik P, Schulz R, Guth BD, Schade A, Paffhausen W, Gross R, Heusch G (1991) Measurement of regional myocardial blood flow with multiple colored microspheres. Circulation 83(3):974–982

Kurkijarvi JE, Nissi MJ, Kiviranta I, Jurvelin JS, Nieminen MT (2004) Delayed gadolinium-enhanced MRI of cartilage (dGEMRIC) and T2 characteristics of human knee articular cartilage: topographical variation and relationships to mechanical properties. Magn Reson Med 52(1):41–46

Maehara N (2003) Experimental microcomputed tomography study of the 3D microangioarchitecture of tumors. Eur Radiol 13(7):1559–1565

Mallat Z, Silvestre JS, Le Ricousse-Roussanne S, Lecomte-Raclet L, Corbaz A, Clergue M, Duriez M, Barateau V, Akira S, Tedgui A, Tobelem G, Chvatchko Y, Levy BI (2002) Interleukin-18/interleukin-18 binding protein signaling modulates ischemia-induced neovascularization in mice hindlimb. Circ Res 91(5):441–448

Mow VC, Ratcliffe A (1997) Structure and function of articular cartilage and meniscus. In: Mow VC, Hayes WC (eds) Basic orthopaedic biomechanics. Lippincott-Raven, Philadelphia, pp 113–177

Nieminen MT, Rieppo J, Silvennoinen J, Toyras J, Hakumaki JM, Hyttinen MM, Helminen HJ, Jurvelin JS (2002) Spatial assessment of articular cartilage proteoglycans with Gd-DTPA-enhanced T1 imaging. Magn Reson Med 48(4):640–648

Nieminen MT, Menezes NM, Williams A, Burstein D (2004) T2 of articular cartilage in the presence of Gd-DTPA2. Magn Reson Med 51(6):1147–1152

Odgaard A, Gundersen HJ (1993) Quantification of connectivity in cancellous bone, with special emphasis on 3-D reconstructions. Bone 14:173–182

Ortiz MC, Garcia-Sanz A, Bentley MD, Fortepiani LA, Garcia-Estan J, Ritman EL, Romero JC, Juncos LA (2000) Microcomputed tomography of kidneys following chronic bile duct ligation. Kidney Int 58(4):1632–1640

Palmer AW, Guldberg RE, Levenston ME (2006) Analysis of cartilage matrix fixed charge density and three-dimensional morphology via contrast-enhanced microcomputed tomography. Proc Natl Acad Sci USA 103(51):19255–19260

Prinzen FW, Glenny RW (1994) Developments in non-radioactive microsphere techniques for blood flow measurement. Cardiovasc Res 28(10):1467–1475

Rai B, Oest ME, Dupont KM, Ho KH, Teoh SH, Guldberg RE (2005) Quantitative microcomputed tomography analysis of angiogenesis and osteogenesis in platelet-rich plasma loaded three-dimensional polycaprolactone-tricalcium phosphate composites implanted in rat nonunion femoral defects. Tissue Engineering Society International Conference and Exposition, Shanghai, China

Rodriguez-Porcel M, Lerman A, Ritman EL, Wilson SH, Best PJ, Lerman LO (2000) Altered myocardial microvascular 3D architecture in experimental hypercholesterolemia. Circulation 102(17):2028–2030

Samosky JT, Burstein D, Eric Grimson W, Howe R, Martin S, Gray ML (2005) Spatially-localized correlation of dGEMRIC-measured GAG distribution and mechanical stiffness in the human tibial plateau. J Orthop Res 23(1):93–101

Scholz D, Ziegelhoeffer T, Helisch A, Wagner S, Friedrich C, Podzuweit T, Schaper W (2002) Contribution of arteriogenesis and angiogenesis to postocclusive hindlimb perfusion in mice. J Mol Cell Cardiol 34(7):775–787

Silvestre JS, Tamarat R, Senbonmatsu T, Icchiki T, Ebrahimian T, Iglarz M, Besnard S, Duriez M, Inagami T, Levy BI (2002) Antiangiogenic effect of angiotensin II type 2 receptor in ischemia-induced angiogenesis in mice hindlimb. Circ Res 90(10):1072–1079

Silvestre JS, Tamarat R, Ebrahimian TG, Le-Roux A, Clergue M, Emmanuel F, Duriez M, Schwartz B, Branellec D, Levy BI (2003) Vascular endothelial growth factor-B promotes in vivo angiogenesis. Circ Res 93(2):114–123

Simopoulous DN, Gibbons SJ, Malysz J, Szurszewski JH, Farrugia G, Ritman EL, Moreland RB, Nehra A (2001) Corporeal structural and vascular micro architecture with X-ray micro computerized tomography in normal and diabetic rabbits: histopathological correlation. J Urol 165:1776–1782

Tiderius CJ, Olsson LE, de Verdier H, Leander P, Ekberg O, Dahlberg L (2001) Gd-DTPA2-enhanced MRI of femoral knee cartilage: a dose-response study in healthy volunteers. Magn Reson Med 46(6):1067–1071

Tiderius CJ, Olsson LE, Leander P, Ekberg O, Dahlberg L (2003) Delayed gadolinium-enhanced MRI of cartilage (dGEMRIC) in early knee osteoarthritis. Magn Reson Med 49(3):488–492

Van Oosterhout MF, Willigers HM, Reneman RS, Prinzen FW (1995) Fluorescent microspheres to measure organ perfusion: validation of a simplified sample processing technique. Am J Physiol 269(2 Pt 2): H725–H733

Watrin A, Ruaud JP, Olivier PT, Guingamp NC, Gonord PD, Netter PA, Blum AG, Guillot GM, Gillet PM, Loeuille DH (2001) T2 mapping of rat patellar cartilage. Radiology 219(2):395–402

Williams A, Gillis A, McKenzie C, Po B, Sharma L, Micheli L, McKeon B, Burstein D (2004) Glycosaminoglycan distribution in cartilage as determined by delayed gadolinium-enhanced MRI of cartilage (dGEMRIC): potential clinical applications. Am J Roentgenol 182(1):167–172

Williams A, Sharma L, McKenzie CA, Prasad PV, Burstein D (2005) Delayed gadolinium-enhanced magnetic resonance imaging of cartilage in knee osteoarthritis: findings at different radiographic stages of disease and relationship to malalignment. Arthritis Rheum 52(11):3528–3535

Wilson SH, Herrmann J, Lerman LO, Holmes DR Jr, Napoli C, Ritman EL, Lerman A (2002) Simvastatin preserves the structure of coronary adventitial vasa vasorum in experimental hypercholesterolemia independent of lipid lowering. Circulation 105(4):415–418

Advances in Scaffold Biomaterial Research and Applications

Materials Selection and Scaffold Fabrication for Tissue Engineering in Orthopaedics

Min Wang

Department of Mechanical Engineering, Faculty of Engineering, The University of Hong Kong, Pokfulam Road, Hong Kong, China
e-mail: memwang@hku.hk

Abstract

Tissue engineering of bone, articular cartilage, etc., in the orthopaedic field has been one of the main focuses of research ever since the discipline of tissue engineering emerged nearly 20 years ago, and yet great efforts are still needed to develop clinically usable tissue-engineered bone or cartilage for the general public. In this chapter, with our own experience in research on bone tissue engineering, candidate materials, scaffold fabrication technologies and strategies for developing bone tissue engineering scaffolds are reviewed and some important influencing factors are analyzed. Polymer-based biodegradable composite scaffolds appear to have great potential in bone tissue engineering. The successful scaffold fabrication technologies will be those that can produce good-quality scaffolds which are also of consistent quality. The capability of the technology to produce scaffolds in relatively large quantities at a reasonable cost is another important consideration. The selection of scaffold material(s) and scaffold production technology must be considered together when one embarks on developing tissue engineering scaffolds.

Introduction

Tissue engineering (TE), since the definition and use of the term appeared in open literature in 1988 (Skalak and Fox 1988), has attracted great attention in science, engineering, medicine and the society (Arnst and Carey 1998; Griffith and Naughton 2002; Langer and Vacanti 1993; Lysaght and Hazlehurst 2004; Mooney and Mikos 1999). The societal issues arising from TE, such as the use of embryonic stem cells from aborted fetus, should never be underestimated (Lloyd-Evans 2004; McIntire 2003; Williams 2004). But these issues are beyond the scope of this chapter and hence not discussed in the chapter. As a new and multidisciplinary endeavor, TE holds the promises of (a) eliminating re-operations by using biological substitutes, (b) using biological substitutes to solve problems of implant rejection, transmission of diseases associated with xenografts and shortage in organ donations, (c) providing long-term solutions in tissue repair or treatment of diseases, and (d) potentially offering treatments for medical conditions that are currently untreatable such as fulminant hepatic

failure. It has made rapid advances over the past two decades (McIntire 2003; Skalak and Fox 1988) due to more knowledge being gained in biology and clinical sciences, the advancement in physical sciences and technology, and more willingness for collaboration and actual deeper collaboration among clinicians, engineers and scientists. The government support in terms of research funding in this field in industrialized as well as developing countries has also played a crucial role. In essence, TE uses living cells, together with extracellular components, to form implantable devices for the regeneration of tissues in damaged or diseased parts of the human body. Living cells are anchorage dependent and will die if they are not provided with a suitable adhesion substrate. Synthetic scaffolds are designed to provide a structural framework as well as a microenvironment for the selected cells and to facilitate the formation of new tissues. It has been generally agreed in the TE community that one of the key issues in TE is the development of suitable biodegradable scaffolds (Lanza et al. 2000). Different application situations require scaffolds of different characteristics.

Researchers around the world are exploring possibilities of applying the TE concept in orthopaedics, dentistry, artificial organs, etc., to treat patients where TE approaches have significant advantages over conventional medical treatments. For TE in orthopaedics, research for the regeneration of bone, articular cartilage, tendon and ligaments, and muscles are being conducted. As the mechanical and biological requirements for these tissues are different (Fung 1993; Lindsay 1996), the approaches to their respective regeneration are thus different.

This chapter focuses on scaffold materials and scaffold manufacture for bone TE, with an additional, small coverage on hydrogel tubes for nerve tissue regeneration. Since 1988, "tissue engineering" has been given various definitions (Langer and Vacanti 1993; Lanza et al. 2000; McIntire 2003; Nerem 1992; Patrick et al. 1998; Skalak and Fox 1988). This chapter uses the term "tissue engineering" in its broadest sense, also extending it slightly to cover the broader area of tissue repair.

Current Strategies for Tissue Engineering Scaffolds

Currently, there are a number of strategies for TE scaffolds. Biomaterials experience with biodegradable polymers in the pre-TE decades, i.e. the time before the U.S. National Science Foundation's panel meeting on tissue engineering in 1987 (Skalak and Fox 1988), has heavily guided researchers towards using medical-profession-accepted and the U.S. Food and Drug Administration (FDA)-approved biopolymers such as poly(lactic acid) (PLA) and poly(lactic acid-co-glycolic acid) (PLGA) for constructing TE scaffolds. The medical device industry and the medical profession had gained sufficient knowledge of these biodegradable materials and using them for TE scaffolds, rather than developing newer and more appropriate materials for such purposes, as was perceived, could shorten the time to get tissue-engineered medical products (TEMPs) from concept/a research laboratory to the general public. Indeed, there has been an abundance of literature on scaffolds made of these polymers (Lanza et al. 2000; McIntire 2003).

For all porous structures, their strengths decrease drastically with an increase in porosity (Gibson and Ashby 1997). Tissue engineering requires highly porous struc-

tures, with the ideal porosity being up to 97%. The inherent weakness of polymeric scaffolds, due to both low mechanical properties of bulk polymers and high porosity levels of the scaffolds, has led to the exploration of using porous metals or ceramics as substrates for bioactive scaffolds (Fujibayashi et al. 2004; Jiang and Shi 1998). Metals and ceramics possess higher strength and stiffness than polymers, and metals are also ductile. Porous bioinert ceramics, such as alumina, can be coated with hydroxyapatite (HA), which is a ceramic material and is osteoconductive (Wang 2002), and thus have the potential for bone tissue repair. An apatite coating can also be deposited on titanium, which is a corrosion-resistant and biocompatible metal that has been widely used for implants, through biomimetic processes (Kokubo et al. 2004). Porous titanium coated with a thin layer of apatite can be another useful system for bone tissue repair. Making a metal foam ("metal foam" is interchangeable with "metallic scaffold" and "porous metal" in this chapter), as opposed to a polymer foam, boosts strength and stiffness, while, in comparison with a porous ceramic, important advantages are expected in terms of toughness and formability. Using non-degradable metallic or ceramic materials for TE scaffolds may contradict the common notion of TE; it nonetheless provides potentially new means for tissue regeneration and thus should be considered as part of the overall TE effort.

The past three decades have witnessed the tremendous progress that was made on bioceramics (the term "bioceramics" used in this chapter encompasses ceramics, glasses and glass-ceramics that are/can be used inside human bodies for prosthetic, diagnostic or therapeutic applications). There is now a comprehensive understanding of structures and properties of bioactive bioceramics, such as HA, tricalcium phosphate (TCP) and Bioglass® (Wang 2002), and these materials have been successfully used in various forms in orthopaedics and dentistry. This group of biomedical materials, viz., bioactive (and for some of them, biodegradable as well) bioceramics, has actually been underestimated for their potential in TE, as polymeric scaffolds have all along been preferred by "tissue engineers". Nevertheless, porous bioactive bioceramic structures have been made and studied for potential TE applications (Callcut and Knowles 2002; Pereira et al. 2005; Yang and Wang 1999).

The concept of using analogous materials for bone tissue substitution was introduced more than two decades ago (Bonfield et al. 1981). These bone analogues are synthetic composites based on polymer matrices since bone is a natural composite material that consists of nano-sized apatite and collagen (Wang 2003). Some of these bioactive ceramic-polymer composites are now in clinical use. Using the same rationale of imparting bioactivity (i.e. osteoconductivity, as implied in this chapter) on polymer substrates through the composite strategy with the use of secondary phase of bioactive (i.e. osteoconductive) bioceramics, polymeric TE scaffolds can be made bioactive and also strengthened with the help of bioactive bioceramics. There are two approaches for making bioceramic-polymer composite scaffolds: (a) incorporating bioceramic particles in the scaffold, rending the composite scaffold bioactive (Wang et al. 2001); or (b) coating the polymer scaffold with a thin layer of apatite through biomimetic processes (Chen et al. 2005a), with the apatite layer thus formed stiffening the original polymer scaffold and making the scaffold bioactive.

The polymers used for these scaffolds, natural or synthetic, have almost always been biodegradable biopolymers.

The strategies outlined above have been adopted by various research groups in different countries, and some of the scaffolds thus developed show promises for bone TE. Provided with more knowledge on properties of currently developed scaffolds and with further understanding of specific cell-scaffold interactions, there certainly will be development of new strategies in TE scaffolds.

Candidate Materials for Tissue Engineering Scaffolds

The judicious selection of materials for TE scaffolds obviously should be considered together with the type of scaffolds that will be used, which in turn must be considered in a wider context of the regeneration of a specific tissue in vitro and in vivo.

Biomedical Polymers

Biodegradable Polymers

Traditionally, polyesters such as PLA and PLGA are materials of choice for TE (not only the TE of bone, cartilage, etc., but also the TE of skin, heart valve and other tissues). The degradation rate of these polymers is affected by the average molecular weight of the polymer (Li 1999); therefore, scaffolds made of PLA or PLGA of different average molecular weights have been studied. Furthermore, other factors, such as crystallinity of the polymer, can also affect the degradation rate (Iannace et al. 2001). Another important consideration is the effect of porosity level on degradation rate of scaffolds (Sultana and Wang 2007), as porous structures have larger surface areas than non-porous bulk polymers, which accelerates the degradation. The emphasis on achieving high interconnectivity of pores in tissue engineering scaffolds further promotes scaffold degradation. Other synthetic polymers, such as poly(ε-caprolactone) (PCL) and poly(propylene fumarate) (PPF), have also been investigated for making TE scaffolds (Hutmacher 2000; Lanza et al. 2000). Biodegradable polymers developed for controlled drug release purposes, e.g., some poly(ortho esters) (Leong et al. 1985), may also be considered for constructing TE scaffolds.

Natural polymers, including collagen (which is a main component of body tissues), chitosan (which is derived from chitin which occurs mainly in crustacea, molluscs and insects where it is an important constituent of the exoskeleton) and polyhydroxybutyrate (PHB, which is made by many microorganisms under the conditions of nitrogen deficiency), are also potential materials for TE scaffolds. They may have the advantage over synthetic biodegradable polymers as their degradation products are part of the body or body fluids (Kohn et al. 2004; Yannas 2004).

"Biostable" Polymers

Polymers have been widely used in medicine for several decades now due to a number of reasons. Their main advantages include ease of fabrication into desired shapes as compared with metals and ceramics and also low cost. Biocompatible polymers, such as polyethylene (PE), polypropylene (PP), polyurethane (PU), polytetrafluoroethy-

lene (PTFE), poly(vinyl chloride) (PVC), polyamides (PA), poly(methyl methacrylate) (PMMA), polyacetal, polycarbonate (PC), poly(ethylene terephthalate) (PET), polyetheretherketone (PEEK) and polysulfone (PSU), when used in general engineering applications, are considered "stable" in comparison with some biodegradable (i.e. "environmentally degradable", to be precise, in the outdoor environment rather than in the human body environment) polymers for general use such as starch polymers and cellulose, and hence they have also been labeled as "biostable" as compared with biodegradable (i.e. degradable in the human body environment) polymers such as PLA and PLGA; however, the human body environment is very hostile to foreign materials, and any polymer, whether it is termed "biodegradable" or "biostable" by the general engineering profession, will degrade in the body over a short period or over several years after implantation. The current practice of using accepted biodegradable polymers for tissue engineering scaffolds probably can and should be extended to include the use of "biostable" polymers, such as Kevlar, which has been used in the fibrous form for tendon and ligament repair. The use of "biostable" polymers in TE can be viewed as (a) a natural inclusion of degradable materials, which have much longer degradation time as compared with existing, accepted biodegradable polymers, but eventually will degrade in the human body, for their utilization in tissue regeneration; or (b) employing a new category of materials, as in the case of using porous metals (stable or non-stable in the body), which is discussed later in this chapter, for bone tissue repair.

Hydrogels

Polymeric hydrogels are cross-linked macromolecular networks formed by hydrophilic polymers swollen in water or biological fluids. They offer unique properties that could be used for drug delivery and/or TE (Li 2004). There are chemical hydrogels and physical hydrogels, depending on the bonding type of the cross-links. Polymer networks of chemical hydrogels are formed by chemical cross-linking through covalent bonding, and hence chemical hydrogels are also called permanent hydrogels. Physical gels are continuous, disordered and three-dimensional hydrophilic polymer networks formed by cohesion forces capable of constituting non-covalent cross-links. These cohesion forces include ionic bonding, hydrogen bonding, van der Waals forces, etc. As physical gels are not covalently cross-linked, the formation of the physical cross-links is largely dependent on parameters such as local temperature, pH, salt type, ionic strength, etc. This characteristic makes it possible to utilize physical hydrogels for tissue engineering. Hydrogels, as water-swollen polymers, can be used as scaffolds (in this situation, for encapsulating cells) and provide an ideal microenvironment for cells which have been distributed in the hydrogels before their injection into the defect sites (ideally, to treat irregularly shaped defects). Hydrogels of both natural polymers, such as collagen (Yang et al. 2004), alginate (Heywood et al. 2004) and chitosan (Mwale et al. 2005), and synthetic polymers such as poly(N-isopropylacrylamide) (Stile et al. 1999), have been investigated for TE purposes.

Bioceramics

Biodegradable Bioceramics

Over the years, HA, TCP and biphasic calcium phosphates (BCP, which contains HA and TCP in different proportions) have been made in the porous form and used as implants in orthopaedics. HA is normally considered to be non-biodegradable as the dissolution rate of non-porous implants of stoichiometric HA is very low in the body environment (Wang 2002), whereas TCP and BCP are biodegradable. The degradation rate of BCP can be controlled by the HA:TCP ratio (Bagot D'Arc and Daculsi 2003). Histological analysis of porous HA, TCP or BCP implants showed bone apposition in the porous structures (Hing et al. 1999; Bagot D'Arc and Daculsi 2003). As there is now a comprehensive understanding of the calcium phosphate family, of which HA and TCP are prominent members, producing scaffolds of HA or TCP appears to be appealing to a number of research groups which have for a few years now conducted research into these scaffolds for bone TE.

Biological apatites constitute the mineral phase of calcified tissues such as bone, dentin and enamel in the body, and also some pathological calcifications. They are similar to synthetic HA, but they differ from HA in composition, stoichiometry, and physical and mechanical properties (LeGeros and LeGeros 1993). Biological apatites are usually calcium-deficient as a result of various substitutions in regular HA lattice points. Among the variety of HA-based bioceramics, carbonated hydroxyapatite (CHA) is a promising material for bone TE as it is bioresorbable and also more bioactive in vivo than stoichiometric HA. HA synthesized in the normal environment is CHA. There are two types of carbonate (CO_3^{2-}) substitution: the carbonate ions can substitute for both the hydroxyl (A-type CHA) and phosphate (B-type CHA) groups in the HA structure. Through theoretical calculations, it has been shown that B-type or PO_4^{3-} substitution is energetically preferred to A-type or OH^- substitution (Astala and Stott 2005), which explains why most CHA synthesized is B-type substituted HA. Recently, through a nanoemulsion process, nanospheres of B-type CHA were synthesized (Zhou et al. 2005). These CHA nanospheres (Fig. 1) can be either utilized on their own to form bone TE scaffolds or incorporated into biodegradable polymers to form osteoconductive composite scaffolds (Zhou et al. 2006).

Bioactive Glasses

Bioglass® is the first and also the most well-known bioactive glass that has been developed specifically for human body tissue repair. Since its invention in 1969, Bioglass® has been extensively researched (Hench 2001). It has been traditionally used in the non-porous form for orthopaedic and dental implants (Wang 2002). Bioglass® of different compositions dissolves at different rates after implantation in the body and Bioglass® 45S5 is the most bioactive material which can bond not only to bone but also to soft tissues. Recently, efforts have been made to form porous Bioglass® structures for TE applications (Pereira et al. 2005). This new exploration can give a new life to Bioglass®, which has commanded a very prominent position in the bioceramics field.
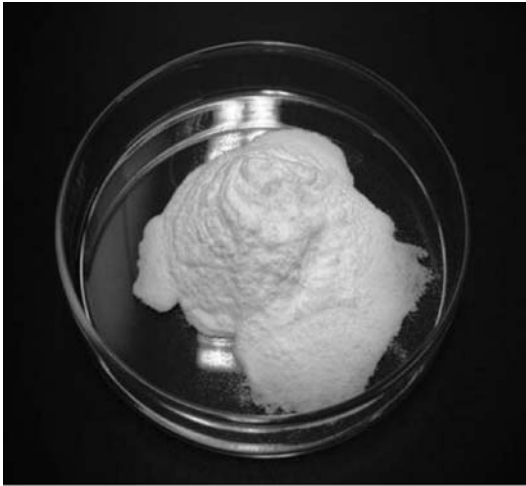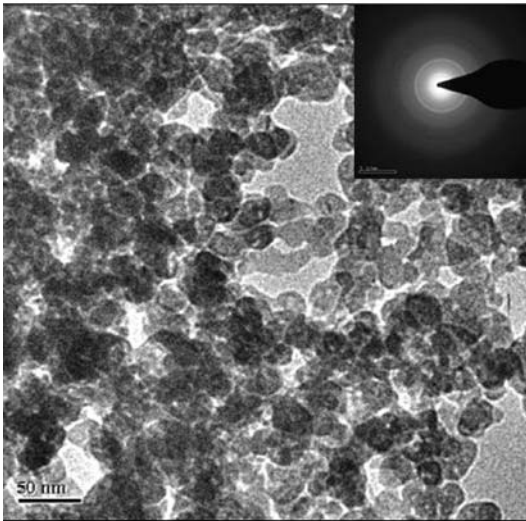
Figure 1 a,b. Carbonated hydroxyapatite (CHA) nanospheres synthesized through a nanoemulsion process. **a** Freeze-dried powder. **b** A transmission electron microscopy image and SAD pattern (*inset*) of the CHA powder

A series of studies have found that another bioactive glass, Biogran®, can be useful in the particulate form for bone TE (Huygh et al. 2002). After 2 months of implantation, the glass granules became excavated. After 6 months of implantation, bone formation in the excavated lumen was observed.

Investigations have been made to make new bioactive glasses for tissue repair. Fibres have been produced from some of these glasses, which in turn could be used to form three-dimensional glass fibre constructs (Shah et al. 2005). The glass fibres were shown to support the proliferation and differentiation of human masseter muscle-derived cells.

Bioinert Bioceramics

Bioceramics such as alumina (Al_2O_3) and toughened zirconia ceramics (ZrO_2) are biocompatible and also very stable in the human body environment, and hence they are currently used for mainly hard tissue repair in the non-porous form. Even though toughened zirconia ceramics possess higher fracture toughness than alumina (fracture toughness is a very important property for brittle materials such as ceramics), there are still a few problems for the application of zirconia ceramics in the orthopaedic field (Wang 2002); therefore, among bioinert bioceramics, only alumina has been used so far in the porous form as the substrate of HA coatings (Jiang and Shi 1998). Like the current use of non-porous alumina for the femoral head of hip prostheses, porous alumina for bone tissue repair should be of the medical grade, i.e. the alumina must have high purity ($\geq$ 99.5%) and high density ($\geq$ 3.90 g/cm^3) and be fine-grained ($<$ 7 μm in grain size) (Wang 2002). The compressive strength and fracture toughness of this grade of alumina in the non-porous form are expected to be $\sim$ 4500 MPa and 5 $\sim$ 6 MPa $\cdot$ m$^{1/2}$, respectively. But for porous alumina, the strength is expected to be much lower, as the strength of a porous structure decreases exponentially with the level of porosity (Gibson and Ashby 1997; Yang and Wang 1999). The pore size of porous alumina should be between 200 and 400 μm, just as what is required for tissue engineering scaffolds made of polymers. The HA or other bioactive coatings formed on the pore surfaces of alumina substrates should not be too thick to reduce the average pore size significantly, nor should they block the channels between pores. The interconnectivity of pores of porous ceramics structures must be retained after the coating process.

Implantable Metals

Titanium and Alloys

Current orthopaedic metals, such as stainless steel and Co-Cr alloys, and the emerging Ti-Ni shape memory alloys (SMA), contain Ni whose ions can be released into the surrounding tissue after implantation and thus cause adverse biological effects. These metallic materials are not suitable as porous metal substrates for apatite coatings because the thin apatite layer cannot stop the release of Ni ions from the metal substrate into the surrounding tissue in the long term. (These metals have served well in the past as implant materials. Unless surface modifications of these metals can inhibit Ni ion release from the substrate, whether it is in the non-porous or porous form, in the long term, these metals should be eliminated from being used inside human bodies.) Ti and its alloys have emerged strongly as metallic biomaterials for implants that require strength, toughness and suitable stiffness (Helsen and Breme 1998). Compared with other metals currently used for implants, Ti is light (density of 4.5 vs 7.9 g/cm^3 for 316L stainless steel and 9.2 g/cm^3 for wrought Co-Ni-Cr-Mo alloy) and possesses good mechanical strength (which is much higher than those of biomedical polymers) and a closer-to-bone elastic modulus ($\sim$ 110 vs 190 GPa for stainless steel and 210 GPa for Co-Cr alloys, whereas the modulus of human cortical bone is 7 $\sim$ 30 GPa.), and it does not have the problem of release of heavy metal ions. Furthermore, Ti is known

to have the special property of "osseointegration" (Branemark et al. 2001), which has been successfully utilized in dentistry and also for cementless hip prostheses. Ti and its alloy Ti-6Al-4V therefore appear to be the materials of choice for forming metallic foams on which apatite is deposited. Compared with porous alumina, porous Ti has the advantage of being much tougher and much less fragile.

Magnesium and Alloys

Magnesium ion is the fourth most abundant cation in cellular organisms. The relatively high natural abundance of Mg and its many favourable physical and chemical properties have resulted in the assimilation of Mg^{2+} for many vital biological functions (Cowan 1995). Magnesium plays a very important role within the cell and affects many biological functions within the body. Yet Mg has been underestimated as a biomaterial due to several reasons. The main weakness of Mg, i.e. having poor corrosion resistance in the context of general engineering applications (Song 2005), may be turned into an advantage for Mg in the TE field, as scaffolds are normally desired to be degradable and the human body environment is very corrosive.

The Mg ions from modified bioceramic substrata ($Al_2O_3-Mg^{2+}$) were shown to have effects on human bone-derived cell (HBDC) adhesion, integrin expression and activation of intracellular signaling molecules (Zreiqat et al. 2002). It was demonstrated that adhesion of HBDC to Al_2O_3-Mg^{2+} was increased compared with that on the Mg^{2+}-free Al_2O_3. The HBDC grown on the Mg^{2+}-modified bioceramic expressed significantly enhanced levels of β1-, α5β1- and α3β1-integrins receptors compared with those grown on the unmodified Al_2O_3. Mg^{2+} supplementation of bioceramic substrata appeared to be able to improve integration of bioceramic implants to local tissues. Because of the importance of Mg in bone growth, HA with Mg substitutions was synthesized and studied (Kim et al. 2003). In a recent investigation of the biocompatibility of Mg, it was found that Mg had no inhibitory effects on marrow cell growth and that there were no signs of cellular lysis (Li et al. 2004); however, alkali- and heat treatment improved the corrosion resistance of Mg, which may not be conducive to the TE applications of this metal.

Composites

Biopolymer-Based Composites

As stated previously, on the basis of mimicking the structure and matching mechanical properties of bone, non-porous bioactive ceramic-polymer composites can be made and used to replace diseased or damaged bone. These materials are synthetic composites and are fabricated through a number of techniques (Wang 2003). The natural extension of the biomimicking concept to the production of bioactive polymer-based composite scaffolds has led to extensive research in this area in recent years. The main purpose for composite scaffolds to contain bioactive bioceramics is the utilization of osteoconductivity of these bioceramics (Weng et al. 2002). There could be an additional effect of strengthening and stiffening of the scaffolds due to the presence of bioceramics (Wang and Ni 2004; Chen et al. 2005a). A number of composite scaffolds have been investigated for bone TE, which include HA/PLGA (Devin et al. 1996),
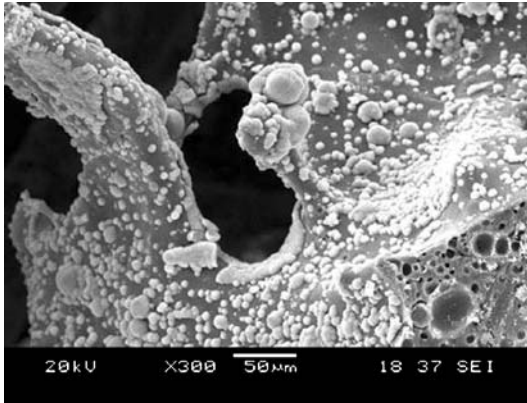
Figure 2. Formation of bone-like apatite on a Ca–P/PLLA composite scaffold during immersion in a simulated body fluid

TCP/PPF (Peter et al. 1998), HA/PLLA (Zhang and Ma 1999), HA/collagen (Du et al. 1999), HA/PCL (Zein et al. 2002), calcium phosphate/chitosan (Zhang and Zhang 2001), calcium phosphate/PLLA (Weng et al. 2002), and Bioglass®/PLLA (Roether et al. 2002). Bioceramic particles incorporated in the polymer scaffolds have been shown to render the scaffolds bioactive (Fig. 2). As can be seen from the aforementioned composite scaffolds, the matrices of these scaffolds are dominantly biodegradable polymers. There are signs, through, that a few researchers are considering using some biocompatible and "biostable" polymers, especially in the fibrous form and with apatite coatings, for TE applications.

The selection of constituents for the composite forming the scaffold is very important, as this leads directly to the success or failure of a TE strategy. Several factors must be considered, which come from potential constituents of the composite and also from the scaffold fabrication technology, as the issues involved cannot be separated simply into two sides:

1. Composite
   a. Polymer matrix: its mer unit, average molecular weight, etc., which affect the physical, mechanical and degradation properties of the scaffolds
   b. Bioceramic phase: its level of bioactivity, particle size, particle shape, etc.
   c. Interactions between the polymer matrix and the bioceramic phase during scaffold production and also in the as-produced state
   d. Interactions between the polymer matrix and the bioceramic phase during biodegradation in the in vitro and/or in vivo environment
   e. Cell and tissue reactions to respective constituents of the composite and also the composite as a whole at the initial non-degradation stage and during the subsequent biodegradation process (in the process, the degradation product(s) is/are an important factor)
   f. Material cost: whether the constituting materials are at an affordable cost
2. Scaffold production
   a. The manufacture technology/route: whether it is a simple and easy process, or a complicated and time-consuming process

  b. The manufacture technology/route: whether it is a laboratory-scale-only process or an industrial process, and whether the laboratory-scale production can be upscalable and up-scaled relatively easily
  c. The fabrication technique: whether it can produce scaffolds of good quality and of consistent quality
  d. The fabrication technique: whether it requires expensive equipment or the production is a costly process
3. Consideration of economy: whether the scaffold is made fully justifying the cost incurred, as assessed by the benefit/cost ratio and also in comparison with the cost of current treatment method of the disease/trauma (this point can be applied to all TE scaffolds)

Under many circumstances, the decision to use a particular polymer with a particular bioceramic to form a composite scaffold has already led to the decision as to which scaffold production technique is to be used.

Bioceramic-Based Composites

Even in the non-porous form, bioactive calcium phosphates, such as HA and TCP, are weak and fragile (Wang 2002). Pores in these ceramics make them even weaker. With high porosity (>50%), the strength of sintered HA is very low (Yang and Wang 1999). An effective way to strengthen and toughen HA is to add a small amount of biocompatible or both biocompatible and bioactive glass to HA, which can significantly increase the strength and toughness of the sintered product (Wang and Yong 2001). Glass-toughened bioactive bioceramic scaffolds can be considered as composite scaffolds (with glass being the secondary constituent, albeit in a small quantity) and have been produced and investigated (Callcut and Knowles 2002). Glass toughening provides a means to improve the mechanical properties of HA scaffold while maintaining the osteoconductivity of the porous structure.

Scaffold Fabrication

Depending on the material or materials (polymer, metal, ceramic or composite) to be used for a TE scaffold, scaffold fabrication techniques differ greatly.

Conventional Technologies

These technologies are "conventional" as they have been used commonly in chemical engineering, ceramic engineering, metal production and forming, composite technology and other fields for purposes other than biomedical applications or for producing porous structures that are not intended for the biomedical industry. Tissue engineering uses these technologies to produce various scaffolds for the regeneration of tissues or organs.

Technologies for Polymeric Scaffolds

As stated previously, due to historical reasons and also quite a number of other factors, making biodegradable polymer scaffolds together with their characterization and evaluation was the earliest and has been the main focus in TE scaffold studies worldwide since TE was started in the 1980s; therefore, the technologies for producing biodegradable polymer scaffolds have been well documented (Atala and Lanza 2002; Hollander and Hatton 2004; Lanza et al. 2000). These technologies include, but are not limited to, fibre bonding, compression/injection moulding and particulate-leaching, solvent casting and particulate leaching, and phase separation/freeze drying. The two techniques, viz., solvent casting and particulate leaching, and phase separation/freeze-drying, appear to be popular among researchers, as they can be used to produce highly porous structures with interconnecting pores; however, the polymer scaffolds produced have been based mainly on PLA- and PLGA-type polymers. In a recent study, it was shown that through an emulsion freeze-drying process, scaffolds based on PHB and polyhydroxybutyrate-co-valerate (PHBV) natural polymers could be produced (Sultana and Wang 2007). Also, using this technique, highly porous structure with controlled pore morphologies could be achieved (Fig. 3). The mechanical behaviour of such PHB and PHBV scaffolds, as illustrated in Fig. 4, is the same as those of highly porous structures (polymer or metal foams). It is certain that using the aforementioned techniques, which are commonly employed in chemical engineering, to produce polymer scaffolds, factors such as polymer solution concentration, porogen type and size, freeze-drying parameters, etc., play very important roles in forming the scaffolds of desired porous structures (pore geometry, pore size and size distribution, pore interconnectivity, thickness of pore walls, etc.) and hence mechanical performance (Weng et al. 2002; Weng and Wang 2001a; Sultana and Wang 2007). Figure 5 shows the effect of solution concentration of chitin polymer during the solvent-casting process on the pore morphology and thickness of pore walls of chitin scaffolds produced.

Carefully modifying the manufacture procedures used for pure polymer scaffolds (Wang 2003), polymeric composite scaffolds containing bioactive ceramic particles,
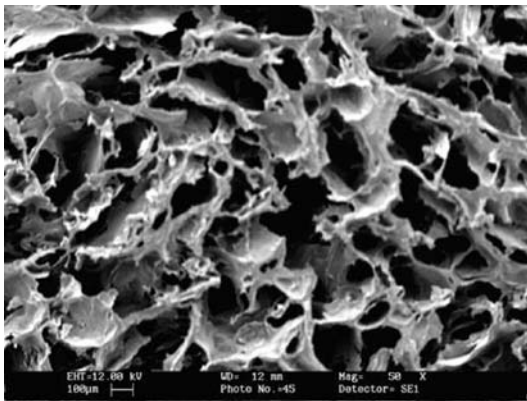
Figure 3. A PHBV scaffold produced through an emulsion freeze-drying process
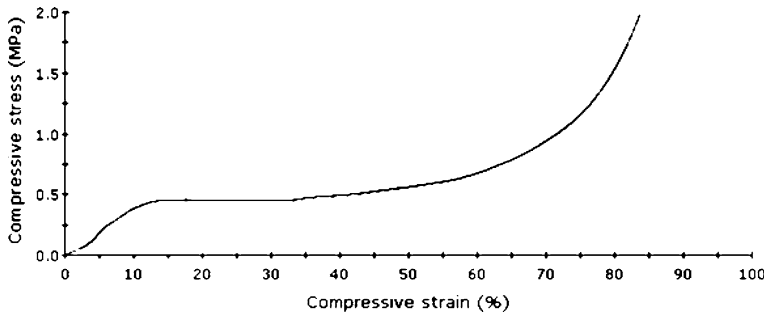
Figure 4. Compressive behaviour of a PHBV scaffold produced through the emulsion freeze-drying process
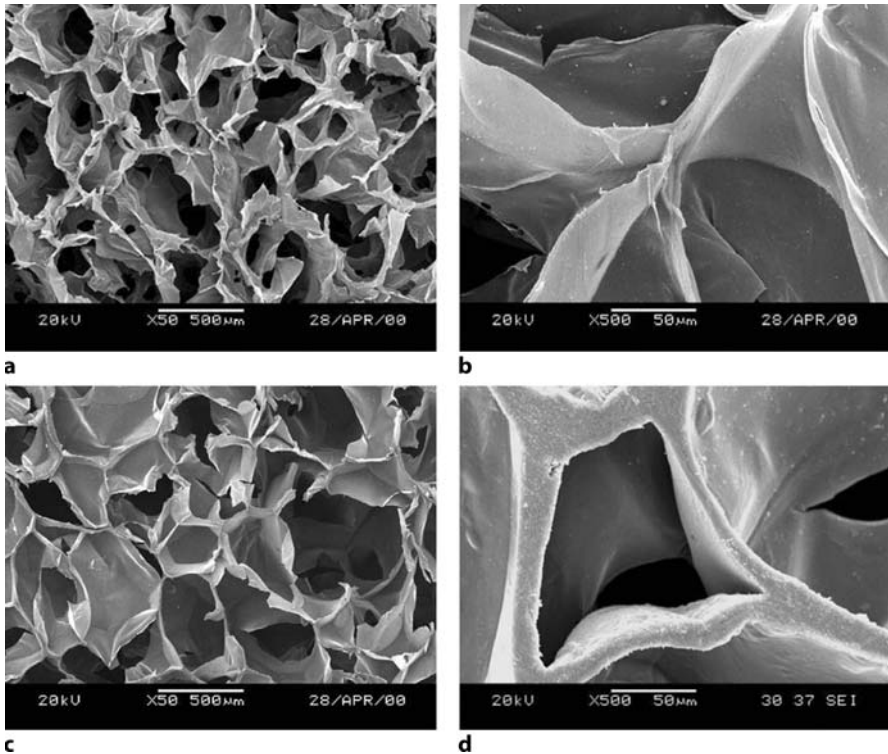
Figure 5 a–d. Chitin scaffolds formed from chitin polymer solutions of different concentrations: **a,b** 0.5% (w/w) chitin solution; **c,d** 1.5% (w/w) chitin solution

such as microspheres of HA (Weng et al. 2002) or nanospheres of CHA (Sultana and Wang 2007), could be produced; however, there is certainly a limit for the amount of particulate bioceramics to be incorporated in composite scaffolds.
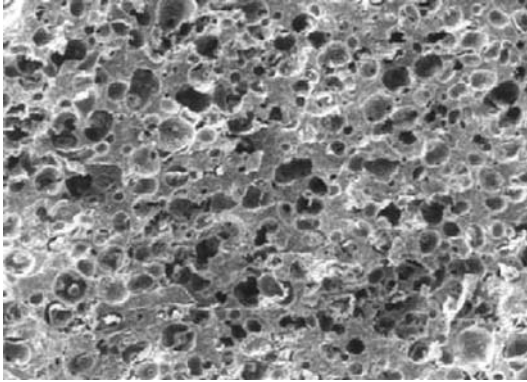
Figure 6. Porous HA made via a modified slip-casting process

Technologies for Bioceramic Scaffolds

There are a variety of methods that can be used to form porous objects of bioactive bioceramics such as HA and TCP; they include deproteinization and sintering of animal bones, hydrothermal conversion of corals, solid reaction route, foaming, sintering of microspheres, etc. (Wang 2002). Coating a polymeric sponge with bioceramic particles in slurry with subsequent burn-off of the sponge can result in a porous bioceramic structure (Fabbri et al. 1995). Using polymer granules as porogens in greenbodies, using gas (hydrogen peroxide) foaming, and using a modified slip-casting technique has appeared to work well in producing porous HA or TCP (Wang and Wang 2000; Yang and Wang 1999). Figure 6 shows a sintered porous HA made through the modified slip-casting process. When tested in the biaxial flexural deformation mode, porous HA discs still exhibited a brittle fracture behaviour (Fig. 7a), and it is evident that a high porosity level rendered porous HA very weak (Fig. 7b).

Recent investigations into forming porous Bioglass® (Pereira et al. 2005) and other bioactive glasses for TE applications undoubtedly provide new impetus into the further development of bioceramics. The manufacture of bioactive calcium phosphate or glass fibres is another notable new development of bioceramics with regard to their use in TE (Shah et al. 2005).

Another direction in making bioactive porous ceramics for tissue repair is to coat bioinert ceramics, such as alumina, with a thin layer of bioactive bioceramics (discussed later). The manufacture of porous technical ceramics, such as alumina, is beyond the scope of this chapter. Information on general ceramic processing can be found elsewhere (Rahaman 2003; Rice 2002).

Technologies for Metallic Foams

There are a number of techniques to make metallic foams (Ashby et al. 2000; Degischer and Kriszt 2002), including foaming, powder metallurgy, and positive replica processing. These techniques have been used to mainly produce porous Ti and Mg for possible hard tissue repair.

A "polymer sponge replication" procedure was used to make highly porous and strong Ti-6Al-4V (Li et al. 2005). In this process, a polymeric sponge, impregnated
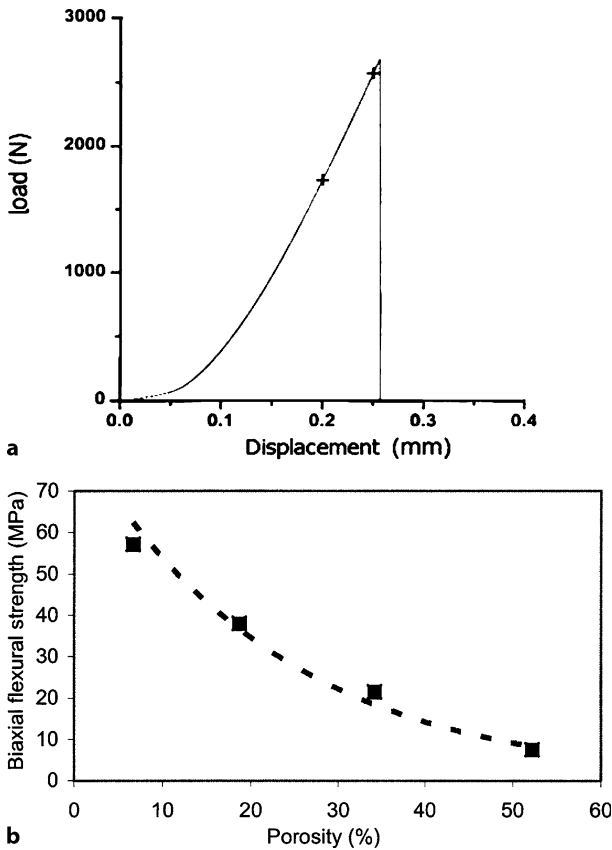
Figure 7 a,b. Mechanical testing results of porous HA. **a** A typical load-displacement curve of porous HA tested under the biaxial flexural deformation mode. **b** Influence of porosity on biaxial flexural strength of HA

with a Ti–6Al–4V slurry prepared from Ti–6Al–4V powders and binders, was firstly subjected to drying pyrolyzing to remove the polymeric sponge and binders. After sintering at a high temperature and under high vacuum, a porous Ti–6Al–4V was produced. It was found that the porous Ti–6Al–4V made had a three-dimensional porous structure with interconnected pores ranging from 400 to 700 μm and a total porosity of ~ 90%. Its mechanical properties (compressive strength and modulus of elasticity) were similar to those of cancellous bone and hence it appeared to be a suitable material and structure for bone tissue repair. In a recent investigation, the plasma spraying technology was used to make porous Ti structures on solid Ti posts (Wu and Wang, in press). In this study, commercially pure Ti powders (feedstock particle size: 40 μm) were plasma sprayed onto Ti rods (Φ10 mm) using controlled spray parameters so as to form a porous structure rather than a compact coating on the Ti rods (Fig. 8). A medium level of porosity and a controlled pore size could be achieved through this process.

Efforts have also been made to produce porous Mg for bone substitution. Two methods, viz., a "replica-casting" process (Wen et al. 2000) and a powder metallurgy technique (Wen et al. 2001), have been used, respectively, to fabricate porous Mg and
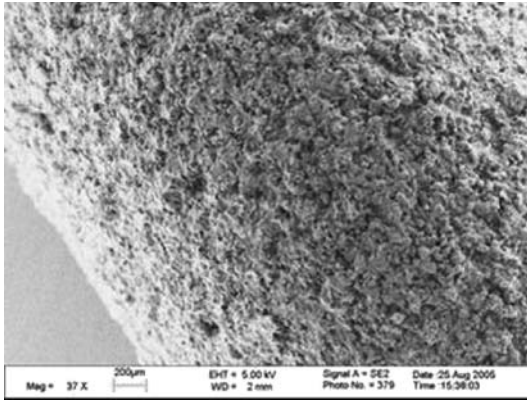
Figure 8. Porous Ti structure produced by plasma spraying of fine Ti powders

its alloy. An open-cell structure of Mg alloy was made through the replica-casting process and its mechanical behaviour under compression was similar to those of other cellular metals. In the powder metallurgy route, the porous morphology, pore size, and porosity of Mg could be controlled via the appropriate choices of spacers. The Mg foams also exhibited an open-cell structure and the pores were in the range of $200-500\,\mu m$, which were intended to simulate the cancellous bone structure. The Mg foams could have a compressive strength of 2.33 MPa and modulus value of 0.35 GPa, which were assumed to be strong enough for handling during implantation and for in vivo loading. Work has been started on a new process to form Mg foams for possible tissue engineering applications (M. Wang, unpublished data).

Rapid Prototyping Technologies

Rapid prototyping (RP) technologies have been widely used in the traditional manufacturing industry (Cooper 2001; Chua et al. 2003). In recent years, they have found applications in the TE field for the production of mainly polymer-based scaffolds. Unlike most other scaffold production techniques currently used by various research groups, RP technologies are mature, industrial processes which offer opportunities to produce scaffolds with consistent pore characteristics in potentially large quantities. The RP technologies are thus strongly appealing in the TE field when they are used to mass-produce scaffolds of consistent quality and also of good quality if the scaffolds are properly designed and made, which is essential for the commercialization of scaffolds. Furthermore, scaffold architecture, which can affect cell behaviour and tissue formation, can be easily designed and changed (manipulated) (Yang et al. 2002). There is also the added advantage of using computer files generated by modern medical imaging techniques (such as MRI) to produce custom-made TE scaffolds for individual patients through various RP technologies which design the appearance (shape and size) of products using computer software. Examples of RP technologies for TE scaffold fabrication include fused deposition modelling (Zein et al.

2002), three-dimensional printing/robotic dispensing (Lam et al. 2002) and selective laser sintering (SLS) (Lee et al. 2005).

Among the various RP technologies, SLS appears to be advantageous for scaffold fabrication because it can process a wide range of biomaterials and produce tailor-made scaffold architectures to meet complex anatomic requirements; however, as SLS has been developed primarily for industrial applications (Cooper 2001), it is not financially feasible at present to use commercial, unmodified SLS machines for biopolymer scaffold production, because the amount of material required is quite large and most commercial, biodegradable polymers for medical applications are still very expensive. In a recent investigation, to minimize the material consumption, a miniature sintering platform, which consisted of two small powder supply chambers, one small build cylinder and recycle bins, was built and installed in the build cylinder of a commercial SLS machine (Zhou et al. 2006). With this modification, TE scaffold could be manufactured from powders of either PLA (Lee et al. 2005) or CHA/PLA composite (Zhou et al. 2006). Another critical issue in using the SLS technology to produce scaffolds is the feedstock powder. Only powders of very fine particles (≤ 70 µm in diameter) can be used as the raw material for sintering; thus, particulate biopolymers in the as-supplied state are too large in size to be used for the SLS process. Therefore, for producing polymer-based scaffolds, fine powders of PLA had to be made from as-supplied PLA granules through a single emulsion process (Lee et al. 2005) and microspheres of CHA/PLA nanocomposite were produced using a bioceramic-nanoemulsion-co-polymer-emulsion technique (Zhou et al. 2006). Figures 9 and 10 exhibit PLA and CHA/PLA microspheres for SLS. As can be seen from Fig. 10b, CHA nanospheres synthesized through the nanoemulsion process were encapsulated in the microsphere.

The RP technologies can also be used to produce bioceramic scaffolds. It was reported that HA scaffolds with interconnecting square pores were created indirectly through stereolithography (SLA)(Hollister et al. 2002). These HA scaffolds had compressive moduli of 1.4 GPa and ultimate compressive strength of 30 MPa, which are similar to those of coralline HA.
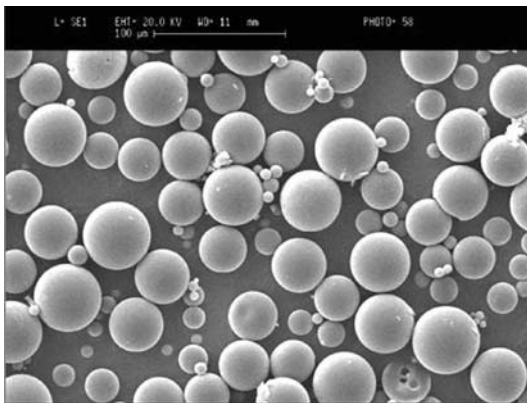
Figure 9. The PLA microspheres for the production of tissue engineering scaffolds using the selective laser sintering technology
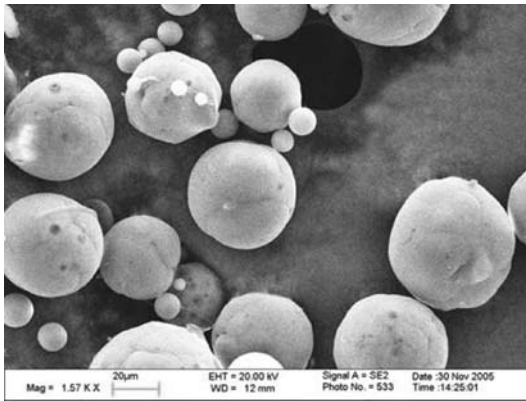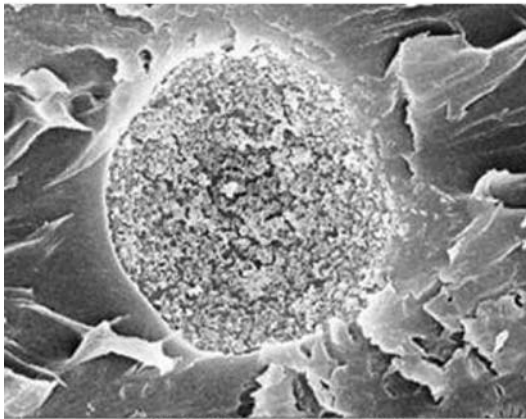
Figure 10 a,b. Microspheres of CHA/PLA nanocomposite for the production of tissue engineering scaffolds using the selective laser sintering technology. **a** General morphology of composite microspheres. **b** Cross-section of a composite microsphere

Technologies for Fibre Production

Textile technologies for producing polymer fibres may have great promise for TE scaffolds as the fibres produced (of diameters in the nanometre to micrometre range) can be used in meshes or in the aligned format (including braided structures) for tissue regeneration. Indeed, in the early days of TE, meshes of biodegradable fibres of micrometres in diameter were used as scaffolds (Atala and Lanza 2002; Langer and Vacanti 1993; Lanza et al. 2000). Recent attention, however, has been focused on biodegradable fibres which have diameters in the nanometre range, as it is considered that the proper in vivo phenotype cannot be consistently achieved if cells are presented with fibres with diameters equal to or greater than the cell size. Among technologies for making polymer fibres of nanometre dimensions, electrospinning is the most appealing and the process is relatively simple (Fong and Reneker 2000). Some electrospun fibres have already been investigated for TE applications (Li et al. 2002; Yang et al. 2005). A study was recently conducted on electrospin-

ning of PHB and PHBV polymers (Tong and Wang 2006). It was found that electrospinning parameters (polymer solution concentration, solution feeding rate, injection needle diameter, electrical voltage and working distance) all had significant effects on the resultant fibres. When electrospinning parameters were optimized, bead formation on nanofibres could be avoided (Fig. 11). With careful experimentation, CHA/PHBV composite nanofibres containing CHA nanospheres could be produced. Figure 12a displays the composite fibres and the EDX spectrum from a fibre, as shown in Fig. 12b, which was obtained from the circled area of Fig. 12a, revealed the presence of Ca and P, indicating the incorporation of CHA particles in the fibre.

Phosphate-based glass fibres of the diameters around $6.5\,\mu m$ could be produced for possible TE applications (Shah et al. 2005). The glass fibres produced could be arranged as (a) separate and spread, (b) a bundle or (c) a mesh. The three-dimensional glass fibre construct appeared to encourage muscle cell attachment and proliferation, indicating its potential use in the TE of craniofacial muscle.
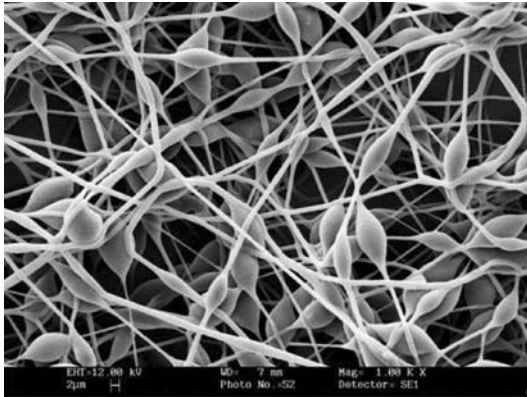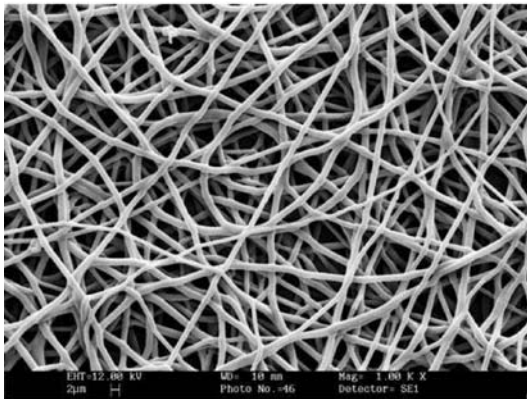
Figure 11 a,b. Electrospun PHBV nanofibres **a** with the formation of beads on fibres, and **b** without the formation of beads on fibres
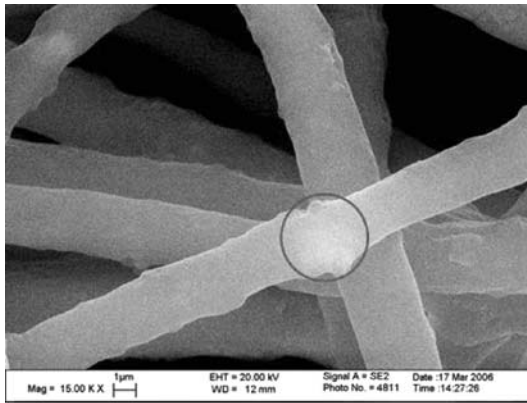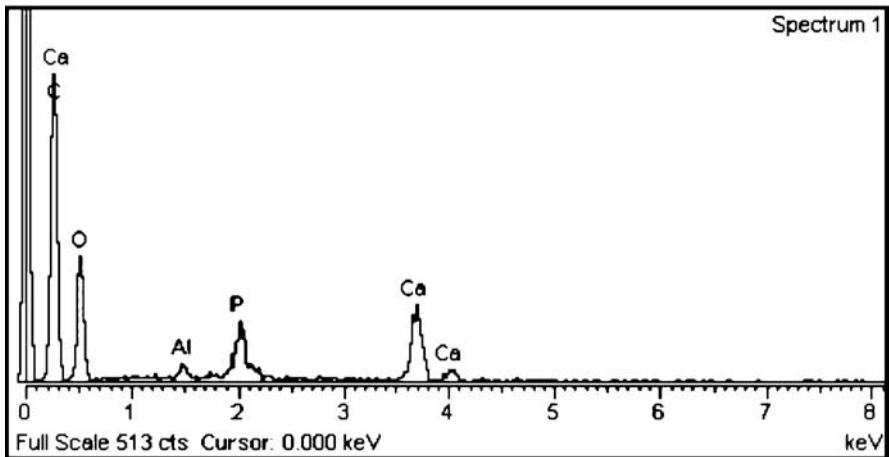
Figure 12 a,b. Electrospun CHA/PHBV composite nanofibres: **a** morphology; **b** EDX spectrum of the circled area in **a**, indicating the existence of CHA nanospheres inside the fibre

Technologies for Bioceramic Coating Formation

As discussed previously, there are two ways of making bioceramic-polymer composite scaffolds. The first approach, i.e. incorporating bioceramic particles in the scaffolds themselves during scaffold production, has already been discussed. The second approach, namely, coating the polymer scaffold with a thin layer of apatite through biomimetic processes, is another attractive route for developing bone TE scaffolds. Coating biodegradable polymer scaffolds with apatite (Chen et al. 2005a) or apatite/collagen composite (Chen et al. 2005b, 2006a) coatings using accelerated biomimetic processes have been successful. Apatite and apatite/collagen composite coatings could be observed on pore surfaces of PLLA scaffolds (Fig. 13). It was found that the apatite coating and apatite/collagen composite coating could improve interactions between osteoblasts and PLLA scaffolds, and that the composite coat-
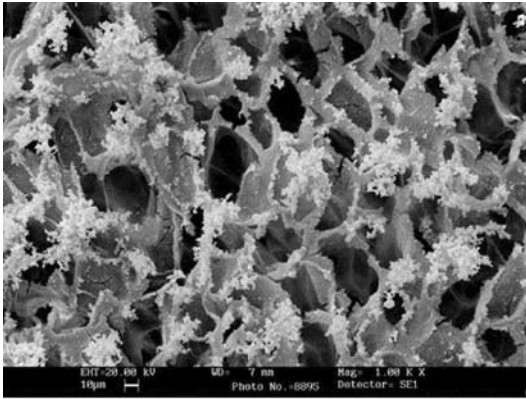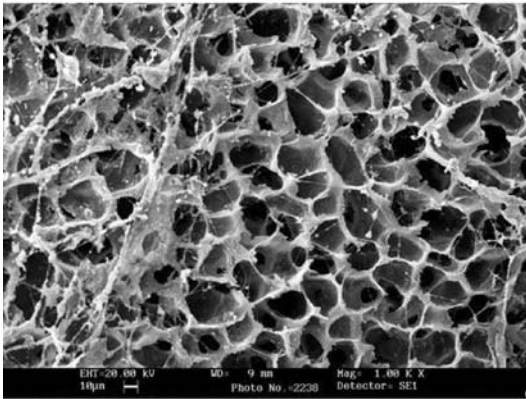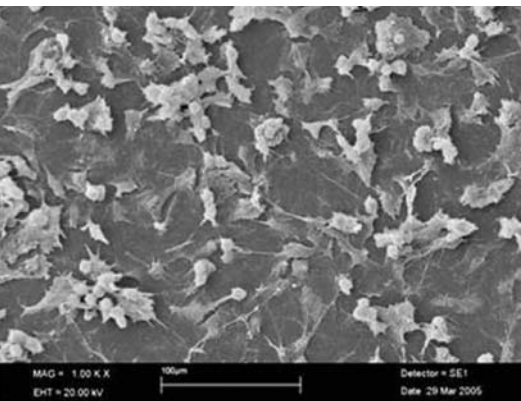
Figure 13 a,b. Formation of bioactive coatings on pore surfaces of PLLA scaffolds through accelerated biomimetic processes: **a** apatite coating; **b** apatite/collagen coating

Figure 14. Osteoblast-like cells attaching to the apatite/collagen composite coating formed on PLLA through an accelerated biomimetic process

ing was more effective than apatite coating in improving such interactions (Chen et al. 2006b). Figure 14 shows that osteoblast-like cells could attach and proliferate on the apatite/collagen coating. One of the key issues in this biomimetic coating approach is to achieve the desired uniform formation of coatings on pore surfaces inside

scaffolds. It appeared that with a dynamic environment, biomimetic apatite coatings could be formed on pores inside the scaffolds (Chen 2006).

Coating porous alumina with HA or bone-like apatite is a reasonable strategy for bone-tissue repair. There are a number of ways in depositing these bioactive coatings on alumina (Jiang and Shi 1998, 1999; Shi and Jiang 1998). Obviously, as the alumina substrate is highly chemically stable and very heat- and steam resistant up to very high temperatures, unlike biodegradable polymeric substrates, there is a large scope for exploration for porous alumina as far as the apatite deposition methods are concerned. In addition, alumina (and, in this aspect of only considering the coating process, also other "non-degradable" substrates) does not have the problem of in-process degradation, which biodegradable polymeric scaffolds are facing, during apatite deposition in an aqueous environment and hence there is no absolute need to accelerate the deposition process if the apatite deposition involves aqueous solutions; however, for achieving high coating efficiency, there is the need to shorten the deposition time. The follow-up study showed that the HA deposited on porous alumina possessed in vitro bioactivity (Shi et al. 2000).

Using titanium as the material for scaffolds on which apatite coatings are formed may be a better option than using alumina, as titanium is now an established material in orthopaedics and dentistry and is much tougher than alumina. Extensive work has been conducted to investigate methods to make titanium bioactive (Kokubo et al. 2004; Wu and Wang, in press), and it was found that bone-like apatite formed on pore surfaces of porous titanium (Fujibayashi et al. 2004). Using a low-temperature approach, which eliminated heat treatment and thus possible thermal damage to the Ti substrate, different types of titania (anatase, rutile or a mixture of anatase and rutile) could be formed on Ti which in turn could induce the formation of apatite in vitro and in vivo (Wu et al. 2006a,b,c; Wu et al., in press). Figure 15 displays FTIR spectra of
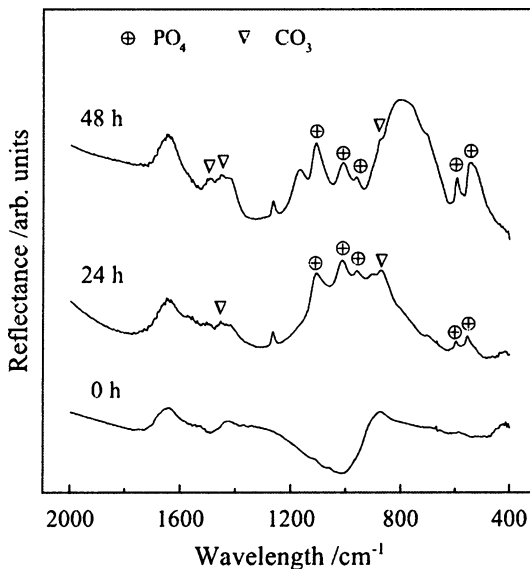
Figure 15. The FTIR spectra of Ti samples soaked in SBF for various times. (The Ti samples had been pre-treated in the low-temperature H_2O_2 oxidation process to form a surface titania layer before their immersion in SBF.)
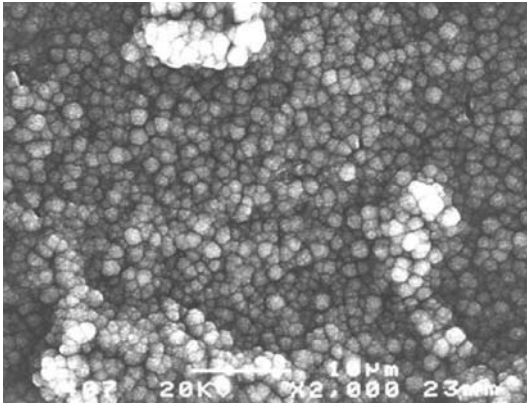
Figure 16. Apatite formed in vitro on a pre-treated Ti sample

Ti samples that were soaked in simulated body fluid (SBF) for various times, exhibiting the emergence of PO_4^{3-} and CO_3^{2-} bands which indicated the existence of CHA (These Ti samples had been pre-treated in the low-temperature H_2O_2 oxidation process to form a surface titania layer before their immersion in SBF.). Figure 16 shows the morphology of apatite formed on one of these Ti samples after 48 h soaking in SBF. Future studies will include optimization of the porous structure (pore size and pore interconnectivity) of Ti and shortening the apatite deposition time.

Methods for Hydrogels

There are a number of methods to make hydrogels of both synthetic and natural polymers (Peppas 2004). Investigations were conducted into making hydorgels of chitin (and its composites) and chitosan for different medical applications (Weng and
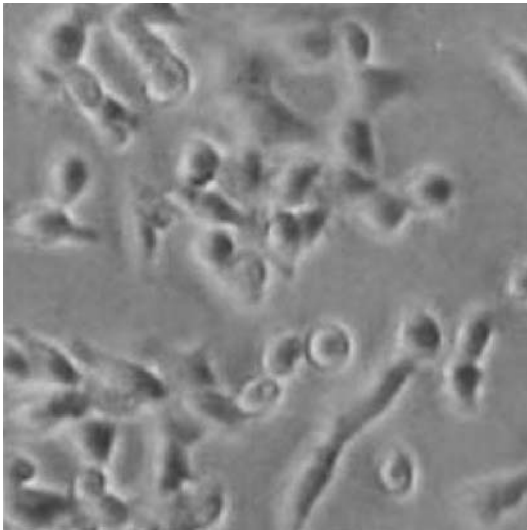
Figure 17. Fibroblasts growing on a chitosan hydrogel membrane
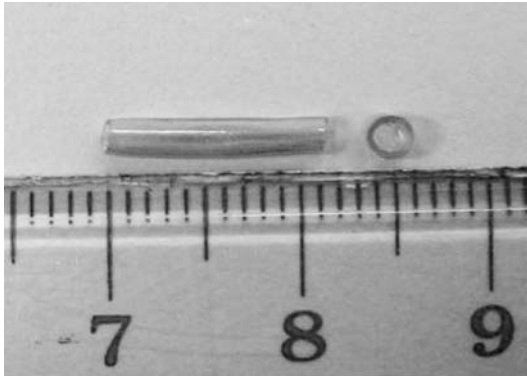
Figure 18. Chitosan hydrogel tubes in the hydrated state

Wang 2001a,b; Wang et al. 2006). In a recent investigation, chitosan hydrogel tubes were produced for potential application in peripheral nerve regeneration (Wang et al. 2006). Both chitosan membranes and tubes of consistent quality could be made by dissolving chitosan flakes in acetic acid and then casting the solution. In vitro evaluation of cast chitosan membranes revealed that fibroblasts grew on the membranes (Fig. 17), indicating no cell toxicity. For producing tubes, the chitosan solution could be used to coat repeatedly a rotating glass rod that was driven by a motor at a low speed. Once the desired thickness of the tube was reached through repeated coating, the chitosan tube could be removed from the glass rod and neutralized with a sodium hydroxide solution. The chitosan tubes were then washed thoroughly and hydrated and stored in ultra-pure de-ionized water. Figure 18 shows chitosan tubes in the hydrated state. The in vivo evaluation of chitosan hydrogel tubes in peripheral nerve regeneration is currently performed.

Concluding Remarks

For TE in orthopaedics, there are a relatively large number of candidate materials for constructing TE scaffolds, and many techniques can be used for scaffold fabrication. Biodegradable polymers have been and will remain as the dominant group of materials for TE of bone, articular cartilage, tendon and ligaments, etc., but efforts are being increasingly made to produce polymer-based composite scaffolds for bone TE. Bioceramics and their composites are possible contenders as bone TE materials. There are also even possibilities of using porous metals for bone tissue repair. The availability and diversity of technologies for fabricating TE scaffolds are both encouraging and challenging. The selection of a particular scaffold-manufacturing technique is influenced by several factors. The successful scaffold fabrication technologies will be those that can produce good-quality scaffolds which are also of consistent quality. The capability of the technology to produce scaffolds in relatively large quantities at a reasonable cost is another important factor. When one embarks on developing TE scaffolds, the selection of scaffold material(s) and the selection of scaffold production technology must be carefully considered together. Among the scaffolds that

have been investigated, are currently under investigation, or will be studied in the future, only some of them will be eventually used in clinical practice.

Apart from science and technology, there are also a few other important factors that can have strong influence on the success or failure of a TE strategy. Due to the nature of TE, as has been witnessed in the first two decades of TE, ethical issues are perpetually linked to this new endeavor in tissue repair. Governments of countries where R&D in TE has been strong have established regulations, or the framework of regulations, in anticipation of possible problems/conflicts (a few of them have already become reality) in dealing with human cells and tissues. The impact of TE on the society, not only in health care but also in other areas of people's lives, can be huge and should be managed.

On the issue of economy, as with other medical treatments for the general public, a TE approach to treat patients must be cost-effective. The competitive edge of TE rests perhaps strongly on its ability to provide long-term solutions in tissue repair, offer treatments for medical conditions that are currently untreatable, and solve the problem of shortage in organ donations; therefore, the benefit of TE can be huge. However, TE may not have any advantage in areas where current conventional treatment methods do not incur high costs and yet do give satisfactory results. The R&D costs in TE are very high and the financial investment in some TE efforts, which may prove successful eventually in treating certain diseases, may not be recouped. The cost of a medical treatment via TE can be a crucial factor in deciding whether or not the general public can eventually benefit from it.

References

Arnst C, Carey J (1998) "Biotech bodies". Business Week, Issue 3588 (07/27/98), pp 56–63

Ashby MF, Evans A, Fleck NA, Gibson LJ, Hutchinson JW, Wadley HNG (2000) Metal Foams: a design guide, Butterworth–Heinemann, Boston

Atala A, Lanza RP (eds) (2002) Methods of tissue engineering, Academic Press, San Diego

Astala R, Stott MJ (2005) First principles investigation of mineral component of bone: CO_3 substitutions in hydroxyapatite. Chem Mater 17:4125–4133

Bagot D'Arc M, Daculsi G (2003) Micro macroporous biphasic ceramics and fibrin sealant as a moldable material for bone reconstruction in chronic otitis media surgery. A 15-year experience. J Mater Sci Mater Med 14:229–233

Bonfield W, Grynpas MD, Tully AE, Bowman J, Abram J (1981) Hydroxyapatite reinforced polyethylene: a mechanically compatible implant material for bone replacement. Biomaterials 2:185–186

Branemark R, Branemark P-I, Rydevik B, Myers RR (2001) Osseointegration in skeletal reconstruction and rehabilitation: a review. J Rehab Res Develop 38:175–181

Callcut S, Knowles JC (2002) Correlation between structure and compressive strength in a reticulated glass-reinforced hydroxyapatite foam. J Mater Sci Mater Med 13:485–489

Chen Y (2006) Developing bioactive composite scaffolds for bone tissue engineering. PhD Thesis, Hong Kong Polytechnic University, Hong Kong

Chen Y, Mak AFT, Li J, Wang M, Shum AWT (2005a) Formation of apatite on poly(α-hydroxy acid) in an accelerated biomimetic process. J Biomed Mater Res Appl Biomater 73B:68–76

Chen Y, Mak AFT, Wang M (2005b) Formation of apatite/collagen composite coating on poly(L-lactic acid) scaffolds in an accelerated biomimetic process. Trans Soc Biomater 30th Annual Meeting, Memphis, Tennessee, p 442

Chen Y, Mak AFT, Wang M, Li J (2006a) Composite coating of bone-like apatite particles and collagen fibers on poly (L-lactic acid) formed through an accelerated biomimetic coprecipitation process. J Biomed Mater Res B 77B:315–322

Chen Y, Mak AFT, Wang M, Li J, Wong MS (2006b) PLLA scaffolds with biomimetic apatite coating and biomimetic apatite/collagen composite coating to enhance osteoblast-like cells attachment and activity. Surface Coatings Technol 201:575–580

Chua CK, Leong KF, Lim CS (2003) Rapid prototyping: principles and applications, 2nd edn. World Scientific, Singapore

Cooper KG (2001) Rapid prototyping technology: selection and application. Dekker, New York

Cowan JA (ed) (1995) The biological chemistry of magnesium. VCH, New York

Degischer H-P, Kriszt B (eds) (2002) Handbook of cellular metals: production, processing, applications, Wiley–VCH, Weinheim

Devin JE, Attawia MA, Laurencin CT (1996) Three dimensional degradable porous polymer–ceramic matrices for use in bone repair. J Biomater Sci Polymer Ed 7:661–669

Du C, Cui FZ, Zhu XD, de Groot K (1999) Three-dimensional nano-HAp/collagen matrix loading with osteogenic cells in organ culture. J Biomed Mater Res 44:407–415

Fabbri M, Celotti GC, Ravaglioli A (1995) Hydroxyapatite-based porous aggregates: physico-chemical nature, structure, texture and architecture. Biomaterials 16:225–228

Fong H, Reneker DH (2000) Electrospinning and the formation of nanofibers. In: Salem DR (ed) Structure formation in polymeric fibers. Hanser Publishers, Munich, pp 225–246

Fujibayashi S, Neo M, Kim HM, Kokubo T, Nakamura T (2004) Osteoinduction of porous bioactive titanium metal. Biomaterials 25:443–450

Fung YC (1993) Biomechanics: mechanical properties of living tissues, 2nd edn. Springer, Berlin Heidelberg New York

Gibson LJ, Ashby MF (1997) Cellular solids: structure and properties, 2nd edn. Cambridge University Press, Cambridge

Griffith L, Naughton G (2002) Tissue engineering: current challenges and expanding opportunities. Science 295:1009–1013

Helsen JA, Breme HJ (eds) (1998) Metals as biomaterials. Wiley, Chichester

Hench LL (2001) The story of Bioglass®: from concept to clinic. In: Pashley DW (ed) Imperial college inaugural lectures in materials science and materials engineering. Imperial College Press, London, pp 203–229

Heywood HK, Sembi PK, Lee DA, Bader DL (2004) Cellular utilization determines viability and matrix distribution profiles in chondrocyte-seeded alginate constructs. Tissue Eng 10:1467–1479

Hing KA, Best SM, Tanner KE, Bonfield W, Revell PA (1999) Quantification of bone ingrowth within bone-derived porous hydroxyapatite implants of varying density. J Mater Sci Mater Med 10:663–670

Hollander AP, Hatton PV (eds) (2004) Biopolymer methods in tissue engineering. Humana Press, Totowa

Hollister SJ, Maddox RD, Taboas JM (2002) Optimal design and fabrication of scaffolds to mimic tissue properties and satisfy biological constraints. Biomaterials 23:4095–4103

Hutmacher DW (2000) Polymeric scaffolds in tissue engineering bone and cartilage. Biomaterials 21:2529–2543

Huygh A, Schepers EJG, Barbier L, Ducheyne P (2002) Microchemical transformation of bioactive glass particles of narrow size range, a 0–24 month study. J Mater Sci Mater Med 13:315–320

Iannace S, Maffezzoli A, Leo G, Nicolais L (2001) Influence of crystal and amorphous phase morphology on hydrolytic degradation of PLLA subjected to different processing conditions. Polymer 42:3799–3807

Jiang G, Shi D (1998) Coating hydroxyapatite on highly porous Al_2O_3 substrate for bone substitutes. J Biomed Mater Res (Appl Biomater) 43:77–81

Jiang G, Shi D (1999) Coating hydroxyapatite on porous alumina substrate through a thermal decomposition method. J Biomed Mater Res (Appl Biomater) 48:117–120

Kim SR, Lee JH, Kim YT, Riu DH, Jung SJ, Lee YJ, Chung SC, Kim YH (2003) Synthesis of Si, Mg substituted hydroxyapatites and their sintering behaviour. Biomaterials 24:1389–1398

Kohn J, Abramson S, Langer R (2004) Bioresorbable and bioerodible materials. In: Ratner BD, Hoffman AS, Schoen FJ, Lemons JE (eds) Biomaterials science: an introduction to materials in medicine, 2nd edn. Academic Press, San Diego, pp 115–127

Kokubo T, Kim HM, Kawashita M, Nakamura T (2004) Bioactive metals: preparation and properties. J Mater Sci Mater Med 15:99–107

Lam CXF, Mo XM, Teoh SH, Hutmacher DW (2002) Scaffold development using 3D printing with a starch-based polymer. Mater Sci Eng 20:49–56

Langer R, Vacanti JR (1993) Tissue engineering. Science 260:920–926

Lanza RP, Langer R, Vacanti J (eds) (2000) Principles of tissue engineering, 2nd edn. Academic Press, San Diego

Lee SH, Zhou WY, Cheung WL, Wang M (2005) Producing polymeric scaffolds for bone tissue engineering using the selective laser sintering technique. Trans Soc Biomater 30th Annual Meeting, Memphis, Tennessee, p 348

LeGeros RZ, LeGeros JP (1993) Dense hydroxyapatite. In: Hench LL, Wilson J (eds) An introduction to bioceramics. World Scientific, Singapore, pp 139–180

Leong KW, Brott BC, Langer R (1985) Bioerodible polyanhydrides as drug carrier matrices I: characterization, degradation and release characteristics. J Biomed Mater Res 19:941–955

Li J (2004) Polymer hydrogels. In: Teoh SH (ed) Engineering materials for biomedical applications. World Scientific, Singapore, pp 7–1 to 7–18

Li JP, Li SH, Van Bltterswijk CA, de Groot K (2005) A novel porous Ti6Al4V: characterisation and cell attachment. J Biomed Mater Res 73A:223–233

Li L, Gao J, Wang Y (2004) Evaluation of cytotoxicity and corrosion behaviour of alkali-heat-treated magnesium in simulated body fluid. Surface Coatings Technol 185:92–98

Li S (1999) Hydrolytic degradation characteristics of aliphatic polyesters derived from lactic and glycolic acids. J Biomed Mater Res (Appl Biomater) 48:342–353

Li WJ, Laurencin CT, Caterson EJ, Tuan RS, Ko FK (2002) Electrospun nanofibrous structure: a novel scaffold for tissue engineering. J Biomed Mater Res 60:613–621

Lindsay DT (1996) Functional human anatomy. Mosby, St. Louis

Lloyd-Evans M (2004) Regulating tissue engineering. Materials Today 7:48–55

Lysaght MJ, Hazlehurst AL (2004) Tissue engineering: the end of the beginning. Tissue Eng 10:309–320

McIntire LV (ed) (2003) WTEC panel on tissue engineering research: final report. Academic Press, San Diego

Mooney DJ, Mikos AG (1999) Growing new organs. Sci Am 280:38–43

Mwale F, Iordanova M, Demers CN, Steffen T, Roughley P, Antoniou J (2005) Biological evaluation of chitosan salts cross-linked to genipin as a cell scaffold for disk tissue engineering. Tissue Eng 11:130–140

Nerem RM (1992) Tissue engineering in the USA. Med Biol Engin Comput 30:CE8–CE12

Patrick CW Jr, Mikos AG, McIntire LV (eds) (1998) Frontiers in tissue engineering. Pergamon, Oxford

Peppas NA (2004) Hydrogels. In: Ratner BD, Hoffman AS, Schoen FJ, Lemons JE (eds) Biomaterials science: an introduction to materials in medicine, 2nd edn. Academic Press, San Diego, pp 100–107

Pereira MM, Jones JR, Hench LL (2005) Bioactive glass and hybrid scaffolds prepared by sol-gel method for bone tissue engineering. Adv Appl Ceram 104:35–42

Peter SJ, Miller ST, Zhu G, Yasko AW, Mikos AG (1998) In vivo degradation of a poly(propylene fumarate)/β–tricalcium phosphate injectable composite scaffold. J Biomed Mater Res 41:1–7

Rahaman MN (2003) Ceramic processing and sintering, 2nd edn. Dekker, New York

Rice RW (2002) Ceramic fabrication technology. Dekker, New York

Roether JA, Boccaccini AR, Hench LL, Maquet V, Gautier S, Jerome R (2002) Development and in vitro characterisation of novel bioresorbable and bioactive composite materials based on polylactide foams and Bioglass® for tissue engineering applications, Biomaterials 23:3871–3878

Shah R, Sinanan ACM, Knowles JC, Hunt NP, Lewis MP (2005) Craniofacial muscle engineering using a 3-dimensional phosphate glass fiber construct. Biomaterials 26:1497–1505

Shi D, Jiang G (1998) Synthesis of hydroxyapatite films on porous Al_2O_3 substrate for hard tissue prosthetics. Mater Sci Engin C 6:175–182

Shi D, Jiang G, Wen X (2000) In vitro bioactive behavior of hydroxyapatite-coated porous Al_2O_3. J Biomed Mater Res (Appl Biomater) 53:457–466

Skalak R, Fox CF (eds) (1988) Tissue engineering. Liss, New York

Song G (2005) Recent progress in corrosion and protection of magnesium alloys. Adv Engin Mater 7:563–586

Stile RA, Burghardt WR, Healy KE (1999) Synthesis and characterization of injectable poly(N-isopropylacrylamide)-based hydrogels that support tissue formation. Macromolecules 32:7370–7379

Sultana N Wang M (2007), Fabrication and characterisation of polymer and composite scaffolds based on polyhydroxybutyrate and polyhydroxybutyrate-co-hydroxyvalerate, Key Engineering Materials, 334–335:1229–1232

Tong HW Wang M (2006), Electrospinning of PHBV fibers: the processing window and elimination of defects, Proceedings of the Biomedical Engineering Conference BME2006, Hong Kong, 2006, pp 55–58

Wang CX, Wang M (2000) Fabrication and characterisation of porous tricalcium phosphate. Proc 10th Int Conf on Biomedical Engineering, Singapore, pp 547–548

Wang M (2002) Bioceramics. In: Ikada Y (ed) Recent research developments in biomaterials. Research Signpost, Trivandrum, pp 33–76

Wang M (2003) Developing bioactive composite materials for tissue replacement. Biomaterials 24:2133–2151

Wang M, Ni J (2004) In vitro evaluation of bioactive and biodegradable composites based on polyhydroxybutyrate. Ann Chimie 29:17–28

Wang M, Yong HS (2001) Production and evaluation of a glass reinforced hydroxyapatite composite. Proc 5th Asian Symp on Biomedical Materials, Hong Kong, pp 101–102

Wang M, Chen LJ, Ni J, Weng J, Yue CY (2001) Manufacture and evaluation of bioactive and biodegradable materials and scaffolds for tissue engineering. J Mater Sci Mater Med 12:855–860

Wang M, Shum DKY, Chu CS, Lam KO (2006) Fabrication and evaluation of chitosan devices for peripheral nerve regeneration: an initial study. Proc Biomedical Engineering Conference BME2006, Hong Kong, pp 47–50

Wen CE, Yamada Y, Shimojima K, Mabuchi M, Nakamura M, Asahina T (2000) Mechanical properties of cellular magnesium materials. Mater Sci Forum 350:359–364

Wen CE, Mabuchi M, Yamada Y, Shimojima K, Chino Y, Asahina T (2001) Processing of biocompatible porous Ti and Mg. Scripta Materialia 45:1147–1153

Weng J, Wang M (2001a) Producing chitin scaffolds with controlled pore size and interconnectivity for tissue engineering. J Mater Sci Let 20:1401–1403

Weng J, Wang M (2001b) In vitro formation of bone-like apatite on the surface of solution-cast partially crystalline hydroxyapatite/chitin composite. Key Eng Mater 192–195:657–660

Weng J, Wang M, Chen J (2002) Plasma sprayed calcium phosphate particles with high bioactivity and their use in bioactive scaffolds. Biomaterials 23:2623–2629

Williams D (2004) Benefit and risk in tissue engineering. Materials Today 7:24–29

Wu JM, Wang M (in press) Surface modification of titanium and its alloys for orthopaedic and dental applications. In: Tanaka J (ed) Surface design and modification of biomaterials for clinical application. Research Signpost, Trivandrum

Wu JM, Wang M, Hayakawa S, Tsuru K, Osaka A (2006a) In vitro bioactivity of hydrogen peroxide modified titanium: effects of surface morphology and film thickness. Key Engin Mater 309–311:407–410

Wu JM, Wang M, Li YW, Zhao FD, Ding XJ, Osaka A (2006b) Crystallization of amorphous titania gel by hot water aging and induction of in vitro apatite formation by crystallized titania. Surface Coatings Technol 201:755–761

Wu JM, Wang M, Osaka A (in press) Bioactive composite coating on titanium implants for hard tissue repair. Key Engin Mater

Wu JM, Zhang S, Zhao FD, Li YW, Wang M, Osaka A (2006c) Influence of film thickness on in vitro bioactivity of thin anatase films produced through direct deposition from an aqueous titanium tetrafluoride solution, Surface and Coatings Technology 201:3181–3187

Yang HY, Wang M (1999) Investigation into manufacture of porous hydroxyapatite via three different routes and effects of porosifiers. Bioceramics 12:349–352

Yang F, Murugan R, Wang S, Ramakrishna S (2005) Electrospinning of nanomicro scale poly(L-lactic acid) aligned fibers and their potential in neural tissue engineering. Biomaterials 26:2603–2610

Yang S, Leong KF, Du Z, Chua CK (2002) The design of scaffolds for use in tissue engineering. Part II. Rapid prototyping techniques. Tissue Eng 8:1–11

Yang XB, Bhatnagar RS, Li S, Oreffo ROC (2004) Biomimetic collagen scaffolds for human bone cell growth and differentiation. Tissue Eng 10:1148–1159

Yannas IV (2004) Natural materials. In: Ratner BD, Hoffman AS, Schoen FJ, Lemons JE (eds) Biomaterials science: an introduction to materials in medicine, 2nd edn. Academic Press, San Diego, pp 127–137

Zein I, Hutmacher DW, Tan KC, Teoh SH (2002) Fuse deposition modeling of novel scaffold architectures for tissue engineering applications. Biomaterials 23:1169–1185

Zhang R, Ma PX (1999) Poly(alpha-hydroxyl acids)/hydroxyapatite porous composites for bone–tissue engineering. I. Preparation and morphology. J Biomed Mater Res 44:446–455

Zhang Y, Zhang M (2001) Synthesis and characterization of macroporous chitosan/calcium phosphate composite scaffolds for tissue engineering. J Biomed Mater Res 55:304–312

Zhou WY, Wang M, Cheung WL (2005) Synthesis of nanospheres of carbonated hydroxyapatite by nanoprecipitation, Proceedings of the 3rd International Symposium on Apatite and Correlative Biomaterials, Wuhan, China, p 107

Zhou WY, Lee SH, Cheung WL, Wang M Ip WY (2006), Selective laser sintering of porous scaffolds from poly(L-lactide) microspheres and its nanocomposite with carbonated hydroxyapatite nanospheres, Proceedings of the 20th European Conference on Biomaterials (ESB2006), Nantes, France, p 175

Zreiqat H, Howlett CR, Zannettino A, Evans P, Schulze-Tanzil G, Knabe C, Shakibaei M (2002) Mechanisms of magnesium-stimulated adhesion of osteoblastic cells to commonly used orthopaedic implants. J Biomed Mater Res 62:175–184

Quantification of Porosity, Connectivity and Material Density of Calcium Phosphate Ceramic Implants Using Micro-Computed Tomography

Hiu-Yan Yeung (✉) [1], Ling Qin[1], Kwong-Man Lee[2], Kwok-Sui Leung[1], and Jack Chun-Yiu Cheng[1]

[1] Department of Orthopaedics and Traumatology, The Chinese University of Hong Kong, Hong Kong SAR, China
e-mail: byeung@cuhk.edu.hk
[2] Lee Hysan Clinical Research Laboratory, The Chinese University of Hong Kong, Hong Kong SAR, China

Abstract

Calcium phosphate ceramics have been widely investigated in orthopaedic tissue engineering and surgery as bone extensor. Attention has been given to manufacturing of a porous ceramic that mimics the trabecular bone structure for better osteoconduction. Although different methods have been applied to manufacture the porous structure, they have been unable to quantify the pores and their interconnection within the ceramics. With the advances in biomedical imaging technologies, the study attempted to quantify the pore structure of different ceramics using high-resolution micro-computed tomography (micro-CT). Three kinds of ceramic blocks with product names (BSC, ChronOS and THA, respectively) were synthesized by three methods from three different manufactures and evaluated in the study. The specification claimed that the porosity of the ceramic ranged from 40 to 80%. Six blocks of each ceramic were evaluated by conventional water immersion method and μCT. The pore size and connectivity of the pores were evaluated with standardized protocols. By the water immersion method, the porosity of three ceramics ranged from 60 to 78%. The three-dimensional analysis of the pores by μCT showed that the porosity of the ceramics was 26.2% for BSA, 59.9% for ChronOS, and 67.7% for THA. The pore connectivity was 2.7 for BSC, 39.7 for ChronOS, and 7.1 for THA. The ChronOS had more functional pores (200–400 μm in diameter) than the BSC (52.8%) and THA (43.2%) did ($p < 0.05$). It was shown that the distribution of the pore size of three different ceramics has different characteristics. We speculated that different combinations of structure parameters may have different in vivo properties in osteogensis, whereas the chemical properties of the ceramics cannot be neglected in the in vivo performance. Providing objective information on the functional pores, the micro-CT evaluation serves as a good standard for specification of the ceramic-related implants in the future characterization of scaffold biomaterials for orthopaedic and related medical applications.

Introduction

Calcium phosphate ceramics (CPC) have been studied extensively in the past for their orthopaedic applications especially in spinal fusion and large bone defect. Although autograft is still the gold standard in orthopaedic and reconstructive surgery, the limited supply of autograft, the risk of infection, and the accompanied complication during the autograft harvest cause the search for synthetic or natural biomaterials to replace live bone. Calcium phosphate ceramics (CPC) become the natural choice since hydroxyapatite (HA) is the main component of CPC as well as the inorganic ingredient of bone. The advantages of the CPC are its biocompatibility (Wilke et al. 1998), osteoconductivity, osteogenicity and in vivo radiographic accessibility (Spivak and Hasharoni 2001; Tay et al. 1999). The CPCs are also studied for their effectiveness as drug-delivery system for various growth factors and, in particular, the bone morphogenetic proteins (BMP; Alam et al. 2001; Cheng et al. 2002; Guo et al. 2002; Urist 1994). In addition to being a drug carrier to the treatment sites, porous CPC is also used as a scaffold for cell-based bone tissue engineering. It has been shown that the porous ceramic scaffolds in combination with mesenchymal stem cells have been a possible alternative for autograft in the repair of bone lesions (Adachi et al. 2005; Bruder et al. 1998a,b; Cancedda et al. 2003; Hollister et al. 2005; Morishita et al. 2006; Peterson et al. 2005).

In the early study of the effects of the pore size on the bony ingrowth to the calcium aluminate ceramic, it had been shown that the interconnected macropores between 50 and 150 μm would promote the formation of osteoid when a pore size > 150 μm was important for the induction of mineralized bony tissue to form inside the ceramics. Small pore size ranging from 5 to 15 μm only had fibrous tissue formed within the ceramics (Hulbert et al. 1970; Klawitter 1979). Recent studies showed that the physical property of a ceramic could affect the osteogenesis induced by BMP. With smaller pores (90–120 μm), the porous HA was able to induce chondrogenesis and subsequent osteogenesis (Kuboki et al. 2001; Tsuruga et al. 1997); however, better bone ingrowth (osteoconduction) was observed in ceramics with larger pore size ranging between 200 and 400 μm in diameter as a result of the better facilitation of blood vessel formation (Guo 1993; Tsuruga et al. 1997).

Apart from pore size, other important variables related to the physical characteristics of ceramics in orthopaedic applications are the porosity (density of pores) and the interconnectivity of these pores (Bignon et al. 2003; Erbe et al. 2001; Hulbert et al. 1970; Klawitter 1979; Predecki et al. 1972; Shors 1999; van Blitterswijk et al. 1986). This information is usually provided by the manufacturers, where the porosity and the "interconnection" of pores are determined by porositmetry (Oya et al. 2002). The "interconnection" claimed in studies was mainly descriptive in nature, which often overestimated the volume fraction of "pores" or "space". Mimicking the structure of trabecular bone, the pores of the ceramics are able to enhance angiogenesis and cell migration into the material (Erbe et al. 2001; Tancred et al. 1998). Up to now, it is well accepted that the porosity and the pore size of the ceramics were evaluated by mercury intrusion porosimetry in which a cylindrical pore model was assumed (Oya et al. 2002); therefore, an objective alternative to characterize the "functional"

structural parameters of both the porosity and interconnection without any shape assumption for the research and development (R&D) of porous ceramics is very necessary.

With the advance of biomedical imaging through micro-computed tomography (micro-CT), the trabecular bone structure and its mineral density can be quantified objectively. Using image processing techniques and three-dimensional reconstruction, the morphological parameters measured by micro-CT can be compared directly with the actual volume of bone (Ruegsegger et al. 1996). Unlike conventional histomorphometry, the new micro-CT evaluation is not based on any presumed shape-based calculation model and does not require any assumption on the morphology of the structure and stereological manipulation (Hildebrand et al. 1999; Muller et al. 1994). Moreover, the porous ceramic may have similar structural property as trabecular bone and similar X-ray attenuation property as the bone.

The aim of this chapter was to establish evaluation protocols of a high-resolution cone-beam micro-CT installed for our institution for orthopaedic, bone mineral and biomaterial research by comparing differences in material porosity, interconnection and the material density of three different CPC implants developed for orthopaedic applications.

Establishment of Evaluation Protocols of Micro-CT for Studying CPC Porosity, Interconnection and the Material Density

Materials

Three different CPCs from three different sources were obtained for comparison. One CPC was made by the Biomaterial Center, Sichuan University (BSC), which was composed of 60% hydroxyapatite (HA) and 40% β-tricalcium phosphate (β-TCP). The second CPC, made by the Department of Orthopaedics, the Beijing 301 Hospital, was a pure HA ceramic (THA). The third CPC was "ChronOS" made by Synthes (Switzerland), which was a pure β-TCP ceramic. The porosity of the ceramics specified by the manufacturers was 75% for THA, 40% for BSC and 70% for ChronOS, respectively. Each material was prepared to a standard 5 × 5× 6-mm block for the volume fraction evaluation using conventional "water immersion" method (Qu et al. 1994) and subsequently structural evaluation using micro-CT.

Quantification of Porosity and Interconnection of Ceramics

Water Immersion Method

The porosity of the blocks was determined by Archimedes method by immersion into water (Qu et al. 1994). The blocks ($n = 6$) were submerged into a certain volume of water in a test tube and placed to a vacuum chamber to remove the air trapped inside the ceramics. The volume of displaced water was recorded as the volume of the material. The "porosity" or "space volume fraction" was calculated by dividing the material volume by the apparent physical dimension of the block.

Micro-Computed Tomography

Scanning Protocol   The high-resolution micro-CT (μCT40, Scanco Medical, Bassersdorf, Switzerland) was used with a spatial resolution of 16 μm for scanning. The cubic voxel has a side length of 16 μm. An optimized threshold was used to isolate the ceramic from the background for the evaluation of different morphological parameters.

Two-Dimensional Image Acquisition   Directly acquired from the scanning, 23 slices of images were sampled at a regular interval for the analysis of material area fraction, porosity, material surface fraction, and material perimeter by traditional histomorphometry. Material area fraction was defined as the percentage of area of the material within the porous block area. The porosity was calculated from the 2D images by the percentage of void area within the porous block area. The material surface fraction was the ratio of material perimeter to the material area.

Three-Dimensional Structural Evaluation   The volume of interest was reconstructed. The material volume fraction and surface fraction was evaluated directly on the 3D images by the image analysis program of μCT40 without any assumption on the shape of the structure. Similar to the 2D image analysis, the material volume fraction was the percentage of material volume over the volume of interest. The material surface fraction was the ratio of material surface to the material volume. In this study, the shapes of the ceramics and the pores were unknown. It was therefore important to use a model-independent method to evaluate the structure. In the traditional stereological methods, the shape of the structure was assumed to be plate-like, which did not fit to the present evaluation where the shapes of the material or the pore were not plate-like (Hildebrand et al. 1999; Hildebrand and Ruegsegger 1997); thus, a model-free method to evaluate the structure of the material in this study was used (Hildebrand et al. 1999; Hildebrand and Ruegsegger 1997). Material mean thickness and material separation were evaluated by filling maximal spheres into the structure with distance transformation (Hildebrand et al. 1999; Hildebrand and Ruegsegger 1997). Porosity of the material was calculated as the void volume of the ceramic. The pores were visualized by converting the void volume to a solid image that was evaluated for the pore connectivity. In the evaluation of connectivity of the pore with the Conn-Euler

Table 1. Porosity and pore connectivity of three different bioceramics compared between water immersion and micro-CT

Bioceramics	Porosity by water Immersion		Micro-CT 3D evaluation			
			Porosity (%)		Pore connectivity	
	Mean±SD	CV (%)	Mean±SD	CV (%)	Mean±SD	CV (%)
THA ($n = 6$)	77.8±2.5	3.2	67.6±4.5	6.7	7.1±1.8	24.8
BSC ($n = 6$)	60.4±8.7	14.4	26.2±2.7*	10.3	2.7±1.5	56.0
ChronOS ($n = 6$)	74.7±1.4	1.9	59.9±1.1	1.9	39.8±9.4*	23.8

* $p < 0.05$ by one-way ANOVA to compare between three ceramics

method of Odgaard and Gundersen (1993), the unconnected objects in the evaluation were not included for the suppression of the boundary/edge problem. The result represented the dominant connected component within the volume of interest. In addition to the connectivity of the pores, pore size and distribution of all the pores were also evaluated. Since it has been shown that the pores within 200–400 μm are "functional" macropores (Guo 1993), the pore size distribution was evaluated with subcategorizing different ranges of pore size as < 200 μm or between 200 and 400 μm, or > 400 μm. The grouping of the different sizes was through the image processing program of the micro-CT workstation. After the pore size was labelled on each pore, a filter was applied to select the function pores.

Evaluation of the Material Mineral Density of the CPC Blocks   A density phantom was used to calibrate the hydroxyapatite (HA) density with corresponding X-ray attenuation value of the material. A linear regression was generated by the workstation for the calculation of mineral density of the materials. The mineral density was expressed as milligram of HA per cubic centimeter.

Statistical Analysis

The SPSS version 10.0 (SPSS, Chicago, Ill.) was used for statistical analysis. The values of different parameters were expressed as mean with standard deviation. One-way ANOVA was applied to compare the mean difference. Statistical significance was determined at $p < 0.05$.

Results

Water Immersion Test

The water immersion method provided quantitative measures for the volume or empty space with micropores in the material. The "porosity" or empty space of the ceramics was calculated accordingly. The "porosity" of the three ceramics was found to be 70.8% for THA, 60.4% for BSC and 74.7% ChronOS (Table 1).

Micro-CT Quantification

From the micro-CT scanning, a stack of 2D X-ray images was generated for structural analysis (Fig. 1). By applying a threshold to the image, the ceramic was extracted from the original image and evaluated for material area fraction, porosity, material perimeter, and material surface fraction in 2D manner, and material density (Table 2).

Porosity
With the 2D images, different parameters were measured with traditional histomorphometric methods as shown in Table 2. The ceramic blocks were then reconstructed from the 2D images by the workstation of μCT40 (Fig. 2). Table 3 showed the different parameters measured directly from the reconstructed block of the ceramics.
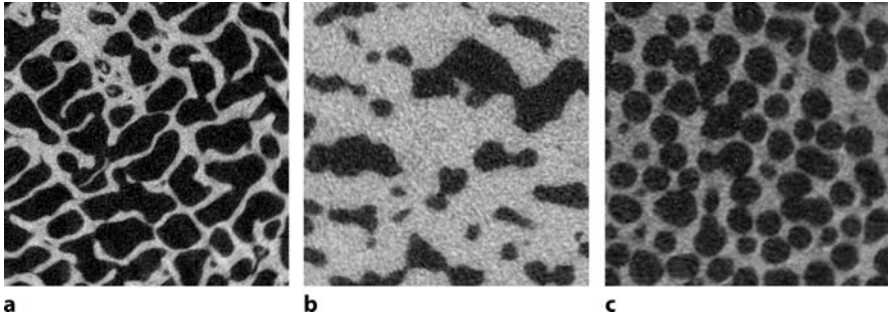
Figure 1 a–c. Representative cross-sectional images of the materials generated from micro-CT. **a** THA; **b** BSC; **c** ChronOS

Table 2. Micro-CT 2D histomorphometry compared among three different bioceramics

	THA ($n = 6$)		BSC ($n = 6$)		ChronOS ($n = 6$)	
	Mean ± SD	CV (%)	Mean ± SD	CV (%)	Mean ± SD	CV (%)
Material fraction (%)	32.18 ± 4.52	14.0	73.82 ± 2.68*	3.6	40.17 ± 0.92	2.3
Porosity (%)	67.82 ± 4.52	6.7	26.18 ± 2.68*	10.2	59.83 ± 0.92	1.5
Material surface fraction (1/mm)	18.05 ± 1.07	5.9	6.60 ± 0.36*	5.5	20.82 ± 0.56	2.7
Material perimeter (mm)	42.56 ± 4.87	11.4	27.98 ± 2.14*	7.6	35.76 ± 0.43	1.2

* $p < 0.05$ by one-way ANOVA to compare between three ceramics

Interconnection of Functional Pores

Using the built-in image processing program, the pores of the three CPCs were visualized, as shown in panel B of Fig. 2. After removal of disconnected pores, ChronOS and THA were shown to have more connected pores within the material when compared with the pores of BSC (Fig. 2, panel C). The connectivity of pore was quantified and it was shown that ChronOS (39.8 ± 9.4) and THA (7.1 ± 1.8) had significantly higher pore connectivity than that of the BSC (2.7 ± 1.5; $p < 0.05$; Table 1). With the image processing technique to threshold the different pore sizes, it was possible to depict the pores at certain size as shown in Fig. 3, in which the pores were > 200 µm in diameter. In addition, the distribution of the different pore sizes of the three CPC blocks can be elucidated (Fig. 4). It was shown that the three CPCs had different ranges of pores. ChronOS had the narrower range of pore size (16 – 368 µm) as compared with that of the other two CPC (BSC: 16 – 496 µm; THA: 16 – 656 µm). It was observed that the pore size of ChronOS was more concentrated at 200 – 400 µm. When different pore sizes were grouped together, it was shown that 87.8 ± 0.5% of the pores in ChronOS had a diameter of 200 – 400 µm, which was significantly more

Table 3. Micro-CT 3D histomorphometry compared among three calcium phosphate ceramics

	THA ($n = 6$)		BSC ($n = 6$)		ChronOS ($n = 6$)	
	Mean±SD	CV(%)	Mean±SD	CV(%)	Mean±SD	CV(%)
Material fraction (%)	32.4 ± 4.5	14	73.8 ± 2.7*	3.7	40.1 ± 1.12	2.8
Material mean thickness (mm)	0.15 ± 0.006	4.2	0.325 ± 0.017*	5.2	0.118 ± 0.002	1.7
Material separation (mm)	0.416 ± 0.052	12.6	0.22 ± 0.033*	14.9	0.263 ± 0.002	0.8
No. of material element	2.15 ± 0.21	10	2.91 ± 0.2*	7	4.18 ± 0.07	1.6
Material connectivity	8.36 ± 1.56	18.62	1.42 ± 0.65*	45.4	45.4 ± 2.24	4.9
Porosity (%)	67.6 ± 4.6	6.7	26.2 ± 2.7*	10.3	59.9 ± 1.1	1.9
Surface fraction (%)	15.38 ± 0.76	4.9	5.35 ± 0.26*	4.8	17.71 ± 0.43	2.4
Material density (mgHA/cm^3)	1251.9 ± 33.2	2.6	869 ± 24.6*	2.8	635.7 ± 25.5	4

* $p < 0.05$ by one-way ANOVA to compare between three ceramics
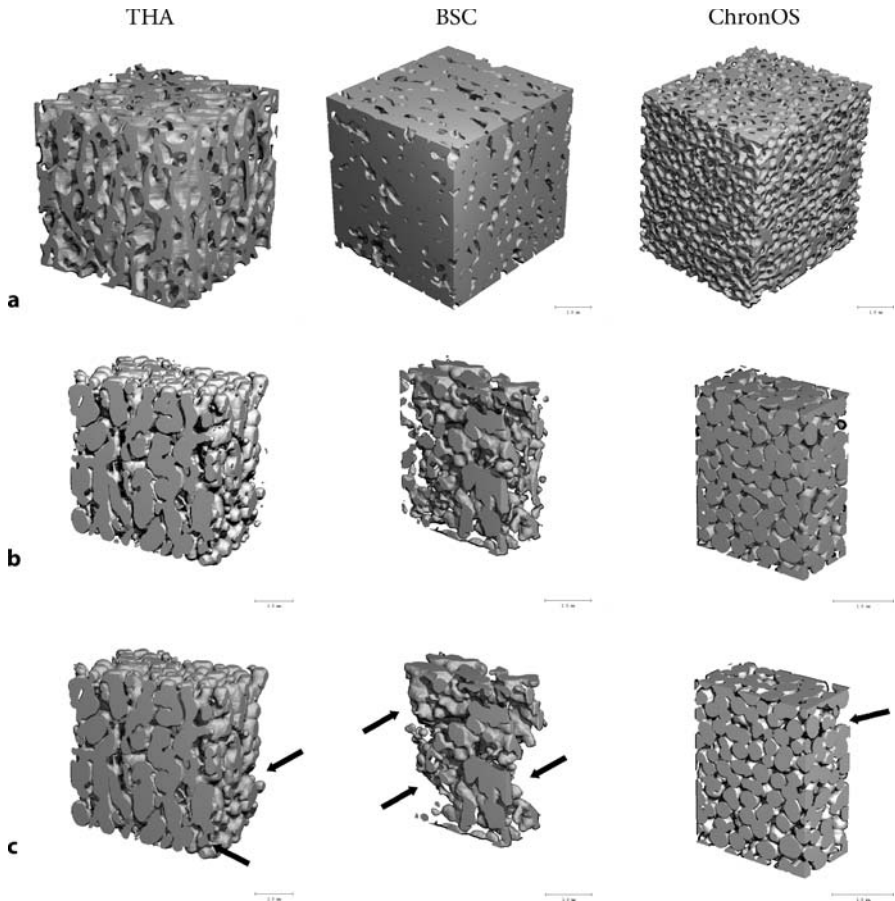
Figure 2. A 3D reconstruction of the material and the porous structure with in the material by micro-CT. The 3D image of the material THA, BSC and ChronOS (panel **a**). With the image processing technique, the materials are made transparent and the pores are converted to visible pixels (panel **b**). During the calculation of the connectivity of the porous structure, the disconnected pores are removed from the intact entity and the connectivity of the pores is calculated accroding to images with connected pores only (panel **c**)
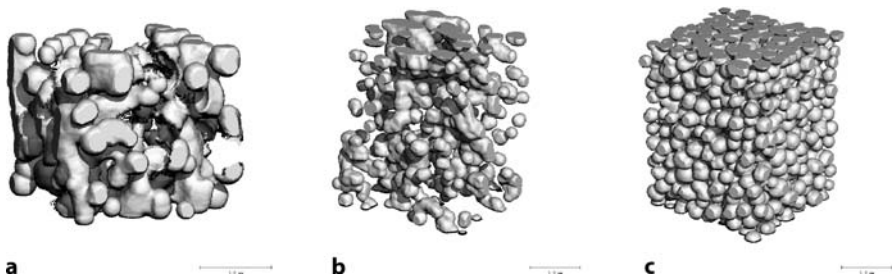
Figure 3 a–c. Functional pores within the three calcium phosphate ceramics. **a** THA; **b** BSC; **c** ChronOS
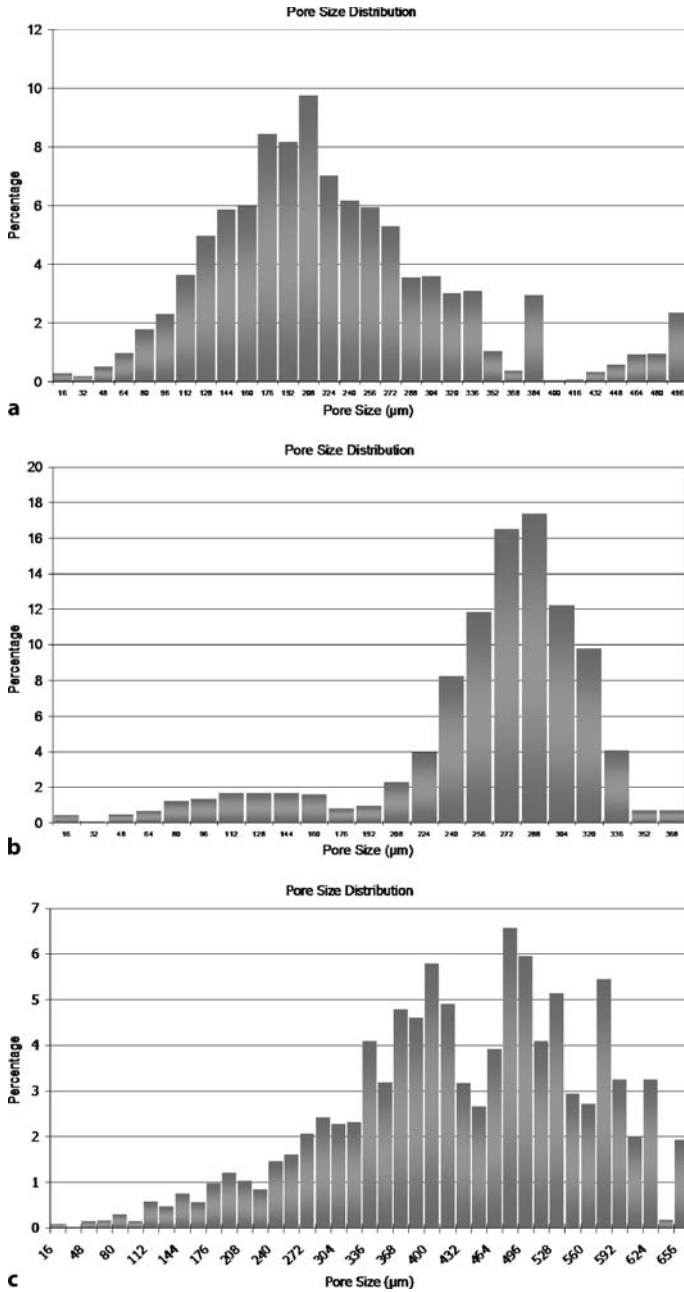
Figure 4. The representative distribution of the different pore sizes of the three calcium phosphate ceramics
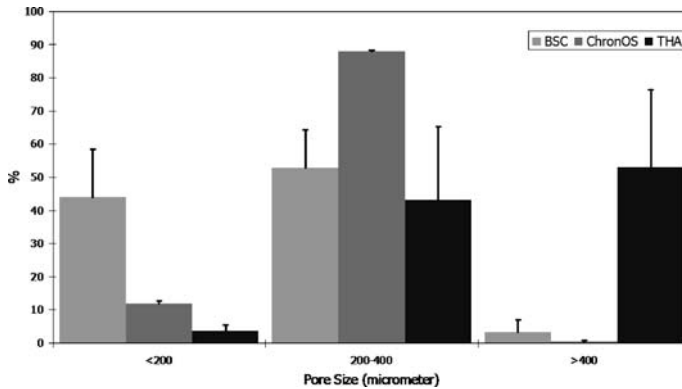
Figure 5. The percentage of different pore size ranges in the three calcium phosphate ceramics. ($p < 0.05$ by one-way ANOVA to compare between different ceramics)

than those of BSC which had $52.8 \pm 11.5\%$ and THA which had $43.2 \pm 22.1\%$ (Fig. 5; $p < 0.05$). The BSC had the most pores with $< 200\,\mu m$ (43.9%) and ChronOS and THA had 12.0 and 3.7% of pores $< 200\,\mu m$, respectively. The THA had more pores with $> 400\,\mu m$ in diameter ($p < 0.05$) than the other two CPCs.

Material Density

The material density was quantified for the content of HA within a given volume. The THA had the highest material density ($1251 \pm 33.2\,mg\,HA/cm^3$) when compared with BSC ($869.0 \pm 24.6\,mg\,HA/cm^3$) and ChronOS ($635.7 \pm 25.5\,mg\,HA/cm^3$; Table 3).

Scanning Electron Microscopy Description

The surface of the three ceramics was visualized by scanning electron microscopy (SEM) and is shown in Fig. 6. It was observed that the surface of THA and BSC was more rough and with many different sizes of ceramic granules. On the other hand, the surface of ChronOS was smoother and the size of the micro-structure was more uniform. The micropores of the three CPCs were interconnected.
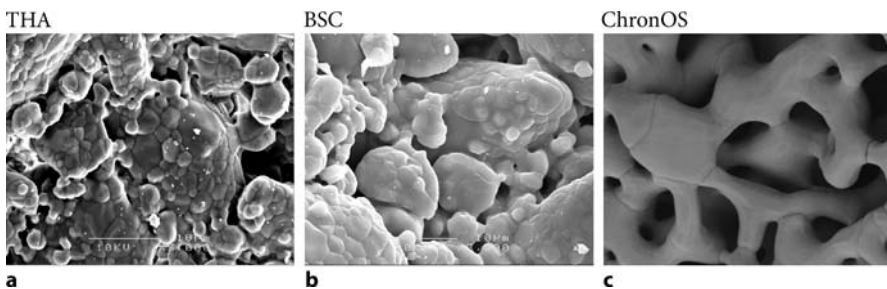
Figure 6. The scanning electron microscopic images of the three calcium phosphatate ceramics

Data Interpretation and Discussion

We use micro-CT intensively in our institution for orthopaedic, bone mineral and biomaterial research (Gong et al. 2005; Lai et al. 2005; Qin et al. 2005; Siu et al. 2004; Yeung et al. 2005). We presently developed and presented a simple objective method to use micro-CT for quantifying the pores of different CPCs, which is important in orthopaedic applications. Since this technique is non-destructive and possibly applicable in a sterilized environment, one can use the analyzed CPC blocks for testing the in vivo effect of different physical parameters of the material and pores.

Apart from providing the porosity and pore size of the ceramic, the 3D evaluation of micro-CT additionally characterizes the connectivity or interconnection of the pores which is essential for bone ingrowth (osteoconduction) associated with both angiogenesis and osteogenesis (Grenga et al. 1989; Guo 1993; Kuboki et al. 2001; Tsuruga et al. 1997) as well as for evaluating quality of structure integration (Shors 1999). It is generally accepted that a pore size > 100 μm is necessary for bone ingrowth (Liu 1997; Lu et al. 1999). In a previous study, it was shown that even if the pore size was larger than 100 μm, the formation of bone could be through either endochondral ossification or membranous ossification (Kuboki et al. 2001). With the advances in imaging and 3D structural image analysis of micro-CT, the present study demonstrates that the variation of the material structure and the porous structure might be significant depending on the manufacturing methods.

Comparison of Water Immersion and Micro-CT in Quantification of Material Porosity

In the present study, a discrepancy existed in the porosity measured by water immersion and the micro-CT. The main reason is that, in water immersion method, all the pores were counted into the porosity, regardless of whether they were micro- or macro-pores. On the other hand, the pores evaluated with micro-CT depended on the resolution of the images and the actual percentage of the micropores within the material. Since the lowest resolution in micro-CT is 36 μm, it is more appropriate to evaluate the macropores with > 36 μm.

The mercury porosimeter is based on the physical principle that a non-wetting liquid does not penetrate fine pore until sufficient pressure is applied. The required pressure is inversely proportional to the size of the pores according to the Washburn equation with the assumption that the pore is cylindrical and well connected (Washbrun 1921); therefore, the pore size distribution obtained from mercury porosimeter does not represent pore diameters but the size of the interconnections between pores (Klawitter and Hulbert 1971). This method provides information on the interconnected size, but not the actual pore size and the overall interconnection of the pores. The porous ceramics as shown in the present study have spherical pores with 3D interconnected structure. The mercury porosimetry only provides partial information on the entire porous structure.

The SEM is a very useful method to demonstrate the micropore structure; however, the quantification of the pore structure is dependent on the image analysis of 2D images obtained from the scan. In a previous study (Filmon et al. 2002), micro-

CT had been used to depict the pore and material structure of the porous biomaterial; however, the pore size and the interconnection of the pores were evaluated from the 2D images of micro-CT. The network of the pore structure was in a 3D manner which required a 3D method to analyze it; therefore, together with the previous study on pore structure by micro-CT (Filmon et al. 2002), the present micro-CT and its related image processing and analysis become a complementary means to further provide comprehensive information on the physical distribution, size and connectivity of the pores within the porous ceramics in a 3D manner.

"Functional Porosity" Quantified by Micro-CT

Unlike the water immersion method and SEM evaluation, micro-CT is a method that provides information on "functional porosity" and 3D interconnection apart from delivering a detailed report on parameters of the material structure objectively. The porosity of the ceramics measured by micro-CT can be calculated based on the void volume of the ceramics. In addition, the micro-CT also evaluates the pore size by using a model-independent method. With this method, the pore size is measured by filling spheres directly into the 3D structure, which is either the material and pores, rather than using 2D images and serology to derive the 3D morphometry (Hildebrand and Ruegsegger 1997). The detailed algorithms used in the program have been discussed from the previous studies (Hildebrand and Ruegsegger 1997; Muller et al. 1994; Odgaard and Gundersen 1993). The evaluation method of micro-CT has been validated using microradiography and histological sections as standard methods (Engelke et al. 1993; Muller et al. 1998; Schmidt et al. 2003). It was shown that a highly significant correlation exists between conventional histomorphometry and micro-CT analysis for material volume fraction and the material surface fraction (Muller et al. 1998; Schmidt et al. 2003). From the images generated by micro-CT, the pores inside the three ceramics in the present study are more or less spherical; therefore, the evaluation method based on sphere space-filling technique and shape-independent calculation matches the material structure very well (Hildebrand and Ruegsegger 1997).

Having the detailed pore size information, the distribution of different ranges of pore size was objectively depicted as shown in the present study. In a classical study, Klawitter and Hulbert (1971) clearly demonstrated the importance of the size of the interconnected pores in conducting the bony ingrowth to the CPC in vivo. In their study, the minimum size of the interconnected pores showing the potential for bone ingrowth was found between 40 and 100 µm. Other previous studies showed that the pore size played an important role in the induction of osteogenesis or chondrogenesis inside the pore of the ceramics (Kuboki et al. 2001; Tsuruga et al. 1997). Micro-CT provides objective evaluation of pore size and distribution of the functional pores. Furthermore, micro-CT also provides the total surface area of the pores and their connectivity. It has been reported experimentally that the osteoconductivity of ceramics is dependent on the surface area as well as other pore structural parameters (Kurioka et al. 1999; Shors 1999). The present study showed that ChronOS and THA have better pore surface fraction than that of BSC. Whether findings of this compara-

tive study indicate that ChronOS and THA have better capacity for bone ingrowth to the ceramics remains a subject for further investigation. Nevertheless, these technical advantages provided by micro-CT are very helpful for research and development or modification of available orthopaedic ceramics for clinical applications.

"Interconnection of functional porosity" Quantified by Micro-CT

A unique parameter of the pore structure provided by micro-CT is the pore connectivity that is evaluated according to the method developed for evaluation of cancellous bone connectivity by Odgaard and Gundersen (1993). The higher the pore connectivity is, the better the pores are linked together. It has been reported that the pore interconnection is important for angiogenesis and osteogenesis inside the ceramics by improving the fluid flow and nutrient supply (Angel et al. 1985; Boden et al. 1995; Grenga et al. 1989; Kuboki et al. 2001). In the present study, ChronOS exhibited higher pore connectivity and more functional pores than those of BSC and THA; however, THA has high percentage of the pores with > 400 µm in diameter. In the present evaluation of the connectivity by micro-CT, it is possible that the evaluation considered the connected large pores as one big entity and did not count it as one connection, even though the 3D image shown in Fig. 2 indicates that most of the pores are interconnected; thus, the pore connectivity in THA is only 7.1, which is much lower than that of ChonOS. Further studies are required to prove that ChronOS may show better functional outcome in terms of better osteo-integration and bony ingrowth when compared with BSC and THA.

"Material Density" Quantified by Micro-CT

As mentioned previously, micro-CT is unable to depict the micropores as effective as the macropores due to the limitation in scanning resolution; however, the surrogate in describing the micropores in the present micro-CT system is the measurement of the material density of CPCs. The specific gravity of hydroxyapatite powder is 1.33, whereas that of the crystal hydroxyapatite is 3.08. In the present study, it was shown that the material densities of the three CPCs were smaller than those of pure hydroxyapatite powder. This indicates that the material observed from the images of the micro-CT does not contain the material itself. There are micropores the insides of which can be easily shown with SEM. On the other hand, the crystalline structure of the CPC should be considered in the estimation of porosity of CPC with micropores. In the present study, the CPC consists of either pure hydroxyapatite or pure β-TCP, or a mixture of both; thus, the material density of the three components also affects the X-ray attenuation and gives material densities different from those given by micro-CT. Although there is significant difference in material density between the three CPCs, we cannot draw the conclusion that the β-TCP had the lowest material density in the present evaluation protocol as β-TCP consists of more micropores. It is necessary to further investigate the micropores inside the materials and their correlation with the material density measurement by micro-CT before application in the evaluation of the micropores inside the ceramics can be confirmed.

The Role of Chemical Properties in Biomaterial Studies

Apart from the differences in structure between these orthopaedic ceramics, the difference in the chemical property of CPC may also influence the in vivo performance after implantation (Tay et al. 1999). A relatively faster absorbable pure *β*-TCP (ChronOS) may have different effects in inducing osteogenesis in vivo when compared with the HA/TCP composite (BSC) and pure HA (THA), which are of relatively slower resorption rate due to the presence of the hydroxyapaptite (Braye et al. 1996; LeGeros et al. 1988; Shors 1999). When the osteoconductivity of the ceramics with different pore size and connectivity are compared, the chemical property and degradation of the materials also play an important role in the performance of the materials. The overall performance will require further investigation to prove our speculation on the effect of different structural properties on osteogenesis.

Conclusion

Based on the foregoing discussion, it is clear that the characteristics of the different CPCs manufactured by different methods can be elucidated when information on the material and porous structure of the CPCs provided by the micro-CT is available. Having these objective characteristics, further evaluations of the in vivo performance of these CPCs can be carried out for the development of a better CPC for both osteocondution and osteo-induction in orthopaedic applications.

References

Adachi N, Ochi M, Deie M, Ito Y (2005) Transplant of mesenchymal stem cells and hydroxyapatite ceramics to treat severe osteochondral damage after septic arthritis of the knee. J Rheumatol 32:1615–1618

Alam MI, Asahina I, Ohmamiuda K, Takahashi K, Yokota S, Enomoto S (2001) Evaluation of ceramics composed of different hydroxyapatite to tricalcium phosphate ratios as carriers for rhBMP-2. Biomaterials 22:1643–1651

Angel MF, Swartz WM, Ramasastry SS, Brown ML, Hanley EN Jr, Herbert DL (1985) Vascularization of tricalcium phosphate, an artificial bone substitute: preliminary observations. Microsurgery 6:175–181

Bignon A, Chouteau J, Chevalier J, Fantozzi G, Carret JP, Chavassieux P, Boivin G, Melin M, Hartmann D (2003) Effect of micro- and macroporosity of bone substitutes on their mechanical properties and cellular response. J Mater Sci Mater Med 14:1089–1097

Boden SD, Schimandle JH, Hutton WC (1995) An experimental lumbar intertransverse process spinal fusion model. Radiographic, histologic, and biomechanical healing characteristics. Spine 20:412–420

Braye F, Irigaray JL, Jallot E, Oudadesse H, Weber G, Deschamps N, Deschamps C, Frayssinet P, Tourenne P, Tixier H, Terver S, Lefaivre J, Amirabadi A (1996) Resorption kinetics of osseous substitute: natural coral and synthetic hydroxyapatite. Biomaterials 17:1345–1350

Bruder SP, Kraus KH, Goldberg VM, Kadiyala S (1998a) The effect of implants loaded with autologous mesenchymal stem cells on the healing of canine segmental bone defects. J Bone Joint Surg Am 80:985–996

Bruder SP, Kurth AA, Shea M, Hayes WC, Jaiswal N, Kadiyala S (1998b) Bone regeneration by implantation of purified, culture-expanded human mesenchymal stem cells. J Orthop Res 16:155–162

Cancedda R, Mastrogiacomo M, Bianchi G, Derubeis A, Muraglia A, Quarto R (2003) Bone marrow stromal cells and their use in regenerating bone. Novartis Found Symp 249:133–143

Cheng JCY, Guo X, Law LP, Lee KM, Chow DH, Rosier R (2002) How does recombinant human bone morphogenetic protein-4 enhance posterior spinal fusion? Spine 27:467–474

Engelke K, Graeff W, Meiss L, Hahn M, Delling G (1993) High spatial resolution imaging of bone mineral using computed microtomography. Comparison with microradiography and undecalcified histologic sections. Invest Radiol 28:341–349

Erbe EM, Marx JG, Clineff TD, Bellincampi LD (2001) Potential of an ultraporous beta-tricalcium phosphate synthetic cancellous bone void filler and bone marrow aspirate composite graft. Eur Spine J 10 (Suppl 2):S141–S146

Filmon R, Retailleau-Gaborit N, Grizon F, Galloyer M, Cincu C, Basle MF, Chappard D (2002) Non-connected versus interconnected macroporosity in poly (2-hydroxyethyl methacrylate) polymers. An X-ray microtomographic and histomorphometric study. J Biomater Sci Polym Ed 13:1105–1117

Gong H, Zhang M, Yeung HY, Qin L (2005) Regional variations in microstructural properties of vertebral trabeculae with aging. J Bone Miner Metab 23:174–180

Grenga TE, Zins JE, Bauer TW (1989) The rate of vascularization of coralline hydroxyapatite. Plast Reconstr Surg 84:245–249

Guo X (1993) Histomorphological studies on the loosening and infection processes of bony structure around the Schanz screws in the sheep tibiae. Medical School of University Essen, Germany

Guo X, Lee KM, Law LP, Chow HK, Rosier R, Cheng CY (2002) Recombinant human bone morphogenetic protein-4 (rhBMP-4) enhanced posterior spinal fusion without decortication. J Orthop Res 20:740–746

Hildebrand T, Ruegsegger P (1997) A new method for the model-independent assessment of thickness in three-dimensional images. J Microsc 185:67–75

Hildebrand T, Laib A, Muller R, Dequeker J, Ruegsegger P (1999) Direct three-dimensional morphometric analysis of human cancellous bone: microstructural data from spine, femur, iliac crest, and calcaneus. J Bone Miner Res 14:1167–1174

Hollister SJ, Lin CY, Saito E, Lin CY, Schek RD, Taboas JM, Williams JM, Partee B, Flanagan CL, Diggs A, Wilke EN, Van Lenthe GH, Muller R, Wirtz T, Das S, Feinberg SE, Krebsbach PH (2005) Engineering craniofacial scaffolds. Orthod Craniofac Res 8:162–173

Hulbert SF, Young FA, Mathews RS, Klawitter JJ, Talbert CD, Stelling FH (1970) Potential of ceramic materials as permanently implantable skeletal prostheses. J Biomed Mater Res 4:433–456

Klawitter JJ (1979) A basic investigation of bone growth in porous materials. Clemson University, Clemson, South Carolina

Klawitter JJ, Hulbert SF (1971) Application of porous ceramics for the attachment of load bearing internal orthopedic applications. J Biomed Mater Res 5:161–229

Kuboki Y, Jin Q, Takita H (2001) Geometry of carriers controlling phenotypic expression in BMP-induced osteogenesis and chondrogenesis. J Bone Joint Surg Am 83 (Suppl 1):S105–S115

Kurioka K, Umeda M, Teranobu O, Komori T (1999) Effect of various properties of hydroxyapatite ceramics on osteoconduction and stability. Kobe J Med Sci 45:149–163

Lai YM, Qin L, Yeung HY, Lee KK, Chan KM (2005) Regional differences in trabecular BMD and micro-architecture of weight-bearing bone under habitual gait loading: a pQCT and microCT study in human cadavers. Bone 37:274–282

LeGeros RZ, Parsons JR, Daculsi G, Driessens F, Lee D, Liu ST, Metsger S, Peterson D, Walker M (1988) Significance of the porosity and physical chemistry of calcium phosphate ceramics. Biodegradation-bioresorption. Ann NY Acad Sci 523:268–271

Liu DM (1997) Influence of porous microarchitecture on the in vitro dissolution and biological behavious of porous calcium phosphate. In: Liu DM, Dixit V (eds) Porous materials for tissue engineering. Trans Tech Publications, Zurich, pp 183–208

Lu JX, Flautre B, Anselme K, Hardouin P, Gallur A, Descamps M, Thierry B (1999) Role of Interconnections in porous bioceramics on bone recolonization in vitro and in vivo. J Mater Sci Mater Med 10:111–120

Morishita T, Honoki K, Ohgushi H, Kotobuki N, Matsushima A, Takakura Y (2006) Tissue engineering approach to the treatment of bone tumors: three cases of cultured bone grafts derived from patients' mesenchymal stem cells. Artif Organs 30:115–118

Muller R, Hildebrand T, Ruegsegger P (1994) Non-invasive bone biopsy: a new method to analyse and display the three-dimensional structure of trabecular bone. Physics Med Biol 39:145–164

Muller R, Van Campenhout H, Van Damme B, Van Der PG, Dequeker J, Hildebrand T, Ruegsegger P (1998) Morphometric analysis of human bone biopsies: a quantitative structural comparison of histological sections and micro-computed tomography. Bone 23:59–66

Odgaard A, Gundersen HJ (1993) Quantification of connectivity in cancellous bone, with special emphasis on 3-D reconstructions. Bone 14:173–182

Oya M, Takahashi M, Iwata Y, Jono K, Hotta T, Yamamoto H, Washio K, Suda A, Matuo Y, Tanaka K, Morimoto M (2002) Mercury intrusion porosimetry used to determine pore-size distribution. Am Ceram Soc Bull 81:52–56

Peterson B, Zhang J, Iglesias R, Kabo M, Hedrick M, Benhaim P, Lieberman JR (2005) Healing of critically sized femoral defects, using genetically modified mesenchymal stem cells from human adipose tissue. Tissue Eng 11:120–129

Predecki P, Stephan JE, Auslaender BA, Mooney VL, Kirkland K (1972) Kinetics of bone growth into cylindrical channels in aluminum oxide and titanium. J Biomed Mater Res 6:375–400

Qin L, Zhang G, Hung WY, Shi Y, Leung K, Yeung HY, Leung P (2005) Phytoestrogen-rich herb formula "XLGB" prevents OVX-induced deterioration of musculoskeletal tissues at the hip in old rats. J Bone Miner Metab 23 (Suppl):55–61

Qu SX, Chen WQ, Weng J, Zhang XD (1994) The early dissolution of the biphasic calcium ceramics implanted in dogs and rabbits. In: Anderson OH, Yli-Urop A (eds) German Ceramic Society, Cologne, pp 91–95

Ruegsegger P, Koller B, Muller R (1996) A microtomographic system for the nondestructive evaluation of bone architecture. Calcif Tissue Int 58:24–29

Schmidt C, Priemel M, Kohler T, Weusten A, Muller R, Amling M, Eckstein F (2003) Precision and accuracy of peripheral quantitative computed tomography (pQCT) in the mouse skeleton compared with histology and microcomputed tomography (microCT). J Bone Miner Res 18:1486–1496

Shors EC (1999) Coralline bone graft substitutes. Orthop Clin North Am 30:599–613

Siu WS, Qin L, Cheung WH, Leung KS (2004) A study of trabecular bones in ovariectomized goats with micro-computed tomography and peripheral quantitative computed tomography. Bone 35:21–26

Spivak JM, Hasharoni A (2001) Use of hydroxyapatite in spine surgery. Eur Spine J 10 (Suppl 2):S197–S204

Tancred DC, McCormack BA, Carr AJ (1998) A synthetic bone implant macroscopically identical to cancellous bone. Biomaterials 19:2303–2311

Tay BK, Patel VV, Bradford DS (1999) Calcium sulfate- and calcium phosphate-based bone substitutes. Mimicry of the mineral phase of bone. Orthop Clin North Am 30:615–623

Tsuruga E, Takita H, Itoh H, Wakisaka Y, Kuboki Y (1997) Pore size of porous hydroxyapatite as the cell-substratum controls BMP-induced osteogenesis. J Biochem 121:317–324

Urist MRB (1994) The search for and the discovery of bone morphogenetic protein (BMP). In: Urist MRB, O'Connor BT, Burwell RG (eds) Bone grafts, derivatives and substitutes. Butterworth-Heinemann, Oxford, pp 315–362

van Blitterswijk CA, Grote JJ, Kuijpers W, Daems WT, de Groot K (1986) Macropore tissue ingrowth: a quantitative and qualitative study on hydroxyapatite ceramic. Biomaterials 7:137–143

Washbrun W (1921) Note on a method of determining the distribution of pore sizes in a porous material. Proc Natl Acad Sci 7:115–116

Wilke A, Orth J, Lomb M, Fuhrmann R, Kienapfel H, Griss P, Franke RP (1998) Biocompatibility analysis of different biomaterials in human bone marrow cell cultures. J Biomed Mater Res 40:301–306

Yeung HY, Zhu F, Qiu Y, Tang SP, Qin L, Lee KM, Cheng CY (2005) Trabecular bone microarchitecture in adolescent idiopathic scoliosis compared between concave and convex site of the facet joints. Chin J Surg 43:777–780

Bone Densitometries in Assessing Bone Mineral and Structural Profiles in Patients with Adolescent Idiopathic Scoliosis

Jack Chun-Yiu Cheng (✉) [1], Vivian Wing-Yin Hung[1], Ling Qin[1], and Xia Guo[2]

[1] Department of Orthopaedics and Traumatology, The Chinese University of Hong Kong, Hong Kong, China
   e-mail: jackcheng@cuhk.edu.hk
[2] Department of Rehabilitation Sciences, The Hong Kong Polytechnic University, Hong Kong, China

Abstract

Scoliosis is a three-dimensional (3D) structural spinal deformity characterized by both vertebral rotation and lateral curvature greater than 10°. Idiopathic scoliosis is the most common type of structural scoliosis and this chapter focuses on bone mineral and structure parameters in girls with adolescent idiopathic scoliosis (AIS) assessed using various bone densitometries, including dual-energy X-ray absorptiometry (DXA), peripheral quantitative computed tomography (pQCT), quantitative ultrasound (QUS), and micro-computed tomography (micro-CT). We found that systemic low bone mass was manifested in 30% of AIS girls. With the use of different modalities of bone densitometry, AIS girls were found to have a significantly lower areal and volumetric bone mineral density (BMD) at various skeletons including spine, proximal femur, and distal extremities. Moreover, poor bone quality reflected by QUS technique was also found in AIS girls. Clinical application of bone densitometry in relation to the curve severity and prognostic value in predicting curve progression may enhance the clinical management and treatment planning for scoliosis patients.

Scoliosis

Scoliosis is a three-dimensional (3D) structural spinal deformity characterized by both vertebral rotation and lateral curvature greater than 10° (Fig. 1; Lonstein 1995b). Idiopathic scoliosis is the most common type of structural scoliosis. There are three types of idiopathic scoliosis based on the age of onset: infantile (0–3 years of age); juvenile (4–9 years of age); and adolescent idiopathic scoliosis (AIS; age from 10 years to maturity around age 16 years; Lonstein 1995a).

The prevalence rate acquiring AIS is approximately 2–4% (Cheng et al. 2000; Lonstein 1995a; Roach 1999; Weinstein 1999). Girl-to-boy ratio is about 4:1 (Weinstein 1999). Progression of scoliosis was found to be strongly associated with growth
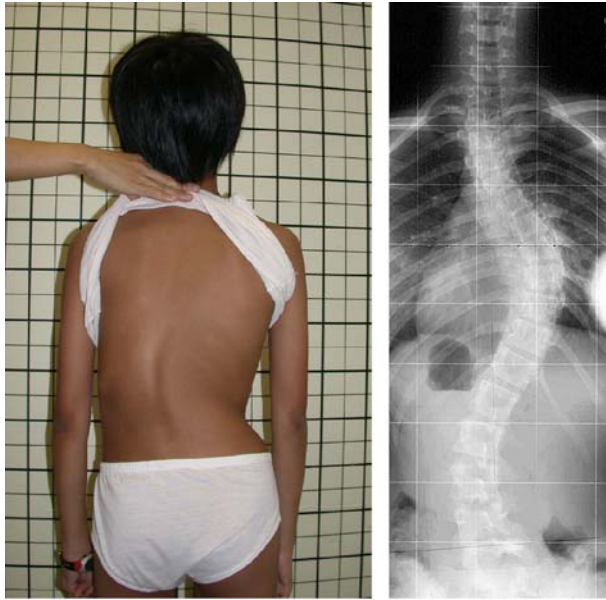
Figure 1. Clinical photo (*left*) and radiography (*right*) of a girl with adolescent idiopathic scoliosis (AIS)

spurt, which usually occurred at ages 10–13 years for girls and about 2 years later for boys (Tanner and Whitehouse 1976). The timing of this rapid growth is typically gauged by Tanner staging, skeletal age, menarche, and Risser sign of iliac apophyseal ossification (Sanders et al. 2003).

The AIS accounts for approximately 80% of all types of idiopathic scoliosis (Morcuende and Weinstein 2003). Despite extensive ongoing research, the etiology of AIS remains unknown. Many studies suggested that the cause of AIS was generally regarded as a multifactorial disorder (Burwell and Dangerfield 2000; Lowe et al. 2000; Weinstein 1994; Willner 1994; Winter and Lonstein 1992). Factors that were suggested to be the etiological ones included: genetic (Carr et al. 1992; Wynne-Davies 1968); hormonal effects (melatonin-related; Bagnall et al. 1996; Dubousset and Machida 1998; Willner et al. 1976); growth disturbances (Nissinen et al. 1993; Willner 1975); connective tissue defect (Hadley-Miller et al. 1994; Taylor et al. 1981); neural mechanism (Zadeh et al. 1995); thrombocytic abnormalities (Yarom et al. 1982); and skeletal muscle abnormalities (Ford et al. 1988; Low et al. 1983).

Bone Mineral and Structural Profiles in AIS Girls Assessed by DXA, pQCT, and QUS

Abnormalities in anthropometric measurements, BMD, as well as bone morphology of long bone and spinal column were found in AIS girls as compared with age- and gender-matched normal controls (Burwell 1977; Cheng et al. 2001; Cheung et al. 2003; Guo et al. 2003; Leong et al. 1982; Nicolopoulos et al. 1985; Shohat et al. 1988; Willner 1974). In our clinical experience, osteoporotic bone can be observed during implantation of spinal surgery in some scoliosis patients. Bone densitometry with minimal

radiation dosage is one of the best non-invasive tools to assess the bone mineral status in patients with scoliosis.

Dual Energy X-ray Absorptiometry

Dual energy X-ray absorptiometry (DXA) has been commonly used in diagnosing osteoporosis in the clinical setting, as well as for pediatric studies (Abes et al. 2003; Adams 1998; Giampietro et al. 2003; Ruegsegger 1996). The DXA is a planar technique with regions of interest (ROI) of BMD measurement being the lumbar spine and the proximal femur in most cases. Parameters that can be obtained from a DXA measurement include bone mineral content (BMC; in grams), bone area (in square centimeters), and areal BMD (aBMD; in grams per square centimeter), which is calculated from the measured bone mass (BMC) over the bone area (Fuerst et al. 1998). The scanning resolution is normally 1 mm. The DXA has several advantages such as low radiation dose, ability to measure axial skeleton, and short scanning time; however, it only provides areal BMD and not volumetric BMD. According to the World Health Organization (WHO) criteria, postmenopausal women with a T-score (calculated with respect to the peak bone mass of the specific normal reference population) ≤ -2.5 standard deviations (SD) are classified as osteoporosis (WHO 1994). In pediatric studies, Z-score, calculated with respect to the age- and gender-matched normal reference, should be used for discriminating children with low bone mass; however, the cut-off value of the Z-score is not well defined, with a cutoff at -1 SD being generally accepted and used in scoliosis research (Cheng et al. 1999; Cheng et al. 2000; Cheng and Guo 1997; Cook et al. 1987; Courtois et al. 1999; Thomas et al. 1992).

Low bone mass in AIS patients has been well documented in our previous studies and by others (Cheng and Guo 1997), where low bone mass in AIS was shown to be a systemic problem rather than a localized problem (Burner et al. 1982; Cheng et al. 1999; Cheng et al. 2000; Cheng and Guo 1997; Courtois et al. 1999; Thomas et al. 1992). Cheng and Guo (1997) conducted a cross-sectional study, with 81 AIS girls and 220 age- and gender-matched normal controls, to study the bone mineral profile in AIS girls. All subjects were divided into three age groups (12, 13, and 14). The BMD of the spine and both proximal femora (Fig. 2) were obtained by DXA (XR-36, Norland Medical System, Fort Atkinson, Wis.). Results revealed that AIS girls had significantly lower BMD in both the spine and hip regions than controls in all age groups, and the percentage differences ranged from -6.9 to -30.4 (Table 1).

However, BMD value of the spine measured using DXA is affected by the vertebral rotation (Cheng et al. 2001; Girardi et al. 2001). Cheng et al. (2001) performed an in vitro study, using cadaver vertebrae L2-L4, to study the effect of vertebral rotation of the lumbar spine on DXA measurement. They demonstrated that there was a significant positive correlation between the degree of axial rotation and the measured bone area ($r = 0.747$; $p < 0.01$) and a significant negative correlation between the degree of rotation and BMD value ($r = -0.665$; $p < 0.01$); however, no significant correlation was found between degree of rotation and BMC ($p = 0.966$). The measured bone area increased approximately 24% and BMD decreased approximately 19% when the vertebrae were rotated by 45° (Table 2). This can be explained by the fact
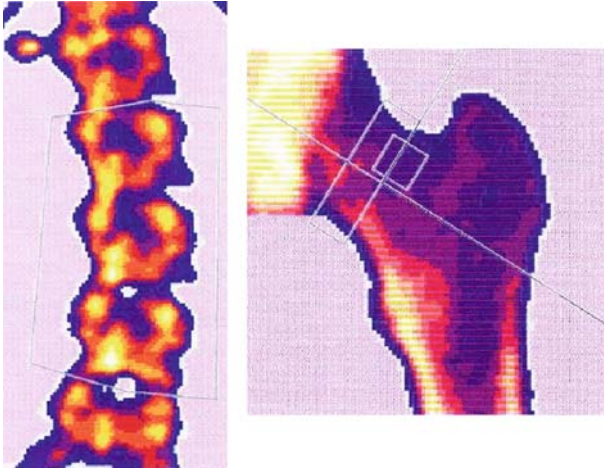
Figure 2. A dual-energy X-ray absorptiometry image of scoliotic spine (*left*) and hip (*right*)

that the posterior elements, such as the transverse processes, of the vertebra are exposed on the projectional area under axial rotation; therefore, the projected bone area is increased. Since BMD is calculated by BMC over the projected bone area, BMD will be underestimated. The BMC is the value of bone mass as a whole, and hence BMC remains constant regardless of the degree of rotation. A similar study has been done by Girardi et al. (2001) and comparable results were obtained; therefore, BMC of the spine or proximal femur is suggested as being a more reliable measuring parameter for patients with spinal deformity.

Table 1. Lumbar and proximal femoral bone mineral density in girls 12–14 years of age. (From Cheng and Guo 1997)

Measuring site	Age (years)	Normal control	AIS	Difference	Difference (%)
Lumbar spine (L2-L4)	12 ($n = 117$)	0.77 ± 0.12	0.71 ± 0.11	$-0.06 \pm 0.12^*$	-7.8
	13 ($n = 107$)	0.84 ± 0.12	0.76 ± 0.11	$-0.08 \pm 0.12^*$	-9.5
	14 ($n = 76$)	0.87 ± 0.11	0.81 ± 0.13	$-0.06 \pm 0.12^{**}$	-6.9
Femoral neck	12	0.76 ± 0.12	0.71 ± 0.10	$-0.05 \pm 0.10^*$	-7.8
	13	0.82 ± 0.11	0.74 ± 0.11	$-0.08 \pm 0.11^*$	-9.8
	14	0.86 ± 0.13	0.77 ± 0.12	$-0.09 \pm 0.13^*$	-10.5
Trochanter	12	0.68 ± 0.14	0.60 ± 0.08	$-0.08 \pm 0.13^{**}$	-11.8
	13	0.72 ± 0.09	0.60 ± 0.09	$-0.12 \pm 0.09^*$	-16.7
	14	0.73 ± 0.09	0.64 ± 0.10	$-0.09 \pm 0.09^*$	-13.5
Ward's triangle	12	0.82 ± 0.14	0.61 ± 0.13	$-0.21 \pm 0.14^*$	-27.4
	13	0.87 ± 0.14	0.61 ± 0.10	$-0.26 \pm 0.13^*$	-29.9
	14	0.92 ± 0.14	0.64 ± 0.12	$-0.28 \pm 0.13^*$	-30.4

Student's t-test significance: * $p < 0.01$; ** $p < 0.05$

Table 2. The DXA measurement of bone area, BMC, and BMD for cadaveric L3 vertebra in different degrees of rotation (results expressed as mean ± SD). (Adapted from Cheng et al. 2001)

Degree of rotation	Nash and Moe index	Outline of L3 Vertebra	Measured area (cm^2; % of baseline value at 0° rotation)	BMC (g; % of baseline value at 0° rotation)	BMD (g/cm^2; % of baseline value at 0° rotation)
0° (AP view)	0		12.96 ± 0.60 (100)	12.36 ± 0.85 (100)	0.95 ± 0.04 (100)
7.5°	I		13.16 ± 0.58 (101.5)	12.37 ± 0.86 (100.1)	0.94 ± 0.04 (98.9)
15°	I		13.45 ± 0.58 (103.8)	12.38 ± 0.85 (100.2)	0.92 ± 0.04 (96.8)
22.5°	II		14.24 ± 0.48 (109.9)	12.39 ± 0.82 (100.2)	0.87 ± 0.05 (91.6)
30°	II		14.74 ± 0.47 (113.7)	12.38 ± 0.81 (100.2)	0.84 ± 0.05 (88.4)
37.5°	III		15.38 ± 0.49 (118.7)	12.42 ± 0.80 (100.5)	0.81 ± 0.04 (85.3)
45°	III		16.07 ± 0.58 (124.0)	12.38 ± 0.80 (100.2)	0.77 ± 0.04 (81.05)

Numbers in parentheses are percentages

Peripheral Quantitative Computed Tomography

Peripheral quantitative computed tomography (pQCT) is a 3D multi-slice scanner which measure the true volumetric BMD (vBMD, in grams per cubic centimeters) of the peripheral skeleton with low radiation dose (Ruegsegger 1996). The ROIs for vBMD measurement are distal radius and tibia. Parameters to be obtained include the integral or total BMD (iBMD); the trabecular (tBMD) and cortical (cBMD) compartments of the distal extremities, with the scanning resolution of 0.3 mm using Densiscan system (Densiscan 2000, Scanco, Bassersdorf, Switzerland; Fig. 3). The pQCT allows the assessment of purely trabecular bone, which, due to its greater metabolic activity compared with cortical bone, may provide a more sensitive measure of frac-

ture risk (Formica et al. 1998; Grampp et al. 1995, 1997). Axial QCT is widely available and may have the strongest power in prediction of vertebral fracture compared to DXA or pQCT (Formica et al. 1998). However, radiation dose of axial QCT incurred five to ten times more than DXA or pQCT which confines the potential clinical application for bone mineral research especially in children (Njeh et al. 1997).

The girls with AIS had generally lower vBMD at the distal extremities than the age- and gender-matched normal controls. Cheng et al. (2000) examined the vBMD at the distal radius and tibia, using pQCT Densiscan system, to confirm whether low bone mass is a local or generalized phenomenon in AIS patients. Results demonstrated 34.5% AIS girls had vBMD value below –1 SD when compared with age-matched normal controls. When the criteria of osteopenia was set to Z-score BMD at -2, a higher percentage of AIS girls were observed to have low vBMD (8.1%) than aBMD (4.1%). This indicated that pQCT is more sensitive in detecting low BMD in trabecular-rich region when compared with DXA.

In addition to the abnormality of BMD at appendicular skeletons, disproportional growth of the anterior and posterior vertebral body was also found in AIS girls. Relative overgrowth at anterior spinal column in AIS has been reported in morphological studies (Porter 2001; Roth 1981). A recent magnetic resonance imaging (MRI) study on the vertebral morphometry of thoracic vertebrae of AIS girls demonstrated that the ratio of differential growth in the AIS group was significantly larger than that in the controls ($p < 0.01$ for all vertebrae; Guo et al. 2003). This evidence may imply that there is an uncoupling of bone growth between endochondral and membranous ossification. In the previous sections, we showed that AIS girls had generalized low
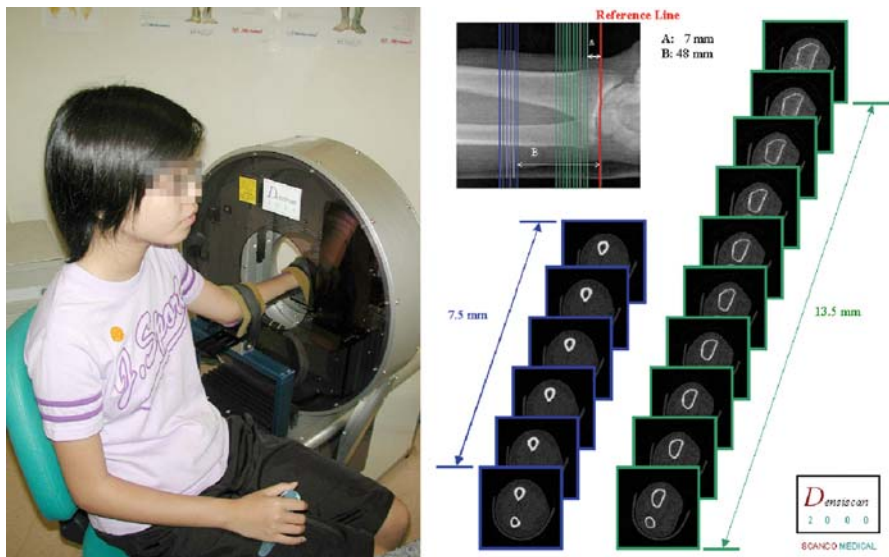
Figure 3. A multi-layer pQCT-machine (Densiscan 200) image of a girl with AIS, during distal radial scanning (*left*), with images of tomography at the distal radius (*right*)

bone mass at the distal radius and tibia as well as proximal femur. These are the regions that had growth plate for longitudinal growth, driven by endochondral ossification, during puberty; thus, suboptimal BMD in long bones and anterior overgrowth in the vertebral body may indirectly support our hypothesis on the abnormal bone growth in AIS patients. Moreover, membranous ossification during adolescence can be reflected by the circumferential growth of long bone.

The authors recently evaluated the cortical vBMD at midshaft of the radius using pQCT and the study consisted of 78 AIS girls and 44 age-matched healthy girls. The results demonstrated that AIS girls had significantly lower cortical vBMD at the cortical shell of the radial midshaft ($1608.8 \, \text{mg/cm}^3 \pm 48.6$) than that of the controls ($1636.7 \, \text{mg/cm}^3 \pm 35.8$; $p = 0.047$). This may imply that the abnormal mineralization of the bone matrix in AIS girls may be the bone-remodeling problem manifested in the BMD at tissue level. These findings may be substantiated by a significantly less osteocyte count reported in the trabecular bone biopsies in AIS patients. Cheng et al. (2001) performed a histomorphometric study on iliac crest biopsy of surgically treated AIS patients. Results revealed significantly lower mean trabecular thickness, absolute osteoid area, and mean osteoid width when compared with normal reference data. The histomorphometric data was also correlated with age, Cobb angle and femoral neck BMD of the patients. It showed that cell number was positively correlated with femoral neck BMD ($r = 0.55$, $p = 0.024$), whereas cell distance was negatively correlated with femoral neck BMD ($r = -0.516$, $p = 0.049$); however, age and Cobb angle were not significantly correlated with the histomorphometric data ($p > 0.4$ for all).

Quantitative Ultrasound

Quantitative ultrasound (QUS) is an alternative method to DXA, pQCT, or QCT in assessing bone quality, quantity, structure, and mechanical properties (Gluer 1997; Gluer et al. 1993; Faulkner et al. 1991; Han et al. 1996; Langton 1996; Nicholson et al. 1993; Njeh et al. 1997; Trebacz and Natali 1999; Wu et al. 2000). Ultrasound is a mechanical wave which causes both trabecular and cortex network to vibrate on a microscale when it passes through bone. The parameters provided by QUS include broadband ultrasound attenuation (BUA), velocity of sound (VOS), and their derived indices, such as Stiffness or Soundness (SI; Hans et al. 1999; Njeh et al. 1997; Stewart and Reid 2002). Clinical studies showed that QUS parameters were able to detect the age-related bone loss in postmenopausal women (Hung et al. 2004; Schott et al. 1998; Welch et al. 2004). Moreover, the ability in predicting fracture risk in QUS was also found in prospective longitudinal studies (Hans et al. 1996; Huang et al. 1998; Pluijm et al. 1999). The BUA measured at the heel using QUS has been reported as having higher predictive power of relative osteoporotic fracture risk at hip than the spine and distal radius (Dubois et al. 2001; Frost et al. 2002; Njeh et al. 1997); however, the precision error of the QUS is relatively high, ranging from 1.3 to 6.0% for BUA and 0.2 to 1.5% for VOS, which confines the clinical application on longitudinal studies (Hans et al. 1996; Huang et al. 1998; Pluijm et al. 1999).

Correlation between QUS and BMD, measured by DXA or pQCT, were modest. The correlation coefficients generally ranged from 0.21 to 0.83 (Gregg et al. 1997; Hung et al. 2004; Njeh et al. 2001; Prins et al. 1998). Prins et al. (1998) reviewed a number of papers on the correlation between QUS parameters and DXA-BMD at different sites. Results suggested that BUA of calcaneus correlates better with DXA-BMD of the same region (calcaneus) than other sites (spine or hip; $r = 0.66$ for calcaneus and $r = 0.47$ for both spine and hip). They support the statement that better correlations can be found if the same region of interest is measured by different techniques or using the same technique to measure different skeletal sites.

Despite extensive research on the bone mineral profile of AIS girls as mentioned above, there are no published studies on the evaluation of bone quality or bone strength in AIS patients using QUS. A preliminary study on the bone quality status in 32 AIS girls and 28 age-matched normal healthy girls was performed by our group. The QUS machine (Paris, Norland Medical Systems) was used to measure the ultrasonic parameters on the non-dominant leg of calcaneus. Results showed that AIS had lower BUA (118.5 ± 15.6 and 124.7 ± 9.3; $p = 0.062$), VOS (1444.0 ± 42.8 and 1448.1 ± 36.7; $p > 0.08$), and SI (357.2 ± 79.4 and 386.4 ± 57.2; $p > 0.07$) than controls. These data might imply poor bone quality or potentially microarchitectural abnormalities in addition to low bone mass in AIS girls as shown by our previous histomorphometric study on evaluation of bone biopsy obtained from surgically treated AIS girls (Cheng et al. 2001).

Potential Clinical Applications of Bone Densitometry in Scoliosis Research

Association Between Low Bone Mass and Curve Severity in AIS

Curve severity was inversely associated with areal and volumetric BMD in AIS patients. A large study of 619 AIS and 300 healthy girls was performed to investigate the association of low bone mass and curve severity in AIS during the rapid growth period (Lee et al. 2005). Results showed that there was a negative correlation between BMD and curve severity (correlation coefficient ranged from -0.083 to -0.115; $p < 0.05$). Moreover, when AIS patients were sub-classified into moderate (Cobb angle between 10 and 39°) and severe (Cobb angle $\geq 40°$) groups, there was a significantly higher percentage of osteopenic AIS girls in severe group than in the moderate group with respect to volumetric BMD of the distal tibia (percentage of osteopenic AIS: moderate vs severe group (28.4 and 40.2%; $p = 0.03$; Lee et al. 2005). The clinical relevance of this finding is that scoliosis-related osteopenia weakens the spinal architecture and may contribute to the progression of spinal deformity during growth.

Low Bone Mass is a Risk Factor in Prediction of Curve Progression in AIS Girls

Scoliosis is an irreversible process of spinal deformity. The currently available active therapies of AIS subjects are non-invasive orthotic spinal bracing and surgery. Appropriate bracing at the early stage is effective in a certain proportion of cases in

arresting curve progression rather than correcting the curvature during the rapid adolescent growth phase; however, the brace should be worn for over 20 hours a day until skeletal maturity, and the self-reported compliance rate was not reliable which may affect the treatment outcome (Carr 2003). For progressive and severe scoliosis patients, spinal fusion is the only treatment to prevent further deterioration of the curve; however, back pain and other complications are the long-term consequences of surgery. In order to prevent curvature from progressing, it is important to identify the risk factors related to curve progression in AIS patients. The well-accepted risk factors in progression can be summarized as follows:

1. The younger the patient at the time of diagnosis, the greater the risk of progression.
2. There is a greater risk of progression before the onset of menarche in females.
3. The lower the Risser grade at curve detection, the greater the risk of progression.
4. The larger the initial magnitude of the curve, the greater the risk of progression (Bunnell 1986; Lonstein and Carlson 1984; Peterson and Nachemson 1995; Soucacos et al. 2000; Weinstein 1994; Weinstein 1999; Yamauchi et al. 1988).

According to our previous discussion, 30% AIS girls had low bone mass and the BMD was inversely correlated with curve severity in AIS girls. The predictive power of low bone mass in curve progression is of great clinical interest. A prospective longitudinal study on the prognostication of curve progression in AIS was performed by our group. In addition to the well-known prognostic factors, BMD was added as an additional factor to investigate whether low bone mass could be a prognostic factor in curve progression. Hung et al. demonstrated that AIS patients who had low bone mass (Z-score $\leq -1\,SD$) had double the risk of progression (Hung et al. 2005). Table 3 shows the results of independent variables associated with curve progression of adolescent idiopathic scoliosis in univariate and multiple logistic regression analyses (95% confidence interval). Results demonstrated that initial Cobb angle > 30° has the greatest predictive power in progression (the adjusted odds ratio = 4.7), whereas low bone mass at concave side of femoral neck BMD was also found to be a significant risk factor in predicting curve progression (odds ratio = 2.3; $p = 0.02$). These results revealed the potential clinical application of DXA measurement in AIS patients for prognostication of curve progression.

Furthermore, the low bone mass may persist (Cheng et al. 1999; Thomas et al. 1992) and eventually lead to substantially reduced peak bone mass, thereby increasing risk of osteoporotic fracture later in life (Saggese et al. 2001). Studies have shown that maintaining a high-calcium diet and participating in weight-bearing exercise have a positive association with bone mineral accretion in growing children (Weaver 2002). Programmed weight-bearing exercise and supplementation of calcium intake could be the treatment options for osteopenic AIS patients to improve their BMD and hopefully to alter the natural history of scoliosis.

Table 3. Independent variables associated with curve progression of adolescent idiopathic scoliosis in univariate and multiple logistic regression analyses (95% confidence interval). *n.s.* non-significant. (Adapted from Hung et al. 2005)

Independent variables	Univariate analysis		Multivariate analysis	
	Odds ratio	*p*-value	Adjusted odds ratio	*p*-value
Age at diagnosis (years)				
14 – 16[a]	1		1	
11 – 13	3.01 (1.91 – 4.74)	< 0.001	2.06 (1.07 – 3.96)	0.03
Years since menarche				
Started[a]	1		1	
Not yet started	6.13 (3.05 – 12.30)	< 0.001	2.48 (1.02 – 6.02)	0.044
Risser grade				
2 – 5[a]	1		1	
0 – 1	7.31 (4.09 – 13.08)	< 0.001	4.68 (2.21 – 9.92)	< 0.001
Spinal Z-score BMD				
Normal BMD[a]	1			
Osteopenia	1.60 (0.98 – 2.62)	0.063		
Convex-side femoral neck Z-score BMD				
Normal BMD[a]	1			
Osteopenia	1.99 (1.14 – 3.48)	0.016		
Convex-side trochanter Z-score BMD				
Normal BMD[a]	1			
Osteopenia	1.42 (0.85 – 2.36)	0.178		
Concave-side femoral neck Z-score BMD				
Normal BMD[a]	1		1	
Osteopenia	2.14 (1.27 – 3.61)	0.004	2.25 (1.13 – 4.49)	0.021
Concave-side trochanter Z-score BMD				
Normal BMD[a]	1			
Osteopenia	1.93 (1.14 – 3.29)	0.015		
Curve pattern				
Lumbar[a]	1			
Thoracic	8.01 (1.77 – 36.38)	0.007		
Thoraco-lumbar	4.98 (1.05 – 23.62)	0.043		
Triple	5.95 (1.09 – 32.53)	0.040		
Initial Cobb's angle				
10 – 19°[a]	1		1	
20 – 29°	0.58 (0.34 – 1.02)	0.057	1.21 (0.57 – 2.56)	n.s.
30 – 39°	1.66 (0.82 – 3.35)	0.156	4.77 (1.92 – 11.85)	0.001
≥ 40°	1.99 (0.73 – 5.42)	0.177	4.58 (1.32 – 15.93)	0.017

Hosmer and Lemeshow goodness-of-fit test: $\chi^2 = 4.22$; $df = 8$; $P = 0.84$

Due to missing data for some variables, 288 patients could be included in the multivariate analyses

The following non-significant variables were excluded by stepwise procedure and were not included in the final model: spinal Z-score BMD; convex-side femoral neck Z-score BMD; convex-side trochanter Z-score BMD; concave-side trochanter Z-score BMD; and curve pattern

[a] Reference category

Limitations and Future Study in the Bone Mineral Profile of AIS Patients

Many studies on the bone mineral status of AIS have been conducted using different types of bone densitometry; however, many of them are correlation or association studies which do not directly examine the affected region: the spine. The DXA machine is able to measure lumbar spine region; however, it only provides 2D areal BMD and cannot differentiate between trabecular and cortical compartments. Moreover, previous studies have shown that BMD value may vary if vertebral rotation has occurred; therefore, DXA measurement of spine is not a reliable technique in assessing bone mineral density for scoliotic patients. Axial QCT is an alternative non-invasive technique for BMD measurement; however, because of the high radiation dose and cost, the clinical application in patients with spinal deformities has never been explored.

Magnetic resonance imaging has been reported to be able to provide qualitative information of bone and provide the structural changes in microarchitecture of trabecular bone (Majumdar and Genant 1995; Quinn and McCarthy 1993). Bone density and architecture, which have different magnetic properties, can be detected by the distinct loss of signal; therefore, although MRI cannot measure BMD, it can provide images of the structure of osteoporotic bone, such as morphological changes in trabecular microarchitecture and occult fractures in the proximal femur (Quinn and McCarthy 1993). Although MRI cannot be used to measure quantitative bone density, it is currently used to diagnose subtle osteoporotic fractures (Levis and Altman 1998). Possible clinical applications for diagnosis of low bone mass in AIS children may need further investigation.

A recently developed pQCT scanner, XtremeCT (Scanco Medical, Switzerland http://www.scanco.ch), is one of a new breed of imaging devices capable of high resolution which provide information of both volumetric BMD and 3D bone architecture non-invasively. Traditionally, bone architecture could only be assessed by histomorphological method of surgical biopsies. Recent clinical study, using XtremeCT, has demonstrated that the trabecular number of the distal radius was 15% less in osteopenic women and 23% less in women with osteoporosis. Cortical thickness was 29% less in osteopenic women and 39% less in osteoporotic women. In addition, there was 27% more trabecular separation in osteopenic women and 38% more in osteoporotic women than in premenopausal women. Trabecular distribution was 61% less homogenous in women with osteoporosis (Boutroy et al. 2005). Non-invasive and minimal radiation assessment of bone microarchitecture may provide more information on bone structure in AIS patients and hence may help us in understanding the etiopathogenesis of scoliosis.

Conclusion

Systemic low bone mass was manifested in 30% of AIS girls. With the use of different modalities of bone densitometry, AIS girls were found to have a significantly lower areal and volumetric BMD at various skeletons including spine, proximal femur, and

distal extremities. Moreover, poor bone quality reflected by the QUS technique was also observed in AIS girls. Clinical application of bone densitometry, in relation to curve severity and prognostic value in predicting curve progression, may enhance the clinical management and treatment planning for scoliosis patients.

References

Abes M, Sarihan H, Madenci E (2003) Evaluation of bone mineral density with dual X-ray absorptiometry for osteoporosis in children with bladder augmentation. J Pediatr Surg 38:230–232

Adams J (1998) Single- and dual-energy: X-ray absorptiometry. In: Genant HK, Guglielmi G, Jergas M (eds) Bone densitometry and osteoporosis. Springer, Berlin Heidelberg New York, pp 305–334

Bagnall KM, Raso VJ, Hill DL, Moreau M, Mahood JK, Jiang H, Russell G, Bering M, Buzzell GR (1996) Melatonin levels in idiopathic scoliosis. Diurnal and nocturnal serum melatonin levels in girls with adolescent idiopathic scoliosis. Spine 21:1974–1978

Boutroy S, Bouxsein ML, Munoz F, Delmas PD (2005) In vivo assessment of trabecular bone microarchitecture by high-resolution peripheral quantitative computed tomography. J Clin Endocrinol Metabol 90(12):6508–6515

Bunnell WP (1986) The natural history of idiopathic scoliosis before skeletal maturity. Spine 11:773–776

Burner W, Badger V, Sherman F (1982) Osteoporosis and acquired back deformities. J Pediatr Orthop 2:383–385

Burwell R (1977) Anthropometry. In: Pynsent PB, Fairbank JCT, Carr AJ (eds) Assessment methodology in orthopaedics. Oxford Press, Boston, pp 123–163

Burwell R, Dangerfield P (2000) Adolescent idiopathic scoliosis: Hypotheses of causation. In: Burwell RG, Dangerfield PH, Lowe TG, Margulies JY (eds) Spine: state of the art reviews. Hanley and Belfus, Philadelphia, pp 319–334

Carr AJ, Ogilvie D, Wordsworth BP, Priestly LM, Smith R, Sykes B (1992) Segregation of structural collagen genes in adolescent idiopathic scoliosis. Clin Orthop Rel Res 274:305–310

Carr W (2003) Bracing in scoliosis. In: DeWald RL (ed) Spinal deformities: the comprehensive text. Thieme, New York, pp 755–760

Cheng JC, Guo X (1997) Osteopenia in adolescent idiopathic scoliosis. A primary problem or secondary to the spinal deformity? Spine 22:1716–1721

Cheng JC, Guo X, Sher AH (1999) Persistent osteopenia in adolescent idiopathic scoliosis. A longitudinal follow up study. Spine 24:1218–1222

Cheng JC, Qin L, Cheung CS, Sher AH, Lee KM, Ng SW, Guo X (2000) Generalized low areal and volumetric bone mineral density in adolescent idiopathic scoliosis. J Bone Miner Res 15:1587–1595

Cheng J, Sher H, Guo X, Hung V, Heung A (2001) The effect of vertebral rotation of the lumbar spine on dual energy X-ray absorptiometry measurements: observational study. Hong Kong Med J 7:241–245

Cheung CS, Lee WT, Tse YK, Tang SP, Lee KM, Guo X, Qin L, Cheng JC (2003) Abnormal peri-pubertal anthropometric measurements and growth pattern in adolescent idiopathic scoliosis: a study of 598 patients. Spine 28:2152–2157

Cook S, Harding A, Morgan E, Nicholson R, Thomas K, Whitecloud T, Ratner E (1987) Trabecular bone mineral density in idiopathic scoliosis. J Pediatr Orthop 7:168–174

Courtois I, Collet P, Mouilleseaux B, Alexandre C (1999) Bone mineral density at the femur and lumbar spine in a population of young women treated for scoliosis in adolescence. Revue Rhumatisme 66:705–710

Dubois E, van den Bergh J, Smals A, van de Meerendonk C, Zwinderman A, Schweitzer D (2001) Comparison of quantitative ultrasound parameters with dual energy X-ray absorptiometry in pre- and postmenopausal women. Netherlands J Med 58:62–70

Dubousset J, Machida M (1998) Melatonin. A possible role in the pathogenesis of human idiopathic scoliosis. In: Fairbank J (ed) Proc 10th Int Philip Zorab Symposium on Scoliosis. Oxford Press, Oxford

Faulkner KG, Gluer CC, Majumdar S, Lang P, Engelke K, Genant HK (1991) Noninvasive measurements of bone mass, structure, and strength: current methods and experimental techniques. Am J Roentgenol 157:1229–1237

Ford D, Bagnall K, Clements C, McFadden K (1988) Muscle spindles in the paraspinal musculature of patients with adolescent idiopathic scoliosis. Spine 13:461–465

Formica CA, Nieves JW, Cosman F, Garrett P, Lindsay R (1998) Comparative assessment of bone mineral measurements using dual X-ray absorptiometry and peripheral quantitative computed tomography. Osteoporosis Int 8:460–467

Frost M, Blake G, Fogelman I (2002) A comparison of fracture discrimination using calcaneal quantitative ultrasound and dual X-ray absorptiometry in women with a history of fracture at sites other than the spine and hip. Calcif Tissue Int 71:207–211

Fuerst T, Guglielmi G, Cammisa M, Genant H (1998) Comparison of quantitative computed tomography and dual X-ray absorptiometry at the lumbar spine in the diagnosis of osteoporosis. In: Genant HK, Guglielmi G, Jergas M (eds) Bone densitometry and osteoporosis. Springer, Berlin Heidelberg New York, pp 365–378

Giampietro P, Peterson M, Schneider R, Davis J, Raggio C, Myers E, Burke S, Boachie-Adjei O, Mueller C (2003) Assessment of bone mineral density in adults and children with Marfan syndrome. Osteoporosis Int 14:559–563

Girardi FP, Parvataneni HK, Sandhu HS, Cammisa FP Jr, Grewal H, Schneider R, Lane JM (2001) Correlation between vertebral body rotation and two-dimensional vertebral bone density measurement. Osteoporosis Int 12:738–740

Gluer CC (1997) Quantitative ultrasound techniques for the assessment of osteoporosis: expert agreement on current status. The International Quantitative Ultrasound Consensus Group. J Bone Miner Res 12:1280–1288

Gluer CC, Wu CY, Genant HK (1993) Broadband ultrasound attenuation signals depend on trabecular orientation: an in vitro study. Osteoporosis Int 3(4):185–191

Grampp S, Lang P, Jergas M, Gluer C, Mathur A, Engelke K, Genant H (1995) Assessment of the skeletal status by peripheral quantitative computed tomography of the forearm: short-term precision in vivo and comparison to dual X-ray absorptiometry. J Bone Miner Res 10:1566–1576

Grampp S, Genant HK, Mathur A, Lang P, Jergas M, Takada M, Gluer CC, Lu Y, Chavez M (1997) Comparisons of noninvasive bone mineral measurements in assessing age-related loss, fracture discrimination, and diagnostic classification. J Bone Miner Res 12:697–711

Gregg EW, Kriska AM, Salamone LM, Roberts MM, Anderson SJ, Ferrell RE, Kuller LH, Cauley JA (1997) The epidemiology of quantitative ultrasound: a review of the relationships with bone mass, osteoporosis and fracture risk. Osteoporosis Int 7:89–99

Guo X, Chau W, Chan Y, Cheng J (2003) Relative anterior spinal overgrowth in adolescent idiopathic scoliosis. Results of disproportionate endochondral-membranous bone growth. J Bone Joint Surg (Br) 85:1026–1031

Hadley-Miller N, Mims B, Milewicz D (1994) The potential role of the elastic fiber system in adolescent idiopathic scoliosis. J Bone Joint Surg (Am) 76:1193–1206

Han S, Rho J, Medige J, Ziv I (1996) Ultrasound velocity and broadband attenuation over a wide range of bone mineral density. Osteoporos Int 6:291–296

Hans D, Fuerst T, Uffmann M (1996) Bone density and quality measurement using ultrasound. Curr Opin Rheumatol 8:370–375

Hans D, Wu C, Njeh CF, Zhao S, Augat P, Newitt D, Link T, Lu Y, Majumdar S, Genant HK (1999) Ultrasound velocity of trabecular cubes reflects mainly bone density and elasticity. Calcif Tissue Int 64:18–23

Huang C, Ross PD, Yates AJ, Walker RE, Imose K, Emi K, Wasnich RD (1998) Prediction of fracture risk by radiographic absorptiometry and quantitative ultrasound: a prospective study. Calcif Tissue Int 63:380–384

Hung VW, Qin L, Au SK, Choy WY, Leung KS, Leung PC, Cheng JC (2004) Correlations of calcaneal QUS with pQCT measurements at distal tibia and non-weight-bearing distal radius. J Bone Miner Metab 22:486–490

Hung VW, Qin L, Cheung CS, Lam TP, Ng BK, Tse YK, Guo X, Lee KM, Cheng JC (2005) Osteopenia: a new prognostic factor of curve progression in adolescent idiopathic scoliosis. J Bone Joint Surg (Am) 87:2709–2716

Langton CM (1996) The clinical role of BUA for the assessment of osteoporosis: a new hypothesis. Clin Rheumatol 15:414–415

Lee WT, Cheung CS, Tse YK, Guo X, Qin L, Lam TP, Ng BK, Cheng JC (2005) Association of osteopenia with curve severity in adolescent idiopathic scoliosis: a study of 919 girls. Osteoporosis Int 16:1924–1932

Leong J, Low W, Mok C, Kung L, Yau A (1982) Linear growth in southern Chinese female patients with adolescent idiopathic scoliosis. Spine 7:471–475

Levis S, Altman R (1998) Bone densitometry: clinical considerations. Arthrit Rheum 41:577–587

Lonstein J (1995a) Idiopathic scoliosis. In: Lonstein JE, Winter RB, Bradford DS, Ogilvie JW (eds) Moe's textbook of scoliosis and other spinal deformities. Saunders, Philadelphia, pp 219–256

Lonstein J (1995b) Patient evaluation. In: Lonstein JE, Winter RB, Bradford DS, Ogilvie JW (eds) Moe's textbook of scoliosis and other spinal deformities. Saunders, Philadelphia, pp 45–86

Lonstein J, Carlson J (1984) The prediction of curve progression in untreated idiopathic scoliosis during growth. J Bone Joint Surg (Am) 66:1061–1071

Low W, Chew E, Kung L, Hsu L, Leong J (1983) Ultrastructures of nerve fibers and muscle spindles in adolescent idiopathic scoliosis. Clin Orthop Relat Res 217–221

Lowe T, Edgar M, Margulies J, Miller N, Raso V, Reinker K, Rivard C (2000) Etiology of idiopathic scoliosis: current trends in research. J Bone Joint Surg (Am) 82:1157–1168

Majumdar S, Genant HK (1995) A review of the recent advances in magnetic resonance imaging in the assessment of osteoporosis. Osteoporosis Int 5:79–92

Morcuende JA, Weinstein SL (2003) Idiopathic scoliosis: general considerations, natural history, and treatment guidelines. In: DeWald RL (ed) Spinal deformities: the comprehensive text. Thieme, New York, pp 752–754

Nicholson P, Haddaway M, Davie M, Evans S (1993) Vertebral deformity, bone mineral density, back pain and height loss in unscreened women over 50 years. Osteoporosis Int 3:300–307

Nicolopoulos K, Burwell R, Webb J (1985) Stature and its components in adolescent idiopathic scoliosis. Cephalo-caudal disproportion in the trunk of girls. J Bone Joint Surg (Br) 67:594–601

Nissinen M, Heliovaara M, Seitsamo J, Poussa M (1993) Trunk asymmetry, posture, growth, and risk of scoliosis. A three-year follow-up of Finnish prepubertal school children. Spine 18:8–13

Njeh C, Boivin C, Langton C (1997) The role of ultrasound in the assessment of osteoporosis: a review. Osteoporosis Int 7:7–22

Njeh CF, Fuerst T, Diessel E, Genant HK (2001) Is quantitative ultrasound dependent on bone structure? A reflection. Osteoporosis Int 12:1–15

Peterson LE, Nachemson AL (1995) Prediction of progression of the curve in girls who have adolescent idiopathic scoliosis of moderate severity. Logistic regression analysis based on data from The Brace Study of the Scoliosis Research Society. J Bone Joint Surg (Am) 77:823–827

Pluijm SM, Graafmans WC, Bouter LM, Lips P (1999) Ultrasound measurements for the prediction of osteoporotic fractures in elderly people. Osteoporosis Int 9:550–556

Porter RW (2001) Can a short spinal cord produce scoliosis? Eur Spine J 10:2–9

Prins SH, Jorgensen HL, Jorgensen LV, Hassager C (1998) The role of quantitative ultrasound in the assessment of bone: a review. Clin Physiol 18:3–17

Quinn SF, McCarthy JL (1993) Prospective evaluation of patients with suspected hip fracture and indeterminate radiographs: use of T1-weighted MR images. Radiology 187:469–471

Roach JW (1999) Adolescent idiopathic scoliosis. Orthop Clin North Am 30:353–365

Roth M (1981) Idiopathic scoliosis and Scheuermann's disease: essentially identical manifestations of neuro-vertebral growth disproportion. Radiol Diagn 22:380–391

Ruegsegger P (1996) Bone density measurement. In: Broll H, Dambacher MA (eds) Osteoporosis: a guide to diagnosis and treatment. Karger, Basel, pp 103–116

Saggese G, Baroncelli GI, Bertelloni S (2001) Osteoporosis in children and adolescents: diagnosis, risk factors, and prevention. J Pediatr Endocrinol Metabol 14:833–859

Sanders JO, Moreland MS, Bassett GS (2003) Idiopathic scoliosis: prevalence and natural history. In: DeWald RL (ed) Spinal deformities: the comprehensive text. Thieme, New York, pp 669–683

Schott AM, Cormier C, Hans D, Favier F, Hausherr E, rgent-Molina P, Delmas PD, Ribot C, Sebert JL, Breart G, Meunier PJ (1998) How hip and whole-body bone mineral density predict hip fracture in elderly women: the EPIDOS prospective study. Osteoporosis Int 8:247–254

Shohat M, Shohat T, Nitzan M, Mimouni M, Kedem R, Danon Y (1988) Growth and ethnicity in scoliosis. Acta Orthop Scand 59:310–313

Soucacos PN, Zacharis K, Soultanis K, Gelalis J, Xenakis T, Beris AE (2000) Risk factors for idiopathic scoliosis: review of a 6-year prospective study. Orthopedics 23:833–838

Stewart A, Reid D (2002) Quantitative ultrasound in osteoporosis. Semin Musculoskelet Radiol 6:229–232

Tanner JM, Whitehouse RH (1976) Clinical longitudinal standards for height, weight, height velocity, weight velocity, and stages of puberty. Arch Dis Child 51:170–179

Taylor T, Ghosh P, Bushell G (1981) The contribution of the intervertebral disk to the scoliotic deformity. Clin Orthop Relat Res 156:79–90

Thomas K, Cook S, Skalley T, Renshaw S, Makuch R, Gross M, Whitecloud T, Bennett J (1992) Lumbar spine and femoral neck bone mineral density in idiopathic scoliosis: a follow-up study. J Pediatr Orthop 12:235–240

Trebacz H, Natali A (1999) Ultrasound velocity and attenuation in cancellous bone samples from lumbar vertebra and calcaneus. Osteoporosis Int 9:99–105

Weaver CM (2002) Adolescence: the period of dramatic bone growth. Endocrine 17:43–48

Weinstein S (1994) Adolescent idiopathic scoliosis: prevalence and natural history. In: Weinstein SL (ed) The pediatric spine: principles and practice. Raven Press, New York, pp 463–478

Weinstein S (1999) Natural history. Spine 24:2592–2600

Welch A, Camus J, Dalzell N, Oakes S, Reeve J, Khaw KT (2004) Broadband ultrasound attenuation (BUA) of the heel bone and its correlates in men and women in the EPIC-Norfolk cohort: a cross-sectional population-based study. Osteoporosis Int 15:217–225

World Health Organization (1994) Assessment of fracture risk and its application to screening for postmenopausal osteoporosis: report of a WHO study group. World Health Organization, Geneva

Willner S (1974) A study of growth in girls with adolescent idiopathic structural scoliosis. Clin Orthop Relat Res 101:129–135

Willner S (1975) A study of height, weight and menarche in girls with idiopathic structural scoliosis. Acta Orthop Scand 46:71–83

Willner S (1994) Adolescent idiopathic scoliosis: etiology. In: Weinstein SL (ed) The pediatric spine: principles and practice. Raven Press, New York, pp 445–462

Willner S, Nilsson K, Kastrup K, Bergstrand C (1976) Growth hormone and somatomedin A in girls with adolescent idiopathic scoliosis. Acta Paediatr Scand 65:547–552

Winter R, Lonstein J (1992) Juvenile and adolescent idiopathic scoliosis. In: Rothman RH, Simeone FA (eds) The spine. Saunders, Philadelphia, p 373

Wu C, Hans D, He Y, Fan B, Njeh CF, Augat P, Richards J, Genant HK (2000) Prediction of bone strength of distal forearm using radius bone mineral density and phalangeal speed of sound. Bone 26:529–533

Wynne-Davies R (1968) Familial (idiopathic) scoliosis. A family survey. J Bone Joint Surg (Br) 50:24–30

Yamauchi Y, Yamaguchi T, Asaka Y (1988) Prediction of curve progression in idiopathic scoliosis based on initial roentgenograms. A proposal of an equation. Spine 13:1258–1261

Yarom R, Meyer S, More R, Robin G (1982) Metal impregnation abnormalities in platelets of patients with idiopathic scoliosis. Haemostasis 12:282–288

Zadeh HG, Sakka SA, Powell MP, Mehta MH (1995) Absent superficial abdominal reflexes in children with scoliosis. An early indicator of syringomyelia. J Bone Joint Surg (Br) 77:762–767

Application of Nano-CT and High-Resolution Micro-CT to Study Bone Quality and Ultrastructure, Scaffold Biomaterials and Vascular Networks

Phil L. Salmon (✉) and Alexander Y. Sasov

Skyscan, Antwerp, Belgium
e-mail: phil.salmon@skyscan.be

Abstract

The application of micro-CT technology to biomedical and bone research is considerable and growing. This chapter focuses on applications requiring particularly high spatial image resolution in micro- and nano-CT imaging. Specific examples described here include the analysis of bone for fine-scale architecture and material quality, the study of synthetic bone scaffolds for orthopaedic research and the imaging of vascular networks. The range of potential research applications of microtomographic technology is both facilitated and limited by technical and physical factors related to the technology. Some technical requirements can be mutually exclusive, such as increased X-ray source power for dense materials and decreasing micro-focus X-ray source spot size for better spatial resolution. Such challenges necessitate innovative solutions at the forefront of the developing technology and include (a) attaining submicron resolution ("nano-CT") tomographic imaging, (b) obtaining optimum resolution and image quality from a desktop system over a wide range of sample sizes, and (c) obtaining sufficient X-ray transmission and detection to image high-density samples at a useful resolution The first of these challenges is addressed by the development by Skyscan of the 2011 nano-CT scanner. This employs an X-ray source using new technology to obtain a spot size of $0.3\,\mu m$, combined with an extremely high precision sample manipulator and highly sensitive X-ray camera. With this instrument, pixel sizes of down to $150\,nm$ are possible. Structural features linked to bone quality, such as osteocytes and microcracks in bone, and resorption lacunae, are readily visualised. The latter two challenges relate to more "conventional" micro-CT applications are addressed by the unique design of the Skyscan 1172 scanner with adaptive geometry in which both the sample and the X-ray camera can move in order to optimise X-ray imaging geometry. Also, the use of a very large 10-megapixel camera format broadens the possible scan parameters to very small pixel sizes and large objects.

Introduction

Technological advances are described which permit high spatial imaging resolution in a new nano-CT instrument and a "conventional" desktop micro-CT scanner. The

nano-CT instrument allows clear visualisation of structures on the level of cells, provided that X-ray contrast is present. The example of the mouse fibula is described in which osteocyte cells are visible, and also cellular resorption and formation sites on the bone surface, as well as submicron cracks of interest to biomechanical bone research. The internal ultrastructure of individual human bone trabeculae can also be imaged by nano-CT. The fibula is a useful site for nano-CT imaging of bone due to the requirement of this technique for very small samples for attaining optimum resolution. The desktop high-resolution scanner cannot attain submicron resolution, but can analyse a much wider size range of samples, due in part to an innovative "adaptive geometry" and use of a large-format camera. Some example applications are described, such as murine bone (including trabecular bone) imaged in vitro and in vivo, bone scaffold biomaterials and vascular networks contrasted by the setting contrast agent Microfil.

Method

The Nano-CT Scanner

The laboratory Nano-CT system is based on a newly designed X-ray source with spot size of 0.3 μm, a highly sensitive array detector and a positioning system with 100-nm accuracy. The X-ray source is of the open type, with internal vacuum maintained with a vacuum pump. Applied X-ray voltage is up to 65 kV. The scanner comprises the X-ray source with associated electronics, a multi-axis precision object manipulator, an intensified X-ray camera, a system controller and a computer for instrument control. It can attain a spatial resolution of 150 – 400 nm (object material dependent). The scanned object remains in normal environmental conditions without any preparation and can be wet or in a liquid medium.

Histomorphometric Analysis of Mouse Fibula by Nano-CT Imaging

A section of the fibula of a 2-month-old mouse was scanned in the Skyscan 2011 nano-CT scanner, using an X-ray source spot size of 300 nm and a pixel size of 290 nm. The applied source voltage was 25 kV, the tomographic rotation 180°, the rotation step 0.8° and the scan duration 35 min. A section of fibula 100 μm long was analysed. Histomorphometric indices were measured using Skyscan CT-analyser software. The whole fibular cross-section was analysed except for a small peripheral segment containing a blood vessel. Osteocyte size and spatial distribution was measured on the basis of enclosed small cavities in the fibula. Resorption surfaces were visible as scalloped surfaces, and formation sites as fuzzy boundaries with an adherent soft tissue (low density) layer (Fig. 1).

High-Resolution Desktop Micro-CT Instruments, for In Vivo and Ex-Vivo Scanning

The Skyscan in vivo micro-CT scanner (model 1076) and the in vitro scanner (model 1172) both employ a microfocus X-ray source with a spot size of about 6 μm.
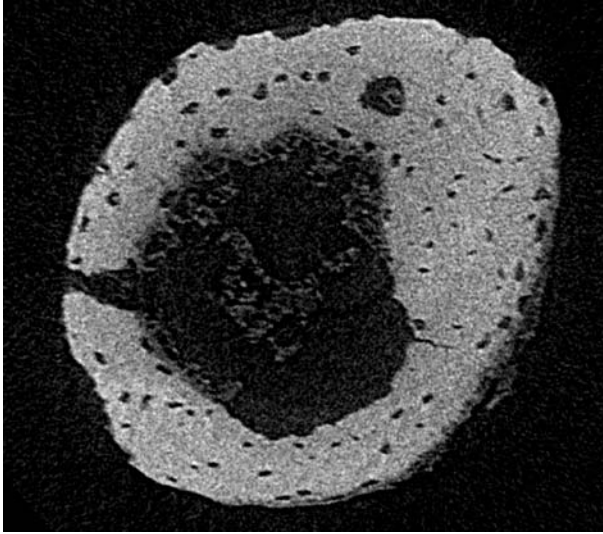
Figure 1. Reconstructed cross-section of a juvenile mouse fibula, scanned in the Skyscan 2011 nano-CT at a pixel size of 290 nm. Osteocytes are clearly resolved. Resorption surfaces are visible as scalloped surfaces, and formation sites as fuzzy boundaries with an adherent soft tissue (low density) layer. Blood vessels are visible (1 and 9 o'clock) crossing the fibular wall. A small radial crack is also visible, at 4 o'clock

X-ray applied voltage is variable over the range 20 – 100 kV. Adjustment of applied voltage and use of a range of X-ray filters allow flexibility in modifying the polychromatic X-ray energy spectrum generated by the tungsten microfocus source target. In both the 1076 and 1172 scanners a large-format X-ray camera (10-megapixel coupled CCD) allows both high-resolution and flexibility of resolution and scanning time with the option of variable pixel binning. The in vivo 1076 scanner has a physiological monitoring system giving real time data on breathing and heart rate, and support for synchronised imaging to remove breathing movement artefacts while scanning the thorax. The 1172 scanner has a unique adaptive geometry allowing the camera to be moved closer to the object and source for substantial improvement in X-ray detection efficiency and scanning speed over a wide range of resolutions. With all these systems, image reconstruction is by a modified Feldkamp algorithm for cone beam (Feldkamp et al. 1984).

Results and Discussion

Nano-CT Histomorphometry of the Mouse Fibula

A novel range of histomorphometric indices can be measured non-destructively in the mouse fibula from nano-CT imaging, with submicron resolution. A cross-section slice from a scan of a mouse fibula is shown in Fig. 2.

To illustrate the possibilities for static histomorphometric study of the mouse fibula with images of this resolution, a range of parameters were measured from

Figure 2. A reconstructed cross-section image of a discreet human trabecula, pixel size 580 nm, also showing osteocytes. The major (long) axis of the trabecular cross-section is 350 μm

the 3D data set of the mouse fibula shown in Fig. 1. These parameters are listed in Table 1. The fibula overall morphometry is quantified, including periosteal and endosteal surfaces. Formation and resorption surfaces are quantified, possibly for the first time from a CT image of bone. And osteocyte distribution and volume are also quantified. A lateral remodelling drift was visible in the fibula cross-section as angu-

Table 1. Histomorphometric parameters of the juvenile mouse fibula measured by nano-CT

Parameter	Unit	Value
Bone area	μm^2	21,353.065
Endosteal perimeter	μm	478.602
Periosteal perimeter	μm	764.934
Endosteal formation surface	μm	252.557
Endosteal percent formation surface	%	52.770
Endosteal resorption surface	μm	115.852
Endosteal percent resorption surface	%	24.206
Periosteal formation surface	μm	219.034
Periosteal percent formation surface	%	728.634
Periosteal resorption surface	μm	299.274
Periosteal percent resorption surface	%	39.124
Osteocyte lacuna diameter	μm	2.506
Osteocyte lacuna separation	μm	17.513
Osteocyte lacuna number	μm^{-1}	0.00779
Osteocyte lacuna percent volume	%	1.957
Osteocyte lacuna anisotropy		2.602 (0.616)

lar separation of the resorption and formation sites on the endosteal and periosteal surfaces. Small cracks were also clearly resolved in the fibula, with crack widths down to well below a micron.

Nano-CT imaging of the murine fibula is a new model providing insight into bone ultrastructural quality. For the first time, static histomorphometry-type parameters have been obtained from a non-destructive CT scan. Of particular interest is the ability to observe and measure formation and resorption surfaces. Osteocytes are imaged very clearly in the mouse fibula by the nano-CT, and quantification of their morphometry and distribution could be a useful tool in the study of the role of osteocytes. Intercommunication between osteocytes is believed to be a key component of bone "mechanotransduction", i.e. the ability of bone to remodel its architecture in response to a changed regime of mechanical load (Noble et al. 2003).

High-resolution Micro-CT Scans of Murine Bone Ex Vivo

The mouse is probably the most important preclinical model in bone research, and being very small, its bones present a challenge to achieve both high image spatial resolution in micro-CT analysis to resolve the finest architecture, and also to scan mouse bones at resolution adequate for bone morphometry at a high speed and throughput. Mouse bone can be imaged in the desktop 1172 scanner at pixel sizes down to about 1 μm. For routine scans, such as for bone morphometry, with durations of half an hour or less, a pixel size of 4–5 μm can be employed. Scans at higher resolution, e.g. 2.45 μm in the case of the juvenile mouse tibia shown in Fig. 3, require scan duration of around 1 h or more. At this resolution architectural features below 10 μm can be clearly seen, such as the fine primary spongiosal network just below the growth plate, and blood vessel canals in the bone cortical wall.

a   b
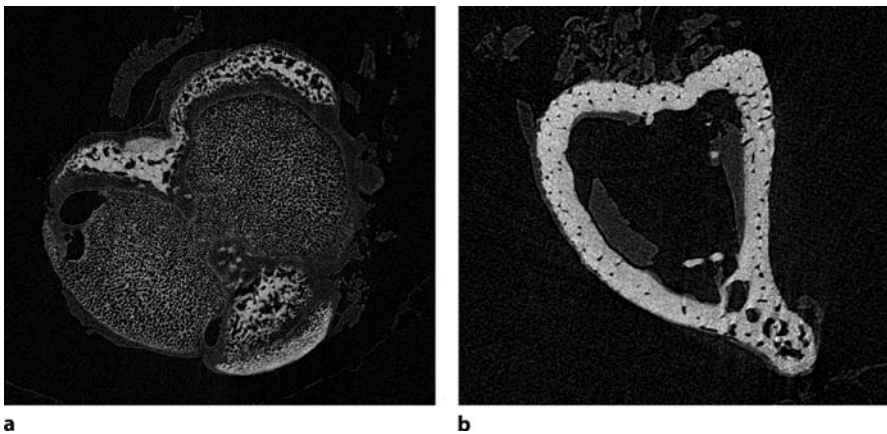
Figure 3 a,b. Higher resolutions (here 2.45 μm pixels) can be attained in vitro, allowing visualisation of primary spongiosal structures (**a**) and cortical blood vessels (**b**) in juvenile murine proximal tibia

High-Resolution Micro-CT Scans of Murine Bone In Vivo

This tomographic imaging technology has perhaps the most potential in biomedical research pertaining to in vivo imaging of the mouse and rat. The tissues that can be imaged on the basis of natural X-ray contrast, bone and lung (due to the presence of calcium phosphate and air respectively) present the principle requirements for the highest possible imaging resolution, to resolve as much as possible of trabecular bone and alveolar-septal-bronchial lung architectures. Trabecular bone in the mouse model is heterogeneous in architecture, including relatively thick plate structures near to and parallel with the endocortical boundary, and a much thinner fine lattice of rod-like structures in the central medulla with a diameter of < 25 μm. To image the whole murine trabecular structure including the central fine lattice, pixel sizes of well below 10 μm are ideally required. In vivo micro-CT imaging presents a challenge to obtain the best resolution possible in the face of several limitations: limited scan time and radiation dose and volume of tissue and breathing movement (Salmon et al. 2003). The Skyscan 1076 in vivo scanner achieves a pixel size of 8.9 μm, and this requires an exposure time of the X-ray camera of several seconds. Due to the camera electronic timing and to the need for image processing during a scan, plus rotation between steps, it has previously been necessary to acquire images during alternate camera cycles only. So the system was only collecting image data for half of the scan time; however, recent improvements to the method and speed of image processing have resulted in a change to a continuous imaging mode in which image data is being collected for almost 100% of the scan time, and the time to obtain high-resolution images in vivo is therefore reduced by half. This has important implications, e.g. in imaging mouse trabecular bone where high-resolution images of

a   b
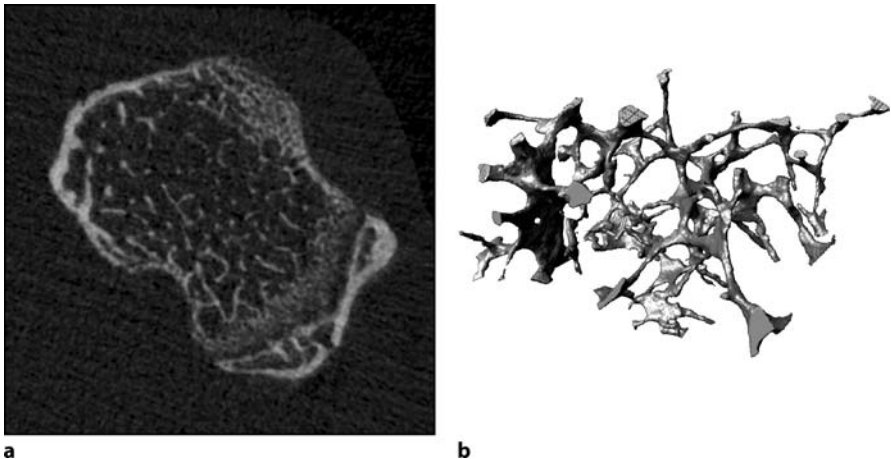
Figure 4 a,b. Mouse knee trabecular bone imaged by a 20-min scan in the Skyscan 1076 in vivo scanner: the 8.9 μm pixel size is at the upper limit of the pixel size required to image the fine murine trabecular lattice. **a** Cross-sectional image. **b** Surface-rendered 3D model image of trabecular structures
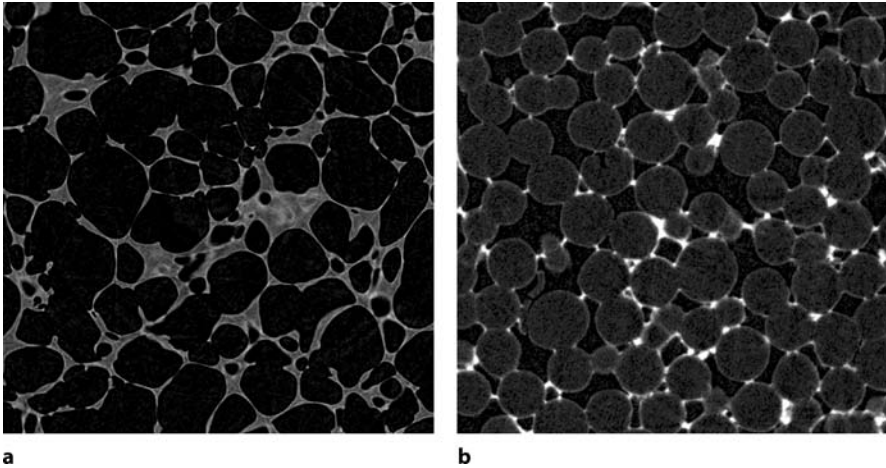
Figure 5. a A PLA/PLGA scaffold matrix, scanned at a pixel size of 5.5 μm, and **b** a synthetic bone scaffold consisting of hydroxyapatite-coated polythene spheres, scanned with 2.8 μm pixel

the mouse knee, suitable for morphometric analysis, can now be obtained in vivo in < 20 min. Such scans allow the trabecular structure around the mouse knee to be reasonably well resolved, as shown in Fig. 4. In vivo bone imaging allows sequential imaging of a bone site in individual animals (Waarsing et al. 2004), with substantial advantages in researching bone structure changes which are only beginning to be realised in bone research.
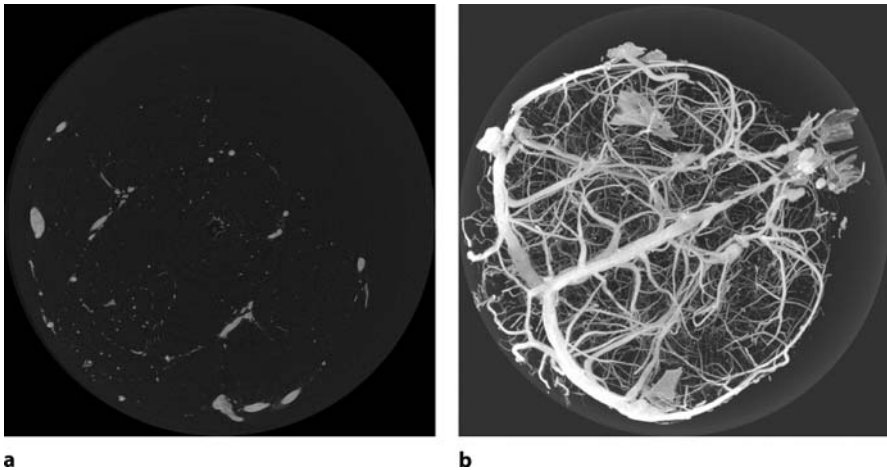
Figure 6 a,b. The vascular network of a mouse's brain, contrasted by injection of the agent Microfil (a resin-containing lead chromate). Scanned in the Skyscan 1172, ex vivo, pixel size 4.2 μm. **a** Reconstructed cross-sectional image. **b** Reconstructed model for 3D viewing by the maximum intensity projection method

Micro-CT Imaging of Bone Biomaterial Scaffolds and Vascular Network Casts

Scaffold biomaterials for the support of bone regeneration in orthopaedic medicine also presents a requirement for detailed 3D imaging in the research and development of optimum materials and architectures required for the scaffolds to achieve their therapeutic objectives. Many different approaches to bone biomaterial scaffolds have been investigated which cannot be fully covered here. Micro-CT scan images of two types of synthetic bone scaffold are shown in Fig. 5. These are the PLA/PLGA type scaffolds, and an array of polythene spheres coated in a 10-μm layer of calcium hydroxyapatite. Such scaffolds present architectures which are superficially similar to some bone samples such as trabecular structures, although their characteristics of density and attenuation of X-rays necessitate different micro-CT scan settings. Low-density scaffolds, such as the PLA/PLGA type, require unfiltered low-energy tungsten-emission X-rays for optimal results, whereas most bone and calcified samples require aluminium-filtered micro-focus X-rays for adequate micro-CT imaging. Low-energy unfiltered X-rays are also suitable for scanning vascular networks which have been cast by a setting resin contrast agent such as Microfil. The use of agents such as Microfil in imaging vascular networks in the context of research into angiogenesis and vascular architecture is becoming more widespread and represents another important application where micro-CT can provide useful and informative 3D image information. The micro-CT scan of a mouse brain, in which the arterial network has been perfused with Microfil, is shown in Fig. 6.

Conclusion

In primary imaging modalities, such as micro- and nano-CT, "what you see is what you get", i.e. the quality and image resolution is largely evident from viewing the image. Biological tissues, such as trabecular bone and lung, possess fine networked structure facilitating the highest available image resolution, both in vivo and ex vivo. The Skyscan nano-CT currently represents the extreme of spatial image resolution attainable in a laboratory tomographic instrument, and opens up new applications for tomographic imaging in biomedicine, including research in bone ultrastructure and biomechanical properties. For example, the internal ultrastructure of human bone trabeculae, including calcification inhomogeneities and osteocyte distribution (see Fig. 3), provides information relevant to assessing origins of osteoporotic spinal compression fractures, which are of considerable clinical significance. Nano-CT occupies what was hitherto a significant gap in imaging technology, for a tomographic 3D modality with resolution in the range of hundreds of nanometers and sample sizes of the order of a millimetre.

Due to the requirement of very small samples by nano-CT, the application of high-resolution CT imaging for the largest range of biomedical and bone research samples remains the province of "conventional" desktop micro-CT scanners. Here resolution levels are well above 1 μm but samples of several millimetres or centimetres diameter with a wide range of densities can be imaged and studied. Advances

discussed here in desktop micro-CT technology include the use of a large-format X-ray camera and adaptive geometry of the X-ray camera and source, to broaden the range of sample types that can be scanned as well as maximising attainable image resolution. The application of desktop micro-CT is illustrated here by examples of murine bone, scanned both ex vivo and in vivo, and samples linked to other important bone-related research areas, namely bone biomaterial scaffolds and infiltrated casts of vascular networks.

References

Feldkamp LA, Davis LC, Kress JW (1984) Practical cone-beam algorithm. J Opt Soc Am 1 (6):612–619

Noble BS, Peet N, Stevens HY, Brabbs A, Mosley JR, Reilly GC, Reeve J, Skerry TM, Lanyon LE (2003) Mechanical loading: biphasic osteocyte survival and targeting of osteoclasts for bone destruction in rat cortical bone. Am J Physiol Cell Physiol 284 (4):C934–C943

Salmon PL, Buelens E, Sasov AY (2003) Performance of in vivo micro-CT analysis of mouse lumbar vertebral and knee trabecular bone architecture. J Bone Miner Res 18 (Suppl 2):S256

Waarsing JH, Day JS, van der Linden JC, Ederveen AG, Spanjers C, De Clerck N, Sasov A, Verhaar JAN, Weinans H (2004) Detecting and tracking local changes in the tibiae of individual rats: a novel method to analyse longitudinal in vivo micro-CT data. Bone 34:163–169

Bio-imaging Technologies in Studying Bone-Biomaterial Interface: Applications in Experimental Spinal Fusion Model

Chun Wai Chan (✉) , Jack Chun-Yiu Cheng, Hiu-Yan Yeung, and Ling Qin

Musculoskeletal Research Laboratory, Department of Orthopaedics and Traumatology,
The Chinese University of Hong Kong, Hong Kong SAR, China
email: chanwai@cuhk.edu.hk

Abstract

Spinal fusion in orthopedic surgery is commonly used to treat spinal deformity and degenerative diseases such as scoliosis and degenerative disc disease. To advance surgical and outcome efficacy and study the biological regulations, different animal models of spinal fusion have been established, including rats, rabbits, dogs, sheep, goats, and even non-human primates. With novel biological factors, biomaterials, biophysical devices and gene therapy, and stem-cell-based-therapy being developed, many medical imaging assessment techniques are being adopted further to evaluate their potential in facilitating spinal fusion experimentally before clinical application. Many bio-imaging evaluation technologies have been developed and their potential has been explored in evaluation of bone and biomaterial interface integration both preclinically and clinically. This chapter reviews some of the conventional and advanced techniques being applied for evaluation of rate and quality of spinal fusion, especially the experimental spinal fusion models based on our own studies. These techniques are summarized in the following categories in studying fusion complex or materials properties: (a) low resolution X-ray; quantitative CT, MRI, and clinical densitometry; (b) high-resolution micro-CT, 2D and 3D histomorphometry with both static and dynamic indices; and (c) macro- and microbiomechanical tests. The general advantages and limitations of the technologies are also briefly summarized. This overview might serve as a reference for future studies concerning study design and selection of technologies for qualitative and quantitative evaluation of spinal fusion based on availability of these methods and potential local and international collaborations.

Introduction

The years 2000–2010 have been designated by the World Health Organization (WHO) as "The Bone and Joint Decade" (BJD) with the mission of promoting the prevention and treatment of musculoskeletal disorders. Spinal disorder is one of the top five musculoskeletal conditions defined by BJD. In correction of spinal deformities,

bone grafting is one of the most common procedures in spinal surgery. It has been estimated that more than 500,000 bone-grafting procedures are conducted in the U.S. per year, with around half of these procedures related to spinal fusion or spinal arthrodesis (Greenwald et al. 2001; Boden 2002).

There are three types of spinal fusion, i.e., anterior interbody, posterior intertransverse, or interlaminar fusion. Posterior spinal fusion (PSF) is the commonest surgical procedure used for treatment of spinal disorders ranging from congenital disease, deformity, and degenerative disease, benign and malignant tumors to spinal fractures. Decortication of lamellar bone of the spinal processes and grafting of autogenous iliac crest have been the gold standard for spinal fusion because of the osteogenic, osteoinductive and osteoconductive effects; however, harvesting of autograft is associated with complications such as high non-union rate of 5–45%, limited supply, donor-site morbidity, pain, increased operation time, blood lost, host metabolic hindrances, and unsuitability in smokers, diabetics, and osteoporotic patients (Greenwald et al. 2001; Boden 2002). On the other hand, allografts from a donor after death are also utilized to substitute autograft. Allograft provides an osteo-inductive and osteoconductive effect on spinal fusion; thus, it is less effective than autograft. It also requires bone bank, storage, sterilization, and quality-control facilities. Infection, viral transmission (including HIV), and availability of the allografts are also problematic (Meding and Stambough 1993; Linovitz and Peppers 2002). Biomaterials as bone substitutes are therefore highly desirable.

Many biomaterials have been used as bone substitutes in spinalcfusion models; these range from demineralized bone matrix, natural coral, or ceramics, such as calcium phosphate, hydroxyapatite, or their composite as hydroxyapatite-tricalcium phosphate (HA-TCP) with or without augmentation with bone marrow or bone morphogenetic proteins (BMP). The efficacy of these materials or factors in enhancing fusion can be assessed by evaluating spatial and temporal changes at the fusion site structurally and functionally with respect to biocompatibility, biodegradablility, osteoconductivity, or osteo-inductivity (Boden and Schimandle 1995; Boden et al. 1995, 1999a,b; Ludwig and Boden 1999; Greenwald et al. 2001; Guo et al. 2001, 2002; Vaccaro et al. 2001; Linovitz and Peppers 2002; Cheng et al. 2002; Chan et al. 2003, 2004, 2005a,b; Yeung et al. 2003). In addition, biophysical interventions have been as used for accelerating spinal fusion, including methods such as electrical stimulation, magnetic field, and low-intensity pulsed ultrasound (Cook et al. 2001; Linovitz et al. 2002; Chan et al. 2003, 2004; Hodges et al. 2003).

Currently, plain-X-ray, CT, and MRI are the conventional means used in the evaluation of spinal fusion clinically; however, these non-invasive methods for assessing fusion status are not fully accurate because of lower resolution. It is difficult to evaluate fusion quality in terms of material property and mechanical strength. Although the presence of residual segmental motion generally reflects non-union, lack of motion on stress radiographs does not necessarily imply solid fusion, especially in the presence of rigid internal fixation (Meding and Stambough 1993; Boden 1998, 2002; Greenwald et al. 2001); therefore, carefully designed animal experiments with objective evaluation using various technologies are prerequisites to the study and documentation of successful fusion before extending this to human clinical trials.

Preclinical Evaluation of Spinal Fusion: Animal Models and Enhancement Methods

Various animal models have been used as spinal fusion experimental studies; these include small animal models using mice and rats (Hasharoni et al. 2005; Moazzaz et al. 2005), medium-sized animals, such as rabbit (Boden et al. 1995; Cheng et al. 2002; Guo et al. 2002; Chan et al. 2005a,b), large animal models such as dogs (Zerwekh et al. 1992), goats or sheep (Magin and Delling 2000), and non-human primates (Boden et al. 1999b; Suh et al. 2002). The most commonly used experimental spinal fusion model for evaluating biological effect of bone-graft substitutes, growth factors, and biophysical interventions in the above-mentioned experimental studies is the lumbar intertransverse process fusion model. Discussions on the technological assessment methods applied to spinal fusion models below are basically based on or applied to this model.

Bio-imaging Technologies for Assessment of Experimental Spinal Fusion

The currently used technologies for bone-biomaterial interface evaluations include radiological imaging techniques, 2D and 3D histomorphometry, non-invasive bone mineral densitometry (BMD), and biomechanical testing.

Radiographic Imaging Techniques

Radiological imaging techniques can be classified as macro- or microradiography. Macroradiological techniques are non-destructive, including plain X-ray (Fig. 1), computed tomography (CT; Fig. 2), and magnetic resonance image (MRI; Fig. 3a,b). They are routinely used in in vivo monitoring or ex-vivo studies (Boden et al. 1995; Boden 1998; Greenwald et al. 2001; Guo et al. 2002); however, these methods generally have lower resolution. For plain X-ray, calcium-phosphate-based biomaterials, such as beta-tricalcium phosphate and hydroxyapatite, are radio-opaque. Biomaterials are implanted onto the transverse processes; thus, they mask bone regeneration on anterior-posterior (AP) views. Newly formed mineralized bone is merely observed on the rim of biomaterials and is only seen in the later stages of spinal fusion. Most bone formation takes place beneath biomaterials because of osteoconductive effect. Plain X-ray is usually used for monitoring any dislocation of biomaterial in vivo. For CT, the basic scanning plane is cross-sectional. Complete spinal fusion can be assessed by reconstruction of 2D images. It depends on the function of computer software to perform reconstruction longitudinal section. The basic principle of MRI relates to the magnetic properties of the 2D data in a hydrogen molecule and its interaction with an external magnetic filed. Water content-rich tissues, e.g. spinal cord, intervertebral disc, and muscle, generate higher signal than bony tissue; therefore, MRI is not frequently used to assess bone fusion.

High-resolution radiography is used for precision measurements of fusion mass and fusion rate of fusion complex after sample harvesting. Microradiological techniques include contact microradiography and recent technological advancement in

Figure 1. Plain X-ray anteroposterior view of hydroxyapatite-tricalcium (HA-TCP; *H*) implanted onto L5-L6 transverse processes with decortication procedure in adult rabbit spinal fusion at 7 weeks post-operation. Calcium phosphate based biomaterials are radio-opaque. Bone regeneration is observed only on the lining of biomaterials but not beneath biomaterials
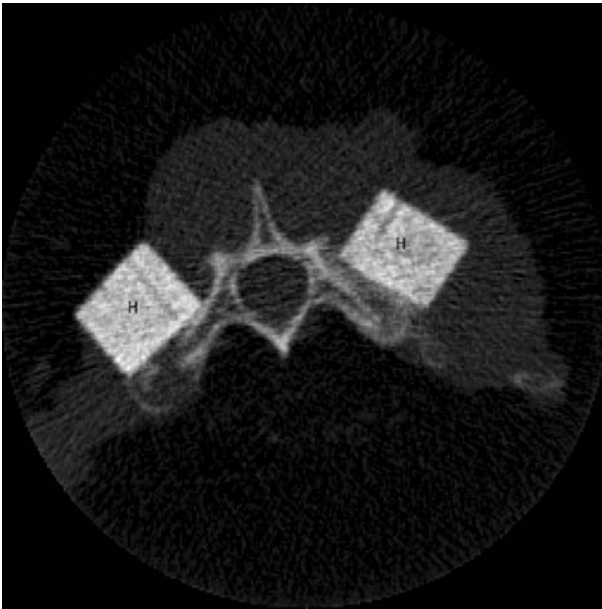
Figure 2. The cross-sectional CT image of hydroxyapatite-tricalcium phosphate (*H*) implanted rabbit posterior spinal fusion scanned by pCQT (Densiscan 2000, Scanco Medical, Basel Switzerland) in vivo. The mineral density, mineral content and volume of the newly formed mineralized tissue are measured under HA-TCP implant

high-resolution CT, i.e., micro-CT. Micro-CT scans the specimens to generate 2D image (Fig. 4a). By reconstruction of 2D images, a powerful static 3D histomorphological assessment technique with resolution as well as 7 μm, allows objective 3D structural assessment of bone and ceramic biomaterials with the fusion com-
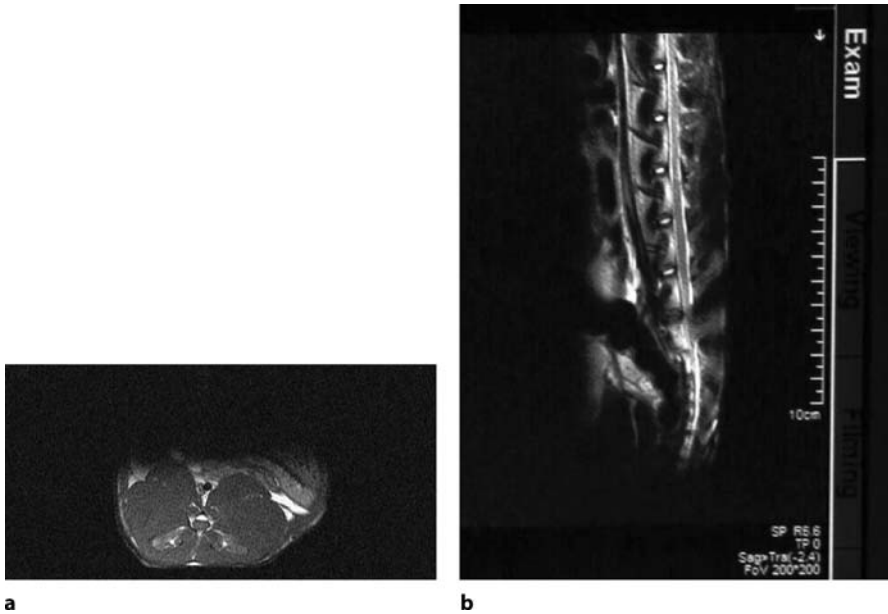
Figure 3 a,b. The MRI image of rabbit spine (T1) is scanned in cross-sectional plane (**a**) and sagittal plane (**b**). The water content rich tissues, e.g. spinal cord and cartilage, are visualized in high intensity in T1-weighted image, whereas the bony tissue is shown in *dark colour* of grey scale

plex intact or without sectioning the specimens for quantification (Fig. 4b,c). This technique is currently used mainly in osteoporosis studies (Schmidt et al. 2003; Siu et al. 2004) or characterization of biomaterial structures (Jung et al. 2003; Yeung et al. 2005); however, some biomaterials, such as hydroxyapatite and beta-tricalcium phosphate, is similar to bone in terms of X-ray attenuation; thus, it is difficult to distinguish these biomaterials from the fusion bone by threshold adjustment.

Contact microradiography is a technique that requires harvested samples to be embedded with resin such as glycomethacylate and methylmethacrylate (MMA) for undecalcified histological sections (Guo et al. 2001; Chan et al. 2004, 2005a,b). The samples are sectioned with two parallel surfaces for studying bone matrix mineralization (Zetterqvist et al. 1995; Qin et al. 2001; Guo et al. 2002). The sections can be examined by high-resolution X-ray film (Fig. 5) or photoplate. During the process of spinal fusion, inter-transverse process distance becomes narrower until fusion is complete. The inter-transverse process distance can be measured by micro-CT or contact microradiography images. Reconstructive 3D image from micro-CT give more accurate distance measurement by adjustment of different viewing angle (Fig. 6; Chan 2005a). For contact microradiography, the distance of inter-transverse process can be measured at relatively low cost using image analysis software, but it depends on the sectioning plane (Fig. 5).
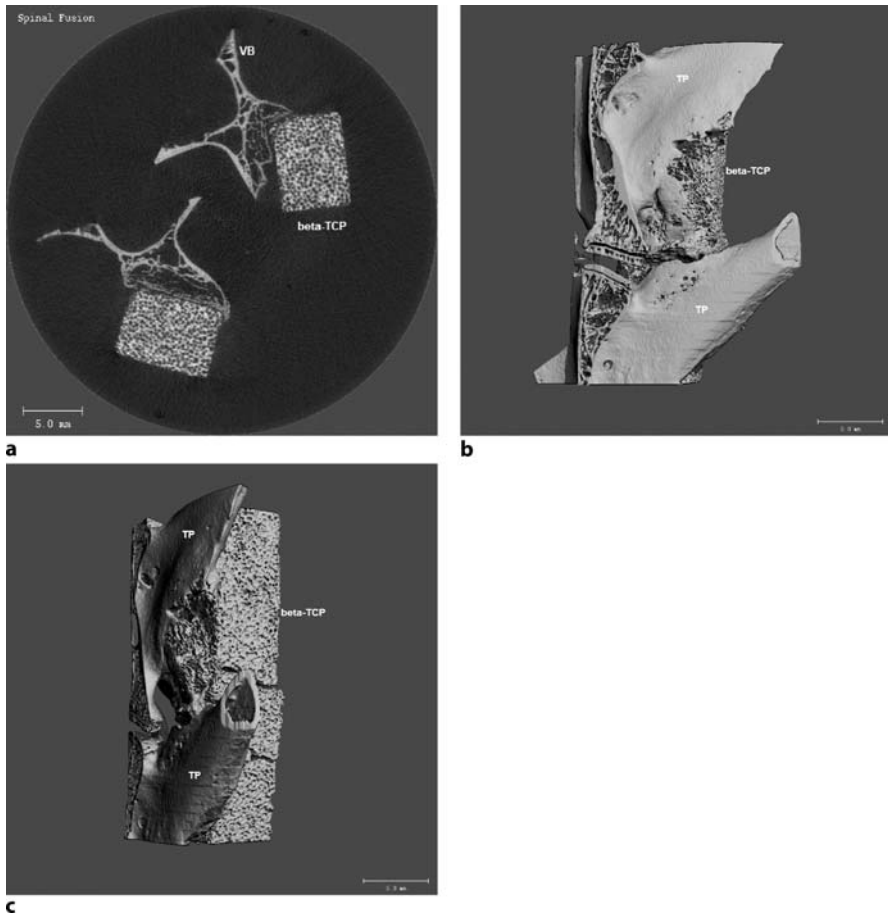
Figure 4 a–c. The micro-CT images of rabbit spinal fusion sample. The vertebral segment is cut into two halves longitudinally after the sample is harvested at 7 weeks post-operation. The samples are scanned in coronal plane to generate serial 2D images (**a**). The serial layers of 2D images are reconstructed into 3D image and presented in ventral view (**b**) and lateral view (**c**) to measure shortest inter-transverse process gap distance. *VB* vertebral body, *beta-TCP* beta-tricalcium phosphate ceramics, *TP* transverse process

    In addition, X-ray photoelectron spectroscopy is also a method of choice, one that analyses the chemical composition and mechanical properties of bone-biomaterials at fusion interface (Guo et al. 2001; Collier et al. 2002).

Histomorphology and Histomorphometry

Conventional light microscopy equipped with either commercially available or custom-made histomorphometric programs (imaging qualification program) is used for both descriptive and quantitative histology in the study of both temporal and spa-
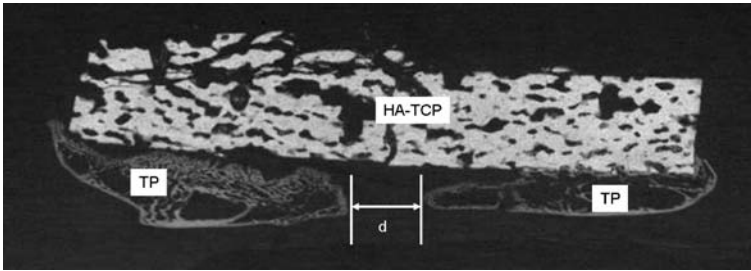
Figure 5. Micro-radiography of spinal fusion with HA-TCP implanted in rabbit posterior spinal fusion model. The samples are sectioned sagittally and perpendicular to the plane of transverse processes (*TP*). The inter-transverse processes gap distance (*d*) is measured between two processes parallel to the axis of ceramics
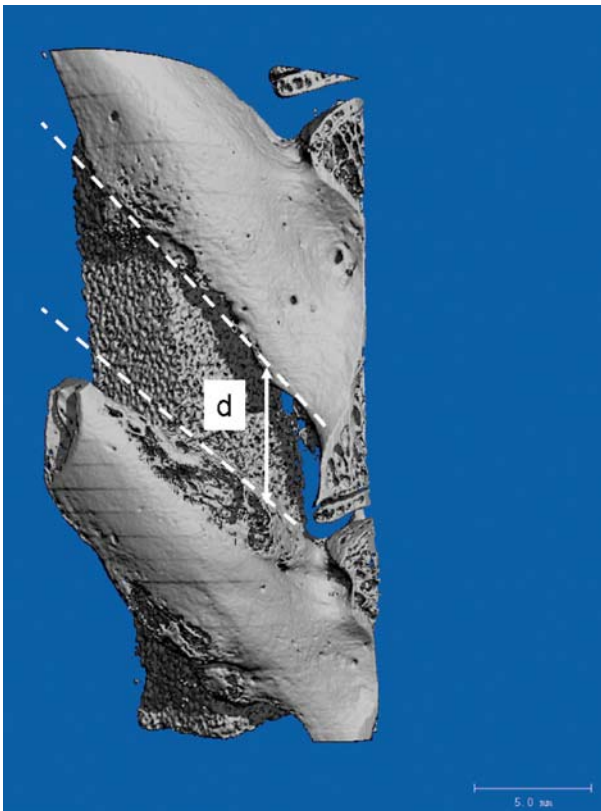
Figure 6. The bone-marrow-derived stem cells treated with basic fibroblat growth factor and osteogenic supplement including dexamethansone, ascorbic acid and β-glycerophosphate in vitro. The cells are loaded on β-TCP. The cell-ceramics composite is implanted at L5 and L6 transverse processes in rabbit posterior spinal fusion at week 7. After micro-CT scanning, 3D fusion model is reconstructed for measurement of intertransverse processes gap distance (*d*) by the shortest distance of two processes underneath the ceramics

tial changes of fusion process and fusion mass (Chan et al. 2003, 2004, 2005a,b; Yeung et al. 2003).

Early Changes at Molecular Level

Fusion mass and adjacent tissues can be studied histologically for gene expression of collagens and bone matrix proteins in the early phase of fusion process (within first 2–3 postoperative weeks), including bone morphogenetic proteins using molecular biology techniques (Boden and Schimandle 1995; Boden et al. 1999b; Ludwig and Boden 1999; Sandhu et al. 2001).

Changes at Cellular, Subcelluar, and Matrix levels

In the early stage of fusion (within 4–5 postoperative weeks), many spatial and temporal osteogenic and chondrogenic responses at the bone-biomaterial interface can be evaluated, including intramembranous, endochondral, transchondroid bone formation, as well as the progress after implantation of biomaterials (Zerwekh et al. 1992; Boden and Schimandle 1995; Boden et al. 1995, 1999a,b; Zetterqvist et al. 1995; Sandhu et al. 1997; Magin and Delling 2001; Guo et al. 2002; Linovitz et al. 2002; Chan et al. 2005b). In these studies many special staining techniques have been adapted or further developed to highlight the cellular or matrix composition both qualitatively (histology) and quantitatively (histomorphometry) based on methodologies summarized by Parfitt (1983), Dickson (1984), and von Recum (1999). In the preparation, serial undecalcified sections normally at around 100 μm or decalcified sections at 7–10 μm perpendicular to the long axis of the implant are prepared. Toluidine blue or basic fusin staining are used for undecalcified sections while hematoxylin and eosin (H&E; Fig. 7), and Safranin O/Fast green are used for proteoglycan-rich cartilaginous tissue (Fig. 8; Chan et al. 2004). Other immunohistochemical staining methods are used to study specific cellular or tissue responses to the implant, e.g., vascular endothelial growth factor (VEGF; Fig. 9; Chan et al. 2005b). In the later phases, these studies focus mainly on evaluation of fusion quality in terms of fusion mass particularly mature osseous tissue, and tissue response or integration with implanted biomaterial with or without growth factor augmentation, and with or without biophysical intervention.
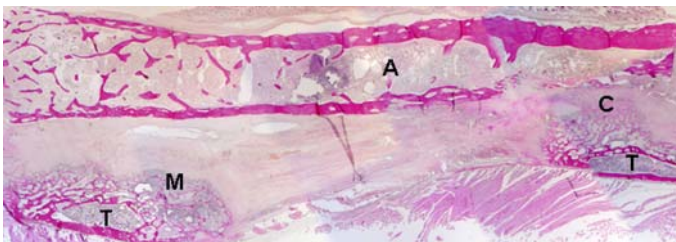
Figure 7. The allograft (*A*) of iliac crest implanted at L5 and L6 transverse processes (*T*) in rabbit posterior spinal fusion at week 5. The spinal processes grow towards each other. Cartilaginous tissue (*C*) and mesenchymal like cells (*M*) found in fusion bed. (Hematoxylin and eosin, ×16)
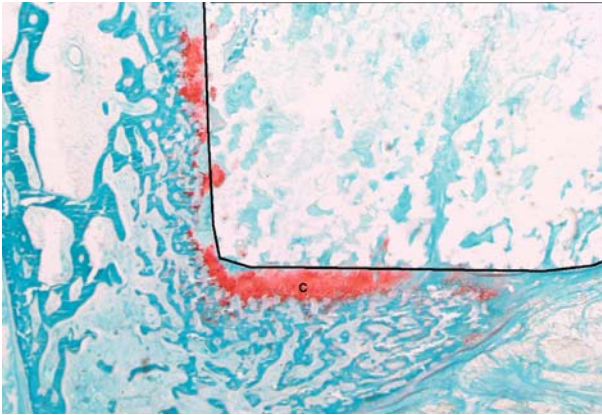
Figure 8. The proteoglycan rich cartilage (*c*) is stained in red colour by safranin O/fast green at week 7 post-operation with HA-TCP implanted at L5 and L6 transverse processes. The samples are sectioned with 15 μm of thickness sagittally and perpendicular to the plane of transverse processes. The area in *black line* is the original region of HA-TCP block
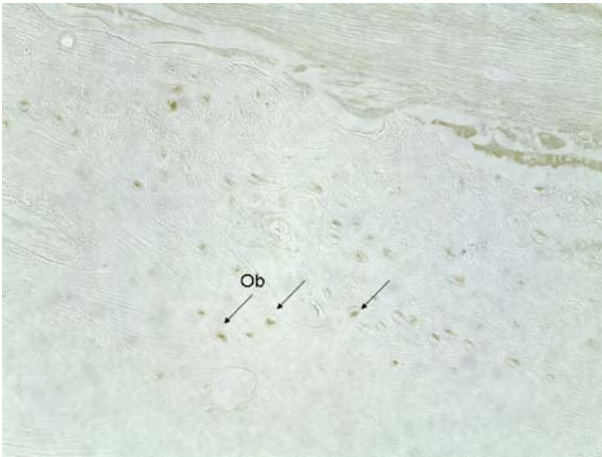
Figure 9. Immunohistochemistry of VEGF in rabbit allograft implanted posterior spinal fusion at week 5 post-operation. The VEGF is expressed moderately in osteoblast and osteocyte in newly formed bone (*Ob*) between intertransverse processes fusion bed (*arrows* denote VEGF positive cell, ×200)

Other Types of Microscopy and Accessories

Conventional light microscopy (Fig. 10a) equipped with florescence and polarization accessories is useful in studying dynamic bone remodeling with sequential florescence labeling (evaluation of osteogenesis at various time points on the same specimen; Fig. 10b) and matrix collagen maturity in terms of collagen fiber alignment (Fig. 10c), It has been used mainly to study bone remodeling of intact bone more than
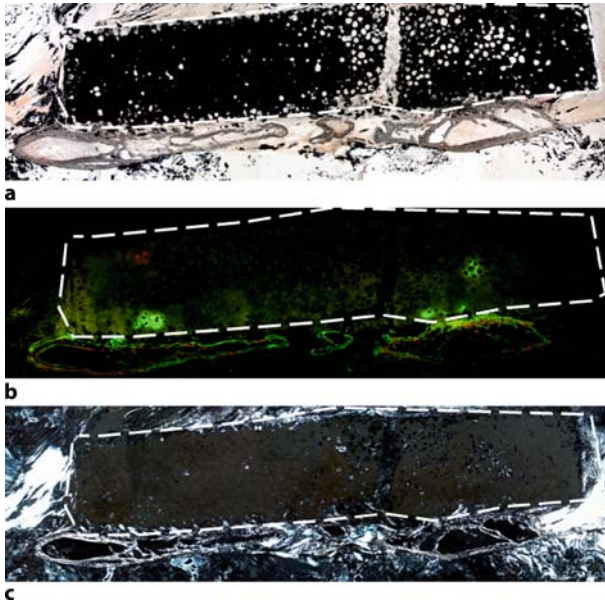
Figure 10 a–c. Sections of rabbit posterior spinal fusion harvested at week 7 post-operation. The area of *dotted line* shows the β-TCP ceramics implant. **a** Unstained section embedded with methyl methacrylate and cut and polished to 100 μm in thickness. **b** Unstained section of Fig. 9 observed under florescence microscopy. The fluorochrome, xylenol orange and calcein was injected intramuscularly at weeks 4 and 6 respectively. The fusion dynamics could be assessed. **c** Unstained section of Fig. 9 under polarised light microscopy. The mature and organized collagen fibre exhibited high intensity. The lamellar bone which showed high intensity had higher maturity. (Magnification ×1)

fracture repair (Parfitt 1983; Qin et al. 1999; O'Brien et al. 2002) and recently also has been adapted for evaluating temporal and spatial osteogenesis in experimental spinal fusion (Guo et al 2002; Chan et al. 2004; Chan et al. 2005a,b).

Some biomaterials are made of porous materials. In the macropores, newly formed bone is not easily observed under conventional light microcopy (Fig. 11a). Fluorescent microscopy can clearly demonstrate bone formation due to fluorochrome deposition with mineral apposition (Fig. 11b). Polarized microscopy showed not only mature lamellar bone but also thick collagen fiber (Fig. 11c).

Transmission and scanning electron microscopy (TEM, SEM) are useful for studying sectioned materials at cellular and subcellular levels or surface materials at cellular and matrix levels, respectively. They may not be useful tools for evaluating fusion mass because of difficulty in sampling or selection of region of interests for quantification, except for studying wear debris (Katz and Meunier 1997; Qin et al. 2004); however, backscatter SEM, used for studying bone matrix and orthopedic biomaterials, is useful for assessing fusion quality by evaluating maturity or mineralization of bone matrix (Zetterqvist et al. 1995). In addition, under identical
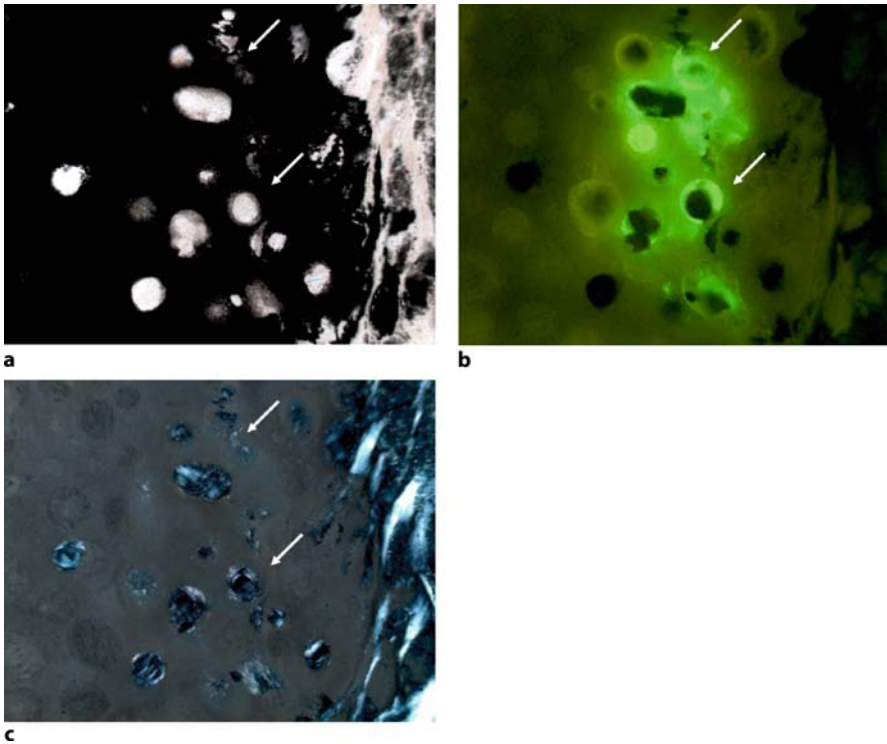
Figure 11a–c. The bone ingrowth found in β-TCP of rabbit spinal fusion at 7 weeks post-operation by different methods. **a** Observed under conventional light microscopy (*arrows*). **b** Observed under fluorescence microscopy, and the fluorochrome deposition demonstrates bone ormation inside the macropores of beta-TCP (*arrows*), although it was not shown clearly in conventional light microscopy. **c** Observed under olarized light microcopy, with the maturity of bone matrix (*arrows*) which was related to the organization of collagen fibres. (Magnification ×50)

preparation and staining conditions, our recent experimental studies showed that the staining intensity of tissue matrix can also be quantified to reflect of bone matrix mechanical properties (Qin et al. 2001; Qin et al. 2004). As bone formation and mineralization is associated with bone blood supply, a recent study determined semi-quantitatively the interosseus origin of the new blood vessels in an intertransverse process fusion mass fixed with in vivo injected colored silicone (Toribatake et al. 1998). Assessment with 3D micro-CT technique is introduced, which has been reported to provide significantly better quantitative results in other organs (Ortiz et al. 2000). In line with the application of 3D techniques, confocal scanning laser microscopy with non-destructive layer-by-layer evaluation strategies, currently used in orthopedic biomaterials experimental research (Iyama et al. 1997; Takagi et al. 2001), may also be applicable in experimental spinal fusion studies.

Bone Densitometry

Non-invasive bone densitometry is widely used in osteoporosis studies for quantifying bone mineral density (BMD) and content (BMC), including areal BMD measurement with dual-energy X-ray absorptiometry (DXA), and volumetric BMD using axial and peripheral quantitative computer tomography (aQCT and pQCT). This has also been adapted for studying the state of mineralization, changes over time, fusion rate, and fusion mass, clinically and experimentally (Sandhu et al. 1997; Cheng et al. 2000; Cheng et al. 2002; Kandziora et al. 2003; Chan et al. 2004, 2005a); however, due to its lower resolution, it is not possible to differentiate bone and implant interface. The newest development of in vivo high-resolution micro-CT for animals (Jaecques et al. 2004) can be adopted for experimental spinal fusions studies in the future for in vivo monitoring of fusion dynamics.

Biomechanical Testing

Although biomechanical testing may not conventionally be considered a bio-imaging method, we still integrate it into this chapter as mechanical testing of the properties of bone-biomaterial fusion complex can be regarded as the "gold standard" or "end point" in evaluating the implanted biomaterials for enhancing spinal fusion experimentally.

Methods for Testing the Quality of Fusion Complex

Both semi-quantitative and quantitative biomechanical measurements have been reported (Boden et al. 1995; Sandhu et al. 1997; Cook et al. 2001; Glazer et al. 2001; Chen et al. 2002; Guo et al. 2002); these include (a) manual palpation, tested at the level of the fused motion segment, and at the levels of the adjacent motion segments proximally and distally to differentiate the union from non-union or rate of pseudoarthrosis, and (b) mechanical testing, including push-out, torsion, compression or tensile

Figure 12. Micro-indentation can reveal Vicker's hardness of the host tissues and implanted materials within the fusion complex using a Microhardness Tester (Microhardness Tester FM; Future-Tech, Tokyo, Japan). The Vickers diamond pyramidal indenter was compressed at 25 g compression load onto the region of interest for a dwell time of 10 s. An indentation mark formed on the region of interest during the compression of the indenter, and the diagonal length of the indentation mark was then measured for the calculation of Vicker's hardness

tests, is conducted using uni-axial or biaxial material testing machines and custom-made testing jigs or metal frames on specially prepared specimen. The variables used to reflect fusion quality include load, strength, stiffness, and energy required to testing the fusion complex to failure. Failure modes are also important to record and used as relevant evidence for fusion quality with specific reference to the region of interests within the fusion complex.

Methods for Testing the Material Properties

The material properties of fusion mass can be examined on undecalcified histological sections by using (a) non-destructive nano- or microindentation test reported for testing intact bone material properties (Qin et al. 2001, 2006) and recently also adapted for studying quality of spinal fusion experimentally (Fig. 12; Guo et al. 2001), and (b) non-contact high-frequency scanning acoustic microscopic evaluations at microlevels currently only seen in studying mechanical properties of intact bone
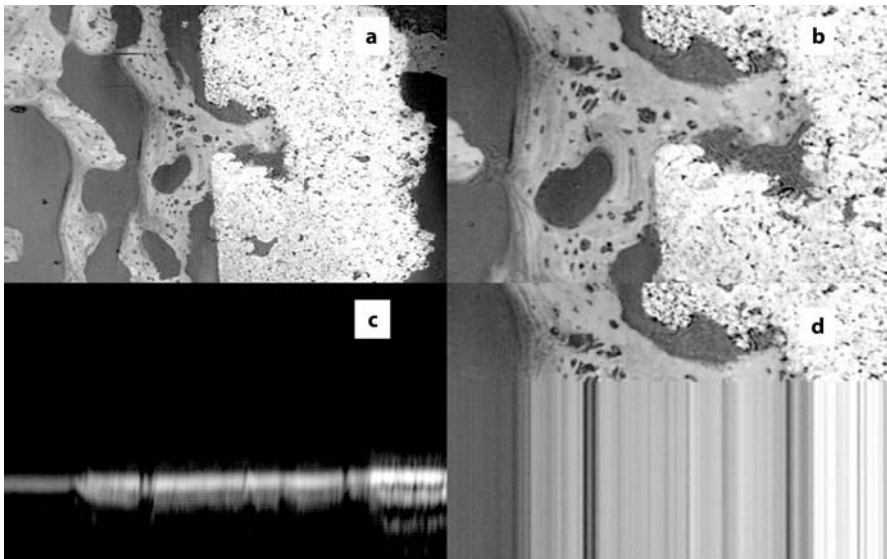
Figure 13a–d. High-frequency scanning acoustic microscopy (SAM) measurement (400-MHz burst mode, resolution 2.5 μm). **a,b** An SAM micrograph from a region of host bone and implanted HA-TCT block from a sagittal section of fusion complex embedded in MMA (×200). **c** X-Z scan on the horizontal axis (scan line) along the regions of interest, i.e. the host bone and implanted HA-TCP from **a**. **d** An SAM reflection impedance pattern of the scan line of **b**. The resulting interference pattern is due to the interaction of the surface and longitudinal acoustic waves providing acoustic information that is related to the specimen's elastic properties along the scanned line. The *narrow band on the left* represents the empty space filled with MMA and reflects lower stiffness, whereas the *wide band on the right* reflects the higher stiffness of the HA-TCP, when compared with SAM image of **c**. The variations in acoustic band long the bone matrix reflects their material stiffness due to differences in degree of mineralization, i.e. stiffer or more mineralized matrix shows wider acoustic band

or bone-dental implant interface (Katz and Meunier 1997; Wang et al. 1998; Turner et al. 1999; Qin et al. 2001, 2004). Nano- or microindentation can reveal the potential degradation of hardness or Young's modules or Vicker's hardness of the host tissues and implanted materials within the fusion complex while high-frequency scanning acoustic microscopy (SAM) measures the impedance of the sound reflection of the materials and gives information about material mechanical properties (Wang et al. 1998; Qin et al. 2006). The SAM also provides high-resolution images comparable to those of conventional light microscopy, which can be used for histomorphological and histomorphometric evaluations (Fig. 13; Katz and Meunier 1997; Qin et al. 2001, 2004).

Discussion

The advantage of conventional 2D histomorphometry enables us to quantify differences of host tissues and implanted biomaterials and the osteo-integration at cellar, subcellular, as well as tissue matrix levels; however, the disadvantages of conventional histomorphometric techniques are time-consuming in terms of specimen preparation, evaluation and interpretation (Parfitt 1983; Qin et al. 2001). A major drawback is the damage and preparation artifacts of specimens during sectioning. The recent technical advances in "non-invasive" 3D evaluation of biological tissues or materials with micro-CT and confocal laser microscopy can overcome some of these problems (Iyama et al. 1997; Ortiz et al. 2000; Takagi et al. 2001). Because of the relatively lower resolution of clinical densitometry, images provided by both DXA or aQCT and pQCT may only be used as reference for prediction of spinal fusion quality. Due to complexity of the fusion spatial patterns in various animal models with differences in anatomy and size, no single standard mechanical testing method has been or can be recommended for spinal fusion experiments. A few macromechanical testing methods, such as nanoindentation and high-frequency scanning acoustic microscopy, may be introduced for future studies aimed at evaluation of fusion quality based on undecalcified sections of fusion complex with or without biomaterial implantation (Guo et al. 2001).Since one single orthopedic research unit is not likely to be equipped with the above-mentioned research facilities or manpower, our recommendation is to facilitate local and international collaborations, which is a "cost-effective" way to conduct modern scientific research demanding state-of-the-art research facilities and expertise (Guo et al. 2001; Qin et al. 2001; Cheng and Qin 2002).

All the above-mentioned technologies used for experimental spinal fusion studies and bone-biomaterial interface studies have both strengths and limitations in their applications. Current molecular biology research has shown that the spinal fusion process is multifactorial and extremely complex. The combined use of these macro- and microassessment tools can definitely deepen our understanding of the quality and fusion dynamics at the bone-biomaterial interface. With the advent of improved animal models, experience gained in the evaluation technology, the basic science behind spinal fusion, will be further clarified. This will further contribute to research and development of new biomaterials for enhancing spinal fusion clinically. Joint ef-
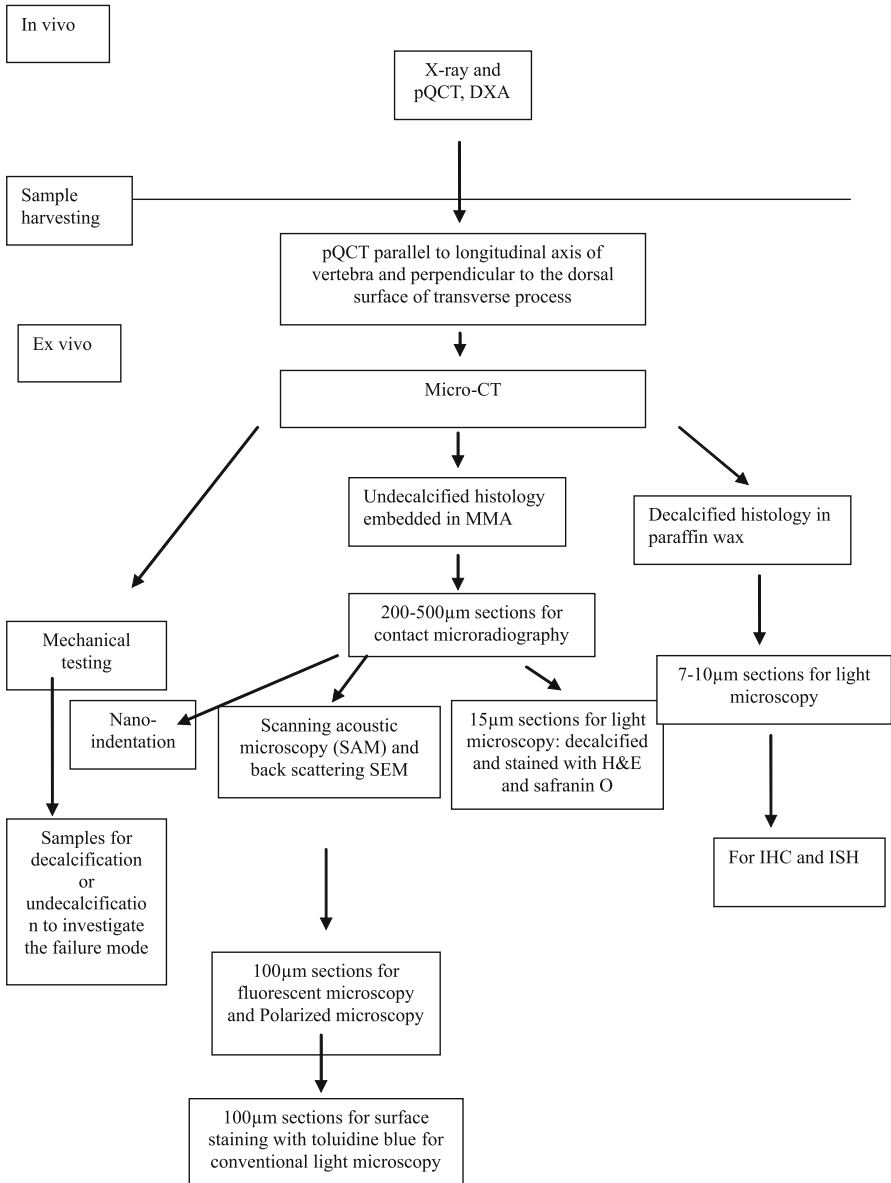
Figure 14. The flow chart shows the sample handling procedures developed in the authors' laboratory. Non- or minimally destructive assessments should be performed before subsequent serious destructive imaging and mechanical assessments. *ICH* immunohistochemistry, *ISH* in situ hybridization

forts and collaborations made not only by biomaterial scientists and engineers, but also by medical doctors and clinical scientists, biologists, and technologists are necessary in promoting all these advances.

Considering the large spectrum of animal models and evaluation techniques at molecular, cellular, tissue, and organ levels used for the assessment of spinal fusion after biological, biomaterial, and biophysical interventions, evaluation strategies have to be defined and validated for specific "end-point(s)" set by investigators for defined experiments. The availability of expertise, manpower, funding supports, research facilities, and not least of all the cost-effectiveness, are all relevant in research planning, implementation, data analysis, and interpretation of findings. In general, smaller animal models, such as mice and rats, were used for evaluation of early events at both molecular and cellular levels (Salamon et al. 2003), whereas large animals, such as rabbits, dogs (Zerwekh et al. 1992; Jung et al. 2003), goats, or sheep (Magin and Delling 2001), and non-human primates (Boden et al. 1999b; Suh et al. 2002), were selected to provide large samples for studying spinal fusion histologically, radiographically, as well as mechanical properties. Rabbit might be a compromised model for satisfying both purposes mentioned above and also cost-effective (Boden et al 1999a, 1995; Guo et al 2001, 2002; Suh et al. 2002). Anti-bodies, which may not cross species, was also a major restriction in selection of animal models (Boden and Schimandle 1995; Boden 1998; Guo et al 2002; Salamon et al. 2003).

Conclusion

This chapter introduces many bio-imaging evaluation technologies that are developed and adopted for potential application in evaluation of bone-biomaterial interface integration both preclinically and clinically. Special emphasis is placed on some of these conventional and advanced techniques being applied to evaluate dynamic processes and quality of spinal fusion. We are not able to make a direct comparison to compare and contrast the techniques in relation to the end-point evaluation at various levels as well as costs in order to offer a guide to selecting appropriate techniques and animal models, but it may serve as a reference for future studies concerning study design and selection of bio-imaging technologies for qualitative and quantitative evaluation of bone-biomaterial interface integration such as experimental and clinical spinal fusion, with or without biological or biophysical argumentation.

References

Boden SD (1998) Bone repair and enhancement clinical trial design. Spine applications. Clin Orthop 355(Suppl):S336–S346

Boden SD (2002) Overview of the biology of lumbar spine fusion and principles for selecting a bone graft substitute. Spine 27(16 Suppl 1):S26-S31

Boden SD, Schimandle JH (1995) Biologic enhancement of spinal fusion. Spine 20(24 Suppl):113S–123S

Boden SD, Schimandle JH, Hutton WC (1995) An experimental rabbit lumbar intertransverse process spinal fusion model. Radiographic, histologic, and biomechanical healing characteristics. Spine 20(4):412–420

Boden SD, Martin GJ Jr, Morone M, Ugbo JL, Titus L, Hutton WC (1999a) The use of coralline hydroxyapatite with bone marrow, autogenous bone graft, or osteoinductive bone protein extract for posterolateral lumbar spine fusion. Spine 24(4):320–327

Boden SD, Martin GJ Jr, Morone MA, Ugbo JL, Moskovitz PA (1999b) Posterolateral lumbar intertransverse process spine arthrodesis with recombinant human bone morphogenetic protein 2/hydroxyapatite-tricalcium phosphate after laminectomy in the nonhuman primate. Spine 24(12):1179–1185

Chan CW, Lee KM, Yeung HY, Chiu YM, Qin L, Leung KS, Cheng JCY (2003) Low intensity pulsed ultrasound enhanced the increase in bone volume of spinal processes with implantation of calcium phosphate bioceramics in rabbits posterior spinal fusion model. Hong Kong J Orthop Surg 7(Suppl):S112

Chan CW, Lee KM, Yeung HY, Qin L, Leung KS, Cheng JCY (2004) Low-intensity pulsed ultrasound increased fusion mass in hydroxyapatite/tricalcium phosphate implanted posterior spinal fusion. Hong Kong J Orthop Surg 8:S12

Chan CW, Fan HB, Lee KM, Qin L, Wong KHK, Yeung HY, Hu YY, Cheng JCY. (2005a) Stem cell based therapy in posterior therapy in posterior spinal fusion: an animal study. Hong Kong J Orthop Surg 9:S28

Chan CW, Yeung HY, Lee KM, Chiu YM, Guo X, Chow P, Tabata Y, Cheng J (2005b) Temporal and spatial expression pattern of VEGF and VEGF receptor in the posterior spinal fusion with allograft. Key Eng Mater 288–289:491–494

Chen WJ, Lai PL, Chang CH, Lee MS, Chen CH, Tai CL (2002) The effect of hyperbaric oxygen therapy on spinal fusion: using the model of posterolateral intertransverse fusion in rabbits. J Trauma Injury Infect Crit Care 52(2):333–338

Cheng JCY, Qin L (2002) Biotechnologies in studying bone-biomaterial interface in experimental spinal fusion: a review. Proc 12th Interdisciplinary Research Conference on Biomaterials (GRIBIO 2002), 14–17 March 2002, Shanghai, China, pp 70–72

Cheng JCY, Qin L, Cheung SK, Sher A, Lee SM, Ng E, Guo X (2000) Generalized low areal and volumetric bone mineral density in adolescent idiopathic scoliosis. J Bone Miner Res 15(8):1587–1595

Cheng JCY, Guo X, Law LP, RN Rosier (2002) How does recombinant human bone morphogenetic protein-4 enhance posterior spinal fusion? Spine 27(5):467–474

Collier JH, Camp JP, Hudson TW, Schmidt CE (2002) Synthesis and characterization of polypyrrole-hyaluronic acid composite biomaterials for tissue engineering applications. J Biomed Mater Res 50(4):574–584

Cook SD, Salkeld SL, Patron LP, Ryaby JP, Whitecloud TS (2001) Low-intensity pulsed ultrasound improves spinal fusion. Spine J 1(4):246–254

Dickson GR (1984) Methods of calcified tissue preparation. Elsevier, Amsterdam

Glazer PA, Spencer UM, Alkalay RN, Schwardt J (2001) In vivo evaluation of calcium sulfate as a bone graft substitute for lumbar spinal fusion. Spine J 1(6):395–401

Greenwald AS, Boden SD, Goldberg VM, Khan Y, Laurencin CT, Rosier RN (2001) American Academy of Orthopaedic Surgeons. The Committee on Biological Implants. Bone-graft substitutes: facts, fictions, and applications. J Bone Joint Surg [Am] 83A Suppl 2 Pt 2:98–103

Guo LH, Guo X, Leng Y, Cheng JC, Zhang X (2001) Nanoindentation study of interfaces between calcium phosphate and bone in an animal spinal fusion model. J Biomed Mater Res 54(4):554–559

Guo X, Lee KM, Law LP, RN Rosier, Cheng JCY (2002) Recombinant human bone morphogenetic protein-4 (rhBMP-4) enhanced posterior spinal fusion without decortication. J Orthop Res 20(4):740–746

Hasharoni A, Zilberman Y, Turgeman G, Helm GA, Liebergall M, Gazit D (2005) Murine spinal fusion induced by engineered mesenchymal stem cells that conditionally express bone morphogenetic protein-2. J Neurosurg. Spine 3(1):47–52

Hodges SD, Eck JC, Humphreys SC (2003) Use of electrical bone stimulation in spinal fusion. J Am Acad Orthop Surg 11(2):81–88

Iyama S, Takeshita F, Ayukawa Y, Kido MA, Suetsugu T, Tanaka T (1997) A study of the regional distribution of bone formed around hydroxyapatite implants in the tibiae of streptozotocin-induced diabetic rats using multiple fluorescent labeling and confocal laser scanning microscopy. J Periodontol 68(12):1169–1175

Jaecques SV, Van Oosterwyck H, Muraru L, Van Cleynenbreugel T, De Smet E, Wevers M, Naert I, Vander Sloten J (2004) Individualised, micro CT-based finite element modelling as a tool for biomechanical analysis related to tissue engineering of bone. Biomaterials 25(9):1683–1696

Jung H, Kim HJ, Hong S, Kim KD, Moon HS, Je JH, Hwu Y (2003) Osseointegration assessment of dental implants using a synchrotron radiation imaging technique: a preliminary study. Int J Oral Maxillofac Implants 18(1):121–126

Kandziora F, Pflugmacher R, Scholz M, Schollmeier G, Schmidmaier G, Duda G, Raschke M, Haas NP (2003) Dose-dependent effects of combined IGF-I and TGF-beta1 application in a sheep cervical spine fusion model. Eur Spine J 12(5):464–473

Katz JL, Meunier A (1997) Scanning acoustic microscopy of human and canine cortical bone microstructure at high frequencies. In: Lowet G et al. (eds) Bone research in biomechanics. IOS Press, Amsterdam, pp 123–137

Linovitz RJ, Peppers TA (2002) Use of an advanced formulation of beta-tricalcium phosphate as a bone extender in interbody lumbar fusion. Orthopedics 25(5 Suppl):585–589

Linovitz RJ, Pathria M, Bernhardt M, Green D, Law MD, McGuire RA, Montesano PX, Rechtine G, Salib RM, Ryaby JT, Faden JS, Ponder R, Muenz LR, Magee FP, Garfin SA (2002) Combined magnetic fields accelerate and increase spine fusion: a double-blind, randomized, placebo controlled study. Spine 27(13):1383–1389

Ludwig SC, Boden SD (1999) Osteoinductive bone graft substitutes for spinal fusion: a basic Science summary. Orthop Clin North Am 30(4):635–645

Magin MN, Delling G (2001) Improved lumbar vertebral interbody fusion using rhOP-1: a comparison of autogenous bone graft, bovine hydroxylapatite (Bio-Oss), and BMP-7 (rhOP-1) in sheep. Spine 26(5):469–478

Meding JB, Stambough JL (1993) Critical analysis of strut grafts in anterior spinal fusions. J Spinal Disord 6(2):166–174

Moazzaz P, Gupta MC, Gilotra MM, Gilotra MN, Maitra S, Theerajunyaporn T, Chen JL, Reddi AH, Martin RB (2005) Estrogen-dependent actions of bone morphogenetic protein-7 on spine fusion in rats. Spine. 30(15):1706–1711

Ortiz MC, Garcia-Sanz A, Bentley MD, Fortepiani LA, Garcia-Estan J, Ritman EL, Romero JC, Juncos LA (2000) Microcomputed tomography of kidneys following chronic bile duct ligation. Kidney Int 58(4):1632–1640

Parfitt AM (1983) The physiologic and clinical significance of bone histomorphometric data. In: Recker RR (ed) Bone histomorphometry: techniques and interpretation. CRC Press, Boca Raton, pp 143–223

Qin L, Leung KS, Chan CW, Fu LK, Rosier RN (1999) Enlargement of remaining patella after partial patellectomy in rabbits. Med Sci Sports Exer 31(4):502–506

Qin L, Hung LK, Leung KS, Guo X, Bumrerraj S, Katz JL (2001) Staining intensity of individual osteons correlated with elastic properties and degrees of mineralization. J Bone Miner Metabol 19(6):359–364

Qin L, Bumrerraj S, Leung KS, Katz JL (2004) Grey levels of osteons correlated with their elastic properties: a scanning acoustic micrography study. J Bone Miner Metabol 22(2):86–89

Qin L, Fok PK, Lu HB, Shi SQ, Leng Y, Leung KS (2006) Low intensity pulsed ultrasound increases the matrix hardness of the healing tissues at bone–tendon insertion: a partial patellectomy model in rabbits. Clin Biomechan 21(4):387–394

Recum AF von (1999) Handbook of biomaterials evaluation: scientific, technical, and clinical testing of implant materials, 2nd edn, Taylor and Francis, Philadelphia

Salamon ML, Althausen PL, Gupta MC, Laubach J (2003) The effects of BMP-7 in a rat posterolateral intertransverse process fusion model. J Spinal Disord Tech 16(1):90–95

Sandhu HS, Kanim LE, Toth JM, Kabo JM, Liu D, Delamarter RB, Dawson EG (1997) Experimental spinal fusion with recombinant human bone morphogenetic protein-2 without decortication of canine osseous elements. Spine 22(11):1171–1180

Sandhu HS, Khan SN, Suh DY, Boden SD (2001) Demineralized bone matrix, bone morphogenetic proteins, and animal models of spine fusion: an overview. Eur Spine J 10(Suppl 2):S122-S131

Schmidt C, Priemel M, Kohler T, Weusten A, Maller R, Amling M, Eckstein F (2003) Precision and accuracy of peripheral quantitative computed tomography (pQCT) in the mouse skeleton compared with histology and microcomputed tomography (microCT). J Bone Miner Res 18(8):1486–1496

Suh DY, Boden SD, Louis-Ugbo J, Mayr M, Murakami H, Kim HS, Minamide A, Hutton WC (2002) Delivery of recombinant human bone morphogenetic protein-2 using a compression-resistant matrix in posterolateral spine fusion in the rabbit and in the non-human primate. Spine 27(4):353–360

Siu WS, Qin L, Cheung WH, Leung KS (2004) Deterioration of microarchitecture of cancellous bone in OVX goats measured with microCT and pQCT. Bone 35(1):21–26

Takagi M, Santavirta S, Ida H, Ishii M, Takei I, Niissalo S, Ogino T, Konttinen YT (2001) High-turnover periprosthetic bone remodeling and immature bone formation around loose cemented total hip joints. J Bone Miner Res 16(1):79–88

Toribatake Y, Hutton WC, Tomita K, Boden SD (1998) Vascularization of the fusion mass in a posterolateral intertransverse process fusion. Spine 23(10):1149–1154

Turner CH, Rho J, Takano Y, Tsui TY, Pharr GM (1999) The elastic properties of trabecular and cortical bone tissues are similar: results from two microscopic measurement techniques. J Biomech 32(4):437–441

Vaccaro AR, Sharan AD, Tuan RS, Kang JD, An HS, Morone MA, Savas PE, Hilibrand AS, Abitbol JJ (2001) The use of biologic materials in spinal fusion. Orthopedics 24(2):191–197

Wang RR, Meyers E, Katz JL (1998) Scanning acoustic microscopy study of titanium-ceramic interface of dental restorations. J Biomed Mate Res 42(4):508–516

Yeung HY, Cheng JCY, Guo X, Lee KM, Chiu YM, Chan CW, Chow PY, Tabata Y (2003) Enhanced vascularization in posterior spinal fusion model by hydrogel incorporated with vascular endothelial cell growth factor. J Bone Miner Res 18(Suppl):S301

Yeung HY, Qin L, Lee SM, Zhang M, Leung KS, Cheng JCY (2005) Novel approach for quantification of porosity for biomaterial implants using microcomputed tomography (μCT) J Biomed Mater Res B Appl Biomater 75B(2):234–242

Zerwekh JE, Kourosh S, Scheinberg R, Kitano T, Edwards ML, Shin D, Selby DK (1992) Fibrillar collagen-biphasic calcium phosphate composite as a bone graft substitute for spinal fusion. J Orthop Res 10(4):562–572

Zetterqvist L, Anneroth G, Nordenram A, Wroblewski R (1995) X-ray microanalytical and morphological observations of the interface region between ceramic implant and bone. Clin Oral Implants Res 6(2):104–113

Assessment of Bone, Cartilage, Tendon and Bone Cells by Confocal Laser Scanning Microscopy

Chris W. Jones[1,2], Kirk H.M. Yip[2], Jiake Xu[2], and Ming-Hao Zheng[2] (✉)

[1] School of Mechanical Engineering, The University of Western Australia, Australia, Nedlands, 6009, WA, Australia
[2] Department of Orthopaedic Surgery, School of Surgery and Pathology, The University of Western Australia, Nedlands, 6009, WA, Australia
e-mail: zheng@cyllene.uwa.edu.au

Abstract

Confocal laser scanning microscopy (CLSM) is a type of high-resolution and comparatively non-destructive fluorescence imaging technique that overcomes the limitations of conventional wide-field microscopy and facilitates the generation of high-resolution 3D images from relatively thick sections of tissue. In addition, CLSM enables the in situ characterization of tissue microstructure. Images generated by CLSM have been utilized for the study of articular cartilage, bone, muscle, tendon and ligament, and in the field of orthopaedics. More importantly, recent evolution in techniques and technologies have facilitated a relatively widespread adoption of this imaging modality, with increased "user friendliness" and flexibility; therefore, applications of CLSM exist in the rapidly advancing field of orthopaedic implants and the investigation of joint lubrication. Accordingly, this chapter focuses on the specific applications, as well as the recent and future direction of developments of CLSM in orthopaedic research in tissues of orthopaedic interest.

Introduction

The principle of confocal microscopy was initially developed by Marvin Minsky in 1955 for imaging neurons in the brain, which requires improved-resolution images over those offered by traditional microscopes (Minsky 1988). In 1972 this concept was revisited, when the first biological images were obtained and published by the laser scanning confocal microscope (LSCM; Hader 1992). Technological developments, including the laser in the early 1960s, "off-axis" (stationary sample) beam scanning in the early 1970s (Sheppard 1994) and the availability of the powerful desktop computer of the 1990s, have all contributed to the present advances in development of the confocal microscope.

In many orthopaedic research applications detailed information regarding tissue microstructure is often required. Traditional histological approaches have utilized destructive mechanical biopsy and standard processing techniques coupled

with conventional or polarized light microscopy to provide such data (Pastoureau et al. 2003); however, these techniques often result in unquantified shrinkage or swelling of the tissue during histological processing; thus, conventional histology inherently prevents the true examination of tissue in the unaltered physiological state, thereby inhibiting simultaneous observation of viable cell response to external mechanical (or internal physiochemical) stimuli. Remarkably, confocal laser scanning microscopy (CLSM), overcomes these limitations and non-destructively generates high-resolution 3D images from relatively thick sections of tissue (Brakenhoff et al. 1997).

In this chapter the specific applications and development of CLSM in orthopaedic research are addressed. in particular we describe the use of CLSM in skeletal tissue and living cells for reconstruction of tissue architecture, cell and subcellular morphology and dynamics.

Confocal Laser Scanning Microscopy

Fluorescent Confocal Microscopy

The modern CLSM running in florescent mode uses a laser light source to excite a fluorescing contrasting agent within an imaged sample. An illumination light is launched from a gas or solid-state laser of a specific wavelength or several wavelengths and then filtered to produce the specific wavelengths required. Areas of interest are imaged by using a specific excitation wavelength that is close to the contrasting agent peak excitation wavelength. The contrasting agent, when excited by a light source, emits a longer wavelength that is then directed back along the same optical path as the illumination beam. A beam splitter or dichroic mirror, only reflecting light below or above a certain wavelength, is then used to divert the florescent emission towards a photodetector, usually a photo multiplier tube (PMT). Before the light hits the photodetector, it passes through set of filters (low pass and high pass) allowing only a narrow bandwidth of light to pass constituting the wavelength range of the peak of the emission wavelength curve. The light is then focused though a detection aperture (confocal pinhole), enabling out-of-focus light to be eliminated before it is registered by the photodetector. Internal reflections within the optic path of the microscope that normally generate noise within the image are also blocked by the detector aperture, thereby reducing blurring of the acquired image due to an improved signal-to-noise (s/n) ratio. In addition, confocal microscopy also has the advantage of being able to utilize less complex (cheaper) objectives lenses through the use of monochromatic light sources that introduce fewer aberrations into the system.

As elegantly noted by Shaw, it is "human nature that the most interesting information is just beyond what is observable", CLSM has been developed in an attempt to surpass the theoretical resolution limitations of polarized light microscopy (0.25 μm; Shaw 1994). The theoretical resolution limitations of confocal microscopy are currently considered between 0.21 and 0.58 μm in both the x- and y direction (parallel to the tissue surface), and between 0.44 and 3.44 μm in the z direction (perpendicular

to the tissue surface; Lee 2000). This lack of temporal resolution limits the ability to record transient cell shape changes, and restricts the capacity to accurately define nuclear surface area (Guilak 1995). Despite the current limitations, confocal microscopy is ideally suited to the analysis of complex 3D tissue architecture, and offers superior resolution to wide-field fluorescent microscopy (Harvath 1997). Moreover, current developments in instrumentation lead to image-acquisition rates that will parallel those achieved by flow cytometry technologies (Rigaut et al. 1992).

Reflectance mode confocal microscopy utilizes a similar set to florescence confocal microscopy, using the reflected light from the specimen in place of an excitable contrast agent. The equality of the excitation and emission wavelengths is maintained through the appropriate selection of filters. This method of confocal imaging is best utilized for the imaging of surface features or surface-texture analysis. Reflectance-mode imaging sometimes suffers from noise at detection due to the illumination light interfering with the detection light through interference. This problem can be minimized by panning the scanning area to a separate area of the objective, thereby avoiding interference artefacts. Sample illumination is achieved by the use of in-phase photon-coherent laser light, which creates improved sample edge detection by the phenomenon of destructive interference (Holst 1996).

Fiberoptic Confocal Microscopy

Single-mode fiberoptics are commonly used in modern confocal microscopy. The optical fibre provides a flexible light path for both the excitation and emission light path, and also acts as a spatial filter equivalent confocal pinhole in rigid systems (Ghiggino 1992). The use of a fibre optic system allows much greater flexibility as the launch and detection hardware can be separated. A recently developed laser scanning confocal arthroscope (LSCA) takes advantage of this by miniaturization of the faster scanning device enabling a confocal system to fit inside a 4.5-mm cannula, thereby facilitating in vivo confocal imaging on in situ samples (Smolinski et al. 2003). The LSCA is able to image sub-surface tissue up to depths of approximately 200 μm (depending on tissue density and contrasting agent penetration), although "cell shadows" currently restrict full field images to 50 μm. This ability makes possible the subsurface study of tissue previously only able to be diagnosed using physical biopsy (Jones et al. 2004).

Two-Photon Confocal Microscopy

Two-photon microscopy (TPM) was first demonstrated in 1990 by Denk et al. (1990). Like confocal microscopy it obtains high-resolution images of fluorophore prepped tissue through laser scanning the image plane. In TPM, a "confocal pinhole" is not required, thereby increasing signal sensitivity, although pinhole may be used to slightly increase resolution, if needed. Unlike confocal microscopy, TPM uses two photons fired nearly simultaneously to interact at the focal point of the objective, thus producing a single photon containing the total energy of the individual photons. This setup limits photo damage and photobleaching to the focused plane, a trait which is advantageous in thicker specimens. Two-photon microscopy holds an advantage over

confocal microscopy in that it can penetrate samples far deeper by utilizing near-infrared light sources that scatter less in tissues (Dunn et al. 2000).

Three-Dimensional Reconstruction

Optical sectioning of the specimen allows for the acquisition of a series of fully focused images at fixed increments along the objective's axis (z-axis). By combining these image stacks, a focused 3D model of an imaged sample can be reconstructed (Fig. 1). This method eliminates the possibility of processing artefacts sometimes introduced by physically sectioning tissue samples, as would be required using wide-field microscopy. Unfortunately, signal attenuation with increasing depth or image distortion due to the sample refractive index mismatch may possibly introduce image artefacts for CLSM during this process (Rigaut et al. 1992).

Deconvolution is another method available to confocal microscopists to improve the resolution of the gained images post-acquisition. This method enables to produce a resolution surpassing Rayleigh's criterion and is termed "super resolution". The mathematical algorithm uses a point-spread function (PSF) which contains information on how the microscope deviates from the perfect Airy profile, thus introducing out-of-focus light. The image plane above and below the one being deconvoluted is used to remove out-of-focus light from the desired image plane.

CLSM Assessment of Cartilage

The hyaline articular cartilage (AC) of synovial joints is subject to high levels of mechanical stress and wear, and is vulnerable to injury and other disease processes that can lead to extensive tissue degeneration. Due to its non-vascular nature and lack
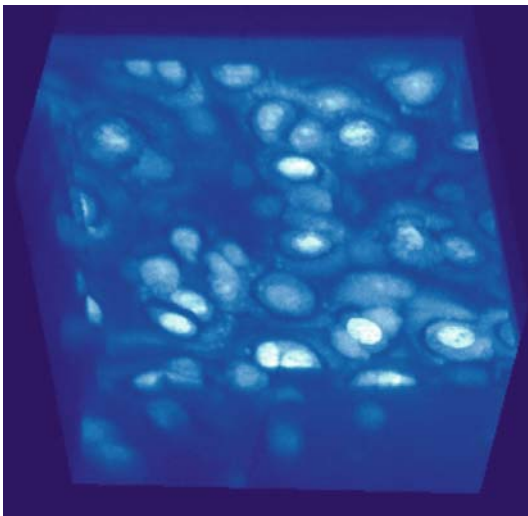
Figure 1. A 3D reconstruction of cartilage tissue with field of view of $100\,\mu m^2$

of other inherent regenerative capabilities, the metabolic and enzymatic responses of AC fail to provide sufficient rate of matrix regeneration to repair even a minimal defect.

While cartilage injury is often associated with damage to other tissues of the diarthroidal synovial joint, it is much more difficult to detect than osseous or osteochondral fractures that are readily identified via magnetic resonance imaging (MRI) techniques. Indeed, there is currently no clinical imaging modality of sufficient sensitivity to detect damage to the chondral matrix and/or cells without visible disruption to the articular surface (Buckwalter 2002).

In AC research, CLSM has been used to characterize both healthy and degenerated cartilage. The major studies in this field and the CLSM techniques that they have employed are reviewed below.

Characterization of Healthy and Degenerate Articular Cartilage

For the assessment of AC condition, CLSM has been used in a number of studies to validate the ultra-structural models (Fig. 1) of AC (Clarke 1974; Stockwell 1997), and to study the physiology and ultrastructures of AC (Hedlund et al. 1994). In addition, CLSM has also been used to assess the early degenerative changes associated with the progression of osteoarthritis (OA). It is noted that in contrast to many of the existing arthroscopically accessed cartilage scoring systems for the clinical assessment of AC lesions and matrix degeneration, which only give little detail with regard to subsurface tissue micro-architecture (Dougados et al. 1994), the use of CLSM has been successful in obtaining detailed 3D microscopic representations of the tissue architecture (Fig. 2; Bush and Hall 2003; Chiang et al. 1997; Hirsch et al. 1993).

Confocal imaging has also been indicated as a relevant tool for the research of articular elastin fibres (De Carvalho and Taboga 1996). In this role, CLSM pro-
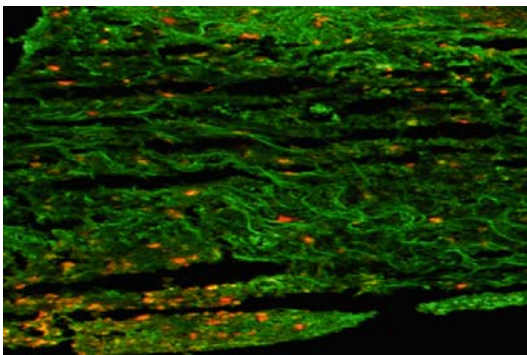
Figure 2. Matrix-induced autologous chondrocyte implantation (MACI). Human autologous chondrocytes labeled with PKH26 (Sigma) were inoculated into the type-I/III collagen scaffold. These cells were implanted into the compartment of cartilage defect in a joint for the regeneration of cartilage. The PKH-26-labeled chondrocytes (*red*) can be monitored in vivo for up to 2 weeks after surgery for the cell migration and survival in the collagen scaffold (*green*)

vides distinct advantages over conventional histological techniques by facilitating the use of thicker sections while simultaneously providing improved resolution capable of imaging finer microstructural details (De Carvalho and Taboga 1996). Furthermore, CLSM has been used to characterize the morphology of chondrocytes from OA and non-OA human AC, and examine the appearance and frequency of multiple elongated processes radiating into the ECM (Holloway et al. 2004). Immunofluorescent staining of the cytoskeletal protein vimentin was used to test the hypothesized morphological difference between OA and non-OA chondrocytes (Holloway et al. 2004).

Cartilage Compression: the Deformation Behaviour of Articular Chondrocytes

The mechanical properties of AC have been the subject of extensive research (Korhonen et al. 2002). On the cellular level, compression experiments have often utilized CLSM as a means of measuring changes in chondrocyte morphology, usually quantified in terms of changes in surface area or volume. Chondrocyte morphology has been established as a key link in describing the behaviour of AC under compression, both in terms of the biomechanics of load bearing and strain distribution, and also with regard to the specific cellular biosynthetic response. For this search, studies have been performed by using CLSM to characterize chondrocyte regulation of metabolic activity via mechanical signal transduction. Results found that the use of CLSM for volumetric analysis correlates well with findings from conventional stereological techniques (Guilak 1995; Guilak et al. 1994, 1995, 1999).

Along with tissue explants, CLSM has also been used to quantify the deformation behaviour of chondrocytes cultured within labelled agarose gels (Knight et al. 1998; Lee et al. 2000). Utilizing the post-imaging 3D morphological analysis, CLSM reported specific cell-shape changes due to compression (spherical to ellipsoidal, with volume conserved) and quantified the relationship between cell membrane and cell-nucleus deformation (Knight et al. 2002).

The issue of chondrocyte death due to cyclical loading was recently the topic of a viability study using live and dead fluorescent assays with CLSM imaging to identify cell apoptosis (Chen et al. 2003). A quantitative analysis of cell death was performed employing the "area method" in order to establish the depth and extent of cell death within the AC structure. This study concluded that the extent of chondrocyte death in compressed cartilage explants was "time, stress and location dependent", with a strong dependence on the "location and extent of collagen damage" (Chen et al. 2003).

Characterization of Collagen

In any collagen-reinforced structure, the 3D architecture of the collagen fibrils is of interest to researchers from the pathological and biomechanics perspective. The CLSM has been used to enable the measurement of the septal fibre angles that define the biomechanical properties of both the perimysial and endomsial septa (Dolber and Spach 1993; Niyibizi et al. 1996).

As the primary functional unit in AC, establishment of the type and distribution and organization of collagen within the chondron has important implications in the mechanotransduction between the chondrocyte and the matrix in which it resides (Poole et al. 1992). Visualization of type-VI collagen via CLSM detailed the interaction between the fibrous pericellular matrix and the chondrocyte membrane (Poole et al. 1992). In addition, CLSM has also been used for a comparative and systematic analysis of the differences in distribution patterns of type-VI collagen between normal and osteoarthritic AC (Chang et al. 1997; Hambach et al. 1998). Using this investigation technique the turnover of collagen in normal cartilage was demonstrated and an increase in collagen synthesis in the middle and deep zones of OA cartilage was reported (Hambach et al. 1998).

Investigation of Cartilage Repair Techniques

While focal chondral lesions are typically assessed via conventional arthroscopy, the emergence of novel surgical and pharmacological cartilage repair techniques has prompted the need for clinical methods to monitor cartilage repair, regeneration or degeneration (Hunziker et al. 2001; Mori et al. 1999). In this role CLSM has been employed in a number of studies to assess the relative efficacy of alternative cartilage repair techniques. The CLSM has permitted the ex-vivo and in vitro characterization of articular chondrocytes and their mechanical environment, a trait which has been used in the assessment of newly developed autologous chondrocyte transplantation techniques. A recently developed confocal arthroscope shows great promise in this field (Jones et al. 2004).

In addition, CLSM has been employed to assess the factors affecting the efficacy of bovine chondrocyte transplantation in vivo (Manolopoulos et al. 1999), to accurately establish chondrocyte viability in vitro following radiofrequency energy (RFE) treatment (Lu et al. 2001), to investigate the efficacy of cell-coating methods for promoting the adherence of chondrogenic progenitor cells to specific matrix molecules, and to compare the surgical techniques following allografts transplantation in an ovine model (Gole et al. 2004) concluded that chondrocyte condition can be determined with significant reliability when assessed via CLSM in combination with metabolic, histological and biomechanical measures.

CLSM Assessment of Bone

Traditional methods of preparing bone specimens required thin sectioning followed by preparation techniques such as decalcification. These methods have their faults including distortion of tissue structures (Mawhinney et al. 1983; Zheng et al. 1997). The difficulties associated with the sectioning of bone for conventional imaging have, as in cartilage research, led to the employment of CLSM for the examination and assessment of bone architecture (Fujii et al. 1998; Zheng et al. 1997). The use of confocal microscopy for the examination of thick tissue sections is flourishing. The ability of CLSM to generate optical sections of a higher resolution than conventional polarized

light microscopy was used to characterize the unembedded histopathology of fresh bone and bone allografts (Fujii et al. 1998; Zheng et al. 1997). In this role, confocal imaging was found to be of particular benefit in the imaging and assessment of the cellular architecture (Figs. 3 & 4: of bone by retaining structural details, minimizing visualization artefacts and enabling the examination of bone-cement interfaces. The CLSM has also been employed to visualize the four-dimensional remodelling of bone labelled with dual osteotropic assays in vivo (Konijn et al. 1996).

Kazama et al. (1993) reported on the use of confocal laser scanning microscopy for the observation of bone specimens. As sections > 20 µm in thickness could not be imaged with the conventional light microscope, bone cells could only vaguely be seen; however, confocal microscopy allowed imaging of the bone at higher magnification with great clarity. The ruffled borders of osteoclasts could be seen at 400× magnification. The lamellar structure of bone could also be seen with the confo-
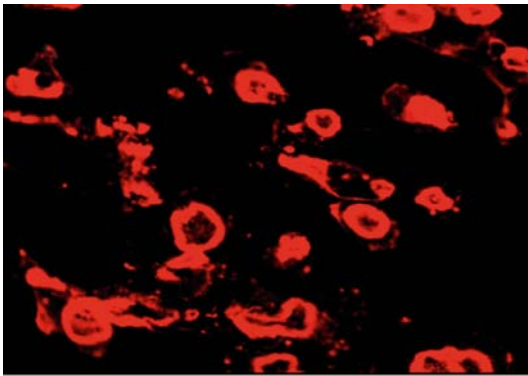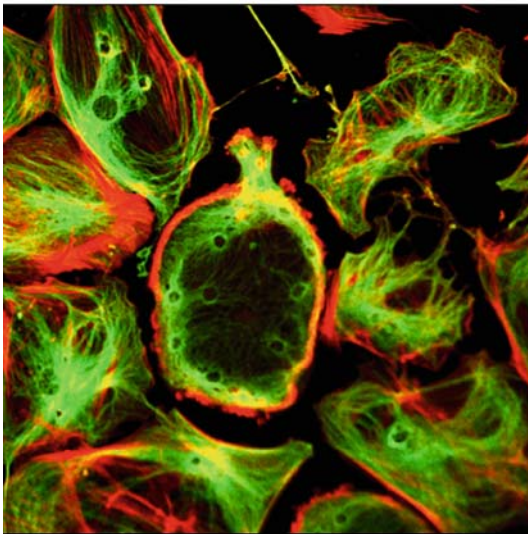
Figure 3. a Confocal micrographs of bone-resorbing osteoclasts. Primary osteoclasts were mechanically disaggregated from the long bones of neonatal rats and cultured on de-vitalized bovine cortical bone slices for 48 h. Cells were then fixed and permeabilized before immunostaining with a rhodamide-conjugated phalloidin antibody to visualize filamentous actin (F-actin). **b** High-magnification confocal image of osteoclasts cultured on glass coverslip. Cells were fixed and immunostained with specific antibodies to visualize F-actin (*red*) and microtubules (*green*)

cal microscope, revealing concentric layers of bone surrounding a central vascular channel. Five-micron sections provided acceptable images with both light and fluorescence microscopy. It was noted, however, that these specimens shrunk by an average 20% when compared with confocal images of the adjacent tissue. The current use of bone biopsy in renal disease is for morphological assessment. As noted, thin sectioning of non-decalcified bone can lead to shrinkage, and as such, Kazama et al. (1993) suggested that this method of bone morphometry should be avoided as much as possible. It was also suggested that confocal microscopy only could produce accurately focused images suitable for detailed bone morphometry of non-decalcified biopsy tissues. Lamellar structure could also be observed, a feature usually lost when imaging with plain light microscopy. Additionally, CLSM has the advantage of being able to construct 3D images; tissues only require a simpler preparation method, which they suggested would allow rapid pathological diagnosis (Fig. 4)

With the development of greater computing power in the mid-1990s, researchers were able to reconstruct 3D images of newly formed bone which tremendously facilitated the study of bone tissue. Konijn et al. (1996) utilized confocal microscopy to assess bone remodelling in a rabbit model and examine the whole calvarial specimen from surface to the deepest layers without any prior treatment. In addition, Zheng et al. (1997) reported on a rapid method for visualizing bone in 100 to 400 μm sec-
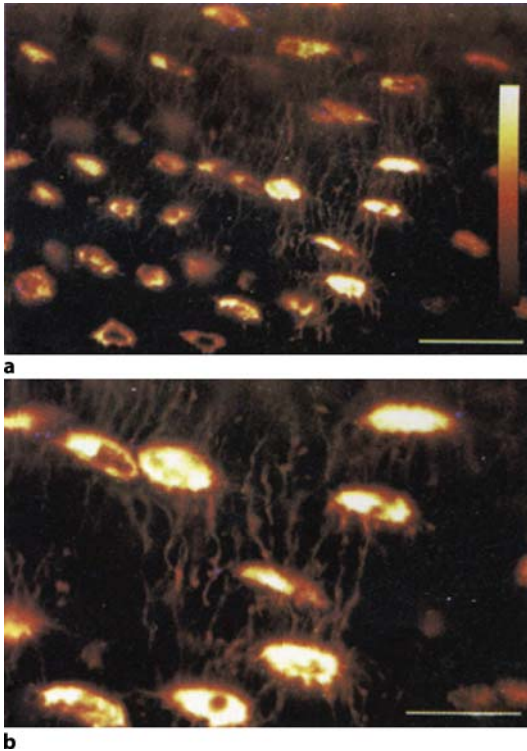
Figure 4. a Confocal images of human cortical bone stained with eosin. Extended focus merged image of 22 optical sections taken at 1 μm intervals demonstrated the architecture of the osteocytic and canlicular network. *Bar* = 50 μm. **b** High magnification of the dentritic network of osteocytes. *Bar* = 25 μm

tions. By taking tissue from sheep and human frozen bone, they were able to assess the cellular detail of bone by confocal microscopy, suggesting that this method of examination might help in pathological diagnosis as optical sectioning can replace many of the time-consuming aspects of preparing bone for histological examination. Moreover, this imaging technique has also been used to investigate 3D distribution of osteocyte processes (Kamioka et al. 2001), the role of ultra-microcracks microdamage in fragility of osteoporotic bone (Fazzalari et al. 1997; Burr et al. 1997), its response to bending (Boyce et al. 1998) and its correlation with age (Ziopus et al. 2001).

CLSM Assessment of Ligament and Tendon

Ligamentous collagen fibrils attach to bone by first passing through non-mineralized and mineralized fibrocartilage present at the ligament-bone interface. The role of this fibrocartilaginous zone of the ligament-bone interface is thought to be important in minimizing mechanical stress. Several studies employing CLSM and immunofluorescence techniques have been conducted in order to characterize the collagens present in isolated ligaments. During the course of their extensive studies of the ligament-bone interface, Niyibizi and Visconti have identified cartilage collagen types I, II, V, IX, X and XI (Niyibizi et al. 1994, 1996), which have important implications for emerging tissue-engineered therapeutic treatments.

In addition, by using CLSM, Visconti et al. (1996) have examined the collagen fibrils at the ligament-bone interface of bovine ligaments to investigate the cellular composition and ECM organization with consideration in its biochemical constituents and biomechanical function. This study illustrated that the presence of cartilage-specific collagens (II and IX) indicates that the ligamentous insertions of the MCL and ACL are fibrocartilaginous, and phenotypic differences were found between these collagens and similar collagens isolated from the AC of the same animals thus implying that the cartilaginous components of the ligamentous insertion play roles in both anchorage, load carriage and stress modulation (Visconti et al. 1996).

The CLSM was also employed by Provenzano et al. (2002) to examine subfailure damage in ligaments at the cellular level using rat medial collateral ligament (MCL). Importantly, the results of this study suggest that, when analyzed as a function of applied strain, tissue stretch-induced structural damage and cellular damage display very different patterns.

While much of the ligament research previously discussed has primarily involved biomechanical property investigation, CLSM has also been employed for purely anatomical studies. In an effort to elucidate the role of oxytalan in periodontal ligament, Chantawiboonchai et al. (1998) sought to improve CLSM techniques for examining the distribution of oxytalan fibres in mice and study of skin ligaments (SL) in subcutaneous regions (Nash et al. 2004) for the reason that CLSM enables preservation of fine fibrous structures with less artefactual damage than conventional H&E histology technique.

In a similar fashion to cartilage compression experiments, the in situ changes in cell morphology and nucleus deformation in tendons under tensile load have also

been analyzed utilizing CLSM, with particular attention being paid to cellular biome-chanical tension relationships (Arnoczky et al. 2004).

The study of tail-tendon cell morphology was conducted by Arnoczky et al. (2002), who used CLSM to examine the in situ deformation of cell nuclei under tensile load. While unable to establish exact cell morphology due to a lack of volumetric analysis, this study was able to show a weak correlation between local and whole-tissue strain, thereby supporting the hypothesis that mechanical loads placed on tendons result in a concomitant in situ deformation of the cell nucleus. This association is thought to have important implications with regard to cell signalling. It is though that this deformation of the cell and nucleus leads to downstream intracellular signalling.

In further demonstration of the versatility of CLSM and the broad range of applications of this imaging modality, Soler et al. (2004) have recently conducted a study into the development of muscles and tendons of the Drosophila leg. Drosophila are small two-winged fruit flies frequently used in genetic research, in this case via the use of a green fluorescent protein (GFP) marker for the tracking of leg development. Using CLSM, muscle development was shown to be closely associated with the formation of internal tendons.

In an ophthalmic study, CLSM imaging with the technique of double-fluorescent labelling and 3D reconstruction has been utilized by Blumer et al. (2003) for examining the innervation pattern of muscle spindles (MSps) and Golgi tendon organs (GTOs) in bovine calf extraocular muscle. Muscles were also imaged with light microscopy and transmission electron microscopy. The CLSM imaging following double staining of nerve terminals with synaptophysin and a-bungarotoxin demonstrated the fine structural features thereby confirming their proprioceptive nature. In this application, the resolution and fine detail provided by CLSM enabled definition of the spatial arrangement of the GTO tissue components and provided unique information on the morphology and proprioceptive nature of MSps and GTOs (Blumer et al. 2003).

CLSM Assessment of Prothesis

Confocal microscopy has been used to evaluate the contact between prosthetic implants and bone. Takeshita et al. (1997) further evaluated the bone formation around HA-coated implants using confocal microscopy. This study compared the bone reaction to HA implants as compared with titanium (Ti) implants and evaluated the bone formation around HA implants using CLSM. Sixty-five rats were divided into two groups, 60 for histological observation and 5 for time-labelling. Cylindrical HA and Ti implants were inserted into the diaphyseal region of the tibia. Thirty-five HA implants and 30 Ti implants were inserted. For the time-labelling experiment, 5 rats with HA implants had oxytetracycline injected intraperitoneally at 7 days, then calcein at 14 days, then alizarin at 28 days. The rats were killed at 5, 7, 14, 28, 84 and 168 days after implantation. Tibial specimens were fixed in ethanol and embedded in resin for histological processing. Sections were taken for light microscopy. Titanium implants revealed a covering of thick lamellar bone. Fibroblast cells were seen

to interrupt the junction between bone and implant. The HA implants showed complete encapsulation with bone with thinner surrounding bone tissue. It was thought that the thicker bone around the titanium implants might reflect a foreign-body reaction. Histomorphometric observation revealed a significant difference in percent bone contact between Ti and HA in all experiments (Takeshita et al. 1997).

More recently, investigators have been drawn to other methods of coating implants in order to improve their biocompatibility and, hence, stability. In a study using CLSM, Kajiwara et al (2005) reported improved bone formation around implants coated with pamidronate, a bisphosphonate. Bisphosphonates enhance bone formation through many mechanisms of action. The aim of their study was to compare the quantity of new bone formed around a new pamidronate-coated implant. Moreover, Zheng et al. (1997) have used CLSM for the morphological analyses of fresh unembedding human cortical bone, bone allograft and bone-cement interfaces, which showed that CLSM provided a relatively easy and rapid means for assessment of the histology of normal and pathological bone.

Future Developments

Recent technological advances in CLSM have created more powerful imaging devices that continue to approach the theoretical resolution limitation, with improved operating systems increasing the "user-friendliness". This progress, along with advances in post-imaging analysis capabilities and constant developments in fluorescence and immunofluorescence staining techniques, suggest that the future of CLSM in orthopaedic research applications is promising indeed. The potential combination of LSCA monitoring with the use of GFP marker tracking may one day provide a contrast-agent-free method for long-term monitoring of therapies such as matrix-induced autologous chondrocyte implantation (MACI; Jones 2004).

References

Arnoczky SP, Lavagnino M, Whallon JH, Hoonjan A (2002) In situ cell nucleus deformation in tendons under tensile load; a morphological analysis using confocal microscopy. J Orthop Res 20:29–35

Arnoczky SP, Tian T, Lavagnino M, Gardner K (2004) Ex vivo static tensile loading inhibits MMP-1 expression in rat tail tendon cells through a cytoskeletally based mechanotransduction mechanism. J Orthop Res 22:328–333

Blumer R, Konakci KZ, Brugger PC, Jose M, Blumer F, Moser D, Schoefer C, Lukas JR, Streicher J (2003) Muscle spindles and Golgi tendon organs in bovine calf extraocular muscle studied by means of double-fluorescent labeling, electron microscopy, and three-dimensional reconstruction. Experimental Eye Res 77:447–462

Boyce TM, Fyhrie DP, Glotkowski MC, Radin EL, Schaffler MB (1998) Damage type and strain mode associations in human compact bone bending fatigue. J Orthop Res 16:322–329

Brakenhoff GJ, Blom P, Barends PJ (1997) Confocal scanning light microscopy with high aperture immersion lenses. J Microsc 117:219–232

Buckwalter JA (2002) Articular cartilage injuries. Clin Orthop Relat Res 402:21–37

Burr DB, Forwood MR, Fyhrie DP, Martin B, Schaffler MB, Turner CH (1997) Bone microdamage and skeletal fragility in osteoporotic and stress fractures. J Bone Miner Res 12:6–15

Bush PG, Hall AC (2003) The volume and morphology of chondrocytes within non-degenerate and degenerate human articular cartilage. Osteoarthritis Cartilage 11:242–251

Carvalho HF de, Taboga SR (1996) The applicability of hematoxylin-eosin staining plus fluorescence or confocal laser scanning microscopy to the study of elastic fibers in cartilages. Life Sci Cell Biol 319:991–996

Chang J, Nakajima H, Poole CA (1997) Structural colocalisation of type VI collagen and fibronectin in agarose cultured chondrocytes and chondrons extracted from adult canine tibial cartilage. J Anat 190:523–532

Chantawiboonchai P, Warita H, Ohya K, Soma K (1998) Confocal laser scanning-microscopic observations on the three-dimensional distribution of oxytalan fibres in mouse periodontal ligament. Arch Oral Biol 43:811–817

Chen CT, Bhargava M, Lin PM, Torzilli PA (2003) Time, stress, and location dependent chondrocyte death and collagen damage in cyclically loaded articular cartilage. J Orthop Res 21:888–898

Chiang EH, Laing TJ, Meyer CR, Boes JL, Rubin JM, Adler RS (1997) Ultrasonic characterisation of in vitro osteoarthritic articular cartilage with validation by confocal microscopy. Ultrasound Med Biol 23:205–213

Clarke IC (1974) Articular cartilage: a review and scanning electron microscope study. J Anat 118:261–280

Denk W, Strickler J, Webb W (1990) Two-photon laser scanning fluorescence microscopy. Science 248:73–76

Dolber PC, Spach MS (1993) Conventional and confocal fluorescence microscopy of collagen fibers in the heart. J Histochem Cytochem 41:465–469

Dougados M, Ayral X, Listrat V, Gueguen A, Bahuaud J, Beaufils P, Beguin JA, Bonvarlet JP, Boyer T, Coudane H, Delaunay C, Dorfmann H, Dubos JP, Frank A, Kempf JF, Locker B, Prudhon JL, Thiery J (1994) The SFA system for assessing articular cartilage lesions at arthroscopy of the knee, arthroscopy. J Arthrosc Relat Surg10:69–77

Dunn AK, Wallace VP, Coleno M, Berns MW, Tromberg BJ (2000) Influence of optical properties on two-photon fluorescence imaging in turbid samples. Appl Opt 39:1194–1201

Fazzalari NL, Parkinson IH (1997) Fractal properties of subchondral cancellous bone in severe osteoarthritis of the hip. J Bone Miner Res 12:632–640

Fujii H, Wood DJ, Papadimitriou JM, Zheng MH (1998) Technique report: application of confocal laser scanning microscopy in bone. J Musculoskeletal Res 2:65–71

Ghiggino KP, Harris MR, Spizzirri PG (1992) Fluorescence lifetime measurements using a novel fiber-optic laser scanning confocal microscope. Rev Sci Instruments 63:2999–3002

Gole MD, Poulsen D, Marzo JM, Ziv I (2004) Chondrocyte viability in press-fit cryopreserved osteochondral allografts. J Orthop Res 22:781–787

Guilak F (1994) Volume and surface area measurement of viable chondrocytes in situ using geometric modelling of serial confocal sections. J Microsc 173:245–256

Guilak F (1995) Compression-induced changes in the shape and volume of the chondrocyte nucleus. J Biomech 28:1529–1541

Guilak F, Ratcliffe A, Mow VC (1995) Chondrocyte deformation and local tissue strain in articular cartilage a confocal microscopy study. J Orthop Res 13:410–421

Guilak F, Jones WR, Ting-Beall HP, Lee GM (1999) The deformation behaviour and mechanical properties of chondrocytes in articular cartilage. Osteoarthritis Cartilage 7:59–70

Hader DP (1992) Image analysis in biology. CRC Press, Boca Raton, pp 17–21

Hambach L, Neureiter D, Zeiler G, Kirchner T, Aigner T (1998) Severe Disturbance of the distribution and expression of type VI collagen chains in osteoarthritic articular cartilage. Arthritis Rheum 41:986–996

Harvath L (1997) Overview of fluorescence analysis with the confocal microscope. In: Javois LC (ed) Methods in molecular biology. Humana Press, Totowa, New Jersey, pp 1–69

Hedlund H, Bismar H, Mengarelli-Widhilom S, FPR, Svensson O (1994) Studies of the cell columns of articular cartilage using UV-confocal scanning laser microscopy and 3D image processing. Eur J Exp Musculoskel Res 3:93–98

Hirsch MS, Hartford Svoboda KK (1993) Confocal microscopy of whole mount embryonic cartilage: intracellular localization of F-actin, chick prolyl hydroxylase and type-II collagen mRNA. Micron 24:587–594

Holloway I, Kayser MV, Lee DA, Bader DL, Bentley G, Knight MM (2004) Increased presence of cells with multiple elongated processes in osteoarthritic femoral head cartilage. Osteoarthritis Cartilage 12:17–24

Holst GC (1996) CCD arrays, cameras, and displays. SPIE Optical Engineering Press, Bellingham, Washington

Hunziker EB (2001) Articular cartilage repair: basic science and clinical progress. A review of the current status and prospects. Osteoarthritis Cartilage 10:432–463

Jones CW, Keogh A, Smolinski D, Wu JP, Kirk TB, Zheng MH (2004) Histological assessment of the chondral and connective tissues of the knee by confocal arthroscope. J Musculoskelet Res 8:75–86

Kajiwara H, Yamaza T, Yoshinari M, Goto T, Iyama S, Atsuta I, Kido MA, Tanaka T (2005) The bisphosphonate pamidronate on the surface of titanium stimulates bone formation around tibial implants in rats. Biomaterials 26:581–587

Kamioka H, Honjo T, Takano-Yamamoto T (2001) A three-dimensional distribution of osteocyte processes revealed by the combination of confocal laser scanning microscopy and differential interference contrast microscopy. Bone 28:145–149

Kazama JJ, Gejyo F, Ejiri S, Okada M, Ei I, Arakawa M, Ozawa H (1993) Application of confocal laser scanning microscopy to the observation of bone biopsy specimens. Bone 14:885–889

Knight MM, Lee DA, Bader DL (1998) The influence of elaborated pericellular matrix on the deformation of isolated articular chondrocytes cultured in agarose. Biochem Biophys Acta 1405:67–77

Knight MM, van de Breevaart Bravenboer J, Lee DA, van Osch GJVM, Weinanas H, Bader DL (2002) Cell and nucleus deformation in compressed chondrocyte-alginate constructs: temporal changes and calculation of cell modulus. Biochem Biophys Acta 1570:1–8

Konijn GA, Vardaxis NJ, Boon ME, Kok LP, Rietveld DC, Schut JJ (1996) 3-D confocal microscopy for visualisation of bone remodelling. Path Res Pract 192:566–572

Korhonen RK, Laasanen MS, Toyras J, Rieppo J, Hirvonon J, Helminen HJ, Jurvelin JS (2002) Comparison of the equilibrium response of articular cartilage in unconfined compression, confined compression and indentation. J Biomech 35:903–909

Lee DA, Knight MM, Bolton JF, Idowu BD, Kayser MV, Bader DL (2000) Chondrocyte deformation within compressed agarose constructs at the cellular and sub-cellular levels. J Biomech 33:81–95

Lu Y, Edwards III RB, Kalscheur VL, Nho S, Cole BJ, Markel MD (2001) Effect of bipolar radiofrequency energy on human articular cartilage: comparison of confocal laser microscopy and light microscopy. Arthroscopy 17:117–123

Manolopoulos V, Wayne Marshall K, Zhang H, Trogadis J, Tremblay L, Doherty PJ (1999) Factors affecting the efficacy of bovine chondrocyte transplantation in vitro. Osteoarthritis Cartilage 7:453–460

Mawhinney WHB, Ellis HA (1983) A technique for plastic embedding of mineralised bone. J Clin Pathol 37:1197–1199

Minsky M (1988) Memoir on inventing the confocal scanning microscope. Scanning 10:128–138

Mori R, Ochi M, Sakai Y, Adachi N, Uchio Y (1999) Clinical significance of magnetic resonance imaging (MRI) for focal chondral lesions. Magn Reson Imaging 17:1135–1140

Nash LG, Phillips MN, Nicholoson H, Barnett R, Zhang M (2004) Skin ligaments: regional distribution and variation in morphology. Clin Anat 17:287–293

Niyibizi C, Visconti CS, Kavalkovich K, Woo SL-Y (1994) Collagens in an adult bovine medial collateral ligament: immunofluorescence localization by confocal microscopy reveals that type XIV collagen predominates at the ligament–bone junction. Matrix Biol 14:743–751

Niyibizi C, Visconti CS, Gibson G, Kavalkovich K (1996) Identification and immunolocalization of type X collagen at the ligament–bone interface. Biochem Biophys Res Commun 222:584–589

Pastoureau P, Leduc S, Chomel A, De Ceuninck F (2003) Quantitative assessment of articular cartilage and subchondral bone histology in the meniscectomized guinea pig model of osteoarthritis. Osteoarthritis Cartilage 11:412–423

Poole CA, Ayad S, Gilbert RT (1992) Chondrons from articular cartilage. Immunohistochemical evaluation of type VI collagen organisation in isolated chondrons by light, confocal and electron microscopy. J Cell Sci 103:1101–1110

Provenzano PP, Heisey D, Hayashi K, Lakes R, Ray Vanderby RJ (2002) Subfailure damage in ligament: a structural and cellular evaluation. J Appl Physiol 92:362–371

Rigaut JP, Carvajal-Gonzalea S, Vassy J (1992) Confocal image cytometry: quantitative analysis of three-dimensional images obtained by confocal scanning microscopy. In: Hader DP (ed) Image analysis in biology. CRC Press, Boca Raton, pp 109–133

Shaw P (1994) Deconvolution in 3-D optical microscopy. Histochem J 26:687–694

Sheppard CJR (1994) Confocal microscopy: basic principles and system performance. In: Cheng PC, Lin TH, Wu WL, Wu JL (eds) Multidimensional microscopy. Springer, Berlin Heidelberg New York, pp 1–19

Smolinski D, Wu JP, Jones CW, Zheng MH, O'Hara LJ, Miller K (2003) The confocal arthroscope as a cartilage optical biopsy tool. Osteoarthritis Cartilage 11:S111–S112

Soler C, Daczewska M, Da Ponte JP, Dastugue B, Jagla K (2004) Coordinated development of muscles and tendons of the Drosophila leg. Development 131:6041–6051

Stockwell RA (1979) The biology of cartilage cells. Cambridge University Press, Cambridge

Takeshita F, Iyama S, Ayukawa Y, Akedo H, Suetsugu T (1997) Study of bone formation around dense hydroxyapatite implants using light microscopy, image processing and confocal laser scanning microscopy. Biomaterials 18:317–322

Visconti CS, Kavalkovich K, Wu JJ, Niyibizi C (1996) Biochemical analysis of collagens at the ligament–bone interface reveals presence of cartilage-specific collagens. Arch Biochem Biophys 328:135–142

Zheng MH, Bruining HG, Cody SH, Brankov B, Wood DJ, Papadimitriou JM (1997) A rapid method for the assessment of bone architecture by confocal microscopy. Histochem J 29:639–643

Ziopus P (2001) Accumulation of in vivo fatigue microdamage and its relation to biomechanical properties in ageing human cortical bone. J Microsc 201:270–278

Specific Applications of Advances in Musculoskeletal and Scaffold Biomaterial Imaging Technologies

In Assessment of Osteoporosis and Treatment

TEM Study of Bone and Scaffold Materials

Shu-Xin Qu[1] (✉) , Xiong Lu[1,2], and Yang Leng[2]

[1] Key Lab of Advanced Technologies of Materials, Ministry of Education, School of Material
Science and Engineering, Southwest Jiaotong University, Chengdu 610031, China
e-mail: qushuxin@home.swjtu.edu.ch
[2] Department of Mechanical Engineering, Hong Kong University of Science
and Technology, Hong Kong, China

Abstract

This chapter summarizes the application of transmission electron microscopy (TEM) to study the structure of normal and pathological bone, the interface between bone and scaffold materials, and the nucleation and structure of calcium phosphate on various scaffold materials. The principles of different TEM techniques, including bright-field image, dark-field image, electron diffraction, and high-resolution TEM are also briefly reviewed. The protocol of biological tissue processing for TEM is introduced. The typical TEM applications in investigation of bone and scaffold materials are highlighted as reference for related study and application.

Introduction

According to the review by Rubin and Jasiuk (2005), bone is a natural composite material with a hierarchical structure. Five structural levels can be distinguished in bone: (a) at macrostructural level: entire bone organ; (b) at mesostructural level: trabecular and cortical bone; (c) at microstructural (or lamellae) level ($10-500\,\mu m$): single osteons and trabeculae (trabecular pockets); (d) at sub-microstructural level ($1-10\,\mu m$): single lamellae; and (e) at nanostructural level (below $1\,\mu m$): collagen fibrils and apatite crystals (Rubin and Jasiuk 2005). The nanostructural level of bone can be investigated by transmission electron microscopy (TEM), including various techniques such as bright field image, dark field image, and high-resolution TEM. The TEM gives insight into the debated characteristics of normal and diseased bone structure, such as the exact crystal shape, size, and its three-dimensional (3D) relationship with collagen fibrils.

TEM in Bone Research

There are a number of studies focusing on the mineralization mechanism and ultra-structure of bone. Bone is one of the few tissues with a mineral density high enough to

be imaged by TEM without staining. The TEM is useful in examining the morphological and crystalline arrangement of mineral apatite and crystal-collagen interaction. Su and coworkers observed the organization of apatite crystals in human wove bone by TEM (Su et al. 2003). It was shown that the apatite crystals in woven bone were platelet-shaped similar to the mature crystals of lamellar bone, but the average crystal dimensions were considerably smaller than those of apatite crystal in lamellar bone due to the high rate of the old bone resorption and new bone formation in wove bone (Su et al. 2003). Apatite crystals were noted on the collagen fibrils in woven bone. In densely packed woven bone, the periodicity of mineral deposited on individual fibrils was in registration over many fibrils. In addition to their association with collagen surfaces, crystals also obviously were distributed in both extrafibrillar and intrafibrillar collagen region. In both cases, the minerals were crystalline and defect-free (Su et al. 2003).

Lees (1996) reported that there were two sets of seemingly contradictory data relating to the ultrastructure of mineralized collagenous tissue. Moreover, there have been some reports regarding with the structure of bone disease, such as osteoporosis, Paget's bone disease, the age-induced transparent dentin, and damaged bone (Chappard et al. 1998; Porter et al. 2005; Rubin et al. 2003; Rubin and Jasiuk 2005; Sahar et al. 2005). It was shown that the lamellar structure of osteoporotic human trabecular and cortical bone had equivalent collagen organization within the lamellae at the microstructural level. But the plywood-like structures routinely were observed in cortical bone, twisted, rotated or orthogonal, and existed in both normal and osteoporotic human trabecular bone; however, one of the differences involved a more pristine lamellar organization in normal trabecular. There was evidence of lamellar structure alteration by the osteocyte network (Rubin et al. 2003; Rubin and Jasiuk 2005). This gives insight into the difference between normal and osteoporotic trabecular bone including lower bone mineral density (BMD) and thinner (or missing) trabecular. High-resolution TEM revealed that the intertubular mineral crystallites were smaller in transparent dentin, wherein the dentinal tubules become occluded with mineral as a natural progressive consequence of aging (Porter et al. 2005). The intratubular mineral (larger crystals deposited within the tubules) was chemically similar to the surrounding intertubular mineral. These observations support the "dissolution and reprecipitation" mechanism for the formation of transparent dentin (Porter et al. 2005).

Carter et al. (2002) reported the effect of deproteination on bone mineral morphology, which may provide an insight into the biomaterials for scaffold materials and natural bone aging. The TEM can also be used to examine the cell morphology as well as to observe the morphology and structure of inorganic mineral of bone. The TEM examination confirmed the presence of cells with apoptotic changes at various regions of the regenerate (Li et al. 2003).

The TEM was also used to investigate comparatively the morphology and organization of apatite crystallites in natural bone and synthetic hydroxyapatite (HA) materials. It was shown that the mineralization of collagen comprising osteoid was preceded by the formation of apatite crystallites within the fibers at selected periodic sites along their length. Moreover, the very presence in this inorganic material of distinct fibers composed of the crystallites was demonstration of inter-crystallite

bonding. The crystallites of the synthetic HA materials did not display any of these ultrastructural features (Rosen et al. 2002).

TEM Study of Scaffold Materials

In the field of orthopedic surgery, clinical cases often involve various bony defects, which need to be filled and reconstructed. The current bone-repairing or bone-replacing materials include autografts, allografts, and various kinds of synthetic materials such as bioceramics, polymers, metallic materials, and their composites. Calcium phosphate (CaP) biomaterials, such as HA and tricalcium phosphate (TCP), show excellent biocompatibility and bioactivity due to their similar component to the mineral of nature bone; therefore, CaP-based biomaterials, such as CaP bioceramics, CaP cement, CaP bioactive glass, and CaP coating on metal implants have been applied in clinical practice for several decades as scaffold materials. In general, the success of implantation, besides physical and biochemical factors, is strongly dependent on the events which take place along the tissue-implant interface. Several light microscopy investigations have demonstrated that no intermediate layer is detectable at the interface between bone and bioactive biomaterial. Furthermore, the ultrastructure of this interface has been investigated by various TEM techniques (De Lange et al. 1990; Gross et al. 1981; Murai et al. 1996; Neo et al. 1992a,b; Serre et al. 2003; Steflik et al. 1990; Tracy and Doremus 1984).

Gross et al. (1981) reported the TEM observations of the interface between bone and scaffold material (glass ceramics). This study showed that areas with bone connection displayed collagen fibers and deposits of apatite crystals in close relationship to the bulk glass ceramic as well as small particles derived mainly from the glassy phase of the implant (Gross et al. 1981). Tracy and Doremus (1984) examined directly the bone-HA interface by using several TEM techniques, including bright- and dark field image, electron diffraction, and high-resolution imaging. Conventional and high-resolution images of TEM demonstrated the direct chemical bonding formed between HA and bone. The bone at the ceramic surface was the same as normal bone away from the interface.

Neo et al. (1992a,b) studied the differences in ceramic-bone interface among four kinds of surface-active ceramics and resorbable ceramics by TEM. They found that surface-active ceramics bonded to bone through a thin CaP rich layer consisting of fine apatite crystals, to which collagen fibers of the bone reached. It was speculated that the chemical bonding existed between surface-active ceramics and bone. On the other hand, it was confirmed that no apatite layer was presented at the interface between resorbable ceramic and bone. The surface became rough due to degradation, and bone grew into the finest surface irregularities. De Lange et al. (1990) observed the ultrastructural appearance of the HA-bone interface by TEM. They found that there was intimate, direct bone contact without any visible interruption. The bone was of normal lamellar type and continuously connected with the trabecular bone. Bone grew into the finest surface irregularities of the implant. Collagen fibers of the calcified bone matrix were observed within a distance < 500 Å from the implant surface. The thin (20–100 Å) electron dense layer at the bone-implant interface resem-

bled the lamina of organic bone matrix, also seen at the inner walls of the osteocyte lacunes. Moreover, the bone-titanium contact was examined by TEM. It was shown that ultrastructurally a 20- to 50-nm thin amorphous zone, a slender cell layer, and/or a poorly mineralized zone were interposed between the bone and titanium (Murai et al. 1996). Steflik et al. (1990) also reported that an unmineralized collagen fiber matrix initially was laid down directly at the implant surface, and that this matrix then was mineralized. The induction of a calcifying matrix was studied in vitro and compared for three biomaterials [collagen sponge, HA materials, and a mixture of both (biostite)] cultured with human osteoblast-like cells. The TEM showed that osteoblasts proliferated and synthesized a new matrix constituted of fibrillar and nonfibrillar element. A deposition of a mineral substance in this newly formed matrix was observed with the collagen sponge and biostite, which were identified as HA crystals (Serre et al. 2003). The authors reported that the fine acicular crystals, which were <100 nm in length, formed on the HA-tricalcium phosphate (HA-TCP) surface in vivo. These acicular crystals have no preference orientation. EDS identified the HA-TCP by detecting only Ca and P, and new bony tissue on the HA-TCP surfaces by detecting S, K, Na as well as Ca and P (Qu et al. 2002). Sautier and coworkers (1992) also reported that there was an electron-dense layer between surface active biomaterials and the neighbouring cells, which was visible and free of collagen before bone formation.

Additionally, there are a number of reports about the CaP nucleation, phase, and structure of the scaffold materials in vivo or in vitro. It was reported that the crystals formed in vitro in dynamic simulated body fluid (SBF) were identified as octacalcium phosphate (OCP), instead of apatite. Most of the precipitated crystals in vivo samples had an HA structure, whereas OCP and dicalcium phosphate (DCPD) were also identified by the authors (Leng et al. 2003). Xin et al. (2005) studied formation of CaP on various bioceramics, including bioglass, A-W glass-ceramics, HA, α-tricalcium phosphate, and β-tricalcium phosphate, showed that ability of inducing CaP formation in SBF was similar among bioceramics, but considerably varied among bioceramics in vivo (Xin et al. 2005). They found that sintered β-TCP exhibited a poor ability of inducing CaP formation both in vitro and in vivo. Our recent TEM study of the formation of CaP on alkali- and heat-treated titanium surfaces revealed that OCP, instead of HA, directly nucleates from amorphous calcium phosphate. The OCP crystals continuously grew on the titanium surface rather than transforming into apatite. Calcium titanate was also identified by electron diffraction (Lu and Leng 2004). The TEM micrograph of self-assembled HA/collagen composite showed that crystal nuclei formed inside the self-assembled collagen fibers, which was in situ nucleated HA nanocrystals (Roceri et al. 2003). The TEM, including electron diffraction pattern, was used to observe the morphologies of precipitated crystals and EDS was employed to analyze the chemical composition (Chang et al. 2000). The TEM confirmed that the precipitated crystals showed different morphologies and were the hexagonal of whitlockite and column ones of wollastonite mainly. The EDS results demonstrated that the precipitated crystals were non-stoichiometic with Si in whitlockite and Mg in wollastonite (Chang et al. 2000). The TEM was used to study the CaP formation in reverse microemulsion. The results showed that the minerals in the deposition were

mainly monetite (DCPA) and the nano-sized needle-like DCPA exhibited preferential orientation along (200) direction (Kong et al. 2005).

In summary, TEM has enough resolution to study the ultrastructure of bone and scaffold materials. Additionally, the electron diffraction and EDS techniques are beneficial for intensifying the phase structure and composition of specimens.

Working Principles

The TEM is an imaging technique whereby a beam of electrons is focused onto a specimen causing an enlarged grey-scale image to appear on a fluorescent screen or film; therefore, it can examine objects on a very fine scale. Electron microscopes (EM) were developed due to the limitation of the magnification and resolution of light microscopes (LM), which depend on the wavelength of light (Eq. 1). The magnification of LM reaches to 1000× and a resolution of LM is generally 0.2 µm. In the early 1930s this theoretical limit had been reached and there was a scientific desire to see the fine details of the interior structures of organic cells (nucleus, mitochondria, etc.). This required 10,000× plus magnification, which was just not possible using LM. The TEM uses electrons as "light source" and their much shorter wavelength make it possible to get a resolution 1000 times better than that of a light microscope. You can see objects to the order of a few angstroms (10^{-10} m) under TEM. For example, you can study small details in the cell or different materials down to near atomic levels. The possibility for high magnifications has made TEM a valuable tool in the medical, biological and material research.

TEM Working Principles

The TEM operates on the same basic principles as the LM but uses electrons instead of light as illumination source (Fig. 1). In optical microscopy, light is used to form the image. As mentioned previously, this restricts the maximum magnification to around 1000 times. As the name suggests, the light passes through the sample in transmitted LM. In TEM, the "light source" at the top of the microscope actually is a filament that can emit electrons. If the filament is heated and a high voltage (the accelerating voltage) of between 40 and 500 kV is passed between it and the anode, the filament will emit electrons. These electrons are accelerated to an anode (positive charge) placed just below the filament, some of which pass through a tiny hole in the anode, to form an electron beam which passes down the column as shown in Fig 1. Instead of glass lenses focusing the light in the light microscope, the TEM uses electromagnetic lenses to focus the electrons into a very thin beam and guide the electron beam path. The electron beam then travels through the specimen put on the sample stage. Depending on the density of the material of the specimen, some of the electrons are scattered and disappear from the beam. At the bottom of the microscope the transmitted electrons hit a fluorescent screen, which gives rise to a grey-scale image:

$$d = \frac{0.61\lambda}{n \sin \alpha} \, , \tag{1}$$
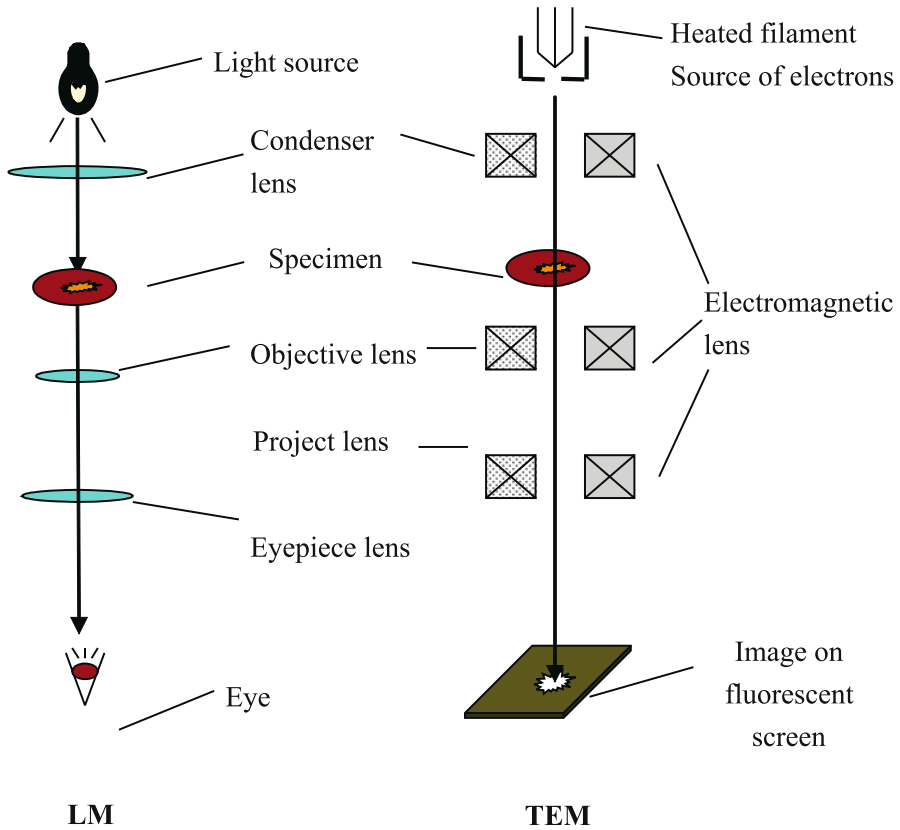
Figure 1. Comparison of imaging acquisition between light microscopy (*LM*) and transmission electron microscope (*TEM*)

where d is resolution of microscopy. The mini distance between two points can be distinguished on the image. The smaller the d, the higher the resolution is. λ is the wavelength of incident beam. n is the relatively refractive coefficient of the medium. $n \sin \alpha$ is numerical aperture.

The high-voltage accelerated electrons in the microscope strike the sample at a high speed and various reactions can occur as shown in Fig. 2. The reactions noted on the top side of the diagram are utilized when examining thick specimens through the techniques such as scanning electron microscopy (SEM), energy dispersive spectrometer (EDS), X-ray photoelectron spectroscopy (XPS) and Auger electron spectrometer (AES), whereas the reactions on the bottom side are those examined in thin specimens by TEM. The electrons interact with the specimen in two ways: inelastic and elastic scattering. Inelastic scattering must be avoided since it contains no local information. The TEM extracts specimen structural information carried by the elastic scattered electrons. The conventional TEM only uses two elastic signals, namely, the transmitted beam and the diffracted beams, because the lattice and the defects of the specimen modulate amplitude and phase of the transmitted electron beam
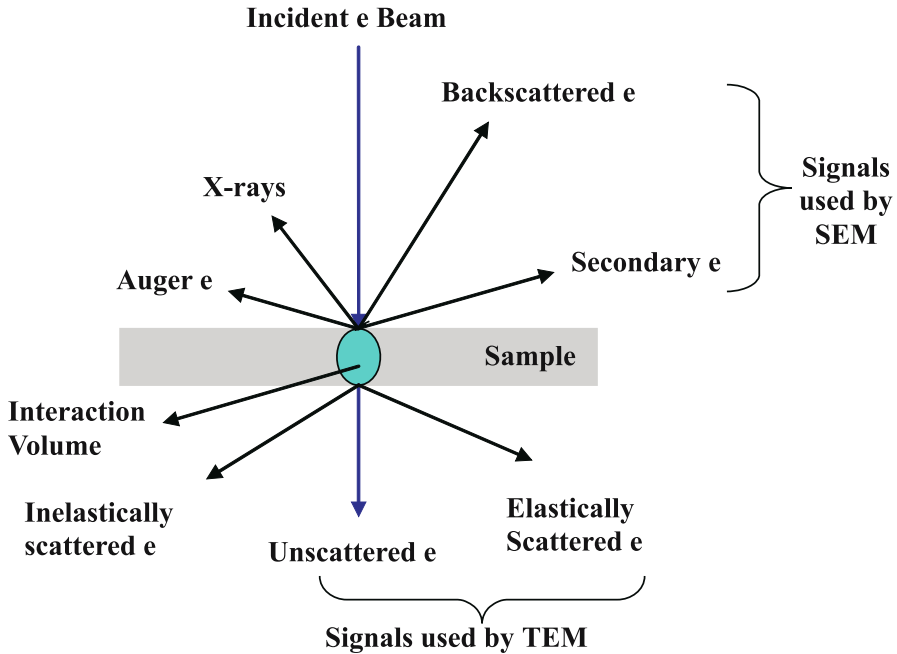
Figure 2. Signals generated when an electron beam interacts with a thin specimen. *SEM* scanning electron microscopy

and the diffracted electron beams. These two signals lead to the two basic operation modes of TEM, namely the image mode and diffraction mode. The information such as the morphology, particle size, defects and grain boundaries can be obtained in the image mode, whereas lattice parameters, crystal orientation and symmetry can be determined in the diffraction mode. The ray paths of TEM system in different mode are shown Fig. 3.

Diffraction Mode Working Principles

Electron diffraction is a collective elastic scattering phenomenon with electrons being scattering by a plane of atoms in crystal materials. The incident electron beam interacts with the atom planes, and diffracted beams are generated when the scattered electron waves interfere with each other constructively, i.e., reinforcement at certain scattering angles. Electron diffraction provides the information of the structure of crystals materials, which tend to generate very strong electron diffraction patterns; however, the amorphous materials, such as polymer and biological specimens, generate very weak diffraction signals. As in X-ray diffraction (XRD), the scattering event can be described as a reflection of the beams at planes of atoms (lattice planes; Fig. 4). The relationship between the interplanar distance, d, of the specimen and diffraction angle, θ, can be described by Bragg's law:

$$2d \sin \theta = n\lambda \ . \tag{2}$$

Diffraction Mode   **Image Mode**
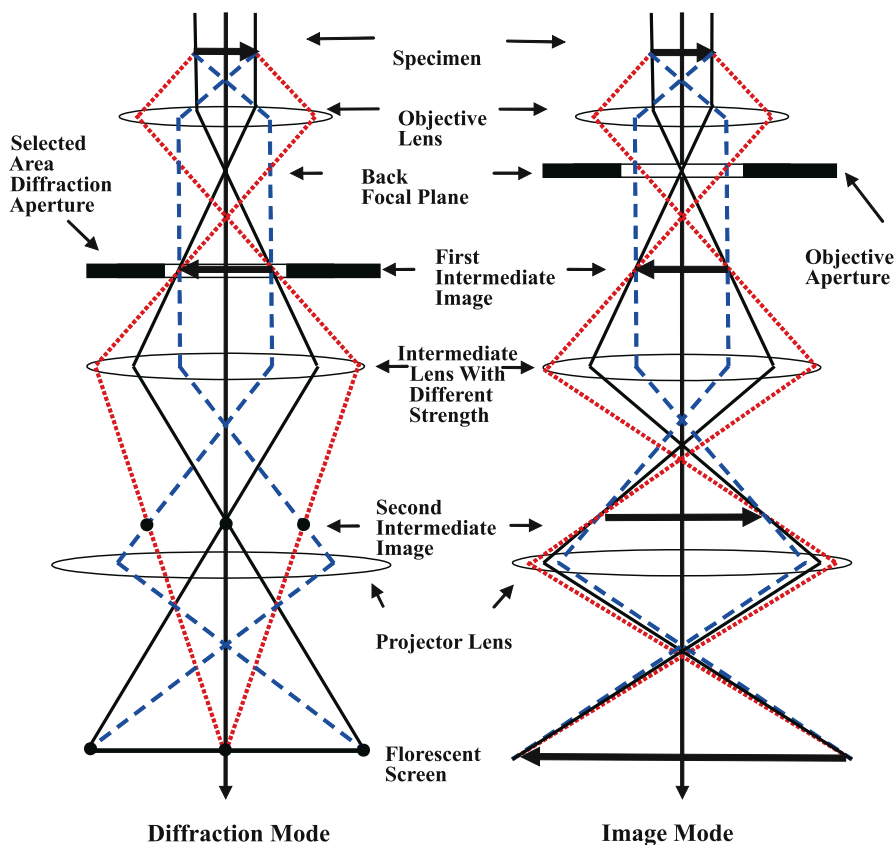
Figure 3. The ray paths at the diffraction mode and image mode. The specimen and its image are demonstrated by the direction of the *horizontal arrow*

There are two ways to obtain a diffraction pattern from a specific area in the specimen being studied. We can either focus the electron beam onto the area of interest or we can select the area using an aperture which encloses only the area of interest. The former technique is known as convergent beam electron diffraction (CBED) and the latter is known as selected area diffraction (SAD). Here we only discuss SAD because it is widely used for identifying inorganic crystalline materials in bone.

The experimental setup for recording the diffraction pattern is shown schematically in Fig. 5. The incident beam and each diffraction beam give a diffraction spot on the screen at a distance of L from the specimen. A flat screen is used because the curvature of the Ewald sphere is usually neglected in electron diffraction. For a diffracted spot at a distance of R from the central spot due to the incident beam, we obtain

$$R = L \tan 2\theta \ . \tag{3}$$

For electron diffraction, 2θ usually is as small as $1 \sim 2$ degree, so that we obtain

$$\mathrm{tg}2\theta \approx 2 \sin \theta \ . \tag{4}$$
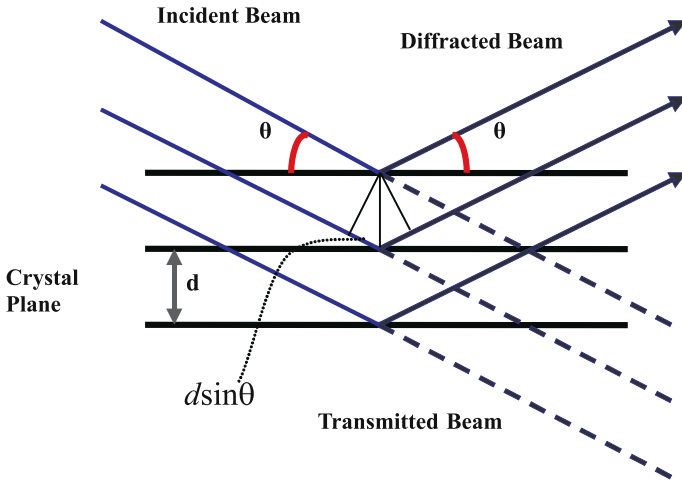
Figure 4. Bragg's law demonstrates the two diffracted beams' interfere constructively. d is the interplanar distance and $d \sin \theta$ is the path difference

From Bragg's law,

$$2 \sin \theta = \frac{\lambda}{d} \, . \tag{5}$$

When $n = 1$, that represents the first-order diffraction; therefore, combining Eqs. (3)–(5) we obtain

$$d = \frac{\lambda L}{R} \, . \tag{6}$$

Equation (6) reveals that the R in the diffraction pattern can be directly used for the calculation of the interplanar distance of the specimen. It also should be pointed out
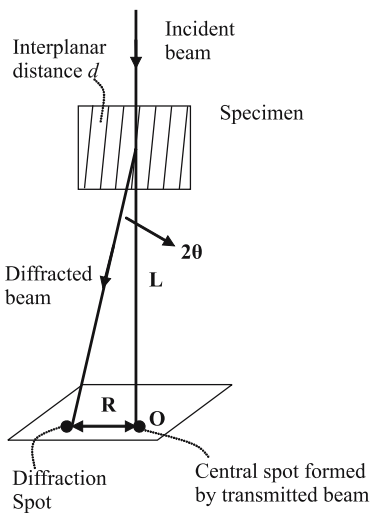
Figure 5. The single crystal diffraction pattern formation in TEM. The geometry relationship of the parameters is given in Eq. (5)
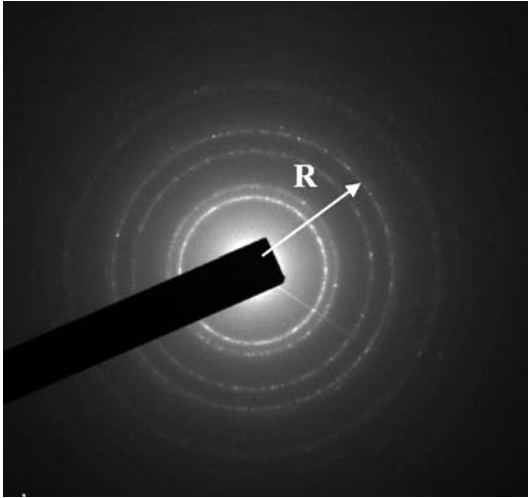
Figure 6. The typical polycrystal diffraction rings. *R* is the radius of diffraction ring and can be used to deduce the crystal structural information of polycrystals according to Eq. (6)

that the diffraction pattern also carry the symmetry information of the crystal specimen. In this way, crystallographic information can be obtained from the electron diffraction pattern of the specimen.

In case of polycrystals being examined under TEM, the diffraction pattern from a large number of randomly oriented small crystals forming the polycrystals is a pattern of several discontinuous sharp rings (Fig. 6). The diameters of these rings are characteristic for the crystal structure. Structural information can be deduced from the ratios of the radii of the diffraction rings using Eq. (6). Generally, we can obtain diffraction pattern and image of a specimen at the same area of the specimen and index the diffraction patterns so that we can relate the crystallography information to the image.

Image Mode Working Principles

An observable image must display contrast, which is defined as the relative intensity difference between an image point and its surroundings. The origin of the TEM image contrast arises from the scattering of the incident beam by the specimen. Several contrast mechanisms play those roles in the TEM imaging. The electron wave can change both its amplitude and its phase as it transmits the specimen, and both these kinds of changes can give rise to image contrast, referred to as amplitude contrast and phase contrast. In most situations, both types of contrast actually contribute to an image simultaneously, although one tends to dominate. Amplitude contrast has two principal types, namely, mass-thickness contrast and diffraction contrast.

Mass-Thickness Contrast

Mass-thickness contrast is the most critical contrast mechanism for amorphous materials such as polymers and biological materials. It arises from two factors, the mass/atomic number of the element contained in the specimen and the thickness

of the specimen. The interaction of electrons with heavy atoms is stronger than with light atoms. If the thickness is homogeneous, areas containing heavier elements appear darker than such with lighter atoms in the resulting TEM image due to the scattering of the electrons in the sample; thus, it forms mass contrast (Fig. 7). This is the reason that, in the cases of TEM examination on soft tissue or cells, it is possible to observe the ultrastructures of the specimen by staining the specimen with heavy materials. On the other hand, more electrons are scattered in thick areas than in thin areas of the specimen, and therefore thick areas appear dark in the resulting TEM image. This forms thickness contrast. Combining two contrast mechanisms together, we get mass-thickness contrast of the image. Certainly, there exist cases in which a thick area with light elements might have the same contrast as a thinner area with heavier atoms.
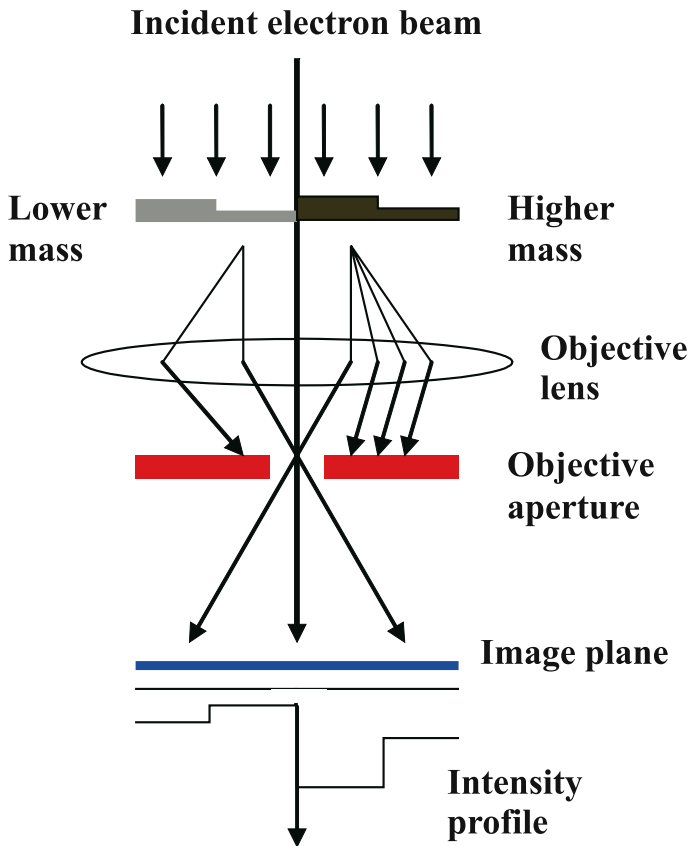
Figure 7. The mechanism of mass-thickness contrast in an TEM image. Thicker or higher mass areas of the specimen will scatter more electrons off axis than thinner or lower mass areas, and therefore more scattered electron will be blocked by the objective aperture; thus, fewer electrons from the thicker or higher mass areas will reach the image plane and give low intensity. Consequently, these areas appear dark in the final image

Diffraction Contrast

As mentioned previously, electron diffraction is caused by the constructive interference electron scattering especially from crystal planes, and therefore it is controlled by the crystal structure and orientation of the specimen. We can use electron diffraction to create contrast in TEM images. Diffraction contrast is simply a special form of amplitude contrast because the scattering occurs at special (Bragg) angles. Basically, diffraction contrast depends on the orientation of a crystalline area in the sample with regard to the direction of the incident electron beam; thus, each crystal of a specimen consisting of many randomly oriented crystals will have its own grey-level in a TEM image. This forms the diffraction contrast. From diffraction-contrast images, different materials, as well as individual crystals and crystal defects, can be easily identified.

The two most basic ways to form diffraction-contrast image are bright-field imaging (BF) and dark-field imaging (DF), which are formed by selectively allowing only the transmitted beam (BF) or one of the diffracted beams down to the microscope column by means of an objective aperture (Fig. 8). The size of the objective aperture in BF mode directly determines the information to be emphasized in the final image. If the sample has crystalline areas, many electrons are strongly scattered by Bragg diffraction, especially if the crystal is oriented along a zone axis with low indices. The area appears with dark contrast in the BF image if the objective aperture size is chosen so as to exclude those diffracted beams; thus, we obtain diffraction contrast on the BF image.

In summary, in the case of a crystalline specimen oriented to excite a particular diffracted beam, all scattered electron beams are deflected away from the optical axis and blocked by the objective aperture, and the corresponding areas appear dark on
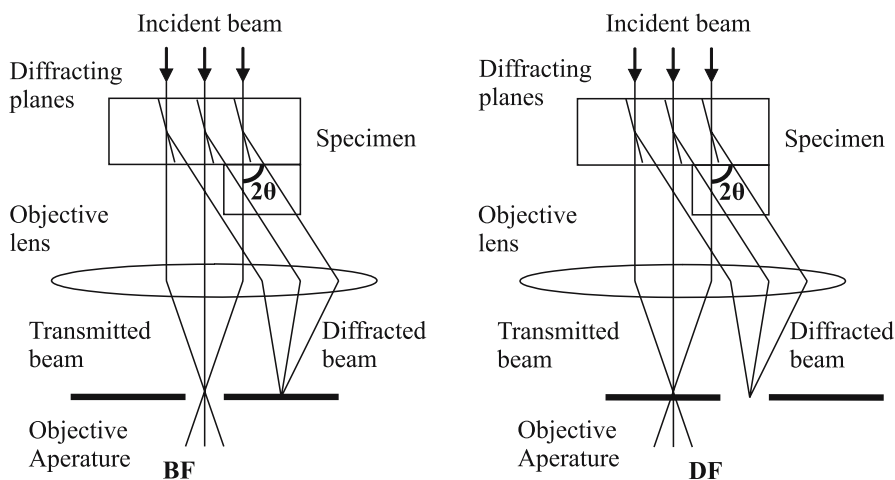
Figure 8. In *BF* image, the (000) transmitted beam contributes to the image, whereas in *DF* imaging, the (000) beam is blocked by the objective aperture and only diffracted beam contributes to the final image

the BF image. As for DF imaging mode, one or more diffracted beams are allowed to pass the objective aperture while the transmitted beam is blocked by the aperture. In this case, the diffracted beam has interacted strongly with the specimen, and often very useful information relevant to crystal-lattice defects is present in DF images.

Note that in DF image mode, we only collect the diffracted beam to form image, and therefore DF image contains pure diffraction contrast; however, in BF image mode an aperture is placed in the back focal plane of the objective lens which allows only the direct beam to pass. In this case, both the mass thickness and diffraction contrast will contribute to BF image: thick areas, areas containing heavy atoms and certain crystalline areas have the same orientation as zone axis and will appear with dark contrast; thus, BF image is suitable for both crystalline and amorphous materials.

When we examine the interface of bone tissue and scaffold materials under TEM, we need to observe inorganic crystal materials in the bone and scaffold materials and organic amorphous tissue at surrounding areas; thus, the BF image mode will be suitable for most cases of bone/implanted material interface observation. In other words, the TEM images of the bone and scaffold materials are generally contributed from both diffraction contrast and mass-thickness contrast.

In conclusion, mass-thickness contrast and diffraction contrast are important amplitude contrast mechanism in TEM imaging.

High-Resolution TEM

High-resolution TEM (HRTEM) is one of the key imaging techniques that has been widely and effectively used for analysing crystal structures and lattice defect in various specimens, including scaffold medical materials. The HRTEM is used for extremely high-magnification studies of materials, and its superior resolution makes
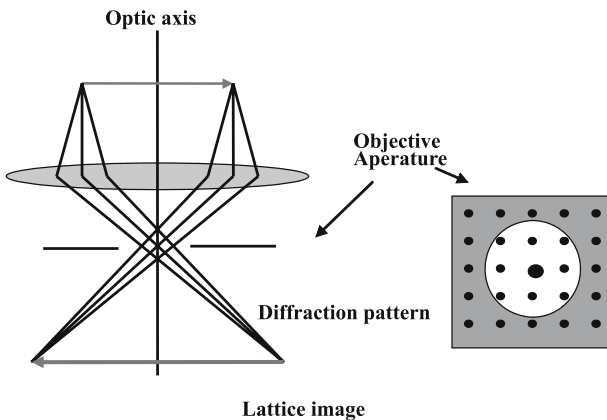
Figure 9. Ray path geometry for HRTEM, which shows that the phase of the central and scattered waves under the imaging conditions interfere with each other and form a crystal structure lattice image. Note that the objective aperture is large enough to allow many beams to pass through simultaneously. Those beams in the *grey area* are blocked by the aperture

it ideal for imaging materials on the atomic scale. Generally, HRTEM can provide structural information at better than 0.2-nm spatial resolution.

The HRTEM is a lattice image that originates from phase contrast. To obtain lattice images, a larger objective aperture has to be used which allows many diffracted beams, including the direct transmitted beam, to pass. Consider a very thin slice of crystal that has been tilted so that a low-index direction (zone axis) is exactly aligned with the incident electron beam. All lattice planes approximately parallel to the electron beam will be close enough to satisfy Bragg's law and will diffract with the primary beam. Then the image is formed by the interference of the many diffracted beams with the incident beam. The incident parallel electron beam also could be regarded as a plane wave, interacts elastically while passing through the specimen and the resulting modulations of its phase and amplitude are presented in the electron wave leaving the specimen (Fig. 9). If the point resolution of the microscope is sufficiently high and a suitable sample is oriented along a zone axis, then high-resolution TEM (HRTEM) images are obtained.

Tissue Processing

The tissue processing procedure is shown in Fig. 10. Briefly, the mended specimens are fixed in 2.5% buffered glutaraldehyde solution, rinsed in phosphate buffered solu-
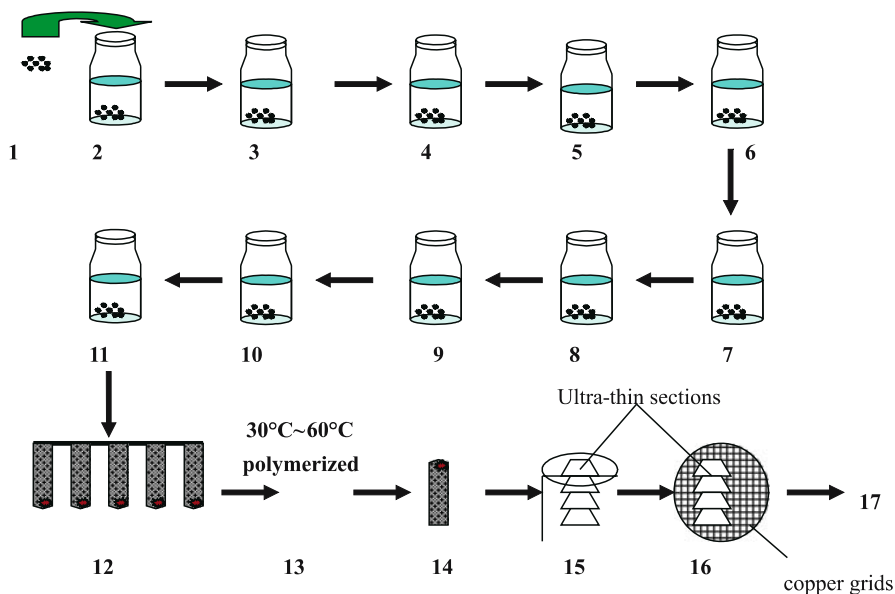
Figure 10. The routine tissue processing procedure. 1 Specimens; 2 fixed in buffered glutaraldehyde; 3 rinsed with buffered solution; 4 postfixed in osmium; 5 – 10 dehydrated in the graded series of ethanol and acetone; 11 infiltrated with Spurr resin; 12 embedded in Spurr resin; 13 polymerized Spurr resin; 14 mended the embedded specimens; 15 cut ultra-thin sections; 16 stained with uranyl acetate and lead citrate; 17 TEM observation

tion (PBS) or other buffered solution, postfixed in 1% osmium tetroxide, dehydrated in an ethanol and acetone series (30, 50, 70, 80, 90, 100%), infiltrated with a graded series of acetone and three changes of Spurr resin, and finally embedded in fresh Spurr resin in capsules. Ultra-thin sections (90–100 nm) of bone specimen are then cut with a diamond knife and picked up on 300-mesh and Formvar coated copper grids. Then the ultra-thin sections are stained with uranyl acetate for 30 min and lead citrate for 15 min. The optimal time for every step depends greatly on the size and tissue type of sample.

Application of TEM to Study Bone and Scaffold Materials

In our study, various TEM techniques, including BF image, DF image, electron diffraction and high-resolution TEM, were used to study bone scaffold materials. Figure 11 shows the BF image of the CaP biomaterial surface which had been implanted in the bone of rabbit. There were a number of needle-like crystals growing on the CaP biomaterial surface. The results of EDS identified the composition of the dark area to be Ca and P elements mainly, whereas the compositions of needle-like substance were shown to be Na, K and S besides Ca and P (Fig. 12). It is well known that Na and K are necessary elements for cellular activity and osmosis, whereas S element indicates the appearance of proteoglycans and glycoproteins in this area; therefore, it was deduced that the dark area was CaP implant, whereas the needle-like area was newly formed bone. The DF image of CaP crystal derived from CaP
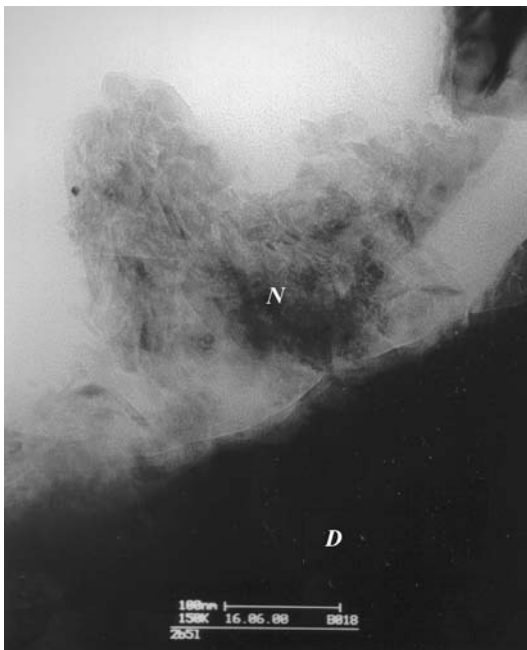
Figure 11. The bright field image of the surface of CaP implant, which is implanted in the bone of animal. *D* The dark area. *N* The needle-like area. The compositions of these two areas are shown in Fig. 12
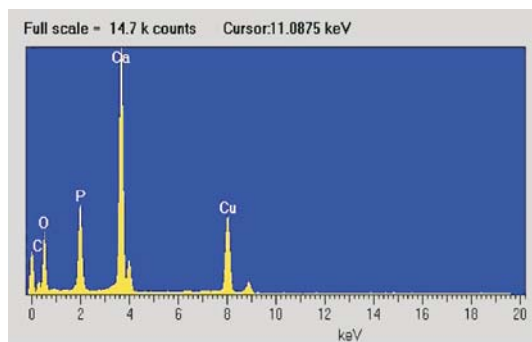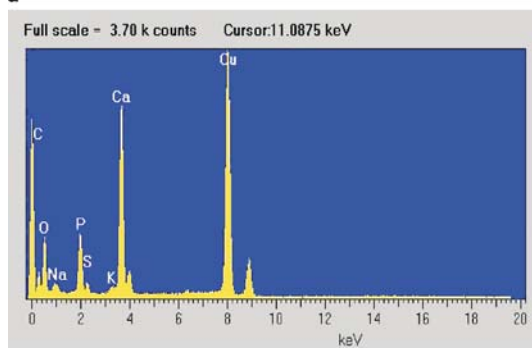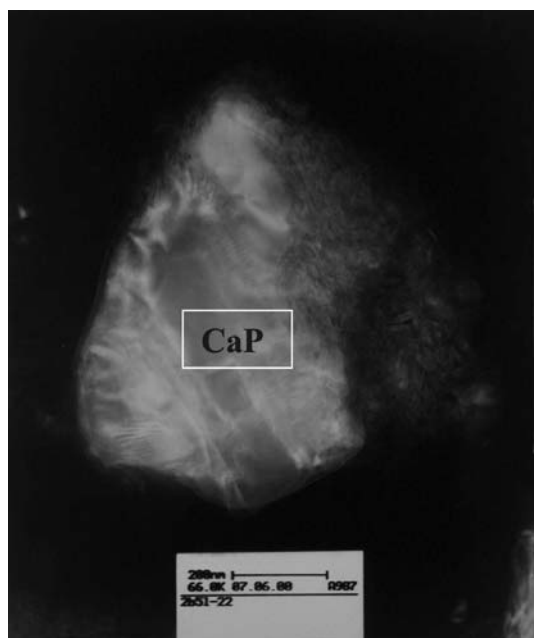
Figure 12 a,b. The results of energy dispersive spectrometer (EDS). **a** The compositions of dark area (*D* in Fig. 11). **b** The compositions of the needle-like area (*N* in Fig. 11)

Figure 13. The dark-field image of CaP crystal derived from CaP implant
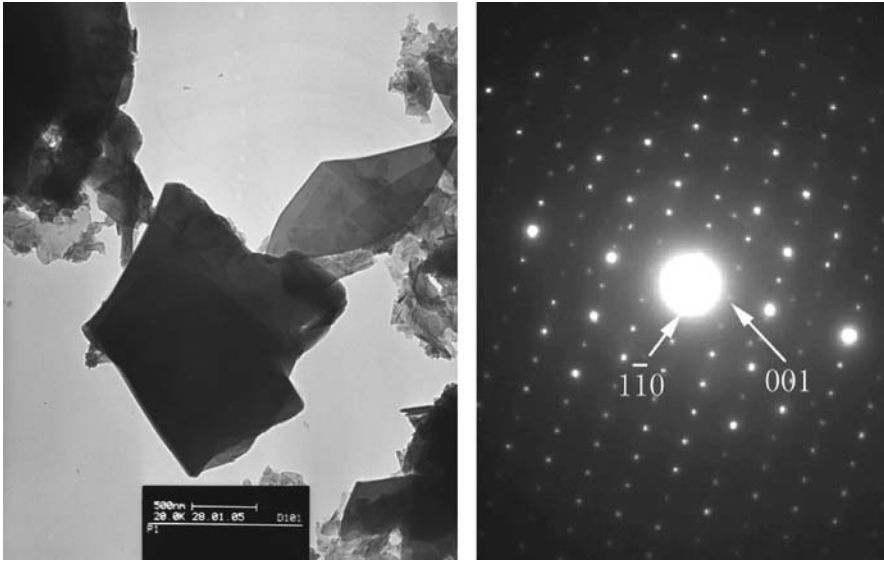
Figure 14. The bright-field image and electron diffraction pattern of precipitated CaP crystal on titanium substrate

implant is shown in Fig. 13. Contrarily, the light area is CaP implant due to the heavy mass.

In our study in vitro, for the TEM sample preparation, ultrasound vibration methods were used (Leng et al. 2003). In brief, the samples were immersed in ethanol solution and ultrasound vibration was applied to separate precipitates from the titanium substance. Then the precipitates were carefully extracted in the solution and
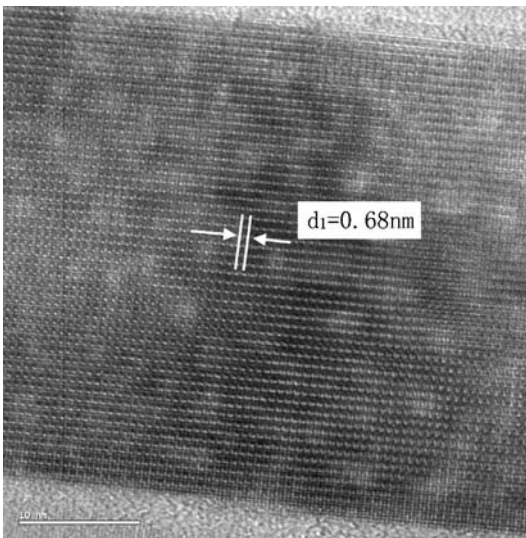
Figure 15. The HRTEM image of octacalcium phosphate, a kind of bioactive ceramics, reveals that the spacing between the crystal planes indexed by the *arrows* is equal to 0.68 nm, which matches the interplanar spacing of octacalcium phosphate (0 0 1)

picked up using TEM copper meshes with carbon film coating. This method has been demonstrated to be efficient to prepare the ultra-thin sections for TEM (Leng et al. 2003; Xin et al. 2005; Lu and Leng et al. 2004). The BF image and corresponding electron diffraction pattern is shown in Fig. 14. The highly crystallized precipitates were revealed to be octacalcium phosphate (OCP) by electron diffraction pattern. The OCP is one kind of bioactive ceramic, an intermediate phase, which transforms into apatite under certain conditions (Feng et al. 1999).

The HRTEM result of precipitated CaP on titanium substrate is shown in Fig. 15. The HRTEM image of octacalcium phosphate OCP reveals that the spacing between the crystal planes indexed by the arrows is equal to 0.68 nm, which matches the plane spacing of octacalcium phosphate (0 0 1).

Limitations of TEM

Every imaging technique has its drawbacks, and TEM is no exception. The TEM has two main drawbacks: tedious sample preparation process and damage to the specimen during TEM examination. Firstly, sample preparation of TEM is very tedious, especially for biological materials. The poor penetrating power of electrons means that the specimens must be as thin as to 50 – 100 nm in order to allow electrons to pass through. Although various methods have been developed to prepare thin specimen nearly covering all types of materials, preparing a thin specimen with uniform thickness, and being electron transparent without changing its structural characteristics and chemistry, is an arduous job and highly dependent on experience. For examining biological materials, such as bone, under TEM, another great obstacle is to dry and fix samples without any distortion. Since the material must be exposed to a very high vacuum (10^{-5} – 10^{-8} Torr) when being examined, it must be dried at some stage in its preparation. To keep the ultrastructure of the biological specimen close to physiological condition during the drying process, certain techniques are used to stabilize or fix the specimen.

Electron beam damage is another significant limitation of TEM imaging, particularly for biological and polymeric materials generally involved in biomedical engineering. Sample damage can be minimized by lowering the electron accelerated voltage, reducing the electron source intensity and focusing the beam to the area of interest; however, all of these methods cannot fully obviate specimen damage. It is also pointed out that sampling area of the TEM is generally as small as 0.3 mm^3; thus, interpretation of TEM images should be approached with caution and the necessary complementary techniques should be considered if we want a fuller characterization of the specimen (Willams and Carter 1996; Champeness 2001).

Conclusion

The TEM is a powerful imaging tool to study the ultrastructure of bone and scaffold material due to its ultra-high-resolution, despite some known limitations. Combination of other characterization techniques, such as EDS, various TEM techniques,

including BF image, DF image, electron diffraction and high-resolution TEM, may be used to study the quality of bone and biomaterials by observing their morphology and identifying the composition and crystal structure of bone and scaffold materials.

References

Carter DH, Scully AJ, Heaton DA, Young MPJ, Aaron JE (2002) Effect of deproteination on bone mineral morphology: implications for biomaterials and aging. Bone 31:389–395

Champeness PE (2001) Electron diffraction in the transmission electron microscopy. Bios, UK

Chang CK, Mao DL, Wu JS (2000) Characteristics of crystals precipitated in sintered apatite/wollastonite glass ceramics. Ceramics Int 26:779–785

Chappard D, Gaborit NR, Filmon R, Audran M, Basle MF (1998) Increased nucleolar organizer regions in osteoblast nuclei of Paget's bone disease. Bone 22:45–49

De Lange GL, De Putter C, De Wijs FlJA (1990) Histological and ultrastructure appearance of the hydroxyapatite-bone interface. J Biomed Mater Res 24:829–845

Feng QL, Wang H, Cui FZ, Kim TN (1999) Controlled crystal growth of calcium phosphate on titanium surface by NaOH-treatment. J Crystal Growth 200:550–557

Gross U, Brandes J, Strunz V, Bab I, Sela J (1981) The ultrastructure of the interface between a glass ceramic and bone. J Biomed Mater Res 15:291–305

Kong XD, Sun XD, Lu JB, Cui FZ (2005) Mineralization of calcium phosphate in reverse microemulsion. Curr Appl Phys 5:519–521

Leng Y, Chen JY, Qu SX (2003) TEM study of calcium phosphate precipitation on HA/TCP ceramcics. Biomaterials 24:2125–2131

Lees S (1996) A model for the ultrastructure of mineralized tissue. Bone 19:148S

Li G, Dickson GR, Marsh DR, Simpson H (2003) Rapid new bone tissue remodeling during distraction osteogenesis is associated with apoptosis. J Orthop Res 21:28–35

Lu X, Leng Y (2004) TEM study of calcium phosphate precipitation on bioactive titanium surfaces. Biomaterials 25:1779–1786

Murai K, Takeshita F, Ayukawa Y, Kiyoshima T, Suetsugu T, Tanaka T (1996) Light and electron microscopic studies of bone-titanium interface in the tibiae of young and mature rats. J Biomed Mater Res 30:523–533

Neo M, Kotani S, Fujita Y, Nakamura T, Yamamuro T, Bando Y, Ohtsuki C, Kokubo T (1992a) Difference in ceramic-bone interface between surface-active ceramics and resorbable ceramics: a study by scanning and transmission electron microscopy. J Biomed Mater Res 26:255–267

Neo M, Kotani S, Nakamura T, Yamamuro T, Ohtsuki C, Kokubo T, Bando Y (1992b) A comparative study of ultrastructures of the interface between four kinds of surface-active ceramic and bone. J Biomed Mater Res 26:1419–1432

Porter AE, Nalla RK, Minor A, Jinschek JR, Kisielowski C, Radmilovic V, Kinney JH, Tomsia AP, Ritchie RO (2005) A transmission electron microscopy study of mineralization in age-induced transparent dentin. Biomaterials 26:7650–7660

Qu SX, Leng Y, Guo X, Cheng JCY, Chen WQ, Yang ZJ, Zhang XD (2002) Histological and ultrastructural analysis of heterotopic osteogenesis in porous calcium phosphate ceramics. J Mater Sci Let 21:153–155

Roceri N, Falini G, Sidoti MC, Tampieri E, Landi M, Sandri B, Parma A (2003) Biologically inspired growth of hydroxyapatite nanocrystals inside self-assembled collagen fibers. Mater Sci Eng C23:441–446

Rosen VB, Hobbs LW, Specror M (2002) The ultrastructure of anorganic bovine bone and selected synthetic hydroxyapatite used as bone graft substitute materials. Biomaterials 23:921–928

Rubin MA, Jasiuk I (2005) The TEM characterization of the lamellar structure of osteoporotic human trabecular bone. Micron 36:653–664

Rubin MA, Jasiuk I, Taylor J, Rubin J, Ganey T, Apkarian R (2003) TEM analysis of the nanostructure of normal and osteoporotic human trabecular bone. Bone 33:270–282

Sahar ND, Hong SI, Kohn DH (2005) Micro- and nano-structural analyses of damage in bone. Micron 36:617–629

Sautier JM, Nefussi JR, Forest N (1992) Surface-active biomaterials in osteoblast culture: an ultrastructural study. Biomaterials 13:400–402

Serre GM, Papillard M, Chavassieux P, Boivin G (1993) In vitro induction of a calcifying matrix by biomaterials constituted of collagen and/or hydroxyapatite: an ultrastructure comparison of three types of biomaterials. Biomaterials 14:97–106

Steflik DE, Corpe RS, Lake FT, Young TR, Sisk AL, Parr GR, Hames PJ, Berkery DJ (1990) Ultrastructure analyses of the attachment (bonding) zone between bone and implanted biomaterials. J Biomed Mater Res 39:613–620

Su X, Sun K, Cui FZ, Landis WJ (2003) Organization of apatite crystals in human wove bone. Bone 32:150–162

Tracy BM, Doremus RH (1984) Direct electron microscopy studies of the bone-hydroxylapatite interface. J Biomed Mater Res 18:719–726

Willams DB, Carter CB (1996) Transmission electron microscopy: a textbook for materials science. Plenum, New York

Xin RL, Yang Y, Chen JY, Zhang QY (2005) A comparative study of calcium phosphate formation on bioceramics in vitro and in vivo. Biomaterials 26:6477–6486

Material and Structural Basis of Bone Fragility: A Rational Approach to Therapy

Ego Seeman

Department of Endocrinology, Austin Health, The University of Melbourne, Melbourne, Australia
e-mail: egos@unimelb.edu.au

Abstract

This chapter discusses drug therapy used to reduce fracture risk by influencing the material and structural properties of bone. Bone loss is slow before menopause because remodelling is slow. Bone loss accelerates after menopause because remodelling rate increases, reducing bone mineral density (BMD) and bones material rigidity. Anti-resorptive drugs reduce the rate of bone remodelling. Reconstruction the skeleton requires anabolic therapy. Parathyroid hormone (PTH) given intermittently increases bone formation on the endosteal surface increasing both cortical and trabecular thickness. Strontium ranelate reduces vertebral and non-vertebral fractures. The rate of bone remodelling does not appear to be reduced. There may be a reduction the depth of bone resorption while allowing bone formation to continue but remains uncertain.

Determinants of Bone Strength

The material composition and structural organization of bone determine its strength? Its ability to tolerate loads without cracking or failing by fracture. Prevailing loads also determine bone's material composition and structural design so that the bone can accommodate loads placed on it. This is achieved by adaptive modelling and remodelling, the two cellular mechanisms responsible for the attainment of peak bone strength during growth and maintenance of bone strength during ageing (Parfitt 1996). Modelling is achieved by bone formation without prior bone resorption. In bone remodelling damaged bone is removed by focal bone resorption. Following completion of bone resorption, bone formation refills the excavated site with new bone to restore bone's structural integrity. Bone modelling is active during growth and establishes the size and shape of bone. Bone modelling by periosteal apposition, and remodelling, also occur during ageing but markedly less so than during growth (Seeman 2003). Within each bone remodelling unit (BMU), resorption is carried out by osteoclasts. Damaged bone is removed and osteoblasts lay down osteoid that undergoes primary then secondary mineralization.

The completion of growth bone formation in the BMU decreases as reflected in an age-related fall in mean wall thickness (Lips et al. 1978). The BMU balance becomes

less positive, zero or, negative–marking the onset of bone loss. If accompanied by an increase in the volume of bone resorbed, trabecular thinning accelerates and may proceed to loss of connectivity and bone fragility (Van der Linden et al. 2001).

Although adaptive modelling and remodelling are successful during growth, advancing age is accompanied by accumulating abnormalities such as hormonal deficiency and excess, exposure to illness and risk factors, and changes in the cellular constituents of this machinery as well. These accumulating abnormalities compromise the material composition and structural organization of bone producing bone fragility. For example, increased remodelling rate, due to sex hormone deficiency and secondary hyperparathyroidism, alter bone's material composition, decreases its tissue mineral density and so reducing material stiffness of superficial (sub-endosteal) bone (Currey 2002). Less remodelled bone, deep to the endosteal surface, becomes more densely and homogeneously mineralised with a deficient in osteocytes, predisposing to increased production, lengthening and reduced removal of micro-damage. The high rate of remodelling also creates excavation sites that serve as stress concentrators.

While changes in remodelling rate modify material properties, the negative balance between the volumes of bone resorbed and formed in each remodelling site produces bone loss and so compromises structure. The negative balance is initially the result of a reduction in the volume of bone formed (not an increase in the volume of bone resorbed) in each BMU. Evidence of this is found in midlife as a reduction in mean wall thickness. This decline in bone-forming capacity may be due to a decline in the production, work or life span of osteoblasts. The reduced life span of osteoblasts may also compromise osteocyte production and so compromise the reconstruction of the osteocytic-canalicular network during a remodelling cycle.

Bone loss is slow before menopause because remodelling is slow. Bone loss accelerates after menopause because the remodelling rate increases reducing tissue mineral density and rigidity. The excavated resorption pits create stress concentrators predisposing to micro-damage. In midlife in women, sex hormone deficiency accelerates remodelling and worsens the negative BMU balance by increasing osteoclast life span and reducing the life span of osteoblasts (Manolagas 2000). Finally, bone modelling by periosteal apposition is minimal after epiphyseal closure, perhaps due to abnormalities in periosteal osteoblast function, osteocyte signalling or deficiency, and provides little compensatory periosteal bone formation in response to endosteal bone loss.

Anti-resorptive Agents

Anti-resorptive drugs, such as alendronate, risedronate or raloxifene, reduce the rate of bone remodelling (Delmas 2002). When an anti-resorptie agent is given the many BMUs present before treatment go to completion by depositing a volume of new bone that mineralises and BMD increases. New excavated sites appearing during therapy are fewer and probably more shallow; thus, completion of remodelling by bone formation is seen as a reduction in cortical porosity while the appearance of fewer and

probably more shallow resorption cavities during therapy results in a slowing of cortical and trabecular thinning. The slowing of remodelling rate also allows more time for tissue mineral density and stiffness to increase (Parfitt 1980).

Continued structural decay in the placebo group accounts for continued fractures while and the prevention of progression or partial reversal of this decay in the treated group accounts for fewer fractures occurring during treatment. Fractures continue; these drugs do not eliminate fracture risk, although they do reduce it by 30–60% (Delmas 2002).

A small increase in bone tissue mass follows initiation of therapy due to completion of the bone formation component of the many resorption-formation remodelling events taking place before treatment. Subsequent primary mineralisation of this new bone, its secondary mineralisation and continued secondary mineralisation of existing unremodelled bone increase material rigidity. Slower remodelling and less resorption in each of the now fewer BMUs reduces the rate of progression of fragility (which continues in untreated subjects).

The required duration of anti-resorptive treatment is poorly defined. Prolonged suppression of remodelling may do harm because remodelling is the means whereby bone damage is removed. As remodelling is slowed during treatment, more time is available for secondary mineralization; thus, bone becomes more homogeneous in tissue density. There is less obstruction to crack progression and lengthening, and increases tissue stiffness predisposes to increased micro-damage production (Mashiba et al. 2000; Komatsubara et al. 2003). Micro-damage occurs in animals given high doses of bisphosphonates. Evidence of a deleterious effect of bisphosphonates in humans is lacking, but cases of impaired fracture healing are reported (Whyte et al. 2003; Odvina et al. 2005).

Parathyroid Hormone

Reconstruction the skeleton requires anabolic therapy (Neer et al. 2003). Parathyroid hormone (PTH 1-34) given intermittently increases bone formation on the endosteal surface increasing cortical thickness, trabecular thickness and perhaps connectivity. Periosteal apposition has been reported in growing animals, but whether this occurs in human subjects is still to be established. Whether different molecules, such as PTH 1-84, have a different mode of action is unclear. Intermittent PTH reduced the risk of vertebral and non-vertebral fractures (Neer et al. 2003).

Whether PTH is more efficacious than anti-resorptives, and whether anti-resorptive given prior, during or after PTH is better (or worse) than either agent alone, is unknown. Surrogates of efficacy are not valid substitutes for counting fractures. The increase in BMD with PTH is greater than with anti-resorptive drugs, but whether this produces a greater fracture risk reduction is unknown. Remodelling markers decrease using anti-resorptives while they increase with PTH so that the usefulness of marker changes in combined therapy is questionable. Prior alendronate, but not other anti-resorptive, delay the BMD and remodelling marker responses to PTH (Ettinger et al. 2004; Black et al. 2003; Finkelstein et al. 2003; Cosman et al. 2005). When

PTH is stopped, anti-resorptive prevent the BMD decline (Cosman et al. 2005), but whether the protection against fractures after stopping PTH is greater with or without an anti-resorptive is unclear; thus, there is no evidence in human subjects to support the use of combined therapy.

Strontium Ranelate

Strontium ranelate (SR) reduces vertebral and non-vertebral fractures, but the mechanism of response is unclear (Meunier et al. 2002, 2004; Reginster et al. 2005). Although initially believed to be anabolic, this has not been confirmed experimentally. The drug does not reduce remodelling rate but may reduce the depth of bone resorption while allowing bone formation to continue. Tissue mineral density does not increase, yet tissue hardness increases (assessed by nano-indentation), perhaps due to deposition of strontium in the hydroxyapatite crystal. The drug does appear to produce dissociation in the pattern of change in markers of bone resorption that are modestly suppressed while markers of bone formation are modestly increased. These are markers of tissue level remodelling and should not be assumed to reflect differing formation-resorption effects in the BMU. Direct evidence of reduced resorption surfaces and increases in mean wall thickness on histomorphometry are not available. Research is ongoing exploring the mechanisms of action of this interesting drug.

The results of anti-fracture efficacy of this new drug are summarized below (Meunier et al. 2002, 2004; Reginster et al. 2005). In the SR for Treatment of Osteoporosis (STRATOS) trial in 353 women with osteoporosis, there was a 44% reduction fracture incidence in the second year. In the phase-3 Spinal Osteoporosis Therapeutic Intervention (SOTI) study of 1649 postmenopausal women with osteoporosis and at least one vertebral fracture, 2 g SR daily for 3 years had a 49% reduction in risk in the first year and 41% during the 3 years. In the Treatment of Peripheral Osteoporosis (TROPOS) of the 5091 patients, 3640 (1817 SR, 1823 placebo) had spinal X-rays. The vertebral fracture risk was 45% at 1 year and 39% at 3 years. In 66.4% without a prevalent fracture, the risk of a vertebral fracture was reduced by 45%. In the subgroup with at least one prevalent fracture, the risk of vertebral fracture was reduced by 32% over 3 years. In TROPOS at 3 years, the risk for all non-vertebral fracture was reduced by 16 and by 19% for major fragility fractures (hip, wrist, pelvis and sacrum, ribs and sternum, clavicle, humerus). The risk of hip fracture in the ITT population was reduced by 15% (not significant). In a post-hoc analysis of women at high risk of hip fracture (age >74 years and femoral neck BMD T score <2.4 according to NHANES; $n = 1977$), the risk reduction for hip fracture was 36%.

Conclusion

Understanding the pathogenesis of bone fragility provides opportunities for drug development to limit the progression and reverse fragility. Progress has been made. We have anti-resorptive agents that reduce progression of bone fragility mainly by re-

ducing the remodelling rate and probably by reducing resorption in each BMU. Anabolic agents do build new bone and thicken the cortices and trabeculae. Whether this translates into better anti-fracture efficacy than found with anti-resorptive agents is not known. Strontium ranelate is different. It reduces fractures, but how this is archieved is not clear. It does not fit easily into either class of agent, but further studies are likely to resolve these uncertainties and open new opportunities for drug development. The advanced bioimaging methods reviewed in other chapters of this book offer new approaches for scientific evaluations of treatments aimed at preventing fractures.

References

Black DM, Greenspan SL, Ensrud KE, the PTH Study Investigators (2003) The effects of parathyroid hormone and alendronate alone or in combination in postmenopausal osteoporosis. N Engl J Med 349:1207–1215

Cosman F, Nieves J, Zion M, Woelfert L, Luckey M, Lindsay R (2005) Daily and cyclic parathyroid hormone in women receiving alendronate. N Engl J Med 353(6):566–575

Currey JD (2002) Bones: structure and mechanics. Princeton University Press, Princeton, New Jersey, pp 1–380

Delmas PD (2002) Treatment of postmenopausal osteoporosis. Lancet 359:2018–2026

Ettinger B, San Martin J, Crans G, Pavo I (2004) Differential effects of teriparatide on BMD after treatment with raloxifene or alendronate. J Bone Miner Res 19:745–751

Finkelstein JS, Hayes A, Hunzelman JL, Wyland JJ, Lee H, Neer RM (2003) The effects of parathyroid hormone, alendronate, or both in men with osteoporosis. N Engl J Med 349:1216–1226

Komatsubara S, Mori S, Mashiba T, Ito M, Li J, Kaji Y, Akiyama T, Miyamoto K, Cao Y, Kawanishi J, Norimatsu H (2003) Long-term treatment of incadronate disodium accumulates microdamage but improves the trabecular bone microarchitecture in dog vertebra. J Bone Miner Res 18:512–520

Lips P, Courpron P. Meunier PJ (1978) Mean wall thickness of trabecular bone packets in the human iliac crest: changes with age. Calcif Tissue Res 10:13–17

Manolagas SC (2000) Birth and death of bone cells: basic regulatory mechanisms and implications for the pathogenesis and treatment of osteoporosis. Endocr Rev 21:115–137

Mashiba T, Hirano T, Turner CH, Forwood MR, Johnston CC, Burr DB (2000) Suppressed bone turnover by bisphosphonates increases microdamage accumulation and reduces some biomechanical properties in dog rib. J Bone Miner Res 15:613–620

Meunier PJ, Slosman D, Delmas PD, Sebert JL, Brandi ML, Albanese C, Lorenc R, Pors-Nielsen S, De Vernejoul MC, Roces A, Reginster JY (2002) Strontium ranelate: dose-dependent effects in established post-menopausal vertebral osteoporosis. The Stratos 2-year randomized placebo controlled trial. J Clin Endocrinol Metab 87:2060–2066

Meunier PJ, Roux C, Seeman E (2004) The effects of strontium ranelate on the risk of vertebral fracture in women with postmenopausal osteoporosis. N Engl J Med 350:459–468

Neer RM, Arnaud CD, Zanchette JR (2001) Effect of parathyroid hormone(1–134) on fractures and bone mineral density in postmenopausal women with osteoporosis. N Engl J Med 344:1434–1441

Odvina CV, Zerwekh JE, Rao DS, Maaloof N, Gottschalk FA, Pak CYC (2005) Severely suppressed bone turnover: a potential complication of alendronate therapy. J Clin Endocrinol Metab 1294–1301

Parfitt AM (1980) Morphological basis of bone mineral measurements: transient and steady state effects of treatment in osteoporosis. Mineral Electrolyte Metab 4:273–287

Parfitt AM (1996) Skeletal heterogeneity and the purposes of bone remodelling: implications for the understanding of osteoporosis. In: Marcus R, Feldman D, Kelsey J (eds) Osteoporosis. Academic Press, San Diego, pp 315–339

Reginster JY, Seeman E, De Vernejoul (2005) Strontium ranelate reduced the risk of nonvertebral fractures in postmenopausal women with osteoporosis TROPOS study. Strontium ranelate reduces the risk of non-vertebral fractures in post-menopausal women with osteoporosis: Treatment of Peripheral Osteoporosis (TROPOS) Study. J Clin Endosc Metab 90:2816–2822

Seeman E (2003) Periosteal bone formation: a neglected determinant of bone strength. N Engl J Med 349:320–323

Van der Linden JC, Homminga J, Verhaar JAN, Weinans H (2001) Mechanical consequences of bone loss in cancellous bone. J Bone Miner Res 16:457–465

Whyte MP, Wenkert D, Clements KL, McAlister WH, Mumm S (2003) Brief report: bisphosphonate-induced osteopetrosis. N Engl J Med 349:457–463

Application of Micro-CT and MRI in Clinical and Preclinical Studies of Osteoporosis and Related Disorders

Ye-Bin Jiang (✉) [1], Jon Jacobson[1], Harry K. Genant[2], and Jenny Zhao[1]

[1] Osteoporosis and Arthritis Lab and Division of Musculoskeletal Radiology, Department of Radiology, University of Michigan, 4510A MSRB I, 1150 W. Medical Center Drive, Ann Arbor, MI 48109, USA
e-mail: joh.jiang@umich.edu

[2] Professor Emeritus, University of California San Francisco, San Francisco, California, USA
Chairman, Board of Directors, Synarc, Inc., San Francisco, California, USA

Abstract

Advanced imaging techniques, which are noninvasive and nondestructive, can provide structural information about bone beyond simple bone densitometry. As the mechanical competence of trabecular bone is a function of its apparent density and 3D distribution, assessment of 3D trabecular structural characteristics may improve our ability to understand the pathophysiology of osteoporosis, to test the efficacy of pharmaceutical intervention, and to estimate bone biomechanical properties. We studied ovariectomy-induced osteopenia in rats with various treatments. Micro-CT is also useful for studying osteoporosis in mice and phenotypes of mice with gene manipulation. Micro-CT can quantify osteogenesis in mouse Ilizarov leg-lengthening procedures, osteoconduction in rat cranial defect models, and structural changes in arthritic rabbits, rats, and mice. Micro-CT can reproducibly quantify 3D microarchitecture of new bone formation inside the pores of titanium prosthesis implants is rabbits. In clinical studies, we evaluated longitudinal changes in iliac crests in premenopausal and postmenopausal women. Paired bone biopsies from postmenopausal women with osteoporotic fracture shows that 3D trabecular microstructure deteriorates in the iliac crest of postmenopausal osteoporotic women without active treatment. Three-dimensional microstructural parameters can predict fracture. Treatment of PTH in postmenopausal women with osteoporosis significantly improved trabecular morphology with a shift toward a more plate-like structure, increased trabecular connectivity, and increased cortical thickness. Paired bone biopsy specimens from the iliac crest in postmenopausal women with osteoporosis before and after beginning estrogen replacement therapy demonstrated in post-treatment biopsies a significant change in the ratio of plates to rods. High-resolution MR and μMR have received considerable attention both as research tools and potential clinical tools for assessment of osteoporosis. It has been used in studying human specimens or animal models of osteoporosis with various treatment strategies.

MR microscopy has been shown to capable of differentiating trabecular structure in the distal radius and the calcaneus in postmenopausal women with or without os-

teoporotic fracture. It has been used in studying human specimens or animals models of osteoporosis with various treatment strategies. A high field MR study show that ovariectomy in ewes induces deterioration of trabecular microstructure and biomechanical property of the femoral neck. These changes are prevented by calcitonin in a dose-dependent manner. Univariate analysis and multivariate stepwise regression analysis indicate that microarchitecture of trabecular bone contributes significantly to its biomechanical characteristics, independent of BMD measured in the femoral neck. Combination of trabecular microstructure with BMD improves prediction of bone quality.

Introduction

Assessing simple bone densitometry provides important information about osteoporotic fracture risk. Many studies indicate that BMD only partly explains bone strength. Quantitative assessment of 3D structural characteristics, such as geometry, relative trabecular volume, trabecular separation, and connectivity, using advanced techniques such as micro-CT or MR images, may improve our ability to estimate bone strength.

Micro-CT

Micro-computed tomography (micro-CT), an imaging technique originally developed for detecting metal stress defects in the car industry, has found application in the assessments of 3D bone microstructure. The micro-CT system was first introduced by Feldkamp and Goldstein (Feldkamp et al 1989; Kuhn et al. 1990) who used a microfocus X-ray tube as a source, an image intensifier as a 2D detector, and a cone-beam reconstruction to create a 3D object. Instead of rotating the X-ray source and detectors during data collection as in clinical CT, the specimen is rotated at various angles. X-rays are partially attenuated as the specimen rotates in equal steps in a full circle about a single axis. At each rotational position, the surviving X-ray photons are detected by a planar 2D array. A 3D reconstruction array is created directly in place of a series of 2D slices.

Much progress has been made in developing micro-CT for nondestructive assessment of 3D trabecular structure and connectivity. The availability of 3D measuring techniques and 3D image processing methods allows direct quantification of unbiased morphometric parameters, such as direct volume and surface determination (Guilak 1994), model-independent assessment of thickness (Hildebrand and Rüegsegger 1997a,b), and 3D connectivity estimation (Odgard and Gundersen 1993). It has found extensive application in the assessment of bone microstructure.

Applications

The early uses of 3D micro-CT focused on the technical and methodological aspects of the systems, but recent development emphasize the practical aspects of micro-

tomographic imaging. At an early stage, the 3D cone-beam micro-CT was used to image the trabecular bone architecture in small samples of human tibias and vertebrae, ex vivo, with a spatial resolution of 60 µm (Feldkamp et al. 1989). A resolution of 60 µm, although acceptable for characterizing the connectivity of human trabeculae, may be insufficient for studies in small animals like rats, where the trabecular widths average about 50 µm and trabecular separations average 150 µm or less (Kinney et al. 1995). With the introduction of desktop micro-CT devices dedicated to the study of bone specimens (Rüegsegger et al. 1996), it has been used extensively in laboratory investigations. Image processing algorithms, free from the model assumptions used in 2D histomorphometry, have been developed to segment and directly quantify 3D trabecular bone structure (Hildebrand and Rüegsegger 1997a,b).

Human Samples

Human iliac crest bone has been traditionally assessed with bone histomorphometry based on only a few thin 2D sections of the biopsy core from the limited tissue available, which may introduce pronounced variation of calculated structural indices and biases. Analysis of 3D structure of bone biopsies is now possible using micro-CT. This permits measurement of the entire biopsy core, providing more reliable and unbiased estimates of bone structural indices.

One recent study compared iliac crest bone samples from premenopausal women with iliac crest bone samples taken from the same women after menopause. The samples were examined using micro-CT with an isotropic resolution of $20\,\mu m^3$. The postmenopausal samples showed significant changes in 3D trabecular structural parameters. The annual rate of change from plate-like structure to rod-like structure was 12%, which may have important consequences for bone biomechanical properties. Trabecular bone became more isotropic after menopause, with an annual decrease rate in DA of 0.7%. Interestingly, annual change in trabecular thickness (−3.5%) was greater than trabecular number (−1.6%) and separation (+2%; Jiang et al 2000a). These findings are quite different from those of traditional 2D histomorphometry. In histomorphometry, it is still a matter of debate as to whether trabeculae become thin or simply disappear after menopause and with aging. It is possible that the loss of entire elements, because of trabecular perforation, forms the main mechanism of structural changes in osteoporosis. The remaining trabeculae are more widely separated and some may undergo compensatory thickening. Trabecular anisotropy increases. During the early stages of aging in the human there is a preferred loss of horizontal trabeculae leading to an increase in anisotropy (Mosekilde 1993), followed by a period of trabecular perforation and an eventual decrease in anisotropy.

Vertebral fracture is a hallmark of established osteoporosis. We investigated the relationship of the severity of vertebral osteoporotic fractures with trabecular microarchitecture of the iliac crest. We selected 180 postmenopausal osteoporotic women from multi-center, double-blind, placebo-controlled studies. Severity grade of 0, 1, 2, and 3, corresponding to no, mild, moderate, and severe fracture, respectively, was scored on lateral spine radiographs. The most severe grade in each patient was used. Statistical tests for trend by increasing fracture grade using regression model were applied. Postmenopausal osteoporotic patients with increasing severity

of vertebral fractures had progressively worse trabecular microstructural integrity. Assessment of severity of fracture can be considered as a useful surrogate of bone quality evaluation, independent of BMD measurement.

In a paired longitudinal study of postmenopausal women with osteoporotic vertebral fractures, 3D trabecular microstructure deteriorates in the iliac crest of postmenopausal osteoporotic women without active treatment. Trabecular thinning does occur and trabeculae shift from a plate-like structural type to a rod-like pattern, and become less connected.

We scanned bone biopsies from the iliac crest of healthy premenopausal women (Pre), and osteoporotic postmenopausal women without fracture (Post) and with vertebral osteoporotic fracture (Post+Fx). Adjusted for age, most odds ratios (OR) discriminated osteoporotic fracture. Dual phases were observed: deterioration of all 3D parameters in the initial years of osteoporotic postmenopausal women without fracture, and further deterioration of 3D connectivity in the later years with fracture. In the initial years, trabecular thinning does occur. Trabeculae dramatically shift from a plate-like structural type to a rod-like pattern, and become more isotropic. In the later years, the remaining trabeculae became more widely separated and less connected, and some mechanically significant trabeculae may undergo compensatory thickening and reinforcing, resulting in an increase in trabecular anisotropy. Changes in 3D trabecular microstructure play important roles in osteoporotic fracture.

In our analysis the changes of more simple 2D indices pertaining to cancellous bone structure, trabecular number (Tb.N), trabecular thickness (Tb.Th) and trabecular spacing (Tb.Sp), did not reach significance after PTH treatment; however, more stereologically correct indices, such as marrow star volume and micro-CT-based 3D indices, revealed significant changes, further corroborating the superiority of these techniques for structural analysis of small samples, such as bone biopsies. To determine reproducibility of micro-CT examination, 20 specimens from different groups were rescanned and reanalyzed. The root mean square coefficient variation (CV) of the measurements was 2.6% for Tb bone volume fraction (BV/TV), 3.6% for Tb number, 5.9% for Tb thickness, 4.0% for Tb separation, 3.3% for Tb degree of anisotropy, 2.1% for SMI, 3.9% for Tb connectivity density (CD), 2.7% for cortical porosity (Ct.Po), and 2.9% for cortical thickness (Ct.Th). The annualized median percent change in placebo group was −3.3% for BV/TV, 4.6% SMI, −9.2% CD, and −14% Ct.Po, and in PTH treated group 4.7% for BV/TV, −8% SMI, 13% CD, 0.5% for Ct.Po, and 14% Ct.Th; thus, micro-CT can reproducibly quantifies 3D microarchitecture of Tb and cortical bone in the iliac crest biopsy, which may find application in studying pathophysiology of osteoporosis and other bone disorders, and evaluating their therapeutic efficacy (Jiang et al. 2003b).

Micro-CT has been used in evaluating 3D bone microstructure of bone biopsies from patients treated with anti-resorptive agents such as estrogen (Zhao et al. 2002), and bisphosphonate residronate which preserves bone microstructure in postmenopausal osteoporotic women (Borah and Dufresne 2003). We examined bone biopsy specimens from the iliac crest in postmenopausal women with osteoporosis before and an average of 2 years after beginning of estrogen replacement therapy (ERT). Bone biopsies were obtained from one side of the iliac crest before treatment

and from the other side after treatment. Compared with pre-treatment biopsies, post-treatment biopsies showed a 14% change in the ratio of plates to rods, but statistically insignificant changes in trabecular bone volume, thickness, number, separation, and connectivity density. The findings indicate that ERT not only preserves existing 3D trabecular bone microarchitecture, but that it also reverses the shift from plate-like to rod-like patterns that is characteristic of osteoporosis. This reversal may reduce the risk of fractures due to osteoporosis by increasing the biomechanical competence of bone (Zhao et al. 2002).

In addition to the studies of anti-resorptive agents, micro-CT has also been used in evaluating 3D bone microstructure of bone biopsies from patients treated with anabolic agents. In an uncontrolled study of paired biopsies taken before and after treatment with human parathyroid hormone, 3D μCT showed increased 3D connectivity density and confirmed the preservation of 2D histomorphometric cancellous bone volume, and trabecular number and thickness. Cortical width from 2D histomorphometry increased in osteoporotic men treated with PTH and in osteoporotic women treated with PTH and estrogen (Dempster et al. 2000).

In a multi-center, double-blind, and placebo-controlled study, once-daily administration of parathyroid hormone (PTH), the major hormonal regulator of calcium homeostasis, causes increased bone formation and bone mass. After the first report in 1929 of increased skeletal calcium in rats after injection of parathyroid extract, preclinical studies and small clinical trials have shown pronounced anabolic effects of intermittent PTH administration on bone. The effect of injected parathyroid hormone on human cortical bone is controversial. Some small early clinical studies found that appendicular BMD was reduced by PTH treatment, whereas vertebral BMD increased. In other studies, BMD at the predominantly distal radius or femoral neck changed little during PTH administration. These findings led to speculation that the anabolic effects of teriparatide on cancellous bone may be obtained at the expense of cortical bone. Most recently, a large randomized double-blind multicenter study, the Fracture Prevention Trial, tested recombinant human PTH (1-34) [teriparatide, rhPTH(1-34), TPTD] vs placebo, for treatment of osteoporosis in 1637 postmenopausal women. Daily injections of 20 or 40 μg of teriparatide over a mean of 19 months increased bone mineral density (BMD) at the lumbar spine and proximal femur, and significantly decreased the incidence of vertebral and nonvertebral fractures. We examined 51 paired iliac crest biopsy specimens, of sufficient quality for analysis (choosing from 102 patients participated in the biopsy study), from subjects participating in this randomized, multicenter, double-blind, placebo-controlled Fracture Prevention Trial in which postmenopausal women with osteoporosis from 99 centers in 17 countries participated. By 2D histomorphometric analyses, teriparatide significantly increased cancellous bone volume, and reduced marrow star volume. The PTH was not associated with osteomalacia or woven bone, and there were no significant changes in mineral appositional rate or wall thickness. By 3D cancellous and cortical bone structural analyses, PTH significantly decreased the cancellous structure model index, increased cancellous connectivity density, and increased cortical thickness. The PTH improved trabecular morphology with a shift toward a more plate-like structure. These changes in cancellous and cortical bone morphol-

ogy should improve biomechanical competence and are consistent with the substantially reduced incidences of vertebral and nonvertebral fractures (Jiang et al. 2003a).

Rat Studies

Micro-CT has been used to measure trabecular bone structure in rats. Most studies have focused on the trabecular bone in the proximal tibial metaphysis, but the trabecular bone in rat vertebrae is of interest because of its similarity to the human fracture site, and because biomechanical testing is practical (Jiang et al. 1997). Micro-CT with an isotropic resolution of $11\,\mu m^3$ has been used to examine the 3D trabecular bone structure of the vertebral body in ovariectomized rats treated with estrogen replacement therapy (Jiang et al. 1999b). Micro-CT 3D determined trabecular parameters show greater percentage changes than those observed with DXA, and they show better correlation with biomechanical properties. Combining trabecular bone volume with trabecular structural parameters provides better prediction of biomechanical properties than either alone. A study of the anabolic effects of low-dose (5 ppm in drinking water) long-term (9 months) sodium fluoride (NaF) treatment in intact and ovariectomized rats shows that NaF treatment increases trabecular bone volume, possibly by increasing trabecular thickness through increasing bone formation on existing trabeculae, rather than by increasing trabecular number. NaF in sham-operated rats increases trabecular structural parameters and bone mineral, but decreases compressive stress in the vertebral body. NaF partially protects against ovariectomy-induced changes in bone mineral and structure, but this protection does not translate into a corresponding protection of bone biomechanical properties (Zhao et al. 2000ab). A recent study shows that Micro-CT examination of rat tibia showed that PTH (1-34) effectively and dose-dependently increased osseointegration on titanium implants and enhanced implant anchorage in gonadectomy-induced low density trabecular bone (Gabet et al. 2005).

Mice Studies

The wide availability of genetically altered mice has increased the usefulness of the murine model for investigating osteoporosis and other skeletal disorders. Independent genetic regulation of 3D vertebral trabecular microstructure in 12BXH recombinant inbred mice, as measured by micro-CT, contributed information regarding the variation in biomechanical properties among the strains (Turner et al. 2001). Mice homozygous for a null mutation of the PTHrP gene die at birth with severe skeletal deformities. Heterozygotes survive and by 3 months of age develop osteopenia characterized by decreased trabecular bone volume and increased bone marrow adiposity. PTHrP wild type and heterozygous-null mice were ovariectomized at 4 months of age and killed at 5 weeks. The 3D micro-CT was used to examine the trabecular structure of the mice, with an isotropic resolution of $9\,\mu m^3$. Bone specimens from mice heterozygous for the PTHrP null allele demonstrate significant changes as compared with wild-type litter mates in most parameters examined; however, measurements of trabecular number and trabecular thickness were not significantly different between the two groups. These findings support the notion that PTHrP haplo-insufficiency

leads to abnormal bone formation in the adult mouse skeleton (He et al. 2000). Recently, µCT shows restoration of cancellous bone volume and connectivity in OVX mice treated with basic fibroblast growth factor for a short term (3 weeks), which can be maintained following treatment with the anti-resorptive agent residronate for at least 5 weeks after withdrawal of basic fibroblast growth factor (Yao et al. 2005). Micro-CT showed that three signaling-selective PTH(1-34) analogs improved microstructure of trabecular bone in the distal femur, T5 vertebra, and femur mid-shaft cortical thickness in female mice (Yang et al. 2005).

The hematopoietic-restricted protein Src homology 2 containing inositol-5-phosphatase (SHIP) blunts phosphatidylinositol-3-kinase-initiated signaling by dephosphorylating its major substrate, phosphatidylinositol-3,4,5-trisphosphate. SHIP -/- mice contain increased numbers of osteoclast precursors macrophages, osteoclast number due to the prolonged life span of these cells, and to hypersensitivity of precursors to macrophage colony-stimulating factor M-CSF and RANKL. Similar to pagetic osteoclasts, SHIP -/- osteoclasts are enlarged, containing upwards of 100 nuclei, and exhibit enhanced resorptive activity. Moreover, as in Paget's disease, serum levels of interleukin-6 are markedly increased in SHIP -/- mice. Consistent with accelerated resorptive activity, 3D trabecular volume fraction, trabecular thickness, number and connectivity density of SHIP -/- long bones are reduced, resulting in a 49% decrease in biomechanical properties, indicating that SHIP negatively regulates osteoclast formation and function and the absence of this enzyme results in severe osteoporosis (Takeshita et al. 2002). Zmpste24 is an integral membrane metalloproteinase of the endoplasmic reticulum. The most striking pathological phenotype of Zmpste24 deficiency in mice is multiple spontaneous bone fractures—akin to those occurring in mouse models of osteogenesis imperfecta. There is a significant loss in 3D bone microstructure of both cortical and trabecular bone in Zmpste24 -/- mice compared with wild-type (Bergo et al. 2002).

The physiological role of BMP signaling in bone formation in post-natal life remains undefined. Trabecular bone volume, osteoblast numbers, and bone formation rates in proximal tibiae were reduced 27, 38, and 44%, respectively, in Smad1 gene knokout mice compared with control littermates. A 3D micro-CT examination showed that in tibiae and femora, trabecular volume, number, thickness, and connectivity density were decreased, and trabecular separation was increased. In the dnBMPR transgenic mice, there was an identical phenotype to that observed in the Smad1gene knockout mice, namely blockage of BMP signaling, decreased trabecular bone volume, and decreased bone formation rates. These results demonstrate that Smad1 is necessary for normal postnatal bone formation, and suggest that BMPs exert their effects on bone formation through the Smad1 signaling pathway (Chen et al. 2003).

Mice homozygous for an insertional mutation in osteopotentia, a novel transmembrane protein essential for skeletal integrity, develop striking skeletal abnormalities similar to those seen in humans and engineered mouse models having severe forms of the brittle bone disease osteogenesis imperfecta. Abnormalities include inflammation and hemorrhaging around limbs, bowing deformities of the long bones, and poorly healed fractures evidenced by the formation of hypertrophic calluses on

long bones and ribs. Micro-CT shows a decrease in trabecular number and trabecular thickness, with a corresponding increase in trabecular separation.

Because of the increasing technical ability to manipulate and study gene expression in the mouse, there is a growing interest in the use of the aged mouse as an animal model to study age-related bone loss in humans. Indeed, because of the remarkable differences in peak bone mass across mouse strains, much work is now concentrated on seeking genetic loci associated with high and low bone mass; however, the question arises as to whether mice lose bone with age or with deprivation of estrogen, and if so, whether the pattern of loss and change in bone architecture is similar to that in human aging. We have shown that ovariectomy induces short-term high-turnover accelerated deterioration of 3D trabecular structure in mice. In a study using 3-month-old Swiss Webster mice 5 and 13 weeks after ovariectomy, 3D micro-CT trabecular structure was measured in the secondary spongiosa of the distal femur with an isotropic resolution of $9\,\mu m^3$. The trabeculae become more rod-like and more isotropic, thinner, and more widely separated after ovariectomy (Zhao et al. 2000c). The HRT prevented OVX-induced bone loss. Percentage changes in pQCT volumetric BMD were similar to the changes measured by micro-CT but less pronounced.

Other Research Applications

Micro-CT has other research applications, e.g., finite element modeling for evaluation of bone biomechanical properties (Van Rietbergen 2003), assessment of bone tumors and treatment response, quantifying osteogenesis in mouse Ilizarov leg-lengthening procedures, and quantifying osteoconduction in a rat cranial defect model (Jiang et al. 2000). In a model of rheumatoid arthritis in mice, micro-CT can quantify the loss as a result of erosion and increased bone resorption and treatment response. Destruction of cartilage and bone are poorly managed hallmarks of human rheumatoid arthritis (RA). Because p38 MAP kinase has been shown to modulate the activity of key pro-inflammatory pathways in RA, we have shown that oral administration of p38 MAP kinase blockade, an inhibitor of this kinase (SD-282), prevents 3D bone destruction in early- and late-stage mouse model of an RA model induced with bovine type-II cartilage ($100\,\mu g/kg$, subcutaneous on days 0 and 21) and lipopolysaccharide ($50\,\mu g/mouse$, intraperitoneal on day 22). In a model of osteoarthritis in dogs, micro-CT with a nominal resolution of $66\,\mu m$ was used to examine the subchondral bone changes. The 3D micro-CT and 2D histomorphometry showed a decrease in bone volume fraction and an increase in bone surface fraction in the femur and patella of dogs 3 and 6 months after an anterior cruciate ligament transection.

Histomorphometry also shows an increase in bone formation rate. Micro-CT images of the femur showed multiple pits on the bone surface of femoral condyles and femoral trochlear ridges, whereas the gross inspection of the cartilage showed only a discoloration in the corresponding areas, indicating that the subchondral bone erosions preceded articular cartilage damage in the development of osteoarthritis (Han et al. 2001). PTH(1-84) at 5, 10, or $25\,\mu g/kg\ day^{-1}$ increased micro-CT bone volume

fraction with associated increases in trabecular number, thickness, and connectivity density in the thoracic vertebrae of osteopenic rhesus monkeys (Moreau et al. 2005).

We examined the precision of 3D microarchitecture of the new bone formation inside the porous titanium prosthesis implanted in the distal femur of rabbits. The implants have different sizes of pore, and have different coating materials. Micro-CT can reproducibly quantify 3D microarchitecture of the new bone formation inside the pores of the titanium prosthesis implants, which may find application in studying effects of different size of pores and different coating materials on osteogenesis (Jiang et al. 2005 a).

Synchrotron Radiation

The micro-CT method was further enhanced by resorting to synchrotron radiation with a spatial resolution of 2 µm (Bonse et al. 1994), or with applications to live rats (Kinney et al. 1995). Compared with X-ray tube, the X-ray beam from synchrotron radiation has high magnitude of intensity, monochromaticity, high photon flux, and small angular source size. For X-ray tube micro-CT, Smith and Silver (1994) have reported that 3D images from cone-beam scanners are inevitably distorted away from the central slice because the single-orbit cone-beam geometry does not provide a complete data set. These distortions and associated loss of spatial resolution have been particularly evident in samples containing plate-like structures, even when the cone-beam angle is less than 6.5° (Smith and Silver 1994). A recent study with direct comparison of fan-beam (obtained on the central plane) and cone-bone (obtained from a divergent section near the periphery of the volume) techniques over a full cone angle of 9°, using a 100 µm µfocus X-ray tube isotropic 33 µm voxels, showed that the bone volume fraction based on a gray-scale threshold in the excised lumbar vertebrae from normal adult rats was not adversely affected by cone-beam acquisition geometry for cone angles typically used in micro-CT (Holdsworth et al. 2001).

The use of synchrotron radiation X-ray source was first suggested by Grodzins (1983) for high-resolution micro-tomography of small samples. It provides a continuous energy spectrum with a high photon flux. The optimum energy for a given sample can be selected from the synchrotron radiation white beam with a small energy bandwidth (0.1–0.001%) using a crystal monochromator, whereas at the same time keeping the photon flux rate high enough for efficient imaging. The monochromaticity of the beam is very important, whereas conventional polychromatic X-ray sources result in beam-hardening artifacts in the reconstructed images due to the stronger attenuation of the soft X-ray in the sample. The monochromaticity of the beam is especially important to perform accurate density measurement. The high photon flux available and small angular source size from synchrotron radiation X-ray sources lead to negligible geometrical blur, making it possible to obtain images with high spatial resolution and high signal-to-noise ratio. The X-ray intensity of synchrotron radiation is higher in magnitude than X-ray tubes. When scanning time is important, synchrotron radiation is a better choice than X-ray tubes for resolution < 1–5 µm. Adaptation of the X-ray energy to the sample can be optimized by using monochromatic radiation because of the continuous X-ray spectrum of synchrotron radiation, which can minimize radiation exposure for examining small an-

imals in vivo. Synchrotron micro-CT has spatial resolutions of 2 μm because of high brightness and natural collimation of radiation sources (Bonse et al. 1994). It uses parallel beam-imaging geometry, and avoids the distortions and loss of resolution inherent in cone-beam methods, and can make distortionless images of human trabecular bone using a CT at a synchrotron electron storage ring (Bonse et al. 1994). Recently, micro-CT using high intensity and tight collimation synchrotron radiation that achieves spatial resolution of 1 – 2 μm has provided the capability to assess additional features such as resorption cavities (Peyrin et al. 1998).

Synchrotron micro-CT at 23 μm/voxel in the proximal tibial metaphysis of live rats (Lane et al. 1995, 1999) shows that trabecular connectivity decreased 27% by days 5 and 8 post-OVX and continued to decrease up to day 50 after OVX. The trabecular BV/TV decreased 25% by 8 days after OVX, and it continued to decrease through day 50. These changes were more rapid than biochemical markers. Estrogen replacement therapy initiated 5 – 13 days after OVX can restore BV/TV—but not connectivity—to baseline levels by allowing bone formation to continue in previously activated bone remodeling units while suppressing the production of new remodeling units. Intermittent human parathyroid hormone (1-34) treatment in osteopenic OVX rats increased trabecular BV/TV to control levels or higher by thickening existing trabeculae. Human parathyroid hormone (1-34) did not re-establish connectivity when therapy was started after 50% of the trabecular connectivity was lost. At 120 days after OVX, there was a small but significant decrease in trabecular bone volume, and a significant decrease in trabecular plate thickness. The decrease in trabecular thickness was associated with an increase in connectivity, in contrast to the proximal tibia, where connectivity always declines (Kinney et al. 2000).

In addition, synchrotron radiation X-ray micro-tomography (micro-CT) using new X-ray optic components has been designed to assess the ultrastructure of individual trabeculae with a resolution of 1 μm, and to describe microscopic variations in mineral loading within the bone material of an individual trabecular rod. Artifacts from X-ray refraction and diffraction require methods different from those used for other micro-CT techniques. Delicate and minimal individual trabecular specimen handling and no microtome cutting preserve the specimen geometry and internal micro-fractures. The histological features of the mineral ultrastructure can be evaluated using volumetric viewing. The volume, shape, and orientation of osteocyte lacunae and major cannaliculae can be observed. Quantitative measures of trabecular ultrastructure are now being considered including BMU (basic multicellular unit of bone remodeling with activation-resorption-formation sequence) volume, lamellar thickness, and density gradients (Flynn et al. 2001).

The hardware for synchrotron radiation micro-CT, however, is not readily accessible. Electron storage rings are stationary and cannot be operated in a small laboratory and only a few synchrotron radiation centers are available worldwide.

(MRI) Microscopic Imaging

Magnetic resonance imaging is a complex technology. High-resolution MR and μMR, collectively called MR microscopy, have received considerable attention both as research tools and potential clinical tools for assessment of osteoporosis. As a non-invasive, non-ionizing radiation technique, MR can provide 3D images in arbitrary orientations and can clearly depict trabecular bone.

Currently, assessment of trabecular structure using MR microscopy is restricted to the peripheral skeleton, unlike CT which can be applied to the spine and peripheral bones. The parameters derived from the low-resolution images account for 91% of the variation in Young's modulus, suggesting that noninvasive assessment of the mechanical competence of trabecular bone in osteoporotic patients may be feasible (Hwang et al. 1997).

Examination of the distal radius using MRI with a spatial resolution of $156\,\mu m^2$, a slice thickness of 0.7 mm, and a modified gradient-echo sequence using a 1.5-T clinical imager (Majumdar 1998) clearly depicted the loss of the integrity of the trabecular network with the development of osteoporosis. Similar images of the calcaneus of normal subjects showed that the orientation of the trabeculae is significantly different in various anatomic regions. Ellipses, representing the mean intercept length, showed a preferred orientation and hence mapped the anisotropy of trabecular structure. Resolutions of $78-150\,\mu m$ and slice thicknesses of $300\,\mu m$ have been achieved in the phalanges, a convenient anatomic site that is particularly suitable for obtaining high signal-to-noise ratio and high spatial resolution images in vivo, using clinical imagers at 1.5 T with a special radio-frequency coil (Jara et al 1993; Stampa et al. 1998), and quantitative 3D parameters based on an algorithm and model for defining trabecular rods and plates have been derived (Stampa et al. 1998). It has been reported that using trabecular structure or textural parameters from in vivo MR images of the radius or calcaneus can discriminate spine and/or hip fracture (Link et al. 1998; Wehrli et al. 1998).

Although high-resolution MR has been used successfully for in vitro quantitative evaluation of human trabecular bone, application of this technology to small animal bones is more demanding, as resolution requirements are more stringent because of the considerably smaller trabecular size. The need for higher resolution, dictated by the thinner trabeculae, entails a significant penalty for signal-to-noise ratio and acquisition time. Recently, the ability of MRI to assess osteoporosis in animal models has been explored in depth. One study demonstrated that using a small high-efficiency coil in a high-field imager, MRI can provide resolutions sufficient to discriminate individual trabeculae. The MRI of trabecular structure in the distal radius shows trabecular bone loss after OVX. Micro-MRI of a rat tail showed 3D cortical bone, trabecular network, and other soft tissue. The μMRI shows increased bone mass in the distal femoral metaphysis of rats treated with a bisphosphonate, increased cartilage thickness in the growth plate, and corresponding recovery changes after withdrawal of treatment. (The trabecular structure in the femoral neck of a ewe can be clearly shown on MRI.) In this study, with appropriate choices, it was possible to image trabecular bone in rats in vivo and in vitro. Segmenting trabecular bone

from adjacent tissues has been a useful technique in the quantification of trabecular bone in MRI images. In a study of ovariectomy in rats, analysis of MRI demonstrated differences in rat trabecular bone that were not detected by DXA measurements.

A double-blind study evaluated trabecular (Tb) microstructure using MRI microscopy and bone quality in terms of resistance to fracture of the femoral neck of a postmenopausal osteoporotic model in ewes treated with salmon calcitonin (sCT), an osteoclast inhibitor. The femoral neck was examined with an MR imager at 9.4 T in axial, coronal, and sagittal planes, using a spin-echo multislice pulse sequence with TR = 1 s, TE = 1.8 ms, inplane resolution 78 µm, and slice thickness 1 mm. An internal calibration procedure standardizing image analysis was used to adjust the segmentation threshold. Data from all three axial, coronal, and saggital planes were averaged. Compared with Sham, OVX for 6 months induced statistically significant changes in Tb structure: Tb bone volume fraction −18%, Tb separation +23%, number of free ends +28%, number of nodes −39%, number of Tb branches −23%, and mean length of Tb branches −19%. There was a dose response of sCT effect on the Tb structure. Compared with OVX, treatment using sCT at 100 U significantly improved all the Tb structural parameters to the Sham level, whereas at 50 U it significantly increased the mean length of the Tb branches. The OVX significantly decreased Tb biomechanical competence (compressive strain −28%). Treatment with sCT resulted in a significant dose-dependent preservation of compressive stress. In univariate analysis, strength and stiffness were correlated with DXA and several components of microarchitecture. Toughness was correlated with MR but not with BMD. In a multivariate stepwise regression analysis, strength and stiffness correlated with BMD and TV/BV, whereas toughness was related to the mean length of the branches. These results indicate that microarchitecture of trabecular bone contributes significantly to its biomechanical characteristics, independent of BMD measured in the femoral neck. Tb bone volume fraction explained 74% of compressive stress. Combination of all structural parameters in a multivariate regression analysis significantly improved the results to 84%, and the combination of BMD further increased the results to 92%. The effects of sCT on the OVX ewes may help explain reduced fracture risk in postmenopausal osteoporotic women treated with sCT (Jiang et al. 2005b).

The MRI showed ovariectomy induced losses in trabecular bone volume fraction and structure that ERT prevented. There are excellent correlations between MRI with resolution up to $24 \times 24 \times 250\,\mu m$ and histological assessment of intact rat tibiae and vertebrae (Kapadia et al. 1993). It has been reported that rat tibiae were imaged at 9.4 T in vitro with isotropic resolution of $46\,\mu m^3$. It has also been shown that alendronate maintains trabecular bone volume and structure about midway between intact and OVX, whereas prostaglandin E_2 returned them to intact levels (Takahashi et al. 1999).

The MRI shows 3D bone structure and some other tissues at the same time. In the rabbit knee, MRI shows trabecular structure and cartilage. In an osteoarthritis model induced by menisectomy or anterior cruciate ligament transection (Zhao et al. 1999), MRI shows subchondral osteosclerosis, and decreased cartilage thickness. The MRI also shows osteophytes in a rabbit osteoarthritis model; however, radiographs only show subchondral osteosclerosis, whereas osteophytes could not be found in a rabbit osteoarthritis model.

One of the crucial parameters to assess bone quality is the degree of bone mineralization. Water- and fat-suppressed projection MR imaging was used to image the solid matrix content of rat bone specimens. The signal from the medullary cavity (water and fat) is largely suppressed, along with the water and fat signal inside bone tissues. This method provides a means to measure bone matrix density in small animals (Wu et al. 2005). To distinguish osteomalacia from normal bone, hypomineralization was induced in rabbits. The 1-H images were acquired at 400 MHz from excised cortical bone by 3D 1 H solid-state imaging of the tibia at a resolution of 183 μm. Significantly, higher water content was found in animals with osteomalacia than in controls; thus, proton solid-state imaging of bone water can distinguish subtle differences in mineralization density and therefore may provide a new means for noninvasive assessment of degree of mineralization of bone (Anumula et al. 2005).

The usefulness of this powerful tool is balanced by disadvantages: it is expensive to obtain, operate, and maintain, and it is rarely available for routine nonclinical use. Dedicated extremity MR systems, which are low-field and less expensive, can quantify geometry of the cortical bone such as cross-sectional area and cross-sectional moments of inertia (CSMI) in the distal radius, and the muscle mass in the forearms, which contribute significantly to the biomechanical strength of the radius (Jiang et al. 1998). The mechanical behavior of a bone reflects the material property within the bones as well as the bone geometry. The CSMI describes the geometric configuration or distribution of the bone mass around the central axis. The magnitude of the CSMI depends on both the cross-sectional area and the squared distance of each unit area from the sectional neutral axis that always intersects the centroid, or center, of the area of the section. In torsion, deformation would be resisted more efficiently if bone were distributed further away from the neutral torsional axis. Ideally, in bending or torsion, bone should be distributed as far away from the neutral axis of the load as possible.

Summary

Many studies have shown that changes in bone quality and structural characteristics lead to changes in bone biomechanical competence or individual risk of fracture independently of BMD. Structural measurements using 3D assessment contribute to our understanding of osteoporosis and other bone disorders, and provide insight into their pathomechanisms, and treatment response, in various animal models and in humans.

Although advanced imaging is demanding in terms of equipment and technique, it is unbiased, free from the model assumptions used in 2D histomorphometry. Since a true 3D assessment of the trabecular bone structure is possible, rod or plate model assumptions are no longer necessary. They are able to directly measure 3D structure, connectivity, and integrity in a highly automated, fast, objective, non-user-specific manner, with little sample preparation, allowing greater numbers of samples for unbiased comparison between controls and subjects. They can have large sample sizes and therefore less sampling error. They are non-destructive, which allows multiple

tests such as biomechanical testing and chemical analysis on the same sample, and noninvasive, which may permit longitudinal studies. These methods also have weaknesses: they require robust image processing algorithms to segment and quantify bone structure, and may have limitations in spatial resolution for certain structures. They cannot provide information on cellular activities or dynamic mineralization processes. Rather than replacing bone histomorphometry, these imaging methods provide additional and valuable information, and are a useful complement to traditional techniques in the evaluation of osteoporosis and other bone disorders.

References

Anumula SS, Magland J, Zhang H, Ong H, Wehrli SW, Wehrli FW (2005) Multimodality study of the compositional and mechanical implications of hypomineralization in a rabbit model of osteomalacia. J Bone Miner Res 20 (Suppl 1):S332

Bergo MO, Gavino B, Ross J, Schmidt WK, Hong C, Kendall LV, Mohr A, Meta M, Genant H, Jiang Y, Wisner ER, Van Bruggen N, Carano RA, Michaelis S, Griffey SM, Young SG (2002) Zmpste24 deficiency in mice causes spontaneous bone fractures, muscle weakness, and a prelamin A processing defect. Proc Natl Acad Sci USA 99:13049–13054

Bonse U, Busch F, Gunnewig O, Beckmann F, Pahl R, Delling G, Hahn M, Graeff W (1994) 3D computed X-ray tomography of human cancellous bone at $8\,\mu$m spatial and 10^{-4} energy resolution. Bone Miner 25:25–38

Borah B, Dufresne T (2003) 3D micro CT applications in osteoporosis: a clinical perspective. Abstract Book of the First µCT User Workshop, Philadelphia

Chen D, Qiao M, Story B, Zhao M, Jiang Y, Zhao J, Feng J, Xie Y, Huang S, Roberts A, Karsenty G, Mundy G (2003) BMP signaling through the Smad1 pathway is required for normal postnatal bone formation. J Bone Miner Res 18:S6

Dempster DW, Cosman F, Kurland E, Muller R, Nieves J, Woelfert L, Shane E, Plavetic K, Bilezikian J, Lindsay R (2000) Two- and three-dimensional structural analysis of paired biopsies from osteoporotic patients before and after treatment with parathyroid hormone. J Bone Miner Res 15:S194

Feldkamp LA, Goldstein SA, Parfitt AM, Jesioil G, Kleerekoper M (1989) The direct examination of three-dimensional bone architecture in vitro by computed tomography. J Bone Miner Res 4:3–11

Flynn M J, Seifert HA, Irving TC, Lai B (2001) Measurement of bone mineralization in whole trabeculae using 3D X-ray microtomography. Proc Int Symp on Bone Biotechnology and Histotechnology, Phoenix, Arizona, p 28

Gabet Y, Kohavi D, Levy J, DiMarchi R, Chorev M, Müller R, Bab I (2005) Parathyroid hormone 1–34 enhances titanium implant osseointegration and peri-implant bone parameters in rat tibial model of low density trabecular bone: a micro CT analysis. J Bone Miner Res 20 (Suppl 1):S430

Grodzins L (1983) Optimum energy for X-ray transmission tomography of small samples. Nucl Instrum Methods 206:541–543

Guilak F (1994) Volume and surface area of viable chondrocytes in situ using geometric modeling of sense confocal sections. J Microsc 173:245–256

Han B, Brodie T, Shen Y, Triantafillou J, Scates P, Willams J (2001) Subchondral bone changes in an ACLT model of osteoarthritis in the dog. Proc Int Symp on Bone Biotechnology and Histotechnology, Phoenix, Arizona, p 31

He B, Jiang Y, Zhao J, Genant HK, Goltzman D, Karaplis AC (2000) Quantitative assessment of three-dimensional trabecular bone microstructure in PTHrP wild type and heterozygous-null mice using micro-computed tomography. J Bone Miner Res 15:S186

Hildebrand T, Rüegsegger P (1997a) Quantification of bone microarchitecture with the structure model index. Comp Meth Biomech Biomed Eng 1:15–23

Hildebrand T, Rüegsegger P (1997b) A new method for the model independent assessment of thickness in three-dimensional images. J Microsc 185:67–75

Holdsworth DW, Robarts JP, Thornton MM (2001) Validation of cone-beam reconstruction for bone micro-CT. Proc Int Symp on Bone Biotechnology and Histotechnology, Phoenix, Arizona, p 33

Hwang SN, Wehrli FW, Williams JL (1997) Probability-based structural parameters from three-dimensional nuclear magnetic resonance images as predictors of trabecular bone strength. Med Phys 24:1255–1261

Jara H, Wehrli FW, Chung H, Ford JC (1993) High-resolution variable flip angle 3D MR imaging of trabecular microstructure in vivo. Magn Reson Med 29:528–539

Jiang Y, Zhao J, Genant HK, Dequeker J, Geusens P (1997) Long-term changes in bone mineral and biomechanical properties of vertebrae and femur in aging, dietary calcium restricted and/or estrogen-deprived/-replaced rats. J Bone Miner Res 19:820–831

Jiang Y, Zhao J, Augat P, Ouyang X, Lu Y, Majumdar S, Genant HK (1998) Trabecular bone mineral and calculated structure of human bone specimens scanned by peripheral quantitative computed tomography: relation to biomechanical properties. J Bone Miner Res 13:1783–1790

Jiang Y, Zhao J, Prevrhal S, Genant HK (1999b) Three-dimensional trabecular microstructure, bone mineral density, and biomechanical properties of the vertebral body of ovariectomized rats with estrogen replacement therapy. J Bone Miner Res 14(S1):S534

Jiang Y, Zhao J, Recker RR, Draper MW, Genant HK (2000) Longitudinal changes between premenopausal and postmenopausal in three-dimensional trabecular microstructural characteristics of human iliac crest bone biopsies. J Bone Miner Res 15:S184

Jiang Y, Zhao J, Mitlak BH, Wang O, Genant HK, Eriksen EF (2003a) Recombinant human parathyroid hormone (1–34) (teriparatide) improves both cortical and cancellous bone structure. J Bone Miner Res 18:1932–1941

Jiang Y, Zhao J, Eriksen EF, Genant HK (2003b) Reproducibility of micro CT quantification of 3D microarchitecture of the trabecular and cortical bone in the iliac crest of postmenopausal osteoporotic women and their treatment with teriparatide [rhPTH(1–34)]. RSNA'03:571

Jiang Y, Zhao J, An YH (2005a) Three-dimensional microarchitecture of the new bone formation on the prosthetic implant: reproducibility of micro CT assessment. J Bone Miner Res 20 (Suppl 1):S335

Jiang Y, Zhao J, Geusens P, Liao EY, Adriaensens P, Gelan J, Azria M, Boonen S, Caulin F, Lynch JA, Ouyang X, Genant HK (2005b) Femoral neck trabecular microstructure in ovariectomized ewes treated with calcitonin: MRI microscopic evaluation. J Bone Miner Res 20:125–130

Kapadia RD, High W, Bertolini D, Sarkar SK (1993) MR microscopy: a novel diagnostic tool in osteoporosis research. In: Christiansen C (ed) Fourth Int Symp on Osteoprosis and Consensus Development Conference, Hong Kong, 28 pp

Kinney JH, Lane NE, Haupt DL (1995) In vivo, three-dimensional microscopy of trabecular bone. J Bone Miner Res 10:264–270

Kinney JH, Haupt DL, Balooch M, Ladd AJ, Ryaby JT, Lane NE (2000) Three-dimensional morphometry of the L6 vertebra in the ovariectomized rat model of osteoporosis: biomechanical implications. J Bone Miner Res 15:1981–1991

Kuhn JL, Goldstein SA, Feldkamp LA, Jesion G (1990) Evaluation of a microcomputed tomography system to study trabecular bone structure. J Orthop Res 8:833–842

Lane NE, Thompson JM, Strewler GJ, Kinney JH (1995) Intermittent treatment with human parathyroid hormone (hPTH[1–34]) increased trabecular bone volume but not connectivity in osteopenic rats. J Bone Miner Res 10:1470–1477

Lane NE, Haupt D, Kimmel DB, Modin G, Kinney JH (1999) Early estrogen replacement therapy reverses the rapid loss of trabecular bone volume and prevents further deterioration of connectivity in the rat. J Bone Miner Res 14:206–214

Link T, Majumdar S, Augat P, Lin J, Newitt D, Lang T, Lu Y, Lane N, Genant HK (1998) In vivo high resolution MRI of the calcaneus: differences in trabecular structure in osteoporotic patients. J Bone Miner Res 13:1175–1182

Majumdar S, Kothari M, Augat P, Newitt DC, Lin JC, Lang T, Lu Y, Genant HK (1998) High-resolution magnetic resonance imaging: three-dimensional bone architecture and biomechanical properties. Bone 22:445–454

Moreau IA, Smith SY, Guldberg RE, Turner CH, Newman MK, Fox J (2005) Treatment of osteopenic rhesus monkeys with parathyroid hormone 1–84 for 16 months improves vertebral trabecular bone quantity and quality. J Bone Miner Res 20 (Suppl 1):S412

Mosekilde L (1993) Vertebral structure and strength in vivo and in vitro. Calcif Tissue Int 53:S121–S125

Odgaard A, Gundersen HJG (1993) Quantification of connectivity in cancellous bone, with special emphasis on 3D reconstruction. Bone 14:173–182

Peyrin F, Salome M, Cloetens P, Ludwig W, Ritman, Ruegsegger P, Laval-Jeantet AM, Baruchel J (1998) What do micro-CT examinations reveal at various resolutions: a study of the same trabecular bone samples at the 14, 7, and 2 micron level. Presented, Symposium on Bone Architecture and the Competence of Bone, Ittingen, Switzerland pp 3–5

Rüegsegger P, Koller B, Muller R (1996) A microtomographic system for the nondestructive evaluation of bone architecture. Calcif Tissue Int 58:24–29

Smith CB, Silver MD (1994) Comparison between single slice CT and volume CT. In: Czichos HCH, Schnitger D (eds) Int Symp on Computerized Tomography for Industrial Applications, Bundesministerium des Innern, Bundesanstalt fur Materialforschung und-prufung, Berlin, Germany

Stampa B, Kühn B, Heller M and C-C Glüer (1998) Rods or plates: a new algorithm to characterize bone structure using 3D magnetic resonance imaging. Presented at the 13th International Bone Densitometry Workshop, 4–8 October 1998, Wisconsin

Takeshita S, Namba N, Zhao J, Jiang Y, Genant HK, Silva MJ, Brodt MD, Helgason CD, Kalesnikoff J, Rauh MJ, Humphries RK, Krystal G, Teitelbaum SL, Ross FP (2002) SHIP-deficient mice are severely osteoporotic due to increased numbers of hyper-resorptive osteoclasts. Nature Med 8:943–949

Turner CH, Hsieh YF, Muller R, Bouxsein ML, Rosen CJ, McCrann ME, Donahue LR, Beamer WG (2001) Variation in bone biomechanical properties, microstructure, and density in BXH recombinant inbred mice. J Bone Miner Res 16:206–213

Van Rietbergen B (2003) Finite element modeling. Abstract Book of the First μCT User Workshop, Philadelphia

Wehrli FW, Hwang SN, Ma J, Song HK, Ford JC, Haddad JG (1998) Cancellous bone volume and structure in the forearm: noninvasive assessment with MR microimaging and image processing. Radiology 206:347–357

Wu Y, Ackerman JL, Dai G, Chelsler DA, Hrovat M, Snyder BD, Nazarian A, Glimcher MJ (2005) Solid bone matrix of rat femur imaged by water and fat suppressed proton magnetic resonance imaging. J Bone Miner Res 20 (Suppl 1):S223

Yang D, Bouxsein M, Chiusaroli R, Schipani E, Pajevic P, Guo J, Singh R, Bringhurst FR (2005) Signaling selective PTH (1–34) analogs accelerate bone formation. J Bone Miner Res 20 (Suppl 1):S102

Yao W, Balooch G, Nalla R, Zhou J, Jiang Y, Wronski T, Lane N (2005) Restoration of cancellous bone connectivity and strength in ovariectomized mice treated with basic fibroblast growth factor and followed by an anti-resorptive agent. J Bone Miner Res 20 (Suppl 1):S345

Zhao J, Jiang Y, Genant HK (2000a) Three-dimensional trabecular microstructure and biomechanical properties and their relationship in different bone quality models. Radiology 217 (P): 411

Zhao J, Jiang Y, Prevrhal S, Genant HK (2000b) Effects of low dose long-term sodium fluoride on three-dimensional trabecular microstructure, bone mineral, and biomechanical properties of rat vertebral body. J Bone Miner Res 15:816

Zhao J, Jiang Y, Shen V, Bain S, Genant HK (2000c) µCT and pQCT assessments of a murine model of postmenopausal osteoporosis and estrogen therapy. Osteoporosis Int 11 (S3):S11

Zhao J, Jiang Y, Vedi S, Compston JE, Genant HK (2002) Longitudinal changes in three-dimensional trabecular microarchitecture of paired iliac crest bone biopsies before and after estrogen replacement therapy in postmenopausal women. J Bone Miner Res 17:S208

CT-Based Microstructure Analysis for Assessment of Bone Fragility

Masako Ito

Department of Radiology, Nagasaki University School of Medicine, 1-7-1 Sakamoto,
Nagasaki 852-8501, Japan
e-mail: masako@net.nagasaki-u.ac.jp

Abstract

Determinants of bone quality include macro- and micro-architecture, secondary mineralization, bone matrix and micro-damage. Although it is recognized that bone quality is an essential component of bone fragility, no established methods of assessment are currently available for clinical use. Computed tomography (CT) can be adapted to evaluate both macroscopic and microscopic structure of bone. We discuss the application of CT to evaluate bone microstructure from micro-CT or synchrotron micro-CT to clinical high-resolution CT. Micro-CT technology can now provide ultra-high-resolution images of $< 10\,\mu m$. The orientation, shape and connectivity of trabeculae can be appreciated and analysed. Geometrical 3D maps are particularly useful to understand the complicated 3D structure of trabeculae. The analysis of trabecular structure is helpful in evaluating the pathophysiology of osteoporosis and the effects of anti-osteoporotic agents on bone mass and microarchitecture. Micro-CT data, linked with finite element analysis (FEA), can be adapted to estimate stress distribution and bone strength. Synchrotron micro-CT provides a more precise analysis of bone microstructure, such as the characteristics of trabecular surface and the different grade of mineralization. Clinical multi-detector row CT (MDCT) has can assess vertebral microstructure in vivo. Although the spatial resolution is limited compared with micro-CT, in vivo assessment of vertebral microstructure may be useful to evaluate the risk of fracture and the longitudinal efficacy of anti-osteoporotic agents.

Assessment of Trabecular Microarchitecture Using Micro-CT

Microstructural Changes Resulting from Ovarariectomy or Neurectomy

An experimental study using ovariectomized (OVX) rats showed that oestrogen deficiency induced trabecular deterioration, manifested by a decrease in bone-to-tissue volume fraction (BV/TV = bone volume/tissue volume), trabecular number (Tb.N) and connectivity density, as well as an increase in trabecular separation (Tb.Sp) and structure model index (SMI; increases in the ratio of plate-like trabeculae), compared
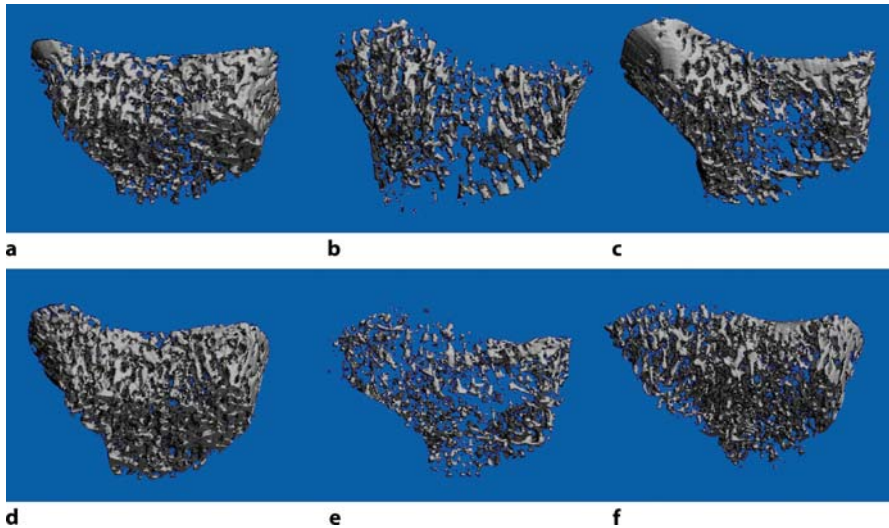
Figure 1 a–f. Three-dimensional micro-CT images of the OVX-sham (**a**), OVX control (**b**), OVX treated with etidronate (EHDP; **c**), NX-sham (**d**), NX control (**e**) and NX treated with EHDP (**f**)

with the sham-operated group (Shiraishi et al. 2002). Trabecular thickness does not always significantly decrease, probably because changes in this parameter depend on the duration of oestrogen deficiency or the age of the animals, and its detection depends on the spatial resolution of micro-CT. The degree of anisotropy (DA) increased after OVX, indicating that trabecular resorption occurs heterogeneously with preservation of the longitudinal trabeculae and disappearance or thinning of the transverse trabeculae. This is attributed to the fact that longitudinal trabeculae are oriented to resist axial loading, whereas transverse trabeculae are not. In contrast, sciatic neurectomized (NX) rats showed marked trabecular deterioration; however, in this case the degree of anisotropy is decreased in contrast to that of OVX rats, since immobilization induces a decrease in all trabecula, both longitudinal and axial.

The study suggests that the increase in DA associated with decreased bone mass, as seen in OVX rats, results from adaptation to loading, which maintains mechanical strength through relative preservation of axial trabeculae, even with a small amount of bone mass. The decrease in cortical area is more prominent in NX than OVX rats. Three-dimensional images of NX rats showed flake-like trabeculae, whereas those in the OVX rats demonstrated preservation of trabecular shape (Fig. 1; Ito et al. 2002a). The reduction of cortical area was more significant in the NX group.

Effect of Anti-osteoporotic Agents on Bone Following Ovariectomy or Neurectomy

We performed a study to evaluate the effect of etidronate (EHDP) on 3D trabecular microstructure in OVX and NX rats (Nishida et al. 2004). Eight-week-old female rats received ovariectomy ($n = 19$) or sham operation (OVX-sham; $n = 10$). The OVX

rats received either vehicle (OVX-control; n = 9) or EHDP (OVX-EHDP; n = 10). Another group of 8-week-old female rats received NX (n = 20) or sham operation (NX-sham; n = 10). The NX rats received either vehicle (NX-control; n = 10) or EHDP (NX-EHDP; n = 10). The EHDP at 5 mg/kg or vehicle was subcutaneously injected 5 days a week. The treatment was initiated 2 weeks after surgery and was continued for 2 weeks. After the treatment, the tibiae were harvested and examined by micro-CT; (μCT20; Scanco Medical). The recovery of structural parameters was not complete in NX rats compared with OVX rats. The 3D micro-CT images showed that the subcortical spongiosa, which was preserved in OVX rats, revealed marked loss in NX rats. Furthermore, these trabeculae were not restored after the EHDP treatment. We concluded that immobility leads to loss of subcortical spongiosa and that etidronate does not prevent this loss in the short term (Fig. 1).

Microstructure and Bone Strength

Trabecular microstructure parameters have a significant correlation with the ultimate load of the ovariectomized rat vertebrae (Fig. 2). This indicates that trabecular microstructure is strongly related to bone strength.

Contribution of Cortical and Trabecular Bone to Biomechanical Property in Vertebrae

To evaluate how much the trabecular and cortical components contribute to bone strength in rats, we developed a finite element analysis (FEA) system using 3D data of micro-CT (Ito et al. 2002b). Twenty-five female rats, 10 months of age, underwent
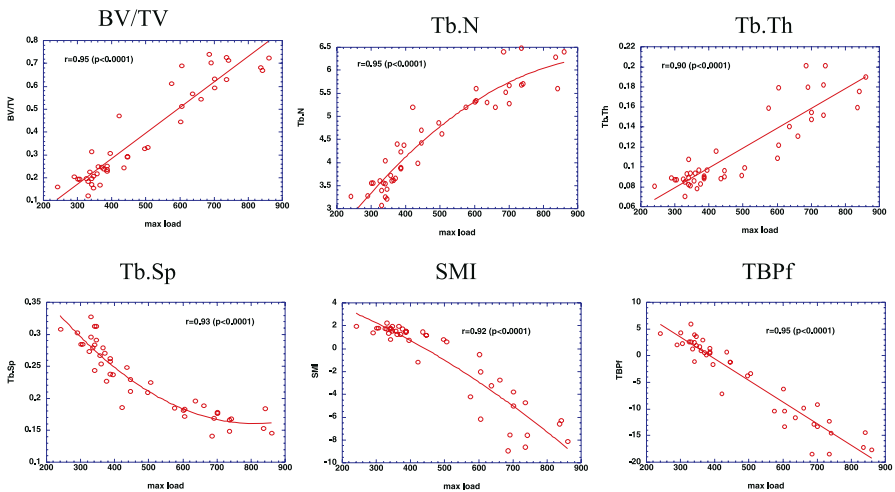
Figure 2. Relationships between microstructural parameters and ultimate load. Microstructural parameters (BV/TV, Tb.N, Tb,Th, Tb.Sp, SMI and TBPf) have significant correlation with the ultimate load of the rat vertebrae. *BV/TV* bone volume fraction, *Tb.N* trabecular number, *Tb,Th* trabecular thickness, *Tb.Sp* trabecular separation, *SMI* structure model index, *TBPf* trabecular bone pattern factor

OVX or sham operation. These rats were classified into three groups: sham control ($n = 6$); OVX control ($n = 4$); and OVX rats treated with alfacalcidol daily dose of zero ($n = 4$), 0.1 mg/kg ($n = 8$) or 0.2 mg/kg ($n = 7$). After 6 months, the excised fifth lumbar vertebral bodies were evaluated by micro-CT. The compressive ultimate load of the specimen was measured by mechanical testing. The yield strength calculated using FEA correlated strongly with load value ($r = 0.90$, $p < 0.0001$). In specimens with a 3D trabecular BV/TV of > 25% ($n = 13$), the strength values showed significant correlations with the values of the cortical area ($r = 0.62$, $p < 0.005$) and BV/TV ($r = 0.87$, $p < 0.0001$). In the specimens with BV/TV of < 25% ($n = 12$), however, the strength showed a significant correlation only with the cortical area ($r = 0.64$, $p < 0.005$). The yield strength values reached a plateau when the micro-CT image of spongiosa selectively reduced at the threshold higher more than a certain level, indicating that spongiosa bears 30–40% of the strength. The mechanical contribution of spongiosa apparently related with the trabecular bone mass, but the critical amount of trabecular bone mass seems to exit where the substantial contribution to the bone strength disappears.

Relationship of Bone Mass, Bone Microarchitecture and Bone Mechanical Property

We evaluated the effect of risedronate on the trabecular microstructure of OVX rat tibiae, using micro-CT, in order to investigate how changes in microstructure contribute to biomechanical property (Ito et al. 2005). Fifty 18-week-old rats underwent sham-operation ($n = 10$) or OVX ($n = 40$). The OVX rats were further divided into four groups ($n = 10$ for each group) treated with risedronate at doses of 0, 0.1, 0.5 or 2.5 mg/kg for 9 months.

The OVX caused deterioration in 3D trabecular microstructure, notably structure model index (SMI) and connectivity density, whereas treatment with risedronate doses at 0.5 and 2.5 mg/kg improved these microstructural changes. Biomechanical property, as assessed by finite element analysis (FEA), correlated significantly with bone volume/tissue volume (BV/TV), and the correlation further increased substantially by adding microstructural parameters, especially SMI and connectivity density, with risedronate therapy; thus, it is suggested that in addition to increasing bone mass, risedronate improves biomechanical property by maintaining a plate-like structure as well as connectivity of trabeculae (Table 1).

The FEA can demonstrate the relationship between biomechanical properties and microstructural changes following administration of anti-osteoporotic agents, although a limitation of FEA system exists, which is probably due to changes of material property after administration of anti-osteoporotic agents.

Assessment of Bone Microarchitecture and Bone Mineralization Using Synchrotron-CT

Synchrotron radiation (SR) provides an intense, laser-like collimated light in the range from infrared to hard X-rays. The use of SR as an X-ray source for high resolution microtomography of small samples was first suggested by Grodzins (1983).

Table 1. The R^2 values of multiple linear regression analysis between microstructural parameters and biomechanical properties in individual groups

	Sham		OVX		RIS 0.1		RIS 0.5		RIS 2.5
	R^2 (BV/TV)	R^2 (BV/TV+)	R^2 (BV/TV+)	R^2 (BV/TV)	R^2 (BV/TV+)	R^2 (BV/TV)	R^2 (BV/TV+)	R^2 (BV/TV)	R^2 (BV/TV+)
Young's modulus	0.85			0.56*	SMI 0.75; ConnD 0.74	0.63	SMI 0.88; ConnD 0.88; Tb.N 0.84	0.80	SMI 0.93; ConnD 0.93; Tb.Th 0.90; Tb.Sp 0.90; Tb.N 0.88
Shear modulus	0.85			0.48*	SMI 0.82; ConnD 0.81; Tb.Sp 0.77; Tb.N 0.75	0.69	ConnD 0.90; SMI 0.89; Tb.N 0.82	0.84	SMI 0.99; ConnD 0.98; Tb.Sp 0.92
Poisson's ratio	0.39*	0.14*		0.14*		0.27*	ConnD 0.75	0.15*	SMI 0.72

The values are shown when their p-values were significant ($p < 0.05$)

* The p-values of R^2 were not significant

Unlike a conventional X-ray tube, SR offers a continuous energy spectrum with a high photon flux. Monochromaticity of the beam is thus absolutely necessary to perform accurate density measurements. The high photon flux from synchrotron X-ray sources and the small angular source size with negligible geometrical blur make it possible to obtain images with high spatial resolution and high signal-to-noise ratio. Because of the characteristic of SR white beam, it has a possibility to provide the different density according to mineralization or to demonstrate bone structure precisely. The SRCT system has been applied to analyze bone microstructure in vivo (Kinney et al. 1995) and in vitro (Bonse et al. 1994, Engelke et al. 1993, Lane et al. 1999, Pateyron et al. 1996, Kinney et al. 1998, 2000) animal studies.

We investigated the ability of SRCT to demonstrate trabecular microstructure, trabecular surfaces and bone mineralization (Super Photon ring-8 GeV; SPring-8; Ito et al. 2003). The SRCT showed high image quality without visible partial volume effect. Three-dimensional SRCT reveals shallow concavities in the bone surface (considered to represent osteoclastic resorption areas (Fig. 3) as well as the connectivity, anisotropy and shape (i.e. rod- or plate-like) of trabeculae, and is almost comparable to scanning electron microscopy (SEM; see Fig. 5). Dilation of vessel canals was demonstrated by SRCT in NX rat tibiae (Fig. 4), which could not be revealed by conventional micro-CT. Two-dimensional SRCT showed different density along the surface of the trabecular bone, indicating the degree of bone mineralization (Fig. 6). These data show that SRCT seems to be a useful tool for delineating trabecular surfaces, evaluating bone mineralization, and for revealing precise trabecular structure.

We quantified and visualized three dimensionally calcium (Ca) density in bone using SRCT. Since mass attenuation coefficients change according to X-ray energy,

a   b
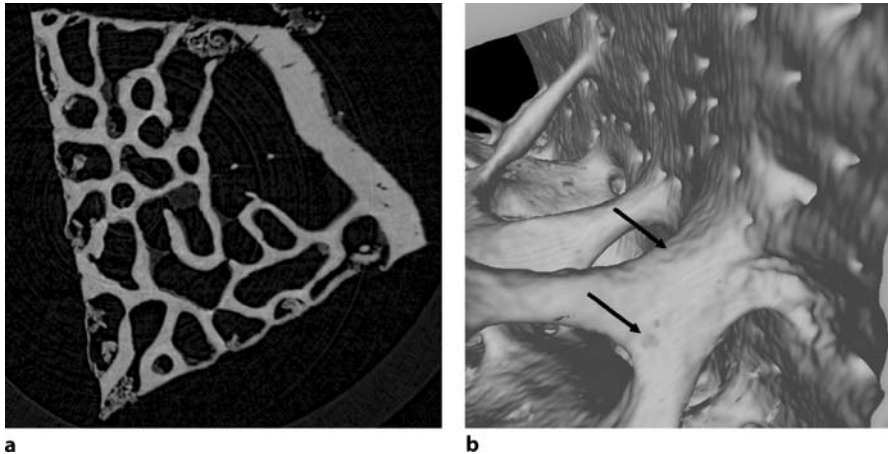
Figure 3 a,b. Two-dimensional and Three-dimensional trabecular microstructure SRCT images of rat vertebra. Two-dimensional image (**a**) shows the sharp border of the trabeculae without visible partial-volume effect. Three-dimensional image (**b**) shows shallow concavities in the trabecular surfaces (*arrows*)
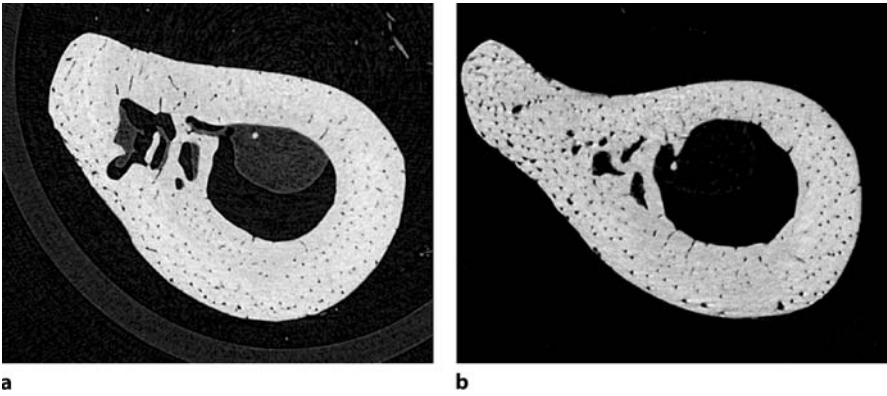
Figure 4 a,b. Two-dimensional axial SRCT images of the rat tibial diaphysis. The NX rat (**b**) shows the dilatation of vessel canals in comparison with the sham-operated rat (**a**)
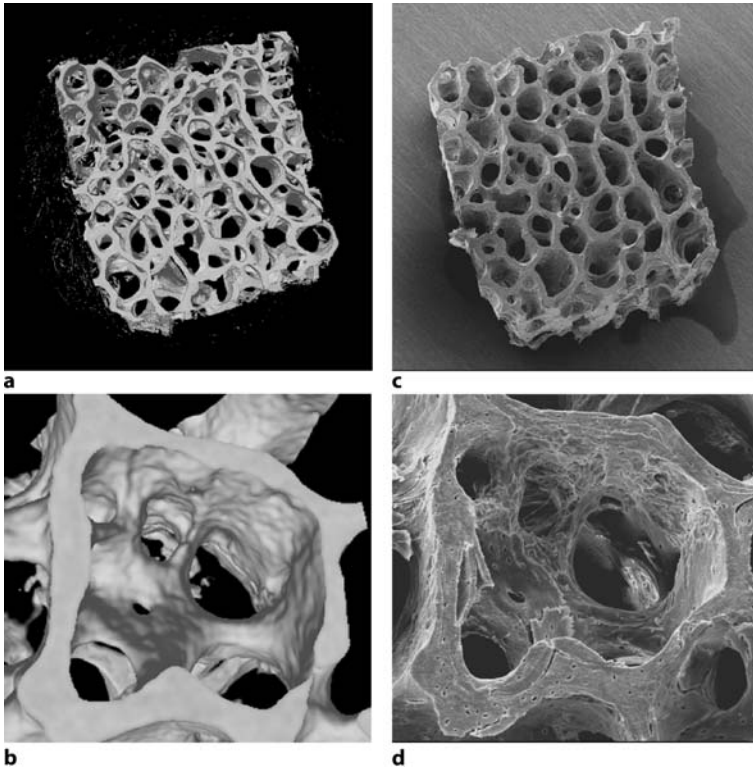
Figure 5 a–d. Three-dimensional SRCT and SEM images of trabecular surface of mini-pig vertebra. The SRCT image (**a**) shows irregularity of trabecular surface (magnified image, **b**). Multiple resorption cavities can be demonstrated using SEM in the same region (**c**) and magnified image (**d**). The SEM image with 8-bit resolution in grey scale
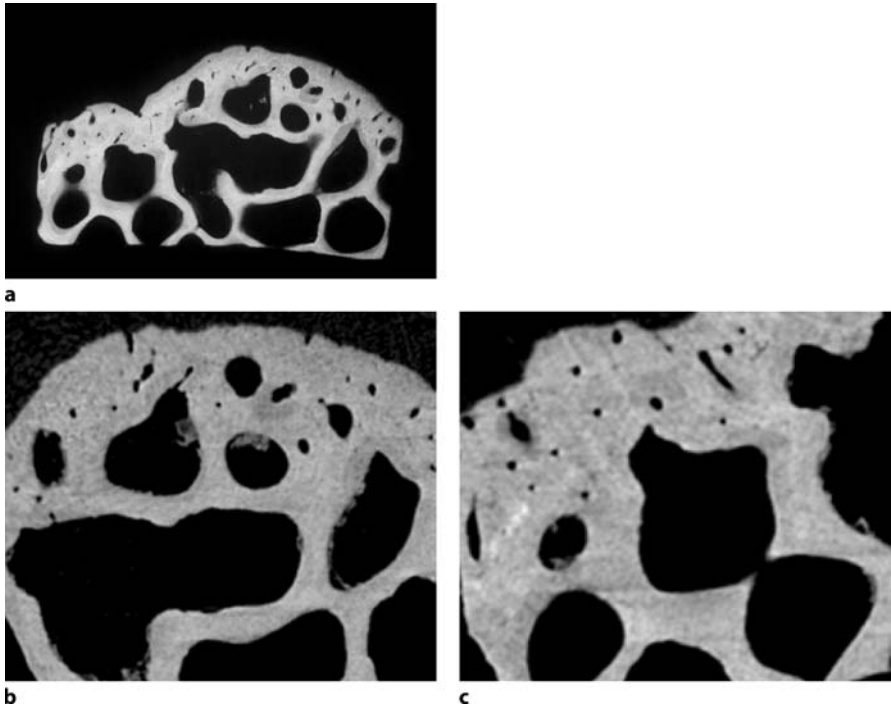
Figure 6 a–c. Two-dimensional SRCT and contact microradiography (CMR) images of the vertebral bone in the mini pig. Different densities can be detected in the surface of the trabeculae by SRCT (**b,c**) as well as by CMR (**a**)
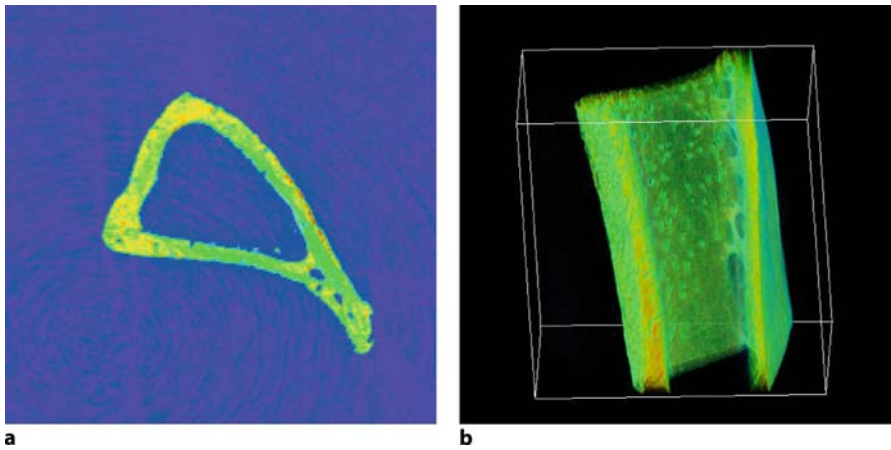
Figure 7 a,b. Two-dimensional (**a**) and 3D (**b**) calcium-density mapping. *Green* indicates the lower Ca concentration, *red* indicates the higher Ca concentration

the coefficients of Ca and carbon (C) were obtained at the various energies of 15, 17, 25 and 40 KeV. The Ca and C density were calculated using the following equation:

$$\mu = \frac{\mu_{Ca}\rho_{Ca}}{\rho_0} + \frac{\mu_C\rho_C}{\rho_0} , \tag{1}$$

where μ is CT value, μ_{Ca}/ρ_0 and μ_C/ρ_0 are mass attenuation coefficients of calcium and carbon, ρ_{Ca} and ρ_C are density of calcium and carbon. Figure 7 shows the 2D and 3D calcium-density mapping. Green signifies a lower Ca concentration, whereas red signifies a higher Ca concentration.

In Vivo Assessment of Bone Microstructure

Assessment of Spinal Microstructure Using MDCT

We developed an in vivo assessment system of microstructure using multi-detector row CT (MDCT). Optimal scanning conditions for evaluation of microstructure of human vertebral bone were first verified using MDCT and micro-CT as reference. Good correlation between bone strength (as assessed by compression testing) and microstructure assessed by both micro-CT and MDCT was obtained using femoral head specimens obtained at surgery.

Finally we evaluated the diagnostic value of in vivo analysis of spinal trabecular microstructure, focusing on the association with spinal fracture. Compared with postmenopausal women without a spinal fracture (Fig. 8), postmenopausal women
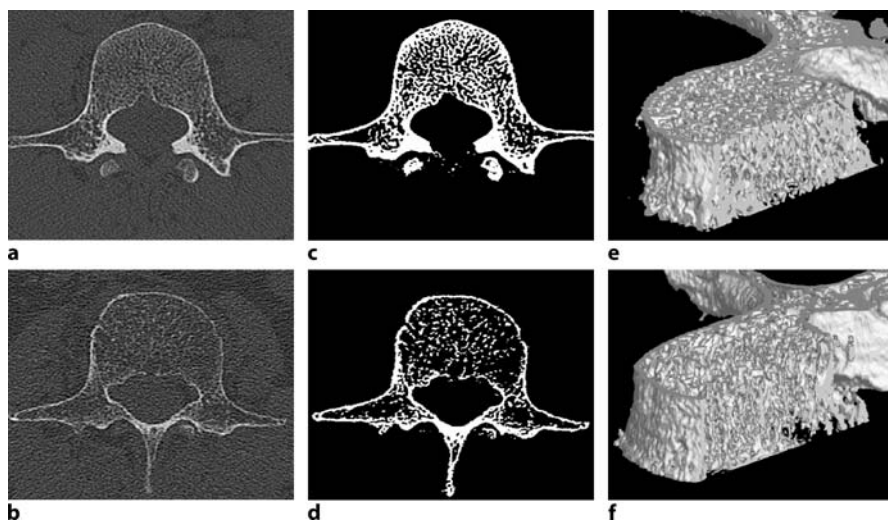
Figure 8 a–f. Representative 2D and 3D MDCT images of the third lumbar spine. Two-dimensional (**a,b**) and 3D (**e,f**) MDCT images of the third lumbar spine were obtained from a 62-year-old woman without vertebral fracture (**a,e**) and from a woman of the same age with a vertebral fracture in her thoracic spine (**b,f**). Binarized images are also shown (**c,d**)

with a vertebral body fracture had a smaller trabecular bone fraction (app BV/TV: 36.1 vs 26.2) in association with fewer trabeculae (app Tb.N: 0.97 vs 0.78), more rod-like structure (SMI: 1.87 vs 2.70) and lower connectivity (Euler's number: −1037 vs −457). The odds ratios of microstructure parameters, such as SMI, Euler's number,

Table 2. The receiver-operating-characteristics analysis and odds ratios of microstructural parameters for their association with spinal fracture. *MDCT* multi-detector-row CT, *app BV/TV* apparent bone volume fraction, *SMI* structure model index, *app Tb.Sp* apparent trabecular separation, *app Tb.N* apparent trabecular number, *app Tb.Th* apparent trabecular thickness, *DA* degree of anisotropy, *BMD* bone mineral density, *DXA* dual X-ray absorptiometry, *AUC* area under the curve, *ROC* receiver-operating curve analysis, *CI* confidence interval

Measurements		AUC (ROC)	Significance (p)	Odds ratio (95% CI)	Significance (p)
MDCT	Microstrucutral parameters				
	SMI	0.928±0.027	0.0001	16.0 (5.3–48.4)	0.0001
	app BV/TV (%)	0.811±0.048	0.0001	13.6 (4.3–42.4)	0.0001
	Euler's number	0.857±0.043	0.0001	13.1 (4.5–38.1)	0.0001
	app Tb.Sp (μm)	0.818±0.048	0.0001	7.4 (2.8–19.8)	0.0001
	Fractal dimension	0.735±0.059	0.0001	7.4 (2.6–20.7)	0.0005
	App Tb.N(1/mm^3)	0.810±0.049	0.0001	6.6 (2.5–17.4)	0.0005
	app Tb.Th (μm)	0.674±0.059	0.01	5.5 (1.6–18.5)	0.01
	DA	0.627±0.063	0.05	3.5 (1.2–10.2)	0.05
	Volumetric BMD (mg/cm^3)	0.870±0.040	0.0001	12.7 (4.4–36.4)	0.0001
DXA	Areal BMD (g/cm^2)	0.647±0.062	0.05	4.8 (1.5–14.8)	0.05

Data are shown as mean ±SD
Odds ratios are presented with 95% CI and *p*-values

Table 3. Correlation of microstructural parameters and BMD with fracture

Volumetric BMD with microstructure parameters			Areal BMD with microstructural parameters		
Measures	R^2	p	Measures	R^2	p
Volumetric BMD	0.366	0.0001	aBMD	0.061	0.0251
SMI	0.486	0.0001	SMI	0.486	0.0001
Tb.Th	0.112	0.0021	Euler's number	0.362	0.0001
Volumetric BMD+SMI	0.508	0.0001	aBMD+SMI	0.486	0.0001
Volumetric BMD+SMI+Tb.Th	0.551	0.0001	aBMD+SMI +Euler's number	0.506	0.0001

Correlation with prevalent vertebral fracture was assessed by multivariate regression analysis

and app BV/TV, for association with prevalent fracture, were much higher than that ratio for association of areal BMD by DXA. The SMI and Euler's number, which represent non-metric features of trabecular structure, would seem to be more useful than metric parameters such as app Tb.N, app Tb.Th or app Tb.Sp (Table 2). It is an advantage of the MDCT scanning system that, in addition to assessing these 3D microstructure parameters, volumetric BMD values can be obtained at the same time by using a reference phantom, and these values correlate highly with the presence of fracture (Table 3).

Comparison with Other Methodologies: Radiography, CT and MRI

In vivo analysis of trabecular microstructure has been investigated using conventional radiography, high-resolution CT, and high-resolution MRI. Conventional radiography has a spatial resolution of up to 40 µm; however, it delivers 2D projectional images of the trabeculae with superimposition of trabecular structure. Conventional high-resolution CT has a spatial resolution of 400 µm. The individual trabeculae that can be seen, however, are subject to partial-volume effects. With high-resolution CT in vivo, analysis of trabecular structure, such as connectivity from a skeletonized representation of the trabecular network (Chevalier et al. 1992), parameters derived from run-length encoding (Ito et al. 1995), and number or area of holes in the trabecular structure (Gordon et al. 1998), is possible. These images had a slice thickness of 1.5 mm and the field of view was reduced to yield an image matrix with a pixel size of 0.31 mm. A good relationship between texture parameters calculated from high-resolution CT images and biomechanical properties have also been reported (Link et al. 1998). Vertebral fracture is the most common osteoporotic fracture, and the presence of fracture indicates a greater risk for future fracture, independently of BMD (Ross et al. 1993). The direct assessment of vertebral microstructure, using MDCT, can be expected to provide greater sensitivity in assessing the risk of spinal fracture; however, this spatial resolution only provides characteristics of trabecular structure, and 2D imaging has limited reproducibility on follow-up examinations.

With the recent advances in MRI) hardware and software, it has become possible to obtain higher-resolution MR images of trabecular bone (Gordon et al. 1997; Majumdar et al. 1997; Link et al. 1998b; Majumdar et al. 1998, 1999) with in-plane resolutions as high as 150 µm and slice thicknesses of 280 µm in vivo (Majumdar et al. 1998). The MR imaging has an advantage of non-ionization, and trabecular microstructure obtained in vivo using high-resolution MR has been demonstrated to be useful in predicting spinal fractures. Structural parameters of the distal radius with a 3D spin-echo sequence (voxel size of $137 \times 137 \times 500 \,\mu m^3$) in 36 women were reported to provide a better index than the BMD of the distal radius (Wehrli et al. 1998). The 3D gradient-echo sequence (voxel size of $156 \times 156 \times 500 \,\mu m^3$) could discriminate between groups with and without a recent hip fracture (Majumdar et al. 1999). A disadvantage of high-resolution MRI in vivo, however, is the relatively long acquisition time of up to 10 ± 20 min. A small field of view is required in order to obtain a high signal-to-noise ratio with fast gradient and optimized coils. Due to these prerequisites and motion artefacts in the axial skeleton, application of high-resolution MRI

is currently limited to peripheral sites such as phalanges, calcaneus, and distal radius (Majumdar et al. 1997; Link et al. 1998b; Lin et al. 1996; Link et al. 1998c). Recently, longitudinal study of MR microstructure has been reported (Chestnut et al. 2005).

References

Bonse U, Busch F, Gunnewig D, Beckmann F, Pahl R, Delling G, Hahn M, Graeff W (1994) 3D computed X-ray tomography of human cancellous bone at 8 mm spatial and 10E-4 energy resolution. Bone Miner 25:25–38

Chestnut CH, Majumdar S, Newitt DC, Shields A, Pelt J, Laschansky E, Azria M, Kriegman A, Olson M, Eriksen EF, Mindeholm L (2005) Effects of salmon calcitonin on trabecular microarchitecture as determined by magnetic resonance imaging: Results from the QUEST study, J Bone Miner Res 20:1548–1561

Chevalier F, Lavel-Jeantet A, Laval-Jeantet M, Bergot C (1992) CT images analysis of the vertebral trabecular network in vivo. Calcif Tissue Int 51:8–13

Engelke K, Graeff W, Meiss L, Hahn M, Delling G (1993) High spatial resolution imaging of bone mineral using computed tomography: comparison with microradiography and undecalcified histologic sections. Invest Radiol 28:341–349

Gordon CL, Webber CE, Christoforou N, Nahmias C (1997) In vivo assessment of trabecular bone structure at the distal radius from high-resolution magnetic resonance images. Med Phys 22:585–593

Gordon CL, Lang TF, Augat LP, Genant HK (1998) Image-based assessment of spinal trabecular bone structure from high resolution CT images. Osteoporos Int 8: 317

Grodzins L (1983) Optimum energy for X-ray transmission tomography of small samples. Nucl Instrum Methods 206:541–543

Ito M Ohki M, Hayashi K, Yamada M, Uetani M, Nakamura T (1995) Trabecular texture analysis of CT images in the relationship with spinal fracture. Radiology 194:55–59

Ito M, Nishida A, Nakamura T, Uetani M, Hayashi K (2002a) Differences of three-dimensional trabecular microstructure in osteopenic rat models caused by ovariectomy and neurectomy. Bone 30:594–598

Ito M, Nishida A, Koga A, Ikeda S, Shiraishi A, Uetani M, Hayashi K, Nakamura T (2002b) Contribution of trabecular and cortical components to the mechanical properties of bone and their regulating parameters. Bone 31:351–358

Ito M, Ejiri S, Jinnai H, Kono J, Ikeda S, Nishida A, Uesugi K, Yagi N Tanaka M, Hayashi K (2003) Bone structure and mineralization demonstrated using synchrotoron rediation computed tomography (SR-CT) in animal models: preliminary findings. J Bone Miner Metab 21:287–293

Ito M, Nishida A, Aoyagi K, Uetani M, Hayashi K, Kawase M (2005) Effects of risedronate on trabecular microstructure and biomechanical properties in ovariectomized rat tibia. Osteoporos Int 16:1042–1048

Kinney JH, Ladd AJC (1998) The relationship between three-dimensional connectivity and the elastic properties of trabecular bone. J Bone Miner Res 13:839–845

Kinney JH, Lane NE, Haupt DL (1995) In vivo, three-dimensional microscopy of trabecular bone. J Bone Miner Res 10:264–270

Kinney JH, Haupt DL, Balooch M, Ladd AJC, Ryaby JT, Lane NE (2000) Three-dimensional morphometry of the L6 vertebra in the ovariectomized rat model of osteoporosis: biomechanical implications. J Bone Miner Res 15:1981–1991

Kuehn B, Stampa, B, Heller M, Glueer C (1997) In vivo assessment of trabecular bone structure of the human phalanges using high resolution magnetic resonance imaging. Osteoporos Int 7: 291

Lane NR, Haupt D, Kimmel DB, Modin G, Kinney JH (1999) Early estrogen replacement therapy reverses the rapid loss of trabecular bone volume and prevents further deterioration of connectivity in the rat. J Bone Miner Res 14:206–214

Lin J, Amling M, Newitt D, Selby K, Delling G, Genant H, Majumdar S (1996) Heterogeneity of trabecular bone structure in the calcaneus using high resolution magnetic resonance imaging (MRI). Osteoporos Int 8:16–24

Link TM, Majumdar S, Lin J, Augat P, Gould R, Newitt D, Ouyang X, Lang T, Mathur AM Genant HK (1998a) Assessment of trabecular structure using high-resolution CT images and texture analysis. J Comput Assist Tomogr 22:15–24

Link TM, Majumdar S, Augat P, Lin JC, Newitt D, Lu Y, Lane NE, Genant HK (1998b) In vivo high resolution MRI of the calcaneus: differences in trabecular structure in osteoporosis patients. J Bone Miner Res 13:1175–1182

Link T, Majumdar S, Lin J, Newitt D, Augat P, Ouyang X, Mathur A, Genant H (1998c) A comparative study of trabecular bone properties in the spine and femur using high resolution MRI and CT. J Bone Miner Res 13:122–132

Majumdar S, Newitt D, Mathur A, Osman D, Gies A, Chiu E, Lotz J, Kinney J, Genant H (1996) Magnetic resonance imaging of trabecular bone structure in the distal radius: relationship with X-ray tomographic microscopy and biomechanics. Osteoporos Int 6:376–385

Majumdar S, Genant HK, Grampp S, Newitt DC, Truong V-H, Lin JC, Mathur A (1997) Correlation of trabecular bone structure with age, bone mineral density and osteoporotic status: in vivo studies in the distal radius using high resolution magnetic resonance imaging. J Bone Miner Res 12:111–118

Majumdar S, Kothari M, Augat P, Newitt DC, Link TM, Lin JC, Lang T, Lu Y, Genant HK (1998) High-resolution magnetic resonance imaging: three-dimensional trabecular bone architecture and biomechanical properties. Bone 22:445–454

Majumdar S, Link TM, Augat P, Lin JC, Newitt D, Lane NE, Genant HK (1999) Trabecular bone architecture in the distal radius using magnetic resonance imaging in subjects with fractures of the proximal femur. Osteoporos Int 10:231–239

Nishida A, Ito M, Uetani M, Nakayama T, Tanaka T (2004) Effect of etidronate on three-dimensional trabecular structure in ovariectomized or sciatic neurectomized rats. J Bone Miner Metab 22:335–340

Pateyron M, Peyrin F, Laval-Jeantet AM, Spanue P, Cloetens P, Peix G (1996) 3D microtomography of cnacellous bone samples using synchrotron radiation. In: Proc SPIE Medical Imaging, vol 96: Physics of medical imaging 2708:417–426

Ross PD, Genant HK, Davis JW, Miller PD, Wasnich RD (1993) Predicting vertebral fracture incidence from prevalent fractures and bone density among non-black, osteoporotic women. Osteoporos Int 3:12–126

Shiraishi A, Higashi S, Masaki T, Saito M, Ito M, Ikeda S, Nakamura T (2002) A Comparison of alfacalcidol and menatetrenone for the treatment of bone loss in an ovariectomized rat model of osteoporosis. Calcif Tissue Int 71:69–71

Wehrli F, Hwang S, Ma J, Song H, Ford J, Haddad J (1998) Cancellous bone volume and structure in the forearm: noninvasive assessment with MR microimaging and image processing. Radiology 206:347–357

Discrimination of Contributing Factors to Bone Fragility Using vQCT In Vivo

Margarita Meta (✉) [1], Ying Lu[1], Joyce H. Keyak[2], and Thomas F. Lang[1]

[1] Department of Radiology, University of California San Francisco, 185 Berry Street, Suite 350, San Francisco CA 94143-0946, USA
e-mail: Margarita.meta@radiology.ucsf.edu

[2] Department of Orthopedic Surgery, University of California, Irvine, California

Abstract

The most serious manifestations of osteoporosis are proximal femoral fractures, affecting over 250,000 elderly in the United States each year and 890,000 in the European Union in the year 2000 alone. The impact on public health and the resultant cost to the health care system highlight the urgency to identify those parameters significant to accurately predict bone quality and fracture risk at the proximal femur. Determinations of the proximal femur are employed to illustrate relevant applications of vQCT with the potential to be extrapolated to other skeletal sites and the research and development of novel biomaterials that could contribute to the restoration or improvement of bone function. We explain the underpinning of parameters for bone mass, BMD, and bone geometry, as well as the structural indices discriminated by vQCT. We further clarify the benefit of sub-regional analysis (trochanteric region separate from femoral neck region) and of compartmental analysis (cortical bone separate from trabecular bone). In order to gain insight into how these factors contribute to bone fragility, we show how vQCT information combined with finite element modeling (FEM) information, a structural analysis tool, allows for estimation of fracture load under various loading conditions including impact from a fall. We typify unique results obtained from studies on aging, drugs with bone impact, and spaceflight, which is difficult to reveal in vivo without vQCT. We show in vivo how aging results in heterogeneous effects in the trochanteric and femoral neck region and how the impact of long-term spaceflight differs between trabecular and cortical bone. We suggest future directions for vQCT, such as the improvement of accuracy and precision for longitudinal studies, the FEM analysis integration into individual patient evaluation for in vivo assessment of simulated fracture conditions, and the development of additional variables for enhancement of bone fragility evaluations.

Introduction

Volumetric quantitative computed tomography (vQCT) has recently emerged as a powerful tool for quantitative skeletal assessment in clinical osteoporosis studies

(Lang et al. 1997, 1999, 2004, Riggs et al. 2004, Li et al. 2006). Osteoporosis is one of the major global public health problems facing the elderly population (Gluer et al. 1994). It is estimated that the worldwide osteoporotic population exceeds 200 million people (Cooper 1999). In the year 2000, the direct cost for osteoporotic fractures in the European Union has been estimated as 32 billion Euros, and it is expected to rise to 77 billion Euros by 2050 (Kanis and Johnell 2005). In the United States, the estimated direct expenditures for osteoporotic hip fractures was $18 billion for the year 2002, and the cost is expected to double or triple during the next decades (NOF 2005). Arguably, the most serious manifestation of osteoporosis are proximal femoral fractures, affecting over 250,000 elderly in the United States each year (Melton et al. 1988; Riggs and Melton 1995) and 890,000 in the European Union in the year 2000 alone (Kanis and Johnell 2005). These fractures result in a 20% mortality rate and substantial loss in quality of life (Cummings and Melton 2002). As a result of the ever increasing life span, the number of new hip fractures is expected to rise to 2.6 million by the year 2025 (Gullberg et al. 1997). The impact on public health and the resultant cost to the health care system highlight the urgency to identify those structural, bone mineral density (BMD), and bone mass parameters significant to accurately predict bone quality and facture risk at the proximal femoral.

Determinations of the proximal femur are illustrated in this chapter to demonstrate useful applications of vQCT in research, diagnosis, and treatment monitoring of osteoporosis. We explain the underpinning of the parameters that can be discriminated by vQCT and can be used in the evaluation of bone fragility. The reported results are from projects conducted in the research laboratory of T. Lang at the Department of Radiology, University of California San Francisco. These analyses can be extrapolated to other skeletal sites and the research and development of novel biomaterials that could contribute to the restoration or improvement of bone function.

Compared with two-dimensional (2D) dual X-ray absorptometry (DXA), three-dimensional (3D) vQCT provides a more detailed framework as to why proximal femoral strength might be impaired. Whole bone strength depends on bone mass, bone material properties, and bone geometry. Analysis of images obtained by vQCT provides quantitative information regarding bone mass, volumetric BMD, and bone geometry of the whole proximal femur, as well as sub-regionally at the trochanteric region and the femoral neck (Fig. 1). Furthermore, vQCT allows for both the analysis of these bone properties as a whole (integral bone determinations) and separately for cortical and trabecular bone (Fig. 1).

Combining the information provided by vQCT with finite element modeling (FEM), a structural analysis tool, is a powerful new approach for evaluating changes in bone. When used alone, vQCT quantifies the changes in specific regions of bone but does not provide a direct measure of the effect of these changes on bone strength; however, QCT-based patient-specific FEM can be used to estimate the whole bone strength of the proximal femur (i.e., fracture load). Hip fracture occurs when the load applied to the proximal femur exceeds the whole bone strength associated with
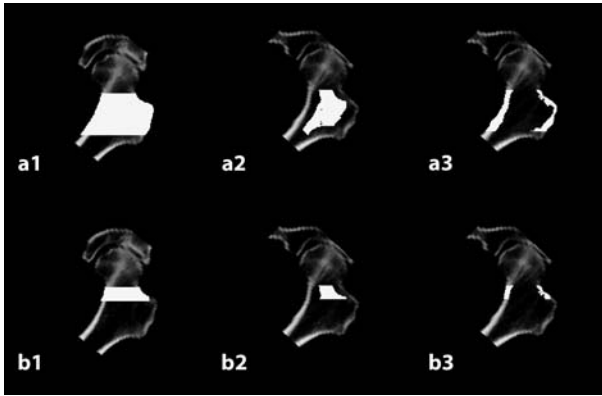
Figure 1 a,b. The vQCT regions of interest (ROI) in the proximal femur. The ROI are white pixels superimposed on image data. vQCT images showing iBMD, tBMD, and cBMD in the (**a**) total femoral and in (**b**) the femoral neck region. The trochanteric region is located outside the femoral neck region but within the overall total femoral region. (From Meta et al. 2006)

a specific activity or "loading condition." Seventy-five to 97% of proximal femoral fractures occur as a consequence of impact from a simple fall from a standing height (Sloan and Holloway 1981; Horiuchi et al. 1988). The remaining proximal femoral fractures occur "spontaneously," in connection with otherwise routine activities, such as walking, turning, or stumbling; thus, impact from a specific type of fall onto the hip and loading during the single-limb stance phase of walking are two examples of the many loading conditions that can cause the proximal femur to fracture, and each of these loading conditions is associated with different whole bone strength.

Specifically, the strength of the proximal femur (i.e., the force required to break the proximal femur) is less under loading from a fall than under loading from normal ambulation (Keyak et al. 2001), partly explaining the high incidence of fracture after a fall.

vQCT Parameters

Bone Mineral Content

Bone mineral content in vQCT is a quantification of the amount of mineralized tissue present in the region of interest (ROI) and therefore is expressed in grams. The BMC estimated by vQCT can be used as a surrogate for the assessment of mass of mineralized bone tissue.

Integral BMC represents the amount of mineralized tissue present in the whole bone–cortical and trabecular–and constitutes a surrogate for whole bone mass (Fig. 1). *Cortical* BMC represents the average amount of mineralized tissue exclusively in the

cortical bone. It can be considered a surrogate of cortical bone mass (Fig. 1). *Trabecular* BMC estimates the mass of mineralized tissue composed of the medullary space of the bone (Fig. 1). When interpreting this parameter, the composition of the bone marrow should be considered. Aging as well as certain treatments, such as glucocorticoids, have an impact on bone marrow fat content and consequently on trabecular BMC determinations. Studies performed to determine the accuracy of vQCT measurements have revealed that increased fat content in the bone marrow results in an underestimation of bone mass (Gluer et al. 1988; Kuiper et al. 1996).

Bone Mineral Density

The vQCT allows for the determination of volumetric BMD (vBMD). It represents the equivalent hydroxyapatite (HA) mass per unit of volume averaged over the voxels contained in the region of interest (ROI) and therefore it is expressed in grams per cubic centimeter. As well as for BMC, vQCT allows for the estimation of integral, cortical, and trabecular vBMD (Fig. 1).

Integral vBMD represents the average BMC per unit of volume in the ROI comprising the whole bone (cortical and trabecular compartments). Therefore, voxels containing bone marrow are included and averaged in the estimation of integral vBMD. Cortical vBMD reflects the average concentration of bone mineral in the cortical region and the porosity of the cortex; however, because of partial-volume averaging, its value depends on cortical thickness, particularly at those locations of the proximal femoral cortex where the cortical thickness is < 2 – 3 mm. In the femoral neck ROI, the cortical ROI is composed primarily of the inferomedial cortex of the proximal femur, for which thickness values exceeding 3 – 4 mm have been reported in humans, but also includes the thin superomedial cortex (thickness 0.3 mm; Bagi et al. 1997); thus, determinations of cortical vBMD at this skeletal site underestimate the actual BMD, with smaller errors for determinations of bone mass (Augat et al. 1998).

Trabecular vBMD values represent the equivalent HA concentration averaged over the voxels contained in the trabecular ROI. Because the trabecular ROI contains voxels with non-bone components and because the spatial resolution of the CT system is larger than the thickness of a trabeculum, trabecular vBMD represents (to a certain degree) the bone volume present in this ROI more than the bone tissue density.

In our laboratory, the precision for vBMD determinations (based on manual registration of ten repeated measurements) range from 0.72 to 1.56%, except for cortical vBMD (2.89%) and trabecular vBMD (5.85%) at the femoral neck (Table 1; Li et al. 2006).

Bone Geometry

Determinations of bone volume (VOL) allow for the estimation of bone size. The VOL is calculated as the volume of all voxels contained within the outer bone margin and is expressed in cubic centimeters. As for BMC and vBMD, it is possible to determine discretely the integral, cortical, and trabecular bone volume (Fig. 1).

Table 1. Precision values obtained by manual and automated registration ($n = 10$). vBMD volumetric bone mineral density, VOL bone volume, CSA cross-sectional area, BSI bone strength index

Variable		Manual registration precision (%)	Automatic registration precision (%)
vBMD (g/cm^3)			
Total femoral	Integral	1.14 ± 0.59	0.87 ± 0.67
region	Cortical	1.36 ± 0.69	1.24 ± 0.86
	Trabecular	0.72 ± 0.30	0.82 ± 0.63
Trochanteric	Integral	1.31 ± 0.81	0.81 ± 0.59
region	Cortical	1.49 ± 0.73	1.42 ± 0.81
	Trabecular	1.20 ± 0.78	0.60 ± 0.43[*]
Femoral neck	Integral	1.56 ± 1.17	1.31 ± 0.80
region	Cortical	2.89 ± 2.30	1.61 ± 1.06[*]
	Trabecular	5.85 ± 3.21	4.53 ± 2.74
Bone geometry: VOL (cm^3) and CSA (cm^2)			
Total femoral	Integral	2.74 ± 1.52	2.54 ± 1.77
region	Cortical	3.37 ± 1.98	2.21 ± 1.45
Trochanteric	Integral	3.79 ± 2.13	2.80 ± 1.60
region	Cortical	4.14 ± 2.26	2.80 ± 1.58
Femoral neck	Integral	3.85 ± 1.74	3.65 ± 2.41
region	Cortical	4.28 ± 2.49	3.07 ± 1.93
Maximum CSA		2.18 ± 1.34	0.48 ± 0.23[*]
Minimum CSA		1.44 ± 0.87	1.51 ± 0.93
BSI (cm^3)			
Femoral neck region	BSI	5.09 ± 3.07	3.66 ± 2.08

Mean ± SD of precision values calculated as the root mean square error of the coefficients of variation of ten repeated measurements
[*] $p < 0.05$ (Li et al. 2006)

Longitudinal increases in integral VOL indicate an increase in whole bone size. This increase in bone size might indicate the presence of periosteal apposition, though presently bone apposition cannot be directly measured by current in vivo CT methods. Changes in cortical VOL would show changes in the size of the cortical ring and might provide insight to the existence of cortical thinning. Partial-volume effects should be taken into consideration when cortical VOL results are been interpreted. The presence of cortices thinner than 1.2 mm can result in overestimation of cortical volume. Studies performed with helical CT have shown that changes in cortical thickness are revealed when cortices are > 1.2 mm and that determinations are more accurate as the CT slice thickness decreases (Prevrhal et al. 1999, 2003). An increase in trabecular VOL indicates an enlargement of the medullary cavity. This suggests the presence of endocortical bone resorption in longitudinal studies.
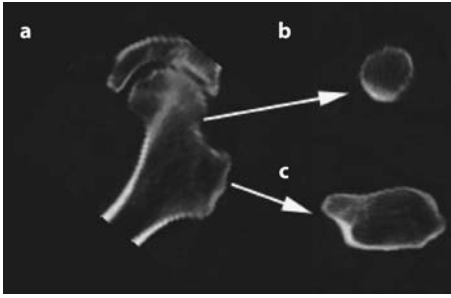
Figure 2 a–c. Definitions of proximal femoral planes for geometric measurements and strength estimates. The vQCT images corresponding to (**a**) coronal projection through hip with *arrows* pointing to (**b**) image of the minimum cross-sectional area (CSA) in the femoral neck region (**c**) image of the maximum CSA in the trochanteric region. (From Meta et al. 2006)

In our laboratory, the in vivo precision for VOL determinations (based on repeated measurements of 10 subjects) range from 2.74 to 4.28%, when the determinations are manually performed (Table 1; Li et al. 2006).

When 3D scanning protocols are used, the images can be formatted to display and quantify additional geometric bone parameters in biomechanically relevant planes, such as the plane perpendicular to the femoral neck axis, where the cross-sectional geometry of the femoral neck can be quantitatively assessed (Lang et al. 1997, 1999, 2004; Riggs et al. 2004). These geometric properties include cross-sectional area (CSA) in the trochanteric region and in the femoral neck region, as well as estimates of cortical thickness (Fig. 2).

For estimates of the periosteal area, we can compute the positions along the femoral neck axis of minimum and maximum CSA, which respectively correspond to the smallest CSA of the femoral neck, and the largest CSA through the trochanteric region (Fig. 2). In vivo precision values for minimum CSA with manual registration are 1.44% and for maximum CSA are 2.18% (Table 1) in our laboratory (Li et al. 2006).

Structural Indices

To estimate the mechanical competence of the proximal femur, structural indices of compressive strength (Compstr, g^2/cm^4) at the trochanteric region and compressive (Compstr, g^2/cm^4) and bending strength (BSI, cm^3) at the femoral neck region can be computed. The compressive strength indices (Compstr) are computed according to methods described by Sievanen (2000): Compstr = $fnvBMD^2 \times fnCSA$; where fnvBMD is the integral BMD of the femoral neck region and fnCSA is the minimum CSA of the femoral neck region.

To calculate BSI, a 2-mm-thick section centered at the location of minimum CSA is reconstructed. The BSI is computed as an effective polar moment of inertia normalized by femoral neck width. To account for heterogeneity, the contribution of each voxel to the polar moment of inertia is weighted by the elastic modulus (e_i)

computed from relationships reported by Keyak et al. (1994). The BSI is computed as:

$$fnBSI = \frac{I_x + I_y}{W} \qquad I_x = \frac{1}{e_b} \sum_i e_i \cdot (x_i - \bar{x})^2 \cdot \mathrm{d}A$$

$$I_y = \frac{1}{e_b} \sum_i e_i \cdot (y_i - \bar{y})^2 \cdot \mathrm{d}A$$

$$W = 2 \cdot \sqrt{\frac{fnCSA}{\pi}}$$

where I_x and I_y are the effective moments of inertia computed about the principal axes of the cross-section and are normalized by e_b, the elastic modulus of cortical bone, x_i and y_i are the distances of voxel i from the principal axes, x and y are the elastic modulus-weighted centroid of the cross section, W is the diameter of a circular cross section of equivalent area, $\mathrm{d}A$ is the CSA of d voxel. Precision for determinations of BSI in the femoral neck region are 5.09% for manual registration (Table 1; Li et al. 2006).

These indices provide insight into mechanical competence of the whole bone; however, they have not been validated as predictors of fracture risk and therefore cannot be considered in that way.

Finite Element Modeling

Finite element modeling (FEM) is a numerical technique that is often used by engineers to perform stress/strain analyses of structures, such as buildings, bridges, airplane wings, engine parts, etc. In the field of osteoporosis, FEM can be used to evaluate the structural behavior of bones such as the hip. Through use of CT scan images, 3D FEM that employs both patient-specific bone geometry and patient-specific material properties can be created. The 3D model may be subjected to loading forces simulating those in normal ambulation (single-legged stance loading condition) or impact from a fall onto the greater trochanter. The analysis results provide a complete description of the 3D stress and strain fields throughout the model of the bone. These results can then be further analyzed to provide an estimation of fracture load.

Keyak and coworkers have developed an automated, CT-based method of generating patient-specific FEMs of bone (Keyak 2001, Keyak et al. 1998, 2001a,b, 2005; Keyak and Rossi 2000). This method takes advantage of the voxel-based nature of vQCT scan data to achieve fully automated mesh generation and, more significantly, to allow heterogeneous material properties to be automatically specified with a high degree of refinement (Figs. 3, 4). For single-legged stance loading, Cody et al. (1999) showed that FEM-computed bone stiffness (force applied to the femoral head divided by displacement of the femoral head) explained at least 20 more variance in proximal femoral strength than DXA-based methods (FE, $r^2 = 0.84$; DXA, $r^2 = 0.57$ to 0.72). Using similar techniques Keyak et al. (2001) has achieved a similar precision to that of Cody et al. (1999) for predicting proximal femur strength under single-legged
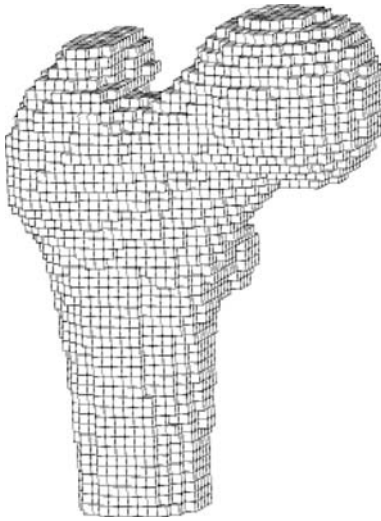
Figure 3. Finite element model (FEM) of a proximal femur generated from vQCT scan data. The model consists of 11,604 linear cube-shaped elements measuring 3 mm on each side
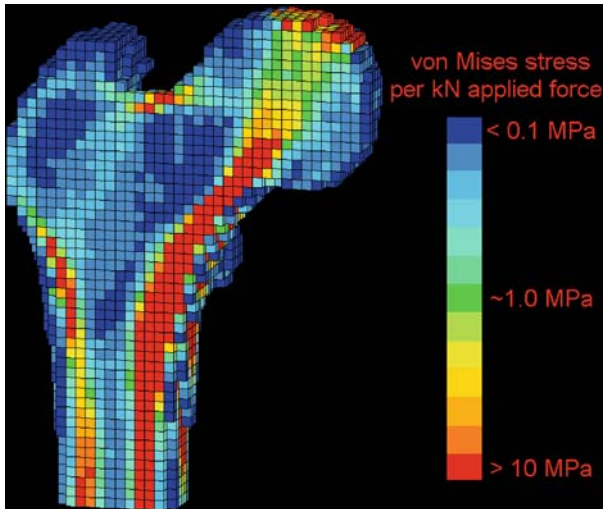
Figure 4. A coronal section of the same FEM as in Fig. 3 illustrates the computed von Mises stress field. Force was applied to the femoral head and directed at 20° to the shaft axis. The distal end of the model was fully constrained. The highest stresses are located primarily in regions of high bone density, illustrating the importance of modeling the variation of material properties

stance loading ($r^2 = 0.93$) and due to impact from a fall onto the greater trochanter ($r^2 = 0.90$; Keyak et al. 1998); thus, based on the extensive data in vitro, it is possible to perform patient-specific FEM calculations to obtain fracture loads that are approximately equivalent to those that would be measured if subjects' bones could be removed and tested to failure in vitro.

In addition to their close correlation with fracture load, the FEM can identify regions of high strain and low factor of safety (local bone material strength divided by the local stress), which occur at the sites where the bones fracture in vitro (Keyak 2001, Keyak et al. 2001a), and where fractures occur in vivo; thus, this technique provides a powerful research tool for studying a variety of factors related to osteoporotic fracture. For example, a study of the effect of force direction on fracture load revealed that the most risky type of fall is an oblique fall onto the posterolateral aspect of the greater trochanter (Keyak et al. 2001b).

Results from Studies

Characterization of Age-Related Changes

The vQCT provides insight into the age-related structural changes that occur at the proximal femur. Fragility fractures at the trochanter and femoral neck have distinct etiologies resulting in an increased ratio of trochanteric to neck fractures with age. The vQCT sub-regional analysis of the proximal femoral contributes to the understanding of the age-related structural changes. In vivo comparisons show differences in proximal femoral compartmental vBMD, BMC, and indices of bone geometry and structural strength between healthy young women near the peak of bone mass and healthy elderly women (Riggs et al. 2004, Meta et al. 2006). Cross-sectional changes in femoral neck BMD and geometry in men and women aged 20–90 years are consistent with the presence of periosteal apposition as a universal skeletal property in men and women (Riggs et al. 2004). The increase in femoral dimensions parallels a loss in trabecular BMD and cortical thickness, and is an apparent adaptation mechanism to preserve strength with respect to the loads exerted in the course of normal physical activity during the aging process. In vivo vQCT studies show how young–elderly differences in these parameters depend on two distinct functional sub-regions of the proximal femur, the trochanteric region and the femoral neck region (Meta et al. 2006). With age there is greater loss of trabecular and cortical bone in the femoral neck region than in the trochanteric region, and a greater increase in bone size at the trochanteric region compared with the femoral neck region (Table 2). For compressive strength indices, the larger bone size in elderly women does not compensate for lower BMD; however, changes in the femoral neck geometry in elderly women appear to protect estimated bending strength, but not compressive strength, despite BMD and cortical volume loss. These findings, which show sub-regional dependence in age-related structural changes at the proximal femur, contribute to understanding the distinctive etiologies in fragility fractures between the trochanteric region and the femoral neck region.

Our most recent study is the first to show in vivo sub-regional dependence in age-related structural changes at the proximal femoral (Meta et al. 2006). The vQCT quantified the way in which changes in the trabecular and cortical compartments differ between the trochanter and the femoral neck.

Table 2. The vQCT values for young vs elderly healthy Caucasian women. BMC bone mineral content, vBMD volumetric bone mineral density, VOL bone volume, CSA cross-sectional area, CS compressive strength. BSI bone strength index

Variable		Young	Elderly
BMC (g)			
Trochanteric region	Integral	19.38 ± 3.56	16.47 ± 4.03[a]
	Cortical	14.58 ± 2.94	11.90 ± 2.99[b]
	Trabecular	2.72 ± 0.69	2.08 ± 0.84[b]
Femoral neck region	Integral	5.05 ± 0.87	4.03 ± 0.97[b]
	Cortical	4.24 ± 0.74	3.27 ± 0.71[b]
	Trabecular	0.35 ± 0.15	0.17 ± 0.20[b]
vBMD (g/cm^3)			
Trochanteric region	Integral	0.313 ± 0.04	0.247 ± 0.04[b]
	Cortical	0.541 ± 0.03	0.525 ± 0.03 (n.s.)
	Trabecular	0.130 ± 0.03	0.086 ± 0.03[b]
Femoral neck region	Integral	0.351 ± 0.04	0.272 ± 0.04[b]
	Cortical	0.515 ± 0.04	0.539 ± 0.04[c]
	Trabecular	0.130 ± 0.04	0.049 ± 0.05[b]
Bone geometry: VOL (cm^3) and CSA (cm^2)			
Trochanteric region	Integral	62.24 ± 10.71	66.63 ± 12.04[a]
	Cortical	26.94 ± 5.02	22.52 ± 4.72[b]
	Trabecular	21.53 ± 5.33	24.78 ± 5.54[b]
Femoral neck region	Integral	14.55 ± 2.75	14.96 ± 3.49 (n.s.)
	Cortical	8.24 ± 1.42	6.06 ± 1.22[b]
	Trabecular	2.65 ± 1.08	3.06 ± 1.35
Maximum CSA		23.88 ± 2.71	27.89 ± 3.35 (n.s.)
Minimum CSA		8.73 ± 1.16	9.78 ± 1.61
Structural indices: CS (g^2/cm^4) and BSI (cm^3)			
Trochanteric region	CS	2.36 ± 0.58	1.74 ± 0.58[b]
Femoral neck region	CS	1.07 ± 0.22	0.73 ± 0.23[b]
	BSI	0.51 ± 0.09	0.45 ± 0.11[a]

The vQCT parameters are mean estimates ± SD. Statistical significance levels for comparing young with elderly women after adjusting for height and weight are given as follows: [a] $p < 0.01$; [b] $p < 0.001$; [c] $p < 0.05$; *n.s.* indicates $p > 0.05$ (Meta et al. 2006)

Evaluation of Osteoporosis Treatments

The vQCT has been used in the evaluation of various osteoporosis drugs, allowing the effects on trabecular and cortical bone as well as sub-regional effects in the proximal femur to be categorized. The evaluation of the effects of parathyroid hormone

(PTH) and alendronate treatment are an example of the results that can be achieved in evaluating osteoporosis treatments as well as in monitoring treatment.

The use of alendronate in the treatment of osteoporosis is an established therapeutic approach. Alendronate constitutes an antiresorptive drug that increases bone strength (Kurland et al. 2000; Rittmaster et al. 2000; Neer et al. 2001; Orwoll et al. 2003). In contrast, PTH increases bone strength but primarily through the stimulation of bone formation (Black et al. 1996; Cummings et al. 1998); therefore, it could be hypothesized that in order to improve osteoporosis treatment, the actions of alendronate and PTH might be beneficially combined (Black et al. 2003). In a randomized double-blind clinical study in postmenopausal women with low BMD at the hip or spine the effects of alendronate alone, PTH alone or both combined was explored by vQCT at the spine and hip (Black et al. 2003). The trabecular vBMD at the spine increased substantially in all groups, but the increase in the PTH group was about double that in the alendronate group or the combination group. The trabecular vBMD at the hip increased in all groups but did not reach significance. Interestingly, the pattern of changes in the cortical bone variables differed from that observed in the trabecular bone. While cortical vBMD at the proximal femur and femoral neck increased in the alendronate group, it decreased significantly in the PTH group, and did not differ in the combination group. Cortical VOL at proximal femoral and at the femoral neck was only increased significantly in the PTH group. When the effect of alendronate alone and the effects of PTH alone were compared with the combination group, only cortical VOL at the femoral neck was significantly increased. No change was observed in BMC.

The results of this study did not show evidence of synergy between the combination of alendronate and PTH (Black et al. 2003). The results further suggest that the simultaneous administration of alendronate may lessen the anabolic effects of PTH (Black et al. 2003). The analysis of the results obtained by vQCT made it possible to distinguish specific responses of trabecular and cortical bone to therapy as well as sub-regional discrepancies in treatment response. These discrepancies between treatments would not have been observed without the use of vQCT.

The use of PTH as a treatment for osteoporosis is limited to 2 years or less. Clinical and experimental studies suggest that gains in BMD achieved with PTH are lost if no antiresorptive treatment follows (Lindsay et al. 1997; Samnegard et al. 2001; Kurland et al. 2004; Lindsay et al. 2004). In a prospective, randomized, double-blinded continuation study of the one previously reported, the effects of follow-up 1-year therapy are reviewed (Black et al. 2005). Women who had received alendronate in the first year continued with alendronate in the second year. Women who had received PTH in the first year were randomly reassigned to one additional year with either placebo or alendronate. Women who had received combination therapy in the first year received alendronate in the second year. Over the treatment period, trabecular vBMD at the spine and hip increased in all groups. At the spine, except for the alendronate-alendronate group, increases in trabecular vBMD were significant, showing the highest increase in the PTH-alendronate group (Black et al. 2005). At the hip, significant increases in trabecular vBMD were observed in the PTH-alendronate group, and the combination-therapy alendronate group (Black et al. 2005). Cortical

vBMD declined slightly in all groups, being not significant only in the combination-therapy-alendronate group, while cortical VOL increased in all groups except for PTH-placebo group (Black et al. 2005). During the second year, women in the PTH-placebo group lost substantial BMD.

In summary, after 1 year of PTH (1–84) gains in BMD appear to be maintained or increased with alendronate, but these gains in BMD are lost if PTH is not followed by an antiresorptive agent (Black et al. 2005).

Evaluation of Treatment Effects in Glucocorticoid-Induced Osteoporosis

Glucocorticoid treatment is the most common cause for secondary osteoporosis in the adult population (Rehman and Lane 2003). Chronic treatment with glucocorticoids has been associated with nearly a 50% incidence of proximal femoral fracture (Lane 2001; van Staa et al. 2002). Analysis of vQCT at the proximal femur shows reduced cortical and trabecular bone in chronically treated patients (Table 3; Lian et al. 2005). These findings are in agreement with results obtained from iliac crest biopsies where trabecular volume, trabecular thickness, and trabecular number is reduced (Dempster et al. 1983). Furthermore, evidence of reduced cortical VOL with no change in integral VOL and minimum CSA suggests the stimulation of endocortical bone resorption by glucocorticoid treatment results in reduced cortical thickness (Lane 2001; Rehman and Lane 2003). The FEM analysis showed that the failure load in both stance and fall loading condition was decreased by similar amounts (Table 3; Lian et al. 2005). These findings are not only consistent with results obtained from experimental studies, but also with results obtained from invasive iliac crest biopsies. Furthermore, the FEM analysis of vQCT images allows for non-invasive evaluation of the impact of treatment on actual bone strength. The identification of changes in the cortical or trabecular compartments, and the identification of sub-regional heterogeneity at the proximal femoral bone, help explain the increase in bone fragility. These finding would not have been possible without the use of vQCT.

Evaluation of the Effects of Long-Term Spaceflight

A recent study by Lang et al. (2004) shows the ability of vQCT to reveal subtle longitudinal changes in bone geometry, even with a small sample size. This study is the first to document periosteal apposition in the femoral neck in a longitudinal protocol. It documents the increase in bone size observed over 1 year for a loss of 10-15% integral bone mass at the femoral neck. It also is the first such study to show differential patterns of cortical and trabecular bone mineral loss at the hip, and to combine these measures to estimate changes in indices of femoral neck strength.

Studies performed with DXA revealed that cosmonauts making flights of 4- to 12-month duration on the Soviet/Russian MIR spacecraft lost bone at an average rate of 1% per month from the spine and 1.5% per month from the hip despite an intense exercise regime (LeBlanc et al. 2000; McCarthy et al. 2000). The vQCT studies on crew members from the International Space Station on 4- to 6-month missions

Table 3. The vQCT values for glucocorticoid-treated vs glucocorticoid-naïve postmenopausal women

Variable		Glucocorticoid treated	Glucocorticoid naïve
BMC g			
Total femoral region	Integral	17.5 ± 4.67	21.5 ± 5.11[a]
	Cortical	12.8 ± 3.61	15.9 ± 3.79[a]
	Trabecular	1.81 ± 0.73	2.27 ± 0.97
Trochanteric region	Integral	13.3 ± 3.91	16.5 ± 4.03[a]
	Cortical	9.53 ± 2.89	11.9 ± 2.98[a]
	Trabecular	1.66 ± 0.69	2.09 ± 0.84
Femoral neck region	Integral	3.43 ± 0.82	4.01 ± 0.97[a]
	Cortical	2.78 ± 0.72	3.27 ± 0.71[a]
	Trabecular	0.12 ± 0.1	0.16 ± 0.19
vBMD (g/cm^3)			
Total femoral region	Integral	0.21 ± 0.04	0.25 ± 0.04[a]
	Cortical	0.49 ± 0.04	0.52 ± 0.04[a]
	Trabecular	0.06 ± 0.02	0.08 ± 0.03[a]
Trochanteric region	Integral	0.21 ± 0.04	0.25 ± 0.04[a]
	Cortical	0.50 ± 0.04	0.53 ± 0.04[a]
	Trabecular	0.07 ± 0.02	0.09 ± 0.03[a]
Femoral neck region	Integral	0.23 ± 0.04	0.27 ± 0.04[a]
	Cortical	0.51 ± 0.04	0.54 ± 0.04[a]
	Trabecular	0.04 ± 0.03	0.05 ± 0.05
Bone geometry: VOL (cm^3) and CSA (cm^2)			
Total femoral region	Integral	81.8 ± 17.2	85.9 ± 15.1
	Cortical	25.9 ± 6.13	30.6 ± 6.09[a]
	Trabecular	27.2 ± 7.57	28.2 ± 6.23
Trochanteric region	Integral	63.1 ± 14.9	66.9 ± 11.3
	Cortical	18.9 ± 4.92	22.6 ± 4.63[a]
	Trabecular	23.9 ± 6.82	24.9 ± 5.16
Femoral neck region	Integral	14.9 ± 2.64	14.9 ± 3.33
	Cortical	5.45 ± 1.18	6.04 ± 1.21
	Trabecular	3.06 ± 1.01	2.99 ± 1.27
Maximum CSA		26.1 ± 3.34	28.0 ± 3.22
Minimum CSA		9.69 ± 1.26	9.70 ± 1.65
Finite element model: stance and fall failure load (kN)			
Stance		6.26 ± 0.94	7.33 ± 1.06[a]
Fall		1.19 ± 0.34	1.41 ± 0.34

The vQCT parameters are mean estimates ± SD. Values are adjusted for age, weight, and duration of hormone replacement treatment. Bonferroni p-value <0.002 was considered significant

[a] $p < 0.002$ (Lian et al. 2005)

were performed to characterize sub-regional distribution of vertebral and proximal femoral bone loss (Lang et al. 2004). Spinal integral vBMD declined at a rate of 0.9% per month ($p < 0.001$), and trabecular vBMD at 0.7% per month ($p < 0.05$; Lang et al. 2004). In the hip, over 90% of bone mass loss was from cortical bone (Table 4; Lang et al. 2004); however, the loss of trabecular BMD at the proximal femur was

Table 4. The vQCT values for pre- vs post-spaceflight crew members. CS compressive strength, BSI bone strength index

Variable		Preflight	Postflight
BMC (g)			
Total femoral	Integral	34.22 ± 6.85	30.66 ± 4.81[a]
region	Cortical	24.84 ± 5.16	22.15 ± 3.78[a]
	Trabecular	5.07 ± 1.16	4.41 ± 0.74[b]
Trochanteric	Integral	26.08 ± 5.31	23.48 ± 3.89[a]
region	Cortical	18.29 ± 3.84	16.39 ± 2.84[a]
	Trabecular	4.37 ± 0.99	3.84 ± 0.68[b]
Femoral neck	Integral	6.31 ± 1.14	5.71 ± 0.83[a]
region	Cortical	5.19 ± 1.01	4.69 ± 0.86[a]
	Trabecular	0.59 ± 0.21	0.48 ± 0.11[a]
vBMD (g/cm^3)			
Total femoral	Integral	0.327 ± 0.03	0.301 ± 0.04[c]
region	Cortical	0.537 ± 0.032	0.526 ± 0.03[b]
	Trabecular	0.141 ± 0.02	0.124 ± 0.02[c]
Trochanteric	Integral	0.325 ± 0.03	0.298 ± 0.04[c]
region	Cortical	0.55 ± 0.03	0.541 ± 0.03[b]
	Trabecular	0.141 ± 0.02	0.124 ± 0.02[c]
Femoral neck	Integral	0.351 ± 0.04	0.328 ± 0.05[c]
region	Cortical	0.537 ± 0.04	0.527 ± 0.04 (n.s.)
	Trabecular	0.128 ± 0.02	0.108 ± 0.22[c]
Bone geometry: VOL (cm^3) and CSA (cm^2)			
Total femoral	Integral	104.9 ± 20.3	79.1 ± 12.0 (n.s.)
region	Cortical	46.0 ± 8.2	41.9 ± 5.5[a]
Trochanteric	Integral	80.2 ± 15.2	79.1 ± 12.0 (n.s.)
region	Cortical	32.8 ± 5.7	30.2 ± 4.3[a]
Femoral neck	Integral	18.3 ± 3.7	17.6 ± 2.7 (n.s.)
region	Cortical	9.6 ± 1.7	8.8 ± 1.2[a]
Maximum CSA		30.76 ± 4.24	31.18 ± 4.24 (n.s.)
Minimum CSA		11.66 ± 1.79	11.66 ± 1.72 (n.s.)
Structural indices: CS (g^2/cm^4) and BSI (cm^3)			
Femoral neck	CS	1.44 ± 0.33	1.26 ± 0.35[c]
region	BSI	2.99 ± 1.64	2.38 ± 0.81[c]

The vQCT parameters are mean estimates ± SD. Statistical significance levels for comparing pre- with post-spaceflight values are given as follows: [a] $p < 0.05$; [b] $p < 0.01$; [c] $p < 0.001$; *n.s.* indicates $p > 0.05$ (Lang et al. 2004)

greater than the loss of cortical and integral bone, tending to be larger at the femoral neck (Lang et al. 2004). These findings are consistent with accelerated loss of trabecular bone in hindlimb unloading (Bloomfield et al. 2002), in spinal cord injury (Frey-Rindova et al. 2000) and in previous spaceflight studies (Vico et al. 2000).

Reduced cortical volume and no change in parameters indicating whole bone size implied that cortical bone loss in the hip occurred primarily by cortical thinning without presence of periosteal apposition (Lang et al. 2004); thus, lower values for structural indices as a result of the changes in cortical and trabecular bone mass indicate that long-duration spaceflight combined with attempts to maintain a rigorous exercise regime still apparently results in a substantial reduction of bone strength (Lang et al. 2004).

Future Directions

Future directions in vQCT comprise various areas of research and development. Research is being done to improve the accuracy and precision of the established methodology especially in longitudinal studies. The increasing integration of FEM analysis into clinical trials, and later into individual patient evaluation, allows for in vivo evaluation of simulated loading conditions, such as a fall to the side. The incorporation of estimates of additional variables related to the pathophysiological mechanism fracture can enhance the evaluation of vQCT images.

In order to improve measurements obtained with vQCT, it would be important to eliminate or minimize user interaction. One study has already been published in this regard (Li et al. 2006). An automated registration algorithm has been developed and optimized for vQCT images of the spine and proximal femoral, and is already integrated to the presently developed software. In follow-up studies, new images are automatically aligned with the baseline images and bone evaluation is initiated based on the morphometric features defined in the baseline images. The algorithm developed for this purpose was based on the mutual information approach, with simplex optimization under a multi-resolution scheme. In a validation study, the implementation of this algorithm showed comparable or improved precision errors compared with those obtained by manual analysis and execution times of 2.3 min for the hip and 1.1 min for the vertebra. This technique can be used in any longitudinal study including clinical trials and monitoring treatment of patients.

The increasing incorporation of FEM to clinical research studies, where not only stance loading but also impact from a fall onto the greater trochanter can be simulated, would help improve understanding through in vivo measurements of how changes in the cortical and trabecular bone compartments lead to in changes in bone strength. The FEM would also allow evaluation of the impact of complex sub-regional changes on whole bone strength and fracture risk.

The vQCT technology also allows for muscle measurements. The integration into one technology of measurements of whole bone strength, sub-regional analysis, and independent measurements of trabecular and cortical bone can offer a fascinating insight into muscle-bone interactions. Furthermore, this integration can allow

for identification and development of unique fracture risk parameters to aid in the diagnosis and treatment monitoring as well as in the development of biomaterials that could contribute to the restoration or improvement of bone function.

References

Augat P, Gordon CL, Lang TF, Iida H, Genant HK (1998) Accuracy of cortical and trabecular bone measurements with peripheral quantitative computed tomography (pQCT). Phys Med Biol 43 (10):2873–2883

Bagi CM, Wilkie D, Georgelos K, Williams D, Bertolini D (1997) Morphological and structural characteristics of the proximal femur in human and rat. Bone 21 (3):261–267

Black DM, Cummings SR, Karpf DB, Cauley JA, Thompson DE, Nevitt MC, Bauer DC, Genant HK, Haskell WL, Marcus R, Ott SM, Torner JC, Quandt SA, Reiss TF, Ensrud KE (1996) Randomised trial of effect of alendronate on risk of fracture in women with existing vertebral fractures. Fracture Intervention Trial Research Group. Lancet 348 (9041):1535–1541

Black DM, Greenspan SL, Ensrud KE, Palermo L, McGowan JA, Lang TF, Garnero P, Bouxsein ML, Bilezikian JP, Rosen CJ (2003) The effects of parathyroid hormone and alendronate alone or in combination in postmenopausal osteoporosis. N Engl J Med 349 (13):1207–1215

Black DM, Bilezikian JP, Ensrud KE, Greenspan SL, Palermo L, Hue T, Lang TF, McGowan JA, Rosen CJ (2005) One year of alendronate after one year of parathyroid hormone (1–84) for osteoporosis. N Engl J Med 353 (6):555–565

Bloomfield SA, Allen MR, Hogan HA, Delp MD (2002) Site- and compartment-specific changes in bone with hindlimb unloading in mature adult rats. Bone 31 (1):149–157

Cody DD, Gross GJ, Hou FJ, Spencer HJ, Goldstein SA, Fyhrie DP (1999) Femoral strength is better predicted by finite element models than QCT and DXA. J Biomech 32 (10):1013–1020

Cooper C (1999) Epidemiology of osteoporosis. Osteoporos Int 9 (Suppl 2): S2-S8

Cummings SR, Black DM, Thompson DE, Applegate WB, Barrett-Connor E, Musliner TA, Palermo L, Prineas R, Rubin SM, Scott JC, Vogt T, Wallace R, Yates AJ, LaCroix AZ (1998) Effect of alendronate on risk of fracture in women with low bone density but without vertebral fractures: results from the Fracture Intervention Trial. J Am Med Assoc 280 (24):2077–2082

Cummings SR, Melton LJ (2002) Epidemiology and outcomes of osteoporotic fractures. Lancet 359 (9319):1761–1767

Dempster DW, Arlot MA, Meunier PJ (1983) Mean wall thickness and formation periods of trabecular bone packets in corticosteroid-induced osteoporosis. Calcif Tissue Int 35:410–417

Frey-Rindova P, de Bruin ED, Stussi E, Dambacher MA, Dietz V (2000) Bone mineral density in upper and lower extremities during 12 months after spinal cord injury measured by peripheral quantitative computed tomography. Spinal Cord 38 (1):26–32

Gluer CC, Reiser UJ, Davis CA, Rutt BK, Genant HK (1988) Vertebral mineral determination by quantitative computed tomography (QCT): accuracy of single and dual energy measurements. J Comput Assist Tomogr 12 (2):242–258

Gluer CC, Cummings SR, Pressman A, Li J, Gluer K, Faulkner KG, Grampp S, Genant HK (1994) Prediction of hip fractures from pelvic radiographs: the study of osteoporotic fractures. The Study of Osteoporotic Fractures Research Group. J Bone Miner Res 9 (5):671–677

Gullberg B, Johnell O, Kanis JA (1997) World-wide projections for hip fracture. Osteoporos Int 7 (5):407–413

Horiuchi T, Igarashi M, Karube S, Oda H, Tokuyama H, Huang T, Inoue S (1988) Spontaneous fractures of the hip in the elderly. Orthopedics 11 (9):1277–1280

Kanis JA, Johnell O (2005) Requirements for DXA for the management of osteoporosis in Europe. Osteoporos Int 16 (3):229–238

Keyak JH (2001) Improved prediction of proximal femoral fracture load using nonlinear finite element models. Med Eng Phys 23 (3):165–173

Keyak JH, Rossi SA (2000) Prediction of femoral fracture load using finite element models: an examination of stress- and strain-based failure theories. J Biomech 33 (2):209–214

Keyak JH, Lee IY, Skinner HB (1994) Correlations between orthogonal mechanical properties and density of trabecular bone: use of different densitometric measures. J Biomed Mater Res 28 (11):1329–1336

Keyak JH, Rossi SA, Jones KA, Skinner HB (1998) Prediction of femoral fracture load using automated finite element modeling. J Biomech 31 (2):125–133

Keyak JH, Rossi SA, Jones KA, Les CM, Skinner HB (2001a) Prediction of fracture location in the proximal femur using finite element models. Med Eng Phys 23 (9):657–664

Keyak JH, Skinner HB, Fleming JA (2001b) Effect of force direction on femoral fracture load for two types of loading conditions. J Orthop Res 19 (4):539–544

Keyak JH, Kaneko TS, Tehranzadeh J, Skinner HB (2005) Predicting proximal femoral strength using structural engineering models. Clin Orthop Relat Res (437):219–228

Kuiper JW, van Kuijk C, Grashuis JL, Ederveen AG, Schutte HE (1996) Accuracy and the influence of marrow fat on quantitative CT and dual-energy X-ray absorptiometry measurements of the femoral neck in vitro. Osteoporos Int 6 (1):25–30

Kurland ES, Cosman F, McMahon DJ, Rosen CJ, Lindsay R, Bilezikian JP (2000) Parathyroid hormone as a therapy for idiopathic osteoporosis in men: effects on bone mineral density and bone markers. J Clin Endocrinol Metab 85 (9):3069–3076

Kurland ES, Heller SL, Diamond B, McMahon DJ, Cosman F, Bilezikian JP (2004) The importance of bisphosphonate therapy in maintaining bone mass in men after therapy with teriparatide [human parathyroid hormone(1–34)]. Osteoporos Int 15 (12):992–997

Lane NE (2001) An update on glucocorticoid-induced osteoporosis. Rheum Dis Clin North Am 27 (1):235–253

Lang T, LeBlanc A, Evans H, Lu Y, Genant H and Yu A (2004) Cortical and trabecular bone mineral loss from the spine and hip in long-duration spaceflight. J Bone Miner Res 19 (6):1006–1012

Lang TF, Keyak JH, Heitz MW, Augat P, Lu Y, Mathur A, Genant HK (1997) Volumetric quantitative computed tomography of the proximal femur: precision and relation to bone strength. Bone 21 (1):101–108

Lang TF, Li J, Harris ST and Genant HK (1999) Assessment of vertebral bone mineral density using volumetric quantitative CT. J Comput Assist Tomogr 23 (1):130–137

LeBlanc A, Schneider V, Shackelford L, West S, Oganov V, Bakulin A, Voronin L (2000) Bone mineral and lean tissue loss after long duration space flight. J Musculoskelet Neuronal Interact 1 (2):157–160

Li W, Sode M, Saeed I, Lang T (2006) Automated registration of hip and spine for longitudinal QCT studies: integration with 3D densitometric and structural analysis. Bone 38 (2):273–279

Lian KC, Lang TF, Keyak JH, Modin GW, Rehman Q, Do L, Lane NE (2005) Differences in hip quantitative computed tomography (QCT) measurements of bone mineral density and bone strength between glucocorticoid-treated and glucocorticoid-naive postmenopausal women. Osteoporos Int 16 (6):642–650

Lindsay R, Nieves J, Formica C, Henneman E, Woelfert L, Shen V, Dempster D, Cosman F (1997) Randomised controlled study of effect of parathyroid hormone on vertebral-bone mass and fracture incidence among postmenopausal women on oestrogen with osteoporosis. Lancet 350 (9077):550–555

Lindsay R, Scheele WH, Neer R, Pohl G, Adami S, Mautalen C, Reginster JY, Stepan JJ, Myers SL, Mitlak BH (2004) Sustained vertebral fracture risk reduction after withdrawal of teriparatide in postmenopausal women with osteoporosis. Arch Intern Med 164 (18):2024–2030

McCarthy I, Goodship A, Herzog R, Oganov V, Stussi E, Vahlensieck M (2000) Investigation of bone changes in microgravity during long and short duration space flight: comparison of techniques. Eur J Clin Invest 30 (12):1044–1054

Melton LJ III, Kan SH, Wahner HW, Riggs BL (1988) Lifetime fracture risk: an approach to hip fracture risk assessment based on bone mineral density and age. J Clin Epidemiol 41 (10):985–994

Meta M, Lu Y, Keyak JH, Lang T (2006) Young-elderly differences in bone density, geometry and strength indices depend on proximal femur sub-region: a cross sectional study in Caucasian-American women. Bone 39 (1):152–158

Neer RM, Arnaud CD, Zanchetta JR, Prince R, Gaich GA, Reginster JY, Hodsman AB, Eriksen EF, Ish-Shalom S, Genant HK, Wang O, Mitlak BH (2001) Effect of parathyroid hormone (1–34) on fractures and bone mineral density in postmenopausal women with osteoporosis. N Engl J Med 344 (19):1434–1441

National Osteoporosis Foundation (2005) Physician's Guide to Prevention and Treatment of Osteoporosis

Orwoll ES, Scheele WH, Paul S, Adami S, Syversen U, Diez-Perez A, Kaufman JM, Clancy AD, Gaich GA (2003) The effect of teriparatide [human parathyroid hormone (1–34)] therapy on bone density in men with osteoporosis. J Bone Miner Res 18 (1):9–17

Prevrhal S, Engelke K, Kalender WA (1999) Accuracy limits for the determination of cortical width and density: the influence of object size and CT imaging parameters. Phys Med Biol 44 (3):751–764

Prevrhal S, Fox JC, Shepherd JA, Genant HK (2003) Accuracy of CT-based thickness measurement of thin structures: modeling of limited spatial resolution in all three dimensions. Med Phys 30 (1):1–8

Rehman Q, Lane NE (2003) Effect of glucocorticoids on bone density. Med Pediatr Oncol 41 (3):212–216

Riggs BL, Melton LJ III (1995) The worldwide problem of osteoporosis: insights afforded by epidemiology. Bone 17 (Suppl 5): 505S-511S

Riggs BL, Melton ILJ III, Robb RA, Camp JJ, Atkinson EJ, Peterson JM, Rouleau PA, McCollough CH, Bouxsein ML, Khosla S (2004) Population-based study of age and sex differences in bone volumetric density, size, geometry, and structure at different skeletal sites. J Bone Miner Res 19 (12):1945–1954

Rittmaster RS, Bolognese M, Ettinger MP, Hanley DA, Hodsman AB, Kendler DL, Rosen CJ (2000) Enhancement of bone mass in osteoporotic women with parathyroid hormone followed by alendronate. J Clin Endocrinol Metab 85 (6):2129–2134

Samnegard E, Akhter MP, Recker RR (2001) Maintenance of vertebral body bone mass and strength created by human parathyroid hormone treatment in ovariectomized rats. Bone 28 (4):414–422

Sievanen H (2000) A physical model for dual-energy X-ray absorptiometry-derived bone mineral density. Invest Radiol 35 (5):325–330

Sloan J, Holloway G (1981) Fractured neck of the femur: The cause of the fall? Injury 13 (3):230–232

van Staa TP, Leufkens HG, Cooper C (2002) The epidemiology of corticosteroid-induced osteoporosis: a meta-analysis. Osteoporos Int 13 (10):777–787

Vico L, Collet P, Guignandon A, Lafage-Proust MH, Thomas T, Rehaillia M, Alexandre C (2000) Effects of long-term microgravity exposure on cancellous and cortical weight-bearing bones of cosmonauts. Lancet 355 (9215):1607–1611

Osteoporosis Research with the vivaCT40

Jürg A. Gasser (✉) and Peter Ingold

Department of Musculoskeletal Diseases, Novartis Institutes for Biomedical Research,
4002 Basel, Switzerland
e-mail: juerg.gasser@novartis.com

Abstract

Non-invasive characterization of trabecular bone structures in rodents by micro-CT is becoming increasingly popular since it is much faster than the labor-intensive histomorphometry and does not require necropsy of animals. We used vivaCT40 from Scanco Medical AG (Bassersdorf, Switzerland) to monitor changes in trabecular structure in skeletally mature rats sequentially treated with the bisphosphonate zoledronic acid (ZOL) and parathyroid hormone (PTH). The results showed that a single i.v. injection of ZOL, in contrast to chronic treatment, did not blunt the bone anabolic effect of PTH. For arthritis research, vivaCT40 allowed imaging of subtle erosive lesions in subchondral bone caused by inflammatory processes in TNFα-transgenic mice. In studies of tumor osteolysis, vivaCT40 allowed monitoring of the progressive osteolytic response following the local administration of 4T1luc2000 tumor cells into the tibia metaphysis of nude mice. The potent protective effect of ZOL on tumor osteolysis was demonstrated. In summary, vivaCT40 is a powerful tool for non-invasive structural measurements in rats and mice to characterize 3D-trabecular micro-architecture accurately, repeatedly, reliably, and quickly.

Introduction

Bone Architecture and Fracture Risk

Neuromuscular function and environmental hazards which influence the risk of falling, the force of the impact, as well as bone strength are all important determinants of fracture risk. Bone mass, its geometric distribution (micro- and macro-architecture), and intrinsic material properties determine a bone's ability to withstand loading (Seeman 2002; Dempster 2003). On average, about 70–80% of the bone strength measured ex vivo is explained by an aerial bone mineral density (BMD) measurement (Kleerekoper et al. 1985; Dempster 2000). The prediction of trabecular bone strength can be greatly improved by including micro-architectural parameters (Parfitt 1992; Goldstein et al. 1990). Trabecular morphometry has traditionally been assessed in two dimensions on histological sections, and the third dimension is added on the basis of stereology (Sosa et al. 2002). Although the histomorphome-

tric method offers high spatial resolution and contrast, it requires substantial time and effort in the preparation of methylmethacrylate sections, and its destructive nature does not allow carrying out measurements in different planes in this anisotropic material. Another limitation is the dependence of stereological methods on a fixed structural model assumption. Typically, Parfitt's "parallel plate" or an ideal rod model is used in bone morphometry (Parfitt et al. 1983), but this model cannot describe trabecular bone structure adequately in conditions where these structures change continuously, such as in ageing and disease (Parfitt 1992; Ding et al. 2002). Such derivations from the ideal model will result in an error of unpredictable magnitude of all indirectly derived parameters. Micro-CT measurements can overcome these limitations of 2D morphometry (model assumptions, destructive nature, lengthy tissue processing) and can now also be carried out in vivo as demonstrated by Kohlbrenner and co-workers (2001).

The primary purpose of our study was to evaluate the ability of vivaCT40 to accurately evaluate changes in trabecular architecture in experimental situations such as osteoporosis in rats, arthritis in TNFα transgenic mice, and to image the tumor osteolytic response in an athymic mouse model. We also wanted to take advantage of the non-invasive nature of this tool to investigate bone phenotyping of transgenic mice.

Osteoporosis

Chronic exposure to the bisphosphonate (BP) alendronate (ALN) has been shown to blunt the bone anabolic response to PTH in rats (Gasser et al. 2000) and humans (Finkelstein et al. 2003). We used vivaCT40 to investigate the potential mechanism behind the BP–PTH interaction and to determine whether a single intravenous ALN injection exerted a different effect to chronic ALN administration. PTH is able to activate flat bone-lining cells into cuboid, collagen-synthesizing osteoblasts within 6 h of administration (Dobnig and Turner 1995). This is a crucial step in the early bone anabolic response to this peptide. We suspected that chronic-BP treatment may be capable of interfering with the cytoskeleton of the osteoblast, similar to the well-known effect in the osteoclast, and therefore prevents the crucial shape change in the lining cells, which is required for the anabolic response to PTH.

Rheumatoid Arthritis

Rheumatoid arthritis (RA) is a systemic chronic inflammatory disease. The most important and most debilitating aspect of RA is an erosive, inflammatory joint disease which develops in one or several diarthrodial joints. The cellular pathology of the disease is characterized by synovitis followed by the formation of fibrous pannus; the latter forms at the junction of cartilage and synovium and is responsible for the marginal erosion of cartilage and subchondral bone, with ultimate destruction of the normal joint architecture. Cells within the pannus are mainly fibroblasts, monocytes, or macrophages. In the sub-synovial tissue, diffuse infiltration of inflammatory cells occurs. The normal adipose structure of this tissue is largely replaced by fibrous tis-

sue. TNFα was been shown to be an important mediator of inflammatory arthritis in mice (Herak et al. 2004). Increased osteoclast activity is a key factor in bone loss in RA. This suggests that osteoclast-targeted therapies may effectively prevent skeletal damage in patients with RA. Zoledronic acid (ZOL) is one of the most potent agents for blocking osteoclast function. We therefore investigated whether ZOL was able to inhibit bone loss associated with chronic inflammatory conditions.

Tumor Osteolysis

Bone is a favored location for cancer metastases, especially from the breast, prostate, kidney, and myeloma. The mechanism that drives some tumor cell types specifically to bone tissue remains largely unknown (Guise and Mundy 1998); however, tumor cells which produce metalloproteinases, growth factors, and various cytokines may facilitate osteoclast recruitment and enhance their resorptive activity resulting in abnormal bone remodeling and proliferation of bone metastases (Thomas et al. 1999; Kitazawa and Kitazawa 2002; Mancino et al. 2001). The BPs are widely used for the treatment of bone metastases. ZOL is a nitrogen-containing BP which, in pre-clinical studies, has demonstrated potent inhibition of osteoclast-mediated bone resorption. ZOL is used in the treatment of Paget's disease, hypercalcemia of malignancy, multiple myeloma, and documented bone metastases from solid tumors, in conjunction with standard anticancer therapy.

Understanding the mechanism of action of ZOL as well as the evaluation of novel therapeutic agents for bone metastases is hindered by the lack of a tumor model where bone metastases follow the growth of the primary tumor in a predictable and reproducible fashion. This problem is partially overcome by the use of experimental bone metastases models, e.g., induced by intra-tibial cell injections; these address issues regarding colonization of tumor cells but not their metastatic behavior. They can, nevertheless, provide valuable insight into the effect of tumor on bone tissue. Apart from vivaCT, the studies described in this chapter also employ 2D and 3D bone densitometry for investigating specific features of osteoporosis in an animal rat model, RA, and bone tumor.

Materials and Methods

All in vivo studies described below were performed according to animal experimentation guidelines approved by the responsible authorities of Basel, Switzerland.

Bone Mineral Density and Structural Evaluation Devices

Dual-Energy X-ray Absorptiometry
Dual-energy X-ray absorptiometry (DXA) was performed ex-vivo using a Hologic QDR-1000 instrument (Watertown, Mass.). Ultra-high-resolution mode (line spacing 0.0254 cm, resolution 0.0127 cm) and a 0.9-cm-diameter collimator were selected for scanning. The excised rat tibiae were placed in 70% alcohol onto a resin platform provided by Hologic for soft tissue calibration.

Peripheral Quantitative Computed Tomography

Peripheral quantitative computed tomography (pQCT) was performed on anesthetized animals using an XCT-Research SA+ (Stratec Medizintechnik, Pforzheim, Germany) fitted with a 0.5-mm collimator (Gasser 2003). Changes in total, cortical, and cancellous bone mass, density, and geometry of rats and mice were monitored except in tumor osteolysis studies, where the heavy local destruction caused by the tumor no longer allowed determination of cortical geometric parameters.

In vivo micro-CT

The vivaCT40 has a rotating gantry, a microfocus X-ray source (45–70 kVp), and detector which rotates around the object. The isotropic spatial resolution of the system is 10–72 μm. Its field of view of 20–38 mm and scan length of 145 mm determine the maximal specimen size and length. For micro-CT measurements, rats or mice were anesthetized with Forene and their hind limb firmly fixed on a special tray for measurement using vivaCT40. For osteoporosis studies in rats, a region of 200 slices starting at a position of 1 mm below the growth plate in the secondary spongiosa was measured at a nominal resolution of approximately 15 μm in rats, and for tumor osteolysis in mice a resolution of 10 μm was chosen. In arthritis studies in rats, a total of 200 slices of 26-μm thickness each was measured, and the resulting scan length of 5.2 mm covered the epiphysis, growth plate, and the secondary spongiosa. One such scan took 9 min for data acquisition. Structural data was calculated from a volume spanning over 60 slices (1.56 mm) in arthritis studies.

Study Design

Osteoporosis Study in Rats

Our aim was to investigate the potential mechanism behind the BP–PTH interaction, and to determine whether a single BP injection exerted a different effect than chronic Alendronate (ALN) administration. Therapeutic dose of the BPs ALN (200 μg/kg) and zoledronic acid (ZOL; 32 μg/kg) were administered as single i.v. injection. A ten times higher dose of ZOL (322 μg/kg) was also administered. Daily s.c. PTH(1-34) treatment (40 μg/kg, five times per week) was initiated 24 h later and continued for 6 weeks. Changes in the mass and density of cancellous and cortical bone, as well as in structural cortical parameters, were measured in the proximal tibial metaphysis (4.5 mm from the proximal end) at 0, 2, 4, and 6 weeks by pQCT (XCT960A or XCT-Research, Stratec Medizintechnik, Germany). For micro-CT measurements on the vivaCT40 (Scanco), a region of 450 slices (6.75 mm) was scanned at a nominal resolution of 15 μm starting from the proximal end of the tibia. Cancellous bone architecture was determined in a region starting at a position of 3.5 mm from the proximal end and approximately 1 mm below the growth plate. Structural data were calculated from a volume spanning over 200 slices (3.0 mm).

Arthritis in TNFα transgenic mice

Human tumor necrosis factor TNFα–transgenic (hTNFtg) mice, which developed severe destructive arthritis as well as osteoporosis, were treated with phosphate-

buffered saline, and single or repeated doses of ZOL at the onset of arthritis at 4 weeks until the age of 10 weeks (Herak et al. 2004).

Tumor Osteolysis in Nude Mice

In this study, we examined the ability of 4T1luc 2000 mouse mammary carcinoma to colonize the tibia of athymic nude mice and the effect of ZOL treatment (0.1 mg/kg, s.c., two times per week). Tumor cells (1×10^5) were injected into the tibia of mice. Their growth was followed in vivo by means of IVIS Xenogen imaging. The osteolytic response was monitored non-invasively in Forene anesthetized mice at baseline and on day 12 after tumor cell injection by pQCT. Total BMD was measured at the site of injection at a distance of 3 mm from the proximal end of the bone. The osteolytic damage was visualized by vivaCT40. A region of 216 slices starting from the proximal end of the bone including the site of tumor-cell injection was measured at a nominal resolution of 12.5 μm. The DXA measurements were performed ex vivo on excised bones.

Statistical Analysis

Statistical analysis was carried out using RS/Client 2.1.2. for Windows (RS/1 version 6.0.1, Domain Manufacturing Corp., Burlington, Mass.). Data were subjected to one-way analysis of variance (ANOVA). Equality of variances was tested by the Levene F-test, and multiple comparisons using the Dunnett test. All statistical tests were two-tailed. All results are expressed as mean ± standard error (SEM).

Results of Above Described Studies

Osteoporosis Rat Model

Our previous data suggested that chronic BP exposure might reduce the ability of PTH to activate bone lining cells into matrix-secreting osteoblasts (Gasser et al. 2000; Dobnig and Turner 1995). The response to PTH was significantly blunted in the tibia of ALN-pretreated rats (Fig. 1). The pQCT measurements indicated a 2-week delay in the anabolic action of PTH in cortical bone ($p < 0.01$ vs Vehicle+PTH, all time points). Also, ALN-pretreated rats did not develop the full anabolic response observed in vehicle-pretreated rats over time. An 8-week washout period (vehicle, green curve) did not restore the "normal" anabolic response to PTH. The blunting of the anabolic response to PTH was also observed in lumbar vertebrae (data not shown) including mechanical competence of vertebrae and femur. In contrast to rats chronically exposed to BPs, a single i.v. injection of ZOL (even ten times the therapeutic dose) or ALN did not impair the response to PTH in rats. Serial measurements of BMD, cortical and trabecular architecture in the proximal tibia metaphysis by pQCT, and in vivo micro-CT indicated a normal bone anabolic response in all

Cortical thickness:
proximal tibia metaphysis by pQCT
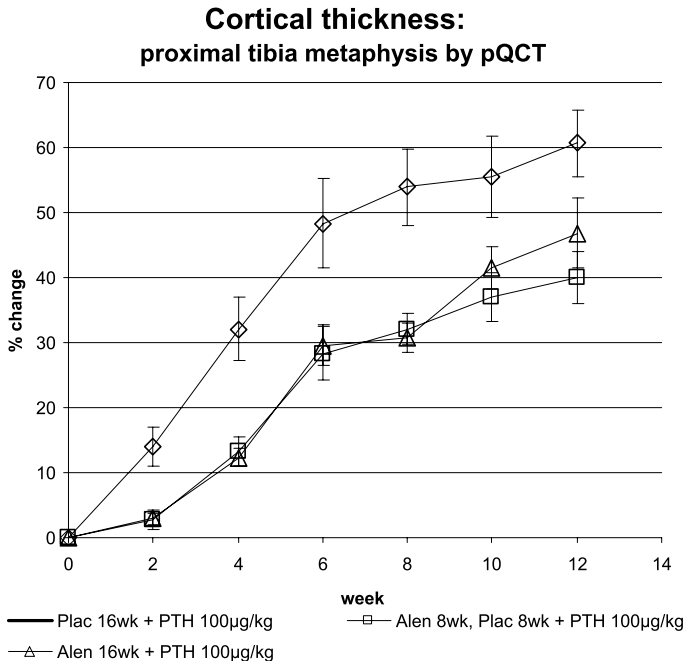
Figure 1. Blunting of the bone anabolic response to $100\,\mu g/kg$ PTH(1-38) in rats pretreated for 4 months with daily s.c. injections $28\,\mu g/kg$ alendronate. The pQCT measurements indicated a 2-week delay in the increase in cortical thickness of ALN-pretreated rats ($p < 0.01$ vs Vehicle + PTH, all time points). Also, ALN-pretreated rats did not develop the full anabolic response observed in vehicle-pretreated rats over time. An 8-week washout period (vehicle, *green curve*) did not restore the "normal" anabolic response to PTH. Data are in mean ± SEM ($n = 10$)

cancellous (Fig. 2) and cortical parameters after single i.v. dosing of ALN- and ZOL-treated animals (n.s. vs vehicle+PTH, at all time points), including those given the supra-pharmacological dose. Single i.v. and chronic BP dosing resulted in very different exposure patterns of osteoblasts, their precursors, and of lining cells to these non-metabolizable compounds. A direct effect of BPs on prenylation of Rap1A in MC3T3-1b cells were shown, which were treated for 24 h with concentrations of $30\,\mu M$ or higher of ZOL and ALN. Inhibition of protein prenylation in osteoblastic cells was seen in the absence of significant toxicity as determined by MTS assay. Cell death at lower concentrations of BPs was the result of compound-induced apoptosis and not necrosis as indicated by Cell Death Detection ELISA (Roche).

Arthritis in TNFα Transgenic Mice

The TNFα transgenic mice presented with multiple erosions in the talus and knee joint. Lesions were clearly visible in the peri-articular area as well as in subchondral bone (Fig. 3), representing the site of local inflammation which triggers an increase in osteoclast activity. Synovial inflammation was not affected by ZOL. In contrast,
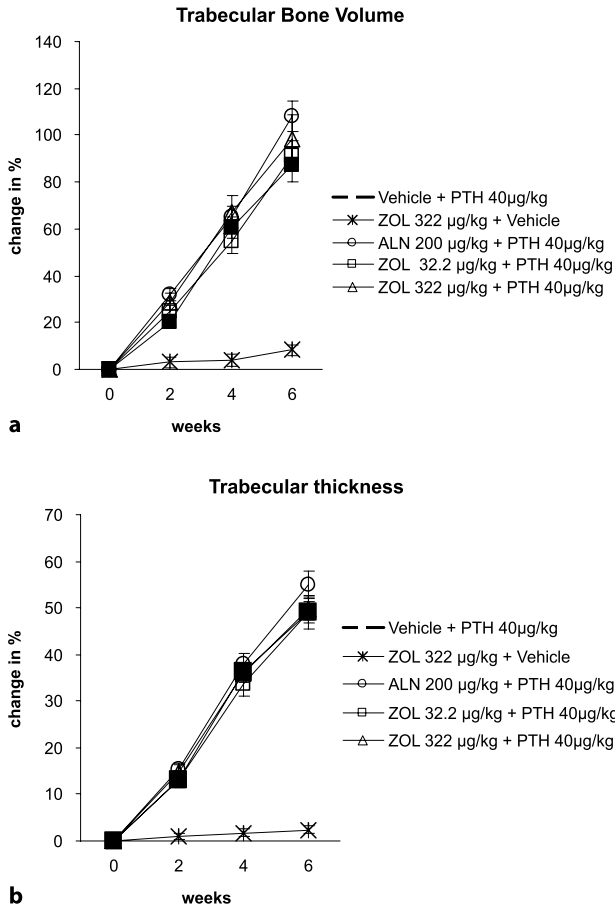
Figure 2 a,b. Micro-CT measurements carried out in vivo at baseline 2, 4, and 6 weeks after start of daily anabolic treatment with PTH(1-38) in rats pre-treated with a single i.v. injection of ZOL or ALN). The bone anabolic response to PTH was found to be identical regardless of previous exposure to single i.v. dose of ZOL or vehicle (all differences BP+PTH n.s. vs vehicle+PTH). **a** Trabecular bone volume increased by approximately 100% after start of PTH treatment. **b** Trabecular thickness increased in all PTH-treated groups by approximately 50%. ANOVA post-hoc Dunnett's test (no significant difference between groups treated with hPTH(1-38). Data are in mean ± SEM ($n = 10$)

bone erosion was retarded by a single dose of ZOL (60%) and was almost completely blocked by repeated administration of ZOL (> 95%). Cartilage damage was partly inhibited, and synovial osteoclast counts were significantly reduced with ZOL treatment. Systemic bone mass dramatically increased in hTNFtg mice after administration of ZOL. This was attributable to an increase in trabecular number and connectivity. In addition, bone resorption parameters were significantly lowered after administration of ZOL.
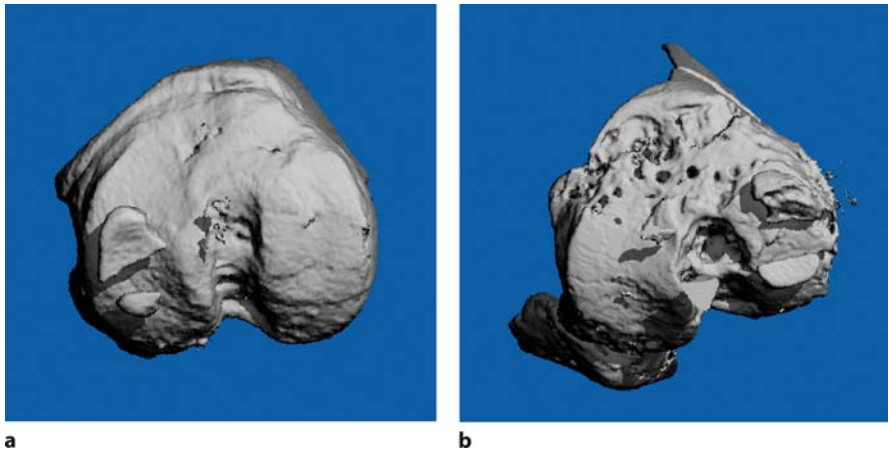
Figure 3 a,b. Images from the proximal tibia of a healthy (**a**) and a TNFα transgenic mouse (**b**), respectively, acquired in vivo on the vivaCT40 at a nominal resolution of 26 μm. Bone erosions resulting from the inflammatory process are visible in the area of subchondral bone

Tumor Osteolysis

Injection of 4T1luc2000 cells into the tibia of female athymic nude mice produced aggressive but localized tumors. By the end of the experiments all mice developed lung metastases and had lost between 10 and 15% of their body weight. The average intra-tibia tumor doubling time was 3.85 days. The ZOL treatment (0.1 mg/kg, s.c., two times per week) had no effect on the tumor growth per se as assessed by IVIS Xenogen bioluminescence; however, the overall body weight loss in ZOL treated
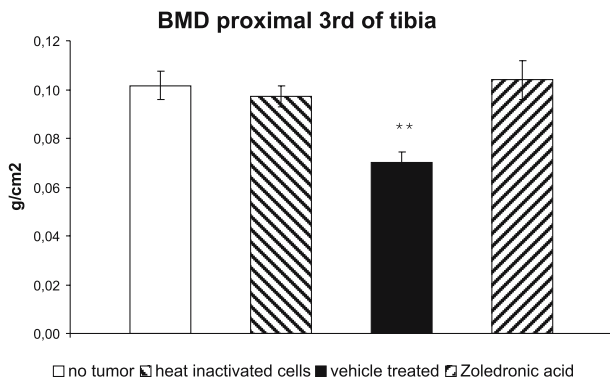
Figure 4. The BMD as determined by DEXA at 3 weeks after intra tibial delivery of 4T1luc2000 cells. The significant decrease in BMD ($p < 0.01$ vs non-tumor-injected mice, Dunnett's test) is completely blocked after administration of ZOL. As expected, heat-inactivated cells did not grow and did not cause osteolysis. Data are in mean ± SEM ($n = 6$)
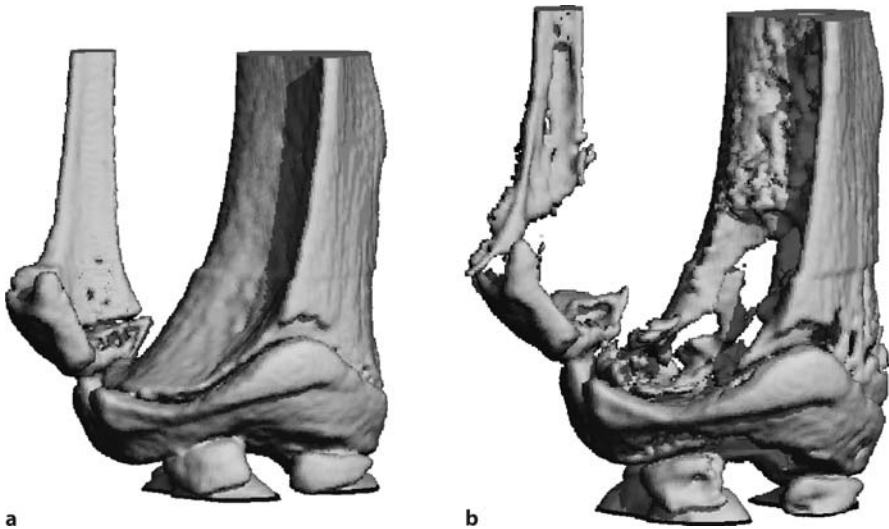
Figure 5. a Image of the proximal tibia metaphysis taken at baseline on the vivaCT40 at a nominal resolution of 12.5 µm in an anesthetized mouse, before the inoculation of 4T1luc2000 cells. **b** Image of the same mouse 3 weeks after tumor cell inoculation shows heavy osteolytic damage

animals of 6.7% was significantly less than that of vehicle-treated animals (13.4%; $p < 0.05$). The pQCT measurements carried out at the site of injection indicated that the BP completely blocked the decrease in BMD of 5.5% observed in vehicle-treated animals ($p < 0.01$; Fig. 4). Ex-vivo measurements of BMD in the proximal third of the tibia by DXA indicated a 27.7% ($p < 0.05$) decrease in BMD, due to tumor-induced osteolysis, which was completely prevented in ZOL-treated animals. Micro-CT images clearly showed that in vehicle-treated mice, osteolysis occurred in the cancellous and cortical compartments (Fig. 5). In many cases the tumor broke through the cortical shell to invade the tibia-fibular space. Bi-weekly s.c. administration of ZOL not only protected animals from cancellous and cortical bone erosions, but it also prevented the tumor from breaking through the cortical shell in all six mice. Injection of heat-inactivated 4T1luc2000 or HBSS did not produce any tumor growth or osteolysis.

Discussion

In our studies, we have taken advantage of the powerful measurement and imaging capability of vivaCT40, which allows monitoring of changes in 3D trabecular micro-architecture resulting from disease processes such as osteoporosis, inflammatory arthritis, and tumor invasion in small rodents. The fast data acquisition time of typically 10–15 min allows, for the first time, the incorporation of this non-invasive technique into large experimental studies along with pQCT and DXA measurements.

Longitudinal studies provide more precise information on the temporal changes in disease processes and allow for detailed monitoring of the efficacy of therapeutic intervention as well as providing information on the time to onset of action.

Our data in rats suggest that chronic BP exposure may reduce the ability of PTH to activate bone lining cells into matrix-secreting osteoblasts. In contrast, a single i.v. injection of BP (even ten times therapeutic dose) did not impair the response to PTH in rats. Single i.v. and chronic BP dosing result in very different exposure patterns of osteoblasts, their precursors, and of lining cells to these non-metabolizable compounds. Although osteoblasts are not generally considered to be a target for BP action, chronic i.v. dosing appears to result in BP accumulation in these cells sufficient to reduce protein prenylation.

We provide evidence that, as with osteoclasts, inhibition of FPP-synthase reduces protein prenylation in osteoblasts, disturbing cytoskeletal function and thereby preventing the shape change required for the activation of bone-lining cells by PTH (Dobnig and Turner 1995). This mechanism is only seen after chronic treatment and may explain the blunting of the anabolic response to PTH observed after chronic exposure of patients and rats to BPs (Gasser et al. 2000; Finkelstein et al. 2003).

In vivo micro-CT is an easy-to-use tool to image the subtle bony erosions in arthritic joints which cannot be detected by any other non-invasive imaging technology (Herak et al. 2004). This can be nicely demonstrated in the analysis of limbs of TNFα-overexpressing mice, in which micro-CT is capable of showing the multiple erosions produced by the osteoclasts in the joint area. At this point we have not attempted to quantify the lesions, but it may be possible to assess the extent of the damaged area and relate this to the total joint surface. The ZOL appears to be an effective tool for protecting bone from arthritic damage. In addition to their role in anti-inflammatory drug therapy, modern BPs are promising candidates for maintaining joint integrity and reversing systemic bone loss in patients with arthritis.

Bone erosion is a central feature of RA. Clinical observations reveal that bone erosion starts early in the course of disease. After a disease duration of only 6 months, >50% of patients with RA experience radiographically detectable skeletal damage, and this proportion might be even higher considering the fact that small bone erosions may escape detection by conventional radiography. A major aim of antirheumatic therapies is to minimize bone damage.

The bone-destructive nature of the 4T1luc2000 tumor in vehicle-treated animals defeated our initial aim to quantify the osteolytic response and assess the protective effects of ZOL on cancellous bone architecture in a longitudinal study. As a result, we were forced to use DXA measurements for quantification, since these areal measurements are less affected by the different growth patterns of the tumors and the osteolytic response evolving in individual animals. Despite these limitations, vivaCT40 enabled us to acquire high-quality images showing the development of osteolytic lesions over time. Overall our data indicate that ZOL, despite having no detectable effect on tumor cell growth per se in this model, is a highly effective treatment for the prevention of tumor-induced osteolysis caused by the intra-tibial inoculation of 4T1luc2000 mouse mammary carcinoma cells in athymic nude mice.

Conclusion

In conclusion, the novel and advanced vivaCT40 has been successfully used in three rodent models to non-invasively monitor changes in trabecular bone architecture, namely a rat model of BP-PTH interaction, a mouse model of inflammatory bone loss and a local tumor osteolysis model in athymic nude mice. We have seen clear differences in the pattern of bone loss between postmenopausal osteoporosis and arthritis, the former showing preferential removal of trabecular elements and a less-pronounced effect on their thickness. In contrast, in TNFα-transgenic mice, the predominant effect of the local inflammatory response affected trabecular thickness without much change in their number. These examples show that the pattern of bone loss can differ considerably between various diseases, and that non-invasive micro-CT measurements can provide the information in a rapid and non-destructive way. Similarly, non-invasive longitudinal measurements provide valuable and reliable information on how drugs, such as BPs, estradiol, or PTH, affect cancellous bone architecture. Our study with PTH in rats clearly showed that the anabolic treatment led to increased trabecular thickness without having any significant effect on their number. The PTH also lowered the structure model index, indicating a morphological change from a rod-like to a more plate-like structure. The non-destructive nature of the measurements does not only save approximately 2 months that would otherwise be required for tissue processing (histomorphometry), it also allows the bones to be used for "destructive" mechanical testing. In addition, the parameters derived from the model-independent 3D reconstruction should be more accurate than the 2D-based histomorphometry parameters.

The vivaCT40 is able to monitor 3D trabecular micro-architecture accurately, repeatedly, reliably, and quickly in living rats and mice under anesthesia. The scanner represents a breakthrough for non-invasive imaging and structural measurements in small rodents.

References

Dempster DW (2000) The contribution of trabecular architecture to cancellous bone quality. J Bone Miner Res 15:20–23

Dempster DW (2003) The pathophysiology of bone loss. Clin Geriatr Med 19:259–270

Ding M, Odgaard A, Linde F, Hvid I (2002) Age-related variations in microstructure of human tibial cancellous bone. J Orthop Res 20:615–621

Dobnig H, Turner RT (1995) Evidence that intermittent treatment with parathyroid hormone increases bone formation in adult rats by activation of bone lining cells. Endocrinology 136:3632–3638

Finkelstein JA, Hayes A, Hunzelman JL, Wyland JJ, Lee H, Neer RM (2003) The effects of parathyroid hormone, alendronate, or both in men with osteoporosis. N Engl J Med 349:1216–1226

Gasser JA (2003) Bone measurements by peripheral quantitative computed tomography in rodents. In: Ralston SH, Helfrich MH (eds) Bone research protocols. Humana Press, Totowa, New Jersey, pp 323–341

Gasser JA, Kneissel M, Thomsen JS, Mosekilde Li (2000) PTH, and interactions with bisphosphonates. J Musculoskelet Neuronal Interact 1:53–56

Goldstein SA, Hollister SJ, Kuhn JL, Kikuchi N (1990) The mechanical and remodeling properties of trabecular bone. In: Mow VC, Ratcliffe A, Woo SLY (eds) Biomechanics of diarthrodial joints, vol 2. Springer, Berlin Heidelberg New York, pp 61–81

Guise TA, Mundy GR (1998) Cancer and bone. Endocrinol Rev 19:18–54

Herak P, Görtz B, Hayer S, Redlich K, Reiter E, Gasser JA, Bergmeister H, Kollias G, Smolen JS, Schett G (2004) Zoledronic acid protects from local and systemic bone loss in TNF-mediated arthritis. Arthritis Rheum 50:2327–2337

Kitazawa S, Kitazawa R (2002) RANK ligand is a prerequisite for cancer-associated osteolytic lesions. J Pathol 198:228–236

Kleerekoper M, Villanueva AR, Stanciu J, Rao DS, Parfitt AM (1985) The role of three-dimensional trabecular microstructure in the pathogenesis of vertebral compression fractures. Calcif Tissue Int 37:594–597

Kohlbrenner A, Koller B, Haemmerle S, Ruegsegger P (2001) In vivo micro tomography. Adv Exp Med Biol 496:213–224

Mancino AT, Klimberg VS, Yamamoto M, Manolagas SC, Abe E (2001) Breast cancer increases osteoclastogenesis by secreting M-CSF and upregulating RANKL in stromal cells. J Surg Res 100:18–24

Parfitt AM (1992) Implications of architecture for the pathogenesis and prevention of vertebral fracture. Bone 13:S41-S47

Parfitt AM, Mathews CHE, Villanueva AR, Kleerekoper M, Frame B, Rao DS (1983) Relationship between surface, volume, and thickness of iliac trabecular bone in aging and in osteoporosis. Calcif Tissue Int 72:1396–1409

Seeman E (2002) Pathogenesis of bone fragility in women and men. Lancet 359:1841–1850

Sosa M, Hernandez D, Segarra MC, Gomez A, Pena E de la, Betancor P (2002) Effect of two forms of alendronate administration upon bone mass after two years of treatment. J Clin Densitom 5:27–34

Thomas RJ, Guise TA, Yin JJ, Elliott J, Horwood NJ, Martin TJ, Gillespie MT (1999) Breast cancer cells interact with osteoblasts to support osteoclast formation. Endocrinology 140:4451–4458

Mechanical Properties of Vertebral Trabeculae with Ageing Evaluated with Micro-CT

He Gong[1,3], Ming Zhang (✉)[1], and Ling Qin[2]

[1] Department of Health Technology and Informatics, The Hong Kong Polytechnic University, Hong Kong, China
   e-mail: htmzhang@polyu.edu.hk
[2] Department of Orthopaedics and Traumatology, The Chinese University of Hong Kong, Hong Kong, China
[3] Department of Mechanics, Nanling Campus, Jilin University, Changchun, 130025, China

Abstract

The aim of this study was to identify the regional variations in the mechanical properties of vertebral cancellous bones at both the apparent and tissue levels, and their relative differences with respect to ageing. Ninety trabecular specimens were obtained from six normal L4 vertebral bodies of six male cadavers in two age groups, three aged 62 years and three aged 69 years, and were scanned using a high-resolution micro-computed Tomography (micro-CT) system. The obtained micro-CT reconstruction models were then converted to micro-finite element models. Micro-finite element analyses were done to determine the apparent Young's moduli and tissue-level von Mises stress distribution for each trabecular specimen in the longitudinal direction (on-axis direction), and medial-lateral and anterior-posterior directions (off-axis directions), respectively. Regional variations about the mechanical properties at both apparent and tissue levels in different transverse layers and vertical columns within and between the two age groups were then analyzed. The results showed significant decreases in the apparent Young's moduli and tissue level von Mises stresses in each direction with ageing; those in the two off-axis directions decreased more with ageing compared with the longitudinal direction, and there were no statistically significant differences between the mechanical properties in the two off-axis directions. The mechanical properties followed their own patterns of regional variations within each group, suggesting both mechanical and age-related adaptation. This study offered an insight into the distributions and variations of mechanical properties within a vertebral body. The mechanical properties calculated from this study may serve as reference for gender and ethnic comparisons and may help us to better understand the regional fracture risk and mechanisms of vertebral fracture, and prevent osteoporotic fracture in older individuals.

Introduction

There are two types of bone in the human body: a dense, compact cortical bone mostly existing in the middle of a long bone (diaphasis); and a porous, spongy tra-

becular bone in the spine and near major joints such as in the ultradistal radius and proximal femur. Trabecular bone is thought to respond faster to metabolic stimuli and has a more frequent occurrence of fragility fractures (Lau et al. 1993; Qin et al. 2002). Osteoporosis is a systemic skeletal disease characterized by low bone mass and microarchitectural deterioration of bone tissue, with a consequent increase in bone fragility and susceptibility to fracture.

At tissue level, the material properties of the trabeculae, in combination with their microarchitectures, determine the strength and stiffness of trabecular bone under loading, i.e., the capacity to withstand load. Some studies have been conducted to quantify changes of the 3D microstructures in central and peripheral trabecular bone caused by ageing (Ding and Hvid 2000; Ding et al. 2002; Gong et al. 2005). To obtain the mechanical properties of trabecular bone, researchers have done direct mechanical tests on the trabecular specimens (Hansson et al. 1987; Keller et al. 1989; Morgan et al. 2003); however, this method may be subject to large errors unless special experimental protocols were designed to minimize the artifact errors (Keaveny et al. 1993, 1997; Morgan et al. 2003). Recently, with the development of computational power and imaging technique, new computer methods have been introduced that, given certain hard tissue properties, allow for the quantification of bone mechanical properties either directly using micro-finite element analysis (µFEA) based on high-resolution micro-CT computer reconstruction image (Van Rietbergen et al. 1995; Judex et al. 2003), or indirectly deriving from the constitutive relationships of bone morphology and elastic properties (Kabel et al. 1999; Van Rietbergen et al. 1998).

It is known that osteoporotic fractures occur most frequently in trabeculae rich skeletal sites and one of the sites most at risk is the spine, particularly in the elderly population (Melton et al. 1992). Our recent study (Gong et al. 2005) using micro-CT scanning technique on the regional variations in microstructural properties of vertebral trabeculae with ageing found significant differences in microstructural parameters, such as BV/TV, Tb.N and DA between 62-year group and 69-year group, and each microstructural parameter followed its own pattern of regional variation within vertebral body in each group. Another computational investigation incorporating finite element analysis with bone-adaptive remodeling theory also suggested that variations existed in trabecular bone Young's modulus within vertebral body (Goel et al. 1995). Keller et al. (1989) identified effects of disc degeneration on regional variations in the compressive properties of lumbar vertebral trabeculae from segments L1–L4 of three human cadavers (71, 78, and 84 years old) using mechanical test; however, the age-related regional variations in the mechanical properties of vertebral trabecular bone need to be investigated. It was found that the trabecular core carried 50–70% of the total load placed on the vertebra, which did not differ between healthy, osteopenic, and osteoporotic vertebrae (Homminga et al. 2001); hence, for lumbar vertebral body, a thorough understanding of the regional variations in the microstructural properties, as well as the mechanical properties, is crucial for diagnosis, prophylaxis, and treatment of the age-related degeneration. It will help to explain the vertebral fracture mechanism, prevent and treat osteoporotic fracture in elder individuals, and choose reasonable physical exercise.

Accordingly, the aims of this study were (a) to identify regional variations in the apparent Young's moduli and tissue-level principal stresses of trabecular bones of L4 vertebral body using high-resolution micro-CT computer reconstruction image-based micro-finite element analysis, and (b) to investigate the effect of ageing on it.

Materials and Methods

Six L4 vertebral bodies were obtained from six male cadaver donors, three aged 62 years (62-year group) and three aged 69 years (69-year group). Human ethics approval was obtained from the Clinical Ethics Committee of the Chinese University of Hong Kong. The specimens were examined using X-ray to rule out potential pathological changes affecting bone structural and mechanical evaluation, including structural deformity and microcallus resulted from potential spinal fracture. For each vertebral body with superior and inferior endplates of $8 \times 8\,mm^2$ with a height
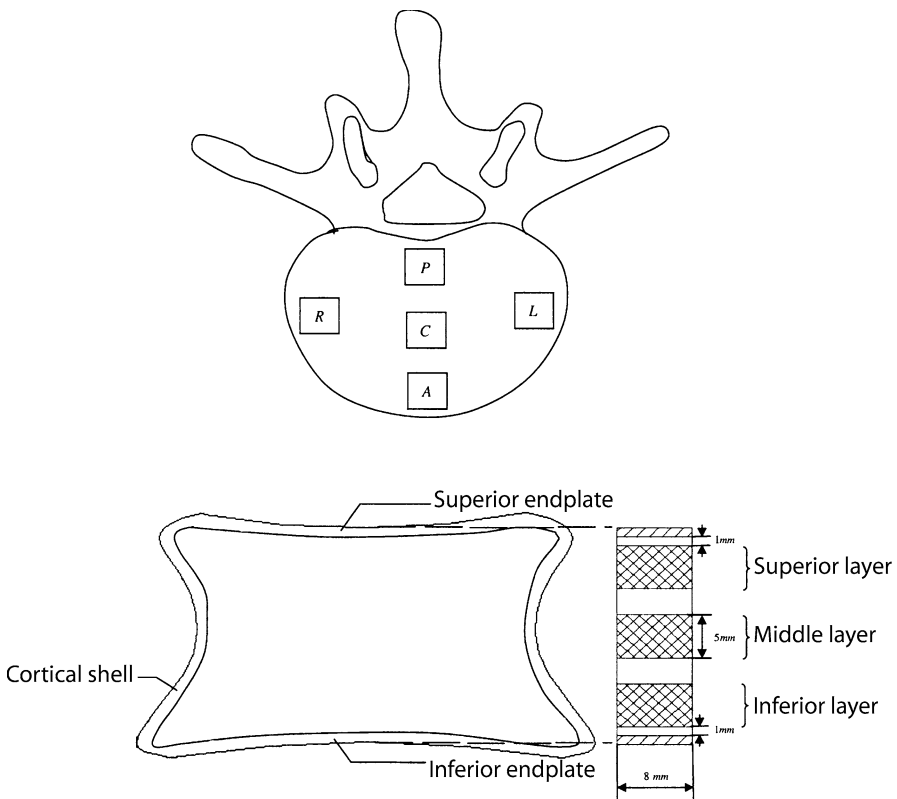
Figure 1. The micro-CT scanning preparation procedure. The superior layer is 1 mm below the superior endplate, and the inferior layer is 1 mm above the inferior endplate and middle layer in between the superior and inferior layers. The three layers and five columns constitute 15 different regions altogether in a vertebral body. *A* anterior, *P* posterior, *C* central, *L* left, *R* right

of about 25 mm were cut from the anterior, posterior, right, left and central regions of the trabecular bone using a standard biopsy drill without damaging trabeculae. The cortical shell was not included in each bone column. A schematic diagram of three layers and five columns within a vertebral body is shown in Fig. 1.

Micro-CT Scanning

A micro-CT system (μCT40, Scanco Medical AG, Bassersdorf, Switzerland) was used to reconstruct the microarchitectures of the trabecular columns. A detailed description of the preparation techniques has been described previously (Gong et al. 2005). The spatial resolution for specimen scanning was set to 20 μm. Each column was scanned three times to obtain three 5-mm-thick transverse layers, i.e., superior layer 1 mm below the superior endplate, inferior layer 1 mm above the inferior endplate, and middle layer between the superior and inferior layers (Fig. 1). The three layers and five columns constituted 15 different regions altogether in each vertebral body. During each scanning, the column was scanned continuously with thickness and increment of 20 μm for 250 slices. The voxel size was $20 \times 20 \times 20 \mu m^3$. After scanning, the micro-CT images of 15 different regions of six vertebral bodies were obtained. The region of interest (ROI) was chosen as a $5 \times 5 \times 5 mm^3$ cube in the center of each region to exclude the boundary artifacts, resulting in a total of 90 vertebral trabecular cubes. The microarchitectural parameters of trabecular cubes were evaluated by the direct method in the micro-CT system for 3D model, which has been reported in detail previously (Gong et al. 2005).

Micro-Finite Element Modeling

Scanco Medical Finite Element Software 1.02 (Scanco Medical AG, Bassersdorf, Switzerland) was used to do μFEA to simulate axial compression tests of each trabecular bone cube in three orthogonal directions: longitudinal; medial-lateral; and anterior-posterior. The 90 mirco-CT reconstruction models were used to construct micro-finite element models by directly converting image voxels representing hard tissue (20 μm in size) to eight-node brick finite elements. A fixed displacement boundary condition was chosen, i.e., all nodes at the bone-platen interface were constrained in the place of the platen with all other surfaces unconstrained to mimic the boundary conditions that occurred during mechanical testing of the bone cubes (Judex et al. 2003; Morgan et al. 2003).

Mechanical testing of the specimens was simulated under displacement control of the platens to mimic mechanical testing conditions. To make the μFEA outcomes of our six L4 vertebral bodies comparable, it was supposed that the mechanical loading on the vertebral body was proportional to the body weight. The average value of BV/TVs of the 15 trabecular cubes in each vertebral body was used to reflect its body weight. A displacement of 1% strain was applied to the central and posterior columns of the vertebral body with the maximum average BV/TV, and the mechanical environments of the other central and posterior columns in the other five vertebral bodies decreased linearly with their average BV/TVs. In each vertebral body,

the mechanical loadings on the central and posterior columns were assumed to be 23% higher than those on the other three columns, based on the observations that the stresses through the nucleus region of the disc were about 30% higher than those through the annulus region (Adams et al. 1996), and that the sectioning procedure used in this study resulted in trabecular cubes from anterior, right, and left columns (peripheral region) that were classified as being covered by the disc annulus, and posterior and central columns (postero-central region) covered by the disc nucleus. Bone material properties at tissue level were assumed to be homogeneous and isotropic with an elastic modulus of 15 GPa. This reflects a quality property of the material itself. The results about tissue-level stresses or strains can be scaled later for any value of the tissue modulus (Kabel et al. 1999). The isotropic Poisson's ratio of bone material was set to be 0.3 (Homminga et al. 2002).

Mechanical properties in the forms of apparent elastic moduli and tissue-level von Mises stresses of the trabecular bone cubes in the three orthogonal directions were obtained. Statistical analyses were done on the mechanical parameters for all 90 trabecular cubes. In each age group, the outcomes of the trabecular cubes from the same layers were pooled to form the layer data sets. In this case, superior, middle, and inferior layers were obtained by grouping the trabecular cubes that formed the same layer but come from different columns and different specimens in the same age group. In the same way, the column data sets can be obtained in the anterior, central, right, left and posterior columns. A single-factor analysis of variance (ANOVA) followed by a Tamhane's T2 post-hoc test was used to compare the mechanical properties between the layers or columns in each group. Student's t-test was performed to compare between the two groups regarding ages. The significance level of p was set to be 0.05. All the statistical analyses were performed using SPSS 12.0 (SPSS, Chicago, Ill.).

Results

μFEA analysis

Table 1 lists the mechanical properties calculated from μFEA for each age group and the differences between the two groups. Each value (mean ± SD) was obtained from 45 data sets grouped in 15 regions for three vertebral bodies in each age group. The value (mean ± SD) for tissue principal stress was calculated for the average von Mises stresses of each trabecular cube in a group. Student's t-test showed significant decreases in the apparent Young's moduli and tissue level von Mises stresses in each direction with ageing, and those in medial-lateral and anterior-posterior directions decreased more with ageing compared with longitudinal direction. A single-factor analysis of variance (ANOVA) showed that in each group, the apparent elastic moduli and the average tissue principal stresses in the longitudinal direction were significantly higher than their counterparts in the other two directions. There were no statistically significant differences in the mechanical properties between medial-lateral and anterior-posterior directions. The trabecular specimens displayed a near transversely isotropic behavior in both age groups; hence, the mechanical properties in

Table 1. The mechanical properties (mean ± SD) in two age groups. *L* longitudinal, *AP* anterior-posterior, *ML* medial-lateral

Parameter	62-year group	69-year group	Difference (%)	Significance level (p)
E_L(Mpa)	259.47 ± 120.75^a	208.19 ± 101.88^a	-19.76	0.01
E_{AP}(MPa)	32.15 ± 42.11	12.84 ± 14.32	-60.06	0.004
E_{ML}(MPa)	26.93 ± 38.74	14.21 ± 13.61	-47.23	0.041
σ_L(MPa)	38.47 ± 11.19^a	29.58 ± 8.88^a	-23.12	0.000
σ_{AP}(MPa)	9.29 ± 8.16	4.67 ± 3.38	-49.72	0.0005
σ_{ML}(MPa)	7.57 ± 6.59	5.30 ± 3.31	-30.00	0.041

[a] ANOVA revealed significant difference from AP and ML directions ($p < 0.001$) in the same age group

medial-lateral and anterior-posterior directions were pooled together to represent as off-axis mechanical properties of the vertebral body in the following results.

Regional Variations of the Mechanical Properties at Different Layers

Table 2 lists mechanical properties of the three layers in the two age groups, and the differences between layers and between age groups.

In the longitudinal direction, no significant difference was found between any layers within either age group for the apparent elastic modulus, as well as for the tissue principal stress. For all three layers, the apparent elastic modulus and tissue principal stress both decreased with ageing, but only the decrease in the latter reached significance level.

In the off-axis directions, there was also no significant difference between any layers within either age group for the apparent elastic modulus, as well as for the

Table 2. The microstructural parameters (mean ± SD) of the three layers in two age groups

Parameter	Layer	62-year group	69-year group	Difference (%)	Significance level (p)
E_L(MPa)	Superior	235.30 ± 110.37	190.58 ± 77.65	-19.01	0.105
	Middle	272.86 ± 120.68	227.71 ± 122.92	-16.55	0.16
	Inferior	270.24 ± 134.68	207.59 ± 105.38	-23.18	0.08
$E_{off-axis}$(Mpa)	Superior	29.67 ± 45.91	10.21 ± 9.07	-65.59	0.024
	Middle	29.97 ± 33.26	14.31 ± 15.12	-52.25	0.017
	Inferior	27.91 ± 35.32	15.51 ± 16.30	-44.43	0.05
σ_L(MPa)	Superior	36.93 ± 10.33	29.57 ± 8.17	-19.93	0.0195
	Middle	40.01 ± 12.43	31.99 ± 10.81	-20.04	0.038
	Inferior	38.48 ± 11.29	27.34 ± 7.46	-28.95	0.002
$\sigma_{off-axis}$ (MPa)	Superior	8.22 ± 7.81	4.50 ± 2.80	-45.25	0.016

tissue principal stress. The apparent elastic modulus and the tissue principal stress in all the three layers from the 69-year group were significantly lower than those in the same layers from the 62-year group.

For both age groups, the mechanical properties at both apparent and tissue level in the longitudinal directions were significantly higher than those in the off-axis directions in all three layers.

Regional Variations of the Mechanical Properties at Different Columns

The mechanical properties at the apparent and tissue level in the different columns of each age group, and their relative differences are listed in Table 3.

In the longitudinal direction, there were no significant differences between the five columns for the apparent elastic modulus in 62-year group; however, for the tissue principal stress, a significant difference was found between the central and posterior columns. In the 69-year group, ANOVA showed significant differences among the five columns for both the apparent elastic modulus and the tissue principal stress. The following Tamhane's T2 post-hoc test found significant differences between the central and anterior columns, the central and right columns, and the central and left

Table 3. The mechanical properties (mean ± SD) of the five columns in two age groups

Parameter	Column	62-year group	69-year group	Difference (%)	Significance level (p)
E_L (MPa)	Central	278.65±103.22	276.59 ± 62.07	−0.739	0.48
	Anterior	263.65±112.33	180.84 ± 68.32	−31.41	0.039
	Posterior	204.44 ± 98.24	254.67±143.56	24.57	0.204
	Right	285.76±140.93	153.77±103.65	−46.19	0.019
	Left	264.82±150.87	180.26 ± 77.58	−31.93	0.077
$E_{off\text{-}axis}$ (MPa)	Central	39.12 ± 39.93	13.86 ± 12.08	−64.57	0.015
	Anterior	12.89 ± 14.93	13.52 ± 18.21	4.89	0.46
	Posterior	37.42 ± 46.20	14.06 ± 14.24	−62.43	0.036
	Right	21.42 ± 19.29	16.26 ± 14.87	−24.09	0.199
	Left	37.98 ± 59.13	14.17 ± 13.45	−62.69	0.063
σ_L (MPa)	Central	49.26 ± 11.46	40.45 ± 6.00	−17.87	0.029
	Anterior	38.22 ± 8.66	27.17 ± 5.25[a]	−28.91	0.003
	Posterior	32.08 ± 5.32[a]	31.29 ± 8.98	−2.45	0.414
	Right	37.86 ± 12.56	23.13 ± 8.43[a]	−38.91	0.005
	Left	34.96 ± 10.27	26.05 ± 3.91[a]	−25.48	0.014
$\sigma_{off\text{-}axis}$ (MPa)	Central	13.21 ± 10.11	6.05 ± 3.25	−54.16	0.009
	Anterior	5.46 ± 4.01	4.74 ± 3.54	−13.30	0.302
	Posterior	9.07 ± 6.10	4.86 ± 3.96	−46.48	0.017
	Right	6.57 ± 4.06	4.43 ± 3.18	−32.56	0.0515
	Left	8.64 ± 9.34	4.74 ± 2.96	−45.20	0.06

[a] Significantly different to central column ($p = 0.05$)

columns, respectively, for the tissue principal stress; however, for the apparent elastic modulus, none of the differences between any two columns reached significance level. If the apparent elastic moduli of the posterior and central columns were further pooled together to form a posterior-central region, and the other three columns form a peripheral or outer region, Student's t-test showed that the apparent elastic moduli of the posterior-central region were significantly higher than those of the peripheral region (p = 0.001). The tissue principal stresses in all the columns decreased significantly with ageing, except the posterior column. The differences in the apparent elastic modulus between the same columns from the two age groups followed different patterns for different columns: those of the columns in the peripheral/outer region decreased severely with ageing, but the difference in the left column did not reach significance level (p = 0.077). In the posterior-central region, the apparent elastic moduli of the central column only decreased slightly; on the contrary, those of the posterior column were higher in the 69-year group.

In the off-axis directions, ANOVA showed no significant difference between any columns within either age group for the apparent elastic modulus, as well as for the tissue principal stress. For all five columns, the tissue principal stress decreased with ageing, but only the decreases in the posterior-central region reached significance level. The apparent elastic moduli in the anterior column were slightly higher in the 69-year group, whereas those in the other four columns decreased with ageing, with the decreases in the posterior-central region reaching significance level.

For both age groups, the apparent Young's moduli and tissue-level von Mises stresses in the longitudinal direction were significantly higher than those in the off-axis direction in all five columns.

Discussion

The mechanical properties of trabecular bone are determined by the properties of its bone tissue and its architecture. Micro-finite element analysis is a state-of-the-art numerical technique used to calculate mechanical properties of trabecular bone as they relate to its microstructure. This chapter aims at quantifying the regional variations in the mechanical properties of L4 vertebral body and exploring the effect of ageing, which may help to gain insight into possible fracture risks in the L4 vertebral body.

As an example, Fig. 2 shows a typical micro-CT reconstruction model of a trabecular cube, and the loading and boundary conditions of its finite element model when compressed in the longitudinal direction and the von Mises principal stress distribution.

A quantitative assessment of bone tissue stresses is essential for the understanding of failure mechanisms associated with osteoporosis, osteoarthritis, loosening of implants, and cell-mediated adaptive bone-remodeling processes at tissue level. With μFEA we determined the apparent elastic moduli in the three orthogonal directions of each trabecular cube. Because of a strong relationship between stiffness and strength (Keaveny et al. 1994), the elastic moduli can provide an estimate of strength as well; thus, the computational work in this chapter may help to demonstrate the re-
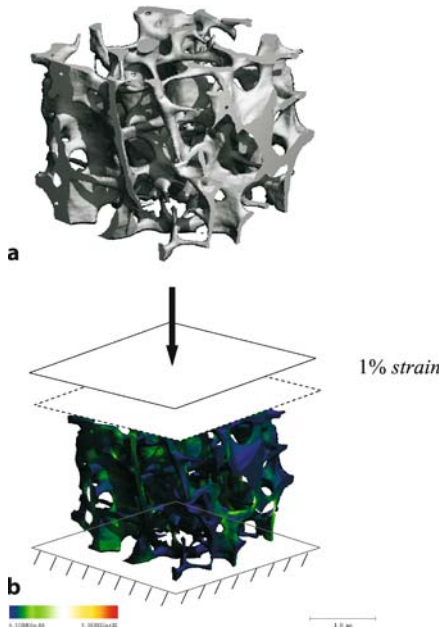
Figure 2 a,b. A typical micro-CT reconstruction model of a trabecular cube, and the loading and boundary conditions of its finite-element (FE) model when compressed in the longitudinal direction and the von Mises principal stress distribution. **a** A typical micro-CT reconstruction model of a trabecular cube. Loading and boundary conditions of its FE model when compressed in the longitudinal direction and the von Mises principal stress distribution. Voxels in the 3D reconstruction are converted to equally shaped brick elements such that the resulting FE model has exactly the same geometry as the reconstruction from which it is derived. **b** Displacements of nodes located at the face z = zmin are suppressed in all directions, those at the face z = zmax are prescribed in the z-direction at a strain value of −1%, and are suppressed in the other directions

gional failure mechanisms of L4 vertebral body at both the apparent and tissue levels associated with ageing.

Vertebral trabecular architectures and mechanical properties were shown to be closely related to their mechanical environment and to age, suggesting both mechanical and age-related adaptation (Adams et al. 1996; Gong et al. 2005; Simpson et al. 2001). Keller et al. (1989) did compressive testing of the mechanical properties of lumbar vertebral segments from three human cadavers with the ages of 71, 78, and 84 years, and found that for normal intervertebral discs, the strength of bone overlying the disc nucleus was 1.25 times that of bone overlying the disc annulus. In our study, the intervertebral discs of our six L4 vertebral bodies did not show macroscopic signs of severe degeneration, and could be classified as normal or only slightly degenerate (Ferguson and Steffen 2003). The data we obtained about the differences in the mechanical properties between the two groups were thus mainly related to different age. The sectioning procedure used in this study resulted in trabecular

cubes from anterior, right, and left columns (peripheral region) that were classified as being covered by the disc annulus, and posterior and central columns (postero-central region) covered by the disc nucleus; hence, our μFEA computational results for the regional variations of the on-axis apparent moduli in the five columns of 69-year group were consistent with the experimental observations by Keller et al. 1989, although their specimens were older than those of ours; however, in our 62-year group, the on-axis apparent moduli in the five columns did not show significant difference. It was suggested that on-axis mechanical properties deteriorated faster for the peripheral region with ageing and off-axis mechanical properties deteriorated faster for the posterior-central region with ageing.

Because of the limited availability of donors, we only studied the mechanical properties of L4 vertebral bodies from two age groups of 62 and 69 years. Statistical analyses showed significant differences between the mechanical properties at both apparent and tissue levels with ageing. Future studies that examine the three-dimensional microstructural properties, as well as mechanical properties of normal vertebral bodies, as well as osteoporotic ones, or ones with degenerated intervertebral discs from a wide age range of ages, may provide additional insight into the structural and mechanical properties, and the changes accompanying ageing, disease, and disc degeneration.

Conclusion

This study offers an insight into the distributions and variations of mechanical properties within a vertebral body. The mechanical properties calculated from this study may serve as reference for gender and ethnic comparisons and may help us better understand regional fracture risks and vertebral fracture mechanism, prevent osteoporotic fracture in elderly individuals, and choose appropriate physical exercise.

References

Adams MA, Mcnally DS, Dolan P (1996) "Stress" distributions inside intervertebral discs: the effects of age and degeneration. J Bone Joint Surg 78B:965–972
Ding M, Hvid I (2000) Quantification of age-related changes in the structure model type and trabecular thickness of human tibial cancellous bone. Bone 26:291–295
Ding M, Odgaard A, Linde F, Hvid I (2002) Age-related variations in the microstructure of human tibial cancellous bone. J Orthop Res 20:615–621
Ferguson SJ, Steffen T (2003) Biomechanics of the aging spine. Eur Spine J 12: S97-S103
Goel VK, Ramirez SA, Kong WZ, Gilbertson LG (1995) Cancellous bone Young's modulus variation within the vertebral body of a ligamentous lumbar spine: application of bone adaptive remodeling concepts. J Biomech Engineering Trans ASME 117:266–271

Gong H, Zhang M, Yeung HY, Qin L (2005) Regional variations in microstructural properties of vertebral trabeculae with ageing. J Bone Miner Metab 23:174–180

Hansson T, Keller TS, Panjabi MM (1987) A study of the compressive properties of lumbar vertebral trabeculae: effects of tissue characteristics. Spine 12:56–62

Homminga J, Weinans H, Gowin W, Felsenberg D, Huiskes R (2001) Osteoporosis changes the amount of vertebral trabecular bone at risk of fracture but not the vertebral load distribution. Spine 26:1555–1561

Homminga J, McCreadie BR, Ciarelli TE, Weinans H, Goldstein SA, Huiskes R (2002) Cancellous bone mechanical properties from normals and patients with hip fractures differ on the structural level, not on the bone hard tissue level. Bone 30:759–764

Judex S, Boyd S, Qin YX, Turner S, Ye K, Muller R, Rubin C (2003) Adaptations of trabecular bone to low magnitude vibrations result in more uniform stress and strain under load. Ann Biomed Eng 31:12–20

Kabel J, van Rietbergen B, Odgaard A, Huiskes R (1999) Constitutive relationships of fabric, density, and elastic properties in cancellous bone architecture. Bone 25:1159–1164

Keaveny TM, Borchers RE, Gibson LJ, Hayes WC (1993) Theoretical analysis of the experimental artifact in trabecular bone compressive modulus. J Biomech 26:599–607

Keaveny TM, Wachtel EF, Ford CM, Hayes WC (1994) Differences between the tensile and compressive strengths of bovine tibial trabecular bone depend on modulus. J Biomech 27:1137–1146

Keaveny TM, Pinilla TP, Crawford RP, Kopperdahl DL, Lou A (1997) Systematic and random errors in compression testing of trabecular bone. J Orthop Res 15:101–110

Keller TS, Hansson TH, Abram AC, Spengler DM, Panjabi MM (1989) Regional variations in the compressive properties of lumbar vertebral trabeculae: effects of disc degeneration. Spine 14:1012–1019

Lau EMC, Woo J, Leung PC (1993) Low bone mineral density, grip strength and skinfold thickness are important risk factors for hip fracture in Hong Kong Chinese. Osteoporos Int 3:66–69

Melton LJ, Chrischilles EA, Cooper C, Lane AW, Riggs BL (1992) Perspective: How many women have osteoporosis? J Bone Miner Res 7:1005–1010

Morgan EF, Bayraktar HH, Keaveny TM (2003) Trabecular bone modulus-density relationships depend on anatomic site. J Biomech 36:897–904

Qin L, Au SK, Leung PC, Lau MC, Woo J, Choy WY, Hung WY, Dambacher MA, Leung KS (2002) Baseline BMD and bone loss at distal radius measured by pQCT in peri- and postmenopausal Hong Kong Chinese Women. Osteoporosis Int 13:962–970

Simpson EK, Parkinson IH, Manthey B, Fazzalari NL (2001) Intervertebral disc disorganization is related to trabecular bone architecture in the lumbar spine. J Bone Miner Res 16:681–687

Van Rietbergen B, Weinans H, Huiskes R, Odgaard A (1995) A new method to determine trabecular bone elastic properties and loading using micromechanical finite-element models. J Biomech 28:69–81

Van Rietbergen B, Odgaard A, Kabel J, Huiskes R (1998) Relationships between bone morphology and bone elastic properties can accurately quantify using high-resolution computer reconstructions. J Orthop Res 16:23–28

MRI Evaluation of Osteoporosis

James Francis Griffith

Department of Radiology and Organ Imaging, The Chinese University of Hong Kong, Hong Kong, China
e-mail:Griffith@ruby.med.cuhk.edu.hk

Abstract

Trabecular architecture is usually studied extremely well by computed tomography (CT) and micro-CT. The limitation of clinical CT is radiation dose. High-resolution clinical magnetic resonance (MR) imaging is also used to study trabecular architecture in the peripheral skeleton, particularly the distal radius and calcaneum. The MR imaging of trabecular micro-architecture has quite good precision and has demonstrated expected changes on longitudinal in vivo study. While clinical MR imaging may currently be limited to examination of fine bone structure only in the peripheral appendicular skeleton, it also has the capacity to study other aspects of bone physiology not readily measurable by other techniques, namely marrow fat content, perfusion and molecular diffusion. Magnetic-resonance-based studies have shown that as spinal bone mineral density decreases, vertebral marrow fat content increases while vertebral marrow perfusion decreases. This reduction in marrow perfusion is an intraosseous phenomenon and is not related to a more generalized circulatory impairment. Females across all groups (normal, osteopaenia and osteoporosis) tend to have slightly higher vertebral fat content than males. Pre-menopausal women have on average lower MR diffusion coefficient than post-menopausal women. In post-menopausal women, the change in fat content or perfusion indices seen with change in bone mineral density does not have any appreciable effect on MR diffusion parameters.

Introduction

All of the efforts put into the screening, diagnosis and treatment of osteoporosis have one goal in mind: to reduce fractures. Increasing incidence of falls and reduced bone strength are the two main determinants of the increased prevalence of spinal, proximal, femoral and radial fractures in the elderly. If bone strength can be maintained, the increased rate of falls may not necessarily translate into an increased incidence of fracture in the elderly. Maintaining or improving bone strength in later years is important. Bone strength is a measure of bone density and bone quality. In other words, bone strength depends not just on bone quantity (as measured by bone density) but also bone quality.

Bone density can be measured accurately and precisely by dual-energy absorpiometry (DXA), which is especially useful in the hip region. Other methods of measuring bone density include quantitative CT examination (QCT; particularly useful in the spine), peripheral QCT, peripheral DXA, radiographic absorpiometry and qualitative ultrasound (QUS).

Bone quality is dependent on the six "M's", i.e. macroarchitecture, microarchitecture, modelling and remodelling (i.e. bone turnover), microfracture accumulation, mineralization and matrix. Currently, MRI can be used to examine two of these parameters, i.e. macroarchitecture and microarchitecture.

Macroarchitecture refers to the overall geometry of the bone and depends on bone size and shape. At the proximal femur, for instance, the parameters studied include hip-axis length (HAL), femoral neck cross-sectional area, femoral neck width and femoral neck-shaft angle. A short hip-axis length and a wide femoral neck cross-sectional area are considered to be protective against proximal femoral fracture. This may explain why men, black women, Asian women and multiparous women have a lower prevalence of proximal femoral fractures compared with Caucasian women of comparable bone density. These macroarchitecture features could be measured by oblique coronal and sagittal magnetic resonance (MR) imaging of the proximal femur, although are usually evaluated by either DXA or CT examination.

Microarchitecture refers to the trabecular and cortical pattern, including the number, arrangement and connectivity of trabecula, as well as the thickness and porosity of the cortex. Trabecula measure from 100 to 400 μm in width. Any imaging technique must have a resolution of 100 μm or less to be able to accurately resolve individual trabeculae. This resolution can now be achieved with high-field-strength (1.5–3.0 T), high-gradient (approximately 30 mT/m) clinical MR units or micro-MRI units (Link et al. 2004; Phan et al. 2006; Vokes et al. 2003). Clinical MRI units using high-resolution gradient-echo sequences can achieve an isotropic resolution of 150 μm. To acquire this high resolution, a small local coil yielding a small field of view needs to be used; therefore, MRI is used currently to study the trabecular pattern in peripheral bones such as the radius and calcaneum (Link et al. 2000; Wehrli et al. 1998). A comparable resolution cannot currently be achieved in the axial skeleton. Trabecular structural measures analysed on MRI examination have been shown to be better than bone mineral density in differentiating patients with and without osteoporotic fractures in transplant patients (Link et al. 2000). Reproducibility of 2–3% can be achieved from two-dimensional structural parameters, whereas the resolution of three-dimensional structural parameters is 4–9% (Newith et al. 2000). Comparing a group of women aged 40–55 years in early menopause treated with oestrogen against a control group showed how micro-MRI can show serial changes (Wehrli et al. 2006; Bauer et al. 1997).

Magnetic resonance relaxometry is another MR-based method whereby trabecular structure can be indirectly assessed from studying the relaxation time of the bone marrow (Link et al. 2000, 2004; Majumdar et al. 1997). The principle underlying MR relaxometry is that changes in trabecular density will affect the microenvironment of the marrow and thereby affect relaxation times. Since high spatial resolution is not as pre-requisite for this technique, it can be performed on clinical MRI units. $T2^*$

(magnetic field heterogeneity relaxation time) and/or its reciprocal relaxation parameter measure, R2* (rate constant for free induction decay) are used as measures in MR relaxometry. The MR relaxometry can be performed more quickly than MR assessment of trabecular pattern, although it has a relatively low precision limiting its usefulness in longitudinal study. All MR-based techniques have the advantage of not utilizing ionizing radiation (as in computed tomography) but are disadvantaged by long examination times (about 20–30 min) and the lack of bone densitometry measurement.

Currently, all of the techniques used to evaluate osteoporosis look at the end result of osteoporosis, i.e. bone loss must be present before the disease is diagnosed. There is no way currently of predicting which patients will develop bone loss and diagnosing osteoporosis before bone loss occurs. Once large defects occur in trabeculae, they may not be able to be replaced. Whereas many risk factors for osteoporosis have been developed, the pathophysiology of osteoporosis remains largely unknown. Magnetic resonance imaging, in addition to assessing bone macroarchitecture and microarchitecture as described above, has the ability to investigate three other aspects of bone physiology not measurable by other techniques, namely MR spectroscopy, perfusion and diffusion (Kugel et al. 2001; Schellinger et al. 2001; Shih et al. 2004; Yeung et al. 2005; Griffith et al. 2005, Griffith et al. 2006). Magnetic resonance spectroscopy allows one to measure the relative ratio of fat vs water in bone marrow. Magnetic resonance perfusion provides a measure of perfusion indices in bone marrow. Marrow diffusion allows one to measure the rate of diffusion of water molecules within bone marrow. Perfusion indices are an indirect measure of blood flow in bone marrow. We conducted some studies in elderly males (Griffith et al. 2005) and post-menopausal females (Griffith et al. 2006), respectively, to investigate the relationship between bone mineral density, bone marrow fat content, diffusion and perfusion as measured by MRI examination.

Studies on Relationship between Bone Mineral Density, Bone Marrow fat Content, Diffusion and Perfusion

Proton (^{1}H) MR Spectroscopy

In vivo ^{1}H MR spectroscopy is a non-invasive technique suitable for the study of metabolic changes in disease processes. In the assessment of bone marrow fat content, a volume of interest within the bone can be selected (Fig. 1) and ^{1}H spectroscopy may be performed using a point-resolved spectroscopy sequence (TR/TE: 2000/25 ms). The relative intensity of water and fat signals may be used to estimate the fat content (FC) present in bone according to the relationship

$$FC = \left(I_{fat}/\left(I_{fat} + I_{water}\right)\right) \times 100 \; [\%] \; , \tag{1}$$

where I_{fat} and I_{water} are the peak amplitudes of fat and water, respectively (Fig. 2).

Recent studies using in vivo ^{1}H MR spectroscopy have shown both a linear increase in vertebral marrow fat content with aging and a higher fat concentration in

Figure 1. Sagittal T2-weighted MR image (TR = 3500 ms/TE = 120 ms) of the lumbar spine shows positioning of the voxel of interest (VOI) for spectroscopy within the L3 marrow cavity
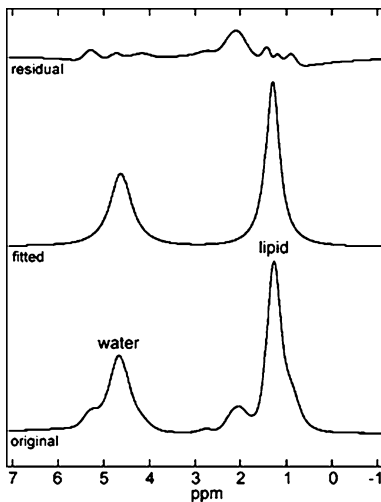
Figure 2. ^{1}H spectrum acquired from this VOI shows a relatively intense lipid peak (1.3 ppm) compared with the water peak (4.65 ppm), indicating increased marrow fat content within the vertebral body. Bottom trace is the original spectrum, whereas the middle shows the fitted spectrum from which peak intensity values were derived and top trace is the residual spectrum

males than females of similar age group (Kugel et al. 2001; Shih et al. 2004). In a study of 53 women (mean age 70 years), marrow fat content was significantly elevated in osteoporotic (mean $65.5 \pm 10\%$) and osteopaenic subjects ($63.5 \pm 9.3\%$) compared with

normal subjects (56.3 ± 11.2%; Griffith et al. 2006). In another study in 90 men (mean age 73 years), vertebral marrow fat content was significantly increased in osteoporotic subjects (mean 58.23 ± 7.83%) and osteopaenic subjects (55.68 ± 10.2%) compared with those with normal bone density (50.45 ± 8.73%; Griffith et al. 2005). Across all bone density groups (normal, osteopaenia and osteoporosis), vertebral marrow fat was significantly higher in women than men.

MR Diffusion-Weighted Imaging

Diffusion-weighted imaging (DWI) is a technique that is sensitive to the mobility or diffusion of water in biological tissues. Measuring the random motion of water molecules within the marrow may indirectly assess changes in the cellular composition of bone marrow associated with osteoporosis. Diffusion-weighted imaging pulse sequences are derived from spin-echo single-shot echo-planar imaging which is sensitized to incoherent motion by a pair of gradient pulses. Varying the gradient amplitude while keeping the gradient duration and separation time constant alters diffusion sensitivity parameters, or b-values. Since diffusion in bone marrow is anisotropic, three diffusion-weighted images are usually acquired for each b-value with the diffusion-sensitization gradient along the readout, phase-encoding and slice directions, respectively. The resultant isotropic diffusion-weighted image can be calculated on a pixel-by-pixel basis according to the following equation:

$$I_b = \sqrt[3]{I_x I_y I_z} \,, \tag{2}$$

where I_b is the resultant isotropic signal intensity of the diffusion-weighted image acquired with a b-value b and I_x, I_y and I_z are the original signal intensities of the diffusion-weighted images obtained with gradient sensitization along the readout, phase-encoding, and slice-selection directions, respectively (Fig. 3).

Apparent diffusion coefficient (ADC) may be calculated according to the relationship $I_b = I_0 \times \exp(-b \times ADC)$, where I_b and I_0 are the mean signal intensities
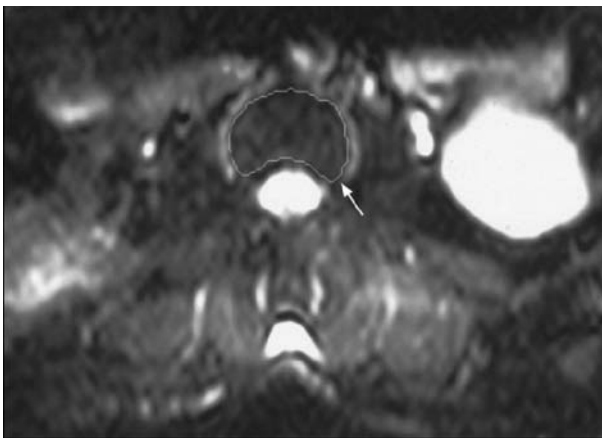
Figure 3. Axial T2-weighted MR image (TR = 2000 ms/TE = 102 ms) of the lumbar spine obtained with a b-value of 0 s/mm^2 shows a manually drawn region of interest (ROI) positioned just within the cortical margins of the L3 vertebral body

in the ROI measured at b-value b and $0\,s/mm^2$, respectively. In a study of 42 women (mean age 70 years) with documented bone mineral density measured by DXA, and 20 normal subjects (mean age 28 years), mean ADC values were significantly lower both in subjects with reduced BMD ($0.41 \pm 0.10 \times 10^{-3}\,mm^2/s$) and normal BMD ($0.43 \pm 0.08 \times 10^{-3}\,mm^2/s$) compared with normal controls ($0.49 \pm 0.07 \times 10^{-3}\,mm^2/s$) (Yeung et al. 2005). Accumulation of fatty bone marrow associated with osteoporosis is reflected by a decrease in ADC.

MR Perfusion Imaging

Dynamic contrast-enhanced MR imaging is another imaging technique that may be useful in the study of micro-circulation or perfusion changes associated with osteoporosis. Dynamic images are usually acquired using a short T1-weighted gradient-echo sequence (TR/TE: 2.9/1.1 ms; pre-pulse inversion time: 400 ms) with a bolus of contrast agent injected at an injection rate of about 2.0 ml/s. A region of interest (ROI; Fig. 4) may be drawn manually to obtain average signal intensity change caused by the arrival of contrast-material within the ROI at each time point (Fig. 5).

Curve fitting is performed on each time-intensity data set to obtain baseline (I_{base}) and maximum signal intensity values (I_{max}). Based on I_{max} and I_{base} values obtained from the fitted time-intensity curve, two perfusion indices may be calculated, namely, maximum enhancement and enhancement slope. Maximum enhancement is defined as the maximum percentage increase ($I_{max} - I_{base}$) in signal intensity from baseline (I_{base}). Enhancement slope was defined as the rate of enhancement between 10 and 90% of maximum signal intensity difference between I_{max} and I_{base}. These

Figure 4. Sagittal T1-weighted MR image (TR = 450 ms/TE = 1 ms) of the lumbar spine shows a manually drawn ROI positioned just within the cortical margins of the L3 vertebral body
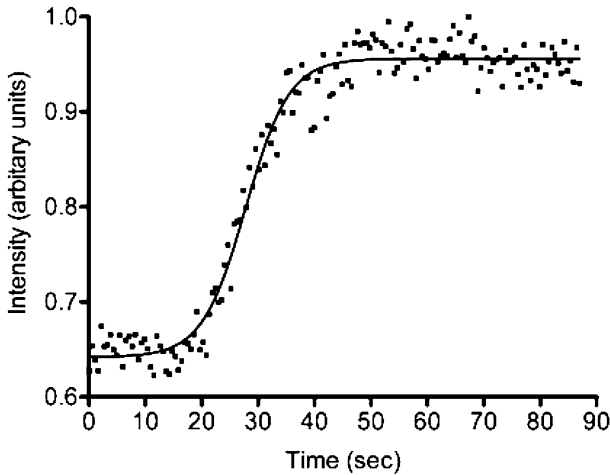
Figure 5. Time-intensity data points based on this ROI were measured from all dynamic images. Typical time-intensity curve for subjects with normal bone density shows high maximum enhancement and steep enhancement slope

perfusion indices are calculated according to the following equations:

$$\text{Maximum enhancement} = \frac{(I_{max} - I_{base})}{I_{base}} \times 100\%$$

and

$$\text{Enhancement slope} = \frac{(I_{max} - I_{base}) \times 0.8}{I_{base} \times (t_{90\%} - t_{10\%})} \times 100\% \, ,$$

where $t_{10\%}$ and $t_{90\%}$ are the time intervals when the rise in signal intensity reaches 10 and 90% of the maximum signal intensity difference between I_{base} and I_{max}, respectively. Both parameters are derived from the first-pass phase of signal enhancement or rapidly rising part of the time-intensity curve and are considered to represent arrival of the contrast material into the arteries and capillaries of the vertebral marrow and its diffusion into the extracellular space.

In a study of 90 male subjects (mean age 73 years), perfusion indices were significantly decreased in osteoporotic subjects (enhancement slope: $0.78 \pm 0.33\%$/s) compared with osteopaenic subjects ($1.15 \pm 0.59\%$/s) or those with normal bone density ($1.48 \pm 0.73\%$/s) [13]. In a similar study in 110 women (mean age 73 years) vertebral marrow perfusion indices were significantly decreased in osteoporotic subjects (enhancement slope: $1.10 \pm 0.51\%$/s) compared with osteopaenic ($1.45 \pm 0.51\%$/s; $p = 0.01$) and normal bone density subjects ($1.70 \pm 0.52\%$/s; $p < 0.001$; Griffith et al. 2006). Erector spinae muscle perfusion indices did not decrease with decreasing bone density, suggesting that the reduction in perfusion indices occurred only within the vertebral body and not in the paravertebral tissues supplied by the same artery (Fig. 6; Griffith et al. 2006).
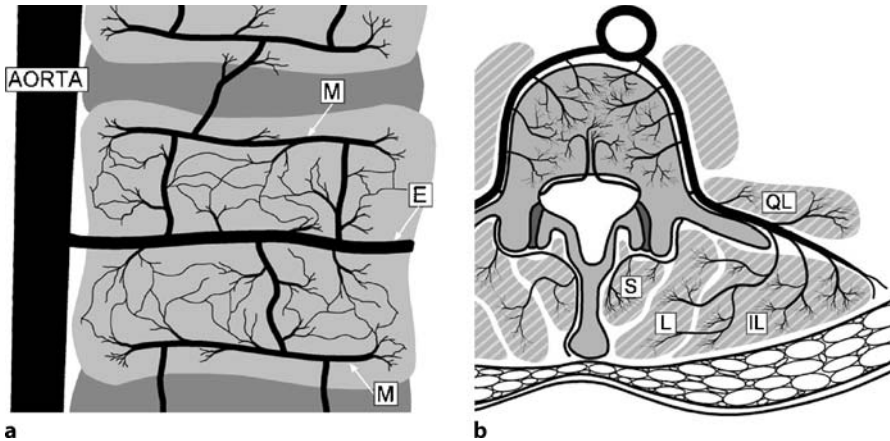
Figure 6 a,b. Blood supply to vertebral body and paraspinal muscle at L3 region. **a** Longitudinal view of surface of vertebral body. Each lumbar artery passes backwards around the waist of the vertebral body as a single trunk. Some branches (equatorial branches, *E*) penetrate into the vertebral marrow, whereas others ascend and descend on the periosteum of the vertebral body. Near the end plates, some of these arteries (metaphyseal branches, *M*) penetrate into the vertebral marrow. **b** Axial view of mid-vertebral body and paraspinal regions. At the intervertebral foramen level, the artery divides to send branches into the spinal canal and the paraspinal muscles. The intraspinal branch gives rise to the nutrient artery, which penetrates the posterior border of the vertebral body. Other branches run dorsally between and supply the quadratus lumborum (*QL*) muscle and the erector spinae muscle complex. The erector spinae muscle complex is composed of three columns, which are from medial to lateral, spinalis (*S*), longissimus (*L*) and iliocostalis (*IL*)

Discussion

Magnetic resonance enables study of the trabecular and cortical pattern in the peripheral parts of the appendicular skeleton. In addition, some aspects of bone physiology not readily quantified by other techniques can be measured, namely fat content, perfusion and diffusion. All of the measurements provided by MR are arbitrary. Fat content is measured as a ratio of fat:water content. Water content seems quite constant in marrow enabling the fat:water content to be accepted as a reliable measure of relative fat content. Neither is perfusion directly measured. Instead, indices of perfusion (usually enhancement slope and maximum enhancement) are measured. Similarly, molecular diffusion is not directly measured, but changes in diffusion coefficient are theoretically considered to represent molecular diffusion and are accepted as such.

As bone mineral density decreases, bone marrow fat content tends to increase while bone marrow perfusion indices decrease, and there is little or no effect on MR diffusion parameters. An identical trend was evident in both males and females. On average, females tended to have higher vertebral marrow fat content irrespective of whether the bone mineral density was categorized as normal, osteopaenia or osteo-

porosis. The decrease in MR perfusion indices observed in subjects with decreased bone density could be caused by a systemic circulatory impairment or a local effect within bone. We therefore compared perfusion indices within the vertebral bone marrow with that in the paravertebral muscle. Both these regions have the same arterial supply, namely the lumbar arteries. If a systemic cause were to blame for the observed reduction in perfusion indices, one would expect both the vertebral marrow and the paravertebral muscles to be similarly affected. This was not the case. The reduction in perfusion indices was only observed within the vertebral marrow, whereas perfusion indices tended to increase, rather than decrease, with decreasing bone mineral density. Longitudinal studies would help to show whether this observed alteration in perfusion is primary or secondary to the development of osteoporosis.

Premenopausal women have, on average, lower MR diffusion coefficients than post-menopausal women. In post-menopausal women, the change in fat content or perfusion indices seen with change in bone mineral density does not have any appreciable effect on MR diffusion parameters.

Conclusion

Magnetic resonance imaging has the potential to investigate not only bone structural detail but also other aspects of bone physiology, namely bone fat content, perfusion and molecular diffusion. Investigation of these parameters may provide insight into the pathophysiology of many bone conditions, including osteoporosis.

References

Baur A, Stabler A, Bartl R, Lamerz R, Scheidler J, Reiser M. MRI gadolinium enhancement of bone marrow: age-related changes in normals and in diffuse neoplastic infiltration. Skeletal Radiol 1997;26:414–418

Griffith JF, Yeung DK, Antonio GE, Lee FK, Hong AW, Wong SY, Lau EM, Leung PC. Vertebral bone mineral density, marrow perfusion, and fat content in healthy men and men with osteoporosis: dynamic contrast-enhanced MR imaging and MR spectroscopy. Radiology 2005;236:945–951

Griffith JF, Yeung DK, Antonio GE, Wong SYS, Kwok T, Woo J, Leung PC. Marrow perfusion, diffusion and fat content in post-menopausal women of varying bone density. Radiology 2006;Epub ahead of print

Kugel H, Jung C, Schulte O, Heindel W. Age- and sex-specific differences in the 1H-spectrum of vertebral bone marrow. J Magn Reson Imaging 2001;13:263–268

Link TM, Majumdar S. Current diagnostic techniques in the evaluation of bone architecture. Curr Osteoporos Rep 2004;2(2):47–52

Link TM, Lotter A, Beyer F, et al. Changes in calcaneal trabecular bone structure after heart transplantation: an MR imaging study. Radiology 2000;217:855–862

Majumdar S, Genant HK, Grampp S, et al. Correlation of trabecular bone structure with age, bone mineral density, and osteoporotic status: in vivo studies in the distal radius using high resolution magnetic resonance imaging. J Bone Miner Res 1997; 12:111–118

Newith DC, Van Rietbergen B, Majumdar S. Processing and analysis of in vivo high resolution MR images of trabecular bone for longitudinal studies: reproducibility of structural measures and micro-finite element analysis derived mechanical properties. Osteoporosis Int 2002;13:278–287

Phan CM, Matsuura M, Bauer JS, Dunn TC, Newitt D, Lochmueller EM, Eckstein F, Majumdar S, Link TM. Trabecular bone structure of the calcaneus: comparison of MR imaging at 3.0 and 1.5 T with micro-CT as the standard of reference. Radiology 2006;239(2):488–496

Schellinger D, Lin CS, Hatipoglu HG, Fertikh D. Potential value of vertebral proton. MR spectroscopy in determining bone weakness. Am J Neuroradiol 2001;22:1620–1627

Shih TT, Liu HW, Chang CJ, Wei SY, Shen LC, Yang PC. Correlation of MR lumbar bone marrow perfusion with bone mineral density in female subjects. Radiology 2004;233:121–128

Vokes TJ, Favus MJ. Noninvasive assessment of bone structure. Curr Osteoporos Rep 2003;1(1):20–24

Wehrli FW, Ilwang SN, Ma J, et al. Cancellous bone volume and structure in the forearm: noninvasive assessment with MR microimaging and image processing. Radiology 1998;206:347–357

Wehrli FW, Ladinsky GA, Vasilic B, Zemel BS, Wright AC, Song HK, Saha PK, Peachy H, Synder PJ. Proc Int Magn Reson Med 2006;14:546

Yeung DK, Griffith JF, Antonio GE, Lee FK, Woo J, Leung PC. Osteoporosis is associated with increased marrow fat content and decreased marrow fat unsaturation: a proton MR spectroscopy study. J Magn Reson Imaging 2005;22:279–285

Multiple Bio-imaging Modalities in Evaluation of Epimedium-Derived Phytoestrogenic Fraction for Prevention of Postmenopausal Osteoporosis

Ge Zhang[1], Ling Qin (✉) [1], and Yin-Yu Shi[2]

[1] Musculoskeletal Research Center, Department of Orthopedics and Traumatology,
   The Chinese University of Hong Kong, Hong Kong SAR, China
   email: lingqin@cuhk.edu.hk
[2] Department of Orthopedics and Traumatology, Shanghai Shu Guang Hospital,
   Shanghai, China

Abstract

Recently, we extracted phytoestrogenic fraction (PF) from herbal Epimedium, which is a kind of traditional Chinese medicine (TCM) known as a "bone-strengthening Chinese herb." This herb has been widely prescribed for musculoskeletal diseases in routine clinical practice of TCM. In this chapter the authors introduce multiple bio-imaging modalities adopted for evaluation of therapeutic efficacy of Epimedium-derived phytoestrogenic fraction (EPF) in two sections. Experimentally, we show that EPF exerted its prevention of estrogen-deficiency-induced osteoporosis in both mechanical and bone-quality indices. Clinically, our clinical placebo-controlled trial using bone densitometry showed that EPF was able to exert beneficial effects on both promotion of periosteal apposition and inhibition of endocortical resorption for improving mechanically structural geometry at osteopenic femoral neck in postmenopausal women. Both preclinical and clinical studies did not document side effects associated with reproductive tissues or organs.

Introduction

It is well known that calcium supplement (CS, a fundamental therapy) and hormone replacement therapy (HRT, a classical therapy) are effective to attenuate bone loss and reduce osteoporotic fracture risks in postmenopausal women (Nieves et al. 1998; Health Initiative Investigators 2002). A meta-analysis of clinical trials demonstrated that the mean increase in bone mineral density (BMD) was 2.5 and 2.7 times higher at the lumbar spine and femoral neck, respectively, when HRT was administrated together with CS as compared with HRT treatment alone. This suggested that HRT exerted its anti-osteoporosis effect through at least one mechanism of an enhancement in intestinal calcium absorption in postmenopausal women (Gallagher et al. 1980;

Heaney et al. 1978; Nieves et al. 1998); however, long-term acceptance and/or compliance rates of HRT are low due to potential side effects on reproductive tissues or organs, which have been recently highlighted by the findings from the Women Health Initiative Trial (Taylor 1997; Health Initiative Investigators 2002); therefore, research and development (R&D) of safe therapies alternatively to HRT is highly desirable for prevention of osteoporosis in postmenopausal women (Eisenberg et al. 1998).

Epimedium has been traditionally used as medicinal herb to treat fractures, bone and joint diseases, and gonad dysfunctions in Asia for thousands of years (Qin et al. 2005a). Now phytoestrogenic fractions were derived from Epimedium (EPF) by a series of standardized extraction and isolation procedures (Lee et al. 2004; Meng et al. 2005; Qin et al. 2005a), which consists of three main phytoestrogenic compounds, i.e., Icariin, Genistein, and Daidzein. Now it is developed and tested as an alternative preparation to relieve menopausal symptoms and to prevent postmenopausal osteoporosis yet with no reported hyperplastic effects on the reproductive tissues or organs both clinically and experimentally (Qin et al. 2005a). The potential mechanism of action of EPF might be explained by its structural similarities to estrogen conformation and their ability to bind to estrogen receptors so as to promote calcium absorption through proposed estrogen receptor pathway of intestinal cells (Arjmandi et al. 1993, 2002; Setchell et al. 2003) and/or regulate bone remodeling through proposed estrogen receptor pathway of bone cells (Chen et al. 2002; Rickard et al. 2003); however, the scientific base of therapeutic efficacy of EPF for prevention of postmenopausal osteoporosis has not been established, especially in the following three aspects:

1. How could EPF protect estrogen-deficiency-induced bone structural deterioration at organ level?
2. How does EPF influence bone envelop at tissue level?
3. At cellular level, if EPF may act via a pathway dependent on an enhancement in intestinal calcium absorption or more on a direct action on bone cells?

Recent epidemiological data implied envelope-dependent pathogenesis of age-related long bone fragility in women. Compared between both sexes, periosteal area increases more in men than in women, whereas endocortical area increases similarly in men and women, then cortical thickness decreases more in women than in men (Ruff and Hayes 1988; Seeman et al. 2003a,b). Accordingly, long bone fragility increases more in women than in men. Furthermore, less age-related periosteal than endocortical widening produced cortical thinning, increasing the risk for structural failure by local buckling in both sexes (Duan et al. 2003). Based on the implied envelope-dependent pathogenesis, a mechanically proposed intervention stratagem for osteopenic hip in women should not only inhibit endocortical resorption but also promote periosteal apposition, which is aimed at improving mechanically structural geometry (see Fig. 1).

For postmenopausal women, there are two kinds of commercially available therapeutics relevant to estrogen, i.e., hormone replacement therapy (HRT) and selective estrogen receptor modulator (SERM). As to HRT, anti-hip-fracture efficacy was documented, whereas increased breast cancer risk was reported (Women's Health Initiative Investigators 2002). As to SERM, reproductive tissue safety was docu-
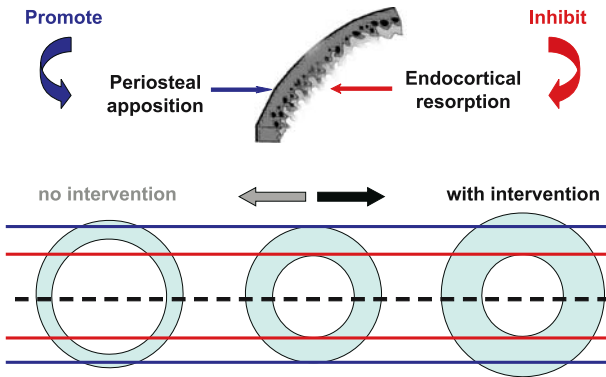
Figure 1. Based on the implied envelope-dependent pathogenesis, a mechanically proposed intervention stratagem for osteopenic hip in women does not only inhibit endocortical resorption but also promotes periosteal apposition. This results finally in an improved mechanical and structural property

mented, whereas anti-hip-fracture efficacy was not reported in (CORE Investigators 2005). In both, inhibiting bone resorption was only involved in their envelop-dependent mechanism (Seeman et al. 2003b; Uusi-Rasi et al. 2006). There is a need, therefore, to explore therapeutic agents, which may not only inhibit endocortical resorption but also promote periosteal apposition, yet with no stimulating effects to reproductive tissues. This is particularly relevant for treatment of osteopenic hip in postmenopausal women as hip fragility fractures associated with postmenopausal osteoporosis have been a global health problem with significant health and socioeconomic burdens, not only to our patients but also to governments and family members (Lau et al. 2001; Keen 2003; Lippuner et al. 2005).

The present chapter contains data from a preclinical study and clinical trial, which investigated the therapeutic efficacy and action mechanism of EPF in postmenopausal osteoporosis.

Preclinical Study

Study Objectives

This part of work was designed to examine the effect of separate or combined therapy of EPF and CS for investigating therapeutic efficacy and action mechanism, by evaluating end-point indices of bone using ovariectomized (OVX) rat model, which included mechanical property, bone mineral density, bone geometry, and bone microarchitecture.

Materials and Methods

Animals, Groups, Treatment, and Sampling

Forty-five 12-month-old female Wistar rats (body weight 440.1 ± 6.0g) were used. During the experimental period, all the rats were fed with standard rat chow that

contained 0.7% phosphorus, 0.9% calcium, and water ad libitum. Animals were randomly assigned into the following five groups: (a) SHAM-operated rats with vehicle (SHAM group); (b) OVX rats with vehicle (OVX group); (c) OVX rats with EPF (EPF group, 10 mg EPF/kg bw day^{-1}; EPF contained 10 mg flavonoids preparation, including 5000 μg Icariin, 250 μg Genistein, 1250 μg Daidzein, and 3500 μg vehicle, which was prepared by Tong Ji Tang Pharmacal Company (Gui Zhou, China; Qin 2005a,b). The supplemental calcium in form of citrate was from Mission Pharmacal Company, Texas.); (d) OVX rats with both CS* and vehicle (CS group, 56 mg calcium/kg bw day^{-1}); and (e) OVX rats with a combination of EPF and CS (EPF+CS group, 10 mg EPF/kg bw day^{-1}, and 56 mg calcium/kg bw day^{-1}). According to the Human-Rat Equivalent Dose Conversion Principle (FDA Guidance for Industry and Reviews 2002; Huang et al. 2004), the experimental dose for EPF and CS in the present study was equivalent to the corresponding clinical prescription dose daily in a 60-kg human. Vehicle, EPF, and CS were all administered orally on day 4 after OVX for 12 weeks. Animals were killed by overdose of Ketamine at the end of 12-week treatment. The uterine was weighed. The left proximal femur was dissected for densitometry, geometry, and envelope by pQCT, 3D trabecula microarchitecture by micro-CT, and failure force by mechanical testing.

Evaluation for End-Point Indices

Mechanical Testing   The left femur was tested in a loading configuration designed to simulate a fall on the greater trochanter (Jamsa et al. 1998; Zhang et al. 2005). Briefly, the distal end of the femur was clamped ante- or retroversion, into an attachment system. The femur was fixed against rotation around the diaphysis axis. Compression test was performed with a 2.5-KN load cell at a speed of 2 mm/min using a material test machine (H25KS Hounsfield Test Equipment, UK). Failure force was used for statistical analysis.

Peripheral Quantitative Computed Tomography   The left proximal femur was fixed with a custom-made plastic rat femur holder for peripheral quantitative computed tomography (pQCT) scanning at the base of femoral neck perpendicularly to the axis of the femoral neck with a multilayer pQCT (Densiscan 2000, Scanco Medical, Bassersdorf, Switzerland). The thickness of each layer was 1 mm and resolution was 220 μm (pixel size). This region was used for designed where the fractures were expected to occur during mechanical test in a fall configuration as reported in our recent study (Qin et al. 2005a,b; Zhang et al. 2005). The contour of the periosteum and endosteum were both defined using the built-in software program for measuring densitometry parameters, including volumetric BMD of integral region inside periosteum (iBMD, g/cm^3) and trabecular region inside the endosteum (tBMD, g/cm^3). The precision error in terms of coefficient variation (CV) was 1.96% for iBMD and 2.25% for tBMD, respectively (Zhang et al. 2002). Cross-sectional moment of inertia (CSMI, mm^4) was used for defining geometrical distribution of cortical bone circumfused by both periosteum and endosteum, Cross-sectional area circumfused with periosteum (CSPA, mm^2) and cross-sectional area circumfused with endosteum (CSEA, mm^2) were measured as bone envelope for quantitative comparisons (Figs. 2, 3).
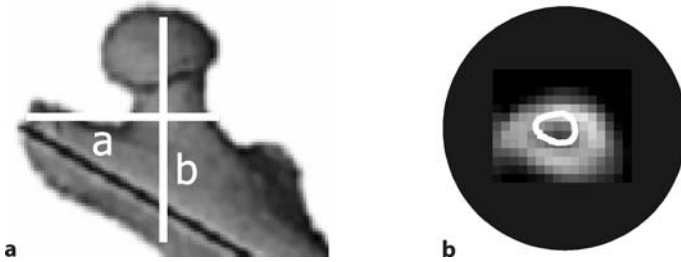
Figure 2. a pQCT scanning at the base of femoral neck in rat. *Line a*: the region at the base of the femoral neck. *Line b*: the axis of the femoral neck. **b** Representative cross-sectional image
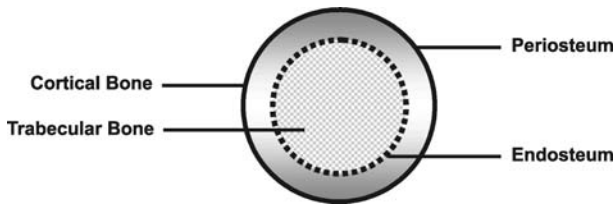
Figure 3. Representative cross-sectional image analyzed by pQCT. The contour of the periosteum and endosteum are both defined automatically using the built-in software program Probability Arithmetic around hand-drawn contour. Then, cortical bone (circumfused by outer periosteum and inner endosteum) is separated from trabecula bone (circumfused by outer endosteum). Cross-sectional moment of inertia (CSMI, mm^4) of cortical bone is calculated to quantify bone geometry. Cross-sectional area (CSA) circumfused with periosteum (CSPA, mm^2) and circumfused with endosteum (CSEA, mm^2) are calculated as bone-envelope parameters

Micro-CT One left femur from each group of animals was scanned with micro-CT (μCT40, Scanco Medical, Bassersdorf, Switzerland). The femoral neck was aligned perpendicular to scanning axis and the total scanning length of 7.9 mm at a resolution of 12 mm per voxel. The selection of representative samples was based on the median value of tBMD from respective groups (Qin et al. 2005a,b). Segmentation parameters for bone from background were fixed (Sigma = 1.2, Support = 2, and Threshold = 214). The trabecular bone within the greater trochanter was extracted with semi-automatically drawn contour at each 2D layer. The volume of interest inside the greater trochanter region was located where femoral neck just met greater trochanter and the 80 continuous CT layers above were chosen for data acquisition. The 3D reconstructed images were used directly to evaluate the microarchitecture parameters (Fig. 4; Qin et al. 2005b; Siu et al. 2004).

Statistical Analysis

Statistical comparisons between vehicle-treated SHAM group and vehicle-treated OVX group were made with a two-tailed *t*-test. The data for all four OVX subgroups was analyzed using a two-factorial ANOVA with body weight as a covariant variable for eliminating its influence on the measurement results, where the two treat-
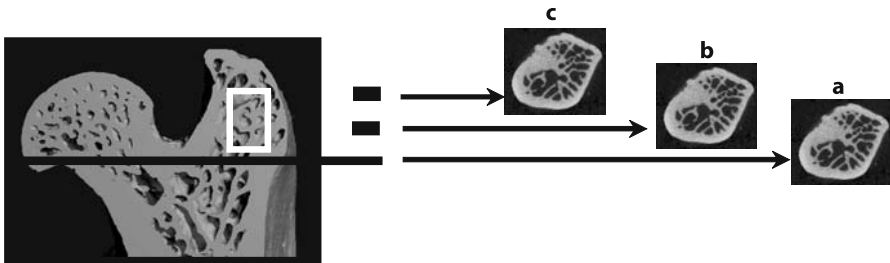
Figure 4. Three-dimensional reconstruction of proximal-rate femur by micro-CT. Reference *layer A* was located where femoral neck just meets the greater trochanter and the 80 continuous layers above. The region between *layer A* and *layer C* is chosen for data acquisition

ment factors were EPF (presence or absence) and CS (presence or absence). In this way, it was determined whether the two different treatments mutually influence each other in a synergetic interactive way (i.e., not a simply additive way). Furthermore, a stepwise multiple regression analysis was used to assess the suitability of both the densitometry parameters (iBMD and tBMD) and geometric parameter (CSMI) for the prediction of the bone strength at structural level (failure force). Statistical significance was set at $p < 0.05$. The results were presented as mean ± SD and all statistical analyses were performed using SPSS 10.0 (Chicago, Ill.).

Results

Body Weight and Uterine Weight
The OVX group showed significantly 15% higher body weight but 80% lower uterine weight than the SHAM group (body weight: 497 ± 19.53 vs 572 ± 22.49 g; uterine weight: 1100 ± 43.20 vs 220 ± 8.65 mg; $p < 0.05$ for both). Body weight and uterine weight were influenced by neither EPF (564 ± 20.34 g for body weight and 222 ± 8.12 mg for uterine weight) nor CS (573 ± 22.04 g for body weight and 226 ± 8.70 mg for uterine weight), when compared with the OVX group ($p > 0.05$ for both). No interaction effect was found between EPF and CS on either body weight (560 ± 22.46 g for EPF+CS group) or uterine weight (228 ± 9.16 mg for EPF+CS group; $p > 0.05$ for both).

Mechanical Testing
The OVX group had 17% lower failure force than the SHAM group (83.57 ± 11.26 N vs 69.56 ± 10.74 N; $p < 0.05$). Compared with the OVX group, failure force was increased 22% by EPF treatment (84.89 ± 8.04 N) and 12% by CS treatment (78.00 ± 15.54 N; $p < 0.05$ for EPF and $p > 0.05$ for CS). The EPF+CS group produced an increase in failure force of only 24% (86.16 ± 20.27 N), which did not show interaction between EPF and CS ($p > 0.05$).

pQCT Evaluation
vBMD and Geometry The OVX group showed 24, 25, and 33% significantly lower iBMD, tBMD, and CSMI, respectively, than that of the SHAM group (iBMD: 1.21 ± 0.07 vs
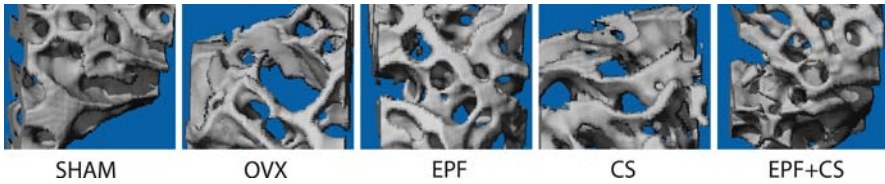
Figure 5 a–e. Representative sample from each group: 3D architecture of trabecula bone within greater trochanter region. **a** Calcium supplement (CS). **b** Epimedium-derived phytoestrogenic fraction (EPF). **c** EPF+CS. **d** Ovariectomized group. **e** SHAM group

$0.91 \pm 0.08 \, \mathrm{g/cm^3}$; tBMD: 1.20 ± 0.07 vs $0.89 \pm 0.07 \, \mathrm{g/cm^3}$; CSMI: 21.54 ± 2.38 vs $14.43 \pm 3.97 \, \mathrm{mm^4}$; $p < 0.05$ for all). All three parameters were significantly higher in the EPF group ($1.20 \pm 0.04 \, \mathrm{g/cm^3}$ for iBMD, $1.19 \pm 0.12 \, \mathrm{g/cm^3}$ for tBMD, and $19.29 \pm 1.50 \, \mathrm{mm^4}$ for CSMI) and CS group ($1.10 \pm 0.08 \, \mathrm{g/cm^3}$ for iBMD, $1.09 \pm 0.09 \, \mathrm{g/cm^3}$ for tBMD, and $18.57 \pm 1.21 \, \mathrm{mm^4}$ for CSMI) than those in the OVX group ($p < 0.05$ for all); however, no interaction was observed between EPF and CS ($p > 0.05$) ($1.21 \pm 0.08 \, \mathrm{g/cm^3}$ for iBMD, $1.20 \pm 0.07 \, \mathrm{g/cm^3}$ for tBMD, and $20.71 \pm 2.12 \, \mathrm{mm^4}$ for CSMI in the EPF+CS group; Fig. 5).

Femoral Neck Envelope The OVX group showed 101% higher CSEA than that of the SHAM group (2.43 ± 2.38 vs $4.90 \pm 0.10 \, \mathrm{mm^2}$; $p < 0.05$). The CSPA was slightly higher in the OVX group than that in the SHAM group (15.90 ± 1.30 vs $16.05 \pm 1.19 \, \mathrm{mm^2}$; $p > 0.05$). Compared with the OVX group, the EPF group showed significantly higher CSPA ($17.33 \pm 0.88 \, \mathrm{mm^2}$; $p < 0.05$), whereas the CS group showed no change in CSPA ($15.89 \pm 1.17 \, \mathrm{mm^2}$; $p > 0.05$). There was no interaction effect on CSPA between PF and CS ($p > 0.05$; $17.16 \pm 0.87 \, \mathrm{mm^2}$ for the EPF+CS group). For CSEA, the EPF treatment ($4.15 \pm 0.69 \, \mathrm{mm^2}$) showed a decrease of 15% and the CS treatment ($4.44 \pm 0.10 \, \mathrm{mm^2}$) showed a decrease of 9% ($p < 0.05$ for both). The EPF+CS group ($2.92 \pm 0.54 \, \mathrm{mm^2}$) produced a further decrease of 40%, which was found to be a synergetic interaction effect on CSEA between EPF and CS ($p < 0.05$; Fig. 5D,E).

Micro-CT Evaluation

The representative samples showed that the vehicle-treated OVX rat had lower value in bone volume / tissue volume(BV/TV), connect density (Conn.D), trabecula number (Tb.N), and trabecula thickness (Tb.Th), and higher value in structure model index (SMI) and trabecula space (Tb.Sp), when compared with the vehicle-treated SHAM rat. Compared with the vehicle-treated OVX rat, the EPF treatment and EPF+CS treatment reversed the above-mentioned findings to the same degree. Interestingly, Tb.Th in the FE rat was highest among all the representative samples, which also exceeded that in the SHAM rat (Fig. 6).
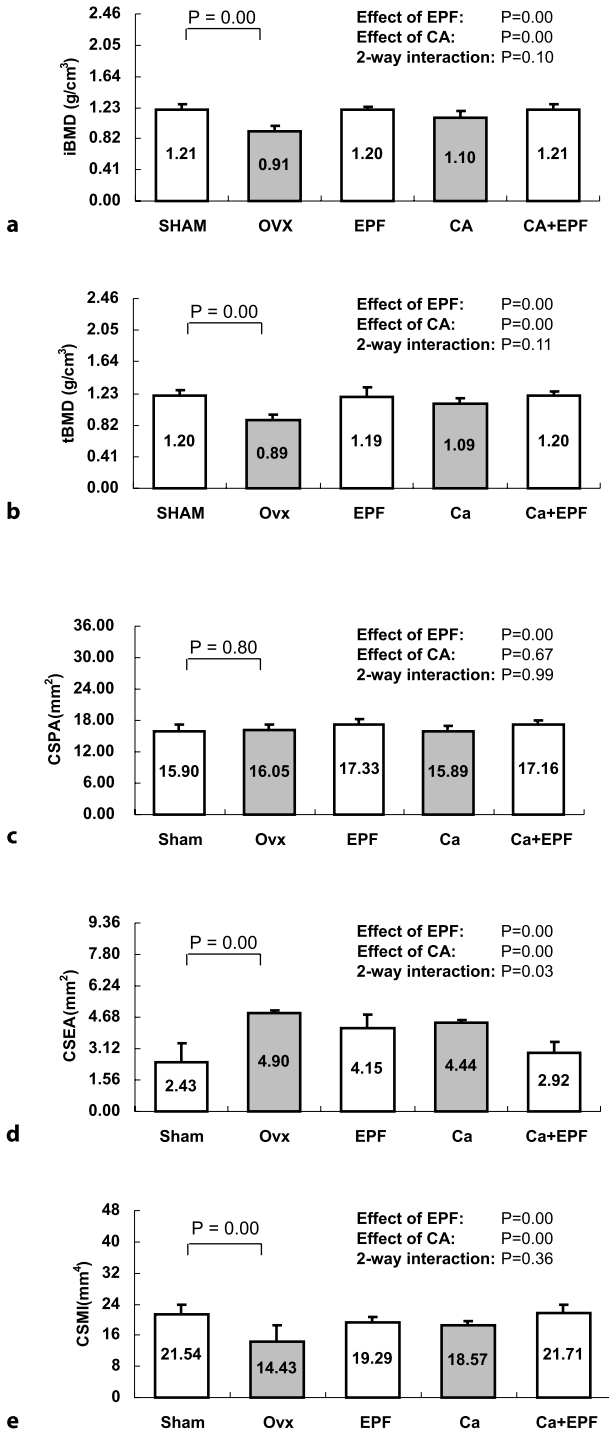
Figure 6a–e. iBMD (**a**), tBMD (**b**), CSPA (**c**), CSEA (**d**), and CSMI (**e**) in respective group. Ovariectomized rats orally received vehicle (*OVX*), epimedium-derived phytoestrogenic fraction (*EPF*), element calcium from calcium citrate (*Ca*) and combination of the EPF and CA. Statistical comparisons between the vehicle-treated SHAM and OVX groups were made with a two-sided *t*-test. The prevention effect of EPF and CA as well as their interaction in ovariectomized rats were analyzed by two-way factorial ANOVA. Each *bar* represents the mean ± SD of nine rats

Regression Analysis

Failure force was best predicted by a stepwise regression model including a combination of tBMD and CSMI (adjusted R^2 = 0.56, $p < 0.05$, standardized coefficient for tBMD = 0.58, $p < 0.05$, standardized coefficient for CSMI = 0.51; $p < 0.05$).

Discussion

This preclinical study used both conventional destructive and advanced non-destructive techniques for evaluation of potential beneficial effects of EPF from herbal Epimedium in prevention of OVX-induced osteoporosis. Factorial design was used for analyzing potential synergetic interaction between EPF and CS.

In the present study, pQCT was used to measure femoral neck vBMD, geometric distribution, and bone envelope. A lower value in iBMD, tBMD, and CSMI was found in the OVX group when compared with the SHAM group, suggesting that reduced bone mass and deteriorated geometry were determinant factors of bone strength in the osteoporotic model, whereas EPF showed its prevention efficacy, which was evidenced by higher value in iBMD, tBMD, and CSMI in the EPF group compared with the OVX group.

A slightly higher value in CSTA was found in the OVX group when compared with the SHAM group, suggesting OVX-induced moderate modeling-dependent bone formation at periosteum aimed at maintaining bone strength for compensation of bone loss (Akhter et al. 2000; Bagi et al. 1993; Erben et al. 1996). Furthermore, EPF showed its anabolic effect on periosteum during estrogen deficiency, as evidenced by a larger CSPA when compared with the OVX group. For CSEA, a larger value was shown in the OVX group when compared with the SHAM group, suggesting OVX-induced endosteum bone resorption (Erben et al. 1996). In contrast, EPF demonstrated its inhibition effect on endosteum bone resorption, as evidenced by a smaller CSEA when compared with the OVX group; however, the limitation of this study was a cross-sectional one, and in vivo monitoring design would be more appreciated for future studies if the potential technical difficulty in repositioning consistency could be achieved with good repeatability. The current in vivo longitudinal studies, either using pQCT or micro-CT, was aimed mainly at anatomically easily assessable proximal tibia (David et al. 2003).

Micro-CT evaluation suggested that 3D architecture of trabecular bone was maintained in the EPF sample compared with the vehicle-treated OVX sample. The Tb.Th in the PF rat was even 22% higher than that in the SHAM rat, which was consistent with our previous study (Qin et al. 2005a). As 15-month-old female Wistar rats already reached mature statues (Alekel et al. 2000; Qin et al. 2005a), the increase in the Tb.Th in response to EPF observed in the present study could not be explained by its anti-resorptive activity through filling remodeling space (Weinhold et al. 1994). Instead, this effect may be only viewed as bone resorption exceeded by bone formation, i.e., the anabolic effect of EPF on trabecular bone. Further systemic histomorphometric evaluations are needed to substantiate this potential underlying mechanism.

In the present study, EPF treatment, but not CS alone, was able to prevent the deterioration of bone mechanical property as evaluated by compression test. No interaction was found between EPF and CS, i.e., supplemental calcium did not further enhance the prevention effect of EPF on OVX-induced reduction in hip failure force. This was also consistent with findings of above non-destructive pQCT indices, suggesting that EPF administration exerted its prevention effect on OVX-induced osteoporosis and was independent of an enhancement in intestinal calcium absorption. In fact, our recent evaluations on bone turnover and calcium metabolism markers also suggested that the preventive effects of EPF were not associated with the enhanced intestinal calcium absorption (Zhang et al. 2006).

In vitro studies substantiated our in vivo findings which showed phytoestrogenic Icariin, Genistein, and Daidzein were able to stimulate osteogenesis in osteoblast and/or osteoprogenitor cells, and to inhibit bone resorption via direct targeting of osteoclast progenitors through estrogen receptor pathways (Meng et al. 2005; Rickard et al. 2003; Setchell et al. 2003). On the other hand, it has also been reported that estrogen receptor-beta pathway was linked to endosteal resorption and periosteal apposition of new bone, whereas estrogen receptor alfa pathway could be linked to the preservative effects on trabecular surfaces (Ke et al. 2002; McCauley et al. 2003; Sims et al. 2002; Windahl et al. 2002). Furthermore, estrogen receptor beta (ERβ) signaling pathway has just been linked to prevention of breast cancer development (Park et al. 2006). Due to diversities of EPF compounds (Icariin, Genistein, and Daidzein) in chemical structure, metabolism and affinity for estrogen receptor (Setchell 1998; Ye et al. 2005), EPF might be involved in a direct action on bone cells through multiple estrogen receptor subtype pathways, and even exert its envelope-specific structural modification with reproductive tissue safety via a novel mechanism involved in selective ER-subtype signaling pathway.

In addition, the present study of regression analysis revealed a combined contribution of non-destructive indices measured by pQCT to destructive failure force, suggesting the predictive power of the non-destructive indices for the destructive end-point in vivo monitoring in future studies.

Conclusion

Calcium supplementation combined with EPF acts not in a synergistic way, but an additive way. The present preclinical study showed that EPF, via an implied direct action on bone cells, was able to inhibit bone resorption at endosteum/trabecula, stimulated bone formation at periosteum/trabeculae, and accordingly prevented osteoporosis without hyperplastic effect on uterus in the OVX rat model.

Clinical Trials

Study Objectives

The present study showed that EPF was able to prevent OVX-induced osteoporosis in rat femoral neck through a unique mechanism associated with both promotion of

periosteal apposition and inhibition of endocortical resorption, which was without hyperplastic effect on reproductive tissues; thus, this small clinical trial, i.e., a single-center, randomized, double-blind, placebo-controlled clinical trial, aimed to confirm above effects and associated underlying mechanism of EPF on both promotion of periosteal apposition and inhibition of endocortical resorption for improving mechanically structural geometry in postmenopausal women with osteopenic femoral neck using a dual-energy X-ray absorptiometry (DXA)-derived hip structure analysis. The safety issue of EPF administration was also documented for reproductive tissue.

Patients and Methods

Subjects
Two-hundred twelve postmenopausal Chinese women from "Women Healthcare Education Club of Bone and Joint" in Shanghai were screened for eligibility. Subjects were included for this study if they were postmenopausal for 8 ~ 12 years with osteopenic femoral neck, i.e., with a T-score of areal BMD (aBMD) between −1SD and −2SD (aBMD between $0.7732 \sim 0.8762 \, \text{g/cm}^2$) measured using DXA (DPX-L, Lunar Corp, Madison, Wis.; Wang 2001). Subjects were excluded if they had bone and related metabolic diseases, drug treatment known to affect bone metabolism in the past 12 months, and fracture history.

Treatment
Finally, 85 subjects were eligible and randomized into EPF group (4 EPF capsules daily; $n = 43$) and Placebo group (matching placebo capsules daily; $n = 42$). All of them received 300 mg element calcium daily. The investigation was double-blind. The EPF capsule (30 mg flavonoids preparation containing 15,000 μg Icariin, 750 μg Genistein, 3750 μg Daidzein, and 10,500 μg vehicle) and placebo capsule were both prepared by Tong Ji Tang Pharmaceutical Co. (Gui Zhou, China). The supplemental element calcium in form of citrate was from Mission Pharmacal Company (Texas). Body weight of each subject was recorded at baseline for covariant analysis (Bingham 2001). The intervention lasted 24 months.

Hip Structure Analysis
Structural properties of the right femoral neck were measured by Lunar DXA based on established "Hip Structure Analysis" (HSA) at baseline, 12, and 24 months (Fig. 7). Periosteal diameter of femoral neck (W, an envelope measure of periosteum) was obtained by dividing femoral neck projection area by the constant height of the scanned region ($K = 1.5 \, \text{cm}$) (Filardi et al. 2004). Cross-sectional area (CSA) of femoral neck (a measure of axial compression strength) was computed as:

$$CSA = \frac{BMD \cdot W}{\rho_m}$$

where P_m is the density of bone mineral in fully mineralized bone tissue ($1.05 \, \text{g/cm}^3$), BMD is aBMD, and W is the periosteum diameter. The assumption that a fully mineralized bone tissue has a mineral density of $1.05 \, \text{g/cm}^3$ (Martin et al. 1984). Estimated
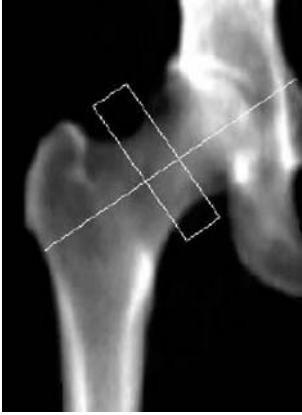
Figure 7. Dual X-ray absorptiometry hip image used for hip structure analysis

endosteum diameter of femoral neck (*ED*, an envelope measure of endosteum) was computed as:

$$ED = 2\sqrt{\left(\frac{W}{2}\right)^2 - f_c \frac{CSA}{\pi}}$$

where $f_c = 0.6$ is the assumed proportion of cortical mass in the femoral neck (Bohr and Schaadt 1985; Kuiper et al. 1997; Bell et al. 1999). Cortical thickness (*CT*) and Buckling ratio of femoral neck (*BR*, a measure of stability for tubular cortices structure) was computed as (Duan et al. 2004; Filardi et al. 2004):

$$CT = \frac{W - ED}{2} \quad BR = \frac{W/2}{CT}$$

Section modulus of cortical bone of femoral neck (*Z*, a measure of bending strength) was computed as (Duan et al. 2004; Filardi et al. 2004):

$$p = 1 - \left[\frac{(1 - f_c)\,CSA}{\pi\left(\frac{ED}{2}\right)^2}\right] \quad CSMI = \frac{\pi}{4}\left(\left(\frac{W}{2}\right)^4 - p\left(\frac{ED}{2}\right)^4\right) \quad Z = \frac{CSMI}{W/2}$$

where *p* is the trabecular porosity.

Converted Calculation of Hip Volumetric BMD

Periosteal diameter of femoral neck (*W*, an envelope measure of periosteum) and the constant height of the scanned region (*K* = 1.5 cm) was used to estimate volume of femoral neck. Bone mineral content (*BMC*) is a direct measure from DXA, and volumetric BMD (vBMD) was then converted according to Center's formula (Center et al. 2004) as:

$$vBMD = BMC/(\pi(W/2)^2\,k)$$

Physical Examination for Reproductive Tissue Safety

At baseline and end point, endometrial thickness of each subject was measured by a same specialist using transvaginal ultrasound (Aloka Echo Camera, model SSD-500; Aloka Co., Tokyo, Japan). Abnormal uterine case was defined as subject with uterine endometrial thickness > 5 mm. At baseline and end point, breast palpating lump was performed by a same specialist. Abnormal breast case was defined as subject with either new lump or advanced lump.

Sample Size

Sample size (n) in each group was computed as (Qin et al. 2005b):

1. $n = 2[(u(+u())s/\delta]2$
2. $S = CV(\%) \times baseline$
3. $\delta = Difference(\%) \times baseline$

Accordingly, a sample of $n = 41$ in each group gave $1 - \beta = 80\%$ power ($\beta = 20\%$, $u_\beta = 0.84$) to detect a 1.8% difference from baseline with respect to the change in DXA-derived periosteal envelope W over 24 months, assuming a CV of 3.3% for W (Khoo et al. 2005) and setting α at 0.1 ($u_\alpha = 1.64$).

Statistics

The DXA-derived data were expressed as mean ± SD, and then percentage changes were calculated as 12-month data or 24-month data minus baseline data. A repeated-measures analysis of variance was used to discern changes between groups at follow-up using both baseline DXA measurements and baseline body weight as covariate (Vickers et al. 2001; Nissen et al. 2005). Abnormal incidence (reproductive tissue safety data) in each group for either breast or uterine was documented. Fisher's exact probability test was performed on abnormal incidence for comparing between-group difference. All tests for significance were two-sided and $p < 0.01$ for DXA-derived data and $p < 0.05$ for safety data was considered statistically significant, respectively. All statistical analysis was conducted with software package SPSS 10.0 for Windows (SPSS Inc., Chicago, Ill.).

Results

Baseline Characteristics and Compliance No anthropometrical and nutritional variations were found between EPF group and Placebo group ($p > 0.1$). Three women dropped out in both groups due to reasons other than treatment.

Hip Structural Analysis The changes from baseline are shown in Fig. 8. For bone envelope parameters, a significant increase from baseline in W was found in EPF group (1.11%, vs baseline, $p < 0.1$), whereas a moderate increase from baseline was found in placebo group (0.85%, vs baseline; $p > 0.1$). The ED increased significantly from baseline in placebo group (1.3%, vs baseline; $p < 0.1$), whereas that changed non-significantly from baseline in EPF group (0.3%, vs baseline; $p > 0.1$). No significant difference was found in all bone envelope parameters at end point of 24 months

(0.6% difference for *W* and −0.6% for *ED*, *PF* vs Placebo, *p* > 0.1, respectively), and repeated-measures analysis demonstrated that a significant interaction between "Time" and "Group" was not for *W* (*p* > 0.1) but for *ED* (*p* < 0.1).

For bone geometry, a significant increase from baseline in *CSA*, *Z*, and *CT* was found in EPF group (2.4% for *CSA*, 7.2% for *Z*, and 7.74% for *CT*, vs baseline, *p* < 0.1, respectively), whereas no significant change from baseline in them was found in Placebo group (−1.2% for *CSA*, −1.4% for *Z*, and −5.2% for *CT*, vs baseline, *p* > 0.1, respectively). The *BR* decreased significantly from baseline in EPF group (−6.14%, vs baseline, *p* < 0.1), whereas that increased significantly from baseline in Placebo group (6.4%, vs baseline, *p* < 0.1). At end point of 24 months, a significant difference in all geometric parameters was shown between EPF group and Placebo group (4.1% difference for *CSA*, 9.7% difference for *Z*, −12.1% difference for *BR*, and 14.3% difference for CT, PF vs Placebo, *p* < 0.1, respectively), and repeated-measures analysis demonstrated that a significant interaction between "Time" and "Group" was found for all geometric parameters (*p* < 0.1; Fig. 8).

BMD Analysis Repeated-measures statistical model showed that there was a significant difference in BMD changes between two groups over time (*p* < 0.1). Slightly increased aBMD or converted vBMD was found in EPF group as compared with their baseline (1.6% for aBMD and 0.3% for vBMD, *p* > 0.1 for both), whereas a significant decrease in either aBMD or vBMD was found in Placebo group (−1.9% for aBMD and −2.6% for vBMD, vs baseline, *p* < 0.1, respectively). As comparison was made for the BMD at the end of the study (24 months), EPF group showed 3.5% higher aBMD and 2.6% higher vBMD than that Placebo group (*p* < 0.1, respectively; Fig. 8).

Reproductive Tissue Safety At the end point of 24 months, two abnormal breast cases were found in EPF group, and four were found in Placebo group. For uterine, three abnormal cases were found in EPF Group, and two were found in Placebo group. There were, however, no significant differences between the two groups (*p* > 0.05 for both).

Discussion

The present clinical trial confirmed the findings obtained from experimental study that a 24-month intervention of EPF, a herb Epimedium-derived phytoestrogenic

---

Figure 8. Changes from baseline up to 24 months after treatment. Parameters are compared between epimedium-derived phytoestrogenic fraction group and placebo group, which are derived from bone densitometry analysis and hip-structure analysis. Repeated-measures analysis of variance showed significant interaction (*p* < 0.1) between time and group (different pattern of effects over time between two groups) for aBMD, vBMD, estimated endosteum diameter (*ED*), cross-sectional area (*CSA*), section modulus (*Z*), buckling ratio (BR), and cortical thickness (CT), except for periosteal diameter of femoral neck (*W*)
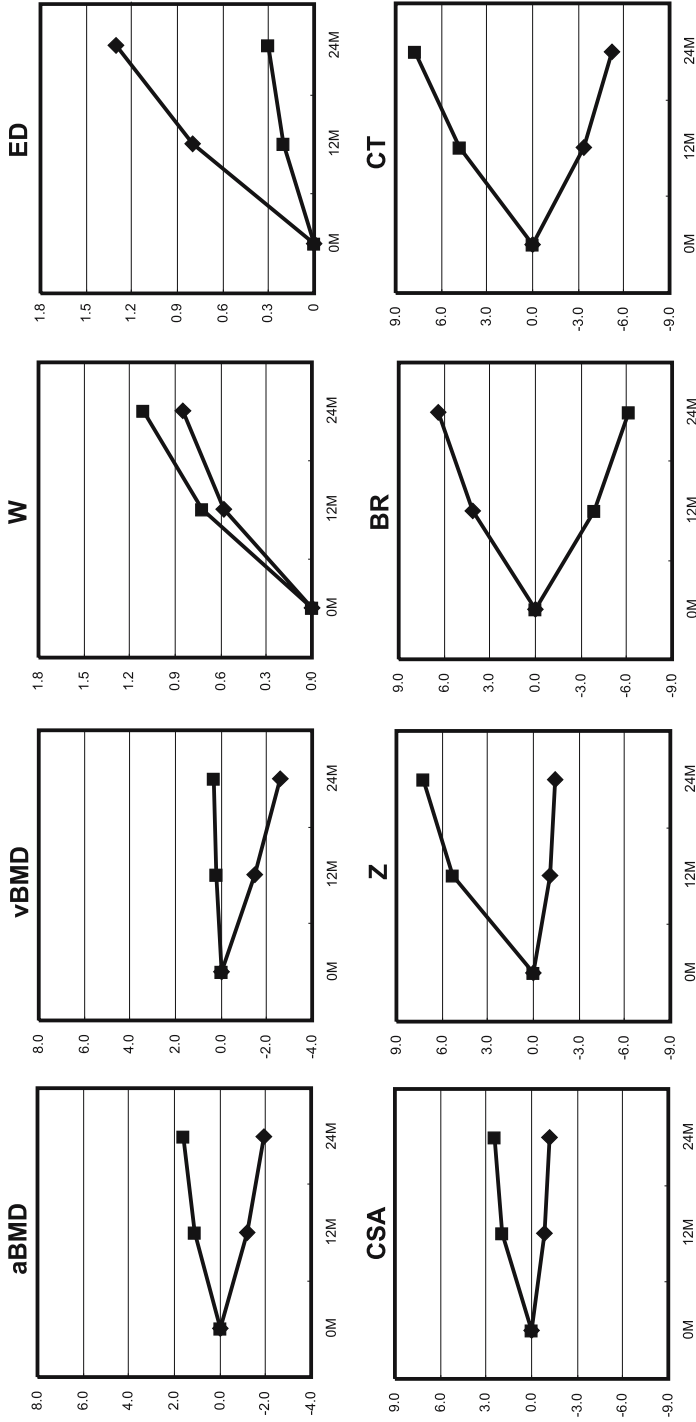
fraction, was able to prevent postmenopausal bone loss at osteopenic femoral neck, without resulting in side effects in reproductive tissues or organs. The findings in this controlled clinical trial supported our hypothesis that EPF was able to exert beneficial effects on both promotion of periosteal apposition and inhibition of endocortical resorption, which implied potentially improved mechanical and structural properties.

Hip Structure Analysis-Based Method

This clinical trial adopted hip structure analysis (HAS)-based method for evaluation of DXA measurement results. The approach provided a more insight into pharmacological treatment efficacy, i.e., information on hip envelope/geometry/densitometry could be obtained when the same data are expressed as aBMD.

Envelope analysis showed that EPF could promote periosteal apposition, which was evidenced by a significantly increased W from baseline in EPF group. On the other hand, EPF was also able to attenuate endocortical bone resorption, which was evidenced by a significantly increased ED found in Placebo group but not in EPF group, suggesting that EPF could exert dual envelop-specific effect, i.e., beneficial effect on both promotion of periosteal apposition and inhibition of endocortical resorption. This was similar to what we found in the above-mentioned animal study.

It is known that structural geometry, which is modified by the above-mentioned envelope-specific biological process, plays an important role in determining mechanical strength. For osteopenic femoral neck, CSA, Z, and BR are the three commonly used HSA-derived geometric parameters involved in biomechanical properties. Those three parameters have been reported to be able to reflect resistance to axial compressive for CSA, bending loads for Z, and susceptibility due to local buckling by increased ratio of W to CT for BR (Uusi-Rasi et al. 2006; Young et al. 1989), respectively.

For geometry analysis, EPF administration could increase both CSA and Z, suggesting improved resistance to both axial compressive and bending load associated with fall configuration. This was also supported by the regression analysis mentioned in our above-mentioned animal experiment. Our above finding was also supported by a recent large population clinical investigation in both sexes, which showed that less age-related periosteal than endocortical widening produced cortical thinning, increasing the risk for structural failure by local buckling of the enlarged thin-walled femoral neck (Duan et al. 2005). In our clinical trial, significantly increased BR from baseline was found in Placebo group, which could be explained by prominent endocortical resorption and moderate periosteal apposition, i.e., thinning cortices (from 0.154 to 0.146 cm) and inadequate periosteal expansion (from 2.941 to 2.966 cm). On the contrary, EPF was able to maintain and even improve structural stability, which was evidenced by significantly reduced BR as well as significantly increased cortical thickness from baseline. These findings indicated the potential role of EPF in promotion of periosteal apposition and inhibition of bone resorption.

Limitations of the Efficacy Study

As compared with animal experimental study shown above, our clinical trial may have a few limitations. Firstly, instead of a true 3D bone measurement, e.g., pQCT

used for above-mentioned animal study, 2D DXA was used clinically for evaluation of both BMD and bone structural variables. The projection-area-based HSA method was involved in crude estimation using linear assumption in image plane. For HSA-derived Z (section modulus), it only evaluates bending in one direction, and no one can determine whether EPF would enhance bending stiffness in the other direction (Beck et al. 2000). For HSA-derived BR, linear assumptions of both cross-sectional shape and the relative fraction of the bone mass in the cortex were used for predi-gestion of non-linear buckling; thus, EPF effects that might disproportionately influ-ence cortical or trabecular bone would not be generally evaluated by this estimation method, and detailed engineering analysis would require more information about the cross section than can be extracted from a single-projection DXA scan (Schafer et al. 2002).

Secondly, the sample size was small, although acceptable. The statistical signif-icance level was just marginally significant in few cases ($p < 0.05$), but was more significant in most cases (p between 0.05 and 0.1). The precision error of measure-ment methodology is one of the major issues which is directly associated with the sample size required. The precision error of DXA was between 1 and 2% for BMD measurement, whereas it was approximately 3.3% for geometrical evaluations (Goh et al. 1995; Khoo et al. 2005). In our clinical trial, a significant 1.1% increase in W (P = 0.098) was found in EPF group ($n = 40$) as compared with its baseline. In order to achieve statistical significance level at $p < 0.05$, a sample size of at least $n = 140$ would be required ($u_{0.05} = 1.96$, $u_{0.8} = 0.84$, CV = 3.3%).

Long-Term Safety

In our 24-month clinical trial, as compared with placebo controls, EPF treatment was not found to be associated with any notable and detectable adverse effects on repro-ductive tissues or organs, including both breast and uterus. This was also supported by our above-mentioned animal study and previous small-scale clinical trial (Qin et al. 2005a). Both preclinical and clinical findings suggested a long-term compliance with EPF administration in postmenopausal women.

Conclusion

The data obtained in our clinical trial support our hypothesis that EPF was able to exert beneficial effects on promotion of periosteal apposition and inhibition of endocortical resorption, which suggested pharmaceutical effects of EPF on anti-postmenopausal osteoporosis and maintenance of hip BMD and geometry. The preser-vation of bone quality under EPF implies mechanical integrity of the hip in post-menopausal women with osteopenic femoral neck. In addition, similar to the animal study described previously, the 24-month administration of EPF was safe for the re-productive tissues or organs. In the future, dose-dependent clinical design should also be performed for confirmation of its efficacy and safety.

References

Arjmandi BH, Salih MA, Herbert DC (1993) Evidence for estrogen receptor-linked calcium transport in the intestine. Bone Miner 21:63–74

Arjmandi BH, Khalil DA, Hollis BW (2002) Soy protein: its effects on intestinal calcium transport, serum vitamin D, and insulin-like growth factor-I in ovariectomized rats. Calcif Tissue Int 70:483–487

Akhter MP, Iwaniec UT, Covey MA (2000) Genetic variations in bone density, histomorphometry, and strength in mice. Calcif Tissue Int 67:337–344

Alekel DL, Germain AS, Peterson CT, Hanson KB, Stewart JW, Toda T (2000) Isoflavone-rich soy protein isolate attenuates bone loss in the lumbar spine of perimenopausal women. Am J Clin Nutr 72:844–852

Bagi CM, Mecham M, Weiss J (1993) Comparative morphometric changes in rat cortical bone following ovariectomy and/or immobilization. Bone 14:877–883

Beck TJ, Looker AC, Ruff CB, Sievanen H, Wahner HW (2000) Structural trends in the aging femoral neck and proximal shaft: analysis of the Third National Health and Nutrition Examination Survey dual-energy X-ray absorptiometry data. J Bone Miner Res 15:2297–2304

Bell KL, Loveridge N, Power J, Garrahan N, Stanton M, Lunt M, Meggitt BF, Reeve J (1999) Structure of the femoral neck in hip fracture: cortical bone loss in the inferoanterior to superoposterior axis. J Bone Miner Res 14:111–119

Bingham SA, Welch AA, McTaggart A, Mulligan AA, Runswick SA, Luben R, Oakes S, Khaw KT, Wareham N, Day NE (2001) Nutritional methods in the European Prospective Investigation of Cancer in Norfolk. Public Health Nutr 4:847–858

Chen XW, Garner SC, Anderson JJ (2002) Isoflavones regulate interleukin-6 and osteoprotegerin synthesis during osteoblast cell differentiation via an estrogen-receptor-dependent pathway. Biochem Biophys Res Commun 295:417–422

Center JR, Nguyen TV, Pocock NA, Eisman JA (2004) Volumetric bone density at the femoral neck as a common measure of hip fracture risk for men and women. J Clin Endocrinol Metab 89:2776–2782

David V, Laroche N, Boudignon B, Lafage-Proust MH, Alexandre C, Ruegsegger P, Vico L (2003) Noninvasive in vivo monitoring of bone architecture alterations in hindlimb-unloaded female rats using novel three-dimensional microcomputed tomography. J Bone Miner Res 18:1622–1631

Duan Y, Beck TJ, Wang XF, Seeman E (2003) Structural and biomechanical basis of sexual dimorphism in femoral neck fragility has its origins in growth and aging. J Bone Miner Res 18:1766–1774

Eisenberg DM, Davis RB, Ettner SL, Appel S, Wilkey S, Van Rompay M, Kessler RC (1998) Trends in alternative medicine use in the United States, 1990–1997: results of a follow-up national survey. J Am Med Assoc 280:1569–1575

Erben RG (1996) Trabecular and endocortical bone surfaces in the rat: modeling or remodeling? Anat Rec 246:39–46

FDA Guidance for Industry and Reviews (2002) Estimating the safe starting dose in clinical trials for therapeutics in adult healthy volunteers, vol 12

Filardi S, Zebaze RM, Duan Y, Edmonds J, Beck T, Seeman E (2004) Femoral neck fragility in women has its structural and biomechanical basis established by periosteal modeling during growth and endocortical remodeling during aging. Osteoporos Int 15:103–107

Gallagher JC, Riggs BL, DeLuca HF (1980) Effect of estrogen on calcium absorption and serum vitamin D metabolites in postmenopausal osteoporosis. J Clin Endocrinol Metab 51:1359–1364

Goh JC, Low S, Bose K (1995) Effect of femoral rotation on bone mineral density measurements with dual energy X-ray asorptiometry. Calcif Tissue Int 57:340–343

Health Initiative Investigators Writing Group for the Women (2002) Risks and benefits of estrogen plus progestin in healthy postmenopausal women: principal results from the Women's Health Initiative randomized controlled trial. J Am Med Assoc 288:321–333

Heaney RP, Recker RR, Saville PD (1978) Menopausal changes in calcium balance performance. J Lab Clin Med 92:953–963

Huang JH, Huang XH, Chen ZY (2004) Dose conversion among different animals and healthy volunteers in pharmacological study. Chin J Clin Pharmacol Ther 9:1069–1072

Jamsa T, Tuukkanen J, Jalovaara P (1998) Femoral neck strength of mouse in two loading configurations: method evaluation and fracture characteristics. J Biomech 31:723–729

Ke HZ, Brown TA, Qi H (2002) The role of estrogen receptor-beta in the early age-related bone gain and later age-related bone loss in female mice. J Musculoskel Neuron Interact 2:479–488

Keen RW (2003) Burden of osteoporosis and fractures. Curr Osteoporos Rep 1:66–70

Kuiper JW, Van Kuijk C, Grashuis JL (1997) Distribution of trabecular and cortical bone related to geometry: a quantitative computed tomography study of the femoral neck. Invest Radiol 32:83–89

Khoo BC, Beck TJ, Qiao QH, Parakh P, Semanick L, Prince RL, Singer KP, Price RI (2005) In vivo short-term precision of hip structure analysis variables in comparison with bone mineral density using paired dual-energy X-ray absorptiometry scans from multi-center clinical trials. Bone 37:112–121

Lau EM (2001) Epidemiology of osteoporosis. Best Pract Res Clin Rheumatol 15:335

Lee SH, Jung BH, Kim SY, Chung BC (2004) Determination of phytoestrogens in traditional medicinal herbs using gas chromatography: mass spectrometry. J Nutr Biochem 15:452–460

Lippuner K, Golder M, Greiner R (2005) Epidemiology and direct medical costs of osteoporotic fractures in men and women in Switzerland. Osteoporos Int 16 (Suppl 2):S8–S17

McCauley LK, Tozum TF, Kozloff KM (2003) Transgenic models of metabolic bone disease: impact of estrogen receptor deficiency on skeletal metabolism. Connect Tissue Res 44:S250–S263

Meng FH, Li YB, Xiong ZL, Jiang ZM, Li FM (2005) Osteoblastic proliferative activity of Epimedium brevicornum Maxim. Phytomedicine 12:189–193

Nieves JW, Komar L, Cosman F, Lindsay R (1998) Calcium potentiates the effect of estrogen and calcitonin on bone mass: review and analysis. Am J Clin Nutr 67:18–24

Nissen N, Hauge EM, Abrahamsen B, Jensen JE, Mosekilde L, Brixen K (2005) Geometry of the proximal femur in relation to age and sex: a cross-sectional study in healthy adult Danes. Acta Radiol 46:514–518

Qin L, Zhang G, Shi YY, Lee KM, Leung PC (2005a) Prevention and treatment of osteoporosis with traditional herbal medicine. In: Deng HW et al. (eds) Current topics of osteoporosis. World Scientific, UK, pp 513–531

Qin L, Zhang G, Hung WY (2005b) Phytoestrogen-rich herb formula XLGB prevents OVX-induced deterioration of musculoskeletal tissues at the hip in old rats. J Bone Miner Metab 23S:55–61

Park BW, Kim KS, Heo MK, Yang WI, Kim SI, Kim JH, Kim GE, Lee KS (2006) The changes of estrogen receptor-beta variants expression in breast carcinogenesis: decrease of estrogen receptor-beta2 expression is the key event in breast cancer development. J Surg Oncol 93:504–510

Rickard DJ, Monroe DG, Ruesink TJ (2003) Phytoestrogen genistein acts as an estrogen agonist on human osteoblastic cells through estrogen receptors alpha and beta. J Cell Biochem 89:633–646

Ruff CB, Hayes WC (1988) Sex differences in age-related remodeling of the femur and tibia. J Orthop Res 6:886–896

Schafer BW (2002) Local, distortional, and Euler buckling in thin-walled columns. J Struct Eng 128:289–299

Seeman E (2003a) Invited review: Pathogenesis of osteoporosis. J Appl Physiol 95:2142–2151

Seeman E (2003b) Periosteal bone formation: a neglected determinant of bone strength. N Engl J Med 349:320–323

Setchell KD, Lydeking-Olsen E (2003) Dietary phytoestrogens and their effect on bone: evidence from in vitro and in vivo, human observational and dietary intervention studies. Am J Clin Nutr 78:S593–S609

Sims NA, Dupont S, Krust A (2002) Deletion of estrogen receptors reveals a regulatory role for estrogen receptor-beat in bone remodeling in female but not in males. Bone 30:18–25

Setchell KDR (1998) Phytoestrogens: the biochemistry, physiology, and implications for human health of soy isoflavones. Am J Clin Nutr 68:S1333–S1346

Siu WS, Qin L, Cheung WH (2004) A study of trabecular bones in ovariectomiezed goats with micro-computed tomography and peripheral quantitative computed tomography Bone 35:21–26

Taylor M (1997) Alternatives to conventional hormone replacement therapy. Compr Ther 23:514–532

Uusi-Rasi K, Beck TJ, Semanick LM (2006) Structural effects of raloxifene on the proximal femur: results from the multiple outcomes of raloxifene evaluation trial. Osteoporos Int 17:575–586

Vickers AJ, Altman DG (2001) Statistics notes: analyzing controlled trials with baseline and follow-up measurements. Br Med J 323:1123–1124

Wang HF, Zhu GY, Wen SF (2001) Studies on establishment and lifestyle determinants of peak bone density in females of Shanghai urban area. Chin J Osteoporosis 7:305–309

Weinhold PS, Gilbert JA, Woodard JC (1994) The significance of transient changes in trabecular bone remodeling activation. Bone 15:577–584

Windahl SH, Andersson G, Gustafsson JA (2002) Elucidation of estrogen receptor functions in bone with the use of mouse models. Trends Endocrinol Metab 13:195–200

Ye HY, Liu J, Lou YJ (2005) Preparation of two derivatives from icariin and investigation of their estrogen-like effects. Zhejiang Da Xue Xue Bao Yi Xue Ban 34:131–136

Young W (1989) Elastic stability formulas for stress and strain. In: Crawford HTS (ed) Roark's formulas for stress and strain, 6th edn. McGraw-Hill, New York

Zhang G, Qin L, Hung Wing (2002) Comparison of pQCT and DXA analysis for establishment of osteoporotic model in proximal femur of mature ovariectomized rats. Chin J Orthop 22:432–436

Zhang G, Qin L, Shi Y, Leung K (2005) A comparative study between axial compression and lateral fall configuration tested in a rat proximal femur model. Clin Biomech 20:729–735

Zhang G, Qin L, Hung WY, Shi Y, Leung PC, leung KS (2006) Flavonoids derived from herbal epimedium brevicornum maxim prevent OVX-induced osteoporosis in rats independent of its enhancement in intestinal calcium absorption. Bone 38:818–825

Areal and Volumetric Bone Densitometry in Evaluation of Tai Chi Chuan Exercise for Prevention of Postmenopausal Osteoporosis

Pauline Po-Yee Lui (✉) , Ling Qin, Wing-Yin Choi, and Kai-Ming Chan

Department of Orthopaedics and Traumatology, The Chinese University of Hong Kong, Prince of Wales Hospital, Shatin, N.T., Hong Kong SAR, China
e-mail: Pauline@ort.cuhk.edu.hk

Abstract

Osteoporosis is a devastating public health problem as it affects hundreds of millions of people worldwide. While oestrogen-replacement therapy or anti-bone resorptive drugs are able to prevent postmenopausal bone loss, they may have certain side effects. Physical activity is an alternative approach. Among different types of physical activity, tai chi chuan (TCC) is a low to moderately intense exercise that is particularly suitable for elderly. The TCC emphasizes steady rhythm, balance, shifting of body weight, muscle relaxation, breathing control, and mind concentration. This chapter reviews the benefits of TCC in retarding bone loss and improving neuromuscular coordination that had been demonstrated in our previous studies and others. The application of bone densitometry techniques for monitoring changes in bone mineral density of elderly practicing TCC is also discussed. The use of pQCT, which has lower in vivo precision error and supports separate analysis of cortical and trabecular bone, allows more accurate and earlier detection of bone mineral changes after TCC exercise.

Epidemiology and Consequence of Osteoporosis and Osteoporotic Fractures

Osteoporosis is a major public health problem, accounting for the association between poor bone quality and fractures. In women, bone loss begins after thirties. The rate of decrease in bone mineral density (BMD) accelerates to its peak level in the first decade after the onset of menopause (Kato et al. 1995). The rate of bone loss can be as high as 5 and 1–2% per year in vertebral bone (Genant et al. 1982; Johnston et al. 1984; Tremollieres et al. 2001) and non-vertebral bone (Riis and Christiansen 1988), respectively, with the decline of circulating sex hormone. It is the deterioration of bone quality coupled with a geriatric fall that results in osteoporotic fracture which makes osteoporosis such a devastating problem for the elderly. The morbidity and mortality that accompany osteoporotic fractures are high. In a study in France, 21% of a group of hip fracture patients died within 3 months of their fracture (Baudoin

et al. 1996). Another study in the U.S. showed that 40% of patients were still unable to walk independently and 60% had difficulty with at least one essential activity of daily living 1 year after hip fracture (U.S. Department of Commerce 1993). After fall or fracture, the elderly become fearful and reluctant to engage in physical activity, resulting in social isolation, depression, and poor quality of life (Borgquist et al. 1992; Calder et al. 1995; Hall et al. 2000; Randell et al. 2000).

Treatment Strategies

The optimal strategies for the prevention of osteoporotic fractures include maximization and maintenance of bone mass as well as minimization of trauma. Physical activity, apart from diet and hormonal changes, is a key determinant of peak BMD. There is also evidence that physical activity during childhood and adolescence modulates the external geometry and architecture of trabecular bone thereby potentially promoting skeletal growth, whereas physical activity during adult life reduces age-related bone loss (Henderson et al. 1998). A 7–8% increase in peak BMD, if maintained throughout the adult years, can be translated into a 1.5-fold reduction in fracture risk (Henderson et al. 1998). It is obvious that the appropriate form of exercises for health and increase or maintenance of BMD varies at different stages of life. Vigorous physical activities, such as weight-bearing, resistance and impact exercises, are good for children and young adults who need to maximize their peak BMD; however, these activities may not be suitable for an aged individual who has developed problems of joint degeneration (Henderson et al. 1998; Li GP et al. 2001; Wolf et al. 1997). Activity modification to limit the impact component of exercise thus becomes necessary. In the older population, activity that is safe can increase/maintain bone mass and improve balance, and thus reduce the risk of falls and fractures. The TCC is a cost-effective exercise that meets these objectives.

Benefits of Tai Chi Chuan

Tai chi chuan is a low to moderately intense exercise that emphasizes steady rhythm, mind concentration, balance, shifting of body weight, muscle relaxation and breathing control (Fig. 1). Numerous studies have reported the therapeutic benefits of TCC

Figure 1. Postmenopausal women practicing Yang-style tai chi chuan exercise, a low to moderately intense exercise that emphasizes steady rhythm, mind concentration, balance, shifting of body weight, muscle relaxation and breathing control

practice with regard to improving quality of life, physical function including activity tolerance and cardiovascular function, pain management, balance, immune response, flexibility, strength, and kinesthetic sense (Hong et al. 2000; Li JX et al. 2001; Li GP et al. 2001; Plummer 1983). This chapter focuses on the benefits of TCC for the prevention of osteoporosis and osteoporotic fractures as well as the application of imaging techniques for the monitoring of BMD and fracture risk of individuals practicing TCC.

Retardation of Bone Loss

The beneficial effects of exercise largely come from studies on high impact or strengthening exercises. The highest BMD values were found in power-trained exercises such as jumping and weight lifting, but not in endurance activities such as swimming or long-distance running (Bass et al. 1998; Block and Smith 1987; Frost 1997). Results regarding the beneficial effects of low impact exercises on bone have been inconsistent (Hatori et al. 1993; Henderson et al. 1998; Kano et al.1998; Uusi-Rasi et al. 1994). Our data demonstrate that low-impact exercise, such as TCC, also carries the beneficial effects of attenuation of bone loss. In our previous study comparing the BMD of postmenopausal women who habitually practiced TCC with another group of age- and sex-matched healthy, sedentary controls, women who regularly practiced TCC showed higher BMD (overall 3.4–7.2%) at the weight-bearing skeletal sites (Qin et al. 2005). Similar results were obtained in another case-control study (Qin et al. 2002). In that study, postmenopausal women who had participated in TCC exercise regularly for an average of more than 8 years had a 10–15% higher areal BMD in the spine and proximal femur and 14% higher volumetric BMD in the distal tibia when compared with the inactive controls. The changes of trabecular BMD (tBMD) of ultradistal tibia (-1.10 ± 1.26 vs $-2.18 \pm 1.60\%$) and the cortical BMD (cBMD) of the distal tibial diaphysis (-0.90 ± 1.36 vs $-1.86 \pm 0.93\%$) were significantly lower in the

Figure 2. Areal BMD measured at both spine and hip using dual-energy X-ray densitometry (DXA; Norland XR-36)

TCC group compared with the control group (Qin et al. 2002). Regular practice of TCC exercise was thus associated with slower rate of bone loss.

To further prove the osteogenic nature of TCC exercise, we also conducted a 1-year prospective controlled study investigating the health benefits of TCC on the rate of bone loss and functions of postmenopausal women. Subjects in the TCC group were assigned to perform TCC for 45 min per day, 5 days per week for 1 year (Fig. 1), whereas the control subjects kept their sedentary lifestyle without participating in active physical exercises. Both dual-energy X-ray absorptiometry (DXA; Fig. 2) and multi-layer peripheral quantitative computed tomography (pQCT; Fig. 3) were used for monitoring changes in BMD. Our results showed that while there was a generalized bone loss in both control and TCC group, the rate of bone loss at spine and femoral neck was slower in TCC group than that of the control group, yet without reaching statistical significance (Fig. 4). The pQCT measurements showed that the rate of bone loss in ultradistal tibia tBMD (-0.53 vs -1.46%) and distal tibial diaphysis cBMD (-0.39 vs -1.40%) were lower in the TCC group compared with that in the control group. The difference between the two groups after 12 months were significant at both regions (ultradistal tibia tBMD: $p = 0.005$; distal tibial diaphysis cBMD: $p < 0.001$). What was more interesting was that reduced rate of bone loss was
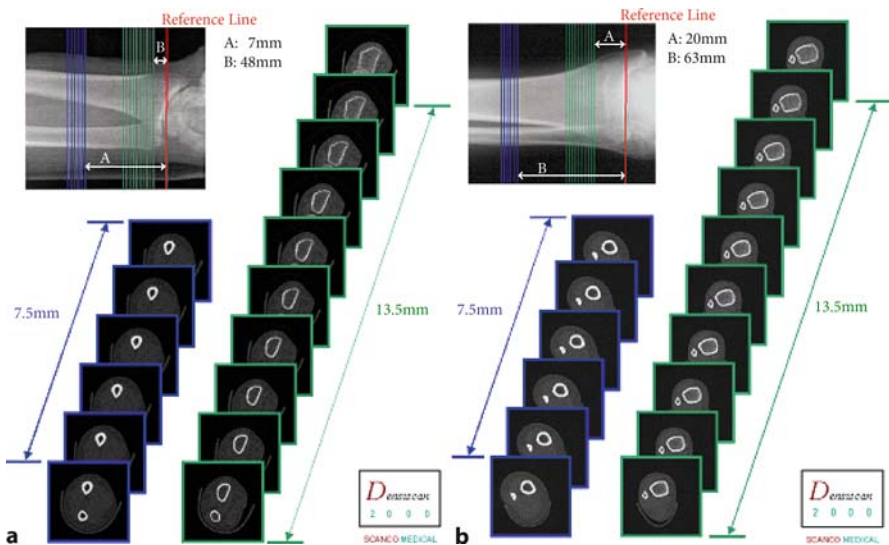
Figure 3 a,b. Volumetric BMD measurement using a highly precise and multi-slice pQCT (Densiscan 2000). Standard 16 tomographs are used to obtain volumetric from distal radius (**a**) and distal tibia (**b**), including a scout view for setting a reference line. The first distal tomogram is scanned at a distance from the end plate (7 mm for radius and 20 mm for Tibia). Ten tomographs in ultradistal distal tibia are used for obtaining trabecular volumetric in a core volume and the integral cortical and trabecular volumetric of the total volume. Six tomograms in the distal tibial diaphysis are scanned 48/63 mm (radius/tibia) proximally (towards the metaphysis) to the tenth tomogram of the distal ones for measuring cortical volumetric. The interval between the individual tomograms is 1.5 mm, with a thickness of 1 mm
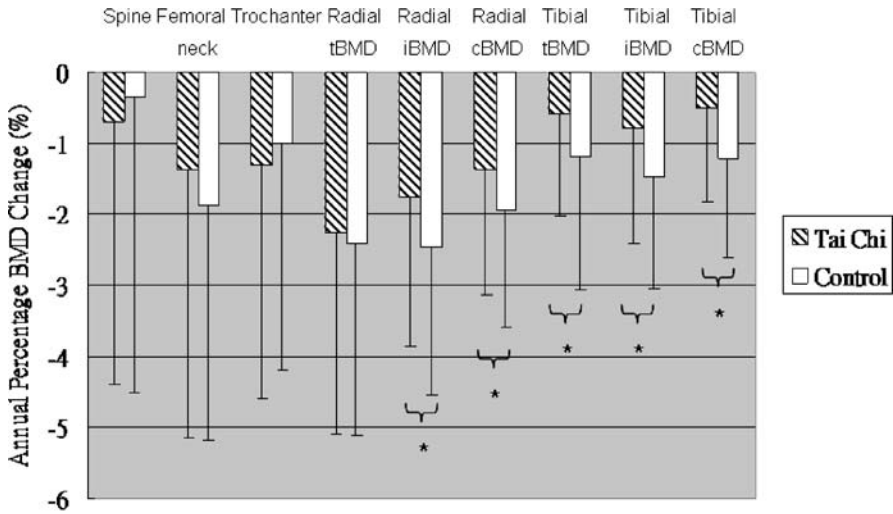
* Significant difference between the CON and TCC in rate of bone loss (p<0.05).

Figure 4. The annual changes (%) of BMD at different anatomical sites measured by pQCT and DXA in control (*CON*) and tai chi chuan (*TCC*) groups (data are mean±SE) as measured by both DXA (spine and hip) and pQCT (distal radius and tibia). No. of subjects in CON = 86; no. of subjects in TCC = 85

also observed in non-weight-bearing regions such as ultradistal-radius iBMD (-2.15 vs -3.41%), and the difference in BMD after 12 months was significant ($p = 0.047$; Fig. 4). The rate of tBMD loss in ultradistal radius (-2.50 vs -3.25%) and cBMD loss in distal radius diaphysis (-1.67 vs -2.84%) were also lower in the TCC group compared with that in the control group, although the BMD at 12 months was not significant (Fig. 4).

The foregoing data show that TCC might have a systematic effect on bone. The factors leading to the systematic retardation of bone loss are not known; however, previous study has shown that the plasma-ionized calcium and 25(OH)D levels decreased, but not bone turnover markers, immediately after strenuous exercise in elderly (Maïmoun et al. 2005). Another study on rats also reported that treadmill exercise transiently decreased the serum calcium level as a result of accumulation of calcium in bone, resulting in an increase in serum 1,25-dihydroxyvitamin D(3) level and a decrease in serum parathyroid hormone level (Iwamoto et al. 2005). Bouassida et al. (2003) also reported that the serum parathyroid hormone of young adults increased during exercise and remained high after 24 h of recovery; however, another study showed no difference in serum levels of parathyroid hormone and calcitriol after exercise (Zittermann et al. 2002). This might be related to the duration and intensity of exercise (Maïmoun et al. 2006). We did not measure the levels of hormones and bone turnover markers in our previous studies on the effect of TCC. Future study should include this as outcomes of the study. Muscle strengthening by TCC might also be responsible for the maintenance of BMD in radius (Pfeifer et al. 2004), which

was evidenced in our recent report on significantly improved hand-grip strength in TCC group (Chan et al. 2005).

As a low-impact exercise, TCC may not be able to increase the BMD, which was also demonstrated in our studies (Qin et al. 2002, 2005; Chan et al. 2004, 2005). It might be explained by the insensitivity of cells in later life to mechanical stimulation (Frost 1999). It has been reported that there was a reduction in estrogen receptor alpha in postmenopausal women, and this would impair the response of bone to mechanical strain (Lee and Lanyon et al. 2004; Tobias 2003); however, TCC exercise could retard the rate of bone loss. While the outcome in terms of BMD may not be as good as the case in high-impact exercise, TCC has the advantage of being safe and is suitable for elderly (Li GP et al. 2001).

Imaging Techniques for Monitoring the Benefits of Exercises on Bone

All of the previous studies on the effects of exercise on BMD used single-photon absorptiometry (SPA), DXA, and more recently multi-slice pQCT for the assessment and monitoring of BMD of individuals. The DXA gives 2D densitometric images, whereas pQCT gives 3D information. The BMD reported using DXA was areal BMD, which is based on bone mineral content in grams over the projected bone area (in square centimeters); however, in the case of pQCT, it measures volumetric BMD (in milligrams per cubic centimeter) based on the multi-slices of 2D image collected. In addition, it provides separate information for the cortical and trabecular bones. Together with the lower precision error of pQCT as compared with DXA (0.3 vs 1%; Lau et al. 1993; Qin et al. 2000), the use of pQCT for the assessment of the effect of exercise is more sensitive and accurate. This allows earlier and more accurate detection of changes in BMD induced by exercise by monitoring the metabolically high-turnover trabecular BMD.

In our studies on the efficacy of TCC in the maintenance of bone mass, we have used both DXA and pQCT to follow the BMD of subjects longitudinally (Figs. 2, 3). Although both DXA and pQCT measurements revealed decelerated rates of bone loss in the TCC group, pQCT was more sensitive and could detect the difference earlier. On the other hand, DXA measurements showed inconsistent changes in BMD in various regions (Fig. 4; Chan et al. 2004; Qin et al. 2002). Longer duration of follow-up is thus required for consistent and statistically significant difference if DXA is used for monitoring the effects of exercise on BMD.

A recent development is the use of in vivo micro-CT (ExtremeCT) for measuring the bone mineral and bone microarchitecture of human. Details of this technology are given in other chapters of this book. This technique has not been applied to study the effect of exercise on elderly, but it is a powerful device that allows better monitoring of treatment effects and improves the assessment of fracture risk.

Tai chi chuan is more suitable than brisk walking as an exercise that can maintain the interest of elderly. In view of the benefits of exercise to health, it deserves greater attention to develop ways to inspire people's interest in exercising. To encourage people's involvement in regular practice is an important and challenging task for health care professionals. Our previous study comparing the benefits of TCC and

brisk walking showed that subjects in the brisk-walking group have a higher dropout rate, and we believe that it might be related to the uninteresting nature of brisk walking (Chan et al. 2005). Of our TCC subjects, 84% continued to practice TCC after the 1-year prospective study, whereas less than 50% of subjects continued brisk walking. In addition, our results showed that TCC exercise (45 min/day, 5 days/week) was superior to brisk walking in retarding bone loss and improving muscle strength. The TCC thus might be a better exercise, compared with brisk walking, for elderly (Chan et al. 2005).

Neuromuscular Function and Postural Control

Fall is common in elderly. About 30% of persons over 65 years of age sustain a fall annually and 90% of osteoporotic fractures are the result of falls (Blake et al. 1998; Lipsitz et al. 1994; Province et al. 1995). Improvement in postural control and proprioception help to prevent osteoporotic fractures. There have been many reports supporting that TCC could strengthen the muscles, especially those in the lower extremities (American College of Sports Medicine Position Stand 1998; Choi et al. 2005; Fong and Ng 2006; Henderson et al. 1998; Hong et al. 2000; Kessenich 1998; Li et al. 2004; Li JX et al. 2001; Qin et al. 2005; Song et al. 2003; Wolf et al. 1996; Wolfson et al. 1996; Wu et al. 2002; Xu et al. 2005, 2006). Results from our cross-sectional study demonstrated that postmenopausal women regularly practicing TCC had significantly greater quadriceps strength (20.2 ± 4.6 vs $14.1 \pm 4.6\,\mathrm{kgf^{-1}}$) and longer single-stance time (114.3 ± 68.1 vs $68.1 \pm 75.5\,\mathrm{s}$) compared with the age- and sex-matched physical inactive controls (Qin et al. 2005). The muscles of lower limbs responded faster to unexpected ankle inversion perturbations in regular TCC practitioners, and it was important for the timely correction of postural disturbances during fall (Xu et al. 2005). Analysis of human biomechanics showed that the duration of each one-leg stance was longer in TCC exercise, and the plantar pressure distribution during the single-leg stance in TCC exercise was different from that during normal walking (Mao et al. 2006a). The research group further demonstrated that the short duration of each step and the frequent change in direction in TCC could simulate the gait challenges that might be encountered in daily activities (Mao et al. 2006b).

As proprioception is significantly and positively associated with posture stability of an individual, it is important to understand whether TCC had any effect on joint proprioception. Fong and Ng (2006) reported that TCC exercise could improve the knee joint position sense of elderly. Moreover, the knee joint proprioceptive acuity of these experienced elderly TCC practitioners was comparable to that of the young controls, indicating that TCC could reverse the effects of aging on proprioception (Tsang and Hui-Chan 2004). Results from our group also demonstrated that elderly people who regularly practiced TCC not only showed better proprioception at the ankle and knee joints than the sedentary controls, but also better ankle kinesthesis than swimmers/runners (Xu et al. 2004). The TCC exercise thus has the advantage of not only retarding bone loss, but also in decreasing the risks of fall. As compared with high-impact exercise, low-weight-bearing TCC exercise has an additional advantage of training the neuromuscular coordination of practitioners.

Directions for Future Research on TCC for Prevention of Osteoporotic Fractures

Although there have been studies on the effect of TCC on bone mass, there are no well-designed, controlled longitudinal studies that include fracture as the primary outcome. Our study recorded higher incidences of fractures in the control group compared with that in the TCC group (Chan et al. 2004); however, it was not a planned outcome of the study. Less fracture in the TCC group might be attributed to skeletal, non-skeletal or environmental factors. Whether the increase in BMD by TCC can be effectively translated into reduced osteoporotic fractures needs to be proved. Future studies should focus on studying the intensity, frequency and duration of TCC on bone and neuromuscular control. There are different styles of TCC, Chen (quick and slow large movements), Yang (slow, large movements; Fig. 1), Wu (mid-paced, compact) and Sun (quick, compact; Jou 1983). It would be important to understand the health benefits of different styles of TCC to the maintenance of bone mass and improvement of neuromuscular coordination. The results of both studies can guide the precise prescription of TCC exercise for different individuals. In vivo micro-CT (ExtremeCT) shall be used in the future as a sensitive and accurate evaluation tool for monitoring the BMD, bone microarchitecture and for predicting bone strength of individuals engaged in different exercise regimes.

References

American College of Sports Medicine Position Stand (1998) Exercise and physical activity for older adults. Med Sci Sports Exerc 30:992–1008

Bass S, Pearce G, Bradney M, Hendrich E, Delmas PD (1998) Exercise before puberty may confer residual benefits in bone density in adulthood: studies in active prepubertal and retired female gymnasts. J Bone Miner Res 13:500–507

Baudoin C, Fardellone P, Bean K et al. (1996) Clinical outcomes and mortality after hip fracture: a 2-year follow-up study. Bone 18 (Suppl 3):S149-S157

Blake AJ, Morgan J, Bendall MJ (1998) Falls by elderly persons at home: prevalence and associated factors. Age Aging 17:365–372

Block JE, Smith R (1987) Overview of exercise and bone mass. In: Genant HK (ed) Osteoporosis update. San Francisco Radiology Research Education Foundation, San Francisco, pp 267–270

Borgquist L, Nilson LT, Lindelow G, Eiklund I, Thorngren KG (1992) Perceived health in hip-fracture patients: a prospective follow-up of 100 patients. Age Ageing 21:109–116

Bouassida A, Zalleg D, Zaouali AM, Gharbi N, Duclos M, Richalet JP, Tabka Z (2003) Parathyroid hormone concentrations during and after two periods of high intensity exercise with and without an intervening recovery period. Eur J Appl Physiol 88:339–344

Calder SJ, Anderson GH, Harper WM, Jagger C, Gregg PJ (1995) A subjective health indicator for follow-up. J Bone Joint Surg (Br) 77:494–496

Chan KM, Qin L, Lau MC, Woo J, Au SK, Choy WY, Lee KM, Lee SH (2004) A randomized, prospective study of the effects of TCC Chun exercise on bone mineral density in post-menopausal women. Arch Phys Med Rehabil 85:717–722

Chan KM, Qin L, Lau MC, Woo J, Lee SH (2005) Health benefits of programmed physical exercise on the prevention of bone loss in post-menopausal women. Research Dissemination Report (Ref 631009), Health Services Research Fund (www.hwfb.gov.hk/grants), pp 1–4

Choi JH, Moon JS, Song R (2005) Effects of Sun-style TCC exercise on physical fitness and fall prevention in fall-prone older adults. J Adv Nurs 51:150–157

Fong SM, Ng GY (2006) The effects on sensorimotor performance and balance with TCC training. Arch Phys Med Rehabil 87:82–87

Frost HM (1997) Why do marathon runners have less bone than weight lifters? A vital biomechanical view and explanation. Bone 20:183–189

Frost HM (1999) Why do bone strength and "mass" in aging adults become unresponsive to vigorous exercise? Insights of the Utah paradigm. J Bone Miner Metabol 17:90–97

Genant HK, Cann CE, Ettinger B, Gordan GS (1982) Quantitative computed tomography of vertebral spongiosa: a sensitive method for detecting early bone loss after oophorectomy. Ann Intern Med 97:699–705

Hall SE, Williams JA, Senior JA, Goldswain PRT, Criddle RA (2000) Hip fracture outcomes: quality of life and functional status in older adults living in the community. Aust NZ J Med 30:327–332

Hatori M, Hasegawa A, Adachi H, Shinozaki A, Hayashi R, Okano H (1993) The effects of walking at the anerobic threshold level on vertebral bone loss in postmenopausal women. Calcif Tissue Int 52:411–414

Henderson NK, White CP, Eisman JA (1998) The roles of exercise and fall risk reduction in the prevention of osteoporosis. Endocrinol Metabol Clin North Am 27:369–387

Hong Y, Li JX, Robinson PD (2000) Balance control, flexibility, and cardiorespiratory fitness among older TCC practitioners. Br J Sports Exerc 34:29–34

Iwamoto J, Takeda T, Sato Y (2005) Effect of treadmill exercise on bone mass in female rats. Exp Anim 54:1–6

Johnston CC, Hui SL, Witt RM et al. (1984) Early menopausal changes in bone mass and sex steroids. J Clin Endocrinol Metab 61:905–911

Jou TH (1983) The tao of TCC chuan: way to rejuvenation, 3rd edn. TCC Foundation, Piscataway, New Jersey

Kano K (1998) Relationship between exercise and bone mineral density among over 5000 women aged 40 years or above. J Epidemiol 8:28–32

Kato T, Chen JT, Katase K et al. (1995) Time course changes in bone metabolic markers after menopause: a cross-sectional study. Acta Obstet Gynaecol Jap 47:43–48

Kessenich CR (1998) TCC as a method of fall prevention in the elderly. Orthop Nurs 17:27–29

Lau EM, Woo J, Leung PC (1993) Low bone mineral density, grip strength and skinfold thickness are important risk factors for hip fracture in Hong Kong Chinese. Osteoporos Int 3:66–69

Lee KC, Lanyon LE (2004) Mechanical loading influences bone mass through estrogen receptor alpha. Exerc Sport Sci Rev 32:64–68

Li F, Harmer P, Fisher KJ, McAuley E (2004) TCC: improving functional balance and predicting subsequent falls in older persons. Med Sci Sports Exerc 36:2046–2052

Li GP, Qin L, Chan KM (2001) Health benefits of TCC Chuan in older individuals. In: Maffuli N, Chan KM, Macdonald R, Malina RM, Parker AW (eds) Sports medicine for specific ages and abilities. Churchill Livingstone, Philadelphia, pp 315–324

Li JX, Hong Y, Chan KM (2001) TCC: physiological characteristics and beneficial effects on health. Br J Sports Med 35:148–156

Lipsitz LA, Nakajima I, Gagnon M (1994) Muscle strength and fall rates among residents of Japanese and American nursing homes: an international cross-cultural study. J Am Geriatr Soc 42:953–959

Maïmoun L, Simar D, Malatesta D, Caillaud C, Peruchon E, Couret I, Rossi M, Mariano-Goulart D (2005) Response of bone metabolism related hormones to a single session of strenuous exercise in active elderly subjects. Br J Sports Med 39:497–502

Maïmoun L, Manetta J, Couret I, Dupuy AM, Mariano-Goulart D, Micallef JP, Peruchon E, Rossi M (2006) The intensity level of physical exercise and the bone metabolism response. Int J Sports Med 27:105–111

Mao DW, Li JX, Hong Y (2006a) The duration and plantar pressure distribution during one-leg stance in TCC exercise. Clin Biomech 21:640–645

Mao DW, Hong Y, Li JX (2006b) Characteristics of foot movement in TCC exercise. Phys Ther 86:215–222

Pfeifer M, Sinaki M, Geusens P, Boonen S, Boonen S, Preisinger E, Minne HW, ASBMR Working Group on Musculoskeletal Rehabilitation (2004) Musculoskeletal rehabilitation in osteoporosis: a review. J Bone Miner Res 19:1208–1214

Plummer JP (1983) Acupuncture and TCC chuan (Chinese shadow boxing): body/mind therapies affecting homeostasis. In: Lau Y, Fowler JP (eds) The scientific basis of traditional Chinese medicine: selected papers. Medical Society, Hong Kong, pp 22–36

Province MA, Hadley EC, Hornbrook MC et al. (1995) The effects of exercise on falls in elderly patients. A preplanned meta-analysis of FICSIT Trials. Frailty and injuries: cooperative studies of intervention techniques. J Am Med Assoc 273:1341–1347

Qin L, Au SK, Chan KM et al. (2000) Peripheral volumetric bone mineral density in pre- and postmenopausal Chinese women in Hong Kong. Calcif Tissue Int 67:29–36

Qin L, Au SK, Choy WY, Leung PC, Neff M, Lee KM, Chan KM (2002) Regular TCC exercise may retard bone loss in postmenopausal women: a case control study. Arch Phys Med Rehabil 83:1355–1359

Qin L, Choy WY, Leung KS, Leung PC, Au SK, Hung WY, Dambacher M, Chan KM (2005) Beneficial effects of regular TCC exercise on musculoskeletal system. J Bone Miner Metab 23:186–190

Randell AG, Nguyenl TV, Bhalerao N, Silvermann SL, Sambrook PN, Eisman JA (2000) Deterioration in quality of life following hip fracture: a prospective study. Osteoporosis Int 11:460–466

Riis BJ, Christiansen C (1988) Measurement of spinal or peripheral bone mass to estimate early postmenopausal bone loss. Am J Med 84:646–653

Song R, Lee EO, Lam P, Bae SC (2003) Effects of TCC exercise on pain, balance, muscle strength, and perceived difficulties in physical functioning in older women with osteoarthritis: a randomized clinical trial. J Rheumatol 30:2039–2044

Tobias JH (2003) At the crossroads of skeletal responses to estrogen and exercise. Trends Endocrinol Metab 14:441–443

Tsang WW, Hui-Chan CW (2004) Effects of exercise on joint sense and balance in elderly men: TCC versus golf. Med Sci Sports Exerc 36:658–667

Tremollieres FA, Pouilles JM, Ribot C (2001) Withdrawal of hormone replacement therapy is associated with significant vertebral bone loss in postmenopausal women. Osteoporos Int 12:385–390

U.S. Department of Commerce (1993) Hip fracture outcomes in people age 50 and over: mortality, service use, expenditures, and long-term functional impairment. Office of Technology Assessment, Congress of the United States, Washington, DC, publication NTIS PB94107653

Uusi-Rasi K, Nygard CH, Oja P, Pasanen M, Sievanen H, Vuori I (1994) Walking at work and bone mineral density of premenopausal women. Osteoporos Int 4:336–340

Wolf SL, Barnhart HX, Kutner NG, McNeely E, Coogler C, Xu T (1996) Reducing frailty and falls in older persons: an investigation of TCC and computerized balance training. Atlanta FICSIT Group. Frailty and Injuries: Cooperative Studies of Intervention Techniques. J Am Geriatr Soc 44:489–497. Comment in: J Am Geriatr Soc 44:599–600

Wolf SL, Coogler CE, Xu T (1997) Exploring the basis for TCC Chuan as a therapeutic exercise approach. Arch Phys Med Rehabil 78:886–892

Wolfson L, Whipple R, Derby C, Judge J, King M, Amerman P, Schmidt J, Smyers D (1996) Balance and strength training in older adults: intervention gains and TCC maintenance. J Am Geriatr Soc 44:498–506

Wu G, Zhao F, Zhou X (2002) Improvement of isokinetic knee extensor strength and reduction of postural sway in the elderly from long-term TCC exercise. Arch Phys Med Rehabil 83:1364–1369

Xu D, Hong Y, Li J, Chan K (2004) Effect of TCC exercise on proprioception of ankle and knee joints in old people. Br J Sports Med 38:50–54

Xu DQ, Li JX, Hong Y (2005) Effect of regular TCC and jogging exercise on neuromuscular reaction in older people. Age Ageing 34:439–444

Xu DQ, Li JX, Hong Y (2006) Effects of long term TCC practice and jogging exercise on muscle strength and endurance in older people. Br J Sports Med 40:50–54

Zittermann A, Sabatschus O, Jantzen S, Platen P, Danz A, Stehle P (2002) Evidence for an acute rise of intestinal calcium absorption in response to aerobic exercise. Eur J Nutr 41:189–196

Enhancement of Osteoporotic Bone Using Injectable Hydroxyapatite in OVX Goats Evaluated by Multi-imaging Modalities

Wing-Hoi Cheung (✉) , Ling Qin, Kam-Fai Tam, Wing-Sum Siu, and Kwok-Sui Leung

Department of Orthopaedics and Traumatology, The Chinese University of Hong Kong, Shatin, N.T., Hong Kong, SAR China
e-mail: louis@ort.cuhk.edu.hk

Abstract

Osteoporotic fracture is very common in aged population, with an average of 1–3% increase per year in most areas of the world because of increase in aging population. Fixation of osteoporotic fracture is difficult, often with implant loosening or backout. Fixation enhancement with various biomaterials and implants is investigated before clinical application. This chapter describes a study investigating the effect of an optimized injectable hydroxyapatite (HA) on enhancing screw fixation in osteoporotic bones. By using radiography, pQCT and micro-CT, the development of osteoporosis in ovariectomized Chinese goats was confirmed. There was an averaged 25% decrease of bone mineral density in the goats after 6-month ovariectomy as well as a significant reduction of trabecular thickness and connectivity. The established osteoporotic goat model was then used for evaluating the efficacy of an optimized injectable HA in screw fixation. With the application of micro-CT and histomorphometry, it was confirmed that the injectable HA was distributed evenly along the screw threads and new bone formation was detected on HA surface without fibrous tissues. The HA increased the contact area between implants and trabecular bones, and hence the holding power to screws. Mechanical test further confirmed the significant increase of screw pull-out force by HA. This study demonstrated the application of multiple non-invasive bioimaging technologies in biomaterial research.

Osteoporosis and Related Fracture

"Osteoporosis is a systemic skeletal disease characterized by low bone mass and microarchitectural deterioration of bone tissue, with a consequent increase in bone fragility and susceptibility to fracture" (Anonymous 1993; WHO 1994), which readily leads to fractures (WHO 1994). Osteoporosis is a known major risk factor of osteoporotic fractures, and of all fractures, hip fracture is particularly serious as it affects mobility and causes severe pain. The frequency of hip fractures is increasing by 1–3% per year in most areas of the world (Cummings and Melton 2002). In Asia it

was reported that the numbers of hip fractures will increase from 68 million in 1990 to 133 million in 2050 (Cummings and Melton 2002). There is also a report showing 4750 elderly suffering hip fractures in Hong Kong annually, which is the fourth major cause of bed occupancy of about 150,000 bed days (Ho and Chan 2003). With longer life expectance and increasing aging population, osteoporosis and related fractures will become a major socio-medical challenge in societies all over the world.

Current Surgical Treatment and Problems

The authors' hospital is a referral centre for treatment of osteoporosis and osteoporotic fractures. We treat over 1000 osteoporotic fractures each year. Many of these fractures need surgery for fixation. Implant loosening or backout is commonly observed, e.g. ~30% femoral neck fractures fixed with hip screws had backout and loss of stable fixation. This is due mainly to the poor holding power of osteoporotic bones with significant bone loss in terms of decrease in bone mineral density (BMD) and deterioration in bone microarchitecture. Many of these cases needed revision surgery and delayed patient rehabilitation. Using different biomaterials to enhance implant-holding properties is therefore clinically indicated, including calcium phosphate compounds, hydroxyapatite (HA) and polymethylmethacrylate (PMMA; Breusch and Kuhn 2003; Larsson and Bauer 2002). Early clinical results of these materials have shown reduced time to full weight-bearing (Larsson et al. 2002). Among these materials, calcium phosphate compounds (CPC) and HA are widely accepted with good pre-clinical (Elder et al. 2000) and clinical (Goodman et al. 1998) results. The manufacturers provide these products in form of blocks, granules or cylinder, etc., which are, however, inconvenient for clinical applications.

Injectable Hydroxyapatite Developed for Enhancement of Osteoportic Fracture Fixation

Injectable HA has been developed recently (Blattert et al. 2002; Larsson and Bauer 2002), and the key advantage is its physical properties to spread evenly along the trabecular space around the screw, which is expected to provide enhanced holding power of implants. With the use of the state-of-the-art densitometric systems, this chapter introduces the evaluations of potential enhancement of an in vitro optimized injectable HA on osteoporotic bone fixation using osteoporotic goat model.

Research Program in Authors' Center with Relation to Studying Osteoporotic Fracture Fixation

Establishment of Osteoporotic Goat Model

To verify the applicability of injectable HA in osteoporotic bones, an osteoporotic large animal model with bone structure similar to human is preferable, as bone size should be large enough to fit the implants used clinically. High similarity of bones between sheep and humans has been reported in terms of anatomical and biome-

Figure 1. Aluminum step wedge as calibrator in place during radiography taking for downstream photodensitometric analysis

chanical aspects (Wilke et al. 1998). Chinese mountain goat is therefore used for establishing osteoporotic model as subtropical climate in Hong Kong is not suitable for sheep keeping.

Sixteen skeletally mature goats (27–32 kg) were bilaterally ovariectomized (OVX) and fed with low-calcium diet (Glen Forrest Stockfeeders, Glen Forrest, Australia) for 6 months (Leung et al. 2001). The development of osteoporosis was monitored and confirmed by using various densitometric approaches: radiography (photodensitometry), and BMD measurement of bone specimens taken at baseline and 6 months after OVX by peripheral quantitative computed tomography (pQCT) and micro-CT.

Photodensitometric Analysis

Development of osteoporosis was monitored on left proximal tibial metaphysic and calcaneus by monthly radiography (X-ray machine SFR-510; Shower X-ray Co., Tokyo, Japan) in the presence of aluminum step wedge (ASW) calibrator (Fig. 1). Radiographs were then digitized using an X-ray imaging system (diagnostix 2048; PACE system, PACE Medical, Freiberg, Germany) for analysis and the outcomes were presented as equivalent thickness of the known ASW calibrator (Leung et al. 2001; Qin et al. 1998). Precision error of the method interpreted by the coefficient of variation (CV) of the repeated measurements of the photodensitometry was about 15%.

In our model establishment, the results showed that the standardized bone density of both regions of interest decreased gradually after the OVX with significant

decrease of 18.9% in proximal tibial metaphyses and 21.9% in calcanei ($p = 0.003$ and $p = 0.023$, respectively, $n = 16$).

Peripheral Quantitative Computed Tomography

Similar to currently popular dual-energy absorptiometry (DXA), photodensitometric analysis is a 2D approach by evaluating BMD in a projectional image, which is, affected by the size of the bone (Qin et al. 1998; Cheng et al. 2001). Peripheral quantitative computed tomography (pQCT) installed in the authors' centre is, a 3D technology that provides true volumetric BMD (in milligrams per cubic centimeter) of both cortical and metabolically more active trabecular of bone (Ruegsegger et al. 1996; Qin et al. 2002). We used a multilayer pQCT (Densiscan 2000, Scanco, Bassersdorf, Switzerland) to scan the iliac crest biopsy specimens with a tomography thickness of 1 mm at a scan resolution of 300 µm. Mean volumetric BMD of five consecutive slices was measured for the central 50% core volume within the entire cross-sectional area (CSA) of the bicortical scan using a built-in software (Leung et al. 2001; Siu et al. 2003).

On average, the median percentage change in metabolically high turnover part, i.e. trabecular BMD, was 25.0% lower in 6 months after OVX as compared with its baseline ($p = 0.006$; Leung et al. 2001). Such decrease in trabecular BMD was caused mainly by the thinning of trabecular bone, but not trabecular matrix mineral density, as measured by micro-computed tomography (micro-CT) as described below.

Micro-Computed Tomography

The microarchitecture of the iliac crest biopsies at baseline and 6 months after OVX were also assessed by using a corn-beam micro-CT system (µCT40, Scanco Medical AG, Bassersdorf, Switzerland; Siu et al. 2004). The spatial resolution was set to 20 µm for scanning and 3D reconstruction. Each biopsy was scanned continuously with thickness and increment of 20 µm for 120 slices. Threshold was set at 122 to gain the best coverage of all trabecular bone and the cortical bone was excluded manually for evaluation (Fig. 2). The evaluation was conducted automatically by the direct method provided by the system for (a) 2D model, including mean trabecular surface area fraction (BS/TV), and (b) 3D model, trabecular number (Tb.N), trabecular thickness (Tb.Th), intertrabecular space (Tb.Sp), trabecular bone tissue volume density (BV/TV), trabecular connectivity (Conn.D), structure model (SMI) and degree of antisotrophy (DA). Moreover, trabecular matrix mineral density of the specimens [defined as BMC/(TV-Tb.Sp), where BMC is bone mineral content, TV is tissue volume, Tb.Sp is intertrabecular space or marrow volume] was also evaluated. A density phantom was used to calibrate the hydroxyapatite (HA) density with corresponding X-ray attenuation value of the material. A linear regression was generated by the workstation for the calculation of mineral density of the materials and the mineral density was expressed as milligrams of HA/cm^3.

The results revealed that BV/TV, BS/TV, Tb.N and Conn.D of the iliac crest biopsy of 6 months after OVX decreased significantly on average by 8.34, 8.01, 8.51 and 18.52%, respectively ($p < 0.05$ each; Siu et al. 2004). The Tb.Sp was 8.26% sig-
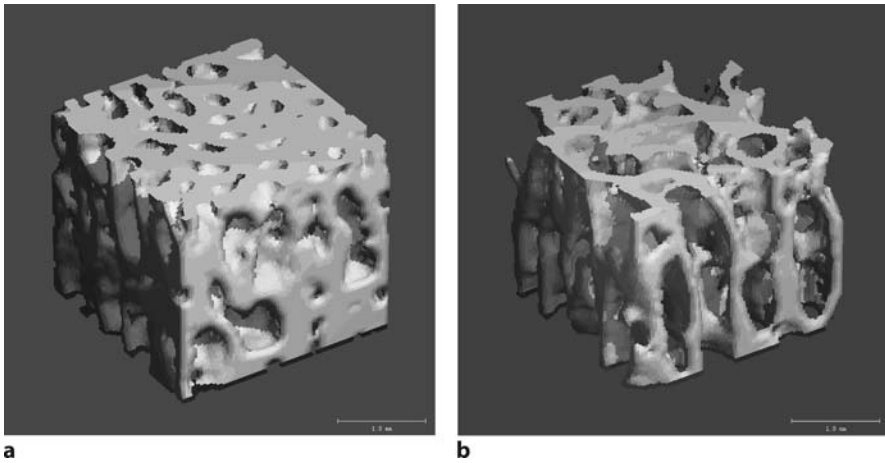
Figure 2 a,b. Osteoporosis was monitored by micro-CT on the iliac crest biopsies of goats. **a** Normal bone. **b** Osteoporotic bone

nificantly greater than baseline after OVX but no significant difference was detected for Tb.Th, SMI and DA values. Also, there was a non-significant 2.3% decrease in trabecular matrix mineral density, suggesting no significant alterations in bone matrix mineral density, but instead mainly trabecular bone thinning as a result of high turnover induced more bone resorption than bone formation. The changes in these structural parameters in the OVX goat model measured by using micro-CT were within the range of the other micro-CT studies from osteoporotic patients or from cadaveric trabecular bone obtained from spine, femur and hip (Ito et al. 1995; Müller et al. 1996; Rauch and Schoenau 2001) to OVX sheep model (Lill et al. 2000). The BV/TV, Tb.N and Conn.D might be the more sensitive variables for early detection of alteration in trabecular structure. This osteoporotic goat model may therefore provide orthopaedic researchers good opportunities to study new techniques and to test new fixation devices and/or biomaterials developed for osteoporotic fracture fixation.

Application of Optimized Injectable Hydroxyapatite in Osteoporotic Bones

We optimized an injectable hydroxyapatite (HA) by dissolving 5 g of bone cement powder (a mixture of tetracalcium phosphate and dicalcium phosphate anhydrous; Ca/P ratio: 1.65–1.67; Stryker Leibinger, Freiburg, Germany) in 0.45 ml/g of 0.25 M Na_2HPO_4 at room temperature (22 °C; Leung et al. 2005). This HA mixture was added into a syringe and mixed inside a shaker (Stryker Leibinger, Freiburg, Germany) at 1000 rpm for 13 s. Both the femoral condyles and the lumbar vertebrae L2–L5 of the established osteoporotic goats were the regions of interest. Two randomly selected lumbar vertebrae of each goat served as HA group with screw insertion and HA injection, whereas the other two lumbar vertebrae acted as controls with screw insertion only. Briefly, 0.15 ml of well-mixed HA was injected into the predrilled

holes (2.7 mm in diameter × 12 mm in depth) of the bone in treatment group. Small stainless steel-titanium cancellous screws (4 mm in diameter) were then inserted into the predrilled holes in both HA and control groups. The goats were euthanized after 1 week, 3 months and 6 months of screw insertion. Bone specimens were collected for micro-CT analysis, histomorphometry and screw pull-out test.

Using Micro-CT

The distribution of injectable HA in bone was assessed by micro-CT system. The spatial resolution was set to 20 μm. Each biopsy was scanned continuously with thickness and increment of 20 μm for 240 slices. The threshold was set at 306 to distinguish the injectable HA and trabecular bone.

The results showed that the injectable HA distributed evenly along the screw threads (Fig. 3), indicating that the viscosity of the injectable HA had been optimized for clinical application and might help to enhance the holding power of implants by increasing the contact area between implants and trabecular bones.

Histomorphometric Analysis

The specimens, with the screw left in situ, were dehydrated and embedded with MMA according to our established protocol (Qin et al. 1999, 2001, 2006). The embedded specimens were sectioned in a longitudinal fashion parallel to the axis of the implant to a thickness of 500 μm using a saw microtome (Leica SP1600, Leica Instruments, Nussloch, Germany), and were further grinded and polished to a thickness of 200 μm using a grinder/polisher (RotoPol-21, Struers, Denmark). The sections were processed for routine histology and examined with a light microscope (Leica DMRXA2, Leica Microsystems, Wetzlar, Germany) and polarized microscope (Leica DMRB, Leica Microsystems, Wetzlar, Germany).
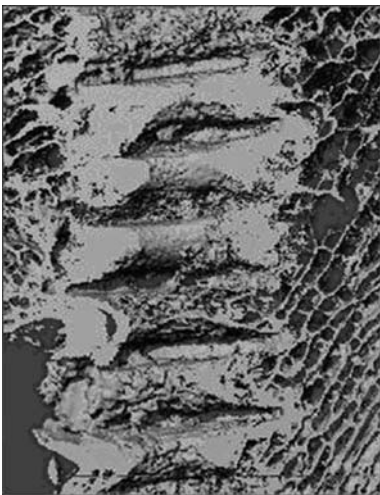
Figure 3. Micro-CT 3D image shows the even distribution of injectable hydroxyapatite around the screw threads

Figure 4. Fibrous tissues were present to hinder the growth of new bone towards the screw threads

Histology showed that in HA group at week 1, the HA filled most of the void space around the screw thread of implants and appeared homogeneous. Meanwhile, a layer of bone was observed on most of the HA surface without intervening fibrous tissue. At month 3 more bone covering the HA was detected with better alignment. At month 6 more properly aligned bone was observed and woven bone completely filled the space without fibrous tissue. In contrast, in control group, much empty space was present at week 1, whereas fibrous tissue was shown to infiltrate the screw and bone interface at month 3. Bone was detected without a good attachment with the screw. At month 6 additional bone was found, but the growth towards the screw was hindered by the fibrous layer (Fig. 4; Leung et al. 2006).

Using Screw Pull-Out Test

Screw pull-out test was performed to determine the pull-out force required for failure using mechanical testing machine (H25K-S, Hounsfield Test Equipment, Salfords, Redhill, UK; Leung et al. 2006). The bone specimen was embedded in a performance polymer (UREOL 2020, Ciba, Hong Kong) with exposing the screw head. A custom-made jig was used to grasp the screw head while the specimen was held rigidly at the other end of the jig. The screw was pulled at 10 mm/min until failure. Force and displacement were recorded in real time at sampling rate of 10 Hz.

There was an immediate increase of screw pull-out force by 54.7% ($p = 0.005$) at baseline (week 1) in HA group, as compared with the control. This revealed an improvement in screw-holding power immediately after HA application. But the differences between HA group and control group were less at 3 and 6 months after implantation (9.8%, $p = 0.069$, and 20.5%, $p = 0.008$, respectively). Failure mode usually occurred in the bone layer in both groups at all time points with more bone attached to the implant of the HA group (Leung et al. 2006).

General Discussion and Clinical Significance

This chapter describes applications of various densitometric assessment techniques for confirming the establishment of osteoporotic goat model and studying the application of the newly optimized bone cement on implant fixation. Those non-invasive densitometric assessments showed their strength in continuous bone density monitoring while micro-CT supplements the bone microarchitectural data for end-point assessment. They are very useful research assessment tools for animal and bone cement research.

In this study, both 2D and 3D densitometric findings confirmed that osteoporotic goat model was successfully established in terms of BMD and microarchitecture by bilateral ovariectomy and low-calcium diet. Due to its similarity of skeletal physiology of goat to human (Qin et al. 1999; Wilke et al. 1998), Chinese mountain goat is a good animal model for osteoporosis research. Optimized bone cement was also verified to significantly augment screw fixation in osteoporotic bones.

In the animal model development, both 2D photodensitometric analysis and 3D pQCT were used for continuous monitoring of bone quality in the OVX goats. The sensitivity of photodensitometry is, however, lower than that of pQCT. The pQCT measurements are more accurate in indicating the BMD changes after OVX. The pQCT is a more accurate technique in osteoporosis studies because it measures the BMD of cancellous bone (Siu et al. 2004). As cancellous bone is eight times metabolically more active than cortical bone (Sheldon 1994), trabecular bone loss in cancellous bone is faster during osteoporosis development (Qin et al. 2001; Chan et al. 2004). Using pQCT to evaluate BMD is a more sensitive and accurate approach to detect BMD change in the animal model as well. The precision error of bone specimen measurements was 0.30–0.35% in our in vitro (Lai et al. 2005) or in vivo study (Qin et al. 2003; Chan et al. 2004); therefore, pQCT should be a recommended method to monitor BMD changes in osteoporotic animal model development, wherever available.

Micro-CT is also used to confirm the deterioration of trabecular microarchitecture in the osteoporotic goat model, as osteoporosis is characterized by low bone density as well as structural deterioration in our series and also others (Anonymous 1993). The micro-CT data correlated to the BMD findings at the same region of interest very well. These results were comparable to those in another clinical study done by Ito et al. (1995) using iliac crest biopsies of osteoporotic patients, which reported a decrease of ~12 – 22% in structural parameters. This implied that our established goat model has similar microarchitectural deterioration during the development of osteoporosis as human. Micro-CT, however, allows measurement of small samples only and cannot serve as a longitudinal monitoring technique, which limits its potential clinical application in follow-up evaluation of bone microarchitectural changes; thus, a non-invasive in vivo micro-CT, such as XtremeCT, may become the trend for such kind of purpose in the near future (Dambacher et al. 2004, 2005; Neff et al. 2004).

Compared with conventional histomorphometry, micro-CT has the advantage of being non-destructive, less time-consuming and highly reproducible. Micro-CT is

a method that can provide reliable 2D or 3D morphometric data on bone microarchitecture and bone matrix or material density in a short time. Despite these advantages, conventional histomorphometry is still a useful assessment technique in which cell distribution or dynamic histomorphometry to assess mineral apposition rate and cellular events can be quantified (He et al. 2003; Parfitt et al. 1987). Also, histomorphometry can help to analyze bone samples with implants (Leung et al. 2005), whereas micro-CT images may generate artefacts interfered by metallic materials; therefore, micro-CT and conventional histomorphometry are supplementary but not exclusive. The choice of which technique to use depends on the objectives of the studies.

Screw pull-out test was used to evaluate the mechanical properties of the bone cement in screw fixation, which serves as a functional test to confirm the efficacy of bone cement in enhancing screw fixation in osteoporotic bones. The results of enhanced screw pull-out force in bone cement group echoes the micro-CT analysis that bone cement increases the holding power of osteoporotic bone to implants by increasing the contact surface area. The fact that the failure mode occurred in the bone layer also indicates that the weak link did not lie in the screw-cement and cement-bone interfaces. This might be explained by the high osteoconductivity of the bone cement and reduction in porosity at the screw-cement interface. In this context, to develop non-destructive imaging methods without limitation of the presence of metal implants to monitor quality of bone-biomaterials-implant complex in in vivo fixation, is a useful approach clinically.

Conclusion

This chapter presents a serial of experimental studies using multiple bioimaging technologies and various densitometric approaches to verify the establishment of osteoporotic animal model and the efficacy of bone cement in screw fixation. These assessment techniques provide useful data on BMD, bone microarchitecture, and bone-cement locations within the osteoporotic bone, which can be adapted effectively into many research areas, including studying biomaterials developed for enhancement of osteoporotic fractures. As non-invasive biomedical imaging or densitometric measurements are valuable for longitudinal evaluation of bone quality, in vivo micro-CT may be the trend for further development and clinical application in the near future, which is the focus of other chapters in this book.

References

Anonymous (1993) Consensus development conference: diagnosis, prophylaxis, and treatment of osteoporosis. Am J Med 94:646–650

Blattert TR, Delling G, Dalal PS, Toth CA, Balling H, Weckbach A (2002) Successful transpedicular lumbar interbody fusion by means of a composite of osteogenic protein-1 (rhBMP-7) and hydroxyapatite carrier: a comparison with autograft and hydroxyapatite in the sheep spine. Spine 27:2697–2705

Breusch SJ, Kuhn KD (2003) Bone cements based on polymethylmethacrylate. Orthopaedics 32:41–50

Chan KM, Qin L, Lau MC, Woo J, Au SK, Choy WY, Lee KM, Lee SH (2004) A randomised, prospective study of the Tai Chi Chun exercise on bone mineral density in postmenopausal women. Arch Phys Med Rehab 85:717–722

Cheng JC, Sher HL, Guo X, Hung VW, Cheung AY (2001) The effect of vertebral rotation of the lumbar spine on dual energy X-ray absorptiometry measurements: observational study. Hong Kong Med J 7:241–245

Cummings SR, Melton LJ (2002) Epidemiology and outcomes of osteoporotic fractures. Lancet 359:1761–1767

Dambacher MA, Neff M, Schmitt S, Schacht E, Qin L, Ito M, Zhao YL (2004) Bone structures in vitro and in vivo in animals and in men: a view into the future. J Bone Miner Metab 3:2–7

Dambacher M, Neff M, Haemmerle S, Rizzoli R, Delmas P, Qin L (2005) "XtremeCT" A new dimension in bone microarchitecture evaluation in vivo in humans. Bone 36:S324

Elder S, Frankenburg E, Goulet J (2000) Biomechanical evaluation of calcium phosphate cement-augmented fixation of unstable intertrochanteric fractures. J Orthop Trauma 14:386–393

Goodman SB, Bauer TW, Carter D (1998) Norian SRS cement augmentation in hip fracture treatment. Laboratory and initial clinical results. Clin Orthop 348:42–50

He Y, Sun XC, Chen HQ, Weng LL, Zheng H, Qiu MC (2003) Bone histomorphometry study on lumbar vertebrae microstructure of ovariectomized goats. Chin J Orthop 38:405–408

Ho KS, Chan WM (2003) Falls in elderly: a "clinical syndrome" and a public health issue. Public Health Epidemiol Bull 12:13–17

Ito M, Ohki M, Hayashi K, Yamada M, Uetani M, Nakamura T (1995) Trabecular texture analysis of CT images in the relationship with spinal fracture. Radiology 194:55–59

Lai YM, Qin L, Hung VWY, Chan KM (2005) Regional differences in cortical bone mineral density in the weight-bearing long bone shaft: a pQCT study. Bone 36:465–471

Larsson S, Bauer TW (2002) Use of injectable calcium phosphate cement for fracture fixation: a review. Clin Orthop Relat Res 395:23–32

Leung KS, Siu WS, Cheung NM, Lui PY, Chow DHK, James A, Qin L (2001) Goats as an osteopenic animal model. J Bone Miner Res 16:2348–2355

Leung KS, Siu WS, Li SF, Qin L, Cheung CH, Tam KF, Lui PP (2006) An in vitro optimized injectable calcium phosphate cement for augmenting screw fixation in osteopenic goats. J Biomed Mater Res B Appl Biomater 78:153–160

Lill CA, Fluegel AK, Schneider E (2000) Sheep model for fracture treatment in osteoporotic bone: a pilot study about different induction regimens. J Orthop Trauma 14:559–565

Müller R, Hahn M, Bogel M, Delling G, Rüegsegger P (1996) Morphometric analysis of non-invasively assessed bone biopsies: comparison of high-resolution computed tomography and histologic sections. Bone 18:215–220

Neff M, Dambacher MA, Qin L (2004) Three dimensional bone microarchitecture assessment in vivo: structures and mechanism of bone loss. Osteology 13:S98

Parfitt AM, Drezner MK, Glorieux FH, Kanis JA, Malluche H, Meunier PJ, Ott SM, Recker RR (1987) Bone histomorphometry: standardization of nomenclature, symbols, and units. Report of the ASBMR Histomorphometry Nomenclature Committee. J Bone Miner Res 2:595–610

Qin L (1998) Application of biomedical imaging methods for musculoskeletal tissues studies. In: Cheng JCY et al. (eds) The laureate of the dragon, vol. 2. Williams and Wilkins Asia-Pacific, Hong Kong, pp 199–206

Qin L, Mak AT, Cheng CW, Hung LK, Chan KM (1999) Histomorphological study on pattern of fluid movement in cortical bone in goats. Anat Rec 255:380–387

Qin L, Hung L, Leung K, Guo X, Bumrerraj S, Katz L (2001) Staining intensity of individual osteons correlated with elastic properties and degrees of mineralization. J Bone Miner Metab 19:359–364

Qin L, Au SK, Leung PC, Lau MC, Woo J, Choy WY, Hung WY, Dambacher MA, Leung KS (2002) Baseline BMD and bone loss at distal radius measured by pQCT in peri- and post-menopausal Hong Kong Chinese women. Osteoporosis Int 13:962–970

Qin L, Dambacher MA, Leung PC, Neff M (2003) Fast and slow bone losers: diagnostic and therapeutic implications in osteoporosis. In: Schneider HPG (ed) Menopause: state of the art. Parthenon, New York, pp 1124–1132

Qin L, Fok PK, Lu HB, Shi SQ, Yang L, Leung KS (2006) Low intensity pulsed ultrasound increases the matrix hardness of the healing tissues at bone-tendon insertion: a partial patellectomy model in rabbits. Clin Biomech. 21:387–394

Rauch F, Schoenau E (2001) Changes in bone density during childhood and adolescence: an approach based on bone's biological organization. J Bone Miner Res 16:597–603

Ruegsegger P, Elsasser U, Anliker M, Gnehm H, Kind H, Prader A (1996) Quantification of bone mineralization using computed tomography. Radiology 121:93–97

Sheldon RS (ed) (1994) Orthopaedic basic science. American Academy of Orthopaedic Surgeons, Washington DC, pp 129

Siu WS, Qin L, Leung KS (2003) pQCT bone strength index may serve as a better predictor than bone mineral density for long bone breaking strength. J Bone Miner Metab 21:316–322

Siu WS, Qin L, Cheung WH, Leung KS (2004) A study of trabecular bones in ovariectomized goats with micro-computed tomography and peripheral quantitative computed tomography. Bone 35:21–26

WHO (1994) Report of a WHO study group: Assessment of fracture risk and its application to screening for postmenopausal osteoporosis. WHO Tech Rep Series 843. World Health Organization, Geneva

Wilke HJ, Jungkunz B, Wenger K, Claes LE (1998) Spinal segment range of motion as a function of in vitro test conditions: effects of exposure period, accumulated cycles, angular-deformation rate, and moisture condition. Anat Rec 251:15–19

In Assessment of Fracture Repair

Quality of Healing
Compared Between Osteoporotic Fracture
and Normal Traumatic Fracture

Ke-Rong Dai (✉) and Yong-Qiang Hao

Department of Orthopaedics, Ninth People's Hospital, Shanghai Jiao Tong University,
School of Medicine, 639 Zhizaoju Road, Shanghai, China
e-mail:krdai@163.com

Abstract

The major clinical consequence of osteoporosis in older people is osteoporotic fracture, which is difficult for fixation and poorer prognosis. Quality of life of patients after surgical intervention is largely affected. How the osteoporotic fracture healing differs from those of normal fracture healing or the nature of the characteristics of healing mechanism of osteoporotic fracture and its healing mode, have not been fully understood. In addition, there are no standards available to evaluate the quality of osteoporotic fracture repair, and the present clinical treatment for osteoporotic fracture is generally the same as that used for general traumatic fracture. Our research focused on studying healing mechanism and quality of osteoporotic fracture systemically at cellular, matrix, tissue, and organ levels compared between osteoporotic fracture rats and non-osteoporotic rats. These studies included evaluations of material property, geometrical morphology, microstructure, bone mineral metabolism, bone density, and mechanical strength of callus evaluated at different fracture healing stages. In order to provide above comprehensive information, we employed evaluation technologies, including transmit and polarized microscopy for histomorphometry, dual-energy X-ray absorptiometry (DXA) for bone mineral density (BMD), and mechanical testing. In addition, the results of our histological evaluations indicated both endochondral bone formation and intramembrane bone formation in osteoporotic fracture repair, yet endochondral bone formation and its ossification played a major role in the repair process. As compared with normal fracture healing, osteogenesis and endochondral ossification were delayed, whereas hard callus remodeling was accelerated, i.e., a faster bone turnover resulting in more bone resorption and less bone formation. In addition, the collagen fibers in the hard callus appeared loosely disorganized and irregular with regard to the direction of the principal stress. The abnormal change of the organizational constitution, microstructure, bone mineral metabolism, and bone mass in osteoporotic fracture repair could result in the decrease of its mechanical strength.

Microscopic Assessment of Osteoporotic Fracture Healing

Experimental Design

Eighty 8-month-old female SD rats were randomized into two groups with 40 in each: the osteoporotic fracture model (OFM) and non-osteoporotic controls, i.e., the traumatic fracture model (TFM). All rats of OPFM group were ovariectomized and all rats of TEM group had sham operation. All rats were operated on once again 3 months later to establish fracture model. The right femur was incised to approach the femur via the septum between the anterior and lateral femoral muscle groups. The femur was cut to broken with scalpels in the mid-shaft and was intramedullary reverse fixed with Kirnische needle 1 mm in diameter (Fig. 1; Hao and Dai 1999, 2002). The callus of each rat was examined by both light and/or polarized microscope (Olympus BH-2, Japan) in 5 days and 1, 2, 4, 6, 8, 12, and 16 weeks postoperatively.

Microscopic Observations

The histological process of the fracture healing in both OFM and TFM groups all shared the common and typical repair processes, including inflammatory stage, repair stage, and the remodeling stage. There was some extent of inter-overlapping in the three developmental stages in both groups; among them, the repair stage evolved from the fibrous callus, the cartilaginous callus to the osseous callus.

Five to seven days after fracture, a huge member of cells aggregated around the fracture site and formed the fibrous callus; among them were mesenchymal cells, fibroblasts, granulocytes, and mononuclear macrophages. At this stage, large numbers of neogenetic capillaries appeared. Around the sub-periosteum of the fracture site, the mesenchymal cells proliferated from periosteum and differentiated into
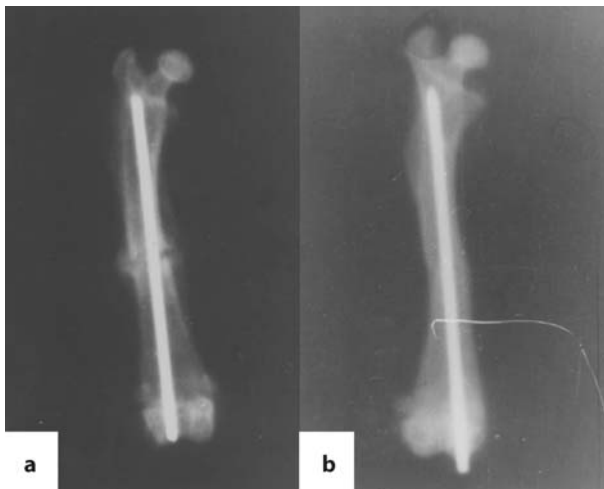
Figure 1 a,b. X-ray of the femur fracture model in rat. **a** 4 weeks. **b** 16 weeks
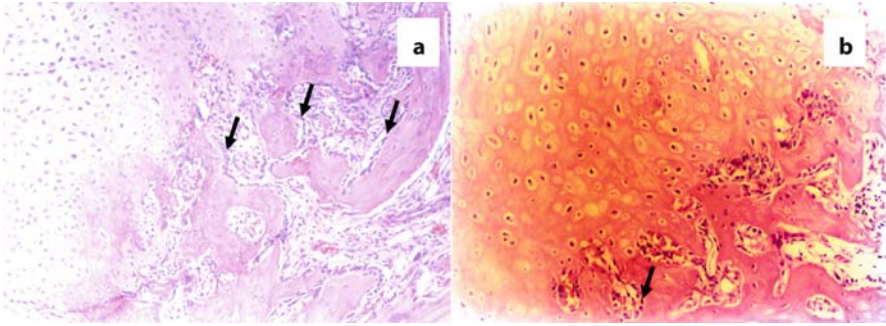
Figure 2 a,b. Representative micrograph of fracture callus at week 2 after fracture (H&E staining: ×100 for both **a** and **b**). **a** From normal fracture group (TFM group): woven bone or immature trabecular bone found around the cartilaginous callus, with numerous osteoblasts lining the surface of the primary trabecular bone (*arrows*). **b** From osteoporotic fracture group (OFM group): immature trabecular bone found around the cartilaginous callus, with less osteoblasts lining on the surface of the primary trabecular bone (*arrow*)

the chondrocytes and the osteoblasts to form woven bone. Comparing with TFM group, the fibrous callus in OFM group was sparse with limited angiogenesis, and the hematoma at the fracture site resorbed slowly.

Two weeks after fracture, the cartilaginous callus formation superseded the fibrous callus and the cartilaginous island appeared in the previous fibrous callus and expended continuously. The chondrocytes around the vessels were of small size and mostly were identified as the round juvenile chondrocytes. With healing over time the chondrocytes around the cartilaginous callus enlarged and part of the cells underwent apoptosis accompanied by formation of woven bone or the primary trabecular
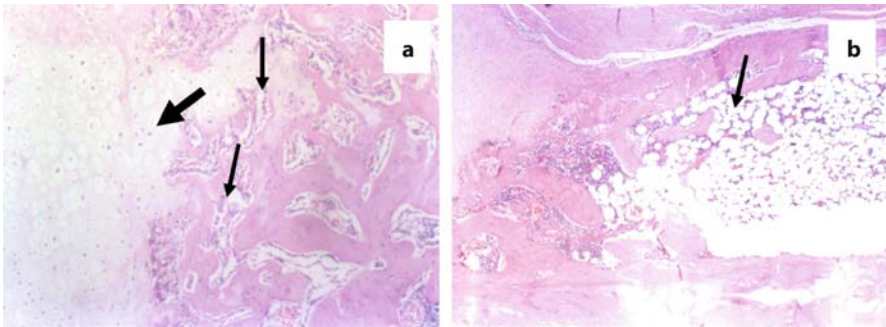
Figure 3 a,b. Representative micrographs of fracture callus at week 6 after fracture (H&E staining: **a**: ×100; **b**: ×40). **a** From normal fracture group (TFM group): hypertrophic chondrocytes found around the cartilaginous callus (*thick arrow*). The cartilaginous callus underwent endochondral ossification and formed woven bone with numerous lining osteoblasts on its surface (*thin arrows*). **b** From osteoporotic fracture group (OFM group): more advanced remodeling of woven bone with widening marrow cavity filled with marrow elements, including more fat cells (*arrow*)
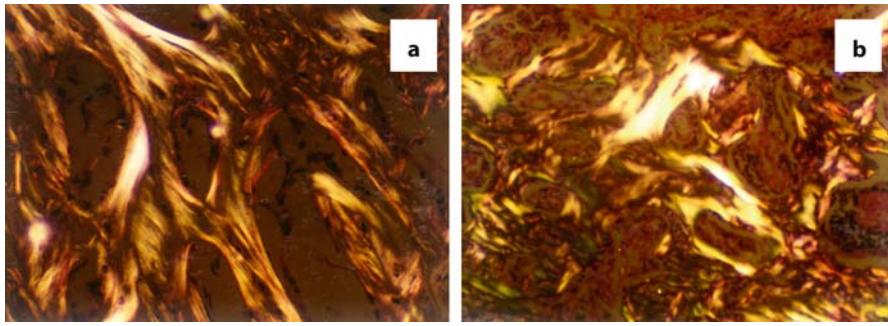
Figure 4 a,b. Representative micrographs of fracture callus at week 6 after fracture observed under polarized microscopy (both **a** and **b**: ×100). **a** Normal fracture group (TFM group): the bone matrix collagens found better aligned. **b** From osteoporotic fracture group (OFM group): less organized than the bone matrix collagens

bone. There were a large number of osteoblasts aligned on the surface of the primary trabecular bone in TFM group (Fig. 2a), whereas in OFM group, less osteoblasts were observed on the surface of the primary trabecular bone (Fig. 2b). Bone marrow elements formed within the marrow cavity within the woven bone or the primary trabecular bone. The observation with the polarized microscope showed that the collagen alignment within the trabecular bone was adapted gradually to the direction of the principal stress in TFM group and the optical refraction was stronger than that found in OFM group. Both the pattern of the trabecular bone and the alignment of collagen fibers within the trabecular matrix in OFM group were irregular.

Six weeks after fracture, the surroundings of the cartilaginous callus were continuously mineralized and replaced by the trabecular bone (woven bone). The chondrocytes previously formed in the primary trabecular bone underwent apoptosis or differentiated and transformed into osteocytes. At the same time, osteoclasts were found to be attaching to the bony surface and "coupled" with the osteoblasts. Both participated in remodeling of the primary bone trabecula into mature trabecula (Fig. 3a). Compared with the TFM group, the bone trabecula resorption in OFM group was faster and more extensive, and bone marrow cavity was formed, which was characterized with trabecular thickening and filled with marrow elements, including a large amount of the marrow fat cells (Fig. 3b). Observation from the polarizer: compared with the OFM group, the thickness of the trabecular bone was uniform in the TFM group and the arrangement direction was identical. The trabecular junction appeared arch and smooth with strong refraction (Fig. 4a). In OFM group, however, the trabecular arrangement was in disorder, i.e., unequal in thickness and in refraction intensity (Fig. 4b).

Sixteen weeks after operation, the soft or cartilaginous callus in the TFM group was gradually replaced by hard or bony callus with woven bone; the latter was then remodeled towards lamellar trabecular bone with collagens aligned to the direction of the principal stress. On the contrary, both the transformation from the cartilaginous callus to the bony callus and from the primary trabecular bone (woven bone)

to the mature trabecular bone (lamellar bone) in OFM group was slower. The mature trabecular bone that had previously formed was mostly resorbed and disappeared.

Discussion

In this study we compared histological differences in healing between normal and osteoporotic fractures. Overall, the repair of osteoporotic fracture was slower but shared the common pathways as normal fracture repair. Similar to a previous study (Sandberg et al. 1993), we also found two main sources of chondrocytes in the cartilaginous callus, one was differentiated from mesenchymal cell linage, and another was the continuous proliferation of the existing chondrocytes. At present, it is usually thought that the former plays the key role in endochondral formation (Sandberg et al. 1989).

The marrow and the periosteum are the important sources of the undifferentiating MSCs. The decrease of estrogen can promote the proliferation of the MSCs between the hematopoietic system in the marrow and the periosteum (Shevde et al. 1996; Jilka et al. 1995; Carl et al. 1993). The "shock effect" of fracture may attract the undifferentiated MSCs to be present around the fracture site and then differentiated into osteoblasts or chondrocytes. The differentiation mode depends on the condition of the local blood supply and the mechanical environment (Anders et al. 1989). In the region close to the fracture ends with poor local blood supply and great stress, the MSCs through the committed chondroprogenitor differentiated as the chondrocyte and formed the cartilaginous callus. After the capillary vessel from the intramembrane callus entering the cartilaginous callus in the periosteum, the cartilaginous osteogenesis was activated (Henricson et al. 1987).

It is noteworthy that during the healing process of the osteoporotic fracture, the bone resorption of the trabecular bone formed from the intra-periosteal osteogenesis and endochondral ossification was remarkably faster than that found in the normal fracture healing, however, with slower and incomplete bone remodeling. After the callus became mature, the woven bone remodeled in a way to adapt the local mechanical requirement. This process was trigged by the osteoclast activation and its "coupling" with the osteoblasts. The osteoclasts are differentiated from the colony forming unit-granulocyte macrophage (CFU-GM), which is produced by the hematopoietic stem cell with the multiple potentialities (CFU-S). In the differentiating process, the uncommitted progenitors proliferated and differentiated and produced the committed osteoclast progenitors; then, it differentiated along the special differentiating way of osteoclast and entered the bone tissue with the vessel movement. Estrogen has been reported to regulate this process through its receptors (Fiorelli et al. 1995) and directly inhibits the functional activity and induces apoptosis (Hughes et al. 1996). The decrease in estrogen can therefore lead to an increase in the osteoclast numbers and enhancement of its functional activity (Shevde et al. 1996). On the other hand, this can also inhibit the proliferation and differentiation of the osteoblasts and the synthesis of the stromatin (Majeska et al. 1994). All these changes may induce bone

loss and the relative deficit of the neogenic bone in the region of the bone absorption, thereby causing poorer healing of the osteoporotic fracture.

In addition, the results of our histological evaluations indicated both endochondral bone formation and intramembrane bone formation in osteoporotic fracture repair, yet the endochondral bone formation and its ossification played a major role in the repair process. As compared with normal fracture healing, the osteogenesis and endochondral ossification were delayed, whereas the hard callus remodeling was accelerated, i.e., a faster bone turnover resulting in more bone resorption and less bone formation. In addition, the collagen fibers in the hard callus appeared loosely disorganized and irregular with regard to the direction of the principal stress.

Histomorphometric Assessment of Osteoporotic Fracture Healing

Static Parameter Measurements and Results

Five rats in each group were killed randomly at postoperative weeks 1, 2, 4, 6, 8, and 12. The callus on the median femur was dissected for fixation in 4% of poly-methanal solution after splashed with natural saline and decalcified in 10% of EDTA solution at pH 7.4 for 3-5 weeks. The solution was then refreshed at 5- to 7-day intervals before dehydration with alcohol and embedding in wax. The specimens were then cut into 5-µm-thick slices and stained with hematoxylon-eosin (H&E) for histomorphometric evaluations of healing callus with VIDAS automatic histomorphometry according to Parfitt's protocol (Parfitt et al. 1987), including (a) trabecular bone volume (TBV), which represents the rate of trabecular bone in overall metaphysical percentage, (b) mean trabecular spacing (Tb.sp) in microns, and (c) mean trabecular plate thickness (MTPT) in microns.

Our measurements showed that the trabecular bone volume (TBV) calculated in group OFM was lower than that calculated in group TFM at all healing time points, with the greatest difference at 12 weeks ($p < 0.05$). The mean trabecular spacing

Table 1. Histomorphometry of fracture callus compared between normal (TFM) and osteoporotic bone (OFM; $n = 5$; data are mean ± SD)

Healing time (weeks)	TBV (µm)		Tb.sp (µm)		MTPT (µm)	
	TFM	OFM	TFM	OFM	TFM	OFM
1	48.7 ± 7.5	50.9 ± 8.8	89.8 ± 23.5	123.0 ± 55.1	58.1 ± 11.3	56.5 ± 18.0
2	46.8 ± 8.8	54.1 ± 7.6	153.6 ± 94.1	157.3 ± 80.0	73.2 ± 33.1	87.4 ± 29.4
4	48.1 ± 2.6	42.3 ± 1.4	133.9 ± 45.4	153.3 ± 44.9	68.6 ± 31.0	78.2 ± 9.2
6	38.7 ± 3.7	24.5 ± 0.4	180.8 ± 41.8	173.2 ± 64.9	94.5 ± 35.5	99.6 ± 33.0
8	37.8 ± 5.3	21.2 ± 5.6	157.4 ± 57.3	180.1 ± 57.2	94.1 ± 24.5	83.0 ± 87.3
12	46.1 ± 5.6*	16.1 ± 10.7	126.2 ± 76.4	186.4±111.9	103.2 ± 32.9	82.6 ± 29.5

*$p < 0.05$ compared between TFM and OFM at the same healing time point

(Tb.sp) and the mean trabecular plate thickness (MTPT) in the OFM group was also lower than that at the latter time point as shown in Table 1.

Bone Dynamic Remodeling and Apposition

For evaluation of bone dynamic remodeling, tetracycline 50 mg/kg and calcein green 20 mg/kg were injected intraperitoneally at 12 and 2 days before killing, respectively. Five rats of each group were killed at 1, 2, 3, and 4 months, postoperatively. The callus specimens were dissected from the adjacent tissues, rinsed with normal saline, and fixed in acetone of 100% for 3 days at 4°. The specimens were then rinsed with running water over night before hydration and de-esterification with increased concentration of ethanol. The specimens were then cleared using dimethylbenzin before sequentially immersion in solution no. 1 composed of 75% of methyl methacrylate and 25% of dimethyl benzine (DBP) for 24 h, and then changes to solution no. 2, which was a combination of solution no. 1 and 2.5 g of benzoyl peroxide (BPO) for 48 h, and finally in solution no. 3 with a combination of solution no. 1 and 6.25 g of BPO for 1-3 days. The embedded specimens were then kept at 50°C over night. After trimming, all the embedded specimens were cut into slices at 15 and 5 μm in thickness with Leica hard tissue microtome. The un-decalcified sections were coated on chromic alum gelatin-coated slides, covered with plastic film and pressed flat, and then kept in an oven at 60°C for 12 h.

The dynamic parameters for bone formation and remodeling were measured by VIDAS histomorphometry under fluorescent microscopy, including the following:

1. Mineral apposition rate (MAR). The ratio of the distance between the twice-marked lines and their time interval (in microns per day). Five visual fields were picked at random under a 10× object glass. The average of three measurements for each pair of marking was used.

2. Fluorescent labeling percentage (LS). By the same method, the percentage rate of the surface length of the double labeling in the overall length of bone surface was measured and calculated. Our findings showed that the MAR of OFM group was higher than that of TFM group at all selected time points ($p < 0.05$ for all), with the

Table 2. Mineral apposition rate (MAR) and percentage fluorescent labeling (LS) of fracture callus compared between normal (TFM) and osteoporotic bone (OFM; $n = 5$; data are mean ± SD)

Healing time (weeks)	MAR (μm/day)		LS (%)	
	TFM	OFM	TFM	OFM
6	1.605 ± 0.815	2.303 ± 0.565	0.564 ± 0.0619	0.457 ± 0.0801
8	2.211 ± 0.239	3.525 ± 1.057	0.558 ± 0.098	0.536 ± 0.0819
12	2.74 ± 0.347[*]	3.846 ± 0.439	0.623 ± 0.0719	0.527 ± 0.0452

[*] $p < 0.05$ compared between TEM and OFM at the same healing time point

greatest difference found at 12 weeks. On the contrary, the LS was lower in the OFM group than in the TFM group (Table 2).

Bone Mineral Status Assessment of Osteoporotic Fracture Healing Using Dual-Energy X-ray Absorptiometry

Experimental Protocol

Forty female 8-month-old SD rats were randomized into osteoporotic fracture model (OFM) group and traumatic fracture model (TFM) group, with 20 for each group. The same surgical intervention was performed as described above. The callus of each rat was then examined by DXA (DPX-L, Lunars) 4, 8, 12, and 16 weeks postoperatively. The energy spectrum of DXA was 38/7 keV with a high voltage stable at ±0.05% and a precision error of 1%.

Five rats in each group were killed at the end of postoperative weeks 4, 8, 12, and 16. The femur specimens were obtained for DXA scanning at 2 cm per stage with the callus as the center and BMD was calculated using a built-in software.

Measurement Results

The BMD values reached peak at 8 weeks and descended thereafter in both groups, faster in group OFM than in group TFM. As compared with week 8 BMD values, the one measured at week 12 was significantly lower ($p < 0.05$; Table 3).

Discussion

The BMD of callus, a quantitative indicator for bone mass in the mineralization of callus, is closely related to its mechanical properties (Alho 1993; Aro et al. 1989). The BMD is decided by the ratio between cartilaginous callus and mature trabecular bone, the degree of mineralization, and the conversion rate of the bone. In the course of the fracture healing, much more cartilaginous callus is produced in rats than in humans (Aro et al. 1989). The extent and degree of the mineralization and absorption of cartilaginous callus have a greater impact on the bone mass in rats. Histologically,

Table 3. Bone mineral density (BMD) of fracture callus compared between normal (TFM) and osteoporotic bone (OFM; $n = 5$; data are mean ± SD, g/cm^2)

Healing time (weeks)	TFM	OFM
4	0.295 ± 0.019[*]	0.287 ± 0.020
8	0.337 ± 0.010	0.338 ± 0.223
12	0.306 ± 0.018[*]	0.272 ± 0.022

[*] $p < 0.5$ compared between TEM and OFM at the same healing time point

the specimens at postoperative week 8 showed an increase of hypertrophic chondrocytes with maximal extended outer diameter. This indicated that extensively and more mineralized cartilaginous callus was the determinant for the increase in BMD. This accounted for the decrease of BMD later at week 16 with absorption and remodeling of the mature and mineralized cartilaginous callus, the lamellar trabecular bone formed, which led to the rapid diminution in its outer diameter. Meanwhile, the decrease in estrogen resulted in an elevated bone turnover (negative balance) and the absorption or removal of mature trabecular bone in great quantity, which was also a factor of decrease in BMD.

Mechanical Properties of Osteoporotic Fracture Healing Callus

Study Design

Forty female 8-month-old SD rats were randomized into two groups osteoporotic fracture model (OFM) group and traumatic fracture model (TFM) group, with 20 rats for each group. Details of the surgical interventions are described above. Animals were killed at postoperative weeks 4, 6, 8, 12, and 16, postoperatively, with a sample size $n = 5$.

Both length and axial or transversal diameters of the femoral fracture callus specimens were measured with a fine caliper. A bone surface of 3×4-cm size on the edge of callus was smoothed with raw sand paper and de-esterified with 100% acetone. When dried, resistance strain gauge (size 1 mm, sensitivity coefficient $2.19 \pm 1\%$, resistance $120 \pm 0.2\Omega$, BF 120-1AA) were stuck on the specimen with contact cement and placed in a universal material strength test machine for torsional tests. The mechanical properties of callus were recorded for analysis.

Findings

Our findings showed that the maximum torsional moment and the modulus of elasticity were higher in the TFM group at both weeks 8 and 12, whereas the maximum angle of torsion was lower at week 16; however, as compared with the OFM group, the modulus of elasticity was lower in the TFM group, whereas the maximum moment of torsion and the maximum angle of torsion was higher (Table 4).

Table 4. Mechanical properties of bone compared between normal (TFM) and osteoporotic bone (OFM; $n = 5$; data are mean $\pm$ SD)

Healing time (weeks)	Modulus of elasticity ($g \times cm^2/deg$)		Maximum moment of torsion ($g \times cm$)		Maximum angle of torsion (deg/cm)	
	TFM	OFM	TFM	OFM	TFM	OFM
8	700 ± 239	323 ± 119	3200 ± 346	3150 ± 1140	3.1 ± 0.9	8.4 ± 5.6
12	445 ± 132	156 ± 51	3600 ± 759	2800 ± 346	9.5 ± 3.4	11.9 ± 9.1
16	203 ± 40	281 ± 26	5400 ± 1201	3400 ± 572	14.8 ± 5.7	9.7 ± 6.6

Discussion

The poorer mechanical properties found in the osteoporotic healing callus may be well explained by both BMD data and histological findings, i.e., inferior composition in organic matrix, especially collagens in callus. In fibrous callus, the early stage in fracture healing, the collagen in the callus is predominantly type III (Ashhurst 1990; Stephen et al. 1995; Sandberg et al. 1989). In the cartilaginous callus stage following the fibrous callus formation, however, the collagen was reported predominantly type II (Ashhurst 1990; Stephen et al. 1995), secreted by chondrocytes, which later became hypertrophic and secreted type-X collagen that was closely related to the mineralization of cartilage (Hiltunen et al. 1993). With the progress of endochondro-ossification, type-II collagen decreased and type-I collagen secreted by osteoblasts became the predominant structural protein and about 90% of overall organic components in the new bone, which demonstrated stronger resistance to mechanical loading with healing over time (Ashhurst 1990; Stephen et al. 1995). This also suggested that the maturity of the callus could be evaluated by determining the ratio of the different types of collagens. In addition, the orientation of collagen fiber arrangement is also important, which defines a position for hydroxyapatite to deposit. The ideal mechanical properties of bone depend on the highly organic combination of the types of collagens and the orientation of collagen fiber arrangement (Ashhurst 1990).

Conclusion

The present study employed comprehensive and objective evaluation on osteoporotic fracture repair using both conventional and polarized microscope for study bone histomorphology, The DXA for evaluating bone mineral statues, and mechanical test for investigating integral healing properties of healing callus. Our study results indicated that both endochondral bone formation and intramembrane bone formation acted in the osteoporotic fracture healing, with the former playing a major role. But during osteoporotic fracture healing process, endochondral bone formation decelerated, and simultaneously, bone callus tissue remodeling (bone resorption more than bone formation) accelerated and resulted in decline of callus quality. The abnormal change of the organizational constitution, microstructure, bone mineral metabolism, and bone mass in osteoporotic fracture repair could result in the decrease of its mechanical strength.

References

Alho A (1993) Mineral and mechanics of bone fragility fractures. A review of fixation methods. Acta Orthop Scand 64:227–232

Anders H (1989) Current concepts of fracture healing. Clin Orthop Relat Res 249:265–284

Aro HT, Wippermann BW, Hodgson SF (1989) Prediction of properties of fracture callus by measurement of mineral density using micro-bone densitometry. J Bone Joint Surg (Am) 71:1020–1030

Ashhurst DE (1990) Collagens synthesized by healing fractures. Clin Orthop Relat Res 225:273–283

Carl CD, Lis M, Birgit S (1993) Cortical bone mass, composition, and mechanical properties in female rats in relation to age, long-term ovariectomy, and estrogen substitution. Calcif Tissue Int 52:26–33

Fiorelli G, Gori F, Petilli M (1995) Functional estrogen receptors in a human preosteoclastic cell line. Proc Natl Acad Sci USA 92:2672–2676

Hao Y, Dai K (1999) An experimental study of vascular endothelial growth factor (VEGF) expression in fracture healing. Chin J Orthop 19:683–686

Hao YQ, Dai KR (2002) The design and establishment of a model of experimental osteoporotic fracture. Orthop J Chin 9:569–572

Henricson A, Hulth A, Johnell O (1987) The cartilaginous fracture callus in rats. Acta Orthop Scand 58:244–248

Hiltunen A, Hannu TA, Eero V (1993) Regulation of extracellular matrix genes during fracture healing in mice. Clin Orthop Relat Res 297:23–32

Hughes DE, Dai A, Tiffee JC (1996) Estrogen promote apoptosis of murine osteoclasts mediated by TGF-beta. Nat Med 2:1132–1136

Jilka RL, Passeri G, Girasole G (1995) Estrogen loss upregulates hematopoiesis in the mouse: a mediating role of IL-6. Exp Hematol 23:500–506

Majeska RJ, Ryaby JT, Einhorn TA (1994) Direct modulation of osteoblastic activity with estrogen. J Bone Joint Surg (Am) 76:713–721

Parfitt AM, Drezner MK, Glorieux FH (1987) Bone histomorphometry standardization of nomenclature symbols and units. Report of the ASBMR Histomorphometry Nomenclature Committee. J Bone Miner Res 2:595–610

Sandberg M, Aro H, Multimaki P (1989) In situ localization of collagen production by chondrocytes and osteoblasts in fracture callus. J Bone Joint Surg (Am) 71:69–77

Sandberg M, Hannu TA, Eero IV (1993) Gene expression during bone repair. Clin Orthop Relat Res 289:292–312

Shevde NK, Pike JW (1996) Estrogen modulates the recruitment of myelopoietic cell progenitors in rat through a stromal cell-independent mechanism involving apoptosis. Blood 87:2683–2692

Stephen HL, Yang RS, AL-Shaikh R (1995) Collagen in tendon, ligament, and bone healing. Clin Orthop Relat Res 318:265–278

Monitoring Fracture Healing Using Digital Radiographies

Gang Li and Mark Murnaghan

The Department of Orthopaedic Surgery, Queen's University Belfast,
Musgrave Park Hospital, Stockman's Lane, Belfast, BT9 7JB, UK
e-mail:g.li@qub.ac.uk

Abstract

Non-invasive imaging of fracture healing is a crucial step in making clinical decisions for optimal outcomes and minimizing risks of fixator removal. Although orthogonal routine radiography remains the most cost effective imaging technique to follow all aspects of fracture healing, it is not reliable to predict bony union or the quality or quantity of the regenerating bone, since an estimated 40% increase in radiodensity is needed to visualize a radiological change, and radiographic changes do not always correlate to mechanical stiffness. Supplemental techniques, including digital radiography, mechanical testing for bone strength and stiffness, dual-energy X-ray absorptiometry (DXA) for bone mineral density (BMD), quantitative computed tomography (QCT) for density and cortical continuity, ultrasound for cyst detection and Doppler or angiography for assessing local blood flow and vascularity, have all been used clinically. Among the methods, digital radiography is a useful, cost-effective and relatively accurate means in the evaluation of new bone formation with time during fracture healing. In animal models of fracture healing, histological data, not the mechanical stiffness of the fracture, showed a positive correlation with the digital radiographic assessment data (relative bone density). The advantages of using digital radiography are the minimal expense and dynamic observation of the healing process through sequential radiographies. The bone-healing qualities can be assessed through the estimated relative bone (mineral) density using phantoms. There is a burning need for a quantitative measure of fracture healing in long bone fractures treated by intramedullary nailing. As there is no prospect of a mechanical measure due to the load-sharing design of the fracture/nail construct, radiological imaging has to be the starting point. After normalization, calibration and registration of serial images, a combination of functional images are be used to monitor the changing mineral content of the tissues in and around the fracture; however, due to its 2D nature, the digital radiographies need to be taken in a standard fashion to allow sequential comparison, and it should be used as a complementary, rather than an absolute, measurement for fracture healing.

Fracture Healing Animal Model

A fracture model is a system employed to study fracture healing, which is of relevance to human fracture healing as encountered in medical practice. The most representative (valid) model would therefore be a human fracture; however, the high validity of a human fracture model must be balanced against poor reliability due to extensive variation between cases in clinical practice. At the opposite extreme, cell culture models are much more reliable but are deficient in validity as a representation of the whole fracture-healing process. Between these extremes lie models in various species and sizes of animal, which offer the possibility of adequate numbers of reasonably similar cases of fracture healing occurring in a whole-organism context, in other words, a balance between reliability and validity.

Model reproducibility is essential for valid investigation and comparison of fracture healing. Several small and large animal models are reported for the investigation of fracture repair in mice (Bunn et al. 2004; Connolly et al. 2003; Li et al. 2005), rats (Bonnarens and Einhorn 1984; Greiff 1978; Olmedo 1994), rabbits (Critchlow 1995), sheep (Claes et al. 1998), dogs (Wu et al. 1984) and goats (Welch et al. 1998). All investigations included variation of important influences on bone repair such as the nature of the fracture, its stability, mechanical stress environment, the fixation device applied and success of fracture reduction. Small animals, such as the mouse, are attractive candidates for investigating bone healing, particularly for studies focused on molecular questions, because of the availability of gene knockouts, antibodies and gene probes (Metsaranta et al. 1991). An externally fixated murine femoral osteotomy model has been developed, validated and used to study various aspects of fracture healing (Bunn et al. 2004; Connolly et al. 2003; Li et al. 2005; Murnaghan et al. 2005).

Monitor Digital Radiographies in Animal Model of Fracture Healing

Standardization of Taking Digital Radiographies

In order to obtain standardized digital radiography, a standardized protocol has to be set up for each study. For instance, we used Faxitron MX-20 digital radiography system for the purposes of taking all X-rays of our animal studies (Fig. 1). Before a day surgery was begun, the machine was turned on and calibrated by taking a series of

Figure 1. Faxitron M20 digital radiography system

eight X-rays (26 kV, 10 ms) to ensure normalization of exposure of radiation. At the end of the surgical procedure (or following induction of a light general anaesthesia for X-rays taken from day 4 onwards), an X-ray jig (Fig. 2) was attached to the cross bar through the two perpendicular portals. This jig contained an aluminium step phantom and allowed for normalization of X-ray penetration between animals and across time points. It also controlled for rotation in all planes, therefore enabling comparison of changes at the fracture within animals.

For taking the X-ray, the animal is carefully placed prone inside the X-ray compartment with its left leg held flexed and in external rotation such that a lateral radiograph of the femur can be taken. The phantom and jig are held flat to the plate using an overlying weight and a crosshair laser is used to centre the area of interest such that a repeatable film may be obtained and comparisons between subsequent pictures can be possible (Fig. 3). The distance from the beam to the plate remains the same throughout the experiment (e.g. 12 cm), and X-rays are taken using a fixed set of exposure setting, such as 24 KPa for 3 s for the mouse. Digital X-rays are then saved in the source computer in the operating theatre as raw data files (*.dat).
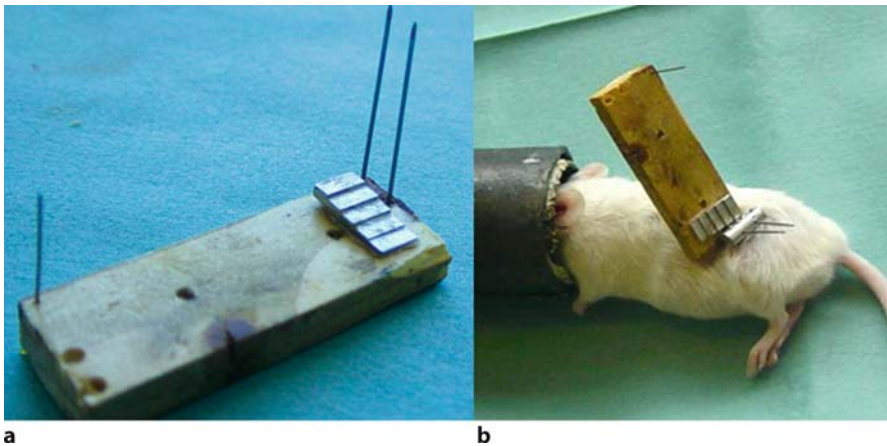
Figure 2. a X-ray jig for mouse fracture model. **b** Mouse with external fixator and the X-ray jig immediately before digital radiography being taken
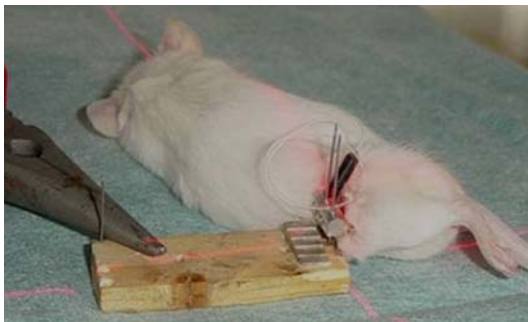
Figure 3. Standardization of the X-ray position. The phantom and jig is held flat to the plate using an overlying weight and a crosshair laser is used to centre the area of interest such that a repeatable film may be obtained and comparisons between subsequent pictures is possible

Analysing Digital Radiographies

The raw data files of the digital radiographies are subsequently analysed using the freely available image analysis software from the University of Texas Health Science Centre San Antonio Dental School (http://ddsdx.uthscsa.edu/). Following several pilot studies into methods of analysis of the data, two standardized techniques are employed for analysing all X-rays. Both methods use the assumption that increasing bone density equates to an increase in pixel density on the radiographs. In each method the bone density at the fracture gap is measured and changes at the site compared across time points and also across drug groups.

The first method is referred to as the "line method". Three parallel lines, 75 pixels in length and centred on the fracture gap, are drawn parallel to the axis of the femoral shaft (Fig. 4). A mean value for each of the 75 points along the femur is calculated from the three lines (Fig. 5a,b). The variances in pixel density of the femur as you pass proximally to distally can then be assessed and plotted as a line graph of pixel density against distance. The 75-pixel length is then divided into three equal 25-pixel sections comprising areas of "normal" bone adjacent to the fracture both proximally and distally alongside a 25-pixel length comprising the fracture gap itself (Fig. 5c). The mean pixel density of the adjacent areas of bone is calculated (solid line) and the difference to this mean (dotted line) for the central section comprising the fracture gap is then calculated from the AUC (shaded area) in Fig. 5d. A comparison can be made as to how the bone content at the fracture gap changes over time. Initially, there is relatively less bone content at the fracture gap, but this becomes positive as callus is laid down during the repair process.

The second method of density assessment is referred to as the "area method" and is performed by measuring the mean pixel density of bone at the fracture gap itself (Fig. 6). Using the image analysis software the mean pixel density of a standardized rectangle centred over the fracture gap approximately 0.5 mm in diameter and extending to the inner edge of the cortices is measured. Alterations in bone density due to variances in X-ray exposure are accounted for by standardization to the alu-
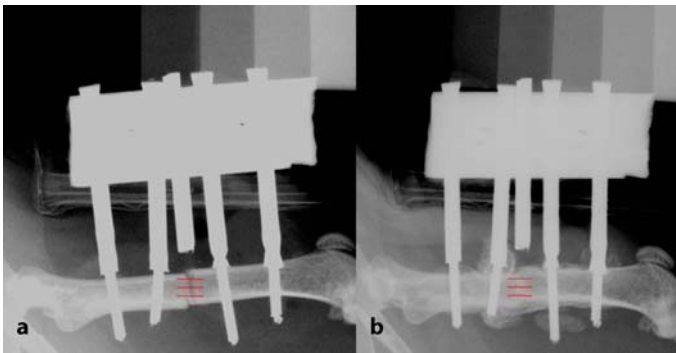
Figure 4 a,b. Mouse femoral fracture digital X-rays shows lines for density analysis at day 0 (**a**) and day 32 (**b**) following fracture
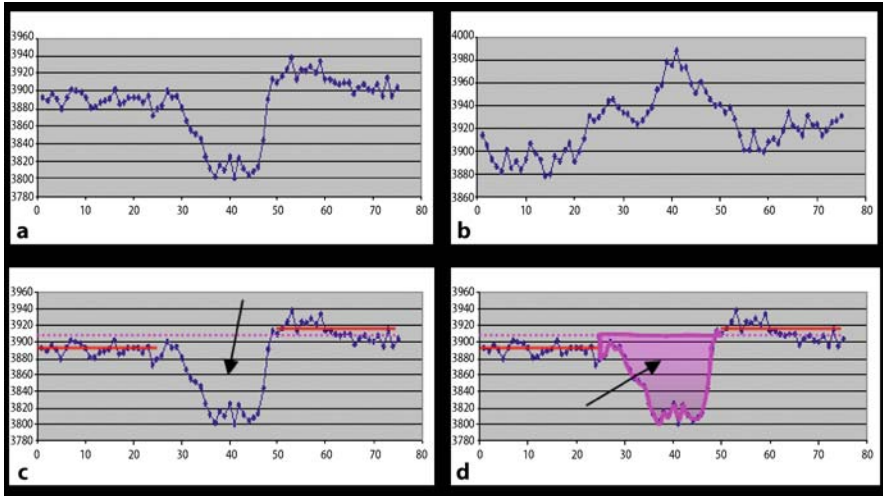
Figure 5 a–d. Line plots of density measurement from a raw data file of digital radiography at day 0 of fracture (**a**) and at day 32 post-fracture (**b**). **c** The 75-pixel length is then divided into three equal 25-pixel sections comprising the areas of "normal" bone adjacent to the fracture both proximally and distally alongside a 25-pixel length comprising the fracture gap itself (*arrow*). **d** The mean pixel density of the adjacent areas of bone is calculated (*solid line*) and the difference to this mean (*dotted line*) for the central section comprising the fracture gap is then calculated from the area under the curve (*shaded area, arrow*)
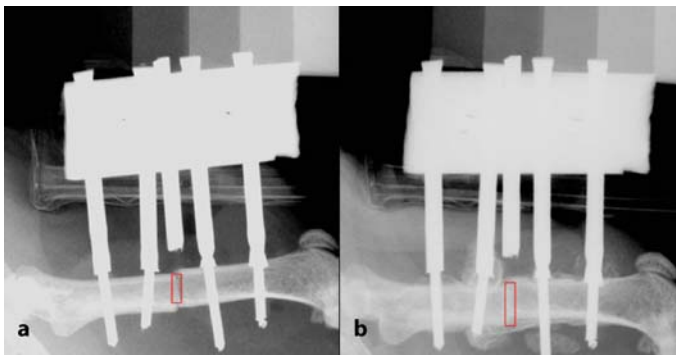
Figure 6 a,b. Density assessment is referred to as the "area method". **a** *Boxed area* represents fracture gap at day 0 of fracture. **b** The *boxed area* represents fracture gap at day 32 following fracture

minium phantom attached to the X-ray jig. The line method also utilizes an internal method of standardization as changes in density are presented as a ratio to the normal femur such that any changes in X-ray exposure will affect both the fracture gap and adjacent normal bone equally.

Reliability of the Digital Radiography Measurement

The intra-observer correlation analysis for the digital radiographic analysis has suggested that the mechanisms of deriving data values and the subsequent analysis of those values are highly repeatable with very low levels of intra-observer errors being observed. By using two independently derived variables across each of the outcome measures [digital X-ray, AUC and region of interest (ROI)]; biomechanical testing, peak loads and stiffness), we have been able to correlate the results both within each outcome measure (i.e. peak load with stiffness; AUC with ROI; Fig. 7a) and across outcome measures (i.e. AUC with histology, AUC with rigidity, etc.; Fig. 7b,c). It has demonstrated that these outcomes correlate very well with strong positive correlations seen both within each of the outcomes (illustrated are ROI with AUC; Fig. 7a); however, there are no significant associations between the day-24 X-ray and biomechanical data. At day 32, however, interestingly there is a strong negative association between the AUC X-ray data and the stiffness of the femurs (Spearman test: $R = -0.687$; $p = 0.010$). The validity of the radiological outcomes used in demonstrating real changes across the fracture gap density between the control and experimental fracture animals (Fig. 8). The technique is capable of differentiating between the changes in the fracture gap density between the two groups of animals, it is also sensitive enough to identify the more subtle decrease in the sham-group density profile (Fig. 8).

Clinical Considerations of Digital Radiography Analysis

Clinical Needs

Orthopaedic surgery has great need of objective and quantitative measures of fracture healing, especially in the reputedly unsolved tibial shaft fracture (Aronson and Shin 2003). In intramedullary nailed fractures stiffness measurements are not possible, which leaves radiological assessment as the only realistic way to monitor the progress of healing. Our pilot study has evaluated the bone mineral density (BMD) of test samples by using digital X-ray images which have been calibrated with a hydroxyapatite reference phantom. Our results compare favourably to results on the same test samples evaluated by DXA, the current gold standard of BMD evaluation. We have also performed preliminary analysis of serial images of nailed tibial fractures that have progressed to union (Fig. 9). The use of imaging phantoms is a common method of evaluating image quality in the clinical setting. These evaluations rely on a subjective decision by a human observer with respect to the faintest detectable signal(s) in the image. Because of the variable and subjective nature of the human-observer scores, the evaluations manifest a lack of precision and a potential for bias. The advantage of digital imaging systems with their inherent digital data provides the opportunity to use techniques that do not rely on human-observer decisions and thresholds (Gagne et al. 2003, 2006).
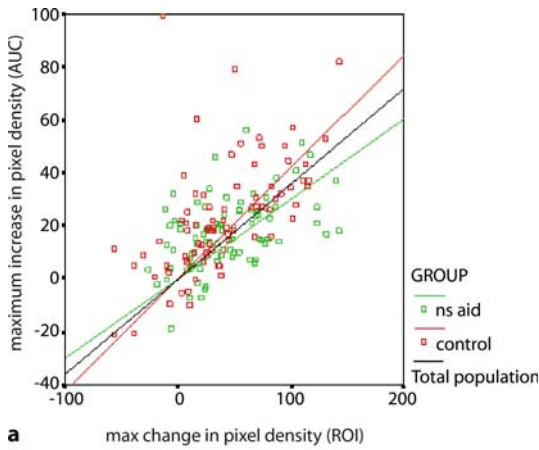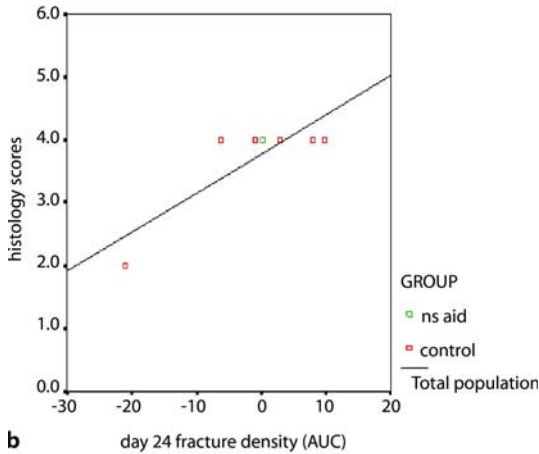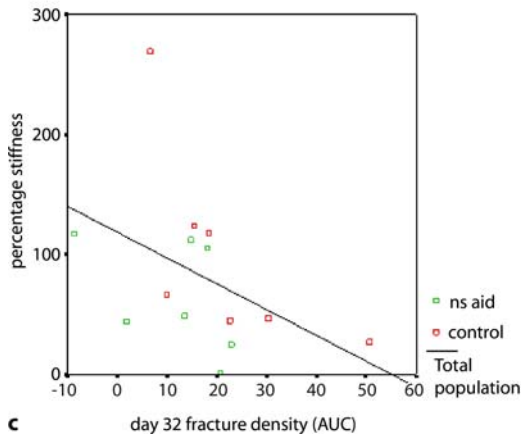
Figure 7 a–c. a Comparisons made between the two methods of radiological assessments, i.e. the area under the curve (AUC) and region of interest (ROI) modalities. To assess this, the maximum change in pixel density from day 0 for each modality is used. Scatter plot of data from AUC and ROI analysis shows a strong correlation between the two methods. **b** At day 32, there is a significant correlation noted between the histology scores and relative fracture density measured from the digital radiographies (Spearman's correlation; $R = 0.626$; $p = 0.013$). **c** Correlations across radiological and biomechanical data produced few statistically significant results. There are no significant associations between the day-24 X-ray and biomechanical data. At day 32, however, there is a strong negative association between the AUC X-ray data and the stiffness of the femurs (Spearman test: $R = -0.687$; $p = 0.010$)
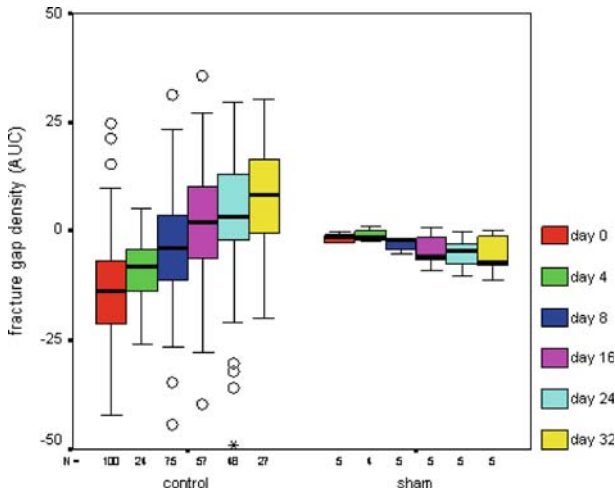
Figure 8. Digital radiography analysis shows changes in the fracture gap density in the two groups (control is the fracture group and sham is the group with fixator but no fracture). The measurement is sensitive enough to identify the more subtle decrease in the sham-group density profile. In the fracture group, the density of the fracture gap at day 16 reaches its peak
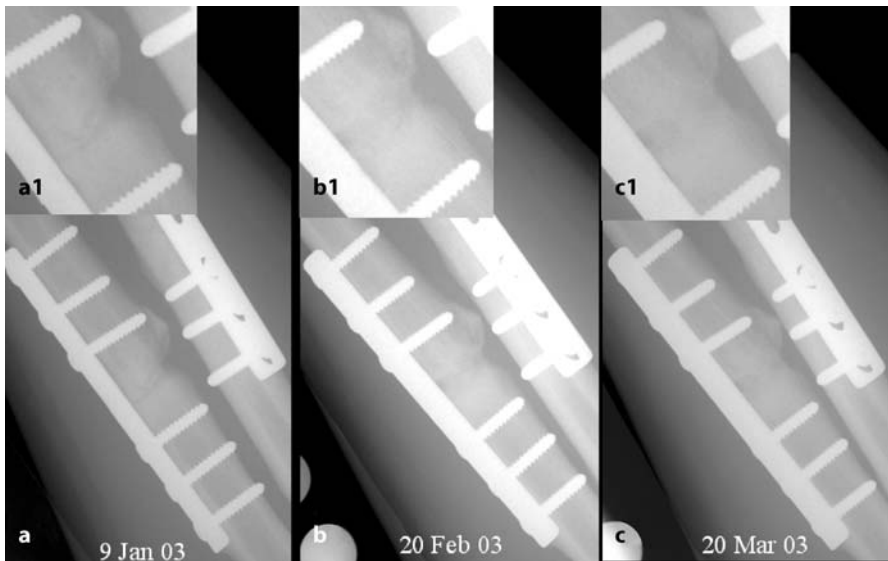
Figure 9 a–c. Serial digital radiographies obtained from a tibial fracture patient with standardised X-ray jig over a 3-month period (**a–c**), showing the progress of fracture healing. *a1–c1* close-ups of the fracture gap in **a–c**

Considerations for Clinical Applications

In clinical practice, before the serial digital radiographies can be used for comparison purposes, the digital images have to be calibrated, normalized and registered. Image registration may be achieved firstly by standardizing the geometry during acquisition of the image using a position control device (Fig. 10), and subsequently by

Figure 10. X-ray jig (*solid arrow*) is applied to control the standard position of the limb for taking X-ray, and settings on the jig (for the limb position and angles) are recorded for each patient and used at subsequent visits. Hydroxyapatite phantoms (*shaded arrow*) are placed on the digital X-ray cassette for measuring relative density

using computer algorithms to match the images to subpixel accuracy. There are still some technical challenges ahead, such as scatter removal via deconvolution and soft tissue removal with beam-hardening correction. Deconvolution is the mathematical process that allows reconstruction of the desired image from the actual radiograph. Once the registration of the image series is completed, the resultant serial images are analysed using functional imaging, morphological description, and 3D reconstruction from two orthogonal views. There is ongoing work in this filed to perfect and standardize the techniques before they can be applied reliably (Gagne et al. 2003; Hazelwood and Burton 2006; Siewerdsen et al. 2006). Nevertheless, animal work has proved that digital radiography can be used as a tool for monitoring fracture healing. Due to the 2D nature of radiography, digital radiographies need to be taken in a standard fashion to allow meaningful sequential comparison, and the facilities for digital radiography follow-up of human fracture healing must be developed with an experienced radiologist, and it is only recommended where this possibility exists. Finally, in animal models of fracture healing, histological data, not the mechanical stiffness of the fracture, show a positive correlation with the digital radiographic assessment data (relative bone density), suggesting that the radiographies shall always be used as a complementary tool in conjunction with clinical and other means of assessment of fracture healing.

Conclusion

Digital radiography is a useful, cost-effective and relatively accurate means of evaluating and following new bone formation during fracture healing. It allows continuous assessment of the healing process through sequential radiographies. In animal models of fracture healing, histological data, but not the mechanical stiffness of the fracture, showed a positive correlation with the digital radiographic assessment data such as relative bone density. The bone-healing qualities can be assessed through the estimated relative bone (mineral) density using phantoms; however, due to its 2D nature, the digital radiographies need to be taken in a standard fashion to allow

sequential comparison, and it should be used as a complementary? Rather than an absolute-measurement for fracture healing.

References

Aronson J, Shin HD (2003) Imaging techniques for bone regeneration analysis during distraction osteogenesis. J Pediatr Orthop 23:550–560

Bonnarens F, Einhorn TA (1984) Production of a standard closed fracture in laboratory animal bone. J Orthop Res 2:97–101

Bunn JR, Canning J, Burke G, Mushipe M, Marsh DR, Li G (2004) Production of consistent crush lesions in murine quadriceps muscle: a biomechanical, histomorphological and immunohistochemical study. J Orthop Res 22:1336–1344

Claes LE, Heigele CA, Neidlinger-Wilke C, Kaspar D, Seidl W, Margevicius KJ, Augat P (1998) Effects of mechanical factors on the fracture healing process. Clin Orthop Relat Res 355 (Suppl): S132-S147

Connolly CK, Li G, Bunn JR, Mushipe M, Dickson GR, Marsh DR (2003) A reliable externally fixated murine femoral fracture model that accounts for variation in movement between animals. J Orthop Res 21:843–849

Critchlow MA, Bland YS, Ashhurst DE (1995) The effect of exogenous transforming growth factor-beta 2 on healing fractures in the rabbit. Bone 16:521–527

Gagne RM, Boswell JS, Myers KJ (2003) Signal detectability in digital radiography: spatial domain figures of merit. Med Phys 30:2180–2193

Gagne RM, Gallas BD, Myers KJ (2006) Toward objective and quantitative evaluation of imaging systems using images of phantoms. Med Phys 33:83–95

Greiff J (1978) A method for the production of an undisplaced reproducible tibial fracture in the rat. Injury 9:278–281

Hazelwood S, Burton D (2006) Images in clinical medicine. N Engl J Med 354:e6

Li G, Bunn JR, Mushipe MT, He Q, Chen X (2005) Effects of pleiotrophin (PTN) over-expression on mouse long bone development, fracture healing and bone repair. Calcif Tissue Int 76:299–306

Metsaranta M, Toman D, De Crombrugghe B, Vuorio E (1991) Specific hybridization probes for mouse type I, II, III and IX collagen mRNAs. Biochim Biophys Acta 1089:241–243

Murnaghan M, McIlmurray L, Mushipe MT, Li G (2005) Time for treating bone fracture using rhBMP-2: a randomised placebo controlled mouse fracture trial. J Orthop Res 23:625–631

Olmedo ML, Weiss AP (1994) An experimental rat model allowing controlled delivery of substances to evaluate fracture healing. J Orthop Trauma 8:490–493

Siewerdsen JH, Daly MJ, Bakhtiar B, Moseley DJ, Richard S, Keller H, Jaffray DA (2006) A simple, direct method for X-ray scatter estimation and correction in digital radiography and cone-beam CT. Med Phys 33:187–197

Welch RD, Jones AL, Bucholz RW, Reinert CM, Tjia JS, Pierce WA, Wozney JM, Li XJ (1998) Effect of recombinant human bone morphogenetic protein-2 on fracture healing in a goat tibial fracture model. J Bone Miner Res13:1483–1490

Wu JJ, Shyr HS, Chao EY, Kelly PJ (1984) Comparison of osteotomy healing under external fixation devices with different stiffness characteristics. J Bone Joint Surg Am 66:1258–1264

Fracture Callus Under Anti-resorptive Agent Treatment Evaluated by pQCT

Yong-Ping Cao[1], Satoshi Mori[2], Tasuku Mashiba[2], Michael S. Westmore[3], and Linda Ma[3]

[1] Department of Orthopedic Surgery, First Hospital of Peking University, Beijing 100034, China
   e-mail: caoyp04@yahoo.com.cn
[2] Department of Orthopedic Surgery, School of Medicine, Kagawa University, Kagawa, Japan
[3] Lilly Research Laboratories, Indianapolis, IN 46285, USA

Abstract

Effects of estrogen, raloxifene, and alendronate on fracture healing were evaluated by a peripheral quantitative computed tomography (pQCT) in an osteoporotic fracture rat model. Three-month-old ovariectomized (OVX; except sham-operated controls) Sprague-Dawley rats were pretreated with vehicle (sham and OVX controls), $0.1\,\text{mg/kg day}^{-1}$ estrogen (17α-ethynyl estradiol), $1\,\text{mg/kg day}^{-1}$ raloxifene, or $0.01\,\text{mg/kg day}^{-1}$ alendronate for 4 weeks before fracture induction. At this point, the pre-fracture groups were killed while transverse osteotomy was performed at the midshaft of both femora in the remaining animals and kept for 6 weeks with drug treatment, and then killed 16 weeks after fracture induction. Excised femora and fracture calluses were analyzed by high-resolution pQCT. At 6 weeks after fracture, the alendronate and OVX groups showed larger calluses at a larger cross-sectional moment of inertia (CSMI) than that of other groups. At 16 weeks after fracture, the calluses in OVX rats were significantly smaller than those observed at 6 weeks, whereas the calluses treated with alendronate did not change in size; therefore, calluses in OVX rats without drug treatment remodeled towards the original geometry in the femoral midshaft faster than drug-treated rats, and on the contrary, the fracture calluses in rats treated with alendronate were the slowest. In conclusion, OVX-induced higher bone turnover and resulted in the fastest remodeling of fracture callus, which was, however, delayed under alendronate treatment. Estrogen and raloxifene treatment showed intermediate callus remodeling between OVX and sham.

Introduction

Osteoporosis is a relatively common disease of postmenopausal women. Antiresorptive agents (estrogen, selective estrogen receptor modulators known as SERMs, and bisphosphonates) are currently available therapies used in the treatment of postmenopausal osteoporosis (Delmas et al. 1997; Grese and Dodge 1998; Ettinger et al.

1999; Sato et al. 1999). They all have a role in preventing the loss of bone by rapidly suppressing the osteoclastic resorption of bone (Bergstrom et al. 2000); however, inhibition of bone resorption has been shown to be followed by a secondary, but powerful, suppression of bone formation activity in rats and women (Fisher et al. 2000; Rodan and Fleisch 1996; Russell and Rogers 1999). The dual suppression of both bone resorption and formation activity results in a substantial reduction in bone turnover.

In the past, emphasis has been largely on the inhibition of fracture incidence; however, with the wide use of anti-resorptive agents, recent attention has been focusing on whether these drugs are deleterious to fracture healing (Hyvonen et al. 1994; Lenehan et al. 1985; Odvina et al. 2005; Pizones et al. 2005). Since osteoporotic patients are prone to fracture, and bone resorption and callus remodeling play an important role in the process of fracture repair, the objective of this study was to ascertain what effect they might have on the ability of the skeleton to repair fractures that might occur during osteoporotic treatment. These data may help to answer the question as to whether or not osteoporotic patients undergoing antiresorptive therapy should consider discontinuing treatment after sustaining a non-traumatic or osteoporotic fracture.

Previous studies showed complex effects of bisphosphonates on fracture repair. A study of the effects of alendronate on fracture healing in dogs (Peter et al. 1996) revealed that fracture calluses were approximately two to three times larger in alendronate-treated dogs compared with controls 16 weeks after a surgically induced middiaphyseal fracture of the right radius. The authors concluded that alendronate treatment before or during fracture healing, or both, resulted in no adverse effects on the union, strength, or mineralization of the callus in mature beagle dogs.

A fracture repair study in humans with Colles' fracture (Van der Poest Clement et al. 2000) showed that bone loss was induced by immobilization of the fracture and adjacent sites. The authors concluded that the bone mineral density (BMD) of the distal radius decreased significantly in the 6 months after fracture and the resulting deficit remained evident at least 1 year after fracture. They found that this bone loss could be prevented by administration of alendronate. The authors stated that fracture healing was excellent during alendronate treatment, but they did not explicitly evaluate and discuss the effects of alendronate on the fracture callus.

Recently, another bisphosphonate, incadronate, was shown to induce enlarged callus but also caused a significant delay in the remodeling process in the fractured femora in rats (Li et al. 1999, 2000, 2001). This delay persisted 49 weeks after fracture. The controversial implications of these studies are that incadronate inhibits the latter stages of the repair process. Fleisch (2001) suggested that strength of the callus was of paramount importance, and that the delay in resorption of the callus was of little consequence, as the organism was able to compensate for any negative effect of the drug on callus composition by alteration of the geometry; however, other investigators (Nyman et al. 1993; Nakamura et al. 1998; Chao et al. 1998) suggested that the process of fracture healing might be considered complete when the fracture line was no longer visible radiologically, and the anatomical architecture and mechanical strength was restored. Li et al. (1999, 2000, 2001) showed that incadronate did not hamper callus strength but did delay radiographic reunion and restoration of nor-

mal architecture. Because incadronate is not currently available, the clinical relevance of these studies is unknown. For this reason, we elected to evaluate the influence of alendronate on fracture callus in the current study.

The role of estrogen in fracture healing is not well understood. A study in New Zealand rabbits (Monaghan et al. 1992) noted the presence of estrogen receptors in the callus. A bimodal distribution of receptors was noted with peaks at days 3 and 16 after fracture. The highest concentration of receptors was noted during endochondral ossification, suggesting a beneficial role for estrogen-stimulated osteoblast differentiation and endochondral ossification in bone regeneration after fracture. To date, the effect of SERMs on the process of fracture healing has not been studied. In the current study, the effects of raloxifene on fracture healing were also evaluated to ascertain possible effects on fracture repair compared with two other currently available osteoporosis therapies.

Materials and Methods

Our study was conducted in 3-month-old OVX Sprague-Dawley rats which were pretreated for 4 weeks prior to establishment of fracture model at both femora and then allowed to heal under treatment for 6 or 16 weeks prior to killing. In this chapter we show the results of fracture callus evaluated by pQCT at the fracture plane and extension region (half callus).

Grouping and Dosing Regimens

Virgin Sprague-Dawley rats (n = 66.2 months of age; Japan SLC, Hamamatsu, Japan) were acclimated for 1 month and housed in rooms at 20°C on a 12-h light/ 12-h dark cycle and free access to lab rat chow (Oriental Yeast, Tokyo, Japan) and water. The rats were randomly allocated into three groups based on their body weight: sham group (sham-operated rats); OVX group (ovariectomized rats); and alendronate group (ovariectomized rats with alendronate). Rats were pretreated subcutaneously for 4 weeks with 0.9% saline vehicle (OVX and sham groups), or alendronate (0.01 mg/kg, Lilly, Indianapolis, Ind.), respectively. At 4 months of age, transverse osteotomies were performed at the midshafts of both femora in all animals. Surgery was performed under general anesthesia with pentobarbital sodium (50 mg/kg, intraperitoneally; Abbott Laboratories, Chicago, Ill.). A fine-toothed circular saw mounted on an electrical drill (Kiso Power Co, Osaka, Japan) was used to perform the osteotomies. A stainless steel intramedullary wire (diameter 1.5 mm; Zimmer, Warsaw, Ind.) was inserted into the medullary cavity to stabilize the fracture site. The wire was cut on the surface on the intercondylar groove to make sure that the movement of the knee was not affected. Unrestricted ambulation was allowed after recovery from anesthesia. Body weights were measured weekly and injection dosages were adjusted accordingly. The same dosing regimen was continued post-fracture.

High-Resolution Quantitative Computed Tomography

Computed tomography (CT) was performed using a CT system from Enhanced Vision Systems (EVS, London, Ontario, Canada). Fracture calluses were imaged with 22.6-μm isotropic voxels (the resolution was the same in all three orthogonal directions). The region from just above the fracture plane to the distal end of the femoral shaft was imaged (about 1 cm total). The same anatomical region was scanned in the non-fractured bones. Excised femora were imaged in 70/30% ethanol/water and calibrated using the gray-level values for ethanol-water and an SB3 block (SB3 is a cortical bone mimicking material; Gammex RMI, Middleton, Wis.). Analyses were conducted on the fracture plane and on a region extending from 1.5 to 6 mm below the fracture plane. The reason for conducting both analyses was that biomechanical testing revealed that the bones did not always break in the original fracture plane. Since the fracture plane was not necessarily the weakest point, it was important to quantify the geometry and properties of the half callus in addition to parameters for the fracture plane.

Within the fracture plane, the image was thresholded into bone and non-bone voxels for CSMI calculations. The threshold level was set half way between the gray level values of ethanol/water and SB3. The bone voxels were used to calculate the following parameters: CSMI; bone area; total bone mineral content (BMC); and average BMD.

An accurate measurement of the CSMI is required for the calculation of material properties from biomechanical data. Due to the non-uniformity and variability of the mineral composition of fracture calluses, we calculated a weighted CSMI, taking into account the BMD distribution within the callus. An equation was developed in which the CSMI was normalized by the average BMD within the fracture plane:

$$I = \frac{\sum BMD_i A y_i^2}{\overline{BMD}} \, ,$$

where I is the CSMI, BMD_i is the BMD of each voxel, A is the area of each voxel, y_i is the perpendicular distance of the each voxel from the central axis, and is the average BMD value.

The region extending from 1.5 to 6 mm below the fracture plane (200 slices) for half calluses was analyzed using a semi-automated deformable boundary technique, slice by slice. The region analyzed was the volume inside the outer boundary of the fracture callus. The parameters extracted were average cross-sectional area (CSA), total BMC, and average BMD. In addition, the area profiles were plotted as a function of distance from the fracture plane.

A subjective parameter was utilized for the 16-week fracture calluses, called the fracture healing index (FHI). This parameter, which measures progression of healing, can have only two arbitrary values, 100 in cases where the fracture plane was not clearly identifiable in the CT image and 0 in cases where the fracture plane was clearly visible in the CT image; therefore, FHI is a subjective parameter that describes the progress of fracture healing.

Statistics

Group differences were assessed by analysis of variance (ANOVA) with pair-wise contrasts examined using Fisher's protected least significant difference (PLSD) where the significance for the overall ANOVA was $p < 0.05$. Statistical analysis was performed using Statview for Windows, version 4.57 (Abacus Concepts, Berkeley, Calif.).

Results

Weeks After OVX But Before Establishing Fracture Model

The QCT parameters for the femoral diaphysis were evaluated at about the site of the fracture for femora from animals 4 weeks post-OVX but just before fracture (Fig. 1; Table 1). The OVX had no effect on bone area, BMC, BMD, or CSMI at the midshaft relative to sham controls. Similarly, treatment with estrogen, raloxifene, or alendronate had no effect on the QCT parameters of the femoral diaphysis relative to sham or OVX controls.

Table 2 summarizes QCT parameters measured in the extended region of the diaphysis and Fig. 2 shows the area profiles. The OVX did not change average area or BMC relative to sham controls but did cause a significant reduction in BMD, which resulted from slight periostial expansion coupled with slight endocortical resorption. Estrogen or raloxifene had no effect on area or BMC relative to sham or OVX controls but did prevent the reduction in BMD due to OVX. Treatment with alendronate did not cause significant changes in average area, BMC, or BMD relative to sham or OVX controls, with the BMD value being intermediate between sham and OVX. The area
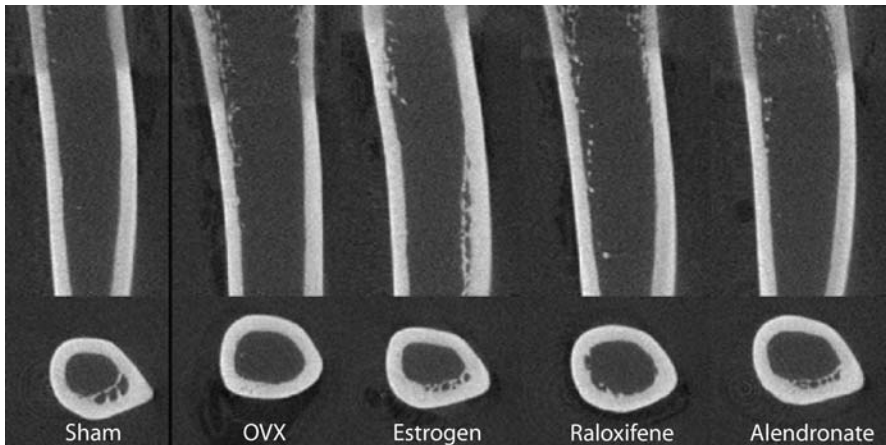
Figure 1. Representative CT images from the pre-fracture groups. The *top images* show vertical slices through the bottom half of the femur. The *bottom images* show the transverse slices that were analyzed corresponding to the approximate location of fracture in the fracture groups. These planes are near the bottom of the vertical slices. Visually, all groups appeared similar at this time point

Table 1. The QCT analysis before and after fracture

Group	Sham	OVX	Estrogen	Raloxifene	Alendronate
Pre-fracture					
Bone Area (mm^2)	5.46 ± 0.22	5.37 ± 0.17	5.79 ± 0.18	5.60 ± 0.19	6.04 ± 0.12
BMC (mg)	0.166 ± 0.007	0.164 ± 0.005	0.174 ± 0.005	0.169 ± 0.005	0.182 ± 0.003
BMD (mg/cm^3)	1344 ± 4	1352 ± 7	1331 ± 10	1338 ± 10	1332 ± 8
Moment of inertia (mm^4)	3.8 ± 0.4	4.4 ± 0.2	4.2 ± 0.2	4.0 ± 0.3	4.8 ± 0.3
6 weeks post-fracture					
Bone area (mm^2)	12.64 ± 0.80^{A}	14.84 ± 1.47^{A}	11.85 ± 1.38^{A}	13.08 ± 0.61^{A}	$19.27 \pm 2.00^{S,O,E,R}$
BMC (mg)	0.284 ± 0.010^{A}	0.299 ± 0.024^{A}	0.251 ± 0.028^{A}	0.278 ± 0.013^{A}	$0.402 \pm 0.032^{S,O,E,R}$
BMD (mg/cm^3)	1010 ± 35	907 ± 28	946 ± 22	943 ± 22	942 ± 31
Moment of inertia (mm^4)	19.2 ± 2.2^{A}	35.2 ± 7.5^{R}	19.3 ± 2.4^{A}	$17.6 \pm 1.6^{O,A}$	$44.8 \pm 8.8^{S,E,R}$
16 weeks post-fracture					
Bone area (mm^2)	11.07 ± 1.01^{A}	9.57 ± 0.80^{A}	8.67 ± 0.37^{A}	10.11 ± 0.56^{A}	$17.41 \pm 1.76^{S,O,E,R}$
BMC (mg)	0.286 ± 0.016^{A}	0.243 ± 0.016^{A}	0.244 ± 0.008^{A}	0.271 ± 0.011^{A}	$0.440 \pm 0.037^{S,O,E,R}$
BMD (mg/cm^3)	1167 ± 37^{E}	1135 ± 20^{E}	$1250 \pm 22^{S,O,A}$	1196 ± 27	1132 ± 31^{E}
Moment of inertia (mm^4)	14.6 ± 2.4^{A}	14.1 ± 1.7^{A}	9.5 ± 1.0^{A}	13.0 ± 1.7^{A}	$35.6 \pm 7.1^{S,O,E,R}$

Data are mean $\pm$ standard error with significant differences from Sham, OVX, Estrogen, Raloxifene, or Alendronate, indicated by S, O, E, R, or A, respectively ($p < 0.05$, Fisher's PLSD)

Table 2. The pQCT analysis on fracture callus (data are mean ± SE)

Group	Sham	OVX	Estrogen	Raloxifene	Alendronate
Pre-fracture: 4 weeks post-ovariectomy					
Average area (cm²)	0.078 ± 0.005	0.085 ± 0.003	0.078 ± 0.003	0.077 ± 0.004	0.087 ± 0.004
BMC (mg)	32.5 ± 1.2	33.1 ± 0.9	33.6 ± 1.1	33.0 ± 1.2	35.7 ± 0.8
BMD (mg/cm³)	929 ± 26°	$860 \pm 18^{S,E,R}$	952 ± 1.9^{O}	$947^{O} \pm 19$	909 ± 23
6 weeks post-fracture					
Average area (cm²)	$0.146 \pm 0.007^{O,A}$	$0.207 \pm 0.018^{S,E,R}$	$0.151 \pm 0.009^{O,A}$	$0.138 \pm 0.005^{O,A}$	$0.198 \pm 0.019^{S,E,R}$
BMC (mg)	50.3 ± 1.5^{A}	55.9 ± 5.0^{A}	55.7 ± 2.7^{A}	52.6 ± 2.0^{A}	$79.9 \pm 5.1^{S,O,E,R}$
BMD (mg/cm³)	$768 \pm 22^{O,R,A}$	$599 \pm 22^{S,E,R,A}$	$821 \pm 16^{O,A}$	$843 \pm 20^{S,O,A}$	$915 \pm 28^{S,O,E,R}$
16 weeks post-fracture					
Average area (cm²)	$0.152 \pm 0.016^{E,A}$	0.136 ± 0.008^{A}	$0.112 \pm 0.006^{S,A}$	0.128 ± 0.007^{A}	$0.198 \pm 0.016^{S,O,E,R}$
BMC (mg)	$59.7 \pm 5.8^{O,E,A}$	$46.1 \pm 1.6^{S,A}$	$49.1 \pm 1.9^{S,A}$	53.2 ± 2.0^{A}	$83.0 \pm 5.3^{S,O,E,R}$
BMD (mg/cm³)	$880 \pm 28^{O,E}$	$761 \pm 30^{S,E,R,A}$	$972 \pm 24^{S,O}$	929 ± 28°	942 ± 31°

Data are mean followed by standard error with significant differences from Sham, OVX, Estrogen, Raloxifene, or Alendronate, indicated by S, O, E, R, or A, respectively ($p < 0.05$, Fisher's PLSD)
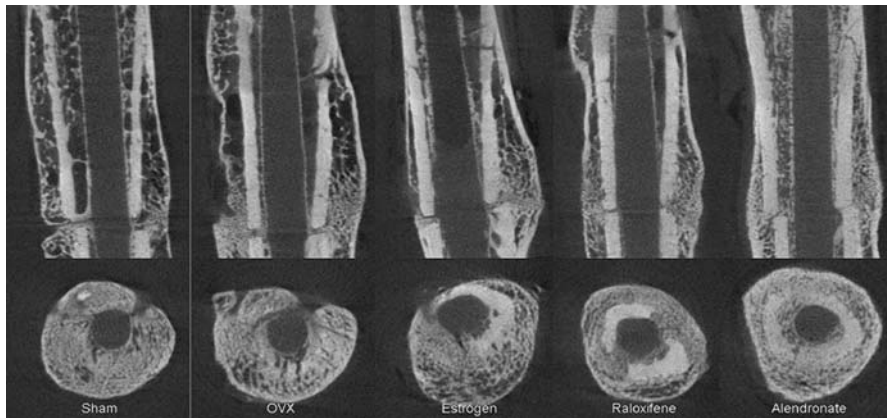
Figure 2 a–c. Area profiles for **a** pre-fracture, **b** 6-week post-fracture, and **c** 16-week post-fracture. This figure illustrates that the calluses in OVX group were large initially but were then remodeled, whereas that of the alendronate group remained

profiles (Fig. 2) suggested an approximately 10% pre-fracture increase in area for the OVX and alendronate groups, even though the average areas were not significantly different at this time point.

Six Weeks After Fracture

The fracture-plane QCT analysis (Fig. 3; Table 1) revealed that OVX bone area, BMC, BMD, and CSMI were not significantly different from sham. Treatment with estrogen had no significant effect on bone area, BMC, BMD, or CSMI relative to sham or OVX controls. Treatment with raloxifene had no effect on bone area, BMC, or BMD, but CSMI was significantly reduced relative to OVX. This was due primarily to geometry, as the raloxifene calluses tended to be smaller than OVX. Treatment with alendronate caused larger calluses to form, as evidenced by the bone area and BMC values, which were both significantly larger than for all other groups. Alendronate BMD was not significantly different from the other groups, but CSMI was significantly larger than all but the OVX controls; therefore, calluses from the alendronate group were larger than estrogen or raloxifene calluses at 6 weeks post-fracture, because the latter treatments tended to form smaller calluses that were more similar to sham than OVX, whereas alendronate calluses tended to be geometrically more like OVX, but with more mineral.

The extended region QCT analysis (Table 2) showed that ovariectomy induced the formation of a callus that was larger than sham. Average area was significantly greater than for sham controls, whereas BMC was not significantly different, and so BMD was significantly reduced relative to sham. Treatment with estrogen reversed ovariectomy effects towards sham levels. Estrogen average area, BMC, and BMD were not different from sham controls, whereas average area was significantly reduced relative to OVX controls, and BMD was significantly greater than for OVX controls. Raloxifene had effects similar to those of estrogen with average area less
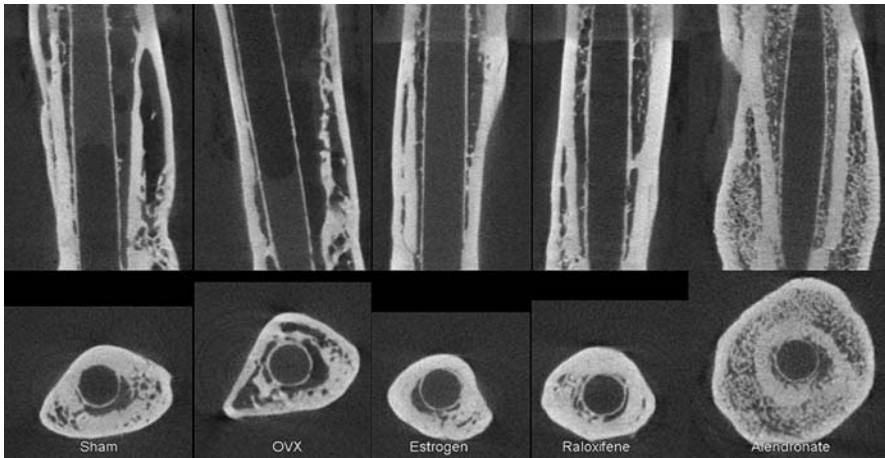
Figure 3. Representative CT images from the 6-week post-fracture groups. The *top images* show vertical slices through the bottom half of the femur. The *bottom images* show the transverse slices that were analyzed corresponding to the fracture plane. Fracture calluses in OVX and alendronate group were larger than that of sham, estrogen, and raloxifene group. It also appears as though the calluses in the other groups had started to remodel more than the calluses in the alendronate group

than OVX and BMD greater than OVX and sham controls. Treatment with alendronate caused the formation of the largest calluses. Alendronate average area was significantly greater than all but OVX controls, whereas both BMC and BMD were significantly greater than all other groups, showing that alendronate induced greater mineralization around the fracture site at 6 weeks post-fracture. The area profiles (Fig. 2) showed a similarity in outer callus geometry between the alendronate and OVX groups, as well as between the raloxifene, estrogen, and sham groups after 6 weeks of fracture healing.

Sixteen Weeks Post-fracture

At 16 weeks post-fracture, the fracture plane was not always discernible at 22.6-μm resolution, especially for the OVX calluses (Fig. 4), so the fracture plane was estimated in cases in which the fracture had healed. This estimation was performed by placing the bones in the imaging fixture the same way every time, assuming that the fractures were all in approximately the same anatomical location. Visually, it appeared that the fracture-healing process consisted of a new cortical shell being formed on the periphery of the fracture callus with the original cortical shell being resorbed. At the 16-week time point, this process appeared to be most advanced in the OVX group and least advanced in the alendronate group where the original cortical shell remained intact but porous. This explains why the fracture plane was still evident in the majority of the alendronate specimens.

At this time point, OVX had no effects on bone area, BMC, BMD, or CSMI relative to sham (Table 1). Estrogen had no effect on bone area, BMC, or CSMI relative to
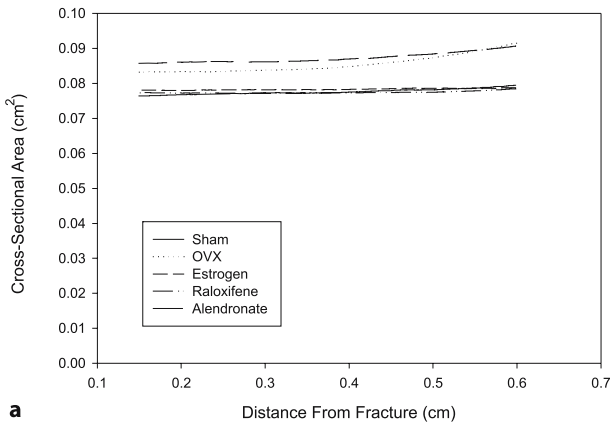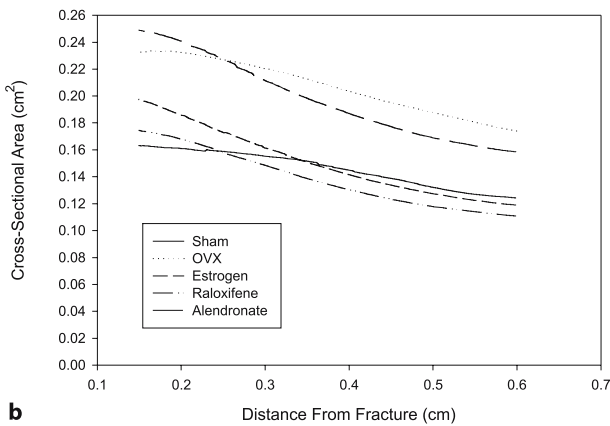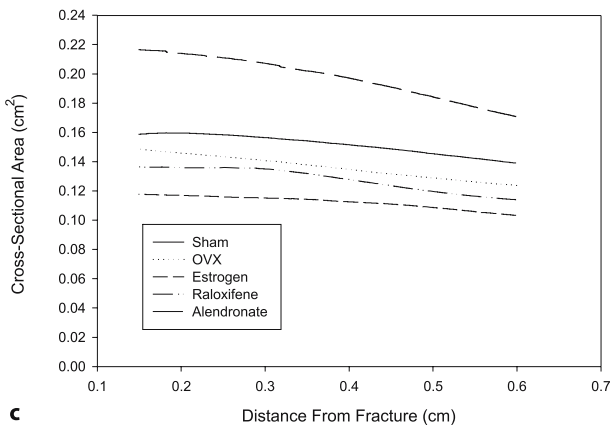
Figure 4 a–c. Representative CT images from the 16-week post-fracture groups. The *top images* show vertical slices through the bottom half of the femur. The *bottom images* show the transverse slices that were analyzed corresponding to the fracture plane. Calluses in alendronate group were much larger than that of other groups. Also, the original cortex was still clearly visible in the alendronate calluses, whereas it had been resorbed to varying degrees in other groups. In the OVX group, calluses around the original cortex were almost completely remodeled. It was also much easier to see the original plane of fracture calluses in the alendronate group

sham or OVX but did increase BMD relative to sham and OVX. Raloxifene had no effect on bone area, BMC, BMD, or CSMI relative to sham and OVX. Alendronate increased bone area, BMC, and CSMI above all other groups, whereas BMD was significantly reduced relative to estrogen.

The 16-week post-fracture extended-region analysis showed that OVX had lower BMC and BMD compared with sham (Table 2), but OVX had no effect on average area. Estrogen reversed the effect of OVX on BMD. In fact, BMD was significantly greater than that in sham and OVX group; however, BMC was still significantly less than sham, and average area was also significantly reduced for estrogen relative to sham. Raloxifene treatment had average area, BMC, and BMD that were not different from sham, whereas BMD was significantly greater than OVX. For the alendronate group, average area and BMC were significantly greater than for all other groups, whereas BMD was significantly greater than OVX. The area profiles (Fig. 2) showed that the calluses in alendronate group had greater dimensions and more mineral than that of all other groups, whereas callus geometry of OVX group decreased back into the range of that of the sham, estrogen, and raloxifene groups. Interestingly, alendronate treatment resulted in the worst FHI (Fig. 5), whereas the fracture plane could not be observed in any of the calluses in OVX group, suggesting that fracture repair progressed the farthest in the OVX group followed by the estrogen, raloxifene, and sham groups.

Discussion

It was reported that alendronate (10 mg) improved dual-energy X-ray absorptiometry (DXA) BMD in the vertebra and femoral necks of postmenopausal women by
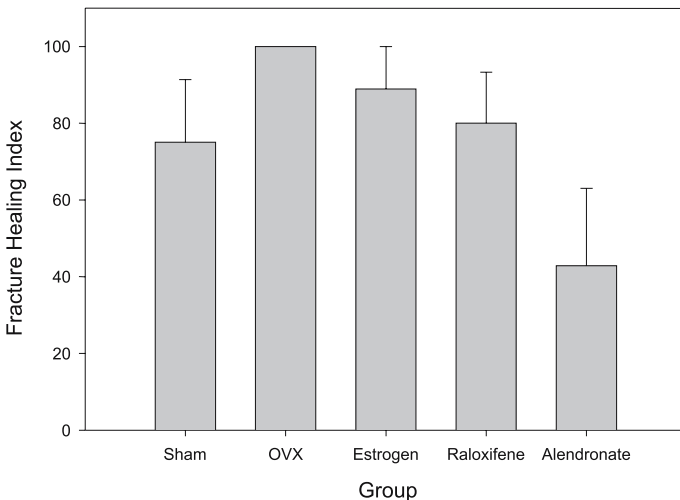
Figure 5. Fracture healing index evaluated at 16 weeks post-fracture. *Error bars* indicate standard errors

9% and 6%, respectively, in 3 years relative to placebo controls (Devogelaer et al. 1996; Black et al. 1996). Also, a 50% reduction in fracture incidence was observed for the spine with reductions of up to 90% for osteoporotic women with multiple spinal fractures (Liberman et al. 1995). Clinical studies with the SERM raloxifene (60 mg) increased DXA BMD by 2.4% in the spine compared with placebo controls after 2 years, which was associated with a 50% reduction in the incidence of vertebral fractures (Delmas et al. 1997; Ettinger et al. 1999). These data suggested a non-linear relationship between BMD and reduction in fracture incidence for the spine.

However, fewer data are available to understand the effects of bisphosphonates or SERMs on the incidence of non-vertebral fractures and what happens to the fracture-repair process of non-vertebral fractures; therefore, we evaluated the effects of estrogen, raloxifene, and alendronate on the fracture-repair process in femora in an effort to model what may happen in women on osteoporosis therapy who sustained osteoporotic fractures.

The QCT data of the present study showed the formation of large calluses in the alendronate and OVX groups at 6 weeks post-fracture. By 16 weeks post-fracture, the calluses in the OVX group had dwindled to the range of the other groups, whereas the calluses in the alendronate group had not changed. In this sense, the OVX group was the fastest to approach the original geometry of the bone, whereas the alendronate group was the slowest. The estrogen and raloxifene calluses were similar in size to the sham calluses at 6 weeks. By 16 weeks, the calluses in estrogen group were significantly smaller than those of sham group, whereas the calluses in raloxifene group were intermediate between that of the sham and estrogen group. The large increase in CSA of the alendronate-treated bones also translated into large increases in the total amount of bone mineral and in the CSMI. The BMC increase was even significant relative to the OVX group at 6 weeks, despite the large CSA of the calluses in OVX group at 6 weeks; however, increases in CSA and BMC did not correlate with a visual determination of fracture healing.

We also reported results of radiography, mechanical testing, and histomorphometry previously (Cao et al. 2002). Interestingly, the 6-week calluses tended to break in the fracture plane, but this was frequently not the case for the 16-week calluses as predicted by the FHI. This parameter was only evaluated at 16 weeks post-fracture with the alendronate group faring the worst. Estrogen and raloxifene were comparable to sham in FHI of the fracture callus. This subjective parameter indicated that treatment with alendronate induced a delay in fracture callus remodeling as the fracture site persisted radiologically in rats treated with alendronate.

The OVX and treatment with compounds induced significant geometrical, compositional, and biomechanical differences among groups; however, the whole callus appeared to be able to compensate for any negative effects of OVX or treatment by morphological adaptation, as shown previously in fracture studies in intact animals with incadronate (Li et al. 1999).

A fracture repair study in humans with Colles' fracture (Van der Poest Clement et al. 2000) showed that bone loss induced by fracture and immobilization at the fracture and at adjacent sites could be prevented by alendronate. This study differed from the current study in that it evaluated the effects of alendronate on bone loss

due to immobilization of a fractured bone at a non-weight-bearing site, rather than evaluating the effects of treatment on the fracture-healing process at a weight-bearing site. The authors did not discuss the effects of alendronate on the fracture callus in this study. For this reason, the implications of these two studies may be quite different.

Conclusion

The OVX-stimulated bone turnover actually seemed to result in the fastest progression of fracture repair in terms of radiographic reunion and the return of normal geometry. Treatment with estrogen or raloxifene did not significantly impair the progression towards radiographic reunion and the return of normal geometry. Alendronate resulted in the large calluses with stiffness significantly greater than sham after 16 weeks of healing; however, there was a significant delay in radiographic reunion and the return of normal geometry highlighting the delay in callus remodeling induced by alendronate.

References

Bergstrom JD, Bostedor RG, Masarachia PJ (2000) Alendronate is a specific, nanomolar inhibitor of farnesyl diphosphate synthase. Arch Biochem Biophys 373:231–241

Black DM, Cummings SR, Karpf DB, Cauley JA, Thompson DE, Nevitt MC, Bauer DC, Genant HK, Haskell WL, Marcus R, Ott SM, Torner JC, Quandt SA, Reiss TF, Ensrud KE (1996) Randomised trial of effect of alendronate on risk of fracture in women with existing vertebral fractures. Fracture Intervention Trial Research Group. Lancet 348:1535–1541

Cao YP, Mori S, Mashiba TK, Westmore MS, Ma L, Sato M, Akiyama T, Shi LP, Komatsubara S, Miyamoto K, Norimatsu H (2002) Raloxifene, estrogen, and alendronate affect the processes of fracture repair differently in ovariectomized rats. J Bone Miner Res 17:2237–2246

Chao EY, Inoue N, Elias JJ, Aro H (1998) Enhancement of fracture healing by mechanical and surgical intervention. Clin Orthop 355 (Suppl):S163-S178

Delmas PD, Bjarnason NH, Mitlak BH, Ravoux AC, Shah AS, Huster WJ, Draper M, Christiansen C (1997) Effects of raloxifene on bone mineral density, serum cholesterol concentrations, and uterine endometrium in postmenopausal women. N Engl J Med 337:1641–1647

Devogelaer JP, Broll H, Correa-Rotter R, Cumming DC, De Deuxchaisnes CN, Geusens P, Hosking D, Jaeger P, Kaufman JM, Leite M, Leon J, Liberman U, Menkes CJ, Meunier PJ, Reid I, Rodriguez J, Romanowicz A, Seeman E, Vermeulen A, Hirsch LJ, Lombardi A, Plezia K, Santora AC, Yates AJ, Yuan W (1996) Oral alendronate induces progressive increases in bone mass of the spine, hip, and total body over 3 years in postmenopausal women with osteoporosis. Bone 18:141–150

Ettinger B, Black DM, Mitlak BH, Knickerbocker RK, Nickelsen T, Genant HK, Christiansen C, Delmas PD, Zanchetta JR, Stakkestad J, Gluer CC, Krueger K, Cohen FJ, Eckert S, Ensrud KE, Avioli LV, Lips P, Cummings SR (1999) Reduction of vertebral fracture risk in postmenopausal women with osteoporosis treated with raloxifene: results from a 3-year randomized clinical trial. Multiple Outcomes of Raloxifene Evaluation (MORE) Investigators. J Am Med Assoc 282:637–645

Fleisch H (2001) Can bisphosphonates be given to patients with fractures? J Bone Miner Res 16:437–440

Fisher JE, Rodan GA, Reszka AA (2000) In vivo effects of bisphosphonates on the osteoclast mevalonate pathway. Endocrinol 141:4793–4796

Grese TA, Dodge JA (1998) Selective estrogen receptor modulators (SERMs). Curr Pharm Des 4:71–92

Hyvonen PM, Karhi T, Kosma VM (1994) The influence of dichloromethylene bisphosphonate on the healing of a long bone fracture, composition of bone mineral and histology of bone in the rat. Pharmacol Toxicol 75:384–390

Lenehan TM, Balligand M, Nunamaker DM (1985) Effect of EHDP on fracture healing in dogs. J Orthop Res 3:499–507

Li J, Mori S, Kaji Y, Mashiba T, Kawanishi J, Norimatsu H (1999) Effect of bisphosphonate (incadronate) on fracture healing of long bones in rats. J Bone Miner Res 14:969–979

Li J, Mori S, Kaji Y, Kawanishi J, Akiyama T, Norimatsu H (2000) Concentration of bisphosphonate (incadronate) in callus area and its effects on fracture healing in rats. J Bone Miner Res 15:2042–2051

Li C, Mori S, Li J, Kaji Y, Akiyama T, Kawanishi J, Norimatsu H (2001) Long-term effect of incadronate disodium (YM-175) on fracture healing of femoral shaft in growing rats. J Bone Miner Res 16:429–436

Liberman UA, Weiss SR, Broll J, Minne HW, Quan H, Bell NH, Rodriguez-Portales J, Downs RW Jr, Dequeker J, Favus M (1995) Effect of oral alendronate on bone mineral density and the incidence of fractures in postmenopausal osteoporosis. The Alendronate Phase III Osteoporosis Treatment Study Group. N Engl J Med 333:1437–1443

Monaghan BA, Kaplan FS, Lyttle CR, Fallon MD, Boden SD, Haddad JG (1992) Estrogen receptors in fracture healing. Clin Orthop 280:277–280

Nakamura T, Hara Y, Tagawa M, Tamura M, Yuge T, Fukuda H, Nigi H (1998) Recombinant human basic fibroblast growth factor accelerates fracture healing by enhancing callus remodeling in experimental dog tibial fracture. J Bone Miner Res 13:942–949

Nyman MT, Paavolainen P, Lindholm TS (1993) Clodronate increases the calcium content in fracture callus. An experimental study in rats. Arch Orthop Trauma Surg 112:228–231

Odvina CV, Zerwekh JE, Rao DS et al. (2005) Severely suppressed bone turnover: a potential complication of alendronate therapy. J Clin Endocrinol Metab 90:1294–1301

Peter CP, Cook WO, Nunamaker DM, Provost MT, Seedor JG, Rodan GA (1996) Effect of alendronate on fracture healing and bone remodeling in dogs. J Orthop Res 14:74–79

Pizones J, Plotkin H, Parra-Garcia JI et al. (2005) Bone healing in children with osteogenesis imperfecta treated with bisphosphonates. J Pediatr Orthop 25:332–335

Rodan GA, Fleisch HA (1996) Bisphosphonates: mechanisms of action. J Clin Invest 97:2692–2696

Russell RG, Rogers MJ (1999) Bisphosphonate: from the laboratory to the clinic and back again. Bone 25:97–106

Sato M, Grese TA, Dodge JA, Bryant HU, Turner CH (1999) Emerging therapies for the prevention or treatment of postmenopausal osteoporosis. J Med Chem 42:1–24

Van der Poest Clement E, Patka P, Vandormael K, Haarman H, Lips P (2000) The effect of alendronate on bone mass after distal forearm fracture. J Bone Miner Res 15:586–593

In Assessment of Osteonecrosis

Volumetric Measurement of Osteonecrotic Femoral Head Using Computerized MRI and Prediction For Its Mechanical Properties

Zi-Rong Li and Zhen-Cai Shi (✉)

Department of Orthopedics, China-Japan Friendship Hospital, Beijing 100029, China
e-mail: shizhencai@sina.com

Abstract

Our study investigated the location and accuracy of osteonecrotic lesions measured by a computed magnetic resonance imaging (MRI, T1-weighted) and coronal data sets in patients with femoral osteonecrosis (ON). A total of 29 patients (38 hips) with ON at the femoral head, who underwent total hip arthroplasty, were recruited into this study. All patients were subjected to MR imaging acquisition before operation. The MRI (T1-weighted) coronal data sets were transferred to a computer in DICOM format using import and export images software (Mimics). A 3D model of ON of the femoral head was restructured. The volume of both femoral heads and the necrotic lesions was calculated. The risk of collapse in patients with different osteonecrotic volume of the femoral head was evaluated using 3D finite element analysis (FEA). Our measurement results showed that the necrotic lesions were located at the anterolateral and superior portion of the femoral head in the restructured 3D model, which matched well with the anatomical location of the osteonecrotic lesions. Our results also revealed that if the necrotic volume was more than 30% of the entire femoral head, there was also a larger collapsed region. Our study suggested that the 3D ON model at the femoral head can be restructured precisely using computed MRI technique. This will be helpful for orthopedic surgeons to understand the shape and location of the necrotic lesion at the femoral head of patients non-destructively.

Introduction

Osteonecrosis of the femoral head (ONFH) is a common disease of the hip joint. According to the nature history, collapse of the femoral head occurs within 1–3 years in 80% patients with ONFH who did not receive any treatment (Ohzona et al. 1991; Sakamoto et al. 1997). Although non-traumatic ONFH occurs in patients of all ages, it tends to occur predominantly in young and middle-aged adults. Hip-replacement surgery is an effective means for releasing pain and restoration of joint function. Long-term outcomes are, however, not known in these patients. This implies that

it is necessary to seek an effective joint-preserving treatment, as not all ONFH will progress to joint collapse.

For patients in early stages of ONFH, it is important and also cost-effective to predict the risk of collapse accurately and to identify patients who may benefit from joint-preserving or conservative treatment. To date, magnetic resonance imaging (MRI) is the most sensitive non-invasive examination for detecting ONFH. The size and location of the necrotic lesion are the main factors related to the risk of ONFH collapse.

Materials and Methods

Patients with ONFH

Thirty-eight hips in a consecutive series of 29 patients with ONFH were recruited into this study. There were 23 men and 6 women with an age range of 26–68 years (mean age 45.5 years). Nine patients had bilateral involvement, and 20 patients were unilateral. The etiology of ONFH was associated with use of steroid use in 18 hips (14 patients), with use of ethanol in 17 hips (12 patients), and idiopathic in 3 hips (3 patients). Among 38 hips, 9 were at stage III and 30 were at stage IV confirmed radiographically, according to the Association Research Circulation Osseous (ARCO) international staging system proposed in 1993 (Gardenlers 1993). Total hip arthroplasty (THA) was then performed for all 38 hips.

MRI Analysis

MR Imaging
All patients were subjected to MR imaging before THA. The MRI was performed with extremity coils on a 1.5-T MR imaging apparatus (Gyroscan, Philips, Eindhoven, The Netherlands) and consisted of T1-weighted SE imaging [repetition time (TR)/echo time (TE) 501/18 ms, matrix size 400 × 400, slice thickness 2 mm without interslice gaps, field of view (FOV) 375 mm, imaging time 5 min 24 s]. During MR imaging, the position of the hip was standardized in neutral abduction-adduction at 0° of flexion and internal rotation of 10°. All imaging data was transferred digitally to a personal computer by DICOM format.

MRI Osteonecrotic Lesion Volume Measurement
The MR imaging data was transferred into a Mimics project document which was then exported to a bitmap paper (Figs. 1, 2). Outlines of the necrotic lesion defined as the sector demarcated by the serpiginous line corresponding to the band-like hypointense margin on serial MRI images, as well as an outline encircling the femoral head, were traced manually or automatically with the magical stick using image analysis software (Adobe Photoshop; Fig. 3). A 3D model of ONFH was restructured using style sculpt software (Magics; Fig. 4). The volume of the femoral head and the volume of the necrotic lesion were calculated using built-in software. Lesion size was expressed as a percentage of the volume of the entire femoral head.

Figure 1. Hip MRI with osteonecrotic bilateral femoral heads (mimics version transferred from DICOM formal)

Figure 2. Hip MRI with osteonecrotic bilateral femoral heads (exported BMP version)

Establishment of MRI Finite Element Model

A 3D finite element model was constructed using MRI data of a normal hip joint. The interface between the femoral head and the acetabulum was treated as a direct contact. The acetabulum was regarded as a rigid body. A load of 3000 N was applied
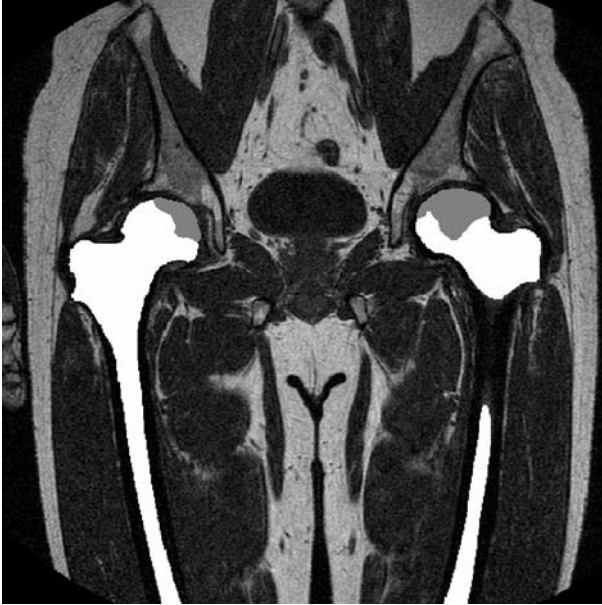
Figure 3. Outline of the necrotic margin traced manually using image-analysis software (Adobe Photoshop)
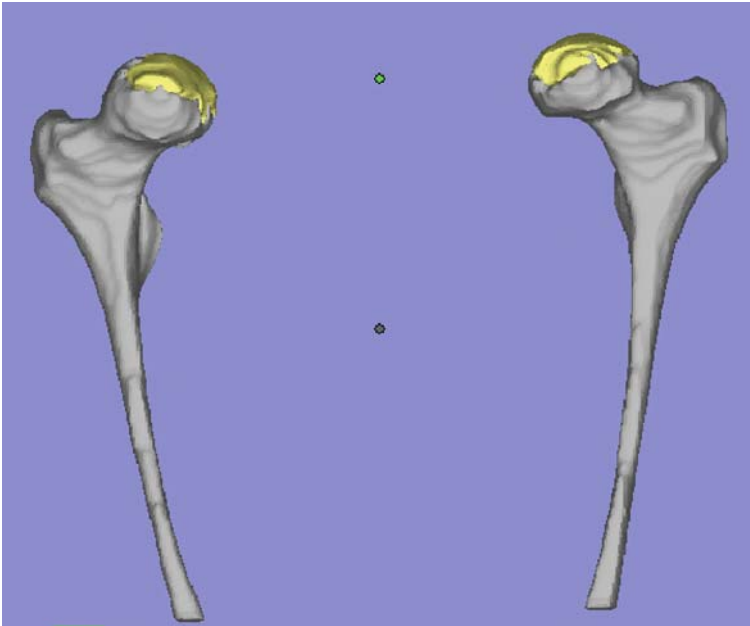
Figure 4. A 3D reconstructed hip model (STL version) with bilateral osteonecrotic femoral heads

15° away from the direction of gravitational force towards the femoral side. The stress index was defined as probability of fracture. The physiological level of the stress index in the necrotic portion was not more than 0.1. If the stress index was above the physiological level at the deep necrotic portion and subchondral region, the femoral head was regarded as being at risk of collapse (Yang et al. 2002). The ratios of the volumes between the necrotic lesion in anterolateral part and the entire femoral head were categorized as 15, 25, 30, 40, and 50%. The risk of collapse in ONFH with different osteonecrotic volumes was evaluated using 3D finite element analysis (FEA).

Anatomic Measurement of ON Lesion

After surgical removal of ONFH, the juncture of the femoral head and neck was identified. The femoral head was then parted from the neck by a hand-motion hacksaw. The remainder of the femoral head was placed into a glass and filled with 300 ml 0.9% sodium chloride solution. The femoral head was then taken out and the fluid volume remaining in the glass was measured. The volume of the entire femoral head (cm^3) was 300, i.e., the remaining fluid volume. Three repeated measurements were done and the mean value was obtained for statistical analysis. The femoral head was then cut into five to six slices and the separated ON areas and cartilage were removed in each cut. The volume of the necrotic lesion was measured using this fluid displacement method. We compared the different volumes using two methods, i.e., computer and anatomical measurement.

Statistical Data Analysis

The SPSS 10.0 software (SPSS, Chicago, Ill.) was used for paired t-test and regression test for studying coefficient correlation between the two different methods of ON lesion volume measurements.

Results

Figure 5 shows the restructured ONFH 3D mode. The necrotic region was labeled, which was located at the anterolateral and superior portion of the femoral head and anatomically anterior to the teres ligament.

The volume of the entire femoral head in 38 hips calculated using built-in software and anatomical methods was $49.0 \pm 4.6\,cm^3$, ($35.6 \sim 60.6\,cm^3$) and $49.3 \pm 4.5\,cm^3$ ($35 \sim 60\,cm^3$), respectively; and the difference in volume measured by these two approaches was $0.59 \pm 0.9\,cm^3$($-1.56 \sim 2.16\,cm^3$, -3.6 to 4.5% of the whole volume of the FH using anatomical methods), which was not statistically significant (paired t-test = -1.592; $P = 0.120$). The necrotic volume of the femoral head measured from MRI and direct anatomical method was $20.1 \pm 6.6\,cm^3$ ($10.7 \sim 38.9\,cm^3$) and $20.2 \pm 6.5\,cm^3$ ($11 \sim 38\,cm^3$), respectively; and the difference in volume was $0.31 \pm 0.53\,cm^3$(-0.96 to $0.99\,cm^3$, -1.8 to 2.1% of the whole volume of the FH using anatomical methods), which did not show significant difference (paired t-test =
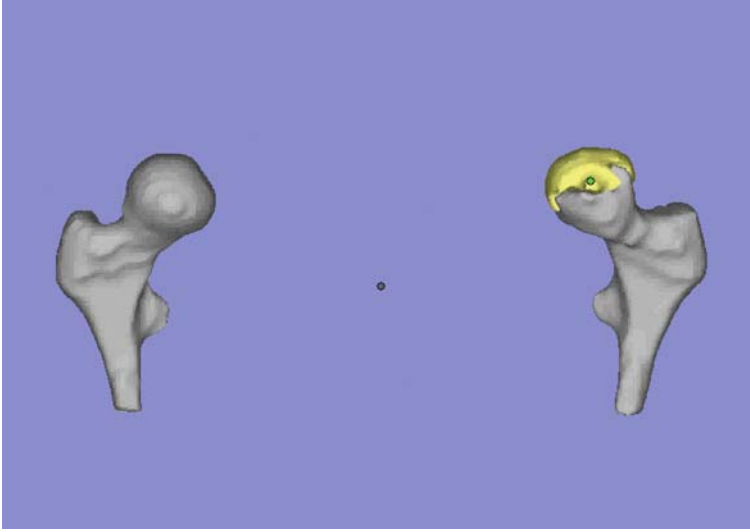
Figure 5. A 3D reconstructed model with osteonecrotic femoral head

−0.965; P = 0.341). The mean volume of the entire femoral head and necrotic lesion measured by anatomical method was 1.19 and 1.53%, respectively, which was greater than that measured by MRI. Regression analysis showed linear relationship or agreement between these two methods for both the entire and necrotic volume of the femoral head (r = 0.976, P = 0.000, and r = 0.996, P = 0.000, respectively). The volume fraction of the necrotic lesion was 40.8±11.6% (range 21.6–66.7%) of the entire femoral head using anatomical and measurement in 38 hips (and 41.5 ± 11.3% (range 22–68%) on MRI measurement, including 16 (17%) hips with a volume of the necrotic lesion larger than 40%, 15 (15%) hips with a volume of the necrotic lesion between 30 and 40%, and only 7 (6%) hips less than 30% necrotic.

The FEA revealed that the fracture or collapse was located in the deep necrotic portion near the necrotic-viable interface, rather than at the surface of the necrotic portion. This was identical to collapse found in the femoral head in pathological specimens. The larger the necrotic volume, the greater the stress index (>0.1), implying higher probability of the femoral head collapse. When the necrotic volume was more than 30% of the entire femoral head, a large area of collapse resulted.

Discussion

Magnetic resonance imaging is widely used in the diagnosis of ONFH with high sensitivity and specificity. Many methods have been developed to estimate the size of ON lesion on radiographs or MR scans, yet the difference in agreement of measurement methods was has been (Sugano et al. 1994; Nishii et al. 2002; Cherian et al. 2003). Much of the current dilemma on selection of the treatment options for ONFH is

caused by the lack of an agreed efficient quantitative system for evaluation and staging; hence, to develop or identify a method or to establish criteria for accurate quantification of the necrotic volumes in ONFH and to assess its prediction power for later collapse of individual patients was the objective of this study.

In the past, several studies used MR imaging or radiographs to assess the extent of ON using different quantitative methods. In 1984, Steinberg et al. (1984) included the size of the necrotic lesion in their system for staging ON of the femoral head. Later, ARCO proposed to quantify the extent of ONFN by categorizing the severity of ONFN into three groups based on the volume of necrosis, i.e., <15, 15% ~ 30, and >30% (Gardenlers 1993). Early studies used the percentage size of the necrotic lesion presented in the entire femoral head on radiography to quantify the severity of ONFH (Sugano et al. 1994; Aaron et al. 1989). Although this radiographic method was simple and useful, it was not an accurate one, as the anterior and posterior parts of the necrotic lesions were overlapped on the anteroposterior radiographs. Once ONFH is demonstrable on radiography, it has already entered a late stage, i.e., collapse of the femoral head, which predisposes to osteoarthritis of the hip (Nishii et al. 2002). It is therefore not sensitive to use a radiography for predicting collapse of the femoral head. When the extent of lesion size and its relation to weight-bearing area of the necrotic involvement were estimated on coronal T1-weighted images of MRI, Shimizu et al. (1994) reported that 21 of 66 hips progressed to collapse after a follow-up of an average of 32 months, and the femoral heads with mixed signals on coronal T1-weighted images of MRI showed a high tendency to collapse; the next were those with high signal and with low signal, respectively.

Li et al. (2003) followed 40 patients (56 hips) with ONFH who accepted joint-preserving treatment and presumed that the femoral head with less than 30% necrotic lesion in the entire head had a low risk of collapse, as compared with a moderate or high risk of collapse if the necrotic lesion was 30 ~ 60% or over 60%. On the mid-coronal and midsagittal T1-weighted images, the lesion size was estimated by measuring the angle of the arc of the necrotic segment from the center of the femoral head, which was defined as the necrotic arc angle. The necrotic arc angle on the mid-coronal and midsagittal images were designated A and B, respectively. The index of necrotic extent was calculated as $(A/180) \times (B/180) \times 100$. But the reproducibility of this method was poor because of inconsistency found among observers (Cherian et al 2003). Cherian et al (2003) modified this method by measuring the necrotic arc angles on the images that area of maximal involvement in the sagittal (A) and coronal (B) planes. This method was confirmed to be able to estimate the true necrotic lesion in ONFH better than the previous method.

Although the methods mentioned above are useful and allow indirect estimation of the volume of ON, they are still not a precise quantitative approach. Hernigou and Lambotte (2001) transferred electronic data to a multiprocessing computer and the area of the necrotic area was outlined on each slice using an imaging-analysis program and the total necrotic volume was then calculated by summarizing the necrotic volume of each slice calculated by multiplying the necrotic area of each slice and its thickness. The area of necrosis was considered to be the sector demarcated by the serpiginous line histologically corresponding to the band-like hypointense margin,

and the inner border of this low intensity was assumed to represent the edge of the necrotic area. This formed an adequate basis for a precise volume measurement of the necrotic bone, which was adopted for the present study. Using this method, minor inter-observer variation or intra-observer variation (measurement done by a single person at different times) was reported, with an average 5% difference, i.e., <1.5 and $1.7 \, mm^3$, respectively, in measurement of the necrotic volume. The volume of ON quantified by MR imaging method with 2-mm slices was only 0.98% smaller than that measured by anatomical method.

In our study, a 3D model of ON lesion in the femoral head was reconstructed by special medical software from MRI (T1-weighted) coronal data sets. This available function will be helpful for orthopedic surgeons to understand the shape and location of necrotic lesion of the femoral head. The volume of ON can be determined accurately by the computer program, which matches well with the anatomic volume of ON lesion. The volume of the ON lesion in the femoral head was reported to be strongly correlated with the risk of collapse by Nishii et al. (2002), who found that hips with ON lesion volume greater than 30% of the femoral head showed a high incidence of collapse among 80% of the cases. In our series of 38 hips with late ONFH of stage III and above, there were 32 hips (84%) with ON lesion volume >30% and 6 hips (16%) with ON lesion volume <30%. Some of the hips collapsed despite having ON lesion volume <30% of the femoral head; therefore, defining the location of the ON lesion is essential. When the ON lesion developed in the anterosuperior portion of the femoral head, the risk of collapse was high, regardless of the size of ON lesion. In ONFH with greater ON lesion volume, no significant relationship was observed between ON lesion location and risk of its collapse. One possible explanation was that the ON lesion occurring in anterosuperior portion of the femoral head was mostly large in size; thus, to define ON lesion location from the reconstructed 3D MR imaging may increase the power to predict the risk of femoral head collapse in patients with small- or medium-size ON lesions.

The relevance of ON lesion size and its location for prognosis of ON treatment has also been documented in biomechanical studies using 3D FEA. The FEA model of ONFH designed for the present study was simple and optimized. If the necrotic volume of the ONFH was >30%, the risk of later collapse was high. In the near future, development of special software that allows automatic image processing of the ON pattern recognition and segmentation, rather than the current manual approach (Zoroofi et al. 2001), is highly desirable for both reducing the time for image analysis and increasing measurement accuracy. These two factors are essential for facilitating routine clinical application of 3D ON lesion reconstruction and FEA in risk prediction of collapse resulting from development of ON lesions in the femoral head.

Conclusion

We investigated the location and accuracy of ON lesions measured by MRI. The measurement results showed that the necrotic lesions were located at the anterolateral and superior portion of the femoral head in the restructured 3D model, which

matched well with the anatomical location of the ON lesions. Our study suggested that the 3D ON model at the femoral head can be restructured precisely using computed MRI technique. This will be helpful for orthopedic surgeons to understand the shape and location of the necrotic lesion at the femoral head of patients non-destructively.

References

Aaron RK, Lennox D, Bunce GE, Ebert T (1989) The conservative treatment of osteonecrosis of the femoral head: a comparison of core decompression and pulsing electromagnetic fields. Clin Orthop 249:209–218

Cherian SF, Laorr A, Saleh KJ, Kuskowski MA, Bailey RF, Cheng EY (2003) Quantifying the extent of femoral head involvement in osteonecrosis. J Bone J Surg 85A:309–315

Gardenlers JWM (1993) ARCO committee on terminology and staging (report on the committee meeting at Santiago De Compostela). ARCO Newslett 5:79–82

Hernigou P, Lambotte JC (2001) Volumetric analysis of osteonecrosis of the femur. Anatomical correlation using MRI. J Bone Joint Surg 83B:672–675

Li ZR, Zhang NF, Shi ZC (2003) Predicting collapse and treatment selection for osteonecrosis of the femoral head. J Clin Orthop 23:193–196

Nishii T, Sugano N, Ohzono K, Sakai T, Sato Y, Yoshikawa H (2002a) Significance of lesion size and location in the prediction of collapse of osteonecrosis of the femoral head: a new three-dimensional quantification using magnetic resonance imaging. J Orthop Res 20:130–136

Nishii T, Sugano N, Ohzono K, Sakai T, Haraguchi, Yoshikawa H (2002b) Progression and cessation of collapse in osteonecrosis of the femoral head. Clin Orthop 400:149–157

Ohzona K, Saito M, Takaoka K, Saito S, Nishina T, Kadowaki T (1991) Natural history of non-tramatic avascular necrosis of the femoral head. J Bone Joint Surg 73B:68–72

Sakamoto M, Shimizu K, Iida S, Akita T, Moriya H, Nawata Y (1997) Osteonecrosis of the femoral head: a prospective study with MRI. J Bone Joint Surg 79B:213–219

Shimizu K, Moriya H, Akita T, Sakamoto M, Suguro T (1994) Prediction of collapse with magnetic resonance imaging of avascular necrosis of the femoral head. J Bone Joint Surg 76A:215–223

Steinberg ME, Hayken GD, Steinberg DR (1984) A new method for evaluation and staging of avascular necrosis of the femoral head. In: Arlet J, Ficat RP, Hungerford DS (eds) Bone circulation. Williams and Wilkins, Baltimore, pp 389–403

Sugano N, Takaoka K, Ohzono K, Takaoka K, Ono K (1994) Prognostication of nontraumatic avascular necrosis of the femoral head: significance of location and size of the necrotic lesion. Clin Orthop 303:155–164

Yang JW, Koo KH, Lee MC, Yang P, Noh MD, Kim SY, Kim KI, Ha YC, Joun MS (2002) Mechanics of femoral head osteonecrosis using three-dimensional finite element method. Arch Orthop Trauma Surg 122:88–92

Zoroofi RA, Nishii T, Sato Y, Sugano N, Yoshikawa H, Tamura S (2001) Segmentation of avascular necrosis of the femoral head using 3D MR images. Comput Graph 25:511–521

Biomedical Engineering in Surgical Repair of Osteonecrosis: the Role of Imaging Technology

Shi-Bi Lu[1], Jiang Peng[1], Ai-Yuan Wang[1], Ming-Xue Sun[1], Jie-Mo Tian[2], and Li-Min Dong[2]

[1] Institue of Orthopedics, General Hospital of Chinese PLA, Beijing 100853, China
[2] Institute of Nuclear Energy Technology, Tsinghua University, Beijing 100084, China

Abstract

We fabricated biomimetic biphasic calcium phosphate (BCP) for tissue engineering in repair of avascular necrosis (AVN) or osteonecrosis (ON) and observed its outcome of reconstructiion in ON femoral head of dogs. Firstly, BCP ceramic scaffolds were fabricated with three-dimensional (3D) gel-lamination technique according to the two-dimensional (2D) images of trabecular structure of dog femoral head. Then, the 3D structure of the scaffolds was scanned and reconstructed using micro-CT for characterization of 3D patterns of its material structure related to trabecular parameters, including bone volume fraction (BVF-BV/TV), bone surface/bone volume (BS/BV), trabecular thickness (Tb.Th), trabecular number (Tb.N), trabecular spacing (Tb.Sp), structure model index (SMI), and trabecular pattern factor (Tb.Pf). After coating marrow stromal cells (MSCs) as seed cells onto biomimetic porous BCP constructed in vitro, the tissue-engineered bones were implanted into the bony defects of dog femoral head through trap-door procedure for 30 weeks. The femoral heads in control group were compacted with autograft bone chips for comparison. Results showed similar micro-CT data between control samples and experimental group implanted with BCP scaffolds, except that a more plate-like "trabecular" was pattern found in BCP scaffolds. Thirty weeks after operation, the contour and integrity of the femoral heads were basically maintained and the BCP scaffold showed trabecular bone formation and integration. On the other hand, the femoral heads in control group collapsed and presented osteoarthritic changes. These findings suggested that the biomimetic porous BCP scaffolds developed for this study coated with MSCs might be an effective approach in repair of the bony defect in ON of the femoral head.

Introduction

Avascular necrosis of the femoral head (ANFH) is a refractory disease that may progress to collapse of the subchondral and articular cartilage of the joint. Despite all efforts made in the past, there are still no effective methods developed for prevention of collapse of the femoral head in many patients. With the development of tissue

engineering and biotechnologies, we are able to adopt these techniques into research and development of methods for potential effective treatment of difficult ANFH.

The bone scaffolds are indicated for implantation in bone defects of critical size, such as the bone defect in the loading area of femoral head, which sustains substantial mechanical loading in daily life. A fundamental issue in designing the tissue-engineered scaffold materials is to provide a biomimetic environment to facilitate functional and sufficient porosity for cell migration and cell/gene delivery (Lin et al. 2004). Accordingly, many variables must be taken into consideration in designing biomimetic scaffold materials. For example, in order to mimic tissue stiffness, especially in design of bone substitute for repair of bone defect, material stiffness and porosity similar to bone is required for both load bearing and cell migration or delivery material (Bruder et al. 1998). In other words, apart from the biomechanical properties, scaffolds in bone tissue engineering must have other characteristics such as pore size, pore interconnectivity, pore volume fraction, permeability, and material surface chemistry, which may, however, influence strength and tissue regeneration. Many investigators have suggested principles for designing tissue-engineered scaffolds for bone application. Yaszemski et al. (1995) stated that scaffolds developed for bone tissue engineering should possess mechanical stiffness matching the low range of trabecular bone stiffness of 50–100 MPa. Hutmacher (2000) proposed that scaffold should match the native tissue stiffness which for trabecular bone ranged from 10 to 1500 MPa. Van Cleynenbreugel et al. (2002) proposed a lattice-structured scaffold to replace trabecular bone. Although this approach may help construct bone scaffold with ideal porosity, it is uncertain if the constructed materials may provide an inner structure of the scaffold, which meets the demand of the local stress distribution. Although a number of researchers have postulated scaffold design principles, and numerous fabrication techniques have been also developed, few methods have been specifically developed for bone scaffold design for application in treatment of ANFN.

This chapter describes a new and novel approach for constructing the scaffold for bone tissue engineering in treatment of ANFN. A high-resolution micro-CT is used for designing and production of a biomimetic porous scaffold. The usefulness of this material is validated in a femoral head bone defect model in dogs.

Materials and Methods

This study comprised (a) scaffold material development and fabrication, (b) characterization of the fabricated scaffold, (c) in vitro tissue engineering, and (d) in vivo efficacy study using the tissue-engineered scaffold material for implantation into the femoral head bone defect in dogs.

Preparation of Porous Hydroxyapatite Bioceramic Scaffolds

We selected BCP (biphasic calcium phosplate) powder as the ceramic phase, which was synthesized via chemical precipitation technique from the aqueous solutions of triammonium phosphate trihydrate and calcium nitrate tetrahydrate. D-9300 (Beijing Eastern Rohm and Haas Co., China) was used as dispersant. Sodium alginate

(Beijing Xudong Chemical Plant, China) was adopted as the gelling polymer, and calcium chloride as initiator (Tianjin Tanggu Dengzhong Chemical Plant, China). Sodium lauryl sulfate (Tianjin Chemical Plant, China) was used as foaming agent and lauryl (Beijing Yili Fine Chemical Ltd., China) as foaming stabilizing agent. The BCP powder was mixed together with deionized water, D-9300, sodium lauryl sulfate, lauryl, and sodium alginate solution to form a foamy ceramic slurry by means of ball milling within a polyethylene jar.

Porous biphasic calcium phosphate (BCP) ceramic scaffolds were fabricated using 3D gel-lamination technology with sodium lauryl sulfate as foaming agent and lauryl as foaming stabilizing agent (Van Cleynenbreugel et al. 2002). With gelling system of sodium alginate and calcium chloride, the foamy hydroxyapatite (HA) and β-tricalcium phosphate (β-TCP) slurry were gelled layer by layer on the 3D gel-lamination machine (Institute of Nuclear Energy Technology, Tsinghua University, China) to fabricate the porous ceramic scaffolds with proper speed and compounding according to the 2D images of canine femoral head. Then the 3D gel-lamination specimens were dried under room temperature and high humidity. After drying, they were burned out at 300–500°C at a reasonably slow heating rate to drive off the volatiles, followed by sintering at 1250°C for 2 h.

Scaffold Structure Evaluation

Eight trabecular bone specimens were obtained from healthy hybrid dog femoral heads along the longitudinal axis of the femur with a trephine of 10 mm in diameter under water-cooling condition. Then these bone specimen and eight BCP scaffolds (diameter×height: 10×10 mm) were scanned using a desktop MicroCT system (μCT-40, Scanco Medical, Bassersdorf, Switzerland). Serial cross-section images were obtained along the longitudinal axis of femur with an isotropic voxel dimension of 20 μm. The 3D structure of these specimens were reconstructed by computer according to the series micro-CT images of these specimens and evaluated using built-in software. A semi-automatic contouring method was used to select a volume of interest exclusively containing the cylindrical core. The resulting image was then segmented using a low-pass Gaussian filter to remove noise, and a fixed threshold to extract the mineralized bone phase as described by others (Tian et al. 2005; Laib et al. 2000; Ding et al. 1999). From the binary images, structural indices were assessed with 3D techniques that do not rely on model assumptions of the trabecular structure (Laib et al. 2000; Muller et al. 1998). All structural parameters were calculated for consecutive millimeter increments and they included bone volume fraction (BVF,BV/TV), bone surface/bone volume (BS/BV), trabecular thickness (Tb.Th), trabecular number (Tb.N), trabecular spacing (Tb.Sp), structure model index (SMI), and trabecular pattern factor (Tb.Pf).

Mechanical Testing

Five specimens of porous scaffolds were cylindrical (diameter×height: 12 mm × 10 mm) in shape with a length to diameter ratio of 1.2:1. An mechanical tester

(MTS, 858 Mini Bionix) with 2 kN load cells was used for the compression test. The crosshead speed was set at 0.4 mm/min, and the load was applied until the scaffold was crushed completely. The elastic modulus was calculated as the slope of the initial linear portion of the stress-strain curve. The yield strength was determined from the cross point of two tangents on the stress-strain curve at the maximum stress (Callister et al. 2003).

Preparation and Seeding of Marrow Stromal Cells

The MSC were derived from iliac wing aspiration and expanded in tissue culture flasks according to related method (Maniatopoulos et al. 1988). Briefly, 2 ml of each canine bone marrow in experimental group was collected from the humerus using a bone marrow needle connected to a heparinized 10-ml syringe. A 0.5-ml portion of the aspirate was cultured in an 80-cm^2 flask with 20 ml of Dulbecco's modified Eagle's medium with a low glucose concentration (DMEM-LG) and 10% fetal bovine serum (FBS). The cells were cultivated at 37°C under 5% CO_2. The medium was changed twice a week until the cells were 80% confluent. Non-adherent cells, such as hematopoietic cells, were removed by the medium change procedure. Subsequently, adherent cells were collected. Cells were released from the flasks by exposure to 0.05% trypsin and were passaged in other flasks. Before surgery, the cells were harvested and centrifuged at 100 g for 10 min and after washing with culture medium at a concentration of 6×10^6 cells/ml in medium containing 15% FBS. The scaffolds were then statically seeded by dropping 0.5 ml of cell suspension on each side of the scaffolds. The constructs were incubated at 37°C for 2 h to allow cell attachment. These scaffolds were cultured for 7 days in FBS medium with 10 nM dexamethasone and 10 mM b-glycerophosphate (DEX and BGP, Sigma) that showed to stimulate MSCs to differentiate into osteogenic linage in both rat and human (Maniatopoulos et al. 1988; Mendes et al. 2002).

Animals and Implantation

Twenty adult hybrid canines (12 ~ 24 months, 14 ~ 16 kg), obtained at least 4 weeks prior to surgery, were randomly divided into experimental group ($n = 10$) and control group ($n = 10$). The surgical procedures were performed under standard conditions. After shaving and disinfection of the hip area, a central skin incision from iliac crest to upper leg was made to expose the muscle fascia and femoral head through an anterolateral approach, in which the lateral circumflex branch of the profunda femoris was preserved. At the top of the femoral head, a 14-mm-diameter trap-door composed of articular cartilage and its underlaying subchondral bone was removed with a thin chisel. The size of the trap-door corresponded to the size (40% of the femoral head in volume and 80% of the main loading region of the femoral head) that has been observed in human clinical studies (Ohzono et al 1991; Nishii et al 2002; Lafforgue et al 1993; Shimizu et al. 1994; Koo et al. 1995). Under constant saline cooling, central guide hole was drilled before 12-mm trephine bone defect in the femoral head

was made to mimic trap-door technique (Mont et al. 2001). The femoral heads in experimental group were implanted with the scaffolds coated with differentiated MSCs, and the femoral heads in control group were packed with autograft bone chips taken from the ilium through the same incision. The implants were press-fit placed into the bone defect (see Fig. 3a). Then the cartilage-bone flap was replaced flush with surrounding articular surface and held in place by three 5-0 sutures. After closing the capsule, the hip abductors were sutured tight to the greater trochanter. The fascia was closed with a non-resorbable suture. The skin was closed in two layers. All animals were observed daily for wound healing and received one preoperation dose and three postoperative doses of antibiotics (gentamicin, 4 mg/kg). Animals were killed by an overdose of pentobarbital after 30 weeks. Femoral heads were obtained for histology and histomorphometry, which were fixated in 4% formaldehyde, dehydrated by graded ethanol series, and embedded in polymethylmethacrylate. Semi-thin sections were made with a sawing microtome (Leica 1600, Nussloch, Germany). The coronal midsection of each sample was used for histomorphometry.

Results

Ceramic Scaffold Structure Evaluations

Micro-CT measurements showed that the ceramic scaffold contained 62% of macroporous porosity. Mechanically, the average compressive modulus and ultimate strength reached 464 ± 36.03 and 5.62 ± 0.78 MPa, respectively. On the contrary, the average compressive modulus and ultimate strength of the trabecular samples of canine femoral heads was 566.10 ± 56.84 and 12.06 ± 3.24 MPa, respectively.

When micro-CT measurements were compared between trabecular bone samples of canine femoral heads and BCP scaffolds, no significant difference was revealed in BV/TV, Tb.Th, Tb.N, and Tb.Pf (Figs. 1, 2; Table 1).

Table 1. Micro-CT measurements compared between BCP scaffold and trabecular bone of dog femoral head

Groups	Micro-CT measurements						
	BV/TV	BS/BV (mm^{-1})	Tb.Th (μm)	Tb.N (mm^{-1})	Tb.Sp (μm)	SMI	Tb.Pf (mm^{-1})
BCP scaffold	38.77± 3.66	15.68± 0.99	167.3± 25.3	1.88± 0.31	405.7± 47.7	0.38± 0.33	−2.27± 1.06
Trabecular bone	40.25± 12.81	21.70± 0.46	191.1± 12.5	2.06± 0.05	308.1± 37.23	0.91± 0.11	−2.52± 0.38
T	2.094	13.42	2.297	1.373	4.949	3.735	0.548
p-value	0.086	0.000*	0.069	0.225	0.004*	0.009*	0.603

*$p < 0.01$
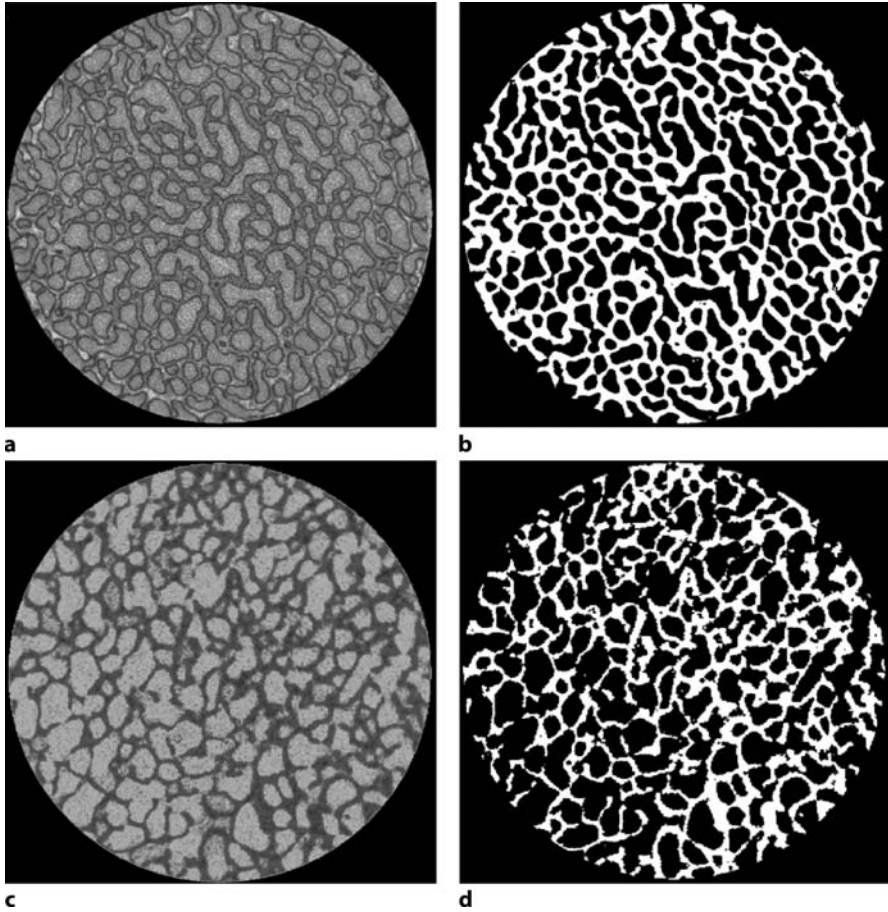
Figure 1 a–d. Micro-CT image of biomimetic BCP scaffold and dog trabecular bone specimen. Compared with trabecular bone, the biomimetic BCP scaffold (**a,b**) shows that the "trabecula" of the scaffold have uniform distribution with homogeneous thickness similar to that of trabecular bone (**c,d**). **a,c** The original micro-CT images. **b,d** Binary image of the micro-CT images

Preparation and Seeding of Marrow Stromal Cell

Cell biocompactibility test indicated MSCs survival and cell attachment onto the surface of the BCP trabecular was good (Fig. 3).

Animals and Implantation

Thirty weeks after operation, the contour of the femoral head in the experimental group maintained, whereas joint collapse was found in the control group (Figs. 4, 5). New bone (trabecular bone) was formed on the cavity surface of the implanted BCP
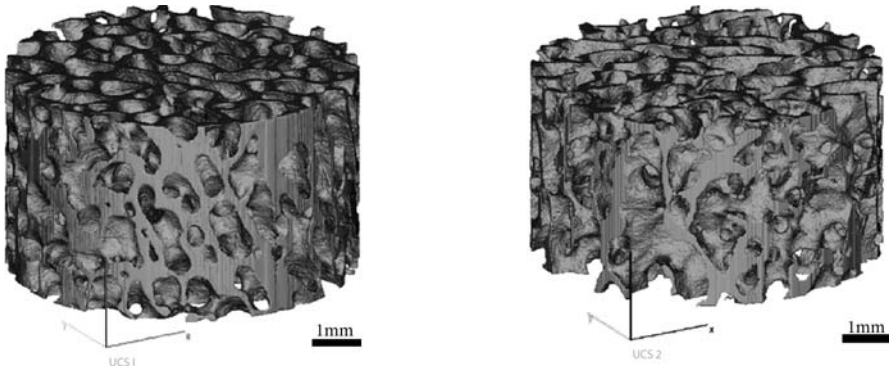
Figure 2 a,b. A 3D micro-CT reconstructed BCP scaffold (**a**) and trabecular bone of the dog femoral head (**b**). The SMI of BCP scaffold and femoral head are, on average, 0.38 and 0.91, respectively, suggesting more plate-like model in BCP scaffold
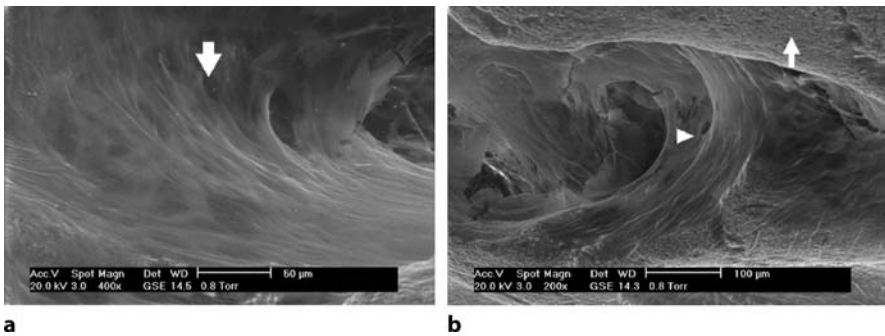
Figure 3 a,b. Scanning electron microscopy images with BMCs loaded onto the BCP scaffolds and grow well. **a** The scaffold's surface was covered by a layer of MSCs (*arrow*). **c** The MSCs (*arrowhead*) are growing on the pore surface in the scaffold (*arrow*)

scaffold and excellent tissue integration was found at the BCP scaffold and host bone, characterized with trabecular bone ingrowth (Fig. 4).

Discussion

Femoral Head with Bone Grafting

Bone grafting as a treatment way for the bone defect of the femoral head combined with osteonecrosis had been adopted by many investigators. These grafting methods included iliac-crest (Rosenwasser et al 1994), strut bone graft (Mont et al. 2001), and tibial bone-grafting (Smith et al. 1980); however, these methods do not provide effective support for the femoral head loading, so patients with femoral head ON must be restricted weight-bearing for a long time in order to facilitate the graft integration after operation (Mont et al. 2001). This suggests the needs structural tissue engineer-
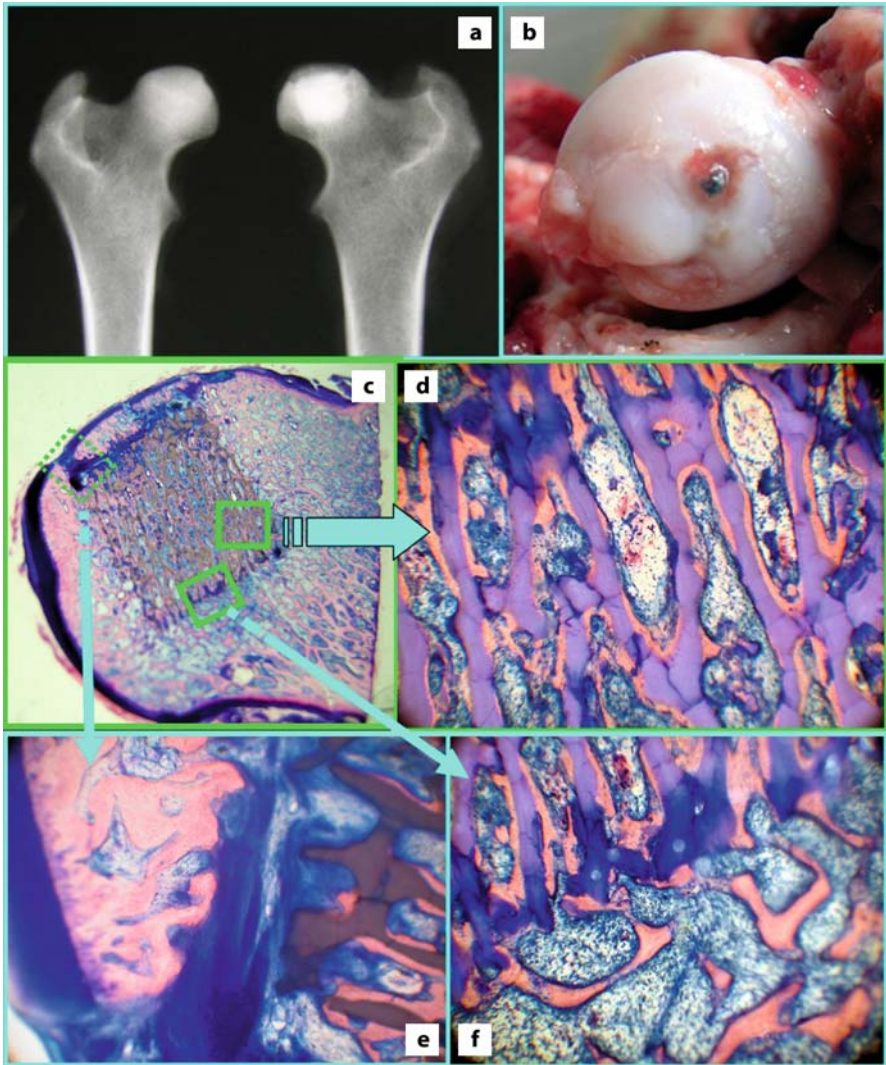
Figure 4. a Representative radiograph of femoral head in experimental group after 30 weeks show that the contour of the femoral head kept integrity. **b** A general view of the femoral head in experimental group (30 weeks). **c** A representative histological section of the femoral head in experimental group 30 weeks after surgery with well-preserved femoral head. **d** The magnified region of the implanted BCP scaffold from one framed area of **c** (*arrows*) shows new bone (trabecular bone) formation on the cavity surface of the implanted BCP scaffold. **e** The conjugate region between the scaffold and bone-cartilage flap region was not good as expected. **f** Excellent healing between the scaffold and trabecular bone

ing for bone grafting. Accordingly, we fabricated a tissue-engineering scaffold in our research group which meets the local stress and strain distribution in the femoral head as shown the present study.
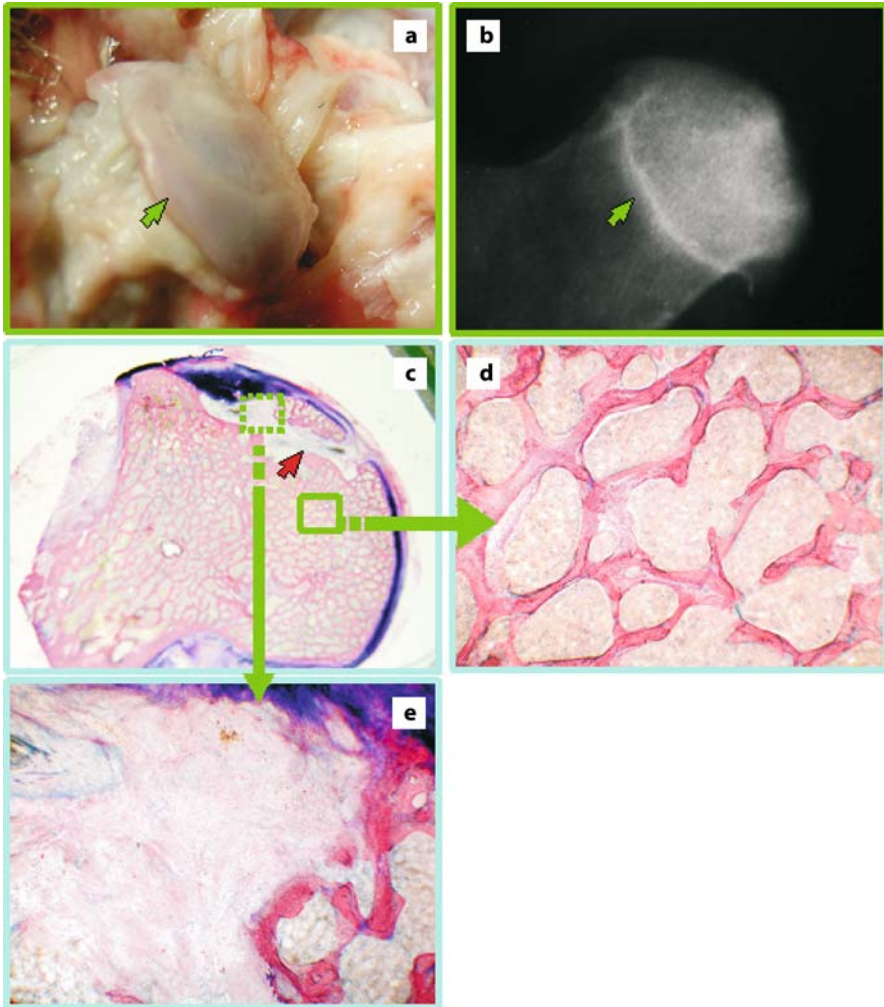
Figure 5. a General view of the femoral head (*arrow*) in experimental group (30 weeks). **b** Representative radiograph of femoral head (*arrow*) in control group after 30 weeks shows that the contour of the femoral head has lost integrity. **c** Representative histological section of the femoral head (*red arrow*) in control group 30 weeks after surgery. **d** Good healing within the inner femoral head (*arrow* spanning **c** to **d**). **e** Poor integration in the conjugate region (*arrow* spanning **c** to **e**) between the scaffold and bone-cartilage flap region

ON Models

Numerous studies have been devoted to develop relevant ON models. The efforts made to date have achieved partial success recently (Conzemius et al. 2002). Apart from emus, no animal model has shown joint collapse, which was the end stage of ON in patients (Gold et al. 1978; Malizos et al. 1993; Kawai et al. 1985). On the con-

trary, the defect model is useful in study of femoral-head ON in simulating the defect created for evaluation of treatment effects at the late stage of ON. In the femoral head defect model, the trabecular bone in the femoral head was removed, which is like the trap-door procedure or its modifications tested by many studies (Buckley et al. 1991; Itoman et al. 1989; Meyers et al. 1983; Mont et al. 1998; Rosenwasser et al. 1994). Mont et al. (2001) summarized the essentials in establishment of ON model as (a) femoral head as the region of interests, (b) model with subchondral defect, (c) to have structural compromise, and (d) similar to defects made for treatment involving vascularized bone grafting. As a result, we chose the bone defect model for our experiment.

Scaffold Production, Evaluation, and Experimental Results

The repair of the bone defect in loading area of the femoral head is a puzzling problem for many researchers. Tissue-engineering technique may be an effective way to target this problem. In the development of scaffold materials for tissue engineering, the scaffold should pursue the following characters: Apart from maintaining the porosity of the scaffold, we must improve scaffold strength, which appeared sometimes more important for the bone defect of the loading place in the femoral head. Over the past decades, considerable effort has been made and focused on fabricating bone scaffolds into a 3D interconnected macroporous scaffold to guide bone reconstruction through rapid vascularization, bone growth and remodeling (Ohgushi et al. 1992; Yoshikawa et al. 1996; Li et al. 2002). Scaffolds developed for bone regeneration should have a homogenous interconnected porous structure with good mechanical properties to withstand loading during bone formation. There are two ways to achieve or improve the strength of the scaffolds. Firstly, we can improve the original intensity of the scaffold with new material (Ramay and Zhang 2004). Secondly, we can improve the inner structure of the scaffold to fit the local stress distribution of the affected place. The latter way may be much more effective for bone scaffold fabricating. According to Wolff's trajectorial hypothesis (Van Rietbergen et al. 1999), the trabecular architecture should be adopted to meet the tissue stresses. This paradigm at least suggests that, normally, stresses and strains should be distributed rather evenly over the trabecular network. This has been partly certified in finite element analysis by Van Rietbergen et al. (1999), which was developed to calculate stresses and strains in complex 3 D structures based on micro-CT images.

A biomimetic scaffold should meet the demands of local stress and strain distribution, rapid vascularization, and bone growth. Wolff's trajectorial principle may also apply to bone scaffold production. In our study, we adopted the approach by improving the inner structure of the scaffold, for experimental studies. Through 3D gel-lamination techniques, we fabricated porous biomimetic BCP ceramic scaffolds with oriented trabecular structure, which was verified by the 3D data set from the micro-CT images. The macro-porous porosity of the BCP scaffold is 62%, which satisfies the need of making bone scaffold in tissue engineering. The average compressive modulus and ultimate strength along the axis of the scaffolds reached 464 ± 36.03 and 5.62 ± 0.78 MPa, respectively. Although the strength of BCP scaffold is lower than that

of trabecular bone from the femoral head, the compressive modulus of BCP scaffold is close to that of the femoral head, which is good for healing of bone defects and implants. Compared with trabecular bone specimens, the BCP scaffolds in our study have a similar appearance and similar value in BV/TV, Tb.Th, Tb.N, and Tb.Pf, but we need further study to certificate that stress and strain distribution in the femoral head is uniform in the inner scaffold after planting. This can be proved by finite-element analysis based on micro-CT images, which our group is doing.

Overall, the animal experiment results show that the bone formation in the scaffold is very good. The trabeculae of the entire BCP scaffold were covered by a layer of new bone. The femoral heads in the experimental group had kept integrity by the time of harvest. In comparison, cartilage repair was less than satisfactory in our study.

Conclusion

We adopted BCP scaffold, prepared by 3D gel-lamination technology incorporated with a foaming method. The MSCs were loaded onto the BCP to fill the bone defect in the canine femoral head in order to prevent collapse of the femoral head. Radiographic and biomechanical studies indicated that the healing of bone region was excellent in the bone–cartilage defect of the femoral head. The conjugate region between bone–cartilage and scaffold was not as good as expected. Further study, including tissue engineering bone–cartilage complex grafting, may be an effective way to meet the related demands and applications.

References

Bruder SP, Kraus KH, Goldberg VM, Kadiyala Y (1998) Critical-sized canine segmental femoral defects are healed by autologous mesenchymal stem cell therapy. Trans 44th Annual Meeting of the Orthopaedic Research Society, p 147

Buckley PD, Gearen PF, Petty RW (1991) Structural bone-grafting for early atraumatic avascular necrosis of the femoral head. J Bone Joint Surg 73A:1357–1364

Callister WD (2003) Materials science and engineering, an introduction, 6th edn. Wiley, New York

Conzemius MG, Brown TD, Zhang Y, Robinson RA (2002) A new animal model of femoral head osteonecrosis: one that progresses to human-like mechanical failure. J Orthop Res 20:303–309

Ding M, Odgaard A, Hvid I (1999) Accuracy of cancellous bone volume fraction measured by micro-CT scanning. J Biomech 32:323–326

Gold EW, Fox OD, Weissfeld S, Curtiss PH (1978) Corticosteroid-induced avascular necrosis: an experimental study in rabbits. Clin Orthop 135:272–280

Hutmacher DW (2000) Scaffolds in tissue engineering bone and cartilage. Biomaterials 21:2925–2943

Itoman M, Yamamoto M (1989) Pathogenesis and treatment of idiopathic aseptic necrosis of the femoral head. Clin Immunol 21:713–725

Kawai K, Tamaki A, Hirohata K (1985) Steroid-induced accumulation of lipid in the osteocytes of the rabbit femoral head. A histochemical and electron microscopic study. J Bone Joint Surg 67A:755–763

Koo KH, Kim R, Ko GH, Song HR (1995) Preventing collapse in early osteonecrosis of the femoral head: a randomized clinical trial of core decompression. J Bone Joint Surg 77-B:870–874

Lafforgue P, Dahan E, Chagnaud C (1993) Early stage avascular necrosis of the femoral head: MR imaging for prognosis in 31 cases with at least 2 years of follow-up. Radiol 187:199–204

Laib A, Barou O, Vico L, Lafage-Proust MH, Alexandre C, Rugsegger P (2000) 3D micro-computed tomography of trabecular and cortical bone architecture with application to a rat model of immobilisation osteoporosis. Med Biol Eng Comput 38:326–332

Li HS, De Wijn JR, Layrolle P, de Groot K (2002) Synthesis of macroporous hydroxyapatite scaffolds for bone tissue engineering. J Biomed Mater Res 61:109–120

Lin CY, Kikuchi N, Hollister SJ (2004) A novel method for biomaterial scaffold internal architecture design to match bone elastic properties with desired porosity. J Biomech 37:623–636

Malizos KN, Quarles LD, Seaber AV, Rizk WS, Urbaniak JR (1993) An experimental canine model of osteonecrosis: characterization of the repair process. J Orthop Res 11:350–357

Maniatopoulos C, Sodek J, Melcher AH (1988) Bone formation in vitro by stromal cells obtained from bone marrow of young adult rats. Cell Tissue Res 254:317–330

Mendes SC, Tibbe JM, Veenhof M, Bakker K, Both S, Platenburg PP, Oner FC, de Bruijn JD, van Blitterswijk CA (2002) Bone tissue-engineered implants using human bone marrow stromal cells: effect of culture conditions and donor age. Tissue Eng 8:911–920

Meyers MH, Jones RE, Bucholz RW, Wenger DR (1983) Fresh autogenous grafts and osteochondral allografts for the treatment of segmental collapse in osteonecrosis of the hip. Clin Orthop 174:107–112

Mont MA, Einhorn TA, Sponseller PD, Hungerford DS (1998) The trapdoor procedure using autogenous cortical and cancellous bone grafts for osteonecrosis of the femoral head. J Bone Joint Surg 80B:56–62

Mont MA, Jones LC, Elias JJ, Inoue N, Yoon TR, Chao EY, Hungerford DS (2001) Strut-autografting with and without osteogenic protein-1: a preliminary study of a canine femoral head defect model. J Bone Joint Surg 83A:1013–1022

Muller R, Van Campenhout H, Van Damme B, Van Der Perre G, Dequeker J, Hildebrand T, Ruegsegger P (1998) Morphometric analysis of human bone biopsies: a quantitative structural comparison of histological sections and micro-computed tomography. Bone 23:59–66

Nishii T, Sugano N, Ohzono K, Sakai T, Haraguchi K, Yoshikawa H (2002) Progression and cessation of collapse in osteonecrosis of the femoral head. Clin Orthop 400:149–157

Ohgushi H, Okumura M, Yoshikawa T, Inoue K, Senpuku N, Tamai S, Shors EC (1992) Bone formation process in porous calcium carbonate and hydroxyapatite. J Biomed Mater Res 26:885–895

Ohzono K, Saito M, Takaoka K, Ono K (1991) Natural history of nontraumatic avascular necrosis of the femoral head. J Bone Joint Surg 73-B:68–72

Ramay HR, Zhang M (2004) Biphasic calcium phosphate nanocomposite porous scaffolds for load-bearing bone tissue engineering. Biomaterials 25:5171–5180

Rosenwasser MP, Garino JP, Kiernan HA, Michelsen CB (1994) Long term followup of thorough debridement and cancellous bone grafting of the femoral head for avascular necrosis. Clin Orthop 306:17–27

Shimizu K, Moruya H, Akita T (1994) Prediction of collapse with magnetic resonance imaging of avascular necrosis of the femoral head. J Bone Joint Surg 76A:215–233

Smith KR, Bonflglio M, Montgometry WJ (1980) Non-traumatic necrosis of the femoral head treated with tibial bone-grafting. A follow-up note. J Bone Joint Surg 62A:845–847

Tian JM, Wang XY, Dong LM (2005) Preparation of porous hydroxyapatite scaffolds. Key Eng Mater 282:1541–1544

Van Cleynenbreugel T, Van Oosterwyck H, Vander Sloten J, Schrooten J (2002) Trabecular bone saffolding using a biomimetic approach. J Mater Sci Mater Med 13:1245–1249

Van Rietbergen B, Muller R, Ulrich D, Ruegsegger P, Huiskes R (1999) Tissue stresses and strain in trabeculae of a canine proximal femur can be quantified from computer reconstructions. J Biomech 32:443–451

Yaszemski MJ, Payne RG, Hayes WC, Langer R, Mikos AG (1995) Evolution of bone transplantation: molecular, cellular, and tissue strategies to engineer human bone. Biomaterials 17:175–185

Yoshikawa T, Ohgushi H, Tamai S (1996) Immediate bone forming capability of prefabricated osteogenic hydroxyapatite. J Biomed Mater Res 32:481–492

Contrast-Enhanced MRI and Micro-CT Adopted for Evaluation of a Lipid-Lowering and Anticoagulant Herbal Epimedium-Derived Phytoestrogenic Extract for Prevention of Steroid-Associated Osteonecrosis

Ling Qin (✉) [1], Ge Zhang[1], Hui Sheng[1], James F. Griffth[2], Ka Wai Yeung[2], and Kwok-Sui Leung[1]

[1] Department of Orthopaedics and Traumatology, The Chinese University of Hong Kong, Hong Kong, China
     e-mail: lingqin@cuhk.edu.hk
[2] Department of Radiology and Organ Imaging, The Chinese University of Hong Kong, Hong Kong, China

Abstract

We developed an alternative steroid-associated osteonecrosis (ON) rabbit model using a combination of a single injection of low-dose lipopolysaccharide (LPS) and three subsequent injections of pulsed high-dose methylprednisolone (MPS). The usefulness of this experimental ON model was evaluated using both conventional and advanced bio-imaging techniques, including contrast-enhanced dynamic MRI and a high-resolution micro-CT. Details on establishment of methodology are described, which were adopted into an efficacy study on a herbal Epimedium-derived phytoestrogenic extract (HEPE) developed for prevention of steroid-associated ON using an established rabbit model. The underlying mechanisms of HEPE for prevention of steroid-associated ON were found to be associated with inhibition of both intravascular thrombosis and extravascular bone marrow lipid deposition, the two known mechanistic pathways in pathogenesis of ON. Our experimental results provide for potential clinical trials or applications of HEPE in the prevention of ON among high-risk patients undergoing steroid treatment.

Introduction

Indications of Steroids and Its Side Effects Related to Osteonecrosis

Osteonecrosis (ON) is a severe skeletal disease that can result from trauma, alcohol abuse, and life-saving pulsed steroid. Steroids are routinely indicated for treatment of many medical conditions such as rheumatoid arthritis (RA), infectious diseases,

organ transplantation, and hemodialysis (Assouline-Dayan et al. 2002). Epidemiologic survey shows that there are approximately 20,000 new ON patients diagnosed per year in U.S., and the prevalence of ON in Asia is even two to three times higher (National Osteonecrosis Foundation; Wang et al. 2004). Steroid-associated ON has even become a socio-economic problem in Hong Kong and mainland China since the outbreak of several virus infectious diseases, including severe acute respiratory syndrome (SARS; Griffith et al. 2005; Li et al. 2006; Hong and Du 2004; Koller et al. 2000; Miller et al. 2002; Scribner et al. 2000; Shen et al. 2004; So et al. 2003).

The pathogenesis of steroid-induced ON is thought to be intravascular thrombosis-induced occlusion and extravascular lipid-deposit-induced compression, leading to an impaired structure-function of intraosseous blood supply system. The impaired intraosseous blood supply induces ischemia, necrosis lesion, and subchondral bone collapse. Some patients may end up with total joint replacement (Aaron et al. 1998; Assouline et al. 2002; Lieberman et al. 2002; Qin et al. 2006; Wang et al. 2000). Unfortunately, the prognosis of total joint replacement is not satisfactory, especially in patients with steroid-induced ON (Aaron et al. 1998; Saito et al. 1989). This implies that prevention of ON development is essential for high-risk patients, including those undergoing steroid treatment (Qin et al. 2006; Wang et al. 2000).

Research and Development in Prevention of Steroid-Associated ON

Based on the pathogenesis of steroid-associated ON, anti-thrombosis agents, such as warfarin, and lipid-lowering agents, such as statins, have been clinically used to prevent steroid-associated ON; however, due to side effects (bleeding for warfarin and abnormalities in liver for statins) occurring during long-term administration, their routine clinical use for prevention of steroid-associated ON among risk patients is limited (Expert Panel 2001; Glueck et al. 2005; Martin et al. 2004; Motomura et al. 2004; Pritchett et al. 2001; Wortmann et al. 2002; Schulman et al. 1999; Wang et al. 2000). It is therefore highly desirable to develop therapeutic agents for long-term use that may target both intravascular thrombosis and extravascular lipid deposition, with fewer no side effects for preventing steroid-induced ON.

The SARS outbreak in China in 2003 provided a unique opportunity where a remarkable difference in incidence of steroid-associated ON was diagnosed using MRI, with up to 32.7% ON (23% ON at hip alone) found in SARS patients in Beijing (Li et al. 2005), whereas only 5–6% in Hong Kong and Guang Zhou (Griffith et al. 2005; Shen et al. 2004). Apart from potential dose variations in steroid use, frequency of herb preparation used for SARS patients during pulsed steroid treatment was much higher in southern China (Hong Kong and Guang Zhou) than in North China (Beijing); thus, we speculate that the much lower ON incidence in Hong Kong and Guang Zhou might be attributed to potential preventive effects of herbs involved in conventional anti-inflammatory traditional herbal medicine including phytoestrogenic extraction from herbal Epimedium during life-saving standard pulsed steroid for treatment of SARS patients (Lau and Leung 2005; Liu et al. 2006), whereas no such conventional approach was introduced for treatment of SARS patients in Beijing (Li et al. 2005).

Herbal *Epimedium* is known as a kidney-tonifying "bone-strengthening" herb. An Epimedium-derived phytoestrogenic extract (HEPE) has been developed as an alternative preparation for long-term and safe administration to prevent postmenopausal osteoporosis (Qin et al. 2005a,b; Zhang et al. 2006). To date, a group of phytoestrogen fractions have been derived from *Epimedium* by a series of standardized extraction and isolation procedures, which mainly consist of three phytoestrogenic compounds (Icariin, Genistein and Daidzein; Lee et al. 2004; Meng et al. 2005; Qin et al. 2005a).

Interestingly, phytoestrogen has also been shown to be able to decrease low-density lipoprotein and increase high-density lipoprotein (Anderson et al. 1995; Clifton-Bligh et al. 2001; Lamon-Fava et al. 2000). This may imply potential beneficial effects on reversing cholesterol transport, i.e., a potential capability in inhibiting lipid deposition in peripheral tissues. In fact, studies have shown that phytoestrogen also has potential anti-thrombotic activity through maintaining a balance between coagulation and fibrinolysis (Choo et al. 2002; Wang et al. 2004). These observations motivated the investigators of this chapter to establish the following hypothesis that HEPE might prevent steroid-associated ON through a unique mechanism associated with inhibition of both thrombosis and lipid deposition. In order to confirm this hypothesis, animal experiments are essential to investigate whether HEPE is able to prevent steroid-associated ON development experimentally, as no clinical trials with controlled conditions are ethically possible to confirm the above-mentioned epidemiologic observations.

Current Available Osteonecrosis Animal Models and Their Limitations

The steroid-associated ON animal models developed in the past include both quadrupeds (mice, rats, rabbits, dogs, pigs, dogs, and horses, etc.) and bipeds (chicken and emeses). All these models may not be able to produce joint collapse, which has been found in ON patients; however, they are still useful for studying the pathogenesis of steroid-associated ON and evaluation of pharmaceutical agents or biophysical means developed for prevention of ON development. Among the above-mentioned animal models, the rabbit ON model is the most frequently used model (Expert Panel 2001; Glueck et al. 2005; Lang et al. 1989; Martin et al. 2004; Motomura et al. 2004; Pritchett et al. 2001; Schulman et al. 1999; Qin et al. 2006; Wortmann et al. 2002; Wang et al. 2000).

Steroid-Associated ON in Rabbit Model

There are two protocols commonly used for establishing steroid-associated ON model in rabbits. One protocol is to use a single injection of high-dose methylprednisolone (MPS; i.e., H-MPS × 1); however, this has a low incidence of ON (43%; Yamamoto et al. 1997). The other protocol is to use two injections of high-dose lippolysaccharide (LPS) combined with subsequent three injections of high dose MPS (i.e., H-LPS×2−H-MPS×3), but this carries a high mortality (50%; Yamamoto et al. 1995). For developing intervention strategies for steroid-associated ON, there is a need to

develop protocols for establishing animal model with a high incidence but low mortality. Recently, a steroid-independent ON rabbit model was successfully established with a single injection of low-dose LPS, which showed a higher incidence of ON lesion (77%) and lower mortality (11%) as compared with the protocol (i.e., H-LPS×2–H-MPS×3) due to avoidance of severe LPS-induced shock by lowering the given dose (Irisa et al. 2001). The authors of this chapter recently confirmed that a single low-dose LPS injection combined with three subsequent injections of pulsed high-dose MPS did induce a high incidence of ON but low or even no mortality in rabbits (Qin et al. 2006). The first part of the chapter reviews the development of imaging methods for studying alterations of blood circulation under the influence of steroid treatment.

Development of a Steroid-Associated ON Rabbit Model

Animals and Inductive Protocols

Twenty-eight-week-old male New Zealand white rabbits with body weight of 45 kg were used. Fourteen rabbits were assigned to the treatment group and received LPS injection (i.v. 10 μ g/kg) (*Escherichia coli* 0111:B4, Sigma-Aldrich). Twenty-four hours later, three MPS injections (i.m. 20 mg/kg; Pharmacia and Upjohn) were given intramuscularly at a time interval of 24 h. Six rabbits were used as control and injected with 0.9% normal saline. The rabbits in both groups were killed 6 weeks after the last MPS injection (Qin et al. 2006).

Imaging Methods Established for Monitoring and Confirmation of ON Development

Contrast-Enhanced MRI for Monitoring Blood Perfusion In Vivo

Contrast-enhanced dynamic MRI was performed for bilateral proximal and distal femora before LPS injection and 6 weeks after the last injection of MPS, using a 1.5-T superconducting system (ACS-NT Intera; Philips, The Netherlands). An extremity coil (transmit-receive surface coil) was used on the target site of the rabbits under sedation with Katamin (i.m. 0.25 ml/kg). T1-weighted MRI images [repetition time (TR) / echo time (TE)=425/13 ms] were used for analysis of the target side with a section thickness of 3 mm. A total of 200 dynamic images were obtained in 90 s. A bolus of dimeglumine gadopentetate (0.8 mmol/kg; Magnevist, Schering, Berlin, Germany) was rapidly administered manually via a previously placed 21-gauge intravenous catheter in the right ear vein, immediately followed by a 6-ml saline flush at the same injection rate. The dynamic scan started as soon as the injection of the contrast medium commenced. Signal intensity (SI) was then measured in operator-defined ellipse-like regions of interest (ROIs) over the target site beneath the joint space in the mid-coronal T1-weighted images (Fig. 1) using a cursor and graphic display device. The SI values derived from the ROIs were plotted against time as time-intensity curve (TIC). The baseline value (SI_{base}) of the SI in a TIC was calculated as the mean SI value in the first three images. The maximum SI (SI_{max}) was defined as the peak enhancement value at a given time interval of 90 s after contrast injection
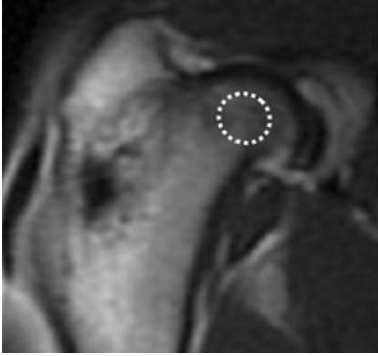
Figure 1. A T1-weighted coronal MRI image of rabbit proximal femur (TR/TE = 425/13 ms) after Gd-DTPA administration. The region of interest in the central part of femoral head with a size of $8 \sim 10$ pixels ($64 \sim 80\,mm^2$) was defined for analysis of local intraosseous perfusion

during the early phase of the first pass. Perfusion index "maximum enhancement" was calculated as:

$$\text{Maximum enhancement} = \frac{\text{SI}_{max}\text{SI}_{base}}{\text{SI}_{base}} \times 100\%$$

The mean of the maximum enhancement values measured at bilateral proximal femur of each rabbit was used for data analysis (Lang et al. 1989; Qin et al. 2006).

Development of a Micro-CT-Based Microangiography for Intraosseous Vessels

Under general anesthesia with sodium pentobarbital the abdomen cavity of the animals was opened and a scurf-needle with 25-mm syringe was inserted in the ab-
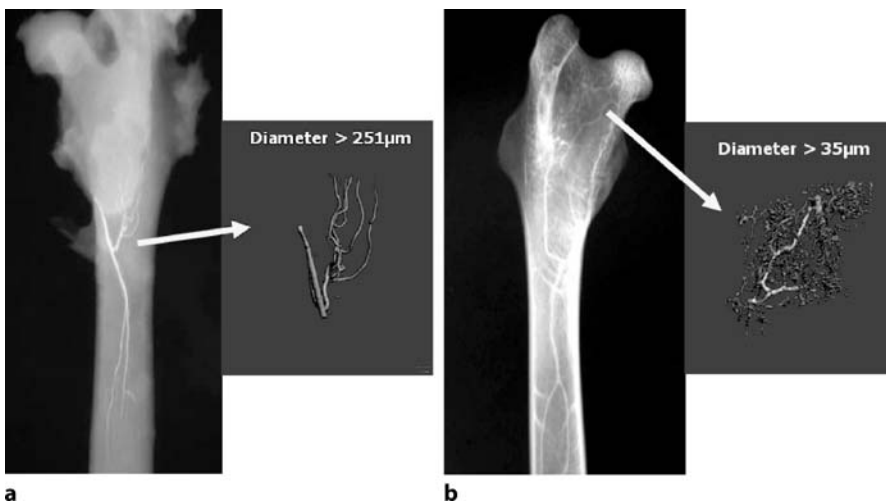
Figure 2 a,b. Comparison of two perfusion mediums for in vivo angiography. **a** Perfusion with clinically used barium sulfate only reached vessels in diaphysis larger than 251 μm (*arrow*) as measured by micro-CT. **b** Perfusion with Microfil lead chromate reached small vessels (*arrow*) in proximal femur as measured by micro-CT used for this study
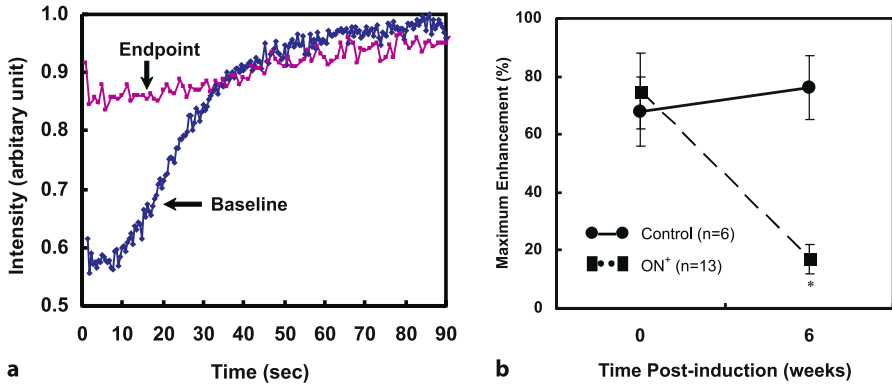
Figure 3. a Representative dynamic MRI time-intensity curves of a rabbit with osteonecrotic proximal femur. Significant decrease in the perfusion index "maximum contrast enhancement" found at the end of the experiment as compared with its baseline. **b** Significant decrease in perfusion index maximum contrast enhancement found at proximal femur of the necrotic rabbits as compared with that of the controls. *Asterisk: p < 0.05*, compared with baseline and control rabbits, respectively

dominal aorta distal to the heart with ligation of that proximal to the heart. The vasculature was flushed with 50 U/ml heparinized normal saline at 37 °C and at a flow speed of 20 mm/min via an automatic pump apparatus (PHD 22/2000, Harvard Apparatus). As soon as the outflow from an incision of the abdominal vein was limpid, 10% neutral buffered formalin (37 °C) was pumped into the vasculature to fix the nourished skeletal specimen (Bentley et al. 2002; Duvall et al. 2004; Jorgensen et al. 1998; Qin et al. 2006; Simopoulos et al. 2001). The formalin was then flushed from the vasculature using the heparinized normal saline, and the vasculature was injected with clinically used barium sulfate in our pilot study, which was only able to demonstrate diaphysial vessels (Fig. 2a) and was not able to meet our requirement for studying intraosseous vessels at both proximal and distal femura of rabbtis; therefore, we adopted the method of others (Bentley et al. 2002; Duvall et al. 2004; Simopoulos et al. 2001) using a lead chromate-containing confected radiopaque silicone rubber compound based on the manufacturer's protocol (Microfil MV-122, Flow Tech; Carver, Mass.; http://www.flowtech-inc.com/microfil.htm), which demonstrated much better perfusion results for micro-CT scanning of the vessels presented at the metaphysial regions (Fig. 2b).

After completion of perfusion, animals were killed and stored at 4° for 1 h to ensure polymerization of the contrast agent before microangiography. Bilateral femoral samples were then harvested and fixed in paraformaldehyde (4%) for decalcification with Ethylenediaminetetraacetic Acid (EDTA, 10%, pH 7.4). Then, both proximal third and distal third of both femoral samples, i.e., four dissected parts for each rabbit, were obtained for micro-CT scanning and evaluation using μCT-40 (Scanco Medical, Bassersdorf, Switzerland).

The micro-CT scan was performed perpendicular to the shaft and initiated from a reference line 10 mm away from the bottom with an entire scan length of 10 mm (refer to the X-ray images of Fig. 4a). The scan resolution selected was 36 μm per voxel with 1024×1024 pixel image matrix. For segmentation of blood vessels from background, noise was removed using a low pass Gaussian filter (Sigma = 1.2, Support = 2) and blood vessels was then defined at a threshold of 85. In order to reconstruct 3D architecture of vasculature, the blood vessels filled with Microsfil was included with semi-automatically drawn contour at each 2D section. A histogram was subsequently generated to display the distribution of vessel size and a color-coded scale was mapped to the surface of the 3D images to produce a visual representation of the vessel size distribution (Duvall et al. 2004).

Results of Blood Perfusion Imaging Analysis

Pathophysiologic Pathway for Intraosseous Blood Supply

A significant decrease ($p < 0.05$) in the "maximum enhancement" of both proximal and distal femur was found in the ON^+ rabbits as compared with baseline, whereas no significant change ($p > 0.05$) was found in the control rabbits (Fig. 3).

Micro-CT-Based Evaluation on Intravascular Pathogenic Events

The control samples showed normal vascular network, whereas the ON^+ samples showed a blocked stem vessel surrounded by small disconnected vessels and disseminated leakage substance (Microfil; Fig. 4a). Quantitatively, histograms were compiled to show the blood vessel size frequency distribution in both ON^+ samples and the controls. As compared with the control samples, the necrotic ones showed an increase in small, collateral-sized-like vessels (200–400 μm), reduced perfusion to conduit vessels (400–600 μm), and dilated vessels (800–1000 μm; Fig. 4b).

Discussion and Conclusion

We used advanced bio-imaging methods (dynamic contrast-enhanced MRI and micro-CT-based microangiography) to demonstrate that pathogenic events and pathophysiologic pathways responsible for intraosseous ischemia.

In a pilot study, we also explored if clinical angiography using radiopaque substance barium sulfate would be a better approach to monitor steroid-associated emboli in the intraosseous vascular network; however, due to its larger particle size with lower solubility in solution, only blood vessels larger than 250 μm were visualized to be perfused radiographically. Microfil (lead chromate) is a radiopaque solution with a smaller particle size, which was recently used for quantitative micro-CT analysis of collateral vessel development after ischemic injury (Duvall et al. 2004), and successfully adopted into the present micro-CT angiographic study. Our findings showed that the formation or presence of intravascular thrombosis was well demonstrated by micro-CT-based microangiography, where the thrombi blocked the vasculature

Figure 4. a Representative images of micro-CT-reconstructed 3D micro-angiography of proximal femur from a necrotic (*upper*) and control rabbit (*lower*), which were evaluated from the region of interest (ROI) within the white frame, respectively (refer to Fig. 1 for the definition of ROI). As compared with control specimen, the necrotic one demonstrated blocked stem vessels with numerous disconnected small vessels and disseminated formless radiopaque substances by leaking in downriver region. Note that the two left images were generated from the corresponding left ones after removing the disconnected small blood vessels by removing the vessels with diameter smaller than 252 µm for better visualization of the blocked stem vessels in necrotic specimen. **b** Representative histogram with distribution of blood vessel sizes in both control and necrotic samples. The necrotic sample shows more small, collateral-sized vessels (200 – 400 µm), reduced perfusion to conduit vessels (400 – 600 µm), and dilated vessels (800 – 1000 µm)
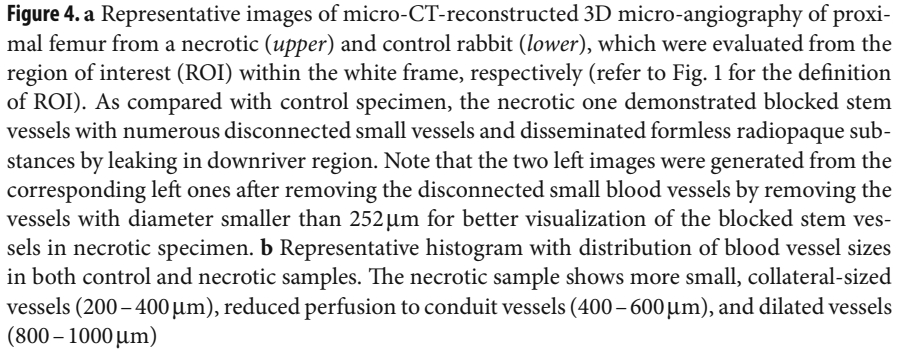
as revealed by both upstream-dilated stem vessels and downstream-reduced conduit vessels localized to the necrotic lesions in decalcified 3D micro-CT intraosseous vascular network.

The above-mentioned perfusion techniques were validated by our previous intravascular hematology and histopathology study, which showed intravascular thrombosis using the same inductive protocol. In ON[+] rabbits, a significant decrease from baseline ($p < 0.05$) induced by LPS was found in the ratio of t-PA/PAI-I before the first MPS injection. Twenty-four hours after the last MPS injection, the decreasing tendency for activated partial thromboplatin time (APTT) was maintained, whereas a rapid decreasing tendency for ratio of t-PA/PAI-I became apparent. It implied imbalance between coagulation and fibrinolysis, such that thrombi occurred histopathologically (Qin et al. 2006).

Structural changes of vasculature were also found to be associated with time-course changes in plasma ratio of low-density lipoprotein to high-density lipoprotein (LDL/HDL ratio) in ON[+] rabbits, which showed a significantly increased ratio from the baseline 24h later after LPS injection, a tendency which was further significantly enhanced 24h after the last MPS injection. This was evidenced in histopathologic findings, which demonstrated increased fat cell size in the necrotic marrow, accompanied by substantially reduced marrow space (Qin et al. 2006). In fact, higher LDL/HDL ratio was considered to reflect the prominent lipid transport to the peripheral tissues, which might result in extravascular marrow compression from lipid deposition (Glueck et al. 2003).

Both intravascular and extravascular events contributed to the impaired perfusion of intraosseous blood supply. This was evidenced by the significantly decreased "maximum enhancement," an index of blood perfusion measured by dynamic MRI in ON[+] rabbits in the present study.

The high incidence (93%), and even no mortality, using this protocol might be attributed to both the combined administration of LPS-MPS and a single low-dose LPS. The histopathologic features of ON in this rabbit model were similar to those observed in human ON specimens we obtained from SARS patients (see Fig. 5). The significance of the protocol used in this study with high ON incidence but low or no

a

Light blue: 36-108 um   Pink: 144-216um   Orange: 252-360um
Yellow: 396-504um   Green: 540-648 um   Light pink: 686-999um

Necrotic bone

Control bone

b

■ Necrotic bone

● Control bone
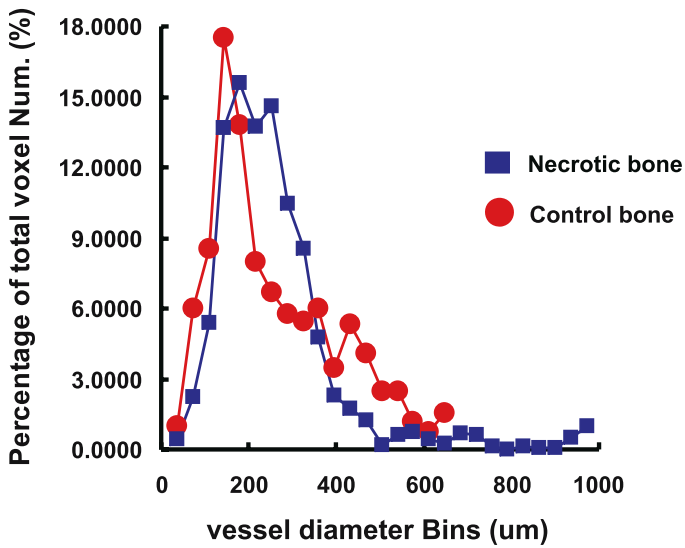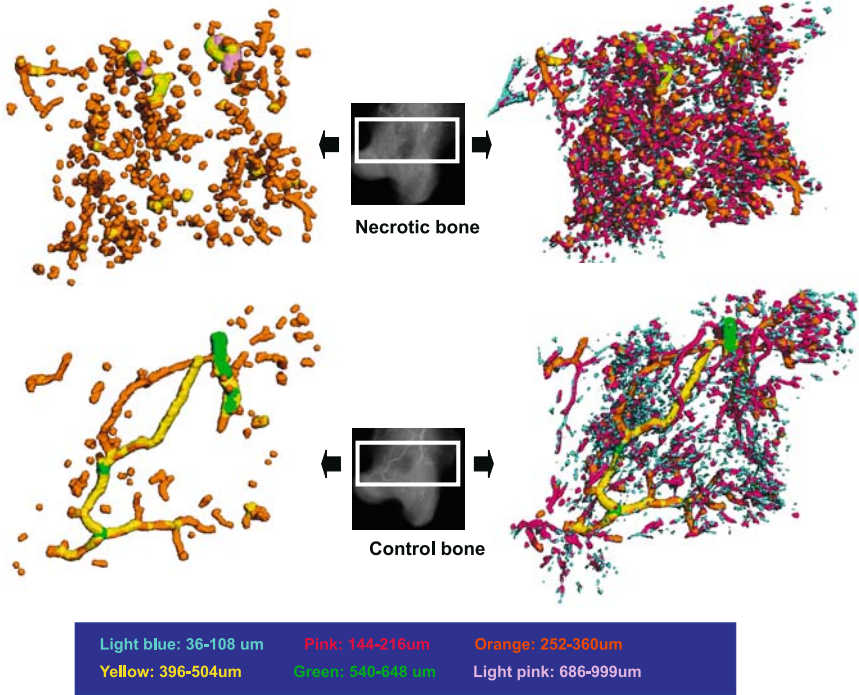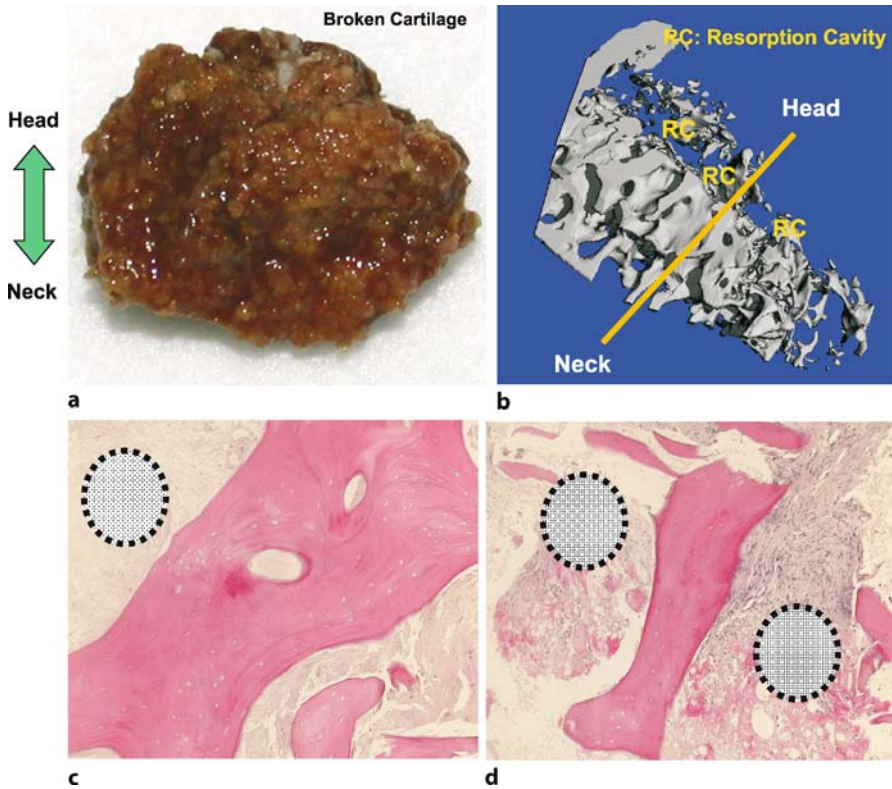
Figure 5 a–d. Osteonecrotic femoral head from a severe acute respiratory syndrome (SARS) patient. **a** Specimen from necrotic femoral head of a patient recovered from SARS. **b** A 3D reconstruction of subchondral necrotic lesion with resorption cavity by micro-CT. **c** Histopathologic section with fibrotic scar formation around the necrotic bone within the *dotted circle* (H&E staining, ×200). **d** Histopathological section with granulation tissue penetration into the necrotic bone with resorption cavity within the *dotted circles* (H&E staining, ×200). *RC* resorption cavity

mortality was obvious, at least in terms of reducing the number of experimental animals required for intervention at studies and increasing the validity of the evaluation results (Motomura et al. 2004).

In conclusion, static and dynamic bio-imaging modalities, including advanced contrast-enhanced dynamic MRI and micro-CT-based angiography, were unique and non-destructive for studying local blood perfusion. The present experimental study showed that our experimental protocol with a single injection of low-dose LPS and subsequent pulsed high-dose MPS injections were an effective way to induce ON in rabbits with a high incidence and no mortality. The ON model established in the present study therefore forms a solid foundation for investigating the efficacy of potential intervention strategies for prevention of steroid-associated ON.
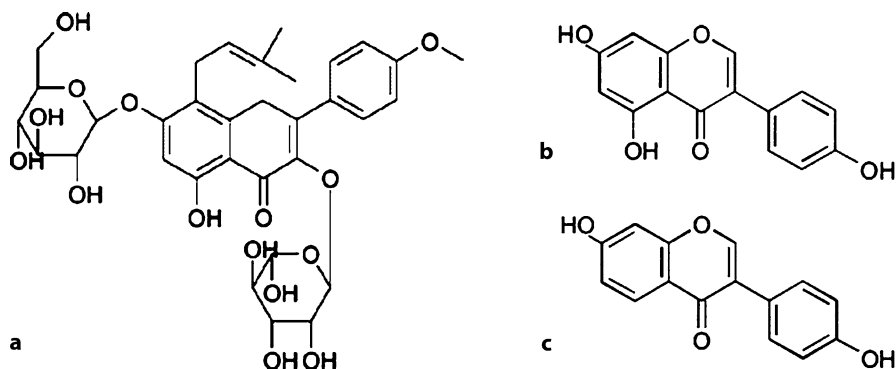
Figure 6a–c. Chemical structures of three main phytoestrogenic components in herbal Epimedium-derived phytoestrogen extraction (HEPE). **a** Icariin (50%). **b** Genistein (2.5%). **c** Daidzein (12.5%)

HEPE Developed for Prevention of Steroid-Associated ON in Rabbit Model

Materials and Methods

Grouping and Treatment

Thirty 28-week-old male New Zealand white rabbits received an established steroid-associated ON inductive protocol as described and also as published recently (Qin et al. 2006). Animals were then divided into control group (CO; $n = 14$) and HEPE group ($n = 16$). Rabbits in HEPE group received HEPE (5 mg/kg/bw day^{-1}) at the first day of intervetion. The known bioactive compounds in HEPE in 5 mg HEPE contained 2500 μg Icariin, 125 μg Genistein, 625 μg Daidzein, and 1750 μg vehicle; Fig. 6) was commercially available (Tong Ji Tang Pharmacal Company, Gui Zhou, China; Zhang et al. 2006).

Evaluations on Intravascular and Extravascular Events of Intraosseous Pathogenesis

Local Blood Perfusion In Vivo Contrast-enhanced dynamic MRI was performed on both femora for local intraosseous perfusion before LPS injection and 6 weeks after the last injection of MPS. (Details of the method are mentioned above in section on ON model evaluation.)

Micro-CT-Based Microangiography Six weeks after inductive injection, both femora were dissected after decalcification.

Histopathology After microangiography, all the decalcified samples were embedded in paraffin, then cut into 6-mm-thick sections along the coronal plane for the proximal parts and the axial plane for the distal parts. The ON lesions and intravascular/extravascular pathologic evidence was evaluated. Sections were stained with hematoxylin/eosin (H&E) for evaluation of osteonecrosis and calculation of fat cell

size. Phosphotungstic acid hematoxylin (PTAH) was the staining specifically employed for examination of fibrin thrombus (Prophet et al. 1992).

Regarding evaluation of ON, entire areas of each dissected part of femoral samples, including epiphysis and metaphysis, were examined for the presence of ON, which were judged blindly by two pathologists based on the characteristic histopathologic features with empty lacunae or pyknotic nuclei of osteocytes in the trabeculae, accompanied by surrounding necrotic bone marrow (Yamamoto et al. 1995, 1997). All rabbits that had at least one ON lesion in the examined sections were defined as ON^+, whereas those with no ON lesions were ON^-.

Regarding calculation of extravascular marrow fat cell size, the fat cell size of each rabbit was calculated as the average of the Feret's diameter of all bone marrow fat cells with clearly defined profile of each dissected part of the femur samples. The histologic sections were digitized into a microscope imaging system (Zeiss Aixoplan with Spot RT digital camera, Zeiss, Germany) for quantification using image analysis software (ImageJ 1.32j, National Institutes of Health, Bethesda, Md.).

Hematology A 5-ml blood sample was collected in a fasting state from each rabbit through the auricular arteries immediately before injection of LPS, and at weeks 1 and 2 after LPS injection. Half was stored at $-70°C$ for evaluating intravascular thrombotic status, including t-PA/PAI-I (ratio of tissue-type plasminogen activator to plasminogen activator inhibitor) as intravascular fibrinolysis indicator by enzyme-linked immunosorbent assay technique using corresponding mouse monoclonal anti-human antibodies (Manufacturer's Datasheet, Xitang Biotechnology, Shanghai, China) and APTT as intravascular coagulation indicator by Automatic Blood Coagulation Analysis Apparatus (SysmexCA-50, Japan).

Statistics Comparison of the incidence of ON between the control group and the HEPE group was performed using Fisher's exact probability test. Student's t-test was used to compare the difference in all the histopathologic measurement data between the control group and the HEPE group. The longitudinal data of dynamic MRI perfusion parameter from each group were analyzed by the program "General Linear Model Based Repeated Measures." All data were expressed as the mean ± SD and statistical significance was set at $p < 0.05$.

Results

End-Point Evaluations for Safety and Efficacy
Safety No rabbits died in either group throughout the experimental period. Rabbits in the HEPE group were found to be physically more active compared with control rabbits.

Treatment Efficacy The incidence of ON in the HEPE group was 31% (5 of 16), which was significantly lower than 93% (13 of 14) in the CO group ($p < 0.05$). The ON lesions with typical features were found in all the ON^+ rabbits (Fig. 7).
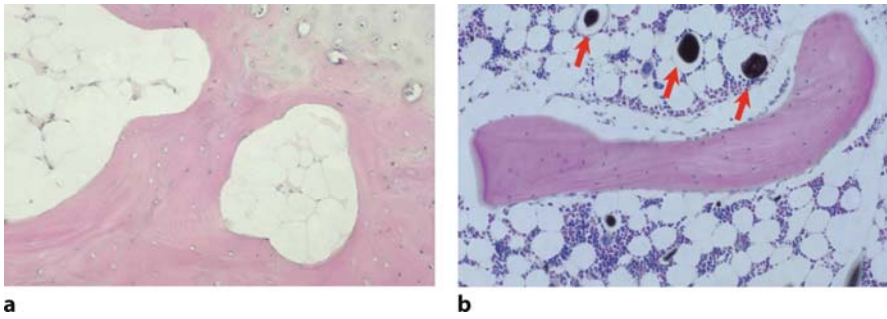
Figure 7 a,b. Histopathologic features compared between representative ON[+] sample in the non-treatment ON group and representative ON[+] sample in the HEPE group. **a** Representative ON[+] sample in the non-treatment control group characterized by more empty lacunae in the trabecular matrix, which were surrounded by more and larger marrow fat cells. **b** Representative ON[−] sample in the HEPE group showed vital bone with normal osteocytes. Considerable space was preserved for marrow hematopoietic cells and vessels containing radiopaque substance (Microfil), indicated by *arrows*

Pathophysiologic Pathway for Intraosseous Blood Supply   Dynamic MRI-based perfusion study showed that the maximum enhancement at both proximal and distal femur decreased significantly from baseline in the CO group, whereas no change was found at those sites in the HEPE group ($p < 0.05$; Fig. 8).

Regarding the micro-CT-based vascular network, the ON[+] samples in the CO group showed a blocked stem vessel surrounded by many small disconnected ves-
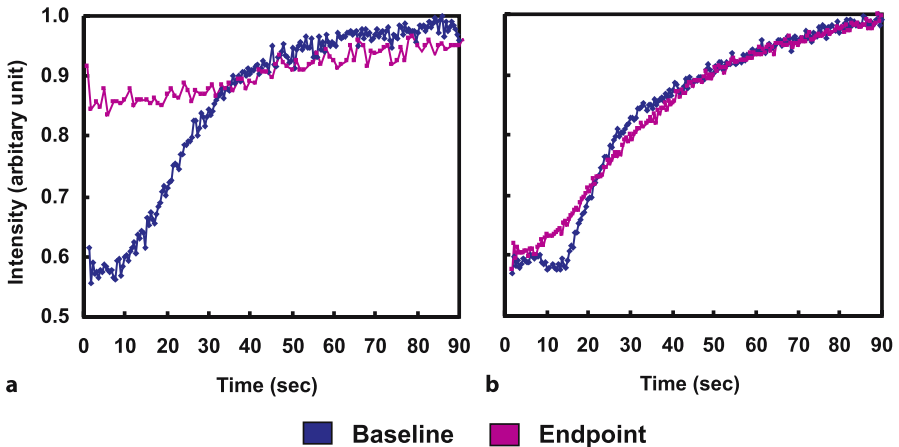
Figure 8 a,b. Representative time-intensity curves (arbitrary unit) by dynamic MRI on proximal femur. **a** Maximum enhancement showed a significant decrease in perfusion function in the non-treatment control group. **b** No significant alteration in perfusion function was found in the HEPE group

sels and disseminated leakage of contrast material (Microfil), whereas there was no blocked stem vessel in the ON$^-$ samples of the HEPE group.

Intravascular/Extravascular Pathogenic Events

Intravascular Hematologic Indicators For coagulation, the APTT in the CO group showed a significant decrease from baseline at week 1 after LPS injection and increased towards baseline later, whereas a prominently attenuated tendency was found in the PE group than the CO group throughout the experimental period ($p < 0.05$). For fibrinolysis, the tPA/PAI-I in the CO group significantly declined from baseline at week 1 after LPS injection and increased towards baseline later, whereas an evidently attenuated tendency was found in the PE group throughout the experimental period ($p < 0.05$; Fig. 9).

Extravascular Histopathologic Indicators Histopathologically, the Feret's diameter of marrow fat cell in the HEPE group ($48.17 \pm 3.54\,\mu m$) was significantly smaller ($p < 0.05$) than that in the control group ($63.71 \pm 6.41\,\mu m$). In the HEPE group, considerable space was preserved for marrow hematopoietic cells and vessels in ON- rabbits; however, little space was left for marrow elements due to enlarged fat cell size in the ON+ rabbits of the control group (Figs. 7, 10).

Discussion and Conclusion

The present study shows, for the first time, that the herbal Epimedium-derived phytoestrogenic extract (HEPE) was able to prevent steroid-associated ON through
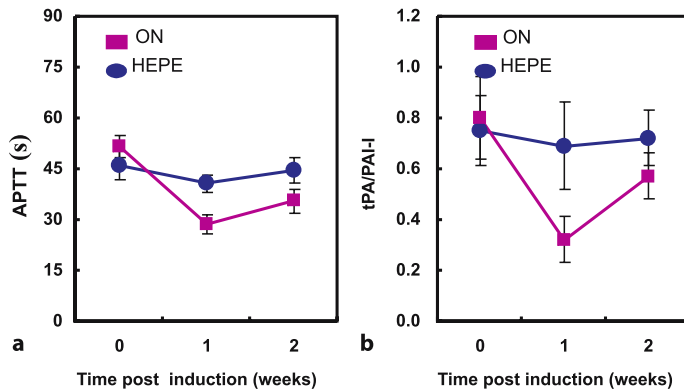
Figure 9 a,b. Hematologic data compared between both non-treatment control group and the HEPE group. **a** Significant decrease in APTT found in non-treatment ON group (ON) at week 1 after LPS injection and restored back to the baseline level afterwards, whereas no significant fluctuation was shown in the HEPE group. **b** The tPA/PAI-I in the non-treatment ON group significantly declined from baseline after LPS injection, whereas there were no measurable changes in HEPE treated group. *Asterisk:* significant difference compared between two groups
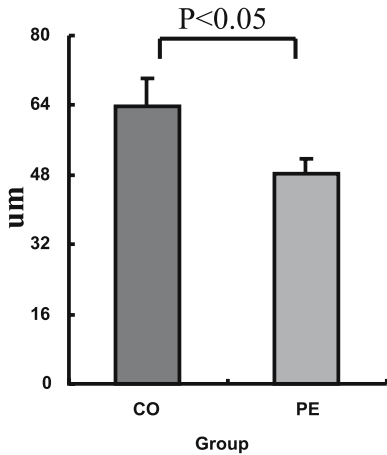
Figure 10. Size of the fat cell was significantly larger in the non-treatment ON group than that of the HEPE group ($p < 0.05$)

a unique mechanism associated with inhibition of both thrombosis and lipid deposition.

In the present study, a single daily oral administration of HEPE effectively reduced threefold the ON incidence (31%) as compared with the control group (93%). Neither animal death nor bleeding event were documented in the HEPE-treated rabbits throughout the experimental period. This may suggest a potential long-term clinical application with more required safety than the available anticoagulants tested clinically (Motomura et al. 2004). Our results may also support, or partially explain, the clinical observations of significantly lower ON incidence in SARS patients in the two cities (Hong Kong and Guang Zhou) in southern China (5–6%; Griffith et al. 2005; Shen et al. 2004) as compared with that in a northern city (Beijing) in China (32.7%; Li ZR et al. 2005), as herb preparations were much more frequently given to SARS patients during pulsed steroid treatment in southern than in northern China (Lau et al. 2005; Liu et al. 2006), apart from steroid dose variations.

The effects of HEPE on the final pathophysiologic pathway to ON, i.e., an impaired structure-function of intraosseous blood supply system, were confirmed by contrast-enhanced dynamic MRI and micro-CT-based angiography. Our findings indicate the potential of HEPE in maintaining local blood circulation and vasculature integrity, functionality, and structure. Functionally, MRI intraosseous perfusion parameter time/intensity-curve-derived maximum enhancement showed a higher value in the examined sites of the ON$^-$ rabbits in the HEPE group than those of the ON$^+$ rabbits in the control group. Structurally, microangiography showed the capability of HEPE to maintain intraosseous vasculature, as evidenced by no blocked stem vessels in ON$^-$ samples of the HEPE group compared with ON$^+$ samples in the CO group.

The mechanistic pathway of HEPE was also indicated by its effects on both intravascular and extravascular events. Histopathologically, fat cell size has been commonly defined as a direct indicator of local lipid deposition (Miyanishi K et al. 2001). In the present study, HEPE was shown to be able to inhibit local lipid deposition,

which was evidenced by smaller fat cell size in the HEPE group than the CO group ($p < 0.05$). Hematologically, it suggested that intravascular indicators (both APTT and tPA/PAI-I) implied that HEPE prevented ON development partially via a potential pathway maintaining balance between coagulation and fibrinolysis. Recent experimental findings indicate that pulsed steroids stimulate adipocytic pathway in marrow (Li X et al. 2005), and phytoestrogen showed potential inhibition effects on adipogenesis (Cooke and Naaz 2005; Dang et al. 2003; Dang and Lowik 2004). Our unpublished preliminary in vitro data has also demonstrated significantly decreased adipogenic PPARγ_2 gene expression in marrow cells from steroid-associated ON rabbits with HEPE prevention.

In this study, HEPE decreased ON incidence to 31%, whereas a combination of anticoagulant plus a lipid-lowering agent decreased ON incidence to 5% in an experimental study (Motomura et al. 2004); however, the combination of therapeutics in Motomura's study started 1-2 weeks before inductive injection, and HEPE in our study started immediately before inductive injection. So, direct comparisons between those two experimental studies could not be made. The first limitation of our study was that it was without a dose-effect design, and the prevention efficacy profile of HEPE, thus far, remains unclear.

In conclusion, we provide evidence supporting our hypothesis that HEPE was able to prevent steroid-associated ON in rabbits through a unique mechanism associated with inhibition of both thrombosis and lipid deposition.

Conclusion

We developed a steroid-associated ON rabbit model with high ON incidence and no mortality. This experimental ON model was adopted for efficacy study on an herbal Epimedium-derived phytoestrogenic extract (HEPE) developed for prevention of steroid-associated ON. The underlying mechanisms of HEPE for prevention of steroid-associated ON were found to be inhibition of both intravascular thrombosis and extravascular bone marrow lipid deposition, evaluated using both conventional and advanced bio-imaging techniques, including contrast-enhanced dynamic MRI and a high-resolution micro-CT. Our experimental results support further clinical study and the potential application of HEPE in the prevention of ON development in high-risk patients undergoing steroid treatment.

References

Aaron RK (1998) Osteonecrosis: etiology, pathophysiology and diagnosis. In: Callaghan JJ, Rosenberg AG, Rubash HE (eds) The adult hip. Lippincott-Raven, Philadelphia, p 457

Anderson JW, Johnstone BM, Cook-Newell ME (1995) Meta-analysis of the effects of soy protein intake on serum lipids. N Engl J Med 333:276–282

Assouline-Dayan Y, Chang C, Greenspan A, Shoenfeld Y, Gershwin ME (2002) Pathogenesis and natural history of osteonecrosis. Semin Arthritis Rheum 32:94–124

Bentley MD, Ortiz MC, Ritman EL, Romero JC (2002) The use of microcomputed tomography to study microvasculature in small rodents. Am J Physiol Regul Integr Comp Physiol 282:1267–1279

Choo MK, Park EK, Yoon HK, Kim DH (2002) Antithrombotic and antiallergic activities of daidzein, a metabolite of puerarin and daidzin produced by human intestinal microflora. Biol Pharm Bull 25:1328–1332

Clifton-Bligh PB, Baber RJ, Fulcher GR, Nery ML, Moreton T (2001) The effect of isoflavones extracted from red clover (Rimostil) on lipid and bone metabolism. Menopause 8:259–265

Cooke PS, Naaz A (2005) Effects of estrogens and the phytoestrogen genistein on adipogenesis and lipogenesis in males and females. Birth Defects Res A Clin Mol Teratol 73:472–473

Dang Z, Lowik CW (2004) The balance between concurrent activation of ERs and PPARs determines daidzein-induced osteogenesis and adipogenesis. J Bone Miner Res 19:853–861

Dang ZC, Audinot V, Papapoulos SE, Boutin JA, Lowik CW (2003) Peroxisome proliferator-activated receptor gamma (PPARgamma) as a molecular target for the soy phytoestrogen genistein. J Biol Chem 278:962–967

Duvall CL, Robert Taylor W, Weiss D, Guldberg RE (2004) Quantitative microcomputed tomography analysis of collateral vessel development after ischemic injury. Am J Physiol Heart Circ Physiol 287:302–310

Expert Panel on Detection, Evaluation, and Treatment of High Blood Cholesterol in Adults (adult treatment panel III) (2001) Executive summary of the third report of the National Cholesterol Education Program (NCEP) J Am Med Assoc 285:2486–2497

Glueck CJ, Freiberg RA, Sieve L, Wang P (2005) Enoxaparin prevents progression of stages I and II osteonecrosis of the hip. Clin Orthop Relat Res 435:164–170

Griffith JF, Antonio GE, Kumta SM, Hui DS, Wong JK, Joynt GM, Wu AK, Cheung AY, Chiu KH, Chan KM, Leung PC, Ahuja AT (2005) Osteonecrosis of hip and knee in patients with severe acute respiratory syndrome treated with steroids. Radiology 235:168–175

Hong N, Du XK (2004) Avascular necrosis of bone in severe acute respiratory syndrome. Clin Radiol 59:602–608

Irisa T, Yamamoto T, Miyanishi K, Yamashita A, Iwamoto Y, Sugioka Y, Sueishi K (2001) Osteonecrosis induced by a single administration of low-dose lipopolysaccharide in rabbits. Bone 28:641–649

Jorgensen SM, Demirkaya O, Ritman EL (1998) Three-dimensional imaging of vasculature and parenchyma in intact rodent organs with X-ray micro-CT. Am J Physiol Heart Circ Physiol 275:1103–1114

Koller E, Mann M, Malozowski S, Bacsanyi J, Gibert C (2000) Aseptic necrosis in HIV seropositive patients: a possible etiologic role for megestrol acetate. AIDS Patient Care STDS 14:405–410

Lamon-Fava S (2000) Genistein activates apolipoprotein A-I gene expression in the human hepatoma cell line Hep G2. J Nutr 130:2489–2492

Lang P, Jergesen JE, Genant HK, Moseley ME, Schuylte-Monting J (1989) Magnetic resonance imaging of the ischemic femoral head in pigs. Dependency of signal intensities and relaxation times on elapsed time. Clin Orthop Relat Res 244:272–280

Lau TF, Leung PC (2005) Using herbal medicine as a means of prevention experience during the SARS crisis. Am J Chinese Med 33:345–356

Lee SH, Jung BH, Kim SY, Chung BC (2004) Determination of phytoestrogens in traditional medicinal herbs using gas chromatography-mass spectrometry. J Nutr Biochem 15:452–460

Li X, Jin L, Cui Q, Wang GJ, Balian G (2005) Steroid effects on osteogenesis through mes-
enchymal cell gene expression. Osteoporos Int 16:101–108

Li ZR, Sun W, Qu H, Zhou YX, Dou BX, Shi ZC, Zhang NF, Cheng XG, Wang DL, Guo WS
(2005) Clinical research of correlation between osteonecrosis and steroid. Zhonghua Wai
Ke Za Zhi 43:1048–1053

Lieberman JR, Berry DJ, Montv MA, Aaron RK, Callaghan JJ, Rayadhyaksha A, Urbaniak JR
(2002) Osteonecrosis of the hip: nanagement in the twenty-first century. J Bone Joint Surg
Am 84:834–853

Liu X, Zhang M, He L, Li YP, Kang YK (2006) Chinese herbs combined with Western medicine
for severe acute respiratory syndrome (SARS). Cochrane Database Syst Rev1:CD004882

Martin JL, Fry ET, Sanderink GJ, Atherley TH, Guimart CM, Chevalier PJ, Ozoux ML, Pen-
syl CE, Bigonzi F (2004) Reliable anticoagulation with enoxaparin in patients undergoing
percutaneous coronary intervention: the pharmacokinetics of enoxaparin in PCI (PEPCI)
study. Catheter Cardiovasc Interv 61:163–170

Meng FH, Li YB, Xiong ZL, Jiang ZM, Li FM (2005) Osteoblastic proliferative activity of
Epimedium brevicornum Maxim. Phytomedicine 12:189–193

Miller KD (2002) High prevalence of osteonecrosis of the femoral head in HIV infected adults.
Ann Intern Med 137:17–25

Motomura G, Yamamoto T, Miyanishi K, Jingushi S, Iwamoto Y (2004) Combined effects of an
anticoagulant and a lipid-lowering agent on the prevention of steroid-induced osteonecro-
sis in rabbits. Arthritis Rheum 50:3387–3391

National Osteonecrosis Foundation website. http://www.nonf.org/index.html

Pritchett JW (2001) Statin therapy decreases the risk of osteonecrosis in patients receiving
steroids. Clin Orthop Relat Res 386:173–178

Prophet EB, Mills B, Arrington JB, Sobin LH (eds) (1992) Armed Forces Institute of Path-
ology Laboratory Methods in Histotechnology. American Registry of pathology, Wash-
ington DC, p 98

Qin L, Zhang G, Shi YY, Lee KM, Leung PC (2005a) Prevention and treatment of osteoporosis
with traditional herbal medicine. In: Deng HW et al. (eds) Current topics of osteoporosis.
World Scientific, UK, pp 513–531

Qin L, Zhang G, Hung WY (2005b) Phytoestrogen-rich Herb Formula "XLGB" prevents OVX-
induced deterioration of musculoskeletal tissues at hip in old rats. J Bone Miner Metabol
23S:55–61

Qin L, Zhang G, Sheng H (2006) Multiple imaging modalities in evaluation of experimental
osteonecrosis induced by a combination of lippolysaccharide and methylprednisolone.
Bone 39:863–871

Saito S, Saito M, Nishina T, Ohzono K, Ono K (1989) Long-term results of total hip arthroplasty
for osteonecrosis of the femoral head. A comparison with osteoarthritis. Clin Orthop Relat
Res 244:198–207

Schulman S (1999) The effect of the duration of anticoagulation and other risk factors on the re-
currence of venous thromboembolisms. Duration of Anticoagulation Study Group. Wien
Med Wochenschr 149:66–69

Scribner AN, Troia-Cancio PV, Cox BA, Marcantonio D, Hamid F, Keiser P, Levi M, Allen B,
Murphy K, Jones RE, Skiest DJ (2000) Osteonecrosis in HIV: a case-control study. J Acquir
Immune Defic Syndr 25:19–25

Shen J, Liang BL, Zeng QS, Chen JY, Liu QY, Chen RC, Zhong NS (2004) Report on the inves-
tigation of lower extremity osteonecrosis with magnetic resonance imaging in recovered
severe acute respiratory syndrome in Guangzhou. Zhonghua Yi Xue Za Zhi 84:1814–1817

Simopoulos DN, Gibbons SJ, Malysz J, Szurszewski JH, Farrugia G, Ritman EL, Moreland RB, Nehra A (2001) Corporeal structural and vascular micro-architecture with X-ray micro-computerized tomography in normal and diabetic rabbits: histopathological correlation. J Urol 165:1776–1782

So LK, Lau AC, Yam LY, Cheung TM, Poon E, Yung RW, Yuen KY (2003) Development of a standard treatment protocol for severe acute respiratory syndrome. Lancet 361:1615–1617

Wang GJ (2000) The pathogenesis and prevention of steroid-induced osteonecrosis. Clin Orthop 370:295–310

Wang W, Zhu GJ, Zu SY (2004) Effects of 17β Estradiol and Phytoestrogen α-Zearalanolon coagulation and fibrinolysis in Rats. Chin J Arterioscler 12:139–142

Wortmann RL (2002) Lipid-lowering agents and myopathy. Curr Opin Rheumatol 14:643–647

Yamamoto T (1997) Effects of pulse methylprednisolone on bone and marrow tissues: corticosteroid-induced osteonecrosis in rabbits. Arthritis Rheum 40:2055–2064

Yamamoto T, Hirano K, Tsutsui H, Sugioka Y, Sueishi K (1995) Corticosteroid enhances the experimental induction of osteonecrosis in rabbits with Shwartzman reaction. Clin Orthop Relat Res 316:235–243

Zhang G, Qin L, Hung WY (2006) Flavonoids derived from herbal Epimedium Brevicornum Maxim prevents OVX-induced osteoporosis in rats independent of its enhancement in intestinal calcium absorption. Bone 38:818–825

Nanomechanics of Bone
and Bioactive Bone-Cement Interfaces

Guo-Xin Ni[1], William Wei-Jia Lu (✉)[1], Alfonso Hing-Wan Ngan[2], and Keith Dip-Kei Luk[1]

[1] Department of Orthopaedics and Traumatology, The University of Hong Kong, Pokfulam Road, Hong Kong, China
e-mail: wwlu@hkusua.hku.hk
[2] Department of Mechanical Engineering, The University of Hong Kong, Pokfulam Road, Hong Kong, China

Abstract

Nanoindentation is an ideal technique to investigate mechanical behaviour at the bone/implant interface. A viscoelasticity correction method was developed and validated for use on biological specimens. Using this new technique the nanomechanics of the interface between strontium-containing hydroxyapatite (Sr–HA) bone cement with cancellous and cortical bone were investigated under weight-bearing conditions. At 6 months after implantation, Young's modulus and hardness at the interface between cancellous bone and Sr–HA cement were significantly higher than those at the cancellous bone and Sr–HA cement, whereas Young's modulus and hardness at interface between cortical bone and Sr–HA cement were significantly lower than those at cortical bone, but significantly higher than Sr–HA cement These results were supported by histological observation and chemical composition. Osseointegration of Sr–HA cement with cancellous bone was observed. An apatite layer with a high content of calcium and phosphorus was found between cancellous bone and Sr–HA cement; however, no such apatite layer was observed at the interface between cortical bone and Sr–HA cement. And the contents of calcium and phosphorus of the interface were lower than those of cortical bone. The mechanical properties indicated that these two interfaces were diffused interfaces, and cancellous bone or cortical bone was grown into Sr–HA cement 6 months after the implantation.

Bioactive Bone-Cement and Bone-Bonding Behaviour

Since Charnley (1960) introduced polymethylmethacrylate (PMMA) bone cement for prosthetic fixation, it has been widely used in orthopedic surgery. Although it is clinically successful, there are several problems associated with the use of this cement. The most serious one is its non-adhesiveness to bone, namely, the formation of a fibrous layer between the bone surface and the cement (Freeman et al. 1982; Jasty

Table 1. Types of biomaterial-tissue attachment and their classifications

Type of implant	Type of attachment	Example
Nearly inert	Mechanical interlock (morphological fixation)	Metals, alumina, zirconia, polyethylene (PE)
Porous	Ingrowth of tissues into pores (biological fixation)	Hydroxyapatite (HA), HA-coated porous metals
Bioactive	Interfacial boding with tissue (bioactive fixation)	Bioactive glasses, HA, Bioactive glass-ceramics
Resorbable	Replacement with tissues	TCP, polyactic acid

et al. 1990). This is a major contributory factor to the loosening of cemented femoral components. The PMMA cement relies on mechanical interlocking with bone, rather than adhesive chemical bonding to form a stable cement-bone union (Freeman et al. 1982).

A solution to overcome this problem at the interface is to use bioactive bone cement. Various types of bioactive fillers, based on calcium phosphates, hydroxyapatite (HA) powders and bioactive glass or glass–ceramic powder, may be used (Dalby et al. 2001; Kenny and Buggy 2003; Dickens et al. 2004; Walsh et al. 2004). These fillers can be combined with a resin such as bisphenol-a-glycidyl methacrylate (Bis-GMA), or PMMA, to produce bioactive cements.

Biomaterials can be classified according to the different types of implant-tissue attachment, which are summarised in Table 1. A bioactive material (see Table 1) is one that elicits a specific biological response at the interface of the material, resulting in the formation of a bond between the tissues and the material. Since direct bone bonding to bioactive glasses was first observed (Hench et al. 1971), considerable progress has been made in understanding the basic mechanisms of bone-biomaterial bonding and its effect on bone formation. This progress resulted mainly from two approaches. One approach focused on studying the bone-biomaterial interface in vivo. Examination of the bonding zone revealed the consistent presence of an interfacial hydroxyapatite layer (Hench et al. 1971; Neo et al. 1993b). The other approach used in vitro immersions in simulated physiological fluids or cell-containing media (Kokubo et al. 1990; El-Ghannam et al. 1997). These analyses revealed that reactions occurred at the implant material surfaces such as dissolution, precipitation and ion exchange. These reactions were accompanied by adsorption and incorporation of biological molecules (Hyakuna et al. 1989; El-Ghannam et al. 1999). This combination of in vivo and in vitro studies led to a better understanding of surface reactions of bioactive ceramics and their effect on bone formation and cell function.

Although various bioactive bone cements show the capability of bone bonding under both non-weight-bearing conditions and weight-bearing conditions (Senaha et al. 1996; Matsuda et al. 1997; Fujita et al. 1998; Fujita et al. 2000), different types of biomaterials exhibit different bone-bonding behaviours due to differences in chemical composition, crystallisation and solubility (Kotani et al. 1991; Neo et al. 1992a,b, 1993a; Tamura et al. 1995; Davies and Baldan 1997; Okada et al. 2001; Fujita et al.

2003). Bioactive glass/glass-ceramics bone cement was reported to bond with bone through a so-called Ca-P rich layer (Kobayashi et al. 1997, 1998; Okada et al. 2001), whereas an apatite layer did not form on β-TCP particles (Okada et al. 1999). The intervening apatite layer in hydroxyapitite (HA) specimen was indistinct and sometimes absent depending on the size of HA particles (Okada et al. 1999; Neo et al. 1993a).

Strontium-Containing Hydroxyapatite Bone Cement

Strontium-containing hydroxyapatite (Sr–HA) bone cement consists mainly of Sr–HA (97.5 wt%) and fumed silica (2.5 wt%) as the inorganic filler and bisphenol-a-glycidyl methacrylate (Bis-GMA; Bis-GMA/TEGDMA) resin as the organic matrix
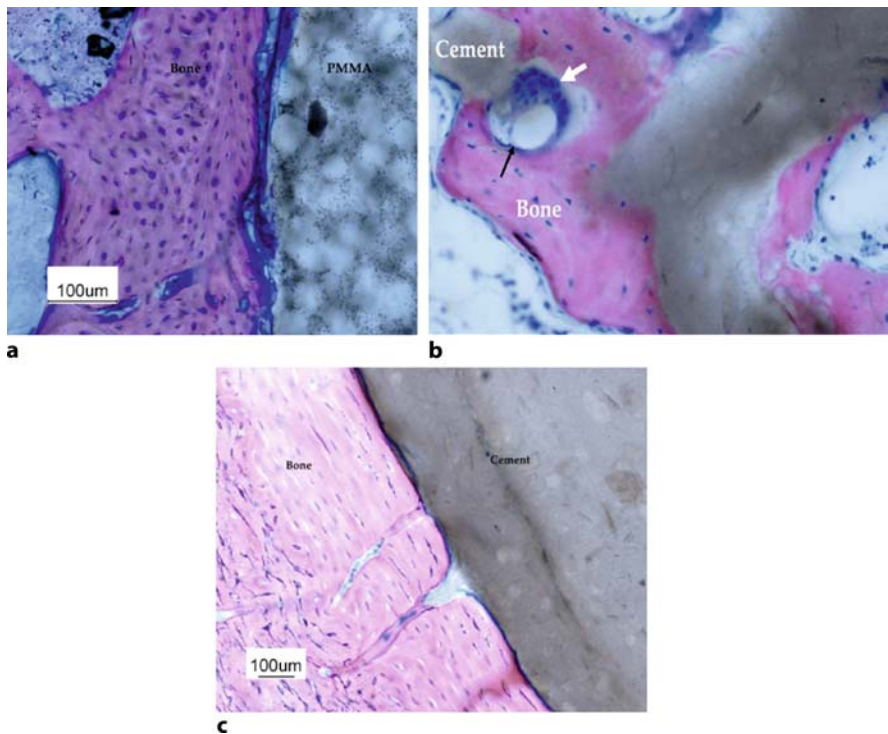
Figure 1 a–c. Undecalcified specimen with Giemsa and eosin staining. **a** An intervening soft tissue layer approximately 10 μm thick was consistently observed at the bone-PMMA cement interface. **b** Intimate contact between the Sr-HA cement and cancellous bone without fibrous layer intervening was widespread. Many multinucleus cells (*white arrow*) covered the surface of the cement, and resorbed the superficial layer of the cement. Cement void is seen. Osteoblast cells are also nearby to form new bone (*black arrow*). New bone infiltrated into the Sr-HA cement. **c** Intimate contact was found between cortical bone and Sr-HA cement, without any fibrous layer intervening. No multinucleus cell was observed at the surface of Sr-HA cement
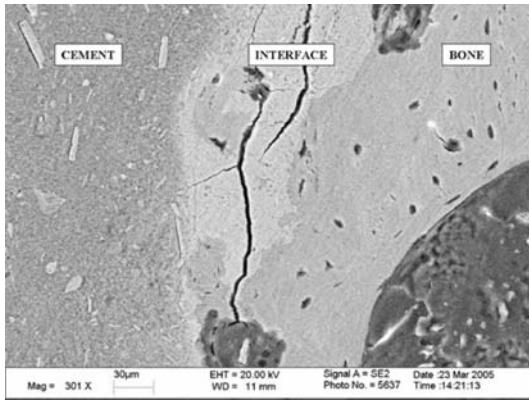
Figure 2 a–c. The SEM micrographs and EDX mapping analysis of an area containing cancellous bone and Sr-HA cement from an undecalcified metaphyseal section (**a**). **b,c** The calcium and phosphorus contents, respectively, from the EDX mapping analysis. The calcium and phosphorus contents at the interface were similar to those of cancellous bone, and were higher than those of the Sr-HA cement
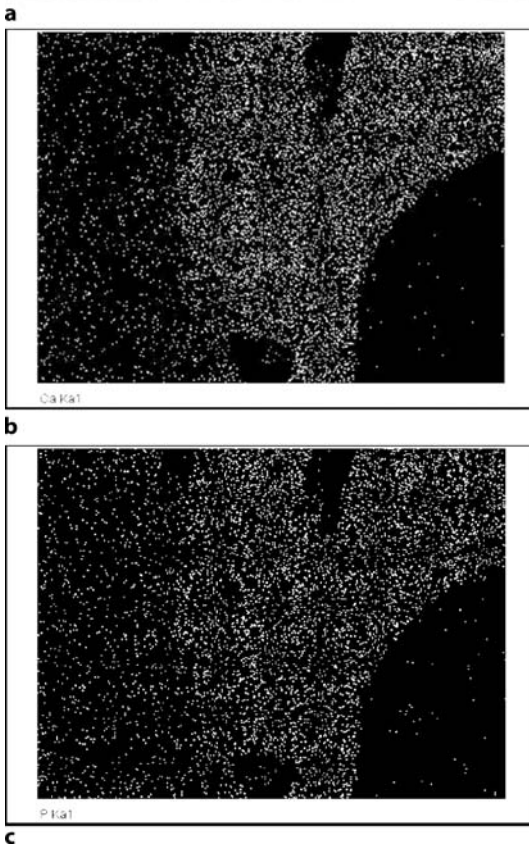
(Li et al. 2000; Lu et al. 2001). The uniqueness of this bone cement is that 10% of the calcium ions in HA are substituted by strontium. Strontium (Sr) belongs to the same element group as barium and calcium, is radiopaque and has been shown to stimulate bone formation (Canalis et al. 1996) and inhibit bone resorption in vitro (Matsumoto et al. 1988) and in vivo (Marie and Hott 1986; Grynpas et al. 1990). Recently, strontium

salts have been shown in clinical trials to be an effective in osteoporosis, being are one of the few drugs that act by promoting bone formation (Boivin et al. 1996; Reginster 1997; Meunier et al. 2002). On the other hand, increased HA solubility and decreased crystal growth in the presence of strontium was confirmed by Christoffersen et al. (1997) and Okayama et al. (1991). It has been suggested that substitution of calcium (Ca) by strontium causes crystal lattice expansion due to the larger atomic radius of strontium, which in turn alters the mineral solubility.

An in vivo study by Chen et al. (2004) using high-resolution transmission electron microscopy (HRTEM) investigated how Sr–HA cement bonds to cancellous bone after implantation into rabbit ilium. The results indicated the following dissolution–precipitation process:

1. The crystalline HA transforms into amorphous HA.
2. The amorphous HA dissolves into the surrounding solution, resulting in over-saturation.
3. The nanocrystallites are precipitated from the over-saturated solution in the presence of collagen fibres.

Ni et al. (2006) further evaluated Sr–HA bone cement in a rabbit hip hemi-arthroplasty model. Six months after surgery, unlike PMMA bone cement with a fibrous tissue layer intervening with bone (Fig. 1a), Sr–HA bone cement was found to bond directly with both cancellous bone and cortical bone, although in a different manner for each type of bone. The Sr–HA cement–cancellous bone interface was examined from metaphyseal sections. At the surface of the Sr–HA cement, giant, multi-nucleated cells were found to have absorbed the cement, leading to irregular surface pitting ("moth-eaten appearance"; Figs. 39.1B). Osteoblast cells were found nearby forming new bone, which might infiltrate into the Sr–HA cement; however, this phenomenon was not observed at the Sr–HA cement–cortical bone interface (Fig. 1c).

Scanning electron microscopy (SEM) revealed that the surface of Sr–HA cement was covered with an apatite layer (Fig. 2a). High content of calcium (Ca) and phos-
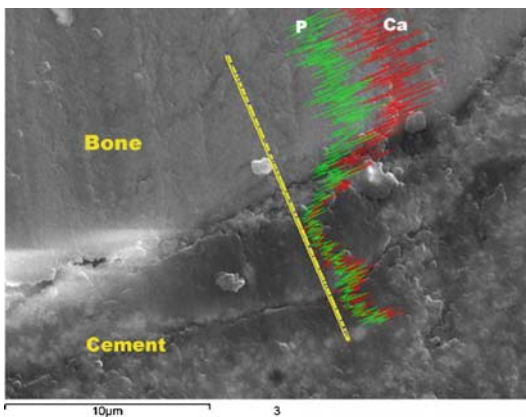
Figure 3. The SEM micrographs and line-scan EDX analysis of an undecalcified diaphyseal section. The EDX scan direction is indicated by the *straight line*. The contents of calcium and phosphorus decreased from the cortical bone to the Sr-HA cement, through the interface. *Ca* calcium, *P* phosphorus

phorus (P) at the Sr–HA cement-cancellous bone interface was suggested by calcium and phosphorus mapping energy-dispersive X-ray (EDX) analysis (Fig. 2a). Figure 2b and 2c shows that the contents of calcium (Ca) and phosphorus (P) at the interface are comparable to those of bone, but are much higher than those of Sr–HA cement. A relatively radiolucent layer was observed between Sr–HA cement and cortical bone on SEM. Line-scan EDX analyses revealed that the contents of calcium and phosphorus at the interface were lower than those of bone, but higher than Sr–HA cement (Fig. 3).

Nanoindentation and Data Analysis

The cement-bone interface is crucial to the stability of the cemented femoral component. The mechanical properties and chemical composition of the newly formed tissues at the interface under load-bearing conditions significantly influence the quality of the bone/bone cement union; however, the mechanical properties of the bone/bone cement interface are not fully understood, because of technical difficulties associated with preparing an intact interface and performing quantitative analyses (Masuda et al. 1998). Traditional mechanical tests, such as bend testing, tension, and compressive testing, are not suitable for evaluating bone/bone cement interface because of specimen size requirements (Keaveny et al. 1997).

Nanoindentation, also known as depth-sensing or instrumental indentation, is a very important technique for the measurement of the mechanical properties in submicron or nanometer length scales (Doerner and Nix 1986; Oliver and Pharr 1992; Pharr 1998). Recently, this technique has been employed to measure the mechanical properties of bone (Rho et al. 1997; Hengsbergers et al. 2002; Fan and Rho 2003). Because of its unique ability to measure the mechanical properties in very small material volumes, the high-spatial resolution of nanoindentation makes it an ideal technique to investigate mechanical behaviours at the bone/implant interface. Guo et al. (2001) successfully used nanoindentation to evaluate the mechanical properties of the interface between bone and calcium phosphate in a rabbit spinal fusion model. The results of nanoindentation of the tissue and the implants were supported by differences in chemical composition.

In the nanoindentation technique, the most commonly used method for data analysis is the Oliver-Pharr method (Oliver and Pharr 1992), which assumes that the tip-sample contact is purely elastic during unloading. In this method, the elastic modulus E is calculated from

$$\frac{1}{E_r} = \frac{(1 - v^2)}{E} + \frac{(1 - v_i^2)}{E_i} ,$$

(1)

where E_i is the elastic modulus of the indenter tip, v and v_i are the Poisson ratio of the sample and the indenter tip, respectively, and E_r is the reduced modulus calculated from

$$E_r = \frac{\sqrt{\pi}}{2} \frac{S}{\sqrt{A_c}} ,$$

(2)

where the S is the tip-sample contact stiffness measured at the onset of an unloading step, A_c is the contact area calculated from a pre-calibrated tip calibration area function $A_c = f(h_c)$. The h_c is the contact depth, which can be obtained by

$$h_c = h_m - \varepsilon \frac{P_m}{S} \ , \tag{3}$$

where h_m and P_m are the depth and load at the onset of unloading, and ε is a constant, which for a Beckovich tip is 0.75. The nanohardness H is obtained as

$$H = \frac{P_m}{A_c} \ . \tag{4}$$

When applied to soft samples, such as biological tissues, the Oliver-Pharr method is known to suffer from one major limitation, namely, the viscoelastic effect during unloading may severely influence measurement accuracy (Tang and Ngan 2003; Ngan et al. 2005). In this study, a method developed by Ngan et al. (2005) was employed to correct for viscoelastic effect during nanoindentation measurements. In this method, the real tip-sample contact stiffness S_e is obtained by

$$\frac{1}{S_e} = \left(\frac{1}{S} - \frac{\dot{h}_h}{\dot{P}_u} \right) \frac{1}{(1 - \dot{P}_h/\dot{P}_u)} \ , \tag{5}$$

where S is the observed or apparent contact stiffness at the onset of unloading, and $\dot{P}_h$ and $\dot{h}_h$ are, respectively, the loading rate and displacement rate just before the unloading, and $\dot{P}_u$ is the unloading rate just after the onset of unloading. The S_e obtained from Eq. (4) is to replace S in Eqs. (1) and (2) in the calculation of the reduced modulus and the hardness.

Viscoelasticity correction has been demonstrated to be important on soft materials or biomaterials including polypropylene, amorphous selenium or bone tissues. In another experiment (Tang et al. 2006), we used Oliver-Pharr and our correction method to calculate the mechanical properties of bone samples from two species of mice, C57 and ICR, respectively. Large variations were found when we used Oliver-Pharr method (non-correction method) under different loading rates (see Fig. 4a); however, the mechanical properties measured from the correction method showed reliable outcomes (see Fig. 4b).

Nanomechanics of Interfaces between Sr-HA Bone Cement and Bone

Using this viscoelastic correction method, the mechanical properties of the interfaces between Sr-HA cement with cancellous and cortical bone were determined (Tables 2, 3). Different nanomechanics profiles were observed between the two interfaces. For the Sr-HA cement-cancellous bone interface, both Young's modulus and hardness values increased at the interface compared with cancellous bone values, and then declined to much lower levels for Sr-HA cement. For the Sr-HA cement-cortical bone interface, both Young's modulus and hardness values decreased at the interface compared with cortical bone, but remained higher than those for Sr-HA cement.
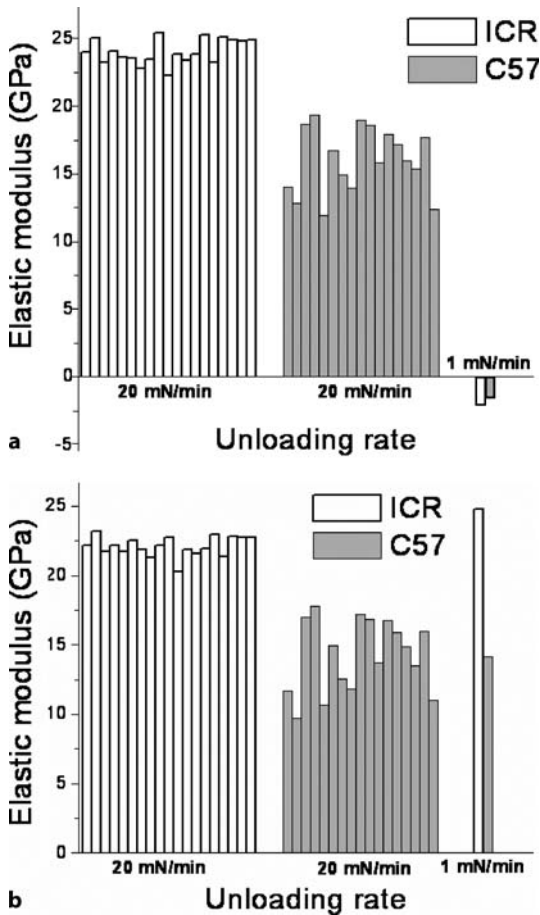
Figure 4. a Elastic moduli of the femur samples calculated from the Oliver-Pharr (non-correction) method. When loading rate changes, large variations are found. **b** Elastic moduli of the femur samples calculated from the viscoelasticity correction method (data from Tang et al. 2006)

The different mechanical properties between Sr-HA bone cement/cancellous bone interface and Sr-HA cement/cortical bone interface may be explained by the different responses of cancellous bone and cortical bone to Sr-HA cement, as well as the different chemical composition of the newly formed tissue at the interfaces.

Table 2. Young's modulus and hardness compared among cancellous bone, interface and Sr-HA cement

	Cancellous bone (n = 32)	Interface (n = 20)	Sr-HA cement (n = 28)
Young's modulus (GPa)	12.7 ± 1.7	17.6 ± 4.2[*a]	5.2 ± 0.5
Hardness (MPa)	632.7 ± 108.4	987.6 ± 329.2[*a]	265.5 ± 39.2

[*] p < 0.05: cancellous bone vs interface
[a] Interface vs cement

Table 3. Young's modulus and hardness compared among cortical bone, interface and Sr-HA cement

	Cortical bone (n = 49)	Interface (n = 7)	Sr-HA cement (n = 44)
Young's modulus (GPa)	12.9 ± 2.2	6.3 ± 2.8[*a]	3.6 ± 0.3
Hardness (MPa)	887.9 ± 162.0	417.4 ± 164.5[*a]	239.1 ± 30.4

[*] $p < 0.05$: cancellous bone vs interface
[a] Interface vs cement

For the interface between Sr-HA cement and cancellous bone, multinucleated cells covered the surface of the cement and resorbed the superficial layer of the cement. This phenomenon was also reported by Ooms et al. (2002) after calcium phosphate cement was injected into rabbit's cancellous bone. New bone infiltrated into Sr-HA cement, leading to osseointegration with Sr–HA cement. The SEM and EDX analysis revealed that Sr-HA bone cement bonded with cancellous bone through an apatite layer with high content of calcium and phosphorus. This chemical bonding of an apatite layer, with high content of calcium and phosphorus, as well as biological interdigitation (or incorporation) of collagen fibres with Sr-HA cement, demonstrated by Chen et al. (2004), may contribute to the higher mechanical properties of the interface shown in this study. Combined with the results from histological observation and chemical composition, the results from nanoindentation could provide further evidence to show that the interface between Sr-HA cement and cancellous bone was a well-integrated interface.

Due to its low solubility, the mechanism of formation of the intervening apatite layer of HA may be different from that of other surface-active materials (Neo et al. 1993a). The HA sometimes bonds to bone directly and sometimes through an intervening apatite layer that is very thin and indistinct (Okada et al. 2001; Neo et al. 1993a); however, the solubility of HA may be different with the change of its structure. Porter et al. (2004a,b) demonstrated that the dissolution rate of HA in vivo increases if silicate ions are incorporated into the HA lattice, and the change in solubility would lead to a difference in morphology of the deposits apposed to implants. Also, the substitution of Ca by strontium could cause crystal lattice expansion due to the larger atomic radius of Sr, which in turn alters solubility (Christoffersen et al. 1997). For Sr-HA cement, 10% of the calcium ions in HA are substituted by strontium. It is believed that a bioactive material's bonding to bone depends not only on the material, but also on the type of bone to which it bonds. Cancellous bone differs from cortical bone in many respects, including vascularity and density (Black and Hastings 1998; Lu et al. 1998). The apatite precipitation on HA does not begin until the surrounding environment becomes appropriate for bone mineralization or apatite formation (Neo et al. 1992a). It is assumed that when bonded with cancellous bone, Sr–HA bone cement may dissolve and the high ion intensity should therefore favour apatite formation. Conversely, relatively little Sr-HA cement may dissolve when opposing cortical bone.

Differences in bone-bonding mechanism of Sr-HA bone cement to cancellous bone and cortical bone lead to different interfaces, a relatively radiopaque layer with high calcium level (with cancelllous bone) and a relatively radiolucent layer with low calcium level (with cortical bone), contributing to the difference in nanomechanics for these two interfaces.

Summary and Conclusion

A number of bioactive bone cements have been developed to substitute for conventional bone cement. Different types of biomaterials exhibit different bone-bonding behaviours due to differences in chemical composition, crystallisation and solubility of materials used. Due to its low solubility, the mechanism of formation of the intervening apatite layer of HA is indistinct and sometimes absent depending on the size of HA particles (Okada et al. 1999; Neo et al. 1993a). The substitution of calcium (Ca) by Sr causes a crystal lattice expansion and in turn alters the solubility of the mineral. Dissolution of Sr-HA cement was indicated after implanted into rabbit ilium (Chen et al. 2004).

Bonding behaviour of Sr-HA bone cement also depends on the type of bone to which it bonds. The nanomechanics of Sr-HA cement-cancellous bone interface are quite different from that of Sr-HA cement-cortical bone, indicating a different response of Sr-HA cement to cancellous bone and cortical bone. Nanoindentation with the viscoelastic correction method described may provide an insight into the mechanical properties of the bone-cement interfaces as well as the bone-bonding behaviour of bioactive bone cement. The results of nanoindentation of the interfaces are supported by differences in histological observation and chemical composition.

References

Boivin G, Deloffre P, Perrat B, Panczer G, Boudeulle M, Mauras Y, Allain P, Tsouderos Y, Meunier PJ (1996) Strontium distribution and interactions with bone mineral in monkey iliac bone after strontium salt (S 12911) administration. J Bone Miner Res 11:1302–1311

Black J, Hastings G (eds) (1998) Cortical bone and cancellous bone. In: Handbook of biomaterial properties. New York: Chapman and Hall, pp 3–24

Canalis E, Hott M, Deloffre P, Tsouderos Y, Marie PJ (1996) The divalent strontium salt S12911 enhances bone cell replication and bone formation in vitro. Bone 18:517–523

Charnley J (1960). Anchorage of femoral head prosthesis to the shaft of the femur. J Bone Joint Surg 42B:28–30

Chen QZ, Wong CT, Lu WW, Cheung KM, Leong JC, Luk KD (2004) Strengthening mechanisms of bone bonding to crystalline hydroxyapatite in vivo. Biomaterials 25:4243–4254

Christoffersen J, Christoffersen MR, Kolthoff N, Barenholdt O (1997) Effects of strontium ions on growth and dissolution of hydroxyapatite and on bone mineral detection. Bone 20:47–54

Dalby MJ, Silvio L di, Harper EJ, Bonfield W (2001) Initial interaction of osteoblasts with the surface of a hydroxyapatite-poly(methylmethacrylate) cement. Biomaterials 22:1739–1747

Davies JE, Baldan N (1997) Scanning electron microscopy of the bone–bioactive implant interface. J Biomed Mater Res 36:429–440

Dickens SH, Kelly SR, Flaim GM, Giuseppetti AA (2004) Dentin adhesion and microleakage of a resin-based calcium phosphate pulp capping and basing cement. Eur J Oral Sci 112:452–457

Doerner MF, Nix WD (1986) A method for interpreting the data from depth-sensing indentation instruments. J Mater Res 1: 601

El-Ghannam A, Ducheyne P, Shapiro IM (1997) Formation of surface reaction products on bioactive glass and their effects on the expression of the osteoblastic phenotype and the deposition of mineralized extracellular matrix. Biomaterials 18:295–303

El-Ghannam A, Ducheyne P, Shapiro IM (1999) Effect of serum protein adsorption on osteoblast adhesion to bioactive glass and hydroxyapatite. J Orthop Res 17:340–345

Fan Z, Rho JY (2003) Effects of viscoelasticity and time-dependent plasticity on nanoindentation measurements of human cortical bone. J Biomed Mater Res 67:208–214

Freeman MAR, Bradley GW, Revell PA (1982) Observation upon the interface between bone and polymethylmethacrylate cement. J Bone Joint Surg 64B:489–493

Fujita H, Nakamura T, Tamura J, Kobayashi M, Katsura Y, Kokubo T, Kikutani T (1998) Bioactive bone cement: effect of the amount of glass–ceramic powder on bone-bonding strength. J Biomed Mater Res 40:145–152

Fujita H, Ido K, Matsuda Y, Iida H, Oka M, Kitamura Y, Nakamura T (2000) Evaluation of bioactive bone cement in canine total hip arthroplasty. J Biomed Mater Res 49:273–288

Fujita R, Yokoyamaa A, Nodasaka Y, Kohgo T, Kawasaki T (2003) Ultrastructure of ceramic-bone interface using hydroxyapatite and β-tricalcium phosphate ceramics and replacement mechanism of β-tricalcium phosphate in bone. Tissue Cell 35:427–440

Grynpas M, Marie JP (1990) Effects of low doses of strontium on bone quality and quantity in rats. Bone 11:313–319

Guo L, Guo X, Leng Y, Cheng JCY, Zhang X (2001) Nanoindentation study of interfaces between calcium phosphate and bone in an animal spinal fusion model. J Biomed Mater Res 54:554–559

Hench L, Splinter R, Greenlee T, Allen W (1971) Bonding mechanisms at the interface of ceramic prosthetic materials. J Biomed Eng 2:117–141

Hengsberger S, Kulik A, Zysset P (2002) Nanoindentation discriminates the elastic properties of individual human bone lamellae under dry and physiological conditions. Bone 30:178–184

Hyakuna K, Yamamuro T, Kotoura Y, Kakutani Y, Kitsugi T, Takagi H, Oka M, Kokubo T (1989) The influence of calcium–phosphate ceramics and glass–ceramics on cultured cells and their surrounding media. J Biomed Mater Res 23:1049–1066

Jasty M, Maloney WJ, Bragdon CR, Haire T, Harris WH (1990) Histomorphological studies of the long-term skeletal responses to well fixed cemented femoral component. J Bone Joint Surg 72A:1220–1225

Keaveny TK, Pinilla TP, Crowford RP, Kopperdahl DL, Lou A (1997) System and random errors in compression testing of trabecular bone. J Orthop Res 15:101–110

Kenny SM, Buggy M (2003) Bone cements and fillers: a review. J Mater Sci Mater Med 14:923–938

Kobayashi M, Nakamura T, Tamura J, Kokubo T, Kikutani T (1997) Bioactive bone cement: comparison of AW-GC filler with hydroxyapatite and beta-TCP fillers on mechanical and biological properties. J Biomed Mater Res 37:301–313

Kobayashi M, Takashi N, Okada Y, Fukumoto A, Furukawa T, Kato H, Kokubo T, Kobayashi M, Takashi N, Kikutani T (1998) Bioactive bone cement comparison of

apatite and wollastonite containing glass-ceramic, hydroxyapatite, and beta-tricalcium phosphate fillers on bone-bonding strength. J Biomed Mater Res 42:223–237

Kokubo T, Kushitani H, Sakka S, Kitsugi T, Yamamuro T (1990) Solutions able to reproduce in vivo surface–structure changes in bioactive glass–ceramic A–W. J Biomed Mater Res 24:721734

Kotani S, Fujita Y, Kitsugi T, Nakamura T, Yamamuro T, Ohtsuki C, Kokubo T (1991) Bone bonding mechanism of β-tricalcium phosphate. J Biomed Mater Res 25:1303–1315

Li YW, Leong JCY, Lu WW, Luk KDK, Cheung KMC, Chiu KY, Chow SP (2000) A novel injectable bioactive bone cement for spinal surgery: a development and preclinical study. J Biomed Mater Res 52:164–170

Lu JX, Gallur A, Flautre B, Anselme K, Descamps M, Thierry B, Hardouin P (1998) Comparative study of tissue reactions to calcium phosphate ceramics among cancellous, cortical, and medullar bone sites in rabbits. J Biomed Mater Res 42:357–367

Lu WW, Cheung KMC, Li YW, Luk KDK, Holmes AD, Zhu QA, Leong JCY (2001) Bioactive bone cement as a principal fixture for spinal burst fracture: an in vitro biomechanical and morphologic study. Spine 26:2684–2691

Marie PJ, Hott M (1986) Short-term effects of fluoride and strontium on bone formation and resorption in the mouse. Metabolism 35:547–551

Masuda T, Yliheikkila PK, Felton DA, Cooper LF (1998) Generalization regarding the process and phenomena of osseointegration. Part I. In vivo studies. Int J Oral Maxillofac Implants 13:17–29

Matsuda Y, Ido K, Nakamura T, Fujita H, Yamamuro T, Oka M, Shibuya T (1997) Prosthetic replacement of the hip in dogs using bioactive bone cement. Clin Orthop 336:263–277

Matsumoto A (1988) Effect of strontium chloride on bone resorption induced by prostaglandin E2 in cultured bone. Arch Toxicol 62:240–241

Meunier PJ, Slosman DO, Delmas PD et al. (2002) Strontium ranelate: dose-dependent effects in established postmenopausal vertebral osteoporosisa: 2-year randomized placebo controlled trial. J Clin Endocrinol Metab 87:2060–2066

Neo M, Kotani S, Fujita Y, Nakamura T, Yamamura T, Bando Y, Ohtsuki C, Kokubo T (1992a) Differences in ceramics–bone interface between surface-active ceramics and resorbable ceramics: a study by scanning and transmission electron microscopy. J Biomed Mater Res 26:255–267

Neo M, Kotani S, Fujita Y, Nakamura T, Yamamura T, Bando Y, Ohtsuki C, Kokubo T (1992b) A comparative study of ultrastructures of the interfaces between four kinds of surface-active ceramics and bone. J Biomed Mater Res 26:1419–1432

Neo M, Nakamura T, Ohtsuki C, Kokubo T, Yamamuro T (1993a) Apatite formation on three kinds of bioactive material at an early stage in vivo: a comparative study by transmission electron microscopy. J Biomed Mater Res 27:999–1006

Neo M, Nakaruma T, Yamamuro T, Ohtsuki C, Kokubo T (1993b) Transmission microscopic study of apatite formation on bioactive ceramics in vivo. In: Ducheyne P, Kokubo T, van Blitterswijk CA (eds) Bone-bonding biomaterials. Leiderdorp, The Netherlands: Reed Healthcare Communications, pp 111–120

Ngan AHW, Wang HT, Tang B, Sze KY (2005) Correcting power-law viscoelastic effects in elastic modulus measurement using depth-sensing indentation. Int J Solids Struct 42:1831–1846

Ni GX, Lu WW, Chiu KY, Li ZY, Fong DYT, Luk KDK (2006) Strontium-containing hydroxyapatite (Sr–HA) bioactive cement for primary hip replacement: an in vivo study. J Biomed Mater Res 77B:409–415

Okada Y, Kobayashi M, Fujita H, Katsura Y, Matsuoka H, Takadama H, Kokubo T, Nakamura T (1999) Transmission electron microscopic study of interface between bioactive bone cement and bone: comparison of apatite and wollastonite containing glass-ceramic filler with hydroxyapatite and b-tricalcium phosphate fillers Inc. J Biomed Mater Res 45:277–284

Okada Y, Kobayashi M, Neo M, Kokubo T, Nakamura T (2001) Ultrastructure of the interface between bioactive composite and bone: comparison of apatite and wollastonite containing glass–ceramic filler with hydroxyapatite and β-tricalcium phosphate fillers. J Biomed Mater Res 57:101–107

Okayama S, Akao M, Nakamura S, Shin Y, Higashikata M, Aoki H (1991) The mechanical properties and solubility of strontium-substituted hydroxyapatite. Biomed Mater Eng 1:11–17

Oliver WC, Pharr GM (1992) An improved technique for determining hardness and elastic modulus using load and displacement sensing indentation experiments. J Mater Res 4:1564–1583

Ooms EM, Wolke JGC, van der Waerden JPCM, Jansen JA (2002) Trabecular bone response to injectable calcium phosphate (Ca–P) cement. J Biomed Mater Res 61:9–18

Pharr GM (1998) Measurement of mechanical properties by ultra-low load indentation. Mater Sci Eng A253:151–159

Porter AE, Botelho CM, Lopes MA, Santos JD, Best SM, Bonfield W (2004a) Ultrastructural comparison of dissolution and apatite precipitation on hydroxyapatite and silicon-substituted hydroxyapatite in vitro and in vivo. J Biomed Mater Res 69A:670–679

Porter AE, Patel N, Skepper JN, Best SM, Bonfield W (2004b) Effect of sintered silicate-substituted hydroxyapatite on remodeling processes at the bone–implant interface. Biomaterials 25:3303–3314

Reginster JY (1997) Miscellaneous and experimental agents. Am J Med Sci 313:33–40

Rho JY, Tsui TY, Pharr GM (1997) Elastic properties of human cortical and trabecular lamellar bone measured by nanoindentation. Biomaterials 18:1325–1330

Senaha Y, Nakamura T, Tamura J, Kawanabe K, Iida H, Yamamuro T (1996) Intercalary replacement of canine femora using a new bioactive bone cement. J Bone Joint Surg 78B:26–31

Tamura J, Kitsugi T, Iida H, Fujita H, Nakamura T, Kokubo T, Yoshihara S (1995) Bone-bonding behavior of three types of bioactive bone cement containing bioactive glass or glass–ceramic powder. Bioceramics 8:219–223

Tang B, Ngan AHW (2003) Accurate measurement of tip-sample contact size during nanoindentation of viscoelastic materials. J Mater Res 18:1141–1148

Tang B, Ngan AHW and Lu WW (2006) Viscoelastic effects during depth-sensing indentation of cortical bone tissues. Philosophical Magazine 86:5653–5666

Walsh WR, Svehla MJ, Russell J, Saito M, Nakashima T, Gillies RM, Bruce W, Hori R (2004) Cemented fixation with PMMA or Bis-GMA resin hydroxyapatite cement: effect of implant surface roughness. Biomaterials 25:4929–4934

In Assessment of Osteoarthritis

Subchondral Bone Microarchitecture Changes in Animal Models of Arthritis

Susanne X. Wang

Director of Orthopaedics and Tissue engineering, MDS Pharma Services,
20011 30th Drive 5E Bothell, WA 98021, USA
e-mail: susanne.wang@mdsinc.com

Abstract

Animal models of osteoarthritis (OA) and rheumatoid arthritis (RA) are used to study the pathogenesis of joint degeneration and evaluate potential antiarthritic drugs for clinical use. Subchondral bone change in arthritis plays an important role in the development of the disease. The study of the subchondral bone change in human arthritis is limited by the access of human tissues especially in the earlier stage. Animal models provide the possibility of studying the pathogenesis of the disease at different stages and with easier usage of tissues. The development of high-resolution micro-computed tomography (micro-CT) scanner, capable of 3D reconstruction at a resolution of 6–50 μm, enables researchers to evaluate the changes in trabecular subchondral bone in animal models of arthritis. This chapter reviews the 3D microstructure changes in OA and RA animal models, as well as describing the application of micro-CT in evaluation of subchondral bone changes using 3D and 2D methods.

Introduction

Arthritis actually consists of more than 100 different conditions. Osteoarthritis (OA) is the most common form of arthritis, and rheumatoid arthritis (RA) is the second most common form. Osteoarthritis is one of the most frequent causes of physical disability among adults. More than 20 million people in the United States have OA. Some younger people suffer from OA as a result of joint injuries, but this disease most often occurs in older people. In fact, more than half of the population aged 65 years and above may show X-ray evidence of OA in at least one joint.

Osteoarthritis is characterized by the progressive destruction of articular cartilage and concomitant changes in subchondral bone. Clinical research on OA has been limited because it often presents at a late stage of the disease and there is a lack of markers indicative of disease progression. The etiology of primary OA is unknown, but secondary OA has multiple causes such as trauma, synovial disease, etc. The pathological mechanisms of OA are poorly understood and current therapy is not directed at the origin of the disease and is mostly symptomatic.

Rheumatoid arthritis is an autoimmune disease that causes chronic inflammation of the joints. It affects up to 1% of the world population. Rheumatoid arthritis can also cause inflammation of the tissue around the joints, as well as other organs in the body. Bone change in RA affects the periarticular and axial skeleton and is a major cause of disability. Osteoporosis of the skeleton has long been recognized in RA patients (Suzuki and Mizushima 1997). The localized osteopenia/osteoporosis seen around inflamed joints is the earliest sign of RA seen on radiographs and is used in RA diagnostics. The presence of focal marginal joint erosions have been regarded as the radiographic hallmark of RA (Sharp et al. 1991; Goldring and Polisson 1998; Goldring and Gravallese 2000). Standard radiographic techniques have demonstrated that these focal bone changes tend to progress throughout the course of the disease, and in general, the presence of extensive erosions tends to correlate with more severe disease activity (Sharp et al. 1991; van Zeben et al. 1993).

A variety of animal models of arthritis have been developed to study disease pathogenesis and to evaluate potential anti-arthritis drugs for clinical use. Animal models of OA include spontaneous OA in guinea pigs (Bendele and Hulman 1988; Meacock et al. 1990; Jimenez et al. 1997) and cynomolgus macaques (Carlson et al. 1994), meniscectomy and ligament transection in guinea pigs (Bendele et al. 1991), meniscectomy in rabbits (Colombo et al. 1983), and anterior cruciate ligament (ACL) transection in rabbits (Yoshioka et al. 1996) and dogs (Manicourt et al. 1999). Animal models of RA include collagen-induced arthritis (CIA) models in mouse and rat, adjuvant-induced arthritis (AIA), antigen-induced arthritis, and transgenic/knockout mice.

Bone Changes in Human Arthritis

It has long been debated whether initiating OA changes occur primarily in the cartilage or first in the underlying bone, with subsequent cartilage pathology. Unfortunately, studies that address OA changes in a kinetic way in both tissues are limited. Although significant changes in the subchondral cancellous bone, such as sclerosis and cyst formation, are frequently observed in patients with OA, little attention has been paid to changes in the subchondral bone, because they have always been considered to be secondary. More than 40 years ago Johnson (1962) suggested that bone remodeling, a natural accompaniment of aging, could lead to irregularities of the articular surface, and consequently, cartilage degeneration. Hutton et al. (1986) showed that in hand OA the increase in isotope concentration was identified in joints with OA prior to the onset of radiographic changes and was predictive of subsequent radiographic abnormalities of joint space loss and osteophyte formation. In human osteoarthritis increased subchondral bone activity, as judged by enhanced uptake of technetium-labeled diphosphonate, was shown to predict cartilage loss (Dieppe et al. 1993). These results suggest that cartilage lesions did not progress in the absence of significant subchondral activity. More recent studies have shown that increased subchondral bone remodeling results in thicker subchondral bone (Grynpas et al. 1991) and increased stiffness (Burr and Schaffler 1997); however, these newly formed arthritic bones are

under-mineralized (Grynpas et al. 1991; Li and Aspden 1997). The weaker bone within thickened subchondral cortical plate and trabeculae of OA joints causes subarticular osteoporosis (Buckland-Wright 2004). These concepts gained credence from histological and histomorphometric analysis of tibial condyles that showed cartilage degeneration to be influenced by remodeling of underlying subchondral bone (Matsui et al. 1997).

Rheumatoid arthritis is a progressive illness that has the potential to cause joint destruction and functional disability. It exhibits significant bone change, including bone erosion and remodeling. The relationships between subchondral bone changes, cartilage damage, and synovium inflammation are not yet fully understood; however, the bone and joint destruction in RA have been confirmed by biochemical markers and gene expression alterations during RA progression (Goldring 2002; Anastassiades and Rees-Milton 2005; Tchetina et al. 2005).

Bone Changes in OA Animal Models

It is evident that changes in the bone occur both in instability and spontaneous OA models. After ACL transection in dogs, the regions of pronounced periarticular cancellous bone mineral density (BMD) adaptation (Boyd et al. 2000a) and microstructural changes (Boyd et al. 2000b) corresponding to focal cartilage defects were already observed at week 3 and appeared more prominent at week 12. Similar studies in rabbits identified a correlation between enhanced blood flow and bone adaptation (Shymkiw et al. 2001). In contrast, studies in meniscectomized guinea pigs demonstrated early bone loss at the subchondral level at 1 month, but increased bone density at 3 months, after meniscectomy (Pastoureau et al. 1999).

The consequences of altered subchondral bone for the overlaying cartilage layer remain unclear. It has been suggested that only the bone density close to the cartilage surface is a major determinant in altered impact loading of the cartilage, and more detailed analysis of focal bone changes, close to expected cartilage lesion sites, is warranted. Interestingly, an increase of ossification is noted in the medial meniscus and not in the lateral meniscus of aging Hartley guinea pigs (Kapadia et al. 2000). Since bone remodeling and cartilage degeneration in this strain is evident with aging in the medial joint compartment, it is suggested that increased ossification of the meniscus alters joint biomechanics and underlies OA joint destruction.

Several animal experiments (Bailey and Mansell 1997; Dedrick et al. 1993) and human biopsy (Grynpas et al. 1991) studies have reported that thickening of the subchondral bone plate correlates to articular cartilage degradation. Simon et al. (1972) promoted the notion that OA begins in the bone by demonstrating that stiffening of subchondral bone preceded cartilage damage in guinea pigs.

In other OA animal models, changes in both bone and cartilage occur as a result of mechanical or surgical alteration of joint loading. For example, impulsive loading of rabbit knees, resulting in increased bone volume, is followed by progressive changes in articular cartilage during the following 6 months (Radin et al. 1984).

Taken together, these results demonstrate that subchondral bone remodeling is linked to cartilage destruction in both humans and animals; however, the mechanism by which changes in subchondral bone result in damage to articular cartilage is not readily apparent.

Micro-CT Imaging in Arthritis

There are increasing demands on arthritis imaging to identify early bone change and erosive joint damage, and to predict future structural and functional deterioration. Unfortunately, conventional radiography has been shown to be insensitive for insignificant bone change and erosions, particularly in early stages of the disease. Computed tomography (CT) offers advantages over projectional radiography. Micro-CT is a fast, accurate, and powerful method for studying skeletal structures. Micro-CT provides superior signal contrast between bone and soft tissue, making it especially appropriate for applications involving measurements of bone density (Genant et al. 1999). High-resolution micro-CT allows the quality spatial view of cancellous and cortical bone. A number of studies have applied micro-CT techniques to non-destructive evaluation of trabecular bone (Borah et al. 2001; Gross et al. 1999; Kapadia et al. 1998), and it has been confirmed to be an accurate tool to precisely measure changes in bone stereology (Kuhn et al. 1990; Feldkamp et al. 1989; Goulet et al. 1994; Odgaard and Gundersen 1993) as well as bone volume and microarchitecture (Goulet et al. 1994; Buchman et al. 1998).

Three-dimensional imaging of human OA is still limited to late stages of the disease. The strength of X-ray-based techniques, such as micro-CT, is that they offer an excellent visualization of bone and exciting features for diagnosis of disease stages and for disease monitoring. Micro-CT provides spatial resolution better than 10 μm, but the size of the objects that can be scanned is only a maximum of 12–15 cm; therefore, the main application of micro-CT in arthritis has been the measurements of bone density and the analysis of 3D microstructure of the bone in animal models, in vivo animal total body scanning (small rodents), human peripheral scanning, and human bone biopsies.

The arthritis animal models mentioned in the previous section developed arthritic pathological changes that carry many characteristics of human arthritis. With application of micro-CT, it is possible to monitor the prominent bony alterations such as volumetric BMD (vBMD), 3D microstructure, bone erosion, osteophyte formation trabecular remodeling (BV/TV), subchondral bone plate thickness, and subchondral sclerosis (Dedrick et al. 1993; Wachsmuth and Engelke 2004; Batiste et al. 2004).

In addition to applications involving measurements of vBMD, BV/TV, and joint space, micro-CT data sets can be rendered and reconstructed into 3D isosurfaces and subsequently used for examination of bone surface irregularities such as osteophyte formation and bone erosions. Batiste et al. (2004) developed a method for volumetric quantification of osteophyte. Briefly, the osteophytes were manually outlined within each contiguous coronal image section. The total volume of osteophytic tissue was then determined in cubic millimeters, based on the known voxel volume.

Methodology of Using Micro-CT in Arthritis Research

In our experiments mentioned below we used GE micro-CT scanner (Explore Locus SP micro-CT Scanner, GE Healthcare, London, ON, Canada).

Sample Preparation

For in vitro scanning, specimens (usually the hind legs) were dislocated from the animal (rabbit, guinea pig, rat, and mouse) body; soft tissue could be intact to scan the whole joint, or be dissected off to scan a single bone. Specimens were prefixed with 10% natural buffered formalin or other fixatives, or freshly dissected and immersed in fixative when scanning. (Freezing of the sample should be avoided since the ice crystals can alter the fine microstructure within the bone, causing inaccurate measurement.)

Scanning Procedures

Samples should be firmly fixed in a water-filled specimen tube in a position such that the main axis is kept as parallel as possible to the Z-axis of the micro-CT image coordinate system. This minimizes any beam-hardening effects, since the X-ray beam crosses a minimal volume of bone tissue. It is suggested that a sufficient space remain between the edges of the sample to the cylinder wall in order to avoid interference to the scanned image from the test tubes.

The eXplore CT acquisition software (GE Medical Systems) was used in our studies to create different protocols according to animal size. For example, mouse and rat bones were scanned at 8-μm isotropic voxel size, with 499 projections, and a total scanning time of 150 min. Rabbit and guinea pig bones were scanned at 20-μm isotropic voxel size, with 299 projections, and a total scanning time of 45 min.

The scan was corrected following image acquisition using data acquired from an empty scan in which bright and dark images were gathered. Correction accounts for variations in temperature and attenuation of the X-rays (Feldkamp et al. 1989). The reconstructed tibia images were analyzed with MicroView 2.0 software (GE Healthcare, London, ON, Canada) in two and three dimensions.

Reconstruction

A volumetric data set of 512^3 voxels was reconstructed from the 499 (or 299) projections using the reconstruction software. Three-dimensional bone analyses were conducted in the reconstructed images. Using MicroView 2.0 analysis software, different regions of interest (ROIs) were selected according to the study purpose. In our guinea pig spontaneous OA model, two of the ROIs were rectangular, with dimensions of $1.85 \times 1.85 \times 0.6$ mm, and were positioned in the middle of the lateral and medial epiphysis to measure the 3D microarchitecture of the secondary spongiosa. Figures 1a and 1b illustrate the location of the epiphyseal ROIs. A third ROI (Fig. 1c), a cylinder $2 \times 2 \times 1$ mm in size, was placed 1 mm below the growth plate to measure the 3D microarchitecture of the primary spongiosa.
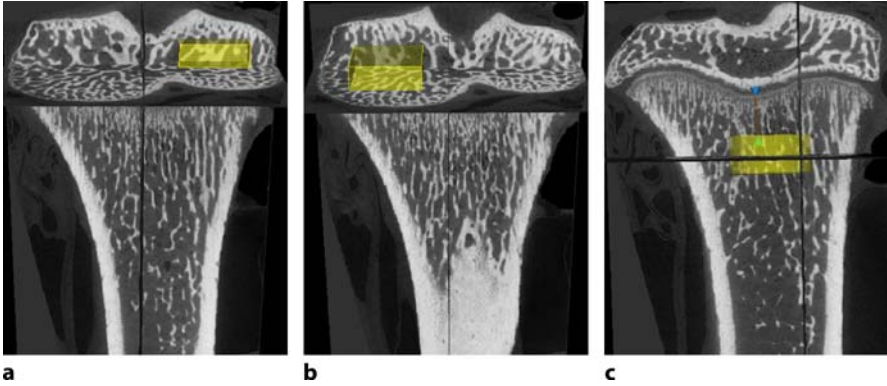
Figure 1 a–c. Locations of the regions of interest analyzed using the bone analysis application of MicroView. Regions highlighted in **a** and **b** have dimensions of $1.85 \times 1.85 \times 0.6$ mm and are placed in the medial and lateral proximal epiphysis, respectively. The *line* in **c** is 1 mm in length and marks the start of the cylindrical metaphyseal ROI analyzed. This ROI has dimensions of $2 \times 2 \times 1$ mm

Three-Dimensional Analysis

Micro-CT images were viewed and analyzed using MicroView software. In 3D analysis, the tissue volume (3D-TV, mm^3) and trabecular bone volume (3D-BV, mm^3)

Table 1. Micro-CT analysis of 3D structure changes during the development of spontaneous OA in two strains of guinea pigs. The DH strain showed significantly lower bone mass than the GOHI strain

		Medial		Lateral		
	STRAIN	Anterior	Posterior	Anterior	Posterior	Average
Volume of	GOHI	0.46 ± 0.02	0.50 ± 0.03	0.46 ± 0.03	0.44 ± 0.03	0.46 ± 0.02
Bone (mm^3)	DH	0.36 ± 0.02	0.45 ± 0.02	0.43 ± 0.02	0.44 ± 0.02	0.42 ± 0.01
P-value		0.005	0.228	0.498	0.845	0.042
Bone mineral	GOHI	504 ± 13.6	541 ± 12.1	497 ± 21.6	494 ± 17.5	509 ± 9.7
density (mg/cc)	DH	439 ± 24.9	501 ± 13.0	481 ± 16.3	487 ± 15.8	477 ± 12.5
P-value		0.033	0.033	0.566	0.761	0.055
Bone volume	GOHI	0.47 ± 0.03	0.51 ± 0.03	0.46 ± 0.03	0.45 ± 0.02	0.47 ± 0.02
fraction	DH	0.37 ± 0.02	0.47 ± 0.02	0.44 ± 0.02	0.45 ± 0.02	0.43 ± 0.01
P-value		0.009	0.251	0.674	0.915	0.077
Surface area	GOHI	6.88 ± 0.22	6.51 ± 0.19	6.78 ± 0.18	6.93 ± 0.13	6.77 ± 0.10
(mm^2)	DH	5.19 ± 0.23	5.68 ± 0.13	5.95 ± 0.17	5.55 ± 0.13	5.59 ± 0.07
P-value		0.000	0.002	0.002	0.000	0.000
Trabecular	GOHI	3.42 ± 0.24	3.97 ± 0.25	3.50 ± 0.28	3.22 ± 0.20	3.53 ± 0.16
thickness (pixels)	DH	3.67 ± 0.23	4.07 ± 0.23	3.78 ± 0.29	4.11 ± 0.26	3.91 ± 0.09
P-value		0.470	0.774	0.494	0.013	0.048
Trabecular	GOHI	5.5 ± 0.4	5.2 ± 0.4	6.0 ± 0.6	5.7 ± 0.4	5.6 ± 0.3
seperation (pixels)	DH	10.2 ± 1.1	6.7 ± 0.4	6.9 ± 0.4	7.4 ± 0.5	7.8 ± 0.3
P-value		0.000	0.024	0.197	0.012	0.000

were measured directly, and the fractional trabecular bone volume (3D-BV/TV, %) was calculated. The trabecular thickness (3D-Tb.Th, μm), trabecular number (3D-Tb.N, N/mm), and bone mineral density (v-BMD) were measured directly on 3D images (Hildebrand et al. 1999). Another parameter obtained was the structure model index (SMI) established by Hildebrand and Ruegsegger (1997). The SMI represents the plate-rod characteristics of trabecular structure. A negative number is indicative of a plate-like structure containing holes, 0 represents an ideal plate-like structure, and 3 represents the ideal rod (cylindrical) structure. Larger SMI values indicate that trabecular structure contains a more rod-like structure in older or diseased bone.

Table 1 is a micro-CT analysis from our spontaneous OA study using two strains of guinea pigs. Three-dimensional analysis revealed the DH strain to have a significantly lower bone mass than the GOHI strain: lower bone mineral density, smaller bone volume fraction, and bone surface area; however, the subchondral bone trabeculae were thicker and more distinctly separated in the DH than in the GOHI strain. Each of the aforementioned changes was most severe on the medial side of the joint, particularly in the anterior region.

Three-Dimensional Isosurfaces

A 3D isosurface image of the specimen was obtained by rendering of image data and reconstructed into a 3D surface view. This isosurface's function facilitated visualization of bone surface irregularities, assisting with early detection of morphological changes related to disease progression. Osteohpyte volume can be quantified using the method described previously (Batiste et al. 2004).

Figure 2a is a 3D reconstructed isosurface of a 12-month-old guinea pig femur from our research. Spontaneous OA was developed in the knee joint of this animal,
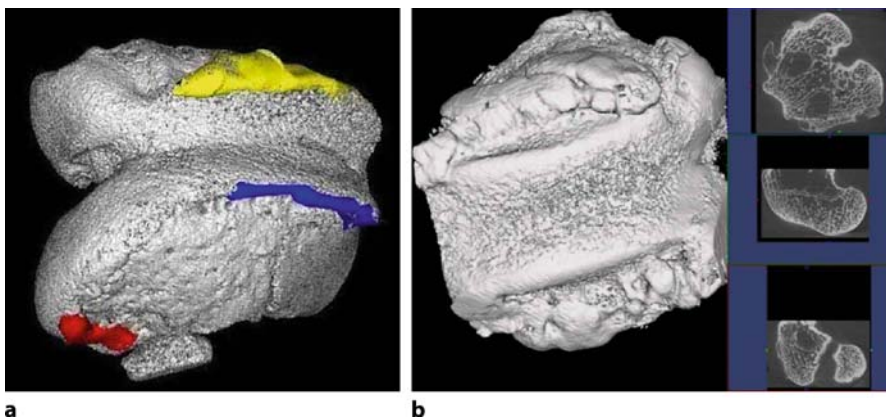
Figure 2. a Three-dimensional reconstructed isosurface of a 12-month-old guinea pig femur to show the out growth of bonny osteophyte (highlighted in *color*). **b** A rabbit femur at 8 weeks after anterior cruciate ligament transection shows massive osteophyte formation

and typical osteophytes were formed (highlighted in color). Figure 2b is a 9 month old rabbit femur at 8 weeks after ACLT, showing massive osteophyte formation. Figure 3 shows horizontal (Fig. 3a) and vertical (Fig. 3b) views of rabbit distal femur segmentations. Osteophytes were also segmented. The osteophyte located at the upper left site of Fig. 3b reveals thinner cortical shell and much less trabeculae.

We studied bone changes in a cell wall antigen-induced rat rheumatoid arthritis model. Figure 4a shows a 3D reconstructed isosurface of a rat proximal tibia. Compared with the normal control tibia (Fig. 4b), the erosions of tibia plateau are clearly visualized. The method mentioned previously (Batiste et al. 2004) can also be used to quantify the volume of erosion by calculating the necessary volume needed to fill the eroded space.
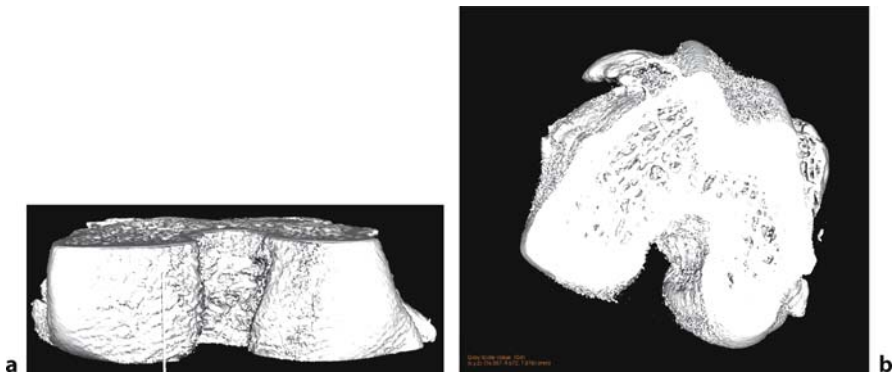
Figure 3 a,b. Segmentations of distal femur horizontal (**a**) and vertical (**b**). Osteophytes were also segmented. The osteophyte located at the upper left side of **b** revealed thinner cortical shell and much less trabeculae
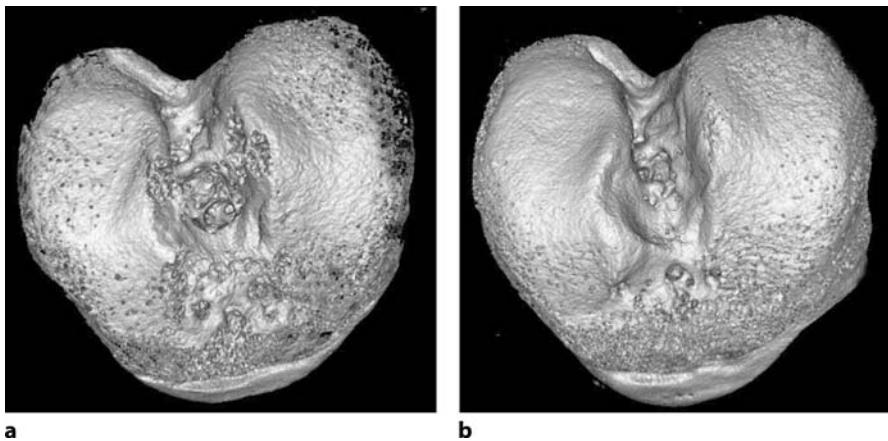
Figure 4. a Isosurfaces of proximal rat tibiae show the erosions at articular bone of the epiphysis in the arthritis-induced rat. **b** A smooth intact surface in a healthy rat tibia
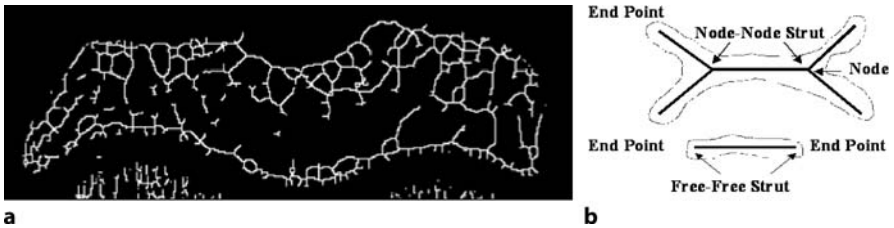
Figure 5 a,b. The area of cancellous bone analyzed by strut analysis (**a**) defines strut connectivity parameters (**b**)

Two-Dimensional Subchondral Bone Analysis

Three coronal sections of proximal tibia were obtained from each 3D reconstructed tibia image: anterior; central; and posterior (1 mm apart for rat and guinea pig tibiae). The subchondral trabecular bone structure and connectivity in the epiphyseal region of the proximal tibia were analyzed using an image processing and analysis system (Quantimet 570, Leica, Germany) on the 2D micro-CT images. After thresholding, a binary image was obtained at the medial and lateral side of the epiphyseal region to analyze the structure parameters according to the ASBMR guidelines (Parfitt et al. 1987): fractional trabecular bone volume (2D-BV/TV, %); trabecular thickness (2D-Tb.Th); and trabecular number (2D-Tb.N, N/mm).

The subchondral bone plate thickness (Sb.Pl.Th, mm) was also measured on the central section of the 2D micro-CT proximal tibia images using individual point-to-point distance measures. The thickness was calculated by averaging 12 measurements per tibia. All measurements were made in a standardized viewing area by a single observer who was blinded to the experiment.

Cartilage Imaging Using Micro-CT and Micro-MRI

Cartilage cannot be seen directly on micro-CT images; however, it can be calculated indirectly from the joint space between the two bony edges. The use of contrast agents may help in some circumstance to image cartilage and other soft tissues, but this still limits the application of micro-CT in evaluating cartilage in vivo.

As compared with X-ray-based imaging devices, MRI provides better soft tissue contrast and the ability to directly visualize articular cartilage, synovium, menisci, and other non-osseous structures both in vivo and ex vivo. Despite its theoretical advantages, due to the inadequacy of the MRI spatial resolution (no better than $100\,\mu m$), the current commercially available high-resolution micro-MRI cannot provide sufficient tissue contrast in order to accurately quantify the cartilage damage in animal models (rodents), especially for smaller lesions (Hutton and Vennart 1995).

The Future of Micro-CT in Arthritis Research

SkyScan (Aartselaar, Belgium) is a company specialized in the development and manufacturing of systems for 3D non-destructive investigation of an object's internal

microstructure. They have put effort into developing high-resolution micro-CT scanners. The Skyscan 2011 nano-CT scanner obtained a spot size of 0.3 μm, which could reduce the pixel size to 150 nm. This instrument enables the observation of small osteocytes and microcracks in bone. This dedicated technique gives better quality to micro-CT in studying detailed bone microarchitecture and material quality.

Scanco Medical AG (Bassersdorf, Switzerland) has advanced the in vivo application of the micro-CT system. Its in vivo micro-CT measurements provide information in a rapid and non-destructive way, which also gives a good resolution up to 12.5 μm. One has to consider the negative effects of the radiation dose of in vivo micro-CT and potential contraindication in clinical and preclinical applications. The effective radiation dose for a standard measurement with the "XtremeCT" (in vivo CT for humans) is 3 mSv, which is the same dose as the natural background radiation per year, and is much lower than the exposure of one-time intercontinental flight (50 mSv); however, the applied dose to the animals during in vivo CT is much higher due to the high resolution; therefore, it is important to minimize the radiation dose without sacrificing the image-quality requirements prior to an animal study.

References

Anastassiades T, Rees-Milton K (2005) Biochemical markers for osteoarthritis: from the present to the future and back to the past. J Rheumatol 32:578–579

Bailey AJ, Mansell JP (1997) Do subchondral bone changes exacerbate or precede articular cartilage destruction in osteoarthritis of the elderly? Gerontology 43:296–304

Batiste DL, Kirkley A, Laverty S, Thain LM, Spouge AR, Gati JS, Foster PJ, Holdsworth DW (2004) High-resolution MRI and micro-CT in an ex vivo rabbit anterior cruciate ligament transection model of osteoarthritis. Osteoarthritis Cartilage 12:614–626

Bendele AM, Hulman JF (1988) Spontaneous cartilage degeneration in guinea pigs. Arthritis Rheum 31:561–565

Bendele AM, Bean JS, Hulman JF (1991) Passive role of articular chondrocytes in the pathogenesis of acute meniscectomy-induced cartilage degeneration. Vet Pathol 28:207–215

Borah B, Gross GJ, Dufresne TE, Smith TS, Cockman MD, Chmielewski PA, Lundy MW, Hartke JR, Sod EW (2001) Three-dimensional microimaging (MRmicro and microCT), finite element modeling, and rapid prototyping provide unique insights into bone architecture in osteoporosis. Anat Rec 265:101–110

Boyd SK, Muller R, Matyas JR, Wohl GR, Zernicke RF (2000a) Early morphometric and anisotropic change in periarticular cancellous bone in a model of experimental knee osteoarthritis quantified using microcomputed tomography. Clin Biomech (Bristol, Avon) 15:624–631

Boyd SK, Matyas JR, Wohl GR, Kantzas A, Zernicke RF (2000b) Early regional adaptation of periarticular bone mineral density after anterior cruciate ligament injury. J Appl Physiol 89:2359–2364

Buchman SR, Sherick DG, Goulet RW, Goldstein SA (1998) Use of microcomputed tomography scanning as a new technique for the evaluation of membranous bone. J Craniomaxillofac Surg 9:48–54

Buckland-Wright C (2004) Subchondral bone changes in hand and knee osteoarthritis detected by radiography. Osteoarthritis Cartilage 12 (Suppl A): S10-S19

Burr DB, Schaffler MB (1997) The involvement of subchondral mineralized tissues in osteoarthrosis: quantitative microscopic evidence. Microsc Res Tech 37:343–357

Carlson CS, Loeser RF, Jayo MJ, Weaver DS, Adams MR, Jerome CP (1994) Osteoarthritis in cynomolgus macaques: a primate model of naturally occurring disease. J Orthop Res 12:331–339

Colombo C, Butler M, O'Byrne E, Hickman L, Swartzendruber D, Selwyn M, Steinetz B (1983) A new model of osteoarthritis in rabbits. I. Development of knee joint pathology following lateral meniscectomy and section of the fibular collateral and sesamoid ligaments. Arthritis Rheum 26:875–886

Dedrick DK, Goldstein SA, Brandt KD, O'Connor BL, Goulet RW, Albrecht M (1993) A longitudinal study of subchondral plate and trabecular bone in cruciate-deficient dogs with osteoarthritis followed up for 54 months. Arthritis Rheum 36:1460–1467

Dieppe PA, Cushnaghan J, Young P, Kirwan J (1993) Prediction of progression of joint space narrowing in osteoarthritis of the knee. Ann Rheum Dis 52:557–563

Feldkamp LA, Goldstein SA, Parfitt AM, Jesion G, Kleerekoper M (1989) The direct examination of three-dimensional bone architecture in vitro by computed tomography. J Bone Miner Res 4:3–11

Genant HK, Gordon C, Jiang Y, Lang TF, Link TM, Majumdar S (1999) Advanced imaging of bone macro and micro structure. Bone 25:149–152

Goldring SR (2002) Bone and joint destruction in rheumatoid arthritis: what is really happening? J Rheumatol 65 (Suppl):44–48

Goldring SR, Polisson RP (1998) Bone disease in rheumatological disorders. In: Avioli L, Krane SM (eds) Metabolic bone disease, 3rd edn. Academic Press, San Diego, pp 621–635

Goldring SR, Gravallese EM (2000) Pathogenesis of bone erosions in rheumatoid arthritis. Curr Opin Rheumatol 12:195–199

Goulet RW, Goldstein SA, Ciarelli MJ, Kuhn JL, Brown MB, Feldkamp LA (1994) The relationship between the structural and orthogonal compressive properties of trabecular bone. J Biomech 27:375–389

Gross GJ, Dufresne TE, Smith T, Cockman MD, Chmielewski PA, Combs KS (1999) Bone architecture and image synthesis. Morphologie 83:21–24

Grynpas MD, Alpert B, Katz I, Lieberman I, Pritzker KP (1991) Subchondral bone in osteoarthritis. Calcif Tissue Int 49:20–26

Hildebrand T, Ruegsegger P (1997) Quantification of bone microarchitecture with the structure model index. Comput Methods Biomech Biomed Engin 1:15–23

Hildebrand T, Laib A, Muller R, Dequeker J, Ruegsegger P (1999) Direct three-dimensional morphometric analysis of human cancellous bone: microstructural data from spine, femur, iliac crest, and calcaneus. J Bone Miner Res 14:1167–1174

Hutton CW, Vennart W (1995) Osteoarthritis and magnetic resonance imaging: potential and problems. Ann Rheum Dis 54:237–243

Hutton CW, Higgs ER, Jackson PC (1986a) 99mTC-HMDP bone scanning in generalized osteoarthritis II: The four hour bone scan image predicts radiographic change. Ann Rheum Dis 45:622–626

Hutton CW, Higgs ER, Jackson PC (1986b) 99mTC-HMDP bone scanning in generalized osteoarthritis I: comparison of standard radiographs and four hour bone scan image of the hand. Ann Rheum Dis 45:617–621

Jimenez PA, Glasson SS, Trubetskoy OV, Haimes HB (1997) Spontaneous osteoarthritis in Dunkin Hartley guinea pigs: histologic, radiologic, and biochemical changes. Lab Anim Sci 47:598–601

Johnson LC (1962) Joint remodelling as a basis for osteoarthritis. J Am Vet Med Assoc 141:1237–1241

Kapadia RD, Stroup GB, Badger AM, Koller B, Levin JM, Coatney RW, Dodds RA, Liang X, Lark MW, Gowen M (1998) Applications of micro-CT and MR microscopy to study preclinical models of osteoporosis and osteoarthritis. Technol Health Care 6:361–372

Kapadia RD, Badger AM, Levin JM, Swift B, Bhattacharyya A, Dodds RA, Coatney RW, Lark MW (2000) Meniscal ossification in spontaneous osteoarthritis in the guinea-pig. Osteoarthritis Cartilage 8:374–377

Kuhn JL, Goldstein SA, Feldkamp LA, Goulet RW, Jesion G (1990) Evaluation of a microcomputed tomography system to study trabecular bone structure. J Orthop Res 8:833–842

Li B, Aspden RM (1997) Mechanical and material properties of the subchondral bone plate from the femoral head of patients with osteoarthritis or osteoporosis. Ann Rheum Dis 56:247–254

Manicourt DH, Altman RD, Williams JM, Devogelaer JP, Druetz-Van Egeren A, Lenz ME, Pietryla D, Thonar EJ (1999) Treatment with calcitonin suppresses the responses of bone, cartilage, and synovium in the early stages of canine experimental osteoarthritis and significantly reduces the severity of the cartilage lesions. Arthritis Rheum 42:1159–1167

Matsui H, Shimitzu M, Tsuji H (1997) Cartilage and subchondral bone interaction in osteoarthrosis of human knee joint: a histological and histomorphometric study. Micro Res Tech 37:333–342

Meacock SC, Bodmer JL, Billingham ME (1990) Experimental osteoarthritis in guinea-pigs. J Exp Pathol (Oxford) 71:279–293

Odgaard A, Gundersen HJ (1993) Quantification of connectivity in cancellous bone, with special emphasis on 3-D reconstructions. Bone 14:173–182

Parfitt AM, Drezner MK, Glorieux FH, Kanis JA, Malluche H, Meunier PJ, Ott SM, Recker RR (1987) Bone histomorphometry: standardization of nomenclature, symbols, and units. Report of the ASBMR Histomorphometry Nomenclature Committee. J Bone Miner Res 2:595–610

Parisien M, Mellish RW, Silverberg SJ, Shane E, Lindsay R, Bilezikian JP, Dempster DW (1992) Maintenance of cancellous bone connectivity in primary hyperparathyroidism: trabecular strut analysis. J Bone Miner Res 7:913–919

Pastoureau PC, Chomel AC, Bonnet J (1999) Evidence of early subchondral bone changes in the meniscectomized guinea pig. A densitometric study using dual-energy X-ray absorptiometry subregional analysis. Osteoarthritis Cartilage 7:466–473

Radin EL, Martin RB, Burr DB, Caterson B, Boyd RD, Goodwin C (1984) Effects of mechanical loading on the tissues of the rabbit knee. J Orthop Res 2:221–234

Sharp JT, Wolfe F, Mitchell DM et al. (1991) The progression of erosion and joint space narrowing scores in rheumatoid arthritis during the first twenty-five years of disease. Arthritis Rheum 34:660–668

Shymkiw RC, Bray RC, Boyd SK (2001) Physiological and mechanical adaptation of periarticular cancellous bone after joint ligament injury. J Appl Physiol 90:1083–1087

Simon SR, Radin EL, Paul IL, Rose RM (1972) The response of joints to impact loading II: in vivo behaviour of subchondral bone. J Biomech 5:267–272

Suzuki Y, Mizushima Y (1997) Osteoporosis in rheumatoid arthritis. Osteoporosis Int 7 (Suppl 3): S217-S222

Tchetina EV, Squires G, Poole AR (2005) Increased type II collagen degradation and very early focal cartilage degeneration is associated with upregulation of chondrocyte differentiation related genes in early human articular cartilage lesions. J Rheumatol 32:876–886

van Zeben D, Hazes JMW, Zwinderman AH et al. (1993) Factors predicting outcome of rheumatoid arthritis: results of a follow-up study. J Rheumatol 20:1288–1296

Wachsmuth L, Engelke K (2004) High-resolution imaging of osteoarthritis using micro-computed tomography. Methods Mol Med 101:231–248

Yoshioka M, Coutts RD, Amiel D, Hacker SA (1996) Characterization of a model of osteoarthritis in the rabbit knee. Osteoarthritis Cartilage 4:87–98

Microarchitectural Adaptations
of Primary Osteoarthrotic Subchondral Bone

Ming Ding

Orthopaedic Research Laboratory, Department of Orthopaedics O,
Odense University Hospital, Clinic Institute, University of Southern Denmark Sdr.
Boulevard 29, 5000 Odense C, Denmark
e-mail: ming.ding@ouh.regionsyddanmark.dk

Abstract

Interest in the concept of bone quality has increased recently, with new imaging techniques and computer modeling abilities capable of assessing bone microarchitecture and bone strength. These novel imaging methods have enabled a detailed and versatile quantification of three-dimensional microarchitecture of bone tissue. Osteoarthrosis (OA) has an unclear pathogenesis and is one of the commonest age-related degenerative joint disease. Little is known about microarchitectural changes in human early OA. Difficulty in obtaining cartilage-bone samples for research in human OA has stimulated the development of animal models. In this chapter, an intensive investigation of the subchondral microarchitectural adaptations of human early OA and primary guinea pig OA is presented. Human early OA subchondral cancellous bone was shown to be significantly thicker and markedly plate-like, but weaker in mechanical properties. The increased trabecular thickness and density but relatively decreased connectivity indicated a mechanism of early-stage OA bone remodeling: a process of filling trabecular remodeling cavities. This process led to a progressive change of trabeculae from rod-like to more plate-like, opposite to that of normal aging. Guinea pig OA subchondral plate was shown to have a markedly increased volume fraction and thickness prior to OA initiation. Subchondral cancellous bone displayed a significant decreased volume fraction in the early stage, but increased volume fraction and trabecular thickness with age, and changing from a rod-like to typical plate-like structure with advancing OA. Subchondral cortical bone had an increased cross-sectional area in severe stage OA. This suggested that a significant microarchitectural adaptation followed by bone matrix density changes resulted in changed mechanical properties and hence decreased bone quality.

Current Understanding of Osteoarthrotic Subchondral Bone Microarchitecture

Osteoarthrosis (OA) stands alongside cancer and heart disease as one of the major causes of suffering and disability amongst the elderly. Changes related to OA occur in all elements of the joint, in particular articular cartilage and subchondral bone

tissues. These changes are thought to be important etiological elements in the pathogenesis of OA. Most previous investigations have focused on human moderate and late OA, whereas little is known about the changes in subchondral cancellous bone quality in human early OA.

Osteoarthrosis is a long-term disease with unclear pathogenesis. It is barely possible to follow the entire process of human OA. Difficulty in obtaining articular cartilage-bone samples for research in human OA has stimulated the development of animal models that resemble human condition. Some experimentally induced arthropathies involve intraarticular intervention which leads to rapidly progressive joint diseases similar to secondary or post-traumatic OA. There are also several naturally occurring animal OA models. Male Dunkin-Hartley strain guinea pig has been well documented to develop spontaneous primary age-related knee joint OA (Bendele and Hulman 1988; Watson et al. 1996). The knee joint arthropathy of this guinea pig OA model closely resembles primary OA in human; however, little is known about the naturally occurring mechanism of the microarchitectural and mechanical adaptations of subchondral bone tissues in this OA model.

Bone quality includes important factors such as the rate of remodeling (bone turnover), degree of mineralization, microarchitecture, bone size, bone geometry, and microdamage accumulation. Interest in the concept of bone quality has increased recently, with new imaging techniques and computer modeling abilities capable of assessing bone microarchitecture and bone strength. These methods have enabled a detailed and versatile quantification of 3D architecture of bone tissue (Odgaard 1997; Hildebrand and Rüegsegger 1997).

Assessment of Human OA Cancellous Bone Microarchitecture

Human Early OA Cancellous Bone Sample

We obtained human cancellous bone specimens from ten early-stage OA proximal tibiae (seven men, three women; mean age 73 years), and ten normal age- and gender-matched proximal tibiae (mean age 72 years). A total of 120 specimens, three from each medial and lateral condyle, were produced. The specimens were allocated to four groups (30 in each group): medial OA; lateral control; normal medial; and normal lateral controls. The degree of OA was defined according to Mankin's criteria and confirmed histologically (Mankin et al. 1971). Early OA was defined by the presence of macroscopically fibrillated cartilage. Normal tibiae had no macroscopic pathology or history of musculoskeletal disease (Ding et al. 2003).

Micro-CT Scanning and Microarchitectural Analysis

A high-resolution micro-CT system (μCT 20, Scanco Medical, Bassersdorf, Switzerland) was used to scan the specimens resulting in a cubic voxel size of $22 \times 22 \times 22 \mu m^3$. Each 3D image data set consisted of approximately 350 micro-CT slide images (512×512 pixels) with 16-bit-gray-levels. To obtain accurate 3D data sets,
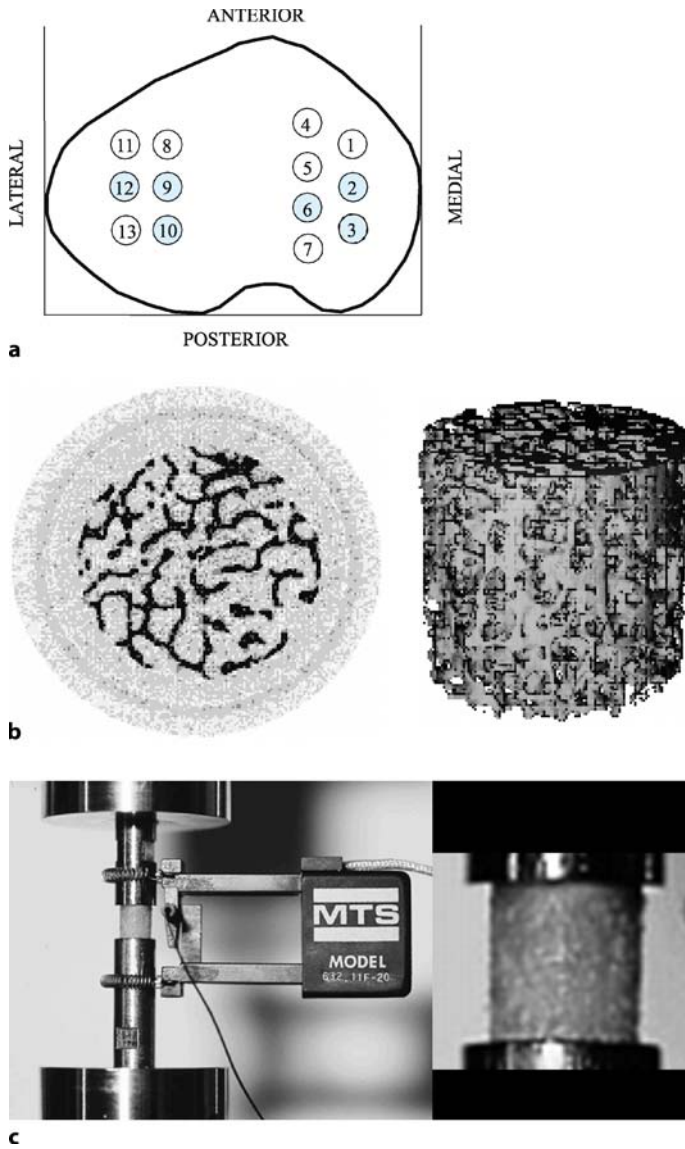
Figure 1 a–c. Study design for human proximal tibial cancellous bone. **a** A plastic template, which was available in different scales. They were used for obtaining specimens from the standardized locations of tibial condyles. Three cylindrical cancellous bones were randomly produced from each medial and lateral condyle. **b** Bone samples were micro-CT scanned to quantify their microarchitectural properties. **c** After scanning, bone samples were tested in axial compression to determine their mechanical properties

micro-CT images were segmented using optimal thresholds so that the bone volume fraction of the data sets corresponded to Archimedes'-based volume fraction (Ding et al. 1999). From the segmented accurate 3D micro-CT data sets, microarchitectural properties were calculated based on true, direct, unbiased, and assumption-free 3D methods (Fig. 1). These microarchitectural parameters include bone volume fraction (BV/TV), structure model index (SMI), trabecular thickness (TbTh, micron), bone surface-to-volume ratio (BS/BV, mm^{-1}), bone surface density (BS/TV, mm^{-1}), architectural anisotropy (DA), connectivity density (mm^{-3}), mean trabecular volume (μm^3), mean marrow space volume (μm^3), and trabecular spacing (micron).

Compression Mechanical Test

After scanning compressive mechanical tests were performed on a 858 Bionix MTS hydraulic material testing machine (MTS Systems Corp., Minneapolis, Minn.). A 1-kN load cell was used and a static strain gauge extensometer (Model 632.11F-20, MTS) was attached to the upper and lower testing columns close to the specimen. After 10 pre-conditioning cycles, the specimens were tested destructively in compression with a strain rate of 0.002/s to calculate ultimate stress (strength), Young's modulus (stiffness), and failure energy (energy absorption to failure; Fig. 1; Ding et al. 1997).

Computation of Elastic Modulus Using Finite Element Analysis

One cylindrical sample was chosen at random from the medial and the lateral condyle of human proximal tibia, and was scanned by micro-CT. The tissue modulus of each specimen was calculated using a combination of finite element modeling and mechanical testing (van Rietbergen et al. 1995). This method was used because it enables one to evaluate the tissue modulus separately from the trabecular architecture. All voxel micro-CT data were coarsened first then converted to cubic elements with an edge length of 66 μm. A bone volume-preserving algorithm was used during the coarsening procedure (Ulrich et al. 1999). After the coarsening procedure, the data was converted to a finite element mesh of 8-node cubic elements. All elements were assigned an arbitrary tissue elastic modulus of 1 GPa and a Poisson ratio of 0.3 (Day et al. 2001), and boundary values were assigned to simulate an unconstrained compressive test with no friction at the platens. The apparent modulus obtained from the finite element model could be simply scaled to match the apparent modulus from mechanical testing, since the finite element analysis was linear elastic. The resulting scaling factor was considered the effective bone tissue modulus of the sample (van Rietbergen et al. 1995).

Assessment of Guinea Pig Subchondral Bone Microarchitecture

Guinea Pig Bone Samples

We investigated age-related progressive changes in 3D microarchitecture of subchondral plate, cancellous and cortical bone tissues in a guinea pig osteoarthrotic model

that covered the entire range of OA, progressing from initiation to severe stage OA (Ding et al. 2006). The proximal tibiae of male Dunkin-Hartley Charles River strain guinea pigs were harvested at the age of 3 (child), 6 (young), 9 (adult), 12 (middle), and 24 (old age) months, ten in each group. The degree of OA was defined according to Mankin's criteria and confirmed histologically (Mankin et al. 1971). The proximal tibiae were examined by micro-CT. Unbiased, assumption-free 3D methods were used to quantify the microarchitectural properties of bone tissue (Fig. 2).
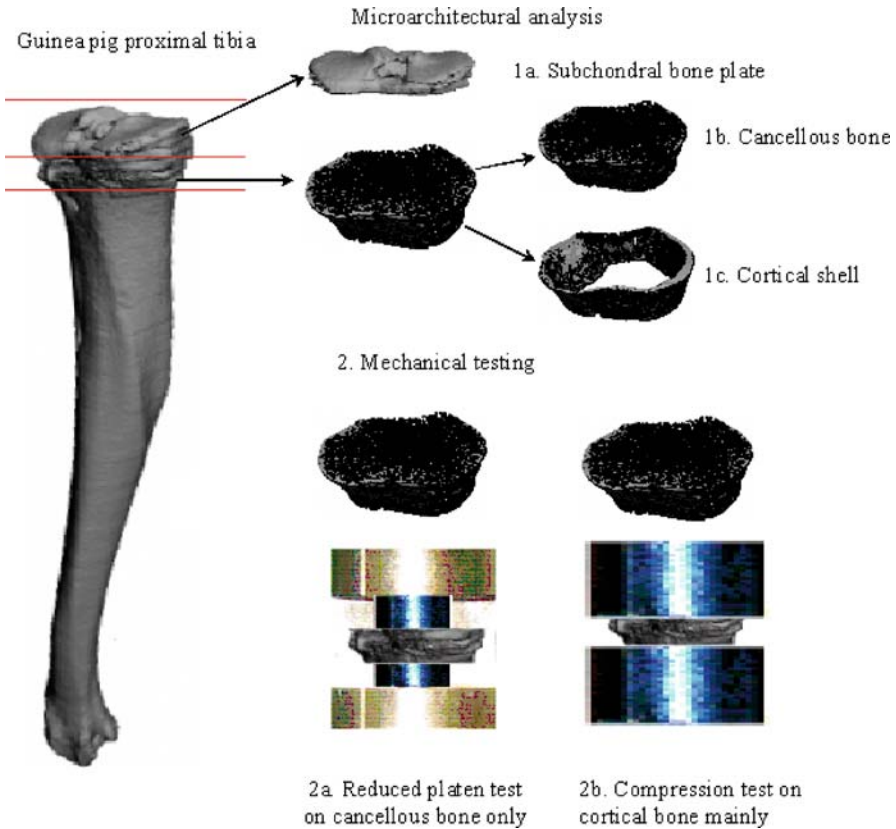
Figure 2. Study design for guinea pig proximal bone samples. The proximal tibiae of the guinea pigs were harvested. After removing soft tissue carefully, the 4-mm-thick proximal tibiae were micro-CT scanned for quantification of 3D microarchitecture of subchondral bone plate. Then a first cut was made 0.5 mm beneath subchondral bone plate and a further cut at distal part was made to produce 3-mm-thick cancellous-cortical bone complex specimen. This complex was micro-CT scanned to quantify the microarchitecture of subchondral cancellous and cortical bones. The cartilage-bone complex, including subchondral plate, was embedded for histology analysis for assessment of cartilage damages. Reduced platen test was first performed on cancellous bone only using an individual testing anvil (diameter 1.2 – 4.5 mm) that fitted to individual cross-sectional area of cancellous bone, then compression test was done on remaining cortical bone to determine their mechanical properties

Micro-CT Scanning and Microarchitectural Analysis

A high-resolution micro-CT system (μCT 40, Scanco Medical AG, Bassersdorf, Switzerland) was used to scan proximal tibial specimens, resulting in 3D reconstruction of cubic voxel sizes $16 \times 16 \times 16 \mu m^3$. Each 3D image data set consisted of approximately 400 micro-CT slide images of proximal tibia and 300 slice images of subchondral bone tissue (1024×1024 pixels) with 16-bit-gray levels. Two scans were performed. The first scan was performed on the 4 mm of proximal tibia to quantify the 3D microarchitecture of the subchondral plate. The proximal tibia was then sawed 0.5 mm beneath the subchondral bone plate and a further cut was made distally to produce a 3 mm thick cancellous-cortical bone specimen using a Leitz Microtome 1600 (Ernst Leitz Wetzlar Gmbh, Wetzlar, Germany). The second scan was performed on this specimen to quantify the 3D microarchitecture of cancellous and cortical bone (Fig. 2; Ding et al. 2005).

Three-Dimensional Microarchitectural Properties of Subchondral Bone Plate

Subchondral bone plate was defined as starting from the calcified cartilage-bone junction and ending at the marrow space (Carlson et al. 1996). To obtain accurate 3D data sets of subchondral bone plate, micro-CT images were segmented using optimal thresholds (Ding et al. 1999). The meaningful microarchitectural parameters
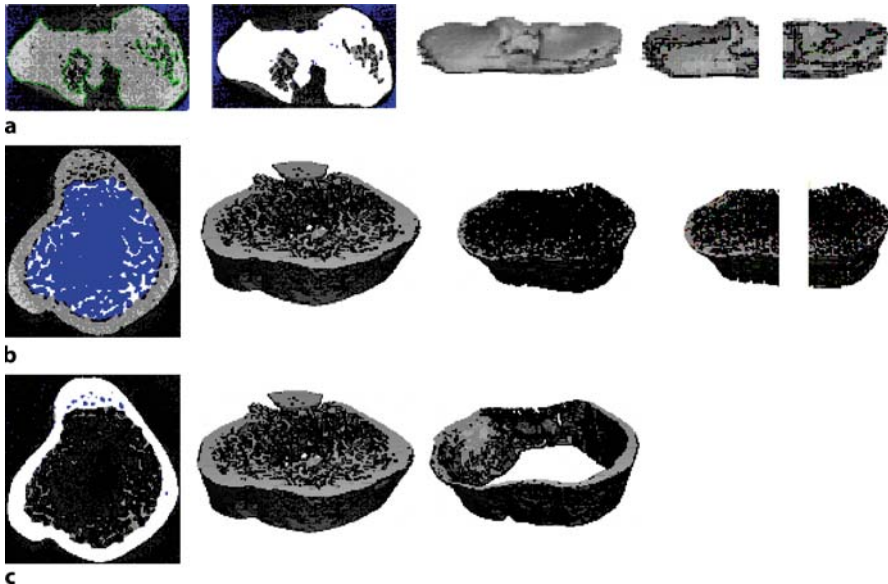
Figure 3 a–c. Quantification of subchondral bone tissues. **a** The 4-mm thick proximal tibiae were micro-CT scanned for quantification of 3D microarchitecture of subchondral bone plate. Then the 3-mm-thick cancellous-cortical bone complex specimen produced 0.5 mm beneath subchondral bone plate was micro-CT scanned for quantification of 3D microarchitecture of both cancellous bone (**b**) and cortical bone (**c**)

for the subchondral bone plate, i.e., plate volume fraction (%), plate thickness (micron), surface density (mm^{-1}), and plate perforation (mean pore size, in micron) were calculated. These calculations were done first on total subchondral plate, then on the medial and lateral condyles (Fig. 3a; Ding et al. 2005). A detailed description for quantification 3D microarchitecture of cortical bone has been presented (Ding et al. 2005).

Three-Dimensional Microarchitectural Properties of Subchondral Cancellous Bone

Subchondral cancellous bone was defined as the epiphyseal cancellous bone region beneath the thin layer of the subchondral plate. The subchondral cancellous bone was segmented using the optimal threshold described above to get accurate 3D data sets. The cancellous bone was defined and separated from the cortical shell. The microarchitectural properties were calculated using the same methods as for human cancellous bone. These calculations were done first on total subchondral cancellous bone, then on medial and lateral condyles (Fig. 3b; Ding et al. 2006).

Three-Dimensional Microarchitectural Properties of Subchondral Cortical Bone

The meaningful microarchitectural parameters of subchondral cortical bone were determined from segmented 3D data sets. The cortical thickness (μm), bone volume fraction (%), bone surface density (mm^{-1}), and cortical bone porosity (cavity/perforation, %) were calculated. The cross-sectional area (mm^2) of cortex was the mean value obtained from subchondral cortical bone (Fig. 3c; Ding et al. 2006).

Compression Testing of Guinea Pig Proximal Tibial Metaphysis

The mechanical tests of proximal tibial bone tissues were performed on a 858 Bionix MTS hydraulic material testing machine (MTS Systems, Minneapolis, Minn.), using a 1-kN load cell. Proximal tibia 3-mm bone specimen was isolated that included whole bone tissue (cortical and cancellous bone). The mechanical testing of proximal cortex was first performed using a so-called reduced platen testing that compressed to 5% on the central cancellous bone only leaving the cortex intact (Hogan et al. 2000). After this testing, compression test was performed again on the cortical bone mainly (including partial cancellous bone) between testing columns and bone specimen (Fig. 2; Ding et al. 2006).

Microarchitectural Adaptation of Human OA Subchondral Bone

Microarchitectural Adaptation of Early OA Subchondral Bone in Humans

Examples of 3D micro-CT image reconstruction of cancellous bone for OA and three controls are shown in Fig. 4. The microarchitectural properties and statistical analysis were presented in Fig. 5. Significant microarchitectural changes in the cancellous
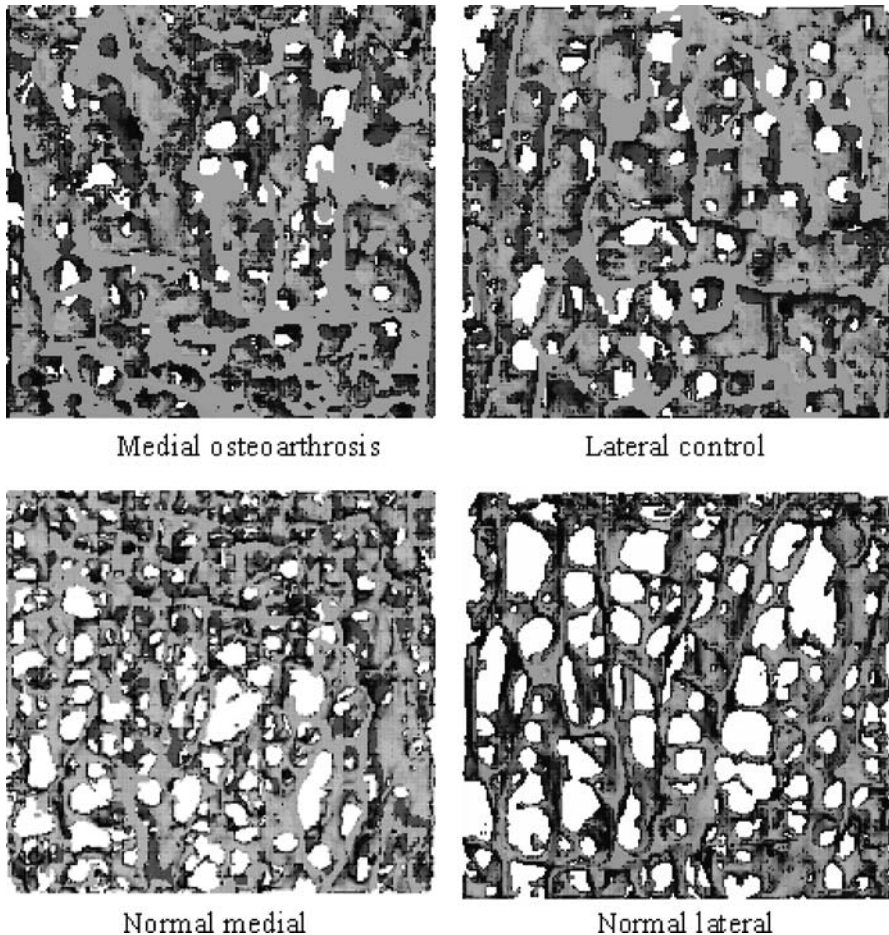
Figure 4. A 3D rendering of human tibial cylindrical cancellous bone specimens from micro-CT scans. The sample selection was based on the median value of bone volume fraction. Comparing the four specimens, the medial osteoarthrosis (OA; *upper left*) had the highest bone volume fraction and trabecular thickness, typical plate-like structure and the lowest bone strength; and the lateral control (*upper right*) had higher bone volume fraction and trabecular thickness, more plate-like structure, and lower bone strength. The normal medial (*lower left*) had lower bone volume fraction and trabecular thickness, more rod-like structure, and the highest bone strength, and the normal lateral (*lower right*) had the lowest bone volume fraction and trabecular thickness, typical rod-like structure, and relative higher bone strength

bone of OA specimens have been observed. The OA cancellous bone was significantly thicker and markedly plate-like but lower in mechanical properties. Similar microstructural changes were also observed for the lateral control with no sign of cartilage damage suggesting early alteration in the subchondral bone prior to cartilage damage.
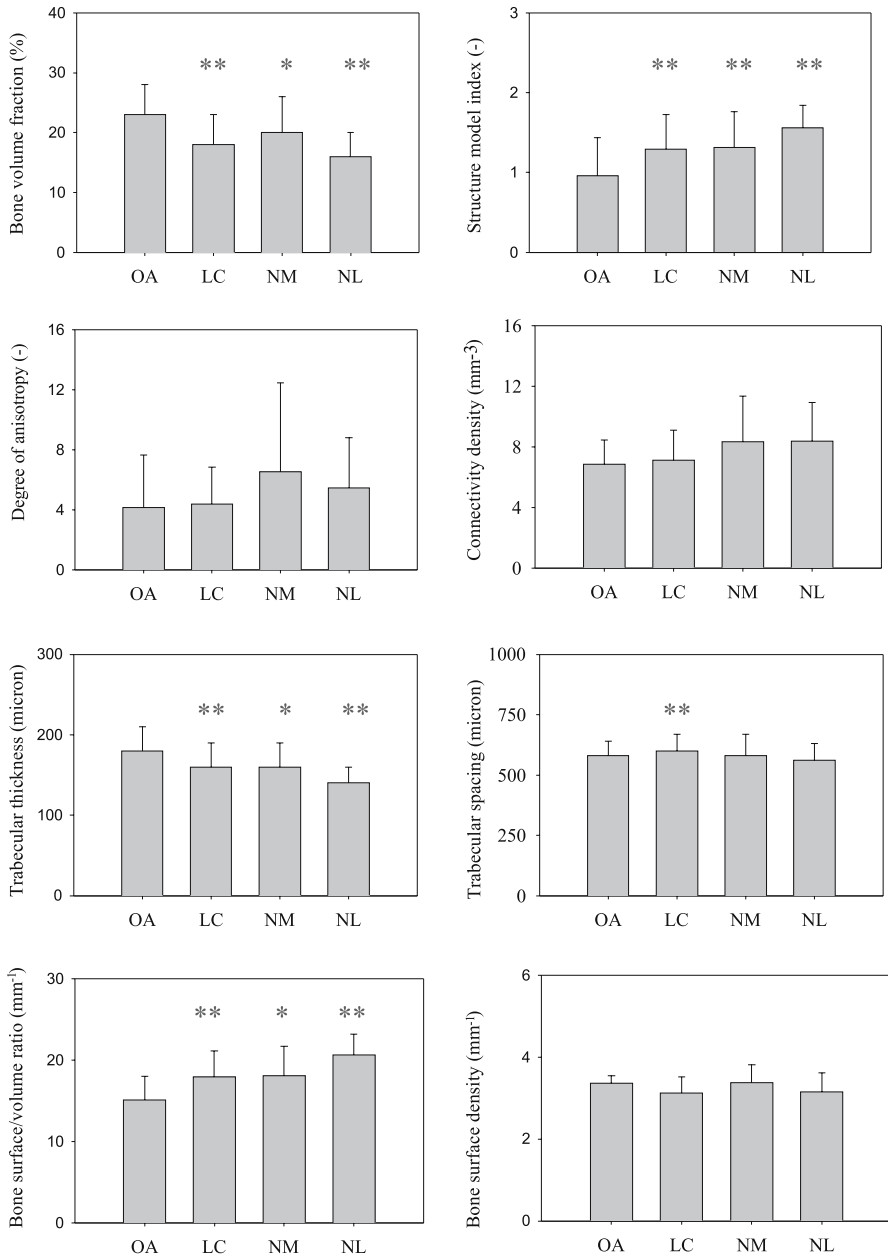
Figure 5. Microarchitectural properties of human early OA cancellous bone and the three control groups, and significant differences between OA and the three controls, are indicated. Compared with OA group, $^{*}p < 0.05$ and $^{**}p < 0.01$. *LC* lateral control, *NM* normal medial, *NL* normal lateral

Structure model index was the best predictor of the mechanical properties of OA cancellous bone; however, only 21–24% of the variance of the mechanical properties could be explained in the OA group. In normal controls, 42–71% of the variance of the mechanical properties could be explained by the structure model index alone (Ding et al. 2003).

Using finite element analysis of micro-CT data, we have demonstrated that effective bone tissue stiffness is decreased and bone quantity is increased in the presence of mild cartilage damage. The reduction of tissue stiffness caused greater tissue deformation than was compensated for by increased bone volume. It is likely that this process leads to a loss of the normal mechanical equilibrium between cartilage and bone (Ding et al. 1998; Day et al. 2001).

Microarchitectural Adaptation of Moderate and Severe OA Subchondral Bone in Humans

Subchondral cancellous bone structural changes in moderate and severe OA have also been described as differences in trabecular surface and shape compared with normal control groups (Fazzalari and Parkinson 1997). Osteoarthrosis is known to be associated with an increased cancellous bone density (Burr and Schaffler 1997). Horizontal trabecular thickness increased earlier followed by changes in the vertical trabeculae (Buckland-Wright et al. 1996). Bone mineral density increases in both the axial and peripheral skeleton with progression of OA (Dequeker 1997). Osteoarthrosis may have an abnormal low mineralization pattern at the late stage, even though OA is associated with a thickening of the subchondral bone plate (Grynpas et al. 1991). The stiffness of OA subchondral cancellous bone increases more slowly as density increases than does the stiffness of normal cancellous bone (Li and Aspden 1997).

Microarchitectural Adaptation of Guinea Pig OA Subchondral Bone

Examples of 3D micro-CT image reconstruction of guinea pig proximal tibial cancellous bone and cortical bone are shown in Fig. 6.

Our study demonstrated a significant bone remodeling-adaptation mechanism and property changes and quality deterioration in OA bone tissues. For subchondral bone plate, plate thickness remained relatively unchanged after 6 months of age. This result suggested that subchondral bone plate was not a major contributor in this OA model (Fig. 7). For subchondral cancellous bone, trabeculae changed from rod-like towards more plate-like which was opposite to that seen in human aging (Figs. 6, 8).

Assessment of OA Subchondral Bone Microarchitecture and Bone Quality

Assessment of Human OA Cancellous Bone Microarchitecture and Bone Quality

Our investigations demonstrated that the mechanical properties of early-stage OA cancellous bone were significantly decreased, despite a significant increase in bone
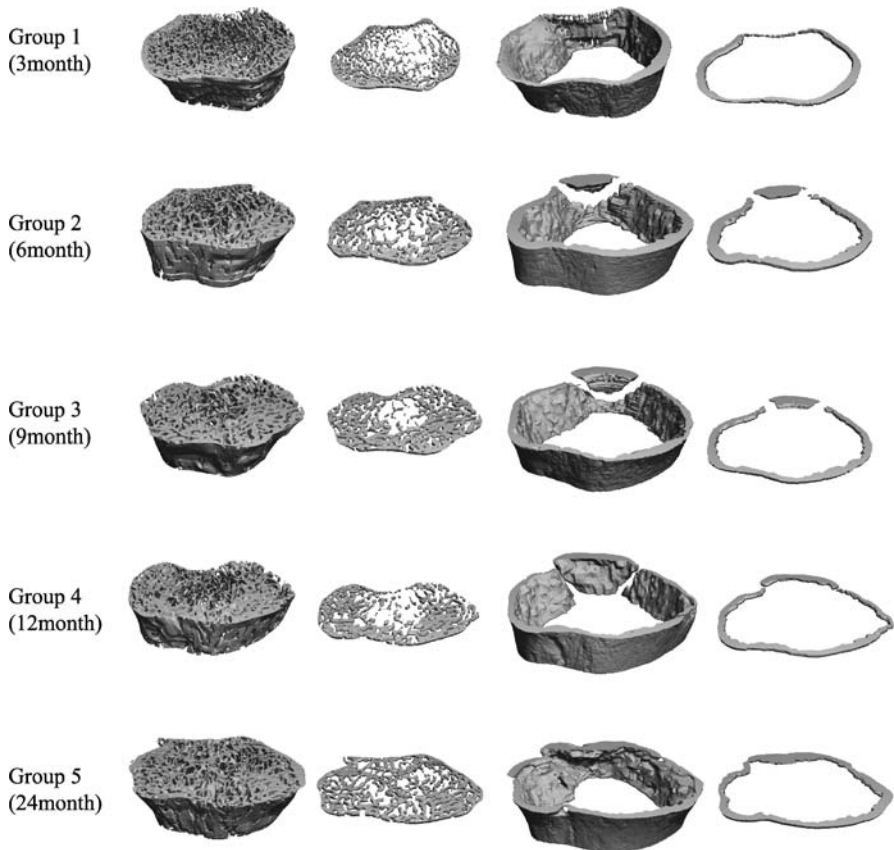
Figure 6. A 3D reconstruction of micro-CT images for guinea pig left proximal tibial cancellous bone and cortical bone 0.5 mm beneath subchondral bone plate in five age groups. The sample selection was based on the median value of bone volume fraction. Significant differences in microarchitecture are seen

density. The increase in the amount of defective bone tissue in early-stage OA could not compensate leading to a loss in mechanical properties (Ding et al. 2001).

Our data support the hypothesis that significant mechanical property and quality deterioration occur in early OA subchondral cancellous bone. The OA cancellous bone is mechanically inferior to normal medial control, despite higher density in OA bone tissue. Structure model index, rather than density, is the best predictor for the mechanical properties in OA and three controls; however, the ability of structure model index to explain mechanical properties in OA cancellous bone is largely reduced (Ding et al. 2003).

Cancellous bone was unusually plate-like in the OA group, whereas a combination of plate and rod structure was observed in the control groups. Interestingly, OA cancellous bone had a lower degree of anisotropy and connectivity. These results suggested that OA cancellous bone was less well organized than normal cancellous
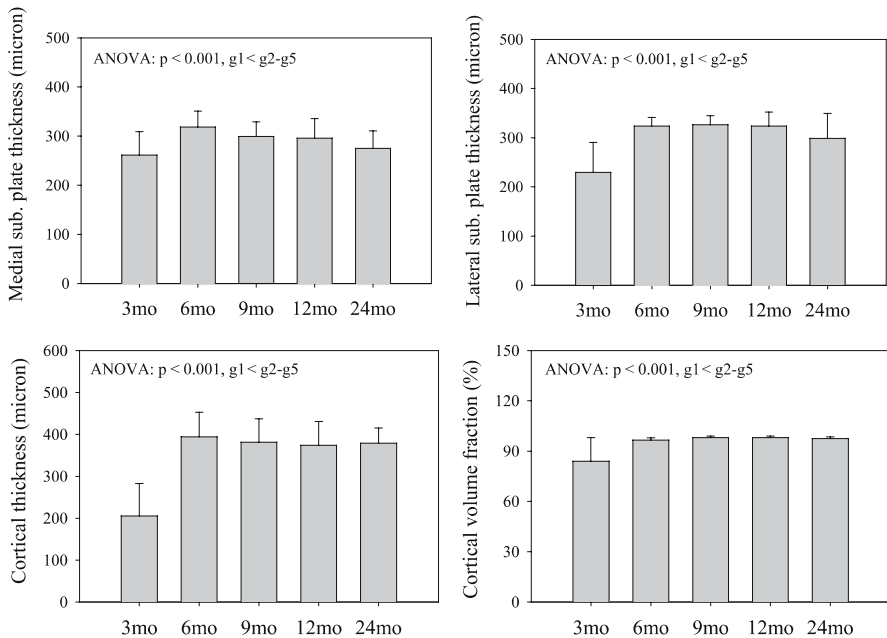
Figure 7. Microarchitectural properties of guinea pig subchondral plate and subchondral cortical bone. Significant differences in properties are indicated

bone (Ding et al. 2003). We have also observed a significant deterioration in elastic modulus of early OA cancellous bone at both apparent and tissue levels (Ding et al., 2001; Day et al. 2001). The decreased correlation between mechanical properties and density-microstructure indicated bone quality deterioration in early OA cancellous bone.

Assessment of Animal OA Cancellous Bone Microarchitecture and Bone Quality

Using micro-CT imaging and mechanical testing, we were able to quantify the subchondral bone microarchitectural adaptation over time that covered the entire range of guinea pig OA initiation and progression.

Volume fraction and thickness of the subchondral plate were markedly increased from 3 to 6 months prior to OA initiation, indicating early involvement of the subchondral plate. Volume fraction of the subchondral cancellous bone was significantly decreased at 6 months suggesting accelerated bone remodeling (absorption). Volume fraction and trabecular thickness increased with age, and changed from rod-like to plate-like structure with advancing OA, reflecting an important role of cancellous bone in OA initiation and development. In severe OA, the cross-sectional area of the subchondral cortical bone was increased, possibly due to osteophyte formation. Young's modulus was maximal at 6 months, whereas ultimate stress and failure energy increased with age with maximal values at 24 months. Bone collagen to mineral
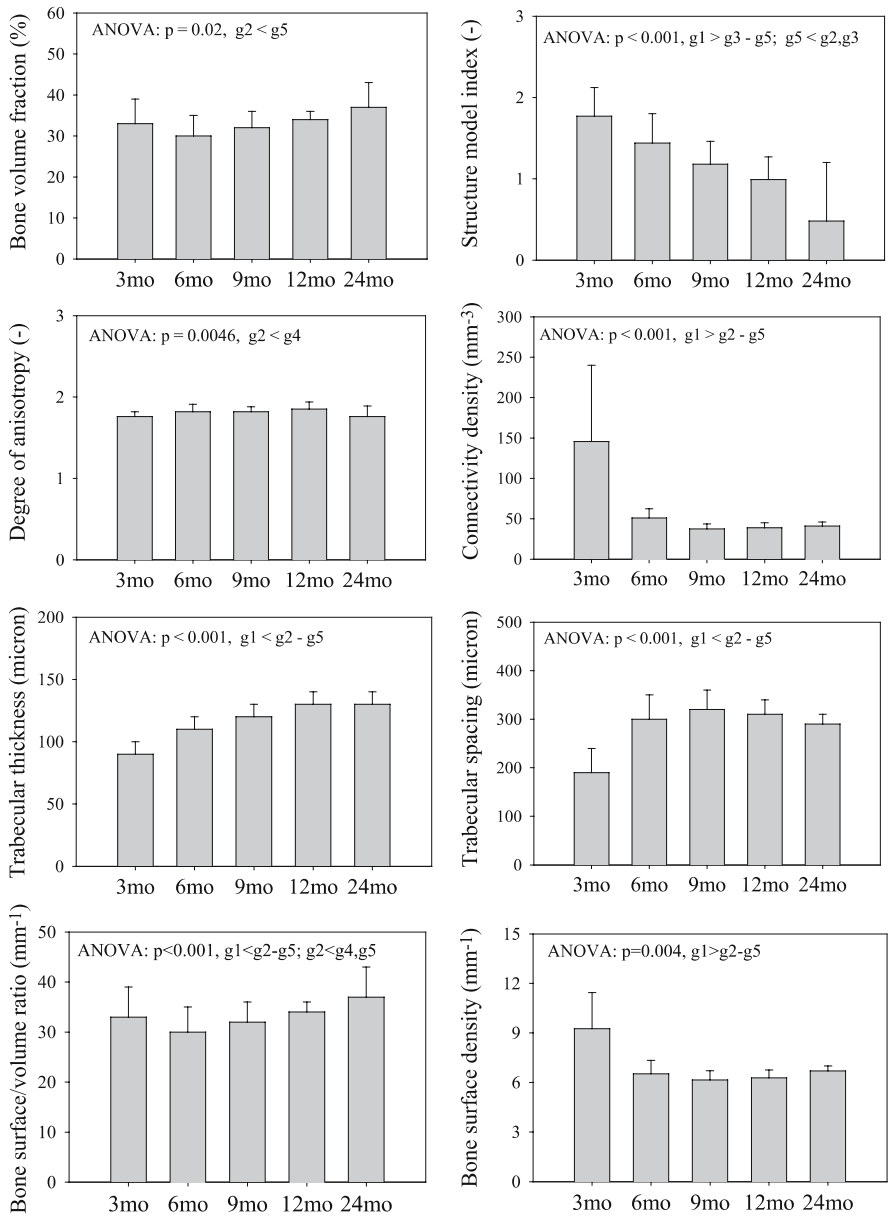
Figure 8. Microarchitectural properties of guinea pig cancellous bone. Significant differences in properties are indicated

ratio was significantly increased after OA initiation, reflecting undermineralization of bone tissues. These findings suggest different mechanisms of microarchitectural adaptation in the subchondral bone. The primary mechanism might be microarchi-

tectural alternation followed by changes in bone matrix density resulting in a change in mechanical properties and hence decreased bone quality (Ding et al. 2001, 2003, 2005).

References

Bendele AM Hulman JF (1988) Spontaneous cartilage degeneration in guinea pigs. Arthritis Rheum 31:561–565

Buckland-Wright JC, Lynch JA, Macfarlane DG (1996) Fractal signature analysis measures cancellous bone organisation in macroradiographs of patients with knee osteoarthritis. Ann Rheum Dis 55:749–755

Burr DB Schaffler MB (1997) The involvement of subchondral mineralized tissues in osteoarthrosis: quantitative microscopic evidence. Microsc Res Tech 37:343–357

Carlson CS, Loeser RF, Purser CB, Gardin JF, Jerome CP (1996) Osteoarthritis in cynomolgus macaques. III: Effects of age, gender, and subchondral bone thickness on the severity of disease. J Bone Miner Res 11:1209–1217

Day JS, Ding M, van der Linden JC, Hvid I, Sumner DR, Weinans H (2001) A decreased subchondral trabecular bone tissue elastic modulus is associated with pre-arthritic cartilage damage. J Orthop Res 19:914–918

Dequeker J (1997) Inverse relationship of interface between osteoporosis and osteoarthritis. J Rheumatol 24:795–798

Ding M, Dalstra M, Danielsen CC, Kabel J, Hvid I, Linde F (1997) Age variations in the properties of human tibial trabecular bone. J Bone Joint Surg Br 79:995–1002

Ding M, Dalstra M, Linde F, Hvid I (1998) Changes in the stiffness of the human tibial cartilage-bone complex in early-stage osteoarthrosis. Acta Orthop Scand 69:358–362

Ding M, Odgaard A, Hvid I (1999) Accuracy of cancellous bone volume fraction measured by micro-CT scanning. J Biomech 32:323–326

Ding M, Danielsen CC, Hvid I (2001) Bone density does not reflect mechanical properties in early-stage arthrosis. Acta Orthop Scand 72:181–185

Ding M, Odgaard A, Hvid I (2003) Changes in the three-dimensional microstructure of human tibial cancellous bone in early osteoarthritis. J Bone Joint Surg Br 85:906–912.

Ding M, Christian DC, Hvid I (2005) Effects of hyaluronan on three-dimensional microarchitecture of subchondral bone tissues in guinea pig primary osteoarthrosis. Bone 36:489–501

Ding M, Danielsen CC, Hvid I (2006) Age-related three-dimensional microarchitectural adaptations of subchondral bone tissues in guinea pig primary osteoarthrosis. Calcif Tissue Int 78:113–122

Fazzalari NL Parkinson IH (1997) Fractal properties of subchondral cancellous bone in severe osteoarthritis of the hip. J Bone Miner Res 12:632–640

Grynpas MD, Alpert B, Katz I, Lieberman I, Pritzker KP (1991) Subchondral bone in osteoarthritis. Calcif Tissue Int 49:20–26

Hildebrand T Rüegsegger P (1997) Quantification of bone microarchitecture with the structure model index. Comput Methods Biomech Biomed Engin 1:15–23

Hogan HA, Ruhmann SP, Sampson HW (2000) The mechanical properties of cancellous bone in the proximal tibia of ovariectomized rats. J Bone Miner Res 15:284–292

Li B Aspden RM (1997) Composition and mechanical properties of cancellous bone from the femoral head of patients with osteoporosis or osteoarthritis. J Bone Miner Res 12:641–651

Mankin HJ, Dorfman H, Lippiello L, Zarins A (1971) Biochemical and metabolic abnormalities in articular cartilage from osteo-arthritic human hips. II. Correlation of morphology with biochemical and metabolic data. J Bone Joint Surg Am 53:523–537

Odgaard A (1997) Three-dimensional methods for quantification of cancellous bone architecture. Bone 20:315–328

Ulrich D, van Rietbergen B, Laib A, Ruegsegger P (1999) The ability of three-dimensional structural indices to reflect mechanical aspects of trabecular bone. Bone 25:55–60

van Rietbergen B, Weinans H, Huiskes R, Odgaard A (1995) A new method to determine trabecular bone elastic properties and loading using micromechanical finite-element models. J Biomech 28:69–81

Watson PJ, Hall LD, Malcolm A, Tyler JA (1996) Degenerative joint disease in the guinea pig. Use of magnetic resonance imaging to monitor progression of bone pathology. Arthritis Rheum 39:1327–1337

Ultrasonic Characterization of Dynamic Depth-Dependent Biomechanical Properties of Articular Cartilage

Yong-Ping Zheng and Qing Wang

Department of Health Technology and Informatics, The Hong Kong Polytechnic University, Hong Kong, China
e-mail:ypzheng@ieee.org

Abstract

This chapter introduces ultrasonic characterization of dynamic depth-dependent biomechanical properties of articular cartilage. The ultrasound-swelling and ultrasound-elastomicroscopy systems are used, which show potentials for the investigation of the transient deformations of articular cartilage at different depths under dynamic loading. Ultrasound approaches inherently provide non-destructive assessment of articular cartilage. With the miniaturization of the ultrasound probes, these ultrasound techniques can be potentially used together with arthroscopes for in vivo assessment of articular cartilage. Studies suggest that these ultrasound approaches can also be potentially applied for dynamic mechanical assessment of other biological tissues, tissue engineered tissues, biomaterials and non-biomaterials.

Introduction

Articular cartilage is the thin layer of connective tissue that covers the articulating bony ends in diarthrodial joints. Because of the spatial variations of the water content, the proteoglycan concentration and the orientation of the collagen fibrils, the mechanical properties of articular cartilage are different at different depths (Mankin et al. 1994; Mow et al. 1991). To measure the depth-dependent properties of the articular cartilage is important not only for the investigation of the multilayered structure of the articular cartilage, but also for the study of cartilage degeneration, such as osteoarthritis, as well as for cartilage tissue engineering.

The zonal variations of the mechanical properties of articular cartilage have been measured in tension (Guilak et al. 1994; Roth and Mow 1980; Woo et al. 1976) and in compression (Chen et al. 2001; Setton et al. 1993) using carefully excised tissue slides at different depths. It is noted that the overall integrity of articular cartilage could not be protected during these measurements. The non-homogeneous deformation distribution within the full-thickness cartilage layer was theoretically predicted (Mow et al. 1980; Wang et al. 2001). In the 1990s the inhomogeneity of the mechanical properties of articular cartilage was directly measured using a confocal microscope (Guilak

et al. 1995) and a video microscope (Schigagl et al. 1996, 1997). A new optical method was developed for investigation of the non-uniform strain distribution with the cartilage layer during free-swelling induced by varying the concentration of the bathing saline solution (Narmoneva et al. 1999). These optical methods demonstrated that the strain distribution of cartilage was significantly depth dependent; however, the strain map was measured along one side of the excised specimen in the optical methods. It is not clear whether the depth-dependent material properties of articular cartilage obtained in such a "destructive" way would be the same as those in its natural intact state.

Ultrasound has been used to characterize the acoustical parameters of cartilage including ultrasound speed, attenuation, frequency spectrum, reflection coefficient, etc. It has been demonstrated that the sound speed varies in articular cartilage due its heterogeneous structure along the depth direction using a scanning laser acoustic microscope (Agemura et al. 1990) and a non-contact ultrasound method (Patil et al. 2004). Associated with compression or indentation, ultrasound has been used to facilitate the direct measurement of the depth-dependent mechanical properties of articular cartilage, such as the transient Poisson's ratio (Fortin et al. 2000), and the compressive strain (Zheng et al. 2002). Cohn et al. (1997a,b) extended the elastography technique (Ophir et al. 1991, 1999) to an elastic ultrasound microscope system. A 2D ultrasound elastomicroscopy system was developed to map deformations of articular cartilage (Zheng et al. 2004b). During the past few decades, the swelling behaviour of articular cartilage has attracted a tremendous amount of interest from researchers because of its important role in the unique biomechanical behaviour of articular cartilage. It has been found that the zonal distributions of proteoglycan concentration, water volume fraction and collagen fibrils govern the inhomogeneous swelling strain distribution (Lai et al. 1991; Maroudas 1976; Narmovena et al. 1999). Recently, ultrasound has also been used to investigate the depth dependence of swelling behaviour of articular cartilage in situ (Wang and Zheng et al. 2005; Zheng et al. 2005b).

In this chapter we describe specimen preparation, experimental setups of ultrasound-swelling system and ultrasound-elastomicroscopy system, data acquisition for ultrasound A-mode signals, ultrasound B-mode and M-mode image, and data processing used for the measurement of the echo displacement and the extraction of biomechanical parameters and images for articular cartilage.

Specimens and Methods

Specimen Preparation

Cylindrical cartilage-bone plugs approximately 3 mm thick were cored from fresh mature bovine patellae without obvious lesions using a metal punch with a diameter of 6.35 mm as shown in Fig. 1a. Specimens were wrapped in wet gauze soaked with physiological saline, and stored in a refrigerator at −20°C until testing. It has been previously reported that cryopreservation, freezing and thawing of the specimen may not affect its biomechanical and acoustic properties (Agemura et al. 1990; D'Astous
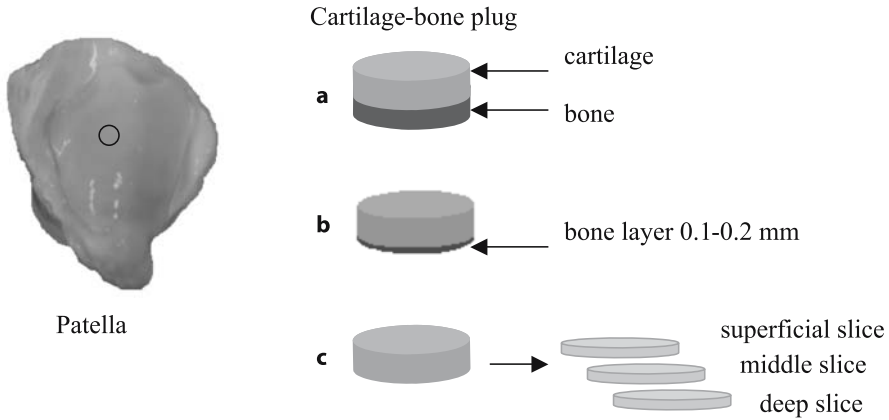
Figure 1. a Cylindrical cartilage-bone plugs with thickness of approximately 3 mm (≈ 6.35 mm) were cored from fresh mature bovine patellae for the ultrasound-swelling test. **b** The bone layer of the plug was prepared to be $0.1-0.2$ mm thick for the ultrasound-compression test. **c** The full-thickness cartilage layer was cut into the superficial, middle and deep slices for the measurement of the depth dependence of the sound speed

and Forster 1986; Dhillon et al. 2001; Kiefer et al. 1989; Kim et al. 1995; Kwan et al. 1992). The specimens were thawed in physiological saline for 1 h before testing.

Specimens with a bone layer approximately $0.1-0.2$ mm thick (Fig. 1b) were prepared from the cartilage-bone plugs using a lower speed diamond saw in the ultrasound-compression test. The reason for leaving this thin layer of bone was to maintain the integrity of cartilage tissue and to prevent the soft cartilage tissue from being squeezed into the slit in the specimen platform during compression. The slit was used to transmit an ultrasound beam into the articular cartilage specimen.

To measure the depth dependence of the sound speed, a thin surgical blade was used to cut the cartilage layer into three horizontal slices parallel to the cartilage surface, i.e. the superficial, middle and deep slices with approximately equal thickness as shown in Fig. 1c.

Experimental Setups

Ultrasound-Swelling System

The ultrasound swelling measurement system was developed to monitor and compare the normal and degenerated articular cartilage specimens in terms of the transient depth-dependent swelling behaviour induced by changing the concentration of bathing saline (Fig. 2a). A 3D translating stage with a specimen container and micrometers (Fig. 2b; Model R301MMX/2201MMXY, Ball Slide Positioning Stages, Deltron Precision) was designed to align the focused ultrasound beam into the cartilage specimen to obtain the maximum echo amplitude. During the swelling test, the cartilage-bone plug was fixed on the bottom of the container, surrounded by rubber gel (Blu-Tack, Australia) and submerged in the saline solution. An ultrasound pulser/receiver (model 5601A, Panametrics, Waltham, Mass.) was used to

drive a 50-MHz focused ultrasound transducer (focal length 12.3 mm and −6 dB focal zone approximately 1 mm in length and 0.1 mm in diameter; Panametrics, Waltham, Mass.). Ultrasound waves propagated through the tissue and the generated ultrasound echoes were received and amplified by the ultrasound pulser/receiver. The received ultrasound signals were digitized by an 8-bit A/D converter card with a sampling rate of 500 MHz (CompuScope 8500PCI, Gage, Ontario, Canada) installed in a computer. The ultrasound signals were displayed on the monitor in real time and automatically saved into the hard disk for offline data analysis.

Ultrasound-Elastomicroscopy System

The ultrasound elastomicroscopy system consisted of a compression system and a backscatter ultrasound biomicroscope system. As shown in Fig. 2c, the specimen
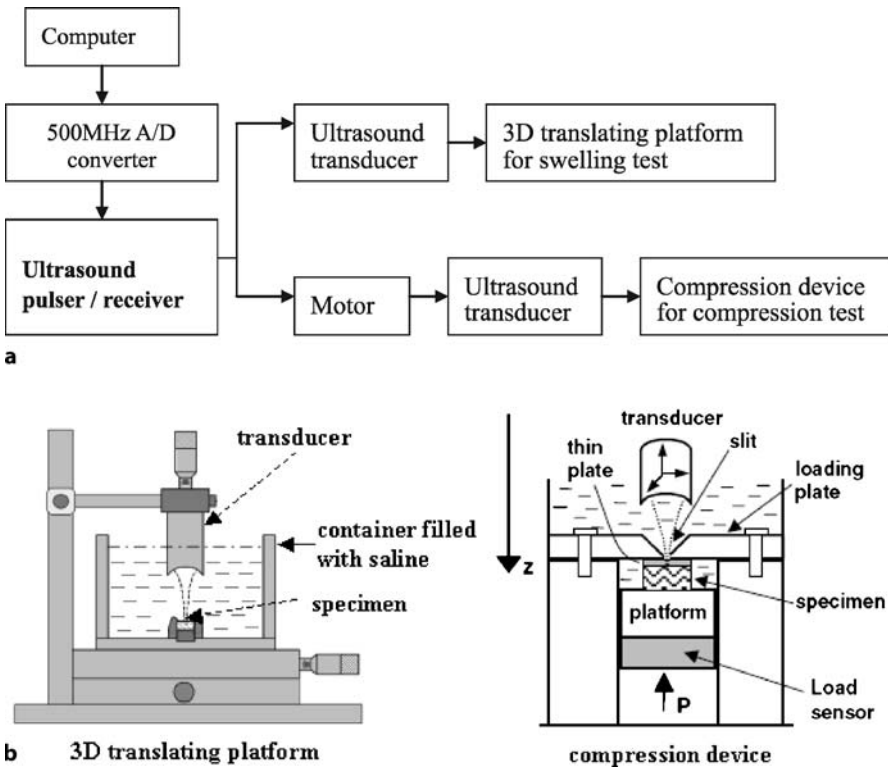
Figure 2. a Block diagram of the experiment setups. **b** The ultrasound-swelling system (Wang and Zheng 2005). The specimen was fixed in the bottom of the container. c The ultrasound-elastomicroscopy system (Zheng et al. 2004b). The specimen was installed between the loading plate and the platform, and load was applied from the bottom. The specimen was scanned along the slit (1 mm in width and 12 mm in length). To measure the ultrasound speed in the superficial, middle and deep cartilage layers, the container in **a** is replaced with a special designed container to facilitate the installation of the specimen slices

platform, in-series with a load cell (25 N, Model ELFS-T3, Entran Devices) on its bottom, could be manually moved up and down. The specimen was installed on the top of the specimen platform, and covered by a rigidly fixed plate. As the specimen was pressed against the plate, the load applied to the specimen was measured using the load cell.

A custom-built computer-controlled stepper-motor system (Sofratest, Ecquevilly, France) allowed the movement of the transducer along the length of the slit. The scan began at one lateral edge of the specimen and continued across the specimen to the opposite edge. At each compression level and scan site, the backscattered radio-frequency (RF) signal was digitized at 500 MHz and 8 bits using a digital oscilloscope (9350AL, LeCroy) and transferred to a computer for offline processing. After a scan was completed at one compression level, the specimen platform was moved upwards to compress the tissue specimen further, and a 15-min delay was applied before continuing data acquisition to allow the tissue to achieve equilibrium state. The echoes from the specimen surface and from the compressing platform beneath the specimen were acquired using the computer-controlled ultrasound system as described above.

Data Acquisition

Ultrasound A-mode Signals

Figure 3a shows a typical histological image of the central portion of a cartilage specimen with a Safranin-O stain. The ultrasound echoes (A-mode signals) that reflected from the surface of the cartilage tissue and from the cartilage-bone interface and scattered inside the cartilage layer were continuously recorded using the ultrasound biomicroscopy system. Figure 3b shows a frame of typical ultrasound RF signals collected from a cartilage specimen.

Ultrasound M-mode Images

The ultrasound M-mode image (Fig. 3c) was formed by the A-mode RF signals to represent transient information. The echoes at different measurement times were drawn line by line to form an image with the grey levels indicating the amplitude of the ultrasound signals. Each horizontal trace in the M-mode image indicated the transient displacement of the cartilage tissues at different depths, induced by the compression or the osmotic pressure.

Ultrasound B-mode Images

The ultrasound signals were also displayed in a B-mode image to represent information of a section of the specimen at different depths. In the experiment, the transducer scanned the cartilage specimen along the length of the slit. The A-mode RF signals at different measurement positions along the slit were drawn line by line to the B-mode ultrasound image (Fig. 4). The grey levels of the image linearly represent the amplitudes of the RF signals, i.e. uniform grey level (128) is baseline while black (0) and white (255) are maximum negative and maximum positive amplitudes in the recorded range.
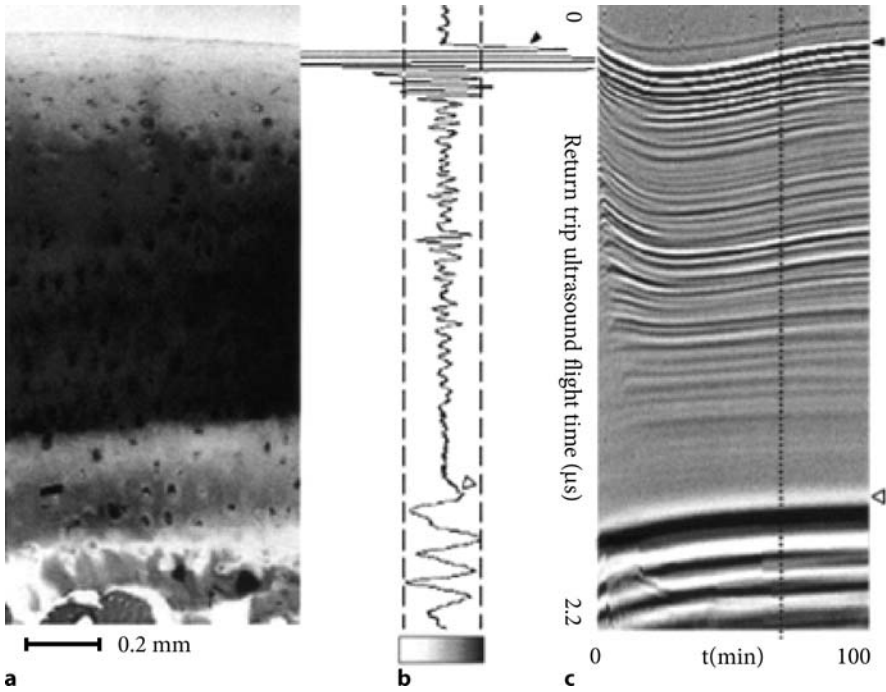
Figure 3. a Histological image of a typical articular cartilage specimen with the *red colour* (darkness in the grey image) indicating the concentration of proteoglycan stained with Safranin-O. **b** A-mode ultrasound signal obtained from a specimen. **c** M-mode representation of the ultrasound signals collected during swelling. The grey levels along the *vertical dotted line* in **c** indicate the signal amplitude shown in **b**. Each horizontal trace in the M-mode image indicates the transient deformations of the cartilage tissues at different depths, induced by the change in saline concentration. *Solid triangle* indicates the first positive half cycle of the reflection signal from the cartilage surface; *open triangle* indicates that from the cartilage-bone interface. (From Zheng et al. 2004a)

Data Processing

Measurement of Echo Displacement

The time of flight (T) of the ultrasound signal transmitted from the cartilage surface to the cartilage-bone interface and back to the cartilage surface can be obtained from the recorded ultrasound echoes. If the average ultrasound speed in the tissue is c, the thickness h of the entire cartilage layer can be calculated using the equation:

$$h = c \times T/2 \ . \tag{1}$$

The displacement of echo signals at different depths during compression or swelling was derived using a cross-correlation echo-tracking method. The cross-correlation technique is generally used for the study of the similarity between two signals. The normalised correlation coefficient of two series of discrete values
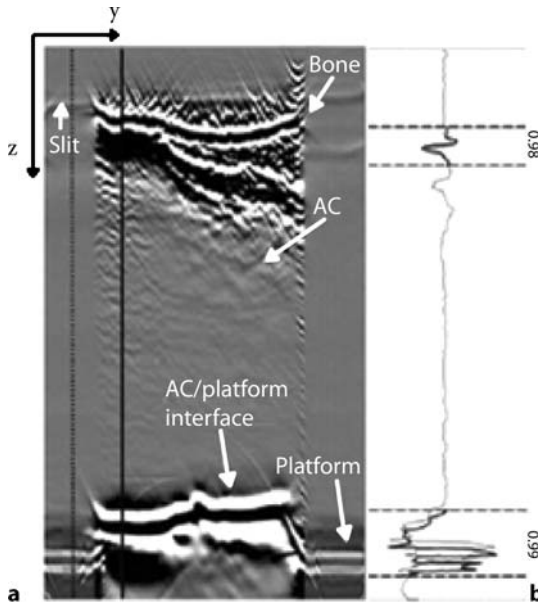
Figure 4. a B-mode ultrasound image (10 mm in width and 3 mm in height) of a typical cartilage specimen. The ultrasound transducer was moved along the length of the slit (the y direction). The ultrasound beam propagated through articular cartilage along the z direction. The grey levels of the image linearly represent the amplitudes of the radio-frequency (RF) signals. The RF signals in **b** correspond to the position indicated by the *solid line* in **a**. The pairs of horizontal *dashed lines* in **b** formed tracking windows to follow the movements of the corresponding ultrasound echoes during the compression procedure. The values beside the tracking windows indicate the correlation coefficients of the cross-correlation operations for the corresponding echoes before and after the compression was applied. (From Zheng et al. 2004b)

$$X = \{x(0), x(1), \dots, x(N-1)\}$$
$$Y = \{y(0), y(1), \dots, y(N-1)\}$$

can be written as

$$R = \frac{\sum_{i=0}^{N-1} [x(i) - \overline{X}][y(i) - \overline{Y}]}{\sqrt{\sum_{j=0}^{N-1} [x(j) - \overline{X}]^2 \sum_{k=0}^{N-1} [y(k) - \overline{Y}]^2}} , \qquad (2)$$

where $\overline{X}$ is the mean of X, and $\overline{Y}$ is the mean of Y. The normalised correlation coefficient R indicates the similarity between the two signals. If they are exactly the same, then $R = 1$, and, if they have no similarity, then $R = 0$. $R = -1$ indicated that the two signals are exactly inverted about the amplitude. The cross-correlation method provides the time shift value of the selected echoes. Then displacement is equal to the product of the sound speed and the time shift value. This method has been used

for the ultrasound elastography of soft tissues (Ophir et al. 1991; Zheng et al. 2004b) and tracking the movements of the selected tissue portions at different depths within the cartilage layer induced by mechanical force (Zheng et al. 2001, 2002, 2005a) or osmotic pressure (Zheng et al. 2004a, 2005b; Wang and Zheng 2005).

Calculation of Ultrasound Speed in Saline and Cartilage

An in vitro non-contact ultrasound method was developed to measure the sound speed in the cartilage (Patil et al. 2004). Figure 5 shows the representation of the calculation of the ultrasound speed in cartilage and saline solution. T_1, T_2, and T_3 represent the time of flight of the round trips of ultrasound echoes from the transducer to the upper surface of the cartilage slice, the lower surface of cartilage slice, and the bottom of the container through the specimen, respectively. T_4 and T_5 represent the time of flight of the round trip from the transducer to the bottom of the container without the presence of the specimen while the transducer is at the original position and the transducer is moved vertically down by the distance of d_T, respectively. The difference between the flight times obtained at the two positions was used to calculate the ultrasound speed in the saline solution (c_S) as follows:

$$c_S = \frac{2d_T}{(T_4 - T_5)} \ . \tag{3}$$

Based on a series of mathematic calculations (refer to Patil et al. 2004), the ultrasound speed in the cartilage tissue (c_{AC}) is obtained from

$$c_{AC} = \frac{T_4 - T_3 + T_2 - T_1}{T_2 - T_1} * c_S \ . \tag{4}$$

Calculation of the Osmosis-Induced Swelling Strain

In the free-swelling experiment, the Donnan osmotic loading was induced by the alternation of the concentration of the bathing saline solution from physiological saline
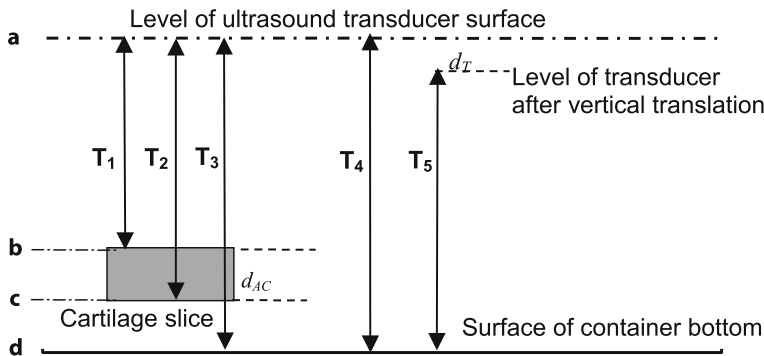
Figure 5. The elements involved in the calculation of the sound speed in cartilage and saline. d_{AC} is the thickness of articular cartilage slice; a represents the original position of the transducer. $T_1 - T_5$ are the flight times of the round trips of ultrasound from the transducer to different interfaces. (From Patil et al. 2004)

(0.15 M NaCl) to hypertonic saline (2 M NaCl) and back to physiological saline. Due to the electrochemomechanics of articular cartilage, the tissue swells and shrinks while the concentration of the external solution is reduced and increased, respectively. The time shift of the interested ultrasound echo can also be obtained using the cross-correlation algorithm. Consequently, the displacement of the cartilage surface (d) was given by

$$d = c'_S \times T'_1/2 - c_S \times T_1/2 , \tag{5}$$

where c_S and c'_S are the sound speeds in the saline before and after the concentration was changed, and T_1 and T'_1 are the time of flight from the transducer to the cartilage surface before and after changing the saline solution. The swelling and shrinkage strain of the full-thickness cartilage layer (ε) is calculated as

$$\varepsilon = \frac{d}{h}, \tag{6}$$

where h is the thickness of the cartilage layer. The equilibrium strains of different layers at different depths are given by

$$\varepsilon_i = \frac{d_i}{h_i}, \tag{7}$$

where d_i is the deformation of the ith sub-layer and h_i is the original thickness of the ith sub-layer.

Extraction of Ultrasound Elastomicroscopic Image

During the compression test, the cartilage surface was covered using a rigidly fixed plate. As the specimen was pressed at a compression rate of 0.1 mm/min for two steps, the applied load and the movement of the tissue were recorded using a load cell and an LVDT load sensor, respectively. It was assumed that the speed of ultrasound in cartilage did not change after a small compression (Zheng et al. 2004b). This ultrasound-compression method is similar to the ultrasound-indentation approach (Suh et al. 2001). The ultrasound speed in cartilage is given by

$$c_{AC} = \frac{T_3 - T_{3a}}{T_0 - T_{0a}} * c_S , \tag{8}$$

where T_0 and T_{0a} are the time of flight from the upper surface to the specimen-platform interface before and after the compression, respectively, and T_3 and T_{3a} represent the time of flight between the specimen upper surface and the surface of the specimen platform in saline before and after the compression, respectively. After the sound speed was estimated for a specimen, the deformation induced by compression could be achieved. A 2D auto-segmentation and displacement measurement using the cross-correlation algorithm were applied in the region of interest (ROI; Zheng et al. 2004b). The displacement image was mapped. The local strains of the tissues at intermediate depths were then calculated from the displacements of the tissue at two adjacent depths. A strain image was formed from the local strain profiles along each ultrasound signal. The grey levels of the strain image indicate the local strain values (Zheng et al. 2004b).

Results and Discussion

Depth-Dependent Swelling Behaviour of Articular Cartilage

During the swelling and shrinkage processes, the cartilage surface tended to deform rapidly and then moved upwards or downwards gradually close to equilibrium in approximately 1 h after changing the concentration of the saline solution. We called this interesting phenomenon as "overshoot-relaxation" phenomenon (Fig. 6). The absolute peak value of the shrinkage strain and swelling strain were $1.01 \pm 0.62\%$ (mean ± SD) and $0.40 \pm 0.33\%$, respectively. This phenomenon might be caused by the anisotropic mechanical properties and ion diffusion rates of articular cartilage; however, it has not been clarified. Further explanation to this finding requires more theoretical and experimental study.

In the previous studies, the equilibrium swelling strain of cartilage ranged from 3% (using the water-weight-gain method; Mow and Schoonbeck 1984) to less than 1% (using a uniaxial confined compression method; Eisenberg and Grodzinsky 1985). The inconsistency of the swelling strains reported in the literature could be due to individual variation of the specimen location, joint, species, age, degeneration status, specimen configuration, and measurement technique.

From the M-mode image (Fig. 3c), it is clearly shown that the ultrasound signals at different depths shift differently. The averaged values of the swelling strains for deep (30% of the total thickness), middle (55%), and surface (15%) zones (Mow et al. 1991) were successfully measured using ultrasound (Fig. 7). The non-uniformity of the swelling strains at different zones was observed, which was similar to the study by Narmoneva et al. (1999). It has been known that most of the proteoglycans are located in the middle zone of cartilage and the fixed negative charges along proteoglycans play a primary role in swelling (Maroudas 1976; Mow et al. 1991); therefore, the swollen middle layer may cause a compressive stress on the deep zone. In addition, the in situ configuration with the deep zone attached to the bone might give a rigid support to place the cartilage matrix in a state of compression. It is also known that
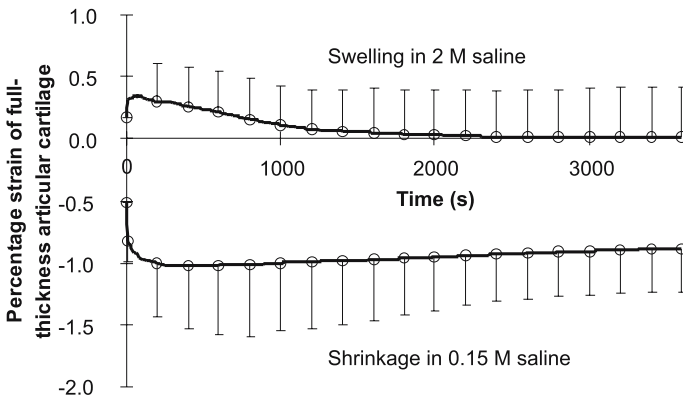
Figure 6. Shrinkage strain and the swelling strain vs the measurement time. The *error bars* represent the standard deviations of the results of 20 specimens. (From Wang and Zheng 2005)
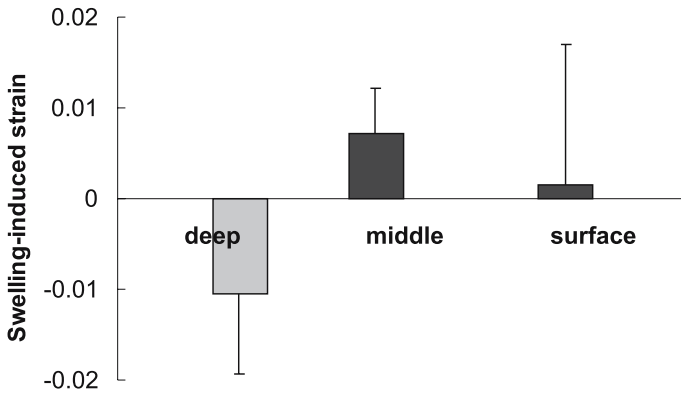
Figure 7. Non-uniform swelling-induced strains in cartilage grouped into three zones. The *error bars* represent the standard deviations of the results of 14 specimens. (From Zheng et al. 2005b)

collagen fiber organization in cartilage is highly non-uniform and anisotropic. Fibers are oriented tangential to the surface at the superficial zone to confine the swelling stress (Eisenberg and Grodzinsky 1985; Lai et al. 1991; Maroudas et al. 1986). This may be a reason why the tensile strain of the surface layer is lower than that of the middle zone. Further studies are definitely needed to better understand the reasons for the compressive strains in the deep zone while the full-thickness cartilage experienced an overall tensile strain during the free swelling test.

Depth-Dependent Ultrasound Speed in Articular Cartilage

The ultrasound speeds in the superficial, middle and deep cartilage layers in physiological saline were measured to be 1574 ± 29, 1621 ± 34 and 1701 ± 36 m/s, respectively (Fig. 8). It was found that the sound speed of cartilage significantly increased with depth ($p < 0.001$), similar to the results reported previously (Agemura et al. 1990). The anisotropic behaviour of the sound speed in the cartilage tissue may be due to the anisotropic mechanical properties and microstructures of articular cartilage (Kempson et al. 1980; Mankin et al. 1994; Mow et al. 1991); however, the excision of the cartilage layers caused the swelling and curling of the specimen (Myers et al. 1984; Setton et al. 1998) and might affect the measurement of the sound speeds in the different cartilage layers. The in vivo depth dependence of the ultrasound speed in cartilage is not yet evident and requires further investigation.

Depth-Dependent Mechanical Properties of Articular Cartilage

The mean equilibrium strains of sublayers at different depths after two incremental compressions and subsequent relaxations are shown in Fig. 9. It was noted that the average compressive strain at the superficial 0.2-mm-thick layer was 0.35 ± 0.09 significantly larger ($p < 0.05$) than that at the deeper layers (0.01 ± 0.02) after the first compression. The superficial layer incurred most of the deformation applied on the specimen, whereas the strains in the middle zones were relatively much smaller.
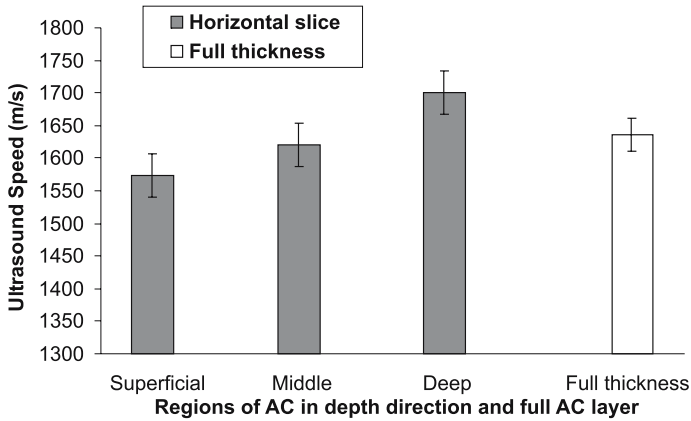
Figure 8. Sound speeds of the horizontal slices and full-thickness layer were measured with the ultrasound beam perpendicular to the cartilage surface. The error bars represent the standard deviations of the results of 18 specimens. (From Patil et al. 2004)
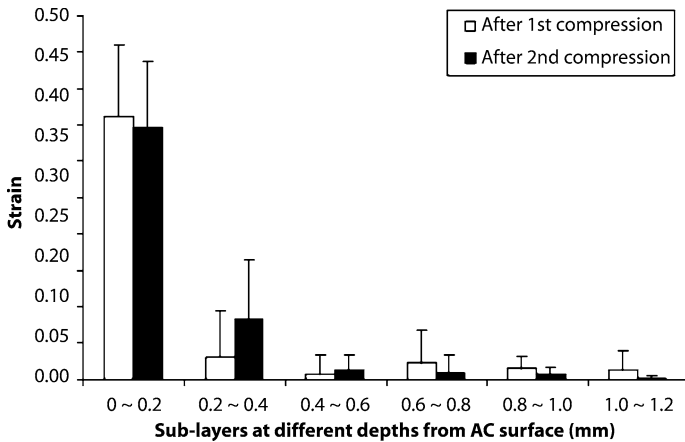
Figure 9. The mean equilibrium strains of sub-layers at different depths after two incremental compressions and subsequent relaxations were applied. The *error bars* represent the standard deviations of the results of ten specimens. (From Zheng et al. 2002)

These findings were similar to those reported using optical microscopic methods (Guilak et al. 1995; Schinagl et al. 1996, 1997).

The region of interest was selected in B-mode ultrasound image (Fig. 10a). Two conjunctive frames of image before and after compression (with a compression of 0.042 mm and average stress changed from 17.4 to 24.1 kPa) were used for cross-correlation calculation. In the corresponding local strain image (Fig. 10c), the grey level indicates the value of strain. Brighter pixels in the lower portion of the image (near the cartilage-platform interface, i.e. the superficial portion of the tissue) indicate that larger strain occurred near the articular surface in comparison with zones
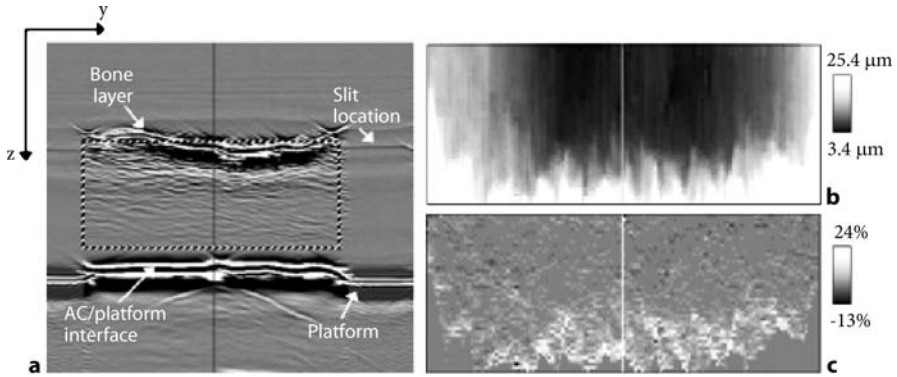
Figure 10. a B-mode ultrasound image (10 mm in width and 3 mm in height). The *dashed rectangle* indicates the ROI for the displacement and strain images (6.2 mm in width and 1.0 mm in height). **b** The image formed by the local displacements within the ROI. Brighter pixels in **b** represent larger tissue movements in the upward direction. **c** The corresponding local strain images of the ROI. Brighter pixels in **c** represent larger strains in the upward direction. (From Zheng et al. 2004b)

near the bone layer. This finding agrees with the results of the 1D transient measurement previously reported (Zheng et al. 2002). It should be paid attention that the material placed between the scanning transducer and the compressed tissue must be kept to a minimum because of the elevated attenuation of ultrasound at high frequencies.

Conclusion

This chapter introduces our studies on the ultrasonic characterization of dynamic depth-dependent biomechanical properties of articular cartilage. The ultrasound-swelling and ultrasound-elastomicroscopy systems have potential for investigation of the transient deformation of articular cartilage at different depths under dynamic loading. Ultrasound approaches can inherently provide non-destructive assessment of articular cartilage. With miniaturization of the ultrasound probes, these ultrasound techniques can be potentially used together with arthroscopes for in vivo assessment of articular cartilage. It is also expected that these ultrasound approaches can be potentially applied to dynamic mechanical assessment of other biological tissues, tissue engineered tissues, biomaterials and non-biomaterials.

References

Agemura DH, O'Brien WD, Olerud JE, Chun LE, Eyre DE (1990) Ultrasonic propagation properties of articular cartilage at 100 MHz. J Acoust Soc 87A:1786–1791

Chen AC, Bae WC, Schinagl RM, Sah RL (2001) Depth- and strain-dependent mechanical and electromechanical properties of full-thickness bovine articular cartilage in confined compression J Biomech 34: 112

Cohn NA, Emelianov SY, Lubinski MA, O'Donnell M (1997a) An elasticity microscope: Part I. Methods IEEE Trans Ultrason Ferroelectr Freq Control 44:1304–1319

Cohn NA, Emelianov SY, O'Donnell M (1997b) An elasticity microscope: Part II. Experimental results IEEE Trans Ultrason Ferroelectr Freq Control 44:1320–1331

D'Astous FT, Foster FS (1986) Frequency dependence of ultrasound attenuation and backscatter in breast tissue. Ultrasound Med Biol 12:795–808

Dhillon N, Bass EC, Lotz JC (2001) Effect of frozen storage on the creep behavior of human intervertebral discs. Spine 26:883–888

Eisenberg SR, Grodzinsky AJ (1985) Swelling of articular cartilage and other connective tissues: electromechanochemical forces. J Orthop Res 3:148–215

Fortin M, Soulhat J, Shirazi-Adl A, Hunziker EB, Buschmann MD (2000) Unconfined compression of articular cartilage: nonlinear behavior and comparison with a fibril-reinforced biphasic model. J Biomech Eng 122:189–195

Guilak F, Ratcliffe A, Lane N, Rosenwasser MP, Mow VC (1994) Mechanical and biochemical changes in the superficial zone of articular cartilage in canine experimental osteoarthritis. J Orthop Res 12:474–484

Guilak F, Ratcliffe A, Mow VC (1995) Chondrocyte deformation and local tissue strain in AC: a confocal microscopy study. J Orthop Res 12:410–422

Kempson GE (1980) The mechanical properties of articular cartilage. In: Sokoloff L (ed) The joints and synovial fluid, vol II. Academic Press, New York, pp 177–238

Kiefer GN, Sundby K, McAllister D, Shrive NG, Frank CB, Lam T, Schachar NS (1989) The effect of cryopreservation on the biomechanical behavior of bovine articular cartilage. J Orthop Res 7:494–501

Kim HK, Babyn PS, Harasiewicz KA, Foster FS (1995) Imaging of immature articular cartilage using ultrasound backscatter microscopy at 50 MHz. J Orthop Res 13:963–970

Kwan MK, Hacker SA, Woo SLY, Wayne JS (1992) The effect of storage on the biomechanical behavior of articular cartilage: a large strain study. J Biomech Eng T ASME 114:149–153

Lai WM, Hou JS, Mow VC (1991) A triphasic theory for the swelling and deformation behaviors of articular cartilage. J Biomech Eng 113:245–258

Mankin HJ, Mow VC, Buckwalter JA, Iannotti JP, Ratcliffe A (1994) Form and function of articular cartilage. In: Simnon SR (ed) Orthopaedic basic science. American Academy of Orthopedic Surgeons, Rosemont, Illinois, pp 2–44

Maroudas A (1976) Balance between swelling pressure and collagen tension in normal and degenerate cartilage. Nature 260:808–809

Maroudas A, Mizrahi J, Katz EP, Wachtel EJ, Soudry M (1986) Physicochemical properties and functional behavior of normal and osteoarthritic human cartilage. In: Kuettner KE, Schleyerbach R, Hascall VC (eds) Articular cartilage biochemistry. Raven Press, New York, pp 311–329

Mow VC, Schoonbeck JM (1984) Contribution of Donnan osmotic pressure towards the biphasic compressive modulus of articular cartilage. In: Trans 30th Annual Orthop Res Soc, Altanta, Georgia, pp 262

Mow VC, Kuei SC, Lai WM, Armstrong CG (1980) Biphasic creep and stress relaxation of articular cartilage in compression: theory and experiment. J Biomech Eng 102:73–84

Mow VC, Zhu W, Ratcliffe A (1991) Structure and function of articular cartilage and meniscus. In: Mow VC, Hayes WC (eds) Basic othopaedic biomechanics. Raven Press, New York, pp 143–198

Myers ER, Lai WM, Mow VC (1984) A continuum theory and an experiment for the ion-induced swelling behavior of articular cartilage. J Biomech Eng 106:151–158

Narmoneva DA, Wang JY, Setton LA (1999) Nonuniform swelling-induced residual strains in articular cartilage. J Biomech 32:401–408

Ophir J, Cespedes I, Ponnekanti H, Yazdi Y, Li X (1991) Elastography: a quantitative method for imaging the elasticity of biological tissues. Ultrason Imaging 13:111–134

Ophir J, Alam SK, Garra B, Kallel F, Konofagou E, Krouskop T, Varghese T (1999) Elastography: ultrasonic estimation and imaging of the elastic properties of tissues. Proc Inst Mech Eng 213:203–233

Patil SG, Zheng YP, Wu JY, Shi J (2004) Measurement of depth-dependency and anisotropy of ultrasound speed of bovine articular cartilage in vitro. Ultrasound Med Biol 30:953–963

Roth V, Mow VC (1980) The intrinsic tensile behavior of the matrix of bovine articular cartilage and its variation with age. J Bone Joint Surg 62:1102–1117

Schinagl RM, Ting MK, Price JH, Sah RL (1996) Video microscopy to quantitate the inhomogeneous equilibrium strain within articular cartilage during confined compression. Ann Biomed Eng 24:500–512

Schinagl RM, Gurskis D, Chen AC, Sah RL (1997) Depth-dependent confined compression modulus of full-thickness bovine articular cartilage. J Orthop Res 15:499–506

Setton LA, Zhu W, Mow VC (1993) The biphasic poroviscoelastic behavior of articular cartilage: role of the surface zone in governing the compressive behavior. J Biomech 26:581–592

Setton LA, Tohyama H, Mow VC (1998) Swelling and curling behaviors of articular cartilage. J Biomech Eng 120:355–361

Suh JKF, Youn I, Fu FH (2001) An in situ calibration of an ultrasound transducer: a potential application for an ultrasonic indentation test of articular cartilage. J Biomech 34:1347–1353

Wang Q, Zheng YP (2005) Non-contact evaluation of osmosis-induced shrinkage and swelling behavior of crticular cartilage in situ using high-frequency ultrasound. Instrum Sci Technol 34:317–334

Wang CCB, Hung CT, Mow VC (2001) An analysis of the effects of depth-dependent aggregate modulus on articular cartilage stress-relaxation behavior in compression. J Biomech 34:75–84

Woo SLY, Akeson WH, Jemmott GF (1976) Measurements of nonhomogeneous, directional mechanical properties of articular cartilage in tension. J Biomech 9: 785

Zheng YP, Ding CX, Bai J, Mak AFT, Qin L (2001) Measurement of the layered compressive properties of trypsin-treated articular cartilage: an ultrasound investigation. Med Biol Eng Comput 39:534–541

Zheng YP, Mak AFT, Lau KP, Qin L (2002) An ultrasonic measurement for in vitro depth-dependent equilibrium strains of articular cartilage in compression. Phys Med Biol 7:3165–3180

Zheng YP, Shi J, Qin L, Patil SG, Mow VC, Zhou KY (2004a) Dynamic depth-dependent osmotic swelling and solute diffusion in articular cartilage monitored using real-time ultrasound. Ultrasound Med Biol 30:841–849

Zheng YP, Bridal L, Shi J, Saied A, Lu MH, Jaffre B, Mak AFT, Laugier P (2004b) High resolution ultrasound elastomicroscopy imaging of soft tissues: system development and feasibility. Phys Med Biol 49:3925–3938

Zheng YP, Niu HJ, Mak AFT, Huang YP (2005a) Ultrasonic measurement of depth-dependent transient behaviors of articular cartilage under compression. J Biomech 38:1830–1837

Zheng YP, Wang Q, Niu HJ (in press) Extraction of mechanical properties of articular cartilage from osmotic swelling behavior monitored using high-frequency ultrasound. J Biomech Eng

Mechanical Property of Trabecular Bone of the Femoral Heads from Osteoarthritis and Osteoporosis Patients

Cheng-Kung Cheng (✉) , Yu-Su Lai, Shih-Sheng Sun, Hsin-Wen Shen, Chan-Tsung Yang, and Hung-Wen Wei

Orthopaedic Biomechanics Laboratory, Institute of Biomedical Engineering,
National Yang Ming University, Taipei, Taiwan
e-mail: ckcheng@ortho.ym.edu.tw

Abstract

Osteoarthritis (OA) and osteoporosis (OP) are the two most common musculoskeletal diseases in the elder population. This study was designed to (a) compare the mechanical properties of trabecular bone of femoral head in OA and OP patients, (b) investigate the effect of the geometry and material properties changes on trabecular tissue by finite element analysis, and (c) study the influence of mechanical property changes of the subchondral plate, the femoral head, and the femoral neck on stress distribution at the articular cartilage from the patients with OA and OP using finite element analysis (FEA). Our analysis showed that parameter of the trabecular number (density and volume) were sensitive for bone strength. The material properties were sensitive for bone strength compared with index parameters. Stronger material properties resulted in a low proportion of elements exceeding yield strain, suggesting stronger trabecular bone tissue. The results revealed that in OA patients, bone density was much higher than in OP patients, and supported the observation that OA might be more likely to occur in those people with stiffer bone in the proximal femur.

Introduction

Osteoarthritis (OA) and osteoporosis (OP) are the two most common musculoskeletal diseases in the elder population. Many studies have reported that these two diseases do not coexist (Cooper et al. 1991; Schnitzler et al. 1992; Wand et al. 1992). Despite numerous data showing that OA protects against or retards the development of OP, the biological explanation for this correlation is not clear. Osteoarthritis is often considered to be a disease of cartilage failure with secondary bone changes, such as marginal osteophytes and subchondral sclerosis, whereas OP is considered as an age-related disease characterized by a reduced amount of bone mass, leading to diminished strength of the bone and an increased risk of fracture.

Presently, evidence is being accumulated that primary OA might primarily be a bone disease rather than a cartilage disease. The OA cases have better preserved bone mass (Moore et al. 1994); however, the relationship between the OA and OP disease remains unclear. Normal bone undergoes a functional adaptation response (bone remodeling) due to physical stimulation and the bony structure may change. In addition, the bone's biomechanical characteristics may be altered due to the change in the bone's internal microstructure influenced by aging. Articular cartilage wear and OA were not frequently observed in the femoral head in elderly patients with femoral neck fracture (FNF) caused by falling that underwent hip replacement. On the other hand, the elderly people with no FNF had a higher incidence of OA (Dretakis et al. 1998). From the biomechanical point of view, the thicker bone in femoral head could result in greater mechanical stress to both bone and articular cartilage, or vice versa.

A few researches have determined the bone property of the femoral head through biomechanical methods (Li and Aspden 1997); however, it is difficult to determine bone properties quantitatively due to the complicated nature of human tissue and errors are often encountered. Li and Aspden (1997) used ultrasound to perform a mechanical analysis on femoral neck fracture induced by osteoporosis in osteoarthrosic compared with normal femoral heads by taking the subchondral plates from the superior, inferior, anterior, posterior, medial, lateral, and central regions of the femoral head. Bone samples were taken from three sections of the femoral head for testing. They were situated (a) well within the main infarct, (b) at the fibrotic/sclerotic margin of the infarct, and (c) immediately subjacent to the margin. A 5-mm cube testing sample was taken from each section for analysis. Even though the above two studies evaluated the biomechanical properties of the femoral head taken from different sections, due to the non-isotropic and non-homogeneous of human bone, analysis results would be influenced by location and direction of the force applied during testing, which might produce different outcomes. Besides, the above studies also concentrated on the retrieved subchondral bone plates. We know that energy absorption does not occur solely in this region, as trabecular bone also has been shown to have absorption properties (Dequeker and Johnell 1995). Due to the complicated material property of the human bone, a rational methodology is needed to establish bone mechanical properties. Here we hypothesize that a direct relationship exists between cartilage wear and the principal compressive group.

It has been widely suggested that health and integrity of the overlying articular cartilage is influenced by the mechanical properties of its bony bed (Radin and Rose 1986). If the bone became unable to attenuate loads, for example by being much stiffer, the articular cartilage would be subject to greater stress, particularly from a load impact, leading to overloading and tissue breakdown. Conversely, an increase in bone compliance may offer a protective effect for the cartilage, such as in OP cases, where compliance comes from bone loss. Epidemiological surveys suggest a negative correlation between OA and OP incidences (Dequeker et al. 1995) and support the argument that OA and OP are two distinct diseases which are not solely related to aging. In other words, cartilage degeneration could be affected by change in the mechanical properties of the underlying bone.

Some finite element models studies assessed juxtaarticular stress distribution due to subchondral plate stiffening and thickening (Anderson et al. 1993). These finite element models, which investigated either the overall stress within the cartilage or the shear stress within the deepest layer of the articular cartilage, showed a slight increase in the stress values when the subchondral bone modulus was elevated. Also, increase in subchondral plate thickness had minimal effect on elevation of the stress. Proliferation of the underlying trabecular bone may lead to increase in stiffness of the bulk material; therefore, it is not sensible to analyze bone performance based solely on the subchondral plate. The contact at the articular surface is a highly dynamic and non-linear phenomenon. Some finite element models studied dynamic juxtaarticular stress transmission, but none addressed the influence of the modulus on a large amount of bone material, including the subchondral plate, the femoral head, and the femoral neck of the proximal femur. We hypothesized that stiffness change in the underlying bones would play an important role on dynamic stress distribution in the articular cartilage.

In order to test above-mentioned hypothesis, we conducted three tests. The first test was to compare the mechanical properties of trabecular bone of the femoral head in OA and OP patients. The second test was to investigate the effect of geometry and material properties changes on trabecular tissue by finite element analysis (FEA). The third test was to use FEA to study the influence of mechanical property change in the subchondral plate, the femoral head and the femoral neck on stress at the articular cartilage in patients with OA and OP.

Materials and Methods

The Mechanical Property of the Femoral Head Evaluated Using Compression Test

The femoral heads used for this study were divided into two groups, i.e., 7 specimens with primary OA and 7 specimens with OP. These specimens were all retrieved from patients who underwent total hip arthroplasty. Diseases such as osteonecrosis, rheumatoid arthritis, infection, and developmental dysplasia of hip were excluded from the two groups. Patients' data for each femoral head specimen including age,

Table 1. Details of groups from which femoral heads were removed. *OA* osteoarthritis, *OP* osteoporosis

Group	No. of femoral heads	Gender (F/M)	Age (years)	Body height (cm)	Body weight (kg)	Head diameter (mm)
OA	7	3/4	78 (62 – 89)	163.1 ± 6.1 (156 – 175)	74.9 ± 9.4 (58 – 79)	50.3 ± 2.5 (47 – 52)
OP	7	5/2	75 (55 – 85)	159.4 ± 5.8 (152 – 168) $p = 0.26$	78.7 ± 8.6 (48 – 78) $p = 0.22$	46.1 ± 2.0 (44 – 49) $p < 0.05$

sex, body height, weight, as well as femoral head diameter were recorded (Table 1). Dual-energy X-ray absorptiometry (DXA; Hologic QDR-1500, Bedford, Mass.) was used for determining the bone mineral density (BMD) for each femoral head before biomechanical testing. The specimens were then frozen and stored at $-10\,°C$ and defrosted 24 h before the biomechanical testing. A linear precision saw (Ismet 5000, Buehler) was used for obtaining a 1-cm cube from the principal compressive region in the femoral head (Fig. 1).

Two testing samples were cut from each femoral head. The material testing machine (Bionix 858, MTS System) was used for compression test. All specimens were loaded in the superior-inferior direction which coincides with the principal stress direction and two parallel plates were confirmed contacting on the upper-lower surface of the testing sample (Fig. 1c). The strain rate of 0.04 mm/s was set for the loading condition (Brown et al. 1981). The stress-strain curve was analyzed to obtain both Young's modulus and yielding stress. An average of the Young's modulus and yielding stress was calculated for each specimen to compare the difference between OA and OP groups. Since human bone is classified as a viscoelastic material with an anisotropic and non-homogenous nature, it is very difficult to incorporate the influence of Poisson's ratio after compression; therefore, the influence was ignored in this study. The slope of the straight segment of the stress-strain curve was taken as
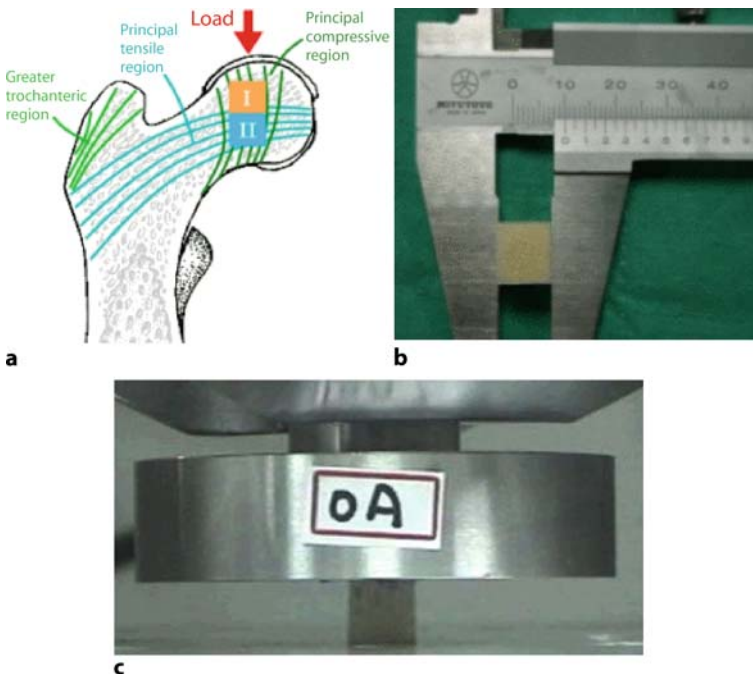
Figure 1 a–c. The illustration of the testing sample. **a** The site from which samples of trabecular bone were removed on the femoral head. **b** One-centimeter-cube testing sample was taken for testing. **c** The setup of mechanical test
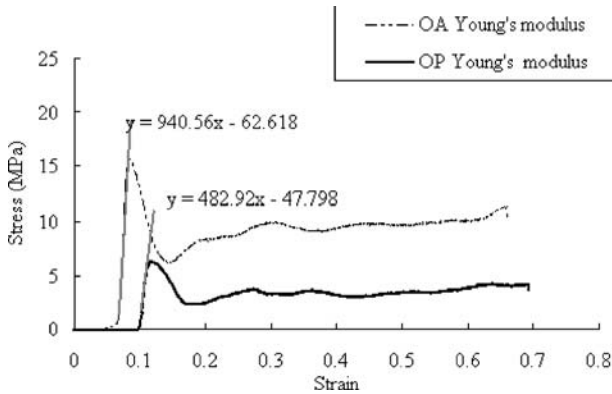
Figure 2. The stress-strain relationship. The slope of the straight segment of the stress-strain curve is taken as the Young's modulus and the maximum value of the curve was defined as the yielding stress. All the analytical data were defined as the same criteria

the Young's modulus (elastic modulus, E) and the yielding stress (σ_y) was taken as the largest value on the curve (Fig. 2). For normalization analysis, all the values, including BMD, E, and σ_y, were normalized to body height, body weight, and femoral head diameter, respectively, to determine which parameter was the major influencing factor of mechanical property. In addition, a linear regression analysis between BMD and the Young's modulus in all samples was done to determine its relationship between the two testing methods. The Student's t-test was used for statistical analysis and a level of significance was set at $p = 0.05$.

The Mechanical Property of the Femoral Head Evaluated Using FEA

Before mechanical testing, all specimens were scanned with high-resolution micro-computed tomography (micro-CT) with a similar cutting face and scan direction to reduce scan error. The conditions set for radiography were as follows: (a) projection resolution was 50 μm (Max); (b) reconstruction resolution was 150 μm; (c) energy intensity was 40 kVp (max); (d) photon values were 17–20 kV; (e) current was 0.6 mA; and (f) the radiography time was 0.5 s. The three-dimensional (3D) image was reconstructed from three directions (x, y, and z axes), as shown in Fig. 3a.

The radiographs were judged by an orthopedic surgeon to determine the boundary between bone marrow and bone. Using this standard to define the gray-scale threshold, images with higher gray level than the threshold were cortical bone, whereas images with lower gray level than the threshold were deemed as bone marrow. By this method, the images were divided into two portions (Fig. 3b).

Many studies indicated have shown the relationship between the mechanical property and density of trabecular bone (Wirtz et al. 2000; Carter et al. 1980; Knauss et al. 1981). They used dry weight and volume of trabecular bone derived from Archimedes' principle to obtain the density and then used a formulate to estimate the stiffness of each block. According to the estimation method published by Wirtz et al. (2000), the formula of longitudinal and transverse Young's modulus were $E = 1904\rho^{1.64}$ and $E = 1157\rho^{1.78}$ (ρ: bone density), respectively. Longitudinal and transverse compression strength were $\sigma = 40.8\rho^{1.89}$ and $\sigma = 21.4\rho^{1.37}$, respectively.
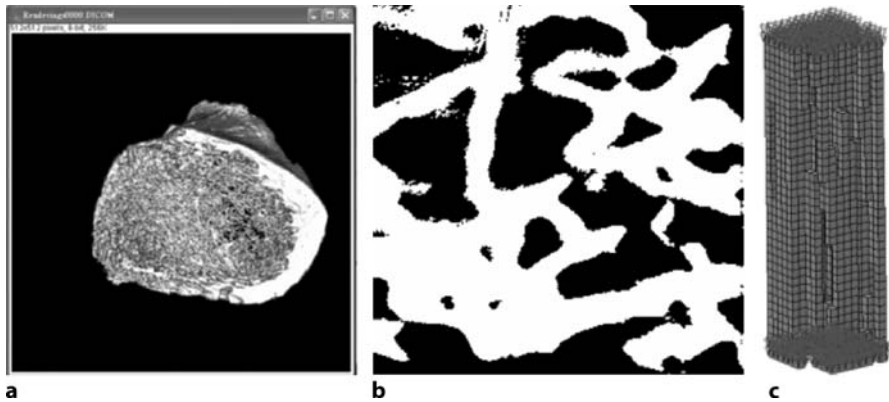
Figure 3. a The 3D image of trabecular bone was recombined from three directions (x, y, and z axes). **b** The processed image with higher gray level than the threshold was bone and lower gray level than the threshold was bone marrow. **c** The 3D trabecular bone model and boundary conditions

Referring to the estimation method published by Carter et al. (1980), the corresponding tensile strength was 3 15MPa within $0.2 - 0.5 \, g/cm^3$ and the shear modulus was $8 - 40$ MPa according to Knauss et al. (1981) within $0.1 - 0.8 \, g/cm^3$. The latter two values were derived from linear regression method.

The FEA was conducted with the general-purpose finite element software AN-SYS 8.0 (Ansys, Canonsburg, Pa.). In order to eliminate errors, only medial portion of the images were used. The 3D model was established by the contour of CT images (Fig. 3c). The bottom plane of the model was fixed in z-direction and given 1% strain (Rietbergen et al. 1995) to simulation the compression condition. Trabecular bone was simplified as homogenous linear-elastic and isotropic material. Young's modulus and shear modulus were both assumed as 1000 MPa and Poisson's ratio was assumed as 0.3. Young's modulus derived from finite element method was compared with that derived from the previous formula.

The following parameters were used to describe the shape of trabecular bone because of its irregular shape (Table 2): TV, BV, and BS were measured and estimated from micro-CT images. BV/TV and BS/TV were derived from the above-

Table 2. Related parameters of trabecular bone

TV	Tissue volume
BV	Bone volume
BS	Bone surface
BV/TV	Bone volume fraction
BS/TV	Relative bone surface
Tb.Th	Trabecular thickness
Tb.N	Trabecular number
Tb.Sp	Trabecular spacing

mentioned values. Tb.Th, Tb.N and tb.Sp were derived from the following formulas: Tb.Th = 2 / (BS / BV); Tb.N = (BV / TV) / Tb.Th; and Tb.Sp = (1 / Tb.N) − Tb.Th.

The Influence of Mechanical Property Changes of the Subchondral Plate Evaluated by FEA

A 2D finite element model (Wei et al. 2005) was constructed to simulate the hip and supporting tissues for contact analyses with Abaqus/Standard 6.3-1 software (Abaqus, Pawtucket, Rhode Island; Fig. 4). The 2D hip joint model, composed of a part of the pelvis and a proximal part of the femur, was generated based on a roentgenogram of a normal hip, representing a projection of the joint onto a vertical plane. Each region was assumed to be homogeneous, isotropic, and linearly elastic. The material properties of the various tissue regions of a normal hip joint are given in Table 3. The thickness of the femoral cartilage was set at 2.0 mm and the thickness of subchondral plate was set at 0.6 mm as for a normal hip joint model (Shepherd and Seedhom 1999).

 This finite element model contained 4974 four-node bilinear elements and 38 three-node bilinear elements. Two two-node linear truss elements were used to model the abductor and the adductor. The loads of 600-N body weight, 2000-N abductor muscle force, and 100-N adductor muscle force were loaded to the model. (Note that the 600-N body weight is the sum of the five 120-N loads, respectively, applied along the five upper boundary nodes on the mid-plane of the symmetrical body as shown in Fig. 4; Ueo et al. 1985). Regarding the boundary conditions, the pelvis component was allowed to displace in the sagittal plane only and the distal end of the femur was allowed to displace in the transverse plane only.

 Dynamic analysis was performed by ABAQUS/Explicit 6.3-1. In dynamic analyses, the overall underlying bones are defined as the combination of the subchondral

Table 3. Material properties of the finite element model (shown in Fig. 4)

Region		Elastic modulus (MPa)	Poisson's ratio	Density (kg/m^3)
Cortical bone				
1	Pelvis cortex	17,000	0.3	1800
9	Femoral neck cortex	2000	0.3	1800
11	Femoral cortex	17,000	0.28	1800
Subchondral plate				
3	Subchondral bone of acetabulum	700	0.3	1068
6	Subchondral bone of femoral head	1100	0.3	1068
Trabecular bone				
2	Pelvic trabecular bone	600	0.3	1000
7	Femoral head	600	0.3	1000
8	Femoral neck	1000	0.3	1000
10	Femoral trabecular bone	600	0.3	1000
Articular cartilage				
4	Acetabulum	15	0.45	1000
5	Femoral head	15	0.45	1000

Region no.	Material name
1	Pelvis cortex
2	Pelvic cancellous bone
3	Subchondral bone of acetabulum
4	Acetabulum cartilage
5	Femoral head cartilage
6	Subchondral bone of femoral head
7	Femoral head cancellous bone
8	Femoral neck cancellous bone
9	Femoral neck cortex
10	Femoral cancellous bone
11	Femoral cortex
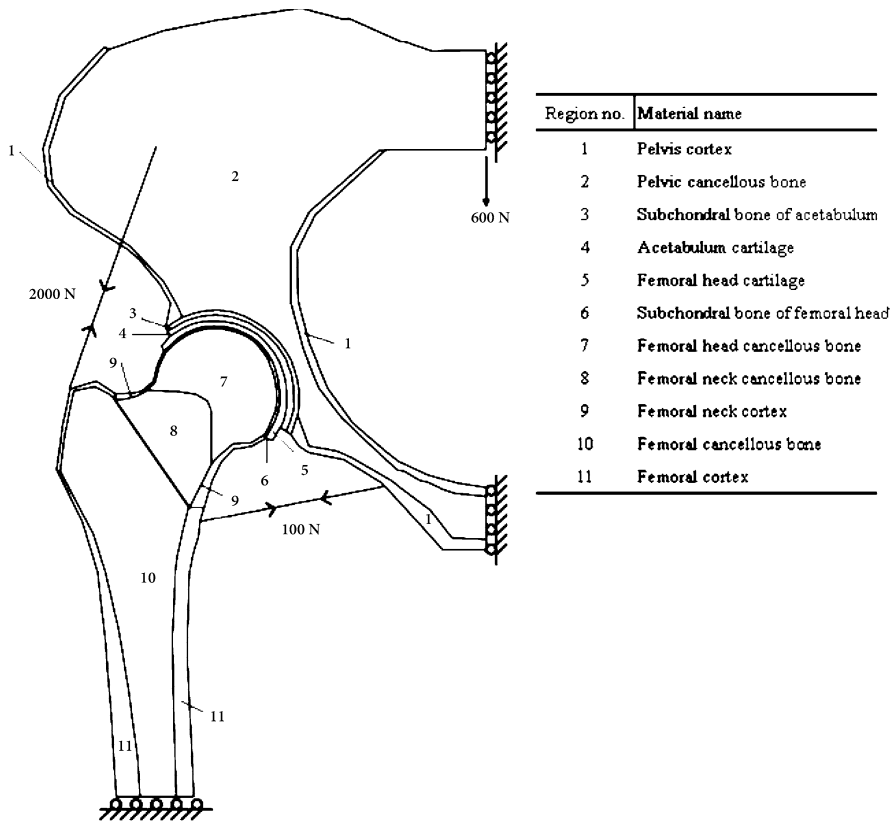
Figure 4. Material property regions of the finite element model. (See Table 3 for their corresponding moduli.)

plate, the femoral head, and the femoral neck, with their elastic moduli denoted, respectively, as E_s, E_h, and E_n. In addition to the normal case, denoted as $Model_{normal}$, using original E_s, E_h, and E_n values as given in Table 3, 5 other cases of parametric analyses with varying elastic moduli in the FE model were performed. Each case of the FE model is denoted with a pertinent subscript as given below:

1. $Model_{Esx2}$: stiffening of the subchondral plate. Only E_s was doubled and denoted as E_{sx2}.
2. $Model_{Es,hx2}$: stiffening of both the subchondral plate and the femoral head. Both E_s and E_h were doubled.
3. $Model_{Enx2}$: stiffening of the femoral neck: only E_n was double. Note that both the cortex bone ($E_{n.ct}$) and the trabecular bone ($E_{n.cn}$) in the neck were doubled.
4. $Model_{Es,h,nx2}$: stiffening of the overall underlying bones. All three moduli in the cases discussed above, E_s, E_h, and E_n (both $E_{n.ct}$ and $E_{n.cn}$) were doubled.

5. Model$_{Es,h,nx0.5}$: softening of the overall underlying bones. All three moduli in the cases discussed above, E$_s$, E$_h$, and E$_n$ (both E$_{n.ct}$ and E$_{n.cn}$) were reduced by half.

The stress distributions along a path including 53 nodes on the cartilage surface and along a corresponding path at the bone/cartilage interface were both evaluated. The damping in ABAQUS for the cartilage was assigned with such a value that the transient oscillatory response of the articular cartilage on the femoral head in the second cycle decayed to about 60% of that of the first cycle, which was considered reasonable in view of the normal body response to an impact (Bader and Kempson 1994). The peak of the first oscillation was used to analyze the stress distribution on the cartilage surface and at the bone/cartilage interface. The strain energy up to 0.1 s, typical heel-strike duration, in each model was analyzed for comparison among these cases.

Results

The Mechanical Property of the Femoral Head Evaluated Using Compression Text

The results showed the average BMD of the OA group was 1.064 ± 0.127 g/cm^2, whereas for the OP group the average was 0.559 ± 0.116 g/cm^2. The BMD of the OA group is significantly higher than that of the OP group ($p < 0.05$). From mechanical testing, comparing the E value of the two specimens taken from each OA femoral head (OAI-top; OAII-bottom; Fig. 5a,b), it was found that the E value of OAI was 791.4 ± 3.9 Mpa, whereas OAII had a slightly higher value of 865.7 ± 259.9 Mpa; however, there was no significant difference between OAI and OAII ($p > 0.05$). The σ_y also had no significant difference between OAI (17.2 ± 3.9 MPa) and OAII (17.2 ± 4.8 MPa). The E-value and σ_y value for OPI and OPII groups did not show any significant difference ($p > 0.05$ for both cases). The E values were 338.5 ± 178.0 MPa (OPI) and 387.5 ± 136.3 MPa (OPII). The σ_y values were measured to be 5.3 ± 2.3 MPa (OPI) and 6.2 ± 2.4 MPa (OPII).

In order to investigate the influence of individual factors in this study, the obtained BMD, E values, and σ_y values which were normalized to the body height, weight, and femoral head diameter, the major influential factor was found by comparing the ratio of OA/OP. The original OA/OP ratios of BMD, E value, and σ_y value were 1.9, 2.28, and 3.01, respectively (Fig. 5c). The OA/OP ratios (normalizing to body height) of BMD, E value, and σ_y value decreased to 1.85, 2.23, and 2.93, respectively. While normalizing to body weight, the OA/OP ratios were 1.76, 2.12, and 2.77, respectively. While normalizing to femoral head diameter, the OA/OP ratios were 17.3, 2.08, and 2.77, respectively. The results showed that normalizing to femoral head diameter had the strongest influence when comparing other individual factors (Fig. 5c). The femoral head diameter was the most important factor that influenced the result, and the body height had the lowest effect. In the linear regression analysis, the OA specimens (square points) had higher BMD value and higher Young's modulus when compared with OP specimens (rhombus points) that had relatively lower BMD value and Young's modulus (Fig. 6). Taking all of OA and OP specimens into consideration,

the correlation coefficient was $R^2 = 0.72$. This showed that the relationship between BMD value and Young's modulus had a tendency of linear correlation.

The Mechanical Property of the Femoral Head Evaluated by FEA

The BMD of OA group was 1.064g/cm^3 and of OP group was 0.559g/cm^3, and the material properties of blocks were estimated by the experience formula (Table 4). The Young's modulus of block was determined by finite element software (Table 5). The real Young's modulus of trabecular bone was determined by the character of
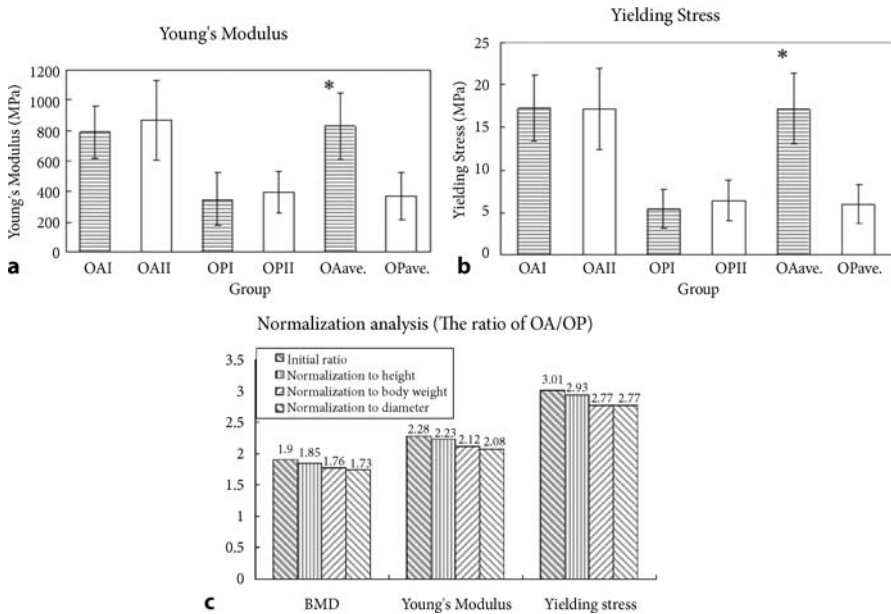
Figure 5 a,b. The mechanical properties of various sites from the OA and OP femoral heads. **a** Young's modulus (MPa). **b** Yielding stress (MPa). *Asterisk:* Statistically different between OA group and OP group ($p < 0.05$). Note that the OA I and OA II indicate the result of the upper and lower specimens in OA femoral head, respectively. The same meanings are indicated in OP I and OP II. **c** All the data including BMD, E value, and σ_y value were normalized by individual factor and then shown as OA/OP ratio. The femoral head diameter had the strongest influence

Table 4. The material properties of blocks (MPa)

	OA-I	OA-II	OP-I	OP-II
Axial Young's modulus	775.6	881.7	798.9	282.7
Lateral Young's modulus	436.1	501.2	98.1	145.5
Axial compress strength	14.8	16.7	3.0	4.5
Lateral compress strength	10.1	11.2	3.2	4.3
Tension strength	15.1	17.0	2.0	4.5
Shear modulus	21.8	24.0	6.9	9.7

linear elastic. The linear relationship of those two values was determined by comparing the values obtained by finite element software and recognized formula. Figure 4 shows the proportion of elements that exceeded yield strain in the four models after finite element analysis when subjected to compression fracture. The proportion of elements in group OA-I was 76.78%, OA-II was 72.97%, OP-I was 87.84%, and OP-II was 84.76%.
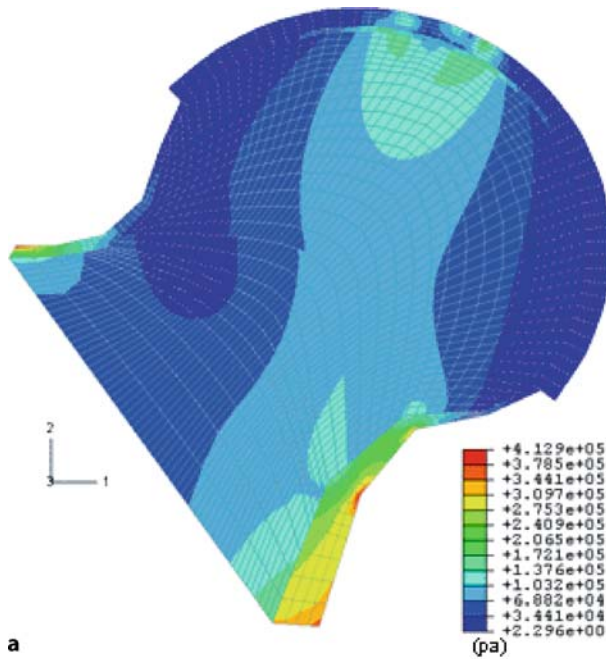
Figure 6. a A contour plot of the von Mises stress in the region including the cartilage, the subchondral plate, the femoral head, and the neck for the normal model. **b** A roentgenogram taken at a femoral head shows patterns similar to those seen in the stress distribution as shown in **a**

Table 5. Values of index parameters in different blocks

	OA-I	OA-II	OP-I	OP-II
TV (mm^3)	0.062500	0.062500	0.062500	0.065200
BV (mm^3)	0.039766	0.047016	0.020906	0.028859
BS (mm^2)	5.796250	6.566875	3.386250	4.433125
BV/TV	0.636	0.752	0.335	0.462
BS/TV (mm^{-1})	92.74	47.12	54.18	70.93
Tb.Th (mm)	0.0137	0.0143	0.0123	0.0131
Tb.N (mm^{-1})	46.42	52.59	27.24	35.54
Tb.Sp (mm)	0.0078	0.0047	0.0244	0.0151

The Influence of Mechanical Property Changes of the Subchondral Plate Evaluated by FEA

Figure 6a shows the von Mises stress contour plot of the region including the cartilage, the subchondral plate, the femoral head, and the neck. It is noted that the pattern of the stress distribution is similar to that observed on the roentgenogram, which can show to some extent the approximate structural orientation of bone materials (Fig. 6). The roentgenogram shows brighter (lighter) lines in Fig. 6 running in the similar direction as the high stress zone of Fig. 6a, i.e., at a small angle clockwise from the vertical direction. The brighter lines indicate higher bone density in the roentgenogram. Weight-bearing function of the primary trabeculation system of the femoral head is clearly demonstrated with the high (compressive) stress lying in the direction from the cartilage surface distally toward the medial neck cortex. The level of the compressive stress developed laterally in the lateral neck cortex due to bending effects of the joint reaction force was found to be mild because of the counteraction exerted by the abductor muscle.

The effects of the underlying bone stiffening on the Tresca (maximum shear) stress distribution on the cartilage surface of the femoral head are shown in Fig. 7. The contact region is defined along a path shown in the explanatory thumbnail. The largest stress values as well as the percentage of change with respect to the normal case (Model$_{normal}$) on the cartilage surface and at the bone/cartilage interface for cases of dynamic analyses are shown in Table 6. Generally, the underlying bone stiffening produced a slight increase in the largest Tresca stress in the cartilage surface. The results of Model$_{Esx2}$ show that doubling the modulus in the subchondral plate led to an increase of 2.2% in the largest Tresca stress. Model$_{Es,hx2}$, doubling the modulus in the subchondral plate and the femoral head, led to 2.0% increase. Model$_{Enx2}$, doubling the modulus in the femoral neck, led to 1.4% increase. Model$_{Es,h,nx2}$, doubling the modulus in the overall underlying bones, led to 4.7% increase. Model$_{Es,h,nx0.5}$, reducing the modulus by 50% in the overall underlying bones, led to 3.9% decrease. These results demonstrated that the largest maximum shear stress was more sensitive to subchondral plate stiffening than to a combination of the subchondral plate, femoral head stiffening, and femoral neck stiffening.
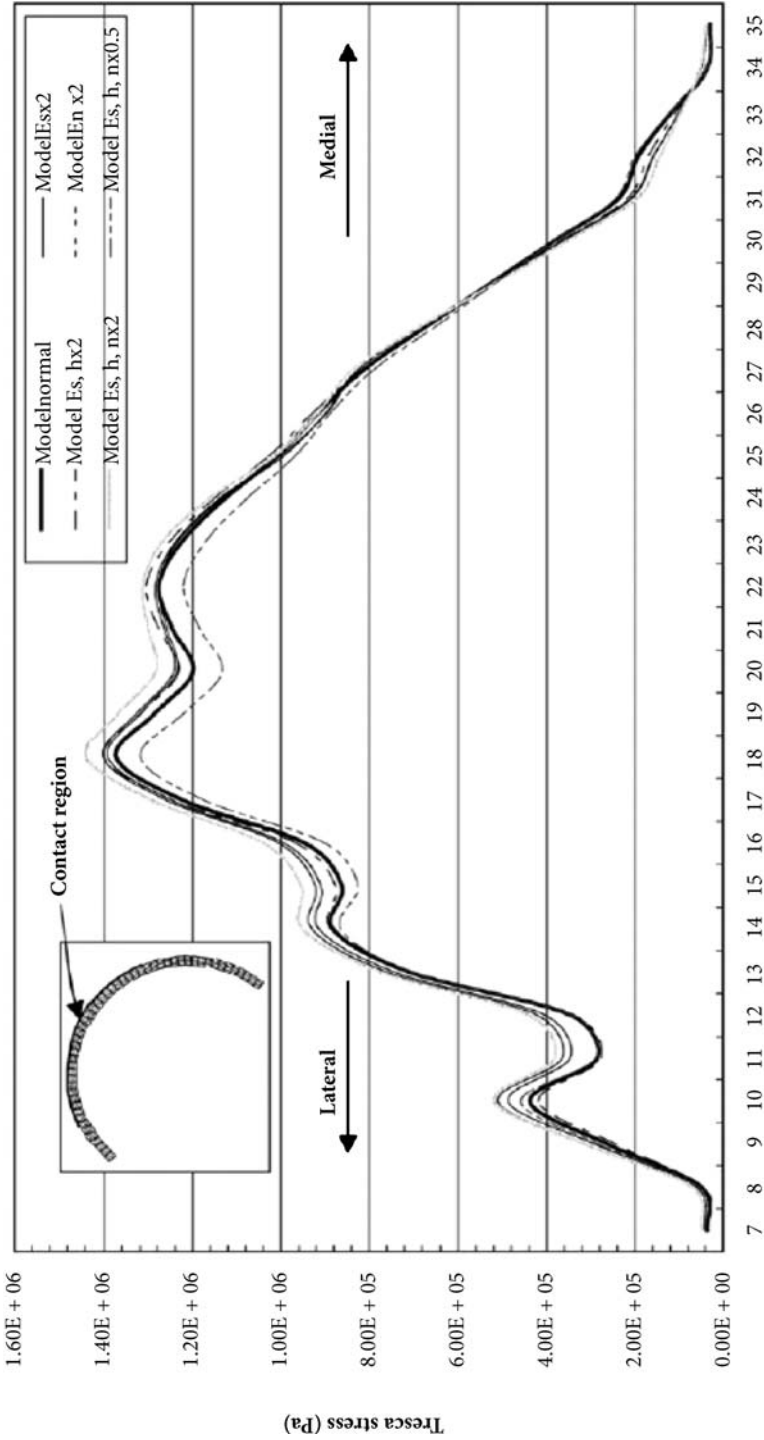
Figure 7. Distributions of the Tresca stress on the cartilage surface for the six cases of parametric studies with varying bone modulus along the path of contact in the thumbnail of a finite element model shown in the *upper left corner*

Table 6. The largest stress in each model and percentage increase (in parentheses) of the largest stress relative to Model$_{normal}$ on the cartilage surface and at the bone/cartilage interface

Model	Largest stress (Pa)			At bone/cartilage interface, Tresca stress
	On cartilage surface			
	Tresca stress	Max. principal stress	Min. principal stress	
Model$_{normal}$	1.373×10^6	0.01×10^6	-0.754×10^6	1.361×10^6
Model$_{Esx2}$	1.403×10^6 (2.2)	0.022×10^6 (57.1)	-0.774×10^6 (2.7)	1.396×10^6 (2.6)
Model$_{Es,hx2}$	1.401×10^6 (2.0)	0.016×10^6 (14.3)	-0.784×10^6 (4.0)	1.391×10^6 (2.2)
Model$_{Enx2}$	1.392×10^6 (1.4)	0.023×10^6 (64.3)	-0.768×10^6 (1.9)	1.384×10^6 (1.7)
Model$_{Es,h,nx2}$	1.438×10^6 (4.7)	0.024×10^6 (71.4)	-0.807×10^6 (7.0)	1.433×10^6 (5.3)
Model$_{Es,h,nx0.5}$	1.319×10^6 (−3.9)	0.013×10^6 (−7.1)	-0.698×10^6 (−7.4)	1.301×10^6 (−4.4)

Model$_{Esx2}$: Stiffening of the subchondral plate only
Model$_{Es,hx2}$: Stiffening of both the subchondral plate and femoral head
Model$_{Enx2}$: Stiffening of the femoral neck
Model$_{Es,h,nx2}$: Stiffening of the overall underlying bones
Model$_{Es,h,nx0.5}$: Softening of the overall underlying bones

Discussion

The Mechanical Property of the Femoral Head Using Compression Test

Osteoarthritis and OP are the two main musculoskeletal diseases among the aged population, but the occurrence of a patient suffering from both diseases is very rare. Bone mass in OA patients is higher than that of normal subjects. Cartilage wear is commonly seen in these patients. This observation is opposite to that seen in OP patients: cartilage wear is usually rare and bone mass is lower to increase susceptibility to femoral neck fractures. At present, the exact physiological mechanism is not known. This study provides a new standpoint to investigate this phenomenon by material testing methods.

From Wolff's law we know that the arrangement of trabecular bone in the femoral head is dependent on the direction of the force sustained; thus, the mechanical properties of the specimens are also influenced by the direction of the force sustained or the region of femoral head. Due to this dependent relationship, there is a significant difference between various origins of the testing specimens. In order to avoid this discrepancy, testing samples were cut from the principal compressive group of the femoral head for mechanical testing in this study. As compared with the results of Li et al. (1997), there was a 56% increase in Young's modulus in OA group compared with OP group in our results, but only a 28% increase in their results. In addition, there was a 67% increase in the yielding stress in our results, but a 42% increase in

their results. Consequently, there is a more significant difference of material properties between OA and OP femoral head, especially in the principal compressive region. Moreover, there are no studies that further estimate which individual factors influence bone mechanical property. In the current study, we performed normalization analysis to individual factors. We found that femoral head diameter strongly influenced mechanical property between OA and OP group when compared with body weight and body height.

Our results showed a significantly larger BMD, Young's modulus, and yielding stress value for the OA group when compared with the OP group, with a respective OA/OP ratio of 1.9, 2.28, and 3.01. If the bone becomes stiffer, it may be less able to absorb impact loads, which may lead to more peak stress and wear in the cartilage. On the contrary, the femoral heads of OP patients are more able to absorb the energy due to the decreased bone strength. Consequently, the stress on cartilage is reduced, decreasing its extent of wear; however, the chance for femoral neck fracture is also elevated because of this decreased bone strength.

The Mechanical Property of the Femoral Head Evaluated by FEA

According to the results of this study, OA patients' BMD was much higher than that of OP patients. The FEA showed that the trabecular stiffness of femoral neck in OA patients was also much higher than in OP. This result not only could represent the reliability of this study, but also showed the dependability in verifying the experiment by measuring bone density. In addition, the difference in size of femoral head between OA and OP patients was not significant in this study. From the biomechanical point of view, larger femoral heads could bear more stress than smaller ones, if only size is considered; however, errors occur when size of the femoral head is ignored.

The results also showed that the higher the numbers and density of the trabecula, the lower the proportion of trabecular bone that exceeded yielding strain. Larger porosity of trabecular decreased the structure strength of trabecular bone. There were no relationships between the index parameters of area ratio, thickness, etc., and structure strength. With regard to material property, the proportion of trabecular bone that exceeded yielding strain decreased, regardless of the values of the stiffness of structure, shear modulus, and Young's modulus of trabecular bone.

The BMD of OA ($1.064\,g/cm^3$) was twice as high as those of OP ($0.559\,g/cm^3$). The results showed that the bone quality of OA was stronger than that of OP in both biomechanical and BMD analysis. The bone strength was too strong compared with articular cartilage in OA patients; therefore, the force was loaded primarily on cartilage. The high load caused cartilage wear. On the contrary, the bone strength was weak in OP patients: the force loaded on the cartilage was low enough to damage cartilage.

The parameters of the trabecular number (density and volume) were sensitive for bone strength; the others were not. The material properties were sensitive for bone strength compared with index parameters, and the result presented a positive correlation. Stronger material properties meant that a low proportion of elements exceeded yield strain. This means that the strength of trabecular bone tissue was greater.

The Influence of Mechanical Property Changes of the Subchondral Plate Evaluated by FEA

The subchondral plate plays two roles in the joint under loading. Primarily, the plate acts as a cartilage support, i.e., as an underlying semi-rigid bed on which the articular cartilage sits. Secondarily, it acts as a weight-distributing arch, transferring the joint loading from the central contact area to the boundary. Increasing the modulus in the subchondral plate may reduce its ability to absorb energy, which could in turn lead to high risk of cartilage breakdown. Our analysis showed that the largest maximum shear stress on the cartilage surface or at the bone/cartilage interface in the cartilage were all more sensitive to the subchondral plate stiffening alone than to the stiffening of both the subchondral plate and femoral head stiffening or to the stiffening of only the femoral neck. These results indicate that, mechanically, subchondral plate stiffness is a major factor in the initial degeneration of the cartilage in OA.

A relatively high percentage of patients with OA have been found to be associated with a higher bone mass. Werner et al. (1996) developed the formulas appropriate for such cases, where the loss of BMD was closely connected to the loss of a structure, e.g., the loss of stiffness was due to trabecular thinning. Our results showed that rise in the overall underlying bone modulus had a mild increase in the largest maximum shear stress in the cartilage, and vice versa. These findings supported the observation that OA might be more likely to occur in those people with stiffer underlying bones in the proximal femur.

The femoral neck is cantilevered when under loads, resulting in substantial bending in the neck. Our results showed that there was a significant increase of the largest maximum tensile stress at the bone/cartilage interface as the modulus of the femoral neck doubled. In addition to shear stress, tensile stress was suggested as a possible cause of surface injuries in articular cartilage under impact loading (Li et al. 1995). Our study corroborates the explanation that the etiology of OA was related to the changes in the mechanical properties of the femoral neck.

Limitations of the Study

There are some limitations to this study. In compression testing, while obtaining the values of the Young's modulus, it was difficult to incorporate the effect of increased cross-sectional area of the specimen due to compression into the analysis; therefore, the influence of Poisson's ratio was ignored, and thus errors might arise from this assumption. Moreover, normal specimens are very difficult to obtain among Asian countries, especially in Taiwan.

In the mechanical property of the femoral head evaluated using FEA, we could not precisely take the sample which was the site of compressed region in the femoral head. This might cause an error. In addition, this study measured the bone density in every patient, and analyzed the relationship between biomechanical properties and bone density. We analyzed the bone biomechanical properties of two diseases but did not consider the condition in vivo. We also ignored the difference that the transportation during the test might induce the sample weakness.

In the influence of mechanical property using FEA, we performed 2D analysis instead of full 3D. Although 3D analysis gives more accurate results, the 2D analysis provides the benefit of having a clear and straightforward comparison of the parametric analyses of the dynamic contact model due to modulus change along the interface. Another simplification that all materials were assumed linear elastic, homogeneous, and isotropic, instead of non-linear viscoelastic tissue properties, limits the resulting interpretation only to the modulus effect. Also, the resulting interpretation was limited by simplification of the loading and boundary conditions, which did not represent complicated physical activity. Although the 2D results could not be directly extrapolated for 3D general predictions, they served to provide quantitative trends by capturing the primary biomechanical interactions between bones.

Conclusion

Our analysis showed that the parameters of the trabecular number (density and volume) were sensitive for bone strength. The material properties were sensitive for bone strength compared with index parameters. Stronger material properties led to low proportion of elements exceeding yield strain, suggesting better strength of trabecular bone tissue. The results revealed that OA patients' bone density was much higher than that of OP patients and supported the observation that OA might be more likely to occur in people with stiffer underlying bones in the proximal femur.

References

Anderson DD, Brown TD, Radin EL. The influence of basal cartilage calcification on dynamic juxtaarticular stress transmission (1993) Clin Orthop Relat Res 286:298–307

Bader DL, Kempson GE (1994) The short-term compressive properties of adult human articular cartilage. Biomed Mater Eng 4:245–256

Brown TD (1981) Mechanical characteristics of bone in femoral capital aseptic necrosis. Clin Orthop 156:240–247

Carter DR, Schwab GH, Spengler DM (1980) Tensile fracture of cancellous bone. Acta Orthop Scand 51:733–741

Cooper C, Cook PL, Osmond C, Fisher L, Cawley MID (1991) Osteoarthritis of the hip and osteoporosis of the proximal femur. Ann Rheum Dis 50:540–542

Dequeker J, Johnell O (1995) Osteoathritis protects against femoral neck fracture: the MEDOS study experience. Bone 14: S51-S56

Dequeker J, Mokassa L, Aerssens J (1995) Bone density and osteoarthritis. J Rheum 22 (Suppl 43):98–100

Dretakis EK, Steriopoulos KA, Kontakis GM (1998) Cervical hip fractures do not occur in arthrotic joints. Acta Orthop Scand 69:384–386

Knauss P (1981) Material properties and strength behaviour of spongy bone tissue at the coxal human femur. Biomed Technol 26:200–210

Li B, Aspden RM (1997) Mechanical and material properties of the subchondral bone plate from the femoral head of patients with osteoarthritis or osteoporosis. Ann Rheum Dis 56:247–254

Li X, Haut RC, Altiero NJ (1995) An analytical model to study blunt impact response of the rabbit P-F joint. J Biomech Eng 117:485–491

Moore RJ, Fazzalari NL, Manthey BA, Vernon-Roberts B (1994) The relationship between head-neck-shaft angle, calcar width, articular cartilage thickness and bone volume in cartilage of the hip thickness and bone volume in arthrosis of the hip. Br J Rheum 33:432–436

Radin EL, Rose RM (1986) The role of subchondral bone in the initiation and progression of cartilage damage. Clin Orthop Relat Res 213:34–40

Rietbergen BV, Weinans H, Huiskes R, Odgaardt A (1995) A new method to determine trabecular bone elastic properties and loading using micromechanical finite element models. J Biomech 28:69–81

Schnitzler CM, Mesquita JM, Wane L (1992) Bone histomorphometry of the iliac crest, and spinal fracture prevalence in atrophic and hypertrophic osteoarthritis of the hip. Osteoporosis Int 2:186–194

Shepherd DE, Seedhom BB (1999) Thickness of human articular cartilage in joints of the lower limb. Ann Rheum Dis 58:27–34

Ueo T, Tsutsumi S, Yamamuro T, Okumura H, Shimizu A, Nakamura T (1985) Biomechanical aspects of the development of aseptic necrosis of the femoral head. Arch Orthop Trauma Surg 104:145–149

Wand JS, Hill ID, Reeve J (1992) Coxarthrosis and femoral neck fracture. Clin Orthop 278:88–94

Wei HW, Sun SS, Jao SH, Yeh CR, Cheng CK (2005) The influence of mechanical properties of subchondral plate, femoral head and neck on dynamic stress distribution of the articular cartilage. Med Eng Phys 27:295–304

Werner HJ, Martin H, Behrend D, Schmitz KP, Schober HC (1996) The loss of stiffness as osteoporosis progresses. Med Eng Phys 18:601–606

Wirtz DC, Schiers N, Pandorf T, Radermacher K, Weichert D, Forst R (2000) Critical evaluation of known bone material properties to realize anisotropic FE-simulation of the proximal femur. J Biomech 33:1325–1330

Index